ISSN 0289-842X

RIKEN Accelerator Progress Report

2000

vol. 34

理化学研究所
RIKEN (The Institute of Physical and Chemical Research)

RIKEN Accelerator Progress Report 2000
January-December

vol. 34

理化学研究所
RIKEN (The Institute of Physical and Chemical Research)
Wako, Saitama, 351-0198 JAPAN

CONTENTS

I. PREFACE

This issue of RIKEN Accelerator Progress Report reports research activities of the RIKEN Accelerator Research Facility (RARF) during the calendar year of 2000. The research programs have been coordinated in the framework of the project entitled Multidisciplinary Researches on Heavy Ion Science. The project involves a variety of fields such as: nuclear physics, atomic physics, nuclear chemistry, radiation biology, condensed matter physics in terms of accelerator or radiation application, basic studies on energy production, basic studies on plants mutation using heavy-ion beams, material characterization, application to space science, accelerator physics and engineering, laser technology, and computational technology. The construction of main cyclotron building of RI Beam Factory has been started this year. These activities involved 12 laboratories in RIKEN, RBRC (RIKEN-Brookhaven Research Center at Brookhaven National Laboratory), and more than 300 researchers including users from domestic and foreign institutions. Thirty-six universities and institutes from within Japan and 33 institutes from 10 countries are included.

Major research activities of the RARF are based on the heavy-ion accelerator complex consists of the $K = 540$ MeV RIKEN Ring Cyclotron (RRC) and the energy-variable heavy-ion linear accelerator (RILAC) and the $K = 70$ MeV azimuthally variable field cyclotron (AVF), which have altogether provided a beam time (on the target) of more than 4000 hours through the year. Those statistic numbers are slightly shorter than those of previous years because of the planned shutdown due to the construction-program of RI Beam Factory.

The three accelerators deliver heavy-ion beams of a variety of elements with energies ranging from a few A MeV to 135A MeV. The two-injector machines (AVF and RILAC) are equipped with ECR heavy ion sources. The AVF is additionally equipped with a polarized ion source for vector and tensor polarized deuterons. The three accelerators have been used in various configurations. The RRC operate with the AVF or the RILAC as the injector. The AVF has been providing beams of ions of mass number up to 60 and the RILAC has been providing beams of ions of mass number larger than that. In addition, the AVF and the RILAC were used separately, when they are not used as the injector, for low energy applications. Recently, low energy (5A MeV) beam of ^{84}Kr has been accelerated for the study of superheavy elements. The beam current as high as 0.8 particle μA was delivered on the target.

Two thirds of the RRC research beam time (~3500 hours in total) goes to nuclear physics and one third is used by atomic physics, material science, nuclear chemistry, radiation biology and others. While the RILAC and the AVF beam time were used for fields other than nuclear physics. The research beam time at the AVF is 2100 hours and 800 hours at the RILAC. RILAC beam time was very little because of the construction of booster linac for charge stripping used in RIBF.

The use of radioactive-ion (RI) beams is the main emphasis of the science at the RRC. Major subjects pursued are: (1) exotic nuclear structure and new dynamics of extremely neutron-rich nuclei (such as those with a neutron halo or skin), (2) nuclear astrophysics involving unstable-nucleus reactions, (3) synthesis of new unstable isotopes far from the valley of stability, (4) extensive measurements of nuclear moments. Characteristic features of intermediate-energy direct reactions are often exploited for such studies.

One of the highlights in nuclear physics is a discovery of a new magic number $N = 16$. It is the first magic number that appears only in neutron-rich nuclei. The another success was the use of secondary beam for another fragmentation reaction and the observation of γ-rays from very neutron rich nuclei, for example ^{36}S. New determination of magnetic moments (^{15}C, ^{17}C) and a quadrupole moment (^{17}B) of neutron-rich nuclei continue steadily. An experiment on the production of superheavy elements has been restarted using GAIRIS spectrometer. This spectrometer is being moved to RILAC experimental room. Experiments with higher intensity beam (up to 10 particle μA) are planned in near future. In theory, outstanding results have been obtained and continue to coming out from Monte-Carlo Shell model calculations. Many properties of nuclei far from the stability lines have been correctly predicted using Alphleet parallel computer in RARF. The study of polymer states with alpha clusters and loosely bound neutrons are of special interest.

Starting this issue, contributions are presented from the RBRC. The RBRC has been established in 1997 for study of high-energy nuclear physics. In theory group, non-parturbative QCD studies are the central subject. In experimental group, the construction of experimental system (PHENIX) as well as the Siberian snake at the relativistic heavy ion collider (RHIC) are close to completion. The origin of nucleon spin is the main subject of the study.

The RI beams were useful for other domains of science as well. In particular, application to condensed matter science has been developed to a large extent by exploiting on-line capability of Mössbauer and PAC

spectroscopies that are feasible only with RI beams.

Intermediate-energy heavy ions from the RRC have found their own applicability. A strikingly efficient mutagenic effect has been observed when the embryo of a Tobacco plant is shot by heavy ions. High-energy heavy ions were irradiated to the plants naturally placed in the air for desirable amount of LET through sample. It has opened a new scheme of mutant production that is efficient and well controlled. The method is so efficient that it is expected to offer new possibilities of bioscience research through comparison between normal and mutagenic samples. For more detailed information such as cross talks between cells is planned to be studied by developing a micro beam.

The RARF carries many international collaborations, among them are large-size two international-collaboration programs using overseas accelerator facilities: one is the muon science project at ISIS in collaboration with the Ratherford-Appleton Laboratory (RAL), and another is the spin physics program at RHIC in collaboration with the Brookhaven National Laboratory (BNL). The pulsed muon beam facility at ISIS has been operated steadily. At RHIC facility, the first heavy-ion beam and the first polarized proton beams have been successfully accelerated. Studies of quark-gluon spin structure functions at BNL/RHIC are waiting for the commissioning of RHIC operation early next year. The large computer system for the analysis (CC-J) has been installed in Wako site.

The RI beam factory project is going reasonably fast. Ground has been broken for the facility building.

I. Tanihata
Director
RIKEN Accelerator Research Facility

II. OPERATION OF ACCELERATORS

RILAC Operation

E. Ikezawa, M. Kase, A. Goto, S. Kohara, M. Fujimaki, O. Kamigaito, N. Fukunishi, Y. Miyazawa, T. Aihara,* T. Ohki,* H. Hasebe,* H. Yamauchi,* and Y. Yano

The upgrade of RILAC began in the spring of 2000 as a result of collaboration with the Center of Nuclear Science (CNS) of Tokyo University. For installation works, regular RILAC operation was discontinued from April 1 through November 30, 2000. Figure 1 shows the layout of RILAC.

We carried out the following installation works.

(1) A shield door and a part of the wall between the No. 1 and No. 2 target rooms of RILAC were dismantled in June of 2000. The target rooms were modified. A new beam transport line to the RIKEN Ring Cyclotron (RRC) and five new target lines were installed in the target rooms.

(2) The seven resonators of a Charge-State Multiplier system (CSM) were installed after the existing accelerator of RILAC. The first two acceleration resonators and the last deceleration resonator of these are of variable-frequency type. Their frequency tunable range is 36 to 78 MHz. The other four acceleration resonators are operated only at the frequency of 76 MHz. The maximum energy of RILAC using the CSM will be 6 MeV/nucleon. Therefore, the radiation safety control system of RILAC will be replaced with a new one.

(3) A GAs-filled Recoil Isotope Separator (GARIS) was moved from the E1 experiment room of RRC to the No. 1 target room of RILAC.

(4) A 90° bending magnet, a switching magnet (0°, 30°, and 60°), and an 85° bending magnet were fabricated. The three new magnets and the two existing 60° bending magnets were installed in the target rooms after the CSM in September of 2000.

(5) Four compact quadrupole triplet magnets with a field gradient of 25 T/m and their power supplies were fabricated. The new magnets, which have also function as steering magnets, were installed in a narrow space between two resonators of the CSM. Each new magnet power supply has a GPIB interface module, and is connected to the Ethernet LAN through a LAN/HP-IB Gateway E2050.

(6) A new deionizer watercooling system was installed in September of 2000. The cooling capacity is 1.3 MW. This system has been used for the CSM, for quadrupole triplet magnets, and for the power supplies of the magnets.

From January through March, RILAC was in steady operation and supplied various kinds of ion beams for various experiments. Table 1 presents the statistics of RILAC operation in 2000. One day of scheduled beam time was forced to be cancelled owing to the failure of an rf feeder in the No. 5 resonator. The days taken for the overhaul and improvement, as shown in Ta-

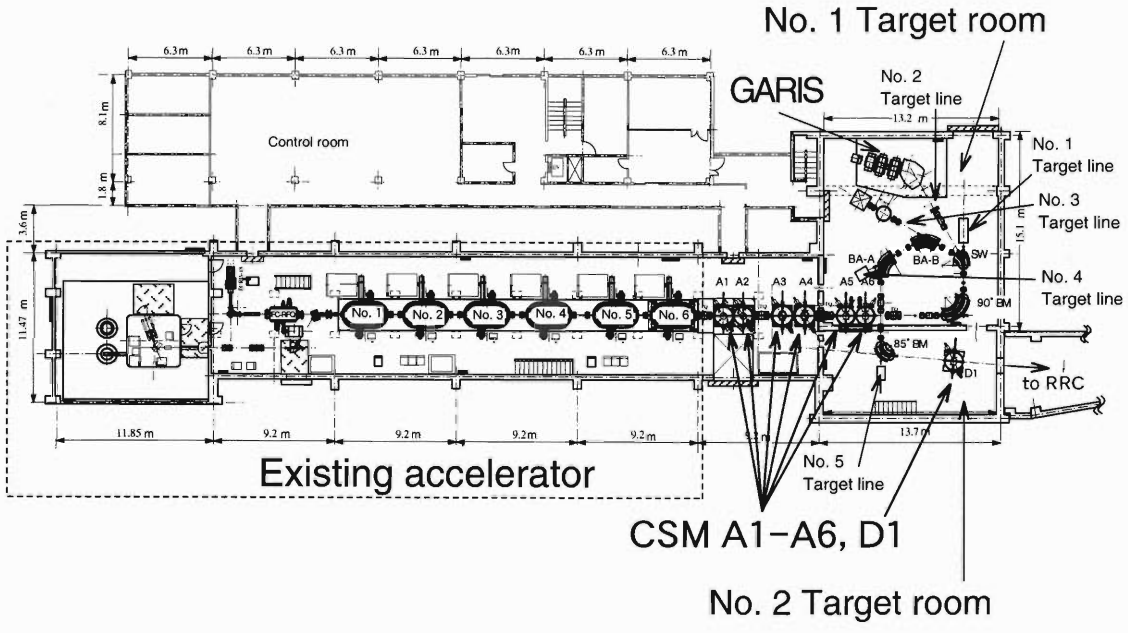

Fig. 1. The layout of RILAC. The CSM A1–A6 are the six acceleration resonators of the CSM. The CSM D1 is a deceleration resonator of the CSM.

* SHI Accelerator Service, Ltd.

Table 1. Statistics for RILAC operation from January 1 through December 31, 2000.

	Days	%
Beam time	52	14.2
Overhaul and improvement	194	53.0
Periodic inspection and repair	10	2.7
Machine trouble	1	0.3
Scheduled shutdown	109	29.8
Total	366	100

Table 2. Beam time allocated for different research groups.

	Days	%
Atomic physics	4	7.7
Radiation chemistry	11	21.2
Material analysis and development	4	7.7
Accelerator research	2	3.8
Beam transport to RRC	31	59.6
Total	52	100

ble 1, include 165 days of installation works. Table 2 summarizes the number of days allotted to different research groups. The percentage of beam time used by the RRC group was approximately 60% of the total. The ^{7}Li, ^{58}Ni, ^{84}Kr, ^{86}Kr, ^{136}Xe, and ^{181}Ta ions accelerated by RILAC were injected to RRC. Tables 3 and 4 present the statistics of the RILAC ion beams delivered using a Cockcroft-Walton injector with an 8 GHz ECR ion source (NEOMAFIOS) and those delivered using a variable-frequency RFQ with an 18 GHz ECR ion source, respectively. Ion beams of 12 elements were used for the experiments and beam acceleration tests. The percentage of beam time using metallic ions amounted to approximately 19% of the total.

Table 3. Statistics of the RILAC ion beams delivered using a Cockcroft-Walton injector with an 8 GHz ECR ion source.

Ion	Mass	Charge states	Days
He	4	1,2	7
Li	7	1,2	4
C	12	4	1
N	14	4	4
Ne	20	4	1
Ar	40	8	2
Kr	84	13	1
		Total	20

Table 4. Statistics of the RILAC ion beams delivered using a variable-frequency RFQ with an 18 GHz ECR ion source.

Ion	Mass	Charge states	Days
O	16	4	2
Ar	40	8	1
Ni	58	9	3
Kr	84	17	3
Kr	86	10	16
Xe	136	20	4
Ta	181	16,24	3
		Total	32

We experienced the following machine troubles during this reporting period.

(1) The cooling pipes in the rf feeder of the No. 5 resonator melted due to too high rf currents. This problem occurred at the acceleration frequency of 25.4 MHz.

(2) Two quadrupole magnets in the drift tube (DT1-1 and DT2-17) of the No. 1 and No. 2 resonators suffered insulation failure in their tape coils and the beam was accelerated without these magnets excited during the operation of RILAC. The magnets and the drift tubes will be replaced with new ones in the upcoming year.

RRC and AVF Cyclotron Operations

M. Kase, A. Goto, S. Numata, T. Kageyama, M. Nagase, S. Kohara, T. Nakagawa, K. Ikegami, J. Fujita, O. Kamigaito, M. Kidera, M. Komiyama, A. Yoneda, I. Yokoyama, H. Isshiki,* H. Akagi,* R. Abe,* N. Tsukiori,* K. Takahashi,* T. Maie,* R. Ohta,* K. Kobayashi,* M. Nishida,* and Y. Yano

Statistics of the RRC operation during the year 2000 are shown in Table 1. The total operation time for the RRC was 5840 hours and of these, 4440 hours were spent for experiments. The history of the RRC operation for these fourteen years is shown in Fig. 1. The operations of RRC and AVF were interrupted frequently due to the rearrangement of experimental apparatus and beam lines from April to December 2000. Moreover, since RILAC has been stopped since April 2000 due to an energy upgrade program using CSM (Charge State Multiplier), RILAC-RRC operation was limited to 8% of the total operation. Nevertheless, operation of the RRC during the year 2000 was carried out efficiently and steadily, as shown in Fig. 1.

Table 1. Statistics of RRC Operation in 2000.

Operation Time of RRC	5840 hr
Beam Service Time	4440 hr
Nuclear Physics Experiment	84%
Non-Nuclear Physics Experiment	16%
RILAC-RRC Operation	8%
AVF-RRC Operation	92%

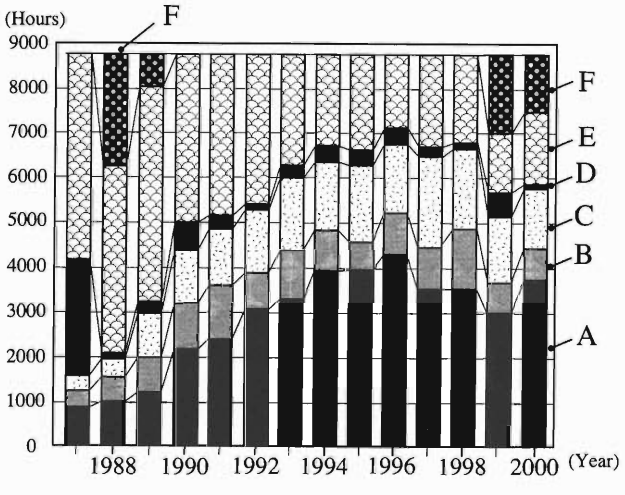

Fig. 1. History of the RRC operation for fourteen years from 1987 to 2000. A: nuclear physics experiments, B: non-nuclear physics experiments, C: beam-tuning time, D: unscheduled shutdown due to machine trouble, E: holidays and maintenance, and F: scheduled shutdown due to construction work.

* SHI Accelerator Service, Ltd.

In a collaboration between RIKEN and the Center of Nuclear Science (CNS) of Tokyo University, many rearrangements of RARF (the RIKEN Accelerator Research Facility) were carried out in 2000. Two large experimental apparatuses were newly imported from outside of RIKEN. A spectrometer (CRIB) was installed in the E7 target room ((a) in Fig. 2) and the particle analyzer (PA) was installed in the E2 target room ((b) in Fig. 2). In order to make space for these large apparatuses, some old beam lines in RARF were removed simultaneously. The ASCHRA chamber in the E2A beam course was moved out of the beam line and stored in the corner of the E2 target room ((c) in Fig. 2) for future use. The slow-beam apparatus in E7B were scrapped and the beam lines from RRC to the E7 target room were removed completely. Hereafter, E7 is used only for beams directly from AVF. The construction of new beam transport lines, which directly connect AVF with the present beam lines of RRC, was started in the summer 2000 and will be completed in the spring 2001 ((d) in Fig. 2). It ensures that the stand-alone use of AVF will be extended to all present beam lines of RARF during future operation of RIBF. A rotational bending magnet was installed in the injection beam line of AVF at the end of 2000 and hence the switching of several ion sources becomes possible. In 2001, three sets of ECR ion sources for AVF injection will be arranged around this magnet in the ion source room. Therefore, the time which is spent for changing the beam at an ion source will be saved in many cases and the development regarding the ion source will be done easily.

The beam courses in the E1 target room were also changed drastically in 2000. The GARIS in the E1A beam course was transferred to the RILAC target room. Although research on superheavy elements with GARIS is still possible in E1A for the next two years until the RIBF will start, a more efficient use of heavy-ion beams for the research is expected in RILAC after its energy is upgraded using six acceleration cavities of CSM. While the AVF-RRC operation is and will be dominated until the RIBF starts, the superheavy experiment become available by stand-alone use of RILAC. A new bending magnet was moved to the E1 target room in advance, which will be used in the transport line from RRC to RIBF in the future. The E1C beam course was improved as the test course of RIPS. For example, a detector test for RIPS using a secondary beam is now available in the E1C beam course ((e) in Fig. 2).

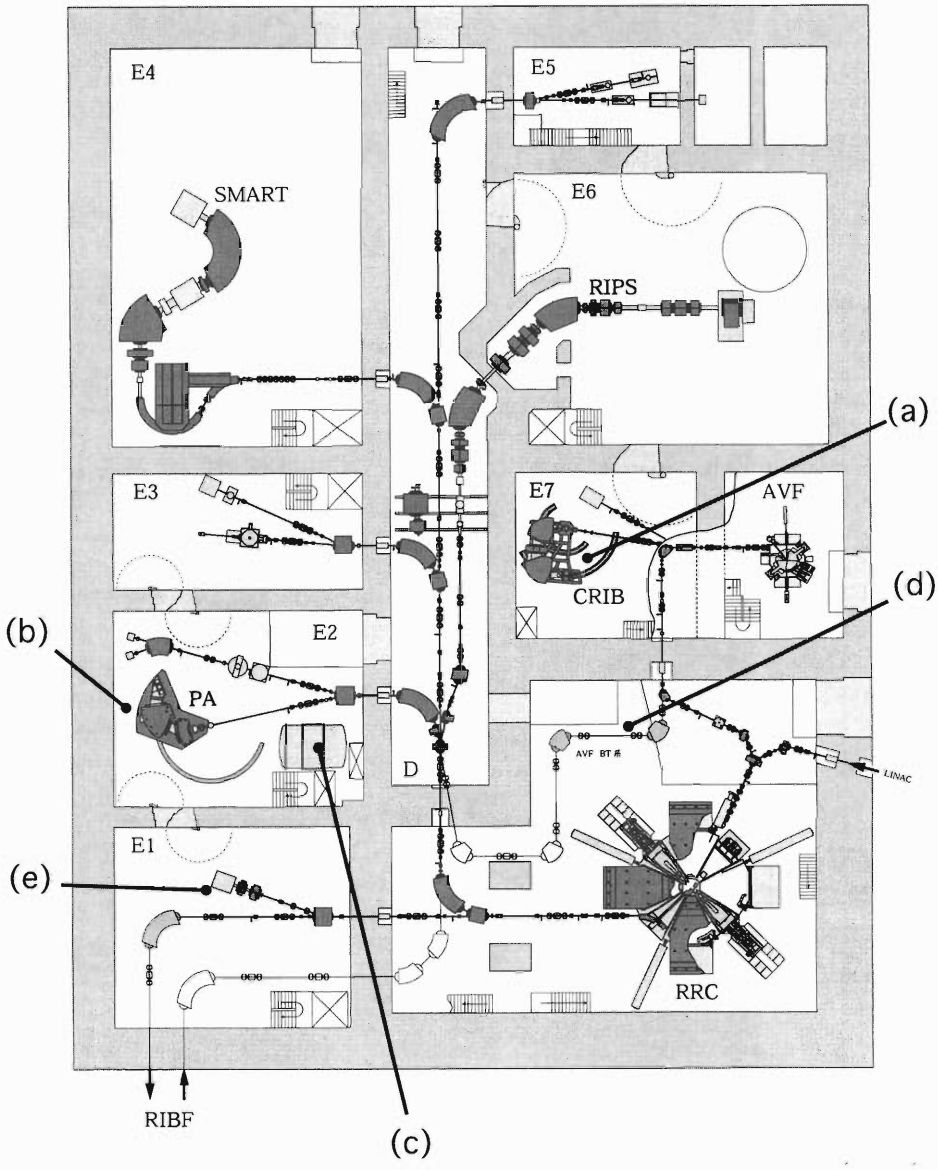

Fig. 2. Layout of beam lines of the RRC and AVF. See text for (a), (b), (c), (d), and (e).

Last spring (2000), the cables of RRC sector magnets were found to be partially damaged after a long operation of fourteen years. Their insulation cover became very hard and lost its flexibility. Some parts of them cracked and a copper conductor was exposed in the worst case. Last summer (2000), the cables were partially replaced by a new type of cable (type: WL1) which can withstand higher temperatures and maintain the same flexibility compared to the former ones.

In order to reproduce the isochronous magnetic field of RRC more easily, a new power supply was added to one of the trim coils (#11–12), which had been supplied with a dc current by one power supply in series with another trim coil (#18–19). As a result, the flexibility of the combination of trim coil currents was enhanced. The new power supply with a maximum current of 300 A is very compact, because the switching mode regulation was applied for the first time in the present facilities. This type of dc power supply is going to be used very widely in IRC as well as SRC of the RIBF project which is now under construction.

Operation of the Tandem Accelerator

K. Ogiwara, T. Urai, K. Watanabe, and E. Yagi

The 1.7 MeV tandem accelerator was operated for 98 days in total for experiments, except for the machine inspection and a beam test, during the annual reporting period from Nov. 1, 1999 to Oct. 31, 2000. For the cesium-sputter ion source, a new type of ionizer was used. However, after a few cycles of operation, it no longer functioned because of a reduction in the electric power supplied to the sheath heater of the ionizer. Through various test operations it was clarified that the trouble resulted from an electrical short circuit which formed between the heater wire and its sheath due to the condensation of cesium from its vapour. Therefore, by covering the end of the sheath heater with insulating ceramics, the functioning of the ionizer was restored. The tandem machine has been operated without any other serious problems as it was before transfer to the present experimental hall.

Experimental studies on the following subjects have been performed, and some are still in progress.

(1) Rutherford backscattering spectroscopy (RBS).

(a) Behaviour of Xe atoms implanted into iron.

(b) Channelling analysis of dopants in semiconducting materials.

(c) RBS analysis of polystyrene surfaces and glassy carbon films modified by ion implantation.

(2) Nuclear reaction analysis (NRA).

(a) Lattice location of hydrogen in niobium alloys by means of the channelling method.

(3) Particle-induced X-ray emission (PIXE).

(a) Application of the PIXE method in biomedical and materials sciences: Trace element analysis using energy-dispersive X-ray spectrometry.

(b) Trace element analysis of feathers to monitor environmental pollution.

(c) Development of an in-air high-resolution PIXE system for chemical state analysis.

(d) Characterization of the II-VI ternary semiconducting crystals.

III. RESEARCH ACTIVITIES

1. Nuclear Physics

Contribution of the Spin-Orbit Interaction for $1/2^+$ in Be Isotopes

N. Itagaki,[*1] S. Okabe,[*2] and K. Ikeda

[Cluster structure, Light neutron-rich nuclei]

A shift of the closed-shell structure is a characteristic behavior of systems with weakly bound neutrons. The contributions of the *sd* shell have been analyzed in $N = 8$ nuclei. For example, a calculation has shown that the slow β-decay of ^{12}Be to ^{12}B can be explained by an admixture of the *sd* shell in ^{12}Be ($N = 8$) in which the closed *p*-shell component must be less than 30%. This shows that the concept of magic numbers is vague in ^{12}Be.

The main purpose of this work is to show the mechanism for the appearance of this $(1/2^+)^2$ configuration in low-lying energy in detail, not only in ^{12}Be, but also in other Be isotopes. According to our previous results for ^{10}Be,[1] the dominant configuration of the two valence neutrons for the second 0^+ state is $(1/2^+)^2$, and the level inversion between $1/2^-$ and $1/2^+$ in ^{9}Be also holds in ^{10}Be. Here, the two valence neutrons stay along the α-α axis, and reduce the kinetic energy by enhancing the α-α distance (up to around 4 fm). Therefore, the $1/2^+$ orbit in this case is not a spherical *s*-wave, but a polarized orbit with the *d*-wave component.

If the $1/2^+$ state consists of the pure *s*-orbit, naturally there is no contribution of the spin-orbit interaction. In Be isotopes, the state contains the *d*-orbit component. However, the spin-orbit interaction again vanishes, when the two valence neutrons are located along the α-α axis, since two neutrons with the same spatial distribution construct only the spin-singlet state. This has been the situation in traditional molecular-orbital (MO) models. However, when one of the valence neutrons deviates from the α-α axis, the spin-triplet state can be constructed, and the spin-orbit interaction strongly acts between this state and the original $(1/2^+)^2$ configuration with the spin-singlet. An extension of the model space also enables us to improve the description of the neutron tail. We have estimated the reduction of the kinetic energy due to the improvement of the neutron tail.

The total wave function is fully antisymmetrized and expressed by a superposition of terms centered at different relative distances between the two α clusters with various configurations of the valence neutrons. All nucleons are described by Gaussians with the oscillator parameter (b) equal to 1.46 fm.

$$G_R = \left(\frac{2\nu}{\pi}\right)^{\frac{3}{4}} \exp[-\nu(\vec{r} - \vec{R}], \qquad \nu = 1/2b^2, \quad (1)$$

Each valence neutron ($\phi_{ci}\chi_{ci}$) around the α-α core is expressed by a linear combination of local Gaussians based on the MO picture,

$$\phi_{ci}\chi_{ci} = \sum_j g_j G_{R_n^j}\chi_{ci}. \quad (2)$$

The effective nucleon-nucleon interaction is Volkov No. 2 for the central part and the G3RS spin-orbit term for the spin-orbit part; all parameters are determined from the $\alpha + n$ and $\alpha + \alpha$ scattering phase shifts and the binding energy of the deuteron.

At first, we discuss the contribution of the spin-orbit interaction for the second 0^+ state of ^{10}Be. The calculated 0^+ energy shows that the smaller is the α-α distance, the larger is the contribution of the coupling with the spin-triplet state. When the α-α distance is 5 fm, the coupling of $S = 1$ to the original $(1/2^+)^2$ increases the binding energy by about 3 MeV; however, when the α-α distance is 3 fm, the coupling increases the binding energy by about 4.5 MeV. Therefore, the coupling with the spin-triplet becomes stronger as the α-α distance becomes small.

Next, the large contribution of this spin-orbit interaction is discussed concerning ^{12}Be.[2] In ^{12}Be, four valence neutrons rotate around two α clusters and, mainly, two configurations are important for the 0^+ ground state. One is $(3/2^-)^2(1/2^-)^2$ for the four valence neutrons, which corresponds to the closed *p*-shell configuration of the neutrons at the zero limit of the α-α distance. The other configuration is $(3/2^-)^2(1/2^+)^2$, where two of the four valence neutrons occupy the σ-orbit. It is necessary to compare the energy of these two configurations as a function of the α-α distance. When it is small, for example 2 fm, the dominant configuration of the four valence neutrons is $(3/2^-)^2(1/2^-)^2$ for the ground state, which corresponds to the closed *p*-shell configuration at the limit of the α-α distance, zero. On the other hand, the $(3/2^-)^2(1/2^+)^2$ configuration for the four valence neutrons becomes lower as the α-α distance is increased. Due to the spin-orbit coupling, the energy is almost the same as that of $(3/2^-)^2(1/2^-)^2$, corresponding to the closed *p*-shell configuration. Furthermore, the energy of $(3/2^-)^2(1/2^+)^2$ is suggested to become even lower than $(3/2^-)^2(1/2^-)^2$ when the pairing effect between $(3/2^-)^2$ and $(1/2^-)^2$ is taken into account. These effects play crucial roles in accounting for breaking of the $N = 8$ magic number.

*1 Department of Physics, University of Tokyo
*2 Center for Information Multimedia Studies, Hokkaido Univ.

References
1) N. Itagaki et al.: Phys. Rev. C **61**, 044306 (2000).
2) N. Itagaki et al.: Phys. Rev. C **62**, 034301 (2000).

Nuclear Polymer States in C Isotopes

N. Itagaki,[*1] S. Okabe,[*2] K. Ikeda, and I. Tanihata

[Cluster structure, Neutron-rich nuclei]

A survey of the molecular-like structure is one of the most challenging subjects in light neutron-rich nuclei. In Be isotopes, recently, decay into fragments of He isotopes (^{4}He, ^{6}He, ^{8}He) has been observed from the excited states of ^{10}Be and ^{12}Be, and the presence of a two-center configuration is suggested. From the theoretical side, these states are studied by various models by which molecular-orbital (MO) nature of the weakly bound neutrons around the two α-clusters has been revealed.[1,2] As for multi-cluster configurations in light α-nuclei beyond the two-center systems, the existence of $N\alpha$ states has been predicted around the threshold energy in the so-called Ikeda diagram. For example, it has been suggested that the second 0^+ state of ^{12}C has a 3α-like molecular configuration. However, according to many theoretical analyses, the state is not necessary to have a linear-chain of 3α, but is described as a weak-coupling state with a triangular shape or the ^{8}Be+α configuration.

In this work, the MO approach introduced for the Be isotopes is applied to a study of C isotopes. The stability of the linear-chain states against the breathing-like path and the bending-like path are shown to be increased by adding valence neutrons around a 3α core. Two orbitals are introduced based on MO: when the distribution of the neutron is perpendicular to the 3α-axis, it is called π-orbit: if it is along the axis, it is called a σ-orbit corresponding to a higher nodal orbital.

We start with the stability of the linear-chain states against the breathing-like path. The relative distance between α-clusters is expressed by the parameter d. If there are no valence neutrons, although the 3α-system (^{12}C) has minimal energy at around $d = 3.5$ fm, the energy pocket is too shallow to conclude the stability of the linear-chain state. On the contrary, in ^{14}C with two valence neutrons in $3/2^-_\pi$, there appears to be evident minimal energy at around $d = 3$ fm. The energy (~ -82 MeV) is lower than ^{12}C by 11 MeV and also the energy pocket is much deeper. Therefore, the π-orbit is found to stabilize the linear-chain structure and to prevent a breathing-like break-up of the system. This ^{14}C$(3/2^-_\pi)^2$ configuration corresponds to an excitation energy of 18 MeV from the ground state, which is calculated by introducing a MO around the 3α-core with an equilateral-triangle configuration. In the case of the σ-orbit for the two valence neutrons (^{14}C$(1/2^-_\sigma)^2$), the excitation energy is higher by about 14 MeV in comparison with ^{14}C$(3/2^-_\pi)^2$. It is rather surprising that the difference is only 14 MeV in spite of the fact that $3/2^-_\pi$ has only one node and $1/2^-_\sigma$ has three nodes. This is due to the α-α-α clustering of the core. The higher nodal orbits along the symmetry axis (σ-orbit) become low-lying as a result of the clustering.

We have shown that ^{14}C$(3/2^-_\pi)^2$ is stable against the breathing-like path. Next, the stability against the bending motion is examined. The curvature of the 0^+ energy against the bending angle is rather monotonic and the energy minimum does not clearly appear. This situation does not drastically change even if the orthogonality between the linear-chain configuration and low-lying states with the equilateral triangle 3α-configuration is taken into account. This effect works, but not sufficiently to push up the energy of the state with a finite bending angle.

The 3α linear-chain state of ^{14}C with two valence neutrons in the π-orbit is found to be stable against the breathing-path, but not stable against the bending-path. Therefore, we next increase the number of the valence neutrons and survey the stability of the linear-chain state in ^{16}C based on the $\alpha + \alpha + \alpha + 4n$ model. The lowest configuration for the four valence neutrons is $(3/2^-_\pi)^2(1/2^-_\pi)^2$, where all of the valence neutrons occupy the π-orbits. The 0^+ energy curve of ^{16}C$((3/2^-_\pi)^2(1/2^-_\pi)^2)$ shows an energy pocket at -86 MeV around $d = 2.5$–3.0 fm, which is deep enough for stability against the breathing-like path. However, ^{16}C$((3/2^-_\pi)^2(1/2^-_\pi)^2)$ does not have any minimal energy against the bending-like path. Next, two of the valence neutrons are introduced to occupy the σ-orbit, and ^{16}C$((3/2^-_\pi)^2(1/2^-_\sigma)^2)$ is also found to be stable against the breathing-like path. The minimal 0^+ energy is higher by 5 MeV than ^{16}C$((3/2^-_\pi)^2(1/2^-_\pi)^2)$, and the excitation energy corresponds to $\sim$25 MeV. The rotation band of this linear-chain states has an energy slope of $\frac{\hbar^2}{2I} = 150$ keV. Furthermore, ^{16}C$((3/2^-_\pi)^2(1/2^-_\sigma)^2)$ is also stable against the bending-like path, since there appears a sharp increase of the 0^+ energy against the bending angle. This feature is much different from ^{14}C$((3/2^-_\pi)^2)$ and ^{16}C$((3/2^-_\pi)^2(1/2^-_\pi)^2)$.

In summary, the configuration of valence neutrons consisting of combination of the π- and the σ-orbit is promising to stabilize the linear-chain state. The excited state in ^{16}C is one candidate.

*1 Department of Physics, University of Tokyo
*2 Center for Information Multimedia Studies, Hokkaido Univ.

References

1) N. Itagaki and S. Okabe: Phys. Rev. C **61**, 044306 (2000).
2) N. Itagaki, S. Okabe, and I. Ikeda: Phys. Rev. C **62**, 034301 (2000).

Halo Structure in ^{19}C: A Glauber Model Analysis†

R. Kanungo, I. Tanihata, Y. Ogawa,[*1] H. Toki,[*2] and A. Ozawa

[Halo, Glauber model]

The recently available $^{19}C + ^{12}C$ interaction cross-section data at $E_{lab} = 960A$ MeV as well as the longitudinal momentum distribution data at $E_{lab} = 910A$ MeV and $88A$ MeV have been analyzed in a Glauber-model approach to investigate the possible ground-state configuration of the ^{19}C nucleus. A comparative analysis of both of these experimental data fails to yield a consistent conclusion regarding a possible ground-state configuration within the 1σ error bar of the experimental data. It is suggested that a considerable change of the core of ^{19}C from a bare ^{18}C nucleus may take place.

† Condensed from the article in Nucl. Phys. A **677**, 171 (2000)

*1 Van de Graaff Accelerator Laboratory, Faculty of Science, Osaka University

*2 Research Center for Nuclear Physics, Osaka University

Enhancement of Low-Energy Dipole Strength in Light Drip-Line Nuclei

H. Sagawa,[*1] T. Suzuki,[*2] H. Iwasaki,[*3] and M. Ishihara

[Electric dipole strength, Loosely-bound nucleon, Drip-line nuclei]

We have studied the electric-dipole transition strength in three nuclei with loosely bound nucleons ($^{12}_{4}Be_8$, $^{14}_{4}Be_{10}$ and $^{13}_{8}O_5$) by large-scale shell-model calculations including the configuration space up to $3\hbar\omega$ excitations. We found large low-energy E1 peaks below 3 MeV in both $^{12}_{4}Be_8$ and $^{13}_{8}O_5$. The calculated results in $^{12}_{4}Be_8$, $E_x = 2.36$ MeV and B(E1) = 0.063 e^2 fm^2, show good agreement with the recently observed 1^- state at $E_x = 2.68(3)$ MeV with B(E1) = 0.051(13) e^2fm^2 by Coulomb excitation.[1] In $^{14}_{4}Be_{10}$, the lowest 1^- state is predicted to be around 7 MeV, which is much higher than the energy in $^{12}_{4}Be_8$. A large low-energy E1 strength is predicted in ^{13}O at $E_x = 2.92$ MeV with B(E1) = 0.056 e^2fm^2. The low-energy E1 strength in $^{12}_{4}Be_8$ and $^{13}_{8}O_5$ can be interpreted as a sign of melting of the energy gaps at $N = 8$ and $Z = 8$ near to the drip lines. We pointed out two key issues to obtain the extremely enhanced E1 strength at low energy.[2] The first one is the effect of extended wave functions, which enlarges the single-particle transition matrix elements, and also induces decoupling of the enhanced low-energy E1 strength from the GDR strength. The second one is coherence in the transition amplitudes between the loosely bound nucleons, and also between the core and the loosely bound nucleons. In addition, the hole-vibration coupling picture is used to interpret the splittings of both the energies and the strength in $^{13}_{8}O_5$. Further experimental and theoretical efforts are definitely needed to study a new coherent effect on the E1 transitions as well as the change in the shell structure near to the drip lines.

References

1) H. Iwasaki et al.: Phys. Lett. B **491**, 8 (2000).
2) T. Suzuki, H. Sagawa, and P. F. Bortignon: Nucl. Phys. A **662**, 282 (2000).

*1 Center for Mathematical Sciences, University of Aizu
*2 Department of Physics, Nihon University
*3 Department of Physics, University of Tokyo

Pygmy and Giant Dipole Resonances in Neutron-Rich Nuclei within the Quasiparticle Representation of the Phonon Damping Model

N. Dinh Dang, V. Kim Au,[*1] T. Suzuki,[*2] and A. Arima

[Giant dipole resonance, Neutron-rich nuclei, Pygmy resonance, Photonuclear reactions]

Recent years have seen intensive studies of effects due to varying the ratio of the proton (Z) and neutron (N) numbers on different nuclear-structure characteristics as nuclei deviate from their valley of β-stability. One of the phenomena is the pygmy dipole resonance (PDR) in neutron-rich nuclei or soft dipole mode in neutron halo nuclei. The PDR leads to an enhancement of the dipole strength below the region of the usual giant dipole resonance (GDR). The PDR, by itself, is not a new subject, because it was observed experimentally in photonuclear reactions in ^{18}O more than two decades ago. The renewed interest in this phenomenon arises mainly due to the prospects of using radioactive-isotope (RI) beams to study unstable nuclei. With the recent method of utilizing the electromagnetic (EM) excitation process at high energies, the E1 strength distribution can be studied up to the region of GDR in light neutron-rich isotopes.[1)]

One of the challenges in the theoretical study of exotic nuclei is how to go from the valley of β-stability, where predictions given by various models for major fundamental nuclear properties are similar, to the region of nuclei with extreme N/Z ratios, where theoretical predictions become quite model-dependent. The PDR was predicted by several theoretical models starting from an application of the cluster model (CM), where the low-lying dipole mode is described as a result of oscillation of neutron excess against the core, the Skyrme-Hartree-Fock model, the Hartree-Fock plus random-phase approximation model, to the large-scale shell-model (LSSM). The LSSM uses an interaction, which is determined as a least-square fit of the particle-hole (ph) two-body matrix elements to the binding and excitation energies of nuclei with mass number $A = 10$–20. The width of GDR was not explicitly calculated in these theoretical studies. Instead, it was introduced as a width parameter from the Gaussian or Breit-Wigner distribution. The recent preliminary experimental results at GSI[1)] have shown that the energy-weighted sum (EWS) of the PDR strength does not follow the prediction of CM. The prediction given by LSSM agrees qualitatively with the preliminary data for the EM cross sections of PDR in ^{20,22}O,[1)] but the GDR shapes given by LSSM disagree with the well-established experimental systematic for photonuclear reactions cross sections in ^{16,18}O. Given the rather scarce experimental data on GDR and PDR in neutron-rich nuclei at present, it is desirable to have an extension toward the region with $N \gg Z$ based on a theoretical model, which properly includes the damping mechanism and satisfactorily describes the well-known systematic of GDR shapes in β-stable nuclei.

In the present paper the quasiparticle representation of the phonon damping model (PDM)[2)] is developed to include the superfluid pairing correlations microscopically. The formalism is applied to calculate the photoabsorption and the EM differential cross sections of E1 excitations in neutron-rich oxygen and calcium isotopes. The calculated photoabsorption cross sections agree reasonably well with the available data for ^{16,18}O and ^{40,48}Ca. The fractions of EWS of strength in the region of PDR ($E_\gamma \leq 15$–16 MeV) and the PDR peaks in the EM cross sections for ^{20,22}O are also found in reasonable agreement with experimental systematic. The deviation from the prediction given by the CM sum rule shows the importance of the effect of coupling to noncollective degrees of freedom in the damping of pygmy and giant dipole resonances. It is also shown in this work that, using low-energy RI beams at around 50–60 MeV/n, one can observe clean and even enhanced PDR peaks without any admixture with the GDR in the EM differential cross sections of neutron-rich nuclei.

References

1) T. Aumann et al.: GSI Sci. Rep. 1999, **27** (2000).
2) N. Dinh Dang and A. Arima: Phys. Rev. Lett. **80**, 4145 (1998); Nucl. Phys. A **636**, 427 (1998); N. Dinh Dang, K. Tanabe, and A. Arima: Phys. Rev. C **58**, 3374 (1998); Nucl. Phys. A **645**, 536 (1999).

*1 Institute of Theoretical Physics, Vietnam. Address after January 1, 2001: Texas A&M University, USA
*2 Department of Physics, College of Humanities and Sciences, Nihon University

Structure of ^{31}Na Studied by the Monte-Carlo Shell Model

Y. Utsuno,[*1] T. Otsuka,[*2] T. Mizusaki,[*3] and M. Honma[*4]

[NUCLEAR STRUCTURE, Shell model, Unstable nuclei]

Since anomalous properties of ^{31}Na concerning the mass[1] and the ground-state spin and magnetic moment[2] were observed in the 1970's, the structure of neutron-rich nuclei around $N = 20$ has attracted much interest, particularly concerning vanishing of the $N = 20$ magic number. Based on the Monte-Carlo shell model (MCSM),[3] we performed a systematic shell-model calculation for even-even $N \sim 20$ exotic nuclei with full mixing between the normal, intruder, and higher intruder configurations for the first time,[4] and gave a comprehensive picture of the region. As for odd-A nuclei, since we should adopt the J-compressed bases,[3] which require much computational time in the MCSM calculation, such a calculation was unfeasible until the Alphleet computer system[5] was introduced at RIKEN. In this report, the structure of a neutron-rich odd-A nucleus ^{31}Na, which is expected to be in the "island of inversion,"[6] is studied by the MCSM with the Alphleet computer system.

The energy levels of ^{31}Na are shown in Fig. 1. The ground-state spin $3/2^+$ agrees with an experiment, in contrast to the *sd*-shell model prediction of $5/2^+$. The calculated magnetic moment of the ground state is $2.17\,\mu_N$ with free-nucleon g factors being consistent with the experimental value of $2.283\ (38)\,\mu_N$.[2] The present study shows that, while the ground state is dominated by the 2-particle 2-hole ($2p2h$) excitations from the $N = 20$ core, $4p4h$ and higher excited configurations are mixed and lower the ground-state energy by more than 700 keV. This energy gain gives rise to a better two-neutron separation energy. The first excited state obtained by the MCSM calculation is a $5/2^+$ state located at 310 keV, in good agreement with a recent measurement of 350 ± 20 keV.[7] On the other hand, this level was calculated to lie around 200 keV in the $0p0h + 2p2h$ truncation. A comparison between the truncated and full calculations clearly indicates the importance of the higher intruder configurations (*i.e.*, $4p4h$ and higher excited configurations from $N = 20$ core): these configurations lower the ground state more than the first excited state, giving rise to a better agreement with experiment. The higher intruder configurations occupy the ground state by about 10%. The $B\,(E2; 3/2^+ \rightarrow 5/2^+) = 200\ \mathrm{e^2fm^4}$ is obtained with the effective charges $e_p = 1.3\,\mathrm{e}$ and $e_n = 0.5\,\mathrm{e}$, suggesting a strong deformation similarly to the adjacent even-A nucleus, ^{32}Mg. This $B(E2)$ value corresponds to $\beta_2 = 0.53$ by assuming an axially symmetric rotor with $K = 3/2$.

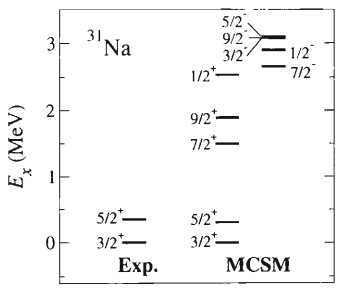

Fig. 1. Experimental energy levels of ^{31}Na (Exp.) compared with those of the MCSM calculation (MCSM).

The negative-parity states are also of interest, partly because the competition and mixing between the $1p1h$ and $3p3h$ configurations can be compared with those of the $0p0h$ and $2p2h$ configurations in the positive-parity states. The present calculation indicates that the yrast negative-parity states shown in Fig. 1 are dominated by $3p3h$ configurations. The truncated shell-model calculation with the same interaction shows that states dominated by $1p1h$ are expected to lie higher than the yrast negative-parity states by more than 1 MeV. This picture is in sharp contrast with the former shell-model prediction,[6] in which the yrast negative-parity states are composed of $1p1h$ configurations for all nuclei in this region.

In order to confirm the validity of our calculation concerning the competition and mixing of various configurations, the role of pf-orbits on the observed quantities is examined in more detail. In the MCSM calculation, the 3^-_1 state of a neutron-rich nucleus, ^{28}Mg, lies at 5.28 MeV, very close to the experimental position of 5.17 MeV. The two-neutron separation energies of $N = 20$ nuclei, which are also very sensitive to the *effective single-particle energy*[4] of the pf shell, are in excellent agreement with an experiment for $N = 20$ isotones ranging from $Z = 10$ to 14.

*1 Japan Atomic Energy Research Institute
*2 Department of Physics, University of Tokyo
*3 Department of Law, Senshu University
*4 Center for Mathematical Sciences, University of Aizu

References

1) C. Thibault et al.: Phys. Rev. C **12**, 644 (1975).
2) G. Huber et al.: Phys. Rev. C **18**, 2342 (1978).
3) T. Otsuka et al.: Phys. Rev. Lett. **81**, 1588 (1998) and references therein.
4) Y. Utsuno et al.: Phys. Rev. C **60**, 054315 (1999).
5) T. Otsuka et al.: Prog. Theor. Phys. Suppl. No.138, 24 (2000).
6) E. K. Warburton et al.: Phys. Rev. C **41**, 1147 (1990).
7) B. V. Prityckenko et al.: submitted to Phys. Rev. Lett.

A Search for a Unified Effective Interaction for Monte-Carlo Shell-Model Calculations (II)

M. Honma,[*1] B. A. Brown,[*2] T. Mizusaki,[*3] and T. Otsuka[*4]

[Shell model, Effective interaction]

The Monte Carlo Shell Model (MCSM)[1] has extended the feasibility of the nuclear shell model far beyond the current limit of the conventional diagonalization technique. We can now study various nuclear properties in the whole pf-shell, or even in heavier mass regions from microscopic viewpoints. At this stage, it is a quite challenging problem to construct a *unified* shell-model effective interaction which is successful over a wide model space, including both the beginning and the middle of the shell.

We can approach to this problem by a "model-independent" method, in which two-body matrix elements and single-particle energies are treated as parameters, and are determined by a least-squares fit to the experimental binding energies and the excitation energies. This technique was successfully applied to the sd-shell, and led to success concerning the USD interaction.[2]

For pf-shell calculations, we have attempted several series of iterative fitting calculations.[3] The shell-model calculations were carried out by a massive parallel computer, Alphleet, at RIKEN. In this report we introduce one promising interaction, called the GF40A[4] interaction, as described below.

Starting from a realistic G-matrix interaction[5] based on the Bonn-C potential, 195 two-body matrix elements and 4 single particle energies were determined by fitting to 635 binding and excitation energy data. We adopted the data of the following 91 nucleids: $^{47-51}$Ca, $^{47-51}$Sc, $^{47-52}$Ti, $^{47-55}$V, $^{48-56}$Cr, $^{50-58}$Mn, $^{52-60}$Fe, $^{54-61}$Co, $^{56-68}$Ni, $^{58-69}$Cu, $^{60-69}$Zn, ^{64}Ga and ^{64}Ge. Nuclei of $A < 47$ are excluded in the fit so as to reduce the effect of the sd-shell configurations. In order to separate well-determined parameters from the rest, we varied 40 linear combinations of the parameters on the basis of the Linear Combination method.[6] We can approximate the MCSM energies by taking only a few dominant (optimized) bases in the form of deformed Slater determinants (few-dimensional approximation; FDA[4]). The FDA can be improved further by adding suitable empirical corrections. The 2-body matrix elements were scaled according to a mass-dependent factor $(A/42)^{-0.3}$ relative to the values at $A = 42$. As a result of the fitting calculations, the GF40A interaction was obtained with an estimated rms error of 255 keV.

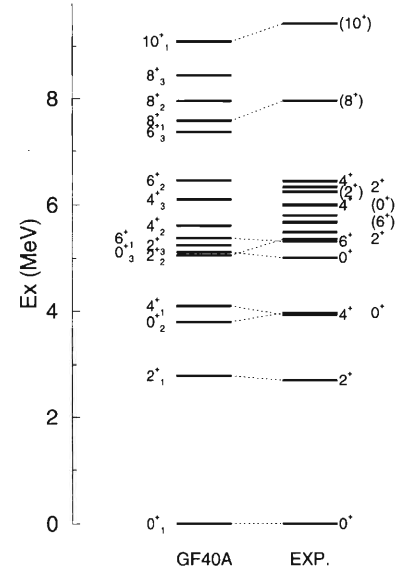

Fig. 1. Energy levels of ^{56}Ni. Experimental data are taken from Ref. 7.

The GF40A interaction was examined from various viewpoints and was found to be quite successful in describing the systematics of binding energies, effective single-particle energies, semi-magic structure of N or $Z = 28$ nuclei, and the isospin structure of the lowest states in $N = Z$ odd-odd nuclei.

As an example, the energy levels of ^{56}Ni are shown in Fig. 1. Levels which are used for the fit are connected by dotted lines. Theoretical values are obtained by the FDA with empirical corrections, except for the 0^+ states, which are obtained by the MCSM with 30 basis states. The agreement between the theory and the experiment is satisfactory.

We are now investigating to what extent we can determine the parameters without uncertainty.

*1 Center for Mathematical Sciences, University of Aizu
*2 Michigan State University, USA
*3 Department of Law, Senshu University
*4 Department of Physics, University of Tokyo

References

1) T. Otsuka et al.: Phys. Rev. Lett. **81**, 1588 (1998).
2) B. A. Brown et al.: Ann. Rev. Nucl. Part. Sci. **38**, 29 (1988).
3) M. Honma et al.: RIKEN Accel. Prog. Rep. **33**, 16 (2000).
4) M. Honma et al.: to be published in Nucl. Phys. A.
5) M. Hjorth-Jensen et al.: Phys. Rep. **261**, 125 (1995).
6) W. Chung: Ph. D. thesis, Michigan State University, 1976.
7) R. B. Firestone et al.: *Table of Isotopes*, (Wiley, New York, 1996).

Monte-Carlo Shell Model Calculation for Medium-Heavy Nuclei

N. Shimizu,* T. Otsuka,* T. Mizusaki, and M. Honma

[Shell model, Nuclear structure, Collective motion, Computational physics]

One of the interesting topics in nuclear physics is an investigation of nuclei which have a triaxial deformed structure. These properties are seen in the Xe-Ba, Pt-Os regions. In 1978, an innovative study was conducted utilizing the O(6) limit of the Interacting Boson Model,[1] and many efforts have continued until now to understand these features more precisely. In this report, we discuss this topic microscopically by utilizing the nuclear shell-model description.

We focus on ^{132}Xe, which is considered to have triaxial deformed features. The excitation energies of ^{132}Xe are shown on the right-hand side of Fig. 1, where we can see such characteristics. For example, the excitation energy of the 2_2^+ state is lower than that of the 4_1^+ state.

In our nuclear shell-model calculation, the single-particle states of the model space are taken as one major shell (N, Z = 50 82), which is sufficiently large to describe the nuclear collective motion. Because the dimension of the Hilbert space becomes too large (larger than 10^7) to diagonalize the shell-model Hamiltonian in a conventional way, we introduce a new version of the Monte-Carlo shell model (MCSM) method using a condensed pair[2] in order to overcome such difficulties. In the former MCSM method which was recently developed by M. Honma *et al.*,[3] the obtained state is presented as a linear combination of a small number ($\sim$ 30) of Slater determinant bases which are selected stochastically. In order to include the contribution of a pairing correlation more efficiently, we replace the Slater determinant by a condensed pair, which is a kind of generalized Cooper pair. The condensed pair basis is written as $(\sum_{ij} \lambda_{ij} \hat{c}_i^\dagger \hat{c}_j^\dagger)^N |-\rangle$[4], where $\hat{c}_i^\dagger$, $|-\rangle$, and λ_{ij} denote the creation operator of a spherical harmonic oscillator, an inert core, and arbitrary amplitudes of the pair, respectively.

The left-hand side of Fig. 1 denotes the theoretical result obtained by the MCSM. This result well reproduces the experimental values, which are drawn on the right-hand side. It shows the characteristics of triaxial deformation discussed before, and we can say that the MCSM result describes the nuclear collective motion sufficiently, including the degree of freedom of a triaxial deformation.

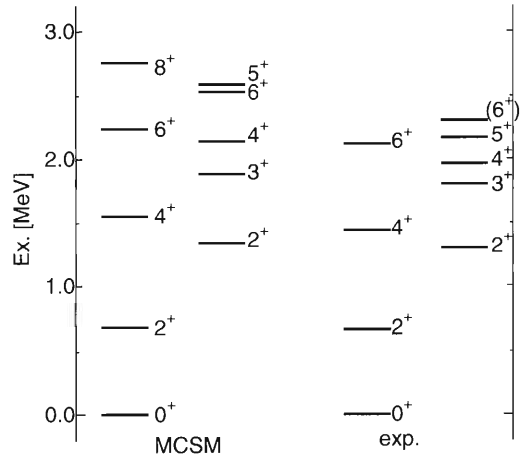

Fig. 1. Energy levels of ^{132}Xe.

These computations were carried out mainly using the Alphleet computer system at RIKEN.

References

1) A. Arima and F. Iachello: Phys. Rev. Lett. **40** 385 (1978).
2) N. Shimizu, T. Otsuka, T. Mizusaki, and M. Honma: Phys. Rev. Lett. **86**, 1171 (2001).
3) Y. Utsuno, T. Otsuka, T. Mizusaki, and M. Honma: Phys. Rev. C **60**, 054315 (1999) and references therein.
4) T. Otsuka and N. Yoshinaga: Phys. Lett. B **168**, 1 (1986).

* University of Tokyo

Normal and Super Deformation in ^{56}Ni†

T. Mizusaki, T. Otsuka, M. Honma, and B. A. Brown*

[Shell model, Shape coexistence]

Investigating the structure of the doubly-magic ^{56}Ni nucleus has become a particularly interesting subject. The spherical ground and low-lying states are a touchstone for the validity of the $N = Z = 28$ doubly closed-shell structure.[1] In addition, salient deformed bands have recently been observed[2] in ^{56}Ni. These collective bands with a large deformation coexist along with the spherical yrast band. For describing this shape coexistence in a single framework, the shell model is quite suitable and the Monte-Carlo shell model (MCSM)[3,4] is one of the powerful tools used to achieve large-scale shell-model calculations. In Refs. 4 and 5, we investigated the yrast band and one of the deformed bands of ^{56}Ni. The level scheme of these bands has been demonstrated to be properly described in full pf-shell calculations with the FPD6 interaction.[6] In this paper, with an enlarged shell-model space, we present a more comprehensive description of the structure of the rotational bands of ^{56}Ni and its neighbor $N = Z$ nuclei.

In Fig. 1, we show a theoretical and experimental[2] level scheme for yrast and two deformed bands. Because there is no candidate for a second deformed band within the pf-shell, the shell-model space should be extended. And because the $g_{9/2}$ orbit has an opposite parity to that of the pf-shell orbits, its effect on low-spin yrast states is expected to be small. However, one-nucleon excitation from pf-shell orbits to the $g_{9/2}$ orbit can take place. In order to investigate this picture, the full pf plus $g_{9/2}$ shell model space is taken into account. For this space, the FPD6 interaction should also be extended, which is discussed in Ref. 7. Such an extended calculation nicely describes these two deformed bands of ^{56}Ni, as shown in Fig. 1.

With the analysis of the MCSM wavefunctions, the first deformed band of ^{56}Ni is a positive parity one and its nature is, on average, 4p4h excitation on top of the ground state within the pf-shell. On the other hand, the second deformed band is a negative parity one where, on average, one nucleon is promoted into the $g_{9/2}$ orbit from the first deformed configuration. With the same interaction, the deformed band of ^{58}Cu[8] can also be well described. In this band, the occupation number of the $g_{9/2}$ orbit is almost two. This picture is quite similar to the Skyrme HF results with the SLy4 interaction.[2,8] In the present calculation, the twinning[2] between the second deformed band of ^{56}Ni and the band of ^{58}Cu is still in question. A further quantitative investigation is needed. A systematic description of large or super deformed bands in the A $\sim$ 60 region within the pf$g_{9/2}$ shell-model space is quite interesting.

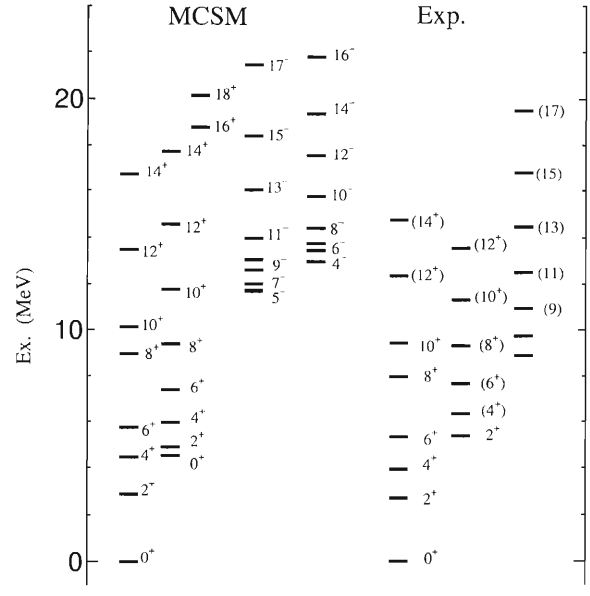

Fig. 1. Experimental levels[2] of ^{56}Ni compared with the MCSM result with an extended FPD6 Hamiltonian.

This work was supported in part by a Grant-in-Aid for Scientific Research (A) (2) (10304019) from the Ministry of Education, Science and Culture. Numerical calculations were carried out partly by a massively parallel computer, Alphleet, at RIKEN. BAB was supported by NSF grants PHY-9605207 and PHY-0070911.

References

1) G. Kraus et al.: Phys. Rev. Lett. **73**, 1773 (1994).
2) D. Rudolf et al.: Phys. Rev. Lett. **82**, 3763 (1999).
3) M. Honma, T. Mizusaki, and T. Otsuka: Phys. Rev. Lett. **75**, 1284 (1995); Phys. Rev. C **53**, 2786 (1996); Phys. Rev. Lett. **77**, 3315 (1996).
4) T. Otsuka, M. Honma, and T. Mizusaki: Phys. Rev. Lett. **81**, 1588 (1998).
5) T. Mizusaki, T. Otsuka, Y. Utsuno, M. Honma, and T. Sebe: Phys. Rev. C **59**, R1486 (1999).
6) W. A. Richter, M. G. van der Merwe, R. E. Julies, and B. A. Brown: Nucl. Phys. A **523**, 325 (1991).
7) T. Mizusaki, T. Otsuka, M. Honma, and B. A. Brown: Phys. Scr. T **88**, 107 (2000).
8) D. Rudolf et al.: Phys. Rev. Lett. **80**, 3018 (1998).
9) T. Mizusaki, et al.: Nucl. Phys. A, in press.

† Condensed from the articles in Phys. Scr. T **88**, 107 (2000)[7] and in Nucl. Phys. A (in press)[9]

* Superconducting Cyclotron Laboratory and Department of Physics and Astronomy, Michigan State University, USA

Effects of the Neutron Spin-Orbit Density on the Nuclear Charge Density in Relativistic Models

H. Kurasawa* and T. Suzuki

[NUCLEAR MODEL, Charge density, Neutron spin-orbit density, Relativistic model]

In recent years, it has been shown that many of the nuclear ground-state properties are well reproduced by Hartree-Fock calculations using the Skyrme effective forces (SHF)[1] and by relativistic mean-field calculations (RMF).[2] For a long time, however, there has remained a problem that SHF and RMF cannot explain the difference between the cross sections for elastic electron scattering from ^{40}Ca and ^{48}Ca. Since they are described as closed-shell nuclei, it was expected that the difference could be easily understood by SHF and RMF; but the problem has not yet been solved.

In 1972, Bertozzi *et al.*[3] took into account the effects of the neutron spin-orbit charge density as a relativistic correction to SHF. The relativistic correction was derived by expanding the Pauli current of the free nucleon in terms of $1/M$, M being the mass of the free nucleon. They found that although the relativistic correction was not negligible, it was not enough to explain the difference between the two cross sections. In 1976, Miller[4] analyzed the same data using RMF, but again could not reproduce the experimental data. The Pauli current made the agreement rather worse between his results and the experiment. Since then, there have been no efforts to solve this problem, as far as the authors know.[5]

Recently, new parameter sets of the Skyrme forces and the relativistic models have been proposed for a better description of the nuclear ground-state properties. By using those sets, we have shown that although RMF with the new parameter sets can well reproduce the experimental data, SHF still fails to explain them.[6] Moreover, we have clarified the relationship between the relativistic and non-relativistic models. In the relativistic models, the effective mass coming from the Lorentz scalar potential yields an additional spin-orbit charge density as a relativistic correction. This correction improves the agreement between the experimental data and the RMF results.

We calculate the cross section for elastic electron scattering using phase-shift analyses. For this purpose we must obtain the nuclear charge density, which is given by

$$\rho_c(r) = \int \frac{d^3q}{(2\pi)^3} \exp(-i\mathbf{q}\cdot\mathbf{r})\langle 0|\hat{\rho}(\mathbf{q})|0\rangle,$$

where $\mathbf{q}$ denotes the momentum transfer from the electron to the nucleus. In relativistic theory, the ground-state expectation value of the time component of the nuclear current is given by

$$\langle 0|\hat{\rho}(\mathbf{q})|0\rangle = \int d^3x\, d^3y \exp(i\mathbf{q}\cdot(\mathbf{x}+\mathbf{y})) \times \sum_\tau \left(G_{E\tau}(y)\rho_\tau(x) + F_{2\tau}(y)W_\tau(x)\right),$$

where the sum of τ is performed with respect to the proton and the neutron, $\tau = p, n$. The functions $G_{E\tau}(y)$ and $F_{2\tau}(y)$ are obtained by inverse Fourier transformations of the Sachs and Pauli form factors, respectively. The nucleon density, $\rho_\tau(x)$, and the spin-orbit density, $W_\tau(x)$, are given by

$$\rho_\tau(r) = \sum_\alpha \frac{2j_\alpha+1}{4\pi r^2}\left(G_\alpha^2 + F_\alpha^2\right),$$

$$W_\tau(r) = \frac{\mu_\tau}{M}\sum_\alpha \frac{2j_\alpha+1}{4\pi r^2}\frac{d}{dr}\left(\frac{M-M^*(r)}{M}G_\alpha F_\alpha + \frac{\kappa_\alpha+1}{2Mr}G_\alpha^2 - \frac{\kappa_\alpha-1}{2Mr}F_\alpha^2\right). \quad (1)$$

In the above equations, G_α and F_α denote the large and small components of the single-particle wave function, respectively, $\kappa_\alpha = (-1)^{j-\ell+1/2}(j+1/2)$ the eigenvalue of $-(1+\boldsymbol{\sigma}\cdot\boldsymbol{\ell})$, and $M^*(r)$ the nucleon effective mass given by $M^*(r) = M - U_s(r)$, where $U_s(r)$ is the Lorentz scalar potential due to the σ-meson.

The relationship between the relativistic and non-relativistic models is very clear. In non-relativistic models, the neutron charge and spin-orbit charge densities are usually neglected in estimating the electron scattering cross section. Bertozzi *et al.*[3] took into account the neutron charge density and a part of the spin-orbit charge density in a non-relativistic framework. Their spin-orbit density was obtained from Eq. (1) by setting $M^*(r) = M$ and neglecting the F_α^2-term.

We have shown that the spin-orbit density due to the effective mass in Eq. (1) is very important in a relativistic model for reproducing the experimental data.[6]

* Department of Physics, Chiba University

References

1) D. Vautherin and D. M. Brink: Phys. Rev. C **5**, 626 (1972).
2) B. D. Serot and J. D. Walecka: Adv. Nucl. Phys. **16**, 1 (1986).
3) W. Bertozzi, J. Friar, J. Heisenberg, and J. W. Negele: Phys. Lett. B **41**, 408 (1972).
4) L. D. Miller: Phys. Rev. C **14**, 706 (1976).
5) H. Feshbach: *Theoretical Nuclear Physics: Nuclear Reactions* (John Wiley & Sons, New York, 1992).
6) H. Kurasawa and T. Suzuki: Phys. Rev. C **62**, 054303 (2000).

Analysis of the Matter Distribution of Nuclei with a Gaussian-Basis Expansion

A. Kohama, S. Yamaji, R. Seki,* and A. Arima

[NUCLEAR REACTION: Matter distribution of nuclei, χ^2-Fitting, Proton-nucleus elastic scattering]

The one-body matter-density distribution, $\rho(\mathbf{r})$, is a fundamental and important quantity for nuclear physics. A consistent study of this quantity for unstable as well as stable nuclei will result in a deeper understanding of nuclear-structure physics.

To this end, we have investigated a method to determine the density distribution of nuclei based on experimental data by a χ^2-fitting.[1] We have demonstrated how it is affected by the quality of data. This was done to prepare for upcoming experiments at the RI-Beam Factory of RIKEN.

For the above demonstration of χ^2-fitting we used pseudo-data which were created from random numbers distributed around the theoretical cross section of the proton-nucleus elastic scattering at various momentum transfers. We took the case of p-^{58}Ni scattering as an example, and generated 25 sets of pseudo-data forming a data-set group. A different data-set group corresponded to a different intensity of the nuclear beam.[2] The density-distribution, $\rho(\mathbf{r})$, was expanded in terms of a Gaussian series[3] in order to avoid any assumption concerning the functional form of the density. The expansion coefficients were determined by minimizing χ^2 between the theoretical cross sections and the pseudo-data;

$$\chi^2 = \sum_{\alpha=1}^{N} \frac{1}{\epsilon_\alpha^2} \left(\frac{d\sigma_\alpha^{\mathrm{data}}}{d\Omega} - \frac{d\sigma_\alpha^{\mathrm{theory}}}{d\Omega} \right)^2 .$$

Here, N is the number of data-points, and ϵ_α is the error of each data-point. The superscript "data" of the cross section implies pseudo-data, and "theory" implies the theoretically obtained value. We used the expression of the first-order optical potential in the Glauber approximation for the theoretical cross section, which includes the density-distribution explicitly.

We have found that the density distributions obtained with the Gaussian-basis functions show similar behavior at the surface, even if the quality of the data becomes worse, *i.e.*, the surface is determined well (Fig. 1). The statistical errors were found to be concentrated in the central region of $\rho(\mathbf{r})$, which is a similar situation to the charge-distribution. To apply the Gaussian-basis function for determining the density-distribution by a χ^2-fitting is a good way to see whether unstable nuclei have an extended structure.[4]

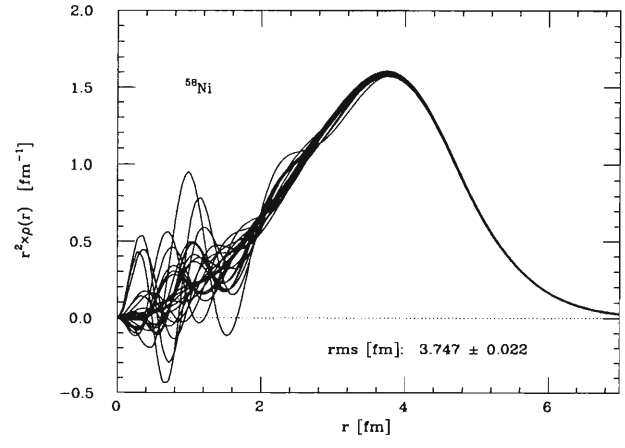

Fig. 1. Example of the results after a χ^2-fitting. The curves show the matter-density distributions, $r^2 \times \rho(r)$, obtained from 25 pseudo-data sets of the cross section. One curve corresponds to one pseudo-data set. The Gaussian-series expansion here contains 20 terms.

References

1) J. L. Friar and J. W. Negele: Adv. Nucl. Phys. **8**, 219 (1975).
2) A. Kohama, S. Yamaji, R. Seki, and A. Arima: in preparation.
3) E. Hiyama and M. Kamimura: Nucl. Phys. A **588**, 35c (1995).
4) I. Tanihata et al.: Phys. Lett. B **160**, 380 (1985).

* Department of Physics and Astronomy, California State University, Northridge, and W. K. Kellogg Radiation Laboratory, California Institute of Technology, USA

Microscopic Foundation of the Fermion Dynamical Symmetry Model: O(6) Limit

Y. M. Zhao,[*1] S. Yamaji, N. Yoshinaga,[*2] and A. Arima

[*SD* pair approximation, Fermion dynamical symmetry model]

The concept of dynamical symmetry has been widely applied in nuclear structure theory. The most successful approach is the interacting *sd* boson approximation of the shell model (IBM).[1] Similar to the IBM, the fermion dynamical symmetry model (FDSM)[2] uses SP(6) or SO(8) *SD* nucleon pairs to construct the subspace. However, the nucleon pairs in the FDSM are assumed to be symmetry dictated. The Hamiltonian in the FDSM is very different from the commonly used one.

Recently, we checked[3] using the *SD* pair approximation of the shell model (the NPA)[4] the assumptions made in the FDSM for a realistic ^{132}Ba nucleus which displays O(6) behavior in both the IBM and the FDSM. It was confirmed that those assumptions are reasonable for this nucleus. Based on this work, we have proposed a correspondence between a *SD*-pair subspace and the FDSM subspace. By applying a pairing plus quadrupole interaction the FDSM Hamiltonian parameters of nucleus ^{132}Ba nucleus are obtained via this correspondence. The parameters obtained in this way are consistent with those taken phenomenologically in the previous studies.[4] The FDSM calculation is performed using the calculated parameters. The calculated results agree with the experimental data very well.

References

1) A. Arima et al.: Ann. Phys. (N.Y.) **99**, 253 (1976); Ann. Phys. (N.Y.) **111**, 209 (1978); Ann. Phys. (N.Y.) **123**, 468 (1979).
2) C. L. Wu et al.: Phys. Rev. C **36**, 1157 (2000).
3) J. Q. Chen: Nucl. Phys. A **626**, 686 (1997); Y. M. Zhao et al.: Phys. Rev. C **62**, 014304 (2000).
4) Y. M. Zhao et al.: Phys. Rev. C **62**, 024322 (2000); Y. M. Zhao, S. Yamaji, N. Yoshinaga, and A. Arima: to be published.

*1 Department of Physics, Southeast University, China
*2 Department of Physics, Saitama University

TDHF Calculation of the Excitation of Isoscalar Giant Resonances

K.-H. Kim, S. Shlomo,[*1] and T. Otsuka[*2]

[Giant resonances, Random-phase approximation, Time-dependent Hartree-Fock]

Recently, experiments on the excitation of the giant resonances have been developed and some experimental data concerning the isoscalar giant monopole resonances (ISGMR) and isoscalar giant dipole resonances (ISGDR) have been obtained for several nuclei, such as ^{90}Zr, ^{116}Sn, ^{144}Sm and ^{208}Pb, by means of inelastic α scattering.[1)]

The situation concerning the ISGMR and ISGDR has changed. The location of the experimental data of the excitation energies of the ISGDR is found to be higher than results obtained from the Hartree-Fock (HF) random-phase-approximation (RPA) approach.[2)] Since the energies of the ISGMR and ISGDR are directly connected to nuclear matter incompressibility,[3)] it would be interesting not only to study the microscopic structure of giant resonances, itself, but also to determine the nulear matter incompressibility, which is important in relation to the equation of state.

It is considered that such a difference between the experimental data and the calculation is mainly due to the absence of full self-consistency between the mean field and particle-hole interaction in the RPA.[2)] In this study, we applied the time-dependent Hartree-Fock (TDHF) method[4)] to a calculation of the excitation of the ISGMR and ISGDR. In this method, the self-consistency is fully satisfied, and the Coulomb and spin-orbit terms, which are neglected in the RPA calculation, are included. Such a fully self-consistent calculation has not been done in RPA calculations so far.

Numerical calculations are now in progress. We calculate the strength function (S(E)) using the transition density obtained from the TDHF calculation and compare it with the result of the usual RPA calculation and the experimental data. We would like to know if only a partially self-consistent calculation is sufficient or whether full self-consistency is necessary, and also if effects of the Coulomb and spin-orbit terms show up in the calculation.

References

1) H. L. Clark et al.: Nucl. Phys. A **649**, 57c (1999).
2) M. L. Gorelik, S. Shlomo, and M. H. Urin: Phys. Rev. C **62**, 044301 (2000).
3) S. Shlomo and D. H. Youngblood: Nucl. Phys. A **569**, 303 (1994).
4) K.-H. Kim, T. Otsuka, and P. Bonche: J. Phys. G **23**, 1267 (1997).

*1 Cyclotron Institute, Texas A&M University, USA
*2 Department of Physics, University of Tokyo

Theoretical Search for Shears Bands in the A∼80 Mass Region

H. Madokoro, J. Meng,[*1] M. Matsuzaki,[*2] and S. Yamaji

[NUCLEAR STRUCTURE ^{84}Rb]

In previous work,[1] we examined the so-called shears band in ^{84}Rb, for which experimental data were obtained.[2] Our result concerning the relativistic mean field (RMF) model shows that this model can nicely reproduce the observed trends of the shears band in ^{84}Rb. In spite of the fact that many high-K bands have been observed in this mass region, very few of them have been assigned as shears bands up to now. It is an interesting topic to clarify, from a theoretical point of view, whether or not there exist other shears bands which have not been observed in this region.

As the first work in this direction, we notice the $N = 47$ isotones, which have the same configuration as the observed shears band in ^{84}Rb, and therefore are considered to be good candidates for new shears bands. Here, we examine ^{82}Br and ^{83}Kr.

We use the RMF model, which is a fully microscopic one with more sophisticated interaction than the simple pairing + QQ force. The RMF model can be generalized to a uniformly rotating frame with a constant rotational frequency, $\boldsymbol{\Omega} = (\Omega_1, \Omega_2, \Omega_3)$.[3,4] The resulting coupled equations of motion are solved by expanding both the nucleon and meson fields in terms of the three-dimensional harmonic oscillator eigenfunctions. A parameter set named NL3 is used in all of our calculations. For ^{82}Br and ^{83}Kr, the proton and neutron configurations in the high-j ($1g_{9/2}$) orbital are assumed to be the same as those of ^{84}Rb. Only those in the low-j (pf) orbitals for protons are different.

The calculated tilt angles (θ) for ^{82}Br and ^{83}Kr, which are measured from the 3-axis in a body-fixed frame are shown in Fig. 1. Also displayed is the result of ^{84}Rb, which is taken from Ref. 1. For ^{84}Rb, it stays at $\theta \sim 55$–$65°$ and is comparable with the predicted property of the shears bands, while in the case of ^{82}Br and ^{83}Kr, the tilt angles are larger and move toward $\theta \sim 90°$ along with an increase in the rotational frequency. This trend is similar to that seen in normal high-K bands in well-deformed nuclei, rather than the shears bands.

Figure 2 shows the $B(\mathrm{M1})/B(\mathrm{E2})$ ratio. We can see that for ^{84}Rb the expected tendency of a smooth decrease is well reproduced. For ^{82}Br and ^{83}Kr, on the other hand, the calculated $B(\mathrm{M1})/B(\mathrm{E2})$ values do not show such a decrease. From these results, we can consider that these two bands calculated for ^{82}Br and ^{83}Kr will not be shears bands. The difference between ^{84}Rb and other isotones can be attributed to the net contribution to the total spin from the low-j pf-shells.

Table 1 shows $\boldsymbol{J}_{pf}^{(p)}$, which represents the net contribution from the low-j (pf) proton levels. Clearly, the main difference between ^{84}Rb and other isotones

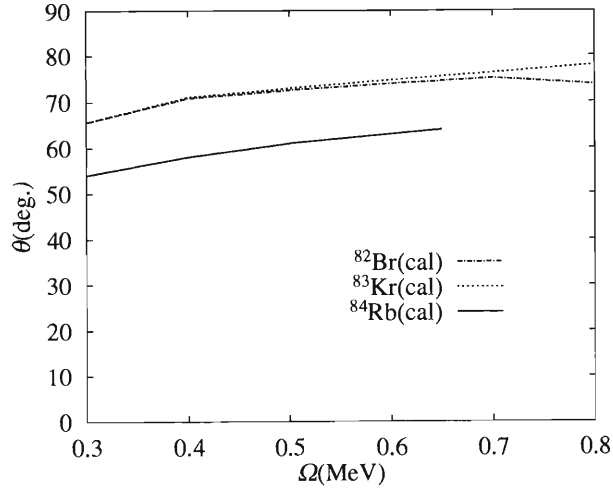

Fig. 1. Tilt angles as functions of the rotational frequency.

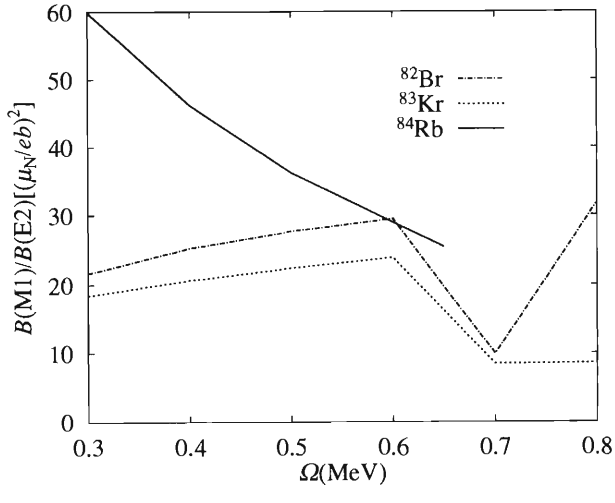

Fig. 2. $B(\mathrm{M1})/B(\mathrm{E2})$ ratio as functions of the rotational frequency.

Table 1. Net contribution from the proton pf-levels.

	$\boldsymbol{J}_{pf}^{(p)}$
^{82}Br	(1.7, 0.0, 0.2)
^{83}Kr	(1.3, 0.0, 0.0)
^{84}Rb	(1.0, 0.0, 2.5)

*1 Department of Technical Physics, Peking University, China
*2 Department of Physics, Fukuoka University of Education

is the 3-component of $\boldsymbol{J}_{pf}^{(p)}$. This difference stems from the fact that in ^{84}Rb only one of the [303]5/2 levels ($k = \pm 5/2$) is occupied, while for other isotones both of the [303]5/2 levels are empty. We can say that the spin-polarization in the [303]5/2 levels is important for the appearance of the shears bands in this case. Systematic studies would be necessary in order to give a definite conclusion on the condition for the appearance of the shears bands.

References

1) H. Madokoro, J. Meng, M. Matsuzaki, and S. Yamaji: Phys. Rev. C **62**, R61301 (2000).
2) H. Schnore et al.: Phys. Rev. Lett. **82**, 4408 (1999).
3) W. Koepf and P. Ring: Nucl. Phys. A **493**, 61 (1989); Nucl. Phys. A **511**, 279 (1990).
4) H. Madokoro and M. Matsuzaki: Phys. Rev. C **52**, R2934 (1997).

Study of Rotational Motion in Unstable Nuclei

T. Nakatsukasa, H. Madokoro, and T. Horibata*

[Rotational motion, Unstable nuclei, Cartesian mesh method]

The aim of this work is to study the structure of unstable nuclei near the drip line which are expected to be produced in the RI-beam factory of RIKEN. The target mass region of our study is light mass deformed nuclei in which the mean-field approximation is considered to be well valid. In the region where we focus our attention, there are several topics, such as the nuclear shape at the high-spin region and the stability of a loosely bound system against rotational motion. Especially the shape of nuclear deformation has great concern with any exotic nuclear rotational motion. Therefore, a detailed study on the density distribution of nucleons near the surface would be indispensable to understand the excitation modes which are expected to be found in this mass region.

As for the numerical technique, a well-adopted method to solve the Hartree-Fock-Bogoliubov (HFB) equations in a self-consistent manner is to expand the wave functions in terms of some basis functions. A typical and frequently used example is the eigenfunction of a three-dimensional harmonic oscillator. This method, however, is not suitable for cases in which we do not know *a priori* the asymptotic form of the wave functions, for example, the case of unstable nuclei near the drip line, which may or may not have halo structures. On the other hand, for a search of exotic deformations, which is also one of the most interesting topics in the study of unstable nuclei, the basis-expansion method is not very good, thus requiring us to optimize the deformation parameters of the basis function.

These shortcomings come from the fact that the assumed shape of the basis functions may affect the resulting shape of the wave functions. Therefore, an alternative method is desired in our case. For such purposes, the Cartesian mesh method based on the Skyrme-type interactions is one of the most promising techniques, and has been frequently employed.[1] The scope of our work is to develop a computer code which can handle the higher order correlations of nuclei as well as the pairing correlation by incorporating the three-dimensional cranking approach, the random-phase approximation, the generator coordinate method as well as the angular-momentum projection technique.

As a first step in our investigation, we have just developed a computer code which can carry out Hartree-Fock calculations based on the relatively simple density dependent force involved in the Cartesian mesh method.[2] A trial calculation of ^{16}O is in progress. In the future, the code will be extended to perform calculations with more sophisticated interactions, such as the Skyrme force (Skyrme-Hartree-Fock) or the relativistic meson exchange force (relativistic mean field).

References

1) P. Bonche, H. Flocard, P. H. Heenen, S. J. Krieger, and M. S. Weiss: Nucl. Phys. A **443**, 39 (1985); N. Tajima, S. Takahara, and N. Onishi: Nucl. Phys. A **603**, 23 (1996); M. Yamagami and K. Matsuyanagi: Nucl. Phys. A **672**, 123 (2000).
2) H. Flocard, S. E. Koonin, and M. S. Weiss: Phys. Rev. C **17**, 1682 (1978).

* Aomori University

Pseudospin Symmetry and Spin Symmetry

K. Sugawara-Tanabe,* S. Yamaji, and A. Arima

[Pseudospin, Spin, Relativistic mean-field, Symmetry, Deformed field]

The pseudospin concept in deformed nuclei is as follows. The single-particle levels with $j_z = \Omega = \ell_z + 1/2$, and $j'_z = \Omega + 1 = \ell_z + 2 - 1/2$ lie very close in energy; these two levels are labeled $j_z = \tilde{\ell}_z - 1/2$ and $j'_z = \tilde{\ell}_z + 1/2$ with $\tilde{\ell}_z = \ell + 1$. In this paper, we compare the pseudospin pair levels, $\tilde{\ell}_z \pm 1/2$, with the spin pair levels, $\ell_z \pm 1/2$, in a relativistic mean-field. The eigenfunction $\psi(\vec{r})$ for the Dirac equation with an axially symmetric deformed potential has two components, *i.e.*, an upper (large) component g and a lower (small) component f. Using a cylindrical coordinates (r, φ, z), each g and f in $\psi(\vec{r})$ has two amplitudes, *i.e.*, $g^{\Omega}_{\pm,k}$ and $f^{\Omega}_{\pm,k}$, where k denotes the other quantum numbers except for Ω, and $\pm$ corresponds to the spin wave function with $s_z = \pm 1/2$. Both of $g^{\Omega}_{\pm,k}$ and $f^{\Omega}_{\pm,k}$ are functions of r and z. By inserting this definition into the Dirac equation, we obtain an equation for $g^{\Omega}_{\pm,k}$ which has a similar form to that for $f^{\Omega}_{\pm,k}$.

Let us assume the case where the exact pseudospin doublet appears, *i.e.*, $\partial V_V/\partial z = 0$, which is equivalent to $\partial V_S/\partial z = 0$, and $\partial V_V/\partial r = 0$, equivalent to $\partial V_S/\partial r = 0$ (see Ref. 1). In the pseudospin pair levels, k corresponds to $[N, n_z, \ell_z]$, and k' to $[N, n_z, \ell_z + 2]$, if we use the asymptotic quantum number. Then, the equation for $g^{\Omega+1}_{+,k'}$ ($f^{\Omega+1}_{+,k'}$) and that for $g^{\Omega}_{-,k}$ ($f^{\Omega}_{-,k}$) become the same form, except for the energy eigenvalue, $E_{\Omega+1,k'}$ and $E_{\Omega,k}$. We wish to mention the other amplitudes of the pseudospin pair levels, *i.e.* $f^{\Omega}_{+,k}$ ($g^{\Omega}_{+,k}$) and $f^{\Omega+1}_{-,k'}$ ($g^{\Omega+1}_{-,k'}$). Under the same conditions to derive the exact pseudospin doublet, they follow different equations. In addition to the difference in $E_{\Omega+1,k'}$ and $E_{\Omega,k}$, the centrifugal term is different. The centrifugal term is proportional to $\Omega - 1/2$ for $f^{\Omega}_{+,k}$ ($g^{\Omega}_{+,k}$) and $\Omega + 3/2$ for $f^{\Omega+1}_{-,k'}$ ($g^{\Omega+1}_{-,k'}$), respectively. Because the pseudospin is for two levels with $[N, n_z, \ell_z]\Omega(= \ell_z + 1/2)$ and $[N, n_z, \ell_z + 2]\Omega + 1 (= \ell_z + 3/2)$, ℓ_z is $\Omega - 1/2$ for the former level and $\ell_z + 2 = \Omega + 3/2$ for the latter level. The amplitudes $f^{\Omega}_{+,k}$ and $f^{\Omega+1}_{-,k'}$ ($g^{\Omega}_{+,k}$ and $g^{\Omega+1}_{-,k'}$) correspond, respectively, to these pair levels, because the centrifugal term corresponds to the z-component of the orbital angular momentum. On the other hand, $f^{\Omega}_{-,k}$ ($g^{\Omega}_{-,k}$) and $f^{\Omega+1}_{+,k'}$ ($g^{\Omega+1}_{+,k'}$) have unnatural $\ell_z = \Omega + 1/2$. Thus, the amplitudes where the pseudospin symmetry is found have unnatural ℓ_z. We name them unphysical amplitudes, and call the amplitudes with natural ℓ_z physical amplitudes. Of course, the energy eigenvalue $E_{\Omega,k}$ is the same for all four amplitudes in the level with the same Ω and k, *i.e.*, $g^{\Omega}_{+,k}$, $g^{\Omega}_{-,k}$, $f^{\Omega}_{+,k}$ and $f^{\Omega}_{+,k}$.

We now consider the spin-pair levels, *i.e.* the levels with $j_z = \ell_z + 1/2$ and $j'_z = \ell_z - 1/2$. In this case the spin pair levels are denoted by $[N, n_z, \ell_z]\Omega(= \ell_z - 1/2)$ and $[N, n_z, \ell_z]\Omega + 1 (= \ell_z + 1/2)$. Then, k equals to k' corresponding to $[N, n_z, \ell_z]$. The physical amplitudes become $f^{\Omega}_{-,k}$ ($g^{\Omega}_{-,k}$) and $f^{\Omega+1}_{+,k}$ ($g^{\Omega+1}_{+,k}$), because both states have $\ell_z = \Omega + 1/2$. On the other hand, $f^{\Omega}_{+,k}$ and $f^{\Omega+1}_{-,k'}$ ($g^{\Omega}_{+,k}$ and $g^{\Omega+1}_{-,k'}$) become unphysical amplitudes.

In a numerical analysis,[1] we have confirmed that the absolute values of the unphysical amplitudes in the large and small components agree each other for the pseudospin pair levels, while the absolute values of physical amplitudes in both of large and small components agree for the spin pair levels. It is very different from the case concerning spherical nuclei, in which the pseudospin symmetry is found in the small component, while the spin symmetry is found in the large component. Another fact we found is that the conditions for the pseudospin symmetry is also the conditions for the spin symmetry in deformed nuclei. Because the deformation mixes ℓ and j, the deformation mixes the spin symmetry and the pseudospin symmetry in the relativistic mean field.

References

1) K. Sugawara-Tanabe, S. Yamaji, and A. Arima: Phys. Rev. C **62**, 052010 (2000).

* Otsuma Women's University

Delta-Hole Interaction in Nuclei and the Gamow-Teller (GT) Strength in ^{90}Nb

A. Arima, W. Bentz,[*1] T. Suzuki,[*2] and T. Suzuki[*3]

[Landau-Migdal parameters, Quenching of Gamow-Teller strength, Δ-hole interaction]

We performed a calculation[1] of the GT sum rule in ^{90}Nb, using the $\pi + \rho$ meson-exchange model. The results are given in Table 1. The calculated quenching factor (S_-/S_{0-}) is consistent with the recently measured value[2] (0.9 ± 0.05) within the error bars, if the quark-model value of the strength of the transition potential, $f_\Delta/f_\pi = \sqrt{72/25}$, is used; but for the Chew-Low model value $f_\Delta/f_\pi = 2$ the theoretical quenching is too strong. The corresponding values for the Landau-Migdal (L.M.) parameter $g'_{\mathrm{N}\Delta}$ are also given in Table 1.

The 'empirical' values of $g'_{\mathrm{N}\Delta}$, determined such as to reproduce the experimental quenching factor, are given in Table 2. The case '$V_{L.M.}$ only' corresponds to the calculation of Ref. 3, which we extended in this work by also including the finite-range parts of the $\pi + \rho$ exchange potentials.

The resulting value of $g'_{\mathrm{N}\Delta}$ is consistent with the meson-exchange pitcure (Table 1) within the error bars, if the quark model value for f_Δ/f_π is used, though a discepancy remains for the Chew-Low model value. An interesting problem is whether or not these relatively small values of $g'_{\mathrm{N}\Delta}$ are in conflict with the absence of pion condensation and precursor phenomena under normal conditions.

Table 1. Quenching factors and values of $g'_{\mathrm{N}\Delta}$.

	(a) $\frac{f_\Delta}{f_\pi} = \sqrt{\frac{72}{25}}$		(b) $\frac{f_\Delta}{f_\pi} = 2$	
	S_-/S_{0-}	$g'_{\mathrm{N}\Delta}$	S_-/S_{0-}	$g'_{\mathrm{N}\Delta}$
π only	0.904	0.25	0.867	0.25
$\pi + \rho$	0.857	0.35	0.805	0.35

Table 2. 'Empirical' values of $g'_{\mathrm{N}\Delta}$.

	(a) $\frac{f_\Delta}{f_\pi} = \sqrt{\frac{72}{25}}$	(b) $\frac{f_\Delta}{f_\pi} = 2$
$V_{L.M.}$ only	0.18 ± 0.09	0.13 ± 0.07
$V_{L.M.} + V_\pi$	0.26 ± 0.09	0.20 ± 0.07
$V_{L.M.} + V_{\pi+\rho}$	0.27 ± 0.09	0.21 ± 0.07

References
1) A. Arima, W. Bentz, T. Suzuki, and T. Suzuki: Phys. Lett. B **499**, 104 (2001).
2) T. Wakasa et al.: Phys. Rev. C **55**, 2909 (1997).
3) T. Suzuki and H. Sakai: Phys. Lett. B **455**, 25 (1999).

*1 Department of Physics, Tokai University
*2 Department of Physics, Nihon University
*3 Department of Applied Physics, Fukui University and RIKEN

Relativistic Hartree-Bogoliubov Approach for Nuclear Matter with Non-Linear Coupling Terms

S. Sugimoto,[*1] K. Sumiyoshi,[*2] and H. Toki[*1]

[Relativistic Hartree-Bogoliubov theory]

We investigated the pairing property of nuclear matter using the Relativistic Hartree-Bogoliubov (RHB) approach. We have extended the RHB approach to be able to include non-linear coupling terms of mesons. We applied it to nuclear matter and observed the effect of non-linear terms on pairing gaps.

Recently, the relativistic mean field (RMF) theory is being widely applied to nuclear matter and finite nuclei. It is known that RMF theory can reproduce nuclear properties quantitatively.[1)] In RMF theory, it is very important to include the pairing interaction on the same footing as the density correlations. Usually, it is implemented by the so-called BCS-type theory as in other mean-field theory. In the BCS-type theory the pairing interaction is implemented by hands outside of the RMF theory. However, we would like for the pairing interaction to be described in a relativistic many-body theoretical manner within the RMF theory. One possibility toward this attempt is the relativistic Hartree-Fock-Bogoliubov theory (RHBF), which was formulated by Kucharek *et al.*[2)] Recently, the Hartree-Fock-Bogoliubov (HFB) theory is being widely used in both the non-relativistic and relativistic mean-field calculations. It can treat the usual mean field and the pairing field simultaneously. The HFB theory has been applied to nuclear matter and finite nuclei, both relativistically and non-relativistically with many interesting results.

However, until now the effect of the non-linear self-coupling terms of mesons was neglected in the pairing channel in the RHB theory. It is known that those non-linear terms are needed to reproduce the properties of nuclear matter and finite nuclei in the RMF theory.[3,4)] We can suppose that those terms have some effect on the pairing correlations. Therefore, we would like the relativistic Hartree-Fock-Bogoliubov theory to include the effect of the non-linear self coupling term of mesons, and to apply it to nuclear matter to see the effect on the pairing gap (Δ).

In Fig. 1 we show the pairing gap at the Fermi momentum (k_F[fm^{-1}]) as a function of the density measured in the Fermi momentum. We use the parameter set TM1,[4)] which has both σ non-linear coupling and ω non-linear coupling terms. In this figure, "With N. L."(solid line) means we include the non-linear term effect on the pairing channel and "Without N. L."(dashed line) means we do not include it. From this figure we can see that the pairing gap is reduced by a few MeV by including the non-linear term of mesons. In our formalism the effect of the non-linear terms appears in the propagators in the pairing channel. It increases the mass parameters of mesons in the propagators and reduces the interaction in the pairing channel. This effect is especially large around $k_F = 1.0$ [fm^{-1}].

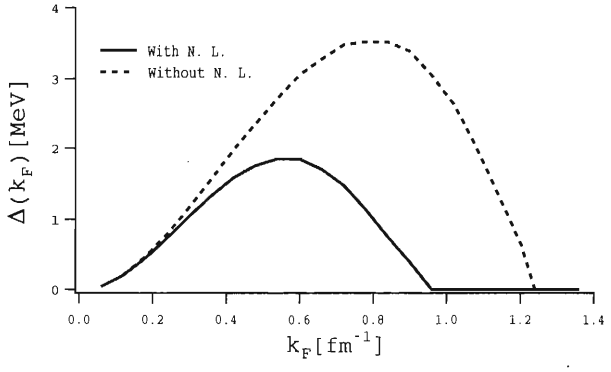

Fig. 1. Pairing gap (Δ) at the Fermi momentum (k_F) in the function of the Fermi momentum. The TM1 parameter set is used. "With N. L."(solid line) corresponds to the case in which the non-linear term of mesons are implemented. "Without N. L." corresponds to the case without them.

We give a brief summary. A new framework has been developed to incorporate non-linear terms of mesons in the pairing channel in the RHFB theory. We have applied the RHB theory to nuclear matter to check the effect of non-linear terms on the p-p channel. We have found that the non-linear terms reduce Δ at the Fermi momentum, especially for the normal-density region. It would be interesting to apply our method to asymmetric nuclear matter or finite nuclei.

References

1) P. Ring: Prog. Part. Nucl. Phys. **37**, 193 (1996).
2) H. Kucharek et al.: Z. Phys. A **339**, 23 (1991).
3) J. Boguta et al.: Nucl. Phys. A **292**, 413 (1977).
4) Y. Sugahara et al.: Nucl. Phys. A **579**, 557 (1994).

*1 Research Center for Nuclear Physics, Osaka University
*2 Numazu College of Technology

Extended Renormalized Random-Phase Approximation†

N. Dinh Dang and A. Arima

[Renormalized random-phase approximation, Ground-state correlations]

The set of linear equations of the random-phase approximation (RPA) is usually obtained within the quasiboson approximation, which treats the particle-hole (ph) pair-creation $B^{\dagger}_{ph}$ and annihilation B_{ph} operators as if they are bosons. This leads to a violation of the Pauli principle. As a consequence, the RPA breaks down at a certain critical value of the interaction strength, where the RPA solution becomes imaginary. The renormalized RPA (RRPA) is an approach to correct for this inconsistency, taking into account the effect of ground-state correlation (GSC) beyond the RPA. This approach has been reformulated in the recent Ref. 1, where an improvement in the estimation of the GCS has been obtained compared to the approach originally proposed by Hara.[2)]

Recently, there has been a renewed interest in the RRPA for its application to microscopic descriptions of single and double beta decays. Further studies of the RRPA and renormalized quasiparticle RPA (RQRPA) have been reported. The studies of RRPA have so far been limited within the ph channel, neglecting the pp and hh interactions. In the RQRPA, this corresponds partly to omission of the so-called scattering terms in the model Hamiltonian, whose effect is strongest for the particle-particle (pp) and/or hole-hole (hh) configurations. It has been suggested that the omission of such terms may be the reason of the strong violation within the RRPA of certain model-independent sum rules, which are well fulfilled within the RPA, such as the Ikeda sum rule for the charge-exchange transitions.

In the present paper, the RPA is fully renormalized to take into account the GSC beyond the RPA, which arises due to the fermion structure of the collective RPA operators. As compared to the conventional renormalized RPA (RRPA), the novelty of the present extended renormalized RPA (ERRPA) is the inclusion of the particle-particle (pp) and hole-hole (hh) GSC beyond the RPA along with the ph ones in the complete set of ERRPA equations. The formalism is illustrated by numerical calculations within a schematic four-level model. The results show that the effects of GSC beyond the RPA due to pp (and hh) transitions can cause a partial or complete compensation of the ones due to ph transitions. This reduces the deviation from the RPA energy-weighted sum of strength within the ERRPA as compared to that within the conventional RRPA.

References

1) F. Catara, N. Dinh Dang, and M. Sambataro: Nucl. Phys. A **579**, 1 (1994).
2) K. Hara: Prog. Theor. Phys. **32**, 88 (1964).

† Condensed from the article in Phys. Rev. C **62**, 024303 (2000)

Exact Form of the Random-Phase Approximation Equation at Finite Temperature Including the Entropy Effect†

K. Tanabe* and N. Dinh Dang

[Thermal random phase approximation, Entropy effect]

Recent experimental studies of the damping of giant dipole resonances (GDR) built on hot nuclei have supplied useful information for checking the theoretical models and methods, which have been successful in describing the properties of the nuclear states in the yrast region, and have been extensively applied to the highly excited states above the yrast line. As such an extension of microscopic formalism, the thermal random-phase approximation (TRPA) equation[1,2] on top of the thermal Hartree-Fock-Bogoliubov (THFB), or the thermal Hartree-Fock (THF) solution when the pairing correlation is not important, is expected to describe the temperature-dependent behavior of the hot GR. For this purpose, the formalism has to be guaranteed not only to smoothly tend to the ordinary RPA in the zero-temperature limit, but also to solve the problem of the discrepancy between the TRPA matrix and the THFB stability matrix.[1)]

In the present paper we have shown detailed steps for the variational derivation of the exact thermal RPA (TRPA) equation whose matrix representation precisely corresponds to the thermal HFB (THFB) stability matrix. This equation describes an interplay between the collective excitation and the entropy effect. It must be noticed that the extended parts of the TRPA matrix represent the temperature effect arising from the ground state correlations modified by the existing collective mode as well as the entropy effect. However, the giant resonance shape is not much affected by the entropy effect unless the coupling of the collective modes to particle-hole (ph) configurations is sufficiently strong, since the entropy effect is described in terms of the second order in the coupling constant. Based on the energy-weighted sum rule (EWSR) extended to a finite temperature, we can point out a possibility that, in case of the GDR, the increasing contributions arising from the entropy effect compensates the decreasing EWSR with temperature so that the sum of both contributions gives a value which does not depend on the temperature. Making use of a simple microscopic model, we have studied the effect of the particle-particle (pp) and hole-hole (hh) configurations on the Landau splitting of the GDR. We find that these configurations play decisive roles in the temperature-dependent phenomena of the GDR built on a hot nucleus. The distortion of the Fermi distribution due to a temperature effect allows the damping of GDR *via* the pp and hh configurations and the Landau splitting width of the GDR increases with increasing the temperature. Since this general mechanism works also in the damping of GDR *via* four-quasiparticle configurations, it can be inferred that the increase in the spreading width is controlled mainly by the $pppp$, $ppph$, $phhh$ and $hhhh$ configurations. This physical picture is consistent with the theoretical expectation based on the standard TRPA in the quasiparticle picture and the recent approaches within the phonon damping model.[3)] It should be remarked that the change of the mean field with temperature, due to the change of pairing correlation and deformation, which are not considered in the present model, are important at low temperatures. Therefore, for the purpose of investigating the temperature dependence of GDR phenomena, it is the most desirable to consider realistic nuclei the TRPA calculations on top of the self-consistent solution to the thermal HFB equation.

References

1) K. Tanabe and K. Sugawara-Tanabe: Phys. Lett. B **172**, 129 (1986).
2) N. Dinh Dang: J. Phys. G **11**, L125 (1985).
3) N. Dinh Dang and A. Arima: Phys. Rev. Lett. **80**, 4145 (1998); N. Dinh Dang, K. Tanabe, and A. Arima: Phys. Rev. C **58**, 3374 (1998).

† Condensed from the article in Phys. Rev. C **62**, 024310 (2000)

* Department of Physics, Faculty of Science, Saitama University

Electromagnetic Cross Sections of Double Giant Dipole Resonances in ^{136}Xe and ^{208}Pb within the Phonon Damping Model†

N. Dinh Dang, V. Kim Au,* and A. Arima

[Anharmonicity, Double giant dipole resonance, Electromagnetic cross section]

The recent observation of double giant dipole resonances (DGDR) in heavy-ion collisions at near-relativistic energies[1] has been a challenge for the theoretical studies of multiphonon excitations. According to the independent-phonon (or harmonic) picture, a DGDR is considered to be a two-dipole-phonon resonance, which is a (single-phonon) giant dipole resonance (GDR) built on top of another (single-phonon) GDR. As such, the DGDR parameters can be calculated by folding two independent GDRs. As a result, the DGDR energy ($E_{\rm DGDR}$) is found to be $2E_{\rm GDR}$ ($E_{\rm GDR}$ is the GDR energy), and the DGDR full width at the half-maximum (FWHM) ($\Gamma_{\rm DGDR}$) is equal to $2\Gamma_{\rm GDR}$ ($\Gamma_{\rm GDR}$ is the GDR FWHM), if folding Lorentzian photoabsorption cross sections is used, or to $\sqrt{2}\Gamma_{\rm GDR}$, if Gaussians are folded. The experimentally extracted energy and width of DGDR differ slightly from these values. The energy shift ($\Delta E \equiv 2E_{\rm GDR} - E_{\rm DGDR}$) is a few hundred keV for ^{136}Xe, while the relation $\sqrt{2}\Gamma_{\rm GDR} \leq \Gamma_{\rm DGDR} \leq 2\Gamma_{\rm GDR}$ has been observed. Anharmonicities are usually referred to as a reason for these deviations from the independent-phonon picture. The most striking result is that the values of the experimentally extracted cross section of electromagnetic (EM) (or Coulomb) excitation for the DGDR are much larger than that given by the folding model. The enhancement is found to be around 178–200% in reactions with ^{136}Xe projectiles at 700 MeV/n kinetic energy, and around 133% using ^{208}Pb projectiles at 640 MeV/n kinetic energy, bombarding a ^{208}Pb target. A number of theoretical approaches has been developed to study the multiphonon giant resonances. Most of them can satisfactorily describe the energy, and even the width, of the DGDR, but a simultaneous description of both the observed GDR and DGDR cross sections is still an open question. Different theoretical models give so far the values of DGDR cross section, which are identical, or quite close, to that of the folding model, *i.e.* much smaller than the experimental values.

Recently, an approach to the multiphonon GDR in heavy nuclei has been proposed,[2] which makes use of the phonon damping model (PDM).[3] This approach allows one to calculate microscopically the strength function of the multiphonon GDR using the same set of PDM parameters, which have been selected to well describe the GDR. The calculated DGDR energy and FWHM are found to be in reasonable agreement with the experimental data. It has also been found that there is a significant difference between the DGDR in open-shell nuclei and that in closed-shell nuclei due to anharmonicities. The DGDR energy-weighted sum of strength in an open-shell nucleus (^{120}Sn) is larger than that given by the folding model by around 30%, while the DGDR in a closed-shell nucleus (^{208}Pb) is found to be rather harmonic.

In the present paper the EM cross sections of DGDR in ^{136}Xe and ^{208}Pb are calculated using the strength functions obtained within PDM. The parameters of the model have been selected to describe reasonably well the single GDR in these nuclei. The results are found to be in overall agreement with the recent experimental data for the DGDR cross sections in exclusive measurements at near-relativistic energies by the LAND collaboration (GSI).

References

1) R. Schmidt et al.: Phys. Rev. Lett. **70**, 1767 (1993); K. Boretzky et al.: Phys. Lett. B **384**, 30 (1996); K. Boretzky et al.: talk at the workshop on "Double Giant Resonance," Trento, Italy, May 10–22, 1999, unpublished.
2) N. Dinh Dang, K. Tanabe, and A. Arima: Phys. Rev. C **59**, 3128 (1999); Nucl. Phys. A **675**, 531 (2000).
3) N. Dinh Dang and A. Arima: Phys. Rev. Lett. **80**, 4145 (1998), Nucl. Phys. A **636**, 443 (1998); N. Dinh Dang, K. Tanabe, and A. Arima: Phys. Rev. C **58**, 3374 (1998).

† Condensed from the article in Phys. Rev. Lett. **85**, 1827 (2000)

* Institute of Theoretical Physics, Vietnam. Address after January 1, 2001: Texas A & M University, USA

Angular-Momentum Effect on the Width of the Hot Giant Dipole Resonance within the Phonon Damping Model

N. Dinh Dang, A. Ansari,* and A. Arima

[Angular momentum, Giant resonances, Thermal and statistical models]

One of the important issues in studying the giant dipole resonance (GDR) built on highly excited nuclei (hot GDR) is to separate the effects due to the temperature (T) and angular momentum (J) on the GDR width. Inelastic α-scattering measurements in ^{120}Sn and ^{208}Pb have shown that the increase in the GDR width with increasing T up to $T \simeq 3.2$ MeV is mainly a temperature effect, since their results, obtained at an averaged $\langle J \rangle$ of $\sim$ 5–20 $\hbar$, coincide with the heavy-ion fusion data obtained at $\langle J \rangle \sim$ 20–45 $\hbar$. Meanwhile, the inclusive heavy-ion fusion measurements of GDR in lighter tin isotopes, ^{106,109,110}Sn, at $T \simeq 1.8$ MeV[1] show an increase in the GDR width by ~ 2 MeV as J increases from 40 to 54 $\hbar$. The angular-momentum effect on the GDR width was studied by several approaches, where the increase in the GDR width as a function of J is induced by averaging over the intrinsic degrees of freedom that describe the thermal fluctuations of the quadrupole shapes.

In the recently developed phonon damping model (PDM),[2,3] it has been shown that the mechanism responsible for the temperature dependence of the GDR width is the coupling of the GDR phonon to particle-particle and hole-hole configurations, which appear due to the fact that the Fermi surface is deformed at $T \neq 0$. This allows the PDM strength functions to be calculated directly in the laboratory frame without any need for an explicit inclusion of the thermal fluctuations of shapes. The PDM is the only up-to-date model that can give a simultaneous and satisfactory description not only for the GDR width,[1] but also for its shape,[4] as well as the integrated yields of γ-emission[3] as a function of T in good agreement with recent experimental data. It is also the only model which can give a consistent description for both the width's increase at low $T \leq 3$ MeV and the width's saturation at high $T \geq 4$ MeV. The angular-momentum effect has not yet been taken into account in the PDM.

In this work the effect of angular momentum on the width of GDR in highly excited nuclei was studied within the phonon damping model by introducing an effective temperature ($\tilde{T}$) as a function of the nuclear temperature (T) and angular momentum (J). The results of numerical calculations for the GDR's width in ^{106}Sn obtained at $T = 1.8$ MeV as a function of J are in good agreement with the recent experimental data. The angular-momentum effect on the GDR width decreases with increasing T and vanishes at $T > 4$ MeV, where the width saturates.

References

1) A. Bracco et al.: Phys. Rev. Lett. **74**, 3748 (1995); M. Matiuzzi et al.: Nucl. Phys. A **612**, 262 (1997).
2) N. Dinh Dang and A. Arima: Nucl. Phys. A **636**, 427 (1998).
3) N. Dinh Dang, K. Tanabe, and A. Arima: Nucl. Phys. A **645**, 536 (1999).
4) N. Dinh Dang, K. Eisenman, J. Seitz, and M. Thoennessen: Phys. Rev. C **61**, 027302 (2000).

* Institute of Physics, Bhubaneswar, India

Thermal Shape and Orientation Fluctuation Corrections for the Hot Giant Dipole Resonance within the Static Path Approximation

A. Ansari,* N. Dinh Dang, and A. Arima

[Giant dipole resonance, Thermal fluctuations of shapes and orientations, Static path approximation]

The study of the giant dipole resonance (GDR) at high temperatures and spins is still an active area of investigations both experimentally and theoretically. There is a need for a fully microscopic approach that employs an effective many-body Hamiltonian, which can reproduce the dependence of the GDR width (Γ) and the shape as a function of the temperature (T) and spin (J). Recently, a microscopic scheme was proposed in Ref. 1 in which the γ-absorption cross section ($\sigma(E)$) as a function of the γ-ray energy (E) is computed in the linear-response theory at finite temperature with averaging over the fluctuating shape parameters within the static path approximation (SPA) to the grand canonical partition function. The angular-momentum dependence is included following the standard cranking approach. Very recently,[2] we applied this approach to study the GDR parameters in ^{120}Sn. It was found that although the increase of Γ with T is very week, the average over the shape fluctuations within SPA can provide a reasonable dependence on J. However, corrections for the fluctuation of the orientation angles of the rotational axis were not included.

As a continuation of the above-mentioned work, we have attempted here to investigate the effect of the orientation fluctuation corrections with numerical calculations performed for ^{106}Sn. Because this nucleus is lighter than ^{120}Sn, we expect a stronger dependence of Γ as well as of the average of deformation parameters on the angular momentum. The γ-absorption cross section of ^{106}Sn is calculated at temperature $T = 2$ MeV and angular momenta $J = 40$ and 55 $\hbar$ following the linear response theory at finite temperature and incorporating the thermal shape as well as orientation fluctuation corrections within the SPA. The orientation fluctuation corrections have been included for the first time in such a calculation, and are found to be rather unimportant. Then, the GDR was calculated without these effects at several more temperature and spin values. We find that at $T = 4$ MeV the GDR width (Γ) shows an increase of only about 1.5 MeV compared to its value at $T = 0.5$ MeV. However, at a fixed temperature of $T = 2$ MeV, the increase in the width at $J = 69\hbar$ is by about 3 MeV compared to its value at $J = 0$. Finally, we also compared the increase of Γ at $T = 2$ MeV as a function of J for ^{106}Sn and ^{120}Sn. The increase is steeper for the lighter isotope, as expected.

References

1) B. K. Agrawal, A. Ansari, and P. Ring: Nucl. Phys. A **615**, 183 (1997).
2) A. Ansari, N. Dinh Dang, and A. Arima: Phys. Rev. C **62**, R011302 (2000).

* Institute of Physics, Bhubaneswar, India

Adiabatic Selfconsistent Collective Coordinate Method for Large-Amplitude Collective Motion†

M. Matsuo,*1 T. Nakatsukasa, and K. Matsuyanagi*2

[Nuclear structure models and methods, Hartree-Fock and random-phase approximations]

Large-amplitude collective motion (LACM), such as fission, shape transitions, anharmonic vibrations and low-energy heavy-ion reactions, are often encountered in studies of nuclear structure and dynamics. Many attempts have been made to construct theories that are able to describe the LACM on a microscopic basis of the nuclear many-body Hamiltonian. In particular, theories based on the time-dependent Hartree-Fock (TDHF) approximation have been extensively investigated. TDHF is a general framework for describing low-energy nuclear dynamics accompanying evolution of a nuclear self-consistent mean field. LACM corresponds to a specific solution of the TDHF equation of motion. Since such a solution forms only a subset of all the TDHF states (Slater determinants), it is often called a collective path, a collective subspace, or a collective submanifold. The collective coordinates are then a set of a small number of variables that parameterize the collective subspace, and the collective Hamiltonian is a function governing the time evolution of the collective coordinates. One of the main purposes of the LACM theories is to provide a scheme to determine the collective subspace and the collective Hamiltonian on the basis of a microscopic many-body Hamiltonian. Although studies of LACM theories form a vast field of research with many recent developments in different directions, realistic applications to nuclear structure problems have been very few.

The adiabatic approximation has often been utilized to formulate a theory of the collective subspace. The adiabatic TDHF (ATDHF) theory[1] is one of the best-known adiabatic theories. The ATDHF theory, however, had a problem of non-uniqueness of the solution.[2] Efforts to settle the non-uniqueness problem have been made and summarized in a consistent way in the formalism of Ref. 3. However, a problem of particle-number conservation arises when applied to superconducting nuclei (*i.e.*, nuclei with pairing correlations).[4]

Theories without an adiabatic approximation have also been developed within the TDHF framework. The early studies in this direction are called local harmonic approximations. Later, a set of general equations that can be used to determine the collective subspace and the collective Hamiltonian were found and formulated in a consistent form, known as the self-consistent collective coordinate method (SCC or SCCM).[5] The theory is purely based on the TDHF with no further approximation. The pairing correlation in superconducting nuclei is easily incorporated within the SCCM by adopting the time-dependent Hartree-Fock-Bogoliubov (TDHFB) equation in place of the TDHF, and the conservation law for the particle number is consistently introduced within the basic framework of the SCCM.[6] However, since the method relies upon an expansion with respect to the collective coordinates, it may not be suitable for the large-amplitude motion of an adiabatic nature, for which the change in the nuclear mean-field is so large that a power-series expansion of the collective coordinates may not be justified.

In this work, we attempted to combine the merits of the two approaches mentioned above, the SCCM and the adiabatic theory, in order to formulate a theory that provides a consistent and practical method that is easily applicable to realistic descriptions of the adiabatic LACM in superconducting nuclei. We have achieved this by introducing an adiabatic approximation within the general framework of the SCCM. Here, we treat superconducting nuclei, since the pairing correlations play essential roles in many cases, like spontaneous fission, tunneling between superdeformed and normally deformed configurations, and coupling between coexisting states with different nuclear shapes (shape-coexistence phenomena). Although the use of the superconducting mean field requires particle-number conservation to be respected, the SCCM allows a simple and consistent treatment of the conservation law. We also avoid the non-uniqueness problem by utilizing principles similar to those of Ref. 3. Furthermore, we show that the equations of the adiabatic SCCM thus formulated can be transformed into another set of equations that have a similar structure as that of the local harmonic approach in adiabatic theories.[3]

† Condensed from the article in Prog. Theor. Phys. **103**, 959 (2000).

*1 Graduate School of Science and Technology, Niigata Univ.
*2 Department of Physics, Kyoto University

References

1) F. Villars: Nucl. Phys. A **285**, 269 (1977).
2) A. K. Mukherjee and M. K. Pal: Phys. Lett. B **100**, 457 (1981).
3) A. Klein, N. R. Walet, and G. Do Dang: Ann. Phys. **208**, 90 (1991).
4) T. Nakatsukasa, N. R. Walet, and G. Do Dang: Phys. Rev. C **61**, 014302 (2000).
5) T. Marumori, T. Maskawa, F. Sakata, and A. Kuriyama: Prog. Theor. Phys. **64**, 1294 (1980).
6) M. Matsuo: Prog. Theor. Phys. **76**, 372 (1986).

Microscopic Description of Damped Collective Motion†

S. Yamaji, H. Hofmann,*1 and F. A. Ivanyuk*2

[Linear response theory, Giant dipole resonance, Fission]

The dissipation of nuclear matter and its evolution as a function of temperature is one of the fundamental properties of nuclear matter.

In the case of the fast collective motion of the isovector mode, the damping mechanism of the giant dipole resonances as a function of spin and temperature has been highly debated. Reviews are given, for example, in Refs. 1 and 2. The theoretical models which are used at present to explain the temperature dependence are the two-body collisional damping model (see, for example, Ref. 3 for collisional damping to the 2p-2h states in the Landau-Vlasov equation, Ref. 4 for collisional damping to the 1p-1h + 1 phonons states, Ref. 5 for collisional damping to 2-phonon states) and the thermal fluctuation model (see, for example, Ref. 6). Whether the temperature dependence arises from collisional damping of nucleons or from thermal fluctuations of nuclear potential landscape is still unclear. Studies of the giant dipole resonance based on transport theory,[7] in which the collisional damping to the 2p-2h states is treated, will shed light on this debate.

As for isoscalar modes at finite excitations, the best information available at present comes from experiments on fission accompanied by the emission of light particles or gamma rays. Nowadays, it seems possible to obtain information on the effective damping rate, $\eta = \gamma/(2\sqrt{M|C|})$, at the saddle and its temperature dependence[8–10], where the coefficients γ, M and C are friction, inertia and local stiffness, respectively. They find an η which increases markedly with T. Such behavior is hard to understand within the macroscopic models (see, for example, Ref. 11).

In the present work,[12] the damping mechanism of the damped collective motion is being studied microscopically on the basis of linear response theory.[7]

As for isovector modes, the calculated strength function of the giant dipole resonance built on highly excited states in ^{208}Pb is compared with the observed one.[13] It is found that our two-body collisional damping model almost reproduces the temperature dependence of the observed width, indicating little room for a contribution due to the thermal fluctuation model.[6]

As for isoscalar modes, slow collective motion like fission, is studied. The calculated effective damping rate η at the saddle is in qualitative agreement with the observed one, which increases markedly with the temperature. A more realistic description of solving the transport equation (see, for example, Ref. 14) is necessary to obtain quantitative agreement. The approximate functional form of the friction is provided for that.

Moreover, it is noticed that the effect of the shell structure on the friction should be taken into account as well as the shell correction energy in theoretical estimate of the production of supper-heavy elements based on the transport equation.

References

1) K. A. Snover: Annu. Rev. Nucl. Part. Sci. **36**, 545 (1986).
2) J. J. Gaardhoeje: Annu. Rev. Nucl. Part. Sci. **42**, 483 (1992).
3) V. Baran, M. Colonna, and M. Di Toro et al.: Nucl. Phys. A **599**, 29c (1996).
4) P. Dontai, N. Giovanardi, P. F. Bortignon, and R. A. Broglia: Phys. Lett. B **383**, 15 (1996).
5) N. Dinh Dang, K. Tanabe, and A. Arima: Phys. Rev. Lett. **80**, 4145 (1998).
6) W. E. Ormand, P. F. Bortignon, R. A. Broglia, and A. Bracco: Nucl. Phys. A **614**, 217 (1997).
7) S. Yamaji, H. Hofmann, and R. Samhammer: Nucl. Phys. A **475**, 487 (1988).
8) P. Paul and M. Thoennessen: Annu. Rev. Nucl. Part. Sci. **44**, 65 (1994).
9) D. J. Hofman, B. B. Back, and P. Paul: Phys. Rev. C **51**, 2597 (1995).
10) I. Dioszegi, N. P. Shaw, I. Mazumdar et al.: Phys. Rev. C **61**, 024613 (2000).
11) J. Blocki, Y. Boneh, J. R. Nix, A. J. Sierk, and W. J. Swiatecki: Ann. Phys. **113**, 330 (1978).
12) S. Yamaji, H. Hofmann, and F. A. Ivanyuk: Proc. Tours Symp. on Nuclear Physics IV, Tours, France (4-7, Sep., 2000).
13) T. Baumann et al.: Nucl. Phys. A **635**, 428 (1998).
14) T. Wada, Y. Abe, and N. Carjan: Phys. Rev. Lett. **70**, 3538 (1993).

† Condensed from the article in Proc. Tours Symp. on Nuclear Physics IV, Tours, France (4-7, Sep., 2000)

*1 Physik-Department der Technischen Universität München, Germany
*2 Institute for Nuclear Research of the Ukrainian Academy of Sciences, Ukraine

Effects of Nuclear Rotation on the Collective Transport Coefficients

F. A. Ivanyuk* and S. Yamaji

[Linear response theory, Friction, Nuclear rotation]

The recent success of the Flerov Laboratory, JINR, Dubna in the synthesis of the superheavy element with $Z = 114$ has provoked considerable theoretical interest in fusion-fission reactions at low excitation energies. Commonly, such reactions are described by solving[1] the Langevin equation for the collective variables which specify the shape of the compound system. Usually, such systems are formed with a rather high angular momentum. However, the effect of rotation on the shell correction, as well as friction and inertia, is completely ignored at present, though one might expect a considerable dependence of the transport coefficients on the rotation, since the rotation greatly changes the single-particle spectrum. This effect was analyzed only in Ref. 2 where a rather strong dependence of the friction coefficient on the angular velocity was found.

To examine the influence of rotation on the potential energy and transport coefficients, we modified the two-center shell model code by taking into account the effects of nuclear rotation. We found that the shell correction is rather stable to nuclear rotation (see Fig. 1). The friction γ and mass M parameters computed within the linear response theory[3,4] turned out to be rather sensitive to such a fine effect as the violation of rotational symmetry by the Coriolis term, $-\omega_{rot}\hat{J}_x$.

To remove the spurious contributions to the transport coefficients, we modified the model of "uniform rotation" and introduced a time-dependent rotational frequency. A similar method was used in Ref. 5 to remove the spurious contributions to the response functions caused by a violation of the particle-number conservation by pairing forces. In the result we obtained the friction and mass, which demonstrated rather reasonable dependence on the rotation (see Fig. 2). For excitations above $T = 2\,\mathrm{MeV}$, where the microscopic shell effects disappear, both γ and M are rather insensitive to rotation. For $1\,\mathrm{Mev} \leq T \leq 2\,\mathrm{MeV}$, we found some increase of γ and M with growing ω_{rot}. Such an effect might be caused by a change in the shell structure due to a re-arrangement of the single-particle states by rotation.

Even a stronger dependence of γ and M on ω_{rot} should be expected for $T \leq 1\,\mathrm{MeV}$ when both the shell and pairing effects are present. As shown,[5,6] the pairing effects change considerably the collective transport at low excitations. The destruction of pairing by rotation can have a considerable effect on the final stage of the fusion reaction and the formation of superheavy elements, which takes place at low excitation energy.

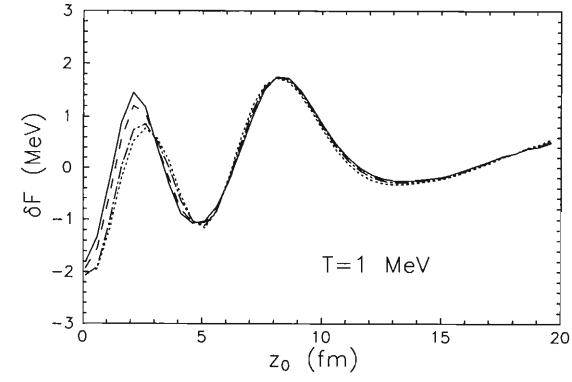

Fig. 1. Shell correction, $\delta F = \delta R - T\delta S$, to the free energy for temperature $T = 1\,\mathrm{MeV}$ as a function of the deformation parameter z_0. The solid, dashed, dotted-dashed and dotted correspond to the values of the rotational moment equal to 0, 20, 40 and $60\hbar$.

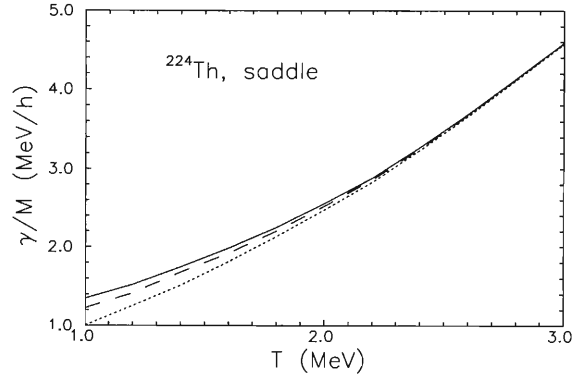

Fig. 2. Reduced friction coefficient, $\beta = \gamma/M$, versus temperature. The dotted, dashed and solid curves correspond to the values of the rotational moment equal to 0, 40 and $60\hbar$.

References
1) Y. Abe et al: Phys. Rep. **275**, 49 (1996).
2) K. Pomorski and H. Hofmann: Phys. Lett. **26**, 164 (1991).
3) H. Hofmann: Phys. Rep. **284**, 137 (1997).
4) S. Yamaji et al: Nucl. Phys. A **475**, 487 (1988).
5) F. Ivanyuk and H. Hofmann: Nucl. Phys. A **657**, 19 (1999).
6) H. Hofmann and F. Ivanyuk: Phys. Rev. Lett. **82**, 4603 (1999).

* Institute for Nuclear Research, Ukraine

Fusion Probability for a Multi-Dimensional Dissipative Barrier

Y. Abe,[*1] J.-D. Bao,[*2] D. Boilley,[*3] and T. Wada[*4]

[Heavy ion fusion, Dissipative barrier, Effect of neck formation]

In the fusion process of massive systems, such as ^{86}Kr+^{208}Pb, with which a Berkeley group claimed to synthesize $Z = 118$ superheavy elements,[1] not only the usual Coulomb barrier, but also the conditional saddle, must be overcome. As for the latter, the passing-over probability is much smaller than a simple barrier penetration for the saddle-point height, leading to what is called fusion hindrance.[2] The reason is that the kinetic energy of the collective motion provided by the incident energy dissipates very quickly into thermal energy, *i.e.*, nucleonic motions, following the compound-nucleus concept by N. Bohr.[3] Therefore, much more energy must be injected than the apparent height of the saddle point. Since there are collective degrees of freedom with heavy inertia mass and nucleonic degrees of freedom quickly thermalized, we can employ the theory of Brownian motion, *i.e.*, dissipation-fluctuation dynamics for collective motions, more precisely, Langevin equation, Kramers equation *etc.*[4]

An analytic solution for a general multi-dimensional parabolic barrier with dissipation has been given by Y. Abe *et al.*,[5] where the probability for passing-over, *i.e.* for fusion, is given simply by the error function. In the one-dimensional case, the extra-push energy which describes the fusion hindrance is given by the following simple expression:

$$E_{extra} = \left(\frac{\beta + \beta'}{2w}\right)^2 \cdot B, \tag{1}$$

where β denotes the reduced friction, γ/m, and $\beta' = \sqrt{\beta^2 + 4w^2}$ with w being the curvature of the saddle point. B is the height of the saddle measured from the energy of the initial point, *i.e.*, the contact configuration of the incident ions. From this expression, one can readily understand that E_{extra} is much larger than B if $\beta \gg w$, which is the case with the one-body model[6] for friction.

The real fusion process would not be described well by a one-dimensional model. It is naturally understood by considering possible shape variations which are parameterized with the fragment distance, the mass asymmetry, the neck radius, *etc.* This indicates that a one-dimensional treatment is an over-simplification and underestimates the probability for reseparation, since there are many possible trajectories sliding down along the multi-dimensional valley back to reseparation, not only along the fusion direction. Therefore, we must take into account the effect properly, but with a reasonal simplicity being maintained.

As a first step, we attempt to take into account the effect of the neck-degree of freedom. Since the barrier height, B, from the contact point depends on the neck parameter, ε, the fusion probability, $P_{fus}(E_{c.m.})$, is given by

$$P_{fus}(E_{c.m.}) = \int_0^1 d\varepsilon \rho(\varepsilon) P_{fus}\left(E_{c.m.}, B(\varepsilon)\right), \tag{2}$$

where $\rho(\varepsilon)$ denotes the distribution of the neck parameter, ε, in contact configurations. Extra-push energy is now obtained by the condition that $P_{fus}(E_{c.m.})$ of Eq. (2) be equal to 1/2, instead of Eq. (1), which is obtained with $P_{fus}(E_{c.m.}, B)$ on the right-hand side of Eq. (2). The problem is how to obtain a distribution, $\rho(\varepsilon)$, which is actually time-dependent. Thus, we must solve a time-evolution of the neck, assuming initial conditions of $\varepsilon(t = 0) = 1.0$ and $\dot{\varepsilon}(t = 0) = 0.0$. The evolution is again described by a Langevin equation,

$$m_\varepsilon \cdot \ddot{\varepsilon} + \gamma_\varepsilon \cdot \dot{\varepsilon} - f_\varepsilon = \sqrt{2\gamma_\varepsilon T} \cdot r_\varepsilon(t), \tag{3}$$

where $f_\varepsilon = -\partial U/\partial\varepsilon$ is approximated to be constant from the liquid-drop model energy surface.[7] $r_\varepsilon(t)$ denotes a random force which is assumed to be Gaussian and Markovian. An essential assumption underlying Eq. (3) is that the ε-degree of freedom is treated with no coupling to the radial motion. The distribution, $\rho(\varepsilon)$, would be given by

$$\rho(\varepsilon) = C_o \cdot \exp\left(-\frac{(\varepsilon - \bar{\varepsilon})^2}{2\sigma^2}\right), \tag{4}$$

where $\bar{\varepsilon}$ and σ are time-averages of the average and the variance of the trajectories over the fusion time. Such an approach leads to a better agreement with the experimental results,[8] for example the ^{100}Mo$-^{100}$Mo system.

*1 Yukawa Institute for Theoretical Physics, Kyoto University
*2 Department of Physics, Beijing Normal University, China
*3 GANIL, France
*4 Department of Physics, Konan University

References
1) V. Ninov: Phys. Rev. Lett. **83**, 1104 (1999).
2) S. Bjornholm and W. J. Swiatecki: Nucl. Phys. A **391**, 471 (1982).
3) N. Bohr: Nature **137**, 344 (1936).
4) Y. Abe et al.: Phys. Rep. C **275**, 49 (1996).
5) Y. Abe et al.: Phys. Rev. E **61**, 1125 (1999).
6) J. Blocki et al.: Ann. Phys. **113**, 330 (1978).
7) K. Sato et al.: Z. Phys. A **290**, 145 (1979).
8) J. D. Bao, D. Boilley, T. Wada, and Y. Abe: to be published.

Dynamics of Contact in ^{86}Kr+^{208}Pb Collisions

Y. Abe*[1] and G. Kosenko*[2]

[Superheavy elements, Heavy ion fusion, Surface friction model]

Recently, ^{86}Kr+^{208}Pb collisions have been used for synthesizing the $Z = 118$ superheavy element at Berkeley.[1] In order to theoretically obtain residue cross sections in such massive systems, it is necessary to calculate the fusion probability, P_{fusion}, by taking into account both the processes of passing over the usual Coulomb barrier and the conditional saddle. In lighter systems, the former process is sufficient for P_{fusion}, but in massive systems the latter process plays a crucial role for P_{fusion}, as discussed with the extra-push or extra-extra-push energy. Therefore, P_{fusion} is given by the following product:

$$P_{fusion} = P_{contact} \cdot P_{formation}, \quad (1)$$

where $P_{contact}$ denotes the probability for the incident system to reach the matter contact, passing over the usual barrier, and $P_{formation}$ denotes that for a composite system (connected di-nucleus system) to reach a spherical compound nucleus, passing over the conditional saddle under strong competition with the so-called quasi-fission and fast-fission. $P_{formation}$ should be calculated by solving the dissipation-fluctuation dynamics of the collective motions, which has not yet been made on the present system, but made on other systems.[2]

In order to perform a dynamical calculation for $P_{formation}$ correctly, the initial conditions are necessary, such as how much flux has overcome the Coulomb barrier, how much incident energy has dissipated into internal excitation, *etc.* These are included in the first factor, $P_{contact}$.

In the present work, the authors have started to obtain $P_{contact}$ by employing the so-called surface friction model,[3] and have solved a number of classical trajectories up to the contact point for ^{86}Kr+^{208}Pb collisions with the incident energy being above the Coulomb barrier.

Physically important points are (i) how much flux can reach the contact point of two nuclear droplet, *i.e.*, at a relative distance equal to the sum of the radii, and (ii) how much energy dissipation, or what is the contact state. Figure 1 shows preliminary results for $P_{contact}$, the probability of reaching the contact point as a function of the energy. Figure 2 shows the radial-momentum distribution at the contact point, from which the radial motion is known to almost reach thermal equilibrium.

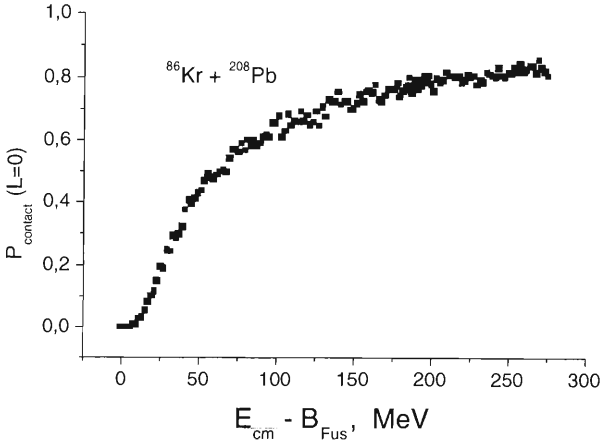

Fig. 1. Contact probability as a function of the incident c.m. energy measured from the Bass barrier, B_{fus}.

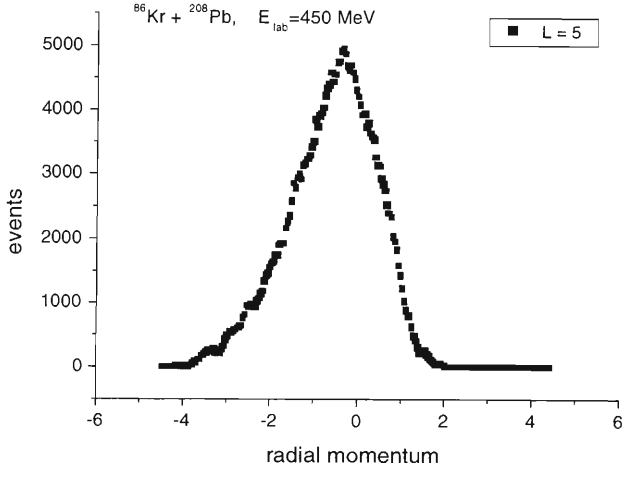

Fig. 2. Distribution of the radial momentum at the contact point $r = R_{12} = R_1 + R_2$ at $E_{lab} = 450$ MeV, where the initial momentum at the barrier top is just outside of the y-axis.

*1 Yukawa Institute for Theoretical Physics, Kyoto University
*2 Department of Physics, Omsk University, Russia

References

1) V. Ninov et al.: Phys. Rev. Lett. **83**, 1104 (1999).
2) Y. Abe et al.: Phys. Rep. **275**, 49 (1996); T. Wada et al.: Proc. DANF98, edited by Y. Oganessian, J. Kilman, and S. Gmuca, (World Scientific, 1999), p.77.
3) D. H. E. Gross and H. Kalinowski: Phys. Rep. **45**, 175 (1978).

New Nuclear Reaction Flow during r-Process Nucleosynthesis in Supernovae: The Critical Role of Light Neutron-Rich Nuclei†

M. Terasawa,*1 K. Sumiyoshi,*2 T. Kajino,*3 G. Mathews,*4 and I. Tanihata

[r-Process, Supernova]

For an r-process study, a reaction network with $10 \leq Z \leq 94$ has usually been adopted for a long time. However, in a very neutron-rich environment, their network can be too narrow for the light-nuclei region. We have therefore extended a network up to the neutron-drip line (see dots in Fig. 1). We compared the final abundance patterns with and without this extension of the network (called 'full network' and the 'small network'). As for $10 \leq Z \leq 94$, we used the nuclear reaction network of Meyer *et al.*[1]

We employed the ν-driven wind models of Sumiyoshi *et al.*[2] We chose the case in which the expansion timescale is as short as $\tau_{\rm dyn} = 0.005$ sec (the mass of neutron star, $M_{\rm NS} = 2.0\,{\rm M}_\odot$; radius, $R_{\rm NS} = 10$ km and; total neutrino luminosity, $L_{\nu,{\rm total}} = 6 \times 10^{52}$ erg/sec). We started a network calculation from the time when the temperature drops to $T = 9.0 \times 10^9$ K and set the time to $t = 0.0$ sec at this time. The initial electron fraction, $Y_e = 0.42$, is taken from hydrodynamical simulations.

It is considered that the r-process path runs through nuclei with almost the same neutron separation energy, $S_n = 2$–4 MeV, at freezout. In the present analysis using our 'full network,' the corresponding S_n-value is about 1 MeV. This result indicates that the r-process path runs through a more neutron-rich region. The r-process path is displayed in Fig. 1 at time $t = 0.57$ sec. At this time, $T = 0.62 \times 10^9$ K and the matter density is 5.4×10^2 g/cm^3. Abundant nuclei are shown by open circles, whose diameters are proportional to the abundance yields. The main reaction path is indicated by arrows.

Figure 2 shows the final abundance distribution. The solid and dotted lines in this figure are the results obtained by using the 'full network' and 'small network,' respectively. The data points are the solar-system r-process abundances from Käppeler *et al.*[3] in arbitrary units. The main reason for this difference between the two cases is that a new nuclear reaction flow opens in the light neutron-rich nuclei.[4]

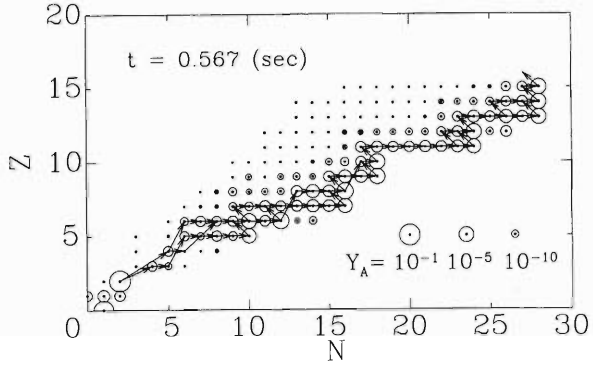

Fig. 1. Abundances and main path for $Z \leq 15$.

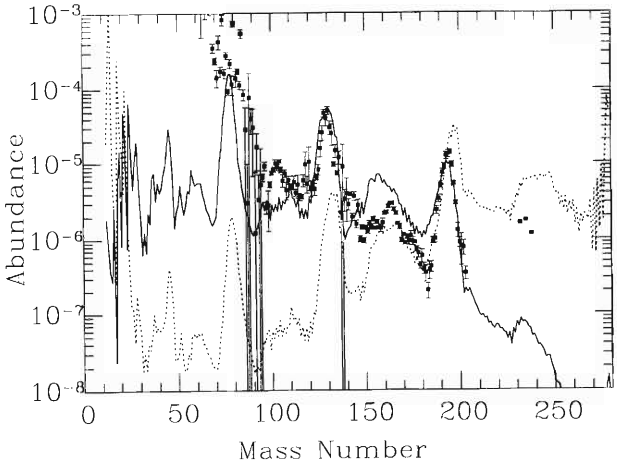

Fig. 2. Final abundances as a function of mass number.

References
1) B. S. Meyer, G. J. Mathews, W. M. Howard, S. E. Woosley, and R. D. Hoffman: Astrophys. J. **399**, 656 (1992).
2) K. Sumiyoshi, H. Suzuki, K. Otsuki, M. Terasawa, and S. Yamada: Publ. Astron. Soc. Jpn. **52**, 601 (2000).
3) F. Käppeler, H. Beer, and K. Wisshak: Rep. Prog. Phys. **52**, 945 (1989).
4) M. Terasawa, K. Sumiyoshi, T. Kajino, I. Tanihata, and G. Mathews: submitted to Astrophys. J. (2001).

† See Terasawa *et al.*[4] for more details

*1 University of Tokyo
*2 Numazu College of Technology (NCT)
*3 National Astronomical Observatory (NAO)
*4 University of Notre Dame, USA

Video: "The Quest for the Origin of the Elements"

Y. Mochizuki, I. Tanihata, and Y. Yano

[Nucleosynthesis]

The authors have produced a video on nucleosynthesis in the Universe. The primary characteristic of this video is that we have employed a number of 2-D and 3-Dimensional visualizations and animations based on an updated understanding of nuclear physics and astrophysics. An outline is given as follows.

Title: "The Quest for the Origin of the Elements"

Planning: RIKEN

Supervision: Y. Mochizuki, I. Tanihata, and Y. Yano

Production: Image Science, Inc.

Time Length: 29' 00" [Restricted by a contract to be broadcast by a program on "Science Channel."]

Type: VHS

Language: Japanese

Target: High-school students intending to take a science course and upward.

Purpose: (1) To bring new researchers into the fields of nuclear physics and astrophysics.
(2) To be used for education in universities and high schools.
(3) Accountability for the RI-Beam Factory Project.

Contents: Chart of the nuclides, Nuclear burning in the Sun, Big-Bang nucleosynthesis, Stellar nucleosynthesis, Heisenberg's valley, The s-process, The r-process, Production of an RI beam, *etc.*

Interviewees: Professors K. Sato, T. Kajino, I. Tanihata, D. Arnett, C. Sneden, K. Langanke, and F.-K. Thielemann.

Theoretical Data are Provided by: Doctors T. Tachibana (for the r-process and the following beta decays), H. Koura (for Heisenberg's valley, chart of the nuclides), K. Kohri (for Big-Bang nucleosynthesis), H. Umeda (for the evolution of the onion-like shell structure of a 15 $M_\odot$ star), T. Shimizu (for a numerical simulation of a supernova explosion).

One of the Emphasized Points: Microscopic physics (*i.e.*, nuclear physics) and macroscopic physics (*i.e.*, astrophysics) are strongly related.

Distribution: Under discussion. Pamphlets for explanation will be prepared.

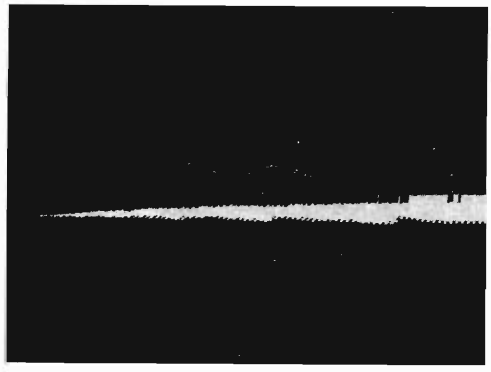

Fig. 1. Solar system abundances are shown by logarithmic scale on the z-axis on the chart of the nuclides.

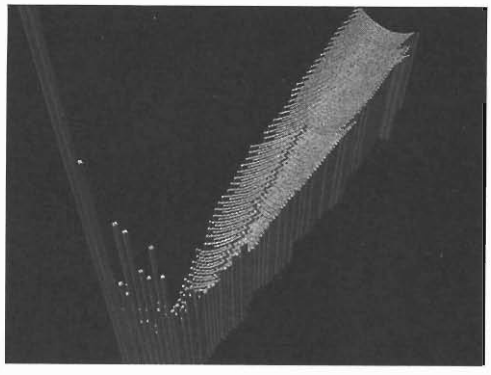

Fig. 2. Heisenberg's valley. The experimental ($A < 8$) and a set of theoretical ($A \geq 8$) atomic mass data are adopted.

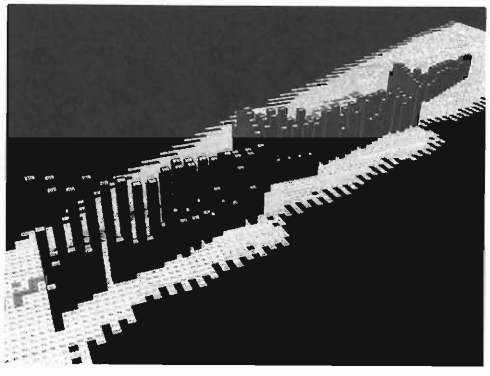

Fig. 3. The r-process path is demonstrated on the z-axis by Log-scaled abundances on the chart of the nuclides.

Nuclear $\bar{K}$ Bound States in ^{3}He and ^{4}He

Y. Akaishi* and T. Yamazaki

[Kaon bound states, Strangeness]

We have investigated theoretically the possible existence of deeply bound nuclear states of $\bar{K}$ in few-body systems. We first constructed phenomenologically a quantitative $\bar{K}N$ interaction model as simple as possible by using free $\bar{K}N$ scattering data,[1] the X-ray data of kaonic hydrogen atom[2] and the binding energy and the width of $\Lambda(1405)$ which can be regarded as an isospin $I = 0$ bound state of $\bar{K}$+N. Then, the $I = 0$ and $I = 1$ $\bar{K}N$ interactions, $v^I_{\bar{K}N}(r)$, $v^I_{\bar{K}N,\pi\Sigma}(r)$ and $v^I_{\bar{K}N,\pi\Lambda}(r)$, are determined. The potential range is set to be the proton size, 0.66 fm. The $I = 0$ interaction produces the unstable bound state of $\Lambda(1405)$ with $E_{\bar{K}N} = -29.5$ MeV (-27 MeV) from the $I = 0$ threshold (from the K^-+p threshold) and $\Gamma = 40$ MeV.

The $\bar{K}N$ g-matrix in nuclear medium is calculated by the g-matrix method, where the binding effects of $\bar{K}$ and N are properly taken into account. Now we search for nuclear $\bar{K}$ bound states in ^{3}He and ^{4}He. By using the normal density distributions we calculate the bound state energies $E_{\bar{K}}$ in such a way that E_{st}, g^I and $E_{\bar{K}}$ become self-consistent. The obtained results are $E_{\bar{K}} = -76$ MeV and $\Gamma = 82$ MeV for $^3_{\bar{K}}$H ($T = 0$), and $E_{\bar{K}} = -69$ MeV and $\Gamma = 66$ MeV for $^4_{\bar{K}}$H. The bindings are fairly large as expected, but the widths are also large, since the bound states are located above the $\Sigma + \pi$ threshold.

Due to the strong $\bar{K}N$ attractive force the bound $\bar{K}$ is expected to act as a kind of glue to combine the nucleons closer. Of course, such a shrinkage effect induced by $\bar{K}$ must be counterbalanced by the strong incompressibility of the core nucleus.

The final results of this size-optimization procedure show substantial lowering of the bound state energies and shrinkage of the core nuclear radii. Figure 1 depicts the optimized $\bar{K}$-nucleus potentials $U_{\bar{K}}$ of the K^- + ^{3}He and K^- + ^{4}He systems with the bound states of $^3_{\bar{K}}$H and of $^4_{\bar{K}}$H, which are extensions of the basic K^- + p system with $\Lambda(1405)$ as its bound state. The predicted bound states are expected to have narrow widths because the states are below the $\Sigma\pi$ emission threshold.

Now let us show that $^3_{\bar{K}}$H ($T = 0$) may be formed and identified in K^- absorption at rest by ^{4}He. The K^- in an atomic orbit falls into the deeply-bound nuclear orbit of $^3_{\bar{K}}$H ($T = 0$), emitting a neutron which helps to form the core nucleus with one neutron less and simultaneously serves as a spectator of the formed state. As shown in Fig. 2, the energy of the emitted neutron is related to the $\bar{K}$ binding energy.

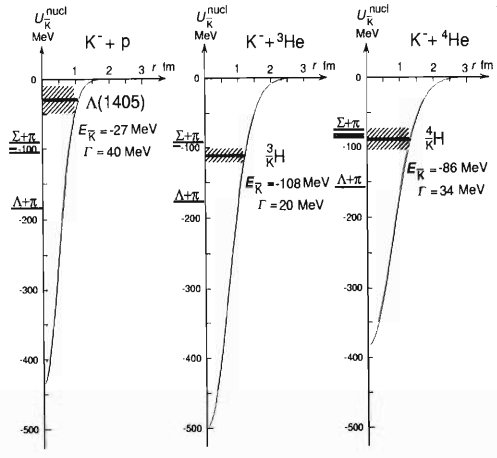

Fig. 1. Calculated $\bar{K}$-N and $\bar{K}$-nucleus potentials and the bound levels, $\Lambda(1405)$, $^3_{\bar{K}}$H and $^4_{\bar{K}}$H for the K^--p, -^{3}He and -^{4}He systems, respectively. The nuclear shrinkage effects are taken into account.

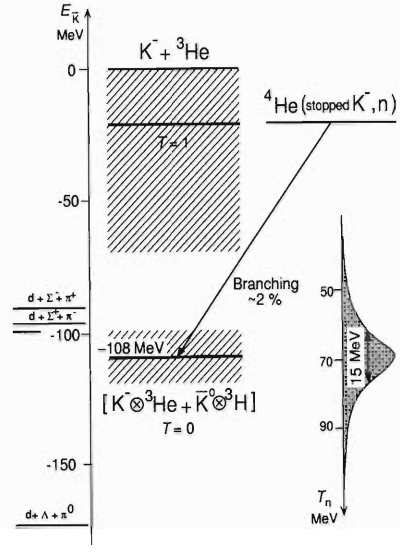

Fig. 2. Energy level diagram of the K^-+^{3}He system. The $T = 0$ state can be excited and signaled with a discrete neutron emission from stopped K^- on ^{4}He. The calculated neutron spectral intensity (branching ratio) is also shown.

References

1) A. D. Martin: Nucl. Phys. B **179**, 33 (1981).
2) M. Iwasaki et al.: Phys. Rev. Lett. **78**, 3067 (1997); T. M. Itoh et al.: Phys. Rev. C **58**, 2366 (1998).

* Institute of Particle and Nuclear Studies, High Energy Accelerator Research Organization

Empirical Deduction of a Medium-Modified Quark Condensate from Deeply-Bound Pionic States in Heavy Nuclei

P. Kienle* and T. Yamazaki

[Pion-nucleus interaction, Nuclear medium effect, Quark condensate]

Although how the hadron properties (mass and structure) are modified in nuclear medium is one of the central problems of hadron nuclear physics, no clear evidence has been available, because of lack of suitable procedures to deduce the in-medium properties from the experimental observables. Recently, a new type of nuclear spectroscopy, namely "hadron mass spectroscopy," has evolved in connection with deeply-bound pionic states,[1] and will be extended to other hadrons. Following the first successful experiment on the ^{208}Pb(d, ^{3}He) reaction to populate the 2p and 1s π^- states in ^{207}Pb,[2] a refined experiment has been carried out on the $\pi^- \otimes {}^{205}$Pb.[3] Further experiments on Sn isotopes will also be carried out soon. Here, we discuss how to obtain information on a possible quark condensate from the experimental data of deeply bound pionic states.

The isovector b_1 parameter in the pion optical potential is related to the pion decay constant through the Tomozawa-Weinberg relation,[4]

$$T^{(-)} = \frac{1}{2}[T_{\pi^- p} - T_{\pi^- n}] = \frac{\omega}{2f_\pi^2}. \tag{1}$$

The pion decay constant (f_π) is the order parameter of chiral symmetry breaking of QCD and is related to a quark condensate ($\langle\bar{q}q\rangle$) through the Gellmann-Oakes-Renner relation,[5]

$$m_\pi^2 f_\pi^2 = -m_q\langle\bar{q}q\rangle, \tag{2}$$

where $m_q = (m_u + m_d)/2$ is the average of the u and d quark masses. If f_π and $\langle\bar{q}q\rangle$ are modified in the nuclear medium to f_π^* and $\langle\bar{q}q\rangle^*$, respectively, they are reflected in the isovector parameter (b_1) of the pion-nucleus potential. Thus, it is essentially important to see how the isovector part of the pion-nucleus interaction is changed from the free value,

$$R = \frac{b_1}{b_1^{\rm free}} = \left(\frac{f_\pi^{*2}}{f_\pi^2}\right)^{-1} = \left(\frac{\langle\bar{q}q\rangle^*}{\langle\bar{q}q\rangle}\right)^{-1}. \tag{3}$$

Recently, the isoscalar and isovector potential parameters of the free πN scattering have been precisely determined as[6,7] $b_0^{\rm free} = (1.7 \pm 1.0) \times 10^{-3}$, and $b_1^{\rm free} = -(90.0 \pm 1.6) \times 10^{-3}$ in units of m_π^{-1}. The well-known in-medium corrections on the potential parameters arising from double πN scattering are

$$b_0^{\rm eff} = b_0^{\rm free} - \epsilon_1[(b_0^{\rm free})^2 + 2(b_1^{\rm free})^2]\left\langle\frac{1}{r}\right\rangle \tag{4}$$

$$= b_0^{\rm free} - \epsilon_1\left[(b_0^{\rm free})^2 + 2(b_1^{\rm free})^2\right]\frac{3k_F}{4\pi} \tag{5}$$

$$\sim -2.08\, b_1^2. \tag{6}$$

The above free πN parameters yield $b_0^{\rm eff} \sim -0.017$ and $b_1 \sim -0.09$. These effective values correspond to a repulsive strength of $V(0) \sim 16$ MeV for ^{205}Pb, and are regarded as giving a starting point, the deviation beyond which might be ascribed to a QCD effect.

The binding energies (B_{nl}) and widths (Γ_{nl}) of the deeply bound 1s states of π^- in heavy nuclei are related nearly uniquely to $V(0)$ and $W(0)$ (irrespectively of the non-local parameters) as

$$V(0) = -455\left[b_0 + \frac{N-Z}{A}b_1\right], \tag{7}$$

$$W(0) = -192\ {\rm Im}B_0\ {\rm MeV}. \tag{8}$$

An experimentally determined $V(0)$ (in MeV) value thus yields a straight line in the b_0–b_1 plane.

We take three typical cases: π^--^{205}Pb, ^{115}Sn and ^{123}Sn. The first one has already been observed, and a new value of $V(0) \sim 26$ MeV has been obtained from the 1s π^- state in ^{205}Pb.[3] Experiments on the Sn isotopes will be performed in the near future.

It is clear that the experimental value, $V(0) = 26$ MeV, for ^{205}Pb deviates significantly from the "effective free" value. If we assert that only the isovector part be primarily renormalized by a QCD effect, it will cause an additional isoscalar repulsion according to Eq. (6). Then, the experimental value $V(0)$ yields

$$b_1 \sim -0.13, \qquad b_0 \sim -0.032, \tag{9}$$

which could indicate that $\langle\bar{q}q\rangle$ is reduced by a factor of ~ 0.7 in the nuclear medium.

An experimental confirmation of the above assertion requires an additional constraint from another nucleus, which has a $\delta = (N-Z)/A$ value different from the first one. The case of ^{123}Sn ($\delta = 0.187$) is nearly identical to the case of ^{205}Pb ($\delta = 0.200$), but the case of ^{115}Sn ($\delta = 0.130$) is very different.

A more direct determination of b_1 is, of course, to compare between the binding energies of different isotopes which have a large enough difference in $\delta = (N-Z)/A$. Let us take the case of ^{115}Sn ($\delta = 0.130$) and ^{123}Sn ($\delta = 0.187$). Starting from the empirical value $V(0) = 26$ MeV for ^{205}Pb, we obtain theoretical estimates of $B_{1s}(^{115}{\rm Sn})$ and $B_{1s}(^{123}{\rm Sn})$ as a function of b_1, as presented in Fig. 1. A measurement of the isotope shift in Sn will thus yield a direct determination of b_1 (and subsequently, of b_0).

* Physik Department E12, Technische Universität München, Germany

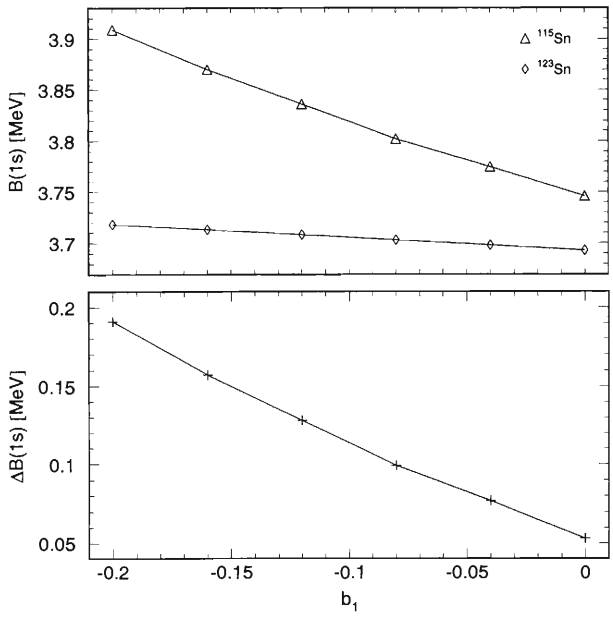

Fig. 1. Calculated 1s π^- binding energies and isotope shifts versus b_1 for the cases of ^{115}Sn-^{123}Sn.

References

1) H. Toki and T. Yamazaki: Phys. Lett. B **213**, 129 (1988); H. Toki, S. Hirenzaki, R. S. Hayano, and T. Yamazaki: Nucl. Phys. A **501**, 653 (1989).
2) T. Yamazaki et al.: Z. Phys. A **355**, 219 (1996); T. Yamazaki et al.: Phys. Lett. B **418**, 246 (1998); H. Gilg et al.: Phys. Rev. C **62**, 025201 (2000); K. Itahashi et al.: Phys. Rev. C **62**, 025202 (2000).
3) H. Geissel et al.: to be published.
4) Y. Tomozawa: Nuovo Cimento A **46**, 707 (1966); S. Weinberg: Phys. Rev. Lett. **17**, 616 (1966).
5) M. Gell-Mann, R. J. Oakes, and B. Renner: Phys. Rev. **175**, 2195 (1968).
6) L. Simon: Phys. Lett. B **469**, 25 (1999).
7) T. E. O. Ericson, B. Loiseau, and A. W. Thomas: Nucl. Phys. A **663/664**, 541c (2000).

ρ-ω Mixing in the Oscillation Model

H. Tezuka*

[Charge symmetry breaking, Isospin mixing]

The Coulomb displacement energies of mirror nuclei, the disagreement between the proton-proton and neutron-neutron scattering lengths without any Coulomb effects and the difference in proton and neutron analyzing powers seem to suggest charge symmetry breaking in the nucleon-nucleon interaction.[1] One explanation of charge symmetry breaking is due to isospin mixing in ρ and ω mesons. We showed in a previous paper that the time development of eigenstates makes isospin mixing because of their mass difference and that the ρ-ω mixing oscillation causes charge symmetry breaking in the nucleon-nucleon interaction.[2] We investigated the effects of breaking with assuming that ρ and ω mesons created by strong interaction are isospin eigenstates.

We here reanalyzed from the stand point that the observed ρ and ω mesons are mass eigenstates. The original isospin mixing Lagrangian density is given by

$$\begin{aligned}\mathcal{L} = &\bar{\psi}\{\gamma^\mu(i\partial_\mu - g_\omega\omega_\mu - g_\rho\tau_3\rho_\mu) - M\}\psi \\ &- \frac{1}{4}F^{(\omega)}_{\mu\nu}F^{(\omega)\mu\nu} + \frac{1}{2}m^2_\omega\omega_\mu\omega^\mu \\ &- \frac{1}{4}F^{(\rho)}_{\mu\nu}F^{(\rho)\mu\nu} + \frac{1}{2}m^2_\rho\rho_\mu\rho^\mu + \epsilon\,\omega_\mu\rho^\mu.\end{aligned}$$

Here, ρ and ω are isospin eigenstates. To eliminate the isospin mixing term ($\epsilon\,\omega_\mu\rho^\mu$) we introduce mass eigenstate vector mesons, A_μ and B_μ:

$$A_\mu = \omega_\mu\cos\theta + \rho_\mu\sin\theta$$

and

$$B_\mu = -\omega_\mu\sin\theta + \rho_\mu\cos\theta.$$

The relation between the mixing coupling constant (ϵ) and the mixing angle (θ) is given by

$$\tan 2\theta = \frac{2\epsilon}{m^2_\omega - m^2_\rho}.$$

We identify A_μ and B_μ with the observed ω and ρ mesons, which are given in the Particle Physics Booklet (PPB).[3] Masses m_ω and m_ρ are given by those of the mass eigenstates m_A and m_B in PPB:

$$m^2_\omega = m^2_A\cos^2\theta + m^2_B\sin^2\theta$$

and

$$m^2_\rho = m^2_A\sin^2\theta + m^2_B\cos^2\theta.$$

To reproduce the branching ratio of ω meson's two-pion-decay, $B(A \to 2\pi) = 0.0221 \pm 0.003$, the mixing angle ($\theta$) should be $2.25° \pm 0.19°$. This mixing angle gives the ρ meson's three-pion-decay branching ratio, 0.00011 ± 0.00002.

Vector mesons ρ and ω, created by strong interactions, are isospin eigenstates, but time development of eigenstates mixes the isospin components. The ω-meson state at time t after creation is given by

$$\begin{aligned}\omega(t) = &(e^{-im_At}\cos^2\theta + e^{-im_Bt}\sin^2\theta)\omega(0) \\ &+ (e^{-im_At} - e^{-im_Bt})\sin\theta\cos\theta\rho(0),\end{aligned}$$

and the ρ state at t is

$$\begin{aligned}\rho(t) = &(e^{-im_At}\sin^2\theta + e^{-im_Bt}\cos^2\theta)\rho(0) \\ &+ (e^{-im_At} - e^{-im_Bt})\cos\theta\sin\theta\omega(0),\end{aligned}$$

where $\omega(0)$ and $\rho(0)$ are the pure isospin 0 and 1 component, respectively.

The ω state and the ρ state at time t are not isospin eigenstates, but linear combinations of two isospin eigenstates, $\omega(0)$ and $\rho(0)$. The existing probabilities of the isospin 0 component and the 1 component oscillate with time. Thus, the vector mesons propagating between nucleons are not isospin eigenstates and the mixing ratios of the isospins are calculated with the mixing angle (θ). The probabilities of the isospin 1 (ρ) component and the isospin 0 (ω) component in the physical ω state at time t are given by

$$\begin{aligned}P(\omega \mid \rho) &= |(e^{-im_At} - e^{-im_Bt})\sin\theta\cos\theta|^2 \\ &= \frac{1}{2}\{1 - \cos(m_A - m_B)t\}\sin^2 2\theta\end{aligned}$$

and

$$\begin{aligned}P(\omega \mid \omega) &= |e^{-im_At}\cos^2\theta + e^{-im_Bt}\sin^2\theta|^2 \\ &= 1 - \frac{1}{2}\{1 - \cos(m_A - m_B)t\}\sin^2 2\theta.\end{aligned}$$

It is shown that the above θ reproduces a disagreement between the scattering lengths. This mixing angle corresponds to the mixing coupling constant, $\epsilon = (0.001207 \pm 0.000102)m_\rho m_\omega$.

* Natural Science Laboratory, Toyo University

References

1) G. A. Miller, B. M. K. Nefkens, and L. Šlaus: Phys. Rep. **194**, 1 (1990).
2) S. Ogushi, M. Terasawa, and H. Tezuka: Phys. Rev. C **56**, 2382 (1997).
3) Particle Data Group: Eur. Phys. J. C **15**, 1 (2000).

Deconfinement by an Infinite Potential

H. Tezuka*

[Confinement, Dirac equation, Vector potential]

Linear-type potentials and harmonic oscillator-type potentials are often used as confinement potentials of quarks in hadrons both relativistically and nonrelativistically. It has been shown that a relativistic particle described by the Dirac equation with linear potentials or harmonic-oscillator potentials cannot be confined if the potential is a vector.[1,2] We also showed that both a monomial vector potential, like ar^n, and a polynomial one, like $\sum_n a_n r^n$, cannot confine a particle in their potentials.[3]

This time we investigated the confinement problem of a vector potential with more general forms. We discussed the possibility of bound states in an infinitely strong attractive vector potential.

The Dirac equation of a particle with mass m in a vector potential $V(r)$ is given by

$$\{\boldsymbol{\alpha}\cdot\boldsymbol{p}+\beta m+V(r)\}\,\psi(\boldsymbol{r})=E\psi(\boldsymbol{r}).$$

The vector potential is assumed to have only the 0-th component and to be spherically symmetric. We consider an infinite potential, such as $V(r)\to\pm\infty$ at $r\to\infty$. The vector potential with $\lim_{r\to\infty}V(r)=+\infty$ is called attractive, because $V(r)$ increases energy with r, while the $\lim_{r\to\infty}V(r)=-\infty$ type vector potential is repulsive.

Rewriting the 4-spinor $\psi(\boldsymbol{r})$ as

$$\psi(\boldsymbol{r})=\begin{pmatrix} i\dfrac{G_{lj}(r)}{r}\,\varphi^l_{jm}(\Omega) \\ \dfrac{F_{lj}(r)}{r}\,\boldsymbol{\sigma}\cdot\dfrac{\boldsymbol{r}}{r}\,\varphi^l_{jm}(\Omega)\end{pmatrix},$$

the Dirac equation for the upper component ($G_{lj}(r)$) is given by

$$\begin{aligned}\frac{d^2G_{lj}(r)}{dr^2}=&-\frac{\dfrac{dV(r)}{dr}}{E-V(r)+m}\frac{dG_{lj}(r)}{dr}\\&-\left[\{E-V(r)\}^2-m^2\right]G_{lj}(r)\\&+\frac{\kappa}{r}\left\{\frac{1+\kappa}{r}-\frac{\dfrac{dV(r)}{dr}}{E-V(r)+m}\right\}G_{lj}(r),\end{aligned}$$

where

$$\kappa=\mp\left(j+\frac{1}{2}\right)\qquad\text{for}\qquad j=l\pm\frac{1}{2}.$$

Because we assume that $V(r)$ becomes infinite as r increases, it is clear that the main part at large r in the second term of the right-hand-side is $-V(r)^2$. If $V(r)\to+\infty$ at $r\to\infty$, $\frac{dV(r)}{dr}>0$, and if $V(r)\to-\infty$ at $r\to\infty$, $\frac{dV(r)}{dr}<0$. Thus $\frac{dV(r)}{dr}\Big/V(r)$ is always positive at large r. We examine whether there is a $V(r)$ which satisfies

$$\frac{\dfrac{dV(r)}{dr}}{V(r)}>V(r)^2.$$

The left-hand-side is the largest part at large r of the first and third terms of the Dirac equation. After integration we obtain

$$-\frac{1}{2V(r)^2}>r+\text{const.}$$

No solution of $V(r)$ can satisfy the equation at $r\to\infty$. We can thus conclude

$$\frac{\dfrac{dV(r)}{dr}}{V(r)}\ll V(r)^2,$$

at $r\to\infty$. Therefore, at large r the main part of the right-hand-side of the Dirac equation is $-V(r)^2$ for an infinite potential. This term is repulsive independent of the sign of the vector potential ($V(r)$). Because the asymptotic equation is given by

$$\frac{d^2G_{lj}(r)}{dr^2}=-V(r)^2G_{lj}(r),$$

the asymptotic wave function oscillates at large r and does not converge. Having no bound states means that the infinitely strong potential does not confine a particle. A particle moving in the vector potential is not confined and exists even at $r\to\infty$.

References

1) Y. Shibata and H. Tezuka: Z. Phys. C **62**, 533 (1994).
2) L. Tomio and P. L. Ferreira: Nuovo Ciment B **107**, 785 (1992).
3) H. Tezuka: Z. Phys. C **65**, 101 (1995).

* Natural Science Laboratory, Toyo University

Measurement of Ortho-Para Effect in Muon-Catalyzed dd-Fusion

A. Toyoda,[*1] K. Ishida, K. Shimomura,[*2] Y. Matsuda, W. Higemoto,[*2] S. N. Nakamura,[*3] T. Matsuzaki, and K. Nagamine

[Ortho-para effect, Muon-catalyzed fusion]

In this report, we provide the final results of a series of experiments about the ortho-para effect in muon-catalyzed fusion (μCF) in solid deuterium (see also a previous report[1]).

One of the most important subjects in a μCF study is to enhance the muon cycling rate, which may be achieved by influencing the muonic molecular formation process. For this purpose, we used deuterium by artificially changing the ratio between ortho deuterium (coupled nuclear spin $I = 0$, 2, rotational state J = even) and para deuterium ($I = 1$, J = odd) (ortho-para ratio) for the first time. The ortho-para effect in μCF was first pointed out by Leon and Cohen[2] and was recently calculated in detail by Faifman.[3] In these references, about a 10% enhancement of the fusion rate in 100% ortho deuterium at around 30 K is predicted.

The second motivation is to understand the unexpected contradiction between the experiments[4,5] and theories in the solid region (below 18.7 K). In some explanations for the contradiction,[6,7] the para deuterium is predicted to play an essential role. Thus, an ortho-para experiment would be possible to determine which explanation is more reasonable.

The experimental setup developed at the RIKEN-RAL[†] Muon Facility consisted of a cryostat to cool down the deuterium target, a target chamber, two pairs of silicon surface barrier (SSB) detectors for fusion proton detection, a Si (Li) detector to cover an energy region of 1.5 keV to 80 keV for X-ray measurement, a pair of plastic scintillators to detect μ-e decay electrons, an ortho-para converter, an ortho-para analyzer to observe the ortho-para ratio of the converted deuterium, and a PC-based Exp 96 data-taking system.[8]

The experiments were carried out at port 3 of the RIKEN-RAL Muon Facility at ISIS. We fitted the measured fusion proton time spectrum with two exponential functions (fast component and slow component), and obtained the fusion proton yield normalized by the muon stopping number, which was estimated by using the μe-decay electrons from the deuterium target. The fast component is expected to be more likely affected by the ortho-para effect. The background was estimated by using the target-out data.

For a comparison between the experimental result and theories with solid effects about an ortho-para effect, we introduce the parameter $R_p = Y_p^{ortho}/Y_p^{normal} - 1$, where Y_p^{ortho} is the fusion proton yield with the fast component in the 99.9% ortho case and Y_p^{normal} is that in the normal (66.7% ortho) case.

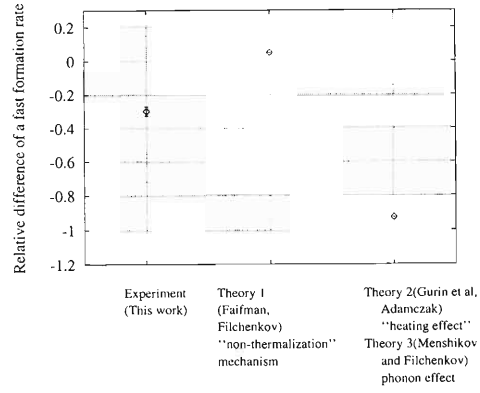

Fig. 1. Comparison between the theories and the experiment about the ortho-para effect.

There have been theoretical proposals for solid effects in μCF:

theory 1, "non-thermalization" mechanism;[9]
theory 2, muonic atom "heating effect";[7]
theory 3, phonon effect.[6]

Figure 1 shows a comparison of R_p between theories and this experiment. From this figure, two of the proposed solid effects, namely, a muonic atom "heating effect" and a phonon creation effect, which are strongly dependent on the ortho-para ratio (in other words, the rotational-state ratio) of deuterium molecules, are understood to be negligibly small. Our result favors the "non-thermalization" effect without a large contribution of dμ atom acceleration.

*1 University of Tokyo
*2 High Energy Accelerator Research Organization
*3 Tohoku University
† Rutherford Appleton Laboratory, UK

References
1) A. Toyoda et al.: RIKEN Accel. Prog. Rep. **33**, 49 (2000).
2) M. Leon and J. S. Cohen: Phys. Rev. A **31**, 2680 (1985).
3) M. P. Faifman: private communication.
4) D. L. Demin et al.: Hyperfine Interact. **101/102**, 13 (1996).
5) P. E. Knowles et al.: Hyperfine Interact. **101/102**, 21 (1996).
6) L. I. Menshikov et al.: Hyperfine Interact. **101/102**, 207 (1996).
7) G. L. Gurin et al.: Hyperfine Interact. **118**, 147 (1999).
8) S. N. Nakamura and M. Iwasaki: Nucl. Instr. Meth. in Phys. Res. A **388**, 220 (1997).
9) V. V. Filchenkov: Hyperfine Interact. **101/102**, 37 (1996).

Temperature-Dependence of Muon Catalyzed Fusion in Solid Deuterium and Tritium Mixtures

N. Kawamura, K. Nagamine, T. Matsuzaki, K. Ishida, S.N. Nakamura,[*1] Y. Matsuda, M. Tanase,[*2] M. Kato,[*2] K. Kurosawa,[*2] H. Sugai,[*2] K. Kudo,[*3] N. Takeda,[*3] and G.H. Eaton[*4]

[Muon catalyzed fusion]

Since the first observation of an unexpected density dependence of the muon cycling rate (λ_c) by Jones *et al.*,[1] its origin has been one of the main subjects in μCF studies, both theoretically[2,3] and experimentally.[4,5] A precursory idea proposed by Vesman[6] succeeded to explain that λ_c was above 10^8 s^{-1} by hypothesizing a resonant $dt\mu$ formation mechanism in a collision between $t\mu$ and D_2 or DT. This theory predicted λ_c to be constant with respect to the target density. Moreover, a theoretical calculation based on Vesman's mechanism[7] predicted for λ_c to decrease steeply with decreasing temperature below 100 K; also, λ_c at 20 K was expected to be one order of magnitude smaller than that at 100 K. However, these theoretical predictions are inconsistent with the experimental results,[4,5] which are summarized as follows:

- *Density dependence*: the muon cycling rate increases with increasing density.
- *Temperature dependence*: the muon cycling rate does not decrease with decreasing temperature below 100 K.

These discrepancies may be due to incomplete knowledge of $dt\mu$ formation.

Some ideas were proposed to revise Vesman's mechanism, *e.g.* quasi-resonance in a three-body collision[2] and the phonon effect,[3] although they are not definitive. In the experimental studies up to the present, the main concentration has been put on the density dependence. However, in order to investigate the $dt\mu$ formation mechanism, an approach from a different aspect, *i.e.* the temperature dependence, can provide new information.

In the present work, we conducted a series of μCF experiments in solid deuterium and tritium mixtures with various tritium concentrations (C_t) from 20% to 70%, and at temperatures from 5 K to 16 K. All of the experiments were carried out at the RIKEN-RAL Muon Facility by observing fusion neutrons and X-rays associated with the muon-to-α sticking phenomenon. A preliminary analysis was performed. Figure 1 shows the temperature dependence of the muon cycling rate (λ_c), which is mainly determined by the fusion-neutron data. As can be clearly seen in this figure, λ_c decreased with decreasing temperature in every C_t case.

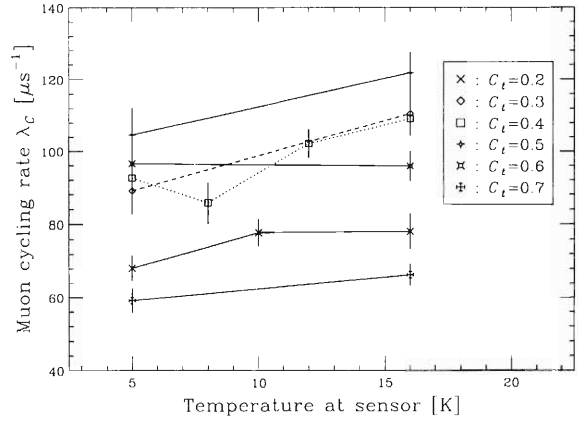

Fig. 1. Temperature dependence of the muon cycling rate, λ_c, in the cases of the tritium concentration, C_t, from 20% to 70%.

Experimentally, we can determine λ_c, and not the $dt\mu$ formation rate ($\lambda_{dt\mu}$). λ_c consists of many parameters, including $\lambda_{dt\mu}$. Although it is the most acceptable interpretation that the observed change in λ_c is caused by a change in $\lambda_{dt\mu}$, other parameters may cause the change in λ_c. In order to determine each parameter independently, a further analysis was performed for the C_t dependence of λ_c at 5 K and 16 K by the method described in the article.[5] Although there still exists some ambiguity, the abovementioned interpretation has been confirmed to be correct. Namely, the observed change in λ_c is explained by the change in $\lambda_{dt\mu}$,

$$\lambda_{dt\mu} : 340\,\mu s^{-1}\,(16\,K) \longrightarrow 200\,\mu s^{-1}\,(5\,K).$$

A theoretical understanding of this result is an urgent subject for the near future.

*1 Present address: Tohoku University
*2 Japan Atomic Energy Research Institute (JAERI)
*3 Electrotechnical Laboratory (ETL)
*4 Rutherford-Appleton Laboratory (RAL), UK

References
1) S. E. Jones et al.: Phys. Rev. Lett. **56**, 588 (1986).
2) L. I. Menshikov et al.: Phys. Lett. B **167**, 141 (1986).
3) K. Fukushima: Phys. Rev. A **48**, 4130 (1993).
4) P. Ackerbauer et al.: Nucl. Phys. A **652**, 311 (1999).
5) K. Ishida et al.: submitted to Phys. Rev. Lett.; Hyperfine Interact. **118**, 203 (1999).
6) E. A. Vesman: Zh. Eksp. Teor. Fiz. Pisma **5**, 50 (1967) (Sov. Phys. JETP Lett. **5**, 91 (1967)).
7) M. P. Faifman et al.: Phys. Lett. B **265**, 201 (1991).

Neutron Energy Spectrum from Muon Catalyzed *t-t* Fusion in a Solid T_2 Target

T. Matsuzaki, K. Ishida, N. Kawamura, S. N. Nakamura,[*1] Y. Matsuda, K. Nagamine, M. Kato,[*2] K. Kurosawa,[*2] H. Sugai,[*2] M. Tanase,[*2] K. Kudo,[*3] N. Takeda,[*3] and G. H. Eaton[*4]

[Muon catalyzed *t-t* fusion]

We have conducted an experiment on muon catalyzed *t-t* fusion in a solid T_2 target by detecting X-rays and neutrons. This experiment is important not only for obtaining supplementary data for the muon catalyzed *d-t* fusion data analysis, but also for a study of the muon catalyzed *t-t* fusion mechanism.

The muon catalyzed *t-t* fusion reaction is expressed as

$$t + t + \mu \rightarrow {}^4\mathrm{He} + n + n + \mu^- + Q\ (11.33\,\mathrm{MeV}) \quad (1)$$

$$(\mu^-{}^4\mathrm{He}) + n + n. \quad (2)$$

We performed an experiment at Port 1 using the same experimental set-up as that for *d-t* μCF studies.[1] The T_2 target gas was purchased from the Chalk River National Laboratory in Canada and installed to an *in-situ* tritium gas handling system.[2] The isotopic enrichment of T was 99.1% with the major remaining components of H (0.67%) and D (0.07%). The ^{3}He impurity originating from tritium β-decay was removed in the tritium gas-handling system. The T_2 gas was then introduced to a target cell cooled by a helium-flow cryostat and solidified at 15 K.[3] The solid T_2 target with a volume of 0.6 cm^3 was formed from the T_2 gas: a volume of 0.574 liter at STP and a radioactivity of 55.2 TBq (1492 Ci). In order to detect the *t-t* fusion neutrons, two calibrated NE213 liquid scintillators (2 inch in diameter and 2 inch in length) were positioned at a distance of 84 cm downstream of the target.[4] A decay μ^- beam with a momentum of 54.5 MeV/c was injected to the T_2 target and about 70μ^- were stopped every muon pulse with a double-pulse time-structure.

The observed recoil proton energy spectrum is shown in Fig. 1 (a). The neutron energy distributes continuously up to 9 MeV, being superimposed on the background from the *d-t* fusion neutrons whose maximum energy is 14.1 MeV. Even if the impurity concentration of the D component in the target T_2 gas is 0.07%, the *d-t* μCF cycling rate is two orders of magnitude larger than the one for *t-t* μCF and the contribution by the *d-t* μCF is not negligible. However, the energy distribution of the *d-t* fusion neutron was well-determined and we could subtract the contribution from the raw spectrum. The obtained spectrum after subtraction is shown in Fig. 1 (b). The spectrum indicates that a large portion of the reaction Q-value is carried away by one neutron in the *t-t* μCF exit channel. This phenomenon is very interesting, and can be well understood by a picture in which the first neutron behaves in strong correlation with a ^{4}He nucleus, like in an intermediate ^{5}He nucleus formation, and the second neutron takes out a large amount of energy with the maximum possible energy (9.4 MeV) being 5/6 of the Q-value. The PSI group has reported a measured neutron energy distribution from *t-t* μCF,[5] but their spectrum drops at the maximum energy of 5 MeV, inconsistent with our observed maximum energy. So far, no theoretical work has been published on the fusion neutron energy distribution from the *t-t* μCF process. Gershtein *et al.* have calculated the energy distribution of (μ^4He) atoms produced in reaction (2) under three assumptions of the statistical distribution, the *n-n* correlation and the *n*-^{4}He correlation.[6] The predicted spectrum gives a distribution of the subtraction between the reaction Q-value and the *t-t* fusion neutron energy distribution in reaction (2). The prediction with the assumption of an *n*-^{4}He correlation supports the present observed neutron energy distribution.

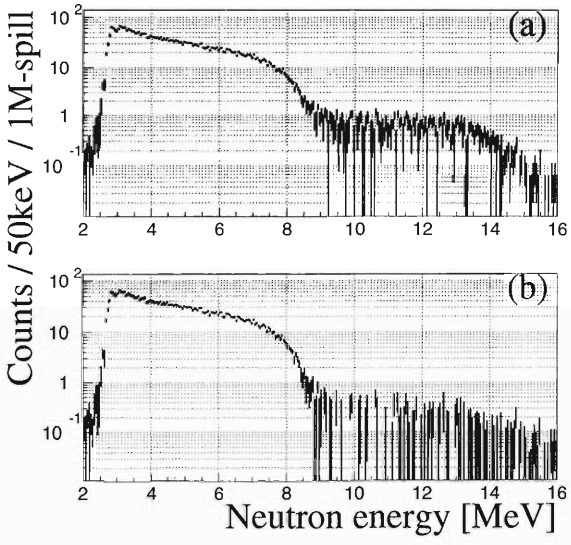

Fig. 1. A recoil proton energy spectrum observed for the fusion neutrons from the *t-t* μCF process. (a) The raw spectrum. (b) The spectrum after subtraction of the *d-t* fusion neutron contribution.

*1 Tohoku University
*2 Japan Atomic Energy Research Institute (JAERI)
*3 Electrotechnical Laboratory (ETL)
*4 Rutherford Appleton Laboratory (RAL), UK

References
1) K. Ishida, K. Nagamine, and T. Matsuzaki et al.: Hyperfine Interact. **118**, 203 (1999).
2) T. Matsuzaki, K. Nagamine, and M. Tanase et al.: Hyperfine Interact. **119**, 361 (1999).
3) K. Ishida, T. Matsuzaki, and K. Nagamine: RIKEN-RAL Annual Report **17** (1997).
4) N. Kawamura et al.: to be submitted to Nucl. Instrum. Methods Phys. Res. A.
5) W. H. Breunlich et al.: Muon Catal. Fusion **1**, 121 (1987).
6) S. S. Gershtein et al.: Sov. Phys. JETP **53**, 872 (1981).

Electron-Nucleus Collider at MUSES

T. Suda, K. Maruyama,* and I. Tanihata

[e+RI collider, Elastic scattering, High resolution spectrometer]

A collider of electrons and a radioactive-ion beam, an e+RI collider, planned in the MUSES project aims at investigating the nuclear structure of many RIs by electron scattering. The charge distributions of unstable nuclei is a main subject to be determined by elastic electron scattering.

We have previously reported the results of our study to clarify the requirements for an electron spectrometer. To achieve an energy-transfer resolution ($\Delta\omega$) to a target nucleus of 1 MeV in the Nucleus-Rest (NR) frame, the required momentum and angular resolutions in the COLlider (COL) frame were found to be 10^{-3} and 1 mrad, respectively, for an optimum electron energy of E_e = 500–700 MeV. We proposed a large acceptance spectrometer (LAS), which tracks electron trajectories in a solenoidal or troidal magnetic field by tracking devices. The LAS covers an azimuthal angle of nearly 2π, which seems to compensate the low luminosity expected in the e+RI collider.

To measure the elastic-scattering cross section of heavier nuclei, however, $\Delta\omega_{NR}$ = 0.1 MeV instead of $\Delta\omega_{NR}$ = 1 MeV will be indispensable. In this case, the momentum resolution, $\Delta p/p$, in the COL frame must be better than 10^{-4}, which forces us to give up LAS and to employ a high-resolution spectrometer (HRS). Obviously, a price to pay for keeping a good $\Delta p/p$ is a smaller solid angle. We have been working to study the feasibility of employing HRS for the e+RI collider. By a careful consideration of the electron-scattering kinematics, the drawback has been found to be overcome by setting the HRS at a very forward angle. At a forward angle, the cross section increases rapidly, and one also gains a larger coverage for the azimuthal angle. For instance, HRS having a ±100-mrad vertical angular acceptance covers more than 20% of 2π at a scattering angle of 5 degrees.

Due to low luminosity, it is not possible to determine the charge form factor up to the high momentum transfer (q_{NR}) region in the NR frame. Depending on the maximum q_{NR}, up to which the form factor is measured, the charge distribution, $\rho_c(r)$, or the mean-square charge radius, $< r_c^2 >^{1/2}$, of an unstable nucleus will be determined. When the form factor is measured up to at least the first diffraction maximum, one can determine $\rho_c(r)$. In the case for very unstable nuclei, whose luminosity is so low that the form factor can be measured only in lower q_{NR} than that for the first dip, $< r_c^2 >^{1/2}$ is determined.

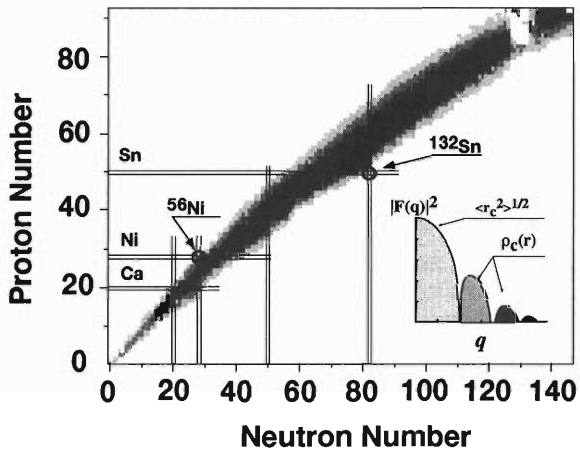

Fig. 1. Accessible form-factor region for each nuclei in a one-week measurement under the given luminosity.

Figure 1 shows the results of a simulation to estimate the accessible form-factor region, as shown by a gradation of gray colors, for each element by a one-week measurement. The simulation uses the luminosity table of the MUSES e+RI collider. A scattering angle of 5–25 degrees is assumed to be covered by a pair of high-resolution spectrometers, whose horizontal and vertical angular acceptances are both ±100 mrad.

As an example, let us briefly discuss the proton magic Sn isotope, which is one of key nuclei for the e+RI collider. The minimum luminosity needed to determine $< r_c^2 >^{1/2}$ and $\rho_c(r)$ is 10^{22} and $10^{26}/\mathrm{cm}^2/\mathrm{s}$, respectively. Since the luminosity for a double-magic nucleus ^{132}Sn is expected to be 6×10^{22}, we will be able to determine $< r_c^2 >^{1/2}$, as can be seen in Fig. 1. Because the luminosity is expected to be larger than $10^{26}/\mathrm{cm}^2/\mathrm{s}$ for $^{108-128}$Sn, these isotopes are candidates for a $\rho_c(r)$ determination.

In summary, it is shown that a forward-angle high-resolution spectrometer can be a solution for the MUSES e+RI collider to determine $< r_c^2 >^{1/2}$ and $\rho_c(r)$ of many isotopes. The solid angle of the spectrometer needs to be 40 msr or more, and the momentum and angular resolution must be better than 10^{-4} and 1 mrad. Since the design of the spectrometer strongly depends on the lattice structure of the collider, discussions are now underway with the MUSES accelerator group.

* Kitasato University

Measurement of the Cross Sections and Analyzing Powers for *d-p* Elastic Scattering at Intermediate Energies

K. Sekiguchi,[*1] H. Sakai,[*1] N. Sakamoto, H. Okamura,[*2] A. Tamii,[*1] T. Uesaka,[*2]
Y. Satou, T. Ohnishi, T. Wakasa,[*3] K. Yako,[*1] S. Sakoda,[*1] K. Suda,[*2]
H. Kato,[*1] Y. Maeda,[*1] M. Hatano,[*1] and J. Nishikawa[*2]

[NUCLEAR REACTIONS, ^{1}H($\vec{d}, d$), E_d = 140, 200, 270 MeV measured: $\sigma(\theta)$, $A_y(\theta)$, $A_{yy}(\theta)$, $A_{xx}(\theta)$, $A_{xz}(\theta)$]

The three nucleon force (3NF) effects in a nucleon-deuteron (Nd) system at intermediate energies ($E/A \geq 60$ MeV) are attracting current interest. This is partly because rigorous numerical calculations are available in terms of Faddeev theory using modern NN forces together with 3NF. Therefore it is becoming possible to compare the calculated results with accurate experimental ones.

In order to study the 3NF effects systematically, we made precise measurements of the cross section and all deuteron analyzing powers (A_y, A_{yy}, A_{xx} and A_{xz}) for *d-p* elastic scattering at E_d = 140, 200 and 270 MeV, covering a wide angular range of $\theta_{c.m.} = 10° - 180°$. A part of the data has been published in Refs. 1 and 2. The CH_2 target was bombarded by polarized deuteron beams. Either scattered deuterons or protons were detected by the magnetic spectrograph SMART, depending on the scattering angle. The beam polarizations were monitored by using a beam-line polarimeter based on *d-p* elastic scattering, and their magnitudes were 60–80% of the theoretical maximum values during the experiments. The statistical errors are within 1.3% for cross sections and ±0.02 or less for A_y, ±0.01 or less for A_{yy}, ±0.02 or less for A_{xx} and ±0.03 or less for A_{xz}, respectively. The uncertainty of the target thickness and charge collection of the beam were also estimated by comparing the measured cross sections for *p-p* elastic scattering with the calculated values by SAID.[3] The ratio of the observed cross sections to the calculated ones is 1.010 ± 0.013 for the measurement at 270 MeV. Thus, the systematic error is estimated to be less than 2%.

In Fig. 1 the experimental results of the cross section and the tensor analyzing power A_{yy} are shown by open circles. Theoretical predictions are also shown.[2,4] The solid curves are calculations with Tucson-Melbourne 3NF[5] and the dashed ones are those which consider only NN forces. The CD BONN potential[6] is used as NN interaction in these calculations. For the cross section, there is a discrepancy in the cross section minimum between the data and the calculated results without 3NF. This discrepancy can be removed by adding 3NF. For A_{yy}, the difference between the data and the calculations without 3NF becomes clearer as the energy increases, while this difference is not described by taking 3NF into account. The agreement is deteriorated when 3NF is included. This feature indicates that the difference in the cross section minimum could be considered as a signature of 3NF, although this 3NF model might have some deficiencies in the spin dependent part.

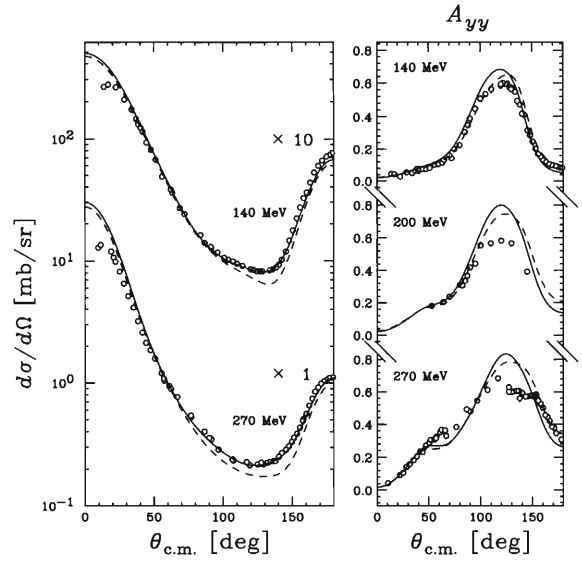

Fig. 1. Cross sections and the tensor analyzing power A_{yy} for *d-p* elastic scattering at 140, 200 and 270 MeV. The dashed curves are the Faddeev calculations in which the CD BONN potential is used as the NN interaction. The solid curves are the Faddeev calculations including the Tucson-Melbourne 3NF.

*1 School of Science, University of Tokyo
*2 Department of Physics, Saitama University
*3 Research Center for Nuclear Physics, Osaka University

References
1) N. Sakamoto, H. Okamura, and T. Uesaka et al.: Phys. Lett. B **367**, 60 (1996).
2) H. Sakai, K. Sekiguchi, and H. Witała et al.: Phys. Rev. Lett. **84**, 5288 (2000).
3) R. A. Arndt and L. D. Roper: *Scattering Analysis Interactive Dial-In program (SAID)*, Virginia Polytechnic Institute and State University (unpublished).
4) H. Witała and H. Kamada: private communications.
5) S. A. Coon et al.: Nucl. Phys. A **317**, 242 (1997).
6) R. Machleidt, F. Sammarruca, and Y. Song: Phys. Rev. C **53**, R1483 (1996).

Measurement of the Polarization Correlation Coefficient for the $^3\vec{\mathrm{He}}(\vec{d},p)^4\mathrm{He}$ Reaction

J. Nishikawa,[*1] T. Uesaka,[*1] A. Tamii,[*2] N. Sakamoto, Y. Satou, T. Wakui, T. Ohnishi, K. Sekiguchi,[*2] K. Suda,[*1] S. Sakoda,[*2] S. Yamamoto,[*3] H. Kato,[*2] M. Hatano,[*2] T. Saito,[*2] N. Uchigashima,[*2] H. Okamura,[*1] and H. Sakai[*2]

[$^3\vec{\mathrm{He}}(\vec{d},p)^4\mathrm{He}$ reaction, E_d = 140, 200, and 270 MeV, Polarization correlation coefficient]

The deuteron D-state wave function is one of the tools used to study the short-range behavior of tensor components in the nucleon-nucleon (N-N) interaction. We are investigating the deuteron D-state by the polarization correlation coefficient ($C_{//}$) for the $^3\vec{\mathrm{He}}(\vec{d},p)^4\mathrm{He}$ reaction.[1] $C_{//}$ is proportional to the D-state density of the deuteron wave function within the framework of the one-nucleon exchange approximation. This $C_{//}$, which is defined as the ratio of the spin-parallel cross section (σ) to spin-unpolarized cross section (σ_0), is given by

$$C_{//}(0^\circ) \equiv \frac{\sigma}{\sigma_0} = 1 + \frac{1}{2}A_{yy}(0^\circ) + \frac{3}{2}C_{y,y}(0^\circ).$$

We have measured $C_{y,y}(0^\circ)$ at the RIKEN Accelerator Research Facility (RARF) to obtain $C_{//}(0^\circ)$, combining it with the tensor analyzing power ($A_{yy}(0^\circ)$), which was measured before.[2]

A polarized deuteron beam was accelerated to E_d = 140, 200, and 270 MeV by the AVF Cyclotron and the Ring Cyclotron. The beam polarization was measured with a polarimeter located at the beam delivery room. The polarized beam was transported to the spectrograph SMART. A polarized ^{3}He target, which was placed in a chamber at the exit of the first dipole magnet (PD1), was bombarded by a polarized beam. Two quadrupole magnets (PQ1 and PQ2) and PD1 were used for beam tuning. ^{3}He gas of 10^{20} cm^{-3} in density enclosed in a glass cell was polarized by the spin-exchange method.[3] The length of the cell was 100 mm and the thickness of the entrance and the exit window was 0.1 mm. The typical polarization of ^{3}He was approximately 13%. Scattered protons were analyzed by subsequent quadrupole (PQ3) and dipole (PD2) magnets and detected by a multiwire drift chamber and plastic scintillators placed in a focal plane. The deuteron beam and the low-energy deuterons were stopped by a beam stopper placed in PD2 and in front of the focal plane.

The proton events were selected by using the time of flight (TOF) from the target to the detector and the energy loss in the plastic scintillators. The proton energy spectrum is shown in Fig. 1. The peak at E_x = 0 MeV is due to the $^3\vec{\mathrm{He}}(\vec{d},p)^4\mathrm{He}$ reaction and is missing in the empty-cell spectrum. The FWHM of the peak is approximately 180 keV.

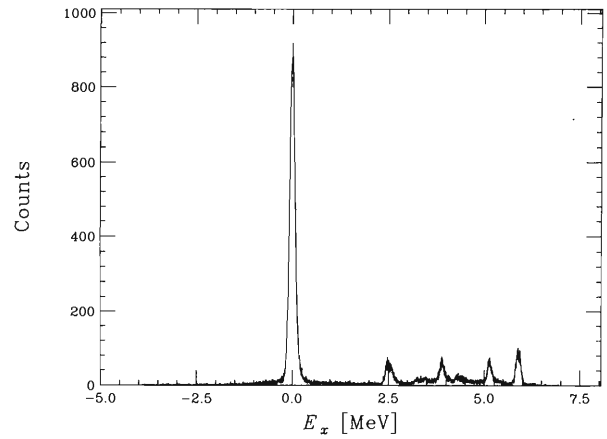

Fig. 1. Excitation energy spectrum for the $^3\vec{\mathrm{He}}(\vec{d},p)^4\mathrm{He}$ reaction at E_d = 200 MeV. The FWHM of the peak at E_x = 0 MeV is approximately 180 keV.

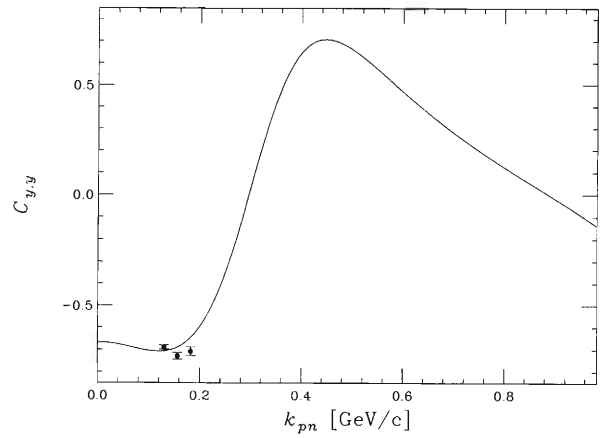

Fig. 2. $C_{y,y}$ for the $^3\vec{\mathrm{He}}(\vec{d},p)^4\mathrm{He}$ reaction at E_d = 140, 200, and 270 MeV, (left, center and right points) respectively. The solid line is a calculated result with the one-nucleon exchange approximation.

$C_{y,y}$ was deduced by using spin-dependent cross sections obtained for all possible combinations of the beam ($P_y = 0, +\frac{2}{3}, -\frac{2}{3}$) and target polarization (up and down). Preliminary results of $C_{y,y}$ are shown in Fig. 2 as a function of the momentum between the proton and the neutron in the deuteron center-of-mass sys-

*1 Department of Physics, Saitama University
*2 Department of Physics, University of Tokyo
*3 Department of Physics, Toho University

tem, k_{pn}. The solid line represents a calculated result with the one-nucleon exchange approximation. Data can be reproduced by the calculation quite well. A detailed analysis is in progress.

References

1) T. Uesaka et al.: Phys. Lett. B **467**, 199 (1999).
2) T. Uesaka et al.: RIKEN Accel. Prog. **33**, 55 (2000).
3) S. Yamamoto et al.: RIKEN Accel. Prog. **34**, 198 (2001).

Measurement of the $^{12}C(d, d')$ Reaction at 270 MeV and a DWIA Analysis Using the Three-Body dN Interaction

Y. Satou, H. Sakai,[*1] H. Okamura,[*2] N. Sakamoto, T. Uesaka,[*2] A. Tamii,[*1] K. Itoh, T. Ohnishi, K. Sekiguchi,[*1] K. Yakou,[*1] S. Sakoda,[*1] K. Suda,[*2] M. Hatano,[*1] H. Kato,[*1] Y. Maeda,[*1] J. Nishikawa,[*2] and H. Kamada[*3]

[Nuclear reaction, Three-body dN interaction]

Light-ion-induced inelastic scattering at bombarding energies above 100 MeV per nucleon has been an appealing probe of nuclear-structure studies because the distorted wave impulse approximation (DWIA) is applicable for reaction calculations. In the IA for the (p, p') reaction, the effective interaction is taken to be the free nucleon-nucleon t-matrix, which can be regarded as being known. In the case of the (d, d') reaction, however, the situation is more complicated, because the structure of the deuteron must be considered. Today, three-nucleon ($3N$) Faddeev calculations make it possible to described the deuteron-nucleon (dN) scattering processes, even at intermediate energies with a reliable accuracy.[1] Therefore, the use of the Faddeev dN t-matrix as an effective interaction could provide a precise DWIA description of the (d, d') reaction. Here, we report on data for the differential cross section for low-lying states in ^{12}C excited via the (d, d') reaction at 270 MeV and compare them with DWIA calculations.

The measurement was performed using the 270 MeV deuteron beam from the Ring Cyclotron by bombarding a 31.3 mg/cm^2 ^{12}C target. The scattered deuterons were analyzed with the magnetic spectrometer SMART. The cross sections for the 2^+, 3^-, 1^+ and 2^- states are shown in Fig. 1 (a). The angular distributions are characteristic of the definite transferred angular momentum (ΔL).

Microscopic DWIA calculations were made by following the description in Ref. 2. The T-matrix is given by

$$T_{dA}^{\mathrm{DWIA}} = \langle X^{(-)}(\vec{R})\chi_{d'}\Phi_{A^*}(\vec{\rho})|t_{dN}e^{i\vec{q}\cdot(\vec{\rho}-\vec{R})}|X^{(+)}(\vec{R})\chi_d\Phi_A(\vec{\rho})\rangle,$$

where the distorted waves in the initial and final channels are denoted by $X^{(+)}(\vec{R})$ and $X^{(-)}(\vec{R})$, the target wave functions by $\Phi_A(\vec{\rho})$ and $\Phi_{A^*}(\vec{\rho})$, and the deuteron spinors by χ_d and $\chi_{d'}$, respectively. $\vec{q}$ is the transferred momentum. The on-shell dN t-matrix (t_{dN}) obtained by $3N$ Faddeev calculations, was used as an effective projectile-nucleon interaction. The distorted waves were generated with the optical potential fitted to elastic-scattering data (see Fig. 1 (b)).

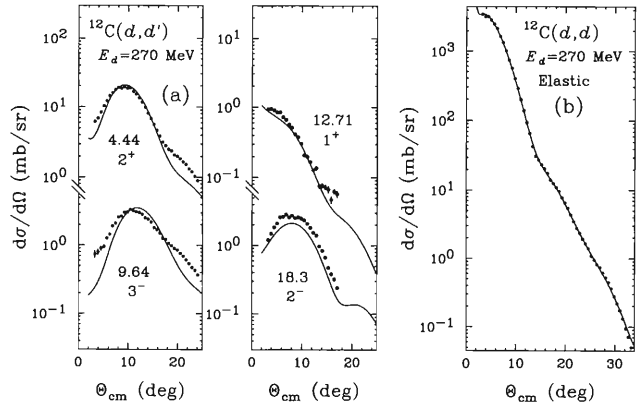

Fig. 1. (a) Measured differential cross sections for the $^{12}C(d, d')$ reaction at 270 MeV leading to low-lying states in ^{12}C (full circles) compared with DWIA calculations (solid lines). (b) Measured differential cross section for the elastic scattering of a deuteron from ^{12}C at 270 MeV. The solid line is the result of an optical-model fit.

The results of DWIA calculations are compared with the data in Fig. 1 (a). The angular-distribution shapes are well reproduced by the calculations. For the 2^+ and 3^- states, a normalization factor of about 2 found in electron scattering[3] was not needed, in agreement with the (p, p') results at incident energies of 100–200 MeV.[4,5] In this energy range the magnitude of the theoretical (p, p') cross section for the 1^+ state is known to depend sensitively on the choice of the effective interaction.[4–6] The present calculation well reproduces the data without introducing any normalization for this state, in agreement with the (p, p') analysis in Ref. 6. The cross section for the 2^- state slightly underestimates in the calculation. The good overall agreement between the data and the calculations indicates that the dN t-matrix obtained from the $3N$ Faddeev calculations gives a sound basis for the projectile-nucleon effective interaction in the DWIA description of the (d, d') reaction at 270 MeV. A striking resemblance between the results of the (d, d') and (p, p') reactions suggests that the former reaction is as sensitive as the latter to the microscopic structure of the target. This is encouraging for a nuclear structure study considering the additional selectivity of the (d, d') reaction to the isoscalar $\Delta T = 0$ transitions.

*1 University of Tokyo
*2 Saitama University
*3 Ruhr University, Germany

References
1) W. Glöckle et al.: Phys. Rep. **274**, 107 (1996).
2) J. Van de Wiele et al.: Phys. Rev. C **50**, 2935 (1994).
3) J. B. Flanz et al.: Phys. Rev. Lett. **41**, 1642 (1978).
4) J. R. Comfort et al.: Phys. Rev. C **24**, 1834 (1981).
5) J. R. Comfort et al.: Phys. Rev. C **26**, 1800 (1982).
6) A. Willis et al.: Phys. Rev. C **43**, 2177 (1991).

Study of Neutron-Rich Nuclides Relevant to the Astrophysics R-Process

Y. Nishi, S. Nishimura, I. Tanihata, K. Morimoto, R. N. Boyd,* and M. Famiano*

[R-process, Nucleosynthesis, β-decay half-life]

The requirements of the r-process (rapid-process) of stellar nucleosynthesis have been well known for several decades.[1] It must produce all nuclei heavier than ^{209}Bi as well as the r-process abundance peaks. And it must do so in a way that does not depend on the preexisting seed nuclei. Several features of the nuclei along the r-processes path are important for abundance predictions. The mass differences between nearby nuclei determine their stability to the (γ, n) process in the hot photon bath in which they are immersed during the r-process. Their lifetimes determine the abundances, if they are at neutron closed shells, of the stable nuclei to which they ultimately decay. Finally, their decay modes, *via* e-, e-n, or something more complex, could produce shifts of the r-process peaks.

At first, we are planning and preparing a β-decay half-life measurement. Clearly, the measurement time for nuclei closer to the neutron drip line will be long, because of the low production rate. We are thus developing 5-layer rotation stopper disks, along with 2-dimensional position-sensitive β-ray detectors and γ-ray detectors, in order to measure many different nuclei concurrently as well as many events within one stopper foil. Figure 1 shows a schematic view of the rotation stopper disks and detectors which we are developing. Each stopper disk has 11 foils. As shown in Fig. 1, a neutron-rich nuclei beam will be implanted to the foil of a certain disk at #1, depending on the range of the nuclide. The stopper disks will be rotated $5/11 \times 2\pi$ [rad] within 300 msec., after which irradiated foils will come to #6 where fixed position-sensitive detectors are located. While the decays of the nuclei in that foil are being measured, another foil will be irradiated.

The detectors consist of a fine plastic-scintilator array and NaI scintilators. Each plastic scintilator has a $4 \times 64\,\mathrm{mm}^2$ effective region and 1 mm or 2 mm thickness. The elements are read out by a 16 ch multi-anode PMT (H6568-10 HAMAMATSU co.). These 16 plastic scintilators are combined into one plate ($64 \times 64\,\mathrm{mm}^2$), and two plates are placed perpendicularly. Hence, two dimensional information concerning the β-rays can be obtained, making it possible to identify the implanted nucleus which we want to detect and to separate that from the backgrounds using position information. NaI scintilators having a 4 cm thickness are placed between the plastic scintilator plates in order to do gamma-ray spectroscopy. Rotation stoppers have already been constructed and confirmed to work well. The design of the detectors has been completed and they are under construction. In early 2001, the first experiment is scheduled using a ^{64}Ni beam, followed by a heavy mass region experiment, executed using ^{104}Ru and ^{136}Xe beams, and so on.

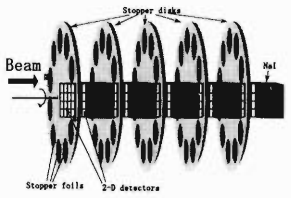

Fig. 1. Schematic view of the rotation stoppers and detectors.

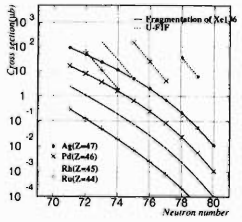

Fig. 2. Cross section of the U-FIF measured at GSI and the expected cross section of the PF estimated by EPAX (ver.2) calculation, where ^{136}Xe is used as the primary beam and Ta as a target.

In order to achieve a higher production cross section of neutron-rich nuclei along the r-process path which is extremely low, we hope to measure and compare the production cross section of the neutron-rich nuclei using Projectile Fragment (PF) for ^{136}Xe and ^{104}Ru, and fission in flight for ^{238}U (U-FIF), if possible. Figure 2 shows the cross section of the U-FIF measured at GSI together with the expected cross section of the PF estimated by the latest EPAX (ver.2) calculation, where ^{136}Xe is used as the primary beam and Ta as a target. It shows that the cross section of U-FIF seems to be larger than that of PF. However, there are parameters which must be taken into account for a realistic scenario, *i.e.* the beam intensity, target thickness, and the acceptance of the RIPS. Especially, it is necessary to investigate the advantage of the U-FIF method for the case of neutron-rich nuclei.

References

1) G. Wallerstein et al.: Rev. Mod. Phys. **69**, 945 (1997).

* Ohio State University, USA

Study of the Secondary Fusion Reaction with the High-Spin Isomer Beam

H. Watanabe, T. Kishida, Y. Gono,[*1] T. Morikawa,[*1] S. Motomura,[*1] T. Fukuchi,[*1] O. Kashiyama,[*1] K. Saitoh,[*1] A. Odahara,[*2] T. Kubo, E. Ideguchi,[*3] B. Cederwall,[*3] T. Bäck,[*3] D. Bucurescu,[*4] and M. Ishihara

[NUCLEAR REACTIONS ^{16}O(^{136}Xe,7n)^{145m}Sm, ^{13}C(^{145m}Sm,xn)$^{158-x}$Er, High-spin isomer beam]

A high-spin isomer beam (HSIB)[1] has been developed at the RIKEN Accelerator Research Facility (RARF). The most remarkable feature of the HSIB compared with a ground-state beam (GSB) is the large intrinsic nuclear spin. Such high-spin isomers have been observed systematically in $N = 83$ isotones with proton number Z from 60 to 68. In recent studies, ^{145m}Sm ($Z = 62$), which has a nuclear spin of $I = \frac{49}{2}$, has been mainly used for a secondary reaction. The ^{145m}Sm beam was produced *via* an inverse-kinematic fusion reaction, ^{16}O(^{136}Xe,7n)^{145}Sm, which led to the beam energy of 5.53 ± 0.11 MeV/nucleon. The experimental technique to obtain the ^{145m}Sm beam intensity of 1–2 $\times$ 10^5 pps on a secondary target was established with the development of a windowless gas target[2] and a superconducting solenoid. By using this beam, the secondary fusion reaction has been investigated. When the fusion reaction is induced by the HSIB, the angular momentum distribution in the compound nucleus is expected to extend toward a higher region due to the vector sum of the isomer spin and the orbital angular momentum brought into the system. Then, the compound nucleus increases in excitation energy only by that of an isomeric state ($\simeq$ 9 MeV) in addition to that carried in by a projectile. Therefore, it may be possible to produce the compound nucleus in a lower energy-higher spin state, namely near to the yrast line. In the present work, the ^{13}C(^{145m}Sm,xn)$^{158-x}$Er reaction was studied. The γ-rays which were emitted from the secondary fusion products ^{154}Er could be identified for the first time in spite of numerous contamination γ-rays in the spectra. The most probable spectrum is shown in Fig. 1, where the γ-rays of ^{154}Er are marked with arrows and energy values reported previously. The yields of γ-rays of interest were in good agreement with the estimated value within the experimental accuracy. However, the amount of angular momenta brought into the system by the HSIB could not be compared with those by the GSB experimentally because of the poor statistics and the large backgrounds. Information concerning the spin distribution formed by the GSB has been already deduced from appropriate experimental probes, *i.e.* the yrast

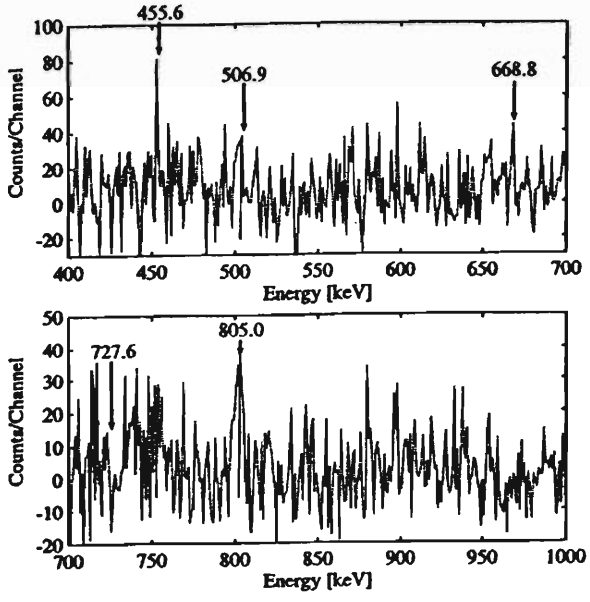

Fig. 1. Background subtracted spectra from the sum of gated spectra in the yrast band of ^{154}Er. The energies of γ-rays in the yrast band are marked with arrows.

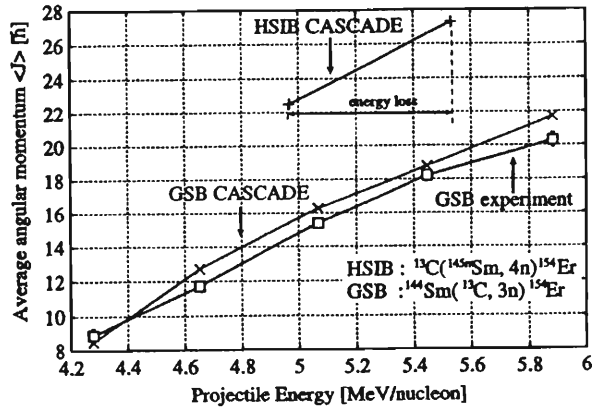

Fig. 2. Averaged angular momenta obtained in the GSB experiment (square) and calculated for the GSB (cross) and the HSIB (plus) as a function of the bombarding energy [MeV/nucleon] for ^{154}Er.

*1 Department of Physics, Kyushu University
*2 Nishinippon Institute of Technology
*3 Department of Physics, Royal Institute of Technology, Sweden
*4 National Institute for Physics and Nuclear Engineering, Rumania

γ-ray flow and the γ-ray multiplicity. These quantities were compared with those resulting from a simulation performed by the code CASCADE. The average angular momenta deduced from the γ-ray multiplicity are shown in Fig. 2. As can be seen, the measured γ-ray multiplicity reflects the amount of angular momentum brought into the system. These results encouraged us to measure the γ-ray multiplicity in the HSIB experiment so as to investigate the difference in the transfered angular momenta between the HSIB and the GSB.

References

1) Y. Gono et al.: Nucl. Phys. A **588**, 241c (1995).
2) T. Kishida et al.: Nucl. Instrum. Methods Phys. Res. A **438**, 70 (1990).

Excitation-Energy Dependence of the GDR in Hot ^{209}Bi Nuclei

Y. Aoki,* K. Yoshida, T. Nakagawa, K. Nakagawa, and J. Kasagi*

[NUCLEAR REACTION, ^{209}Bi+^{209}Bi E/A = 12 MeV/u; Inelastic scattering; Measured high energy γ rays, protons, and residues; Deduced GDR response]

The excitation-energy dependence of the property of the giant dipole resonance (GDR) in ^{209}Bi on the excitation energies up to 500 MeV was studied by measuring the high-energy γ rays in coincidence with the heavy fragment. There have been many studies concerning the GDR of hot nuclei in the Sn region. However, the experimental data are scarce for heavier nuclei.

The excited states of ^{209}Bi were populated by deep inelastic scattering of ^{209}Bi + ^{209}Bi at 12 MeV/nucleon. A beam of ^{209}Bi from the RIKEN RING Cyclotron irradiated a 1 mg/cm^2 ^{209}Bi self-support target. Fragments of the reaction were detected by 3 large PPAC/Ionization chambers. Protons evaporated from the fragments were measured by a crystal ball consisting of 65 BaF_2 poswitch detectors. The excitation energy of each fragment was determined by the kinematics of the detected fragment, and was confirmed by the energy spectra of the protons.

The high-energy γ-rays were measured by 2 sets of high-energy γ-ray detectors consisting of 7 BaF_2 scintillators. The γ-ray spectra were obtained for the four excitation bins of 0–40, 40–100, 100–250, and $\geq$ 250 MeV. The multiplicities of the γ rays were also measured by a crystal ball and used for deducing the angular momenta of the excited fragments.

The obtained spectra were compared with statistical model calculations using the code CASCADE. In the calculation, the initial distribution of the excitation energies and the angular momenta of the fragments were taken from the experimental data. The GDR energies (E_G) and widths (Γ_G) were treated as the parameter and were determined by a χ^2 fitting of the calculated spectra and experimental spectra. The GDR strength was fixed at the value of the full energy-weighted sum rule. We made two different assumptions concerning Γ_G. One was that Γ_G is fixed during the de-exciting cascade. This assumption is commonly used for the GDR analysis. The apparent width (Γ_{app}) is obtained in this assumption, since we neglect the change of Γ_G along with the decay. The other was that Γ_G varies according to the excitation energies of the de-exciting state, so that the variation of Γ_G is properly included in the calculation. Both calculations gave a similar quality of the fits.

In Fig. 1, the obtained Γ_G is plotted against the temperature (T) of the initial state. Temperatures were obtained from the excitation energies by correcting the effect of the angular momenta. Γ_{app}, which was obtained based on the former assumption, are shown as circles in the figure. As can be seen, the apparent widths are varied from 4.8 MeV to 12 MeV along with an increase in the temperature from 0 to 2.5 MeV and saturate for higher temperatures. Although the result agrees well with the theoretical work of Ormand *et al.*[1] and Dang *et al.*,[2] the assumption is not justified, since Γ_G is varied from 4.8 MeV to 12 MeV. The result of the latter assumption, which includes the effect of the varied width, is shown as the solid line of Fig. 1. Γ_G is a similar value to Γ_{app} for $T \leq 2$ MeV, but a rapid increase of Γ_G is seen for $T \geq 2.5$ MeV. This result is in disagreement with the theories, although similar results were experimentally obtained in the Sn region.[3]

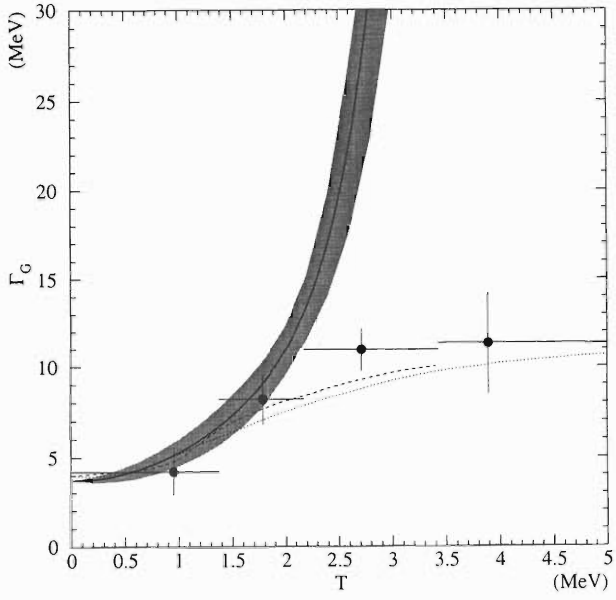

Fig. 1. Temperature dependence of the GDR width of ^{209}Bi. The circles are the results from the fixed-Γ_G calculation. The solid line shows the width deduced from the variable-Γ_G calculation. The gray zone along with the line indicates the uncertainty of Γ_G. The theoretical results from Ormand *et al.*[1] and Dang *et al.*[2] are also shown as dashed and dotted lines, respectively.

The rapid increase of Γ_G indicates that GDR disappeared due to successive broadening of the width. We defined the limiting temperature of the GDR as the temperature at which Γ_G exceeds 30 MeV, and is plotted in Fig. 2 against the mass together with the results of other experiments.[3] As can be seen, the limiting

* LNS, Tohoku University

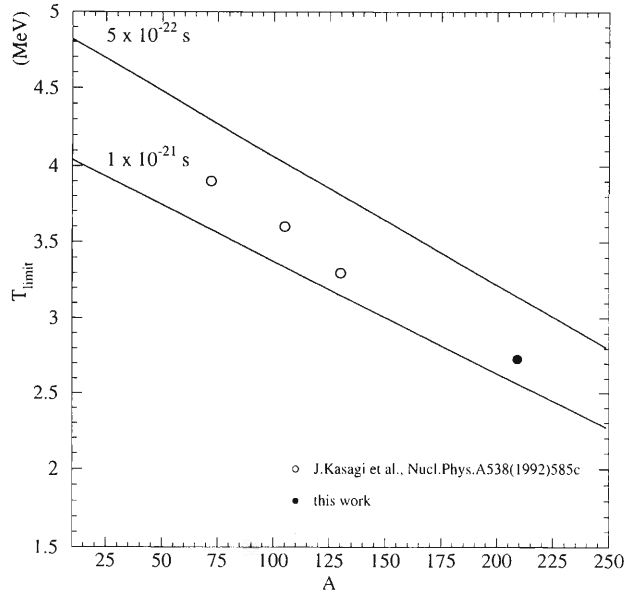

Fig. 2. Limiting temperature of the GDR are plotted as a function of mass A. The temperatures of the excited states corresponding to their lifetimes of 1×10^{-22} and 5×10^{-23} are also shown in the figure.

temperature of the GDR is well-scaled by the lifetimes of the excited states, which are estimated from the statistical model. It can be said that the GDR disappears at a lifetime of about 8×10^{-22} sec.

References

1) W. E. Ormand, P. F. Bortignon, and R. A. Broglia: Phys. Rev. Lett. **22**, 607 (1994).
2) N. Dinh Dang and A. Arima: Nucl. Phys. A **636**, 427 (1998).
3) J. Kasagi, et al.: Nucl. Phys. A **538**, 585c (1992).

Search for a $Z = 118$ Superheavy Nucleus in the Reaction of ^{86}Kr with ^{208}Pb

K. Morimoto, K. Morita, I. Tanihata, N. Iwasa,[*1] R. Kanungo, T. Kato, K. Katori, H. Kudo,[*2] T. Suda, I. Sugai,[*3] S. Takeuchi, F. Tokanai,[*4] Y. Wakasaya,[*5] T. Yamaguchi, A. Yeremin,[*6] A. Yoneda, A. Yoshida, and M. Giurgiu

[NUCLEAR REACTION, Gas-filled recoil separator, Alpha-decays]

Last year, three decay chains were reported by a Lawrence Berkeley Laboratory group[1] in the reaction products of ^{86}Kr with ^{208}Pb. The observed chains have a possibility to be consistent with the formation of $^{293}118$ and its sequential α decays. However, the decay chains are not associated with any known nuclei. The observed production cross section is 2.2 (+2.6, −0.8) pb. This experiment was motivated by a following recent prediction of Smolanczuk,[2] which indicates that the cross section of a cold-fusion reaction of ^{86}Kr with ^{208}Pb is 670 pb. Although the experimental cross section reported is by 3 hundred times smaller than that of the theoretical prediction, we made a followup experiment of the LBL group, because it is still much bigger than the cross section systematics with extrapolation of the experimental values.

The experimental set up is shown in Fig. 1. The Pb target thickness was 320–440 μg/cm^2; it was evaporated onto the downstream side of a 100 μg/cm^2 carbon foil. Furthermore, the target was covered by 20–30 μg/cm^2 carbon with evaporation. Six segments of it were mounted on a wheel that rotated at 600 rpm. The beam energy was 457.6 MeV, and the beam current was 500 particle nanoamperes on the average. The incident beam energy at the center of the target was 449 MeV. To avoid the primary beam from impinging on the silicon detector in the event of a broken target, a carbon foil of 30 μg/cm^2 thickness was mounted as a charge stripper of primary beams. The reaction products recoiling out of the target were separated from the primary beam by using a gas-filled recoil separator, GARIS.[3] The separator was filled with helium gas at one torr. After passing through the separator, the recoiling particles were implanted in a position-sensitive silicon detector (PSD), which had an active area of 60 × 60 mm with a thickness of 300 μm. Light charged particles passing through the PSD were detected by a veto SSD. The total counting rate of the PSD was several counts/sec under the condition with 1000 particle nanoamperes of the beam intensity. The dead time of electronics was reduced by using a double trigger system, which was able to accumulate two 'implanted or decay' events as a one 'electronics' event. It was 20 μs for less than 2 events and 800 μs for more than 3 events. The total system was checked by the reaction of ^{86}Kr with ^{110}Cd.

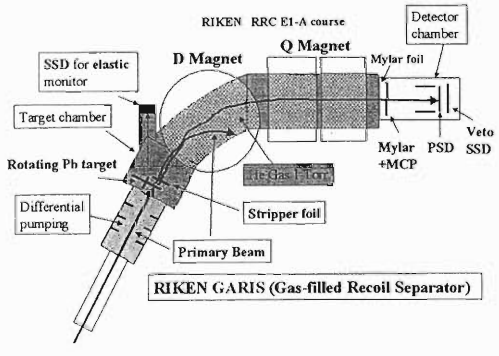

Fig. 1. Schematic view of the experimental set up.

We had machine times in Feb. 2000. The first 4 days were performed for a test of targets, an estimation of the magnetic rigidity (Bρ), calibrations of the detectors and a check of the data-acquisition system. The last 10 days were used to accumulate a dose of 2×10^{18} ions, but no candidate of the evaporation residue was found. In this beam dose, when we assume that the efficiency of GARIS was 0.8 and that one event was observed, the cross section corresponds to 0.6 pb. Since we used a gas-filled separator with helium gas as the LBL group did, a problem of charge changing decay of isometric states in flight would be less significant than the production experiment with a vacuum-type kinematic separator as SHIP at GSI or as LISE at GANIL. We chose the value of the magnetic rigidity of the separator to be 2.1 Tm in order to make the experimental condition as close as that of the LBL group. However, this Bρ value still has an ambiguity as a suitable value for $^{293}118$. Because the mean values of the charge states in the helium gas for such atoms its atomic number larger than 110 have not been well studied experimentally, we should perform a systematic study of them.

*1 Tohoku University
*2 Niigata University
*3 Institute for Particle and Nuclear Studies, High-Energy Accelerator Research Organization (KEK)
*4 Yamagata University
*5 IBM Corporation
*6 Flerov Laboratory of Nuclear Reactions JINR, Russia

References

1) V. Ninov et al.: Phys. Rev. Lett. **83**, 1104 (1999).
2) R. Smolanczuk: Phys. Rev. C **59**, 2634 (1999).
3) K. Morita et al.: Nucl. Instrum. Methods Phys. Res. B **70**, 220 (1992).

Superheavy Hydrogen ^{5}H, Spectroscopy of ^{7}He

A. A. Korsheninnikov, M. S. Golovkov, A. Ozawa, K. Yoshida, I. Tanihata, Z. Fulop, K. Kusaka, K. Morimoto, H. Otsu, H. Petrascu, F. Tokanai, D. D. Bogdanov,[*1] M. L. Chelnokov,[*1] A. S. Fomichev,[*1] V. A. Gorshkov,[*1] Y. T. Oganessian,[*1] A. M. Rodin,[*1] S. I. Sidorchuk,[*1] S. V. Stepantsov,[*1] G. M. Ter-Akopian,[*1] R. Wolski,[*1] W. Mittig,[*2] P. Roussel-Chomaz,[*2] H. Savajols,[*2] E. A. Kuzmin,[*3] E. Y. Nikolskii,[*3] B. G. Novatskii,[*3] and A. A. Ogloblin[*3]

[NUCLEAR REACTION, p(^{6}He,^{2}He)^{5}H, d(^{6}He,p)^{7}He, $E = 36A$ MeV]

Both neutron-rich nuclei ^{5}H and ^{7}He were investigated in numerous experiments for 30 years. However, until now, the existence of ^{5}H as a well-defined resonance was remained unclear. The ground state of ^{7}He, which decays into n+^{6}He, was established very well experimentally, but many attempts to observe an excited state of ^{7}He were unsuccessful. We performed a spectroscopic study of ^{5}H and ^{7}He using radioactive beams.

To search for ^{5}H, we applied an experimental method that is similar to the missing-mass method, but with the detection of unstable recoil particles. In the usual missing-mass experiment, a binary reaction, $A(b,c)D$, is studied, and a measurement of the recoil particle, c, allows one to obtain an excitation spectrum for the residual nucleus, D. If the residual system, D, is very neutron rich, then — generally speaking — the particle c is very proton rich and it can even be unstable, like, *e.g.*, ^{6}Be, that decays into p+p+α, or the similar singlet-state ^{2}He, that decays into p+p. To deal with an unstable recoil nucleus, c, one needs to detect all particles from its decay. Having kinematically complete information on the unstable system, c, one can determine the excitation energy in the residual system, D, and perform its spectroscopy.

For the spectroscopy of ^{5}H we studied the reaction p(^{6}He,^{2}He)^{5}H. The secondary beam of ^{6}He with the energy of $36A$ MeV was obtained using the fragment separator ACCULINA at JINR (Dubna). As a target we used a cryogenic target from GANIL (France), which was filled with hydrogen gas. Two protons from the decay of ^{2}He were detected in coincidence by the RIKEN telescope, which represents a stack of ring-like solid-state strip-detectors. Apart from protons, we also detected tritons from the decay of ^{5}H→t+n+n, using a downstream telescope consisting of a large-area SSD-detector and a BGO-crystal.

Figure 1 shows the preliminary result for the ^{5}H spectrum extracted from the p+p-coincidences and measured in coincidence with tritons from the decay of a ^{5}H-system, p(^{6}He,ppt). The spectrum is shown as a function of the energy of ^{5}H above the decay threshold, t+n+n. The background from measurements with an

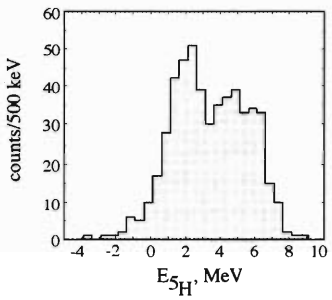

Fig. 1. Missing mass spectrum of ^{5}H from the reaction p(^{6}He,ppt).

empty target (instead of the target filled by hydrogen) was negligible in this spectrum. A cut-off at ~ 7 MeV reflects the detection limit due to the acceptance of the RIKEN telescope.

In the spectrum of Fig. 1, a peak at ~ 2 MeV attracts attention, which is a good candidate for the resonance ^{5}H. An analysis of the data is still in progress. Note that the spectra obtained for different reaction channels (p(^{6}He,pt)^{3}H and p(^{6}He,t)^{4}He) show proper peaks corresponding to the residual nuclei (^{3}H and ^{4}He), which implies the reliability of the obtained results.

To search for excited states of ^{7}He, we performed two experiments. In the first experiment we used a secondary beam of ^{8}He produced by the fragment separator RIPS. We studied the reaction p(^{8}He,d)^{7}He and observed an excited state of ^{7}He which decays into ^{4}He+3n. Most likely, this state has a structure with a neutron in the excited $p_{1/2}$-state coupled to the ^{6}He core, which, itself, is in the excited 2^+ state. These results were recently published.[1)]

In the second experiment, we especially aimed at searching for single-particle states in ^{7}He. The d(^{6}He,p) reaction was investigated using the ^{6}He secondary beam produced by the fragment separator ACCULINA at JINR (Dubna). We used the GANIL cryogenic target, which was filled with deuterium. An analysis of the obtained data is in progress.

*1 JINR, Russia
*2 GANIL, France
*3 Kurchatov Institute, Russia

References

1) A. A. Korsheninnikov et al.: Phys. Rev. Lett. **82**, 3581 (1999).

Observation of an Excited State in ^{7}He with an Unusual Structure†

A. A. Korsheninnikov, M. S. Golovkov, A. Ozawa, E. A. Kuzmin,*1 E. Y. Nikolskii,*1 K. Yoshida, B. G. Novatskii,*1 A. A. Ogloblin,*1 I. Tanihata, Z. Fulop, K. Kusaka, K. Morimoto, H. Otsu, H. Petrascu, and F. Tokanai

[NUCLEAR REACTION, p(^{8}He,d)^{7}He, $E = 50A$ MeV, Nuclear structure]

To perform the spectroscopy of ^{7}He, we studied the reaction p(^{8}He,d)^{7}He. A secondary beam of ^{8}He at $50A$ MeV was produced by the fragment separator RIPS. As a proton target, we used CH_2. Background measurements with a carbon foil and an empty target were also performed. Deuterons were detected by a telescope of ring-like strip-detectors at small angles in a laboratory system corresponding to a high cross section. In addition to the deuterons, we detected particles emitted from the decay of ^{7}He. Neutrons were measured by the neutron walls of plastic scintillators, while charged particles were bent in a dipole magnet and detected by a drift chamber and the plastic scintillators' hodoscope. These parts of the detection system allowed us to investigate the spectra of deuterons detected in coincidence with ^{6}He, ^{4}He, and neutrons. As a result, we obtained the deuteron spectra from the reactions p(^{8}He,d), p(^{8}He,d^{6}He), p(^{8}He,d^{4}He), p(^{8}He,dn), p(^{8}He,dn^{6}He), and p(^{8}He,dn^{4}He).

The obtained spectra show the well-known ground state of ^{7}He at the energy $E_n - {}^6\mathrm{He} = 0.44$ MeV above the decay threshold, n+^{6}He, but also an excited state of ^{7}He at $E_n - {}^6\mathrm{He} \sim 3.3$ MeV. The decay scheme of ^{7}He is shown in Fig. 1.

The most interesting experimental finding is that the revealed excited state of ^{7}He decays predominantly into ^{4}He+3n, in spite of a larger ^{6}He+n decay energy.

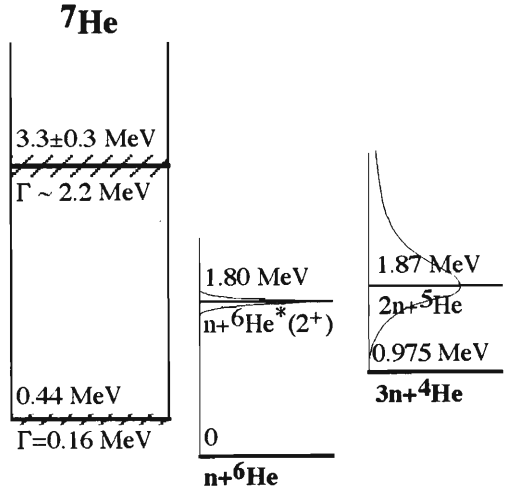

Fig. 1. Decay scheme of ^{7}He.

This reflects an unusual structure of this state.

The structure of the found ^{7}He* level should represent a neutron in an excited state coupled to the ^{6}He-core, which itself is in the excited 2^+-state. The population of such an unusual state in our experiment is consistent with the structure of ^{8}He used as a projectile, because the ground state of ^{8}He contains mainly the ^{6}He-subsystem in the excited 2^+-state.

† Condensed from the article in Phys. Rev. Lett. **82**, 3581 (1999)

*1 Kurchatov Institute, Russia

Search for Neutron Pair Pre-Emission in the Fusion of ^{11}Li Halo Nuclei with Si Target

M. Petrascu,[*1] I. Tanihata, K. Morimoto, T. Kobayashi,[*2] K. Katori, I. Cruceru,[*1] M. Giurgiu, A. Isbāsescu,[*1] H. Petrascu,[*1] R. Ruscu,[*1] M. Chiba,[*2] S. Nishimura, A. Ozawa, T. Suda, K. Yoshida, and C. Bordeanu[*3]

[NUCLEAR REACTIONS; Si(^{11}Li, fusion), E~13 A MeV; Secondary beams; Neutron coincidences]

The pre-emission of neutrons in the fusion of ^{11}Li halo nuclei with Si targets was first reported in Refs. 1–3. The pre-emission of neutron pairs was first analysed in Ref. 4. However, the statistics of n-n coincidences was rather low due to the fact that the detection system was unsuited for such measurements. Reported here are the results of a recent experiment performed by the aid of a new array[4] detector, built within the cooperation between IPNE-Romania and RIKEN-Japan. The diagram of the experimental set-up is similar to the previous one, except for the facts that an array detector was used instead of the RIKEN "Long neutron wall" and a Si detector-target 500 μm thick was placed in the MUSIC chamber instead of the previous 250 μm thick Si detector target. The array detector consists of 81 elements, made of $4 \times 4 \times 12\,\mathrm{cm}^3$ BC-400 crystals, mounted on XP2972 phototubes. The efficiency of the crystals[4] based on a Monte Carlo calculation for 13 MeV neutrons is 34%. The array detector was placed at a distance of 138 cm from the target. A calibration to determine the thresholds of those detectors was performed by means of cosmic rays. The measurements were performed with 13 A MeV ^{11}Li and ^{9}Li beams. The ^{9}Li beam, which had no pre-emissions of neutron pairs, was used for a cross-talk background determination. It was found that the cross-talk coefficient for adjacent detectors (first-order coincidences) is 0.020 ± 0.003, for detectors separated by one detector (second-order coincidences) is 0.0052 ± 0.001, and for detectors separated by two detectors (third-order coincidences) is 0.0017 ± 0.0007

The processing of data obtained with ^{11}Li revealed a remarkable n-n coincidence effect. After subtracting the cross-talk background, 109 ± 23 first-order n-n coincidences, 107 ± 15 second-order n-n coincidences and 98.7 ± 12.4 third-order coincidences remained within the range of the narrow neutron group (the neutrons distribute in a narrow forward angle).

On the basis of the n-n coincidence results, a concentration of $(84 \pm 8)\%$ neutron pairs within a narrow neutron group was estimated. From the obtained coincidence results, the differential cross-section as a function of the angle θ (LS) between the momenta of two neutrons was also derived. For most of the neutron pairs, θ (LS) is less than about 3°.

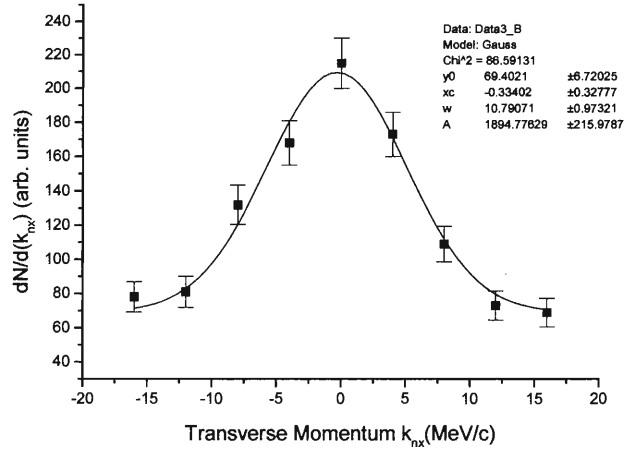

Fig. 1. Transverse momentum distribution of the pre-emitted neutrons in the fusion reaction of ^{11}Li + Si measured along the line parallel to the x-axis. From a Gaussian analysis, it follows that the width of the distribution is (10.7 ± 0.97) MeV/c.

The measurement with the array detector allowed a new, very precise determination of the transverse momentum distribution for the neutrons within the narrow group. It turns out that the FWHM of this distribution is close to 11 MeV/c.

Figure 1 shows the results concerning the determination of transverse momentum of narrow neutron group.

References

1) M. Petrascu et al.: RIKEN AF-NP-237 (1996).
2) M. Petrascu et al.: Phys. Lett. B **405**, 224 (1997).
3) M. Petrascu et al.: Rom. J. Phys. **43**, 307 (1998).
4) M. Petrascu et al.: Rom. J. Phys. **44**, 83 (1999).

*1 National Institute of Physics and Nuclear Engineering, Romania
*2 Tohoku University
*3 Weizman Institute, Israel

Sub-Barrier Fusion of ^{11}Be+^{209}Bi

C. Signorini, A. Yoshida, T. Fukuda, Y. Watanabe, Y. Mizoi, N. Fukuda, H. Sakurai, Y. Watanabe, D. Pierroutsakou, L. Stroe, P. K. Saha, and M. Ishihara

[NUCLEAR REACTION: ^{9,10,11}Be+^{209}Bi, Sub-barrier fusion, α-decay]

Measurements of the sub-barrier fusion cross section in the system of ^{11}Be (halo nucleus) + ^{209}Bi and the comparisons with the ^{9}Be (stable nucleus) + ^{209}Bi one have been extensively studied in parallel.[1,2] The main goal is to investigate whether effects from the halo structure and/or the weak binding energy of the last halo neutron show up in the cross sections. The results up to now show that the fusion cross sections in the above barrier region are reduced by ~30% for both ^{11}Be and ^{9}Be due to the neutron breakup competing process. This may be due to the small binding energy of the last neutron, $S_n = 0.5$ MeV for ^{11}Be and 1.7 MeV for ^{9}Be. In the sub-barrier region, those two fusion cross sections are quite similar. This is rather unexpected and needs to be confirmed by more accurate measurements, since the fusion cross section for this ^{11}Be system consists of the 5n, 4n, and fission channel, but the 3n long-lived channel contribution could not be included. Our experimental setup was improved to measure the 3n evaporation residue, ^{217}Fr ($E_\alpha = 8.32$ MeV, $T_{1/2} = 16\,\mu$s).

^{9,10,11}Be beams were produced by the fragmentation process of a ^{13}C primary beam with 100 A MeV energy and around 100 pnA intensity on a Be production target with 12 mm thickness. Those Be isotopes were separated by the RIPS projectile fragment separator, resulting in a purity of almost 100%. The typical beam intensity of these isotopes was 150 kcps with an energy of $E_{cm} = 47$ MeV $\pm$ 15% (in fwhm) on the Bi target. In order to improve the statistics of fusion events, a stack of 3 thin Bi target foils (800 μg/cm^2 evaporated on 70 μg/cm^2 Mylar foil) was surrounded by 16 large Si surface barrier detectors (SSD) with a size of 48 × 48 mm^2 and a thickness of 300 μm. The detection solid angle for the α-decays from one target was around 80% of 4π. A plastic scintillator counter with a thickness of 1 mm was introduced at the end of the target stack in order to eliminate any non-reaction events where the beam penetrates until the end without fusion. The multi-hit

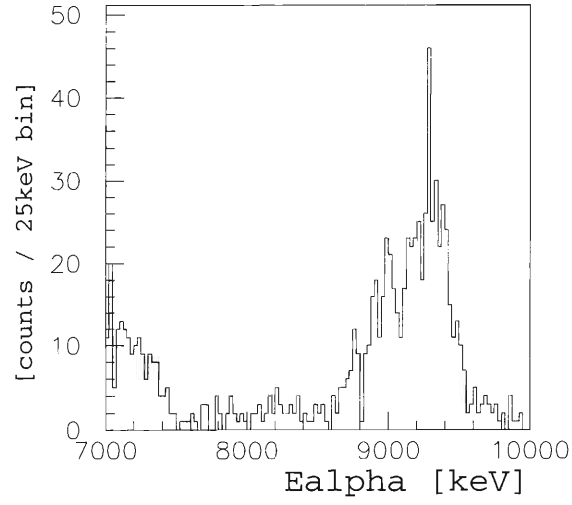

Fig. 1. The α-decay spectra from ^{215}Fr and ^{216}Fr.

TDC was introduced in order to record all the timing within 20 μsec long ADC gate period. Using these methods we can select delayed α-decay events from 3n)^{217}Fr and also select the fission events with the coincidence of beam timing and 2 plane hit of SSD detectors. Figure 1 shows a part of the observed α-decay spectra from the fusion evaporation residue nucleus 5n)^{215}Fr ($E_\alpha = 9.35$ MeV, $T_{1/2} = 86$ ns) and 4n)^{216}Fr ($E_\alpha = 9.0$ MeV, $T_{1/2} = 700$ ns) with the decay timing analysis gate < 2 μsec. We gained the total statistics of these α-decay events by around two-times the previous one. A timing analysis of the TDC is proceeding in order to reduce the background at the 3n)^{217}Fr peak, which is mainly from an elastic scattering of the other beam particle, accidentally coinciding during the long ADC gate period.

References

1) C. Signorini et al.: Eur. Phys. J. A **2**, 227 (1998).
2) C. Signorini et al.: Eur. Phys. J. A **5**, 7 (1999).

Inelastic Alpha-Scattering Reactions on ^{14}O and ^{12}Be

A. Saito,[*1] S. Shimoura,[*2] T. Minemura,[*1] Y. U. Matsuyama,[*1] H. Baba,[*1] H. Akiyoshi, N. Aoi,[*3] T. Gomi,[*1] Y. Higurashi,[*1] K. Ieki,[*1] N. Imai,[*3] N. Iwasa,[*4] H. Iwasaki,[*3] S. Kanno,[*1] S. Kubono,[*2] M. Kunibu,[*1] S. Michimasa,[*2] T. Motobayashi,[*1] T. Nakamura,[*5] H. Sakurai,[*3] M. Serata,[*1] E. Takeshita,[*1] S. Takeuchi,[*1] T. Teranishi,[*2] K. Ue,[*2] K. Yamada,[*1] and Y. Yanagisawa

[NUCLEAR REACTIONS: ^{4}He(^{14}O,^{14}O*), ^{4}He(^{12}Be,^{12}Be*), $E_{\mathrm{lab.}} = 60$ MeV/nucleon, Inelastic Scattering]

Inelastic alpha scattering at intermediate energies is a powerful tool for investigating the excited states of nuclei, especially for giant monopole resonances, in order to discuss nuclear compressibility.[1)] We have measured the inelastic α-scattering cross section on the unstable nuclei ^{14}O and ^{12}Be in inverse kinematics for the first time. The present experiment was aimed at measuring the cross sections to the known 0^+ state and other states and obtaining higher excitation energy spectra by using the invariant mass method for various decay channels.

Radioactive beams of ^{14}O and ^{12}Be were produced by the RIKEN Projectile-fragment Separator (RIPS) by projectile-fragmentation reactions of 135 MeV/nucleon ^{16}O and 100 MeV/nucleon ^{18}O, respectively. The energies of the beams were 59 MeV/nucleon and 60 MeV/nucleon, respectively. The secondary beams were identified event-by-event from time-of-flight (TOF) information between two plastic scintillators of 0.5 mm thicknesses separated by 5.3 m from each other. The secondary beams bombarded a liquid helium target confined within a cell with a window of 24 mm diameter. The direction and position of each beam particle at the secondary target were measured by two sets of Parallel Plate Avalanche Counters (PPAC's) installed upstream from the secondary target.

Outgoing particles were detected and identified by a plastic scintillator array hodoscope located 4 m downstream from the secondary target. The array consists of three layers (ΔE, $E1$, and $E2$) of 5 mm, 60 mm, 60 mm thicknesses, respectively. The energies and scattered angles of the particles were determined by the TOF's and hit positions in the hodoscope, respectively. Each particle was identified by using the TOF-ΔE and TOF-E methods.

An array of sixty-eight NaI(Tl) scintillators of $6 \times 6 \times 12\,\mathrm{cm}^3$ rectangular shape coupled to a 5 cm ϕ photomultiplier tube were set around the secondary target. The segmentation of the array allowed us to correct for any Doppler shifts from moving reaction products.

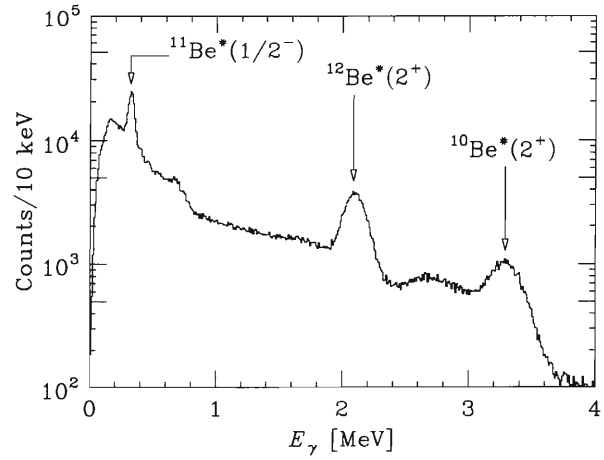

Fig. 1. Doppler-corrected γ-ray energy spectrum obtained in coincidence with the reaction products of Be isotopes.

Figure 1 shows an on-line Doppler-shift-corrected spectrum of γ rays for events identified as Be isotopes at the ΔE hodoscope in the ^{4}He+^{12}Be reaction. De-excitation γ rays were observed at energies of 0.38 MeV, 2.10 MeV, and 3.36 MeV which correspond to the known γ lines from ^{11}Be*(1/2$^-$), ^{12}Be*(2$^+$),[2)] and ^{10}Be*(2$^+$) states, respectively.

Data analyses are now in progress.

References

1) D. H. Youngblood et al.: Phys. Rev. C **57**, 2748 (1998); D. H. Youngblood et al.: Phys. Rev. C **60**, 014304 (1999).
2) H. Iwasaki et al.: Phys. Lett. B **481**, 7 (2000); H. Iwasaki et al.: Phys. Lett. B **491**, 8 (2000).

*1 Department of Physics, Rikkyo University
*2 Center for Nuclear Study, University of Tokyo
*3 Department of Physics, University of Tokyo
*4 Faculty of Science, Tohoku University
*5 Department of Applied Physics, Tokyo Institute of Technology

Measurement of the Magnetic Moment for ^{15}C

H. Ogawa,[*1] K. Asahi, K. Sakai,[*1] H. Ueno, M. Nagakura,[*2] T. Suzuki,[*3] H. Miyoshi,[*1] Y. X. Watanabe, N. Imai,[*4] K. Yoneda, A. Yoshimi, K. Yogo,[*1] T. Suga,[*1] A. Goto,[*1] T. Honda,[*1] Y. Kobayashi, A. Yoshida, T. Kubo, and M. Ishihara

[NUCLEAR STRUCTURE: Spin-polarized radioactive beams, β-NMR, Measured magnetic moment, $^{15}C_{g.s.}$]

The magnetic moment for $^{15}C_{g.s.}$ ($I^\pi = 1/2^+$, $T_{1/2} = 2.449\,s$) has been measured by means of the fragmentation-induced nuclear polarization technique and β-detected nuclear magnetic resonance (β-NMR) spectroscopy. The $I^\pi = 1/2^+$ ground state of ^{15}C in a shell model is to a large extent described by the $^{14}C(0^+) \otimes \nu(2s_{1/2})$ configurations, and its magnetic moment may provide good information abount the neutron g_s factor appropriate in a neutron-rich nucleus.

Fragments of ^{15}C were produced in the fragmentation of ^{18}O ($E/A = 70\,MeV$) projectiles on a ^9Be ($184\,mg/cm^2$) target using RIPS. The fragment emission angle (θ_L) and momentum (p_F) were selected in order to obtain the spin polarization as $\theta_L = 4.2 \pm 2.2°$ and $p_F = 5.51 - 5.57\,GeV/c$, respectively. Then, the polarization, $P \sim 1.4\%$, was observed if a β-ray asymmetry factor $A_\beta = -0.48$ was assumed. Thus, polarized ^{15}C fragments were implanted in a highly purified graphite stopper to which a static magnetic field, $B_0 = 149.35\,mT$, was applied. After the beam-on period, an RF field was applied perpendicular to the B_0 field with its frequency being swept over a specified region. If the Lamor frequency (ν_L) was located within the region of the frequency sweep, the fragment spins were flipped by means of the adiabatic fast passage method of NMR (AFP-NMR), and as a result a change in the β-ray asymmetry was observed.

The NMR spectrum obtained for the measurement of the ^{15}C magnetic moment is plotted in Fig. 1. A tentative analysis gives the resonance frequency $\nu_L = 3916 \pm 20\,kHz$, corresponding to a magnetic moment of $|\mu(^{15}C)| = 1.720 \pm 0.009\mu_N$ (preliminary).

The present value of $\mu(^{15}C)$ is fairly close to the magnetic moment of a pure $s_{1/2}$ neutron configuration, $\frac{1}{2}g_s$. For example, the single-particle magnetic moment is obtained as $\mu(\nu[s_{1/2}])_{eff} = -1.746\mu_N$ if we take the effective M1 operator of Brown and Wildenthal.[1)]

The experimental magnetic moment for $^{15}C_{g.s.}$ is in good agreement with a shell-model calculation using the OXBASH code, taking the effective M1 operators which are commonly used in the region of stability, as shown in Fig. 2.

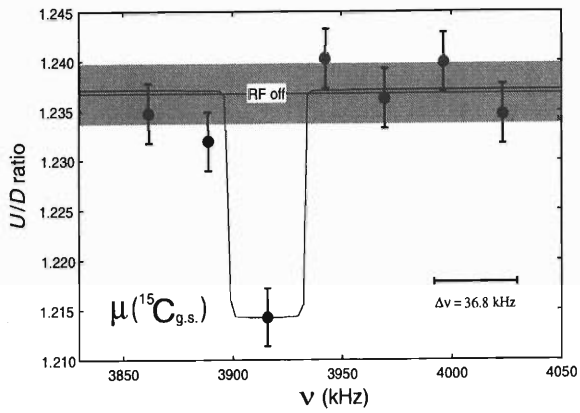

Fig. 1. Spectrum obtained for the ^{15}C magnetic moment measurement. The β-ray up/down ratio is plotted as a function of the oscillating frequency (ν) with its frequency being swept from $\nu - \frac{1}{2}\Delta\nu$ to $\nu + \frac{1}{2}\Delta\nu$.

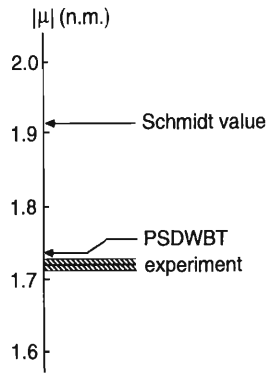

Fig. 2. Comparison between the experimental $\mu(^{15}C)$ value and a shell-model calculation using the PSDWBT interaction[2,3)] in which the effective M1 operator from the work of Arima, Shimizu, Bentz and Hyuga[4)] for protons and that from Brown and Wildenthal[1)] for neutrons are employed.

*1 Tokyo Institute of Technology
*2 Sanwa Newtec Co., Ltd.
*3 Sony LSI Design Inc.
*4 University of Tokyo

References

1) B. A. Brown et al.: Nucl. Phys. A **474**, 290 (1987).
2) E. K. Warburton et al.: Phys. Rev. C **46**, 923 (1992).
3) B. A. Brown et al.: Computer code OXBASH, MSU Cycl. Lab. Rep., No.524 (1986).
4) A. Arima et al.: Adv. Nucl. Phys. **18**, 1 (1987).

Search for Opposite Deformations of the Proton and Neutron Distributions in ^{16}C

A. Krasznahorkay,[*1] T. Motobayashi,[*2] I. Tanihata, H. Baba,[*2] M. Csatlós,[*1] Zs. Dombrádi,[*1] N. Fukuda, Zs. Fülöp,[*1,2] Z. Gácsi,[*1] J. Gulyás,[*1] N. Iwasa,[*3] H. Kinugawa,[*2] S. Kubono,[*2] M. Kurokawa,[*4] X. Liu,[*4] S. Michimasa,[*4] T. Minemura,[*2] A. Ozawa, A. Saito,[*2] S. Shimoura,[*2] S. Takeuchi, P. Thirolf,[*5] Y. Yanagisawa,[*4] and K. Yoshida

[NUCLEAR REACTIONS: ^{208}Pb(^{16}C,^{16}C*), 53A MeV]

Recently, Horiuchi and Kanada-En'yo[1,2] performed systematic calculations for Li, Be, B, and C isotopes within the antisymmetrized molecular dynamics (AMD) model. Although the proton density of C isotopes always has an oblate deformation, the neutron density is predicted to change its deformation from oblate to prolate as a function of the neutron number.

We intended to measure the charge and mass-deformation parameters of ^{16}C using a Coulomb-nuclear interference effect in the inelastic channel populating the 2_1^+ state. The interference between the Coulomb and nuclear excitation in the inelastic scattering of light and heavy ions has been studied by several groups, both experimentally and theoretically.[3,4] The interference manifests itself as a pronounced minimum in the inelastic scattering angular distribution at bombarding energy and scattering angle conditions corresponding to approximately a grazing collision. In addition, the predicted cross sections for similar and opposite deformations of proton and neutron densities differ by about 100% around $\theta = 3°$, assuming an angular resolution of $\Delta\Theta_{CM} \leq 0.2°$.

The experiment was performed at RIKEN, Japan. A ^{18}O primary beam of 100A MeV energy and 380 pnA intensity bombarded a ^{9}Be target of 9.0 mm thickness. A ^{16}C beam was separated by the RIPS fragment separator.[5] The corresponding ^{16}C energy was 53A MeV, and no beam contamination has been observed. The momentum resolution of the separator was set to 0.1%.

The ^{16}C beam bombarded a 50 mg/cm^2 ^{208}Pb target with 99.5% enrichment. The scattering angle was determined by four parallel plate avalanche counters,[6] three of them upstream, and one downstream of the target. Due to mainly multiple scattering in the target, the angular resolution of the system was $\Delta\Theta_{CM} \approx 0.4°$.

Particle identification of the scattered particles was made by a plastic scintillator hodoscope, placed 5 m from the target. The hodoscope[7] consisted of 5 mm thick ΔE and 60 mm thick E plastic scintillators of 1 m length, and covered a solid angle of 5.7 degrees.

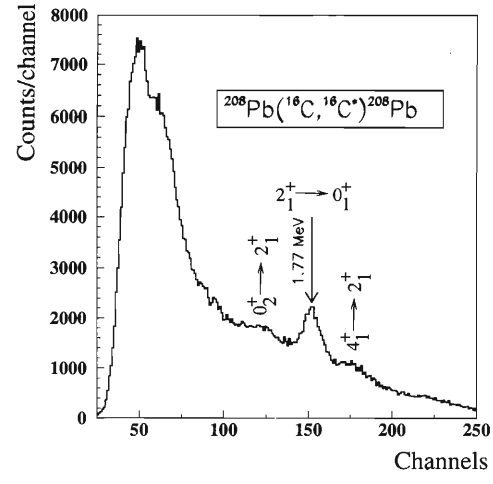

Fig. 1. Doppler shift corrected gamma spectrum collected by the DALI array. The de-excitation of the ^{16}C 2^+ state can be used to select the inelastic scattering reaction channel.

The vacuum chamber of the hodoscope, and the last PPAC detector were separated by a thin Mylar foil. The gamma de-excitation of the inelastic scattered ^{16}C particles was detected by the DALI detector array, consisting of 68 NaI crystals[8] with a size of $6 \times 6 \times 12$ cm^3. The array was shielded by layers of 20 cm paraffin 1 mm cadmium and 10 cm lead.

A Doppler shift corrected γ-spectrum collected by the DALI array can be seen in Fig. 1. The (E_γ = 1766 keV) transition in ^{16}C is clearly seen in the spectrum. Further analysis, *e.g.* angular distribution determination of the scattered ^{16}C particles is in progress.

*1 ATOMKI, Hungary
*2 Rikkyo University
*3 Tohoku University
*4 Center for Nuclear Study, University of Tokyo
*5 Ludwig-Maximilians-Universität, Germany

References
1) H. Horiuchi and Y. Kanada-En'yo: Nucl. Phys. A **616**, 394c (1997).
2) Y. Kanada-En'yo and H. Horiuchi: Phys. Rev. C **55**, 2860 (1997).
3) W. Brückner et al.: Phys. Rev. Lett. **30**, 57 (1973).
4) S. H. Fricke et al.: Nucl. Phys. A **500**, 399 (1989).
5) T. Kubo et al.: Nucl. Instrum. Methods Phys. Res. B **70**, 309 (1992).
6) H. Kumagai et al.: RIKEN Accel. Prog. Rep. **31**, 164 (1998).
7) I. Hisanaga et al.: RIKEN Accel. Prog. Rep. **31**, 162 (1998).
8) T. Motobayashi et al.: Phys. Lett. B **346**, 9 (1995).

Electric Quadrupole Moment of ^{17}B

H. Miyoshi,[*1] H. Ogawa,[*1] K. Asahi, K. Sakai,[*1] H. Ueno, T. Suzuki,[*2] M. Nagakura,[*3]
T. Honda,[*1] Y. X. Watanabe, N. Imai,[*4] K. Yoneda, T. Suga,[*1] A. Yoshimi, K. Yogo,[*1]
Y. Kobayashi, A. Yoshida, T. Kubo, W.-D. Schmidt-Ott,[*5] G. Neyens,[*6] S. Teughels,[*6] and M. Ishihara

[NUCLEAR STRUCTURE, spin-polarized radioactive beams, β-NMR method, measured quadrupole moment of ^{17}B]

The electric quadrupole moment (Q moment) for the neutron-rich isotope ^{17}B ($I^\pi = 3/2^-$, $T_{1/2} = 5.08$ ms) has been determined using a polarized radioactive isotope beam.

The experiment was carried out at RIPS. A ^{17}B beam was produced from the fragmentation of ^{22}Ne projectiles on a 1.07 g/cm^2 thick ^{93}Nb target at an energy of 110 MeV/nucleon. In order to obtain spin-polarized ^{17}B fragments, emission angles of $\theta = 0.5$–$3.8°$ and the fragment momenta of $p = 7.10$–7.54 GeV/c were selected. The obtained polarization is $P \sim -1.0/A_\beta$%, where A_β denotes the β-asymmetry factor. The produced spin-polarized ^{17}B fragments were transported to the final focus of RIPS, and were then implanted in a single-crystal Mg stopper. The measurement of the Q moment for ^{17}B was performed by observing the nuclear magnetic resonance *via* the change in the angular distribution of β-rays (β-NMR method).

The experimental result is shown in Fig. 1. From the result, $|eqQ/h| = 138.1 \pm 4.7$ kHz, the Q moment of ^{17}B was tentatively determined to be $|Q| = 38.8 \pm 1.5$ mb by taking an electric field gradient (q) deduced from Refs. 1 and 2.

The obtained value, $Q(^{17}\mathrm{B})_{\mathrm{exp}}$, is very close to $Q(^{13}\mathrm{B})_{\mathrm{exp}}$, which is for an isotope whose neutron p shell is closed. On the other hand, shell model calculations overestimate $Q(^{17}\mathrm{B})_{\mathrm{exp}}$ by 60%, as shown in Fig. 2. The overestimation by shell-model predictions is removed if the neutron effective charge is taken to be $e_n \approx 0.03$, which is substantially smaller than standard value $e_n = 0.5$ in sd shell.[3] The small e_n is also supported by the result for $Q(^{14}\mathrm{B})_{\mathrm{exp}}$ and $Q(^{15}\mathrm{B})_{\mathrm{exp}}$ previously reported by our group.[4] It may be suggested

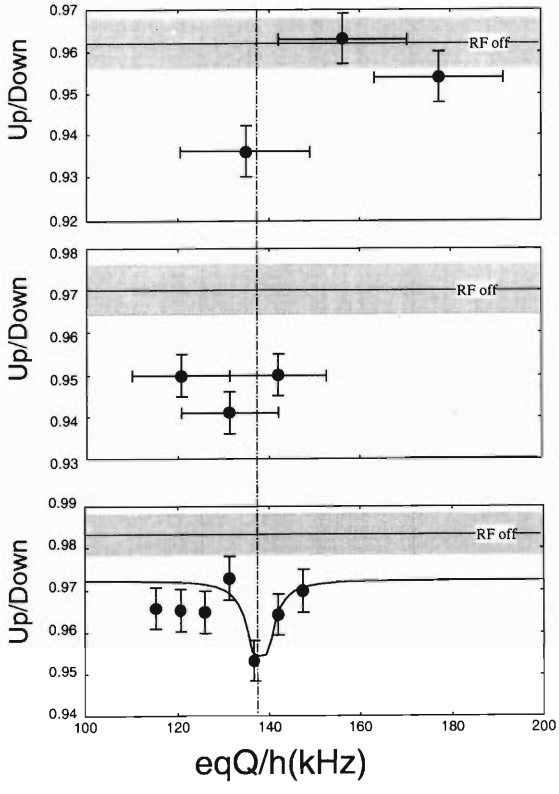

Fig. 1. Up/down ratio of β-ray intensities plotted as a function of eqQ/h, observed for ^{17}B implanted in a Mg crystal.

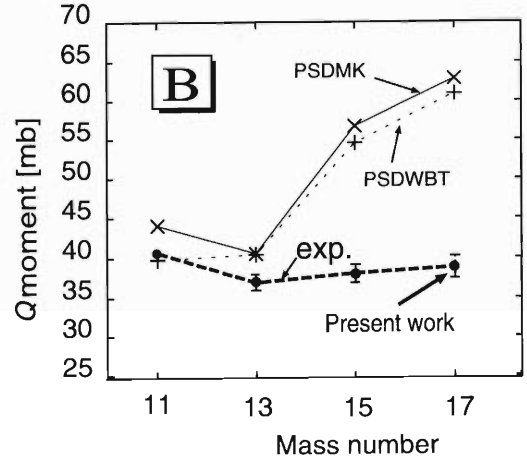

Fig. 2. Comparison between the experimental (exp) and theoretical Q moments for odd-mass B isotopes. The experimental Q moments are assigned a positive sign taken from the value of shell model calculations. The experimental Q are almost constant against the mass number. The value of $Q(^{17}\mathrm{B})$ obtained in the present work is considerably smaller than shell-model calculations with the effective interactions of PSDMK[5,6] and PSDWBT,[5,7] with $e_p = 1.3$ and $e_n = 0.5$.

*1 Tokyo Institute of Technology
*2 Sony LSI Design Inc.
*3 Sanwa Newtec Co., Ltd.
*4 University of Tokyo
*5 II.Physikalisches Institute of University, Germany
*6 University of Leuven, Belgium

that the core polarization induced by excess neutrons tends to diminish as the neutron-richness increases.

References

1) A. Kitagawa et al.: Hyperfine Interact. **60**, 869 (1990).
2) T. Minamisono et al.: Phys. Rev. Lett. **69**, 2058 (1992).
3) B. A. Brown et al.: Annu. Rev. Nucl. Part. Sci. **38**, 29 (1988).
4) H. Izumi et al.: Phys. Lett. B **366**, 51 (1996).
5) Shell model code OXBASH, B. A. Brown et al.: MSU Cycl. Lab. Rep. No.524 (1986).
6) D. J. Millener et al.: Nucl. Phys. A **255**, 315 (1975).
7) E. K. Warburton et al.: Phys. Rev. C **46**, 923 (1992).

Determination of the ^{17}C Ground-State Spin from a g-factor Measurement

D. Kameda,[*1] K. Asahi, H. Ogawa,[*1] H. Ueno, H. Miyoshi,[*1] K. Yoneda, Y. Watanabe, N. Imai,[*2] T. Suga,[*1] K. Ohno,[*1] W. Sato, K. Sakai,[*1] A. Yoshimi, K. Yogo,[*1] Y. Kobayashi, A. Yoshida, T. Kubo, and M. Ishihara

[^{17}C, Ground state spin, β-NMR method]

The ground-state spin for ^{17}C has been studied using several theoretical and experimental approaches.[1–3] Up to now, two candidates, $I^{\pi} = 1/2^{+}$ and $3/2^{+}$, for the ground-state spin remain unexcluded. In order to pin down the spin for ^{17}C, a measurement of the g-factor may play a decisive role, because it is extremely sensitive to whether the spin is $1/2^{+}$ or $3/2^{+}$. In the present work, the g-factor of the ^{17}C ground state was measured by means of the β-NMR method using a spin-polarized fragment beam of ^{17}C.

The beam of ^{17}C was obtained from the fragmentation of ^{22}Ne projectiles at an energy of 110 MeV/nucleon on a ^{93}Nb target of 778 mg/cm^2 thickness. In order to produce spin polarized fragments of ^{17}C, the emission angle (θ_{L}) and the outgoing momentum (p_{F}) were selected for the fragments. For the purpose of seeking the best θ_{L} and p_{F} settings to obtain an optimized polarization, the polarization (P) of ^{17}C was measured by means of the adiabatic field rotation of the holding field method[4] before pursuing a β-NMR search. As a result, at $\theta_{\mathrm{L}} = 3.8 \pm 1.5°$ and $p_{\mathrm{F}} = 7.21$–7.66 GeV/c, a β-ray asymmetry change of $A_{\beta}P = -1.2 \pm 0.4\%$ was observed.

After confirming the polarization, the g-factor was measured by means of the adiabatic fast-passage (AFP) method[5] of NMR. The ^{17}C fragments were implanted in a cooled Pt stopper to which a static magnetic field (B_0) of 99.56 mT was applied for the precession of ^{17}C. The temperature of the stopper was kept at around 75 K. An oscillating field was then applied for the stopper in a direction perpendicular to B_0. $|g(^{17}\mathrm{C})| = 0.5054 \pm 0.0024$ was obtained from the β-NMR spectrum shown in Fig. 1.

First of all, the Schmidt value is about 8-times larger than the experimental g-factor, suggesting the ground state spin to be different from 1/2. In fact, a more elaborate theoretical g-factor for the $1/2^{+}$ state from shell-model calculations[5,6] with the PSDMK and PSDWBT interactions, shown in Fig. 2, also greatly exceeds the experimental g-factor. We can thus clearly exclude the possibility of 1/2 for the ground-state spin from the experimental g-factor. Then, the only remaining possibility for the ground state spin is 3/2. In Fig. 2, the experimental g-factor indeed lies between the predictions for the $3/2^{+}$ state. We therefore conclude that the ground-state spin for ^{17}C is 3/2.

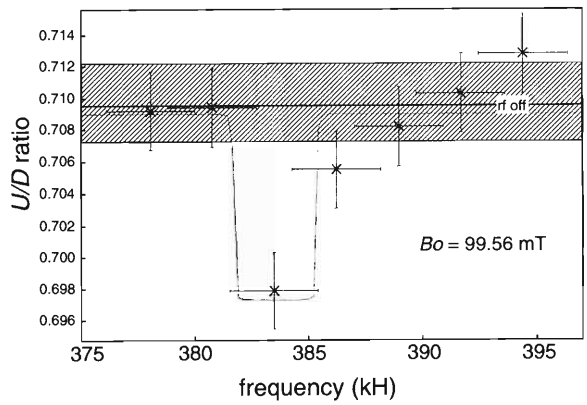

Fig. 1. NMR spectrum obtained for ^{17}C, with bin widths ($\delta\nu/\nu$) of 0.01. For each experimental point the statistical error and the width of the frequency sweep are indicated by the vertical and horizontal bars, respectively. The g-factor is obtained from $g = h\nu_0/\mu_N B_0$. The ν_o is the resonant frequency ($\nu_o = 383.54$ kHz).

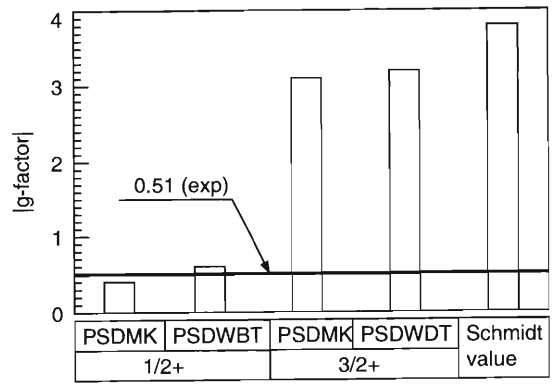

Fig. 2. Comparison of the experimental g-factor (exp) for ^{17}C with theoretical predictions (PSDMK, PSDWBT). For the symbols distinguishing the theories, see figure.

*1 Tokyo Institute of Technology
*2 University of Tokyo

References
1) D. Bazin et al.: Phys. Rev. C **57**, 2156 (1998).
2) T. Baumann et al.: Phys. Lett. B **439**, 256 (1998).
3) E. K. Warburton and B. A. Brown: Phys. Rev. C **46**, 923 (1992).
4) H. Ogawa et al.: Phys. Lett. B **451**, 11 (1999).
5) H. Ueno et al.: Phys. Rev. C **53**, 2142 (1996).
6) B. A. Brown et al.: OXBASH, MSU Cycl. Lab. Rep. No.524, (1986).

Reaction Cross Sections of ^{17}Ne

M. Fukuda,[*1] M. Mihara,[*1] K. Tanaka,[*1] T. Sumikama,[*1] S. Kudo,[*1] K. Matsuta,[*1] T. Minamisono,[*1] T. Izumikawa,[*2] T. Suzuki,[*3] T. Yamaguchi, T. Zheng, T. Onishi, A. Ozawa, and I. Tanihata

[NUCLEAR REACTION: Be(^{20}Ne, ^{17}Ne); E = 135 MeV/nucleon; Measured ^{17}Ne reaction cross sections]

^{17}Ne has attracted much interest as a candidate for a proton-halo nucleus. Based on the β-decay data, it was discussed that the ground state of ^{17}Ne ($I^\pi = 1/2^-$) or the excited state of the daughter nucleus, ^{17}F ($I^\pi = 1/2^+$, E_x = 495 keV), has a proton-halo structure because the β-decay rate is strongly supressed.[1] In order to clarify which nucleus has a proton halo, we investigated the nucleon density distribution of ^{17}Ne through a measurement of reaction cross sections.

The transmission method[2] was employed to measure the reaction cross sections of ^{17}Ne. An unstable nuclear beam of ^{17}Ne was produced by projectile fragmentation of the 135 MeV/nucleon ^{20}Ne primary beam provided from the RIKEN Ring Cyclotron. Nuclide selection was made through the RIPS (RIken Projectile fragment Separator). A beam energy of 40 MeV/nucleon was chosen to gain large nucleon-nucleon total cross sections of about three-times those at the LBL energies, around 700 MeV/nucleon. At 60 MeV/nucleon the cross sections take approximately the middle values in between these two energies.

The experimental setup, the principles for particle identification and for determining the reaction cross sections are basically the same as those used in the previous study.[2] Particle counting and identification before a reaction target were performed by two thin Si counters for a ΔE measurement and three parallel-plate avalanche counters (PPACs) that provided time and position information. Downstream of the reaction target, the identification was made from ΔE taken by Si counters and from the time-of-flight (TOF) taken between the PPACs and plastic counters that were placed 1.7 m downstream from the reaction target. The energy loss in the reaction target was about 20 MeV/nucleon for both energies.

Analyses of the data are now in progress. Figure 1 shows one of the preliminary results for ^{17}Ne on C and Al targets at 63 MeV/nucleon, compared with the systematics of reaction cross sections for stable nuclei by Kox *et al.*[3] This figure indicates that the reaction cross sections of ^{17}Ne are enhanced by ~10% compared with the systematics for stable nuclei. However, this enhancement does not seem to be so large as in the cases of ^{8}B or ^{9}C. The density distribution and detailed discussions will be given after completing the analyses.

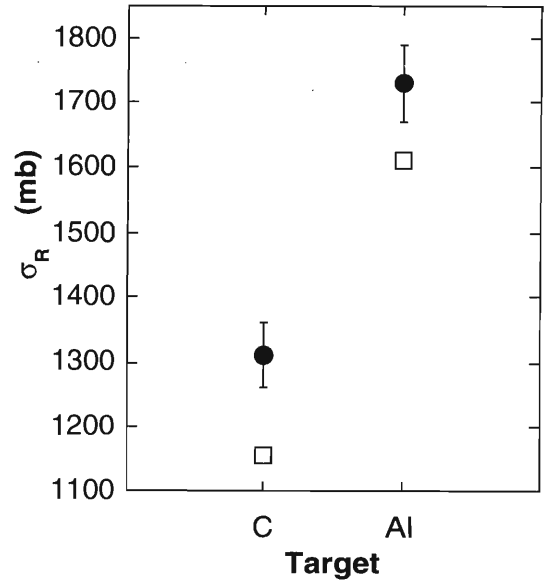

Fig. 1. Comparison between the experimental reaction cross sections of ^{17}Ne at 63 MeV/nucleon and the systematics for stable nuclei. Closed circles show the present data, and open squares the values from the Kox formula.

References

1) M. J. G. Borge et al.: Phys. Lett. B **317**, 25 (1993).
2) M. Fukuda et al.: Nucl. Phys. A **656**, 209 (1999).
3) S. Kox et al.: Phys. Rev. C **35**, 1678 (1987).

*1 Department of Physics, Osaka University
*2 Radioisotope Center, Niigata University
*3 Department of Physics, Niigata University

Search for ^{21}B

A. Ozawa, T. Yamaguchi, T. Zheng, R. Kanungo, T. Onishi, T. Suda, I. Tanihata, K. Yoshida, T. Suzuki,[*1] T. Izumikawa,[*1] T. Kato,[*1] Y. Kawamura,[*1] Y. Yamaguchi,[*1] S. Momota,[*2] and K. Kimura[*3]

[NUCLEAR REACTIONS: ^{9}Be(^{40}Ar, X), $E(^{40}\mathrm{Ar}) = 94.2\ A\,\mathrm{MeV}$]

Recently, we have surveyed the neutron separation energies and the interaction cross sections for neutron-rich nuclei in the *p-sd* and *sd* shell regions, and have found some signature for a new magic number, $N = 16$, near to the neutron drip line.[1] If $N = 16$ near to the neutron drip line is a magic number, very neutron-rich ^{21}B may be bound.[2] The nuclear structure of ^{21}B would be interesting, since its A/Z ratio is over 4, which is the largest number among known nuclei. Because of the exceptional A/Z value, an isotope search with a magnetic rigidity setting optimized for this particular nuclide has not yet been performed. Recent developments of radioactive ion (RI) beam technology now turn to allow searches for such nuclei located very far from the stability line (for example, Ref. 3).

The experimental setup at RIPS is shown in Fig. 1. The ^{40}Ar beam accelerated at the AVF and RIKEN Ring Cyclrotron up to 94.2 AMeV reacted with a 471 mg/cm^2 thick Be target. The target thickness was chosen to maximize the secondary beam intensities based on a semiempirical yield estimation by the INTENSITY code.[4] The primary beam current was monitored by an array of plastic detectors located near to the production target. The typical primary beam intensity was 33 pnA.

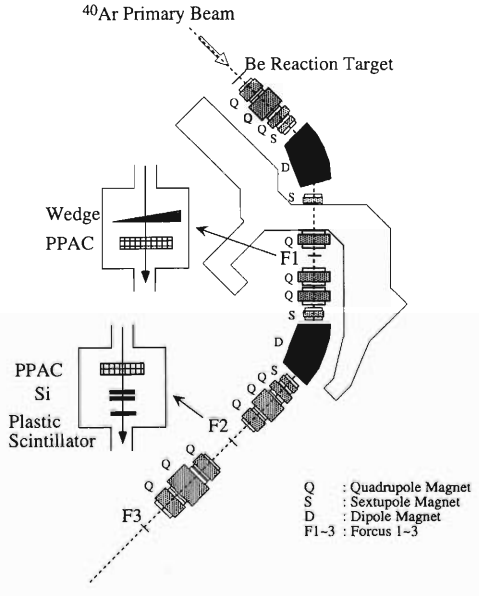

Fig. 1. Experimental setup at RIPS.

The reaction fragments were collected and analyzed by RIPS operated in an achromatic mode with the maximum momentum acceptance and solid angle. The magnetic rigidity of the first half of RIPS was set at 5.40 Tm in order to optimize the yield of the ^{21}B isotopes. To reduce the relative rates of light isotopes, such as ^{3}H, a rather thin aluminum wedge with a mean thickness of 223 mg/cm^2 was used on the momentum-dispersive focal plane (F1). The magnetic rigidity of the second part of the RIPS spectrometer was thereby adjusted to 5.35 Tm.

Particle identification was performed by a standard method on the basis of energy loss (ΔE), time-of-flight (TOF) and magnetic rigidity (Bρ) measured for each fragment. The positions of the fragments at F1 were recorded using a parallel-plate avalanche counter (PPAC) to determine the Bρ values. The F1 PPAC also provided a timing signal. The sensitive area of the PPAC was 15 cm (H) $\times$ 10 cm (V), the horizontal size of which covered a full rigidity acceptance of 6%. The charge-division method was applied for position reading. The fragmentation products reached the achromatic focal point (F2), where a plastic scintillation counter (F2-Pl) with a thickness of 1.5 mm, two silicon detectors (SSDs) with 0.35 mm thickness each, and a PPAC with 10 cm (H) $\times$ 10 cm (V) effective area were installed. The TOF of each fragment was determined from the F2-Pl timing and F1-PPAC timing. The two SSD detectors provided independent energy-loss values (ΔE). The magnetic fields at the two dipoles were monitored by NMR probes.

The Be production target was irradiated for 78 hours in total. We clearly identified ^{17}B and ^{19}B isotopes with 360 events counted for ^{19}B. However, serious backgrounds due to the scattering of light isotopes complicate the identification of ^{21}B. Thus, further analysis is necessary for any conclusive statements.

*1 Niigata University
*2 Kochi University of Technology
*3 Nagasaki Institute of Applied Sciences

References

1) A. Ozawa et al.: Phys. Rev. Lett. **84**, 5493 (2000).
2) M. Beiner et al.: Nucl. Phys. A **249**, 1 (1975).
3) H. Sakurai et al.: Phys. Lett. B **448**, 180 (1999).
4) K. Sümmerer et al.: Phys. Rev. C **61**, 034607 (2000).

Coulomb Dissociation of ^{23}Al

T. Gomi,[*1] T. Motobayashi,[*1] K. Yoneda, S. Kanno,[*1] N. Aoi,[*2] Y. Ando,[*1] H. Baba,[*1] K. Demichi,[*1] Z. Fülöp,[*3] U. Futakami,[*1] H. Hasegawa,[*1] Y. Higurashi,[*1] K. Ieki,[*1] N. Imai,[*2] N. Iwasa,[*4] H. Iwasaki,[*2] T. Kubo, S. Kubono,[*5] M. Kunibu,[*1] Y. U. Matsuyama,[*1] S. Michimasa,[*5] T. Minemura,[*1] H. Murakami,[*1] T. Nakamura,[*6] A. Saito,[*1] H. Sakurai,[*2] M. Serata,[*1] S. Shimoura,[*5] T. Sugimoto,[*6] E. Takeshita,[*1] S. Takeuchi,[*1] K. Ue,[*5] K. Yamada,[*1] Y. Yanagisawa, A. Yoshida, and M. Ishihara

[NUCLEAR REACTIONS: ^{208}Pb(^{23}Al,p^{22}Mg)^{208}Pb, 51 A MeV; Coulomb dissociation]

We performed an experiment to determine the rate of the radiative capture reaction, ^{22}Mg(p,γ)^{23}Al. We employed an experimental technique of intermediate-energy Coulomb dissociation combined with a radioactive isotope beam of ^{23}Al.

It has been pointed out that the ^{22}Na yields obtained from observing the cosmic γ rays are significantly lower compared with the calculated value for the hot Ne-Na cycle (^{20}Ne(p,γ)^{21}Na(p,γ)^{22}Mg($\beta^+\nu$)^{22}Na).[1] This discrepancy might be due to an ambiguity of the employed reaction rates. Therefore, it is important to experimentally determine the rate of ^{22}Mg(p,γ)^{23}Al, which might lead to a decrease of the amount of ^{22}Na.

The ground-state spin and parity, J^π, of ^{23}Al is known to be $5/2^+$, and the proton separation energy is 125 keV. The first excited state ($1/2^+$) is unbound, and the excitation energy has already been measured to be 460 ± 60 keV using the transfer reaction ^{24}Mg(^{7}Li,^{8}He)^{23}Al.[2] This excitation energy being close to the proton separation energy, implies a considerable contribution of the first excited state to the reaction rate. In the present work we studied the reaction ^{23}Al(γ,p)^{22}Mg to determine the $1/2^+ \rightarrow 5/2^+$ transition probability of ^{23}Al using the Coulomb dissociation method.

The experiment was performed in the RIPS beam line. An ^{23}Al beam was produced by the projectile fragmentation reaction of a 135 AMeV ^{28}Si beam on a 1.11 g/cm^2 ^{9}Be target. The energy of the ^{23}Al beam was 51 AMeV at the final focal plane, F3, of RIPS, and the typical intensity was around 2×10^4 cps. The purity of the ^{23}Al beam was about 7%. The ^{23}Al nucleus and a main contaminant, ^{22}Mg (56%), were separated using time-of-flight (TOF) information obtained from the signals of the cyclotron RF and of a 0.5 mm thick plastic scintillator located at the focal plane, F2. The ^{23}Al beam bombarded a 80 mg/cm^2 ^{208}Pb target located at F3. A 38 mg/cm^2 ^{12}C target was also used to estimate the contribution of the nuclear interaction. The position and incident angle of the beam at the target were measured by two sets of parallel-plate avalanche counters placed upstream of the target. A stack of sixty-eight NaI (Tl) scintillators was placed around the target to measure the deexcitation γ rays. The products of the breakup reaction, ^{22}Mg and a proton, were detected by a silicon telescope and a plastic scintillator hodoscope[3] located 56 cm and 4 m downstream of the target.

The telescope consisted of four layers of 0.5 mm thick silicon detectors. The detection area was 150×150 mm^2 with a vacant area of 50×50 mm^2 in the center. This arrangement enabled us to detect the reaction products scattered at angles larger than 2.5°, by suppressing the detection of the secondary beam nuclei. As the first and second layers, position-sensitive detectors were used. They were divided into strips horizontally and vertically, respectively. The width of the strip was 5 mm, which corresponds to an angular resolution of 9 mrad in the laboratory frame. We used single-element detectors as the third and fourth layers. The reaction products, ^{22}Mg, were implanted into the fourth layer, so that the telescope provided ΔE-E information. The hodoscope consisted of ΔE and E plastic scintillators of 5 mm and 60 mm thicknesses. They detected light reaction products which punched through the silicon telescope.

The particle identification of heavy reaction products was performed by the ΔE-E method using a silicon telescope, while the light reaction products, such as protons, were identified by the TOF-ΔE and TOF-E method using the scintillator hodoscope. The energy of ^{22}Mg was obtained from the total energy deposit on the silicon telescope and the velocity of the proton was determined from the TOF information between the target and the hodoscope. In order to deduce the relative energy of the breakup reaction products measured in coincidence, the momentum vectors of the particles were determined from their energies combined with the hit position on the silicon telescope.

An analysis of the data is now in progress.

*1 Rikkyo University
*2 University of Tokyo
*3 ATOMKI, Hungary
*4 Tohoku University
*5 Center for Nuclear Study, University of Tokyo
*6 Tokyo Institute of Technology

References

1) H. Schatz et al.: Phys. Rev. Lett. **79**, 3845 (1997).
2) M. Wiescher et al.: Nucl. Phys. A **484**, 90 (1988).
3) I. Hisanaga et al.: RIKEN Accel. Prog. Rep. **31**, 162 (1998).

β-Delayed Proton Decay of ^{24}Si

V. Banerjee,[*1] T. Kubo, A. Chakrabarti,[*1] H. Sakurai, A. Bandyopadhyay,[*1] K. Morita, S. Lukyanov,[*2] K. Yoneda, H. Ogawa, and D. Beaumel[*3]

[NUCLEAR STRUCTURE; ^{28}Si+Be, Proton-rich nuclei, β-delayed protons]

β-delayed proton spectroscopy has provided very useful information for nuclear structure model calculations and for calculations of the nuclear reaction network tracing the elemental nucleo-synthesis in the *rp* process. The β-delayed proton decay of ^{24}Si, the subject of the present study, has already been studied at GANIL[1] using the projectile fragmentation reaction for production and the projectile fragment separator for the selection of ^{24}Si fragments, which were ultimately stopped in an active detector for the study of delayed proton spectrum. This methodology, although extremely powerful, has the undesirable feature of very high β-ray background[1] which adversely affects the proton spectrum, especially below about 2 MeV.

We have employed a new experimental technique[2] to eliminate the high β-ray background in a measurement of delayed protons from ^{24}Si. The ^{24}Si fragments after separation in the RIKEN Projectile Fragment Separator (RIPS)[3] were implanted at a grazing angle of 15 degrees in a 2.6 μm Al stopping foil placed parallel to a gas ΔE-Silicon E telescope used for a delayed proton measurement along with suppression of the β-background. Prior to implantation in the Al-stopping foil, the fragments were made to pass through a set of Al foils whose total thickness was carefully tuned to serve the dual purpose of energy degradation and filtering out of the isotones — ^{22}Mg and ^{21}Na completely and ^{23}Al to a great extent.

^{24}Si fragments were produced by bombarding a 100 MeV/u ^{28}Si beam of intensity 20 pnA on a 552 mg/cm^2 thick ^{9}Be target. RIPS was operated in the achromatic mode with an aluminum wedge degrader of thickness 221 mg/cm^2 and a momentum acceptance of 0.125%. The isotope identification in flight was done from the ΔE-TOF spectrum. The beam was pulsed ON for 200 ms and a delayed proton measurement was carried out during a beam OFF period of 200 ms.

The 1-dimensional proton energy spectrum for β-delayed protons from ^{24}Si projected from the proton band in 2-dimensional ΔE-E plot is shown in Fig. 1. The high quality of the proton spectrum in terms of almost complete β-rejection is clearly evident. The half-life of ^{24}Si was determined to be $T_{1/2} = 139 \pm 18$ ms,

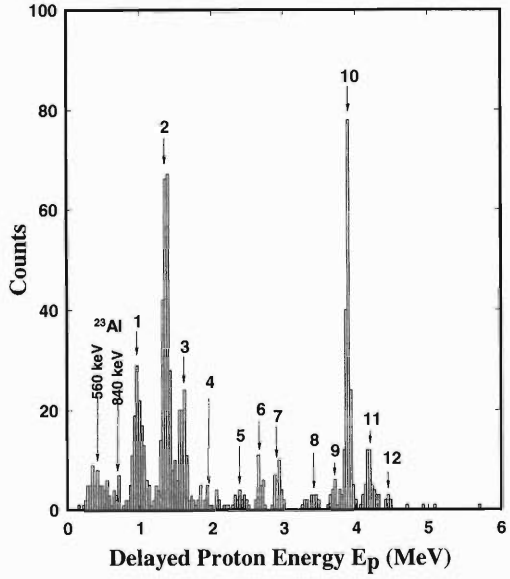

Fig. 1. β-delayed proton spectrum from the decay of ^{24}Si.

in good agreement with a previous measurement of 140 ms.[1] The peaks numbered 9 and 12 in Fig. 1 are two new proton peaks observed in the present work. Two new levels in ^{24}Al at energies of 5.76 and 6.53 MeV are also proposed on the basis of transitions from these levels to the 1.87 MeV level in ^{23}Mg. The excitation energies are deduced by adding the recoil energies to the observed proton decay energies. The level at 5.43 MeV, which could not be unambiguously assigned in a previous study,[1] has been assigned on the basis of a clear peak at 3.42 MeV. The level energies and the relative intensities deduced on the basis of present study are in overall good agreement with those from the earlier study[1] and the shell-model calculations of Brown.[4]

References

1) S. Czajkowski et al.: Nucl. Phys. A **616**, 278c (1997).
2) V. Banerjee et al.: Phys Rev. C **63**, 024307 (2001).
3) T. Kubo et al.: Nucl. Instrum. Methods Phys. Res. B **70**, 309 (1992).
4) B. Brown: private communication.

*1 Variable Energy Cyclotron Centre, India
*2 Joint Institute for Nuclear Research, Russia
*3 Institut de Physique Nucleaire, France

Spectroscopy of ^{34}Si with the (d, d') Reaction in Inverse Kinematics

N. Iwasa,[*1] T. Motobayashi,[*2] H. Sakurai,[*3] H. Akiyoshi, Y. Ando,[*2] N. Aoi,[*3] H. Baba,[*2] N. Fukuda,[*3] Zs. Fülöp,[*4] U. Futakami,[*2] T. Gomi,[*2] Y. Higurashi, K. Ieki,[*2] H. Iwasaki,[*3] T. Kubo, S. Kubono,[*5] H. Kinugawa,[*2] H. Kumagai, M. Kunibu,[*2] S. Michimasa,[*5] T. Minemura,[*2] H. Murakami,[*2] A. Saito,[*2] S. Shimoura,[*5] S. Takeuchi,[*2] Y. Yanagisawa, K. Yoneda, and M. Ishihara

[NUCLEAR REACTIONS, ^{2}H(^{34}Si,^{34}Si γ)^{2}H]

From recent experimental and theoretical studies, the ^{34}Si nucleus is known to be located just outside of the "island of inversion", and its ground state has a closed $\pi(0d_{5/2})^6\nu(sd)^{12}$ configuration.[1] On the other hand, a 0_2^+ (deformed) intruder state was suggested to lie between the 2_1^+ state at 3.328 MeV and the ground 0_1^+ state in order to explain the small B (E2; $0^+ \rightarrow 2^+$) measured at MSU.[2] A recent calculation by Caurier et al. predicted this intruder state to located at 1.8 MeV.[3] We carried out an experiment of the ^{34}Si(d, d') reaction in the inverse kinematics to search for the intruder state by reconstructing the level scheme for ^{34}Si.

A radioactive ^{34}Si beam was produced by the fragmentation of an ^{40}Ar beam at 95 MeV/u in a ^{9}Be target with a thickness of 370 mg/cm^2. The beam was isotopically separated by the RIKEN projectile-fragment separator (RIPS). Particle identification of the secondary beam was performed event-by-event using the time-of-flight (TOF) and ΔE information of two plastic scintillators with a thickness of 0.3 mm installed at the second and third foci (F2 and F3).

A liquid-deuterium target with a thickness of 150 mg/cm^2 was bombarded by the ^{34}Si beam. The beam energy at the center of the target was 40.9 MeV/u. The scattered ^{34}Si was measured by four sets of silicon counter telescopes arranged in a 2×2 matrix placed 135.7 cm downstream from the target. Each telescope consisted of four layers of ion-implanted silicon detectors with an effective area of 50×50 mm^2 and a thickness of 500 μm. The scattering angle and TOF of the scattered ^{34}Si were measured by a parallel-plate avalanche counter (PPAC) placed in front of the silicon detectors. The scattered ^{34}Si stopped in the second or third detector. Particle identification of the reaction products was achieved by utilizing the TOF-ΔE and ΔE-E methods.

The de-excitation γ-rays were detected by a NaI(Tl) array surrounding the target from 40 to 138 degree in coincidence with ^{34}Si detected by the silicon counter telescope. The NaI(Tl) array consisted of 68 NaI(Tl) crystals with a rectangular shape ($6\times6\times12$ cm^3) coupled to 5.1 cm ϕ photomultiplier tubes. A lead shield with a thickness of 5 cm surrounded the NaI(Tl) array for background reduction. The background from neutrons produced in the target was reduced by using the TOF between the target and the NaI crystals.

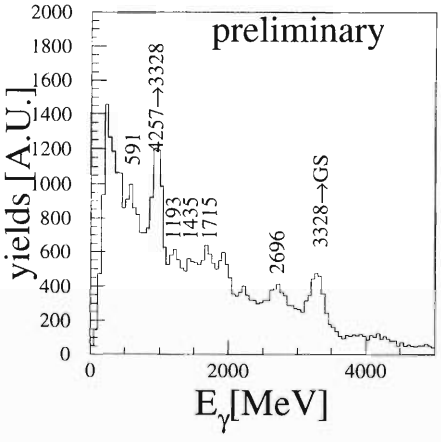

Fig. 1. Doppler corrected γ-ray spectrum in coincidence with ^{34}Si, produced by the ^{34}Si(d, d') reaction.

Figure 1 shows a Doppler-corrected γ spectrum measured in coincidence with the scattered ^{34}Si detected by the silicon detectors. The 3328 keV and 929 keV γ-rays are known to be the $2_1^+ \rightarrow 0_1^+$ and 4257 keV $\rightarrow 2_1^+$ transition, respectively.[4] Recently, the γ lines of the 591, 1053, 1193, 1435, 1715 and 2696 keV were found by β-γ measurements at ISOLDE.[5] These γ lines were observed in this figure. The 591, 1193, and 2696 keV γ-rays were obviously measured in coincidence with the 3328 keV γ-ray. Assuming that the 0_2^+ intruder state is in between the first 2_1^+ state at 3.328 MeV and the ground state, as suggested by Caurier *et al.*,[3] the 1435 keV line is a candidate for the $2_1^+ \rightarrow 0_2^+$ transition among them. A careful analysis of the γ-γ correlation is in progress to establish the level.

*1 Tohoku University
*2 Rikkyo University
*3 University of Tokyo
*4 ATOMKI, Hungary
*5 Center for Nuclear Study, University of Tokyo

References
1) Y. Utsuno et al.: Phys. Rev. C **60**, 054315 (1999).
2) R. W. Ibbotson et al.: Phys. Rev. Lett. **80**, 2081 (1998).
3) E. Caurier et al.: Phys. Rev. C **58**, 2033 (1998).
4) R. B. Firestone et al.: *Table of Isotopes, 8th ed., 1998 update*, (*Wiley, New York, 1998*).
5) S. Nummela et al.: preprint CERN-EP/2000-73 (2000).

New Magic Number, $N = 16$, Near to the Neutron Drip Line

A. Ozawa, T. Kobayashi,[*1] T. Suzuki,[*2] K. Yoshida, and I. Tanihata

[Magic number, Neutron separation energies, Interaction cross-sections]

Recent experiments using a radioactive isotope beam (RI beam) show some signature of the disappearance of the $N = 8$ and $N = 20$ closed shell.[1,2] However, no appearance of a magic number has been shown experimentally so far, although some new magic numbers were theoretically predicted 25 years ago.[3] Recent improvements of RI beam techniques allow us to measure the mass and the interaction cross-sections (σ_I) for nuclei on the neutron drip-line or close to the drip-line for $Z \leq 8$. Thus, we have surveyed the neutron separation energies (S_n) and σ_I for neutron-rich *p-sd* and *sd* shell region to investigate a new magic number.

A neutron (N) number dependence of observed S_n[4] for nuclei with $N \leq 25$ is shown in Fig. 1. A magic number appears as a decrease of S_n along with an increase of N. The traditional magic numbers ($N = 8$, 20) are clearly seen close to the stable nuclei as breaks in the small isospin (T_z) lines. However, the break at $N = 8$ ($N = 20$) disappears at $T_z = 3/2$ ($T_z = 4$), which is also known concerning other experimental quantities. A break in the S_n line appears at $N = 16$ for $T_z \leq 3$, as shown in Fig. 1, which indicates the creation of a new magic number in $N = 16$ near to the neutron drip-line.

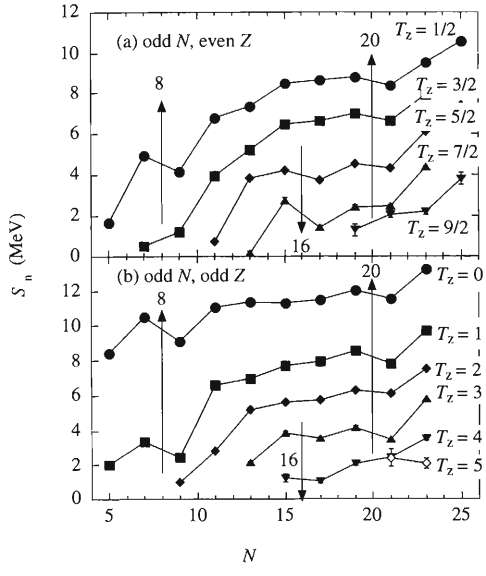

Fig. 1. Neutron (N) number dependence for experimentally observed S_n for nuclei with odd N and even Z (a) and odd N odd Z (b).

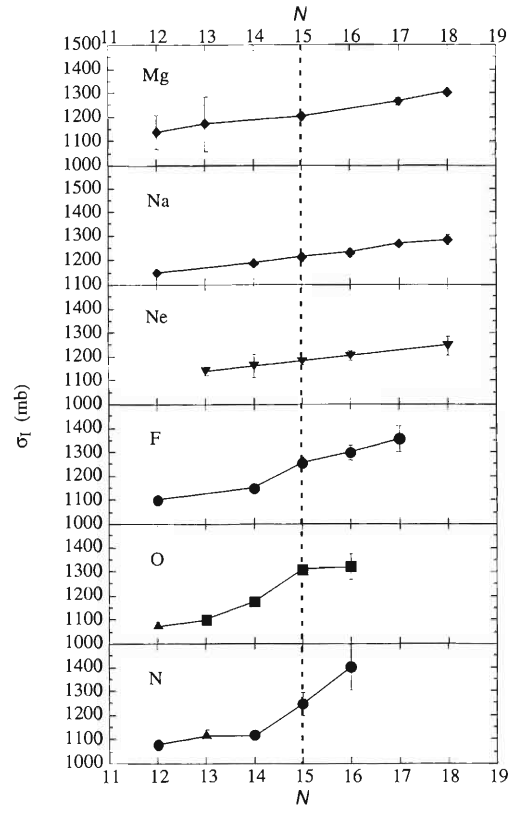

Fig. 2. Neutron (N) number dependence for experimentally observed σ_I for N to Mg isotopes on C targets.

In Fig. 2, a N number dependence of experimentally observed σ_I for N to Mg isotopes is shown.[5] We observed a steep increase of σ_I from $N = 14$ to $N = 15$ for N to F isotopes although, for Ne to Mg isotopes, no steep increase for σ_I is shown. This anomalous increase at $N = 15$ for N to F suggests that a $2s_{1/2}$ orbital is dominant in the valence neutron of the nuclei. This conclusion also supports the creation of a new magic number at $N = 16$ near to the neutron drip-line, since a clear single-particle structure is suggested for $N = 15$. At weakly bound $N = 16$, $2s_{1/2}$ and $1d_{5/2}$ orbitals are filled by neutrons, leaving a large gap to the $1d_{3/2}$ orbital.

*1 Tohoku University
*2 Niigata University

References

1) T. Motobayashi et al.: Phys. Lett. B **346**, 9 (1995).
2) A. Navin et al.: Phys. Rev. Lett. **85**, 266 (2000).
3) M. Beiner et al.: Nucl. Phys. A **249**, 1 (1975).
4) G. Audi and A. H. Wapstra: Nucl. Phys. A **595**, 409 (1995).
5) A. Ozawa et al.: Nucl. Phys. A, in press.

Deeply Bound 1s and 2p States of π^- in ^{205}Pb

H. Geissel,[*1] H. Gilg,[*2] A. Gillitzer,[*2] R. S. Hayano,[*3] S. Hirenzaki,[*4] K. Itahashi,[*5] M. Iwasaki,[*5] P. Kienle,[*2] M. Münch,[*2] G. Münzenberg,[*1] W. Schott,[*2] K. Suzuki,[*3] D. Tomono,[*5] H. Weick,[*1] T. Yamazaki, and T. Yoneyama[*5]

[Pion bound states, Pion transfer reaction]

Following the first successful observation of deeply bound π^- states in ^{207}Pb in the ^{208}Pb(d, ^{3}He) reaction at $T_d = 600$ MeV,[1-4] we carried out another experiment with a ^{206}Pb target. The previous experiment has clarified that (1) the deeply bound π^- states (1s and 2p) in ^{207}Pb indeed exist with narrow widths[5,6] and that (2) they are produced in the (d, ^{3}He) reaction, as theoretically predicted.[7,8] Since this reaction produces deeply bound states of configurations $(nl)_\pi(n'l')_n^{-1}$ at a small momentum transfer, the observed spectrum in the previous experiment is rather complex due to the $3p_{1/2}$ and $3p_{3/2}$ neutron holes separated in energy by 0.89 MeV. The present experiment using ^{206}Pb was purposely undertaken in view of the absence of the $3p_{1/2}$ hole.[9]

The Fragment Separator System of GSI was used as a high-resolution spectrometer at zero degree with sufficient particle identification capability. There was no background of instrumental origin. The observed spectrum, presented in Fig. 1 and Fig. 2, shows two well-resolved peaks of the 1s and 2p pionic components. The absolute energy scale was calibrated by using the p(d, ^{3}He)π_0 reaction, which exhibited a monoenergetic peak in the same spectrometer setting. The instrumental uncertainty in the missing mass energy was 0.04 MeV. The instrumental resolution was estimated

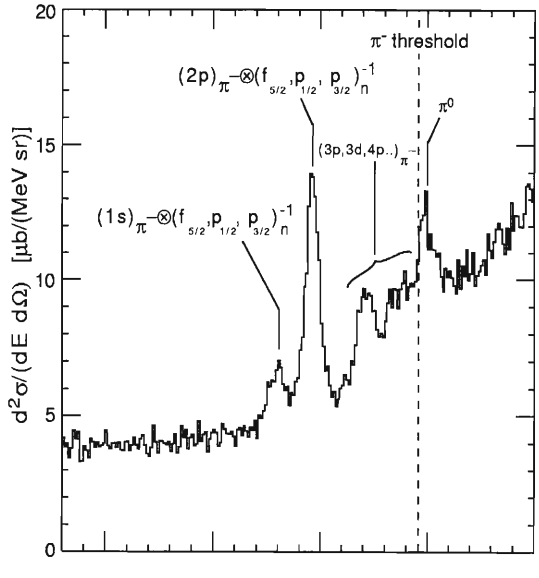

Fig. 1. Excitation spectrum of the ^{206}Pb(d, ^{3}He) reaction measured at an incident deuteron energy of 600 MeV. The π^- emission threshold is shown by the vertical broken line.

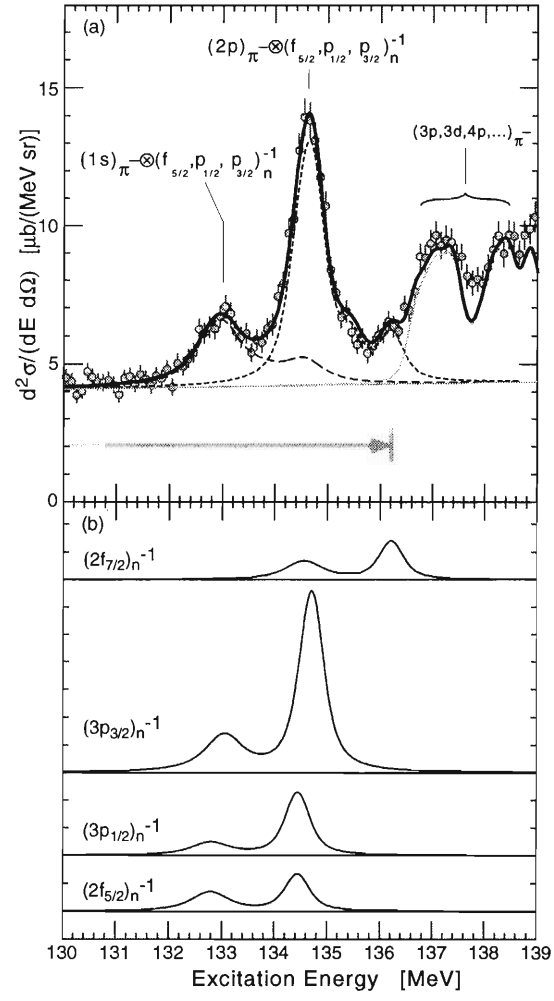

Fig. 2. Fitting result of the excitation spectrum. (a) The data points are fitted by the solid curve, which was obtained in the fit range indicated. The broken and dotted curves are the $(1s)_\pi$ and $(2p)_\pi$ components, respectively. (b) The partial contributions from the four neutron hole states, shown in the same scale as (a). Each component is a sum of two Lorentzian's corresponding to the $(1s)_\pi$ and $(2p)_\pi$ states folded by experimental resolution.

*1 Gesellschaft für Schwerionenforschung, Germany
*2 Physik-Department, Technische Universität München, Germany
*3 Department of Physics, University of Tokyo
*4 Department of Physics, Nara Women's University
*5 Department of Physics, Tokyo Institute of Technology

to be 0.32 ± 0.05 MeV FWHM.

The 1s and 2p peaks were decomposed by assuming the configurations and their relative spectroscopic factors calculated theoretically in Ref. 9 with the binding energies B_{1s} and B_{2p} and widths Γ_{1s} and Γ_{2p} as free parameters. The fitting of the experimental data with theory is excellent and the deduced binding energies and widths are:

$$B_{1s} = 6.768 \pm 0.044\ (stat.) \pm 0.045\ (syst.), \quad (1)$$

$$\Gamma_{1s} = 0.78 \pm 0.14\ (stat.) \pm 0.055\ (syst.), \quad (2)$$

$$B_{2p} = 5.110 \pm 0.016\ (stat.) \pm 0.040\ (syst.), \quad (3)$$

$$\Gamma_{2p} = 0.37 \pm 0.04\ (stat.) \pm 0.05\ (syst.). \quad (4)$$

The obtained binding energies and widths were used to deduce the strength of the s-wave (local) potential.

References

1) T. Yamazaki et al.: Z. Phys. A **355**, 219 (1996).
2) T. Yamazaki et al.: Phys. Lett. B **418**, 246 (1998).
3) H. Gilg et al.: Phys. Rev. C **62**, 025201 (2000).
4) K. Itahashi et al.: Phys. Rev. C **62**, 025202 (2000).
5) H. Toki and T. Yamazaki: Phys. Lett. B **213**, 129 (1988).
6) H. Toki, S. Hirenzaki, T. Yamazaki, and R. S. Hayano: Nucl. Phys. A **501**, 653 (1989).
7) H. Toki, S. Hirenzaki, and T. Yamazaki: Nucl. Phys. A **530**, 679 (1991).
8) S. Hirenzaki, H. Toki, and T. Yamazaki: Phys. Rev. C **44**, 2472 (1991).
9) S. Hirenzaki and H. Toki: Phys. Rev. C **55**, 2719 (1997).

2. Atomic and Solid-State Physics

Charge Transfer in F^{2+} Ions Colliding with He Atoms below keV/u Energies and Its Reverse Process

J. P. Gu,[*1] G. Hirsch,[*1] R. J. Buenker,[*1] M. Kimura, I. Shimamura, C. M. Dutta,[*2] and P. Nordlander[*2]

Charge transfer processes for heavy ion impact are important basic processes in various scientific and technological applications.[1)] Over the past decade, an intense effort from the atomic physics community toward a better understanding of scattering dynamics over a wide range of energies has resulted in a basic understanding of compiled experimental cross section data. As a consequence, a large number of extremely interesting new physics has emerged making the field prosperous and lively. However, although there have been a large number of studies of collisions of $H^+, He^{q+}, \ldots, O^{q+}$ ions with simple atoms and molecules, relatively few investigations have been performed on other heavy ions ($Z > 9$) because of, in part, some difficulties in producing these ions in experiments. However, scattering processes by these ions are particularly interesting and important because not much of spectroscopic information for the ions is available, and these complex systems possibly lead us to a new phenomenon of collision physics.

Recently HF molecules have been detected in interstellar medium, and the origin and formation mechanisms are sought.[2)] From this observation, therefore, F^{q+} ions are expected to be present in interstellar environment, and to play a subtle role for astrochemistry. Also fluorine ions (F^{q+}) and atoms are known to be present in biological systems including the human body, and the knowledge of its interaction with other atoms and molecules are needed for medical and biological study. As a part of our heavy-ion collision project, we present a theoretical investigation on charge transfer in collision of F^{q+} ions with He atoms based on a molecular state expansion method below 1 keV/u. The processes we are concerned with are:
(i) the ground-state ion impact:

$$F^{2+}(^4S) + He(^1S) \longrightarrow F^+ + He^+, \qquad (1a)$$

and
(ii) the excited-state ion impact:

$$F^{2+}(^2D) + He(^1S) \longrightarrow F^+ + He^+. \qquad (1b)$$

The energy defect between the ground $F^{2+}(^4S)$ and the excited $F^{2+}(^2D)$ states is approximately 4.3 eV. Therefore these two ions may be produced simultaneously through γ-ray- or ion-impact ionization in natural environment like the astrophysical environment, or laboratory plasma. Hence it is necessary to put together all information of the effect from these states when modeling scattering dynamics. The adiabatic potential curves of HeF^{2+} are obtained by employing the *ab initio* multireference single- and double-excitation configuration interaction (MRD-CI) method,[3)] with configuration selection at a threshold of 5.0×10^{-8} Hartree. The two electrons in the first (lowest) molecular orbital (MO) are kept inactive in the present CI calculation, and the highest MO is discarded. A semiclassical MO expansion method with a straight-line trajectory of the incident ion was employed to study the collision dynamics. In this approach, the relative motion of heavy particles is treated classically, while electronic motions are treated quantum mechanically. By solving the coupled equations numerically, we obtain the scattering amplitudes for transitions: the square of the amplitude gives the transition probability, and integration of the probability over the impact parameter gives the cross section. Charge Transfer Cross Sections $F^{2+} + He(^1S)$ collisions is summarized and representative results for the Quartet state are shown in Fig. 1 (total, $1^4\Sigma^-$ and $1^4\Pi$ cross sections): This is an exothermic process. The cross sections increase four-fold as the incident energy increases from 0.1 keV/u to 0.6 keV/u, but are found to be rather small with a magnitude of 2×10^{-16} cm^2 even at the highest energy studied. This is a manifestation of the weak coupling which connects between the initial and charge transferred states because both the projectile F^{2+} and the target He atom have tight shells. The partial cross sections for $1^4\Sigma^-$ is larger than those for $1^4\Pi$, and they show a structure at collision energies between 0.2–0.3 keV/u. This is an effect of interference between the initial $2^4\Sigma^-$ and $1^4\Sigma^-$

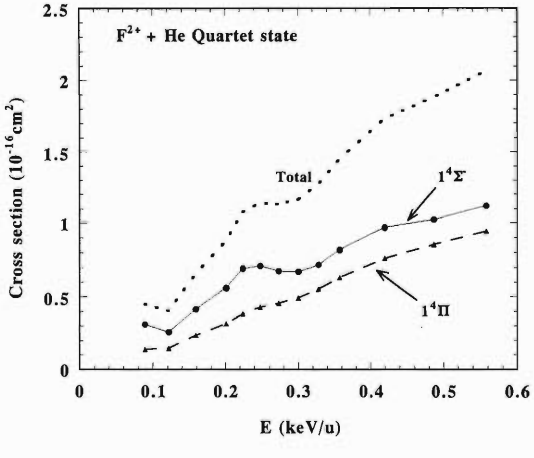

Fig. 1. Charge transfer cross sections for the process (1a) in F^{2+} + He collisions.

*1 Theoretische Chemie, Bergische Universitaet-Gesamthochschule Wuppertal, Germany
*2 Department of Physics and Rice Quantum Institute, Rice University, USA

states. The $1^4\Pi$ state is not involved in the dynamics. The total cross sections reflect this structure. This is caused by the strong peak in the coupling of this $1^4\Sigma^-$ channel with the incoming channel at $R \sim 3.7\ a_0$. The partial cross sections for $1^4\Pi$ increase with the collision energy monotonously.

References

1) R. K. Janev: *Review of Fundamental Processes and Applications of Atoms and Ions* (World Scientific, Singapole, 1993).
2) R. K. Janev: *Atomic and Molecular Processes in Fusion Edge Plasma* (Plenum Press, New York, 1995).
3) R. J. Buenker and S. D. Peyerimhoff: Theor. Chim. Acta **35**, 33 (1974); Theor. Chim. Acta **39**, 217 (1975); R. J. Buenker: Int. J. Quantum Chem. **29**, 435 (1986).

Theoretical Calculation of Double Electron Transfer Processes in Collisions of He^{2+} with Mg

S. Sakaguti,[*1] K. Ohtsuki,[*2] and T. Watanabe[*3]

We study theoretically a double electron transfer process, namely

$$He^{2+} + Mg(3s3s) \longrightarrow He^{**}(nln'l') + Mg^{2+},$$

induced by collision of a He^{2+} ion with a neutral Mg atom at collision energies of 15–40 keV. In this process, valence electrons of the Mg atom are transferred into a doubly excited state $(n, n' \geq 2)$ of He.

This work was stimulated by experimental study by Iemura *et al.*[1,2] They measure energy spectrum of the Auger electrons ejected in the collisions of He^{2+} with alkaline earth atoms Mg, Ca, Sr, and Ba.

In this energy region, the speed of the electronic motion is considered to be fast compared with the relative motion of the atomic cores. Hence, coupled equations derived from a molecular orbital (MO) basis are employed. Also, the de Broglie wavelength of the relative motion of the atomic cores is short enough for treating this motion classically, and its trajectory is nearly along a straight line. Therefore, we adopt the straight-line-trajectory impact parameter method.

The assumption of the straight-line trajectory leads to the relation $\boldsymbol{R} = \boldsymbol{b} + \boldsymbol{v}t$ between time t and the internuclear distance vector $\boldsymbol{R}$, where $\boldsymbol{b}$ is the impact parameter and $\boldsymbol{v}$ is the relative velocity between the nuclei.

The Schrödinger equation for the electronic state of the $(MgHe)^{2+}$ system

$$i\frac{\partial}{\partial t}\Psi_{el}(\boldsymbol{r}, t) = \mathcal{H}_{el}\Psi_{el}(\boldsymbol{r}, t),$$

was considered, where $\boldsymbol{r}$ denotes the position vector of the electrons collectively and $\mathcal{H}_{el}$ is the electronic Hamiltonian. The total electronic wave function $\Psi_{el}(\boldsymbol{r}, t)$ was expanded as

$$\Psi_{el}(\boldsymbol{r}, t) = \sum_n c_n(t, b)\Psi_n(\boldsymbol{r}; R) \times \exp\left[-i\int_{-\infty}^{t} E_n(R)dt\right],$$

in terms of the eigenfunctions $\Psi_n(\boldsymbol{r}; R)$ satisfying the time-independent Schrödinger equation $\mathcal{H}_{el}\Psi_n(\boldsymbol{r}; R) = E_n(R)\Psi_n(\boldsymbol{r}; R)$.

In order to express the adiabatic electronic states

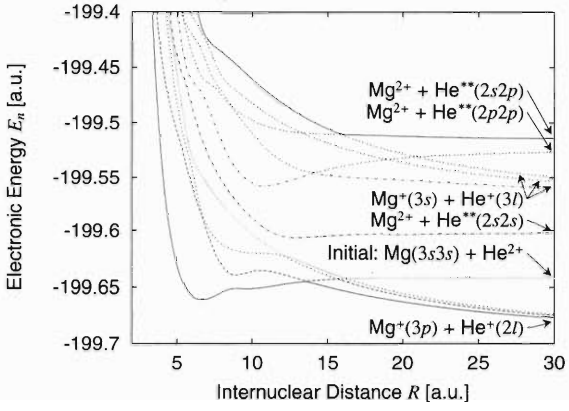

Fig. 1. Adiabatic potentials of $(MgHe)^{2+}$. The origin of energy is the completely broken-up state. The symmetry of each state is $^1\Sigma$.

$\Psi_n(\boldsymbol{r}; R)$, molecular orbitals were constructed from linear combinations of atomic orbitals (LCAO-MO); Slater-type functions (STF) were used as basis functions for constructing atomic orbitals. The basis functions of the Mg atom were taken from Clementi and Roetti[3] and those of the He atom were determine by us. The adiabatic states were constructed by freezing the inner shell electrons and by expressing the two outer electrons as a linear combination of two-electron configurations. We use ALCHEMY II[4] to calculate adiabatic potentials (Fig. 1). We will compute the transition matrix elements to obtain the coefficients $c_n(t, b)$ of the electronic states by solving the first-order coupled differential equations, and will compute the cross sections,

$$\sigma_n = 2\pi\int_0^\infty |c_n(\infty, b)|^2 bdb.$$

References
1) K. Iemura et al.: Physica Scr. T **73**, 205 (1997).
2) K. Iemura et al.: submitted to Phys. Rev. A.
3) E. Clementi and C. Roetti: At. Data and Nucl. Data Tables **14**, 177 (1974).
4) A. D. McLean et al.: in *Modern Techniques in Computational Chemistry: MOTECC-91* (IBM Corporation Kingston, New York, 1991), p. 233.

*1 Graduate School of Science and Engineering, Saitama University
*2 University of Electro-Communications
*3 Japan Science and Technology Corporation

Laser-Assisted Formation of Antihydrogen

R. J. Whitehead,[*1] J. F. McCann,[*2] and I. Shimamura

The interactions of antiprotons $\bar{p}$ with simple atoms has been a subject of great importance since the development of low-energy $\bar{p}$ beams. In particular, the formation of cold antihydrogen $\bar{\mathrm{H}} = (\bar{p}, e^+)$ in reactive collisions of $\bar{p}$ with positronium $\mathrm{Ps} = (e^+, e^-)$, *i.e.*,

$$\bar{p} + \mathrm{Ps} \longrightarrow \bar{\mathrm{H}} + e^-$$

has been of great interest because of the possibility of the spectroscopy of $\bar{\mathrm{H}}$, which would lead to the information on fundamental principles of physics including parity violation.[1)]

We have simulated the above process by the classical trajectory Monte Carlo (CTMC) method. Our main interest is to investigate the effects of the presence of a laser on the $\bar{\mathrm{H}}$ formation rate. The main advantage of the CTMC method is that it is relatively easy to execute for three-body systems without approximation further than the classical treatment. Converged fully quantum mechanical or semi-classical calculations often require large-scale numerical calculations, which may not always be feasible.

The presence of a laser introduces a perturbation which, in the dipole approximation and with the choice of the length gauge, has the form

$$H' = -F(t)\cos(\omega t + \varphi)\sum Z_i \mathbf{r}_i \cdot \mathbf{e},$$

where $\mathbf{e}$ is the direction of polarization of the laser, ω is the angular frequency, φ is the phase, $F(t)$ is the time-dependent electric field amplitude, and Z_i and $\mathbf{r}_i$ are the charge and the position vector of the ith particle in the three-body system. The peak field ($F_{\max}$) is related to the light intensity (I) by $F_{\max} = \sqrt{2I/\varepsilon_0 c}$. In this work the field was ramped smoothly on and off over a time scale τ, the total time period ΔT being chosen to be longer than the collision time:

$$F(t) = F_{\max} \times \begin{cases} \sin^2(\pi t/2\tau), & 0 \le t \le \tau \\ 1, & \tau < t < \Delta T - \tau \\ \sin^2(\pi(\Delta T - t)/2\tau), & \Delta T - \tau \le t \le \Delta T. \end{cases}$$

The CTMC procedure is well documented,[2)] but briefly it consists of the following steps: (1) Monte Carlo sampling of initial conditions, (2) integration of the classical equations of motion, and (3) identification of the exit channel in the asymptotic region $t \to +\infty$.

The dynamics can be solved by integration of the equations of motion in either the Hamiltonian or Lagrangian form. In fact it is simple and efficient to work with the six (independent) second-order differential equations of motion following directly from Newton's second law. These were solved by resolving the equations into their Cartesian coordinates resulting in 12 first-order coupled ordinary differential equations.

The effect on $\bar{p}$ capture due to the presence of a laser has been studied in the Born approximation.[3)] However it has been established that for laser-free collisions this model is inadequate at energies below the ionization threshold. Nonetheless, calculations at high energies using this approximation predicted an enhancement of capture in some cases by a factor of ten or more.[3–5)] However, the laser intensities considered have been shown to lead to rapid photoionization[6)] and thus to depletion of capture. We consider the process over the low energy range of interest to experiment. In particular, we investigate laser-assisted formation of $\bar{\mathrm{H}}$ at two $\bar{p}$ energies 1 keV and 15 keV, for laser wavelengths of $\lambda = 248$ nm and 1064 nm, and consider linearly polarized light with alignment parallel to and perpendicular to the collision axis (direction of the $\bar{p}$ beam).

It was discovered that the addition of the laser field led to enhancement of the formation of antihydrogen of the order of 4–70% for a $\bar{p}$ collision energy of 1 keV and 8% for an energy of 15 keV with $\lambda = 248$ nm. Certainly the classical model has shortcomings, however these preliminary results are promising. It seems that this process is worth studying with a quantal model of low-energy laser-assisted $\bar{p}$ capture by Ps, or equivalently, laser-assisted e^++H scattering leading to the formation of Ps, the latter being the reverse process of the charge conjugate of the former.

References

1) M. Charlton et al.: Phys. Rep. **241**, 65 (1994).
2) R. Abrines and I. C. Percival: Proc. Phys. Soc. **88**, 861 (1966); J. S. Cohen: Phys. Rev. A **27**, 167 (1983).
3) S.-M. Li et al.: Phys. Rev. A **59**, 1697 (1999).
4) S.-M. Li et al.: Phys. Rev. A **61**, 067402 (2000).
5) S.-M. Li et al.: J. Phys. B **33**, 4627 (2000).
6) L. B. Madsen and P. Lambropoulos: Phys. Rev. A **61**, 067401 (2000).

*1 Department of Physics, University of Durham, UK
*2 Department of Applied Mathematics and Theoretical Physics, Queen's University of Belfast, UK

Effects of the Hyperfine Structure on Symmetric Scattering of Muonic Atoms: Hyperspherical Close-Coupling Studies

A. Igarashi,[*1] M. P. Faifman,[*2] and I. Shimamura

Symmetric collisions of muonic atoms in a hyperfine state F with hydrogen isotope nuclei

$$p\mu(F) + p \longrightarrow p\mu(F') + p, \quad (1)$$

$$d\mu(F) + d \longrightarrow d\mu(F') + d, \quad (2)$$

$$t\mu(F) + t \longrightarrow t\mu(F') + t, \quad (3)$$

at low energies ($< 100\,\mathrm{eV}$) take a special place in the general picture of scattering processes in hydrogen-isotope mixtures with negative muons. The cross sections of reactions (1)–(3) provide the important information necessary for proposals and analysis of various experiments, in particular, on the precision measurements of the muon capture by hydrogen isotope nuclei and muon catalyzed fusion. The effective capture rates and the neutron yields of the nuclear fusion in muonic molecules, extracted from experimental data, depend on the populations of the hyperfine states of the muonic hydrogen atoms and on the rates of transitions between them.

On the other hand, calculations of the cross sections for processes (1)–(3) would be a good test for any computational method developed for the study of Coulomb three-body systems. In fact, the cross sections for processes (1)–(3), calculated by use of different methods,[1,2] are in good agreement. However, these cross sections show discrepancies with the experimental data on spin-flip ($F' \neq F$) reactions (2) and (3).[3–5]

The most intriguing is the spin-flip process

$$d\mu(F = 3/2) + d \longrightarrow d\mu(F' = 1/2) + d, \quad (4)$$

in reaction (2). The experimentally observed rates[5,6] of reaction (4) agree well between them but differ from the calculated ones by ~40%. According to the kinetics of muon-catalyzed fusion processes in deuterium,[7] the transitions between hyperfine states $F = 3/2$ and $F = 1/2$ of $d\mu$ atoms can proceed both through the spin-flip process

$$d\mu(F) + \mathrm{D}_2 \longrightarrow d\mu(F') + \mathrm{D}_2, \quad (5)$$

and due to the back-decay process of the intermediately formed molecular complex $(dd\mu)dee$ in reaction

$$d\mu(F) + \mathrm{D}_2 \longrightarrow (dd\mu)dee \longrightarrow d\mu(F') + \mathrm{D}_2. \quad (6)$$

Then the observed spin-flip rates $\lambda_{FF'}$ may be decomposed into the contribution $\lambda^{scatt}_{FF'}$ from reaction (5) and the contribution $\lambda^{bc}_{FF'}$ from process (6) as

$$\lambda_{FF'} = \lambda^{scatt}_{FF'} + \lambda^{bc}_{FF'}. \quad (7)$$

The component $\lambda^{bc}_{FF'}$ extracted from measured data agrees well with theory unlike the rates $\lambda^{scatt}_{FF'}$.

One could mention that for real experiment a molecular target is used, and so it is necessary to take into account not the "bare" nucleus in scattering calculations but the effects of the molecular structure. However, such an attempt could not resolve the existing disagreement between theory and experiment.

This long-standing puzzle about the rates $\lambda_{FF'}$ requires a serious check of the calculations of spin-flip cross sections. Most previous systematic calculations were done in the framework of the traditional adiabatic-state expansion method. The well-known problems with this method, such as the incorrect boundary conditions inherent in it, lead to the use of a large number of states of the "two-center problem," including the continuum states, and a detailed analysis of the convergence of the obtained solution.

In the present work both elastic and spin-flip cross sections of reactions (1)–(3) were calculated with the close-coupling method in the hyperspherical coordinates, as an extension of our previous work in Ref. 2. The advantages and reliability of this method were fully demonstrated in the previous publications.[2,8] In fact, the cross sections calculated in the present work turned out to agree fairly well with the results of the adiabatic-state expansion method, thus leaving the theory-experiment discrepancy still unresolved. On the theoretical part, the molecular effect should probably be considered seriously, now that reactions (1)–(3) have been treated quite accurately.

*1 Faculty of Engineering, Miyazaki University
*2 Russian Research Center Kurchatov Institute, Russia

References

1) L. Bracci et al.: Muon Catal. Fusion **4**, 247 (1989); Phys. Lett. A **134**, 435 (1989); J. S. Cohen: Phys. Rev. A **43**, 4668 (1991); C. Y. Hu et al.: J. Phys. B **28**, 3629 (1995).
2) A. Igarashi, I. Shimamura, and N. Toshima: Phys. Rev. A **58**, 1166 (1998).
3) C. Petitjean et al.: Hyperfine Interact. **118**, 127 (1999).
4) P. Ackerbauer et al.: Nucl. Phys. A **652**, 311 (1999).
5) P. Baumann et al.: Phys. Rev. Lett. **70**, 3720 (1993); B. Lauss et al.: Hyperfine Interact. **118**, 79 (1999).
6) N. I. Voropaev et al.: Hyperfine Interact. **118**, 135 (1999) and references therein.
7) L. I. Men'shikov et al.: Sov. Phys. JETP **65**, 656 (1987).
8) A. Igarashi and N. Toshima: Phys. Rev. A **50**, 232 (1994); A. Igarashi, N. Toshima, and T. Shirai: Phys. Rev. A **50**, 4951 (1994).

Possible Binding of Positron with Molecules

M. Kimura, M. Tachikawa, and I. Shimamura

Study of positron scattering from molecules has attracted a significant interest recent years since the knowledge of interactions and dynamics is expected to provide basic physics at much deeper level by a comparative study between positron- and electron-scattering cases. However, very little knowledge and information for molecular processes by positron impact have been attained due to the lack of systematic experimental and theoretical studies. Positronium (Ps) formation is a channel unique to positron impact which has a threshold of $(E_i - 6.8)$ eV (where E_i is an ionization potential of a target). One path for the Ps formation is a direct process that is regarded as similar to *charge transfer* process in ion-atom collisions. Another path is an indirect process that the positron is temporarily captured by the molecular field before it escapes from it as the Ps, *i.e.*, Ps formation via a resonance. After the Ps formation, the target molecule is left as a molecular ion either in the ground or excited electronic state. For a majority of molecular ions, they are known to strongly couple with dissociation channels, and hence, are not stable. After a short lifetime, they break up producing various smaller fragmented species. The kind of species and their energy distributions after breaking-up should be quite different from those produced by electron impact. Therefore, the precise knowledge of dynamics for the Ps-formation and resonance from various molecular targets would be of fundamental interest for atomic and molecular physics as well as condensed matter physics. Therefore, it is extremely important to understand if positron can attach, at least temporarily, to molecules.

Recently, there are three independent experiments which are strongly indicative of the presence of resonance or bound state of positron: (i) Sueoka and Kimura[1] have observed a strong suppression of Ps formation in fluorinated hydrocarbons (FHCs) compared to their hydrocarbon (HCs) counterparts in the ratio of Ps formation cross section to total cross section near Ps-formation thresholds. As the molecular size increases, these ratios of Ps formation to total from both groups are found to merge. (ii) Surko's group[2] has measured annihilation rates for various molecules by thermal positron impact below 1 eV, and has observed that annihilation rates differ significantly from HCs to FHCs, in which the annihilation rates for HCs are found to be grossly larger by four–five orders of magnitude than those for FHCs. Furthermore they have analyzed from their γ-emission spectrum and speculated that the annihilation tends to occur on C-H bonds in HCs and on F atoms in FHCs.[2] (iii) Xu *et al.*[3] has carried out another type of positron scattering experiment from large molecules, in which they have detected the appearance of various types of fragments when low energy positron with the energy below Ps threshold was introduced into the target. The fragmentation may occur through a resonance state. All three experimental findings that studied completely different aspects of positron scattering may be interpreted consistently by assuming the presence of the positron resonance or bound state for FHCs. If a positron is assumed to be trapped at the far end of the polarization potential where it is isolated from the rest of electrons, then these resonance or bound states are likely to make a positron lifetime longer, hence reducing the annihilation or fragmentation. In a study of Ps formation in liquid halogen-substituted substrates, Wikander[4] has found that in the liquid-FHCs, the Ps formation rate decreases by 10% more in comparison with that in liquid-HCs. The basic underlying physics should share the same origin as in the three experimental results above. In order to provide a rationale to these findings, the theoretical study based on a quantum chemical method based on the Hartree-Fock approach is underway to examine a possible bound state of positron. The preliminary result clearly suggests that some molecules with a strong dipole moment such as LiH can indeed bind a positron with a positron affinity of 0.0055 a.u.

References

1) O. Sueoka and M. Kimura: to be published in Phys. Rev. A.
2) S. J. Gilbert, R. G. Greaves, and C. M. Surko: Phys. Rev. Lett. **82**, 5032 (1999); C. Surko: private communications (2000).
3) J. Xu, L. D. Hulett, Jr., T. A. Lewis, D. L. Donohue, S. A. McLuckey, and O. H. Crawford: Phys. Rev. A **49**, R3151 (1994).
4) G. Wikander: Chem. Phys. Lett. **80**, 361 (1981).

Electron and Positron Scattering from CF_3I Molecules below 600 eV

M. K. Kawada,* O. Sueoka,* M. Kimura, and I. Shimamura

Perfluorocarbon (C_mF_n) molecules have been regarded as important and efficient gases for plasma etching, and have been extensively used in semiconductor manufacturing industries.[1] However, because of their long life in the stratosphere as well as in the atmosphere and hence the introduction of toxic gases into the earth's environment, it has been decided to completely terminate the usage of these gases in the very near future. Therefore, the development of an alternative new gas that is environmentally safe and efficient is urgently required. Strong candidates for these alternative gases are non-perfluorocarbon gases such as CF_3I because the molecule is known to be environmentally safe and to easily release the CF_3 radical. To assess the behavior of these molecules in the plasma environment, it is crucial to understand the fundamental spectroscopic properties of these molecules and their dynamics, particularly the electron scattering processes at low to intermediate energies. Also, a complete set of cross-sectional data for a wide range of collision energies is necessary to assess and evaluate the role of inelastic scattering processes. A comparative study between electron and positron scattering from molecules can provide more detailed insight into interaction and dynamics, and hence is essential. Therefore, we conducted a comparative study of electron and positron scattering from CF_3I molecules for total and elastic cross sections.

Electron Impact: Total cross sections (TCSs) for electrons from CF_3I molecules obtained at selected energies within the range 0.7–600 eV are shown in Fig. 1 along with the previous experimental data.[2] Some interesting general features of the present TCSs for CF_3I can be summarized: (1) The TCSs have a relatively large and broad peak at around 4–11 eV, and the curve drops sharply on both sides of this energy range. The magnitude of the TCS sharply increases from 20×10^{-16} cm^2 at 0.8 eV to the maximum value of 53×10^{-16} cm^2 at around 5 eV, followed by a very slow decrease until the energy reaches 11 eV, where it has a value of 50×10^{-16} cm^2. (2) This large and broad peak appears to consist of two small humps at approximately around 5 eV and 8 eV. (3) Several small structures can be seen at around 25 eV. The broad peak at around 4–11 eV is due to strong enhancement from the shape resonances.

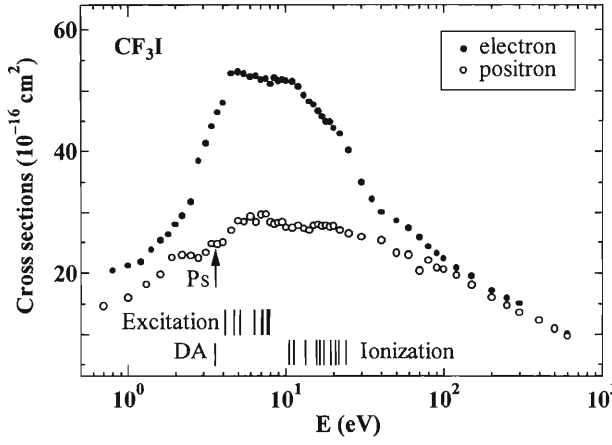

Fig. 1. Total cross sections of electron and positron impacts on CF_3I molecules. Electronic excitations, dissociative attachment and ionization thresholds are also shown in vertical lines.

Positron Impact: TCSs for positron impact are also included in Fig. 1. Over the entire impact-energy range, the TCSs for positrons are always found to be smaller than those for electrons. Starting from a value of 14×10^{-16} cm^2 at 0.7 eV, the TCSs increase with a step-like structure at around 2–3 eV and continue to increase to a maximum value at around 7 eV. This step-like increase is attributable to the opening of a new positronium formation channel at a threshold of 3.43 eV. A few structures can also be observed in the energy region between 4 eV and 20 eV, and these are attributable to the opening of new channels for a series of electronic excitations, and direct ionization where each threshold corresponds to approximately 4.3 eV and above, and 10.23 eV. Other weak structures can also be observed throughout the entire energy range.

References

1) L. C. Christophorou: *Electron-Molecule Interactions and Their Applications* (Academic Press, New York, 1984).
2) T. Underwood-Lemons, D. C. Winkler, J. A. Tossell, and J. H. Moore: J. Chem. Phys. **100**, 9117 (1994).

* Graduate School of Science and Engineering, Yamaguchi University

Elastic Scattering of Electrons from Carbonyl Sulfide

M. Takekawa and Y. Itikawa*

Due to its importance in a field of environmental science, carbonyl sulfide (OCS) is one of the important molecules for a study of electron scattering. A theoretical study is attempted to get detailed information about elastic scattering (more strictly, vibrationally elastic scattering, corresponding to the experimental data available) of electrons from OCS in this investigation.

We mention the present theory here briefly. The details of the theory have been described elsewhere.[1] The *fixed-nuclei, adiabatic-rotation approximation* is employed in the present calculation, that is, we freeze the target nuclei throughout the collision. The electronic excitation probability of the target molecule is expected to be smaller than the elastic scattering probability in the present incident energy region 1.0–60.0 eV. Therefore, the target molecule is assumed to stay in the electronically ground state, in which the OCS molecule is linear. The wave function of the incident electron in the body-fixed frame (*i.e.*, the z-axis is chosen along the molecular axis and the origin of the coordinates is located at the center-of-mass of the molecule) is expanded in terms of the spherical harmonics to yield coupled differential equations for the radial part of the wave function. The coupled differential equations are solved with the scattering boundary conditions to obtain the scattering matrix (S-matrix) in the body-fixed frame. After the frame transformation from the body-fixed to the space-fixed coordinates, differential cross sections are obtained. The closure method (with the adiabatic-rotation version of the point-dipole-Born approximation) is adopted to consider the effect of the long-range dipole interaction. The effect is essential in the forward scattering region.

The interaction between an electron and the target molecule is composed of three terms: static, exchange and correlation-polarization potentials. For electron exchange, a local model potential[2] is adopted. Use is made of a parameter-free correlation-polarization model[3] to take account of the target polarization. This model is constructed by matching local, short-range correlation potential to the long-range polarization potential. The former is evaluated in the local density approximation of electron gas. The quantum chemistry molecular orbital code *GAMESS* is used to generate the multi-centered target wave function.

Figure 1 shows the present differential cross section

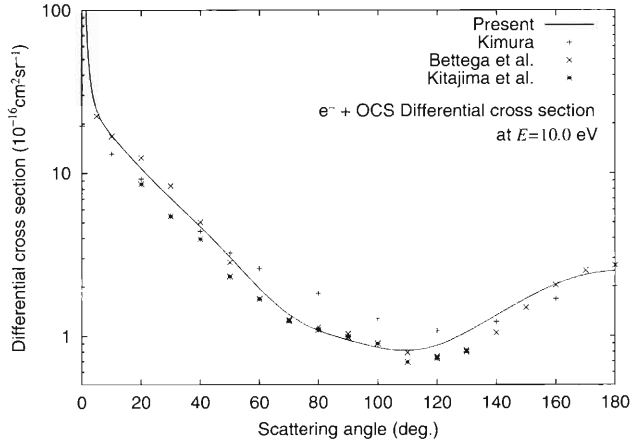

Fig. 1. Differential cross sections for the elastic scattering at 10.0 eV.

(DCS) for the elastic scattering at an incident energy of 10.0 eV. In this figure, the result of the present calculation is compared with the experimental DCS[4] and the theoretical values obtained by the continuum-multiple-scattering method[5] and by the Schwinger multichannel method.[6] The present result reproduces the experimental DCS fairly well and is also in a good qualitative agreement with the other theoretical results except at a scattering angle of 0°. The disagreement at 0° may be due to the difference in the considerations of the long-range dipole interaction in the different calculations. The present closure method does not take into account the molecular rotation properly, but should be reliable unless the scattering angle is extremely small. In principle, a calculation considering the rotational transition is needed to evaluate the appropriate DCSs in the forward scattering region for a polar molecule.[7]

References

1) M. Takekawa and Y. Itikawa: J. Phys. B **29**, 4227 (1996).
2) S. Hara: J. Phys. Soc. Jpn. **22**, 710 (1967).
3) N. T. Padial and D. W. Norcross: Phys. Rev. A **29**, 1742 (1984).
4) M. Kitajima et al.: At. Collision. Res. Jpn. **24**, 10 (1998) and private communication.
5) M. Kimura: private communication.
6) M. H. F. Bettega et al.: Aust. J. Phys. **53**, 399 (2000).
7) Y. Itikawa: Phys. Rep. **46**, 117 (1978).

* The Institute of Space and Astronautical Science

Photoabsorption Spectra in the Continuum of Molecules and Atomic Clusters†

T. Nakatsukasa and K. Yabana*

Since excitation spectra above the ionization threshold are continuum spectra, it is very important to take into account the effect of the electronic single-particle continuum. The random-phase approximation (RPA) with Green's function technique[1,2] is a powerful method to investigate a continuum response of finite systems to electromagnetic fields. However, the applicability was rather limited, namely the method is applicable only to spherical systems. We present alternative methods based on a theory of the time-dependent local density approximation (TDLDA) to calculate the excitation spectra for systems with arbitrary shape at the RPA level.

The exact treatment of the continuum is represented by an outgoing asymptotic behavior of the single-particle Green's functions,

$$G^{(+)}(\mathbf{r},\mathbf{r}';E) = \langle \mathbf{r}|(E - H_{\rm sp} + i\epsilon)^{-1}|\mathbf{r}'\rangle, \qquad (1)$$

which appear in the expression of the response (density correlation) function. Here $H_{\rm sp}$ is the single-particle Hamiltonian of the ground-state Kohn-Sham equation. In order to impose the outgoing boundary condition upon the Green's function, we utilize an equation for the single-particle Green's function,

$$\hat{G}^{(+)}(E) = \hat{G}_0^{(+)}(E) + \hat{G}_0^{(+)}\hat{V}\hat{G}^{(+)}(E), \qquad (2)$$

where $\hat{G}_0^{(+)}$ is a single-particle Green's function for a solvable Hamiltonian H_0 and $\hat{V} = H_{\rm sp} - H_0$. For instance, we may take H_0 as a single-particle Hamiltonian with a spherical Coulomb potential. Solving the Dyson-type Eq. (2) in a three-dimensional coordinate space, now we can exactly treat the continuum. See the paper† for details.

We apply the method to finite electron systems, *e.g.* molecules and clusters. We show photoabsorption spectra of valence electrons of ethylene in Fig. 1. The agreement with experiment is excellent. In this calculation, the highest-occupied molecular orbital (HOMO) is found at $-11.7\,$eV. Thus, for $\omega > 11.7\,$eV, electrons can be excited into the continuum. When the system is polarized by an external electric field, the induced polarization acts as a screening field. The dashed line in the figure shows the result of the independent-particle approximation (IPA) which ignores this dynamical screening. We see that the dielectric effects are essential for reproducing the photoabsorption spectra. We have applied the method to a negatively charged Na_7^- cluster and to other small molecules, silane and acetylene.

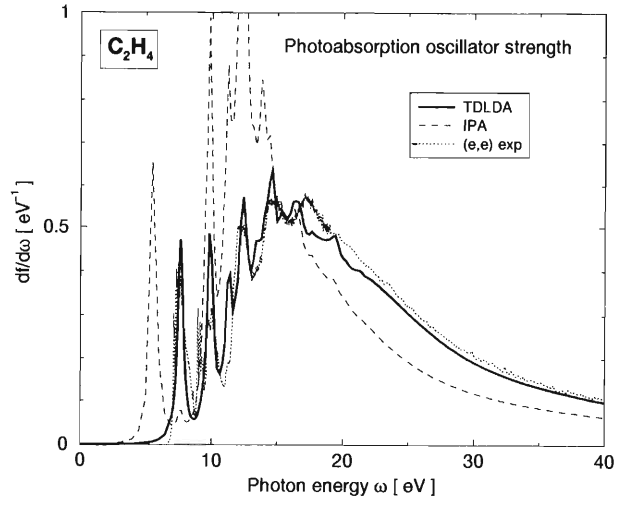

Fig. 1. Photoabsorption spectra of ethylene molecules. The solid and dashed lines are the calculated spectra with and without a dynamical screening effect, respectively. The dotted line indicates experimental data.

Another method we have developed is a real-time method. We calculate the time evolution of a TDLDA state under an external field and demonstrate that the continuum effect may be effectively taken into account by introducing a complex absorbing potential at the edge of the box ($R < r < R + \Delta r$). We adopt an absorbing potential of a linear form,

$$W(r) = -iW_0\frac{r-R}{\Delta r} \quad \text{for } R < r < R + \Delta r. \qquad (3)$$

The WKB analysis provides a condition of minimizing the total reflection,[3]

$$20\frac{E^{1/2}}{\Delta r\sqrt{8m}} < |W_0| < \frac{1}{10}\Delta r\sqrt{8m}E^{3/2}, \qquad (4)$$

where E is the energy of outgoing particles. Advantage of this method over the previous one is the computational feasibility. See the article† for the applications of the real-time method and comparison with the previous method.

References

1) S. Shlomo and G. Bertsch: Nucl. Phys. A **243**, 507 (1975).
2) A. Zangwill and P. Soven: Phys. Rev. A **21**, 1561 (1980).
3) M. S. Child: Mol. Phys. **72**, 89 (1991).

† Condensed from the article in J. Chem. Phys. **114**, 2550 (2001)

* Institute of Physics, University of Tsukuba

Radiative Electron Capture of Swift Heavy Ions

T. Azuma, T. Ito, Y. Takabayashi, K. Komaki, T. Kambara, Y. Kanai, Y. Nakai, T. Kojima, and Y. Yamazaki

Various kinds of X rays have been observed in heavy-ion-solid collisions. The characteristic X rays originating either from projectile ions or target atoms are observed as discrete peaks. The X rays with energy distribution much broader than the above, caused through collisional dynamics between projectile ions and target atoms, are also observed. The typical examples are X rays associated with the electron capture into the discrete states of projectile ions from target atoms to satisfy both the energy and momentum conservations. This process called "radiative electron capture (REC)" was first observed by Schnopper *et al.*[1] Since then a number of experimental REC data have been accumulated.[2] For low energetic projectiles, the REC process is neglibible compared with the non-radiative electron capture process, but it becomes dominant for high Z ions at the high incident energies, since REC cross section is crudely scaled by v_p^{-5} (v_p: projectile velocity) in contrast to the non-REC cross section scaled by v_p^{-11}. The energy width of the X-ray peak associated with the REC process originates from the momentum distribution of the bound electrons of the target atom, *i.e.*, the Compton profile.

In addition these bound electrons have another chance of being captured into the continuum states of projectile ions by emitting photons. This process is sometimes called "radiative electron capture into the continuum states (RECC)" as an analogy to REC.[3] The RECC process is accompanied by the emission of continuum X rays with a maximum edge energy corresponding to that of electrons with velocity of v_p. Electrons once excited into the continuum by the RECC process have a chance to emerge as a "convoy electron" emitted at the zero-degree direction with velocity around v_p.

We investigate these X rays *via* measurements of the energy spectra of emitted X rays at the ion-solid collisions together with coincident measurements of charge-state distribution of emerged projectile ions in the incident energy range of several tens MeV/nucleon. Bare Kr^{36+} ions of 36 MeV/nucleon passed through a 178 μg/cm^2-thick carbon foil tilted by 45° from the beam direction. Emitted X rays at the collisions were observed by a Si(Li) detector located at an angle of 90° from the beam direction. The charge distribution of emerged projectile ions was measured using a combination of a magnetic analyzer and position sensitive 2D-silicon detectors at the downstream end of the beam. The signals from the charge distribution of the projectile ions and X rays were accumulated in a list mode.

The X rays emitted from REC into the K- and L-shell, the continuum X rays from RECC, and the characteristic K_α and K_β X rays of the projectile ions on the shoulder of the curve for the RECC component were observed as shown in Fig. 1 (a). The spectrum of X rays in coincidence with the component of hydrogen-like Kr^{35+} among emerged projectile ions, *i.e.*, the electron captured state is also shown in Fig. 1 (b). It is clearly seen that the peaks associated with the electron capture process are stressed as a result of depression of RECC and other background component. The characteristic X rays are emitted following capture of target electrons into the L or higher states of the projectile ions. The peak energies for the K- and L-REC components are 37.1 and 23.7 keV, respectively. The oberved energies agree well with the theoretical values expected from the relativistic kinematics, which confirms its validity for the REC process. Furthermore, the observed energies of K_α and K_β X rays are 13.5 and 16.0 keV, and are also consistent with the theoretical value.

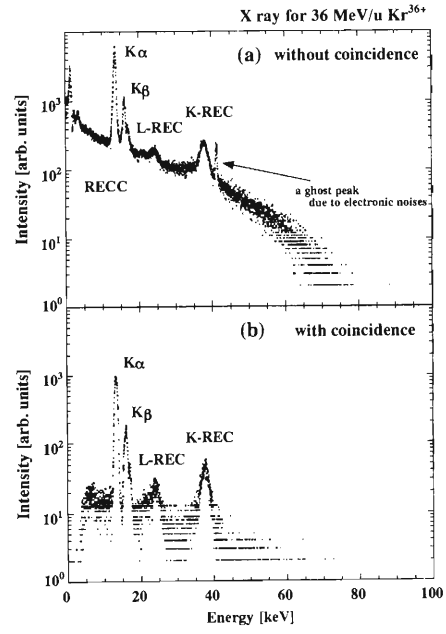

Fig. 1. X-ray energy spectra for 36 MeV/nucleon Kr^{36+} ions. (a) Single spectrum. (b) Spectrum taken in coincidence with the component of Kr^{35+} after passing through a 178 μg/cm^2-thick carbon foil. The correction for the detector efficiencies are not made.

References

1) H. W. Schnopper et al.: Phys. Rev. Lett. **29**, 898 (1972).
2) see references in Th. Stohlker et al.: Phys. Rev. A **51**, 2098 (1995).
3) H. Tawara et al.: Phys. Rev. A **55**, 808 (1997); T. Ludziejewski et al.: J. Phys. B **31**, 2601 (1998).

Elastic Wave from Fast Heavy-Ion Irradiation of Metals

T. Kambara, Y. Kanai, T. M. Kojima, Y. Nakai, Y. Yamazaki, A. Yoneda, and K. Kageyama*

We have observed elastic oscillations in the ultrasonic region from various solid samples irradiated with a pulsed ion beam. We have previously reported the experimental setup at the Ring Cyclotron and the preliminary results[1] with 26 MeV/u Xe ions as well as the procedure used to obtain the short pulse beam.[2]

In recent measurements, we have observed a longitudinal wave pulse with a rise time shorter than 70 ns at the onset of the ultrasonic oscillation for metallic samples. The samples were polycrystalline Al and Cu plates with square-shaped faces of 35 mm × 35 mm and a thickness of 5 or 10 mm. The ion beam was incident on one face at right angles with a spot size of about 3 mm × 3 mm and a piezoelectric ultrasonic sensor was placed at the opposite side of the beam spot. According to calculations, the range of the ions in Al is estimated to be 280 μm and that in Cu to be 110 μm. They are much shorter than the thickness of the samples. Therefore, all the ions were stopped in the material near the incident surface.

Figure 1 shows the ultrasonic waveform from the 5-mm-thick Al sample, along with the microstructure of the beam pulse. The beam spot was at the center of the face of the sample, immediately opposite the sensor. The displayed waveforms are composed of an average of 34 shots.

The waveform from the sensor has an oscillatory structure, as shown in Fig. 1 (a). Figure 1 (b) shows the onset of the ultrasonic oscillation. At the onset, there is a low and sharp pulse with a rise time shorter than 100 ns which is delayed by about 0.8 μs relative to the beam pulse. This arrival time is consistent with that estimated with the tabulated speed of the bulk longitudinal wave denoted as L in Fig. 1 (b). Therefore, we conclude that the observed ultrasonic pulse is a very short longitudinal wave generated at the time of irradiation. On the other hand, there is no such structure evident in the waveform at the expected arrival time of the shear wave. A similar short pulse was observed for 10-mm-thick Al and Cu samples at the expected arrival time of the longitudinal wave.

Figure 2 compares the waveforms for a 10-mm-thick Al sample at different beam spot positions; the beam spot at the center of the face immediately opposite the sensor (0 mm), shifted from the center by 3 mm, 6 mm and 12 mm. The onset waveform depends on the position of the beam spot and it gradually becomes broader as the distance increases. The onset time matches the estimated arrival time of the longitudinal wave denoted by arrows in the figure. We speculate that the increase of the pulse width is due to the finite size of both the beam spot and the ultrasonic sensor.

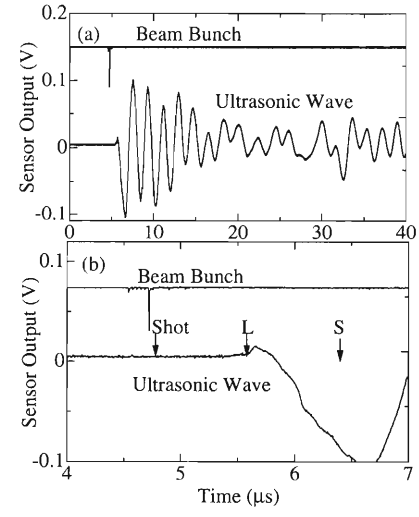

Fig. 1. Ultrasonic waveform from a sensor on the back of a 5-mm-thick Al sample, along with the time structure of an ion bunch. (b) is expansion of (a) near the onset of oscillation. L denotes the arrival time of the bulk longitudinal wave estimated with the tabulated sound velocity.

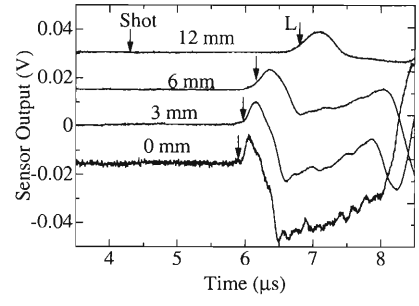

Fig. 2. Ultrasonic waveforms for a 10-mm-thick Al sample at the beam spot on the opposite side of the sensor (0 mm) and at 3–12 mm from the center. Arrows denote the estimated arrival time of the longitudinal wave.

References

1) T. Kambara, Y. Kanai, T. M. Kojima, Y. Nakai, A. Yoneda, K. Kageyama, and Y. Yamazaki: Nucl. Instrum. Methods Phys. Res. B **164/165**, 415 (2000).
2) A. Yoneda and T. Kambara: RIKEN Accel. Prog. Rep. **33**, 203 (2000).

* Department of Mechanical Engineering, Saitama University

Hardening of Fe-Cu Alloys by Swift Heavy Ion Irradiation

T. Hasegawa,[*1,*2] A. Iwase,[*1] Y. Chimi,[*1] N. Ishikawa,[*1] T. Tobita,[*1]
M. Suzuki,[*1] S. Ishino,[*2] and T. Kambara

As irradiation-enhanced precipitation of copper atoms in stainless steels causes the hardening and embrittlement of reactor pressure vessels, it is one of the important phenomena, the understanding of which provides the basis for nuclear reactor safety. For the past decade, much work on irradiation enhanced Cu precipitation in stainless steels and Fe-Cu model alloys has been carried out by using neutron, electron and low energy ion irradiations. It is usually assumed that the thermal motion of point defects produced through elastic collisions dominates the phenomenon. Recently, however, Barbu *et al.* have shown that in Fe-1.3% Cu alloys irradiated with 5.1 GeV Kr ions, the electron excitation along the swift ion beam path induces the Cu precipitation.[1] In this paper, we report the change in hardness of Fe-Cu alloys by GeV heavy ion irradiation at elevated temperatures, and compare the results with those for electron irradiation.

Two model alloys, Fe-0.6% Cu and Fe-1.2% Cu were used for the present experiment. The specimens were irradiated with 3.5 GeV (26 MeV/u) Xe ions using the RIKEN ring cyclotron. The specimen temperature during Xe irradiation was kept constant at 250°C. For comparison, irradiation with 3.8 GeV (21 MeV/u) Ta ions at room temperature was also performed. After the irradiation, the hardness of the specimen in the irradiated and unirradiated areas was measured at room temperature using a Vickers hardness tester with a load of 100 gf.

Figure 1 shows the change in Vickers microhardness by irradiation as a function of dpa (the number of displacements per atom by elastic collisions) which is calculated by using the TRIM computer code.[2] In the figure, the results for 2.5 MeV electron irradiation at 250°C[3] and those for the 3.8 GeV Ta irradiation at room temperature are also plotted. For Fe-1.2% Cu alloys, the change in hardness due to the Xe irradiation is much greater than that due to electron irradiation at the same dpa value, while for Fe-0.6% Cu alloys, the change in hardness is smaller than that for Fe-1.2% Cu. The figure also shows that Ta irradiation at room temperature rarely changes the hardness of Fe-Cu alloys. The present result implies that the electronic excitation by GeV heavy ions contributes to the precipitation of Cu atoms, which causes the increase in hardness. The extent of the contribution depends on the concentration of Cu atoms and the irradiation temperature.

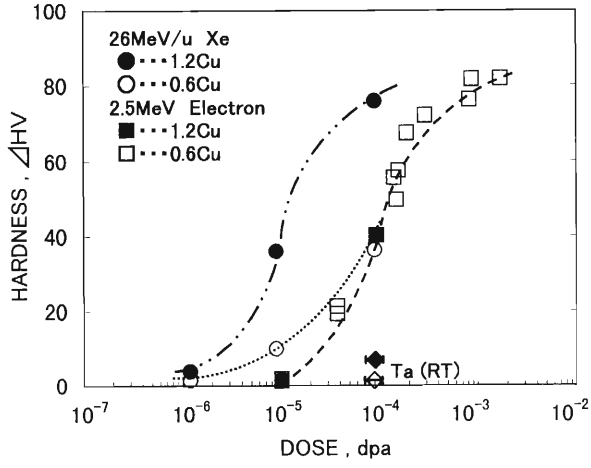

Fig. 1. Change in Vickers microhardness of Fe-Cu alloys by GeV ion and electron irradiations as a function of calculated dpa.

References

1) A. Barbu et al.: Nucl. Instrum. Methods Phys. Res. B **146**, 278 (1998).
2) J. P. Biersack et al.: Nucl. Instrum. Methods B **174**, 257 (1980).
3) T. Tobita et al.: Trans. 15th Int. Conf. on Structural Mechanics in Reactor Technology (SMiRT-15) X-205 (1999).

*1 Japan Atomic Energy Research Institute
*2 Faculty of Engineering, Tokai University

Magnetic Properties of Fe-Ni Invar Alloys Irradiated by High-Energy Heavy Ions

F. Ono,[*1] A. Takahashi,[*1] S. Wei,[*1] H. Inoue,[*1] A. Iwase,[*2] Y. Chimi,[*2] N. Ishikawa,[*2] N. Kuroda,[*2] and T. Kambara

Fe-Ni alloys around the Invar composition of 35 at.% Ni show various anomalies in both mechanical and magnetic properties. Anomalies in the physical properties such as low thermal expansion were interpreted as being due to the large positive value of the magneto-volume effect which cancels out the normal part of the thermal expansion. Anomalies in the magnetic properties are an unusual decrease in the spontaneous magnetization from the Slater-Poling curve and an abrupt increase in the high-field susceptibility.

These anomalies have been understood from the band picture to be a result of the instability of the 3d-band electron ferromagnetism.[1] However, the detailed concentration dependence of the magnetization cannot be explained without taking into account the effect of the concentration fluctuation, as pointed out by Kachi *et al.*[2] The extent of the concentration fluctuation in Fe-Ni Invar alloys made by the conventional alloying method was estimated by adjusting the Gaussian distribution parameter to fit the experimental curve. Using this parameter, magnetic anomalies in Fe-Ni Invar alloys have been explained satisfactorily. Thus, the concentration fluctuation was found to play an important role in the fabrication of Fe-Ni Invar alloys.

We have succeeded in changing the extent of the concentration fluctuation by mixing the powders of the starting elements and mechanically alloying[3] them. The extent of the fluctuation was controlled by annealing the alloys at high temperatures.[4]

The effect of high-energy ion beam irradiation on the magnetization curves of the mechanically alloyed Fe-Ni Invar was investigated using a sample-subtracting-type magnetometer. The irradiations were carried out using 2.86 GeV Xe ions at a fluency of $10^{12}/cm^2$ using the RIKEN Ring Cyclotron. The observed magnetization curves at room temperature before and after the irradiations are shown in Fig. 1. The magnetization for all the samples with different extents of fluctuation decreased upon irradiation. However, the irradiation

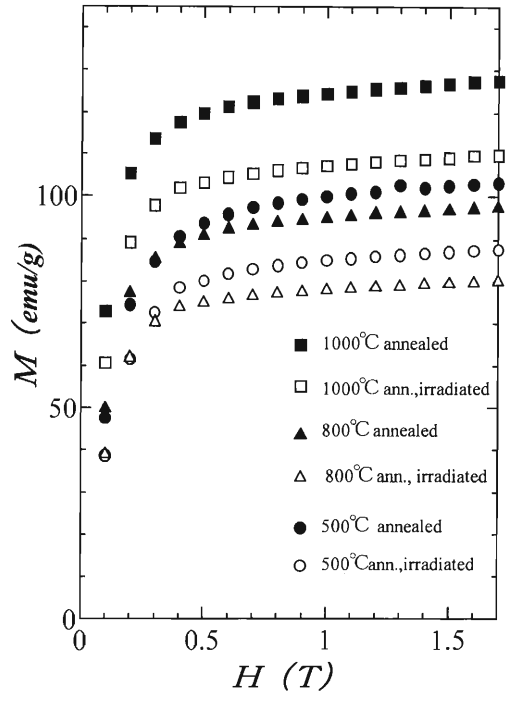

Fig. 1. Magnetization curves for Fe-Ni Invar mechanical alloys at room temperature before and after high-energy ion irradiation.

effect is the smallest in the three samples at the moderate extent of concentration fluctuation, *i.e.*, annealed at 800 °C. This tendency may be associated with other unique characteristics of this extent of fluctuation as shown in Ref. 4.

References

1) P. Entel et al.: Phys. Rev. B **47**, 8706 (1993).
2) S. Kachi et al.: J. Phys. Soc. Jpn. **25**, 285 (1968).
3) F. Ono et al.: Proc. '98 Powder Metallurgy World Congress, Granada, Spain, Vol. 1 (1998), p. 449.
4) S. Wei et al.: J. Magn. Soc. Jpn. **23**, 391 (1999).

*1 Department of Physics, Okayama University
*2 Japan Atomic Energy Research Institute

Magnetic Relaxation in Bi-2223 Tapes Irradiated by Xe Ions

H. Ikeda, N. Ishikawa, A. Iwase, T. Kambara, and R. Yoshizaki*

In the field of power applications it is necessary to fabricate superconducting materials with high critical current densities J_c. Higher J_c is, in general, achieved by increasing in the flux pinning energy in superconductors. However, in the high-temperature (T_c) cuprate superconductors, the large flux creep effect in the magnetization has been reported.[1] Therefore, we have to clarify the origin of the pinning mechanism in high-T_c superconductors. As a first step, we introduced columnar defects in to the Bi-2223 tapes parallel to the aligned c-axis (normal to the tape surface) by Xe-ion irradiation and measured the distribution of the flux pinning energy.[2] In the present research, we study the pinning energy distribution for the Bi-2223 tapes with columnar defects by Xe-ion irradiation.

The Ag-Cu alloy sheathed tapes were prepared by the powder-in-tube method. The details of the preparation method and the fundamental properties of the samples were reported elsewhere.[3] Bi-2223 tapes with $3.0 \times 3.0 \times 0.1\,\mathrm{mm}^3$ typical dimensions were irradiated with 3.5 GeV $^{163}Xe^{31+}$ ion at the RIKEN Ring Cyclotron Facility to introduce columnar defects perpendicular to the tape surface direction. The magnetic properties were measured using a superconducting quantum interference device (SQUID) magnetometer. Pinning potentials were estimated from the decay profiles of the remanent magnetic moment for the nonirradiated and irradiated Bi-2223 tape samples. In the magnetic relaxation measurement, we adopted the following process: the magnetic field was initialized to zero (approximately $20\,\mu\mathrm{T}$), then the sample was loaded at the measurement temperature. After the zero-field cooling, a magnetic field was applied ($H = 1\,\mathrm{T}$) and the relaxation of the magnetization was measured for approximately 10^5 sec.

The relaxation of the remanent moment for the irradiated and nonirradiated samples shows the linear $\ln(t)$ dependence in the entire observed temperature range. In order to study the effects of temperature and irradiation on flux creep, the magnetization M is normalized to the initial magnetization M_0. It is clearly seen that the slope of M/M_0 versus $\ln(t)$ decreases the relaxation rate for the irradiated Bi-2223 tape samples. This result shows that the critical current density (J_c) can be improved in the entire temperature range with irradiation. The standard model for flux creep in superconductors proposed by Anderson[4] has been used to analyze data on high-temperature superconductors. We use the model of Maley *et al.*[5] to analyze the data. Using the rate equation of Beasley, Labusch and Webb:[6] $dM/dt = (B\omega a/\pi d)\exp(-U_{eff}/kT)$, where ω and a are the hop frequency and distance, respectively, for a flux bundle, and d is the grain diameter. This leads to the expression $U_{eff}/k = -T[\ln(dM/dt) - \ln(B\omega a/\pi d)]$ for the effective pinning potential. Here, we have estimated the value of the constant $C = \ln(B\omega a/\pi d)$ empirically by plotting the data as U_{eff}/k versus M at each temperature for the irradiated and nonirradiated Bi-2223 tape samples and adjusting C to obtain the smoothest curve. The constant values are $C = 20$ for the irradiated case and $C = 25$ for the nonirradiated ones, as shown in Fig. 1 (a) and (b). These values imply physically reasonable values. It is considered that the difference in C behavior between the irradiated and nonirradiated cases comes from the difference in the induced defect structure with irradiation. In the case of irradiation, it produces columnar defects (amorphous tracks with diameters of $\approx 6\,\mathrm{nm}$), which yield a large pinning energy of high-temperature superconductors for vortices parallel to the defects.

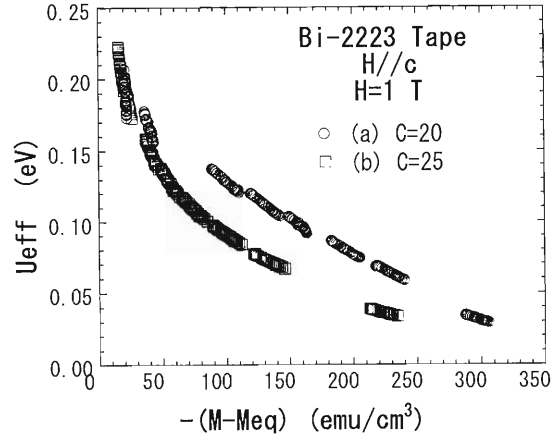

Fig. 1. The effective pinning potential U_{eff} as obtained from the nonlinear equations for flux creep versus the magnetization M for the irradiated Bi-2223 tape and the nonirradiated ones.

We observed the pinning energy distribution for the Bi-2223 tape samples. We used Maley's expression to analyze the data. The change in the distribution of the activation energies with irradiation was determined. Since the number of deeper pinning centers as increased, it is expected that the columnar defects will act as effective pinning centers.

* Institute of Materials Science, University of Tsukuba

References

1) K. A. Muller et al.: Phys. Rev. Lett. **58**, 1143 (1987).
2) H. Ikeda et al.: Physica B **284/288**, 871 (2000).
3) M. Ishizuka et al.: Physica C **252**, 339 (1995).
4) P. W. Anderson: Phys. Rev. Lett. **9**, 293 (1972).
5) M. P. Maley et al.: Phys. Rev. B **42**, 2639 (1990).
6) M. R. Beasley et al.: Phys. Rev. A **181**, 682 (1969).

Scaling of Irradiation Effects by Primary Ionization Rate in Ion-Irradiated Oxide Superconductors

N. Ishikawa, Y. Chimi, A. Iwase, O. Michikami,* H. Wakana,* and T. Kambara

It is customary to analyze the effect of electronic excitation in terms of the electronic stopping power, S_e, which is defined as the energy transferred from incident ions to electrons of the target per unit ion-path length.[1,2] However, in the present study, we have found that the defect production via electronic excitation in ion-irradiated oxide superconductors is dominated by the primary ionization rate rather than the electronic stopping power. Thin films of an $EuBa_2Cu_3O_y$ (EBCO) oxide superconductor were irradiated with various heavy ions (120 MeV Cl, 150 MeV Sc, 90 MeV Ni, 125 MeV Br, 0.71 GeV Kr, 90 MeV I, 3.54 GeV Xe, 3.84 GeV Ta, and 200 MeV Au) in a wide energy range of 90 MeV–3.84 GeV. The ions with the energy of 90–200 MeV were produced at a tandem accelerator at Japan Atomic Energy Research Institute, Tokai Establishment (JAERI-Tokai), and the ions of 0.71–3.84 GeV were produced at the RIKEN Ring Cyclotron. All irradiations were performed at a fixed temperature of 100 K. The values of $\Delta\rho/\rho_o$ were measured *in situ* as a function of ion fluence, Φ, at 100 K by the standard four-probe method, where $\Delta\rho/\rho_o$ is the change in resistivity normalized by the resistivity before irradiation, ρ_o.

An increase in normal-state resistivity and a decrease in superconducting transition temperature, T_c, are observed for all irradiations, indicating that lattice defects are introduced by the irradiations. In Fig. 1, it is found that the initial slope of the resistivity change, $[(\Delta\rho/\rho_o)/\Phi]_{\Phi\to 0}$, can be well scaled by the primary ionization rate. The primary ionization rate is represented by dJ/dx, where J is the number of target atoms primarily ionized by the irradiating ion and x is the path length of the irradiating ion.[3,4] In Fig. 2, it is also found that the change rate in T_c, $(\Delta T_c/T_{co})/\Phi_{total}$, is well scaled by the primary ionization rate. Here, T_{co} is the value of T_c before irradiation, Φ_{total} is the fluence at which the resistivity at 100 K becomes 2.4 times larger than that before irradiation, and $\Delta T_c = T_{co}$-T_c ($\Phi = \Phi_{total}$).

In our previous study,[5] it was found that electronic stopping power is not an appropriate parameter for describing the defect production process in EBCO irradiated with high-energy heavy ions. From these results, it is concluded that the primary ionization rate is a much better parameter than the electronic stopping power for describing the defect production process. This is consistent with the results of our previous study of lattice parameter changes in ion-irradiated EBCO.[6] Successful scaling of the irradiation effects by the primary ionization rate suggests that the atomic displacements are triggered by Coulomb repulsion between primarily ionized atoms.

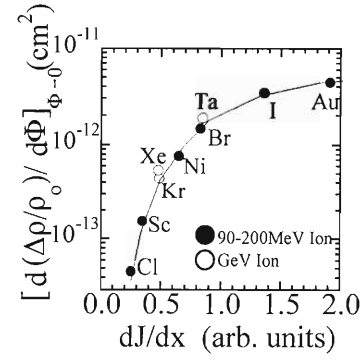

Fig. 1. $[(\Delta\rho/\rho_o)/\Phi]_{\Phi\to 0}$ plotted as a function of the primary ionization rate.

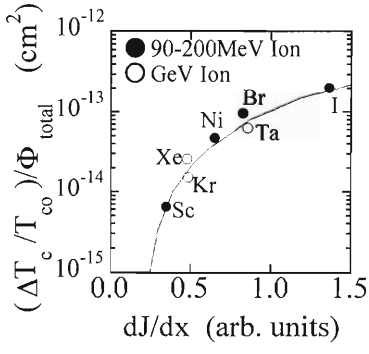

Fig. 2. $(\Delta T_c/T_{co})/\Phi_{total}$ plotted as a function of the primary ionization rate.

References

1) V. Hardy et al.: Nucl. Instrum. Methods Phys. Res. B **54**, 472 (1991).
2) Y. Zhu et al.: Phys. Rev. B **48**, 6436 (1993).
3) H. A. Bethe: Ann. Phys. **5**, 325 (1930).
4) R. L. Fleischer et al.: Phys. Rev. **156**, 353 (1967).
5) N. Ishikawa et al.: RIKEN Accel. Prog. Rep. **32**, 99 (1999).
6) N. Ishikawa et al.: Nucl. Instrum. Methods Phys. Res. B **135**, 184 (1998).

* Faculty of Engineering, Iwate University

In-Beam Mössbauer Study on the Jump Mechanism of Self-Interstitials in Pure Iron

Y. Yoshida,*1 Y. Kobayashi, F. Ambe, E. Yagi, X. Diao, and A. Seeger*2

The jump mechanism of self-interstitials in body-centred cubic metals is still only partially understood. Direct observations of self-interstitials are highly desirable in order to clarify the jump processes on an atomistic scale. In-beam Mössbauer spectroscopy using the ^{56}Fe(d,p)^{57}Fe reaction offers the possibility to study the motion of self-interstitials in iron crystals. By the ^{56}Fe(d,p)^{57}Fe* reaction, ^{57}Fe probes excited to the 14.4 keV level (denoted by ^{57}Fe*, lifetime $\tau_{\text{Mössb}} = 140 \times 10^{-9}$ s) are produced in natural Fe and ejected from their lattice sites approximately in the beam direction with kinetic energies up to about 1 MeV. A certain fraction of the ejected ^{57}Fe* probes end up as self-interstitials in the Fe matrix. Information on the jump vectors of the interstitial ^{57}Fe* may be obtained by measuring the dependence of the Mössbauer spectrum on the crystal orientation.

A single-bunch 8 MeV deuteron beam with repetition period 1.2 μs, pulse width 2 ns, and cross section 3 mm × 10 mm was used to implant the ^{57}Fe* nuclei into an Fe single crystal. The time window was set at 100 to 500 ns, thus suppressing background counts due to short-lived reaction products. The beam current was 75 or 110 nA, corresponding to fluxes of 1.8×10^{12} or 2.8×10^{12} deuterons/(cm^2·s). High-purity Fe single crystals of 5 mm × 12 mm × 1 mm prepared at the Max-Planck-Institut für Metallforschung by strain annealing were chemically etched down to thicknesses of 50 μm and finally purified by anneals for 24 hours at 1123 K under wet H_2 gas and for 24 hours at 923 K under dry H_2 gas. The thickness of the samples guaranteed that virtually no deuterons were stopped in the sample. The orientation of the crystal foil mounted on a sample holder was checked by the Laue method. The deuteron beam direction was 10° from [$\bar{1}$10]. For measurements between 300 and 700 K an infrared lamp heater is used. The vacuum in the chamber was kept at about 10^{-5} Pa throughout the measurements. A parallel-plate avalanche counter (PPAC) detecting the conversion electrons emitted from the Mössbauer absorber is mounted on a Mössbauer transducer. At a detector distance of 0.07 m, typical 14.4 keV γ-ray count rates were about 12 s^{-1} for currents of 75 nA. At a distance of 0.11 m the angular resolution was 5°.

Typical in-beam spectra measured at different temperatures between 150 and 700 K in the [100] direction are shown in Fig. 1. Figure 2 compares the fit parameters, namely (a) total area A, (b) hyperfine field B_{hf}, (c) centre shift δ and (d) full width at half maximum Γ

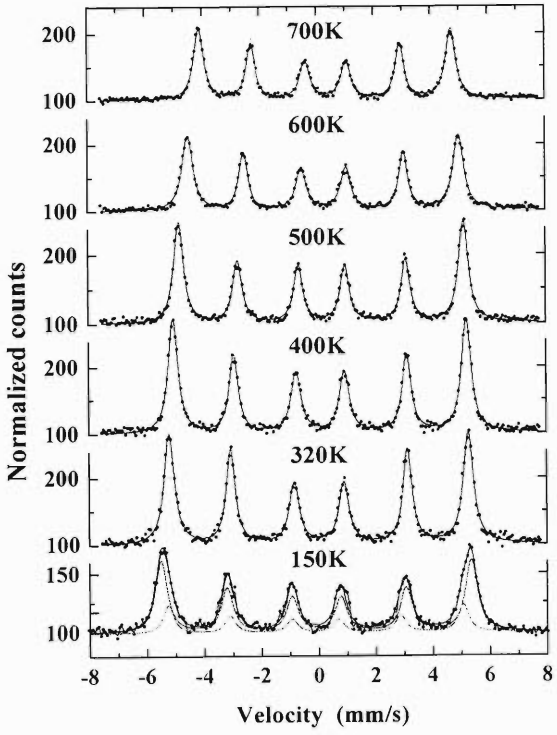

Fig. 1. In-beam Mössbauer spectra of α-Fe between 150 and 700 K measured in [100] at a detector distance of 0.07 m. The 150 K spectrum was obtained in an earlier experiment under otherwise similar conditions.

(full symbols), with those obtained in a conventional laboratory experiment on pure Fe in ultra-high vacuum (open symbols). None of the spectra of Fig. 1 show well-resolved satellite lines. Although at a first glance the spectra appear to be very similar to those of unirradiated Fe, the temperature dependences of the fit parameters are quite different, as may be seen in Fig. 2: (a) The area A decreases much faster than expected from a Debye model with the Debye temperature $\Theta_{\text{D}} = 470$ K of unirradiated Fe. (b) The hyperfine fields B_{hf} are lower than those of unirradiated Fe. (c) Above 550 K the centre shift δ starts deviating from the second-order Doppler shift corresponding to substitutional Fe. (d) The full width Γ of the Mössbauer line at half maximum stays at a constant of about 0.40 mms^{-1}. The spectra at 500 K were also measured along the measuring directions of 0° (= [100]), 14°, 22°, 32° and 45° (= [110]) in the (001) plane. The fit parameters depend strongly on the measuring directions. The facts that B_{hf} and δ do depend on the emission directions and that a peak is superimposed on the gradual decrease of A with increasing θ, show

*1 Shizuoka Institute of Science and Technology
*2 Max-Planck-Institut für Metallforschung, Germany

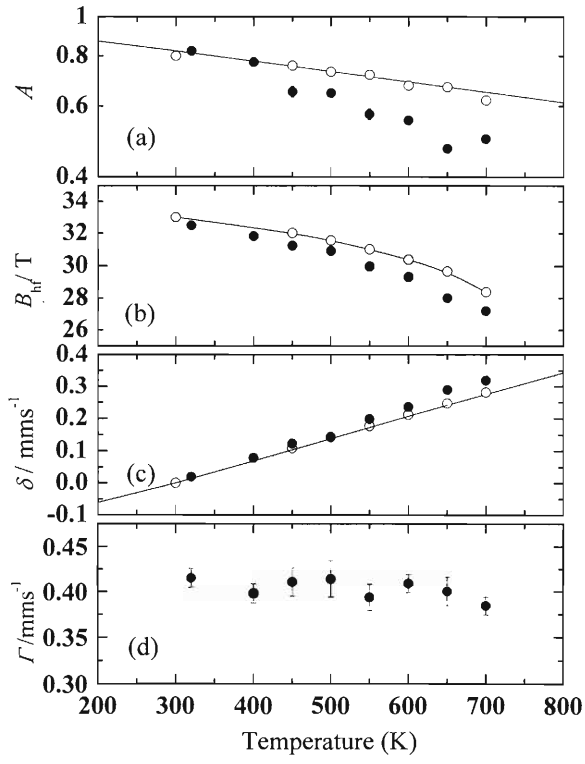

Fig. 2. Temperature dependence of the fit parameters above 300 K; (a) area A, (b) hyperfine field B_{hf}, (c) centre shift δ, and (d) full width at half maximum Γ. Open symbols refer to the control experiment.

that the spectra at elevated temperatures arise from the superposition of several 6-line components. If the spectra consisted of the substitutional Fe component only, the area would show a simple "$\cos\theta$ effect" due to Mössbauer self-absorption, and both the hyperfine field and the centre shift would not change at all. Nevertheless, the data analysis in terms of A, B_{hf}, Γ, and δ was based on one 6-line set only; hence the numerical values must be considered motionally averaged over different contributions to the spectra. The observations will allow us to study the jumps of ^{57}Fe* on non-lattice sites on the time scale 10^{-7} s by comparing the angular dependence of the area with those predicted from different jump models, such as dumb-bell and crowdion models.[1)]

References

1) H. J. Blythe, H. Kronmüller, A. Seeger, and F. Walz: Phys. Stat. Sol. (a) **181**, 233 (2000).

In-Beam Mössbauer Study on Interstitial and Substitutional $^{57}Mn/^{57}Fe$ Jumps in Si

Y. Yoshida,* Y. Kobayashi, K. Hayakawa,* K. Yukihira,* F. Shimura,* A. Yoshida, X. Diao, H. Ogawa, Y. Yano, and F. Ambe

Iron is known to be a fast diffusing impurity in Si, and the diffusion is thought to proceed *via* interstitial sites. However, no direct observation of the jump processes has been achieved at high temperatures. Mössbauer spectroscopy is expected to give us information not only on the lattice sites, but also on the jumping processes of the probe atoms in the material. In order to study the diffusion processes of isolated Fe in Si, there is an experimental difficulty, *i.e.*, an extremely low solubility of ^{57}Fe in Si. For such a low concentration there has not been a measurement particularly with Mössbauer spectroscopy at high temperatures. In order to pursue a Mössbauer experiment with low concentration of 10^{11} Fe/cm^3 in Si wafers, we have developed a new experimental technique of Mössbauer spectroscopy using an on-line isotope separator for projectile nuclear fragments at the RIKEN. This method provides a possibility for direct observation of the diffusion processes of Fe atoms in bulk Si crystals at the atomic scale. The on-line isotope separator (RIPS) produces a radioactive beam of ^{57}Mn, which decays with a half-life of 1.45 min to the 14.4-keV Mössbauer level of ^{57}Fe*. Accordingly, the highly energetic particles with several GeV from the separator can be implanted directly into the depth range of several hundred μm from the surface. Subsequently, the 14.4 keV γ-rays emitted from ^{57}Fe* provide a possibility to measure Mössbauer spectra, which give atomistic information on both the local surrounding and the dynamics of the ^{57}Fe* atoms at the final lattice sites through hyperfine interactions.

Figure 1 shows the Mössbauer spectra of ^{57}Fe* following the decays from ^{57}Mn implanted into FZ-⟨111⟩ Si. The spectra were measured between 350 and 650 K. The spectrum at 350 K can be fitted by two components corresponding to interstitial Fe on the left-hand side ($\delta = -0.76(2)$ mms^{-1}) and substitutional Fe on the right-hand side ($\delta = 0.02(5)$ mms^{-1}). The similar spectra were observed below 300 K in the former experiment on FZ-⟨100⟩Si.[1] The isomer shifts of both interstitial and substitutional lines are in good agreement with those obtained from theoretical calculations.[2] In Fig. 2, the fit parameters are shown as functions of temperature: The total area A (a), the interstitial fraction $F_{\rm int}$ (b) and the centre shifts δ of both components (c). The lines drawn in Fig. 2 (a) and (b) are only for eye-guide. The dotted line in Fig. 2 (a) corresponds to the temperature dependence predicted from a Debye-

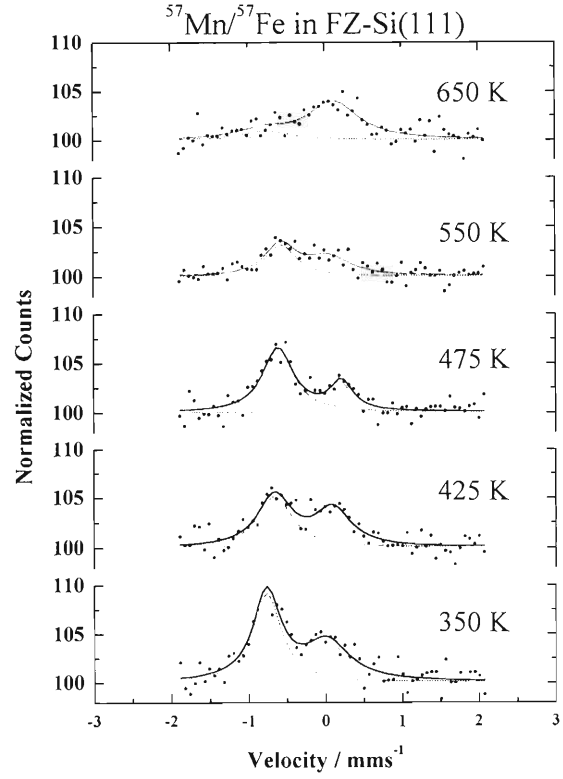

Fig. 1. Mössbauer spectra of $^{57}Mn/^{57}Fe^*$ in FZ-⟨111⟩Si measured between 350 and 650 K.

model with a Debye-temperature of 450 K, which is deduced from the Debye-temperature of Si, 640 K, by taking into account the mass difference. The data points of the total area deviate from the course of the Debye model, which may be related either with an anharmonic effect or with a fast jump process of Fe atoms in Si. The temperature dependence of the centre shift mainly originates from the second-order Doppler shift plotted between the data points in Fig. 2 (c), which is essentially a measure of the mean square velocity of ^{57}Fe* in the Si matrix. The fact that the centre shifts follow the second-order Doppler shift, indicate that both interstitial and substitutional components are well defined up to 600 K. The fraction of the interstitial component, however, starts decreasing at about 500 K, suggesting that the substitutional $^{57}Mn/^{57}Fe^*$ atoms are created by a reaction with other defects. Above 500 K there exist line broadenings on both components, which finally merge into a broad single line at 700 K, *i.e.*, a motional averaging due to a ^{57}Fe* jump process. Using the centre shift value, the average occupation probabilities of Fe atoms at 700 K can be es-

* Shizuoka Institute of Science and Technology

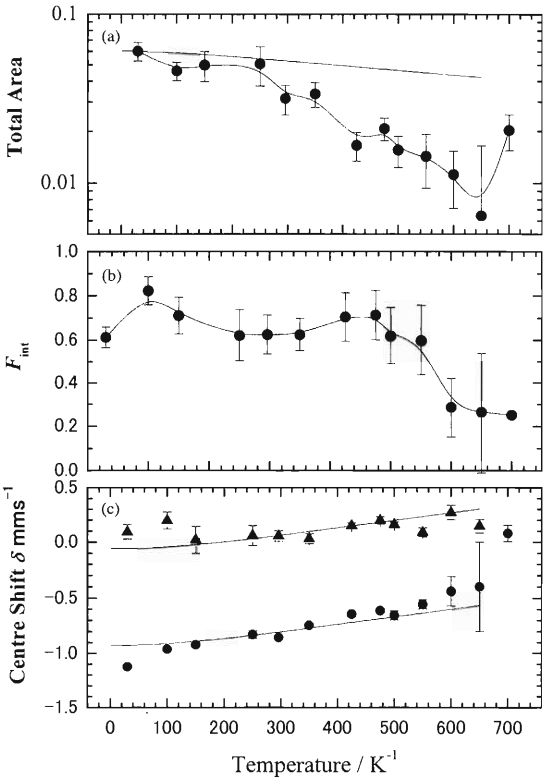

Fig. 2. Temperature dependence of the fit parameters. (a) Total Area A, (b) interstitial fraction $F_{\rm int}$, and (c) centre shift. Circle and triangular symbols refer to the interstitial and substitutional Fe, respectively.

timated to be 30% on the interstitial site and 70% on the substitutional site.

The defect distributions and the related nm-scale structures of the samples, which were used in the present experiments, have been studied using atomic force microscopy (AFM):[3] Two types of the swellings were clearly observed on cleaved Si surfaces, which correspond to defects produced by the slowing-down process of ^{57}Mn probes.

Recently, an ISOLDE group[4] has measured the in-beam Mössbauer spectra of ^{57}Mn/^{57}Fe in Si after the implantation with a rather low energy of 60 keV. They use proton-induced fission at ISOLDE on-line mass separator at CERN. Their results are rather different from the present ones, which may arise from the different implantation energy.

References

1) K. Kobayashi, Y. Yoshida et al.: Hyperfine Interact. **126**, 417 (2000).
2) J. Kübler, A. E. Kumm, H. Overhof et al.: Z. Phys. B **92**, 155 (1993).
3) X. Diao, Y. Yoshida et al.: RIKEN Accel. Prog. Rep. **33**, 94 (2000).
4) G. Weyer: private communication

Depth Profile of Vacancy-Oxygen Pairs in CZ-Si Irradiated with 3.5 GeV-Xe Ions

X. Diao, K. Hayakawa,[*1] F. Shimura,[*1] A. Iwase,[*2] T. Kambara, and Y. Yoshida[*1]

In order to determine the effects of GeV ion irradiation on single-crystal silicon, 3.5 GeV-Xe ion irradiation was performed at room temperature using the RIKEN Ring Cyclotron.[1] For the first time, it was found that vacancy-oxygen pairs are produced in Czochralski-grown (CZ) silicon by GeV ion irradiation. Further studies were carried out and a clear depth profile of vacancy-oxygen pairs along the Xe ion trajectory is described here together with results of the quantitative analysis of defect concentration.

Figure 1 shows the depth profile of IR spectra of the irradiated CZ-Si recorded with a Jasco WS/IR-8000 Micro infrared spectrometer at room temperature. It is known that the two peaks in the spectra, one at $1107\,cm^{-1}$ and another at $830\,cm^{-1}$, represent interstitial oxygen and vacancy-oxygen pairs, respectively. In order to evaluate the concentrations of interstitial oxygen, $[O_i]$, and vacancy-oxygen pairs, [VO], conversion factors of $f_{[O_i]} = 3.14 \times 10^{17}\,cm^{-2}$ for $[O_i]$, and $f_{[VO]} = 6.1 \times 10^{16}\,cm^{-2}$ for [VO] were used according to Bullis[2] and Oates and Newman.[3]

Since each spectrum in the depth profile (Fig. 1) was measured from a very thin irradiated layer at a certain depth ($20\,\mu m$), both VO and interstitial oxygen are assumed distributing homogenously in this layer. Therefore, local concentrations of [VO] and $[O_i]$ along the irradiation depth are obtained based on the spectra. The results are shown in Fig. 2. For comparison, calculated depth dependence, using program TRIM, of energy loss of Xe ions caused by electronic excitation, S_e, and nuclear collision, S_n, is also plotted in Fig. 2. The results show very good agreement among the depth dependences of [VO], $[O_i]$ and the energy

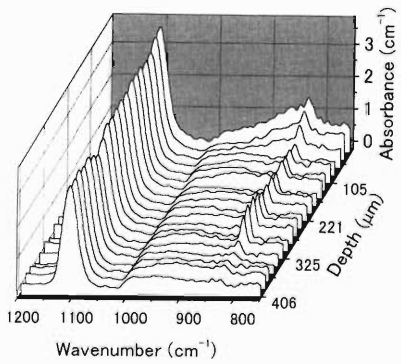

Fig. 1. Infrared absorption spectra of irradiated CZ-Si along the irradiation depth (Fluence = $1.0 \times 10^{13}\,Xe/cm^2$).

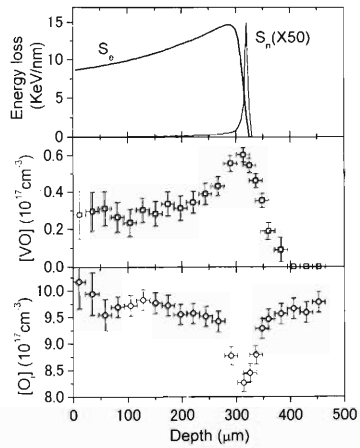

Fig. 2. Depth dependences of [VO] and $[O_i]$ in irradiated CZ-Si (Fluence = $1.0 \times 10^{13}\,Xe/cm^2$), and TRIM-calculated energy loss by electronic excitation, S_e, and nuclear collision, S_n, respectively.

loss of Xe ions. Apparently, the VO complexes were formed through consumption of the original interstitial oxygen; which is clearly observed from the decrease in $[O_i]$ shown in Fig. 2. However the consumption is not quantitatively equivalent to the VO formation, particularly at the depth where [VO] appears at a maximum and $[O_i]$ at a minimum. It may be concluded that, at most, 70% of the lost interstitial oxygen atoms have transferred to VO complexes at such a depth; the remaining 30% probably formed other kinds of defects, which could not be detected in our experiment. An interesting argument arises on the grounds that the interstitial oxygen decreased much more rapidly in the depth region of 275–340 μm than in any other region. This indicates that the undetected defects are mainly distributed in this region. On the other hand, the TRIM calculation predicts that the irradiated Xe ions have completely stopped at the depth of approximately 330 μm, but the VO complexes are still obviously detectable to a depth of 375 μm. We may also conclude from our results that both electronic excitation and nuclear collision contribute to VO formation, each of their contributions being predominant within their own regions.

*1 Shizuoka Institute of Science and Technology
*2 Japan Atomic Energy Research Institute

References

1) X. Diao, Y. Yoshida, K. Hayakawa, F. Shimura, T. Kambara, A. Iwase, and Y. Yano: RIKEN Accel. Prog. Rep. **33**, 90 (2000).
2) W. M. Bullis: in *Oxygen in Silicon*, edited by F. Shimura (Academic Press, 1997), p. 100.
3) A. S. Oates and R. C. Newman: Appl. Phys. Lett. **49**, 262 (1986).

Defects and Their Distribution in Si Produced by GeV-^{57}Mn Irradiation

X. Diao, K. Hayakawa,* Y. Kobayashi, F. Shimura,* and Y. Yoshida*

At the RIKEN RI-beam factory, GeV-ion irradiation is essential for introducing radioactive isotopes into materials for materials science research, and therefore it is very important to understand the defects and their distributions around the isotopes. We reported in the last progress report[1,2] that vacancies and other kinds of defects were produced along ion tracks in silicon upon GeV-heavy-ion irradiation. Although the defects are assumed to be created through both electronic excitation and nuclear collisions, the formation mechanisms of the defects have yet to be understood thus far. In the present experiment, after the irradiation of floating-zone silicon (FZ-Si) with GeV-^{57}Mn which was separated using the RIKEN projectile-fragment separator (RIPS), the defects and their distribution were further studied by X-ray diffraction (XRD) and atomic force microscopy (AFM).

At the E6-beam line of the RIKEN ring cyclotron, an FZ-Si sample was irradiated with ^{57}Mn. The primary energy after the separation was approximately 1 GeV. In order to stop the ions in the sample, a 470-μm-thick Al plate was used as an energy degrader. The irradiation was performed at temperatures between 77 and 3000 K. The total fluence of ^{57}Mn was $5.0 \times 10^{10}/\mathrm{cm}^2$. The incident ion direction was 45° from [110].

After the irradiation, the back of the Si surface was mechanically polished and measured using Cu$K\alpha$ X-rays in reflection geometry by four-axis XRD. The beam was 0.5 mm in diameter. The surface was covered with a 2-mm-wide aluminum aperture as shown in Fig. 1. By shifting the position of the aperture, we were able to obtain XRD patterns at different positions, which may provide information on the lattice defects produced at different depths from the irradiated surface. An obvious split was found at the Si (400) peak, as shown in Fig. 2, for the position corresponding to the depth of 90 μm, *i.e.*, the ion range of ^{57}Mn.

Furthermore, AFM observations were carried out on the same area where the X-ray measurement was performed. In order to obtain a clean and smooth cross section for the observations, the sample was initially cleaved and immediately set into an AFM vacuum chamber. Many hillocks can be observed in the region from the surface to the ion range of approximately 90 μm (Fig. 3). In particular, the number of the hillocks increases around the ion range. Accordingly, the peak shift of (400) observed in the X-ray measurement can be closely related to the lattice defects produced around the ion range. Both experiments are still in progress and the results will be reported elsewhere.

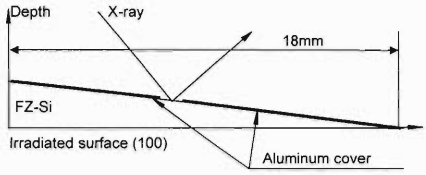

Fig. 1. Schematic view of the experimental arrangement of XRD.

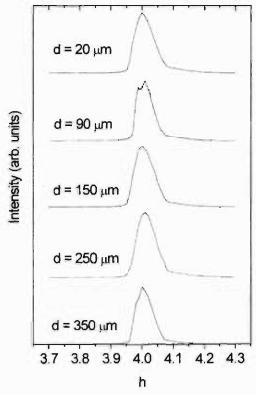

Fig. 2. X-ray diffraction patterns of FZ-Si irradiated with ^{57}Mn. The h-scan was performed from (3.700) to (4.300).

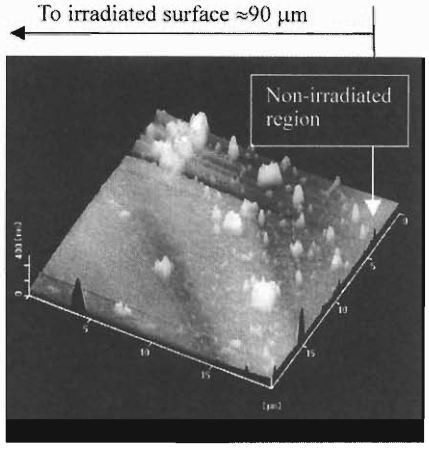

Fig. 3. AFM image observed on a cleaved cross section of FZ-Si irradiated with ^{57}Mn.

References

1) X. Diao, Y. Yoshida, K. Hayakawa, F. Shimura, T. Kambara, A. Iwase, and Y. Yano: RIKEN Accel. Prog. Rep. **33**, 90 (2000).
2) Y. Yoshida, Y. Kobayashi, X. Diao, K. Hayakawa, K. Yukihira, F. Shimura, A. Yoshida, Y. Watanabe, F. Ambe, and Y. Yano: RIKEN Accel. Prog. Rep. **33**, 93 (2000).

* Shizuoka Institute of Science and Technology

Surface Modification on Fe-Ni (31.7at.% Ni) by 3.5 GeV Xe Ion Irradiation

X. Diao, K. Hayakawa,[*1] A. Iwase,[*2] T. Kambara, Y. Yamazaki, and Y. Yoshida[*1]

Irradiation-effect studies of metallic materials began in the early 1950's, stimulated by the advancement of the nuclear industry. The main problems concerned with irradiation effects on metals and alloys are changes in mechanical properties, volume and shape changes, and changes in corrosion resistance. For GeV ion irradiation, only in few materials, *e.g.*, Ni-Zr alloy,[1] have irradiation tracks been found, while in other materials, obvious defects induced by irradiation have never been found. In our experiment, room temperature irradiation on Fe-Ni alloys with 31.7at.% Ni concentration were performed using the RIKEN Ring Cyclotron with 3.5 GeV Xe ions. Off-line observations were carried out using X-ray diffraction (XRD) analysis, scanning electron microscopy (SEM), atomic force microscope (AFM), and Mössbauer spectroscopy.

Three foils of Fe-Ni (31.7at.%) with a thickness of 50.4 μm were overlapped and irradiated successively by 3.5 GeV Xe ions. It is predicted, according to simulation program TRIM, that the Xe ions pass through the first two specimens and stop inside the third one. Therefore, all the measurements were taken on both sides of each specimen except for the Mössbauer spectroscopy measurement, in which the spectra obtained show results from the entire body of each specimen.

SEM results show marked differences before and after irradiation. (1) Morphological structures of the surfaces have been greatly modified by irradiation, except that the back of No. 3 remains roughly the same as that of the original structure, which corresponds to the prediction based on irradiation depth. (2) Bumps and holes are found scattered on the irradiated surfaces and the boundaries of crystal grains are not distinct after irradiation.

Two of the AFM images of the irradiated surface are shown in Fig. 1. The shapes of the bumps are craterlike, indicating that thermal spikes were formed during irradiation. These bumps are distributed heterogeneously on the irradiated surfaces with diameters from 100 nanometers to 2 microns.

XRD results confirm that all three specimens retain their f.c.c. crystal structure after irradiation. However, two obvious modifications on the surfaces have been observed. (1) Crystalline reorientation of lattice directions is observed. The relative ratios among the intensities of diffraction peaks from different lattice indices are significantly changed by the irradiation. The effect appears to be that of recrystallization by heat treatment. (2) Individual peak shifts and splitting are observed after irradiation (Fig. 2). This reveals slight changes in lattice parameters and defects produced by irradiation.

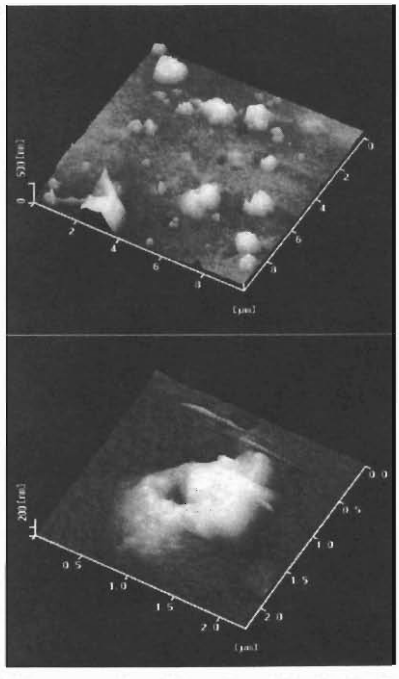

Fig. 1. AFM images of surface of an Fe-Ni (31.7at.%) specimen irradiated with 3.5 GeV Xe ions.

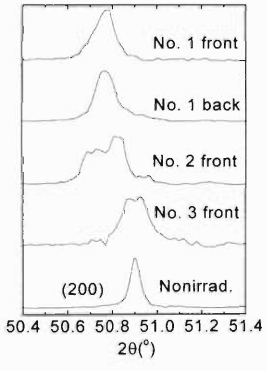

Fig. 2. (200) peaks from XRD patterns of the irradiated and nonirradiated Fe-Ni specimens.

Mössbauer spectra did not show apparent changes as a result of irradiation. The average hyperfine magnetic field has a slight increase compared with that of the nonirradiated Fe-Ni (31.7at.%) alloy.

References

1) A. Barbu, A. Dunlop, A. H. Duparc, G. Jaskierowicz, and N. Lorenzelli: Nucl. Instrum. Methods Phys. Res. B **145**, 354 (1998).

*1 Shizuoka Institute of Science and Technology
*2 Japan Atomic Energy Research Institute

Calibration of a Light Particle Telescope for the ALOS Satellite Using a ^{4}He Beam

H. Matsumoto,* T. Goka,* H. Koshiishi,* and H. Katoh

The Advance Land Observation Satellite (ALOS) will be launched by NASDA into a sun-synchronous orbit in 2003. A light particle telescope (LPT) will be on board this satellite to observe high-energy electrons (0.1–2.9 MeV), protons (1.6–250 MeV), deuterons (7.1–27.9 MeV), tritons (8.3–28.5 MeV), ^{3}He (19.3–102.4 MeV) and ^{4}He (9.1–300 MeV) ions in the inner radiation belt. The LPT consists of a 0.25-mm-thick PIN-type detector for measuring ΔE and four 1.5-mm-thick PIN-type detectors for measuring E. In additions to these thick detectors, a 1.5-mm-thick PIN-type detector is set for use as an anticoincidence detector to eliminate the signals of high-energy particles which penetrate the detector stack. The side of the detector stack is covered by high-Z (tantalum) shielding, which excludes side-penetrating protons up to about 100 MeV. A thin aluminum (0.025 mm thick) window is used to stop photons and charged particles with energy lower than the lower limit of the energy measurement.

Signals from the ΔE and E detectors are pulse-height analyzed simultaneously by fast analog-to-digital converters. A logical analysis of the pulses by the coincidence/anticoincidence circuitry distinguishes electrons from alpha particles and accumulates pulse-height distributions in the memory.

The telescope was tested and calibrated at the E3 target room of the RIKEN ring cyclotron. A ^{4}He beam with an energy of 135 MeV/nucleon was used to measure the fundamental characteristics of the PIN-type detectors used in the telescope and the total performance of the telescope. The energy resolution was tested at four different energies by placing aluminum moderators of different thicknesses before the LPT. In the charge discrimination test, the secondary particles (e, p, d, t, ^{3}He and alpha) produced by the nuclear reactions of the ^{4}He beam with acrylic were measured.

A schematic view of the experimental setup is shown in Fig. 1.

Figure 2 shows typical ΔE-E scatter plots. The separation between different particles is very clear, which makes the assignment of particles ID easy. Two-dimensional contours are applied to the scatter plot for each particle type. An example of such contours for protons is indicated as solid lines enclosing the protons in Fig. 2.

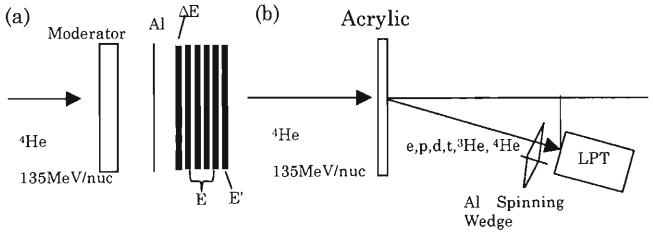

Fig. 1. Schematic view of experimental setup for ^{4}He beam experiment at RIKEN. (a) energy resolution test. (b) charge discrimination test.

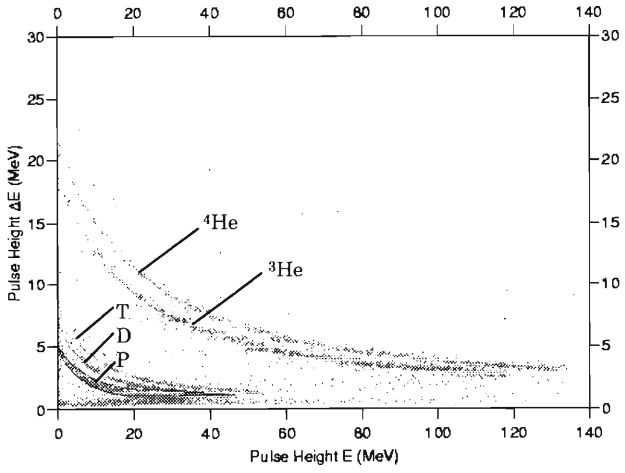

Fig. 2. Two-dimensional scatter plot of 0.25 mm ΔE detector versus 6 mm E-detector pulse heights.

The energy resolution of each individual detector has been confirmed using 5.48 MeV alpha particles from the radioisotope (^{241}Am). The resolution was found to be about 12.64 and 21.23 keV (FWHM) for ΔE and E detectors, respectively.

As a result of the energy resolution test, the peak energy of the pulse-height distribution of each detector comes within 4% from the simulated pulse height, and the full-width at half maximum is also about 4%.

* National Space Development Agency of Japan

Single-Charged Heavy Fragment Ion Production in Fast He^{2+}-C_{60} Collision

Y. Nakai, T. Kambara, A. Itoh,[*1] H. Tsuchida,[*2] and Y. Yamazaki

A number of studies of C_{60} fragmentation have been performed with various excitation probes.[1-7] The distribution of product ions strongly depends on the energy deposit, which is the internal energy of the precursor of fragmentation. In low-energy deposition by electrons, atoms and collisions with the surface, C_{60} emits small neutral clusters in a few micro seconds or a longer time scale after excitation.[2-5] In the latter case, the activation energy and the kinetic energy release associated with C_2 evaporation were estimated. The time-of-flight (TOF) peak profile for each product ion contains information on fragmentation, that is, the kinetic energy release and lifetime. However, a part of such information is often lost due to poor experimental resolution. We have developed a high-resolution TOF mass spectrometer to obtain information on the fragmentation mechanism. Using this spectrometer, we have measured TOF peak profiles in the mass range from C_{50}^+ to C_{58}^+ in the fragmentation by very fast He^{2+} ion impact, as reported in 1999 RIKEN Accelerator Progress Report. We compare them with the simulation of sequential C_2 emission based on the Rice-Ramsperger-Kassel-Marcus (RRKM) formalism. It is shown that the experimental results support high activation energies and a very loose transition state, as discussed in Ref. 8.

Each experimental TOF peak of fullerene-like fragment ions is asymmetric as shown in Fig. 1. The tails on the longer TOF side curve much more gently than those on the shorter TOF side. This asymmetry becomes more obvious with heavier fragment ions. Note that the asymmetric shapes do not arise from the mass difference in C_{60} with a different number of ^{13}C because the peak widths of fragment ions are much wider than those of C_{60} ions. The thermal motion of C_{60} is not the cause the asymmetric peak, either. Roughly, the peak intensities of C_{60-2n}^+ (n = 1 to 5) exponentially decrease with n. This is consistent with other studies of fullerene-like fragment ion production.

We simulated the TOF spectrum by statistical dissociation using two sets of transition states and activation energies. In Fig. 1, we show the simulated TOF spectra. For each set of transition state and activation energies, we determined the internal energy distribution of parent C_{60}^+ ions by assuming the simple exponential functional form so as to reproduce the peak intensity ratios among fullerene-like fragment ions. When the normal transition state and activation energies, 7.1 eV for C_{60}^+, are used, the simulated TOF

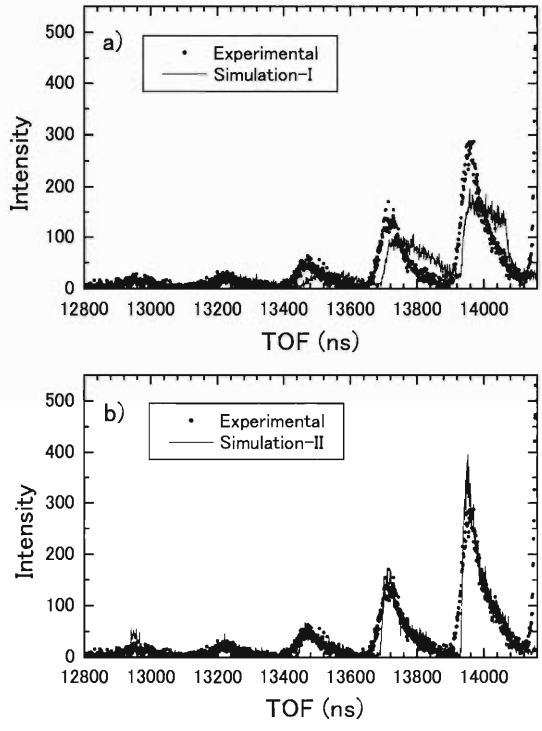

Fig. 1. Comparison of the experimental TOF spectra with simulation results. Solid circles correspond to the experimental results. Solid lines correspond to the simulated results. See text for the difference between (a) and (b).

spectrum does not agree with the experimental TOF spectrum, as shown Fig. 1 (a). However, when the very loose transition state and high activation energy from Ref. 8, 9.5 eV for C_{60}^+ are used, the simulated result agrees with the experimental spectrum fairly well, as shown in Fig. 1 (b). Our results support high activation energies and a very loose transition state and indicate that the dominant process of fullerene-like fragment production is the sequential C_2 emission, even in the collision of C_{60} with fast He^{2+} ion.

References

1) Y. Nakai et al.: J. Phys. B **30**, 3049 (1997).
2) M. Foltin et al.: J. Chem. Phys. **107**, 6246 (1997).
3) P. Weis et al.: J. Chem. Phys. **104**, 6246 (1996).
4) R. Woergoetter et al.: J. Chem. Phys. **101**, 8674 (1994).
5) M. Foltin et al.: J. Chem. Phys. **98**, 9624 (1993).
6) R. K. Yoo et al.: J. Chem. Phys. **96**, 911 (1992).
7) J. Laskin et al.: Chem. Phys. Lett. **242**, 249 (1995).
8) J. Laskin et al.: Int. J. Mass Spectrom. **177**, L9 (1998).

*1 Kyoto University
*2 Nara Women's University

Beam Plasma Experiment at RILAC Facility

A. Sakumi, T. Katayama, M. Nakamura, and Y. Oguri*

In the energy region of hundreds of keV/u, the energy dependence of the stopping power of oxygen ions in a plasma is quite different from that in cold matter.[1,2] Although the experimental investigation has been conducted for a few species, it is not sufficient to explain the physics involved in beam-plasma interaction systematically. With this background, we have experimentally investigated the dependence of the stopping power in the plasma on the atomic number of the projectile with fixed incident energy, ranging from Kr to Bi. These projectiles are available at the CNS (Center for Nuclear Study, Univ. of Tokyo) beam line in the RILAC facility. Figure 1 shows a schematic view of the experimental setup. A beam of 1.4 MeV/u $^{84}Kr^{13+}$ ions is delivered in a single bunch. A dense plasma is produced by irradiating a small lithium hydride (LiH) pellet with a Q-switched Nd-glass laser ($\lambda = 1.054\,\mu$m, 5.5 J and 30 ns (FWHM)). The pellet diameter is approximately 60 μm. The irradiance of the laser on the pellet was 2 TW/cm^2.

The energy loss of ions, which interact with the target plasma, is measured by the time-of-flight (TOF) method. In order to filter the plasma light emission, the TOF detector is operated in the gated mode using a HV pulser. The laser, ion beam and the pulser are synchronized by the digital delay generators.

To model and interpret the measured energy loss precisely, an exact knowledge of the plasma parameters such as temperature and electron density are of fundamental necessity. Plasmas with a temperature of ~10 eV are known to produce a considerable amount of VUV and soft X-ray radiation both as line emission (bound-bound transition) and continuum (free-free transition, free-bound transition).[3] The target plasma should therefore be diagnosed by X-ray and/or VUV spectroscopy. The electron temperature is determined from the slope of the free-bound continuum and the electron density is estimated from the opacity of the resonance line emissions and also from Stark broadening.

The theoretical estimate[1] of the stopping power of the Kr ions as a function of the incident energy is shown in Fig. 2. The target is a plasma with a density of 10^{18} cm^{-3} and a temperature of ~15 eV. We estimate a large enhancement of the stopping power in the plasma compared with that in the cold matter.

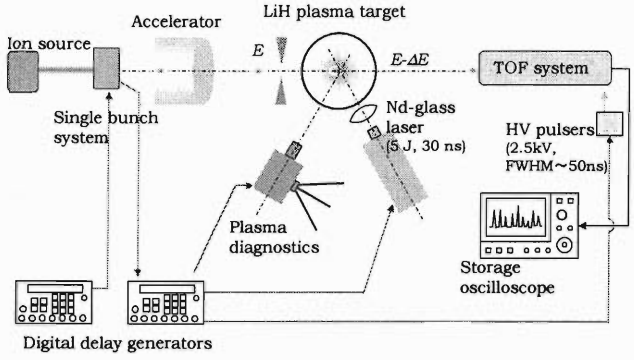

Fig. 1. Schematic view of the experimental setup.

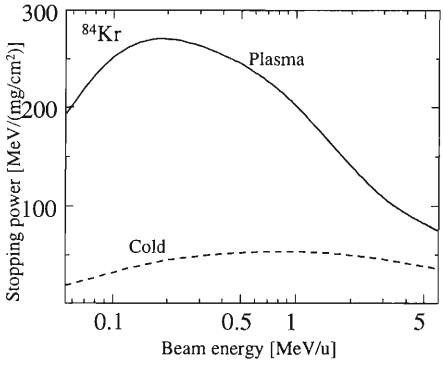

Fig. 2. Stopping power in the LiH plasma estimated for ^{84}Kr projectiles.

References

1) T. Katayama: J. Plasma Fusion Res. **70**, 323 (1994).
2) A. Sakumi et al.: Nucl. Instrum. Methods Phys. Res. A (2001), to be published.
3) P. Nicolosi, E. Jannitti, and G. Tondello: Appl. Phys. B **26**, 117 (1981).

* Research Laboratory for Nuclear Reactor, Tokyo Institute of Technology

Vacancy Formation Energy of Indium Determined by Using the Positron Annihilation Age-Momentum Correlation Technique

N. Suzuki, Y. Nagai,* Y. Itoh, A. Goto, and T. Hyodo

The positron annihilation technique has been used to measure the vacancy formation energy E_v for various metals.

If the material contains only one type of vacancy, E_v is determined through the quantitative analysis of the change in the positron annihilation parameters by assuming the two-state trapping model.[1,2] According to this model, the S-parameter, which is defined as the number of central region of the Doppler-broadened 511 keV annihilation γ-ray energy spectrum divided by the total counts, satisfies,

$$\frac{S - S_f}{S_v - S} \propto \exp\left(-\frac{E_v}{k_B T}\right), \tag{1}$$

where S_f and S_v are the specific S-values corresponding to the positrons in the bulk and in the vacancy, respectively, which are usually assumed to increase linearly with temperature.

Although E_v for indium has been measured by many workers, those values are not mutually consistent but are scattered over 0.39–0.59 (eV).[3] This discrepancy is probably caused by the uncertainty of S_v. Since the positron trapping in indium does not saturate even near the melting temperature, the uncertainty of S_v disturbs the result of the analysis.

In the present study we developed a new method to overcome this difficulty using the positron age-momentum correlation (AMOC) technique. In the present method, the AMOC spectrum $N(p,t)$ is characterized in terms of the time-dependent line-shape parameter $S(t)$, which is defined as

$$S(t) = \frac{\int_{\pm\Delta p} N(p,t)dp}{\int N(p,t)dp}, \tag{2}$$

where Δp is an arbitrarily determined momentum width. Since the lifetime of the trapped positrons is appreciably longer than that in the bulk, S_v can be determined by extrapolation using,

$$S_v = \lim_{t\to\infty} S(t). \tag{3}$$

Thus it is expected that E_v can be determined from the data for the temperatures, where saturation trapping of the positrons does not occur, by fitting the S-parameter using the value of S_v obtained by AMOC.

Figure 1 shows the time-dependent S-parameter $S(t)$ for indium at 413 K. It is seen that $S(t)$ increases gradually with time. It represents the increase in the fraction of the trapped positrons. $S(t)$ almost saturates after about 0.5 ns. This indicates that almost all the positrons in the bulk have annihilated or are trapped in vacancies in this time range. The almost constant value of $S(t)$ in this time range (solid line in Fig. 1) corresponds to S_v.

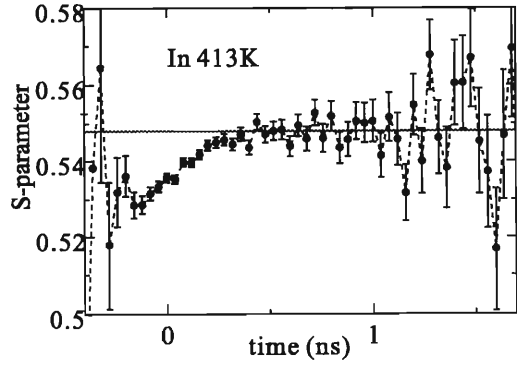

Fig. 1. Time evolution of $S(t)$ for In at 413 K.

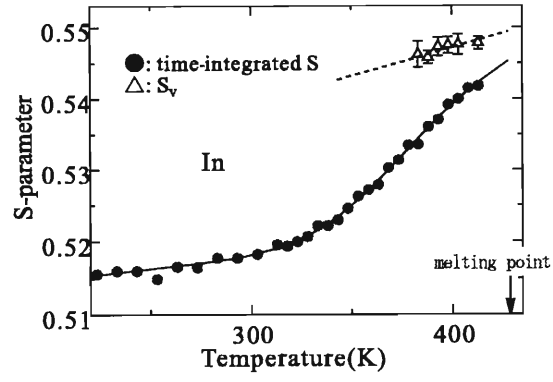

Fig. 2. S-parameter for In plotted against the temperature.

The closed circles in Fig. 2 show the S-parameter obtained by the conventional Doppler broadening measurements and the triangles show the S_v values thus obtained. The solid line and the dashed line represent Eq. (1) and a linear function simultaneously fitted to the data for S and S_v, respectively. The E_v thus determined is 0.48 ± 0.02 (eV).

References

1) B. Bergersen and M. J. Stott: Solid State Commun. **7**, 1203 (1969).
2) D. C. Connors and R. N. West: Phys. Lett. A **30**, 24 (1969).
3) P. Rice-Evans, T. Hlaing, and I. Chaglar: Phys. Lett. A **60**, 368 (1977), and references therein.

* Institute for Material Research, Tohoku University

High-Resolution Soft X-Ray Measurements in 2.3 keV/u $^{15}N^{7+}$ Ions Transmitted through a Capillary

Y. Iwai,[*1] S. Thuriez,[*2] R. Hutton,[*3] Y. Kanai, H. Oyama, K. Ando, H. Masuda,[*4] K. Nishio,[*4] K. Komaki,[*1] and Y. Yamazaki

When a slow highly charged ion approaches a solid surface, the ion resonantly captures target valence electrons into excited states. X-rays emitted from 2.3 keV/u $^{15}N^{7+}$ ions transmitted through a thin Ni microcapillary foil were measured with a high-resolution soft X-ray spectrometer. The microcapillary target was ~1 mm^2 in area with a thickness of ~1 μm and had a multitude of straight holes ~200 nm in diameter. The spectrometer consists of a concave grating and a back-illuminated CCD. For details of the spectrometer, see Ref. 1. Our measurements' energy resolution in FWHM was 3.1 eV at 500 eV, the energy accuracy was 0.5 eV at 500 eV, and the time window, which depends on the width of the slit and the energy of the ion beam, was 37 ps for 2.3 keV/u ions. For this experiment, we used a beam of 2.3 keV/u $^{15}N^{7+}$ ions from a 14.5 GHz Caprice-type electron cyclotron resonance (ECR) ion source at RIKEN.

X-ray spectra were taken at three points downstream of the microcapillary target along the ion beam. The points were immediately downstream of the target ($T = 0$), 0.35 mm downstream ($T = 0.52$ ns), and 2.75 mm downstream ($T = 4.10$ ns). Figure 1 shows the spectrum at the target immediately downstream.

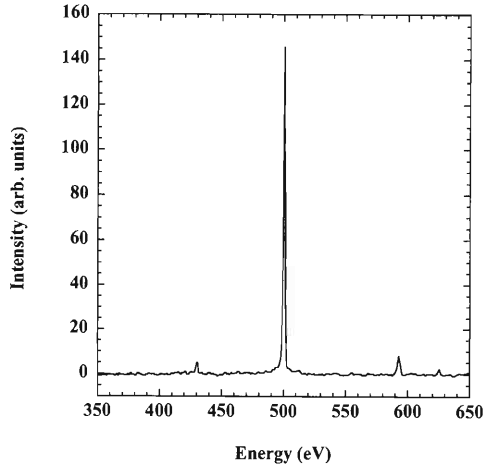

Fig. 1. Spectrum of K X-rays measured with the spectrometer immediately downstream of the target ($T = 0$), for 2.3 keV/u $^{15}N^{7+}$ ions transmitted through a Ni microcapillary. The spectrum has four peaks, at 625.1 ± 0.7 eV, 593.0±0.7 eV, 500.3±0.5 eV, and 430.5±0.4 eV.

*1 Institute of Physics, Graduate School of Arts and Sciences, University of Tokyo
*2 Quantaflow, France
*3 Department of Physics, University of Lund, Sweden
*4 Department of Applied Chemistry, School of Engineering, Tokyo Metropolitan University

Table 1. Electronic core configurations.

Experiment	Ref. data	Configuration	Term
625.1 ± 0.7 eV	625.3 eV[2)]	4p → 1s	$^2P_{3/2} \rightarrow {}^2S_{1/2}$
593.0 ± 0.7 eV	592.9 eV[2)]	3p → 1s	$^2P_{3/2} \rightarrow {}^2S_{1/2}$
500.3 ± 0.5 eV	500.3 eV[2)]	2p → 1s	$^2P_{3/2} \rightarrow {}^2S_{1/2}$
	500.2 eV[2)]	2p → 1s	$^2P_{1/2} \rightarrow {}^2S_{1/2}$
430.5 ± 0.4 eV	430.7 eV[3)]	1s2p → 1s^2	$^1P_1 \rightarrow {}^1S_0$
425.8 ± 0.4 eV	426.3 eV[3)]	1s2p → 1s^2	$^3P_1 \rightarrow {}^1S_0$

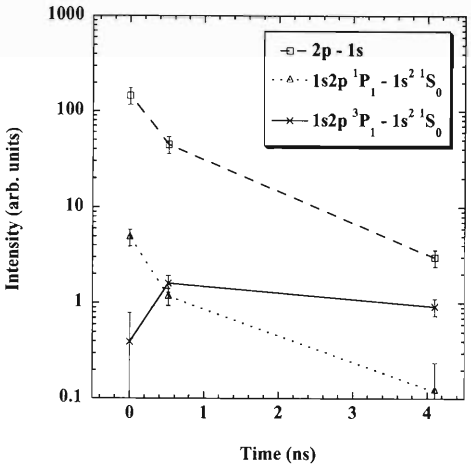

Fig. 2. X-ray decays of the 2p $^2P_{3/2,1/2}$, 1s2p $^1P_1$, and $^3P_1$. The error bars, except for the ^3P first and ^1P last points, are mainly due to the beam stability.

In all, five peaks were observed, at 625.1 ± 0.7 eV, 593.0 ± 0.7 eV, 500.3 ± 0.5 eV, 430.5 ± 0.4 eV, and 425.8 ± 0.4 eV. According to theoretical calculation and reference data, the five peaks are attributed to core electronic transitions of H-like[2)] 4p $^2P_{3/2} \rightarrow$ 1s $^2S_{1/2}$ (625.3 eV), 3p $^2P_{3/2} \rightarrow$ 1s $^2S_{1/2}$ (592.9 eV), 2p $^2P_{3/2,1/2} \rightarrow$ 1s $^2S_{1/2}$ (500.3 eV, 500.2 eV), He-like[3)] 1s2p $^1P_1 \rightarrow$ 1s^2 $^1S_0$ (430.7 eV), and 1s2p $^3P_1 \rightarrow$ 1s^2 $^1S_0$ (426.3 eV). The observed transitions with their core configurations are summarized in Table 1.

Figure 2 shows the X-ray intensities for the 2p $^2P_{3/2,1/2}$, 1s2p $^1P_1$, and $^3P_1$ as a function of the time after the ion leaves the microcapillary target. This result provides information on the decay process related to outer shells.

References

1) Y. Iwai et al.: RIKEN Rev. **31**, 34 (2000).
2) R. L. Kelly: J. Phys. Chem. Ref. Data **16**, Suppl. 1 (1987).
3) W. R. Johnson, D. R. Plante, and J. Sapirstein: Adv. At. Mol. Opt. Phys. **35**, 255 (1995).

Charge State Distribution of Highly Charged Ions Passing through Microcapillaries

D. Dumitriu,[*1] Y. Kanai, Y. Iwai,[*2] Y. Morishita, and Y. Yamazaki

The properties of hollow atoms related with their formation mechanism have been intensively studied by many groups.[1,2] In typical ion-surface experiments the study of the intrinsic nature of hollow atoms in the first generation- hollow atom above the surface (HAA)- is rather difficult, because the time interval between the HAA formation and its arrival at the surface is shorter than its intrinsic lifetime. Beam Capillary Spectroscopy (BCS) is a new and powerful method recently developed[3,4] which allows direct observation of HAA in vacuum by using a thin microcapillary as a target. We have measured the charge state distribution $f(q_f)$ of the ions transmitted through a Ni microcapillary target as a function of the final charge state q_f. 22 keV O^{q+} and N^{q+} ions ($q = 5, 6, 7$) from RIKEN 14.5 GHz ECR ion source were used as incident projectiles. The charge states of the ions transmitted through the target were separated and analyzed by a new charge state analyzer built in Atomic Physics Lab. It consists of two sets of deflectors combined with a ceratron. The deflectors are arranged in a "cascade" type configuration, the beam being deflected on vertical direction in his passing from one deflector towards another, until it reaches the ceratron. The first deflector consists of planar electrodes inclined at 15° (with respect to the beam direction) and the second one is a 128° cylindrical sector type. One of the electrodes for each deflector is grounded. As high voltages up to 20 kV can be applied on both deflectors, the analyzer can in principle separate rather high charge states (13^+ from 14^+) for incident energies in the range of $<$ 25 keV/q. The ceratron is located very close to the exit of the second deflector. A movable Faraday cup located between deflectors is used for adjusting the beam. The Ni microcapillary target (area: 4 mm^2, length: 3.8 μm) is set in front of the analyzer. Results are shown in Fig. 1 and they present the following features: (a) One electron capture ($q_f = q - 1$) dominates in the charge changed fractions, independent of the projectile and initial charge state. (b) Almost neutralized projectiles ($q = 1$) are produced in large quantities and comparable to that for one electron capture. (c) The other charge states fractions ($1 < q_f < q - 1$) are lower than those for $q_f = 1$ and $q_f = q - 1$. (d) For the same initial charge state q, almost similar behavior was found in the final charge state distributions.

The total fraction CF of the all transmitted ions

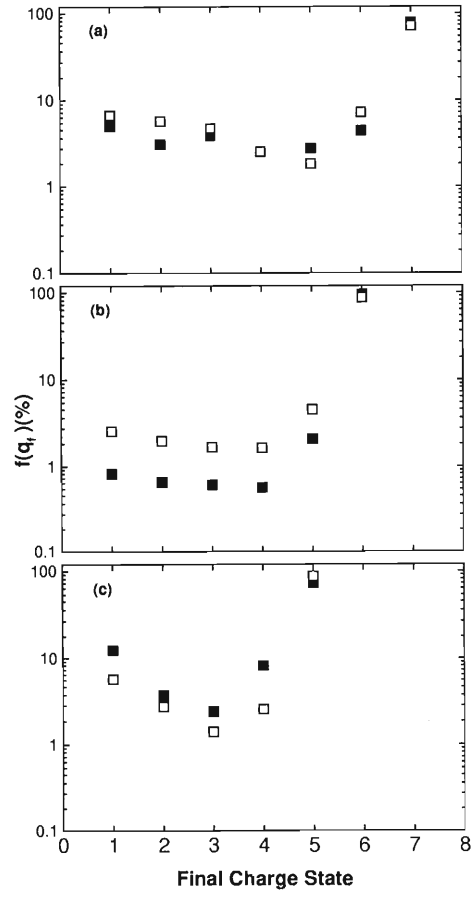

Fig. 1. Charge state distributions $f(q_f)$ of 22 keV O^{q+} (filled symbols) and N^{q+} (open symbols) ions transmitted through the Ni microcapillary target. (a) $q = 7$, (b) $q = 6$, and (c) $q = 5$.

who captured electrons from microcapillary walls can be estimated by CF $= 2d_c/\rho$ with $d_c = (2q)^{1/2}/W$, where d_c is the critical distance for one electron capture, ρ is the nominal radius of the microcapillary and W is the binding energies of the target valence electrons. The CF formula is available under assumptions that the beam is entering parallel with the capillary axis and with the capillaries being of perfect cylindrical shape. The present target has capillaries with radii varying between 50 nm on the backside and 90 nm on the front side. Considering a nominal radius of 50 nm has been chosen the expected CF is ~4.1% for $q = 7$ and decrease to 3.5% for $q = 5$. The total fraction CF measured is larger, probably due to different conditions of the beam and the capillary from the ideal conditions as mentioned above. The present results are in qualitatively agreement with the theoretical one.[5] Also the

*1 Horia Hulubei National Institute for Physics and Nuclear Engineering, Romania
*2 Institute of Physics, Graduate School of Arts and Sciences, University of Tokyo

present measurements for N^{6+} ion beam can be qualitatively compared with a previous measurement with N^{6+} (28 keV) incident projectile on a Ni microcapillary target[6] with a different nominal radius (250 nm) and length (1.5 μm). We found an overall agreement for final charge states distribution pattern in both cases.

In conclusion, the transmitted charge state distribution related to hollow ion formation has been studied for two projectiles O and N, with the same total energy 22 keV and charge states from 5+ to 7+. The transmitted charge state fractions depend both on the initial projectile charge state as well as on the nature of the projectile. We are planning to measure K X-rays emitted by the transmitted ions in coincidence with the final charge states as a next step.

References

1) J. P. Briand et al.: Phys. Rev. Lett. **65**, 159 (1990).
2) A. Arnau et al.: Surf. Sci. Rep. **27**, 113 (1997).
3) Y. Yamazaki et al.: J. Phys. Soc. Jpn. **65**, 1199 (1996).
4) Y. Yamazaki: Int. J. Mass Spectrom. **192**, 437 (1999).
5) K. Tőkési et al.: Nucl. Instrum. Methods Phys. Res. B **164/165**, 504 (2000).
6) S. Ninomiya et al.: Phys. Rev. Lett. **78**, 4557 (1997).

Angular Distribution Measurements of Electron Capture Processes for X^{4+}(X=C, N, O)-He Collisions at Energy Region below 40 eV/u

M. Hoshino,* M. Kitajima,* Y. Nakai, Y. Kanai, H. Tanaka,* and Y. Yamazaki

The study of multi-electron capture processes in highly charged ion (HCI)-atom collisions has been the subject of a number of experimental and theoretical investigations. Angular differential cross-section measurements of very slow collisions are of great interest because the angular differential cross-sections become more sensitive to the shapes of the interaction potential curves as the collision energy decreases. However, since difficulties arise in producing very slow and well-collimated HCI beam below 100 eV/u, experimental studies of very slow collisions between HCI and atoms have been limited. Recently, we have developed a crossed-beam experimental apparatus for angle-resolved energy gain spectroscopy of very slow collisions. We utilize the ion beam from the 14.5 GHz CAPRICE electron cyclotron resonance (ECR) ion source at RIKEN.[1] Here, we present angular distribution measurements of electron capture processes for X^{4+}(X=C, N, O)-He collision below 40 eV/u.

Figure 1 (a) shows the typical energy gain spectrum of C^{4+}-He collision at 23 eV/u and 4 deg. An intense peak due to the double-electron capture process $C^{4+}(1s^2) + He \rightarrow C^{2+}(1s^22s^2) + He^{2+}$ is seen in Fig. 1 (a). The single-electron capture peak was too weak to be resolved from the background in the present measurement. Both single- and double-electron capture processes are seen in the energy gain spectra of a N^{4+}-He collision at 32 eV/u shown in Fig. 1 (b). The most intense single-electron capture peak corresponds to the capture into the N^{3+} ($2p^2$) state, which is the transfer excitation process. Intense peaks due to the capture into the N^{2+} ($2s2p^2$) state is seen for the double-electron capture in the N^{4+}-He collision. We have also measured the energy gain spectra of an O^{4+}-He collision at 20 eV/u. The dominant single-electron capture is the capture into the O^{3+} ($2p^3$) states, which is the transfer excitation process. The dominant double-electron capture peaks are observed for the capture into the O^{2+} ($2s2p^3$) state.

Figure 2 represents the angular distribution of C^{2+} ions produced in the $C^{4+}(1s^2) + He \rightarrow C^{2+}(1s^22s^2) + He^{2+}$ at collision energy of 39 and 23 eV/u. We have calculated differential cross sections for $C^{4+}(1s^2) + He \rightarrow C^{2+}(1s^22s^2) + He^{2+}$ with the close-coupling method using the potential curves of Boyd *et al.*[2] at 39 and 23 eV/u. The calculated results, convoluted with experimental angular resolutions of 1.0 and 1.8 deg. for 39 and 23 eV/u, respectively, are also shown in Fig. 2.

* Department of Physics, Sophia University

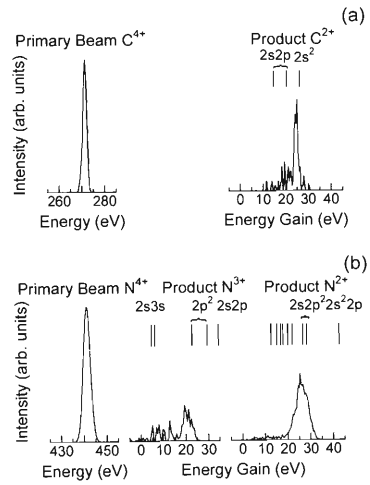

Fig. 1. (a) Energy gain spectrum of C^{4+}-He collision at 23 eV/u and 4 deg. (b) Energy gain spectrum of N^{4+}-He collision at 32 eV/u and 0 deg.

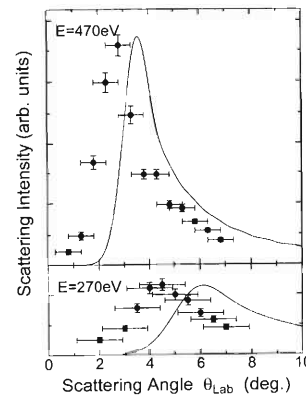

Fig. 2. Angular distribution of C^{2+} ions produced in the $C^{4+}(1s^2) + He \rightarrow C^{2+}(1s^22s^2) + He^{2+}$ at collision energies of 39 and 23 eV/u (•). Calculated differential cross sections convoluted with the experimental angular resolution are shown together (—).

Clear differences in the peak positions between experimental and calculated results are seen for both energies. The peak positions of the calculated results are shifted to larger angles compared to the present experimental results. Much more accurate potential curves are required.

References

1) M. Kitajima, Y. Nakai, Y. Kanai, Y. Yamazaki, and Y. Itoh: Phys. Scr. T **80**, 377 (1999).
2) R. Boyd et al.: J. Chem. Phys. **106**, 6548 (1997).

X-Ray Spectroscopy of Highly Charged Ions Using Superconducting Tunnel Junction Detector

T. Ikeda, Y. Iwai,* Y. Kanai, H. Kato, K. Kawai, H. Miyasaka, Y. Morishita, Y. Nakai, T. Oku, C. Otani, H. Oyama, H. Sato, H. M. Shimizu, Y. Takizawa, H. Watanabe, and Y. Yamazaki

A superconducting tunnel junction (STJ) detector is a newly developed X-ray detector which has merits of single-photon detection and high energy-resolution. For the X-ray energy region, crystal spectrometers and semiconductor-based detectors are widely available. A crystal spectrometer has high energy-resolution but low acceptance. On the other hand, a semiconductor-based detector has a large acceptance and provides timing information, but the energy-resolution is not as good. Measurements using the STJ detectors provide not only high energy-resolution, but also timing information and high counting-rates. The principle of the photon detection in the STJ is based on the excitation of quasiparticles due to the breaking of Cooper pairs in a superconductor. The dissociation energy of one Cooper pair is on the order of meV. However, a semiconductor-based detector needs an excitation energy of ~3 eV for one electron-hole pair. Therefore, the small dissociation energy of the STJ allows more precise energy-dispersive spectroscopy. Moreover, the STJ has a sensitivity for γ-ray, UV, visible, IR and neutral- and charged-particles.

The STJ fabricated at RIKEN has a layer structure of Nb (150 nm thick, lower electrode)/Al (50 nm)/AlO_x/Al (50 nm)/Nb (150 nm, upper electrode). Its sensitive region has an area of $100 \times 100\,\mu m^2$. The STJ characteristics and the fabrication process have been described elsewhere.[1] During measurement, the STJ is cooled to less than 0.4 K and voltage-biased with a magnetic field of 50–300 Gauss to suppress the dc-Josephson current. The output signals are amplified by either a superconducting quantum interference device (SQUID) amplifier or a charge-sensitive amplifier. Our STJ was characterized with 5.9 keV X-rays from an RI source, and energy resolution of 41 eV was achieved.

The STJ was used in an experiment involving collision between highly charged ions (HCI) and a solid target with a Caprice-type ECR ion source at RIKEN. Ions extracted from the ion source were collimated by a four-jaw slit to a size of $6 \times 6\,mm^2$, and then led to a target chamber. The ions were Ne^{9+}, O^{7+} and Ar^{14+} accelerated by 10 kV. The intensity was between 50 and 100 nA. The target was a stainless steel with a flat surface at room temperature, the angle between the target surface and the beam being 45°. X-rays emitted in a direction perpendicular to the beam were detected by the STJ. The distance between the beam center and the STJ surface was 24 mm. Since the STJ must be cooled to about 0.38 K, it was shielded by two 100-nm-thick Al films from thermal radiation by the target. In this measurement, a charge-sensitive amplifier was employed. The beam intensity was controlled so that the counting rate was between 100 and 500 counts per second. Figure 1 shows a raw spectrum of the K_α X-rays from Ne^{9+} ions. In the plot, there are two peaks of X-rays corresponding to the photon absorption in the upper and lower electrodes and a pulsar peak for the evaluation of electronic noise. The observed peak broadening due to the electronic noise of the readout system corresponds to 20–30 eV. The photon absorption in different electrodes can be easily identified by a SQUID amplifier.[2] Under our collision conditions, the K_α peak consists of the satellite X-rays from ions related to different numbers of L-shell holes. For Ne ions, the energy of the satellite X-rays ranged from 840 to 890 eV. The Ne K_α peak shown in Fig. 1 has an asymmetric shape with a tail on the higher-energy side. This can be attributed to the satellite X-rays. The shape is consistent with a high-resolution measurement by Andrä *et al.*[3]

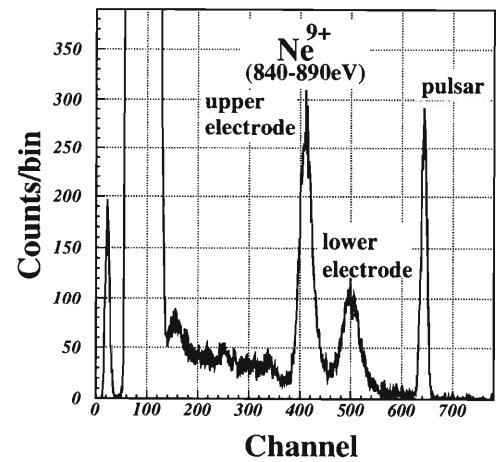

Fig. 1. Energy spectrum of the K_α X-rays from Ne^{9+} ions.

References
1) H. Sato et al.: Jpn. J. Appl. Phys. **39**, 5090 (2000).
2) T. Ikeda et al.: IEEE Trans. Appl. Supercond., in press.
3) H. J. Andrä et al.: Z. Phys. D **21**, S135 (1991).

* Institute of Physics, Graduate School of Arts and Sciences, University of Tokyo

Measurement of Charge State Distributions and Scattering Angular Distributions of 5 keV/q N^{q+} Ions Transmitted through Microcapillaries for Multiple Electron Transfer Study

D. Murakoshi,[*1] N. Okabayashi,[*1] Y. Iwai,[*1] Y. Morishita, H. A. Torii,[*1] Y. Kanai, K. Nishio,[*2] H. Masuda,[*2] K. Komaki,[*1] and Y. Yamazaki

We have been studying interactions between ions and metallic surfaces, using a microcapillary foil as a target. As a slow highly charged ion approaches a metallic surface, target electrons are transferred to the ions when the ions are still far above the surface. Electrons are transferred into highly excited states while the inner shells of the projectile are kept open. Such an atom (ion) with many electrons in highly excited transient states and many inner shell vacancies is called a "Hollow Atom" above the surface. Various experiments so far have proven that the Classical Over Barrier model (COBm) reproduces various aspects of the observations. However, even if hollow atoms are generated above the surface, they hit the target surface immediately after their formation as long as the surface of the target is flat. Ninomiya *et al.*[1] suggested that a micro capillary target enables the extraction of hollow atoms generated above the surface into vacuum, and showed that we can obtain important information on multiple electron capture processes of highly charged ions.

Recently, we measured the final charge state distributions for 800 eV/q Xe^{q+} ($3 \leq q \leq 9$) ions transmitted through Ni microcapillaries,[2] which were well reproduced with the Monte Carlo simulations taking into account Auger cascading processes of hollow atoms (ions).[3]

We also measured scattering angular distributions for 800 eV/q Xe^{6+} incident ions, which are shown in Fig. 1. As is seen in the figure, the angular divergence gets larger as the final charge state increases, which is qualitatively different from a naive expectation. The COBm indicates that the critical distance d_c where electron transfer occurs between an ion and a metallic surface is given by $\sim \sqrt{2q}/W$, where q is the incident charge state and W is the work function of the target metal. In other words, the charge state gets lower as the distance of the ion to the surface gets smaller, which is supported by the same Monte Carlo simulation referred to above.

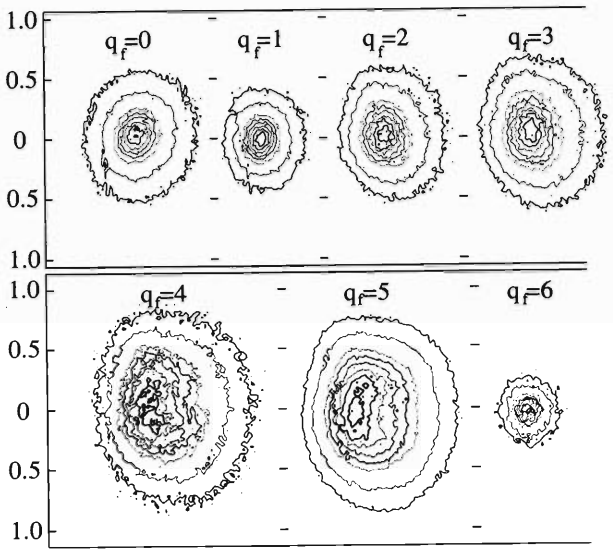

Fig. 1. Contour plots of scattering angular distributions for Xe^{6+} transmitted through Ni microcapillaries, where scattering angles are represented in degree.

To understand this puzzling tendency of the scattering angle, we are now preparing a new experiment on 5 keV/q N^{q+} at RIKEN 14.5 GHz Caprice, employing the new capillary target with significantly straighter pores.

References

1) S. Ninomiya, Y. Yamazaki, F. Koike, H. Masuda, T. Azuma, K. Komaki, K. Kuroki, and M. Sekiguchi: Phys. Rev. Lett. **78**, 4557 (1997).
2) D. Murakoshi, N. Okabayashi, Y. Iwai, Y. Morishita, H. A. Torii, K. Komaki, and Y. Yamazaki: Prog. Rep. Atom. Coll. Res. Jpn., to be published.
3) K. Tokesi, L. Wirtz, C. Lemell, and J. Burgdorfer: Phys. Rev. A **61**, 020901R (2000).

*1 Institute of Physics, University of Tokyo
*2 Tokyo Metropolitan University

Behavior of Ions in Superfluid Helium

R. Saneto,[*1] Y. Fukuyama, Y. Matsuo, and Q. Hui[*2]

We are currently developing a method to trap ion beams in superfluid helium (He II) and to study spectroscopic properties of atoms with short-lived radioactive nuclei, which are produced at accelerator facilities. He II is expected to be a suitable medium for trapping ions because it can instantly stop the ion beams with high kinetic energy.[1] Then, various methods of spectroscopy can be applied for trapped ions and atoms in He II because it is transparent in the wide wavelength region from radio frequency to vacuum ultra violet. Microwave detection combined with the optical pumping method will enable measurement of hyperfine splitting[2,3] of alkali and alkali-earth atoms and ions.

The experiments of laser spectroscopy in He II have been carried out on many kinds of impurity, mainly neutral atoms. However, only a few kinds of ion such as Ba^+ and Yb^+ have been observed thus far.[4,5] It is also necessary to study the physical properties of ions in He II, such as their optical transitions and mobilities, in order to develop a method for observing the unstable nuclei in He II. Recently, we measured the ion current in He II to study the behavior of ions.

The experimental setup is illustrated in Fig. 1. A metal Dewar with quartz windows is filled with He II. The pressure of the He gas in the Dewar is about 6 Torr, which corresponds to that of liquid He at a temperature of about 1.6 K. A quartz cell is placed above the liquid surface and the cell itself is also filled with He II by transferring liquid He utilizing the fountain effect of He II. The liquid surface in the cell is maintained at a full level. A metal sample is held about 1 cm above the quartz cell. An ablation laser beam (532 nm, approximately 20 mJ/pulse) is focused onto the sample through one of the windows. Neutral atoms and atomic ions are produced by laser ablation. Only positively charged ions are injected into He II by the electric field generated at three electrodes that are set in the quartz cell in such a way that the upper electrode stays just 2 mm below the liquid surface. A high voltage is applied to the upper electrode (grid) and a low voltage is applied to the middle one (Frisch grid). The lower collector is connected to the digital oscilloscope through the current amplifier. The distance between the grid and the Frisch grid is 4 mm, whereas that of the Frisch grid and the collector is 1 mm. The ion current detected at the collector is amplified by a factor of 10^9 and monitored with the digital oscilloscope.

Figure 2 shows the observed ion currents of Sr^+ in He II at various electric fields between the grid and the Frisch grid. Laser ablation is performed at time zero

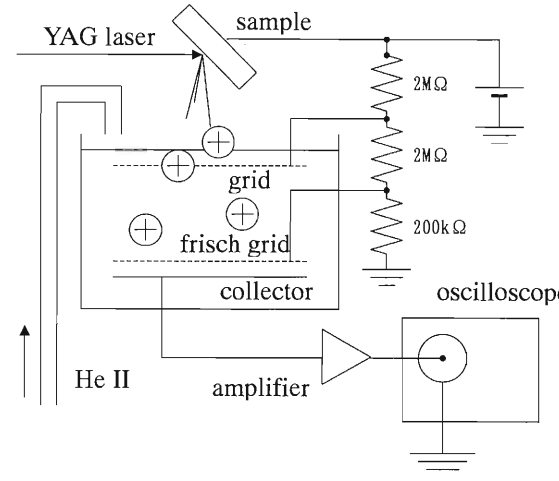

Fig. 1. Experimental setup.

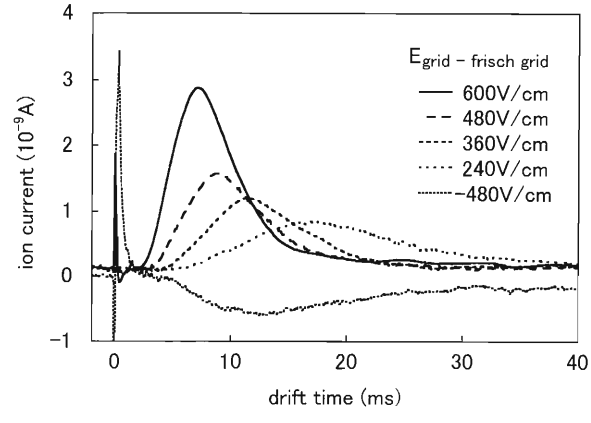

Fig. 2. Observed ion currents.

which is indicated by the current flowing into the Frisch grid. By increasing the applied voltage, the peak position of the ion current appears faster and the width of drift time becomes narrower; the peak intensity of the current becomes stronger, as well. It is estimated from this result that about 10^8 Sr^+ ions, which is much larger than the number required for optical detection (10^4), are introduced into He II. We are now attempting to detect the laser-induced fluorescence (LIF) spectrum of Ba^+ and Sr^+. We are also preparing a new cryostat for on-line spectroscopic measurement of unstable nuclei in He II.

*1 Keio University
*2 University of Electro-Communications

References

1) N. Takahashi et al.: Physica B **284/288**, 89 (2000).
2) T. Kinoshita et al.: Phys. Rev. B **49**, 3648 (1994).
3) T. Yabuzaki et al.: Z. Phys. B **98**, 367 (1995).
4) H. J. Reyher et al.: Phys. Lett. **115**, 238 (1986).
5) Y. Moriwaki: Eur. Phys. J. D, **13**, 11 (2001).

Development of New Technique to Measure Isotope Shift and Hyperfine Shift Using Atomic Beam Deflector

Y. Fukuyama, Y. Matsuo, and I. Tanihata

Now we can create the wide variety of RI atoms from the stable region to near the dripline. There are many atoms whose isotope shift and hyperfine shift have not been measured systematically. So far, most of the isotope shift and hyperfine shift measurements were carried out using mainly collinear laser spectroscopy. For the RI atoms far from stability, this method is not sensitive enough because the laser induced fluorescence whose detection efficiency is not so high is used as detection method. It is required to develop highly efficient way for laser spectroscopic study of RI atoms. In recent years, techniques of laser cooling and trapping neutral atoms have been developed rapidly. They provide us a possibility to manipulate the motion of atoms with laser radiation pressure force. Inspired by these techniques we are developing the atomic beam deflector,[1] which deflect the RI atoms by radiation pressure force only when the frequency of laser beam is nearly resonant to the electric transition of the RI atoms. Deflected atoms reach the forward detector (det.2, see Fig. 1), subsequently beta rays are detected. Since the quantum efficiency of scintillator to detect a beta ray is much higher than that of photomultiplier tube to detect a photon, this system will provide much higher sensitivity to measure the isotope shift and hyperfine shift of RI atoms far from stability.

Figure 1 shows schematic diagram of atomic beam deflector. The atomic beam deflector consists of two pairs of cylindrical mirrors. A concave mirror with $R = 1050$ mm and a convex mirror with $R = 1000$ mm are placed along the concentric circle. Both mirrors have lengths of 200 mm. The laser beam first hit the edge of the convex mirror and travel between two mirrors as shown in Fig. 1. When the incident angle of laser beam is sufficiently small, wavefronts of laser beam are approximately parallel to the surface of cylindrical mirrors. The RI atoms are introduced into atomic beam deflector parallel to the wavefront of laser beam and the frequency of laser is tuned slightly red from the resonance. Atoms absorb the laser light from both side. Atoms travel along the curved trajectory parallel to the wavefront. For the atoms, which escape from the curved trajectory, the absorption rate of the laser light which has the direction to push back atoms to the trajectory is higher than that of the laser light of the opposite direction because of Doppler effect. Atoms move approximately along the wavefront of laser beam after the atomic velocity becomes parallel to the wavefront. The laser frequency should be swept sufficiently slow compared to the beta decay time of RI atoms. It is possible to apply this technique to RI atoms which have the beta decay time less than few seconds.

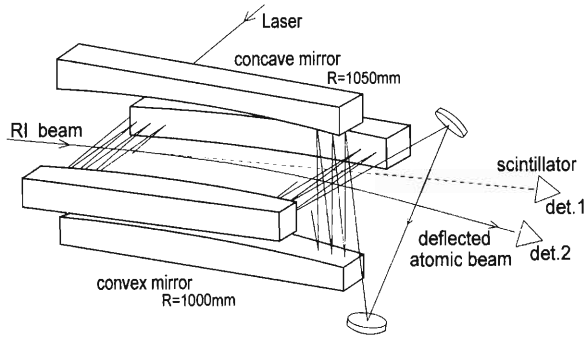

Fig. 1. Illustration of atomic beam deflector.

The minimum radius R of curvature for the atom to follow the wavefront determined from the ratio of momentum transfer rate between atoms and photons $h/2\lambda\tau_s$ and the longitudinal momentum mv of the atom to be $R = 2mv^2\tau_s\lambda/h$, where m and v are the mass and velocity of atom, τ_s the spontaneous lifetime of the upper state and λ the wavelength of the transition. Our primary goal is to measure the isotope shift and hyperfine shift for lithium and magnesium. For lithium atom which has 0.1 eV kinetic energy and incident angular divergence of 0.1 rad, the efficiency of deflection is calculated to be almost 100% and deflected angle is about 0.2 rad. When the distance from the end of deflector to the detector is not less than 150 mm, deflected atomic beam and non-deflected atomic beam will be separated completely. With this method using one to three laser frequencies it is possible to measure 30 kinds of atoms. These atoms are mainly alkaline, alkaline earth, and metastable rare gas atoms which have strong S-P electric transition with closed cycle. To combine this deflector with laser-laser or laser-microwave double resonance, it is possible to obtain the accuracy of the isotope shift and hyperfine shift in frequency dimension determined by the width of laser or microwave spectrum.

In recent years Wada *et al.* are developing the RF ion-guide system[2] to provide low kinetic energy RI atomic beams. We suppose this deflector to be used with the RF ion-guide system. This deflector is expected to be a powerful tool to measure the isotope shift and hyperfine shift of RI atoms which has low kinetic energy and low flux density. Because the efficiency of particle detection is usually much higher than that of optical detection, in ideal case the efficiency of

particle detection is unity. We are currently preparing a CW-laser system for the atomic beam deflector.

References

1) F. Shimizu et al.: Chem. Phys. **145**, 327 (1990).
2) T. Wada et al.: RIKEN Accel. Prog. Rep. **33**, 180 (2000).

Development of a High-Intensity Slow-Positron Source for Cooling Highly Charged Ions II

N. Oshima, T. M. Kojima, D. Dumitriu, A. Mohri, H. Oyama,
T. Kambara, Y. Kanai, Y. Nakai, M. Wada, and Y. Yamazaki

A technique for cooling highly charged ions (HCIs) using positron plasmas is under study, where a large number of positrons must be stored in an electromagnetic trap.[1] In order to capture positrons at a high accumulation rate, a high-intensity slow positron-source is under construction.[2]

Slow positrons are produced by moderation of fast positrons emitted from a β^+ decay radioisotope. The energy spread of slow positrons so prepared is typically a few eV. In our study, a combination of a ^{22}Na radioactive source (1.5 GBq) and a solid neon (Ne) moderator is used.[2]

Figure 1 shows a schematic diagram of the positron source assembly. An encapsulated ^{22}Na positron source is mounted on a cold finger of a refrigerator and is cooled to 5 K so that a rare-gas solid moderator is formed on the front surface of the source. The assembly is electrically floated to accelerate slow positrons to an energy of 0–200 eV.

A schematic drawing of the positron beamline is shown in Fig. 2. The solenoid and coils installed along the beamline yield an axial magnetic field of about 10 mT and guide the slow positrons. The positron beam profile is observed using a multichannel plate (MCP). A scintillation counter is prepared close to the MCP to evaluate the positron beam intensity by measuring the count rate of positron annihilation gamma rays. Since the downstream of the beamline after the solenoid guides not only positrons but also HCIs, a lens and a profile monitor for HCIs are also installed.

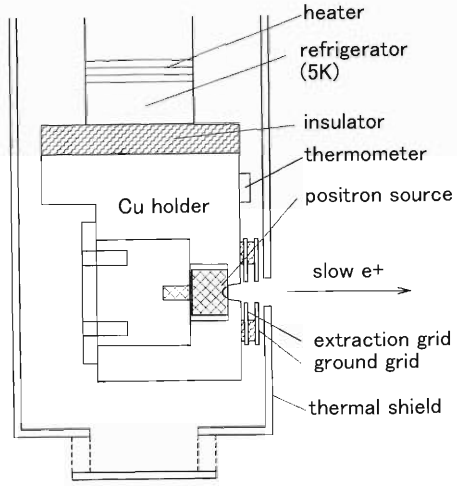

Fig. 1. Schematic diagram of the slow-positron source assembly.

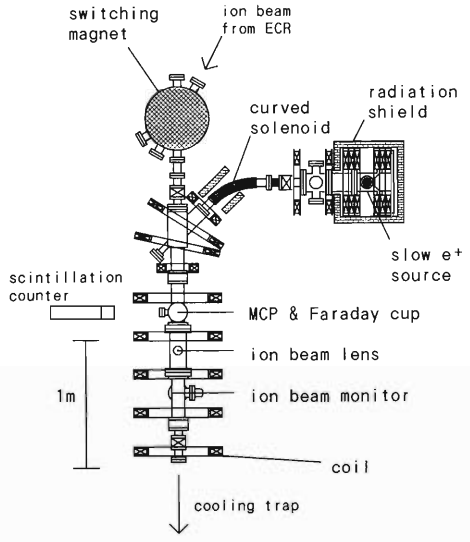

Fig. 2. The slow-positron beam line.

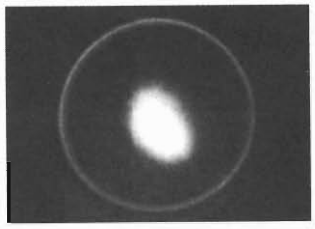

Fig. 3. Positron beam profile observed using the MCP. The MCP active diameter (a ring diameter) is 10 mm.

The profile of the extracted positron beam observed using the MCP is shown in Fig. 3. The beam diameter was approximately 5 mm. The beam intensity was 1.5×10^6/sec and the efficiency of the moderator was determined to be 1.0×10^{-3}, which is defined by the ratio of the number of the extracted slow positrons to the number of β^+ decays of the radioisotope. This moderation efficiency is still 20% of that reported in Ref. 3. Further development of the slow positron-source is underway.

References

1) N. Oshima et al.: Proc. Int. Workshop on Advanced Techniques of Positron Beam Generation and Control, Wako (RIKEN, 1998), p. 64.
2) N. Oshima et al.: RIKEN Accel. Prog. Rep. **33**, 255 (2000).
3) R. G. Greaves et al.: Can. J. Phys. **74**, 445 (1996).

Stable, High-Efficiency Positron Moderator with Tungsten Mesh

Y. Nagashima,[*1] T. Kurihara,[*2] F. Saito, Y. Itoh, A. Goto, and T. Hyodo[*1]

The development of high-efficiency stable moderators has been an essential factor in the development of slow positron beams. The efficiency ϵ of a moderator is defined as the ratio of the number of extracted slow positrons per unit time to the source activity. The highest efficiency has been accomplished by using inert gas solids as the moderation material.[1,2] The value of ϵ for solid neon moderator is reported to be as high as 7×10^{-3}. However, it is not easy to keep such a high efficiency stably for a long time because this moderator requires a cryogenic system.

Tungsten has been widely used for the moderation material because of its stability and relatively high moderation efficiency.[3] The value of ϵ for the transmission moderator of tungsten single crystal foil is reported to be 5.9×10^{-4} and that of tungsten polycrystal foil is 2.6×10^{-4}.[4] Although the backscattering moderator of tungsten single crystal exhibits ϵ of one order of magnitude higher than that of the transmission moderator[5] and is useful for a re-moderator, its efficiency when used as a primary moderator would be low because a significant fraction of the moderated positrons are shielded by the source on the path of the beam.

Several authors have tested stacks of tungsten meshes as moderators.[6–10] Since meshes have large surface areas, high efficiency is expected. Furthermore, the cost is considerably lower than that of thin foils.

In this paper, we report the development of a stable, high-efficiency moderator with tungsten mesh.[11] The moderator consists of a six-overlapping tungsten mesh. The size of each mesh is 7 mm × 24 mm. They are 85% transmission with 20 μm wires. The meshes were annealed in vacuum by passing an electric current through the tungsten foils wrapping the meshes. The temperature was raised and maintained at 2000°C for 2 minutes. After annealing, the meshes were quickly transported in air and installed in the moderator assembly of the beam apparatus.

The moderator is placed 1 mm away from the window of the positron source. It is held with insulating bushings at a potential of +350 V with respect to the chamber and 9 V below the source. The positrons reemitted from the moderator are accelerated to 350 eV by a 95% transmission tungsten grid placed 3 mm downstream from the moderator.

The experimental system used to measure the efficiency of the moderator is magnetically guided positron beam apparatus with a trochoidal $\boldsymbol{E} \times \boldsymbol{B}$ filter. The magnetic transport system provides an approximately uniform axial field of 0.015 T. After leaving the $\boldsymbol{E} \times \boldsymbol{B}$ filter, the beam enters an insulating tube, where the positrons can be accelerated by floating up the whole of the source side. The base pressure of the system is 1.0×10^{-6} Pa.

In order to measure the beam intensity, the beam is incident on a carbon sample of 15 mm in diameter. The number of the positrons which annihilate on the sample are counted by detecting the 511-keV γ-rays using a high purity Ge detector. The efficiency of the detection system is calculated by placing a calibrated ^{22}Na source at the sample position.

The beam intensity is determined to be $6.7 \times 10^4 e^+/s$ when the source activity is 4.5 mCi (166 MBq). This value is almost independent of the beam energy for $E_{e+} > 350$ eV. If we assume that the positron transmission efficiency of the beam apparatus is 100%, the moderation efficiency ϵ is 4.5×10^{-4}.

The moderator is stable. The efficiency measured after a few months was found to be the same as the above value.

The moderation efficiency ϵ is higher than that for any other tungsten mesh moderator reported so far. It is comparable with the single crystal tungsten foil moderator. The mesh moderator has the advantage that the treatment is far easier and the cost is far lower than the single crystal. Further improvement of the efficiency is expected by optimizing the number of overlapping meshes.

References

1) A. P. Mills, Jr. and E. M. Gulikson: Appl. Phys. Lett. **49**, 1121 (1986).
2) R. G. Greaves and C. M. Surko: Can. J. Phys. **74**, 445 (1996).
3) J. M. Dale et al.: Surf. Interface Anal. **2**, 199 (1980).
4) E. Gramsch et al.: Appl. Phys. Lett. **51**, 1862 (1987).
5) A. Vehanen et al.: Appl. Phys. A **32**, 163 (1983).
6) L. S. Fornari et al.: Phys. Rev. Lett. **51**, 2276 (1983).
7) N. Zafar et al.: Hyperfine Interact. **89**, 243 (1994).
8) N. B. Chilton and P. G. Coleman: Meas. Sci. Technol. **6**, 53 (1995).
9) J. P. Merrison et al.: Appl. Surf. Sci. **149**, 11 (1999).
10) R. Zhang et al.: Rad. Chem. Phys. **58**, 639 (2000).
11) Y. Nagashima et al.: Jpn. J. Appl. Phys. **39**, 5356 (2000).

*1 Institute of Physics, Graduate School of Arts and Sciences, University of Tokyo
*2 Institute of Materials Structure Science (IMSS), High Energy Accelerator Research Organization (KEK)

Development of an EBIS Using High-T_c Superconductors

A. Endo,* H. A. Torii,* K. Yoshiki Franzen,* K. Komaki,* and Y. Yamazaki

Electron beam ion source (EBIS) is widely used as an effective source of highly charged ions. The ions are trapped in the magnetically confined electron beam and are successively ionized by the electron impact. The current density of the electron beam is one of the important parameters; it determines the maximum charge of produced ions. In oder to realize a high-density beam, conventionally a superconducting magnet is used. However, the magnet greatly increases the size of the apparatus and the running costs, with high liquid He consumption. Alternatively, a few EBIS (EBIT) without superconducting magnets have been developed.[1–3] The designers preferred downsizing at the cost of a strong magnetic field. Instead of this cost, we are attempting to develop an EBIS using a high-T_c superconducting material. It decreases the size of the EBIS and enables operation at liquid N_2 temperature with a sufficientry strong magnetic field.

The high-T_c superconducting material we used is YBa_2CuO_{7-x}, which has a high critical current density (J_c); its application as a bulk magnet has been investigated.[4] There are different methods to magnetize bulk. Field cooling (FC) using a static magnetic field is an effective method that is widely used. However, it requires an additional strong magnet, which increases the size of the apparatus. Recently, a new method called pulsed field magnetization (PFM) has been developed, in which the magnetizing coil can be kept comparatively small.[5,6] We adopted this type of EBIS, where the magnetizing coil (1.4 mm × 3.0 mm wire, 182 turns) is set in a liquid N_2 reservoir. We used three ring-shaped bulk magnets of 51 mm outer diameter, 15 mm inner diameter and 12 mm thickness each. Figure 1 shows the results of our magnetizing test. By repeatedly applying pulses of 11 ms width at a peak magnetic field of a few tesla, we succeeded in magnetizing bulks up to 1 T at liquid N_2 temperature.

A schematic view of the EBIS is shown in Fig. 2. Three bulk magnets are sealed in a stainless steel container which is in contact with the liquid N_2 reservoir wall. Electrons produced by a Pierce-type electron gun with a 3-mm-ϕ spherical cathode are injected into the magnetic field. The shape and the potential of the electrodes are determined by computer simulations. According to the simulations, a 100 mA electron beam is compressed to a diameter of 100 μm, corresponding to a current density of 1000 A/cm^2 at the center of the drift tube. Both electron gun and electron collector are floated at a negative voltage (up to −30 kV). Electrons are accelerated between the gun and the drift tubes. After passing through the ionizing region, electrons decelerated to 1 keV and are collected by the water-cooled electron collector. Produced ions are accelerated by the same potential, and extracted.

This EBIS is now under construction.

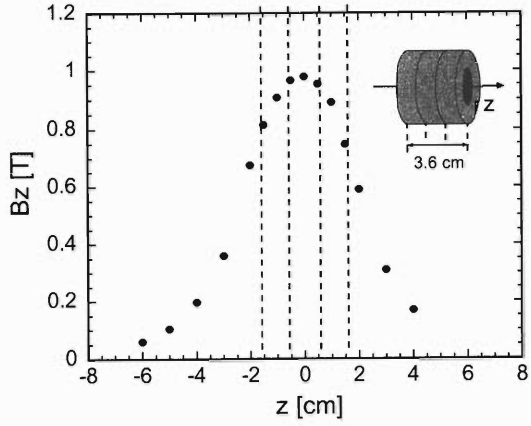

Fig. 1. Distribution of trapped magnetic flux at 77 K.

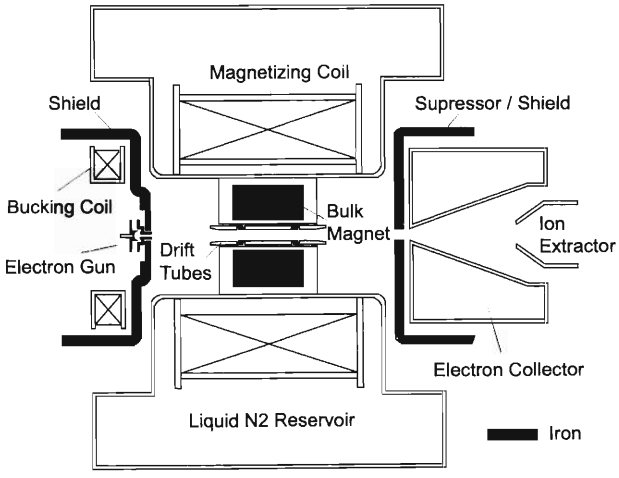

Fig. 2. Schematic view of our EBIS.

References
1) K. Okuno: Jpn. J. Appl. Phys. **28**, 1124 (1989).
2) K. Kusakabe et al.: Phys. Scr. T **73**, 378 (1997).
3) K. Motohashi, A. Moriya, H. Yamada, and S. Tsurubuchi: Rev. Sci. Instrum. **71**, 890 (2000).
4) M. Morita, M. Sawamura, S. Takebayashi, K. Kimura, H. Teshima, M. Tanaka, K. Miyamoto, and M. Hashimoto: Physica C **235/240**, 209 (1994).
5) U. Mizutani, T. Oka, Y. Itoh, Y. Tanagi, M. Yoshikawa, and H. Ikuta: Appl. Supercond. **6**, 235 (1998).
6) T. Oka, Y. Itoh, Y. Yanagi, M. Yoshikawa, H. Ikuta, and U. Mizutani: Physica C **335**, 101 (2000).

* Institute of Physics, University of Tokyo

A Possibility of a New Stripe Ordered State of Spins and Holes in the Overdoped $La_{2-x}Sr_xCu_{1-y}Zn_yO_4$ Studied by μSR

I. Watanabe, M. Aoyama,* M. Akoshima,* T. Adachi,* Y. Koike,* and K. Nagamine

Anomalous behavior of the transport phenomena with suppression of the superconductivity in Zn-substituted $La_{2-x}Sr_xCu_{1-y}Zn_yO_4$ around $x = 0.21$ has been reported Refs. 1–3 suggesting a possibility of the existence of a new stripe ordered state of spins and holes in the overdoped region. We have carried out the muon spin relaxation (μSR) measurements in order to investigate the Cu-spin state in these single-crystals of $La_{2-x}Sr_xCu_{1-y}Zn_yO_4$.[4)]

μSR measurements were carried out at the RIKEN-RAL Muon Facility (RIKEN-RAL) at the Rutherford-Appleton Laboratory in the UK. The two-exponential function of $A_1e^{-\lambda_1 t} + A_0e^{-\lambda_0 t}$ was used for the analysis. A_0 and A_1, λ_0 and λ_1 are regarded as the initial asymmetries and the depolarization rates, respectively.

Figure 1 shows the zero-field μSR time spectra of the Zn-substituted single-crystal obtained at various temperatures down to 0.3 K. The time spectrum deviates from the Gaussian-type at low temperatures below 3.5 K, indicating the appearance of a fast depolarizing component. At low temperatures below 2 K, the asymmetry of the muon spin polarization decreases quickly by nearly two thirds within a time range of 0.5 μsec after the arrival of muons in the sample. No clear coherent precession of the muon spin[5)] has been observed.

Fgiure 2 displays the results of the analysis. The initial asymmetry of the muon spin decreases suddenly around 2 K with decreasing temperature for the Zn-substituted crystal, which correlates with the increase of λ_1. The λ_0 is enhanced with decreasing temperature and exhibits divergence at 2 K. These are typical

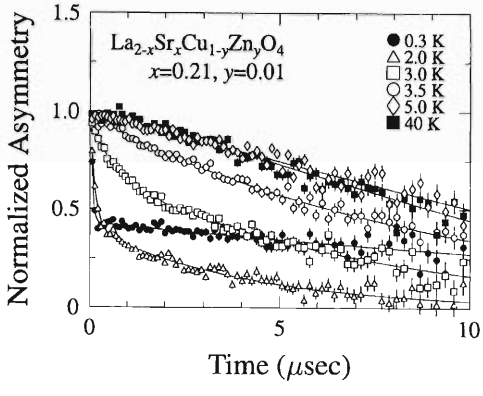

Fig. 1. Zero-field μSR time spectra of the Zn-substituted single-crystal of $La_{2-x}Sr_xCu_{1-y}Zn_yO_4$ with $x = 0.21$ and $y = 0.01$ at various temperatures. Solid lines are the best fit results.

* Graduate School of Engineering, Tohoku University

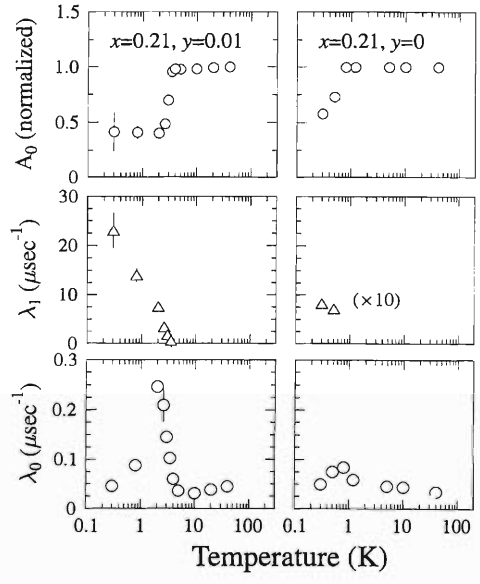

Fig. 2. Temperature dependences of the initial asymmetry of the slow depolarizing component (A_0) and the depolarization rates of the fast (λ_1) and slow (λ_0) depolarizing components in the Zn-substituted ($y = 0.01$) and Zn-free ($y = 0$) single-crystals of $La_{2-x}Sr_xCu_{1-y}Zn_yO_4$ with $x = 0.21$.

characteristics in the case that a static magnetically-ordered state of Cu spins appears in the La-214 systems as observed in the previous μSR studies.[5)]

It has been reported that the resistivity of the present Zn-substituted single-crystal with $x = 0.21$ exhibits upturn below about 80 K in every direction of the crystal axes.[3)] In addition, no Meissner effect has been confirmed at temperatures above 2 K. These results suggest that doped holes tend to be localized at lower temperatures. Since a static magnetically-ordered state of Cu spins are revealed by μSR to appear at low temperatures below 2 K in the same single-crystal, it is suggested that the ground state of this Zn-substituted single-crystal is a sort of coexisting state of statically ordered Cu-spins and localized holes. Therefore, it is plausible that a new stripe ordered state of spins and holes exists in the overdoped region as suggested from the transport measurements.[3)]

References

1) N. Kakinuma et al.: Phys. Rev. B **59**, 1491 (1999).
2) Y. Koike et al.: J. Low Temp. Phys. **117**, 1157 (1999).
3) T. Kawamata et al.: Phys. Rev. B **62**, R11981 (2000).
4) I. Watanabe et al.: Phys. Rev. B **62**, R11985 (2000).
5) I. Watanabe et al.: Hyperfine Interact. **86**, 603 (1994).

Level Crossing Resonance Study of a Two Dimensional Dimer System $SrCu_2(BO_3)_2$

A. Fukaya, I. Watanabe, and K. Nagamine

In low dimensional quantum spin systems, *e.g.* Haldane-gap and spin-ladder systems, the ground state is a non-magnetic singlet state due to quantum effects. In such compounds, muon spin relaxation is not expected, at least, at low temperatures, since a number of thermally excited triplet is quite small. However, in various compounds with the singlet ground state, an anomalous enhancement of the muon spin relaxation (μSR), which means existence of electronic magnetic moment and a spin freezing, is observed at low temperatures. Although an intrinsic property of system or a probe effect of muon has been discussed, the origin has not been clarified yet. At present, we speculate that the origin is that implanted muons locally distort the lattice and the singlet state is locally destroyed. To confirm our speculation, we have applied a level crossing resonance (LCR) method to a two dimensional dimer system $SrCu_2(BO_3)_2$, in which anomalous spin freezing is observed in μSR. If implanted muons locally distort the lattice, it should be reflected in resonance positions and/or line shapes of resonance. Thus, we can study an effect which implanted muons bring to local environment by comparing the result of NQR.[1)]

We have performed LCR measurement at Port 2 of the RIKEN–RAL Muon Facility. A powder sample of $SrCu_2(BO_3)_2$ was used.

In Fig. 1, we show the longitudinal field (LF) dependence of average asymmetry with time region from 5 μs to 10 μs, $A_{\rm ave}$, at 50 K and 3.1 K. We found the decrease of $A_{\rm ave}$ around 90 G, which suggests resonance of muon and some nucleus. The amplitude of resonance decreases at 3.1 K. The resonance position does not depend on temperature. In addition to the decrease of $A_{\rm ave}$ around 90 G, we also found the decrease of $A_{\rm ave}$ around 700 G (inset of Fig. 1). This decrease of $A_{\rm ave}$ is quite small and quite broad.

We can estimate resonance fields from the result of Cu-NQR.[1)] If implanted muons produce neither additional electric field gradient nor distortion of the lattice, the resonance position can be estimated from the function,[2)]

$$\gamma_{\rm N}|\mathbf{H}_{\rm N}^{\rm loc} + \mathbf{H}_{\rm LF}| = \gamma_{\mu}|\mathbf{H}_{\mu}^{\rm loc} + \mathbf{H}_{\rm LF}|, \qquad (1)$$

where $\gamma_{\rm N}$ and γ_{μ} is a gyromagnetic ratio of a nucleus and one of muon. $\mathbf{H}_{\rm N}^{\rm loc}$ and $\mathbf{H}_{\mu}^{\rm loc}$ are, respectively, a local field at the nuclear site and one at the muon stopping site. $\mathbf{H}_{\rm LF}$ is a longitudinal field. Since NQR frequency for ^{63}Cu and ^{65}Cu under zero-field is 23.0 MHz and 21.0 MHz,[1)] the resonance positions of muon-^{63}Cu and muon-^{65}Cu are expected to be, respectively, ~1900 G and ~1700 G. In $SrCu_2(BO_3)_2$, besides ^{63}Cu and ^{65}Cu, three elements of ^{38}Sr, ^{11}B and ^{12}B have a nuclear quadrupole moment. At present, elements which contributes the observed resonance have not been determined yet. To obtain information in more detail, we are planning theoretical calculation and additional LCR experiments.

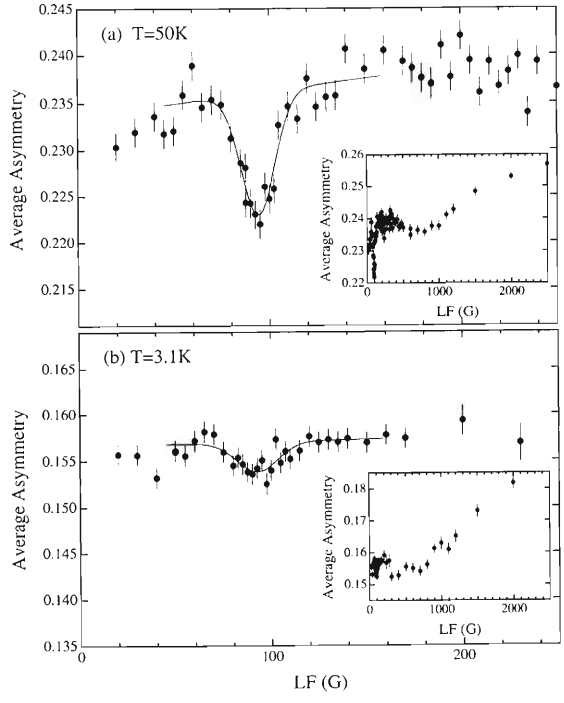

Fig. 1. LCR spectra at (a) 50 K and (b) 3.1 K. The insets show LCR spectra up to 2.5 kG.

References
1) H. Kageyama et al.: Phys. Rev. Lett. **82**, 3168 (1999).
2) G. M. Luke et al.: Hyperfine Interact. **31**, 29 (1986).

μSR Study on Magnetic Properties of p-NPNN·Cu(hfac)$_2$

S. Ohira, I. Watanabe, F. L. Pratt,* and K. Nagamine

p-NPNN (p-nitrophenyl nitronylnitroxide) is the first organic bulk ferromagnet, and is also known to be a ligand for transition and rare-earth metal ions. One such metal ion complex, p-NPNN·Cu(hfac)$_2$ (hfac = hexafluoroacetylacetonate), has a crystal structure which consists of alternating chains of p-NPNN and Cu(hfac)$_2$. The chains are connected by π-π and head-to-tail overlap of the p-NPNN molecules, resulting in a two-dimensional (2D) network.[1] The ac susceptibility (χ_{ac}) shows a cusp at 1.22 K suggesting that 2D antiferromagnetic interchain interaction operates in the 2D network, and the susceptibility also shows a sudden increase at ~0.60 K, suggesting a spin canting. The detailed magnetic properties of this material have not however been investigated by any other methods. We therefore performed a μSR study on p-NPNN·Cu(hfac)$_2$ in order to study the magnetic structure and spin dynamics of the system microscopically and to understand the magnetic properties of p-NPNN by investigating its properties as a ligand.

The experiment was carried out at the RIKEN-RAL Muon Facility in the UK. Polycrystalline samples were mounted on a silver plate with Apiezon-N, and fixed onto the sample holder of a ^{3}He cryostat. ZF- and LF-μSR measurements were carried out from 0.3 K to 80 K using this cryostat.

ZF-μSR time spectra is shown in Fig. 1. Slow relaxation of the muon spin due to nuclear dipole fields was observed above ~2 K, indicating that the system was in a paramagnetic phase. The muon spin relaxation gradually became faster below 2 K, and the shape of the time evolution of the muon spin dramatically changed between 1.2 K and 1.1 K. The initial asymmetry suddenly decreased, and recovery of the muon spin polarization was observed in the time region of $t \geq 6\,\mu$s, indicating the appearance of static internal fields.

The ZF time spectra were well fitted by the following equation:

$$A(t) = A_{\mathrm{power}}\, e^{-(\lambda_{\mathrm{power}} t)^{\beta}} + A_{\mathrm{fast}}\, e^{-\lambda_{\mathrm{fast}} t} + B. \quad (1)$$

The first term describes the muon spin relaxation caused by nuclear and/or electronic spins and the second term the fast spin depolarization of muons which experience large hyperfine fields through forming muonium ($= \mu^+ e^-$) or a muonium radical state. The third term, B, is constant and includes background (A_{bg}) and the finite muon spin polarization held constant at $\frac{1}{3}$ of the initial value by the component of static internal field which is parallel to the initial muon spin direction. Figure 2 shows the temperature dependence of the initial asymmetries, A_{power} and B ($= A_{\mathrm{bg}} + A_{\mathrm{tail}}$). Both A_{power} and B are almost temperature-independent above 1.2 K, while A_{power} suddenly decreases and B increases below 1.1 K. This result suggests that a long-range magnetically ordered state occurs below ~1.2 K.

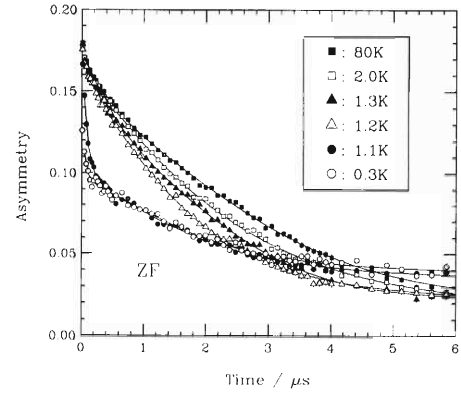

Fig. 1. ZF-μSR time spectra of p-NPNN·Cu(hfac)$_2$.

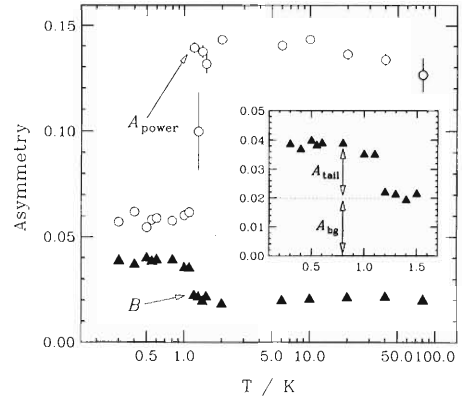

Fig. 2. Temperature dependence of initial asymmetry. The constant value of B above 1.2 K corresponds to background (A_{bg}). The increase of B below 1 K is assigned to the $\frac{1}{3}$-tail of a ZF Kubo-Toyabe component.

Our result is quite different from the susceptibility one. Taking into account the χ_{ac} result, the internal magnetic field between 0.6 K and 1.22 K should be fluctuating due to a short-range ordering. In our μSR study, however, the internal magnetic field at the muon site was static in this temperature region, suggesting a long-range ordered state below 1.2 K with no evidence of any further change at 0.6 K.

References

1) T. Origuchi et al.: Mol. Cryst. Liq. Cryst. **296**, 281 (1997).

* Also University of Oxford

μSR Study on a 2D Weak-Ferromagnetic Organic Radical Crystal

S. Ohira, K. Mukai,* K. Ohiro,* and I. Watanabe

Pure organic radical magnetic crystal, which is namely composed only of light elements such as C, H, N and O, are of much interest in recent years. An organic radical crystal 1,3,5-triphenyl-6-oxoverdazyl (TOV) is known to be a weak-ferromagnet. The magnetic susceptibility measurement on this material showed a broad maximum in the dc susceptibility at 6 K, indicating that the system is the $S = 1/2$ one-dimensional (1D) Heisenberg system, and suggested the appearance of a weak-ferromagnetism by increase of the susceptibility below $\sim$5 K.[1] On the other hand, the result of heat capacity is described by an $S = 1/2$ 2D Heisenberg antiferromagnet with $J/k_B = -4.5 \pm 0.2$ K, and the long-range magnetic ordering was not observed there.[2] We carried out ZF- and LF-μSR experiments on TOV, in order to study the details of the magnetically ordered state microscopically.

The experiment was carried out at the RIKEN-RAL Muon Facility in the UK, using a ^{3}He cryostat down to 0.3 K. Polycrystalline samples of TOV were prepared. They were mixed with Apiezon-N to fix on a silver sample holder.

Figure 1 shows ZF-μSR time spectra of TOV. Above $\sim$5 K, a random static internal field due to nuclear dipolar fields was observed. The changes of internal field and spin dynamics caused by the low-dimensional short-range magnetic ordering were not observed. Below $\sim$5 K, clear muon spin precession was observed, indicating the onset of a *unique* internal magnetic field at the muon site. A magnetic phase transition is expected at $\sim$5 K. The fact that a muon spin precession signal is observed evidences the appearance of a long-range magnetic ordering in the system. This result is consistent with that of the previous susceptibility measurement, and the transition temperature is similar to that obtained from the susceptibility measurement.

The precession frequency of the muon spin can be converted to the magnitude of the internal magnetic field at the muon site by using an equation $\omega = \gamma_\mu H$, where $\omega/2\pi$ is the precession frequency of the muon spin, H the internal field at the muon site, and γ_μ a gyromagnetic ratio of muon, respectively. The temperature dependence of the internal field at the muon site below 5 K shows appearance of spontaneous magnetization in the system, as shown in Fig. 2.

From our μSR study, it was confirmed that a long-range magnetic ordering appeared below $\sim$5 K in TOV. This result supports the previous magnetic susceptibility measurement. Enhancement of the muon spin relaxation associated with a short-range magnetic ordering was not observed in our study.

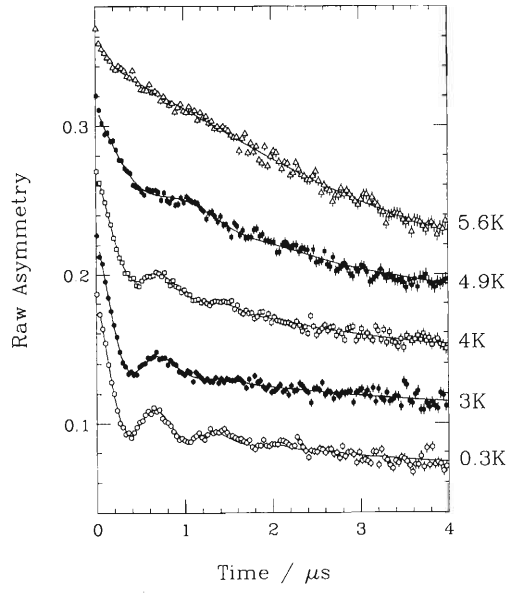

Fig. 1. ZF-μSR time spectra of TOV. Asymmetry includes constant background. The vertical scale refers to 0.3 K data, and the others are shifted by 0.04 for each vertically.

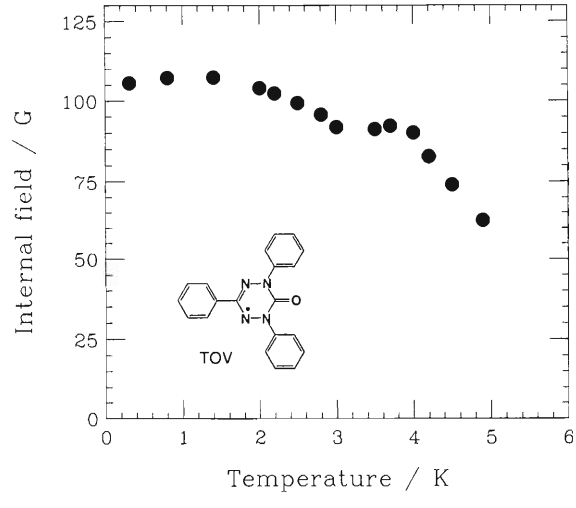

Fig. 2. Temperature dependence of the internal magnetic field at the muon site.

References

1) R. K. Kremer et al.: Chem. Phys. Lett. **230**, 255 (1994).
2) M. Mito et al.: J. Phys. Soc. Jpn. **66**, 2147 (1997).

* Ehime University

First Observation of a Full Dispersion Curve in a Spin-Ladder

K. Katsumata, M. Matsuda, R. S. Eccleston,[*1] S. Brehmer,[*2] and H. J. Mikeska[*2]

Quantum antiferromagnetism in lower dimensions has attracted much attention from condensed matter physicists. In recent years, spin ladder systems have been the subject of intense theoretical and experimental studies.[1)] A spin ladder is composed of n coupled one-dimensional magnets with an interchain (or rung) interaction $J_\perp$ ($J_{\rm rung}$). The most extensively studied spin ladder system is the one in which the magnetic atoms have spin quantum number $S = \frac{1}{2}$ with an antiferromagnetic intrachain (or leg) interaction $J_\parallel$ ($J_{\rm leg}$) as well as an antiferromagnetic $J_\perp$. The magnetic properties of such $S = \frac{1}{2}$ antiferromagnetic ladders (AFLs) change radically depending on whether n is even or odd.[2)] The ground state of an $S = \frac{1}{2}$ AFL with even n is a singlet with an energy gap to the lowest excited triplet. On the other hand, an $S = \frac{1}{2}$ AFL with odd n has no gap in the excitation spectrum. Despite a progress in theoretical studies, little is known experimentally about the low energy excitation spectrum of a spin ladder. Here, we report the first observation of a full dispersion curve for the low energy excitation in a spin ladder material using a pulsed neutron source.

The compound chosen for this study is $La_6Ca_8Cu_{24}O_{41}$. The parent compound $Sr_{14}Cu_{24}O_{41}$ consists of both CuO_2 chains and Cu_2O_3 ladders of copper ions. A number of experiments showed that the two-leg ladder has a spin gap (the bottom of the excitation spectrum) of 28–56 meV.[3)] An important point in the $Sr_{14}Cu_{24}O_{41}$ system is that stoichiometric $Sr_{14}Cu_{24}O_{41}$ contains hole carriers. These holes in the ladder may broaden the excitation spectrum and make the observation difficult. On the contrary, the compound $La_6Ca_8Cu_{24}O_{41}$ has no holes in the ladder, therefore, we expect that a cleaner spectrum will be observed.

The single crystals of $La_6Ca_8Cu_{24}O_{41}$ were grown using a traveling solvent floating zone method. An array of four mutually aligned single crystals was used. The neutron scattering experiments were carried out on the High Energy Transfer Chopper Spectrometer on the ISIS Pulsed Neutron Source at the Rutherford-Appleton Laboratory, UK. The experiments were carried out with incident neutron energies of 150, 300, 500 and 600 meV that were monochromated by a rotating Fermi chopper that was phased to the source.

The dispersion data as obtained from the observed magnetic peak positions are shown in Fig. 1 together with the theoretical fits described below. The signals at 30–60 meV originate from the bottom of the excitation band in the first Brillouin zone and those at 70–200 meV from the excitations in the second and the third zones. As is evident from the figure, when we reduce all the experimental points to a single Brillouin zone, these points constitute a full dispersion curve for the lowest energy excitation. As far as the authors are aware, this is the first experiment[4)] that observed the full dispersion curve in a spin ladder material.

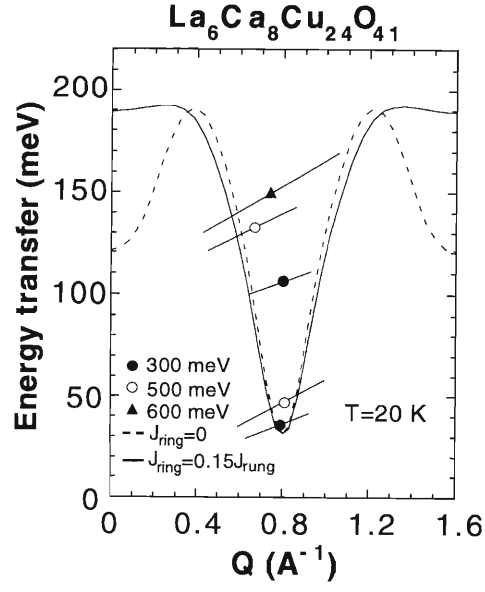

Fig. 1. The dispersion curve for the low energy excitation in the spin ladder material $La_6Ca_8Cu_{24}O_{41}$. The solid and broken curves are theoretical ones discussed in the text.

We have studied theoretically the low energy excitation in an $S = \frac{1}{2}$ two-leg spin ladder. The standard analysis of experimental data for spin ladders uses the two parameters $J_{\rm leg}$ and $J_{\rm rung}$ only, assuming the simplest symmetric structure of the two legged ladder. For this model we have calculated the dispersion of the lowest triplet excitation using the Lanczos method for ladders with 12 rungs (*i.e.* 24 spins) and periodic boundary conditions. With $J_{\rm rung}$ and $J_{\rm leg}$ as only exchange parameters we obtained the best fit to our data for $J_{\rm rung} = 53$ meV and $J_{\rm leg} = 106$ meV, corresponding to $J_{\rm leg}/J_{\rm rung} = 2$, as shown in Fig. 1. They are, however, not consistent with both (i) the expectation from a geometrical consideration that the Cu-O-Cu exchange on legs and rungs should be approximately equal (due to identical exchange paths and approximately equal distances and also in analogy to 2D materials such as La_2CuO_4) and (ii) the results of an exact diagonalization calculation for the electronic state of cuprates performed by Mizuno *et al.*,[5)] which gives $J_{\rm rung} \sim 150$ meV

*1 ISIS Facility, Rutherford Appleton Laboratory, UK
*2 Institut für Theoretische Physik, Universität Hannover, Germany

and $J_{\rm leg}$ ~170 meV, corresponding to $J_{\rm leg}/J_{\rm rung} = 1.1$. We, therefore, considered whether or not the introduction of additional exchange interactions gives a fit to our data with comparable accuracy and concomitantly is consistent with the expectation $J_{\rm rung} \approx J_{\rm leg}$. We calculated the dispersion with an additional ring exchange $J_{\rm ring}$ with the following Hamiltonian,

$$\mathcal{H}_{\rm ring} = 2J_{\rm ring}[(\boldsymbol{S}_1 \cdot \boldsymbol{S}_2)(\boldsymbol{S}_3 \cdot \boldsymbol{S}_4) + (\boldsymbol{S}_1 \cdot \boldsymbol{S}_4)(\boldsymbol{S}_2 \cdot \boldsymbol{S}_3) - (\boldsymbol{S}_1 \cdot \boldsymbol{S}_3)(\boldsymbol{S}_2 \cdot \boldsymbol{S}_4)]. \quad (1)$$

The solid curve in Fig. 1 shows the theoretical one with $J_{\rm rung} = 110$ meV, $J_{\rm leg} = 110$ meV, and $J_{\rm ring} = 16.5$ meV.[4)]

References

1) For a review, see E. Dagotto and T. M. Rice: Science **271**, 618 (1996).
2) E. Dagotto, J. Riera, and D. Scalapino: Phys. Rev. B **45**, 5744 (1992).
3) See for example, K. Kumagai, S. Tsuji, M. Kato, and Y. Koike: Phys. Rev. Lett. **78**, 1992 (1997).
4) M. Matsuda, K. Katsumata, R. S. Eccleston, S. Brehmer, and H.-J. Mikeska: Phys. Rev. B **62**, 8903 (2000).
5) Y. Mizuno, T. Tohyama, and S. Maekawa: Phys. Rev. B **58**, R14713 (1998).

First Results of Laser Spectroscopy of Antiprotonic Helium at the New Antiproton Facility AD of CERN

M. Hori,[*1] J. Eades,[*1] E. Widmann,[*2] H. Yamaguchi,[*2] J. Sakaguchi,[*2] T. Ishikawa,[*2] R. S. Hayano,[*2] H. A. Torii,[*3] B. Juhász,[*4] D. Horváth,[*5] and T. Yamazaki

With the birth of a new antiproton beam facility (the Antiproton Decelerator) at CERN a new experimental program on high precision studies of Antiprotonic Helium was started in 2000 as a part of the Asacusa Collaboration. Antiprotonic Helium is a metastable system of $\bar{p}He^+$ atoms and retains long lifetimes of 3–4 μs even in dense helium targets.[1,2] As much as 3% of the antiprotons stopped in helium are captured into metastable states with large principal ($n \sim 38$) and angular momentum quantum numbers ($l \sim n-1$). Its laser resonance spectroscopy was initiated in 1994,[3,4] and series of experiments were carried out[5–9] at LEAR.

The AD provided a pulsed beam containing 2×10^7 antiprotons, with an energy of 5.3 MeV, a pulse-length of 250 ns, and a repetition rate of 1 pulse per 2 minutes. We made new experimentations including Cerenkov counters for analog detection of delayed annihilation spectra and pulsed laser systems. Metastable $\bar{p}He^+$ atoms were produced by injecting a single antiproton pulse into a cryogenic helium gas target.

The charged pions produced in the annihilation were detected using two Cerenkov counters. The Cerenkov light was measured with a gatable fine-mesh photomultiplier (Hamamatsu Photonics R5505GX-ASSYII)

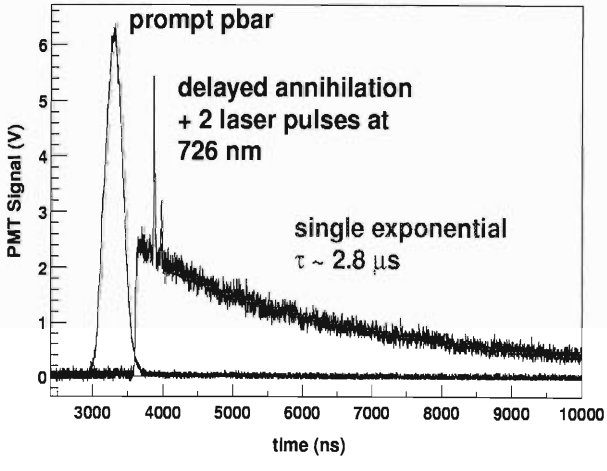

Fig. 1. A typical delayed annihilation time spectrum taken by the analog method.

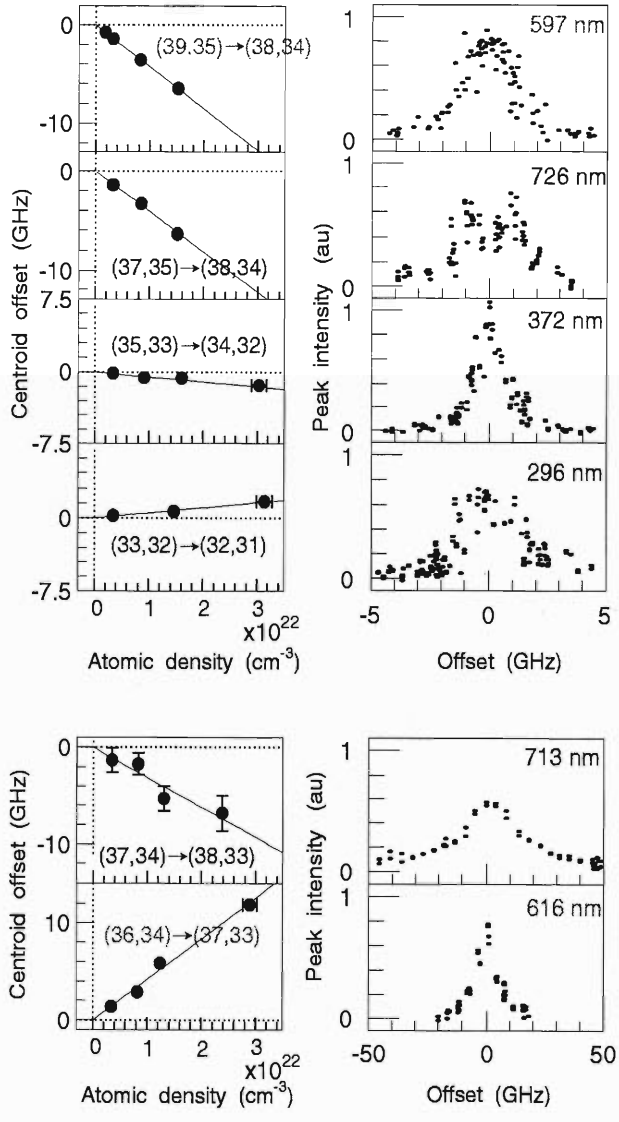

Fig. 2. The density shifts of 6 transitions of metastable antiprotonic helium atoms (left). The resonance profiles of the corresponding transitions (right).

developed especially for this experiment. At the arrival time of the antiprotons, the electron multiplication in the photomultiplier was deactivated by adjusting the voltage potential of the dynodes, thereby suppressing the overwhelming burst of photoelectrons caused by the prompt annihilation. Afterwards the detector was reactivated, producing a continuous pulse lasting more than 15 μs. This waveform, which reflects the delayed annihilation time spectrum, was recorded using a digital oscilloscope with an analog bandwidth of 1 GHz.

*1 CERN, Switzerland
*2 Department of Physics, University of Tokyo
*3 Institute of Physics, University of Tokyo
*4 Institute of Nuclear Research of the Hungarian Academy of Sciences, Hungary
*5 KFKI Research Institute for Particle and Nuclear Physics, Hungary

The metastable atoms were irradiated by a single laser pulse fired into the target, which induced transitions from metastable states to Auger-dominated short-lived states. This forced the annihilation of otherwise long-lived antiprotons and thereby producing a sharp spike in the delayed annihilation time spectrum. A dye laser (Lambda-Physik Scanmate 2E) pumped by the second harmonic ($\lambda = 532\,\mathrm{nm}$) of a Q-switched Nd:YAG laser (Coherent Infinity) was used, to produce laser pulses with a width of 4–6 ns, a diameter of 1 cm, a bandwidth of 0.4–0.6 GHz, and a power density of about 0.1–1.0 $\mathrm{mJ/cm^2}$ per pulse. A typical analog pulse shape is shown in Fig. 1. This was taken as a one-shot pulse, including more than 10^5 delayed annihilation events. With two successive laser pulsed tuned at 726 nm two resonent annihilation spikes were observed.

In the first period we searched for unknown transitions successfully. The frequency shifts of six transitions due to collisions with other helium atoms were measured (Fig. 2), and the zero-density frequencies deduced. Thus, their transition frequencies were determined to a precision down to 1.3×10^{-7}. The results agree with recent three-body QED theories,[10,11] even for transitions involving unstable states of 10-ps lifetime. The best agreement of $\lesssim 2 \times 10^{-7}$ was obtained for two ultraviolet transitions having the smallest frequency shifts of $< 10^{22}\,\mathrm{GHz/cm^3}$. When combined with the known antiprotonic charge-to-mass ratio, the results indicate that the mass (or charge) is in agreement with that of the proton to a precision of 7×10^{-8}, nearly an order of magnitude better than previous values.

References

1) M. Iwasaki et al.: Phys. Rev. Lett. **67**, 1246 (1991).
2) T. Yamazaki et al.: Nature **361**, 238 (1993).
3) N. Morita et al.: Phys. Rev. Lett. **72**, 1180 (1994).
4) R. S. Hayano et al.: Phys. Rev. Lett. **73**, 1485 (1994); Phys. Rev. Lett. **73**, 3181 (1994); F. Maas et al.: Phys. Rev. A **52**, 4266 (1995).
5) T. Yamazaki et al.: Phys. Rev. A **55**, R3295 (1997).
6) E. Widmann et al.: Phys. Lett. B **404**, 15 (1997).
7) H. A. Torii et al.: Phys. Rev. A **59**, 1 (1999).
8) M. Hori et al.: Phys. Rev. A **57**, 1698 (1998).
9) T. Yamazaki et al.: Chem. Phys. Lett. **265**, 137 (1997); B. Ketzer et al.: Phys. Rev. Lett. **78**, 1671 (1997); J. Chem. Phys. **109**, 1662 (1998).
10) V. I. Korobov and D. Bakalov: Phys. Rev. Lett. **79**, 3379 (1997); V. I. Korobov: Hyperfine Interact. **119**, 185 (1999).
11) Y. Kino, M. Kamimura, and H. Kudo: Hyperfine Interact. **119**, 201 (1999).

3. Radiochemistry and Nuclear Chemistry

In-Beam Mössbauer Study on Valence States of ^{57}Fe Decaying from ^{57}Mn Implanted into $KMnO_4$ (I)

Y. Kobayashi, K. M. Kubo,[*1] Y. Yamada,[*2] A. Yoshida, H. Ogawa,[*3] and F. Ambe

Mössbauer spectroscopy combined with an ion implantation technique provides unique information on the final lattice position, dynamical behavior and chemical states of implanted probes in a solid. A lot of emission Mössbauer studies have been performed to investigate ^{57}Fe produced by EC decay of ^{57}Co, as a typical implanted ion, into various matrices. However, there have been only two applications of ^{57}Mn,[1,2] which is also another mother source of ^{57}Fe, in Mössbauer experiments because ^{57}Mn is a short-lived nuclide, $T_{1/2}$ = 1.45 min. About 80% of ^{57}Mn decays directly to the Mössbauer level of 14.4 keV through the β^--decay process. It is known that aftereffects caused by the β-decay around the decaying probes are not very serious compared to those by the EC decay.

Mn sits next to Fe in the periodic table. However, the chemical properties of Mn are much different from those of Fe and Co. Mn occurs in various oxidation states, from 2+ up to 7+, in ordinary solidstate chemistry. Different oxidation states are expected to be synthesized for ^{57}Fe arising from ^{57}Mn decay, compared with that from ^{57}Co. Therefore, Fe species in exotic oxidation states and in an unusual oxygen configuration might be observed after the decay from ^{57}Mn in an appreciate matrix.

In this study, the in-beam Mössbauer technique was applied to obtain information concerning the oxidation state of ^{57}Fe arising from ^{57}Mn in $KMnO_4$, in which Mn ions are in a 7+ state.

In-beam Mössbauer spectra of ^{57}Fe arising from ^{57}Mn in $KMnO_4$ are shown in Fig. 1. Each spectrum was accumulated over 20 hrs. The center shift is given relative to iron metal at room temperature, and the sign of velocity is in the emission Mössbauer experiment. The spectrum obtained at 25 K could be analyzed preliminarily by two singlets, which are indicated by (a) and (b) in Fig. 1. The center shifts of components (a) and (b) were obtained to be 0.80 mm/s and −0.25 mm/s, respectively. The area intensity of component (b) was almost equal to that of component (a) at 25 K.

The results at 25 K were used as a reference to the correlation between oxidation states of Fe and the center shifts of chemical compounds coordinated with octahedral or tetrahedral configurations of oxygen atoms.[3] This correlation is almost ideally linear

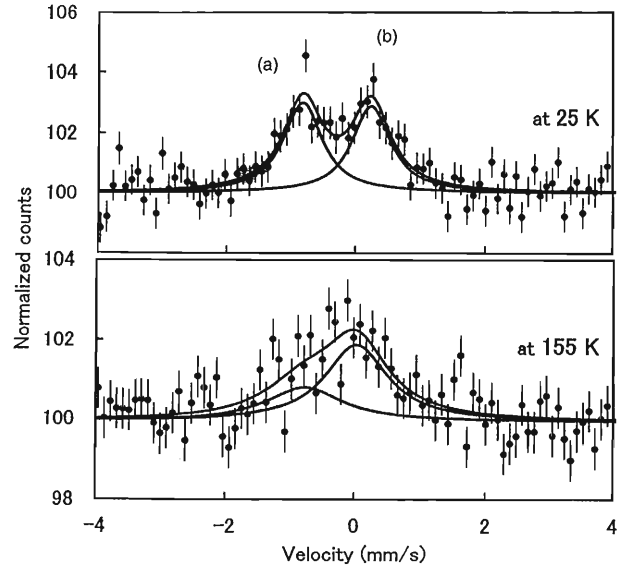

Fig. 1. In-beam Mössbauer spectra of ^{57}Fe arising from ^{57}Mn implanted into $KMnO_4$ at 25 and 155 K.

up to an oxidation state of 4+. However, for the higher oxidation states, the deviation from the linearity becomes obvious because of the increase in the covalency of Fe–O bonding. A preliminary result from this correlation suggests that components (a) and (b) correspond to an ionic Fe^{2+} and a covalent Fe^{5+}, respectively.

The spectrum at 155 K, on the other hand, was not obtained with sufficient statistics, but it could be fitted by the two components in the same manner as that at 25 K. Both resonance lines became broader than the result at 25 K. It is suggested that this phenomenon resulted from a certain effect on dynamics of implanted atoms. Furthermore, to discuss the site occupancies of ^{57}Fe ions, the calculation by molecular orbital methods with SCF-X_α and Gaussian procedures is being performed.

References

1) R. S. Preston and B. J. Zabransky: Phys. Lett. A **55**, 179 (1975).
2) M. Nakada et al.: Bull. Chem. Soc. Jpn. **65**, 1 (1992).
3) N. S. Kopelev: in *Mössbauer Spectroscopy of Sophisticated Oxides*, edited by A. Vertes and Z. Homonnay, (Akademiai Kiado, Budapest, 1997), p. 329.

*1 School of Science, University of Tokyo
*2 Department of Chemistry, Faculty of Science, Science University of Tokyo
*3 Graduate School of Science, Tokyo Institute of Technology

Metabolic Study of Bio-Trace Elements in Pregnant Rats Using the Multitracer Technique (I)

S. Enomoto, H. Tamano, T. Yanagiya, and R. Hirunuma

It is great of interest to study the transfer of trace elements from the placenta to the fetus because the placental organ may be regarded as the first environment of human development. Limited information is available on the transfer of trace elements from the mother to the fetus. Only the transfers of certain trace elements such as Zn and Fe are known, however the uptakes of other trace elements in the placenta and fetus of a rat during pregnancy remain unknown.

In this paper, the multitracer technique was applied to study the maternal transfer of trace elements *via* the placenta to the fetus.

The radioactive multitracer solution was prepared from an Ag target irradiated with a 135 MeV/nucleon ^{12}C, ^{14}N, or ^{16}O beam accelerated in the RIKEN Ring Cyclotron. Chemical separation was carried out, and then the multitracer solutions were obtained. Physiological saline was added to the radioisotopes to prepare the radioactive multitracer solution for injection into pregnant rats.

Seventeen-day-pregnant Wistar rats were used for this experiment. An appropriate amount of the radioactive multitracer saline was injected intravenously into the tail. The rats were sacrificed under ether anesthesia at 3, 12, 24 and 48 hours after injection. The maternal blood, placentas, fetuses, fetus brains, and amniotic fluids were removed from the rats and collected. The activities were determined by γ-ray spectrometry using highly pure Ge detectors. The results are given in the ratio of the percentage of injected dose to the weight of organs of the pregnant rats (uptake %/g).

Multitracer was applied to study the distribution of 18 trace elements in the organs and fluids of the 17-days-pregnant rats.

We examined the time dependence of the uptake amounts for various elements. From these results, we observed a large difference in the time dependency of each element and it was divided into three groups.

In the first group elements, such as Be, V, Sc, As, Y, Zr, Tc, Rh, and Ru move to the placenta from the maternal blood and accumulate only in the placenta. For this first group of elements, the present study revealed high uptake of these elements in the placenta, with no observable activity in the fetus or the amniotic fluid. The transfers of the first group of elements occur, demonstrating that these elements hardly penetrate the placental membrane, but the transfers of these elements are very low.

In the second group of elements, such as Na, Co, Ga, Rb, and Sr were transported to the placenta from the maternal blood and distributed in the placenta, fetus, and amniotic fluid. The uptake rates of Na indicated constant accumulation in all tissues, and did not depend on time after injection. On the other hand, the uptake rate of Rb increased and those of Co, Ga, Sr decreased with time after injection in the maternal blood, fetus, fetal brain and amniotic fluid. Rubidium has been suggested to be an essential trace element, but this remains unproven. It is essentially an intracellular ion, physiologically most similar to K and distributed throughout the body in much the same way. The present study showed uptake of Rb in both placenta and fetus for all times measured. The uptake of Rb is higher in the placenta than in the fetus. This suggests that Rb is able to penetrate the placental barrier. About 43% of Rb in the placenta was transferred to the fetus at 24 hours after injection and the concentration of Rb in the fetus was the same as that in maternal blood.

Metabolic Study of Bio-Trace Elements in Pregnant Rats Using the Multitracer Technique (II)

S. Enomoto, H. Tamano, T. Yanagiya, and R. Hirunuma

During pregnancy, there is an increased demand for minerals that are recognized as nutrients either for the formation of the fetus and the products of conception. The increased demand for these nutritients must be met through dietary intake or homeostatic responses. These homeostatic mechanisms may include the use of body stores, an increase in absorption of the mineral, reduction of excretion and/or slowing down of nutrient utilization or turnover. Some of these homeostatic responses are stimulated the physiological changes that occur with pregnancy. The utilization and turnover rate of most minerals during pregnancy is increased probably because of the synthesis that occurs, but there have been few studies carried out to examine this in animals. From our multitracer studies in report (I), we observed a large difference in the time dependency of each element and it was divided into three groups. In this paper, we discuss the biobehavior of the third group of elements.

In this third group, elements such as Mn, Fe, Zn, and Se were transported to the placenta *via* maternal blood and mainly accumulated in the fetus; they were not detected in the amniotic fluid. The uptake rates of these elements correlated with fetal growth. The fetus requires vast quantities of essential elements for normal development from the mother across the placenta, because the essential elements have important functions and are components of various kinds of proteins and tissues.

Although the amount of Mn in the placenta is not as high as that of Zn, the uptake of Mn in the fetus is very high. The uptake of Mn is approximately 2.8 times higher in the fetus than in the placenta at 24 hours after injection, and mainly accumulates in the fetal brain. Almost of Mn is concentrated in the fetal brain. The present study revealed that the injection of Mn also increased Mn transfer through the placenta to the fetus, and the transfer from placenta to fetus proceeded rapidly. These results suggest that Mn mainly accumulate in the fetal brain because it is related to neural development. The baby can obtain sufficient Mn for normal development after birth because the transfer of Mn from mother to fetus in rats occurs *via* the placenta after 18 days of gestation.

The uptake rate of Zn in the placenta is similar to that in the fetus, reflecting that the same concentration of Zn in the placenta was transferred to the fetus. After uptake into the placenta, the Zn is transferred across the cell layer and through other layers of the placenta and is secreted into the fetal plasma. Finally, it is taken up into the liver and incorporated into metallothionein. The rate of transfer of Zn from mother to fetus was demonstrated to increase at later stages of pregnancy.

The uptake of Fe in the fetus is higher than that in the placenta and maternal blood; more than 2.5 times the concentration of Fe in maternal blood was found in the fetus in 24 hours after injection. It was concluded that the amount of Fe which the fetus requires is higher than the requirement of the placenta and the maternal blood. The transfer of Fe from the maternal blood to the fetus *via* the placenta is related to the concentration of transferrin, and the fetal Fe is derived from maternal transferrin.

Selenium plays an important role in the system of defense against peroxidative damage to lipid membranes. It has high uptake in the placenta, and 33% of the Se in the placenta was transferred to the fetus within 24 hours of the injection. The uptake of Se in the fetus is lower than that of Zn, however, the demand of the fetus for Se is also large. Our results also indicated that Se is rapidly metabolized by the fetus. Similar to the case of Mn, it was suggested that the Se transfer from mother to fetus is influenced by the concentration of Se in the maternal blood.

Based on the results in the reports (I) and (II), we consider that the placenta is highly selective because essential elements such as those in the third group are readily transported across the placental membranes to the growing fetus, whereas nonessential elements such as those in the first group hardly penetrated the placental barrier that protects the fetus from toxic effects.

Uptake of Radioactive Elements in Rat Brain Tumor

H. Tamano, S. Enomoto, R. Hirunuma, and A. Takeda

Nuclear medicine techniques, which are noninvasive methods, play important roles for diagnosis of brain tumors. These techniques can detect tumors by imaging biochemical and metabolic changes of tumors, unlike morphological imaging such as X-ray computed tomography (CT) and magnetic resonance imaging (MRI). ^{18}F-fluorodeoxyglucose (FDG) positron emission tomography (PET) has been widely used in the diagnosis of brain tumors. However, FDG PET often fails to detect brain tumors because of the relatively high uptake of ^{18}F-FDG in the normal brain, in which glucose is actively utilized.[1] Therefore, the development of a tumor-specific imaging agent is necessary for advanced diagnosis of brain tumors.

Zinc, an essential transition metal for animals and humans, has three functions in zinc enzymes, *i.e.*, catalytic, coactive (or cocatalytic) and structural. Zinc is necessary for DNA replication and transcription, and protein synthesis. This metal may play critical roles in the regulation of cell division and growth.[2] Zinc has also been ascribed roles in the metabolism and interaction of tumor cells. Dietary zinc deprivation effectively suppressed the proliferation of transplanted tumors in tumor-bearing animals.[3] Judging from the importance of zinc in cellular proliferation and metabolism, it is considered that zinc uptake may reflect the metabolic activity of tumors. Brain tumors were positively imaged with ^{65}Zn because of the slow turnover of zinc in the brain;[4] these findings suggest the potential of using ^{69m}Zn, a short-half-life gamma emitter (half-life, 13.76 h; energy, 439 keV), for the diagnosis of brain tumors by single-photon emission computed tomography (SPECT).

The multitracer technique has the advantage of determining the metabolism of various trace elements under strictly identical conditions. In the present study, the multitracer technique was applied to determine the distribution of radioactive elements in rat brain tumor in order to find radioactive elements that have selective affinity for brain tumors.

The multitracer solution was prepared from an Ag target irradiated from a heavy-ion beam of 135 MeV/nucleon accelerated by the RIKEN Ring Cyclotron. Male Fisher rats (nine weeks old) were anesthetized with chloral hydrate in physiological saline solution and placed in a stereotaxic instrument. C6 glioma cells ($2 \times 10^5/10\,\mu$l culture media/rat) were injected at a rate of $0.7\,\mu$l/min into the left hippocampus of the rats at the coordinates of -4.7 mm posterior to the bregam, -3.9 mm lateral to the midline suture and -6.2 mm from the dura *via* a microdialysis probe without a dialyzing membrane using a microinjection pump. Fourteen days after tumor implantation, the multitracer solution (0.3 ml/200 g body weight) was intravenously injected into the tail vein of the rats. One hour after the injection of the multitracer solution, the rats were sacrificed after collecting the blood under deep diethyl ether anesthesia. The brain was excised and divided into tumor, cerebral cortex, cerebellum and the rest. The radioactivity in each tissue was measured by γ-ray spectrometry using high-purity Ge detectors. The assignment of the γ-rays was carried out on the basis of their energies and half-lives. The uptake of each radioactive element was given as a percentage of the injected dose per wet weight (% dose/g).

When the multitracer was intravenously injected into C6-glioma-bearing rats, 15 radioactive elements, *i.e.*, ^{7}Be, ^{22}Na, ^{46}Sc, ^{48}V, ^{51}Cr, ^{54}Mn, ^{56}Co, ^{65}Zn, ^{75}Se, ^{83}Rb, ^{85}Sr, ^{88}Zr, ^{95m}Tc, ^{103}Ru, and ^{99}Rh, were detected in the excised brain and/or collected blood 1 h after injection. ^{65}Zn, ^{83}Rb, ^{54}Mn, and ^{22}Na were preferentially taken up by the tumor, compared to other radioactive elements. Their uptake in the tumor ranged from 0.5–0.8% dose/g. The uptake of ^{65}Zn, ^{83}Rb, and ^{54}Mn in the tumor was 5–12 times higher than in any other brain region and significantly higher than that in the blood. The uptake of ^{22}Na in the tumor was also significantly higher than that in any brain regions, whereas it was lower than that in the blood. The uptake of ^{56}Co, ^{99}Rh, ^{85}Sr, ^{75}Se, ^{51}Cr, ^{46}Sc, and ^{48}V in the tumor ranged from 0.2–0.4% dose/g, and was higher than that in any other brain regions. However, the uptake of ^{56}Co, ^{99}Rh, ^{75}Se, ^{51}Cr, and ^{48}V in the tumor was lower than that in the blood, and the uptake of ^{85}Sr and ^{46}Sc in the tumor was roughly similar to the blood level. ^{88}Zr, ^{7}Be, ^{95m}Tc, and ^{103}Ru were hardly taken up in the brain.

The present findings demonstrate that zinc, rubidium and manganese are taken up in large amounts by the tumor in the brain of C6-glioma-bearing rats. This suggests the potential using radioactive rubidium and manganese, in addition to radioactive zinc, for brain tumor imaging.

References

1) R. Hustinx and A. Alavi: Neuroimaging Clin. N. Am. **9**, 751 (1999).
2) B. L. Vallee and K. H. Falchuk: Phys. Rev. **73**, 79 (1993).
3) A. Takeda, K. Goto, and S. Okada: Biol. Trace Elem. Res. **59**, 23 (1997).
4) T. Tamano, S. Enomoto, N. Oku, and A. Takeda: submitted to J. Cereb. Blood Flow Metab.

Metabolic Study of Trace Elements in Se-Excess Rats

R. Hirunuma, H. Tamano, and S. Enomoto

The uptake and distribution of various trace elements in the Se-deficient and Se-excess rats were determined by the multitracer technique, which can be used to evaluate the behavior of many elements simultaneously. This paper describes the synergism and/or antagonism of Se and some other elements containing multitracer in the rat's body.

Male Wistar rats bred from the fetal stage on a Se-deficient diet (Oriental Yeast Co., Ltd.) were used in these experiments as Se-deficient rats. Male Wistar rats (7 weeks old) were used as normal and Se-excess rats in the present study.

Multitracer solution containing various kinds of radionuclides was prepared from an Ag target irradiated with ^{14}N beam of 135 MeV/nucleon using RIKEN Ring Cyclotron. The multitracer solution was injected intravenously into each rat. These rats were sacrificed at several times after injection, and the radioactivity in their organs was measured using high-purity Ge detectors.

Effects of Se-deficiency on the behavior of Se, Fe, and As were evident in various organs. The uptake of Se was higher in the brain of Se-deficient rats than that of normal ones. The uptake of Se in the liver of Se-deficient rats was lower than that of normal ones. In the case of normal rats, the uptake of Se in the liver was much higher than that in the brain. However, in the case of Se-deficient rats, the uptake of Se in the liver was almost comparable to that in the brain. It was reported that a small quantity of Se fed to Se-deficient rats is preferentially absorbed in the brain than in the liver.[1] Higher uptake of Fe and As was observed in the liver of Se-deficient rats than in the liver of normal ones. The concentration of ferritin in Se-deficient rats was found to be higher than that in normal ones. The increase in Fe uptake by Se-deficient rats was considered to be due to an increase in the concentration of Fe-binding proteins, such as ferritin. Selenium was known to enhance As excretion into the bile in rats.[2–4] Higher uptake of As suggested that bile excretion of As was decreased by severe Se deficiency.

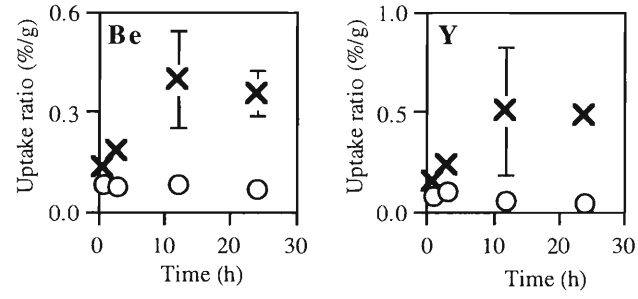

Fig. 1. Uptake of Be and Y in the liver of Se-excess (○) and normal rats (×).

On the other hand, the behavior of Se, As, Be, and Y was affected by Se addition. The uptake of Se in the blood, kidney, and testicles of Se-excess rats was lower than that of normal ones. Also, the uptake of As in the blood of Se-excess rats was lower than that of normal ones. However, there was no difference in the uptake of Se and As in the liver between Se-excess and normal rats. Compared with normal rats, the uptake of Be and Y in the liver of Se-excess rats was low (Fig. 1). Selenium is known to be in a competitive or synergistic relationship with several metals. From the present results on Be and Y, it was newly elucidated that there was also some interaction between these elements and Se.

References

1) D. Behne et al.: Biochim. Biophys. Acta **966**, 12 (1988).
2) O. A. Levander: Environ. Health Perspect. **19**, 159 (1977).
3) O. A. Levander and C. A. Baumann: Toxicol. Appl. Pharmacol. **9**, 98 (1966).
4) O. A. Levander and C. A. Baumann: Toxicol. Appl. Pharmacol. **9**, 106 (1966).

In Vivo Multitracer Detection for Assessment of Dynamics of Elements in Liver and Head of Living Rat

K. Matsumoto, R. Hirunuma, S. Enomoto, and K. Endo

When multitracer solution is intravenously injected into a living animal, each element in the multitracer is distributed to particular organs according to its characteristic affinity. Using a γ-ray detector equipped with a well-defined slit, collimated γ-rays from a particular part of the living animal can be obtained. Time courses of the γ-ray radioactivities provide information on the *in vivo* dynamics of biotrace elements for specific parts of the living animal.

The multitracer was prepared from silver foil. Then, 2 mL of isotonic citrate buffer multitracer solution (pH 6.2) was prepared. Six-week-old male Wistar rats were anesthetized with i.p. injection of pentobarbital. The rat was fixed to a special plastic rat holder with adhesive tape and placed in the desired position. A slit (7.5 mm width, 70 mm length, and 50 mm depth) was placed between the rat holder and a high-purity Ge semiconducting γ-ray detector. Immediately after i.v. administration of 100 μL of multitracer solution, the γ-ray spectra of the liver ($n = 4$) or head ($n = 3$) of the rat were measured. γ-Ray spectra were accumulated over 10 min for the liver and 20 min for the head. Data acquisitions were repeated 6 times for the liver and 4 times for the head. As the standard sample, 10 μL of multitracer solution was measured. In this experiment V, Mn, Co, Zn, As, Se, Rb, Sr, and Y were analyzed. The distribution of each element was indicated as a percentage of the radioactivity of the measured part to that of the standard sample.

The distributions of As, Sr and Y are relatively low in the liver and decrease with time (Fig. 1 (A)). These distributions may depend on the concentration of metals in the blood, and metals may gradually leak from the observed area to particular organs through the bloodstream. A smaller fraction of Rb is also found in the liver but increases gradually with time (Fig. 1 (A)). It appears that Rb gradually diffuses to organs in the observed area. Relatively large fractions of V, Mn, Co, Zn, and Se are found in the liver (Fig. 1 (A) and (B)). Since relatively high uptake rates of V, Mn, Co, Zn, and Se in the liver 1–2 days after i.v. administration was reported,[1–3] the distributions of these elements are considered to reach a plateau at a very early stage, and did not change in the time range examined in this study. The distribution of Se in the liver, however, increased at an early stage. Se can be predicted to have a slower distribution rate than V, Mn, Co, or Zn.

Lower distributions of the elements were observed in the head (Fig. 1 (C) and (D)) than in the liver. V, Sr, and Y, of which the distributions in the head are higher than those of other elements, may diffuse to the skull at a very early stage after administration. The concentrations of V and Y did not change while that of Sr increased during the early stage. This suggests that the distribution rate of Sr may be slower than those of V and Y. Co, Se, and As concentrations seem to decrease in the head while Mn, Zn, and Rb concentrations do not change. Since Mn, Zn, and Rb were observed in the brain removed from the same rat 48 hr after administration, these elements may be considered to accumulate gradually in the brain.

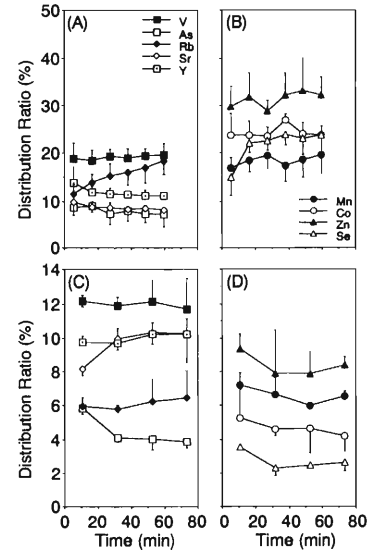

Fig. 1. Time course of radioactivity of several elements obtained by the *in vivo* multitracer analysis technique. The radioactivities were measured ((A), (B)) in the liver, and ((C), (D)) in the head of rats.

These results suggest that differences in the distribution of elements may mainly reflect preferred accumulation in certain organs and/or tissues in the observed area. Elements injected into a rat distribute throughout the whole body within at least 30 sec, and metabolism and excretion begin immediately. The distributions depend on the distribution rate in a very early stage after administration. Therefore, a shorter observation time period is required. The distribution level and/or rate of several elements might be influenced by pathological conditions such as oxidative stress.

References

1) R. Hirunuma et al.: Appl. Radiat. Isot. **48**, 727 (1997).
2) R. Hirunuma et al.: Appl. Radiat. Isot. **50**, 843 (1999).
3) R. Hirunuma et al.: J. Radioanal. Nucl. Chem. **239**, 213 (1999).

Alleviation of Cadmium Cytotoxicity by Manganese

T. Yanagiya, N. Imura,[*1] S. Enomoto, Y. Kondo,[*2] and S. Himeno[*1]

Cadmium (Cd) is an environmental pollutant that causes adverse effects in organisms, but little is known about the mechanism of Cd transport. Previously, we demonstrated that a Cd-resistant cell line (Cd-rB5) derived from immortalized metallorthionein (MT) null mouse fibroblasts exhibits a marked decrease in Cd accumulation, suggesting that the change in Cd transport is responsible for the resistance to Cd in the absence of MT expression.[1] Furthermore, the utilization of the multitracer technique has revealed that the uptake of manganese (Mn) in Cd-rB5 cells was also markedly reduced.[2] Competition studies and kinetic analyses have indicated that a high-affinity transport system for Mn is used for the cellular uptake of Cd in parental cells, whereas this pathway is suppressed in Cd-rB5 cells, leading to the reduced accumulation of Cd.[2]

In this study, to explore whether Mn alleviates cytotoxicity of Cd, we examined the effects of Mn addition to the medium on the cytotoxicity of Cd in Cd-rB5 and parental cells.

Simultaneous addition of $MnCl_2$ in the medium reduced the cytotoxicity of Cd efficiently in parental cells but not in Cd-rB5 cells. As shown in Table 1, the IC_{50} value of $CdCl_2$ for parental cells in the absence of $MnCl_2$ was 1.6 μM, and this value increased up to 18.6 μM by the addition of $MnCl_2$ dose-dependently. On the other hand, the IC_{50} value of $CdCl_2$ for Cd-rB5 cells was 25.0 μM in the absence of $MnCl_2$, but this value was not influenced by the addition of $MnCl_2$. The protective effect of Mn on Cd cytotoxicity in parental cells but not in Cd-rB5 cells suggests that the reduction of Cd cytotoxicity is related to the change in cellular Cd incorporation by Mn.

Previously, we have shown that the uptake of $CdCl_2$ was inhibited by the addition of $MnCl_2$ in parental cells but not in Cd-rB5 cells, suggesting that the Cd/Mn transport system is not functioning in Cd-rB5 cells.[2] However, we examined the mutual inhibitory effects of Cd and Mn uptake only at low dose levels (less than 1.0 μM) in the previous study, based on the result that the uptake of Mn in Cd-rB5 cells was suppressed only at Mn concentrations less than 3 μM. Our conclusion at that time was that there are at least two transport systems for cellular Mn uptake and that only the high-affinity Mn transport system is suppressed in Cd-rB5 cells. In the present study, however, the addition of $MnCl_2$ in the range of 1–30 μM protected against cytotoxicity of Cd in parental cells but not in Cd-rB5 cells. These results implicate that the interaction of Mn and Cd in terms of their incorporation into cells is more complicated than expected; at least one of the low-affinity Mn uptake systems may also be involved in the Cd uptake, or the high-affinity Mn uptake system may be responsible for the modulation of Cd toxicity even when high concentrations of Cd or Mn were applied to cells.

The results of our studies suggest that Mn is involved not only in the transport of Cd but also in the cytotoxicity of Cd. Further studies are needed to elucidate the molecular mechanism of Cd and Mn transport.

References

1) T. Yanagiya et al.: Life Sci. **65**, PL177 (1999).
2) T. Yanagiya et al.: J. Pharmacol. Exp. Therap. **292**, 1080 (2000).

Table 1. Effect of simultaneous addition of $MnCl_2$ on $CdCl_2$ cytotoxicity in Cd-resistant and parental cells.

Mn added in the medium (μM)	Parental cells		Cd-rB5 cells	
	IC_{50} (μM) [a]	Ratio (-fold)	IC_{50} (μM) [a]	Ratio (-fold)
0	1.6	1.0	25.0	1.0
1	3.6	2.3	22.6	0.9
3	8.4	5.3	22.7	0.9
10	16.9	10.6	22.3	0.9
30	18.6	11.6	21.3	0.9

Parental cells and Cd-rB5 cells were exposed to $CdCl_2$ in the absence or presence of 1, 3, 10 or 30 μM $MnCl_2$ for 48 hr, and then the surviving cells were determined by MTT assay.

[a] The concentration of metals required to kill 50% of the cells as calculated by MTT assay.

*1 School of Pharmaceutical Sciences, Kitasato University
*2 Department of Urology, Nippon Medical School

Tissue Uptake Behavior of Sc, Mn, Co, Zn, Se and Rb in Mice Bred under Manganese Deficient and Excessive Diets

Y. Kanayama,[*1] Y. Yabushita,[*1] T. Tarohda,[*2] K. Washiyama,[*1] R. Amano, and S. Enomoto

It is well known that manganese (Mn) uptake is enhanced under conditions of iron (Fe) deficiency and depressed by large amounts of nonheme Fe. Dietary copper (Cu) also induces decreased Mn uptake and retention. Furthermore, addition of essential and nonessential trace elements to the drinking water can result in altered tissue uptake of essential trace elements (including Mn) in normal mice.[1] These observations suggest that Mn interacts with other trace elements in uptake, retention and subsequent tissue distribution. In this experiment, we examined the interrelationships between Mn and other elements in mice using a multitracer solution and mice bred under three levels of dietary Mn concentrations.

The multitracer was obtained from an Ag foil target irradiated by a 135 MeV/nucleon ^{12}C beam accelerated in the RIKEN Ring Cyclotron according to the method of Ambe *et al.*[2–4] The final multitracer solution for injection contained the carrier-free states of ^{46}Sc, ^{54}Mn, ^{58}Co, ^{59}Fe, ^{65}Zn, ^{75}Se, ^{83}Rb, ^{85}Sr and ^{88}Zr in the physiological saline solution (0.9% NaCl in 0.001 NHCl).

The ICR mice (prenatal 16 days) were bred under different Mn-diets until their babies were 3 weeks old. Mn-diets were prepared with three different levels of Mn concentration (0.43 ppm, 31.8 ppm and 300.4 ppm), referred to as Mn-deficient, -adequate and -excessive diets, respectively. The multitracer solution was intraperitoneally (i.p.) injected into the mice (n = 5 for each Mn diet). Forty-eight hours after i.p. injection, the brain, thymus, cardiac muscle, lung, spleen, pancreas, kidney, liver, testis, blood, and parietal bone were excised under ether anesthesia. These organs were weighed and freeze dried. The dried samples were subjected to γ-ray spectrometry using high-purity Ge semiconductive detectors with reference to an appropriate standard. The uptake behavior was evaluated in terms of the organ uptake rate (the radioactivity percentage of injected dose per gram, %dose /g).

Figure 1 compares the organ uptake behavior of ^{46}Sc, ^{54}Mn, ^{58}Co, ^{65}Zn, ^{75}Se, and ^{83}Rb tracers in the mice bred under Mn-deficient, -adequate and -excessive diets. These six elements were traced simultaneously in all samples. The ^{54}Mn uptakes in all organs of Mn-deficient mice were found to be significantly higher than those of Mn-adequate mice. However, there were no significant differences between Mn-adequate and excessive mice. As noted for the other elements (Sc, Co, Zn, Se, and Rb), the ^{58}Co uptake rates in lung, spleen, blood, and kidneys of Mn-deficient mice were higher than those of Mn-adequate mice. Furthermore, significant differences were also found in

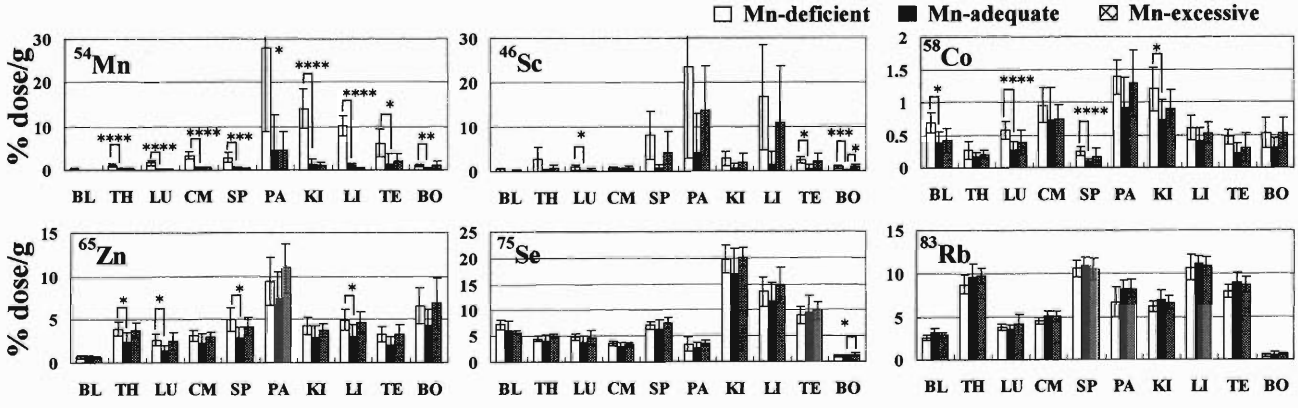

Fig. 1. Organ uptake rates of ^{54}Mn, ^{46}Sc, ^{58}Co, ^{65}Zn, ^{75}Se, and ^{83}Rb in mice bred under three different Mn-diets. Symbols indicate as follows: BL: blood; TH: thymus; LU: lung; CM: cardiac muscle; SP: spleen; PA: pancreas; KI: kidneys; LI: liver; TE: testes; BO: bone. Statistical analysis of data was by t-test: $*p < 0.05$, $**p < 0.01$, $***p < 0.005$, $****p < 0.001$. ICR mice were bred under three different Mn-diets, which are deficient (Mn 0.4 ppm), adequate (Mn 31.8 ppm), and excessive (Mn 300.4 ppm) diets (n = 5 for each group).

*1 School of Health Sciences, Faculty of Medicine, Kanazawa University
*2 Graduate School of Natural Science and Technology, Kanazawa University

the ^{65}Zn uptake rates in thymus, lung, spleen, and liver. On the other hand, comparing Mn-adequate to Mn-excessive mice, there were few differences in all uptakes of Sc, Co, Zn, and Se (except the ^{46}Sc and ^{75}Se bone uptake rates). In all ^{83}Rb uptakes, no significant difference was observed among the three different mice.

In conclusion, the alteration of Mn concentration in the diet influences not only the Mn uptake but also the Sc, Co, Zn, and Se uptakes in various organs except the brain.[5)]

References

1) J. C. K. Lai et al.: in *Manganese and Its Role in Biological Processes* (*Metal Ions in Biological Systems*, Vol. 37), edited by A. Sigel and H. Sigel (Marchel Dekker, New York, 1999), p. 123.
2) S. Ambe et al.: Chem. Lett. **1991**, 149.
3) S. Ambe et al.: Anal. Sci. **7**, Suppl., 317 (1991).
4) S. Ambe et al.: J. Radioanal. Nucl. Chem. **195**, 297 (1995).
5) Y. Yabushita et al.: RIKEN Accel. Prog. Rep. **34**, 134 (2001).

Brain Regional Uptake Behavior of Sc, Mn, Co, Zn, Se, and Rb in Mice Fed Mn-Deficient and Excessive Diets

Y. Yabushita,[*1] Y. Kanayama, T. Tarohda,[*2] K. Washiyama,[*1] R. Amano, and S. Enomoto

Manganese (Mn) is an essential trace element, and it is widely distributed in the tissues of animals. Deficiency of manganese during embryonic development leads to congenital ataxia, and its excess affects the central nervous system, impairing cognitive functions and motor activity.[1)] It is thought that these several symptoms are caused by influences of various element-element interactions rather than by influences of a single element. However, little is known at present about the interrelationships between Mn and the other elements in the brain. In the present research, we determine the brain regional uptakes of multitracer in mice fed three kinds of diets with different Mn concentrations to obtain some information on the biological interactions of Mn with trace elements.

An Mn-deficient diet was purchased and Mn-adequate and excessive diets were prepared by adding $MnCO_3$ to the Mn-deficient diet. ICR mice were fed the Mn-deficient, Mn-adequate or Mn-excessive diets with pure water from prenatal 16 days. Natal baby mice were bred to 3 weeks with their dams. A multitracer solution containing ^{7}Be, ^{46}Sc, ^{54}Mn, ^{59}Fe, ^{58}Co, ^{65}Zn, ^{75}Se, ^{83}Rb, ^{85}Sr, ^{88}Y, and ^{88}Zr was injected intraperitoneally into 3-week-old male mice. Forty-eight hours after injection, they were sacrificed under ether anesthesia. The brain was excised and separated into eight regions. These separated brain regions were measured using γ-ray spectra with high pure Ge detector and evaluated in terms of "brain regional uptake rate (% dose/g)."

On the basis of the results, the multitracer solution enabled a simultaneous tracing of ^{54}Mn, ^{46}Sc, ^{58}Co, ^{65}Zn, ^{75}Se, and ^{83}Rb in all brain regions. Figure 1 shows their brain regional uptakes in Mn-deficient, adequate and excessive mice. The ^{54}Mn uptakes of Mn-deficient mice were clearly higher than those of Mn-adequate mice. However, no significant differences were observed between Mn-excessive and adequate mice. On the other hand, no significant differences among three different diets were observed for all other tracers. As compared among brain regions, ^{54}Mn, ^{58}Co, ^{65}Zn, and ^{83}Rb were distributed evenly in all regions. However, ^{75}Se and ^{46}Sc were region-specific and concentrated in certain brain regions. The ^{75}Se uptake rate was significantly higher in the cerebellum and the olfactory bulb than that in the other

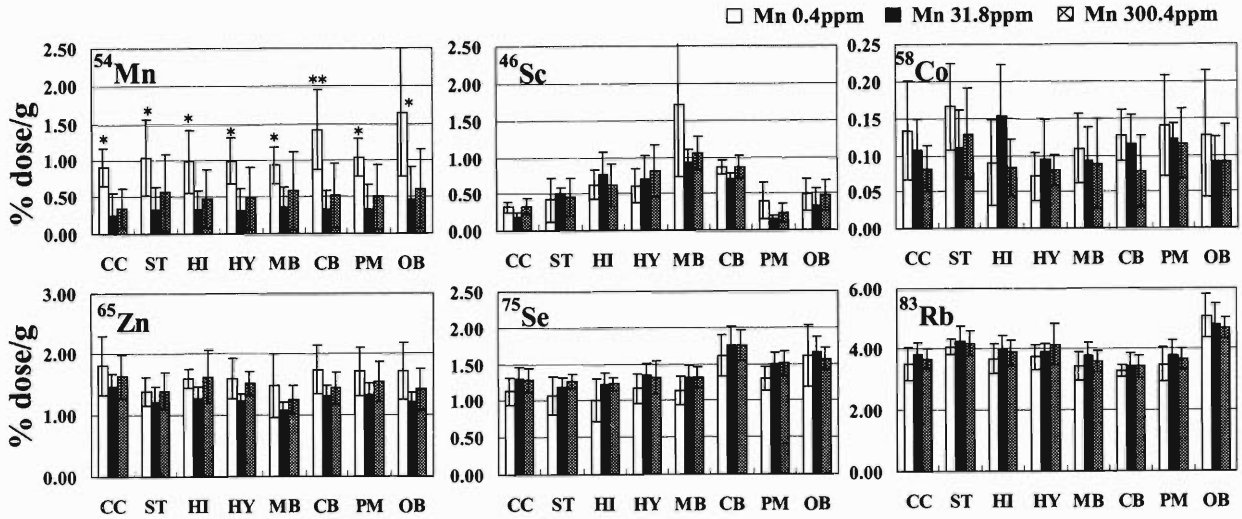

Fig. 1. Brain regional uptakes of Mn, Sc, Co, Zn, Se, and Rb in Mn-deficient, adequate and excessive mice. CC: cerebral cortex; ST: corpus striatum; HI: hippocampus; HY: thalamus and hypothalamus; MB: midbrain; CB: cerebellum; PM: pons and medulla; OB: olfactory bulb. Each bar and line represents the mean $\pm S.D.$ for five animals. Asterisks indicate significant differences (* $p < 0.05$, ** $P < 0.01$) from Mn-adequate mice.

*1 School of Health Sciences, Faculty of Medicine, Kanazawa University
*2 Graduate School of Natural Science and Technology, Kanazawa University

regions, and the ^{46}Sc uptake rate was also higher in the midbrain.

These findings suggest that both Mn-deficient and excessive states do not markedly influence the brain uptake behaviors of the other trace elements in mice fed diets with Mn concentrations from 0.4 to 300.4 ppm in this experiment, although some interactions were clearly observed in the organs except those in the brain of identical mice.[2)]

References

1) R. M. Leach, Jr. and E. D. Harris: in *Handbook of Nutritionally Essential Mineral Elements*, edited by B. L. O'Dell and R. A. Sunde (Marcel Dekker, New York, 1997), p. 335.
2) Y. Kanayama et al.: RIKEN Accel. Prog. Rep. **34**, 132 (2001).

Biobehavior of Multitracers in Brain of 1-, 4- and 8-Day-Old Normal Mice

T. Tarohda,[*1] Y. Yabushita,[*2] Y. Kanayama, R. Amano, and S. Enomoto

Conveniently, the multitracer contains simultaneously both essential and nonessential trace elements in a salt-free and carrier-free state. We have been interested in the investigating the brain functions of essential elements and the neurotoxic effects of nonessential elements. In the previous report, we examined multitracer behavior in the brains of 1-, 3- and 8-week-old mice.[1] In this work, we continuously focused on the studies of multitracer uptake, transportation and retention in the brain during postnatal development.

A carrier-free multitracer was obtained from an Ag (purity: more than 99.99%) target irradiated with a ^{12}C beam of 135 MeV/nucleon in the RIKEN Ring Cyclotron. The multitracer was separated and prepared according to the method of Ambe *et al.*[2–4] at the Radioisotope Center of Kanazawa University. The multitracer solution for injection was prepared as a slightly acidic physiological saline solution.

Sixty normal ICR mice used in this experiment were divided into three groups according to age: 1-, 4- and 8-day-old groups. An appropriate amount of the multitracer solution (0.1 ml/5 g mouse weight) was injected intraperitoneally (i.p.) into each mouse. The mice were dissected and perfused with 0.9% NaCl solution under ether anesthesia 6, 12, 24 and 48 hours after i.p. injection. Brain samples were excised, and then weighed immediately and then freeze-dried. The dried samples were subjected to γ-ray spectrometry using pure Ge detectors. The uptake behavior was evaluated in terms of brain uptake rate, namely the radioactivity percentage of injected dose per gram of the brain of interest (% dose/g).

The multitracer technique enabled simultaneous tracing of the nine elements, Sc, V, Mn, Co, Zn, Se, Rb, Ru, and Rh, in the identical brain samples and an accurate comparison of their biobehavior. Figure 1 compares the brain uptake rates in the 1-, 4- and 8-day-old normal mice 6, 12, 24 and 48 hours after i.p. injection. The brain uptake rates for these elements in the 1-day-old mice were the highest among those of elements in all age-groups examined. The uptake rates of 1- to 8-day-old mice are very higher than the uptake rates of 21- to 56-day-old mice, as reported previously.[1] These high uptake rates are presumably related to the manner of brain growth during neonatal development (the weight of a 1-day-old brain increased by approximately four times over in the three weeks after birth, as shown

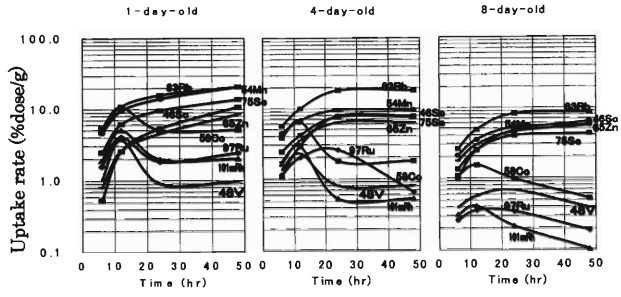

Fig. 1. Brain uptake rates for Sc, V, Mn, Co, Zn, Se, Rb, Ru, and Rh in normal mice 6, 12, 24 and 48 hr after i.p. injection of the multitracer solution. Each uptake rate represents the mean value ±S.D. obtained for five mice.

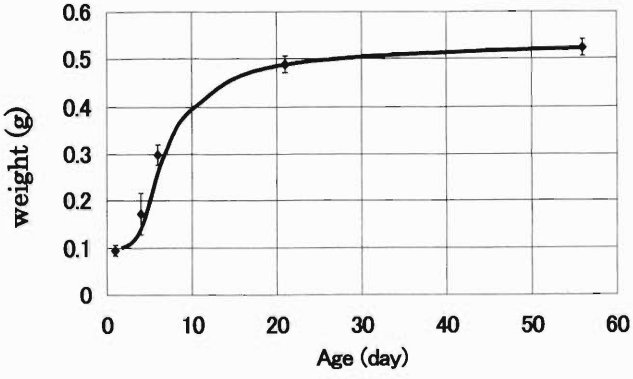

Fig. 2. Developing brain weight of normal mouse.

in Fig. 2). The high uptake rate may also be attributed to the high metabolic rate and the imperfect formation of the blood-brain barrier in infancy. Moreover, there appear to be two uptake patterns in brain; one seems to be increasing with time, as shown in Rb, Sc, Mn, Se and Zn patterns, and the other seems to increase at first and decrease gradually with time as shown in Co, V, Ru and Rh patterns. These patterns were found to be more distinct in the aged brain. This phenomenon may represent a classification of these two groups, owing to the necessity of the different elements in the brain. As to Rb and Sc, Rb may uptake into brain as a substitute for K, but Sc behavior has yet to be determined.

References

1) T. Tarohda et al.: RIKEN Accel. Prog. Rep. **33**, 118 (1999).
2) S. Ambe et al.: Chem. Lett. **1991**, 149.
3) S. Ambe et al.: Anal. Sci. **7**, Suppl., 317 (1991).
4) S. Ambe et al.: J. Radioanal. Nucl. Chem. **195**, 297 (1995).

*1 Graduate School of Natural Science and Technology, Kanazawa University (Asanagawa General Hospital)
*2 School of Health Sciences, Faculty of Medicine, Kanazawa University

Effect of Sodium Iron Ethylendiaminetetraacetic Acid Intake on the Uptake of Trace Elements in Anemic Rats

K. Igarashi,* H. Inage,* Y. Nakanishi,* R. Hirunuma, S. Enomoto, and S. Kimura*

Iron deficiency is one of the major micronutrient deficiencies. With diets that mainly consist of cereals or vegetables, which contain inhibitors of iron absorption, in developing countries, there is a high prevalence of iron deficiency and anemia. One method of improving iron deficiency is by food fortification, which is usually considered the most sustainable approach. Fish sauce is considered as a good vehicle for iron fortification in Asian countries such as Vietnam. Sodium Iron Ethylendiaminetetraacetic Acid (NaFeEDTA) is stable during processing and storage, and is also a highly bioavailable form of iron recommended as an iron fortificant. Davidsson et al. reported that NaFeEDTA dose not reduce the absorption of Zn, although there is a possibility that EDTA might bind to other metals and change the state of these metals. Iron bioavailability depends on food components. Tannic acid, which is contained in vegetable foods, is an inhibitor of iron absorption. We thus select tannic acid as an inhibitor to study.

In this work, we studied the inhibitory effect of tannic acid on iron absorption and various elemental uptakes from NaFeEDTA or ferrous sulfate (FS) and a multitracer additive diet on anemic rats.

Three-week-old Wistar male rats were purchased from Charles River Japan, Inc. and were housed in stainless steel cages. They were made anemic through their diets. The composition of the diets is shown in Table 1. The diets, mineral and vitamin supplements were prepared in accordance with the recommendations of the American Institute of Nutrition (AIN-93). Iron was excluded from the mineral supplement. Ferrous sulfate was used as a control. Three days before the experiment, rats were divided into four groups by dietary control. After 5 weeks feeding, rats were given an experimental diet and orally administered tannic acid or saline. The rats were orally administered a dose of 2 mg tannic acid. Rats were sacrificed 3, 7, 24 and 48 hours after administration of tannic acid or saline. Organs such as liver, spleen, kidney and bone were separated and blood was collected, centrifuged into plasma and clot. The radioactivities of their organs and blood were measured using high-purity Ge detectors.

The concentration of hemoglobin in anemic rats, 9.4 ± 0.13 g/dl, was lower than that in normal controls, which had concentrations from 13 to 17 g/dl. In this study, the multitracer contained the following elements: Na, Sc, Mn, Fe, Co, Zn, As, Se, Rb, Sr, Zr, Tc, and Rh. The uptake rates of Fe and Zn in anemic rat liver are shown in Fig. 1.

The uptakes of Fe and Zn for every group increased with time. In the case of Fe uptake, tannic acid had inhibitory effects on the FS additive diet. On the other hand, tannic acid had few suppressive effects on the

Table 1. Composition of iron deficiency diet (ID).

Ingredient (%)	ID	Experimental diet A	Experimental diet B
Casein	14	14	14
L-Cystine	0.18	0.18	0.18
Corn starch[1]	62.1	38.19	38.19
Sucrose	10	10	10
Soy bean oil	4	4	4
Cellulose	5	5	5
Mineral mix [Fe (-)]	3.5	27.38	27.38
Vitamin mix	1	1	1
Choline bitartrate	0.25	0.25	0.25
Iron compound[2]		FS	NaFeEDTA
Multitracer		+	+

[1] Corn starch was replaced with mineral mix in experimental diet.
[2] 352 mg Fe/kg diet as FS or NaFeEDTA was added (each rat was given iron compounds at a dose of 0.5 mg Fe).

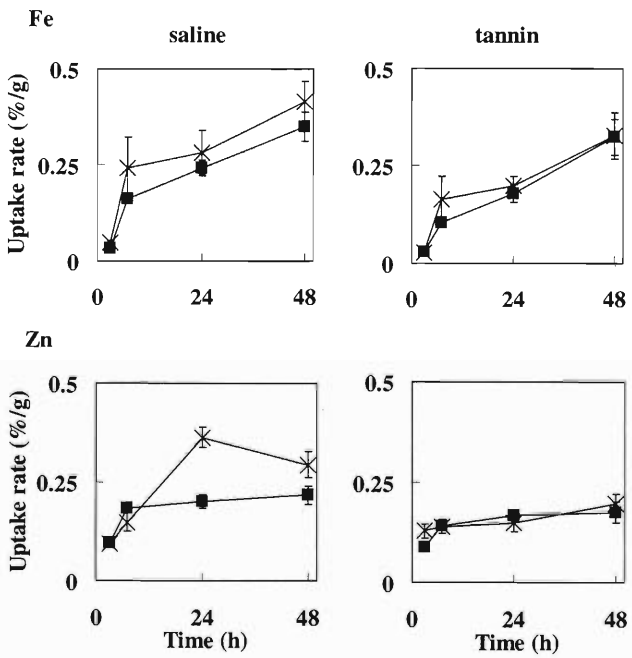

Fig. 1. Uptake rates of Fe and Zn in liver of anemic rats on the FS (×) or the NaFeEDTA (■) diet. Each datum in the figures represents the mean value ± S.E. obtained from at least eight preparations.

* Graduate School of Human Life Sciences, Showa Women's University

NaFeEDTA additive diet. Forty-eight hours after administration, about 22.0% of Fe uptake for the FS diet and about 8.0% of that for the NaFeEDTA diet had decreased. The biodistribution of Zn in anemic rat liver yielded similar results to the Fe uptake. Although Zn uptake for the FS diet was inhibited by 60.0%, that on the NaFeEDTA diet was inhibited by only 16.5% from tannic acid 24 hours after administration. However, the uptake rates of Fe did not show a large difference between the FS and the NaFeEDTA diets with or without tannic acid. Zinc uptake on the FS diet without tannic acid was higher than that on the NaFeEDTA diet without tannic acid 24 and 48 hours after administration. In the case where tannic acid was added, the uptake rates of Zn on the FS and the NaFeEDTA diet had similar levels. These results suggested that NaFeEDTA differed little from FS in the terms of the uptake of Fe with tannic acid and did not affect the uptake of Zn into the liver.

There is great interest in food fortification using NaFeEDTA. The biodistribution of various other elements and other tissues from rats on the FS and the NaFeEDTA diets with or without tannic acid are currently under data analysis. Our results indicate that the multitracer technique is a convenient tool for obtaining information on the behavior of various trace elements in nutritional research.

Study on Distribution of Multitracer in Partially Hepatectomized Rats

A. Nakayama,* H. Yasui,* H. Sakurai,* R. Hirunuma, and S. Enomoto

The multitracer technique has been developed to simultaneously analyze the dynamic behavior of trace elements in animals and plants. In this study, we investigated the effects of liver regeneration on the intestinal absorption and tissue distribution of trace elements in normal rats. The time courses of radioactivity of the multitracers in organs were evaluated using the distribution ratio. Accumulation of trace elements in the tissues significantly changed in the liver and small intestine of partially hepatectomized rats. These results suggest that the liver regeneration may alter the intestinal absorption and hepatic distribution of several trace elements in terms of the requirement of endogenous elements in cell division.

In general, the liver has been considered to function normally owing to its potential ability to maintain homeostasis even if two thirds of it is lost. In addition, the regeneration speed of the liver is so fast that it recovers its normal size within almost 10 days after two thirds of it is removed. In the regeneration period, hepatocytes induce cell division to cover the decreased primal hepatic functions. Since the intestinal absorption of nutrition including trace elements affects protein syntheses in the liver, and nutrients absorbed from the gastrointestinal tract are transferred to the liver through the portal vein, the reduction of the hepatic functions changes the distribution of trace elements in the entire body. Thus, we examined the distribution of essential trace elements in the liver, kidney, and intestines of rats that had been partially hepatectomized by orally administering multitracer elements to elucidate the relationship between the liver regeneration and global disposition of trace elements.

Male Wistar rats (body wt. $\sim$250 g) were divided into three groups; normal, and 1 h or 5 days after the 70% hepatectomy. A multitracer solution containing the radioisotopes of 20 elements was prepared from an Ag target irradiated by a heavy-ion beam of 135 MeV/nucleon accelerated by the RIKEN Ring Cyclotron. The multitracer solution was orally administered to the rats (0.5 ml/rat). The rats were sacrificed 1, 3, and 6 h after the administration, and blood samples were collected and selected organs (liver, kidney, and small intestine) were removed from the rats in each group ($n = 4$). The radioactivity levels in the blood, liver, kidney, and intestine were measured by γ-ray spectrometry. The observed γ-rays were analyzed in terms of their energies and half-lives. The individual behaviors of Be, Na, Ca, Sc, V, Cr, Mn, Fe, Co, Zn, As, Se, Rb, Sr, Y, Zr, Tc, Ru, and Rh were examined. The obtained time courses for the amount of each trace element in each organ were evaluated based on the distribution ratios (% dose/g wet weight of the tissue).

The amounts of the 19 trace elements accumulated in the tissues were simultaneously determined on the basis of the radioactivity. The effects of 70% hepatectomization on the accumulation of the trace elements were marked in the liver and small intestine. Intestinal absorption of Fe and As in hepatectomized rats was enhanced higher than that of normal rats, whereas that of Na and Ca was unchanged between the normal and hepatectomized rats, and that of Zn, Mn, Cr, and V decreased in the hepatectomized rats compared with that of normal rats. In addition, the hepatic uptake of Na, Zn, Se, As, and V significantly increased in the hepatectomized rats. These results suggest that liver regeneration alters the intestinal absorption and hepatic distribution of several trace elements. On the basis of these results, further studies on the relationship between trace element requirements and hepatocyte division will provide important information for analyzing the features of several diseases in terms of trace elements.

* Department of Analytical and Bioinorganic Chemistry, Kyoto Pharmaceutical University

Uptake of Trace Elements in Rat Lens

T. Nabekura,* T. Minami,* R. Hirunuma, S. Enomoto, and Y. Ito*

Transparency is a remarkable and unique characteristic of lenses, and is a basic prerequisite for normal visual acuity. Lens transparency is conditioned by cellular structure, protein structure and constitution and the concentration of electrolytes. To maintain transparency, protective mechanisms, such as glutathione peroxidase and superoxide dismutase, are well developed.

Metals are known to act as activators and/or inhibitors of various enzyme reactions. However, the role of trace elements in lenses has not been fully investigated. The multitracer technique was established at RIKEN and has been successfully applied to many biological systems for comparing the behavior of a number of elements under strictly identical experimental conditions. In the present study, the multitracer technique was applied to the determination of the uptake of trace elements in the lenses of adult and suckling rats.

The radioactive multitracer solution was prepared from silver foil irradiated with a ^{14}N beam of 135 MeV/nucleon from the RIKEN ring cyclotron. Lenses of adult (6-week-old) and suckling (13-day-old) male SD rats were carefully removed by a posterior approach. The lenses were precultured in phosphate-buffered saline (PBS) for consistency at 37 °C under 5% CO_2/95% air atmosphere. After precultivation, the lenses were checked under a microscope, and clear and nondamaged lenses were used in subsequent experiments. The lenses were transferred to 3.9 mL of fresh PBS in 30-mm-diameter dishes. Saline solution (0.1 mL) containing multitracer was added to the medium, and the lenses were cultured at 37 °C under 5% CO_2/95% air atmosphere. The incubation was stopped by removing the lenses from the PBS medium containing multitracer and washing then 3 times in 4 mL of ice-cold PBS. The radioactivities were determined by γ-ray spectrometry using a pure germanium detector. Identification and determination of nuclides were performed on the basis of their energies and half-lives and the peak areas of their γ-ray spectra.

Table 1 shows the uptake of trace elements in adult and suckling rat lenses exposed to multitracer for 4 h. Be, Sc, V, Mn, Fe, Co, As, Se, Rb, Sr, Y, Zr, Ru and Rh were detected. However, uptake rates of trace elements in lenses differed for each element and in adult and suckling rats. Uptake of Se and Rb were higher in the lenses of suckling rats than adult rats (significant different; $p < 0.05$). In contrast, uptake of Sr by adult rat lenses was higher than by suckling rat lenses ($p < 0.05$), and Co and As uptake showed comparable levels in adult and suckling rat lenses ($p > 0.1$). In general, it may be easier for suckling rat lenses to absorb elements from outside, because the barrier function of suckling rat lenses has not fully matured. However, our results showed that some elements were not absorbed by suckling rat lenses to any greater extent. Therefore, uptake of trace elements in rat lenses should be conducted not merely by passive diffusion, but also some specific mechanism of absorption and/or excretion of certain elements. Furthermore, the development affects the transport of trace elements into rat lenses. The present study suggests that different mechanisms, depending on the development, act to transport trace elements into lenses.

Table 1. Uptake of trace elements in adult and suckling rat lenses exposed to multitracer for 4 h.

Element	Adult rat lens (% / mg lens)	Suckling rat lens (% / mg lens)
Be	0.01744±0.0013	0.01398±0.0015
Sc	0.01748±0.0025	0.01340±0.0020
V	0.02017±0.0031	0.01460±0.0020
Mn	0.03380±0.0014	0.02626±0.0031
Fe	0.02153±0.0012	0.01527±0.0019
Co	0.03453±0.0018	0.03320±0.0050
As	0.01702±0.0025	0.01309±0.0013
Se	0.03865±0.0025	0.05009±0.0045
Rb	0.01647±0.0007	0.03156±0.0038
Sr	0.04432±0.0021	0.02222±0.0028
Y	0.01544±0.0021	0.01111±0.0011
Zr	0.01802±0.0032	0.01221±0.0014
Ru	0.04082±0.0016	0.02935±0.0036
Rh	0.03890±0.0022	0.02913±0.0037

Data represent mean ±S.E. of four measurements.

* Kinki University

Effect of Administration Methods of Multitracer Solution on Uptake Rates of Cobalt and Other Trace Elements in Zn-Deficient Mice

T. Ohyama,[*1] T. Yoshida,[*1] H. Maetsu,[*1] M. Noguchi,[*2] H. Suganuma,[*1] R. Hirunuma, S. Enomoto, T. Omori,[*1] and M. Yanaga[*1]

Cobalt is one of the essential trace elements in living organisms. Each male adult contains 1.1 mg of this element. It is absorbed in the intestine and excreted mainly in urine. This element is mainly incorporated into cobalamines, such as vitamin B_{12}, which is an important organic compound for maintaining normal metabolism, growth and functioning as a coenzyme in living organisms.

Previously, we investigated the biobehavior of some essential trace elements, such as Mn, Fe, Co and Zn, in mice using instrumental neutron activation analysis (INAA) and the multitracer technique.[1–6] The results obtained with INAA revealed that Co concentrations in all organs and tissues of Zn-deficient mice (Zn-def. mice) were higher than those of control mice.[1–3,6] The ratio of Co concentrations in various organs and tissues of Zn-def. mice to those of control mice increased until a 3-week treatment period with a Zn-deficient diet from 8 weeks of age and an additional increase in the ratio was not observed in the longer treatment period.[6] We considered that the reason for the increase in the Co concentration in Zn-def. mice was the increase in the Co uptake rate in various organs and tissues. An increase in the Co uptake rate was expected in Zn-def. mice in the less than 3-week treatment period with the Zn-deficient diet. Therefore, the multitracer technique was applied in order to determine the uptake rate of Co and other trace elements in Zn-def. mice which were treated with a Zn-deficient diet for 1 or 3 weeks. However, the results for multitracer experiments did not show a significant difference in the Co uptake rates between Zn-def. mice and control ones.[4,5] In these multitracer experiments, intraperitoneal injection was used as the administration method of multitracer solution into each mouse. The uptake rates obtained by this administration method were not reflective of the change in mucosal functions upon absorption of trace elements in the intestine under a Zn-deficient state. If the increase in the Co concentration in Zn-def. mice depends on the amount of Co absorbed in the intestine, it is necessary to investigate the effect of the administration method on the amount of Co absorbed. Therefore, in the present work, the administration method of multitracer solution was changed to oral administration.

A multitracer solution was prepared from a Ag target irradiated by a heavy-ion beam with 135 MeV/nucleon accelerated by the RIKEN Ring Cyclotron. The multitracer solution for oral administration was adjusted to pH 3 with diluted hydrochloric acid. Other experimental procedures, except for the administration method, were the same as those in our previous works.[4,5]

Figure 1 shows the uptake rates of Zn and Co in various organs and tissues of Zn-def. mice and control ones. As shown in Fig. 1, Co uptake rates of Zn-def. mice were higher than those of control ones. This result showed the increase in the amount of Co absorbed in the intestine in the Zn-deficient state. This may be one of the reasons for the increase in the Co concentration in the Zn-deficient state. On the other hand, Zn uptake rates of Zn-def. mice were also higher than those of control ones. The postulate that Co shares a common intestinal mucosal transport pathway with Fe was reported.[7] In the present case, the result suggests the existence of a common absorption pathway of Zn and Co.

For the other elements, such as Fe and Mn, there were no differences in the uptake rates between Zn-def. mice and control ones. On the other hand, Fe and Mn concentrations of Zn-def. mice were higher than those of control ones in the case of the more than 6-week treatment period with the Zn-deficient diet.[6] In a more severe Zn-deficient state, the change in uptake

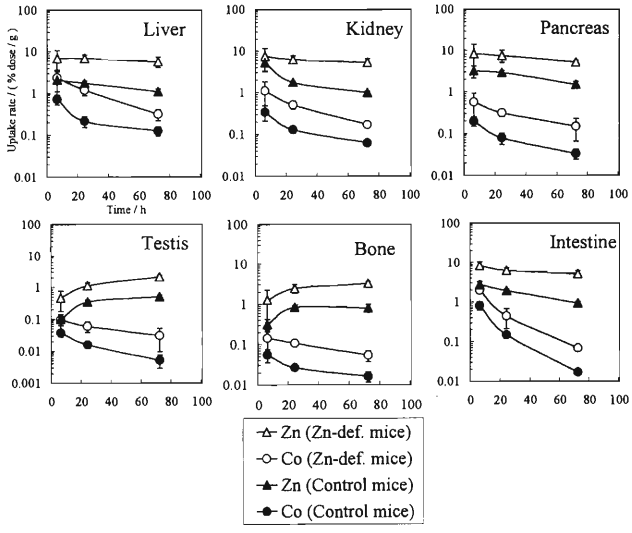

Fig. 1. Zn and Co uptake rates in various organs and tissues after oral administration of multitracer solution (1-week treatment period with Zn-deficient diet).

*1 Radiochemistry Research Laboratory, Faculty of Science, Shizuoka University
*2 Department of Biology and Geosciences, Faculty of Science, Shizuoka University

rates of these elements, such as Mn, Fe and Co, in Zn-def. mice might be observed.

References

1) M. Yanaga, M. Iwama, K. Takiguchi, M. Noguchi, and T. Omori: J. Radioanal. Nucl. Chem. **231**, 187 (1998).
2) M. Yanaga, M. Iwama, K. Shinotsuka, K. Takiguchi, M. Noguchi, and T. Omori: J. Radioanal. Nucl. Chem. **243**, 661 (2000).
3) M. Yanaga, H. Wakasa, T. Yoshida, M. Iwama, K. Shinotsuka, M. Noguchi, and T. Omori: J. Radioanal. Nucl. Chem. **245**, 255 (2000).
4) T. Ohyama, T. Yoshida, M. Iwama, M. Yanaga, M. Noguchi, T. Omori, R. Hirunuma, and S. Enomoto: RIKEN Accel. Prog. Rep. **33**, 118 (2000).
5) T. Ohyama, M. Yanaga, T. Yoshida, H. Maetsu, M. Noguchi, H. Suganuma, T. Omori, R. Hirunuma, and S. Enomoto: J. Radioanal. Nucl. Chem., to be published.
6) M. Yanaga, M. Iwama, T. Yoshida, H. Wakasa, T. Ohyama, M. Noguchi, and T. Omori: to be published.
7) A. B. R. Thomson, L. S. Valberg, and D. G. Sinclair: J. Clin. Invest. **50**, 2384 (1971).

The Absorption of Divalent Cations in Digestive Organs

S. Yoshida,* M. Masuda,* M. Nakayama,* M. Yamasaki,* R. Hirunuma, S. Enomoto, and H. Morikawa*

During pregnancy, the maternal mineral metabolism changes dramatically to satisfy the fetal demand. Intestinal absorption is one of the most essential aspects of mineral metabolism. The purpose of this study is to clarify the principal portion(s) in the intestinal loop responsible for the absorption of calcium and magnesium in a pregnant state.

A multitracer was produced by irradiating a titanium target with a ^{14}N-beam of 135 MeV nucleon from the RIKEN Ring Cyclotron. This contains ^{28}Mg, ^{47}Ca and other radioisotopes. The multitracer solution is dissolved into a buffer solution. Nine-week-old female rats (nonpregnant state and age-matched pregnant rats in the 6th, 13th, 20th day of gestation) were used for the experiment.

The rats were fasted overnight and then anesthetized with pentobarbiturate. Segments of the duodenum, jejunum, ileum and colon of 6 cm length were isolated. Each specimen was everted to prepare a sac with mucosa on the outside. Each gut sac was filled with 600 μl of multitracer solution and then immersed in 10-ml of the buffer solution and incubated with bubbling of 95% O_2 and 5% CO_2 at 37°C for 90 minutes. After incubation, 300 μl of the solution from the serosal side, and 3 ml from the mucosal side were removed. The activity of each tracer in the sample was determined by gamma-ray spectrometry using high-purity Ge detectors. Data were expressed as the S/M ratio (the serosal side content is indecated as S and the mucosal side content as M). An S/M ratio greater than 1.0 can be considered as a mechanism of active transport of the minerals from the mucosal into the serosal side.

The S/M ratio of Ca in the duodenum was significantly greater than 1.0. On the other hand, the S/M ratio of Mg was significantly greater than 1.0 only in the colon, as shown in Figs. 1 and 2. In short, it is suggested that the active transport of Ca from the mucosal side into the serosal side exists only in the duodenum, and that of Mg only in the colon. On the 6th and 13th days of gestation, the S/M ratios of Ca in the duodenum were the same as those in the nonpregnant state. However, on the 20th day of gestation, the S/M ratios in the duodenum increased, which were significantly higher than those in the nonpregnant state. This indicates that the absorption of Ca in the duodenum increases late in the course of pregnancy.

On the other hand, there were no intestinal sites that presented a significant increase of more than 1.0 in the S/M ratio of Mg during gestation. On the 13th and 20th days of gestation, the S/M ratios in the colon were significantly lower than those in the nonpregnant state. These data suggest that the active transport of Mg observed in the colon of nonpregnant rats was not present during gestation.

Other authors[1,2] also reported that the S/M ratio of Ca in the duodenum was greater than 1.0. The S/M ratios in pregnant animals were reported to increase compared with those in nonpregnant subjects.[2] The results of the present study on Ca were consistent with these reports. On the other hand, there are few previous reports about the intestinal absorption of Mg in which the everted gut sac and the single RI tracer

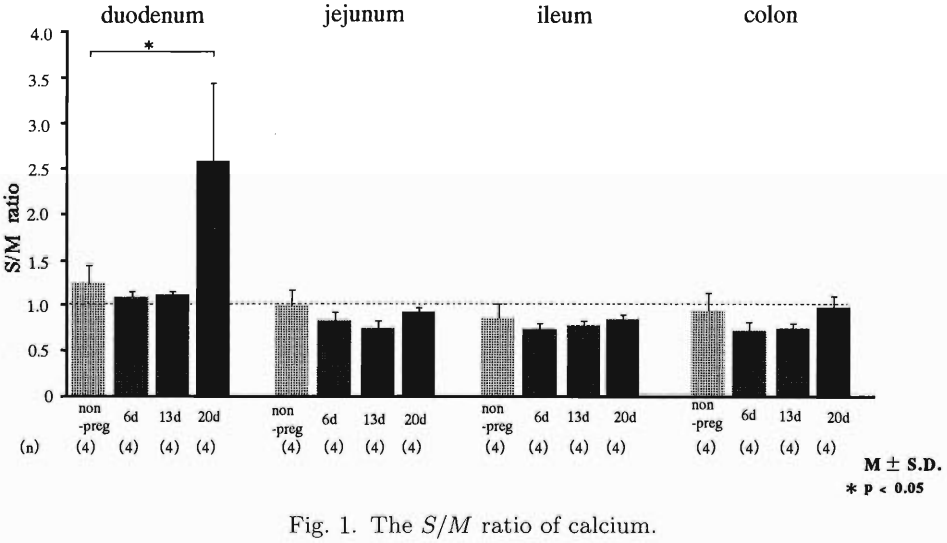

Fig. 1. The S/M ratio of calcium.

* Department of Obstetrics and Gynecology, Nara Medical University

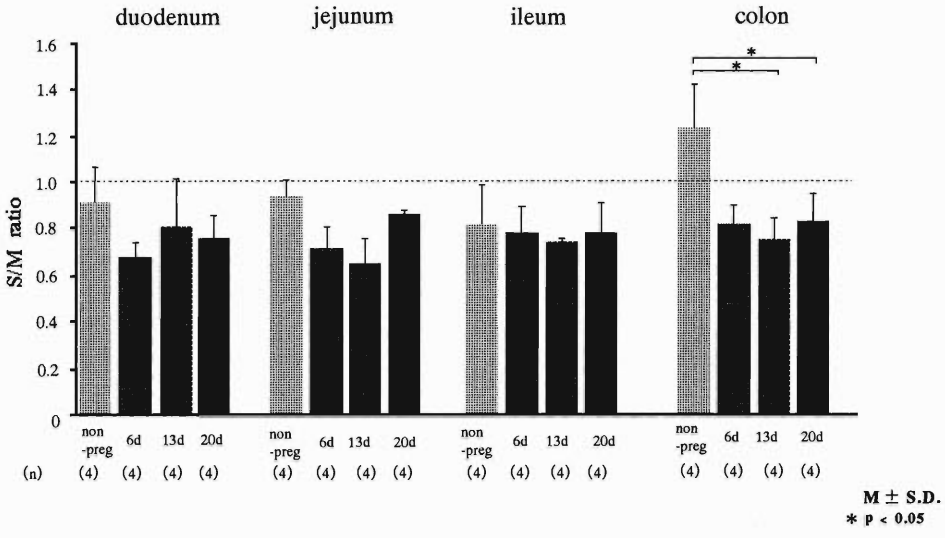

Fig. 2. The S/M ratio of magnesium.

method were used.[3)]

The results of other workers[1–3)] and ours suggest that Mg is absorbed in different segments of the intestine as compared to Ca, and the absorption *via* active transport does not increase during gestation.

In summary, the duodenum is thought to be the principal site for Ca absorption, which showed a significant increase in Ca absorption during pregnancy. The active transport of Mg in the colon may exist in a nonpregnant state, while no such evidence was observed during gestation. The present data suggest that each part of the intestinal loop is responsible for the absorption of a particular cation.

References

1) D. Schachter et al.: Am. J. Physiol. **196**, 357 (1960).
2) K. Takeuchi et al.: Folia Endocrinol. Jpn. **64**, 1175 (1988).
3) L. Hardwick et al.: Am. J. Physiol. **256**, G720 (1990).

Influence of Lanthanum on the Uptake of Various Elements by Marigold

H. Suzuki,[*1] H. Kumagai,[*1] F. Mori,[*2] K. Sakamoto,[*2] K. Inubushi,[*2] and S. Enomoto

More than 20 elements in the periodic table have been detected in plants. C, H, O, N, P, K, S, Mg, Ca, Fe, Mn, Zn, Cu, Cl, B and Mo are currently considered to be essential for all higher plants. Recently, a Research group in China reported on the beneficial effects of small applications of rare-earth elements (REEs) such as La and Ce on the growth of crops in soils of low extractable REEs content.[1] However, the studies conducted by Diatloff and Smith[2] showed that La and Ce was highly toxic to plants. Shinano *et al.*[3] reported that plant growth is related to nutrient uptake ability such as that for N. If the influence of REEs on the uptake of some elements by plants is investigated, it may serve to clarify the role of REEs on plant growth. In this study, the influence of La on the uptake of various elements by plants was studied using the multitracer technique.

Seeds of marigold plants (*Tagetes patula* L. cv. Bonanza spray) sowed in 9-cm pots (240 mL in volume) containing 400 g of river sand applied with (La treatment) or without $La(NO_3)_3$ of 10 μmol La kg^{-1} sand. As the elongation of the root from the marigold seed was seriously affected at La concentrations higher than 50 μmol La kg^{-1} sand, the experiment was carried out at a concentration of 10 μmol La kg^{-1} sand. Plants were grown under biotron with a 16/8 hr day/night regime, 15,000 lux, 65% relative humidity and 25°C. The marigold seedlings were thinned to 1 plant per pot seven days after sowing. Throughout the experiment, the pots were weighed twice a day and watered to 55% of the water holding capacity (WHC) of river sand. The details of the plant nutrient management practice were described in our previous paper.[4]

A multitracer solution was prepared from a Ag target that was irradiated with a 135 MeV/nucleon ^{14}N beam accelerated by the RIKEN Ring Cyclotron. The Ag target was dissolved in HNO_3 and then the Ag was precipitated with HCl as AgCl, leaving another multitracer in solution. The solution was evaporated to dryness, and dissolved in fertilizer solution for the experiments. A multitracer containing the radionuclides of ^{7}Be, ^{22}Na, ^{46}Sc, ^{51}Cr, ^{54}Mn, ^{59}Fe, ^{56}Co, ^{65}Zn, ^{75}Se, ^{83}Rb, ^{85}Sr, ^{88}Y, ^{88}Zr and ^{95m}Tc was applied 29 days after sowing. The chemical forms of the radionuclides on administration were assumed to be Be^{2+}, Na^{+}, Sc^{3+}, Cr^{3+}, Mn^{2+}, Fe^{3+}, Co^{2+}, Zn^{2+}, SeO_3^{2-}, Rb^{+}, Sr^{2+}, Y^{3+}, Zr^{4+}, and TcO_4^{-}.[5] The plants were sampled for analysis 21 days after the multitracer addition. The radioactivities of the plants were measured using Ge semiconductor detectors. The radioactivity applied to the pot was taken as 100% and by comparison, the radioactivity of the plant was expressed as a percentage of the uptake (relative uptake, % of DOSE).

Table 1 shows the relative uptake of radionuclides and the fresh weight by plant. The fresh weight of the aerial parts of marigold was decreased by La application, while the fresh weight of roots was not affected by La application. The relative uptake of ^{7}Be, ^{22}Na, ^{51}Cr, ^{59}Fe, ^{56}Co, ^{65}Zn, ^{85}Sr, ^{88}Y, ^{88}Zr and ^{95m}Tc in La treatment was similar to that in control. The relative uptake of ^{46}Sc in La treatment was larger than that in control, while those of ^{54}Mn, ^{75}Se and ^{83}Rb in La treatment were statistically lower than that in control.

Ishikawa *et al.*[6] reported that La^{3+} impaired the permeability of the plasma membrane of the whole cells in the root-tip portion. Therefore, the uptake of ^{46}Sc, ^{54}Mn, ^{75}Se and ^{83}Rb in La treatment may be affected by the impairment of the permeability of the plasma membrane. As the effect of Rb^{+} and K^{+} on plant absorption is almost the same, the lower uptake of ^{83}Rb in La treatment reveals the inhibition of K uptake by

Table 1. Fresh weight of plant and relative uptake of various radionuclides by plant.[a]

Treatment	Fresh weight (g plant^{-1})		Relative uptake (% of DOSE)													
	A. P.[b]	Root	^{7}Be	^{22}Na	^{46}Sc	^{51}Cr	^{54}Mn	^{59}Fe	^{56}Co	^{65}Zn	^{75}Se	^{83}Rb	^{85}Sr	^{88}Y	^{88}Zr	^{95m}Tc
Control	6.42	3.26	0.1	17.1	1.6	1.2	19.4	1.5	9.8	9.3	22.4	46.9	6.5	2.4	1.2	67.2
La treatment	5.60	2.95	0.1	14.3	2.1	1.6	14.5	1.7	9.9	10.0	18.0	18.5	5.9	2.7	1.3	67.5
Student's t -test[c]	**	n.s.	n.s.	n.s.	*	n.s.	*	n.s.	n.s.	n.s.	*	***	n.s.	n.s.	n.s.	n.s.

[a] Each value is presented as the mean of data from four plants.
[b] Aerial parts: [c] n.s., not significant; *P< 0.05; **P< 0.01; ***P< 0.001.

*1 Radioisotope Research Center, Chiba University
*2 Faculty of Horticulture, Chiba University

La. An example of interference with K^+ transport was also presented by Leonard *et al.*[7] who demonstrated that the short-term influx of ^{86}Rb as a tracer for K^+ into corn root segments was inhibited by $La(NO_3)_3$. Since K and Mn are essential for plant growth, the reduction of the fresh weight of the aerial parts by La application is probably related to the inhibition of Mn and K uptake. However, Se and Sc are not essential for plant growth. Therefore, further study is required to elucidate the relationships among the reduction of the fresh weight of the aerial parts, the increase in ^{46}Sc uptake and the decrease in ^{75}Se uptake by La application.

References

1) P. H. Brown, A. H. Rathjen, R. D. Graham, and D. E. Tribe: in *Handbook on the Physics and Chemistry of Rare Earths*, edited by K. A. Gschneidner, Jr. and L. Eyring, (Elsevier Science, Amsterdam, 1990), p. 423.
2) E. Diatloff and F. W. Smith: J. Plant Nutr. **18**, 1963 (1995).
3) T. Shinano, M. Osaki, S. Yamada, and T. Tadano: Soil Sci. Plant Nutr. **40**, 485 (1994).
4) H. Suzuki, H. Kumagai, K. Oohashi, K. Sakamoto, K. Inubushi, S. Enomoto, and F. Ambe: Soil Sci. Plant Nutr. **46**, 283 (2000).
5) RIKEN Rev., No. 13 (1996).
6) S. Ishikawa, T. Wagatsuma, and T. Ikarashi: Soil Sci. Plant Nutr. **42**, 613 (1996).
7) R. T. Leonard, G. Nagahashi, and W. W. Thomson: Plant Physiol. **55**, 542 (1975).

Chemical Isolation and Purification of ^{95m}Tc from Distilled Waste Fraction during Multitracer Separation of Ag Target

T. Tsuji,[*1] T. Tarohda,[*1] K. Washiyama,[*2] R. Amano, and S. Enomoto

Technetium (Tc) is an artificial radioelement with $Z = 43$. A long-lived ^{99}Tc (2.14×10^5 y) is of great practical importance in the nuclear fuel cycle, and its behavior in the environment requires special consideration.[1] A γ-emitting Tc isotope has been sought for use as a chemical yield tracer for ^{99}Tc (which has only β^--rays and no γ-rays), and can be selected from the following candidates: ^{93}Tc (2.75 h), ^{95}Tc (20 h), ^{95m}Tc (61 d), ^{96}Tc (4.28 d), and ^{99m}Tc (6 h). Some of these candidates exist in the irradiated Ag target during multitracer preparation. The isotope ^{95m}Tc is the most ideal owing to its half-life and its γ-ray energies. In this report, we describe the chemical isolation of ^{95m}Tc and ^{96}Tc from the Ag target irradiated by the RIKEN Ring Cyclotron, and the purification of these isotopes to obtain a pure Tc sample for further instrumental analysis.

Figure 1 shows the flow chart of the process of Tc isolation and purification from a Ag target. A multitracer was obtained from the irradiated Ag target according to the method of Ambe and coworkers.[2–4] Few volatile radioactive species were presented in the multitracer solution to be distilled in the stream of HNO_3 and HCl acid solvent. However, Tc species were transferred with acid distillate into a cooled reservoir. To isolate the Tc species, the distillate (including Tc) was diluted 10 times with pure water, and then the diluted solution was dried on a hot plate under an infrared lamp. The residue was dissolved in pure water, and the resulting solution was poured into an Al_2O_3 column to purify the Tc species. The effluent solution was collected as the purified Tc fraction.

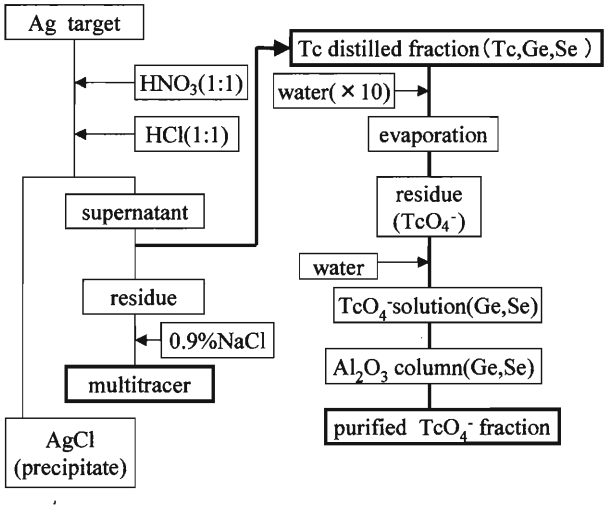

Fig. 1. Flow chart of Tc isolation and purification from irradiated Ag target.

Table 1. The observed γ-emitting nuclides and their activities in Tc fraction and multitracer solution.

Nuclide	Half-Life	γ-Energy (keV)	Branching %	Activity (kBq)
Tc distilled fraction				
^{95m}Tc	61d	582.5	30	8.5
^{96}Tc	4.28d	778.2	99.8	43.2
^{68}Ge	270.8d	1077.4(^{68}Ga)	3(^{68}Ga)	66.4
^{75}Se	119.78d	264.7	58.5	0.9
multitracer solution				
^{7}Be	53.12d	477.6	10.5	1128.7
^{46}Sc	83.79d	1120.5	100	70.9
^{48}V	15.97d	983.5	100	8.8
^{51}Cr	27.7d	320.1	10.1	164.1
^{59}Fe	44.5d	1099.3	56.5	11.9
^{54}Mn	312.3d	834.9	100	90
^{56}Co	77.27d	846.8	100	22.2
^{58}Co	70.86d	810.8	99.5	242.2
^{65}Zn	244.26d	1115.6	50.6	123.9
^{74}As	17.77d	595.8	59	21.9
^{75}Se	119.78d	264.7	58.5	101
^{83}Rb	86.2d	520.4	45	952.9
^{84}Rb	32.77d	881.2	69	109.1
^{85}Sr	64.84d	514	96	1350.9
^{88}Zr	83.4d	392.9	97.2	355.4
^{99}Rh	16.1d	528.2	33	72
^{101m}Rh	4.34d	306.9	94	170.9

(γ-ray measurement was performed on the 20th day after irradiation)

Table 1 shows all of the radionuclides in the Tc fraction and the multitracer solution. The radioactivities of ^{95m}Tc and ^{96}Tc were 8.5 and 43.2 kBq, respectively. The chemical species of the isolated Tc in the distilled (HNO_3+HCl) solution were presumably in the form of $TcCl_7$, which was volatile and transferred with the acid stream into the reservoir. The Tc chemical species were changed to nonvolatile TcO_4^- species by diluting the Tc acid solution 10 times with pure water. Using an Al_2O_3 column, the impurities ^{68}Ge and ^{75}Se were absorbed on Al_2O_3 and removed from the Tc fraction. The final ^{95m}Tc and ^{96}Tc fraction was confirmed to be very high in radionuclidic purity.

*1 Graduate School of Natural Science and Technology, Kanazawa University
*2 School of Health Sciences, Faculty of Medicine, Kanazawa University

References
1) K. H. Lieser: Radiochim. Acta **63**, 5 (1993).
2) S. Ambe et al.: Chem. Lett. **1991**, 149.
3) S. Ambe et al.: Anal. Sci. **7**, Suppl., 317 (1991).
4) S. Ambe et al.: J. Radioanal. Nucl. Chem. **195**, 297 (1995).

Synthesis of Chemical Separator for Metals Produced by the Multitracer Method

Y. Komatsu,* H. Yamada,* M. Sekita,* and S. Enomoto

As multitracer solution has up to 50 elements, a separation technique is very important to separate effective elements for use in medical and biological fields. The layered dihydrogen tetratitanate, $H_2Ti_4O_9{\cdot}nH_2O$, fibres were a useful chemical separator for picking up effective ions in the solution.

The $H_2Ti_4O_9 \cdot nH_2O$ fibres were synthesized from potassium tetratitanate, $K_2Ti_4O_9$, fibres by the flux method. This involved passing hydrochloric acid (1 mol dm^{-3}) through a column to convert $H_2Ti_4O_9$ into layered dihydrogen tetratitanate hydrate fibres. An aqueous standard solution of cobalt(II) ions was prepared by dissolving cobalt(II) chloride in water.

The distribution coefficient, K_d, was calculated as

$$K_d = C_1/\mathrm{g}/(C_2/\mathrm{cm}^3),$$

where C_1 is the amount of adsorbed cobalt(II) ions per 1 g of the solid and C_2 is the concentration of cobalt(II) ions per 1 cm^3 of the aqueous solution.

Figure 1 shows the dependence of the logarithm of the distribution coefficient, K_d, of the layered dihydrogen tetratitanate hydrate fibres on the pH in the aqueous phase for ten different temperatures between 25 and 250°C. In these experiments, the concentration of hydrogen ions in the solid phase was kept constant during the adsorption of cobalt(II) ions. The slopes of the lines for 25°C and 100°C are approximately 2.0. The reaction for the adsorption of cobalt(II) ions to the fibres under these conditions can be expressed by the ion exchange reaction:

$$m\mathrm{Co}^{2+}{}_{(\mathrm{aq})} + \mathrm{H_2Ti_4O_9} \cdot n\mathrm{H_2O}_{(\mathrm{s})} \longrightarrow 2m\mathrm{H}^{+}{}_{(\mathrm{aq})} + \mathrm{Co}_m\mathrm{H}_{2(1-m)}\mathrm{Ti_4O_9} \cdot n\mathrm{H_2O}_{(\mathrm{s})},$$

where the subscripts "aq" and "s" denote the aqueous and solid phases, respectively, and $0 < m < 1$. The slopes of the lines for 125 and 250°C are lower than +2.0, namely, approximately +1.6 at 125–150°C and approximately +1.0 at 175–250°C, respectively.

By plotting $pH_{1/2}$, which is defined as the pH value in the aqueous solution when 50% metal ions was ion exchanged on the fibres, vs. reaction temperatures, the $pH_{1/2}$ values decrease with an increase in the temperature from 25 to 100°C, whereas the values increase with an increase in the temperature from 100 to 250°C. The layered dihydrogen tetratitanate hydrate fibres described above adsorb cobalt(II) ions in aqueous solutions at the temperatures used. This shows that the adsorption of cobalt(II) ions to the fibres is controlled by the original structure of the solids.

* National Institute for Research in Inorganic Materials

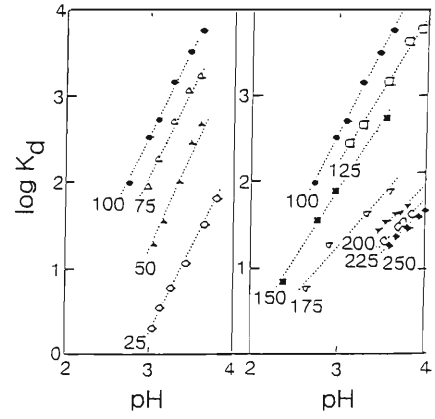

Fig. 1. Distribution coefficient, K_d, of cobalt(II) ions as a function of pH in the aqueous phase at various temperatures.

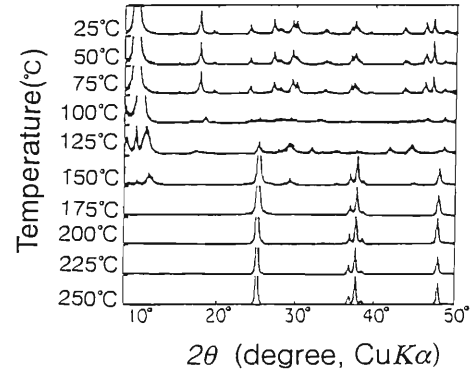

Fig. 2. X-ray powder diffraction patterns of the solid samples treated with aqueous solutions at ten different temperatures.

The dihydrogen tetratitanate hydrate fibres have a layered structure similar to that of potassium tetratitanate.[1] Figure 2 shows the X-ray powder diffraction patterns of the layered dihydrogen tetratitanate hydrate fibres treated with aqueous solution at ten different temperatures between 25 and 250°C. The fibres treated below 100°C show almost the same patterns as the original fibres. This finding indicates that the structure remains virtually unchanged up to 125°C. The solid samples treated at 125–200°C turned powdery, which can be clearly seen in the change of the diffraction patterns as shown in Fig. 2, particularly above 150°C. Based on a detailed analysis of the diffraction patterns, the fibrous structure is changed to anatase and/or these intermediate phases above 125°C which give three peaks in the diffraction pat-

terns. This anatase and/or these intermediate phases are also known to have the capability of adsorbing cobalt(II) ions.

In conclusion, dihydrogen tetratitanate hydrate was synthesized to be capable of adsorbing Co(II) ions from 25 to 250°C. This was applicable to other metal ions when the reaction temperature was 25°C,[1] thus the dihydrogen tetratitanate hydrate can be used as the chemical separator for metals produced by the multi-tracer method.

References

1) T. Sasaki et al.: Sep. Sci. Technol. **18**, 49 (1983).

Ion Exchange Separation of Divalent Metal Ions from Iron (III) through 2,2'-Bipyridyl Complex Formation

Y. Gorai,[*1] Y. Komatsu,[*2] S. Enomoto, and K. Oguma[*1]

The improvement in the selectivity of ion exchange resin to metal ions by complex formation reactions is important and interesting from the standpoint of metal separations as well as the solution chemistry of metal ions. The addition of an organic base to a solution of metal ions, which forms stable complexes with the base added, might prevent the ion exchange adsorption of the metal ions to give lower distribution coefficients (K_d). However, metal ions which do not form complexes with the base added could still give the same distribution coefficients even in the presence of the base. The present study was undertaken to improve the selectivity of iminodiacetate-type chelating resin, Diaion CR 11 (Mitsubishi Chemical Co., Tokyo), to transition-metal ions by the addition of pyridine or 2,2'-bipyridine. These reagents were employed because they are well known to react with various transition-metal ions to form relatively stable complexes. Copper (II), nickel (II), and cobalt (II) in the presence of 2,2'-bipyridine were found to exhibit lower K_d values than those in the absence of 2,2'-bipyridine because of 2,2'-bipyridyl complex formation. Iron (III) gave the same distribution coefficients regardless of the addition of 2,2'-bipyridine.

Distribution coefficients (K_d) were measured by a batch method at 25 °C. A buffer solution containing appropriate amounts of transition-metal ions and Diaion CR 11 in an Erlenmeyer flask was shaken for 24 h and the transition-metal ion in the solution phase was determined by atomic absorption spectrometry or inductively coupled plasma atomic emission spectrometry. The K_d values were calculated using the following equation: K_d = amount of metal on resin (g/g)/ amount of metal in solution (g/ml). The K_d values for transition-metal ions in the media containing pyridine or 2,2'-bipyridine were also calculated in the same manner.

The K_d values for copper (II), nickel (II), cobalt (II), and iron (III) obtained in buffer solutions (without an organic base) are shown in Fig. 1 (A). The selectivity of Diaion CR 11 to transition-metal ions increased with increasing the stability constants of the metal complex with iminodiacetic acid.[1)] The selectivity decreased in the following order: Fe (III) > Cu (II) > Ni (II) > Co (II). The addition of pyridine to the buffer solution did not affect the K_d values of the transition-metal ions tested. This is because pyridine reacts with the transition-metal ions to form complexes of low-

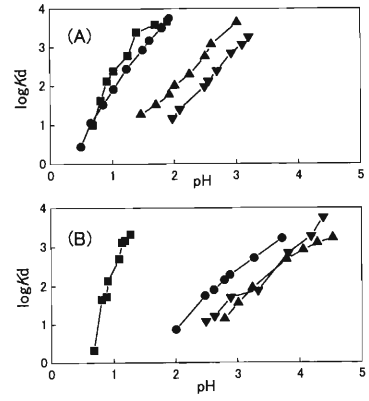

Fig. 1. Distribution coefficients for transition-metal ions on Diaion CR 11 in the absence (A) and presence (B) of 2,2'-bipyridine (10^{-2} M). ■ Fe(III), ● Cu(II), ▲ Ni(II), ▼ Co(II).

stability constants. On the other hand, the presence of 2,2'-bipyridine (10^{-2} M) shifted the adsorption curves of copper (II), nickel (II), and cobalt (II) to the higher pH region (see Fig. 1 (B)). These transition-metal ions are known to form stable 2,2'-bipyridyl complexes[1)] and their adsorption on Diaion CR 11 might be prevented by the presence of 2,2'-bipyridine. Iron (III) does not form stable complexes with 2,2'-bipyridine and its K_d value was not affected by the addition of 2,2'-bipyridine to the buffer solutions.

The selectivity of Diaion CR 11 towards iron (III) was improved by the addition of 2,2'-bipyridine to the buffer solution as described above. Therefore, the separation of iron (III) from copper (II), nickel (II) or cobalt (II) was attempted using CR 11 in combination with the buffer solution (pH 1.3) containing 10^{-2} M 2,2'-bipyridine. A sample solution containing iron (III) and copper (II) (or nickel (II)) was loaded on a Diaion CR 11 column to retain iron (III) on the column. Copper (II) (or nickel (II)) passed through the column and was determined by atomic absorption spectrometry. Iron (III) adsorbed on the column was quantitatively recovered by elution with 1 M hydrochloric acid.

Cobalt (II) reduced iron (III) to iron (II) in the presence of 2,2'-bipyridine, and iron (II) passed through the Diaion CR 11 column as a 2,2'-bipyridyl complex as did copper (II) and nickel (II). Accordingly, it was impossible to separate iron (III) from cobalt (II).

*1 Department of Materials Technology, Faculty of Engineering, Chiba University
*2 National Institute for Research in Inorganic Materials

References

1) L. G. Sillen and A. E. Martell: *Stability Constants of Metal-Ion Complexes* (Chemical Society, London, 1971).

Ion-Size-Selective Masking Effect in Metal Ion Separation

S. Umetani,[*1] S. Tsurubou,[*2] Y. Komatsu,[*3] and S. Enomoto

Application of a masking effect to the solvent extraction method is an effective means for selective separation of metal ions. In the solvent extraction of alkali, alkaline-earth and lanthanide metal ions using chelating reagents, metal ions with small ionic radii exhibit high extractability. On the other hand, the stability of complex formation between macrocyclic ionophores and the above-mentioned metal ions exhibits a different tendency. A solvent extraction system of high selectivity could possibly be developed by the combination of chelating reagents and macrocyclic ionophores. 18-Crown-6 and cryptand [2.2.2] have been shown to be useful ion-size-selective masking reagents in the synergistic extraction of alkaline earths into cyclohexane using 1-phenyl-3-methyl-4-benzoyl-5-pyrazolone (HPMBP) and tri-n-octylphosphine oxide (TOPO).[1–4] In the present study, a novel macrocycle application is proposed.

Extraction of alkaline earth metals in the presence of 18-crown-6. Alkaline earth metals were extracted into cyclohexane using 0.05 M HPMBP and 0.01 M TOPO in the order Mg > Ca > Sr > Ba, which is the order of decreasing ionic radius.[1,2] When 0.03 M 18-crown-6 was added to the aqueous phase, the extractions were carried out in the high pH region. The larger the ionic radius, the higher the pH region the extraction moved to. As a result, the separation among alkaline earth metals, particularly for Ca/Sr and Sr/Ba, has been improved. It is clear that 18-crown-6 works as an ion-size-selective masking reagent in the aqueous phase.

In the synergistic extraction of alkaline earths (M^{2+}) using HPMBP (HA) and TOPO (L), the extraction equilibrium and the extraction constant, $K_{ex,s}$, can be written as follows:

$$M^{2+} + 2HA_o + sL_o = MA_2L_{s,o} + 2H^+ \quad (1)$$

$$K_{ex,s} = D[H^+]^2/[HA]_o^2[L]_o^s, \quad (2)$$

where the subscript o denotes the species in the organic phase and D is defined as $[MA_2L_s]_o/[M^{2+}]$.

The distribution ratio in the presence of 18-crown-6 (CE), D^*, can be expressed by Eq. (3).

$$D^* = [MA_2L_s]_o/\{[M^{2+}] + [M(CE)^{2+}]\} = K_{ex,s}[HA]_o^2[L]_o^s/[H^+]^2\{1 + \beta[CE]\} \quad (3)$$

The separation factor in the absence of crown ether, SF, between two metal ions, M1 and M2, is defined as the difference in the logarithmic value of the respective distribution ratios.

$$SF = \log (D_{M1}/D_{M2} = \log(K_{ex,s,M1}/K_{ex,s,M2}) \quad (4)$$

The separation factor in the presence of crown ether, SF^* {(defined as $\log(D^*_{M1}/D^*_{M2})$}, is expressed as Eq. (5) when s1 and s2 are the same and [CE] is sufficiently high.

$$SF^* = \log (K_{ex,s,M1}/K_{ex,s,M2})(\beta_{M2}/\beta_{M1}) \quad (5)$$

Comparing Eqs. (5) and (6), the separation factor can be improved by as much as β_{M2}/β_{M1}. Separation factors in the presence and absence of crown ether are shown in Ref. 2.

Extraction of alkaline earth metals in the presence of cryptand [2.2.2]. Diazapolyoxabicyclic ligands (cryptands) exhibit a prominent selectivity for alkali and alkaline earth metals. They are soluble in water and their stability in complex formation is sufficiently high for use as a practical masking reagent. Incorporating nitrogen as an element constituting the ring structure, the masking effect of cryptands depends on pH, unlike in the case of crown ethers such as 18-crown-6.[3,4] The extraction using 0.01 M HPMBP and 0.01 M TOPO into cyclohexane in the absence and presence of 0.01 M cryptand [2.2.2] has been examined. The extraction behaviors for Mg and Ca in the presence of cryptand [2.2.2] are quite similar to those in the absence of cryptand [2.2.2]. The log D values for Sr in the presence of cryptand [2.2.2] begin to decrease above pH 5. The log D values for Ba in the presence of cryptand [2.2.2] deviate from those in the absence of cryptand [2.2.2] above pH 4.5.

In order to establish the quantitative extraction-separation system for Ca and Sr, the extraction was carried out at reduced HPMBP and TOPO concentrations of 4×10^{-3} M, keeping the initial concentration of cryptand at 0.01 M. The distribution ratio of Sr decreases rapidly above pH 5.6 as expected, while that of Ca still increases by pH 7.5. Calcium can be separated from Sr quantitatively in the pH range of 7.2 to 8.6 where more than 99% Ca ($\log D > 2$) is extracted into cyclohexane, while more than 99% Sr ($\log D < -2$) remains in the aqueous phase at the same time. Careful control of pH at 7.8 could lead to the most optimum separation: 99.9% extraction of Ca ($\log D > 3$) with 99.9% of Sr ($\log D < -3$) remaining in the aqueous phase.[3]

*1 Institute for Chemical Research, Kyoto University
*2 Department of Chemistry, Asahi University
*3 National Institute for Research in Inorganic Materials

References

1) S. Umetani, M. Matsui, and S. Tsurubou: J. Chem. Soc., Chem. Commun. **1993**, 914.
2) S. Tsurubou, M. Mizutani, Y. Kadota, T. Yamamoto, S. Umetani, T. Sasaki, Q. T. H. Le, and M. Matsui: Anal. Chem. **67**, 1465 (1995).

3) T. Sasaki, S. Umetani, M. Matsui, and S. Tsurubou: Chem. Lett. **1994**, 1195.

4) S. Tsurubou, S. Umetani, and Y. Komatsu: Anal. Chim. Acta **394**, 317 (1999).

Multitracer Study on the Diffusion of Various Ions in the Porewater of Granite

C. Egawa,* Y. Takahashi,* S. Enomoto, R. Hirunuma, and H. Shimizu*

The presence of various elements in micropores of rocks introduced by diffusion of groundwater should be quantified from various environmental aspects. After high-level radioactive waste is disposed of in a deep underground repository, it is possible that some radionuclides are leached from the waste and transported through the surrounding rocks by groundwater.[1] The diffusion also influences dispersal of toxic metals entering the environment as a result of more general human activity such as industrial installation. For evaluating the transport of these elements in the geosphere, it is important to understand the diffusion behavior of the elements introduced in to rocks by groundwater. In this study, diffusion experiments were conducted using a multitracer containing 14 radioisotopes (^{7}Be, ^{48}V, ^{51}Cr, ^{54}Mn, ^{58}Co, ^{59}Fe, ^{65}Zn, ^{74}As, ^{75}Se, ^{83}Rb, ^{85}Sr, ^{88}Y, ^{88}Zr, and ^{103}Ru) to discuss the relationship between differences in the chemical characteristics of these elements and their diffusion behavior.

The apparent effective diffusivity (De) was determined by the through-diffusion method.[2] Granite samples from drilling cores of the Toki granitic rocks (from central Japan) were cut into 5-mm-thick and 30-mm-diameter disks. Each disk was fitted tightly between two cells (volume: 100 cm^3) filled with water (pH 4, NaCl 0.10 M). The multitracer solution prepared from a Ag target was injected into one cell. Radioactivities of the nuclides transported into the other cell were determined using a Ge detector after various time intervals.

Diffusion curves were obtained for two granite samples: a fresh one and a weathered one (Fig. 1). Among the 14 elements studied, the diffusions of Be, Mn, Co, Zn, Se, Rb, Sr, and Y were observed for the weathered granite sample (Fig. 1 (a)). For the fresh granite sample, only the diffusions of Mn, Se, Rb, and Sr were observed (Fig. 1 (b)). The difference may be due to the larger porosity (ε) of the weathered granite (1.0%) than of the fresh one (0.42%). The diffusion curve was fitted by Fick's equation to obtain De values. The De for each element was plotted against the bulk diffusivity in aqueous solution (Dv), as shown in Fig. 2. The De values for Rb, Sr, Zn, Co, and Mn were plotted close to a line indicated by

$$\mathrm{De} = \varepsilon \mathrm{Dv} \tag{1}$$

for both fresh and weathered granites. This result is worthy of note, since the diffusions of various elements in the porewater of granite can be approximately formulated using Dv by such a simple relation. From autoradiography analysis, diffusion pathways were found in grain boundaries and cleavages of biotites and pla-

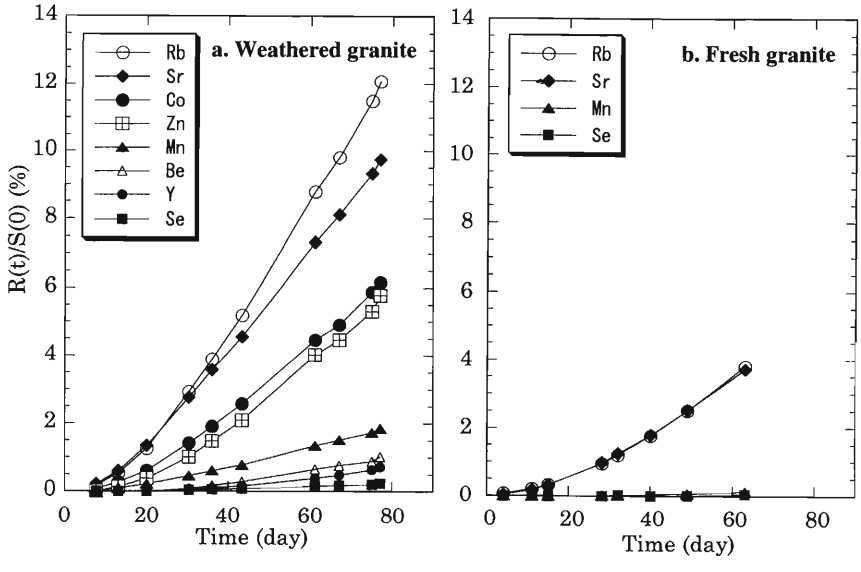

Fig. 1. Diffusion curves through a 5-mm-thick granite disk for (a) weathered and (b) fresh granite. The y axis shows the concentration ratio of each element in the diffusion cell to the initial concentration in the tracer cell.

* Department of Earth and Planetary Systems Science, Graduate School of Science, Hiroshima University

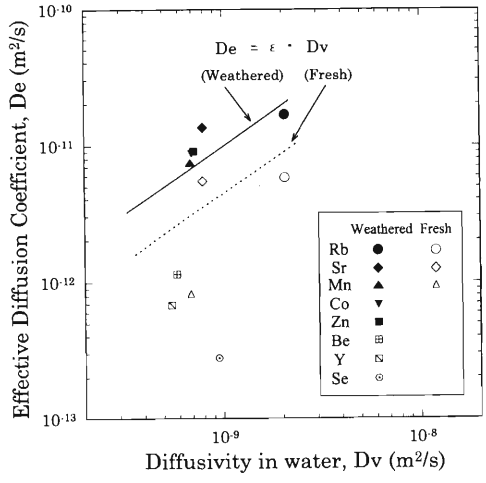

Fig. 2. Relationship between effective diffusion coefficients (De) and diffusion coefficients at infinite dilution in aqueous solution (Dv) for various ions in weathered and fresh granite.

gioclases in the granite. This is consistent with the finding that the diffusion was mainly controlled by the porosity. Biotite separated from the granite using a magnetic separator was employed for batch sorption experiments. The amounts of sorbed Be and Y were larger than those of Rb, Sr, Zn, Co, and Mn. This implies that Be and Y were not diffused through porewater, but through the Donnan phase in the vicinity of the mineral surfaces. This mode of diffusion is referred to as "surface diffusion".[3)]

No diffusion of V, Cr, Fe, As, Zr, or Ru was observed. This can be attributed to two factors: (1) the slow diffusion rate of the elements and (2) the strong affinity of the elements on the mineral surface. From batch experiments, the sorbed fraction of As was less than those of Be and Y which were transported into the other cell. This finding eliminates the second factor as the cause of the lack of diffusion of As. Hence, it is implied that the diffusion rate of As is slow compared with those of other ions such as Be and Y. Under our experimental conditions, As forms oxyanions such as $As(III)O_3^{3-}$ or $As(V)O_4^{3-}$. The present results suggest that the diffusions of the oxyanions are slower in the porewater than those of other cations having similar Dv to these anions. This seems also valid for explaining the slower De of Se, which forms SeO_3^{2-} or SeO_4^{2-}, than those calculated using Eq. (1). For Cr, Fe, and Zr, the batch experiments showed that most of them were sorbed on the biotite surfaces, indicating that the reason the diffusions of these ions were not observed was because of the second factor (*i.e.*, strong affinity for the mineral surface).

References

1) D. G. Brookins: *Geochemical Aspects of Radioactive Waste Disposal* (Springler-Verlag, New York, 1984).
2) T. Yamaguchi and S. Nakayama: J. Contam. Hydrol. **35**, 55 (1998).
3) T. Cole, G. Bidoglio, M. Soupioni, M. O'Gorman, and N. Gibson: Geochim. Cosmochim. Acta **64**, 385 (2000).

Development of New Multitracer with Neutron Fission of ^{235}U

A. Shinohara, S. Shibata, K. Takamiya,* and S. Enomoto

The Division of Radioisotope Technology is preparing multitracer solutions with heavy-ion reactions using the RIKEN Ring Cyclotron (RRC), and providing them to scientists in the various research fields, such as, pharmaceutical, biological and environmental sciences. A multitracer is a tracer solution containing multiple radioactive isotopes without carrier materials. The preparation method was developed by Ambe and coworkers[1–3] at RIKEN approximately ten years ago. However, the available elements are limited by their own half-lives and reaction yields. Therefore, another method of preparing multitracers containing radioactive isotopes, which cannot be produced by heavy-ion reactions, is urgently required. We attempted to prepare a multitracer by the thermal neutron-induced fission of ^{235}U because in nuclear fission, neutron-rich isotopes are produced in relatively high amounts in comparison with charged-particle-induced reaction. In this paper, we report on the preparation of a multitracer by the thermal neutron-induced fission of ^{235}U at Kyoto University Reactor (KUR).[4]

A mixture of $^{nat}UO_2$ and catcher material, in which the fission products recoiled out from the UO_2 were captured, was irradiated by thermal neutrons in KUR. In order to prepare the multitracer solution efficiently, the following parameters for the sample preparation were investigated: (1) catcher material, (2) mixing ratio of UO_2 to catcher material, (3) particle size of the catcher material, and (4) sample shape for irradiation. The samples prepared were irradiated using the pneumatic transferring system (Pn-2) at KUR. The content of the samples and the irradiation times are tabulated in Table 1. The fission products captured by the catcher material dissolved in 0.1 N HCl, while the UO_2 did not. The solution containing fission products was filtered with suction to separate UO_2. Gamma rays from an aliquot of the solution and the UO_2 on the filter paper were measured using a Ge detector to obtain the yields of the products. The capturing efficiency of fission products by catcher materials was evaluated with the ratio of the yield for each product nuclide captured in catcher materials to the total yield.

Figure 1 shows the mean capturing efficiency for each sample as a function of the weights ratio of $W_{catcher}/W_{total}$, where $W_{catcher}$ and W_{total} are the weight of the catcher material and the sample, respectively. The sample mixed with NaCl as a catcher material is efficient for preparing multitracer solutions.

The multitracer solutions prepared above were extensively used for biological research to trace the element distribution in mice. In this research, the multitracer solutions obtained from the sample containing NaCl are particularly suitable, because this physiological salt solution can easily be prepared. Besides biological research, applications to environmental, pharmaceutical and cytological sciences are now being planned.

We are also planning to prepare a new multitracer

Table 1. Contents of irradiated samples.

Catcher Material	Form	Weight /mg UO_2:Catcher	Irrad. Time
NaCl	Powder (coarse)	0.95:2.95	10min
		1.12:9.68	1min
		1.06:29.74	1min
	Powder (fine)	1.09:1.11	5min
		1.07:3.33	5min
		1.05:29.45	1min
	Pellet	5.12:5.18	2min
		2.48:7.72	2min
		1.25:10.85	5min
		0.37:10.43	2min
$MgCl_2$	Powder (fine)	1.00:29.61	5min
LiF	Powder (fine)	0.90:9.60	5min

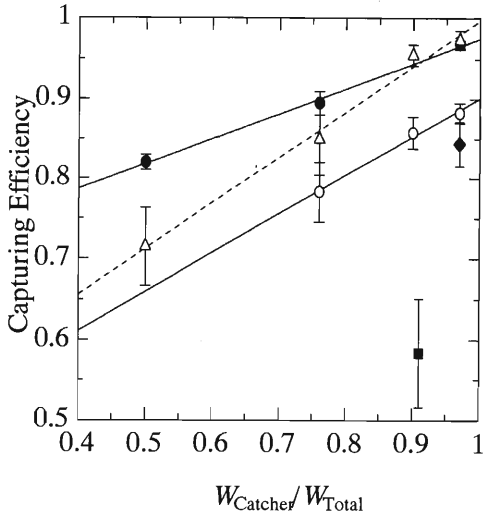

Fig. 1. The mean capturing efficiency for each sample correlated with the weight ratio $W_{catcher}/W_{total}$. Open and closed circles indicate the efficiencies obtained for coarse and fine powder samples with NaCl as the catcher material, respectively. Square and diamond are those with LiF and $MgCl_2$, respectively. The efficiencies obtained for pellet samples with NaCl are also indicated as triangles. Solid and dashed lines indicate the results of the least-squares fitting for the mean efficiencies of powder and pellet samples with NaCl, respectively.

* Research Reactor Institute, Kyoto University

containing short-lived isotopes with KUR or RRC. A new target system containing both the target and catcher materials and a rapid on-line chemical apparatus will be designed for this purpose.

References

1) S. Ambe, S. Y. Chen, Y. Ohkubo, Y. Kobayashi, M. Iwamoto, M. Yanokura, and F. Ambe: Chem. Lett. **1991**, 149.
2) F. Ambe: RIKEN Rev., No. 4, 31 (1994).
3) S. Ambe, S. Y. Chen, Y. Ohkubo, Y. Kobayashi, H. Maeda, M. Iwamoto, M. Yanokura, N. Takematsu, and F. Ambe: J. Radioanal. Nucl. Chem. **195**, 297 (1995).
4) K. Takamiya, M. Akamine, S. Shibata, A. Toyoshima, Y. Kasamatsu, and A. Shinohara: J. Nucl. Radiochem. Sci. **1**, 81 (2000).

Compton Camera for Multitracer

Y. Yang,* S. Motomura,* Y. Gono,* S. Enomoto, Y. Yano, and K. Asahi

In the multitracer technology, many radioisotopes are used simultaneously. Therefore, for a detection system to identify the positions of many tracers, it is necessary to measure the gamma ray energy spectrum with a high energy resolution. Although Compton cameras for single photon imaging consisting of a segmented Ge detector and scintillitors have been proposed for years,[1] it is necessary to use two segmented Ge detectors for multitracer technology. The advantages of a Compton camera over a conventional mechanically collimated gamma camera are a wide field of view, high efficiency, and high image resolution at high gamma ray energy.

Monte-Carlo simulations were performed with the GEANT program to determine the efficiency and resolution of the proposed Compton camera as well as to optimize its detector system. The dependence of the efficiency on gamma ray energy and the distributions of the number of scattering of gamma rays in two segmented Ge detectors were also simulated.[2] The following conclusions were reached. The optimum thicknesses of the first detector and the second detector were 1 cm and from 2 cm to 4 cm, respectively. The optimum distance between the two detectors was about 8 cm in the case when the distance between the source and the first detector was 6 cm. Large areas for the two detectors were preferred. The optimum ratio of the area of the first detector to that of the second detector was about 2/3. A Compton camera can operate for a wide energy range of gamma rays. In a Compton camera, only when gamma rays undergo Compton scattering in the first detector and then the scattered gamma rays are fully absorbed in the second detector can these events be used for image reconstruction. These events are defined as good events. The probability of multiple scattering of 1.332 MeV gamma rays in a 2 cm-thick Ge first detector is about 50 percent for good events. If multiple scattering occurs in more than one segment of the first detector, more than one segment give signals, thus the event can be removed from the coincident events and will not contribute to the background of the image. If multiple scattering occurs within one segment of the first detector, the event cannot be distinguished from single scattering events and will contribute to the background of the image. The probability of multiple scattering of 1.332 MeV gamma rays in a 2 cm-thick Ge second detector is about 90 percent for good events. The average multiplicity is 3. The multiple scattering events occurring within one segment can be directly used for image reconstruction. If multiple scattering occurs in more than one segment, the event can be removed from the total coincident events, which lowers the efficiency. If a tracking algorithm is used to identify the interaction order, some of those events may be tracked and used for image reconstruction.

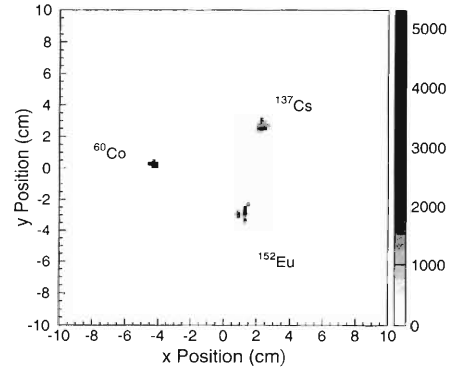

Fig. 1. Two dimensional-image of three sources.

A test experiment was performed using a Compton camera consisting of two existing segmented Ge detectors. Each detector is a planar-type Ge detector of $50 \times 50 \times 20\,\mathrm{mm}^3$ segmented by an electrode into 25 segments of an equal size of $10 \times 10 \times 20\,\mathrm{mm}^3$. Two detectors were placed in parallel and the distance between their centers was 6 cm. Three sources of ^{60}Co, ^{137}Cs, and ^{152}Eu were placed in a plane perpendicular to the center axis of the Compton camera. The distance from the source plane to the center of the first detector was also 6 cm. Only seven segments of the first detector and nine segments of the second detector were used in the experiment due to the availability of the electronic modules. By setting energy windows on the peaks of three sources in the measured gamma ray energy spectrum, two-dimensional images can be obtained. Figure 1 shows the identified positions of three sources. It is seen that the present system functions in a manner suitable for multitracer technology.

As the next step, we plan to develop a Compton camera consisting of two strip Ge detectors. A much better image resolution is expected through the use of this Compton camera. The cost of electronics can also be greatly reduced compared with a Compton camera consisting of two segmented Ge detectors if the segment size is the same as the strip width.

* Department of Physics, Kyushu University

References

1) M. Singh and R. R. Brechner: J. Nucl. Med. **31**, 178 (1990), and references therein.
2) Y. F. Yang, Y. Gono, S. Motomura, S. Enomoto, and Y. Yano: accepted for publication IEEE Trans. Nucl. Sci. (2001).

Separation of ^{18}F from [^{18}O] Water by Electrochemical Method

F. Saito, Y. Nagashima,[*1] T. Kurihara,[*2] N. Suzuki, J. Kim, L. Wei, Y. Itoh, A. Goto, and T. Hyodo[*1]

^{18}F produced from $H_2{}^{18}O$ water irradiated by a proton beam from a cyclotron is widely used in the synthesis of radiopharmaceuticals for PET (positron emission tomography). The ^{18}F is usually separated from the $H_2{}^{18}O$ water before synthesis in order to enable to the use of the $H_2{}^{18}O$ water repeatedly. In this process, the efficiency of the recovery of the ^{18}F as well as the efficiency of the synthesis of radiopharmaceuticals is essential. Currently, ion-exchange resins or fibers are used. Although they are efficient, the preparation of the ion-exchange resins is complex, and residual organic solvent decreases the efficiency of the synthesis of the ^{18}F-labelled chemicals. As a result, the $H_2{}^{18}O$ water is able to be reused only a few times.

We investigated an electrochemical method which was developed for producing a ^{18}F spot source of slow positron beams from $H_2{}^{18}O$ water to separate the ^{18}F from the $H_2{}^{18}O$ water.[1,2] The ^{18}F in the solution was electrodeposited on a graphite rod and then emitted into the ultrapure water in a different cell (Fig. 1 (a)). The PC controlled electrodeposition apparatus (Fig. 1 (b)) has been reported elsewhere.

The ^{18}F of the activities 150–227 mCi (5.55–8.40 GBq) was electrodeposited on a 10 mm ϕ graphite rod with electrodeposition voltage of 200 V, and then emitted into the ultrapure water with an electroemission voltage of 250 V. The efficiency of the electrodeposition for 5 min and the fraction of ^{18}F emitted into the ultrapure water for 5 min were 97% and 89%, respectively. Thus, as much as 86% of the ^{18}F in the $H_2{}^{18}O$ water is available for the synthesis of radiopharmaceuticals for PET.

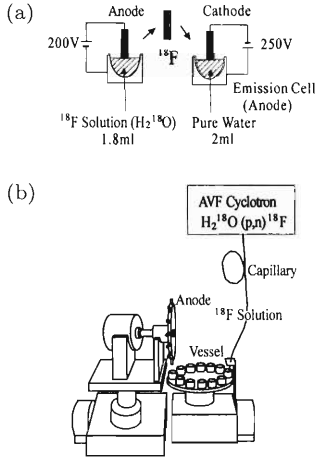

Fig. 1. (a) Diagram of a graphite rod and a platinum cell for electrodeposition and electroemission. (b) PC-controlled electrodeposition apparatus.

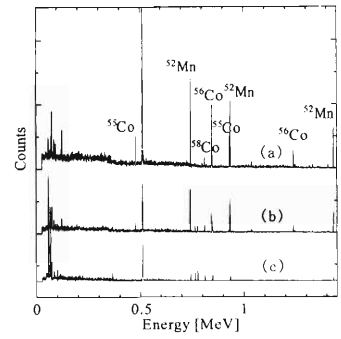

Fig. 2. The energy spectra of γ-rays from the impurity metal RI ions in (a) the residual $H_2{}^{18}O$ water, (b) the graphite rod, and (c) the recovered ^{18}F solution, normalized to the measurement time.

The β^+ emitted from the ^{18}F ionized the H_2O molecules and produced many charge carriers, as a result, the electric conductivity of the ^{18}F solution became higher. Therefore, no charge carrier of ^{19}F was added either to the $H_2{}^{18}O$ target for the electrodeposition or to the pure water for the electroemission. The recovered $H_2{}^{18}O$ water without carrier impurity is much more easily reused than that containing carrier impurity.

The presence of metal ions in the ^{18}F solution affects the yields of the synthesis of [^{18}F] radiopharmaceuticals. Figure 2 shows the γ-ray emission spectra from (a) the residual $H_2{}^{18}O$ water, (b) the graphite rod and (c) the recovered ^{18}F solution. The peaks of the impurity metal ions such as ^{52}Mn, ^{56}Co, ^{57}Co and ^{58}Co in the spectrum of the recovered ^{18}F solution are low, because most of the ions remain in the residual $H_2{}^{18}O$ water. These metal ions were produced by the bombardment of protons on the Harvar foil used for the target holder and recoiled into the $H_2{}^{18}O$ water. Therefore, the metal ions dissolved in the target $H_2{}^{18}O$ water must be efficiently removed from the recovered ^{18}F solution.

In conclusion, this method is promising for routine applications where numerous high-purity fluorides must be produced.

*1 Department of Basic Sciences, Graduate School of Arts and Science, University of Tokyo
*2 Institute of Materials Structure Science (IMSS), High Energy Accelerator Research Organization (KEK)

References

1) F. Saito, Y. Nagashima, T. Kurihara, I. Fujiwara, R. Iwata, N. Suzuki, Y. Itoh, A. Goto, and T. Hyodo: Nucl. Instrum. Methods Phys. Res. A **450**, 491 (2000).
2) F. Saito, N. Suzuki, Y. Itoh, A. Goto, I. Fujiwara, T. Kurihara, R. Iwata, Y. Nagashima, and T. Hyodo: Rad. Phys. Chem. **52**, 755 (2000).

4. Radiation Chemistry and Radiation Biology

Dynamics of Incipient Ion Tracks in Wide-Band-Gap Materials: Electron-Hole Plasma Luminescence from Ion Tracks and Initiation of Defect Formation

K. Kimura, S. Sharma, and A. Popov

We found novel ultra-fast luminescence decay component (UFLDC) from the track core in a number of wide-band-gap materials, by measuring fast luminescence decay and time-resolved spectrum (TRS).[1] Samples used were NaF, LiF, NaCl, KCl, CsCl, KBr, KI, RbI, CsI, BaF_2, MgO, and α-alumina. Thus, the UFLDC appears to be a common phenomenon in wide-band-gap materials except for some kinds of materials such as diamonds and SiO_2. An example, Fig. 1, is an equi-height plot of wavelength-dependent decay curves of an RbI single crystal irradiated with Xe-ions at 6 K. One may recognize the UFLDC in both sides of slower decays at 320 nm due to the σ-self-trapped exciton (STE); σ-band is known to have the lifetime of 3 ns. TRS's were able to be obtained based on Fig. 1 replotted with photons/ion. Consequently, the UFLDC was characterized by the lifetime of 30 ps (by deconvolution), the peak at 4 eV, and the width, 1.5 eV, which are quite different from the known bands.

The UFLDC was largely affected by excitation density (ED). Figure 2 shows the specific intensity of the UFLDC as a function of ED's due to 2.0 MeV/nucleon He-, N-, Ar-, Kr-, and Xe-ions. At this energy, the ion track is dominantly comprised of the core part. Equal ion velocities give nearly equal track radii for the above five ions. Consequently, we can estimate relative ED without the value of the radius. Now, the UFLDC increases largely with increasing ED and moreover its rate is super-linear. This indicates that the UFLDC originates from the multiple interactions among the excited precursors. Considering non-tailing decay curves and their temperature-insensitivity, the precursors must be short-lived similarly to the UFLDC and hence they are limited to electron-hole pairs (e-h pairs) or free excitons. The e-h pairs can be formed so densely here as to exist adjacently since ED for a Xe ion attains 200–600 eV/atom. Adjacent e-h pairs can combine immediately, as are adjacent H atoms, to form electron-hole plasmas. Such bindings give rise to gigantic oscillator strength.[2] The UFLDC may be ascribed to e-h plasma luminescence.

The large shift of the UFLDC from the band gap, quite different from the e-h plasma in semiconductors, is interesting and may be caused by the ion track. Electrons ejected by an ion expand toward radial direction of the ion trajectory, lose the energy, and return back to the holes, which takes 10^{-14}–10^{-13} s. During this period, the dense positive ions and atoms not only lose the binding for the crystal but also they are put under

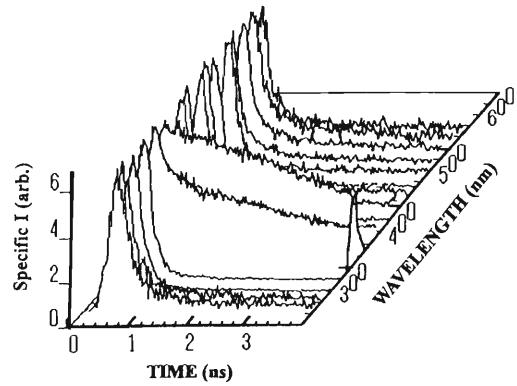

Fig. 1. Wavelength dependent equi-height decay curves of RbI under irradiation with Xe-ions at 6 K.

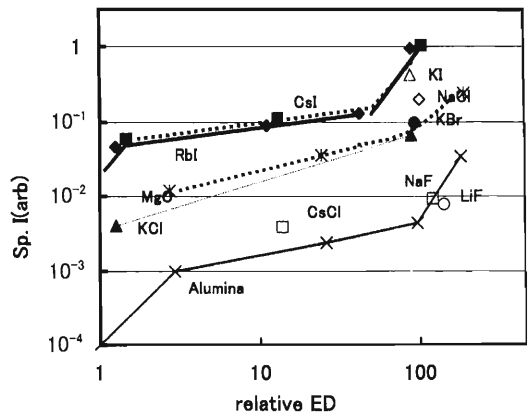

Fig. 2. Excitation-density (ED) dependence of specific intensity of the UFLDC.

huge Coulomb repulsive force, resulting in deformation of crystal and likely bindings among halogen atoms and anions. Thus, the configuration under recombination luminescence of the e-h plasma is deformed and rearranged. They all reduce photon energy like Stokes shift. Simultaneously, this means that the so-called amorphization in the track core takes place already in a short period of about 10^{-13} s, which is a novel model for the ion irradiation effect.

References

1) K. Kimura, J. Kaneko, S. Sharma, W. Hong, and N. Itoh: Phys. Rev. B **60**, 12626 (1999).
2) E. I. Rashba: in *Excitons at High Density* (*Springer Tracts in Modern Physics*, Vol. 73), edited by H. Haken and S. Nikitine, (Springer, Berlin, 1975) p.150.

Ultrafast Luminescence of CsI Scintillator Crystals under Heavy-Ion Irradiation

A. I. Popov, S. Sharma, and K. Kimura

During the last years, there has been a steady increase in the number of studies of CsI single crystals due to the fact that at room temperature these crystals exhibits a fast ultra-violet (UV) emission at 300–305 nm, of which the decay curve can be characterized mainly by two decay times, 10 ns and 35 ns. The fast scintillation property with its high density and good radiation hardness makes CsI one of the most attractive materials for high-resolution electromagnetic calorimetry as well as for positron tomography. On the other hand, when CsI crystals are irradiated at near liquid helium temperatures, the luminescence spectra consist of two self-trapped exciton (STE) bands: singlet (290 nm) and triplet (340 nm) emissions.[1] The singlet band has two decay components of 2 ns and 100 ns at 5 K, whereas the triplet band is composed of 0.6 and 20 μs components.

In this paper, we report the results for pure CsI crystals, irradiated by several kinds of ions: He, N, Ar, and Xe ions accelerated to 2.0 MeV/nucleon. Luminescence decay and time-resolved spectra have been measured using a single-ion and single-photon coincidence (SISP) system.[2]

The main results can be summarized as follows:
(1) We have found ultrafast (< 100 ps) broad luminescence (200–400 nm).
(2) Over this broad luminescence, a narrower but intense band rose precipitously at 300 nm and was also ultrafast (< 100 ps). Its decay curve was followed by a slower decay component, which formed a retarded peak at low temperature. Neither broad nor narrow ultrafast luminescence (UFL) has been found thus far, while the slow component can be assigned to the known STE. The UFLs may be ascribed to electron-hole interactions and plasma formation in the ion track core and its surrounding.
(3) We have found that UFL was almost independent of temperature. As an example, the time-resolved luminescence spectra of CsI irradiated with N ions at 70 K are shown in Fig. 1. As evident in Fig. 1, prominent UFL at 300 nm coexists with less-intensive and slow triplet STE emission, whereas only the latter one can be observed under conventional irradiation conditions.[1]

At room temperature, the 300 nm band has been observed more than once under the electron, γ-, VUV- or X-photon irradiation, but reported decay times are slower than 10 ns. All traditional excitation sources are insufficient in providing the necessary excitation density to create multiple e-h pairs nearby. For example, recently the 300 nm band has been studied by a French research group[3] using the most powerful soft X-ray laser with the specifications, 6×10^{12} photons of 58.5 eV/pulse- 5×10^{-2} eV/Å^3. In our case, the excitation density in an ion track core of 5–10 Å diameter is approximately 6–20 eV/Å^3, which is three orders of magnitude higher. This is why the use of heavy ion irradiation of such high excitation density leads to the formation of a principally new luminescence substance, which has emission decay components shorter than 100 ps.

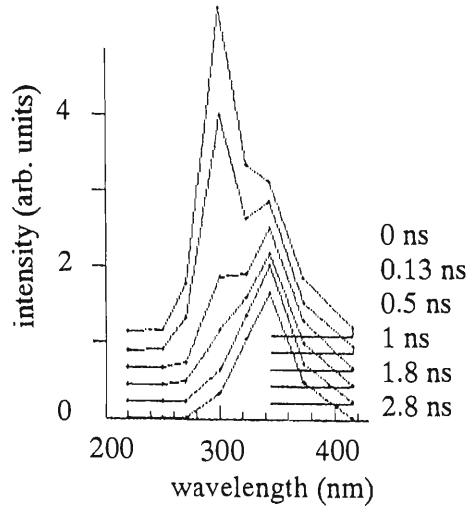

Fig. 1. Time-resolved luminescence spectra of CsI irradiated by N ions at 70 K.

The finding of the ultrafast decay component in 300-nm emission is very important not only for the physics of incipient track effects and electron-hole plasma formation in insulators, but also for further applications of CsI as scintillator detectors.

References

1) H. Lamatsch et al.: Helv. Phys. Acta **45**, 20 (1972).
2) K. Kimura and J. Wada: Phys. Rev. B **48**, 15535 (1993).
3) P. Jaengle et al.: J. Appl. Phys. **81**, 2406 (1997).

Photoconductivity of Nonconductive Oxides: Search for Electric Conduction under Ion Irradiation

N. Matsunami and K. Kimura

When insulating or nonconductive oxides are exposed to ion irradiation, holes in the valence band (VB) and electrons in the conduction band (CB) are generated by electronic excitations. It is interesting to investigate whether the holes in the VB and/or electrons in the CB are electrically conductive or not. If these carriers are not conductive, the electric charge may accumulate and the surface potential may not be zero against the ground during ion irradiation, unlike metals. A nonzero surface potential may cause inaccurate measurements of the beam current and lead to misleading results of the secondary charged particle emission yields.

We have measured the current induced by photon irradiation using a D_2 lamp, a grating in a vacuum of ~0.1 Torr and an electrometer (KEITHLEY 6517). Au of ~100 nm was deposited as electrodes on which Cu leads were attached using Ag paste. The separation between the two electrodes was ~0.1 cm. Figure 1 shows the result of $SrTiO_3$ (STO). It appears that the photocurrent was nearly proportional to the applied bias voltage. The maximum conductivity for STO and MgO was evaluated as $3.6 \times 10^{-8}\,\mathrm{Scm}^{-1}$ at 200 nm and $10^{-9}\,\mathrm{Scm}^{-1}$ at 190 nm, respectively. Here, the thickness d of the effective layer for photon absorption or carrier generation is taken to be the photon wavelength at which the photocurrent takes its maximum.

We have calibrated the light intensity I (Fig. 2). The electron-hole concentration n can be estimated by $n = I\alpha d\tau/v \sim 10^8\,(\mathrm{cm}^{-3})$ at 200 nm, where $I = 3 \times 10^{12}$ photons/s, αd is assumed to be 0.1 (α = absorption coefficient and $d = 200$ nm), τ = lifetime of electrons and/or holes (taken as ~ ns) and v = volume of carrier generation (circle of 5 mm diameter multiplied by $d = 4 \times 10^{-6}\,\mathrm{cm}^3$). Then, the mobility μ is evaluated as $\sim 10^3\,\mathrm{cm}^2/\mathrm{Vs}$ and this value is comparable with that of Si. In conclusion, the carrier mobility in CB of STO is adequate for electric conduction during ion irradiation. Investigation of the carrier density during ion irradiation, and measurements below 200 nm and of other oxides are under way.

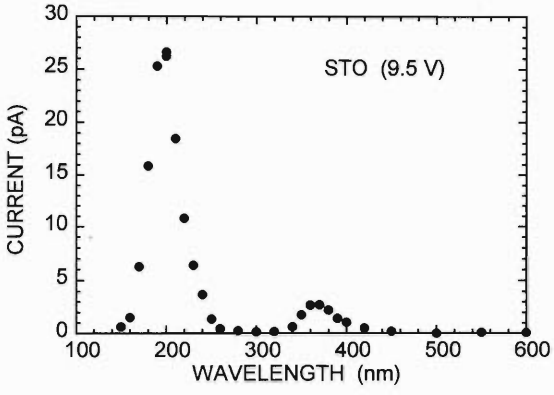

Fig. 1. Photocurrent vs. photon wavelength for $SrTiO_3$ at an applied bias of 9.5 V.

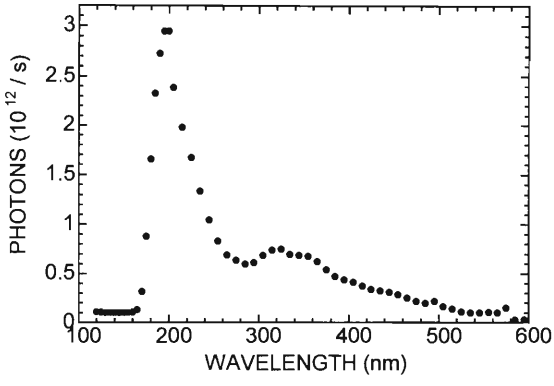

Fig. 2. D_2 lamp intensity at a sample position as a function of photon wavelength.

Recent Progress in Biological Electron Transfer Studies by the Method of Labelled-Electron with Muons: Cytochrome c Oxidase

K. Nagamine, F. L. Pratt,[*1] S. Ohira, I. Watanabe, S. Yoshikawa,[*2] K. Shinzawa-Itoh,[*2] and T. Tsukihara[*3]

In order to obtain microscopic information about electron-transfer in the biological macro-molecule, the μSR method offers a great potential. During the slowing-down process, the injected μ^+ picks up one electron to form a neutral atomic state called a muonium. The muonium is then thermalized followed by chemical bonding to a reactive site on the molecule. Then, depending upon the nature of the molecule, the electron brought-in by the μ^+ can take on several characteristic behaviors including a localization to form a radical state and/or a linear motion along the molecular chain. These behaviours, by setting the time-origin of electron movement, can be detected most sensitively by measuring the spin relaxation process of the μ^+ using the μSR method, which occurs through a magnetic interaction between the μ^+ and the moving electron produced by the μ^+ itself (the method of labelled-electron with muons).

The experimental studies on a series of representative proteins conducted by the RIKEN-KEK-Oxford group mainly at RIKEN-RAL Muon Facility has revealed so far the following important new aspects of electron transfer in proteins.[1,2)]

(i) For the muon-produced electron, topologically linear motion exists along the chain of both cytochrome c and myoglobin. The intra-site diffusion rate along chain $D_{//}$ takes on a value on the order of 10^{12} rad/s, and is almost temperature independent. The cutoff process of the linear motion represents a departure on a longer time scale from the one-dimensional diffusion which occurs on a shorter time-scale. Thus, one can obtain the inter-chain diffusion rate, $D_\perp$. The obtained $D_\perp$ in cytochrome c is dominated by two different process, as can be seen in the temperature dependence. The characteristic change at 200 K of $D_\perp$ seems to be related to the well-known structural change of glass-like transition. On the other hand, $D_\perp$ in myoglobin shows only one component, reflecting the different protein dynamics of this molecule for inter-chain electron-transfer.

(ii) Positive muons, as evidenced by the preliminary paramagnetic measurements as well as theoretical calculations, stop preferentially at the negatively charged sections near to the heme-Fe atom.

(iii) The characteristic electron transfer phenomena in the form of 1/B dependence was not seen neither in lysozyme nor in cytochrome c with Fe(2+) where electron transfer is known not to exist.

In the present experimental studies conducted at RIKEN-RAL Muon Facility, we challenged to explore electron transfer in the cytochrome c oxidase, which

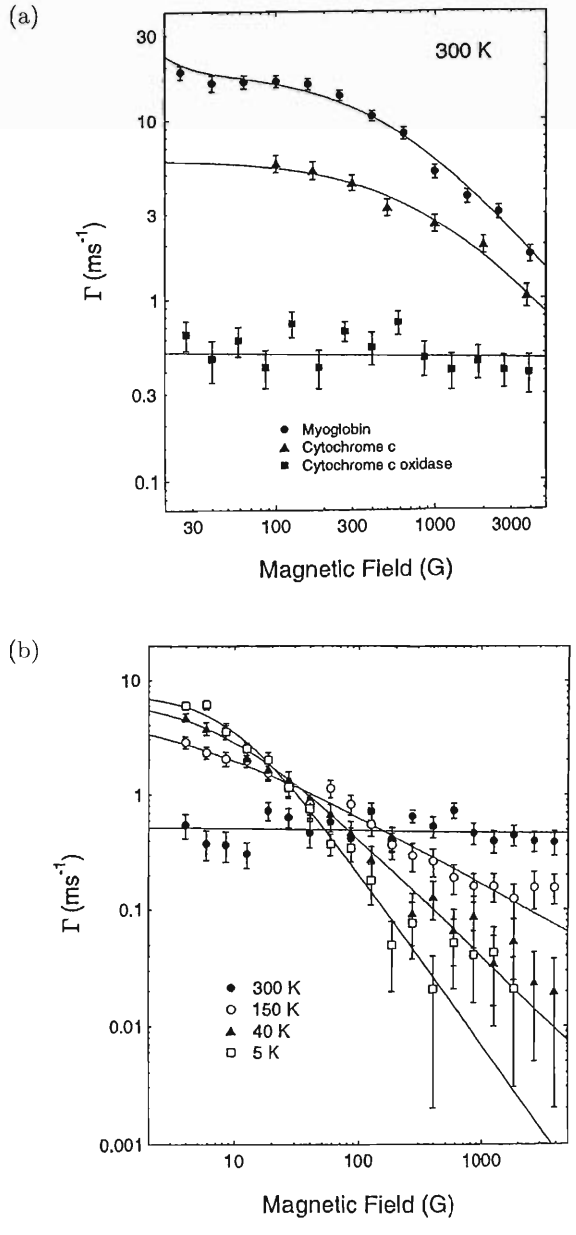

Fig. 1. (a) Observed muon spin relaxation parameters under various external magnetic fields on three typical proteins at room temperature. (b) Same as Fig. 1 (a) for cytochrome c oxidase at various temperatures.

*1 Oxford University, UK
*2 Himeji Institute of Technology
*3 Institute for Protein Research, Osaka University

is known as a terminal protein situated at the final part of mitochondria aspiration chain. Recently, structure studies have been carried out by using a high-resolution X-ray studies.[3] Due to the difficulty in the sample preparation, the actual sample is composed of the Bovine heart cytochrome c oxidase (50%) and the surfactant material Deyl-β-D-maltoside and buffer chemicals of NaH_2PO_4 (altogether 50%).

The results are shown in Fig. 1(a) and (b) in terms of the external field dependence of the relaxation parameter (Γ) obtained by a fit to the data with the Risch-Kehr function representing a relaxation function due to a lineraly moving electron. The following conclusions are readily obtained:
(1) at room temperature, electron transfer along the chain in cytochrome c oxidase is very much suppressed compared to these in cytochrome c and mioglobin.
(2) by reducing temperature, the electron transfer along the chain becomes evident, in particular, below 150 K.

The results may contain contributions of the signals from either surfactant or buffer. Since there exist several heme centers, there might be corresponding signal components. The extended studies are now in progress.

References

1) K. Nagamine: Bull. Mater. Sci. **22**, 485 (1999).
2) K. Nagamine et al.: Physica B **289/290**, 631 (2000).
3) T. Tsukihara et al.: Science **269**, 1069 (1995).

Metal Uptake Mutant of Yeast *Schizosaccharomyces pombe*

Y. Nose* and I. Yamaguchi

The disposal of radioactive wastes and nuclear facility accidents are serious social problems. To reduce the radionuclides in environment, metal uptake activity of various living organisms has received attention. Recently, we demonstrated by using the multitracer technique that the yeast *Saccharomyces cerevisiae* and *Schizosaccharomyces pombe* has ability to take up various radionuclides.[1–3] To determine the metal-uptake mechanisms in yeast, *S. pombe*, transformants were made and their metal uptake abilities were measured.

The *S. pombe* transformants were made by restriction-enzyme-mediated integration (REMI) method, using blastisidin-S resistance gene (BSD) as a marker. Among about 700 transformants, a mutant having high metal uptake abilities was selected by multitracer technique. The multitracer uptake assay was done as follows. Wild type and transformants of yeast were cultured in 1.5 ml of YEL medium. Cells were collected by centrifugation at 1,000 xg for 5 min. Cell pellets were suspended in 1 ml of 10 mM HEPES buffer (pH 6.0) with or without 3% glucose, and incubated at 25°C for 30 min. Ten μl of the multitracer solution containing 1362.2 Bq of ^{7}Be, 18.6 Bq of ^{22}Na, 95.2 Bq of ^{46}Sc, 313.2 Bq of ^{54}Mn, 83.1 Bq of ^{56}Co, 1063.2 Bq of ^{65}Zn, 205.5 Bq of ^{75}Se, 3372.8 Bq of ^{83}Rb, 3024.0 Bq of ^{85}Sr, 1886.4 Bq of ^{88}Y, 1318.8 Bq of ^{88}Zr, and 14.1 Bq of ^{95m}Tc, was added to the cell suspension. After 30 min, cells were collected, washed 3 times with distilled water, and subjected to gamma-ray measurement and protein assay. Figure 1 shows the metal uptake ability of the transformant, designated REMI 7-4. In the presence of glucose, REMI 7-4 took up Sc, Se, Rb, and Zr at higher levels than control. Uptakes of other metals by the transformant were same with wild type. On the other hand, in glucose absent condition, REMI 7-4 took up Co at lower levels than wild type, and no significant changes were observed in other metals. Little are known about the uptake mechanisms of Sc, Se, Rb, Zr and Co. Therefore, the transformant should be the key to analyze the mechanisms. The gene(s) disrupted by REMI event still remained to be identified. The next step is molecular biological analysis of the mutant.

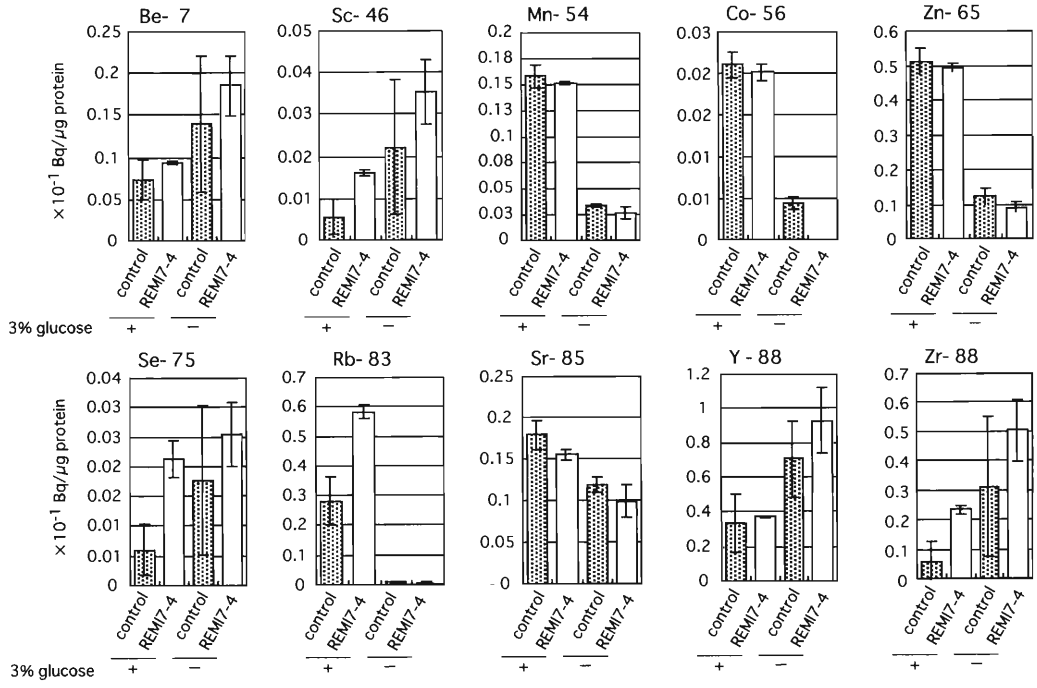

Fig. 1. Uptake of various radionuclides by REMI 7-4. Data represent the gamma-ray activity (Bq) per microgram of cell protein.

References

1) Y. Nose et al.: RIKEN Accel. Prog. Rep. **31**, 141 (1998).
2) Y. Nose and I. Yamaguchi: RIKEN Accel. Prog. Rep. **32**, 128 (1999).
3) Y. Nose and I. Yamaguchi: RIKEN Accel. Prog. Rep. **33**, 137 (2000).

* University of Michigan Medical School, USA

Influence of Nonpathogenic *Fusarium* Strains on Uptake of Radionuclides by Tomato

T. Soshi, T. Arie,* and I. Yamaguchi

Radionuclides released into the environment enter the food chain through, *e.g.*, plants and fish, pose a potential risk to human health. Eliminating the radionuclides from the soil environment or reducing their uptake by food crops would decrease the dose to humans. The possibility of phytoremediation was suggested to reduce the radionuclides in the soil. Transfer of radionuclides from the soil to the plant varies depending on soil characteristics and plant species.[1,2] Rhizosphere microbes are also often known to affect the uptake of radionuclides from the soil by the plant.[3,4] However, the influences of microorganisms on the uptake of radionuclides by plants remain to be elucidated. Aiming at phytoremediation of soils polluted with radionuclides or at increasing the uptake ability of plants, we have analyzed the effect of microbes on the uptake by the plant using the multitracer technique.[1,2] Tomato is one of the plants capable of uptaking and accumulating radionuclides. We found that a tomato pathogenic strain of *Fusarium* (*F. oxysporum*, *F.* spio *rycopersici*) can enhance the uptake of Sr and Cs by the plant through infection.[3] In this paper, we report on the influences of nonpathogenic strains of *F. oxysporum*, *F.* spio *rycopersici* (N.P.F.) on the uptake of radionuclides using the multitracer technique.

N.P.F. (T1, T2, T3, M1, and M2) were isolated from tomato rhizosphere. Tomato seeds were sown in plastic pots containing 150 g of sterilized horticultural soil (Kureha engei baido, Kureha Chemical Industry Co., Tokyo). N.P.F. were cultivated on potato dextrose broth at 25°C for 1 week until sufficient spores were formed. The tomato plants were cultivated in a greenhouse at 25–30°C and under 15,000 to 17,000 lux light for 12 hrs a day. N.P.F. liquid cultures were drenched directly to the soil for inoculation. Two weeks after seeding, a mixture of diluted multitracer and radioactive cesium (^{137}Cs) was applied to each pot. The same amounts of solution were absorbed by filter paper for comparison. In the two weeks that followed, the aerial parts of the plants were collected and dried at 50°C. Then the radioactivity was measured using a hyperpure Ge detector and the results were expressed as the uptake percentage with respect to the initial tracer activity per gram dry weight of the plant.

Figure 1 (a) and (b) show the uptake rate of several elements from the soil to the aerial parts of the plant (Na, Mn, Co, Sr and Cs in Fig. 1 (a); Zn, Tc and Rb in Fig. 1 (b)). The tomato plants treated with T1 showed moderate enhancement of the uptake of Na,

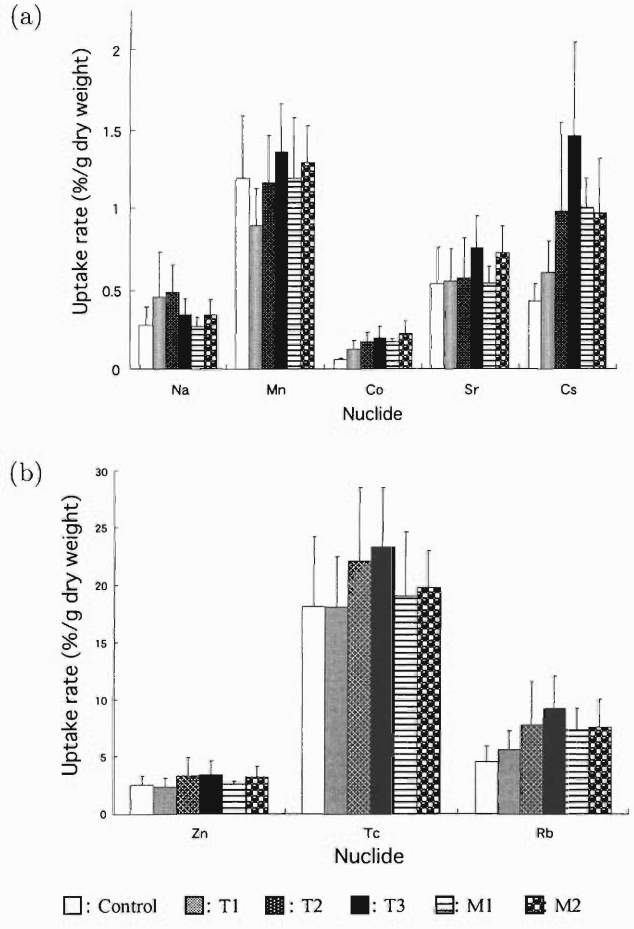

Fig. 1. (a) Uptake rate of five elements by tomato inoculated with nonpathogenic strains of *Fusarium*. (b) Uptake rate of three nuclides (Zn, Tc and Rb) by tomato with nonpathogenic strains of *Fusarium*. Data is expressed as percentage to the activity of the control per gram dry weight of the plant that inoculated with nonpathogenic strains of *Fusarium* (T1, T2, T3, M1 and M2). Error bar shows standard deviation.

Co, Cs and Rb. The uptake rates of Sr and Zn were almost the same as that of the control and the Mn uptake rate was less. T2 increased the uptake of the same elements as T1 as well as Tc. M1 and M2 enhanced uptakes of Co, Cs and Rb. M2 also increased Sr uptake. T3 showed significant increase in the uptake in all elements except for Na. Enhancement of the uptake of both Sr and Cs was observed in T3 and M2-inoculated tomato. In terms of phytoremediation for contaminated soil by long-lived radionuclides such as Sr or Cs, the use of microbes like N.P.F. T3 or M2 to enhance uptake of these elements by plants is sug-

* Faculty of Agriculture, Tokyo University of Agriculture and Technology

gested.

References

1) S. Gouthu et al.: RIKEN Accel. Prog. Rep. **30**, 117 (1997).
2) S. Gouthu et al.: J. Radioanal. Nucl. Chem. **222**, 247 (1997).
3) S. Gouthu et al.: RIKEN Accel. Prog. Rep. **31**, 146 (1998).
4) J. A. Entry: Water, Air Soil Pollut. **88**, 167 (1996).

Variation in Sensitivity to Radiation of Orchid Genetic Resources

K. Furukawa,* M. Kubota,* T. Abe, and S. Yoshida

Orchids are the largest family of higher plants. However, only a few genera of orchids are used for horticultural purposes. Breeding of these orchids has been conducted for more than 100 years and new varieties are released every year. Heavy-ion irradiation is one of the interesting methods of mutation breeding. The effect of N-ion irradiation on mutation breeding of orchids was investigated in this study.

Eight varieties of *Cymbidium*, nine of *Odontoglossum alliances* (eight of *Odontioda* and Vuylstekeara), three of *Zygopetalum*, *Epidendrum* and *Oncidium* were used for heavy-ion irradiation. The protocorm-like body (PLB) was cut to half or a quarter of its size and then 15 pieces of cut PLB were placed on a Petri dish with a solid medium containing Hyponex 20-20-20 (Hyponex Japan, Osaka, N-P-K=20-20-20), sucrose and a gelling agent. Each experiment was repeated at least once or twice. Irradiation treatments of the PLBs were conducted in the dose range of 5 to 100 Gy with ^{14}N ions. After irradiation, PLBs were transplanted to Erlenmeyer flasks with Mukoyama original medium. These flasks were put in the culture room at 20 to 25 °C with a 16 h light/8 h dark fluorescent illumination for 3 to 5 months. Then, the number of green-colored PLBs and elongated shoots was counted and a survival rate was calculated.

PLBs of *Cymbidium* 'Red Angelica' were used to determine the survival rate in the dose range of 5 to 100 Gy (Table 1). PLBs could not survive at doses over 50 Gy. The 50% lethal dose (LD_{50}) value was 9.2 Gy. The LD_{50} value of 'Sweet Devon' was lower than that of 'Red Angelica,' and those of 'Procyon' and 'In The Mood' were higher. The LD_{50} values of the other four cultivars were almost the same as that of 'Red Angelica.' In the case of *Zygopetalum*, 'Pretty Ann' and 'Fire Kiss' have the same parents, however the radiation sensitivity of these cultivars was different. Shoots were differentiated from surviving PLBs of most orchids at doses under 20 Gy. *Odontoglossum alliances* was lesssensitive to radiation than the other genera examined.

Already, orchid plants from the irradiated PLBs have been grown in the greenhouse. Further observations are needed to determine the change of phenotype in the flowers of those juvenile plants.

Table 1. Effect of ^{14}N heavy-ion beam irradiation on frequencies of survival of orchid genera.

Dose (Gy)	Survival (%)							
	Cymbidium.							
	Lady Fire 'Red Angelica'	Enzan Stream 'Orpheus'	New Century 'Coronation'	Enzan Spring 'In The Mood'	Melody Fair 'Marilyn Monroe'	Pearl Dawson 'Procyon'	'Devon Odyssey '	'Sweet Devon'
0	100	100	100	100	100	100	100	72
5	85	90	95	95	85	95	100	14
10	55	50	40	80	45	90	60	0
20	15	-	-	-	-	60	20	0
50	0	-	-	-	-	-	-	-
	Odontioda							
	Lovely Penguin 'Fides'	Lovely Apple 'Ruby Castlehill'	Sleeping Parade 'Orange Sunset'	Lovely Morning 'Sayaka'	Peter Timoney 'Kurara'	Nationhood 'Bossa Nova'	Starlit Night 'Fancifully'	
0	100	100	100	100	100	100	100	
10	84	82	100	96	68	76	100	
20	48	74	80	80	36	40	15	
	Odontioda	*Vuylstekeara*	*Zygopetalum*			*Epidendrum*	*Oncidium*	
	Frontispiece 'Anhelo'	Cambria 'Golden Gate'	B. G. White 'Bogey'	Redvale 'Fire Kiss'	Redvale 'Pretty Ann'			
0	100	100	100	100	100	100	100	
5	-	-	88	80	100	85	75	
10	70	88	52	40	80	60	40	
20	64	80	4	0	32	40	0	
50	35	-	-	-	-	-	-	

* Mukoyama Orchids Ltd.

The Effects of Heavy-Ion Beam Irradiation on PLB Development in Several Orchids

K. Tokuhara,[*1] T. Abe, K. Miyoshi,[*2] and S. Yoshida

Breeding of Orchidaceous plants has been conducted by hybridization for more than 150 years. This takes a long time due to the slow growth of the orchid. Moreover, it is impossible to obtain cultivars by hybridization which have the minimum change of a certain characteristic, such as color of flower. Thus, mutation breeding has been conducted as a useful method for the establishment of new cultivars with minimum changes from the original cultivar in many plant species. Recently, establishment of new cultivars using heavy-ion radiation as an alternative method of mutation breeding has been reported. In the present study, we investigated the effect of heavy-ion beam irradiation on protocorm-like body (PLB) development in several orchids.

PLBs of *Laeliocattleya* (*Lc.*) Melody Fair 'Summer King.' *Oncidium* (*Onc.*) *obryzatum*, *Onc.* sp., and *Phalaenopsis* (*Phal.*) Wedding Promenade 'Purple Queen,' which were micropropagated by shoot tip culture, were used. Fifty PLBs were placed in a plastic Petri dish (6 cm in diameter) containing 5 ml New Dogashima medium supplemented with 10 g/L sucrose and 1.5 g/L gellum gum as a gelling agent. The media were adjusted to pH 5.4 before autoclaving at 120°C and 1 kg/cm^2 for 15 min. Then, these PLBs were irradiated with ^{14}N or ^{20}Ne-ion beams (135 MeV/u) in the dose range of 5 to 50 Gy. Two to five replications were made for each treatment under the present conditions. Three weeks after the irradiation, PLBs were subcultured in square bottles containing fresh medium. Frequencies of PLB mortality were measured 1, 2 and 3 months after irradiation in *Lc.* and 3 months in the other genera.

After irradiation, the frequency of PLB mortality increased with increasing absorbed dose as well as prolongation of the culture period in all genera examined (data not shown). However, the frequency of mortality did not increase after a culture period exceeding three months post-irradiation. Moreover, no significant difference in mortality for *Lc.* was observed between treatment with ^{14}N and that with ^{20}Ne-ion (Table 1). In *Onc.*, all PLBs showed necrosis after irradiation with a dose higher than 50 Gy. *Phal.* was highly sensitive to the treatment. In fact, more than 62% of the PLBs exhibited necrosis after a dose higher than 5 Gy. Differentiation and growth of shoots from surviving PLBs excluding *Phal.* after 50 Gy exposure were slower than from PLBs after lower doses (0, 5, 10 and 20 Gy). Mutated shoots from surviving PLBs in the case of exposure to more than 10 Gy were observed in *Phal.*

In our subsequent experiments we are investigating the effect of irradiation on the growth and characteristics of flowers, in terms of shape and color in the blooming season in our greenhouse.

Table 1. Effects of heavy-ion beam irradiation on PLB development in several orchids.

Ion	Gray	*Lc.* Melody Fair 'Summer King'	*Onc. obryzatum*	*Onc.* sp.	*Phal.* Wedding Promenade 'Purple Queen'
Control	0	6.0 ± 4.2*	0.8 ± 0.4	6.9 ± 2.3	0
N	5	27.9 ± 6.9		12.1 ± 0.9	62.4 ± 5.1
	10	25.4 ± 3.4		30.3 ± 2.7	76.4 ± 3.3
	20	51.0 ± 4.9		40.7 ± 2.7	84.8 ± 2.5
	50	72.4 ± 2.4		60.4 ± 6.0	89.6 ± 2.4
Ne	5	23.8 ± 7.2	2.0 ± 1.4		
	10	26.8 ± 5.3	16.0 ± 3.9		
	20	59.3 ± 4.8	68.0 ± 7.0		
	50	86.3 ± 1.2	100.0		

* Frequency of mortality (%)

*1 Dogashima Orchid Center
*2 Faculty of Bioresource Sciences, Akita Prefectural University

Mutant Flowers of Dahlia (*Dahlia pinnata* Cav.) Induced by Heavy-Ion Beams

M. Hamatani,[*1] Y. Iitsuka,[*1] T. Abe, K. Miyoshi,[*2] M. Yamamoto,[*3] and S. Yoshida

Radiation has been widely adopted in order to induce artificial mutations in various plant species easily and effectively. In our previous research,[1–3] we irradiated dahlias with γ-rays to induce mutations for new agronomic traits such as a high productivity of cut flowers in winter. However, we obtained only mutants with limited color variations, which were assessed with poor marketability. Moreover, promising phenotypes of mutations which were selected in the growing season following the irradiation treatment were not stable in the next season and thus we did not obtain any mutants with genetically stable features. Therefore, we conducted an experiment using treatments of heavy-ion beams as an alternative method for the induction of dahlia mutations which were more stable and more varied than the ones induced using γ-rays.

Irradiation treatments were conducted on the small shoots (approximately 1 cm in length) of the pink-flower dahlia cv. 'Miharu,' which were grown in a modified Murashige-Skoog medium, in the dose range of 5, 10, 20, 50 and 100 Gy for N-ions. We did not obtain distinct experimental results for those plants treated with more than 20 Gy due to their poor growth *in vitro*. Plants treated with 10 Gy grew vigorously *in vitro* as well as in the experimental field, and showed the highest frequency of mutant induction.

The results obtained under experimental field conditions with an increase in exposure dose are as follows: (1) decrease in the frequency of anthesis, (2) increase in the variation of flower diameter, (3) increase in the variation of flower colors and (4) increase in the malformation of flowers. On the other hand, irradiation had little effect on the time of flowering, the length of flower stalks and the frequency of appearance of side-facing flowers.

Flowering frequencies after 5 and 10 Gy apparently decreased compared with those after 0 and 1 Gy. The decrease in the flowering frequency with the increase in the exposure dose has also been observed in the treatment of γ-ray irradiation. As for floral diameter, those of 3–12 cm have been observed. Under the 0 to 5 Gy doses, the percentage of flowers with a diameter of 9–10 cm was 80%, but under 10 Gy, it was 55% and the number of flowers with a diameter of either less than 8 cm or more than 11 cm increased. The mutants, such as those with darker- or paler-colored petals or white-tipped petals were observed in the present

Fig. 1. Variation of mutations. (Arrow indicates a typical flower of 'Miharu.')

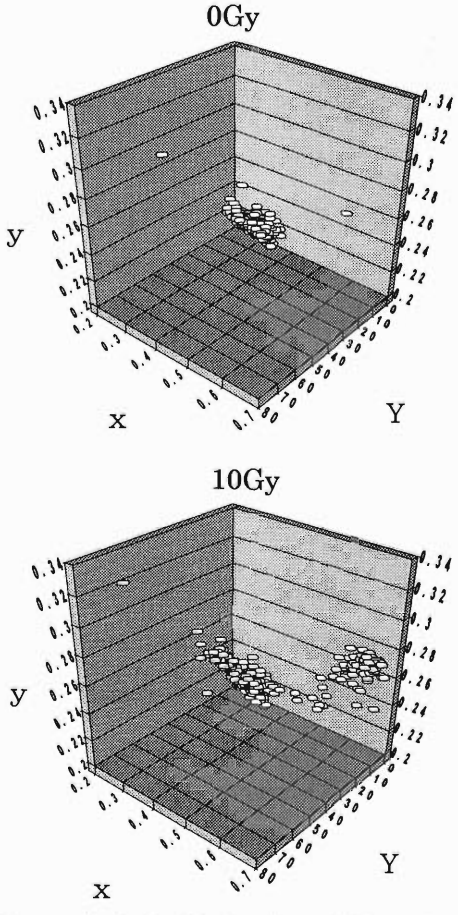

Fig. 2. The analysis for floral colors of the mutants using a chromameter.

*1 Hiroshima City Agriculture and Forestry Promotion Center
*2 Faculty of Bioresource Sciences, Akita Prefectural University
*3 The Hiroshima Botanical Garden

experiment (Fig. 1) as well as in our previous experiment with γ-ray irradiation. Mutants with darker-colored flowers were more commonly observed in N-ion irradiation than in γ-ray irradiation. The frequency of mutants with darker-colored flowers is higher than that of mutants with paler ones. The analysis for the flower color using a chromameter (MINOLTA CR-300) revealed that the mutations of flower colors after 5 and 10 Gy showed two clusters (Fig. 2). More than ten clones were selected as promising strains for the market, such as clones with flowers having pink-tipped or white-tipped petals, those with paler-colored and darker-colored petals and so on. Because changes in the flower traits are sometimes observed in dahlias due to their chimeric characteristics, further experimentation should be conducted to evaluate the stability of these promising strains.

References

1) A. Takai: Ann. Rep. Hiroshima City Agric. For. Prom. Cen. (Hortic. Sect.) **1997**, 115.
2) A. Takai: Ann. Rep. Hiroshima City Agric. For. Prom. Cen. (Hortic. Sect.) **1998**, 80.
3) Y. Iitsuka: Ann. Rep. Hiroshima City Agric. For. Prom. Cen. (Hortic. Sect.) **1999**, 89.

A New Method for Induction of Mutation in Wheat and Barley Using Heavy-Ion Beams

I. Honda,* M. Wada,* T. Abe, T. Asami, and S. Yoshida

Recently, heavy-ion bombardment (HIB) of plants has been investigated to obtain a certain mutant. Abe *et al.* extensively studied and established the application of this method to tobacco plants to obtain a mutant.[1] Applications of this method to other plants such as rice[2] and rose[3] were also studied, however, those to wheat, barley, and maize have not yet been reported. In this study, HIB applications to wheat and barley to obtain a certain mutant were investigated.

The Japanese breeding line of barley (*Hordeum vulgare* L.), Kantohadaka 77 (K77; six-rowed, naked cariopsis, uzu, waxy endosperm) was used as a plant material. Both imbibed (12 hr, 20°C) and dry seeds were irradiated by ^{14}N-ion beams (135 MeV/u) at a dose range of 5 to 400 Gy and grown in the field. The culture condition was not appropriate for barley; only 21.4% of the plants survived even in the control (without HIB) culture. HIB of barley of more than 20 Gy to the imbibed seeds and 200 Gy to the dry seeds severely inhibited their growth. Thus, their M_2 seeds were not obtained. The M_2 seeds were harvested separately from each plant from seeds subjected to lower dose treatments and albino plants were observed from the imbibed seeds subjected to 5 Gy treatment and dry seeds subjected to 10 and 20 Gy treatments. These results indicate that in the HIB of barley, the optimal doses of irradiation are 5 Gy for imbibed and 50 Gy for dry seeds (Table 1).

In the experiment on wheat (*Triticum aestivum* L.), a Japanese bread wheat cultivar, Bandowase, was used as a plant material. Both imbibed (24 hr, 4°C) and dry seeds were irradiated using the same method as that for barley. Treated seeds were sown and cultivated to their two-leaf stages, and then their growth was examined. The growth of imbibed seeds subjected to more than 20 Gy HIB and dry ones subjected to more than 200 Gy HIB was severely inhibited (Table 2). The optimal doses for wheat may be 10–20 and 100 Gy HIB of imbibed and dry seeds, respectively.

The M_2 barley seeds were mixed according to their absorbed doses, aliquots of them were cultivated, and plants with a short culm were observed. In total, 15 plants with a short culm were selected as putative mutants. Some of these plants were selfed as well as crossed with K77 and/or Misatogolden (Misato), and phenotypes of M_3, F_1, and F_2 plants were examined. Among the 15 putative lines with a short culm, one severe dwarf line (d3, selected from 100 Gy HIB dry seeds), and two semidwarf lines (d4 and d5, which were selected from 50 Gy HIB dry and 5 Gy HIB imbibed seeds, respectively) whose leaf expansion is imperfect, were selected as homozygous phenotypes for short culm. Phenotypes of F_1 among these three lines and K77 and Misato were the same as those of K77, and F_1 between K77 and Misato. All their F_2 segregated into mutants and normal plants with a 1:3 ratio, suggesting that all of these three lines are single-gene recessive mutants (Table 3).

These results clearly demonstrate that HIB is effective for the induction of mutation in barley. This unique method may contribute to the development of a novel mutant for crop improvement in the near future.

Table 1. Effects of HIB treatment on barley.

Imbibed seed treatment			Dry seed treatment		
Absorbed dose (Gy)	Normal plants*	Albino plants**	Absorbed dose (Gy)	Normal plants*	Albino plants**
5	111 (11.1)	1	10	131 (16.9)	1
10	12 (1.2)	0	20	124 (16.0)	1
20	0 (0)	0	50	76 (9.8)	0
50	0 (0)	0	100	39 (5.0)	0
100	0 (0)	0	200	0 (0)	0
Cont.	9 (21.4)	0	400	0 (0)	0

*Number of plants showing normal growth (rate (%) in parenthesis).
**Number of M_2 lines with albino plants. Cont.: control.
Number of seeds sown: imbibed HIB 1000, dry HIB 777, Cont. 42.

Table 2. Effects of HIB treatment on wheat.

Imbibed seed treatment		Dry seed treatment	
Absorbed dose (Gy)	Normal plants (%)*	Absorbed dose (Gy)	Normal plants (%)*
5	88.3	10	91.1
10	91	20	82.1
20	51	50	79.3
50	4.5	100	71.7
100	2.4	200	0.5
200	0	400	0
Cont.	91.2	Cont.	84.6

*Rate of plants showing normal growth. Cont.: Control.

Table 3. Segregation of F_2 plants.

Cross	Mutant plant*	Normal plant*	Total plant*	χ^2 value (1:3)	Probability
K77 × d3	8	24	32	0	1
Misato × d4	8	23	31	0.01	0.92
K77 × d5	2	7	9	0.04	0.85
Misato × d5	9	30	39	0.08	0.78

*Number of plants. K77: Kantohadaka 77, Misato: Misatogolden.

References
1) T. Abe et al.: in *Modification of Gene Expression and Non-Mendelian Inheritance*, edited by K. Oono and F. Takaiwa, (National Institute Agrobiological Resources, 1995), p.469.
2) T. Abe et al.: RIKEN Accel. Prog. Rep. **32**, 145 (1999).
3) T. Kitaura et al.: RIKEN Accel. Prog. Rep. **33**, 141 (2000).

* National Agriculture Research Center, Ministry of Agriculture, Forestry and Fisheries

Chromosome Breakage in Wheat Induced by Heavy Ion-Beam Irradiation

H. Tsujimoto,* T. Yamada,* and T. Abe

Because of polyploidy, common wheat (*Triticum aestivum* L. $2n = 6x = 42$) is tolerant to chromosomal aberrations. Many aneuploids and chromosomal deletion lines were produced in this species and used to map genes on a certain chromosome or chromosomal region. We here aim to produce 'micro-chromosome deletion lines' that carry smaller deletions. These lines must be useful in future to isolate and identify wheat genes by map-based cloning method. It is reported that irradiation of heavy ion-beam caused 10 bp- to 10 kb-deletions. Thus, we chose this treatment, instead of chemical mutagen that mainly causes base changes of DNA.

Dry seeds of common wheat cultivar 'Chinese Spring' were irradiated with N and Ne ion (135 MeV/u) within a dose range of 50 to 200 and of 25 to 100, respectively. The linear energy transfer of the N and Ne ion corresponded to 30 and 63 KeV/mm, respectively. One month after sowing on nursery boxes with sterilized soil, the survived plants were counted. Mitosis and meiosis were observed in the root-tip cells and pollen mother cells, respectively. In mitosis, numbers of chromosome breaks were counted in which dicentric and ring chromosomes were regarded to be the productions by two breakage events.

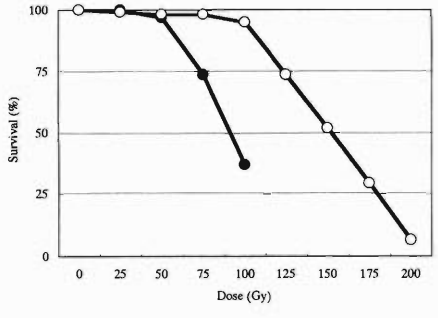

Fig. 1. Survival of plants irradiated with N or Ne ion-beam on 30 days after the irradiation. Open and closed circles indicate N and Ne ion-beam irradiation, respectively.

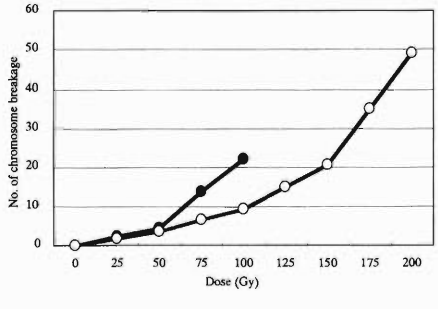

Fig. 2. Number of chromosome breakage in plants irradiated with ion beam. Open and closed circles indicate N and Ne ion-beam irradiation, respectively.

With the increase of dose, the frequency of survival decreased (Fig. 1). The values of LD50 of N and Ne were 90 and 150 Gy, respectively. With dose increase, numbers of chromosome breakage increased (Fig. 2). Ne-ion beam induced chromosome breakage twice as much as N beam did. These data indicated that in wheat LD50 corresponds to 20 chromosome breaks. In mitosis, multi-centric, dicentric, ring chromosomes in addition to simply broken chromosomes appeared (Fig. 3). Appearance of micronuclei in interphase cells indicated that breakage events were not healed yet. In meiosis multivalent appeared, meaning many translocations were included in the plants (Fig. 4).

We found that the doses we irradiated were too strong to produce micro-chromosome deletion lines. We need to investigate plants irradiated with lower doses.

Fig. 3. A mitotic metaphase cell of a plant irradiated with N ion-beam at 100 Gy. Arrows indicate abnormal chromosomes.

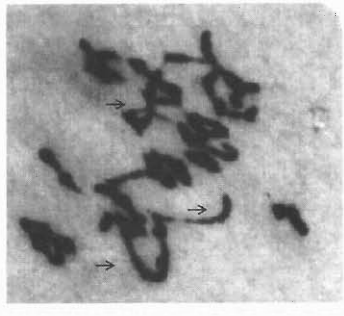

Fig. 4. A meiotic metaphase cell of a plant irradiated with Ne ion-beam at 100 Gy. Arrows indicate multivalents.

* Kihara Institute for Biological Research, Yokohama City University

Dose-Dependent Effects of Heavy-Ion Beam Irradiation on the Testes of Mice

A. Yoshiki, A. Kogiso, N. Hiraiwa, F. Ike, H. Nagase, C. Yoshida-Noro, N. Fukunishi, Y. Yano, and M. Kusakabe

We investigated the effects of heavy ion beams on the germ cells in testes quantitatively by immunohistological methods. C57BL/6J (B6) mice were deeply anesthetized with nembutal solution, fixed on a plastic plate, and exposed to heavy ion beams in the testis region of the body. The ^{12}C, ^{14}N and ^{20}Ne-ion beams were accelerated using the RIKEN ring cyclotron at Linear Energy Transfer (LET) of 135 MeV/u. Histological damage and its recovery in the testes were examined by conventional staining and immunohistochemistry. B6 males were sacrificed at 2, 5 and 10 weeks after heavy-ion beam irradiation, and their testes were removed and fixed in 4% paraformaldehyde solution. The tissues were rinsed in 0.1 M sodium phosphate buffer (pH 7.4), dehydrated with ethanol series, and embedded in polyester wax (B.D.H., England) or Technovit 8100 resin (Heraus Kultzer GmbH, Wehrheim, Germany). Immunohistochemistry was performed using germ cell stage-specific rat monoclonal TRA369 antibodies which can recognize testicular germ cells in stages from early pachytene spermatocytes to spermatids.[1] The degree of tissue damage and recovery of the seminiferous germ cells was expressed by mean scores in three different regions of the testis section as follows: recovery rate (%) = the number of seminiferous epithelial sections without TRA369-positive cells/the total number of seminiferous epithelial sections × 100. Three mice were used for each group.

Several weeks after irradiation, we noted that the black coat hair gradually turned to white in the heavy-ion-beam-exposed region. Although heavy ion beams were irradiated on the ventral side, the degree of hair pigmentation in both the ventral and dorsal skin was reduced in a dose-dependent manner (Fig. 1 A). This finding indicates that the ^{12}C, ^{14}N and ^{20}Ne-ion beams penetrated into and equally affected the inside tissues such as those of the testes. Testis tissues were histologically examined at 2, 5 and 10 weeks post irradiation (Fig. 1 B). The degree of tissue damage was most significant at 5 weeks in all the groups. Immunohistological staining of the testes with TRA369 antibodies revealed seminiferous epithelial sections without differentiating germ cells. We scored the seminiferous epithelial sections with or without TRA369-positive cells and expressed the damage and recovery of the differentiating germ cells as the recovery rate in each experimental group (Fig. 2). These quantitative analyses indicate that histopathological effects of heavy ion beams on the germ cells in the testes occur in a dose-dependent manner, and that the type of the beam differentially affects the histology of testis tissues.

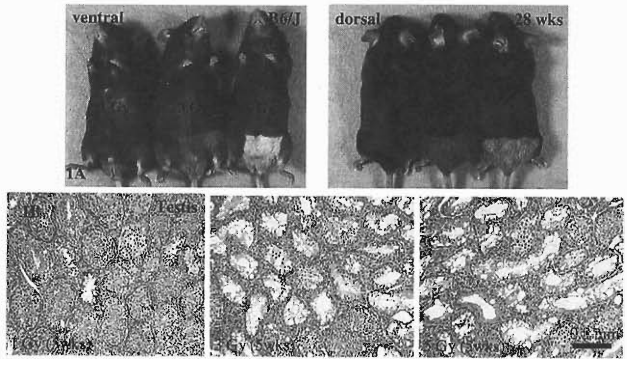

Fig. 1. Change in the coat color and histological damage of testis tissues after nitrogen ion irradiation. (1A) Degree of reduction in hair color detected 28 weeks after irradiation. (1B) Histology of testes 5 weeks after irradiation of 1, 3, and 5 Gy.

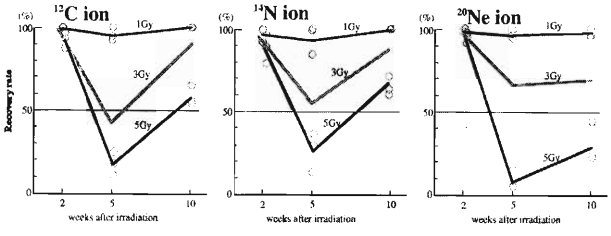

Fig. 2. Quantitative analyses of seminiferous epithelial germ cells after heavy-ion beam irradiation. Please see details in the text.

References

1) D. Watanabe et al.: Mol. Reprod. Dev. **33**, 307 (1992).

Mouse Mutagenesis by Heavy-Ion Beam for the Profiling of Morphogenetic Genes

C. Yoshida-Noro, A. Yoshiki, M. Kusakabe,* T. Matsuyama, and H. Nagase

Mouse mutant archive is a useful resource for the functional genomics in the post-genomic era. We propose here novel systematic approaches for the production, screening, preservation and analysis of morphogenetic mutants (Fig. 1).

(1) Heavy-Ion Beam Mutagenesis

Since on-going ENU (*N*-ethyl-*N*-nitrosourea) chemical mutagenesis primarily induces random single base substitutions, mutations in the genome do not necessarily represent as phenotypes. In order to increase the efficiency of phenotype assessment, we introduced a method using heavy-ion beams accelerated by RIKEN Ring Cyclotron as a mutagen.[1] As this method is expected to cause multiple types of mutation including point mutation, deletion and translocation, it is suitable for the analysis of multi-gene phenotypes such as cancer or developmental defects. It is reported that average size of deletion shows two peaks at about 85 bp and 1,000 bp in relation to the nucleosome structure.[2,3] Frequency of mutation in the genome of a mutant strain (B105) has been investigated and estimated at approximately $1.5\text{–}5.0 \times 10^{-4}$ by using RLGS[4] (restriction landmark genome scanning) and SSLP (simple sequence length polymorphism) analysis.

(2) Fetal Phenotype Screening

Fertilization rate and birth rate are the key factors for getting mutant offspring, which causes difficulty in an effective accumulation of the mutation resource through the analysis of the born offspring. In order to overcome this problem, we apply the phenotype screening at the fetal stage either at G3 (recessive) or G1 (dominant) generations. So far the total appearance rate of developmentally abnormal fetus screened at G3 generation is about 5%.

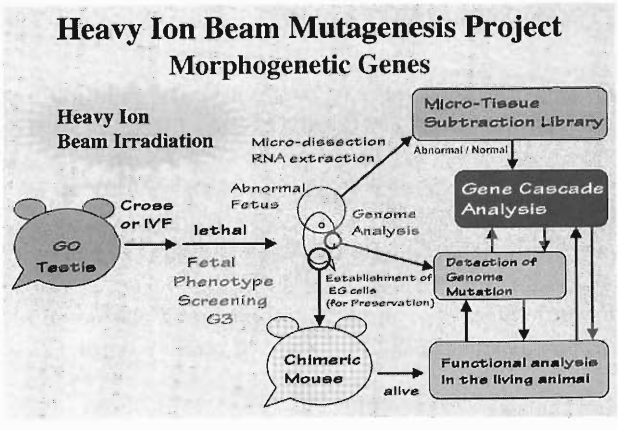

Fig. 1. Schematic overview of HIB mutagenesis project.

(3) Analysis for Expression Profiles in the Mutant Tissues

Gene expression profiles of the abnormal tissues in the mutant are analyzed by using Micro-Tissue cDNA Subtraction Library and *in situ* hybridization with a high-throughput system. By combining these data with genome analysis such as SSLP, RLGS or RDA (Representational Difference Analysis), we study the mechanisms of which the mutagenized gene and resulted changes of gene cascade generate the mutant phenotype. We applied these approaches to a mutant strain B105 with abnormal head morphology found at E10 and E13 G3 fetus, and analyzed its gene expression profiles as well as genome analysis. We got several genes expressed in the wild type head but not in the mutant head. Using these cDNAs as probes, we investigate the causality of genetic defect and morphogenetic abnormality.

(4) Preservation and Functional Analysis Using EG Cells

Primordial germ cells are isolated from the genital ridges in the fetus with mutant phenotype and cultured for establishing embryonic germ (EG) cells. Mutant genetic resource is cryopreserved in the form of EG cells and utilized by the production of chimeric or clone mice. Function of lethal gene mutation in the live animal can be examined by chimeric analysis. This approach is especially important in the screening at G1 generations.

References

1) A. Yoshiki et al.: RIKEN Accel. Prog. Rep. **33**, 148 (2000).
2) W. R. Holley and A. Chatterjee: Rad. Res. **145**, 188 (1996).
3) B. Rydberg: Rad. Res. **145**, 200 (1996).
4) Y. Hayashizaki et al.: Genetics **138**, 1207 (1994).

* Present address: Department of Anatomy, Jikei Medical School

Mutation Induction by Heavy-Ion Irradiation of gpt Δ Transgenic Mice

T. Kurobe,[*1] N. Fukunishi, T. Nohmi,[*2] M. Kusakabe, F. Hanaoka, and F. Yatagai

Transgenic mice can be used to detect mutations accompanied by whole-body exposure to ionizing radiation. Recently, the tumor suppressor gene, p53, has come to be regarded as a guardian of cells. Here, we report on the progress in our current study to examine the involvement of p53 in mutations induced after heavy-ion exposure, by using such transgenic mice system.

An outline of the mutation detection system is schematically illustrated in Fig. 1.[1)] After whole-body irradiation with a 135 MeV/u C-ion beam, the genomic DNA was isolated from various organs and the λ DNA was rescued in the form of a phage. Mutations in the target gene of λ DNA was determined by both gpt assay (6 TG^R colonies) and deletion assay (spi (−) plaques).

Enhancement of the gpt (−) mutant frequency was not observed in liver after whole-body exposure to the C-ion beam (10 Gy). Since point mutation seemed to be in frequently induced, we focused on the spi (−) assay in this study. An approximately 3-fold induction in the frequency of the spi (−) mutant was observed in liver, kidney, and spleen after such C-ion exposure (data not shown).

Similar measurements were performed under different p53 backgrounds. In p53 (−/−) knockout transgenic mice, the spi (−) mutant frequency for DNA recovered from kidney was about 40% higher than those from wild-type (p53 +/+) mice (Fig. 2). Similar enhancement by a defect of p53 was observed in spleen (50%), but not in liver (data not shown).

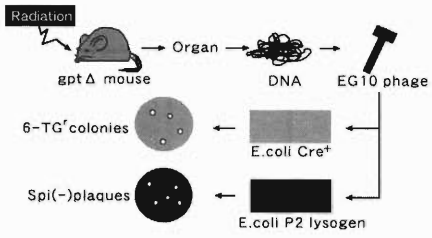

Fig. 1. A scheme of mutation assay. λ EG10 phage was rescued from genomic DNA of liver, kidney. The spi (−) mutation were detected by infecting E coli P2 lysogen, and spi (−) mutant frequency (MF) was calculated by dividing the numbers of spi (−) plaques by that of plaques of the total rescued phages. The gpt mutants, which are resistant to 6-TG, were detected by infecting E coli YG6020. And gpt (−) MF was calculated by dividing the number of 6-TG and CM double resistant colonies by that or CM single-resistant colonies.

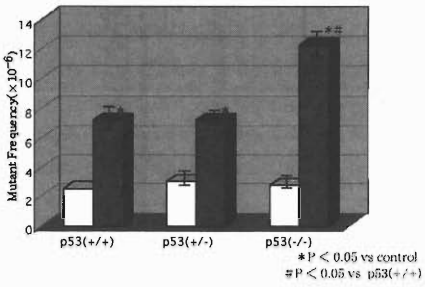

Fig. 2. Spi (−) mutant frequency (MF) for kidney recovered from C-ion irradiated gpt Δ mice. Open and closed column represent the results from un- and 10 Gy-irradiated mice, respectively. The symbol, (+/+), (+/−) and (−/−), mean p53 wild type, hetero- and homo-knockout mice, respectively.

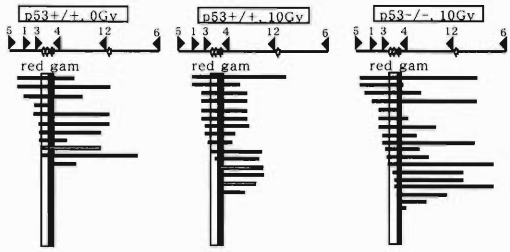

Fig. 3. A deletion map of spi (−) mutants recovered from kidney. A deletion part of the target region is expressed as closed bar. Numbers and arrows represent PCR mapping primers.

The spi (−) mutants recovered from kidney were analyzed by PCR amplification of the region of the target gene, *red/gam*. The population of mutants, providing PCR amplified products, did not differ greatly between p53 (+/+) [32%] and p53 (−/−) [42%]. DNA sequencing analysis for PCR-amplified mutants demonstrated frequent occurrences of the ±1 bp frame shift and relatively short deletion (2–488 bp), but no significant difference in their occurrence was not found between the two types of mice. For the remaining PCR unamplified mutants, we carried out both PCR amplification and DNA sequencing over the wide range of phage DNA beside the target region. As shown in Fig. 3, the mutants extending to primer 6, resulting in long deletion, were more frequently recovered in p53 (−/−) than in p53 (+/+).

These results suggest a possible involvement of p53 in the above mutation induction.

*1 Advanced Research Institute for Science and Engineering, Waseda University
*2 Division of Genetics and Mutagenesis, National Institute of Health Science

References

1) N. Nohmi et al.: Environ. Mol. Mutagen. **34**, 9 (1999).

Cell-Cycle Arrest Delayed Following Heavy-Ion Exposure

S. Goto,[*1] S. Morimoto, T. Kurobe,[*2] M. Izumi, N. Fukunishi, M. Watanabe,[*1] and F. Yatagai

Cellular responses after ionizing-radiation exposure occur to protect cells from radiation damage. The purpose of this study is to assess the question, "Are there different cellular responses between heavy ions and X-rays?" After X-ray irradiation, a variety of DNA damage is produced in cells. Each cell must possess some mechanisms responsible for damage repair, and cell-cycle regulation is considered to be a mechanism to make the repair more effective. Therefore, we examined cell-cycle progression after irradiation to elucidate cellular responses. In fact, after 3 Gy X-ray irradiation, human lymphoblastoid cells, TK6, showed an accumulation of cells at G2/M, the so-called G2/M arrest (Fig. 1 A). Compared to the X-ray case, cell exposure

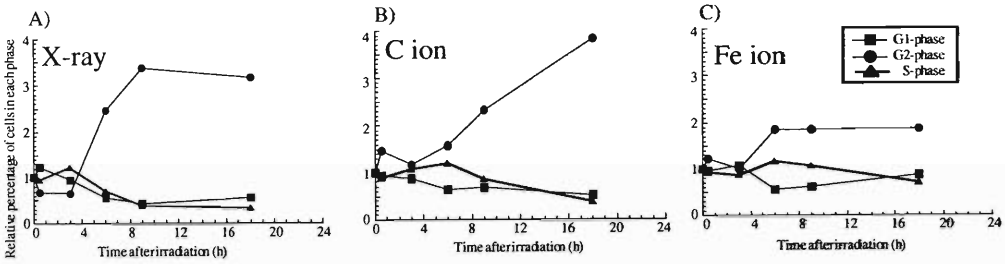

Fig. 1. TK6 cell-cycle progression after irradiation with (A) X-rays, (B) carbon ions (22 keV/μm), and (C) iron ions (1000 keV/μm). Following the radiation exposure, cells were fixed with ice-cold methanol at each postirradiation time and the nuclear region of cells was stained with propidium iodide (PI). Cell-cycle distributions were analyzed by laser scanning cytometry (LSC). The population of cells in a particular phase is expressed as a relative percentage with respect to each phase of the unirradiated sample.

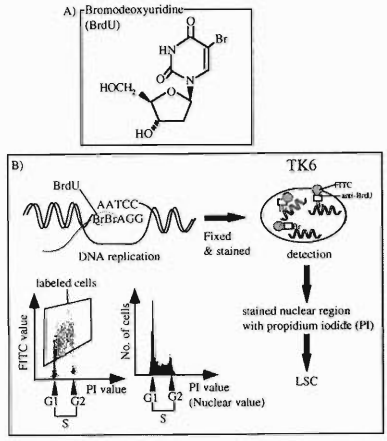

Fig. 2. (A) Chemical structure of bromodeoxyuridine (BrdU). (B) A principle for detection of the transfer pattern of the incorporated BrdU. After adding BrdU into the medium, cells incorporate it during DNA replication. These labeled cells were fixed with ice methanol, and stained with mouse monoclonal BrdU antibody and anti-mouse FITC. If cells incorporate BrdU, they can be detected by their green fluorescence. Moreover, the nuclear region of cell is stained with propidium iodide (PI). Laser scanning cytometry (LSC) reveals the staining patterns of BrdU and PI, which reflects the DNA replication frequency and cell-cycle distribution.

to carbon ions (LET 22 KeV/μm) and iron ions (LET 1000 keV/μm) resulted in the delayed accumulation of G2/M cells (Fig. 1 B, C). To determine whether this delay is due to cell freezing in the S-phase, cells undergoing DNA replication in the S-phase were prelabeled with bromodeoxyuridine (BrdU) before irradiation to follow their cell-cycle progression (Fig. 2). The transfer pattern of cells with incorporated BrdU demonstrated that the heavy-ion exposed cells remained in the S-phase longer (Fig. 3). In terms of cell-cycle progression, cellular responses are clearly different between X-ray and heavy-ion exposure. These results suggest that the repair for heavy-ion produced DNA damage is difficult in the S-phase because the damage is different from that induced by X-ray irradiation.

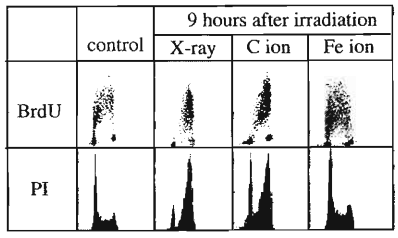

Fig. 3. The transfer pattern of prelabeled BrdU. Before exposure, cells were prelabeled with BrdU for 15 min. The labeled S-phase cells were followed for 9 h after irradiation with different types of radiation (see text).

*1 Department of Health Science, School of Pharmacological Science, Nagasaki University
*2 Faculty of Science and Engineering, Waseda University

Cellular Responses after Low-Dose Exposure to Heavy Ions

S. Morimoto, M. Izumi, N. Fukunishi, F. Hanaoka, and F. Yatagai

Bodily exposure to ionizing radiation is unlikely to occur in day-to-day life. However, we cannot neglect the risk of exposure to accelerated heavy ions in special cases involving individuals who work nearby a nuclear reactor, spend time in a space environment, *etc.* Low-dose effect studies seem to be very important not only for radiation risk estimation but also to obtain a basic understanding of radiation biological effects.

Our previous studies revealed several characteristics of mutations in the human *hypoxanthine phosphoribosyltranferase (hprt)* gene after heavy-ion exposure.[1] The induction pattern of signal-transduction proteins as well as the cell-cycle progression after heavy-ion exposure was also shown to be different from those following X-rays.[2] We recently examined the presence of adaptive responses in the same cell line after pre-exposure (5 to 20 cGy) to C-ions (22 keV/μm) and Fe-ions (1000 keV/μm).[3] A relatively high level induction of the above proteins was observed in cell mass after the pre-exposure; this did not, however, have a clear influence on either the depression of the mutation or on the recovery from lethality following the challenging X-ray irradiation.

The above low-dose exposure is schematically illustrated in Fig. 1. In this study we assess the protein induction in the individual cell instead of the mass state, because such an assay might reveal the cellular responses in an early stage following the heavy-ion exposure. Human lymphoblastoid cell line TK6-E6-20C was irradiated by a low dose (10, 20, 50 cGy) of C-ions or Fe-ions, and then incubated for 2 hours at 37°C to detect the induction of p53 protein by indirect immunofluorescence staining (Fig. 2). The population of p53-induced cells was calculated by immunofluorescence staining (Fig. 3). In contrast with C-ions and X-rays, a much lower population of p53-induced cells

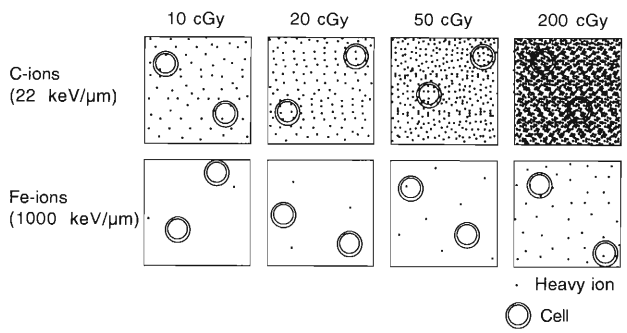

Fig. 1. A schematic illustration of cells hit by primary accelerated C-ions (22 keV/μm) and Fe-ions (1000 keV/μm).

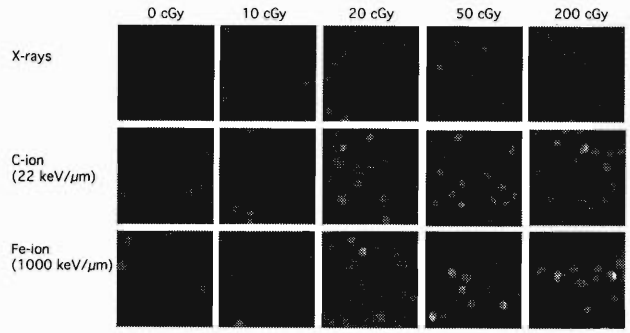

Fig. 2. *In situ* indirect immunofluorescence detection of p53 in TK6-E6-20C after X-rays, C-ions (22 keV/μm), and Fe-ions (1000 keV/μm) exposure. Cells were fixed after 2 hour incubation (37°C), then attached to a coverslip, and stained with monoclonal antibody against p53 (DO-1, Santa Cruz Biotechnology).

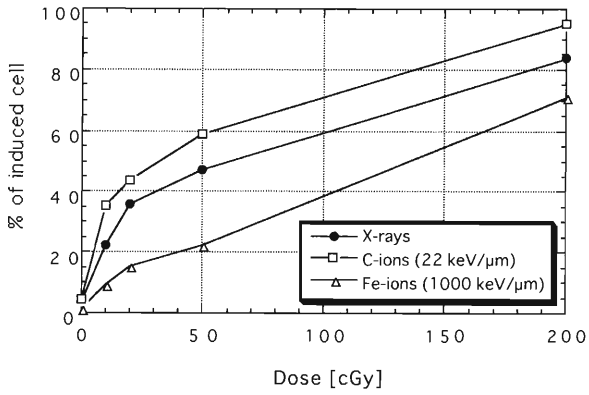

Fig. 3. Population of p53-induced cells after X-rays, C-ions (22 keV/μm), and Fe-ions (1000 keV/μm) exposure. About 100 cells were counted to calculate the percentage from the pictures, as shown in Fig. 2.

as observed in the case of Fe-ions. Immunofluorescence analysis revealed that the population of p53-induced cells is proportional to the probability of the cell being hit by a primary heavy ion. We plan to extend this line of analysis using antibodies against other related proteins to obtain a better understanding of cellular responses in individual cells.

References

1) Y. Kagawa et al.: Mutagenesis, **14**, 199 (1999).
2) A. Gordon et al.: RIKEN Accel. Prog. Rep. **33**, 131 (2000).
3) S. Morimoto et al.: Adv. Space Res. in press (2000).

5. Instrumentation

Production of Secondary Beam through Rigidity Selection

T. Yamaguchi, T. Zheng,[*1,*2] A. Ozawa, I. Tanihata, K. Morimoto, T. Suda, M. Chiba,[*3] and K. Katori

For the multipurpose utilization of radioactive ion beams, the E1C beam line has been rearranged to an intermediate-energy secondary beam line. The previous beam line[1] was used to study the nuclear high-spin states, where the high-spin isomer beam was produced by the heavy-ion-induced fusion reaction and the beam energy was low. On the basis of the old beam line, the present beam line can be used to transport intermediate-energy beams produced by the projectile fragmentation method. Figure 1 shows the layout of this beam line.

In order to obtain a well-separated secondary beam, we combine magnetic rigidity analysis with spatial selection. Secondary beams can be produced by impinging primary beams on a production target. By adjusting the magnetic field of the dipole, a beam with a certain magnetic rigidity can be selected. After passing through the dipole magnet, the beam is dispersively focused on the first focus point (F1), while the primary beam is stopped inside the chamber of the dipole or in the baffle immediately after the dipole. Using the 4 directional slits (4D slits) located at F1, the beam of interest can be selected by spatial distribution. The momentum acceptance of the beam line can also be defined by this slit. Finally, the selected beam is nearly achromatically focused on the second focus point (F2).

The first-order transfer matrix elements calculated by the code TRANSPORT[2] are shown in Fig. 2. Because of the small apertures and small focusing power

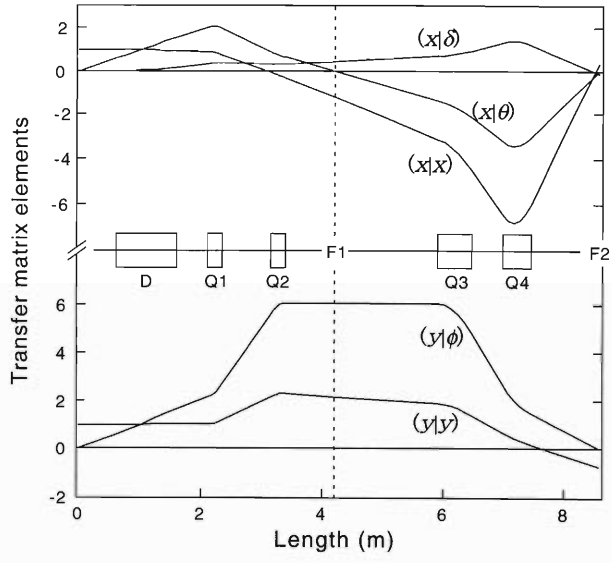

Fig. 2. First-order transfer matrix elements calculated by the code TRANSPORT.[2] $(x|\theta)$ and $(y|\phi)$ are given in m/rad, and $(x|\delta)$ is given in cm/%.

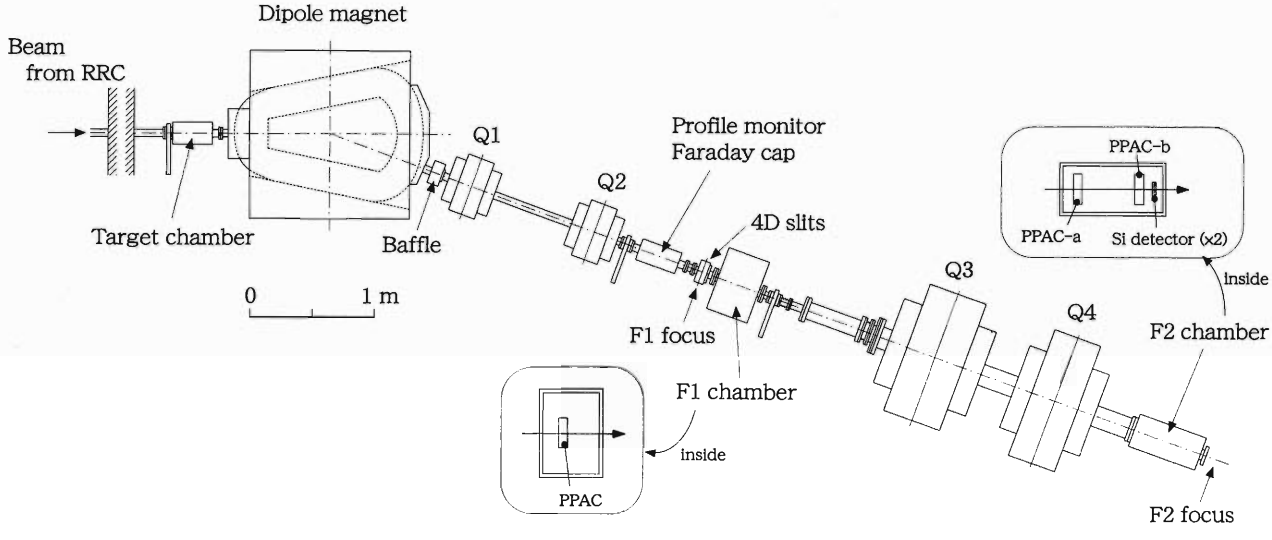

Fig. 1. Schematic view of the present E1C secondary-beam line. In the target chamber, three targets and ZnS can be installed. The opening space of the x direction of baffle is fixed at ± 18 mm, which is the same as the acceptance of the beam line. 4D slits have two sets of movable slits for x (left and right) and y (up and down) directions. In the F1 chamber one PPAC is installed, and in the F2 chamber two PPACs and two Si detectors are installed for secondary beam diagnostics.

*1 Science University of Tokyo
*2 Peking University, China
*3 Tohoku University

Table 1. Basic characteristics of the present secondary-beam line.

Configuration	D-Q-Q-Q-Q
Angular acceptance	θ: 9 mrad, ϕ: 5 mrad
Momentum acceptance	$\pm 4\%$
Max. $B\rho$	3.5 Tm
Deflection angle	20°
Focus at F1	dispersive
Focus at F2	nearly achromatic
Dispersion at F1	$(x\|\delta) = 0.5$ cm/%
Magnification at F1	$(x\|x) = -1.3$, $(y\|y) = 2.1$
Magnification at F2	$(x\|x) = 0.4$, $(y\|y) = -0.8$
Path length	4.2 m (target to F1)
	8.4 m (target to F2)

of Q1 and Q2 quadrupoles, the beam optics for the y direction is designed to be point to parallel (from target to F1), and parallel to point (from F1 to F2). By doing so, a larger angular acceptance is obtained. The basic characteristics of this beam line are listed in Table 1.

For particle identification, several detectors are installed. A parallel-plate avalanche counter, PPAC[3] (charge division type, sensitive area $100 \times 100\,\mathrm{mm}^2$), is placed at F1 to measure spatial distribution of the beam. Two PPACs are placed at F2 to determine beam trajectory. PPACs installed at F1 and F2 can be also used as counters for a time-of-flight (TOF) measurement. Two Si detectors installed inside the F2 chamber measure ΔE. The magnetic field (B) of the dipole is monitored by a Hall probe. Using the $B\rho$-ΔE-TOF method, the secondary beam can be easily identified.

In order to check the performance of this new beam line, we carried out a test experiment. A Be target was bombarded with a 70-AMeV $^{15}N^{7+}$ beam to produce the secondary beam. We were mainly interested in the $N = 8$ isotones such as ^{14}C, ^{13}B, and ^{12}Be. Using the $B\rho$-ΔE-TOF method, particle identification was realized. Figure 3 shows a typical example of the results of ^{14}C production, where Z was deduced from the energy deposit in Si detector, and A/Z was deduced from TOF between target (RF signal of ring cyclotron) and F2 (timing signal from PPAC at F2). In Fig. 3, ^{14}C was clearly identified, and the other nuclei within the same $B\rho$ region were also observed as expected. In order to reduce scattered particles originating from the primary beam, the magnetic rigidity of the dipole was set higher than that of the center of the momentum distribution of the ^{14}C beam, which was calculated by the code INTENSITY.[4] However, many scattered particles still entered the detector system. To minimize such an effect, detailed analysis and further improvements are now in progress.

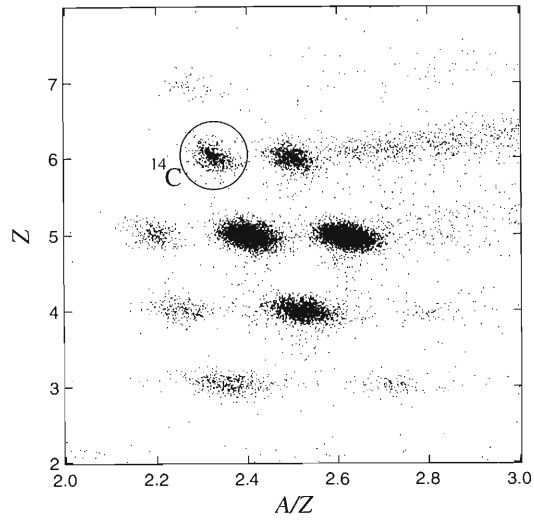

Fig. 3. Result of production of ^{14}C beam. The magnetic field of the dipole was set higher than that of the center of the momentum distribution of the ^{14}C beam. The x-axis shows A/Z and the y-axis shows Z of detected particles.

References

1) T. Kishida et al.: RIKEN Accel. Prog. Rep. **28**, 50 (1995) and references therein.
2) K. L. Brown: Adv. Particle Phys. **1**, 71 (1983).
3) H. Kumagai and K. Yoshida: RIKEN Accel. Prog. Rep. **28**, 127 (1995).
4) J. A. Winger et al.: Nucl. Instrum. Methods Phys. Res. B **70**, 380 (1992).

Development of Low Energy Polarized Radioactive Isotope Beams

H. Miyoshi,[*1] K. Asahi, H. Ogawa,[*1] H. Ueno, and T. Suzuki[*2]

A number of nuclear moments have been measured at the RIKEN Ring Cyclotron during the last decade, by using spin-polarized beams from the fragmentation reaction combined with the nuclear magnetic resonance *via* change in the angular distribution of β rays (β-NMR method). This approach, however, requires several conditions to be fulfilled. One is to find a suitable host material in which spin-polarized nuclei can be implanted, since the spin relaxation time is very sensitive to the chemical properties of an implanted atom and the host material. The size of the β-ray asymmetry parameter, which largely determines the performance of the measurement, is another important factor.

To avoid the difficulties forecast in such requirements when the measurement is extend to the heavier mass region, we attempt to develop a method which involves a low-energy spin-polarized radioactive isotope (RI) beam, which we call the Atomic-Beam RI Polarization method (ABRIP). The advantage of this method is that neither special host material nor a large β-ray asymmetry is required, since the magnetic resonance is performed in-flight and the resonance is detected simply by counting the radiations of the transmitted RI.

In the following, a method to produce low-energy spin-polarized RI beams is proposed. First, the RI atoms are stopped in a noble gas in a cell. The temperature of the gas is kept as low as 80 K. Then, the RI atoms are ejected together with the gas into vacuum from the cell. A nozzle[1)] is mounted on the exit of the cell so that the gas spouts out at forward angles. The spread of the angles of the gas flow can be set within 3–4 degrees, as reported in Ref. 1. A schematic view of the setup is shown in Fig. 1.

A hexapole magnet is installed to converge the beam from the nozzle of the cell. The force on the atoms in a strong magnetic multipole field, $B(r)$, is given as

$$F(r) = \mu \nabla B(r), \tag{1}$$

where μ is the atomic magnetic moment and $B(r)$ the strength of the field $B(r)$. The field distribution $B(r)$ within the magnet bore can be calculated using formulae derived by Halbach.[2)] For a hexapole magnet consisting of M wedge-shaped segments, one finds:

$$B(r) = (r/r_i)^2 B_0 \frac{3}{2}\left(1 - (r_i/r_o)^2\right) \times \cos^3(\pi/M)\sin(3\pi/M)/(3\pi/M), \tag{2}$$

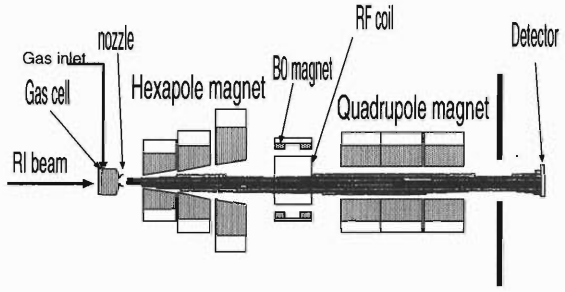

Fig. 1. Schematic view of the ABRIP device. The indicated trajectories for RI atoms are the results of simulation when the RF field is applied.

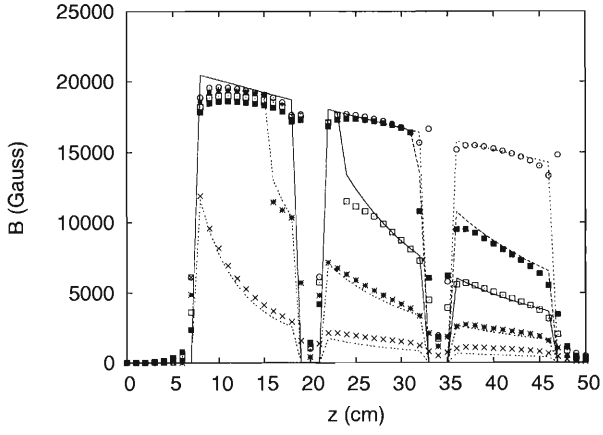

Fig. 2. Comparison of $B(r)$ field obtained from Eq. (2) in the text (dots), with the simulated value from the code OPERA[3)] (dotted lines). The three hexapole magnets are assumed to be 12 cm long each with 2 cm interval spacing.

where r_i and r_o denote the inner and outer radii of the magnet, and B_0 the residual field. In our calculation, the hexapole magnet is assumed to consist of 24 segments of permanent magnets. The magnetic field at the pole tip is about 1.5 T. The radius r_i is varied over a region 0.5–3 cm while r_o is fixed at 7.5 cm. Comparison of the calculated hexapole $B(r)$ with $B(r)$ using the simulation code OPERA[3)] is shown in Fig. 2. The $B(r)$ field evaluated from Eq. (2) is in good agreement with the simulation result. We therefore employed the $B(r)$ value from Eq. (2) to simulate the particle orbit in the hexapole field. In Fig. 1, the simulated trajectories for atoms with spins parallel to the field (low-field seekers) are shown, where convergence of the beam is apparent. At the final stage, a quadrupole magnet is installed to obtain a polarized RI beam. By select-

*1 Tokyo Institute of Technology
*2 Sony LSI Design Inc.

Table 1. Simulation results for the transmission and total efficiency for various mass numbers of RI atoms. For the definitions of the transmission and total efficiency, see text.

A	Transmission (%)		Total efficiency (RF-On)
	RF-On	RF-Off	
20	17.75	0.15	7.69×10^{-6}
30	27.27	0.50	1.18×10^{-5}
40	33.12	0.62	1.43×10^{-5}
50	33.02	1.00	1.43×10^{-5}
60	29.34	1.15	1.27×10^{-5}
70	26.42	1.39	1.14×10^{-5}
80	21.73	1.59	9.42×10^{-6}

ing the beam direction, a high degree of polarization is expected.

In the low-field region located between the hexapole magnet and the quadrupole magnet, an RF field is applied in order to induce transitions between different spin states. The entire setup is arranged so that when the frequency of the RF field is off-resonance the detector located behind the quadrupole magnet counts no transmitted particles. When the resonance is met, the spin transition occurs and the deflection of the flight paths due to the quadrupole field turns and results in counts at the detector. In Table 1 we list the simulated transitions and efficiencies of the apparatus. Here, the "transmission" is defined as the ratio of the number of RI atoms reaching the detector to that of the atoms released from the nozzle. The "total efficiency" is a product of several factors: (transmission) $\times$ (detection efficiency) $\times$ (RF transition efficiency) $\times$ (probability of RI atoms stopping within the gas cell).

In our simulations, the degree of polarization is evaluated as exceeding 99%. Thus, although the total efficiencies may not be very high, the resonance detection is expected to be carried out with very high Signal/Noise ratios, enabling the moments measurements of nuclei in regions far from stability.

References

1) W. J. Hiller and W.-D. Schmidt-Ott: Nucl. Instrum. Methods **139**, 331 (1976).
2) K. Halbach: Nucl. Instrum. Methods **169**, 1 (1980).
3) OPERA-2d and OPERA-3d/TOSCA, Vector Field, Ltd., UK.

Installation of Low-Energy RI Beam Separator CRIB

Y. Yanagisawa, S. Kubono,[*1] T. Teranishi,[*1] Y. Mizoi,[*1] S. Watanabe,[*1] M. Notani,[*1] S. Michimasa,[*1] K. Ue,[*1] Y. Ohshiro,[*1] N. Yamazaki,[*1] S. Shimoura,[*1], S. Kato,[*2] and M. Kase

Low-energy radioactive isotope beams of around 10 MeV/u provide great opportunities to investigate nuclear properties as well as to study nuclear astrophysics. We have installed a low-energy radioisotope separator, called CRIB, which is an inflight separator, in the E7 room. CRIB consists of the magnetic spectrometer DUMAS[1)] and a velocity selector (Wien filter). This separator is installed as a part of the CNS-RIKEN collaboration. The facility enables one to obtain radioactive isotope beams of energies below 10 MeV per nucleon by using the primary beams from the AVF cyclotron.

The DUMAS is designed to be a doubly achromatic spectrometer with an intermediate dispersive focus between the two dipoles. Figure 1 shows a schematic view of the CRIB. Particles produced by nuclear reactions at the primary target, for example, (p, n) and (d, p) reactions, are collected and separated through the spectrometer, and focused downstream where a secondary target is placed for a radioactive beam experiment. The principle of isotope separation is based on the magnetic rigidity analysis and the energy loss of particles. A degrader is placed on the intermediate focus to generate energy loss. The basic specifications of this magnetic system are listed in Table 1.

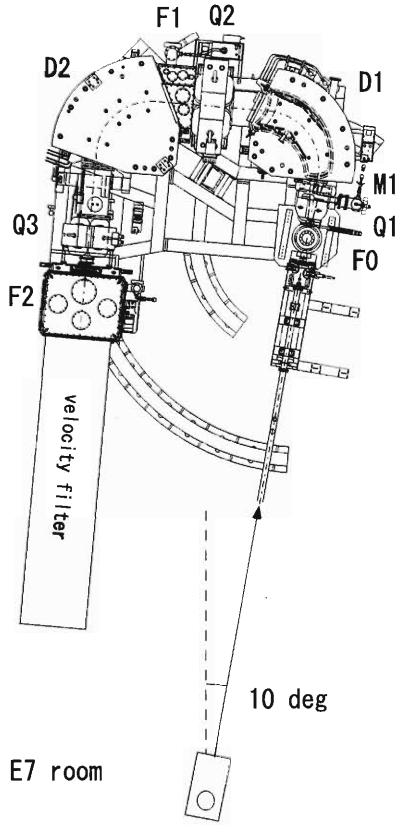

Fig. 1. Schematic view of CRIB.

Table 1. Specifications of CRIB.

Maximum energy	$E_{max} = 110\, Z^2/A$ MeV
Orbit radius	$\rho = 84$–98 cm
Spectrum range	±7.7% in momentum (±15% in energy)
Maximum solid angle	$\Delta\Omega_{max} = 5.6$ msr (75 mr (H) × 75 mr (V))
Deflection angle	185 deg
Length of central orbit	$L = 7.80$ m ($\rho = 90$ cm)
1st focal plane	
Size	40 cm (H) × 8 cm (V)
Energy dispersion	$\Delta x \cdot E/\Delta E$ = 700 mm ($\rho = 98$ cm) = 1015 mm ($\rho = 84$ cm)
Tilted angle	0 deg
Energy resolution	$\Delta E/E = 1/350$
2nd focal plane	
Energy dispersion	0
Magnification	$M_x = 1.5$, $M_y = 0.2$

The spectrometer consists of five main magnets (Q1-D1-Q2-D2-Q3) and two small correction magnets (M1 and M2), as shown in Fig. 1. All these magnets are mounted on a platform which can rotate from −5 deg. to 60 deg. around the center of the F0 scattering chamber. Particles produced at the target are analyzed with respect to their momenta in the first half of the system and are focused dispersively on the first focal plane F1. The first section with the configuration of Q-M-D-Q gives a dispersive focus at F1 and analyzes the magnetic rigidity of reaction products. The primary beam will be stopped on the wall of a water-cooled aluminum faraday cup inside the first dipole. The second section with a configuration of D-M-Q compensates the dispersion of the first section and gives a doubly achromatic focus at F2.

Development of the CRIB facility is in progress. The velocity filter system after F2 focal plane will be installed soon in order to increase purity of the secondary beams. The next plan for the CRIB facility is to install a gas target system[2)] for the production of secondary beams using fusion reactions.

*1 Center for Nuclear Study, University of Tokyo
*2 Yamagata University

References

1) T. Noro et al.: RCNP Ann. Rep. **1983**, 173.
2) T. Kishida et al.: Nucl. Instrum. Methods Phys. Res. A **438**, 70 (1999).

Installation of a Gas-Filled Recoil Separator (GARIS) at the RIKEN Linear Accelerator Facility

K. Morita, M. Kase, Y. Yano, A. Yoneda, K. Morimoto, T. Suda, A. Yoshida, Y. L. Zhao, K. Katori, and I. Tanihata

This year, a gas-filled recoil separator (GARIS)[1] was installed in an experimental hall of the RIKEN Linear Accelerator (RILAC) facility. The separator was designed for fast (in-flight) and effective collection of the nuclear reaction products separating them from an intense primary beam. The GARIS was originally installed in an experimental hall (E1) of the RIKEN Ring Cyclotron (RRC) facility and used mainly for searching for new isotopes which were produced in fusion-evaporation reactions.[2–4]

As part of an RI-Beam Factory (RIBF) project,[5] the E1 experimental hall will be used for a beam transport line from the RRC to a new accelerator area. Thus we need to relocate the entire separator setup from the E1 experimental hall.

A new accelerator-decelerator system (CSM: charge state multiplier) was installed immediately downstream of the existing RILAC also as part of the RIBF project. The CSM consists of an accelerator section, a charge stripping section, and a decelerator section in this order. With the accelerator section of the CSM we obtain a beam with the maximum energy of $5.8A$ MeV, while the highest beam energy available with the RILAC only is $4A$ MeV. This maximum beam energy value, $5.8A$ MeV, is suitable for studying the nuclear fusion-evaporation reaction. This is because, for almost all pairs of beam- and target-nucleus combinations, the energy is sufficiently high to overcome a Coulomb barrier of an incident channel, but is not so high as to excite the fused nucleus excessively. Since the high excitation energy of the compound (fused) nucleus leads the main decay channel to fission, the survival probability of the evaporation residues becomes small.

Under these circumstances we decided to transfer the GARIS from the E1 experimental hall at RRC to an experimental hall behind the accelerator section of the CSM to continue experiments using the GARIS.

An advantage of this relocation is that we expect that we will be able to obtain a more intense beam on target than we have with the RRC because we can greatly reduce the beam path length by skipping the RRC and its long beam line. The figure of merit is expected to be about one order of magnitude in the case of a Kr beam. One of the most interesting applications of the GARIS is the discovery of isotopes of new elements whose atomic number is greater than 113. These elements are the so-called superheavy elements (SHE). Because the production cross section of such a reaction is estimated to be less than 1 picobarn ($10^{-36}\,\mathrm{cm}^2$), the figure of merit is important to the design of this kind of experiment. Here, we estimate the counting rate of such an experiment in order to demonstrate how important the high beam intensity is. We assume that the production cross section (σ) is 1 picobarn ($10^{-36}\,\mathrm{cm}^2$). Typical target thickness (T) is $200\mu\mathrm{g/cm}^2$ ($6 \times 10^{17}\mathrm{atom/cm}^2$), and typical beam intensity (I) from the RRC is 1 particle-μA (6×10^{12} ion/s). Then, if we assume that the total detection efficiency (ϵ) is 0.5 we obtain a counting rate (Y/s) of the event by multiplying these numbers, as

$$\begin{aligned} Y/s &= \epsilon \times \sigma \times T \times I \\ &= 0.5 \times 10^{-36} \times 6 \times 10^{17} \times 6 \times 10^{12} \\ &= 1.6 \times 10^{-6}/\mathrm{s}\ (= 1/7.2\ \mathrm{day}). \end{aligned}$$

This counting rate means that we expect an event in a little more than 1 week, on average. If we obtain ten times higher intensity, we can expect an event every 17.4 hours, on avarage.

We can expect further profit. Now two accelerators, the RILAC and an azimuthaly varying field (AVF) cyclotron, are used as injectors for the RRC. Three years from now, the RRC will be operated mainly through the AVF cyclotron injection, then we will be able to occupy the beam time of the RILAC operation mostly for our experiments. Thus we can expect to have much more beam time than we currently have at the RRC. This situation will allow us to perform a systematic study of the SHE region.

Along with this relocation, we have made some improvements to the GARIS. The original GARIS consisted of three magnets in a D1-Q1-Q2 configuration, where D denotes the dipole magnet and Q denotes the quadrupole magnet, as described in Ref. 1. The distance between Q1 and Q2 was 330 mm. The distance has now been increased to 520 mm. When we designed the Q-magnet, the effect of the large bore radius (150 mm) was not properly taken into account. As a consequence, the focusing power of Q2 was lacking at the highest Bρ value of the D-magnet. By changing only the distance between Q1 and Q2, the focusing power is expected to recover without changing the power supply to the Q-magnet.

Another improvement was made by installing a new D-magnet (D2) between Q2 and the focal plane. In the experiment, incident beams are stopped by a graphite wall in the D1-magnet. A large number of light-charged particles are emitted there. Although the Bρ values of these light-charged particles are far different from the values of the reaction products of interest,

because their source points are not as those of the reaction products, they reach the focal plane by passing through the Q-magnets. These light-charged particles come into the focal plane detectors, and create a main background signal in our detection system. This additional D-magnet sweeps such light-charged particles from the focal point. In this way we expect to realize a low background condition at the highest beam intensity.

Testing experiments for measuring the characteristics of the new GARIS system are scheduled for early 2001.

References

1) K. Morita et al.: Nucl. Instrum. Methods Phys. Res. B **70**, 220 (1992).
2) K. Morita et al.: Z. Phys. A **352**, 7 (1995).
3) Y. H. Pu et al.: Z. Phys. A **357**, 1 (1997).
4) Y. Tagaya et al.: Eur. Phys. J. A **5**, 123 (1999).
5) Y. Yano et al.: Proc. 15th Int. Conf. on Cyclotrons and Their Applications, Caen, France, (IOP, 1998), p.696.

Absolute Calibration of Deuteron Beam Polarization at Intermediate Energies *via* $^{12}C(d,\alpha)^{10}B^*(2^+)$ Reaction

K. Suda,[*1] H. Okamura,[*1] T. Uesaka,[*1] J. Nishikawa,[*1] H. Sakai,[*2] A. Tamii,[*2] K. Sekiguchi,[*2] K. Yako,[*2] S. Sakoda,[*2] H. Kato,[*2] M. Hatano,[*2] Y. Maeda,[*2] N. Sakamoto, Y. Satou, and T. Ohnishi

At RIKEN Accelerator Research Facility (RARF), we are studying nuclear reactions and spin structures of the nucleus using polarized deuteron beam at intermediate energies.[1] Among these studies, the one on the three-nucleon forces (3NF) draws considerable interest.[2] In such studies, highly precise data are required to be compared with rigorous calculations. Accordingly, the accuracy of beam polarization also becomes crucial. The polarization is measured using the *d-p* elastic scattering as polarimetry at RARF. The analyzing powers for the reaction were calibrated against the polarization measured by the $^{12}C(d,p)^{13}C$ reaction or $^{3}He(d,p)^{4}He$ reaction at the exit of the injector AVF cyclotron.[3,4] However, systematic uncertainty arises from the fact that the beam polarization and the analyzing powers for the *d-p* elastic scattering cannot be measured simultaneously. Moreover, systematic uncertainties of the analyzing powers for the two reference reactions mentioned above are already significant in amount. Thus, we proposed to use the $^{12}C(d,\alpha)^{10}B$ reaction at 0° as a new polarization standard for the deuteron beam at intermediate energies.[5] In Ref. 5, we reported on the calibration of the analyzing powers for the *d-p* elastic scattering using the (d,α) reaction at $E_d = 270$ MeV. As we reported, the statistical accuracy of the beam polarization measured using the (d,α) reaction was insufficient because the beam intensity was limited due to a high level of background events. Thus, we performed calibration again with reduced background events at the same deuteron energy. The amount of shield at the back of the beam stopper is increased, because particles from the stopper are thought to be a major source of background events at 0° measurement. The result is shown in Fig. 1. An agreement between the present results and the data from Ref. 3 is fairly good. We also carried out the calibration at $E_d = 140$ MeV. The result agrees with the data from Ref. 4. These results indicate that this method of the calibraion using the (d,α) reaction is useful at intermediate energies.

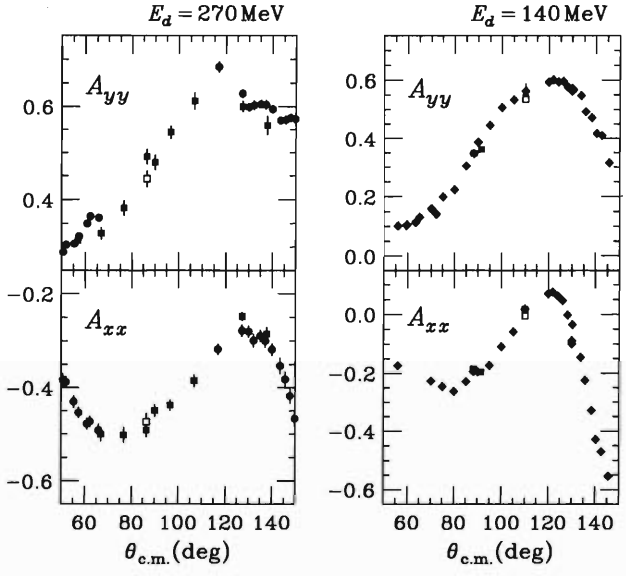

Fig. 1. Analyzing powers for the *d-p* elastic scattering at $E_d = 270$ and 140 MeV. The present results are indicated by open squares in each panel. In the left panel, the data indicated by the closed squares are taken from Ref. 3 and those indicated by circles are from Ref. 2. In the right panel, diamonds represent the data taken from Ref. 6. The errors are statistical ones only.

References
1) For example, H. Okamura et al.: Phys. Lett. B **345**, 1 (1995).
2) H. Sakai et al.: Phys. Rev. Lett. **84**, 5288 (2000).
3) N. Sakamoto et al.: Phys. Lett. B **367**, 60 (1996).
4) T. Uesaka et al.: RIKEN Accel. Prog. Rep. **33**, 153 (2000).
5) K. Suda et al.: RIKEN Accel. Prog. Rep. **33**, 154 (2000).
6) K. Sekiguchi et al.: RIKEN Accel. Prog. Rep. **34**, 50 (2001).

*1 Department of Physics, Saitama University
*2 Department of Physics, University of Tokyo

The Design of a Polarimeter for a Spin-Polarized Positron Beam

J. H. Kim, F. Saito, N. Suzuki, L. Wei, Y. Nagashima, T. Kurihara, A. Goto, Y. Itoh, and T. Hyodo

A new positron polarimeter has been designed and its performance is simulated using a charged-particle trajectory program. The results of the ray tracing are presented along with the details of the design parameters and projected system performance. The positron polarimeter will be used in conjunction with an electrostatic system in which ^{18}F will be generated as a polarized positron source using azimuthal varying field (AVF) cyclotron at RIKEN (The Institute of Physical and Chemical Research). The polarization of the slow positrons will be measured by an ortho-positronium quenching method with incident energies of 0.1 to 30 keV in the presence of magnetic fields (up to 12 kGauss). The design of the polarimeter enables the effective transmission of positrons to the sample by avoiding the reflection of the positrons using electrostatic lenses, which do not change the spin of positrons.

For the polarimeter shown in Fig. 1, slow positrons are accelerated (0.1–30 keV) by a linear-type accelerator (1) and transported to a sample (2) through an electromagnet (5). A set of lenses (3) with a 20 mm inner diameter is used to focus the positrons onto the sample through a hole in the electromagnet pole pieces, producing a magnetic field. The beam profiles shown in Fig. 1 using the lenses to focus (a) and without using the lenses (b) at the incident energy of 4 keV, indicate that the beam diameter at the sample can be reduced from 11 mm to 2 mm. In Fig. 2, the beam diameter (open squares) becomes larger thus the positrons will miss the sample when the beam energy is lower than 4 keV. Using the lenses, the beam diameter (closed circles) is simulated to be 2–6 mm in the range of beam energies from 0.1 to 30 keV.

The reflection of the positrons due to the mirror effect is simulated as a function of the beam energies (0.1–30 keV) and magnetic fields (0–12 kGauss). When the small lenses are not used, the reflection of the positrons occurs at beam energies of less than 5 keV, even under weak magnetic fields (left side of the dotted line in Fig. 3). Focusing the positrons, as indicated by the solid line, can reduce the mirror effect (shaded area).

A ray tracing analysis indicates that this design is capable of effectively transmitting positrons at beam energies varying from 0.1 to 30 keV within the beam diameter of 2–6 mm. However, the observed reflection of the positrons (lower than 2 keV) at 12 kGauss indicated that further refinement of beam design is needed to produce a better positron polarimeter.

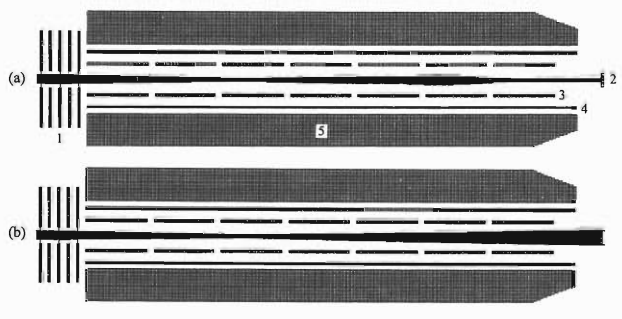

Fig. 1. Ray tracing simulations (with a charged-particle trajectory program) of the polarimeter.

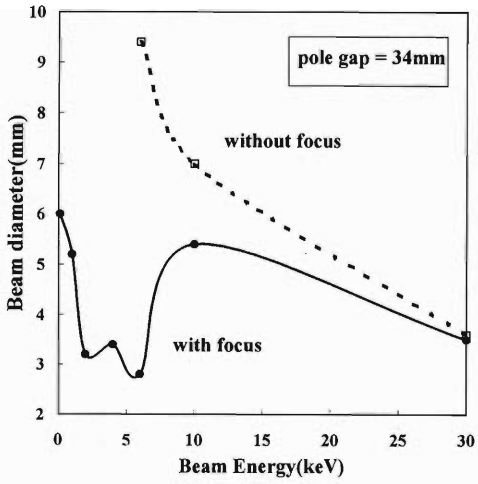

Fig. 2. The beam diameter at the sample as a function of beam energies. The open squares represent the diameter without focusing while the closed circles represent the diameter with focusing.

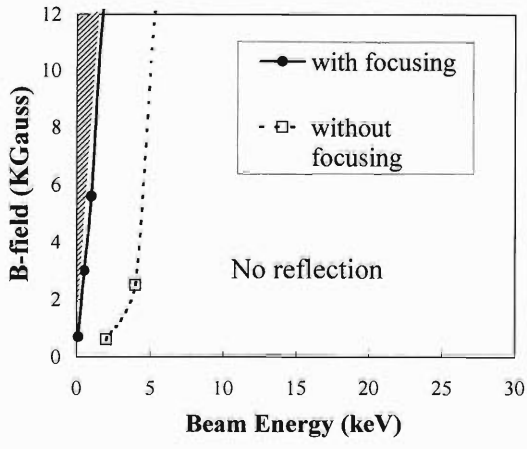

Fig. 3. Magnetic field dependence of the beam reflection as a function of beam energies.

Development of Rotating Target for Big-RIPS in RIBF

A. Yoshida, K. Morimoto, A. Ozawa, M. Fujimaki, Y. Takahashi, and I. Tanihata

A rotating target system for the projectile fragment separator (Big-RIPS) in the RI-Beam Factory (RIBF) has been developed. The assumed maximum heat loss in the target material (beryllium or carbon) is for the case of a ^{238}U primary beam at 400 A MeV, 1 pμA from the Super-conducting Ring Cyclotron (SRC). The stopping range of the beam in the target material is $R = 18$ mm and the optimum target thickness for producing the most intense secondary beams is approximately $d = 6$ mm ($d/R = 0.3$) where the beam penetrates the target. Under this condition, it is expected that 20 kW heat loss occurs in a 1 mm-diameter beam spot size. In order to avoid melting the target, the rotating target method is useful. A prototype was constructed and tested with the maximum intense heavy-ion beam from the present RIKEN Ring Cyclotron (RRC).

The maximum intense beam $^{40}Ar^{9+}$ at 24 A MeV, 1.9 pμA was bombarded on a carbon disk with a beam spot size approximately 3 mm in diameter; the size was determined using a ZnS foil. The range of the beam is a depth of 0.5 mm and the thickness of the target disk was 2 mm, thus the beam stops inside the target and releases its full energy of 1.8 kW in a narrow Bragg peak region. The calculated heat density at this peak region is approximately 690 W/0.12 mm = 5.7 kW/mm, which is almost the same condition as the assumed maximum heat loss for the case of the ^{238}U beam mentioned above, 20 kW/5 mm = 4 kW/mm, if the beam spot size is comparable. The carbon disk, 260 mm in diameter and 1.8 g/cm^3 in density, was tightly fixed by screws on the water- cooled aluminum plate and was rotated in the vacuum chamber (Fig. 1).

The temperature of the beam spot was measured by

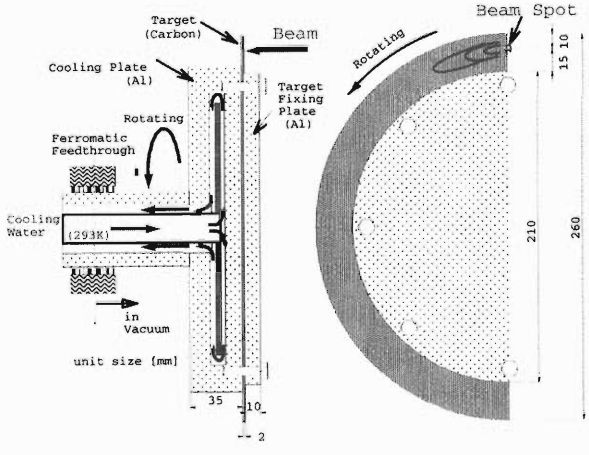

Fig. 1. Cross-sectional view of the rotating target plate (left) and image of the beam spot (right).

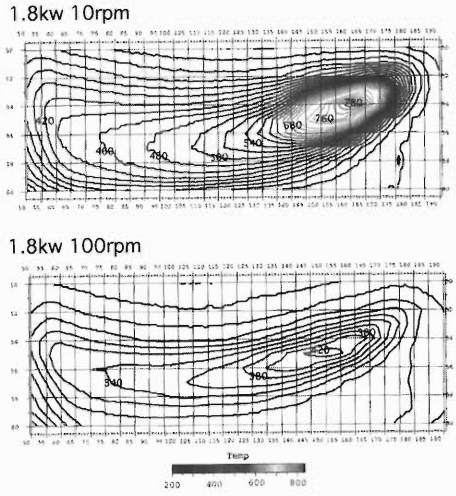

Fig. 2. Contour plots of the temperature distribution near the beam spot with the maximum beam intensity of 1.8 kW at 10 rpm (up) and 100 rpm (down) corresponding to 126 and 1256 mm/s in tangential speed, respectively.

an infrared radiation thermoviewer (TVS-2200, Avionics Japan) which has an InSb detector sensitive to 3–5.4 μm infrared radiation. A BaF_2 glass window was used to allow infrared radiation to penetrate from the vacuum chamber. The emissivity at the surface of the carbon target and the BaF_2 window was calibrated using a thermocouple device and found to be 0.84. A typical temperature distribution of the beam spot is shown in Fig. 2. The position resolution of the thermoviewer is approximately 0.6 mm/pixel, due to the size of its digital image of 256 × 100 pixels. Each pixel has 256 levels of temperature information; its maximum range is −40–2000°C and its minimum resolution is 0.1°C. The refresh rate of one image is 30 flames/sec which is sufficiently fast to achieve the position resolution mentioned above, even at the highest rotation speed of the target disk, 150 rpm.

A series of measurements varying the rotation speed from 10 to 150 rpm and the beam heat loss from 0.2 to 1.8 kW was performed. A saturation effect was observed for the plot (Fig. 3 (a)) of rotation speed vs beam spot temperature under the same heat loss condition, although the target volume in the tangential direction increased linearly with the rotation speed. This may be because the thermal diffusion coefficient is less than the rotation speed. A mostly linear correlation is observed between the heat loss dE vs the beam spot temperature up to 1.8 kW heat loss, as shown in Fig. 3 (b).

When we changed the flow rate of the cooling wa-

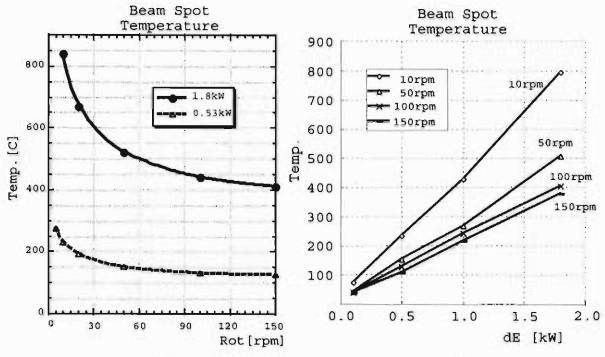

(a) (b)

Fig. 3. Maximum temperature of the beam spot was measured while varying rotation speed and heat loss in the target.

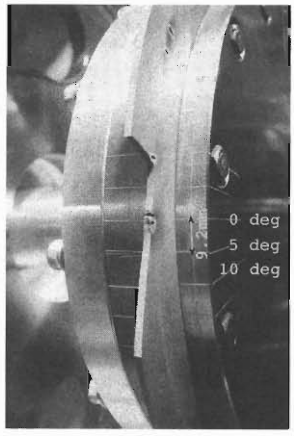

Fig. 4. Holes in the carbon disk target caused by the beam when the rotation stopped. Also, it cracked due to a difference in thermal expansion.

ter at 25°C from 5 to 10 liters/min under the beam heat loss condition of 1.8 kW, we did not observe a clear decrease in temperature at the beam spot, but an increase in temperature at the outlet of the cooling water from $dT = 1.5$°C to 2.8°C was observed. This indicates that the cooling water carried away the heat from 980 W to 1050 W, corresponds to approximately 56% of the total energy released. Calculated thermal radiation at the beam spot temperature of 800°C is sufficiently small at approximately 3 W/cm^2. This indicates that there may be other paths of heat consumption in the target chamber which we have not yet located.

When we stopped the rotation, the beam immediately shot through the target and made a small hole (Fig. 4). The size of the hole was 0.7×1.2 mm, which indicates a smaller beam spot than that measured by the ZnS foil.

We need to develop a simulation program which can explain our data so that we can predict the temperature under the 20 kW heat loss condition which can not presently be reached in the RIKEN accelerator facility. We have installed another rotating target system in the present RIPS facility and we continue to measure the data for higher beam energies $\sim$100 A MeV and with a small beam spot size of 1 mm in diameter.

Development of Ferromagnetic Targets for Radioactive-Isotope Beams and a Detector System for Transient Magnetic Field Experiments

H. Ueno, W. Sato, H. Ogawa,[*1] N. Imai,[*2] K. Yoneda, A. Yoshimi, Y. Kobayashi, D. Kameda,[*1] H. Miyoshi,[*1] K. Sakai,[*1] H. Watanabe, and K. Asahi

It is known experimentally that moving ions experience an effective magnetic field as strong as several kT while slowing down in polarized ferromagnetic targets.[1] This magnetic field, the so-called *transient field*, has been applied to the measurement of g-factors for short-lived nuclear excited states. In the present research, ferromagnetic targets for RI beams and a detector system for transient magnetic field experiments have been developed in order to measure the g-factors of short-lived ($\tau \sim$ ps) excited states for unstable nuclei.

Two types of materials, Fe and Gd, are prepared as targets. An adequate degree of magnetization is achieved by the following method. Iron foils are cleaned and rolled to the required thickness of $\sim 10\,\mathrm{mg/cm^2}$. The foils are first heated to $\sim 800\,\mathrm{K}$ in a colts tube furnace evacuated to a pressure of $< 1\times10^{-6}$ Torr, then hydrogen is leaked into the furnace to a pressure of 1 atm, and the temperature is increased to $\sim$ 1200 K for one hour. Another method of annealing is employed for the preparation of gadolinium (Gd) foils, since Gd is known as an effective hydrogen getter. After being placed in the colts tube furnace, $\sim 10\,\mathrm{mg/cm^2}$ thick Gd foils are heated to 1100 K under a pressure of 1×10^{-6} Torr for 10 minutes. The heating power is then reduced slowly and the foils are cooled to room temperature. Although magnetic anisotropy of hexagonal Gd shows a strong temperature dependence of the angle between the easy direction of magnetization and the crystallographic c-axis, it was reported that well-annealed polycrystalline foils show almost the same magnetization compared to the single crystal.[2]

Figure 1 shows the schematic layout of the detector system. The multilayered target consists of 100-mg/cm^2-thick Pb and the above-described well-annealed Gd foil facing each other and placed in a vacuum chamber. In order to obtain high magnetization of the Gd foil an external magnetic field of $B_{\mathrm{ext}} = 0.3\,\mathrm{T}$ is applied perpendicular to the beam axis using a couple of coils placed outside the chamber. The multilayered target is supported with a Cu cold finger connected to a cold head of a cryostat which is cooled to liquid-nitrogen temperature also for the high magnetization.

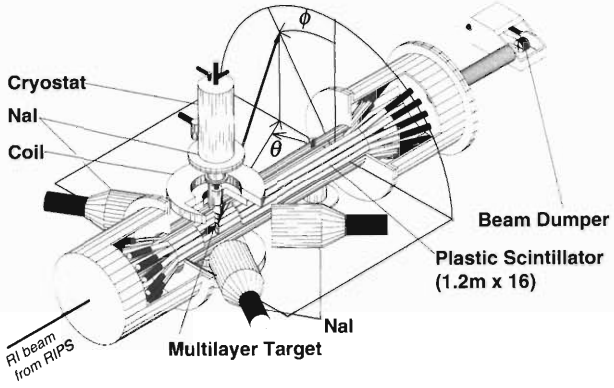

Fig. 1. Schematic layout of the detector system for transient field experiments. For details, see text.

The γ rays emitted from the excited RI-beam particles are measured using four 5.5" × 5.5" NaI(Tl) scintillators in coincidence with scattered RI-beam particles detected with $16\,\ell$ = 1.2-m-long plastic scintillators which are mounted cylindrically with 7.5 cm distance from the beam axis, as shown in Fig. 1. Thus scattering angles $5° < \theta_{\mathrm{Lab}} < 165°$ and $-80° < \phi_{\mathrm{Lab}} < 80°$ and $100° < \phi_{\mathrm{Lab}} < 170°$ are covered. The four NaI detectors are placed at angles $\theta_{\mathrm{Lab}} \sim \pm45°$ and $\pm120°$ relative to the beam axis for measurements of the angular correlation and precession in the transient field. The angles of the γ detectors can be changed to give the maximum slopes of measured particle-γ-angular correlations depending on the nuclear alignment of the excited state. Considering the limited energy resolution of the NaI(Tl) scintillators, a Ge detector is also used to locate contaminant lines in the photo-peak region of the focusing γ transition as well as those fed from higher excited states.

The first experiment using a RI beam is under preparation.

References

1) R. R. Borchers, B. Herskind, J. D. Bronson, L. Grondzins, R. Kalish, and D. E. Murnick: Phys. Rev. Lett. **20**, 424 (1968).
2) O. Häusser, H. R. Andrews, D. Ward, N. Rud, P. Taras, R. Nicole, J. Keinonen, P. Skensved, and C. V. Stager: Nucl. Phys. A **406**, 339 (1983).

*1 Tokyo Institute of Technology
*2 University of Tokyo

A Windowless Solid Hydrogen Target

S. Ishimoto,[*1] T. Kobayashi,[*2] K. Morimoto,[*1] I. Nomura,[*3]
S. Suzuki,[*1] Y. Takahashi,[*4] I. Tanihata, and T. Tsuru[*1]

A windowless solid hydrogen target has been successfully developed[1] for RI-beam-induced nuclear reactions at the RIKEN RI Beam Facility currently under construction.[2] Increasing interest in heavy ion reactions requires a thin and flat solid hydrogen target without any extra materials in the path of the particles. The target is a bare disk of solid hydrogen of diameter 25 mm and thickness 5 mm (40 mg/cm^2) held in vacuum at low temperature. Hydrogen crystal is grown either directly from normal hydrogen gas[3] or from its melt in a cell bored in a 10-mm-thick pure copper block which is cooled by liquid helium as shown in Fig. 1. The two sidewalls of the cell were Teflon-coated stainless-steel flanges, which were tightly pressed to the cell plate by stainless-steel bellows. The bellows were driven by helium gas introduced into them and were precisely controlled by the gas pressure. A 0.8-mm-thick indium gasket was used as a vacuum-tight seal. We employed a pair of step-type flanges when we changed the target thickness.

We found that the following conditions are essential to obtain a uniform crystal of hydrogen. The precooled gas must be introduced at the top of the cell through a vacuum-insulated tube. By these precautions we are able to satisfy the two requirements; keeping the gas inlet free in order to push out the void in the final stage of solidification and producing a gentle upward temperature gradient inside the cell which suppreses the fluid dynamical instabilities in solidification from the melt. It is also important to establish a uniform temperature over the surrounding wall of the cell except for the open end of the inlet tube, which ensures uniform growth of the crystal on the wall as well as preventing fluid dynamical instabilities. Precooling of incoming gas to liquid nitrogen temperature is proved to be pertinent. The vacuum sleeve inside the copper plate keeps the inlet gas at an appropriate constant temperature, which ensures the stable conditions for crystal growth.

Flat hydrogen crystal with high quality has been obtained reproducibly. After completing solidification, the sidewalls of the cell, which are in the path of the particles, are removed in the target cryostat and the crystal is self-supported inside the cell. Thus, there is no extra material in the path near the target. We have obtained a uniform and transparent crystal of normal hydrogen of 25 mm diameter and of either 5 mm or 10 mm thickness.

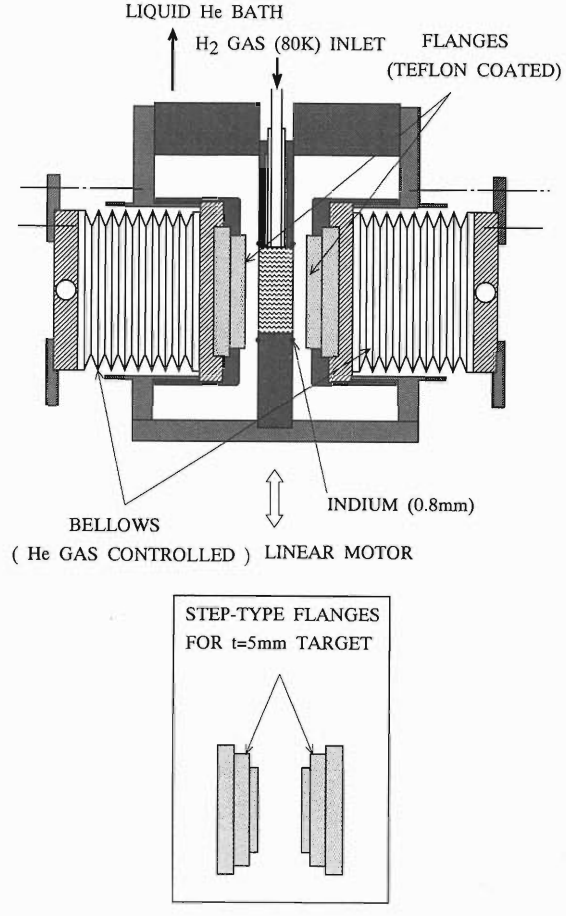

Fig. 1. Assembly of the Teflon-coated flanges and bellows for the sidewalls of the target cell, and a pair of step-type flanges for a 5-mm-thick target.

Figure 2 shows a photograph of the windowless solid hydrogen target of 5 mm thickness. A bare hydrogen crystal is self-supported inside the cell, *i.e.*, inside the copper frame. The crystal is transparent and no visible defects are present. Holding the target at a low temperature prevents the sublimation of hydrogen molecules. At approximately 4.2 K, the sublimation rate agrees with the value calculated from the vapor pressure at thermal equilibrium.[4] The loss is negligible when the target is held below 3 K. The method of crystal growth will be extended to the hydrogen isotopes, HD, D_2, T_2 and possibly to other cryogenic gases such as nitrogen, argon, neon and xenon. The techniques developed here may be applied to various experimental studies in other fields involving neutron scattering, nuclear fusion, optical spectroscopy and solid state physics.

*1 High Energy Accelerator Research Organization
*2 Faculty of Science, Tohoku University
*3 National Institute for Fusion Science
*4 Research Center for Nuclear Physics, Osaka University

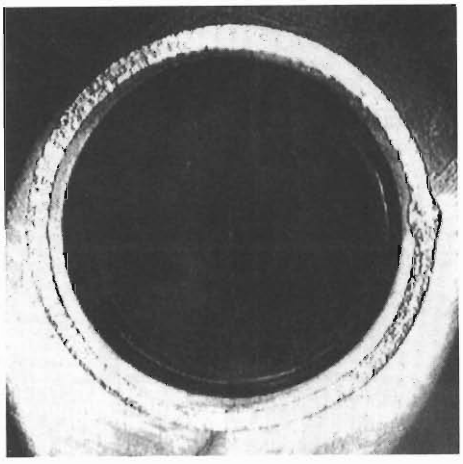

Fig. 2. Bare crystal being held inside the target cell: the windowless solid hydrogen target of 5 mm thickness.

References

1) S. Ishimoto, T. Kobayashi, K. Morimoto, I. Nomura, S. Suzuki, Y. Takahashi, I. Tanihata, and T. Tsuru: RIKEN-AF-NP-348, KEK Preprint 2000-23 H, to be published in Nucl. Instrum. Methods Phys. Res.
2) I. Tanihata: Nucl. Phys. A **588**, 253c (1995).
3) T. Momose, M. Miki, M. Uchida, T. Shimidzu, I. Yoshizawa, and T. Shida: J. Chem. Phys. **103**, 1400 (1995).
4) P. C. Souers: *Hydrogen Properties for Fusion Energy*, (University of California Press, Berkeley, California, 1986).

Construction of Liquid Helium Target

H. Akiyoshi, T. Minemura,[*1] M. Kunibu,[*1] and S. Shimoura[*2]

A helium target system was constructed for a radioactive nuclei induced (α,α') reaction experiment. To overcome the low intensity of the radioactive nucleus beam, helium is liquefied. The liquid helium target system worked well in a series of experiments performed in October of this year.

Numerous cryotargets of ^{4}He have been built in the past to be used in nuclear physics as well as in other fields. In this report we describe the design chosen for the radioactive nuclei induced (α,α') reactions. To detect the γ rays emitted after bombardment of radioactive nuclei from the RIKEN projectile-fragment separator, RIPS, the target is surrounded by NaI scintillators. The amount of material in the path of ejected γ rays should be minimized in order to reduce the absorption of γ rays, while the liquid helium target must be kept at cryogenic temperature, which requires material for cooling and heat shielding. The target cell is isolated in vacuum, which requires additional material. In order to minimize the dead solid angle combining with the existing NaI array system, free space for the target is limited. To use the beam time effectively, the helium target should remain in place for more than two weeks without supplying liquid helium. Consequently, we adopted a liquid helium target liquefied by a small refrigerator.

Figure 1 shows a schematic diagram of the liquid helium target system. All the cryogenic-temperature sections are placed in a cylindrical vacuum chamber made of thin aluminum (K). A target cell (H) is cooled down to approximately 3 K by the second stage of a Gifford-McMahon cycle refrigerator (N) through a connecting component made of copper. The target cell, the connecting part and the second stage of the refrigerator are surrounded by a heat shield (I) attached to the first stage of the refrigerator in order not to receive radiant heat from room temperature parts. A line of pipe (G) wraps around the connecting part, and is lead outside of the vacuum chamber coiling around the refrigerator cylinder. The pipe and the connecting part constitute a heat exchanger (J). Helium is liquefied at the heat exchanger and accumulates in the target cell. Through the pipe, helium gas from a gas cylinder (A) is introduced. The pressure of the helium gas is controlled by a precision pressure regulator (B). The gas pressure in the helium supply pipe is measured by a manometer (C). The flow through the thin pipe causes a pressure difference between the supplying part and the target cell. Therefore, another manometer is used to measure the internal pressure of the target cell through a short-cutting pipe (F) connected to the target cell. The valve E is normally closed. Relief valves are put on both pipes in case of overpressure. Mass flow meters measure the supplied and released gas flow. We can determine the state of liquefying by monitoring the flow rate. Temperatures of the target cell, the heat exchanger, the heat shield, the gas line near 300 K, and the room temperature are measured by silicon diode thermometers. The output voltage of the thermometers, the manometers and the mass flow meters are digitized by a digital multimeter (L), and acquired by a computer (M).

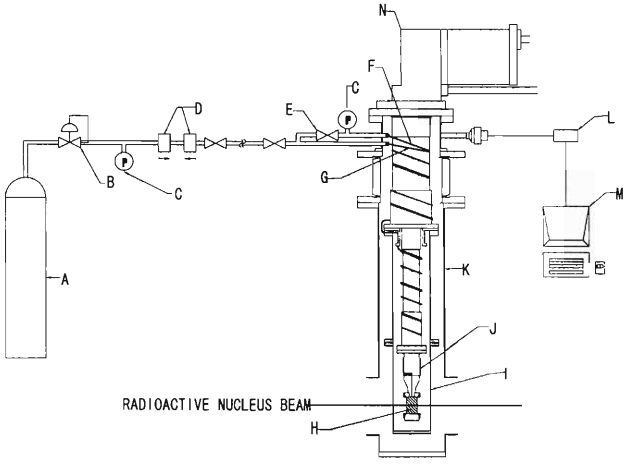

Fig. 1. Schematic diagram of liquid helium target system. Meanings of letters A-M are described in the text.

The target cell is made of aluminum in order to reduce the absorption of γ rays. Havar foils of 6 μm thickness are glued on the cylindrical target cell using Stycast 1266 forming the entrance and exit windows 24 mm in diameter. The windows exhibit high stability and vacuum tightness, but the radioactive nucleus beam may pass through it without large energy losses. The thickness of the target is easily changeable around a few hundreds mg/cm^2. The heat shield is also made of aluminum to reduce γ ray absorption. Two holes in the heat shield 30 mm in diameter allowing the entrance and exit of the radioactive nucleus beam are covered with aluminized Mylar films so as to shield the target from the room temperature parts.

*1 Department of Physics, Rikkyo University
*2 Center for Nuclear Study, University of Tokyo

Construction of a Polarized Proton Target Using a Single Crystal of Aromatic Molecules

T. Wakui, M. Hatano,[*1] H. Sakai,[*1] T. Uesaka,[*2] and A. Tamii[*1]

We have designed and constructed a proton polarizing system in order to develop a polarized proton solid target applicable to experiments using a radioactive isotope beam. The goal of this study is to attain a polarization of more than 50% in a target sample with a diameter of 20 mm and a length of 5 mm. The target will be used to investigate the structure of unstable nuclei through an experiment involving an inverse kinematics. In such an experiment, a proton target which can be polarized in low magnetic fields (100–3000 Gauss) at high temperatures (77–300 K) is desirable because it is necessary to detect low momentum recoiled protons at a large detection solid angle.

Protons in a single crystal of aromatic molecules can be polarized under such conditions by a method called microwave-induced optical nuclear polarization.[1] In this method, guest aromatic molecules doped in the single crystal are optically pumped to the lowest triplet state by laser irradiation. Populations of sublevels in the triplet state are different from each other due to the angular momentum selection rule. Then, the population difference is transferred to proton polarization by means of the integrated solid effect (ISE), a kind of dynamic nuclear polarization method.[2,3] The polarization procedure is described in a previous report.[4]

We use naphthalene and *p*-terphenyl molecules as a host material and pentacene as a guest material. The crystallization procedure is described in Ref. 5.

After crystallization, a section is cut from the crystal and placed in the polarizing system shown in Fig. 1. The system consists of a C-type magnet, a laser system for the optical pumping, a microwave system for the ISE and an nuclear magnetic resonance (NMR) system for measuring the proton polarization.

The magnetic field produced by the C-type magnet is about 3 kGauss. The magnetic field inhomogeneity of 10^{-3} over the target size is required for obtaining a proton polarization of more than 50%. We designed a magnet which satisfies this condition. The diameter of the coil is 150 mm and the gap between the poles is 60 mm. The magnetic field inhomogeneity measured using a NMR teslameter at a field of about 3 kGauss is 3.5×10^{-4} over the target size. The field homogeneity is sufficient for polarizing protons.

We use an Ar-ion laser for the optical pumping. The wavelength of the main mode in the laser, 514 nm, corresponds to the energy of transition to the third excited singlet state in pentacene. To obtain a high population difference in the lowest triplet state, a pulsed laser beam is required because the lifetime of the most populated level in the triplet state is shorter than that of other levels. For pulsing the laser beam, we use an optical chopper. The pulse width and the repetition rate are 20 μs and 1 kHz, respectively. The pulsed laser beam is injected from behind the magnet to the target sample.

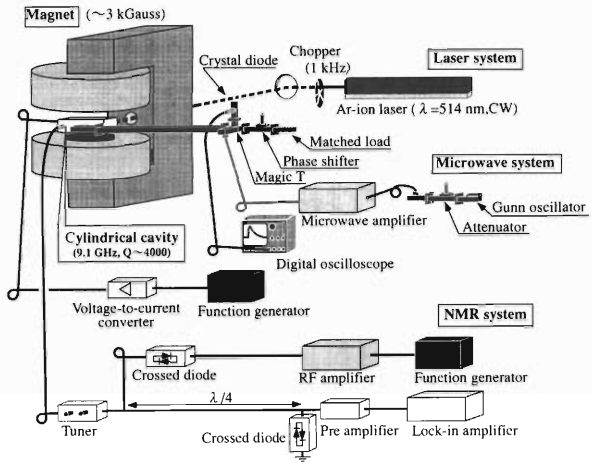

Fig. 1. Experimental setup for proton polarizing system. The system consists of a magnet, a laser system for optical pumping, a microwave system for the ISE and ESR measurements and an NMR system for measuring the proton polarization.

Since the frequency of the electron spin resonance (ESR) in pentacene is about 9.1 GHz under a magnetic field of 3 kGauss, the target sample is placed in a cylindrical microwave cavity. It is necessary that the cavity enables the laser irradiation for the optical pumping, the magnetic field sweep for the ISE and the application of the RF field for the NMR, without impairing the quality factor. Moreover, the target sample has to be kept at a temperature ranging from 77 K to room temperature. We introduced sets of internal RF and field modulation coils into TE_{011} cylindrical cavity; both were placed parallel to the cylinder axis in the cavity, as shown in Fig. 2. Both coils are configured in a two-loop arrangement and are made from four Cu rods with a 2-mm diameter. The quality factor of the cavity is not impaired by the coils as long as the rods are kept parallel to the cylinder axis, and is about 4000 at room temperature. The coil configuration also permits the laser irradiation of the target sample. A quartz tube, on which the target sample is mounted, is placed into a double quartz tube placed among the coil rods along the cylinder axis. Cooled N_2 gas is introduced into the inner quartz tube when

*1 University of Tokyo
*2 Saitama University

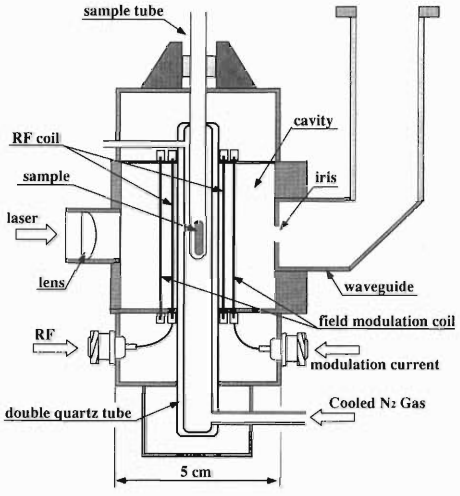

Fig. 2. Schematic view of the TE_{011} cylindrical cavity. The cavity contains sets of internal RF and field modulation coils. The quality factor of the cavity is about 4000 at room temperature.

protons are polarized below room temperature.

The schematic diagram of the microwave system is shown in Fig. 1. A microwave from a Gunn oscillator is pulsed and amplified by a microwave amplifier. Its maximum output power is 20 W and the pulse duration is 10 μs. A circulator attached to the output stage of the amplifier protects it against damage due to unexpected reflection of microwaves. Pulsed microwaves are split with a magic tee, one arm of which is connected to the cylindrical cavity. The other arm (balance arm) is equipped with a phase shifter and a matched load. The impedance of the cavity is matched with that of waveguides by changing the diameter of the iris, a hole between the cavity and a waveguide.

During the pulsed microwave irradiation, the magnetic field is swept through the entire width of an ESR spectrum, whose width is about 30 Gauss, in order to perform the ISE. The field sweep is done by applying a triangular wave of about 50 A_{p-p} to the field modulation coil in the cavity. The current is produced by a voltage-to-current conversion circuit using a high-power operational amplifier.

We observed the ESR spectrum of a sample with a cw microwave so as to align the long molecular axis parallel to the direction of the magnetic field, because the population difference is maximum in this direction. The cw microwave is amplified by the amplifier which is used for the ISE. The maximum output power for the cw microwave is 100 mW. In the measurement, reflected microwaves from the cavity are mixed with those from the balance arm, and are detected with a crystal diode. Figure 3 shows the ESR spectrum of DPPH (2,2-Diphenyl-1-picrylhydrazyl) of about 50 μg. DPPH is used as a standard sample to optimize the microwave system.

A pulsed NMR system is used for measuring the proton polarization. The schematic diagram of the NMR system is shown in Fig. 1. The RF signal produced by a function generator is pulsed and amplified by an RF amplifier, whose maximum output is 500 W. The frequency and the width of the RF pulse are 12.75 MHz and 2 μs, respectively. The power of the RF pulse is adjusted to a level called the 90° pulse, which maximizes the amplitude of transverse magnetization of protons. The pulse is passed through a tuner for impedance matching and applied to the RF coil in the cavity. Then, the NMR signal due to the free induction decay of protons is picked up by the same RF coil. The picked-up signal is amplified by a preamplifier and its proton resonance frequency component is obtained using a lock-in amplifier. Figure 4 shows the NMR signal of the water doped with a paramagnetic impurity.

We are currently tuning the microwave system and the NMR system. These will be completed soon, and we will start to polarize protons subsequently.

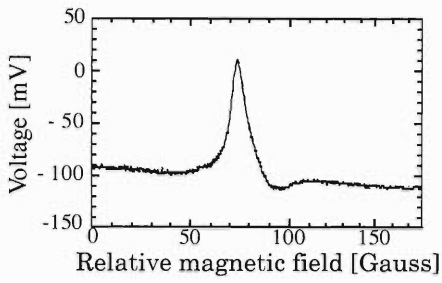

Fig. 3. The ESR spectrum of DPPH (2,2-diphenyl-1-picrylhydrazyl) of about 50 μg in a magnetic field of about 3 kGauss. DPPH is used as a standard sample for optimizing the microwave system.

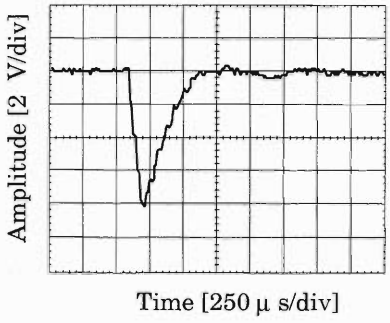

Fig. 4. The free induction decay signal of the water doped with a paramagnetic impurity.

References

1) H. W. van Kesteren et al.: Phys. Rev. Lett. **55**, 1642 (1985).
2) A. Henstra et al.: Phys. Lett. A **134**, 134 (1988).
3) M. Iinuma et al.: Phys. Rev. Lett. **84**, 171 (2000).
4) M. Hatano et al.: RIKEN Accel. Prog. Rep. **33**, 182 (2000).
5) M. Hatano et al.: RIKEN Accel. Prog. Rep. **34**, 196 (2001).

Development of Single Crystals of Aromatic Molecules Doped with Pentacene for a Polarized Proton Target

M. Hatano,[*1] T. Wakui, H. Sakai,[*1] A. Tamii,[*1] and T. Uesaka[*2]

We are now developing a polarized proton solid target applicable at high temperatures ($\geq$ 77 K) and in a low magnetic field ($\leq$ 3 kG). We plan to apply this target to study the structure of an unstable nuclei. We will measure the reactions between an unstable nuclear beam and the polarized proton target in the inverse kinematics condition. We hope to obtain information on the spin of the single particle orbit of a knock-out nucleon by measuring the analyzing power in the $(\vec{p}, 2p)$ or $(\vec{p}, np)$ quasi-free reactions. We can also study the LS interaction between a proton and an unstable nucleus by measuring the elastic scattering between them. In such investigations it is crucial to detect low momentum recoil protons to achieve high angular and energy resolutions. Therefore, a polarized proton target which is applicable in a low magnetic field is especially essential. The polarized proton target is also useful for various experiments, for example, $\vec{d} + \vec{p}$ spin correlation measurement.

As a target material, we use a single crystal of aromatic molecules doped with pentacene ($C_{22}H_{14}$). For the host material we use naphthalene ($C_{10}H_8$, melting point 80.5°C) or p-terphenyl ($(C_6H_5)_2C_6H_4$, melting point 214°C). These host materials are suitable for crystallization with pentacene.

The π-electron of the pentacene molecule has large electron population differences among three Zeeman sublevels in its optical pumped triplet state. This indicates that the electron is polarized. The electron polarization is 73%. This value is independent of temperature and magnetic field. The electron polarization is transferred to the protons by means of the integrated solid effect (ISE).[1,2] Then proton polarization is transferred to the neighboring protons by spin-spin interaction. ISE is a kind of dynamic nuclear polarization. The most significant advantage of this method is that it is applicable in a low magnetic field. Iinuma *et al.* reported that proton polarization of 30% was achieved with this method at a temperature of 77 K and in a magnetic field of 3 kG.[1]

It is known that the higher the purity of the host material, the higher the attainable proton polarization. Therefore, we developed a purification system based on the zone-melting method.[3] The crystallization process is realized by the Bridgman method.[4]

The purification system is shown in Fig. 1. The host material is enclosed in a glass cell. The glass cell is pulled up at a speed of ~20 mm/h through a 20 mmϕ glass tube. Thirty heaters are attached to the glass tube at intervals of 9 cm in order to melt the host material so that melting and solidification of the host material occur alternatingly. Impurities accumulate gradually at the bottom of the glass cell during the passage. Then we remove the part with the impurities and enclose the other part in the glass cell to be purified again in the same way to achieve higher purity. We repeat this procedure tow or three times.

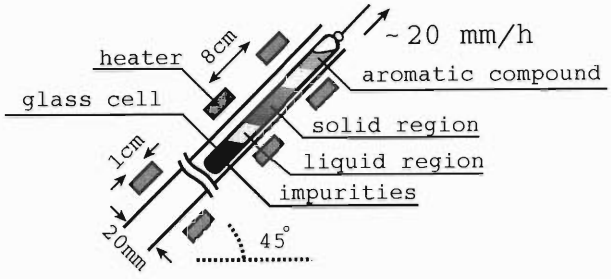

Fig. 1. Aromatic compound purification system. Impurities accumulate gradually at the bottom of the glass cell through the liquid region and the solid region alternately.

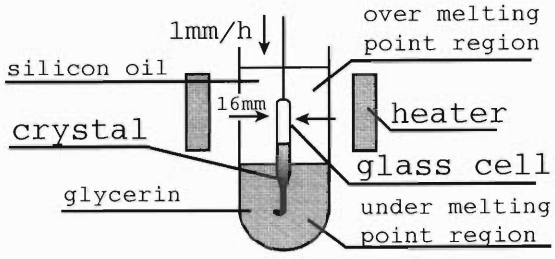

Fig. 2. Aromatic compound crystallization system. The single crystal of aromatic compound grows at the boundary between the temperatures above the melting point and below the melting point.

The crystallization system is shown in Fig. 2. A glass cell enclosing the purified host material and a small quantity of pentacene is pulled down at a speed of ~1 mm/h from the region above the melting temperature toward the region below the melting temperature. In this process, the bottom of the glass cell is cooled down gradually, and a single crystal grows from the bottom of the glass cell.

We have succeeded in fabricating a single crystal of naphthalene doped with pentacene and one of p-terphenyl. Their pentacene molar fractions and crystal sizes are shown in Table 1. The ISE system is being tuned at RIKEN.[5] We will start polarizing protons in a few months.

*1 University of Tokyo
*2 Saitama University

Table 1. Pentacene molar factions and crystal sizes.

host material	molar fractions	size of crystal
naphthalene	0.001 mol %	$10 \times 10 \times 25$ mm^3
p-terphenyl	0.01 mol %	$7 \times 5 \times 15$ mm^3

We are interested in studying other aromatic molecules for a polarized proton target, for example, anthracene ($C_{14}H_{10}$, melting point 216.2°C) doped with phenazine ($C_{12}H_8N_2$). We have already succeeded in making a single crystal of anthracene with a size of $3 \times 3 \times 3$ mm^3.

References

1) M. Iinuma et al.: Phys. Rev. Lett. **84**, 171 (2000).
2) A. Henstra et al.: Chem. Phys. Lett. **165**, 6 (1990).
3) W. R. Wilcox et al.: Chem. Rev. **64**, 187 (1964).
4) G. J. Sloan et al.: *Techniques of Melt Crystallization*, (Wiley-Interscience, New York 1988).
5) T. Wakui et al.: RIKEN Accel. Prog. Rep. **34**, 194 (2001).

Accurate Calibration of ^{3}He Polarization

S. Yamamoto,[*1] T. Uesaka,[*2] T. Wakui, J. Nishikawa,[*2] and H. Sakai[*3]

A RIKEN ^{3}He target polarized by spin exchange with optically pumped Rb vapor[1,2] has been applied in nuclear physics experiments in 1996,[3] 1998[4] and 2000.[5] To obtain the absolute value of ^{3}He polarization, we introduced a method based on the frequency shift of the Rb electron spin resonance (ESR)[6] in a previous work.[7] A typical Rb ESR frequency and shift are 12.203(5) MHz and 7(3) kHz, respectively, in our case. The uncertainty here is expected to be mainly due to instability of the magnetic field produced by main coils. The instability is about 20 mG at a magnetic field of 30 G. Thus, we need to measure the magnetic field with high accuracy in order to improve the precision of the Rb ESR frequency.

For this, we introduced a commercial magnetometer whose measurement range and resolving power are 2 G and 10 μG, respectively. We measured a weak magnetic field generated by current ($\sim$ 5 A) applied to the main coils. The Rb ESR frequency was measured simultaneously with the magnetic field using the method described in Ref. 7. Time dependence of the Rb ESR frequency is shown in Fig. 1 together with that of the magnetic field. We found that the fluctuation of the Rb ESR frequency of 5 kHz is mainly caused by the fluctuation of the magnetic field. We corrected the Rb ESR frequency, taking its magnetic field dependence into account.

The measurements of the Rb ESR frequency were carried out in the cases where ^{3}He nuclear spin $\mathbf{K}$ is parallel ($\downarrow\mathbf{K}\downarrow\mathbf{B}$) and antiparallel ($\uparrow\mathbf{K}\downarrow\mathbf{B}$) to the magnetic field $\mathbf{B}$ of 25 G produced by the main coils. A ^{3}He nuclear spin was flipped using a nuclear magnetic resonance (NMR) setup of adiabatic fast passage. Figure 2 shows the Rb ESR frequency which was alternately obtained for each case. By using the magnetometer, we have succeeded in obtaining a Rb ESR frequency with a precision within less than 1×10^{-5}, which is an improvement from the previous work.[7]

The Rb ESR frequency shift $\Delta\nu$ is given by the Rb ESR frequencies $\nu_{(\downarrow\mathbf{K}\downarrow\mathbf{B})}$ and $\nu_{(\uparrow\mathbf{K}\downarrow\mathbf{B})}$ in Fig. 2 as

$$\Delta\nu = \nu_{(\uparrow\mathbf{K}\downarrow\mathbf{B})} - \nu_{(\downarrow\mathbf{K}\downarrow\mathbf{B})} = \frac{\mu_B g_s}{h\,(2I+1)} \kappa_0 \frac{8\pi}{3} \nu_{\mathrm{He}} [^3\mathrm{He}] \mathrm{P}_{^3\mathrm{He}},$$

where μ_B is the Bohr magneton, g_s is the electron g-factor, $[^3\mathrm{He}]$ is the ^{3}He density, and $\mathrm{P}_{^3\mathrm{He}}$ is the ^{3}He polarization. If ^{3}He polarization is 100%, $\Delta\nu$ is 46.5 kHz in our case.

Figure 3 shows the Rb ESR frequency shift, or the ^{3}He polarization, as a function of the amplitude of the ^{3}He NMR signal. The ^{3}He NMR amplitude corresponds to a relative value of ^{3}He polarization[6] and was measured with an uncertainty of less than 1%. Therefore, the Rb ESR frequency shift should be proportional to the NMR amplitude. The solid line represents the result of least-squares fitting. Although the data points are mostly on the fitted line, there still remain some deviations of less than 0.4 kHz. The deviation corresponds to 8% for the Rb ESR frequency shift. We assume that the deviation was mainly caused by a stray field which was detected by the magnetome-

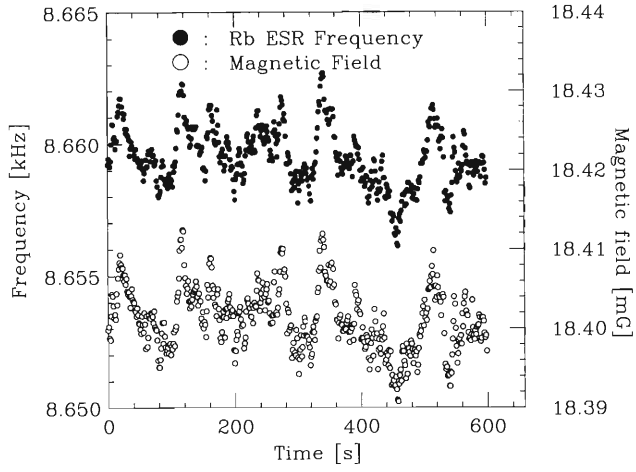

Fig. 1. Time dependence of the Rb ESR frequency and the magnetic field. The Rb ESR frequency was measured simultaneously with the magnetic field.

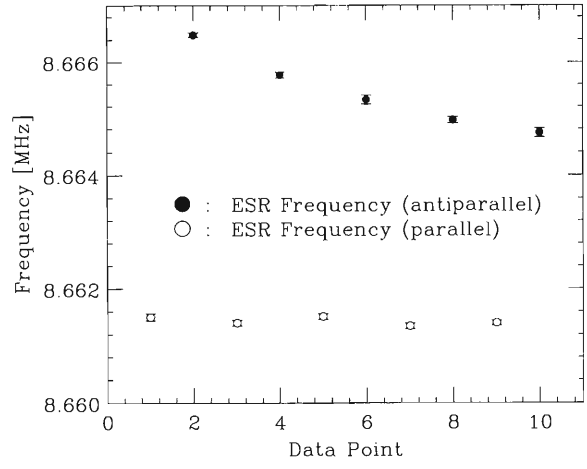

Fig. 2. A typical set of the Rb ESR frequency corrected for the fluctuation of the magnetic field. The Rb ESR frequency was measured in the cases where ^{3}He nuclear spin $\mathbf{K}$ is parallel ($\downarrow\mathbf{K}\downarrow\mathbf{B}$: ○) and antiparallel ($\uparrow\mathbf{K}\downarrow\mathbf{B}$: ●) to a magnetic field $\mathbf{B}$.

*1 Toho University
*2 Saitama University
*3 University of Tokyo

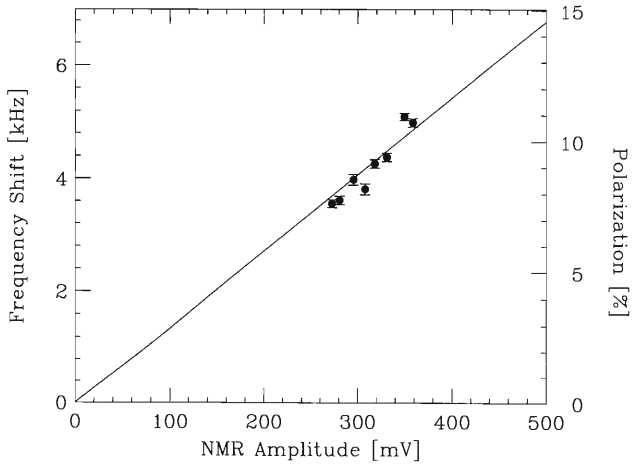

Fig. 3. The Rb ESR frequency shift as a function of ^{3}He NMR amplitude.

ter. We plan to modify the setup to shut off the stray field from the magnetometer.

References

1) R. M. Herman: Phys. Rev. A **137**, 1062 (1965).
2) T. G. Walker and W. Happer: Rev. Mod. Phys. **69**, 629 (1997).
3) T. Uesaka et al.: RIKEN Accel. Prog. Rep. **30**, 139 (1997).
4) M. Kurokawa et al.: personal communication.
5) J. Nishikawa et al.: RIKEN Accel. Prog. Rep. **34**, 51 (2001).
6) M. V. Romalis and G. D. Cates: Phys. Rev. A **58**, 3004 (1998).
7) S. Yamamoto et al.: RIKEN Accel. Prog. Rep. **33**, 156 (2000).

Preparation of Single-Crystal C_{60} for the Implantation of $^{19}F(\leftarrow{}^{19}O)$

W. Sato, K. Asahi, H. Ueno, Y. Kobayashi, H. Ogawa,[*1] A. Yoshimi, K. Yoneda, H. Watanabe, N. Imai,[*2] K. Yoshida, K. Yogo,[*1] H. Miyoshi,[*1] D. Kameda,[*1] and H. Nakahara[*3]

Fullerenes, represented by C_{60}, are novel carbon allotropes of soccer-ball-like shapes consisting of a network of five- and six-membered carbon rings.[1] The unique structure of the molecules shows such intriguing properties as superconductivity, and it is interesting to provide insight into the electronic properties of the fullerene C_{60}. Through our previous study,[2] the time-differential perturbed angular correlation (TDPAC) method has been found to be exceedingly well suited for the study of solid-state fullerenes because it can provide direct information on both static and dynamic interactions between probe nuclei and the extranuclear field. Taking advantage of the spectroscopy, we will apply the TDPAC method in this study using ^{19}F as the probe. For the introduction of the probe ^{19}F, the precursor radioactive nuclides, ^{19}O, as a secondary beam produced by projectile fragmentation of ^{22}Ne are to be implanted in the solid C_{60}. Since the pattern of the TDPAC spectrum, in general, becomes simple when the probes are incorporated in a single crystal, we have started to work on the production of C_{60} crystals, growing them as large as possible. The production method of C_{60} in progress is described in the present report.

For the preparation of C_{60} single crystals, we mostly followed the method developed by Tachibana *et al.*[3] Approximately 50 mg of 99.95% pure C_{60} powder was heated at 250°C under evacuation to $\sim 1\times10^{-5}$ Torr in a Pyrex glass tube with an inside diameter of 8 mm ϕ. The tube was sealed after one-day heat treatment, and placed in a horizontal quartz-tube furnace, on which a kanthal line is coiled to produce the temperature gradients shown in Fig. 1. The C_{60} powder at the end of the Pyrex tube was sublimed at approximately 600°C and an aggregation of small single crystals was deposited at the cold center of the tube after 5 days. The crystals were then sealed in vacuum in a Pyrex glass tube with an inside diameter of 13 mm ϕ. With the crystals kept at the right-side end, the tube was placed in another horizontal quartz-tube furnace having the temperature gradients shown in Fig. 2. In this furnace, the Pyrex tube was moved slowly towards the left at a rate of 5 to 10 mm/day. Large single crystals with sizes of approximately 1 mm were grown at the cold center of the furnace within 3 days.

For the purpose of the present study described above, larger crystals with a size of at least 3 mm are requisite because excessive beam collimation leads to the reduction of the beam intensity, resulting in poor statistics. Further improvement of the apparatus is therefore strongly needed.

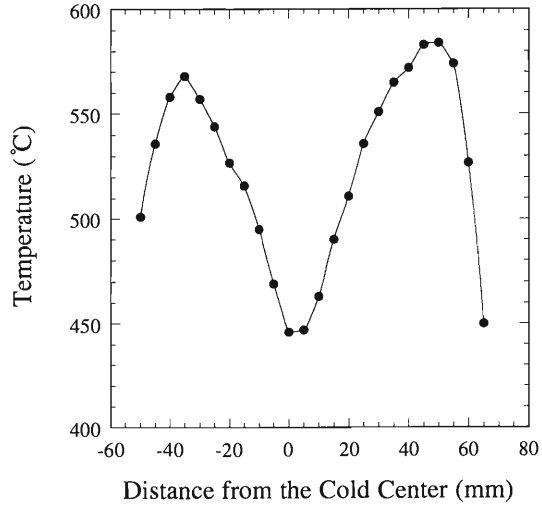

Fig. 1. Temperature profile of the furnace for the sublimation of the C_{60} powder.

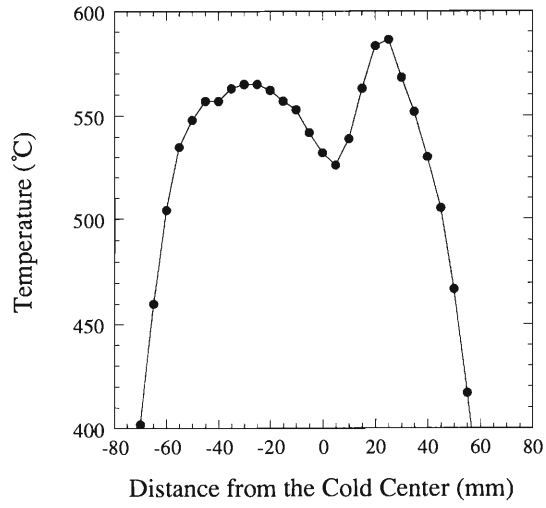

Fig. 2. Temperature profile of the furnace for the growth of single-crystal C_{60}.

References

1) H. W. Kroto et al.: Nature **318**, 162 (1985).
2) W. Sato et al.: Phys. Rev. Lett. **80**, 133 (1998).
3) M. Tachibana et al.: J. Cryst. Growth **166**, 883 (1996).

*1 Department of Physics, Tokyo Institute of Technology
*2 Department of Physics, University of Tokyo
*3 Graduate School of Science, Tokyo Metropolitan University

RF Deflector System for RI Beams on RIPS

K. Yamada,* I. Tanihata, T. Suda, and T. Motobayashi*

There are many nuclei in the neutron-rich side of the nuclear chart which arouse much interest, for instance, the ones involved in the r-process and nuclei with neutron halos. Therefore, various experiments using neutron-rich RI beams have been performed. On the other hand, few experiments have been reported regarding proton-rich RI beams produced by projectile fragmentation. However, proton-rich nuclei are also of interest. For example, the ones along the $N = Z$ line draw much attention due to their special nuclear structures affected by the neutron-proton pairing. Some proton-rich nuclei are involved in the rp-process, the explosive nuclear burning in novae. A major difficulty for fragmentation-based proton-rich beams is in the presence of unwanted nuclei in the secondary beam of interest. Fragment separators such as RIPS[1] select projectile fragments by their magnetic rigidity $\chi_B = B\rho = mv/Ze$. Because the velocities of the fragments are similar to that of the primary beam, the use of a degrader following magnetic analysis enables further separation of nuclei with the same A/Z ratio. However, for a proton-rich nucleus, the tails of the momentum distributions for less proton-rich species are included, because their intensities are much higher than the nucleus of interest. This happens particularly among isotones, because their magnetic rigidities take almost the same value.

To overcome the difficulty discussed above, we are planning to develop a radio frequency deflector system that is expected to be installed in the RIPS beam line to obtain high-purity proton-rich RI beams. Since different particles selected by RIPS have different velocities, the difference of their arrival times is determined among different species. By applying an RF voltage in the direction perpendicular to the beam axis, the secondary beams are deflected depending on their arrival time at the deflector. The frequency and the phase are set so that the beam of interest is not deflected and other unwanted beams are deflected.

Figure 1 shows the outline of the deflector system. It consists of an oscillator synchronized to the cyclotron RF signal, a controller circuit, deflector electrodes, slits that eliminate deflected beams, RF shields, high voltage insulators and a vacuum chamber. The bending direction will be set to be vertical, and the system will be installed between the Q9 lens and the F2 chamber of RIPS by replacing the existing switching magnet. The system design will be realized soon.

References

1) T. Kubo et al.: Nucl. Instrum. Methods Phys. Res. B **70**, 309 (1992).

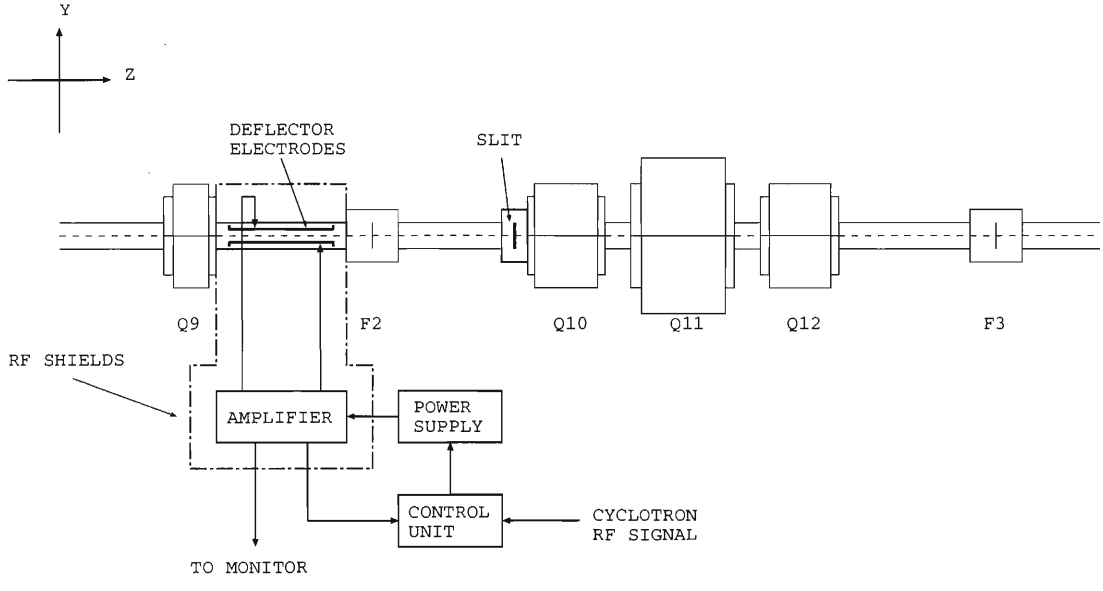

Fig. 1. Outline of the deflector system.

* Rikkyo University

Development of an RF Ion Guide System

M. Wada, Y. Ishida, T. Nakamura, T. Sonoda,[*1] T. Oshima,[*1] Y. Nakai, T. M. Kojima, Y. Kanai, H. Oyama, T. Kambara, Y. Yamazaki, A. Yoshida, T. Kubo, Y. Matsuo, Y. Fukuyama, K. Okada,[*2] K. Noda,[*3] H. Kawakami,[*4] S. Ohtani,[*5] and I. Katayama[*4]

An rf ion guide system was proposed to obtain slow or trapped radioactive nuclear ions which are primarily produced by a projectile fragment separator.[1,2] The energetic ion beams from the fragment separator are firstly energy degraded by passing through a degrader plate. The medium-energy ion beam thus obtained is then injected into the He gas cell to thermalize the ions. The stopped ions should be quickly extracted to the vacuum and transferred to the downstream instruments. In the ordinary ion guide system, the transport of ions in the cell is carried out only by the gas flow. If a large cell were used to stop relatively high energy ion beams, it would take much more time than possible loss processes such as charge exchange and diffusion to the wall.

A fraction of thermalized ions in the He gas is known to be in a singly charged state. The ions can be manipulated by an electric field. However, if a static electric field is applied, the ions would be lost at the cathode electrode since the ion motion in such high-pressure follows the electric force line. If, on the other hand, an rf field were applied in addition to the static field, the average force due to the rf gradient field would become repulsive against the electrode. The effective electric field due to the gradient rf field at the tip of the electrode is

$$E_{\mathrm{eff}} \approx \frac{8m\mu^2}{e}\frac{V^2}{r_0^3}, \qquad (1)$$

where m is the mass, μ the mobility of the ion in the gas, e the electric charge, V the terminal voltage of the rf potential, and r_0 the distance between adjacent electrodes. In general, heavier ions at lower pressure can be driven in a weaker rf field.

In a previous off-line test,[3,4] multiple metallic plates were used to form the rf electrodes and the distance between the electrodes was 2.5 mm. More than 50% transmission efficiency was achieved for Ta ions under the conditions of He pressure of 30 Torr and rf amplitude of 50 V. The pressure used in this test was too low for practical experiments. We set the target pressure at 150 Torr, which corresponds to the stopping capabilities of 5 MeV/u for medium to heavy ions and 2.5 MeV/u for very light ions, if the depth of the cell is 2 m. To operate the rf ion guide mechanism under such high pressure, decreasing the r_0 is the most effective way; increasing the voltage is limited by the discharge problem. According to Eq. (1), transporting Li ions in 150 Torr He gas could be realized if fine structure electrodes with a distance of 0.3 mm or 0.5 mm between electrodes were fabricated.

We fabricated such fine structure electrodes using a flexible printed circuit. Figure 1 shows the electrodes for the nozzle part made of a printed circuit on a polyimide film. The arc pattern lines with an interval of 0.3 mm form ring electrodes by folding the film into a corn shape. The straight part of the print pattern was extended to form a cable as well as a feed-through up to an rf divider circuit board which was placed outside the vacuum. The large funnel structure part was also made of the flexible printed circuit (Fig. 2). The total number of electrodes for this part was more than 400

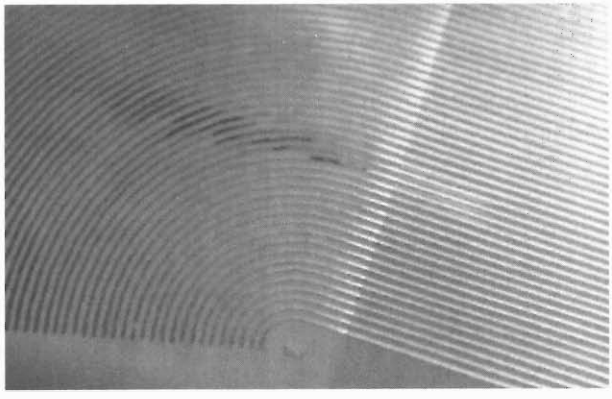

Fig. 1. Printed circuit fabricated on a polyimide film. Nozzle part of the rf ring electrode was formed by folding this print pattern.

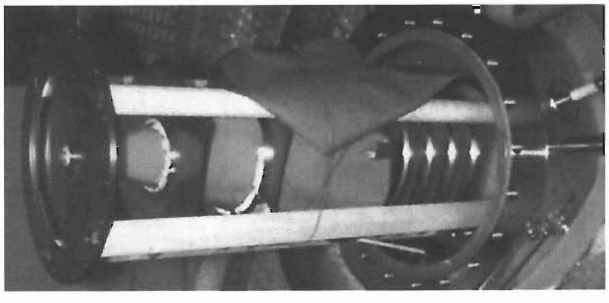

Fig. 2. Funnel structure part of the rf electrode assembled in the gas cell. Diameter of the top (right side in the figure) is 100 mm and the bottom is 5 mm. Nozzle part is to be placed at the left side of this structure.

*1 Cyclotron and Radioisotope Center, Tohoku University
*2 Department of Physics, Sophia University
*3 National Institute for Radiological Science
*4 Institute for Particle and Nuclear Studies, High Energy Accelerator Research Organization
*5 Institute of Laser Science, University of Electro-Communications

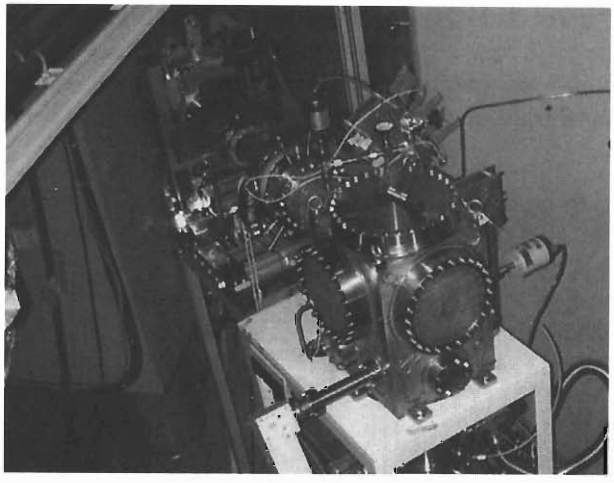

Fig. 3. D2 magnet of RIPS and the rf ion guide test bench.

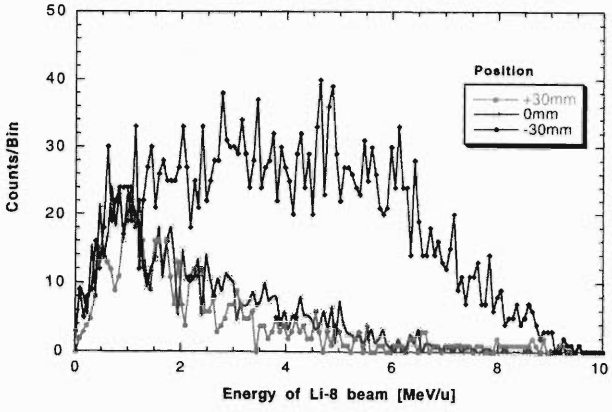

Fig. 4. Energy distribution of the ^{8}Li beam after the wedge degrader measured by a 700-μm-thick Si detector.

and the total capacitance measured at the source terminal of the rf divider circuits was more than 10 nF. Two high-power amplifiers, which were originally designed for a piezo device, were used to drive the rf circuits with a frequency of ~600 kHz and an amplitude of up to 200 V.

On-line test experiments are under way at the RIKEN fragment separator, RIPS. A new beam port was prepared particularly for this development at the side of the second dipole magnet (D2) where the second focal point (F1') from the first dipole (D1) was obtained (Fig. 3). The magnification was 3.9 for the horizontal direction and 8.7 for the vertical direction. The focal point was momentum dispersive and the dispersion was as large as 42 mm/%, which enables us to perform energy compression using a wedge degrader. Figure 4 shows energy spectra of the ^{8}Li beam after the wedge degrader made of Pyrex glass 33 mm in thickness with a wedge angle of 1.6 degrees. The test beam of ^{8}Li was produced from a primary beam of 100-MeV/u ^{13}C and a Be target 0.75 mm in thickness. The yield at the degrader was 1.1×10^{3} atoms/pnA and the beam size was as large as 60 mm in the horizontal and 20 mm in the vertical directions. The stopping capability for Li ions is about 1 MeV/u if a compact-size gas cell with 30 cm length is used for the test. The acceptable beam fraction in such an energy range was as small as 0.5%.

Although the Li beam is one of the most difficult species in terms of the energy spread after the degrader, the stopping capability of the gas cell and the rf voltage required for manipulating ions in the gas cell, we chose ^{8}Li as the test beam since the detection efficiency is very high and we aim at trapping ^{11}Be for future experiments on hfs spectroscopy. A test of the gas cell using the ^{8}Li ion beam is in progress.

References

1) M. Wada et al.: Presented in the Int. Workshop on Ion Guide Isotope Separator On-Line (IGISOL-6), Dubna, (1997), unpublished.
2) I. Katayama et al.: Hyperfine Interact. **115**, 165 (1998).
3) M. Wada et al.: RIKEN Accel. Prog. Rep. **33**, 180 (2000).
4) M. Wada et al.: RIKEN Rev. No.31, 56 (2000).

Performance of Liquid Xe Scintillation Chamber with ^{20}Ne Beam

T. Kato,* T. Doke,* J. Kikuchi,* H. Okada,* F. Nishikido,* Y. Matsui,*
K. Morimoto, and I. Tanihata

In the Radio Isotope Beam Factory (RIBF) project at RIKEN, a variety of RI will be produced, and the discovery of many new isotopes heavier than O is anticipated. To search for new isotopes in a region away from the stability line in the nuclear chart, the amount of beam irradiation required will increase because of the low production cross sections of these nuclei. Therefore, detectors which can withstand radiation damage due to heavy ions are required.

To satisfy such a requirement, the possibility of using liquid rare gas as a detector medium is considered. Recently, a new liquid argon (LAr) ionization chamber was constructed as a calorimeter and used to test for heavy ions with an energy of around 100 MeV/nucleon. Excellent energy resolution of 0.6–0.7% (FWHM)[1] was achieved for Ar and Ca ions, but the pulse heights of the ionization signals changed with the beam intensity as a result of accumulation of Ar^+ ions.

Next, the use of scintillation in liquid xenon (LXe) is considered to eliminate this intensity dependence. The decay time constants (4.3 and 22 ns) of the scintillation light are comparable to those of plastic scintillators, and the scintillation yield (W_{ph} = 14.7 eV) is comparable to that in NaI (Tl). LXe is expected to be the detector medium, functioning as a timer and energy counter with high resolution, high counting rate and resistance to radiation damage.

In order to study the timing and energy responses to heavy-ion beams of scintillation in liquid xenon (LXe), the LAr ionization chamber has been improved. A cross-sectional view is shown in Fig. 1. LXe was compressed in the internal vessel under vacuum. All heavy ions with an energy of 100 MeV/nucleon stop in LXe. Scintillation light produced by heavy ions was observed using two photomultipliers (PMTs; HAMAMATSU, R5900) through a MgF_2 window.

The test experiment was performed with a ^{20}Ne beam at 135 MeV/nucleon at the RIKEN ring cyclotron in September 2000. Aluminum plates of 0, 1, 3, 5, 8 and 10 mm thickness were used as a degrader to change the beam energy. The beam energy was measured after passing the aluminum plates using the time of flight (TOF) between a plastic scintillator and the LXe scintillation chamber. A beam spot of 10 mm diameter was focused on the center of the LXe chamber. An effective area of 1 mm diameter in front of the LXe chamber was selected by a veto plastic counter in off-line analysis.

Figure 2 shows that the intrinsic time resolution with one photomultiplier (PMT) was around 30 ps in sigma up to a beam intensity of 1.3×10^5 cps. The time resolution of the LXe scintillation chamber with two PMTs is given by dividing the intrinsic time resolution of 30 ps by $\sqrt{2}$, giving 21 ps in sigma. It is also shown in Fig. 2 that the energy output was constant for the increase in the beam intensity. The difference was less than 1% and the energy resolution was 1.2–1.4% in sigma. Figure 3 shows the relationship of the energy output to the deposited energy in LXe. Nonlinearity of the amount of scintillation light in LXe for the incident

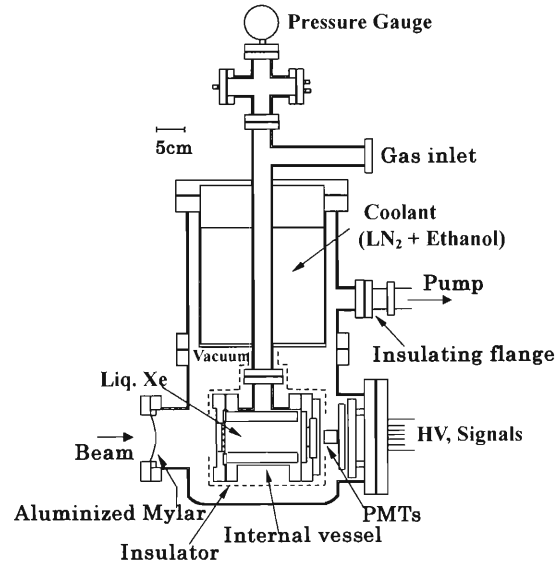

Fig. 1. Cross-sectional view of the LXe scintillation chamber.

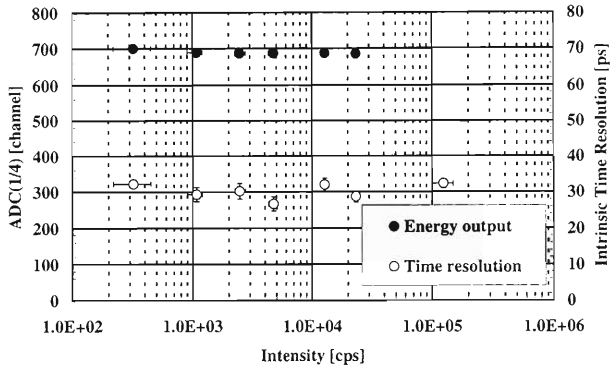

Fig. 2. Intrinsic time resolution and energy output relative to beam intensity. The plot of energy output for 1.3×10^5 cps was discarded, because the measurement was not carried out under good conditions due to the AC-coupling of the ADC (LeCroy 2249 W).

* Advanced Research Institute for Science and Engineering, Waseda University

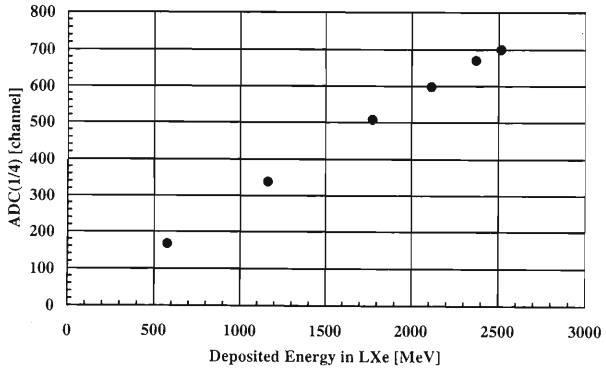

Fig. 3. Relationship between the amplitude of the output signals and the deposited energy in LXe.

energy is fairly small compared to that in other organic and inorganic scintillators.

The number of photons (N) that arrived on a photocathode of each PMT was estimated by the solid angles calculated along the track of the ^{20}Ne beam. The time and energy resolution was fitted by a function of $(a/\sqrt{N}+b)$, where a and b are parameters, and it became obvious that the number of photons determined both resolutions. This finding suggests that both resolutions will be improved by increasing the number of photons. The solid angles were about 2% of 4π in the experiment. We plan to construct a chamber to improve the geometry of the PMTs, and test it with some kinds of heavy-ion beams.

The results of this experiment have been submitted to the Japanese Journal of Applied Physics.

References

1) A. Yunoki et al.: Nucl. Instrum. Methods Phys. Res. A **432**, 332 (1999).

Measurement of Depth of Interaction in a Segmented Planar Ge Detector

E. Ideguchi,[*1] B. Cederwall,[*2] T. Bäck,[*2] L. Milechina,[*2] Y. Gono, Y. Yang, T. Teranishi,[*3] N. Aoi,[*4] D. Bucurescu,[*5] and T. Kishida

Gamma-ray measurements using heavy-ion induced reactions often suffer from the Doppler effect. Due to the finite solid angle of the γ-ray detector, Doppler broadening deteriorates the energy resolution. This effect is particularly serious when one uses so-called inverse reactions. In order to correct for the energy shifts originating from the Doppler effect, it is necessary to detect the directions of γ rays emitted in the reaction and to reduce the solid angle subtended by each Ge detector.

In order to achieve this aim, a detector complex consisting of a segmented Ge detector[1,2] and a clover Ge counter[3] has been developed.[2] The planar Ge crystal of 5 cm $\times$ 5 cm with 2 cm thickness is used as a transmission type ΔE γ-ray counter, for which the cathode is electrically segmented into 25 elements and each segment is of 1 cm $\times$ 1 cm square shape. The clover Ge mainly detects Compton scattered γ-rays from the segmented Ge detector. Doppler broadening is reduced due to the small solid angle of each segment of the planar Ge placed in front.

Recently, new techniques to enable the tracking of γ radiation in primarily Ge detectors are being developed which will allow the determination of the time sequence of γ-ray interactions and their respective positions in a detector, as well as their energies.[4–6] The γ rays are detected by highly segmented Ge detectors. Three-dimensional position determination in the detectors is achieved by analyzing the pulse shapes of net charge signals in the irradiated segments and mirror charge signals of the neighboring segments since they reflect the interaction points of the γ rays in the Ge crystal. Tracking algorithms based on the Compton scatter formula are then applied in order to determine the energy, direction and interaction sequence of incoming γ rays. By applying a tracking technique to the segmented planar Ge detector as well one can obtain a higher effective granularity and therefore a better Doppler correction. A necessary requirement, however, is that a sufficiently high position resolution for γ-ray interactions in the detector volume can be obtained.

In order to determine the dependence of the pulse shapes of signals produced in the Ge detector on the location of the interaction points, it was necessary to introduce experimental conditions where primarily single-interaction events are considered. This was achieved[7] by irradiating the segmented planar Ge detector with a collimated ^{137}Cs γ-ray source and requiring coincidence between this detector and another (coaxial) Ge detector. The coaxial detector was also collimated by a Pb slit collimator in order to detect only γ rays scattered at 90° in the segmented detector. Energy gates were then applied to the detector signals in order to select single Compton scattering events. In this case, the energy of the Compton scattered γ rays is 288 keV and the energy deposited in the planar Ge detector is 374 keV. The hole size of the Pb collimator and the width of the slit were chosen to be 1.5 mm and 2 mm, respectively, in order to obtain a small geometrical uncertainty in the positions of the scattering points due to the size of the collimators while maintaining a reasonable counting rate. Gamma rays were irradiated to the central segment (# 13) of the crystal, and the output signals from the cathode element # 13 and the adjoining cathode elements # 8 and # 12 were used to obtain the net charge and mirror charge pulse shapes. In the measurement, three different interaction depths of 5 mm, 10 mm, and 15 mm in the center of the segment # 13 were chosen as well as one interaction point at a 5 mm depth but 2.5 mm off-center.

A main goal of the present investigation was to identify the pulse shape parameters which may best serve to determine the depth of interaction. By studying averaged pulses, for which the contribution from electric noise has largely been canceled, we may easily identify the main changes in the detector signals as a function of interaction position. Averaged pulses from the anode and the centrally irradiated cathode segment # 13 recorded at the three different depths, 5 mm, 10 mm, and 15 mm, are presented in Fig. 1. The figure shows a clear dependence of the pulse shapes as well as the relative timing of the anode and cathode signals on the depth of interaction.

Clearly also more detailed features of the pulse shapes are sensitive to the depth of interaction. However, in the present work, we have restricted ourselves to the straightforward approach of using only the timing of the anode signal relative to the cathode element # 13, and the rise time of the signal from the cathode element # 13, which we identify as the most important properties for determining the depth of interaction.

In the analysis, we use T_{50} as a measure of the arrival time of the charge at the anode relative to the

*1 Department of Chemistry, Washington University, USA
*2 Department of Physics, Royal Institute of Technology, Sweden
*3 Center of Nuclear Study, University of Tokyo
*4 Department of Physics, University of Tokyo
*5 H. Hulubei National Institute of Physics and Nuclear Engineering, Romania

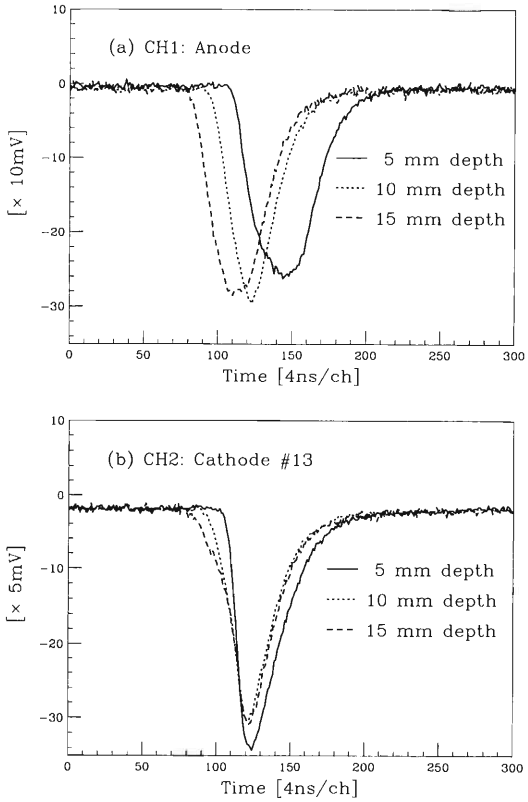

Fig. 1. Averaged pulses for anode (a) and cathode (b) signals obtained by irradiating the center of the segment at three different depths, 5 mm, 10 mm, and 15 mm.

timing of the constant fraction discriminator output of cathode segment # 13. Here, T_{10}, T_{50}, and T_{90} indicate the earliest time at 10%, 50%, and 90% of the maximum amplitude of the pulse, respectively. The difference between T_{90} and T_{10} was taken as a measure of the rise time of the pulse. In order to select events with only a single interaction in the Ge crystal, an energy gate around 374 keV was applied to the integrated anode and cathode element # 13 signals. In Fig. 2 a correlation plot for the two independent time parameters, T_{50} and $T_{90}-T_{10}$, is displayed for four different interaction points in the detector. It can be clearly seen that the (T_{50}, $T_{90}-T_{10}$) pairs are distributed in separate regions of the chart according to the depth of interaction. The distributions due to irradiation in the center at 5 mm depth and 2.5 mm off-center overlap almost completely with the central interaction points at 5 mm depth as expected, since they are due to the same depth of interaction. The overlap at the borders of the distributions probably arises from the geometrical uncertainty due to the Pb collimator, and the wider distributions for the deeper depths of interaction may indicate the effect on the signal from multiple scattering in the crystal.

The finite opening angle of the collimator set-up

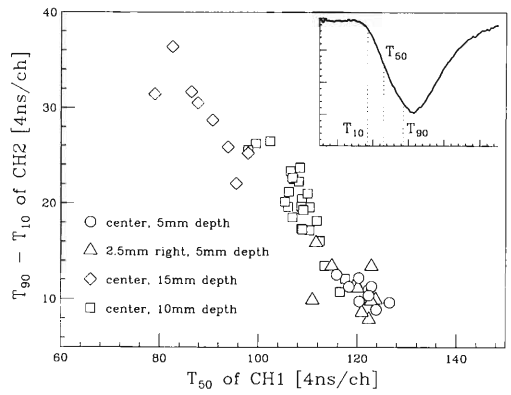

Fig. 2. Correlation diagram between T_{50} and $T_{90}-T_{10}$ for four different interaction points. The inset shows a typical pulse shape used in the analysis and the timing of T_{10}, T_{50}, and T_{90}.

used in the measurement produced a geometrical uncertainty in the distribution of the interaction points of γ rays in the Ge crystal. Monte-Carlo simulations using the code GEANT3[8] were performed[7] to estimate this uncertainty and to compare the result with the distribution of experimental T_{50} values obtained by the pulse shape analysis. The geometrical uncertainties in the depth direction were estimated from the simulation to be 1.13 mm, 1.26 mm, and 1.32 mm for 5 mm, 10 mm, and 15 mm depth, respectively, by assuming that they have Gaussian distributions.

The uncertainties in the T_{50} values are primarily a combination of the geometrical uncertainty due to the Pb collimators and effects intrinsic to the detector such as electric noise, charge trapping *etc.* The intrinsic position resolution of the detector (for single interactions) can therefore be unfolded by removing the geometrical contribution estimated from the simulations. Based on the results[7] of the pulse shape analysis and the simulations, an intrinsic position resolution for single interactions of the order of 1 mm was obtained for the depth direction.

References

1) E. Ideguchi et al.: RIKEN Accel. Prog. Rep. **27**, 121 (1993).
2) Y. Gono et al.: Nucl. Phys. A **588**, 241c (1995).
3) P. M. Jones et al.: Nucl. Instrum. Methods Phys. Res. A **362**, 556 (1995).
4) M. A. Deleplanque et al.: Nucl. Instrum. Methods Phys. Res. A **430**, 292 (1999).
5) K. Vetter et al.: Nucl. Instrum. Methods Phys. Res. A **452**, 223 (2000).
6) J. van der Marel and B. Cederwall: Nucl. Instrum. Methods Phys. Res. A **437**, 538 (1999).
7) E. Ideguchi et al.: to be published.
8) GEANT3, Detector Description and Simulation Tool (CERN, Geneva, 1993).

Ten-Segment Germanium Detector

S. Motomura,* S. Tanaka,* Y. Gono, T. Kishida, H. Watanabe, and K. Asahi

A telescope germanium (Ge) detector was developed. A telescope system was first prepared for the energy correction of Doppler shifted energy of γ-rays which were emitted from recoiling reaction products with a large velocity such as 10% of the velocity of light.[1] In this case, the telescope consisted of a segmented and a clover Ge detector. This system worked well for Doppler correction as well as γ-ray linear polarization measurement.[2,3] However, it was found that Ge detectors in two independent cryostats caused a reduction of detection efficiency in the telescopic mode. To avoid this problem, one Ge crystal was segmented to form the Ge telescope shown in Fig. 1.

Sensitivity for γ-ray linear polarization was higher with square segmentation for the front part of the telescope. This configuration does not allow the same electric field shape to form in all the segments. Therefore it was necessary to test whether the square segmentation coaxial Ge detector could be used to keep high energy and time resolutions. The energy resolutions of all segments as well as efficiencies were measured as listed in Tables 1 and 2. Energy resolutions are the same as or better than those given in the specifications, except that given for 'Full.' The 'Full' signal was taken from the inner n-type electrode which was common for all the segments. This discrepancy must be further examined.

Considering the efficiency, the measured values of the ten-segment Ge detector are consistent within a factor of 2. These values depend strongly on the setting of discriminator levels for signals. Therefore, it is not a straightforward comparison. However, the Ge volumes of the two systems are 198 cm^3 for the ten-segment system and about 500 cm^3 for the 25 segment + clover system. Considering this difference, these results indicate that the ten-segment telescope has very high efficiency compared with that of the 25 segment + clover system.

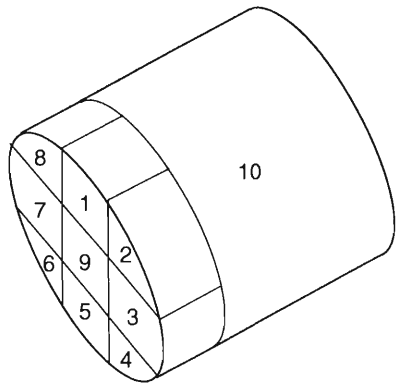

Fig. 1. Ten-segment Ge detector.

Table 1. Energy resolution.

Segment number	FWHM (keV) at 1.33 MeV (Spec.)	FWHM (keV) at 1.33 MeV (Measured)
1	2.93	2.80
2	2.24	1.91
3	2.58	2.24
4	2.11	1.96
5	2.47	2.24
6	2.16	2.13
7	2.83	2.67
8	2.38	2.33
9	2.08	1.93
10	2.92	2.97
Full	3.0	3.56

(Full : Signal combining all charges collected independently on each segment.)

Table 2. Gamma-ray detection efficiency of telescope detectors.

Gamma-ray energy (keV)		Ten-Segment Germanium		25 Segment + Clover
		Measured	Simulation	
122	A	0.011	0.020	0.009
	B	0.0002	0.0001	
344	A	0.0027	0.0046	0.0027
	B	0.0011	0.0022	0.0003
1408	A	0.00044	0.0007	0.0007
	B	0.0008	0.0010	0.00043

A : Segmented Ge only.
B : Telescopic mode.

References

1) Y. Gono et al.: Nucl. Phys. A **588**, 241c (1995).
2) H. Watanabe: Ph. D. Thesis, Kyushu University (2000).
3) H. Tsuchida et al.: KUTL Rep. **6**, 92 (1997).

* Department of Physics, Kyushu University

Development of Ultrahigh Resolution Time-of-Flight Detector for RI Beam at RIKEN

S. Nishimura, M. Chiba, M. Kurata-Nishimura, K. Morimoto, Y. Nishi, I. Tanihata, T. Yamaguchi, and T. Zheng

In the RI beam factory (RIBF) project,[1] it is absolutely critical to develop a new time-of-flight system. The requirements for this are improved timing resolutions below 20 ps with high efficiency, use of fewer materials, and operational at a high beam intensity of more than 10^6 cps as well as sufficient radiation hardness against heavy ions for stable operation. For heavy-ion beams, various kinds of detectors are used as time-of-flight detectors.[2,3] In this report, we focus on the time-of-flight resolution of a well-known scintillation detector for the current RIPS and for the future RIBF at RIKEN.

The test experiment was performed in the E1c beam line at RIKEN in November, 2000. The primary beam of ^{40}Ar is used at an energy of 95 MeV per nucleon. The layout of the experiment is shown in Fig. 1. There are two position-sensitive detectors PPAC (P1, P2)[4] placed upstream of the test detectors for precise position measurement at the position of scintillation detectors. The start timing of the beam is defined by a scintillation detector (S0). In addition, there are four test counters (S1, S2, S3, and S4) installed in the light shield box. Each scintillation detector consists of two identical photomultiplier tubes directly attached to a scintillator with optical coupling of Bicron BC630. Various kinds of scintillators and photomultiplier tubes are tested systematically to investigate the performance of the time-of-flight resolution during the experiment (See Tables 1 and 2.). The precise position measurement of the primary beam within 1 mm is expected using two additional fiber scintillation detectors (FI1, FI2)[5] which are installed downstream of S4.

In this test experiment, signals from photomultiplier tubes are digitized by leading-edge discriminators (Kaizu and Phillips 630) and sent to secondary leading-edge discriminators to reshape the signals after a 100 ns cable delay. The timing measurement was performed using two Kaizu time-to-digital converters (TDC-3781), for which precision of the timing measurement is about 25 ps per channel. The timing resolution of the electronics after the discriminator outputs is evaluated by comparing the timing jitter between two identical outputs from a discriminator channel. The intrinsic timing resolution of our electronics is confirmed to be about 8 ps. The signal coincidence of two photomultiplier tubes from the start counter (S0) is used as a start timing, where low-loss microwave cables (HUBER+SUHNER S-04272-B) are chosen to obtain trigger signals faster than the TDC signals *via* BNC cables (RG-58). All ADCs and TDCs of scintillation detectors were input into a computer *via* CAMAC and stored in a disk for off-line analysis. As a CAMAC crate controller, TOYO-CC/7700 is selected.

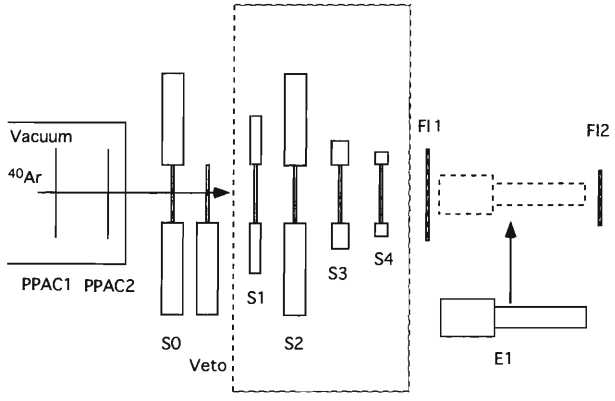

Fig. 1. Experimental setup at the E1c line of RIKEN.

Table 1. Characteristics of different types of photomultiplier tubes.[6] The R3809U-52 is the photomultiplier tube with two microchannel plates inside its tube. R5900-L16 is a metal-channel dynode used for S4, where signal outputs from No. 6–11 in 16 channels are totalled. (PMT: type of photomultiplier tubes, R.T: rise time, T.T.S: transit-time spread, G: gain, and Det.: detector types)

PMT	*R.T* (ns)	T.T.S (ps)	*G* ($\times 10^6$)	*Det.*
R2083	0.7	370	2.5	*S0*, *S2*
R4998	0.7	160	5.7	*S1*
R3809U	0.15	<25	0.2	*S3*
R5900	0.6	180	2.0	*S4*

Table 2. Characteristics of various scintillators[7] used in the experiment. BC422Q is quenched with 0.5% benzophenone to improve timing properties. (Scinti.: type of scintillators, R.T: rise time, L.O: light output, A.L: attenuation length, and Det.: detector types used as default.)

Scinti.	*R.T* (ns)	*L.O* (%)	*A.L* (cm)	*Det.*
BC404	0.7	68	160	*
BC418	0.5	67	100	*
BC422	0.35	55	8	*S0*, *S4*
BC422Q	0.10	19	<8	*S1*, *S2*, *S3*

The timing resolution of each detector was investigated in the off-line analysis. Figure 2 shows our preliminary time-of-flight spectrum between S0 and

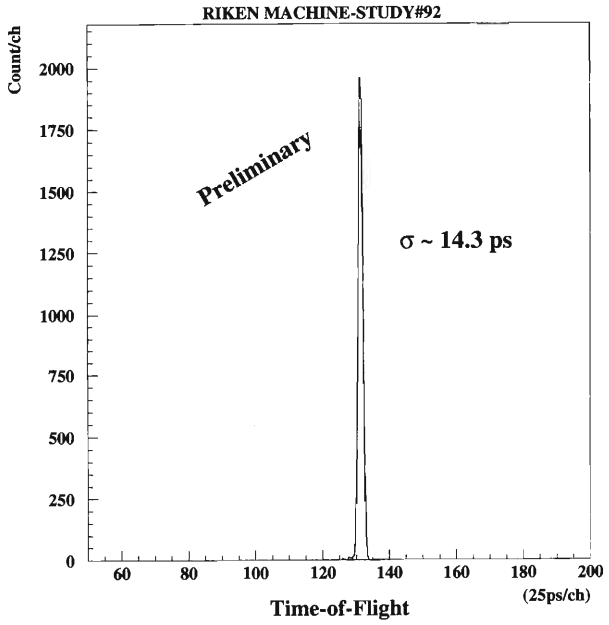

Fig. 2. Time-of-flight spectrum between S0 and S1 after the slewing correction.

S1. As a scintillator, BC422 and BC422Q with dimensions of $50 \times 40 \times 0.5\,\mathrm{mm}^3$ and $40 \times 20 \times 0.5\,\mathrm{mm}^3$ in width $\times$ height $\times$ thickness are chosen for S0 and S1, respectively. About 15% of the improvement in time-of-flight resolution is achieved after the slewing correction using the pulse height information of each photomultiplier tube as well as a correction of timing as a function of position dependence. Notably, our preliminary results show that the time-of-flight resolution between S0 and S1 is about 14.3 ps. This indicates that the intrinsic timing resolution of S0 and S1 is about 10.1 ps(!) on the average, which is nearly the limit of the timing resolution that can be possibly achieved for the current electronics itself and would be the best time-of-flight resolution achieved by a scintillation detector. In the future, it would be possible to achieve a better timing resolution of below 10 ps using faster timing electronics, particularly for the TDC.

A new time-of-flight detector has been developed using fast scintillators and fast photomultiplier tubes. Our preliminary results show that the intrinsic timing resolution of about 10 ps is achieved using ^{40}Ar ions with an energy of 95 MeV per nucleon. Further improvement is expected using faster electronics. While systematic study of the scintillation detector is in progress using scintillators of various sizes, thicknesses, and types as well as different types of photomultiplier tubes. In the future, it is necessary to investigate its radiation hardness as well as its operation under a high beam intensity to evaluate its performance under a realistic environment of the RIBF.

References

1) I. Tanihata: J. Phys. G: Nucl. Part. Phys. **24**, 1311 (1998).
2) T. Chujo et al.: Nucl. Instrum. Methods Phys. Res. A **383**, 409 (1996).
3) F. Tokanai, K. Morimoto, M. Kurata-Nishimura, I. Tanihata, and S. Yamada: submitted to IEEE Trans. Nucl. Sci.
4) H. Kumagai, N. Fukuda, A. Ozawa, K. Summerer, and I. Tanihata: RIKEN Accel. Prog. Rep. **33**, 163 (2000).
5) K. Morimoto, F. Tokanai, M. Kurata-Nishimura, I. Tanihata, Y. Hayashizaki, and S. Yoshida: IEEE Trans. Nucl. Sci. (2000), to be published.
6) Hamamatsu Photonics: Photomultiplier Tubes and Related Products (1998).
7) BICRON: Organic Scintillators, Related Materials and Detectors (1997).

Detection of Heavy Ions by a Superconducting Tunnel Junction

H. Sato, T. Ikeda, K. Kawai, H. Miyasaka, T. Oku, W. Ootani,[*1], C. Otani, H. M. Shimizu, Y. Takizawa, H. Watanabe, K. Morimoto, and F. Tokanai[*2]

One of the important applications of the superconducting tunnel junction (STJ) is as a high-energy-resolution photon detector which exceeds the energy resolution of the conventional semiconductor detectors because of the small gap energy of the superconductor (~meV). We have been developing the STJ,[1,2] and the energy resolution of 41 eV in full width at half maximum (FWHM) for 5.9 keV X rays has been achieved,[1] which is the best result in Japan.

The STJ can also form the basis of a good detector for heavy ions, which is very useful in applications to a beam profile monitor under a heavy radiation dose and to a very fast time-of-flight (TOF) counter. The passage of a heavy ion through an STJ results in quasiparticles being instantaneously generated in a small region called hot spot along the heavy ion track. The superconducting current is assumed to be suppressed at the hot spot causing a decrease in the STJ critical current. If we apply a bias current across the STJ, this decrease switches the STJ voltage from 0 to gap voltage (~mV). Heavy ions can thus be detected by monitoring this voltage switching. The switching speed is expected to be in the order of 1 to 10 ps, which enables a very fast particle detector to be realized. With regard to the radiation hardness, recent study has shown that only slight damage has been observed with Au^{15+} irradiation of 0.92 Grad.[3]

We began the development of the heavy-ion-detection system using the STJ, and the STJ response to heavy ions was experimentally studied at the RIKEN Ring Cyclotron Facility.[4]

We fabricated an Nb-based STJ with a layer structure of Nb (200 nm-thick)/Al (10 nm)-AlO_x/Nb (150 nm) in our fabrication facility at RIKEN. The STJ has a square shape, the upper Nb layer being 20 μm × 20 μm and the lower Nb layer being 40 μm × 40 μm.

An STJ chip was cut out of the fabricated wafer to a size of 5 mm × 5 mm and set in a liquid He cryostat. A plastic scintillator was placed upstream of the cryostat to monitor the beam intensity and to be used as one of the TOF counters. Bias current I_b was supplied to the STJ by a function generator through a variable resistor. A time-to-analog converter (TAC) was triggered by the switching signal of the STJ and stopped by the delayed scintillator signal. The timing spectrum was obtained by constructing a histogram of the pulse height of the TAC output with a multichannel analyzer.

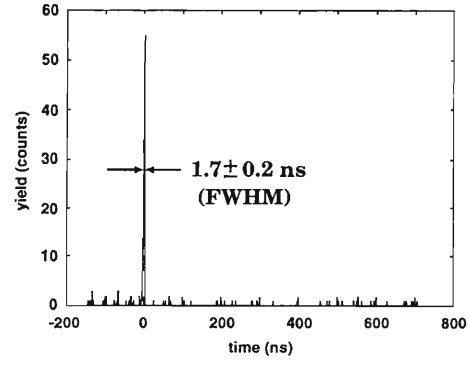

Fig. 1. Time spectrum obtained from the TAC. Full scale on the horizontal axis (1 μs) corresponds to the time range of the TAC.

A ^{40}Ar beam at 95 MeV/nucleon was introduced into the cryostat, and the size of the beam spot was adjusted to a 10 to 15 mm diameter to illuminate the entire chip. The energy of the ^{40}Ar beam was attenuated by passing through the plastic scintillator, the two Al windows at the cryostat and a 43-mm-thick liquid He column and the kinetic energy as it entered the STJ was 44.4 MeV/nucleon.

The incident rate of ^{40}Ar ions was measured by the plastic scintillator as 400 cps, and the voltage switching rate of the STJ was about 1.1 cps. The rate ratio is consistent with the area ratio of the beam cross section and the STJ area. The rise time of the typical output voltage from the STJ was 67 ns, which was predominantly limited by the analog bandpass of the transmission cable connecting the STJ to the amplifier.

The obtained time spectrum is shown in Fig. 1. The time width of the peak was 1.7 ± 0.2 ns in FWHM; this corresponds to the time resolution of the detection system that was determined by the time walk of the discriminators and time jitter of the signals from the STJ and the plastic scintillator. The signal cables and data acquisition system were not adequate for transmitting fast pulses to identify the intrinsic timing characteristics of the STJ. An improved measurement system with more appropriate cables for fast pulse transmission is planned.

*1 International Center for Elementary Particle Physics, University of Tokyo
*2 Department of Physics, Yamagata University

References

1) H. Sato et al.: Jpn. J. Appl. Phys. **39**, 5090 (2000).
2) C. Otani et al.: Jpn. J. Appl. Phys. **39**, 1710 (2000).
3) L. Frunzio et al.: Jpn. J. Appl. Phys. **37**, Suppl. 2, 40 (1998).
4) H. Sato et al.: Nucl. Instrum. Methods Phys. Res. A **459**, 206 (2001).

Tritium Gas Handling System Operation in 1999/2000

T. Matsuzaki, K. Nagamine, K. Ishida, S. N. Nakamura,[*1] M. Tanase,[*2] M. Kato,[*2]
K. Kurosawa,[*2] and H. Sugai[*2]

A tritium gas handling system (TGHS) has been constructed to produce high-purity D-T target gas for precise measurements of the α-sticking probability in the muon catalyzed d-t fusion cycle at the RIKEN-RAL Muon Facility. At the experiment site, the system enables us to purify the D-T target gas by removing the ^{3}He component (a decay product of tritium), to adjust the D/T gas mixing ratio and to measure the hydrogen isotope components. A schematic diagram is shown in Fig. 1. The system is designed to handle the D-T gas with negative pressure and a total volume of 1.1 liter. Tritium gas with the inventory of 56 TBq (1500 Ci) has been operated in the system.

In the period of 1999/2000, we conducted three major works for the TGHS and reported their details as follows.

(1) Replacement of the mass separation column in the radio-gas chromatograph

The radio-gas chromatograph system was originally developed at the Department of Radioisotopes in JAERI in order to separate hydrogen isotope components for tritium gas enrichment and hydrogen isotope analysis.[1)] By connecting a small ion chamber to a gas chromatograph, the tritiated hydrogen components can be measured more quantitatively. The present gas chromatograph system has been compactly designed to allow installation in the glove box. The system consists of a thermal conductivity detector, separation column and ion chamber with 0.5 cm^3 sensitive volume. The separation column of 3 mm diameter and 3 m long is filled by aluminum oxide powder coated with manganese chloride ($MnCl_2$) and is cooled by liquid nitrogen. The gas sampling unit with a volume of 0.8 cm^3 is designed to be remotely operated by the TGHS control system and the sampled gas is transported to the separation column by neon carrier gas.

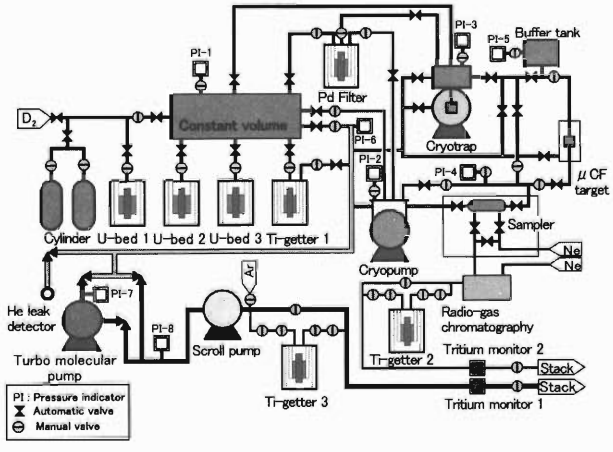

Fig. 1. Diagram of tritium gas handling system.

The separation column deteriorated for an unknown reason and the obtained mass separation of hydrogen isotopes was poorer than the designed performance. Therefore, we manufactured a new separation column with the same specifications and its performance was confirmed at JAERI using deuterium gas before the replacement work. In December 1999, we replaced the separation column of the gas chromatograph with the new one. We measured the mass separation in the gas chromatogram of deuterium gas and the result is shown in Fig. 2. A satisfactory mass separation was obtained between D_2 and HD components, where HD is an impurity in the crude D_2 gas.

(2) Replacement of titanium getter 3

Three titanium getters are installed in the TGHS. Figure 3 shows the cross-sectional view of the triplex structure with double ends. The secondary layer called a "sweep line" is a space for argon gas flow to cool the primary space and sweep away possible permeated tritium. The third layer called a "cooling line" is also a space for argon gas flow to be used as required. This structure minimizes the tritium permeation from the primary space at an elevated temperature because the heater is positioned at the center of the primary space enclosed by two layers with argon flow. The thermocouple located inside the heater enables temperature control with the aid of a PID process controller. Another thermocouple is positioned in the titanium layer as a secondary backup. In Fig. 1, Ti-getter 1 is used to collect the D-T gas in the constant volume for disposal. The other two Ti-getters are used to collect the residual hydrogen in the releasing gas from the

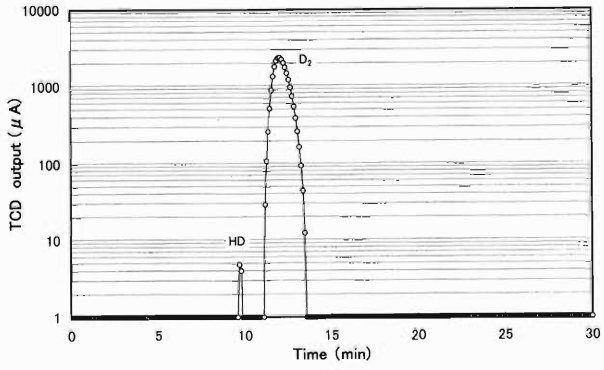

Fig. 2. Obtained gas chromatogram of deuterium gas using the new separation column.

*1 Tohoku University
*2 Japan Atomic Energy Research Institute (JAERI)

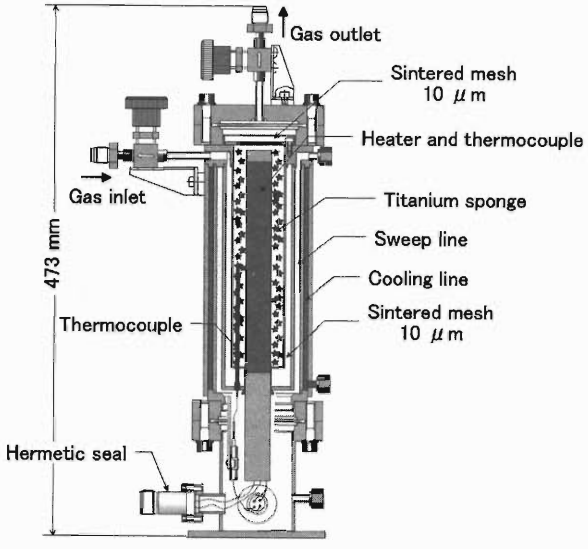

Fig. 3. Cross-sectional view of titanium getter.

radio-gas chromatograph and evacuation system. The titanium sponge of 250 g is loaded around the heater in the primary space and corresponds to the hydrogen gas absorption capability of 46 liters. The releasing gas is introduced into the titanium sponge layer through the sintered mesh. Then, the hydrogen gas is absorbed and the residual gas passes out upward, while the tritiated methane is not absorbed in the Ti-getter. The conditioning of Ti-getters was conducted by evacuation for eight hours at an operating heater temperature of 570°C. The absorption performance of Ti-getter 3 was confirmed by introducing tritium gas and the obtained tritium reduction factor measured by tritium monitor 1 was about 1/5 in the single-pass mode.

Recently, the thermocouple located inside the heater broke down in Ti-getter 3 and the heater temperature could not be controlled. A new titanium getter with the same specification was manufactured and it was installed at the same time as the replacement work of the separation column was carried out in December 1999. After the investigation at the manufacturing company, it was found that the thermocouple wire was broken at the connection part between the thermocouple wire from the heater and the lead wire to the hermetic seal shown in Fig. 3.

(3) Tritium gas supplied by Chalk River Laboratory

In a series of muon catalyzed d-t fusion experiments, we have mainly used tritium gas supplied by JAERI. The tritium gas has been produced there through the ^{6}Li(n, a)T reaction by neutron irradiation to ^{6}Li-Al alloy targets in a nuclear reactor.[2] The tritium gas is extracted from the irradiated ^{6}Li-Al alloy in a vacuum furnace and isotopically enriched by applying the radio-gas chromatograph technique.[1] Removing the ^{3}He component, as a further purification step, is carried out using a palladium filter. The purity of tritium isotope is 99.1% with an impurity of the H component which is originally contained in the ^{6}Li-Al alloy.

In January 2000, we imported tritium gas of 56 TBq (1500 Ci) to UK from Chalk River Laboratory in Canada. At this time, the tritium handling facility at JAERI was under reconstruction and the Chalk River Laboratory is the only organization in the world that supplies tritium gas commercially for scientific research. The tritium gas was placed in two gas cylinders and transported to the RIKEN-RAL Muon Facility. The gas cylinders were then installed in the TGHS and the tritium gas was transferred to the system. In Canada, tritium is extracted from heavy water (D_2O) used at CANDU reactors by the cryogenic distillation method, where tritium is produced in the heavy water by neutron irradiation. The purity of tritium isotope is 99.1% with impurities of D (0.07%) and H (0.67%).

References

1) M. Tanase, M. Kato, K. Kurosawa, S. Motoishi, S. Okane, H. Sugai, M. Fujie, K. Onoma, and H. Yamabayashi: J. Nucl. Sci. Technol. **22**, 147 (1988).
2) H. Kudo, M. Fujie, M. Tanase, K. Kato, K. Kurosawa, H. Sugai, H. Umezawa, T. Matsuzaki, and K. Nagamine: Appl. Radiat. Isot. **43**, 577 (1992).

Optical Detection of Nuclear Spin Precession for the Observation of Nuclear Casimir Effect in ^{131}Xe

K. Yogo,* A. Yoshimi, K. Sato,* K. Sakai,* and K. Asahi

We aim at observing the Casimir effect in a nuclear system which manifests itself in nuclear spin precession. The Casimir effect[1] refers to an observable change in a bound system of charged particles, which occurs when the surrounding vacuum is restricted by placing, for example, a pair of parallel conductingplates. Because of the boundary condition imposed by the plates, the vacuum fluctuation effect differs from the one in free space, resulting in a shift in the energy of the system, depending on the gap between the plates. Recently, observations of the Casimir effect in a neutral atom[2] and macroscopic bodies[3] have been reported.

Here, we use a ^{131}Xe nucleus placed in a static magnetic field B_0 as a probe to observe the vacuum fluctuation. In this case, the effect of the vacuum fluctuation would be dominated by a virtual process in which the ^{131}Xe nucleus jumps from the ground state ($I^\pi = 3/2^+$) to the nearby first excited state ($1/2^+$) and returns, emitting and reabsorbing a virtual photon. If the space around the ^{131}Xe spins is sandwiched by two conducting plates aligned perpendicular to the z-axis (taken parallel to the B_0 field), then the nuclear Zeeman sublevels m are expected to show tiny but finite shifts depending on m; the energy shifts for sublevels $m = \pm 3/2$ are larger than those for $m = \pm 1/2$ since the emission of photons from the $m = \pm 3/2$ is considered to be more restricted than that of photons from $m = \pm 1/2$. Such an effect will be observed in a ^{131}Xe spin precession as three split frequencies, or as "side bands" around the central frequency corresponding to $m = +1/2 \leftrightarrow -1/2$ transition in the Fourier transform of the precession signal. The estimated size of the shifts according to Cheon[4] is $\Delta E \sim 10^{-11} - 10^{-10}\,\mathrm{eV}/b$, where the distance b between the plates is expressed in cm, while recent calculations[5] suggest much smaller values $\Delta E \sim 10^{-19} - 10^{-18}\,\mathrm{eV}/b^2$. The splittings due to the Casimir effect should be clearly distinguished from trivial quadrupolar splittings[6] stemming from a possible shape asymmetry in the ^{131}Xe gas container.

In the planned experiment, ^{131}Xe gas contained in a glass cell is spin-polarized through spin-exchange collisions with Rb atoms, which is polarized by the optical pumping method with circular polarized 795 nm D1 light from a diode laser (Fig. 1). Once ^{131}Xe nuclei are polarized, the pumping light at the cell is turned off

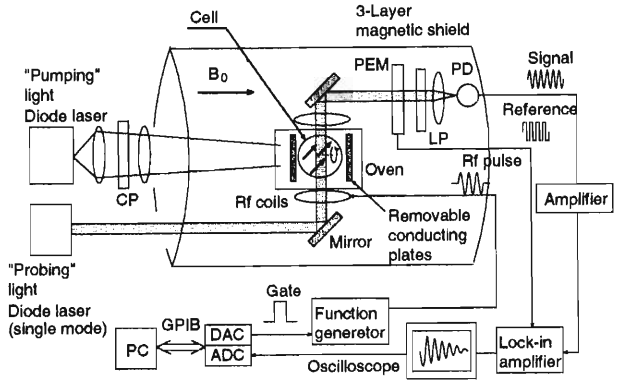

Fig. 1. Setup for the observation of nuclear spin precession with probe light. The conducting plates are removed during the pumping phase. CP: circular polarizer. PEM: photoelastic modulator. LP: linear polarizer. PD: photodiode. PC: personal computer. DAC: digital-to-analog converters. ADC: analog-to-digital converters.

and the conducting plates are placed to modify the vacuum, and an rf field is applied to tilt the spins with respect to the B_0 field. The spin precession thereafter is detected based on the inverse process of the pumping, with linear polarized probe light from a single-mode diode laser. The small amount of circular polarization component is introduced in the probe light after passing through the cell because the Rb vapor in the cell shows circular dichroism due to spin exchange with the polarized Xe nuclei. A photoelastic modulator (PEM), which functions as a chopper of polarized light, enables us to perform a lock-in detection for measuring a slight change in the polarization of the probe light which reflects the Xe polarization. Thus far, we have succeeded to polarize Xe spin. At present, the above detection method for the Xe spin precession is in progress in the RIKEN-TITech collaboration.

References

1) H. B. G. Casimir: Proc. K. Ned. Akad. Wet. **51**, 793 (1948).
2) C. I. Sukenik et al.: Phys. Rev. Lett. **70**, 560 (1993).
3) S. K. Lamoreaux: Phys. Rev. Lett. **78**, 5 (1997).
4) I.-T. Cheon: Hyperfine Interact. **78**, 231 (1993).
5) K. Naito et al.: Prog. Theor. Phys. **97**, 749 (1997).
6) Z. Wu et al.: Phys. Rev. Lett. **59**, 1480 (1987).

* Tokyo Institute of Technology

Development of Nuclear Spin Maser for Low Density Spin System

A. Yoshimi, K. Asahi, K. Yogo,* K. Sato,* and K. Sakai*

We have developed a new type of spin maser which is applicable to low density spin systems. The nuclear spin maser, in which nuclear spin polarization contiguously precesses with a constant transverse polarization, will enable a high-sensitivity detection of a small energy shift of nuclear Zeeman levels. Such a method is necessary for experiments related to fundamental symmetry, such as investigations of electric dipole moments of nuclei.

In a conventional spin maser, the feedback oscillating field which enables spins to precess contiguously in spite of the transverse relaxation is produced by a precession-induced current in a coil wound around the spin system.[1] Therefore a high-density polarized nuclear spin (polarization $P \sim 10\%$), typically $\sim 10^{18}\,\mathrm{cm}^{-3}$, is necessary. We proposed an "active" spin maser which can oscillate at a low spin density where the feedback field is artificially produced based on the detected spin direction.[2] This method can be applied to a nuclear system which cannot be obtained with high density, such as stored neutrons ($\sim 10\,\mathrm{cm}^{-3}$) and radioactive nuclei ($\sim 10^{8}\,\mathrm{cm}^{-3}$).

We have successfully realized the operation of an active spin maser with the polarized ^{129}Xe nuclear system ($I = 1/2$). Spin polarization of ^{129}Xe is produced by the spin exchange interaction with a laser-polarized Rb atom. The precession signal of ^{129}Xe, which is detected by the pickup coil, is sent to the operation circuit in order to produce the feedback signal for realization of the spin maser. The feedback signal is fed to the drive coil to apply the feedback oscillating field onto the precessing spins. The feedback field tends to tilt the polarization vector to the transverse plane so that the spin polarization continues to precess with a constant angle from the quantization axis. The maser signal of Xe in an active feedback operation is shown in Fig. 1 together with that in conventional maser operation. The maser frequency is $\nu \cong 3.5\,\mathrm{kHz}$ which depends on the static field $B_0 \cong 3.0\,\mathrm{G}$.

We are currently developing a new detection system of spin precession for producing the feedback field. The purpose of this development is to realize a maser operation with a frequency ($\sim 10\,\mathrm{Hz}$) at which the spin precession of low-density nuclei can be observed with a high signal-to-noise ratio. The schematic setup is shown in Fig. 2. ^{129}Xe gas is confined in a glass cell consisting of two parts, a masing cell (top) and a probing cell (bottom). The pumping laser light irradiates the masing cell. Rb atoms in the probing cell is not polarized because the spin relaxation of Rb is short, $\sim 1\,\mathrm{msec}$. The spin precession of ^{129}Xe causes the slight polarization of Rb atoms due to the spin exchange collision. Then, the spin precession of ^{129}Xe can be observed by detecting the instantaneous spin direction of the Rb atoms. The spin direction of the Rb atoms is observed by measuring the circular polarization component in the transmitted light which irradiates the probing cell, where the circular polarization is detected by a photoelastic modulator (PEM) after conversion to linear polarization. We are currently arranging the optical setup and designing the cell.

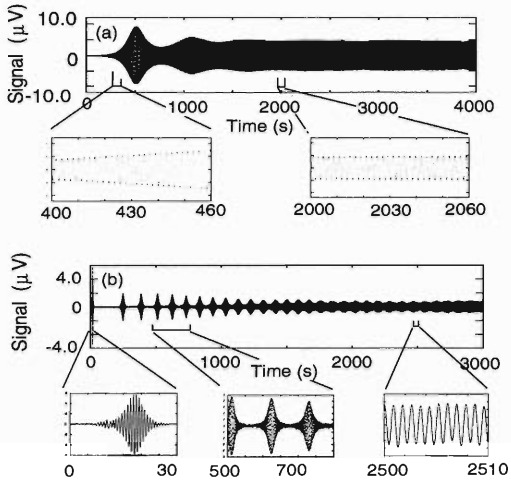

Fig. 1. Maser oscillation signals of ^{129}Xe in (a) a conventional spin maser, and (b) a maser incorporating the artificial feedback system.

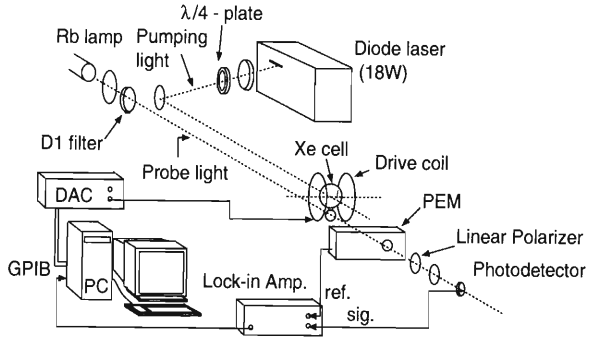

Fig. 2. Schematic setup of a maser incorporating the optical detection system.

References

1) M. G. Richards, B. P. Cowan, M. F. Secca, and K. Machin: J. Phys. B **21**, 665 (1988).
2) K. Asahi et al.: Czech. J. Phys. **50** Suppl. 1, 179 (2000).

* Tokyo Institute of Technology

Calibration of Deuteron Polarimeter DPOL for the Measurement of the $^{12}C(\vec{d}, \vec{d}')$ Scattering in Highly Excited Continuum

H. Kato,[*1] Y. Satou, H. Sakai,[*1] A. Tamii,[*1] K. Sekiguchi,[*1] K. Yako,[*1] S. Sakoda,[*1] M. Hatano,[*1] Y. Maeda,[*1] N. Sakamoto, T. Ohnishi, K. S. Itoh,[*2] H. Okamura,[*3] T. Uesaka,[*3] K. Suda,[*3] J. Nishikawa,[*3] and T. Wakasa[*4]

In order to search for Double Gamow-Teller (DGT)[1,2] resonances, we have measured polarization transfer coefficients of the $^{12}C(d, d')$ scattering. Since the DGT resonances are expected to exist in highly excited continuum of ^{12}C, we have measured the reaction in the excitation energy region of $E_x < 60$ MeV. For this purpose we have calibrated the effective analyzing power of the focal plane Deuteron POLarimeter, DPOL,[3] in the corresponding deuteron energy range, *i.e.*, $210 < E_d < 270$ MeV.

The DPOL is located at the second focal plane of the spectrometer, SMART.[4] A full view of the DPOL is illustrated in Fig. 1. The DPOL consists of two MWDCs, scatterers (SC), a hodoscope (HOD) and a calorimeter (CM). Incoming deuterons are scattered in the SCs and ejectile particles are detected by the second MWDC and the HOD. The SCs are composed of plastic scintillators and polyethylene plates. The DPOL utilizes the $^{12}C(\vec{d}, d)$ reaction for the vector polarization measurement and the $^{1}H(\vec{d}, 2p)$ reaction for the tensor polarization measurement. The vector and tensor polarizations of incoming deuterons can be measured simultaneously.

In the calibration of the DPOL, a faint polarized deuteron beam was directly injected into the SCs. The beam energy was lowered to the appropriate energies by adjusting the thickness of aluminum degraders. The obtained energy dependence of the effective analyzing powers is shown in Fig. 2. iT_{11} is the vector analyzing power of the $^{12}C(\vec{d}, d)$ reaction in a scattering angle range of $5° < \theta < 14°$. T_{20} and T_{22} are the tensor analyzing powers of the $^{1}H(\vec{d}, 2p)$ reaction in ranges of $0° < \theta < 10°$ and $3° < \theta < 12°$, respectively. Relative energies of two protons in the CM system are selected as $E_{rel} < 3$ and $E_{rel} < 10$ MeV in the analysis of T_{20} and T_{22}, respectively. The scattering angle ranges and reaction energy ranges are determined as the figure of merit (FOM) of each analyzing power reaches a maximum. The FOMs and thicknesses of scatterers are compared with those of the polarimeters at Saturne[5,6] in Table 1. The FOMs of the DPOL are smaller than those of Saturne due mainly to the thickness of the scatterers. However, the DPOL has an advantage in that the vector and tensor polarizations can be measured simultaneously, while at Saturne, two different polarimeter systems must be used. Therefore, the DPOL is expected to have fewer systematic errors in the measurement.

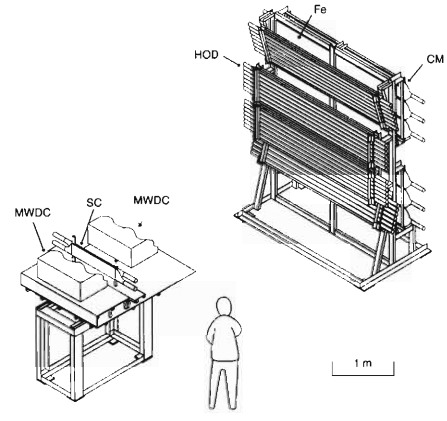

Fig. 1. A full view of the DPOL.

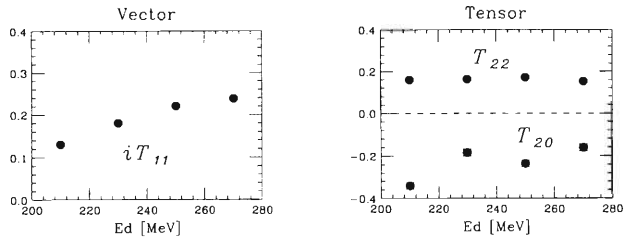

Fig. 2. The energy dependence of the effective analyzing power of the DPOL.

Table 1. FOMs and thicknesses of scatterers. The difinition of the FOMs is adapted to that of Saturne. The FOMs are defined as in Refs. 5 and 6.

	F_{11} (10^{-2})	F_{20} (10^{-2})	F_{22} (10^{-2})	thickness (g/cm^2)
DPOL	1.91	0.60	0.59	C:4.2 H:0.47
Saturne	4.2	1.2	1.0	C:8.2 H:1.1

*1 University of Tokyo, *2 University of Tsukuba
*3 Saitama University, *4 RCNP, Osaka University

References
1) P. Vogel et al.: Phys. Lett. B **212**, 259 (1988).
2) N. Auerbach et al.: Ann. Phys. **192**, 77 (1989).
3) S. Ishida et al.: AIP Conf. Proc. **343**, 182 (1995).
4) T. Ichihara et al.: Nucl. Phys. A **569**, 287c (1988).
5) B. Bonin et al.: Nucl. Instrum. Methods Phys. Res. A **288**, 389 (1990).
6) S. Kox et al.: Nucl. Instrum. Methods Phys. Res. A **346**, 527 (1994).

Computing Environment of the RIKEN Accelerator Research Facility

T. Ichihara, Y. Watanabe, A. Yoshida, and K. Yoshida

In this report, we describe the recent computing environment of the RIKEN Accelerator Research Facility (RARF).

(1) UNIX cluster server

Figure 1 shows the configuration of the UNIX cluster server of RARF, which was installed in 1998. Five nodes of UNIX servers, three of which are True 64 UNIX (alpha) and two of which are Solaris, are connected *via* the Gigabit Ethernet using a 1000 BaseSX multimode optical fiber. The utilization of the Gigabit Ethernet ensures the fast file access of the remote node and eliminates the network traffic jam. RARFAXP is the main server for mail, text processing, user homepages and general computing. RARFAX1, RARFAX2, and RARFSUN are used mainly for intensive data analysis and large-scale calculations. RARFNFS0 is a dedicated Network File Service (NFS) server which is equipped with 2.8 TB (400 GB × 7) raid5 work disks. The Veritas File System (VxFS), which is a kind of logging file system, was adopted for the raid file systems to obtain high performance in file operation and fast file system recovery (fsck) after system failure.

RARFLX1 and RARFLX2 are installed at the 1F counting room to serve the working terminals during the experiment. A Linux OS is adopted for RARFLX1 and RARFLX2. All seven nodes share a common Network Information Service (NIS) and NFS system to form a UNIX cluster. Several kinds of tape drives, including AIT-2, DLT, DDS4, DDS3 and 8 mm ones are connected to the UNIX cluster. A load sharing facility (LSF) is installed for the batch queuing system.

Secure Shell (SSH) was installed for all the nodes. The use of SSH is strongly recommended for remote login and file transfer to ensure security against data sniffing. The Secure Sockets Layer (SSL)-encrypted Internet Message Access Protocol (IMAP) service is available at the RARFAXP. An anonymous ftp service is operating at RIKSUN (ftp.riken.go.jp) which archives 400 GB of useful software for research, including Linux and TeX distributions, GNU software and a large amount of free software for PC, Mac and UNIX systems.

(2) VMS system

Figure 2 shows the old system of the RARF off-line cluster, which consists of nine nodes of Open VMS/AXP system. These nodes are connected by 100 Mbps FDDI and 10 Mbps Ethernet. This VMS cluster was the main off-line system at RARF before 1998. Since users of the VMS systems are migrating to other systems such as the UNIX cluster, termination of the operation of the VMS system is currently under discussion.

(3) Online DAQ system

The VMS-based Data Acquisition (DAQ) system

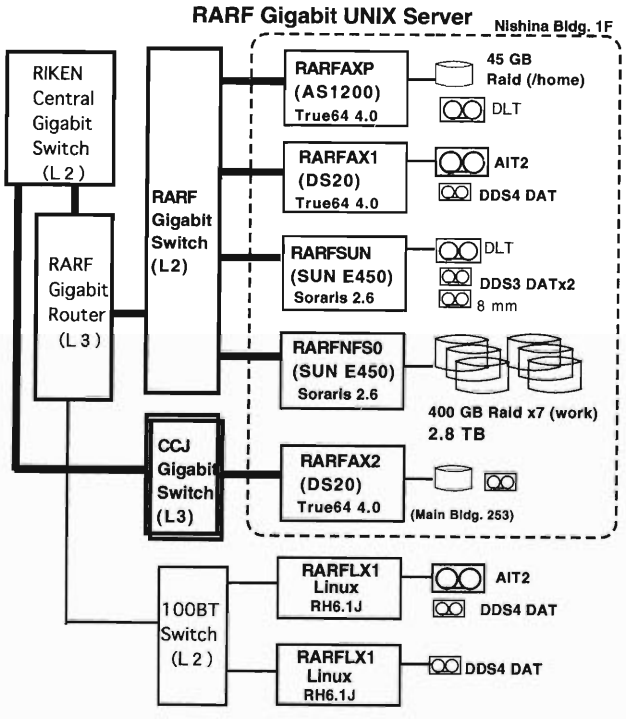

Fig. 1. Configuration of the RARF UNIX cluster.

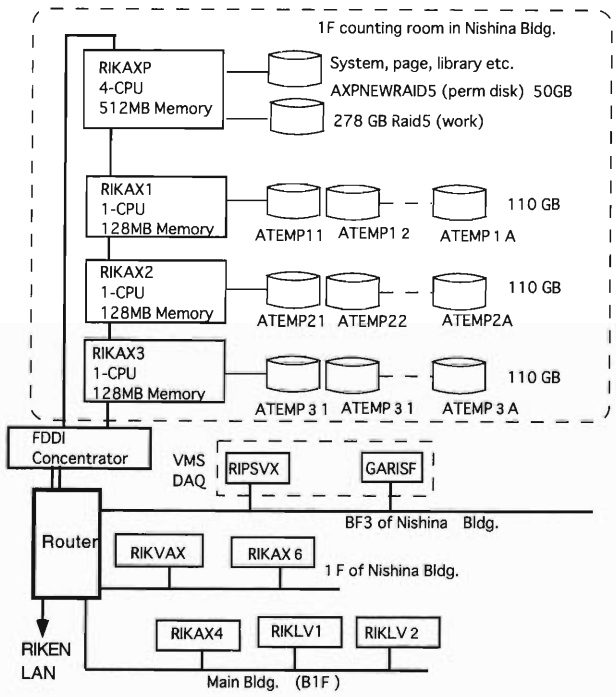

Fig. 2. Configuration of the old VMS cluster.

is used for several experiments including RIPS. The CES 2180 Auxiliary Crate Controller accelerates the CAMAC read operation to approximately 1.4 μs/word read.[1] A Linux-based fast DAQ system was developed recently for a SMART experiment.[2] A CC7700 and PC-Linux-based DAQ system is also available for experiment.[3,4]

(4) Wide-Area Network (WAN) environment

RIKEN is connected to the Inter-Ministry research information network (IMnet) at the speed of 15 Mbps and this bandwidth will be updated to 50 Mbps in early 2001. For the international connection, RARF joined the Asia-Pacific Advanced Network (APAN) which has a bandwidth of 70 Mbps over the Pacific Ocean. Thanks to the APAN, stable access to the USA and Europe ESnet sites has been achieved.

(5) Electronic-mail address

The electronic-mail address for a general user of the RIKEN Accelerator Research Facility is described as follows, where the *userid* should be replaced by user's login name of the RARF UNIX Cluster.

userid@rarfaxp.riken.go.jp

References

1) T. Ichihara et al.: IEEE Trans. Nucl. Sci. **36**, 1628 (1989), see also http://www.rarf.riken.go.jp/rarf/exp/comp/
2) H. Okamura et al.: Nucl. Instrum. Methods Phys. Res. A **443**, 194 (2000).
3) H. Baba et al.: RIKEN Accel. Prog. Rep. **34**, 221 (2001).
4) N. Iwasa: http://rarfaxp.riken.go.jp/~iwasa/cc7700.html

CAMAC Data Acquisition System for the NIRS/HIMAC Facility

H. Otsu* and T. Kobayashi*

A new CAMAC data acquisition system has been developed for experiments at a secondary beam course in the Heavy Ion Medical Accelerator in Chiba (HIMAC). In the facility we have carried out experiments mainly on measuring the $(p, 2p)$ reaction from unstable nuclei. The new porting system has the following characteristics:

- The system is suitable for data production rates typically ranging from 100 to 100 k words/s.
- A cost-effective system can be realized by dividing the system into several, easily exchangeable parts, which leads to lower costs.
- The raw data format can be fully compatible with those of the conventional DAQ system in the RARF/RIPS facility.
- A compact DAQ system is desired, which can be replaced in RARF/RIPS in the near future.

(1) Hardware configuration (see Fig. 1)

This system consists of three computers. One is a CAMAC ACC K3976, which takes typically 1.8 μs for a single CAMAC function. A DAQ software package (EXP9X[1]) is available with a different hardware configuration (K3976-K3929-Linux PC). The other two are linux PCs with Intel Pentium family processors. The upstream linux PC, called the 'front-end,' is specified to transmit data up to 32×16 kB on K3976 memory to memory on the PC. CC7000 and its interface have no direct memory access (DMA) property. Instead, the front-end PC has a device driver specified to transfer 16 kB data at once without other process interruptions. This extension enables the system to achieve a transfer rate of 360 kB/s, about half that of the original EXP96 system. The spill-off transfer (1.5 s for 32×16 kB) is available in the HIMAC synchrotron facility. Thus, no dead time occurs in transferring data to the front-end PC. The data are directly stored on hard disks or tape storages mounted on the front-end PC and partly distributed to the downstream (back-end) linux PC. In the back-end PC, analyzer processes are run. A private network with a crossed Ethernet cable connects two linux PCs. The front-end PC is the core part of this DAQ system.

(2) Software configuration (see Fig. 2)

K3976 programs are almost the same as the original EXP96's. For compatibility with the RARF/RIPS raw data format of a 16 kB unit, several codes are replaced, mainly to realize continuity between units.

The CC7000 Linux device driver, developed and maintained by the SMART group, is used as a base for the front-end PC. The code to transmit 16 kB data

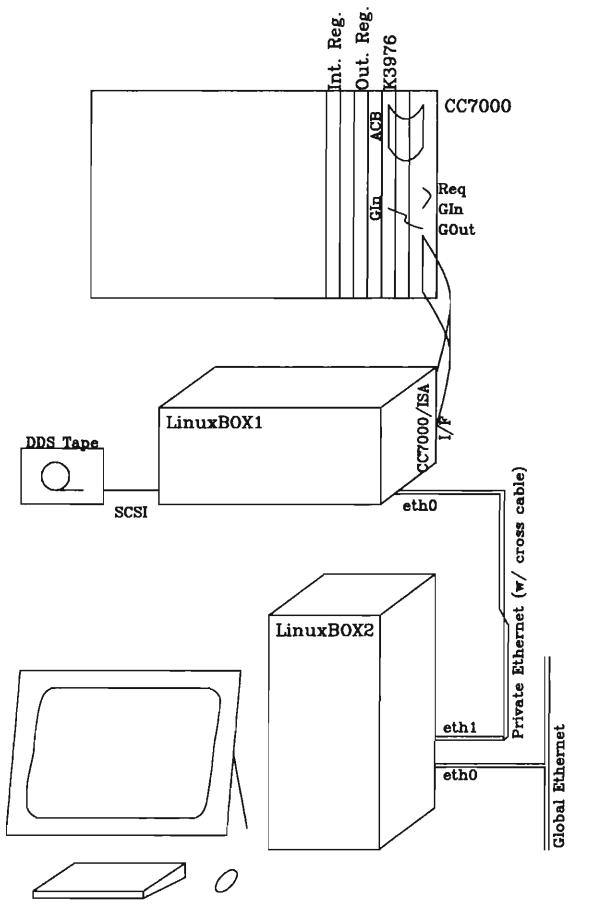

Fig. 1. DAQ system consisting of three computers. ACC K3976 reads module data and stores them in the memory. When the memory is full or a user interruption occurs, these data are transferred to the front-end PC and stored on a disk or a tape.

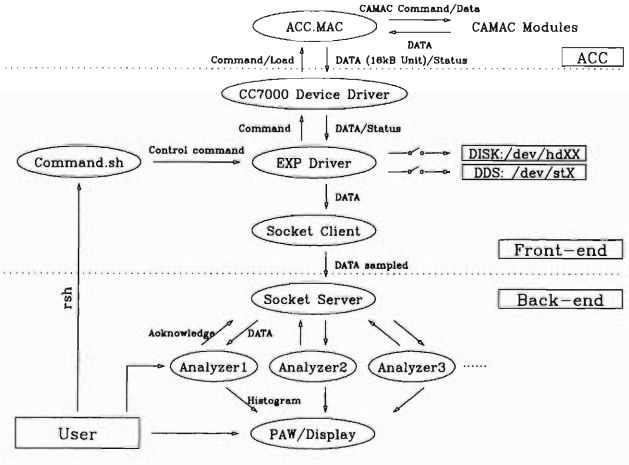

Fig. 2. Block diagram of the software configuration.

* Department of Physics, Faculty of Science, Tohoku University

at once is added in the device driver. As a result, an OS clock is delayed depending on the frequency of data transfer. The OS clock is restored from a CMOS clock on the PC when the stop command is given.

From the front-end PC to the back-end PC, the sampled data are transferred by a client-server program pair with a protocol of TCP. In the back-end PC, data analysis is performed. Codes compatible with those used in the RARF/RIPS facility are available.

In order to conserve the rate of transferring data to the front-end PC, only limited processes are allowed to run. In contrast, many processes are allowed in the back-end PC because they have no influence on the front-end PC.

In summary, it is found that the DAQ system functions well in the HIMAC facility. This system is a candidate for the smooth replacement of the current VAX/J11 system used in the RARF/RIPS facility.

References

1) S. N. Nakamura and M. Iwasaki: RIKEN Accel. Prog. Rep. **30**, 152 (1997).

Development of New Data Acquisition System BabarlDAQ for Nuclear Physics Experiments

H. Baba,[*1] S. Takeuchi,[*1] K. Yamada,[*1] S. Shimoura,[*2] and K. Ieki[*1]

We have developed a new data acquisition (DAQ) system "BabarlDAQ." The previous RIKEN standard CAMAC[†] system[1] consisted of a CES2180 auxiliary crate controller (ACC), a VAX computer, Kinetic 3922 and a Kinetic 2922 Q-BUS Interface for 3922. However, as the CES2180 ACC is out of production and the number of VAX computers is declining, the development of new DAQ systems is necessary for future generation experiments.

BabarlDAQ employs personal computers (PCs) with a RTLinux[2] operating system, Kinetic 3922 crate controller and Kinetic 2915 PCI Interface to 3922. RTLinux is the real-time operating system variant of Linux that is released under the GNU General Public License and can be freely used. The BabarlDAQ processes each event using a PC instead of an ACC. Using RTLinux for event processing, the BabarlDAQ performance is reached at the same level as that of the previous system. For event processing, a user may add a program in the C language instead of the assembler language used in the previous system.

BabarlDAQ includes "Anapaw," which is a useful analysis software that runs under Linux. Anapaw is based on PAW[3] which uses the CERN Program Library[4] and is compatible with "Analys" which is used in the previous system. Anapaw has the same user interface for both on-line and off-line analyses. For on-line use, Anapaw receives data from *Analyzer*, which is one of the components of BabarlDAQ, while Anapaw can also read data from files for off-line analysis.

Thus, BabarlDAQ is very cost-effective and users can change from the previous system to BabarlDAQ easily.

The configuration of BabarlDAQ is shown in Fig. 1. The main components of BabarlDAQ are the *Collector*, *Driver*, *Transfer*, *Database*, *Controller*, *Recorder*, and *Analyzer*. Each component, except for the *Collector*, *Driver* and *Transfer*, can be distributed to PCs that communicate with each other through ethernet. The *Database* manages status data (*e.g.*, run information, current block data, scaler data), and provides these for other components. The *Controller* is the only component which has a user interface, and the user can control BabarlDAQ through the *Controller*. The *Recorder* stores raw data which come from *Transfer* on storage, hard disk or magnetic tape. The *Analyzer*, which is a front-end program for on-line software such as Anapaw and Status Monitor *etc.*, receives block data from the *Database*. The *Collector* loads the *Driver* and executes the *Transfer* when data acquisition is started. The *Driver* acquires data from CAMAC and stores data in a buffer which is located at a shared memory region. The *Transfer* observes a shared memory, and transfers data to the *Recorder* and *Database* when the buffer becomes full. Since the *Driver* and *Transfer* communicate which each other through the shared memory, and the *Collector* is front-end for the *Driver* and *Transfer*, these components must exist in the same computer region. The *Driver* and *Transfer* operations are shown in Fig. 2.

The *Driver* checks the Look-At-Me (LAM) signal every 50 μs using a RTLinux periodic tack. While it takes

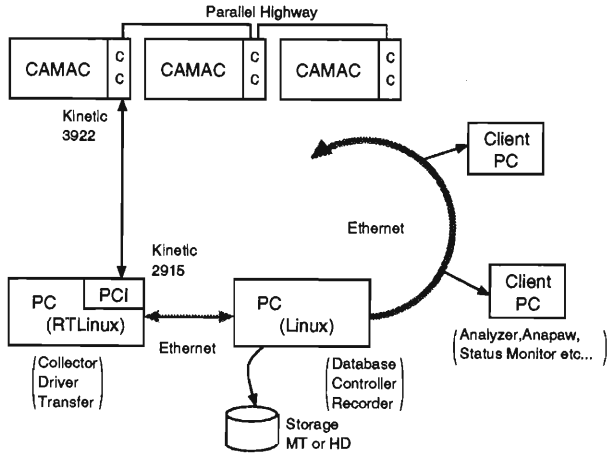

Fig. 1. Typical configuration of BabarlDAQ. Some client PCs can lie on the ethernet.

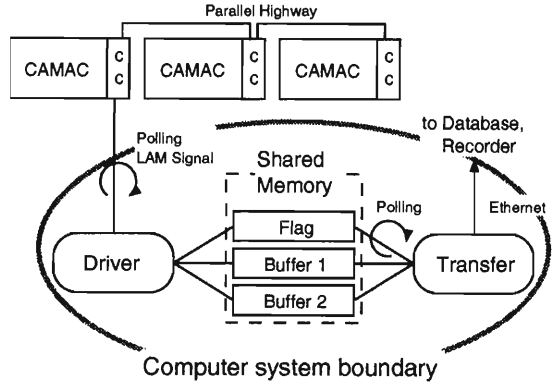

Fig. 2. Operation of the *Driver* and *Transfer*. The *Driver*, *Transfer* and shared memory are located in the same computer region.

[*1] Rikkyo University
[*2] Center for Nuclear Study, University of Tokyo
[†] Computer Automated Measurement and Control

Table 1. Performance of CAMAC access. Interrupt latency is the period between CAMAC set LAM signal and the RTLinux handler is taken up by IRQ that is not used in BabarlDAQ.

		Time (μs)
Single Action	No data transfer	8.5
	1 Word Read	11.0
	1 Word Write	11.0
Block Read Action	Overhead	16.8
	1 Word Read	2.6
Interrupt Latency		4.5

CAMAC: Kinetic 3922 + 2915 PCI Interface
CPU: INTEL Cerelon 450 MHz
OS: Linux 2.2.13 + RTLinux 2.0

up to 600 μs to start a handler in a standard Linux and there could easily be a more than 20 ms latency for a periodic task, a RTLinux periodic task can run within 35 μs of its scheduled time. With two buffers in a shared memory, the *Driver* can acquire data from CAMAC even while the *Transfer* is accessing buffered data.

We have developed a device driver for a Kinetic 2915 interface to a 3922 crate controller running on RTLinux. The performance of CAMAC access is listed in Table 1. Owing to the RTLinux, these times are not affected by any other consumer process. The single action response time is 8.5 μs at the no-data-transfer mode, and 11.0 μs at the read-action or write-action mode. In the Block-read-action mode, which is one of the Kinetic 3922 + 2915 action modes, once the crate address, station number, subaddress, function and transfer-count are set at the 2915 CNAF and the transfer-count register, new data are automatically set at the 2915 FIFO register for the transfer-count times at which each data is read out from the 2915 FIFO register. This mode is useful for LeCroy FERA, FERA-compatible, Memory and Phillips modules that are able to read sequentially. In this mode, it takes up to 58.4 μs to read 16 words, while in the other single-action mode, it takes up to 176 μs.

BabarlDAQ has been introduced for nuclear physics experiments using the RIKEN projectile fragment separator (RIPS). Figure 3 shows the live time of BabarlDAQ in a typical experiment at RIPS. Live time is calculated based on the ratio of the total event number to the accepted event number by CAMAC. In this experiment, typical event size is about 80–90 words and the event rate is 0.2 kcps to 1.8 kcps, and the acquired data is stored on magnetic tape. This result is no worse than that of the previous system. It should be noted that the stored data have no errors, in spite of the high rate and long duration of the experiment.

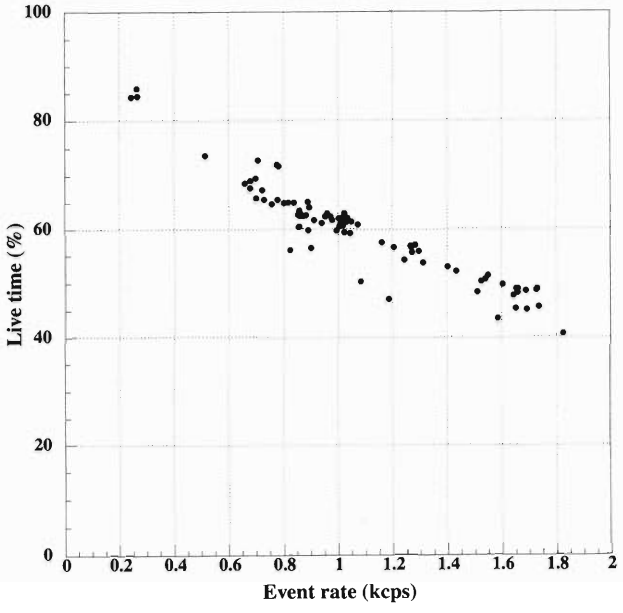

Fig. 3. Live time of BabarlDAQ in a typical experiment at RIPS.

We will continue to explore means of developing of BabarlDAQ in order to achieve performance improvement, for example, not only using CAMAC and PCs but also combining ACC or VME.†

References

1) T. Ichihara et al.: IEEE Trans. Nucl. Sci. **36**, 1628 (1989).
2) http://www.rtlinux.org/
3) http://wwwinfo.cern.ch/asd/paw/
4) http://wwwinfo.cern.ch/asd/cernlib/

† VERSAbus Module Europcard

6. Material Analysis

Fabrication of Nanoparticles in Polymer by Ion Implantation

T. Kobayashi and M. Iwaki

A polyimide film was implanted with Ag, Cu, Fe, K, Pd, and W ions using the four available accelerators with the energy from 100 to 380 keV. The beam was scanned over a set area (400 cm^2 for Ag and W implantation, and 9 cm^2 for the other ions) so that the fluence would be the same for all the irradiated specimen areas. The fluence ranged from 1×10^{15} cm^{-2} to 5×10^{17} cm^{-2}, and the current density was kept to 0.1 to 3 $\mu A cm^{-2}$ at a pressure below 1×10^{-5} Pa.

Cross-sectional transmission electron microscope (TEM) observations were performed to observe any growth of metallic particles using a 200 keV JEOL 2000-FX electron microscope. The implanted specimens were packed in epoxy resin, and the 100-nm thick cross-sectional samples were prepared using a Leica ULTRACUT UCT with a diamond knife. The surface composition was obtained from Rutherford backscattering spectroscopy (RBS) spectra. The RBS measurement was performed using a pelletron accelerator in RIKEN. The energy and the scattering angle of the He ion beam were 1.5 MeV and 160°.

Figure 1 shows the cross-sectional TEM image of specimen implanted with silver ions at a fluence of 1×10^{16} cm^{-2}. The formation of particles of about 5 nm in diameter was observed at around a depth of 50 nm. The diameter of the particles increased with the magnitude of the fluence until it reached about 10 nm in the specimens implanted at a fluence of 1×10^{17} cm^{-2}. These results suggest that silver atoms implanted in polyimide migrate easily during irradiation. The electron diffraction pattern of the specimen implanted at a fluence of 1×10^{17} cm^{-2} shows that implanted silver atoms exist as face-centered cubic (fcc) crystalline particles. The crystalline particles were also observed in the cases of the copper- and palladium-implanted specimens.

In the cases of iron-, potassium-, and tungsten-implanted specimens, no particle formation was observed in the implanted layers. An increase in electron density was observed at around depths of mean ion ranges due to implanted atoms. However, no diffraction pattern related to implanted atoms was observed by electron diffraction spectroscopy.

It was concluded that noble metals implanted in polyimide tend to form nanoparticles and that chemical activities of implanted atoms may control the particle formation.

Figure 2 shows the RBS spectra of a silver- and a tungsten-implanted specimen at a fluence of 1×10^{16} cm^{-2}. The depth profiles of these two ions are almost same. The oxygen concentration in the implanted layer decreased dramatically. The proportion of nitrogen atoms at the surface was difficult to estimate, because its signal overlaps with the signal for oxygen arising from O beneath the implanted layer. At any rate, little difference was seen between these two spectra in the region corresponding to the concentration of nitrogen and oxygen. On the other hand, the spectrum shows that the density of carbon atoms in the tungsten-implanted layer was higher than that of the silver-implanted one. This means that a chemical interaction exists between tungsten and carbon, rather than between tungsten and oxygen. In this case, we can speculate that the formation of metallic particles is suppressed by bonding between the implanted atoms and carbon, which in turn, affects the migration of the implanted atoms.

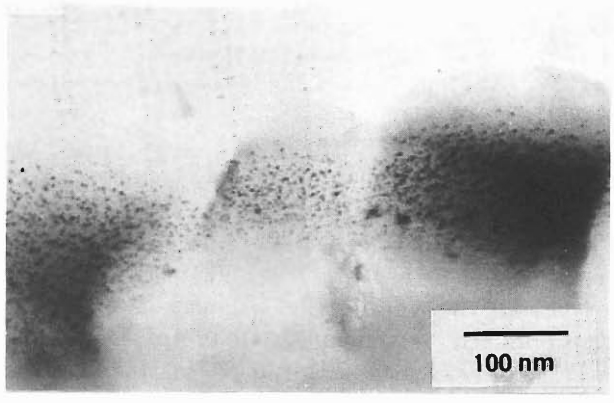

Fig. 1. A cross-sectional TEM image of the specimen implanted with silver at 1×10^{16} cm^{-2}.

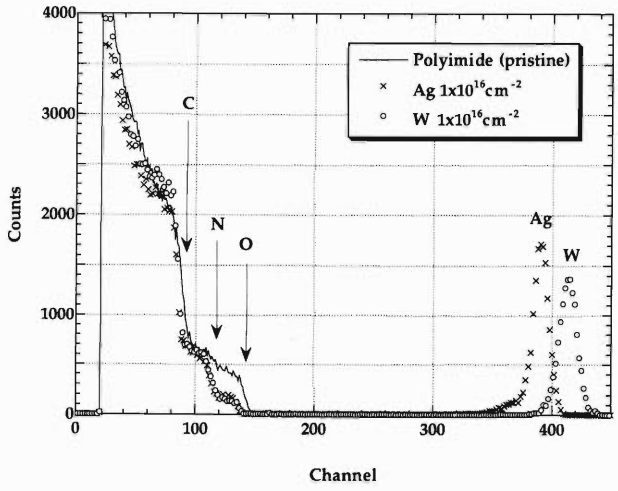

Fig. 2. RBS spectra of silver- and tungsten-implanted specimen at a fluence of 1×10^{16} cm^{-2}.

Direct Speciation of Sulfur in Marine Sediments by High-Resolution PIXE

K. Maeda, T. Hasegawa,[*1] H. Hamanaka,[*1] K. Hasegawa,[*1] and M. Maeda[*2]

We have developed a high-resolution PIXE system for chemical state analysis in atmospheric air.[1,2] In the present work we apply this system to measure the chemical shifts of K$\alpha_{1,2}$ line of sulfur in marine sediments in order to examine the possibility of direct speciation of sulfur in such delicate environmental substances.[3]

The experimental setup is almost the same with that reported in the previous paper[2] except that an entrance slit and a remote controllable XYZ target stage were newly attached to the system. A target sample was placed in air and bombarded with a 2.1 MeV proton beam of 3 mm diameter.The X-rays emitted from the target passed through the entrance slit and were diffracted by a flat analyzing crystal. The diffracted X-rays were then detected by a position-sensitive proportional counter (PSPC) and recorded on a 512 channel analyzer. The entrance slit was made 0.3 mm in width and placed at 5 mm distance from the proton beam spot on the target. It worked to restrict the shape and position of the X-ray source exactly. The target sample was moved repeatedly by a programmable stage controller in order to reduce the sample damage by proton bombardment. The analyzing crystal used was NaCl (200). One channel of the PSPC corresponds to 0.140 eV in the energy region of S K$\alpha_{1,2}$ (2.31 keV). The precision of chemical shift measurements was estimated to be ± 1 channel by measuring S Kα spectra of MoS_2, Na_2SO_3 and Na_2SO_4.

The marine sediment samples were collected in the Sagami Bay, Japan, from the water depth of one thousand meter using a corer. Immediately after the sample collection, the core sample was cut into 1 cm-thick slices, frozen and stored in a freezer. The day before the PIXE measurements the sliced samples were defrosted. Small portion of the samples were collected on membrane filters, washed with a small amount of Milli-Q water and then stored in plastic containers. The membrane filters loading the sediment samples were cut into two or three pieces each, and set on plastic target holders and directly submitted to the PIXE analysis.

Sulfur K$\alpha_{1,2}$ spectra obtained from two depths (6.5 cm and 8.5 cm) in the sediment core sample are shown in Fig. 1 together with the spectra from reference targets MoS_2 (S^{2-}) and Na_2SO_4 (S^{6+}). The peak position of the S K$\alpha_{1,2}$ from the sediment at the depth of 6.5 cm is near to that of MoS_2. On the other hand, the peak position of the S K$\alpha_{1,2}$ from the sediment

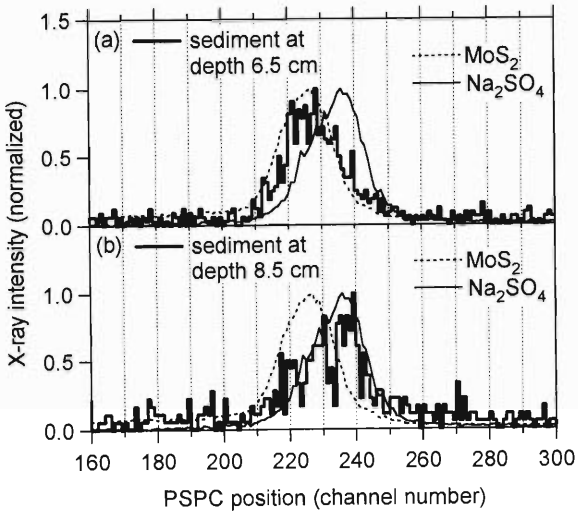

Fig. 1. K$\alpha_{1,2}$ spectra of S in the sediment samples at the depths of (a) 6.5 cm and (b) 8.5 cm. Beam current 80 nA; measuring time (a) 700 s; (b) 600 s: maximum counts (/channel) (a) 32; (b) 18. Sulfur concentrations in these samples were around 1%.

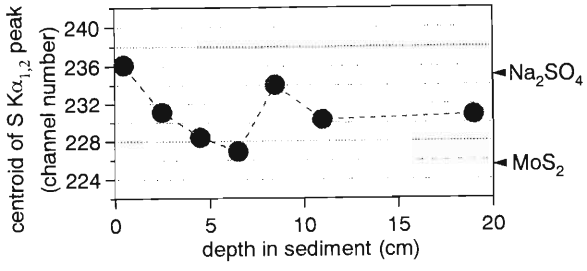

Fig. 2. Centroids of S K$\alpha_{1,2}$ spectra obtained from the sediment samples at different depths in the core sample.

at the depth of 8.5 cm is between those of MoS_2 and Na_2SO_4. The latter spectrum seems to be composed of two or more components.

Measurements of S Kα specta were carried out several times for each sample. Repeated measurements indicated that the sediment samples were oxidized by air to some extent during the handling and measurements.[3] The centroids of S K$\alpha_{1,2}$ plotted against the depth in the sediment core in Fig. 2 were obtained by summing the spectra of duplicate measurements, which were carried out within fifteen minutes after taking the samples from the containers. The centroid positions in each pair of the duplicate measurements agreed within 3 channels although the counting rates were very small. From Fig. 2, we may

*1 College of Engineering, Hosei University
*2 Tokyo University of Fisheries

suppose that the ambience of the sediments near the interface between the sediment and marine water was rather oxidative and the ambience of the sediments at the depth around 6 cm was rather reductive. The high-resolution PIXE is considered to become a useful tool for direct speciation of S in environmental substances, although more rapid measurements are desired. Development of a highly sensitive high-resolution PIXE system is in progress.

References

1) K. Maeda, K. Hasegawa, H. Hamanaka, and K. Ogiwara: Nucl. Instrum. Methods Phys. Res. B **134**, 418 (1998).
2) K. Maeda, A. Tonomura, H. Hamanaka, and K. Hasegawa: Nucl. Instrum. Methods Phys. Res. B **150**, 124 (1999).
3) K. Maeda, T. Hasegawa, H. Hamanaka, K. Hasegawa, and M. Maeda: Int. J. PIXE **10**, 47 (2000).

Slow Positron Yields from Some Porous Materials

L. Wei, N. Suzuki, J. Kim, F. Saito, Y. Itoh, A. Goto, T. Kurihara, Y. Nagashima, and T. Hyodo

The slow positron yields from a solid are affected by many factors, such as positron penetration depth, positron diffusion length, trapping by defects and surface state, and there are several characteristics necessary to realize highly efficient moderator. The positron work function at the surface must be negative. Furthermore, the materials should have high density, so that more positrons can be slowed down quickly in the crystal structure, and then the thermalized positron can be re-emitted at the surface. Finally, the moderator material must have a high positron mobility or long diffusion length, so that the positron can reach to the surface and successfully exit to the vacuum. Besides these characteristics, the effective emission surface also plays an important role which is well clarified by recent studies on porous nickel and tungsten multi-wires. Therefore, there is possibly room for further increases in the slow positron yield. In this work, we report the first measurement of slow positron yields from several porous materials which have a large aspect ratio or surface-to-volume ratio and a stable physical property.

The materials used in this study are β-SiC whiskers, β-SiC beads, tungsten powder and carbon fibers. The slow positron yield measurements were carried out on the magnetically guided slow positron beam lines at RIKEN. The two beam lines are equipped with an E × B energy filter and a bending magnetic solenoid, respectively, to ensure that no fast positron can arrive at the sample chamber. For the calculation of efficiency ε, 100% positron transmission efficiency of the beam line is assumed.

The overall moderation efficiencies ε for β-SiC whiskers, β-SiC beads, tungsten powder and carbon fibers have been measured to be $0.58-0.71 \times 10^{-4}$, 0.17×10^{-4}, 1.2×10^{-4} and $< 0.04 \times 10^{-4}$, respectively. In this experiment, the 1-mm-diameter tungsten powder was pasted on 1.5 mm Al foil. The obtained efficiency, 1.2×10^{-4}, is comparable to that of tungsten polycrystal foil.[1)]

The preparation conditions for the tungsten powder were not optimized in the present study. First, the annealing temperature was 1100°C, which is lower than that conventionally used for tungsten annealing ($\sim$ 2000°C). Secondly, during the preparation of the moderator, the annealed tungsten powder was dipped in ethanol before being pasted onto the Al foil. Finally, the tungsten powder was not pasted uniformly or regularly well onto the Al foil because of our lack of experience. However, by overcoming the above problems in the processing, it seems reasonable to expect that the moderation efficiency for tungsten powder may reach the high 10^{-4} range, the value obtained by using the tungsten overlapping mesh.[2)]

The moderation efficiencies obtained for all the β-SiC moderators are below the 10^{-4} level, which is at least several times lower than the estimate from re-emission measurements, but still tens of times higher than that obtained using transmission film moderator.[3,4)] SiC is a potential candidate for a robust and efficient positron moderator, because of its large negative work function, considerable diffusion length and stable physical and chemical properties. The SiC whiskers and SiC beads have either a large aspect ratio or surface-to-volume ratio, thus they are expected to provide high moderation efficiency. However, the moderation efficiencies obtained are away from the predicted value. One probable reason for this is the process used to prepare the moderator. Another reason may be the surface state, which affects the positron emission. We expect that proper surface treatment and a well-designed SiC/foil arrangement will improve the moderation efficiency.

In conclusion, slow positron yields from several materials with porous structures have been measured on slow positron beam lines in RIKEN. β-SiC whiskers have a proposed moderation efficiency ε in the high 10^{-5} range and tungsten powder in the low 10^{-4} range.

References

1) S. Pendyala and W. McGowan: J. Electron Spectrosc. Relat. Phenom. **19**, 161 (1980).
2) Y. Nagashima, T. Kurihara, F. Saito, Y. Itoh, A. Goto, and T. Hyodo: Jpn. J. Appl. Phys. **39**, 5356 (2000).
3) R. Suzuki, T. Ohdaira, A. Uedono, S. Ishibashi, A. Matsuda, S. Yoshida, Y. Ishida, S. Niki, P. J. Fons, T. Mikado, T. Yamazaki, S. Tanigawa, and Y. K. Cho: Mater. Sci. Forum **714**, 255 (1997).
4) A. Uedono: private communication.

7. RIKEN-BNL Collaboration on Spin Physics Program

Experimental Activities in the RIKEN BNL Collaboration for Spin Physics at RHIC

M. Ishihara and G. Bunce

The RHIC Spin Project is the integrated effort of accelerator, experimental and theoretical physics to study polarization phenomena in high-energy hadron collisions using polarized proton beams at RHIC. We have made significant progress in the project this year achieving the first successful storing and acceleration of polarized proton beams at RHIC.

RHIC provided the first collision of gold ion beams in June, 2000 at $\sqrt{s_{NN}} = 56\,\mathrm{GeV}$, followed by the luminosity run through summer at $\sqrt{s_{NN}} = 130\,\mathrm{GeV}$. In the PHENIX experiment, we have recorded about 5 million events on tape out of 45 millions minimum-bias events, which translates to $4.1\,\mu\mathrm{b}^{-1}$. We have obtained the first set of physics results using the electromagnetic calorimeter (EMCal), transverse energy distribution, transverse momentum distribution of π^0, and inclusive photon.[1,2] In the early phase of the polarized proton operation, these analyses will be extended to the study of gluon polarization (Δg) in the proton with pion production,[3] which is one of the main goals of the project.

The data analyses are in progress at the RHIC Computing Facility (RCF) and the PHENIX Computing Center in Japan (CC-J).[4,5] A database management system has been carefully chosen to ensure identical reference of calibration constants at both RCF and CC-J.[6] Large-scale simulation has just been finished at CC-J and the simulation data is being transferred to RCF.[7]

Towards the full operation of the Muon Arm in 2001, the construction and commissioning of Muon detectors are now at full speed. All Muon Tracking chambers are installed in the Muon Magnet. Signals are read out successfully using partially installed electronics, and the optical alignment system is a key device for achieving $100\,\mu\mathrm{m}$ position resolution and its installation will be completed with CCD readout system.[8]

The Muon Identifier (MuID) has been installed since September, 1998. A part of the system was read out successfully in gold-gold collisions this summer.[9] The MuID is expected to provide a "road" of penetrating track as a seed for both level-1 trigger and track reconstruction with Muon Tracking. A road finding algorithm has been developed and applied for the real events, and performed successfully.[10]

The Muon Arm will be able to provide powerful constraints on Δg through heavy quark productions[11] even in the first year of polarized proton operation.

Since we are interested in rare events such as lepton or photon productions with high transverse momentum, a level-1 trigger is a key device in pp collisions. The development of such a trigger system for Central Arms based on the energy deposit in EMCal is in progress.[12]

In parallel to these efforts in the PHENIX experiment, we prepared for the commissioning of RHIC with polarized proton beams. The first snake magnet was already in its place.

The polarized ion source has been replaced with an intense optically pumped polarized ion source (OPPIS).[13] It can provide high current ($\geq 1\,\mathrm{mA}$) and high polarization ($\geq 80\%$). After the acceleration through linac to 200 MeV, the polarization was typically measured to be $\sim 70\%$ during the commissioning. In the Alternating Gradient Synchrotron (AGS), several depolarization resonances have been overcome and the final polarization was measured to be $\sim 35\%$.

The polarization of the proton beam in RHIC has been measured using a pC CNI polarimeter[14] which was developed last year through experiment E950 at AGS.[15] In the experiment, the single transverse-spin asymmetry $\mathcal{A}_N$ for elastic scattering of proton off carbon was measured as a function of momentum transfer squared t in the Coulomb Nuclear Interference (CNI) region ($10^{-3} \leq -t \leq 10^{-2}\,\mathrm{GeV}^2$). A recoiled Carbon was clearly identified using both time-of-flight and energy detected in the silicon detector. An analyzing power of $\sim 1.5\%$ was found at $-t = 0.01\,\mathrm{GeV}^2$ and it was sufficiently large to be employed for the RHIC polarimeter.[16]

Prior to the installation of the pC CNI polarimeter, the silicon detector has been calibrated in terms of energy at either at the test bench using an α-source or at the Tandem Accelerator Facility using a 10 MeV proton beam. The silicon strips are found to be very uniform in their response.

We have installed four sets of silicon detectors in the RHIC ring at azimuthal angles of 45°, 135°, 225°, and 315°. This configuration enables us to measure the polarization vector in the plane normal to the beam.

The polarized beam was injected to RHIC at $24.3\,\mathrm{GeV}/c$. With the snake off, we have measured vertical polarization. Then, we adiabatically turned on the snake magnet to rotate the spin direction into the horizontal plane while maintaining the polarization. The polarimeter measured horizontal polarization. With an acceleration of $0.7\,\mathrm{GeV}/c$, we expected that the spin direction would be rotated by 180° in the horizontal plane. This expectation has been confirmed using the polarimeter. The polarization was maintained up to $29.1\,\mathrm{GeV}/c$, then lost by further acceleration. Asymmetries are summarized in Fig. 1 as

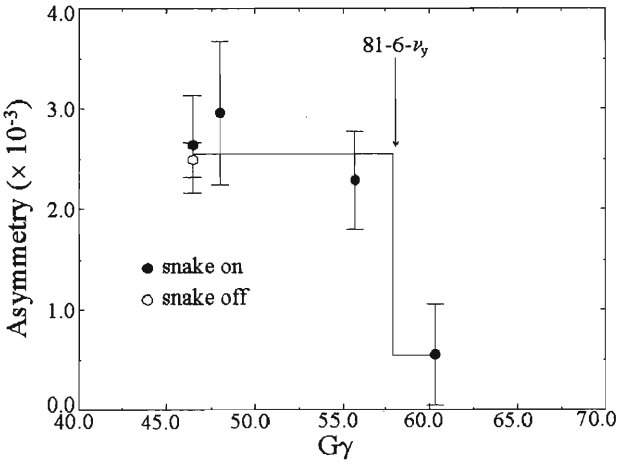

Fig. 1. Asymmetries measured at RIIIC are plotted as a function of $G\gamma$.

a function of $G\gamma$, where G represents the anomalous magnetic moment of the proton. This represents the first storage and acceleration of polarized proton beam at high energy.[14)]

With this success of the polarized proton commissioning, we hope that this project will become very fruitful including future measurements,[17–19)] so that precise information on the spin structure of the nucleon will be obtained by a global analysis.[20)]

References

1) A. Bazilevsky et al.: RIKEN Accel. Prog. Rep. **34**, 232 (2001).
2) H. Torii et al.: RIKEN Accel. Prog. Rep. **34**, 238 (2001).
3) Y. Goto et al.: RIKEN Accel. Prog. Rep. **34**, 248 (2001).
4) T. Ichihara et al.: RIKEN Accel. Prog. Rep. **34**, 252 (2001).
5) Y. Watanabe et al.: RIKEN Accel. Prog. Rep. **34**, 254 (2001).
6) S. Yokkaichi et al.: RIKEN Accel. Prog. Rep. **34**, 256 (2001).
7) N. Hayashi et al.: RIKEN Accel. Prog. Rep. **34**, 258 (2001).
8) J. Murata et al.: RIKEN Accel. Prog. Rep. **34**, 237 (2001).
9) A. Taketani et al.: RIKEN Accel. Prog. Rep. **34**, 230 (2001).
10) Y. Mao et al.: RIKEN Accel. Prog. Rep. **34**, 242 (2001).
11) H. D. Sato et al.: RIKEN Accel. Prog. Rep. **34**, 244 (2001).
12) D. Galanakis et al.: RIKEN Accel. Prog. Rep. **34**, 240 (2001).
13) Y. Mori et al.: Rev. Sci. Instrum. **71**, 1237 (2000).
14) K. Kurita et al.: RIKEN Accel. Prog. Rep. **34**, 229 (2001).
15) I. Alekseev et al.: RIKEN Accel. Prog. Rep. **33**, 170 (2000).
16) J. Tojo et al.: RIKEN Accel. Prog. Rep. **34**, 236 (2001).
17) D. Boer et al.: RIKEN Accel. Prog. Rep. **34**, 249 (2001).
18) A. Deshpande et al.: RIKEN Accel. Prog. Rep. **34**, 251 (2001).
19) J. Murata et al.: RIKEN Accel. Prog. Rep. **34**, 237 (2001).
20) H. Kobayashi et al.: RIKEN Accel. Prog. Rep. **34**, 248 (2001).

The First RHIC Polarimeter Commissioning

K. Kurita, H. Spinka,[*1] D. Underwood,[*1] H. Huang,[*2] W. Glenn,[*2] Z. Li,[*2] W. MacKay,[*2] G. Mahler,[*2] Y. Makdisi,[*2] W. McGahern,[*2] S. Rescia,[*2] T. Roser,[*2] T. Russo,[*2] G. Bunce, G. Igo,[*3] W. Lozowski,[*4] I. Alekseev,[*5] V. Kanavets,[*5] D. Svirida,[*5] H. En'yo,[*6] K. Imai,[*6] J. Tojo,[*6] A. Deshpande, Y. Goto, M. Ishihara, T. Ichihara, N. Saito, A. Taketani, Y. Watanabe, D. Fields,[*7] D. Koehler,[*7] D. Brown,[*8] S. Dhawan,[*9] V. Hughes,[*9] and R. Krisst[*9]

The most critical question for our spin experiments with the Relativistic Heavy Ion Collider (RHIC) is whether it is possible to accelerate polarized protons in RHIC. We finally came to the point of injecting the polarized proton beam into RHIC for the first time in September 2000, after a very long period of hard work.[1–3)]

We will describe in this article our achievements during the two weeks of the polarized proton acceleration commissioning.

It should be noted that we are still in the construction phase and that some necessary equipment was partially instrumented at the commissioning. We had one pC CNI polarimeter to measure the polarization of the beam and a set of helical dipole magnets called a Siberian Snake in a RHIC ring. Two sets of snake magnets are needed to accelerate polarized protons up to the RHIC full energy of 250 GeV, but it was known that one was sufficient to reach 100 GeV if the orbital error is minimal although the stable spin direction becomes horizontal instead of vertical.

Our goals for the commissioning were:

(1) to establish the asymmetry measurement,
(2) to observe the polarization direction change (vertical to horizontal) when the snake is turned on,
(3) to accelerate the polarized proton beams, and
(4) to achieve high polarization at 100 GeV.

The first step was to establish asymmetry measurement with the pC CNI polarimeter by identifying recoil carbons from pC elastic scatterings. The commissioning showed that we can identify pC CNI scattering very clearly, with little background. When the data were combined to measure the vertical polarization, we verified the vertical polarization of the injected beam (Fig. 1 (a)). We reversed the polarization and observed it in reverse (Fig. 1 (b)). We turned off the polarization at the source and observed zero (Fig. 1 (c)). On the basis of these results, we confirmed that the polarimeter was working and we had achieved a polarized beam in RHIC.

We also observed the expected horizontal polarization after we adiabatically turned on the Siberian Snake (in the case of using only one snake, it is necessary to turn it on after injecting the beam) (Fig. 2). We accelerated the beam to cause the polarization to reverse radially and it did, and then we repeated this with the Siberian Snake off and observed no remaining polarization after the same acceleration. This confirmed that we can accelerate polarized protons with the Siberian Snake.

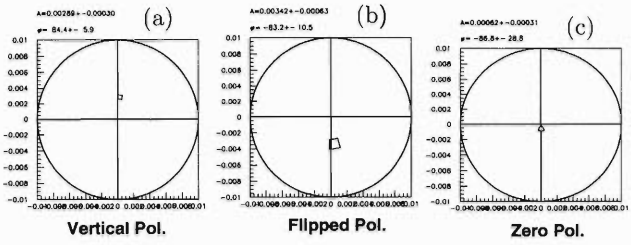

Fig. 1. Polarization vector obtained by the RHIC polarimeter during the establishment of the vertical polarization.

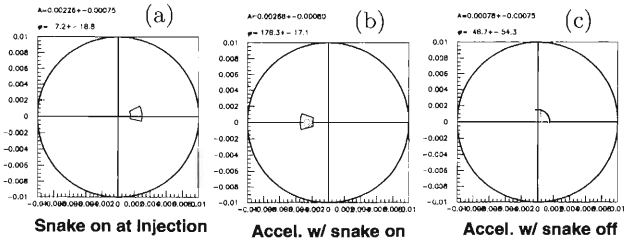

Fig. 2. Study of Snake magnet behavior.

We further accelerated the proton beam up to approximately 32 GeV without appreciable depolarization. However, we were not successful in achieving higher acceleration. We believe that this is due to the large orbit errors which may induce unexpected depolarization resonances. Further study beyond our third goal, including the orbit error correction, will be undertaken during the next RHIC spin run.

This was the first time we observed a polarized proton beam in RHIC and it was a significant milestone for RHIC spin physics. We were greatly encouraged by this commissioning although many challenges still remain.

*1 Argonne National Laboratory, USA
*2 Brookhaven National Laboratory, USA
*3 University of California, Los Angels, USA
*4 Indiana University, USA
*5 Institute of Theoretical and Experimental Physics, Russia
*6 Kyoto University
*7 University of New Mexico, USA
*8 New Mexico State University, USA
*9 Yale University, USA

References

1) J. Tojo et al.: RIKEN Accel. Prog. Rep. **32**, 52 (1999); **34**, 236 (2001).
2) I. Alekseev et al.: RIKEN Accel. Prog. Rep. **33**, 170 (2000).
3) K. Kurita et al.: RIKEN Accel. Prog. Rep. **34**, 234 (2001).

First Commissioning of the PHENIX Muon Identifier by Au-Au Collision

A. Taketani, V. Cianciolo,[*1] H. En'yo,[*2] N. Hayashi, T. Ichihara, K. Imai,[*2] M. Ishihara, L. Kotchenda,[*3] K. Kurita, Y. Mao,[*4] J. Newby,[*5] K. Pope,[*5] K. Read,[*1,*5] N. Saito, H. D. Sato,[*2] and T.-A. Shibata[*6]

The muon identifier (MuID) of the PHENIX experiment was installed in 1998 and has been tested. We integrate MuID detector panels, gas supply, readout electronics, a data acquisition system, high-voltage power supply, online monitoring, and an off-line reconstruction program. The MuID data was collected during the Au-Au colliding beam run in the year 2000 as well as other subsystems of the PHENIX.

The MuID detector is expected to play an important role with the Muon Tracker[1)] (MuTR) in the RHIC spin program[2)] as well as in the heavy-ion program. The MuID can identify muons from other hadron particles by the sandwiching of five absorber steel plates and proportional tubes.[3)] It also functions as a trigger counter and can find course tracks for the more accurate tracking of the muon trajectory at MuTR. The MuID covers 10 to 35 degrees in θ and 360 degrees in ϕ at 7 meters from the interaction point. We segmented a total of 10 gaps. Each gap has four large-sized and two small-sized panels. The detectors are located at the forward and backward regions, the so-called south and north arms, respectively. Each panel has horizontally and vertically oriented tubes. The MuID panels were fabricated[4)] and installed.[5,6)]

At the time of the commissioning, the muon south magnet (MMS) had not yet been installed between the central magnet and the MuID. Therefore, the secondary particles which were generated at the beam pipe were not shielded well. Due to limitations of the available readout electronics, seven small-sized panels at the south arm were prepared for operation. We connected all gas tubing to the gas supply system[7)] and fed pure CO_2 instead of a CO_2 and i-C_6H_{10} mixture. The pure CO_2 has less gas amplification gain and slower drift velocity. However, the beam crossing time of this run is sufficiently long to utilize slower drift velocity and the noise level is suffciently low compared with the signal threshold level, as described later. The flow rate was 3.5 liters per minute, corresponding to one volume exchange per day. In addition, the high-voltage (HV) cables and low-voltage (LV) supply lines were connected between the seven panels and each power supply. A signal cable can handle up to 16 channels of the chamber signal. The small-sized panel has two cables for horizontal orientation and one cable for vertical orientation. Due to the radiation safety issue, all gas tubing and electronics cables of the small-sized panels are located at a place where frequent access is not expected. However, our readout electronics are located at a place which has relatively easy access. Thus, we decided to operate gas, HV, and LV, regardless of the signal cable connection. However, we chose which signal cable(s) was connected to the readout electronics each time.

After establishing the connection, the internal preamps were checked by feeding the test pulser signal. It was amplified by the preamp and checked at the signal cable end using an oscilloscope. All preamps of the seven panels were operational.

After five volume gas exchanges, we started to apply a HV up to 4.2 kV. A HV monitoring program and an automatic voltage control program were developed. The monitoring program displays each HV operation status every 30 seconds. Forty-eight channels of HV can be checked at a glance. The control program monitors the current during ramping. Voltage is increased when the associated current does not exceed the specified threshold, which is typically 6 μA at 4 kV. It takes 15 min to reach a 4.2 kV operational voltage.

During the applying 4.2 kV, the noise level of each signal was measured as 40 mV on average, as expected.

During the first week of MuID operation with a 65 GeV/A Au-Au collision beam, one signal cable was connected to the readout electronics. The signal channels which are at the first gap, horizontal, and closest to the beam were chosen as the highest rate channels for timing tuning purposes. The coincidence of forward-backward beam-beam counters were used for triggers. Figure 1 shows the hit occupancy rate per channel per event. The solid line and plus markers represent the measured value and simulated data, respectively. The simulated data includes HIJING event generation and the detailed detector simulation. The measured and simulated values are matched. We expect that the hit occupancy rate will be reduced to less than 0.1 when the MMS and beam collar are installed. The beam collar will shield the bare beam pipe between the MMS and the MuID and reduce the exposure of secondary particles.

During the last two weeks of the gold-gold collision run, six signal cables were connected to the readout electronics. Horizontal and vertical cables were cho-

*1 Oak Ridge National Laboratory, USA
*2 Kyoto University
*3 State Interphysica, Russia
*4 Chinese Institute for Atomic Energy, China
*5 University of Tennessee, USA
*6 Tokyo Institute of Technology

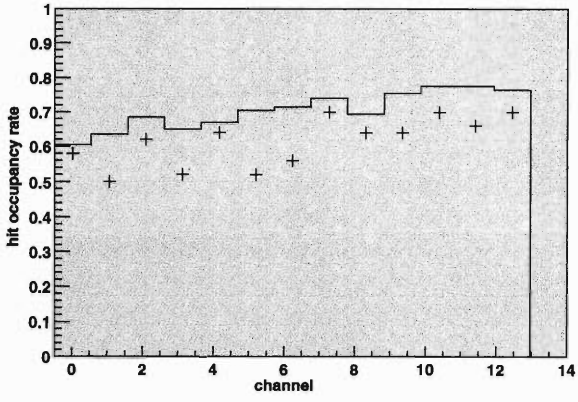

Fig. 1. Hit occupancy rate.

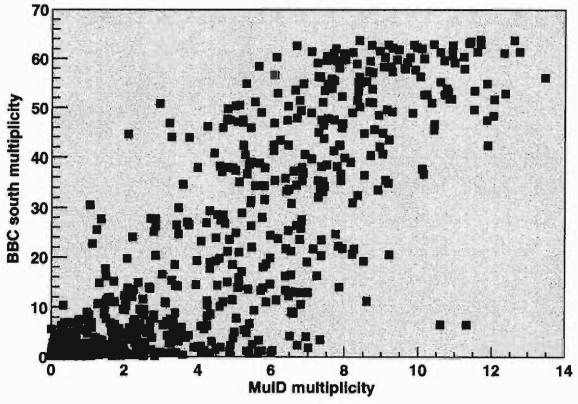

Fig. 2. Multiplicity coincidence.

sen from the second, third, and fifth gaps. Each horizontal and vertical readout channel is lined since it is a requirement for course road finding in the reconstruction program. Mao *et al.* reported details of the reconstruction.[8] We confirmed the reconstructed road in the event display. The 550 k events are recorded into the tape as part of the PHENIX main data stream. Figure 2 shows the coincidence between the MuID hit multiplicity and the beam-beam counter (BBC) hit multiplicity. It has a clear positive correlation, as expected, since the beam-beam counter covers $3 \leq |\eta| \leq 4$ and the MuID covers $1.1 \leq |\eta| \leq 2.4$.

The integration and operation of the partial MuID system was carried out and the commissioning was successfully finished with the Au-Au collision run. We will continue to prepare for the upcoming polarized proton run in 2001.

References

1) J. Murata et al.: RIKEN Accel. Prog. Rep. **33**, 165 (2000).
2) H. En'yo et al.: RIKEN Accel. Prog. Rep. **30**, 34 (1997).
3) Y. Mao et al.: RIKEN Accel. Prog. Rep. **30**, 36 (1997).
4) A. Taketani et al.: RIKEN Accel. Prog. Rep. **31**, 172 (1998).
5) A. Taketani et al.: RIKEN Accel. Prog. Rep. **32**, 50 (1999).
6) K. Kurita et al.: RIKEN Accel. Prog. Rep. **32**, 32 (1999).
7) A. Taketani et al.: RIKEN Accel. Prog. Rep. **33**, 33 (2000).
8) Y. Mao et al.: RIKEN Accel. Prog. Rep. **34**, 242 (2001).

PHENIX EMCal: First Results from RHIC Au-Au Collisions

A. Bazilevsky, G. David,[*1] H. En'yo,[*2] Y. Goto, K. Imai,[*2] E. Kistenev,[*1] N. Saito, and H. Torii[*2]
for the PHENIX Collaboration

PHENIX[1] is one of the two large experiments at the BNL relativistic heavy-ion collider (RHIC). The PHENIX detector is suitable for broad research programs in both heavy-ion and polarized proton collisions. From June 2000, RHIC produced collisions of gold ions at beam energies up to 65 GeV per nucleon. Luminosities of about $5 \times 10^{25}\,\mathrm{cm}^{-2}\mathrm{sec}^{-1}$ were achieved.

The electromagnetic calorimeter (EMCal) of PHENIX showed excellent performance during the 2000 run. Preliminary physics results include transverse energy measurements, and inclusive-photon and π^0 spectra reconstruction. Below we present these results.

Transverse energy is one of the key observables in quark-gluon plasma (QGP) search and study. According to Bjorken,[2] the transverse energy rapidity density dE_T/dy is directly related to the spatial energy density ϵ in a relativistic collision. Many simulation studies based on the HIJING 1.33 event generator[3] and GEANT[4] detector response were performed to determine the relationship between the measured and "true" E_T distribution. The obtained E_T distribution at mid-rapidity is shown in Fig. 1. Two percent of the most central Au-Au collisions gives a mean E_T value of about 550 GeV $\pm$ 10% (*syst*) in a pseudorapidity unit (statistical error is negligible), which is about 40% higher than that obtained in the SPS-NA49 fixed-target experiment for Pb+Pb collisions.[5]

One of the proposed signatures of the QGP is the enhancement of photon radiation. Compton scattering of the gluons enhances the yield of photons at $p_t > 2\,\mathrm{GeV}/c$. Thermal radiation from the hot QGP gas enhances it at lower p_t ($< 2\,\mathrm{GeV}/c$). The dominant source of background for direct photons is π^0 decays; therefore, π^0 measurements are very important for direct photon reconstruction. Reconstruction of π^0 is also important for studying the jet quenching effect, and isospin correlations and fluctuations. The π^0 peak can be clearly identified in the two-cluster invariant mass distribution.[6] After applying the back-

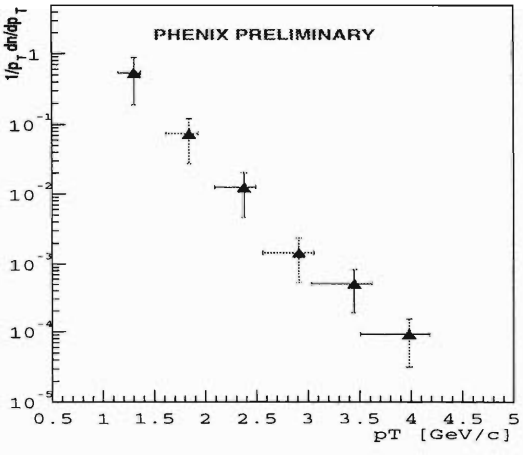

Fig. 2. π^0 p_t spectrum.

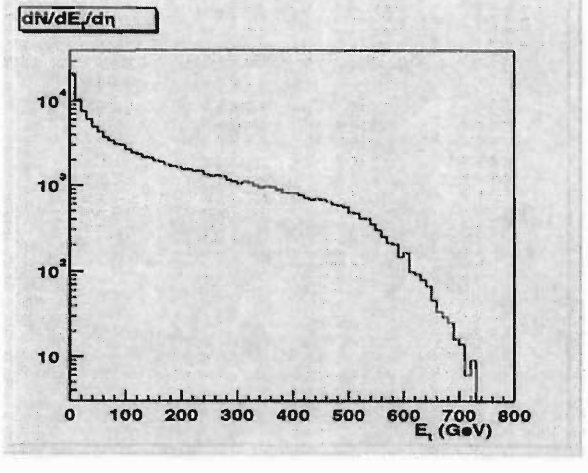

Fig. 1. E_t distribution in Au-Au collisions at $\sqrt{s}$ = 130 GeV/A.

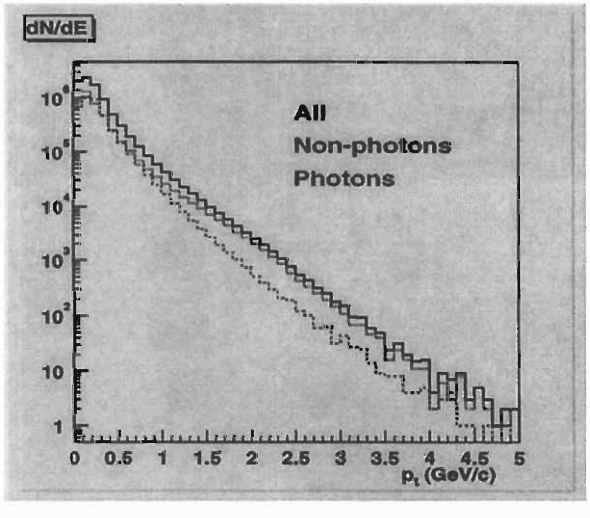

Fig. 3. Inclusive-photon p_t spectrum; solid: all EMCal clusters, dotted: clusters suppressed by EMCal time of flight or shower profile cuts for photons, dashed: clusters surviving EMCal time of flight and shower profile cuts for photons.

*1 Brookhaven National Laboratory, USA
*2 Kyoto University

ground subtraction technique, and acceptance and efficiency corrections,[7] the π^0 p_t spectrum was obtained (Fig. 2). The slope parameter of the exponential fit was estimated to be 303 ± 11 $(stat) \pm 67$ $(syst)$ MeV/c, which is higher than that obtained in the SPS-WA98 experiment for central Pb+Pb collisions:[8] 200 MeV/c for low p_t ($\approx$ 1 GeV/c) and 270 MeV/c for higher p_t ($\approx$ 3 GeV/c). Figure 3 shows the reconstructed inclusive-photon spectrum in EMCal. To identify photons in EMCal, we applied time-of-flight and shower profile cuts. This helps reduce the non-photon background by a factor of 2 to 20 depending on the energy region. The residual contamination varies from 30% for $p_t = 0.7$ GeV/c to $< 15\%$ for $p_t > 2.5$ GeV/c (simulation study). The efficiency of photon reconstruction after these cuts was about 90%.

References

1) D. P. Morrison: Nucl. Phys. A **638**, 565c (1998).
2) J. D. Bjorken: Phys. Rev. D **27**, 140 (1983).
3) X. N. Wang and M. Gyulassy: Phys. Rev. D **44**, 3501 (1991).
4) GEANT 3.2.1, CERN Program Library (1993).
5) T. Alber et al.: Phys. Rev. Lett. **75**, 3814 (1995).
6) H. Torii et al.: RIKEN Accel. Prog. Rep. **34**, 238 (2001).
7) T. Sakaguchi et al.: RIKEN Accel. Prog. Rep. **34**, 261 (2001).
8) M. M. Aggarwal et al.: nucl-ex/0006007; Phys. Rev. C, to be published.

RHIC pC CNI Polarimeter

K. Kurita, H. Spinka,[*1] D. Underwood,[*1] H. Huang,[*2] W. Glenn,[*2] Z. Li,[*2] W. MacKay,[*2] G. Mahler,[*2] Y. Makdisi,[*2] W. McGahern,[*2] S. Rescia,[*2] T. Roser,[*2] T. Russo,[*2] G. Bunce, G. Igo,[*3] W. Lozowski,[*4] I. Alekseev,[*5] V. Kanavets,[*5] D. Svirida,[*5] H. En'yo,[*6] K. Imai,[*6] J. Tojo,[*6] A. Deshpande, Y. Goto, M. Ishihara, T. Ichihara, N. Saito, A. Taketani, Y. Watanabe, D. Fields,[*7] D. Koehler,[*7] D. Brown,[*8] S. Dhawan,[*9] V. Hughes,[*9] and R. Krisst[*9]

A number of possible methods of measuring the polarization at RHIC were considered. The problem is that the process used for low-energy protons, pp elastic scattering at $-t = 0.15$ (GeV/c)^2, appears to have diminishing analyzing power of 1/energy. Therefore, its analyzing power is significantly small for polarimetry at RHIC energies. One new attractive approach uses the asymmetry of inclusive pion production at large x_F and moderate p_T. Such a polarimeter was designed, but was abandoned due to its high cost (roughly \$1.5 million).

To use pC elastic scattering in the Coulomb nuclear interference (CNI) region was a novel suggestion. CNI involves scattering from the anomalous magnetic moment of the polarized proton, an electromagnetic spin-flip amplitude, and a nonflip hadronic amplitude. This method is attractive because

(1) a significant (4%) analyzing power is predicted over the entire RHIC range,[1)]
(2) the figure of merit is high due to its large cross section,
(3) a very thin solid carbon target allows us easy target handling and quick measurements in RHIC, and
(4) it allows inexpensive setup when only the recoil carbons are detected by Si detectors in vacuum.

In the course of the development of the RHIC pC CNI polarimeter, AGS-E950 was performed to measure the analyzing power of pC CNI reaction at the RHIC injection energy.[2,3)] It was found that statistically significant polarization measurements can be performed with pC CNI. According to our experience from performing AGS-E950, the RHIC pC CNI polarimeter was designed to enable the use of the same principle. However, the following RHIC specific issues were considered and new improvements were reflected in the design.

(1) Smooth impedance change is required inside the polarimeter chamber so as not to disturb the beam.
(2) At RHIC full luminosity with 250 GeV beam, the temperature of the target may become significantly high.
(3) Computer simulation of spin orientation dynamics implies that protons far away from the center of the beam might be depolarized.
(4) RHIC requires ultrahigh vacuum in the range of 10^{-9}–10^{-10} Torr and electronics are not allowed in the vacuum.
(5) Up to 250°C baking is required.
(6) To minimize the noise, the distance between the Si detector and the preamplifier has to be small.
(7) A significantly high data-taking rate is required.

Figure 1 shows the RHIC polarimeter installed in one of the RHIC rings (the blue ring). As evident in the photograph, the entrance and exit of the chamber have conical shapes to reduce impedance gap. Resonance peaks in the electromagnetic wave frequency space in the chamber were measured and were found to be sufficiently weak.

The very thin target was made available through development at IUCF. Its thickness, only $\tilde{1}00$ atoms, allows the slow carbon ($\tilde{1}00$ KeV) to escape, thus reducing the scattering rate to a level which can be tolerated by detectors; the target survives beam heating due to its large surface-to-volume ratio. To determine the radial polarization distribution, two target position remote control systems were designed to allow horizontal and vertical scans of the beam. Four Si detectors were placed at 45-degree positions so that none of the detectors fall in the shadow of the target frames. A schematic view of the Si detector arrangement is shown in Fig. 2. In addition to the four Si detector ports, two Si ports were installed in a 90-degree location to allow a better asymmetry measurement for the vertically polarized proton beam because 45-degree detectors can detect only $1/\sqrt{2}$ of the analyzing power of the pC CNI process.

Fig. 1. RHIC pC CNI polarimeter installed in RHIC.

*1 Argonne National Laboratory, USA
*2 Brookhaven National Laboratory, USA
*3 University of California, Los Angels, USA
*4 Indiana University, USA
*5 Institute of Theoretical and Experimental Physics, Russia
*6 Kyoto University
*7 University of New Mexico, USA
*8 New Mexico State University, USA
*9 Yale University, USA

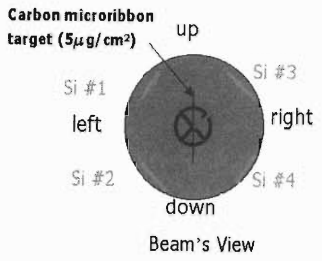

Fig. 2. Schematic diagram of RHIC pC CNI polarimeter as viewed by the beam.

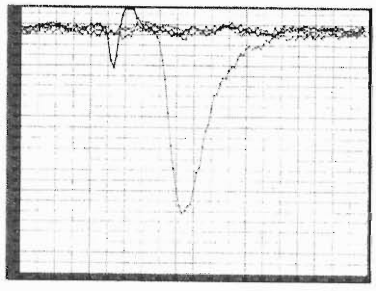

Fig. 3. Typical recoil carbon signal from Si detector recorded by our prototype WFD.

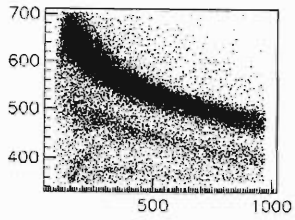

Fig. 4. Arrival time versus pulse height of events in a Si strip.

Only metals and ceramics are allowed to be used in ultrahigh vacuum on the order of 10^{-9}–10^{-10} Torr. Also, the baking requirement excludes the possibility of installing preamplifiers in the vacuum. However, Si detectors have to be in the vacuum to measure very-low-energy recoil carbons because these carbons lose energy very rapidly in any material. It is a well-known fact that the distance between the detector and the preamplifiers has to be minimized. Therefore, we designed a Si-mounting plate, which is made of ceramics and preamlifier cards, which can be mounted directly on the atmospheric pressure side of the feedthrough. With this design, we can remove preamplifier cards without breaking the good vacuuum. Then, the baking can be performed very efficiently.

A potential disadvantage of using very thin carbon target is that the number of carbon atoms can actually become depleted, so that it is important to use the scattering time efficiently. However, this also works out well for an expected lifetime of two to three hours of the beam, and for measurements taking less than ten seconds when the RHIC reaches the full-design luminosity. It is also important to use the scattering time efficiently to measure the polarization many times during proton injection into RHIC without significantly increasing the beam emittance (and decreasing the collision luminosity).

Although currently our main data aquisition (DAQ) system is based on CAMAC FERA modules which limit our data-taking rate, we have developed a prototype wave form digitizer (WFD) which can in principle be made to work without a dead time. This prototype was tested in the RHIC spin-commissioning period in September 2000[4] and was found to work successfully in the RHIC environment. Figure 3 shows a typical recoil carbon signal from the Si detector. A rapid data readout scheme is to be developed next year. WFD also works efficiently in reducing the systematic errors by distinguishing overlapping events from nonoverlapping events.

When we performed RHIC spin-commissioning, we injected only six bunches instead of 120 to allow our DAQ system to work without significant dead time.

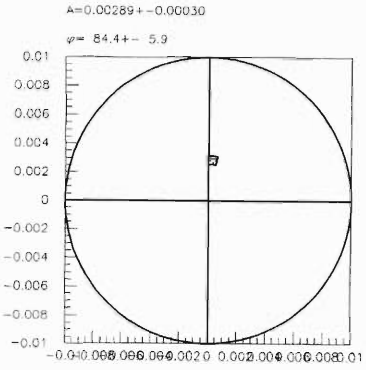

Fig. 5. The first polarization vector measurement (10 sigma effect) with the RHIC pC CNI polarimeter.

The polarization direction was alternated so that we can obtain asymmetry with significantly less systematic errors, which mainly come from the detector acceptance and bunch-by-bunch luminosity variations. Since the Si detectors are located 15 cm from the target, the carbon atoms of interest arrive 60–80 nanoseconds after a bunch passes the target. The signal is observed after prompt products are gone, and before the arrival of the next bunch. (At full luminosity, RHIC bunch spacing is 106 nanosecconds.) The carbon band, along with the alpha band, was clearly observed in the arrival time versus pulse height scatter plot shown in Fig. 4. After the carbons were identified in the carbon band, the asymmetry in the horizontal and vertical directions was calculated. Figure 5 shows the first significant polarization vector measured while we were trying to establish the polarization measurement in RHIC.

References

1) T. D. Lee: Proc. Workshop on Hadron Spin-Flip at RHIC Energies, RIKEN BNL Research Center, 1997-July-Aug., Vol.3 (1997).
2) J. Tojo et al.: RIKEN Accel. Prog. Rep. **32**, 52 (1999); **34**, 236 (2001).
3) I. Alekseev et al.: RIKEN Accel. Prog. Rep. **33**, 170 (2000).
4) K. Kurita et al.: RIKEN Accel. Prog. Rep. **34**, 229 (2001).

Measurement of the Analyzing Power for Proton-Carbon Elastic Scattering in the Coulomb-Nuclear Interference Region at 22 GeV/c

J. Tojo,[*1] I. Alekseev,[*2] M. Bai,[*3] B. Bassalleck,[*4] G. Bunce, A. Deshpande, J. Doskow,[*5] S. Eilerts,[*4] D. E. Fields,[*4] Y. Goto, H. Huang,[*3] V. Hughes,[*6] K. Imai,[*1] M. Ishihara, V. P. Kanavets,[*2] K. Kurita, K. Kwiatkowski,[*5] B. Lewis,[*4] W. Lozowski,[*5] Y. Makdisi,[*3] H. O. Meyer,[*5] B. V. Morozov,[*2] M. Nakamura,[*1] B. V. Przewoski,[*5] T. Rinkel,[*5] T. Roser,[*3] A. Rusek,[*3] N. Saito, B. Smith,[*4] D. N. Svirida,[*2] M. Syphers,[*3] A. Taketani, T. L. Thomas,[*4] D. Underwood,[*7] D. Wolfe,[*4] K. Yamamoto,[*1] and L. Zhu[*1]

Measurement of the analyzing power for proton-carbon (pC) elastic scattering in the Coulomb-nuclear interference (CNI) region provides a unique opportunity to study spin dependence of hadronic interaction and an application to high-energy proton polarimetry at BNL-RHIC as the first polarized proton collider.[1–3] The analyzing power $A_N(t)$ originating from interference between electromagnetic (EM) spin-flip interaction and hadronic spin-nonflip interaction is theoretically predicted,[4–6] ranging from 1–4% in the small momentum transfer region of $10^{-3} < -t < 10^{-2}\,(\mathrm{GeV}/c)^2$.

Experiment E950 involving the first measurement of the $A_N(t)$ was carried out at BNL-AGS in March 1999. The pC elastic scattering from a 21.7 GeV/c polarized proton beam and an ultrathin carbon target was identified by detecting only recoil carbons emitted almost 90° to the beam direction, which had a very low energy ranging from 100 keV to a few MeV. The experimental setup to measure the energy and the time of flight (TOF) of recoil carbons consisted of two left-right detector arms of silicon strip detectors (SSDs) and microchannel plate assemblies (MCP) with thin carbon foils. The details of the experimental setup and the performance are described in detail in Refs. 1 and 2. In this article, we report the preliminary results of the analyzing power measurement.

Recoil carbon events were selected by making use of kinematic relation between energy and TOF. Physics backgrounds of 4.4 MeV C* excitation and Δ production were not kinematically allowed to come into the detector acceptance. Other backgrounds were estimated to be less than 3% from target-empty data. Momentum transfer squared $-t$ was determined kinematically from both energy and TOF. Energy loss of recoil carbons at the carbon target, the thin carbon foil and the dead layer of the SSDs were estimated and corrected to determine $-t$. The $A_N(t)$ was derived using

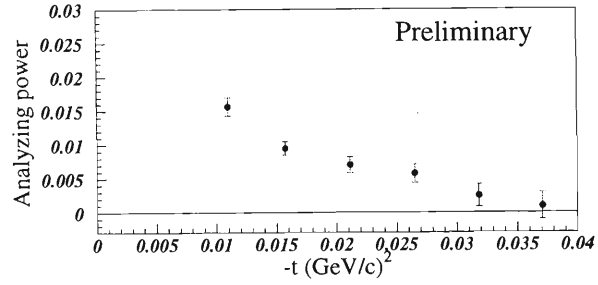

Fig. 1. Preliminary results of the analyzing power A_N as a function of momentum transfer $-t$. The error bars indicate statistical errors only.

a square root formula:

$$A_N(t) = \frac{1}{P_B} \frac{\sqrt{N_L^{\uparrow}(t) \cdot N_R^{\downarrow}(t)} - \sqrt{N_L^{\downarrow}(t) \cdot N_R^{\uparrow}(t)}}{\sqrt{N_L^{\uparrow}(t) \cdot N_R^{\downarrow}(t)} + \sqrt{N_L^{\downarrow}(t) \cdot N_R^{\uparrow}(t)}}. \quad (1)$$

$N_L^{\uparrow}(t)$ ($N_R^{\downarrow}(t)$) represents the number of recoil carbon events at $-t$, which were detected in the right (left) detector arm with beam polarization up (down). P_B represents the beam polarization. It was measured independently and found to be approximately 40%. The preliminary results of $A_N(t)$ are shown in Fig. 1. Error bars indicate statistical errors only. Systematic errors are still under study.

In summary, we succeeded in measuring the analyzing power for pC elastic scattering in the CNI region with high statistical accuracy. The preliminary results were presented. Our data will be compared with a theory including the contribution of hadronic spin-flip amplitude. Hadronic spin-flip amplitude will be constrained from the further analysis.

*1 Department of Physics, Kyoto University
*2 Institute of Theoretical and Experimental Physics, Russia
*3 Brookhaven National Laboratory, USA
*4 Department of Physics and Astronomy, University of New Mexico, USA
*5 Indiana University Cyclotron Facility, USA
*6 Department of Physics, Yale University, USA
*7 Argonne National Laboratory, USA

References

1) J. Tojo et al.: RIKEN Accel. Prog. Rep. **32**, 52 (1999).
2) I. Alekseev et al.: RIKEN Accel. Prog. Rep. **33**, 170 (2000).
3) K. Kurita et al.: RIKEN Accel. Prog. Rep. **34**, 234 (2001).
4) T. D. Lee: Proc. Workshop on Hadron Spin-Flip at RHIC Energies, Vol. 3, 1997-July-Aug., (RIKEN BNL Research Center 1997).
5) B. Z. Kopeliovich: hep-ph/9801414.
6) N. H. Buttimore: AIP Conf. Proc., **95**, p.634 (1983).

Construction of PHENIX South Muon Tracker

J. Murata, M. L. Brooks,[*1] D. S. Brown,[*2] N. Bruner,[*3] D. Fields,[*3] H. Kobayashi, D. M. Lee,[*1] S. Pate,[*2] N. Saito, T.-A. Shibata,[*4] W. Sondheim,[*1] R. Towell,[*1], M. Sugioka,[*4] and C. Velissaris[*2]

Mechanical installation of the PHENIX south muon tracker (MuTr) is now close to completion. The south muon arm was installed in the PHENIX experimental hall by the end of 2000, after completion of the front-end electronics (FEE) installation. In July 2000, all cathode strip chambers, each consisting of three stations (#1, 2, 3) which were mainly constructed by the BNL, LANL and UNM staff, were installed into the south muon magnet. The RIKEN team was responsible for the chamber gas supply system and the optical alignment system, which were constructed and installed.[1] Before the chamber installation, the RIKEN team also performed a resolution measurement of a test chamber using a prototype FEE at LANL in 1999, obtaining $\sigma = 165\,\mu$m which was determined by a simple center-of-gravity method. By using the actual PHENIX FEE with the actual #2 chamber, we obtained a sufficient resolution of $100\,\mu$m by a charge-ratio method in the summer of 2000. The main reason for the improvement is the difference in the position determination method.

Although we have confirmed the sufficient quality of the chamber and the FEE, an optical alignment system is required which monitors accurate chamber geometries in order to obtain the required momentum resolution in the actual PHENIX system. This system consists of a (62.5/125)-μm-diameter fiber optics cable at #1, a 1-cm-diameter convex lens at #2, and a CCD camera with a 8.8×6.6 mm (768×493 pixels) effective region at #3. There are 56 such optic beams monitoring the relative X-Y positions between the three stations. Because the mechanical precision required for each optics component must be within $25\,\mu$m, the lens and optics fiber are aligned to the center of mounting blocks with accuracy of $10\,\mu$m by means of a special optical system. The position offsets of the CCD cameras from the centers of the mounting blocks were measured after tuning the camera position in order to obtain the focal image in the actual system. All optics components were installed inside the muon magnet by the end of 2000.

A data acquisition system for CCD image capturing has also been constructed. The 56 camera signals are fed into a video-signal switching box (Keithley 7001+7011S),[2] which has one output port connected to a frame-grabbing card (Scion Corp., Pr-LG3)[3] on an image-capturing PC. The digital I/O ports of the Pr-LG3 control the switching of the 56 channels. We can control image capturing and also external I/O using the single software, Scion Image for Windows.[3] This simplicity has huge advantage in terms of the stability of such digital systems which undergo frequent interruption. The same macroscript also calculates the center position of the focal image and stores this in an output file which is connected to the database.

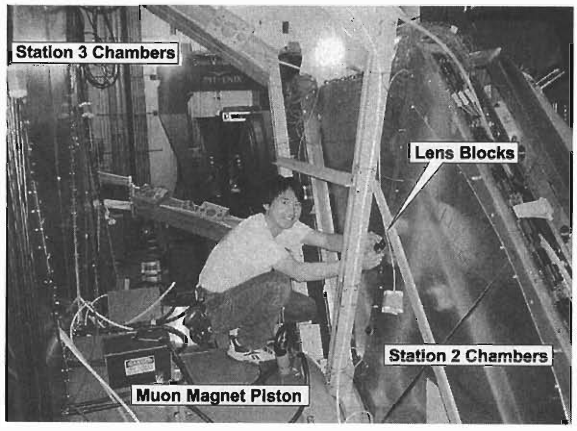

Fig. 1. Installing lens blocks on #2 chambers. The upper half of the PHENIX south muon magnet is shown.

We have also constructed the chamber gas supply system.[4] The requirements of the gas system are: (1) usage of $50\%Ar+30\%CO_2+20\%CF_4$ mixed gas, which was selected mainly for its non-flammability and relatively small Lorentz angle; (2) full recirculation in order to conserve the expensive CF_4 gas; and (3) stable pressure control that protects the thin #2 chamber windows. In order to satisfy these requirements, we have designed and built a gas system which consists of the main control rack, a compressor panel and a distribution panel. The construction of each system is almost completed. Following a system check and construction of the electric read-out system, the alarm system is now under construction.

In addition to these works, the RIKEN team is also going to contribute to the MuTr software and FEE development. The construction of MuTr chambers for the PHENIX north muon arm has just started, and it is expected to be completed in 2001.

*1 Los Alamos National Laboratory, USA
*2 New Mexico State University, USA
*3 University of New Mexico, USA
*4 Tokyo Institute of Technology

References

1) J. Murata et al.: RIKEN Accel. Prog. Rep. **33**, 165 (2000).
2) Keithley Instruments, Inc.: http://www.keithley.com
3) Scion Corporation: http://www.scioncorp.com
4) PHENIX MuTr Gas System Home Page: http://spin.riken.bnl.gov/~jiro/mutrgas.html

Performance of the PHENIX EMCal in First Physics Run

H. Torii,[*1] A. Bazilevsky, G. David,[*2] H. En'yo,[*1] Y. Goto, K. Imai,[*1]
E. Kistenev,[*2] and N. Saito, for the PHENIX Collaboration

In the early summer of 2000, the PHENIX experiment for heavy-ion physics at RHIC has started, and we will start that for spin physics in 2001. In this experiment, the electromagnetic calorimeter (EMCal) plays an important role in detecting photons and electrons/positrons. In order to cover topics in both physics, *e.g.*, thermal photon measurement in heavy-ion physics, and prompt photon, π^0 and weak boson measurement in spin physics, the EMCal needs to cover a wide energy range from a few hundred MeV to 80 GeV. Spin physics also requires the energy measurement to be within 2% accuracy to measure cross sections of prompt photons and π^0 production with 10% errors, because the cross sections have steep transverse momentum (p_T) slopes. The PHENIX EMCal consists of a lead scintillator (PbSc) and lead glass (PbGl). In this paper, we will report only the performance of the PbSc.

To fulfill the physics requirement, several beam tests at BNL/AGS and CERN/SPS[1,2] were performed. From the beam tests, the energy resolution for PbSc is known as $\sigma_E/E = 1.9\% \oplus 8.2\%/\sqrt{E}$ from 0.5 GeV/c to 80 GeV/c, where $\oplus$ represents the quadratic sum. We obtained the energy measurement with 2% accuracy from 0.5 GeV to 80 GeV. This result is consistent with the expected results based on the uncertainty of beam momentum, nonlinearity of photon multiplier tube,[3] readout electronics, and shower leakage effect. At 10 GeV, the result shows 4% deviation, which will be corrected in the future.

Before the physics experiment of 2000, the energy scale for all towers was calibrated using a cosmic muon traversing PbSc module, whose energy deposit is 38 MeV in average. Figure 1 shows the energy distribution using the PHENIX clustering algorithm at $\sqrt{s} = 130\,A$ GeV Au+Au collision. We observed clearly the minimum ionization peak (MIP) by charged hadron. The MIP energy was adjusted in each of the 144 towers of PbSc. After this adjustment, a 2% deviation was observed in a relative energy scale. The time dependence measured by the MIP energy was also corrected.

Figure 2 shows the two-photon invariant-mass spectrum with a π^0 peak after MIP correction. The peak exhibits a nominal π^0 mass within the 2% statistical error. We can conclude that the absolute energy scale has 2% accuracy.

Table 1 shows the summary of performance. It appears to fulfill the physics requirement of 2% accuracy.

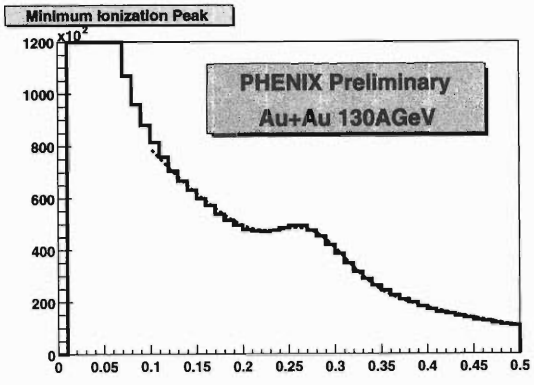

Fig. 1. Preliminary energy distribution by PHENIX Au+Au collision at $\sqrt{s} = 130\,A$ GeV.

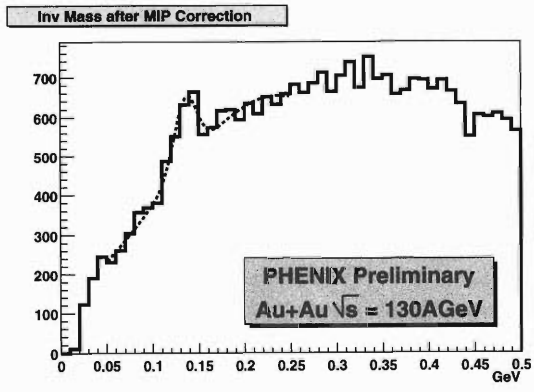

Fig. 2. Preliminary two photon invariant mass distribution in PHENIX Au+Au collision at $\sqrt{s} = 130\,A$ GeV.

Table 1. Summary of the performance of PHENIX EMCal.

Energy scale	
Time dependence	0.4% (after 7% correction)
Relative	2% (after < 6% correction)
Absolute	2%

However, these performance tests are dominated by energy clusters with less than 1 GeV because of the 280 MeV MIP energy and the steep p_T spectrum of π^0. We plan to increase the statistics in the future, and determine the performance up to more than 10 GeV to satisfy the physics requirement. The physics analysis is in progress and results[4] will soon be available.

References

1) Y. Goto et al.: RIKEN Accel. Prog. Rep. **32**, 47 (1999).
2) H. Torii et al.: RIKEN Accel. Prog. Rep. **33**, 168 (2000).

*1 Kyoto University
*2 Brookhaven National Laboratory, USA

3) G. David et al.: IEEE Trans. Nucl. Sci. **42**, 306 (1995).
4) A. Bazilevsky et al.: RIKEN Accel. Prog. Rep. **34**, 232 (2001).

Development of a Level-1 Trigger for the PHENIX Central Detector Arms

D. Galanakis,[*1] Y. Akiba,[*2] K. Shigaki,[*2] H. Sato,[*3] J. Tojo,[*3] V. Cianciolo,[*4] P. Stankus,[*4] A. Wintenberg,[*4] G. Young,[*4] B. Lillie,[*5] G. Bunce, Y. Goto, M. Grosse Perdekamp, N. Hayashi, M. Ishihara, N. Saito, H. Hamagaki,[*6] T. Matsumoto,[*6] K. Oyama,[*6] K. Barish,[*7] M. Bick,[*7] B. Nandi,[*7] W. Xie,[*7] and M. Tamai[*8]

The PHENIX detector is a large multipurpose detector at the Relativistic Heavy-Ion Collider at Brookhaven National Laboratory.[1)] It consists of two spectrometers for muon detection $1.2 < \eta < 2.4$ and two central detector arms $|\eta| < 0.35$ for high resolution detection of electrons, photons and soft hadrons. The design of the PHENIX apparatus was initially optimized for the needs of heavy-ion physics. However, the detector is also being adapted to perform well in an environment of high-luminosity proton-proton collisions. This upgrade is required for the physics program with polarized protons including measurements of the gluon-, quark- and antiquark-polarizations inside the proton.

In this paper, we discuss event selection electronics, the so-called level-1 trigger, which will efficiently select events during high-luminosity proton-proton running. The trigger also has significant applications in heavy-ion physics and will be used, for example, for the selection of J/Ψ events in peripheral Au-Au and light-ion collisions at increased luminosity.[2)] In heavy-ion physics, the total cross section corresponds to a raw event rate of 14 kHz. This is well matched to the 12 kHz bandwidth of the PHENIX data acquisition. In contrast, the maximum raw event rate from spin running will be 12 MHz. Therefore, no spin physics program is possible in PHENIX without a substantial upgrade of the level-1 trigger. The upgraded trigger should efficiently select ($> 80\%$) the interesting physics events and substantially reduce background events. The trigger requirements are further complicated by the necessity to be sensitive in parallel for several physics channels, which have small cross sections (*e.g.*, heavy quark production, W production and Drell-Yan), and the need to be taken in parallel with high event selection efficiency in each single channel. In order to match the different physics channels with the available data acquisition bandwidth, a reduction factor of 5000–10000 is needed in each channel.

We have designed and studied a level-1 trigger for the central detector arms which performs the required event selection and data reduction. The trigger is based on the combined information from the electromagnetic calorimeter (EMC) and the ring imaging Cherenkov counter (RICH); the trigger's principle is presented graphically in Fig. 1. Fast programmable logic combines and processes information from four independent EMC thresholds and the RICH. Detailed studies have confirmed that the trigger efficiently selects electrons, photons and jets of hadrons.[2,3)] Table 1 summarizes a specific trigger scheme in which the RICH threshold is set to the equivalent of three photoelectrons and the four EMC thresholds are set at $E = 0.7, 4.0, 5.0$ and 10.0 GeV. The settings are chosen to simultaneously trigger on single electrons and di-leptons (both as tags for heavy quarks) as well as highly energetic photons (direct photon production) and electrons (W production). The trigger scheme pre-

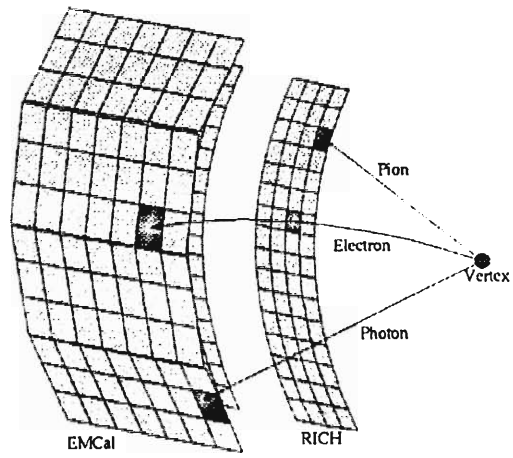

Fig. 1. The PHENIX level-1 trigger for the central detector arms uses coincidences between the EMC and the RICH in order to identify electrons and photons.

Table 1. Possible trigger scheme in the PHENIX central arms. For electrons, the RICH threshold has been set to three or more photoelectrons.

Channel	EMC Thr.	Rej. Fac.	Rate
single e	700 MeV	3000	4 kHz
e-μ	700 MeV	>250000	<0.05 kHz
γ	5 GeV	>40000	<0.3 kHz
e (W)	10 GeV	>40000	<0.3 kHz
Bias	4 GeV	>40000	<0.3 kHz

*1 On leave from Aristoteles University, Greece
*2 High Energy Accelerator Research Organization (KEK)
*3 Kyoto University
*4 Oak Ridge National Laboratory, USA
*5 On leave from Reed College, USA
*6 University of Tokyo
*7 University of California at Riverside, USA
*8 Waseda University

sented in Table 1 reduces the event rates in the central arm to about half the PHENIX data acquisition bandwidth without necessitating a reduction of the event rate prior to the event selection process. Both RICH and EMC are required in order to achieve sufficient raw event rejection.

References

1) D. P. Morrison et al.: Nucl. Phys. A **638**, 565 (1998); N. Saito et al.: Nucl. Phys. A **638**, 575 (1998).
2) T. Matsumoto: Talk at 55th Ann. Meet. of Physical Society of Japan, Niigata, (2000).
3) W. Xie, B. Lillie, and D. Galanakis: Talks and Posters at Division of Nuclear Physics of APS Meet., Williamsburg, (2000).

Event Reconstruction in the PHENIX Muon Identifier

Y. Mao, V. Cianciolo,[*1] A. Glenn,[*2] K. Kurita, J. Murata, J. Newby,[*2] K. Pope,[*2] K. Read,[*2] N. Saito, H. D. Sato,[*3] S. Sorensen,[*2], and A. Taketani

The PHENIX muon detector comprises two arms, each of them includes a muon tracker, consisting of three tracking stations, and a muon identifier, consisting of five gaps instrumented with 8.4 cm-wide Iarocci tubes in horizontal and vertical orientations and interleaved with four layers of steel.[1)]

Essentially, there are two goals for event reconstruction using the PHENIX muon identifier (MuID): (1) to find roads which will be used as initial tracks for the muon tracker (MuTR) software since there are too many combinations if started from the MuTR due to both high multiplicity in gold-gold collision and finer read-out in the MuTR ($\sigma_x \sim 100\,\mu$m), and (2) to do particle identification for reconstructed tracks. To achieve both purposes, a road-finding algorithm with two steps has been developed:[2)] the phase-one road finder, which presents a set of initial roads to the MuTR software focusing on better match between MuTR tracks and MuID roads for a higher muon reconstruction efficiency, and the phase-two road finder, which retraces the roads accepted by the MuTR software and performs a more accurate hit pattern finding for a better hadron rejection.

The phase-one road finding starts with a road seed, which is constructed from a hit found in a seed gap and vertex position measured by a vertex detector, and then finds additional hits that are consistent with the road trajectory. A hit *closest* to the projection of the road to the gap, containing that hit within the search window, is generally accepted. The projection of the road is steered, and the size of the search window is adjusted to allow a deviation from a straight-line trajectory due to multiscattering in the steel absorbers placed between gaps. As a default, two seed gaps are applied to handle the inefficient tubes. The main problem in phase-one road finding is the compromise between high reconstruction efficiency and the least number of ghost roads, in particular those due to relatively large MuID granularity: a tube is approximately 8.4 cm wide and 250–502 cm long. We first focus on higher reconstruction efficiency and then determine the following items to reduce the number of ghost roads: (1) X-Y consistency; (2) X-Y position where the road projects to the z-vertex plane; (3) fit quality of the road to a line; and (4) sharing of hits between two roads. In addition, the phase-two road finding will further reduce the number of ghost roads by combining information from both the MuID and the MuTR. The reconstructed roads are then available for use as input for the MuTR software.

Once the MuTR software accepts the roads and finds associated tracks in the MuTR, the result will be sent back to the MuID software. The phase-two road finding performs two tasks: to further reduce the number of ghost roads and to find all possible hits produced by a single particle penetrating the MuID. The phase-two road finding begins by checking the track identity and keeps the best-matched track/road (least χ^2) if there are multiroads pointing to the same track, which happens when a particle hits the tube overlap region in the MuID. Furthermore, the match quality is also investigated for each matched track/road for ghost-road reduction. The passed roads are retraced and, in general, *all hits* within the search window are accepted in contrast to the phase-one road finding which only accepts the *closest* hit, since hits associated with a road are of crucial importance for the particle identification. Then, we create a group of variables for each road, for instance, the total number of hits in the road and the last gap reached by the road, according to our previous study on hadron/muon identification.

With all possible information for a track/road, particle identification is performed. Currently, a very simple reference table, based on the particle momentum and the last gap, is used to separate muons from hadrons. Two different approaches are being studied: the discriminant function analysis and extended multidimensional reference will be incorporated into the MuID software in the near future.

The software has been intensively tested with simulated single-muon and single-pion events[3)] and the latest result reveals a reconstruction efficiency of approximately 99% for muons in 2.5–5.0 GeV/c and a pion reduction rate of about 0.3% in the same momentum region. We expect a better pion reduction rate after new particle identification software becomes available. The software has also been used to process the MuID data during the last summer run and roads were successfully reconstructed, although the MuID was only partially instrumented.

References

1) PHENIX Collaboration: http://www.phenix.bnl.gov/phenix/WWW/figures/jpg/2_9703phnx1.jpg
2) V. Cianciolo et al.: http://rhip.phys.utk.edu/rhip/Phenix/muideventreconstruction.html
3) Y. Mao et al.: RIKEN Accel. Prog. Rep. **33**, 46 (2000).

*1 Physics Division, Oak Ridge National Laboratory, USA
*2 Physics Department, University of Tennessee, USA
*3 Kyoto University

Gluon Polarization Measurements in the PHENIX Central Arm

A. Bazilevsky, Y. Goto, and N. Saito

Polarized proton collisions, which we will perform at RHIC/PHENIX,[1] are sensitive to gluon polarization, $\Delta g(x)$, in the leading order. By measuring longitudinal spin asymmetry, $A_{LL} = (d\sigma_{++} - d\sigma_{+-})/(d\sigma_{++} + d\sigma_{+-})$, where $d\sigma_{++}$ ($d\sigma_{+-}$) represents the cross section with parallel (antiparallel) beam helicity, $\Delta g(x)$ is extracted.

The PHENIX detector system consists of two central arms and two muon arms. In this report, we discuss physics signals in the central arms. Signals in the muon arms are discussed in another report.[2] In the central arms, each of which cover $|\eta| < 0.35$ and $\pi/2$ azimuthal angle, we will measure prompt photon and neutral/charged pion production using a fine-segment electromagnetic calorimeter (EMCal), tracking chambers and particle-ID detectors. The segmentation of the EMCal is 0.01 radian in both the azimuthal and polar directions.

The dominant process for prompt photon production is the gluon Compton process, $gq \to \gamma q$. We investigate the gluon distribution with a clear theoretical interpretation. The measurement is experimentally challenging because there are many backgrounds, mainly from the two-photon decay of π^0. The PHENIX detector has good background reduction capability with the EMCal. Figure 1 shows the estimated statistical errors of our A_{LL} measurement of the prompt photon in one year of full luminosity, $320\,\mathrm{pb}^{-1}$, at $\sqrt{s} = 200\,\mathrm{GeV}$.[3] The statistics make a clear distinction between three models of GS95 NLO polarized PDF with different integrated gluon polarization values from 1.02 to 1.71 at $Q^2 = 4\,\mathrm{GeV}^2$. The raw ratio of experimental background to the prompt photon yield is 50% to 200% in the p_T region from 10 to $30\,\mathrm{GeV}/c$ at $\sqrt{s} = 200\,\mathrm{GeV}$. Due to the fine-segment EMCal, this ratio can be reduced by mass reconstruction of two photons and an isolation cut down to less than 20%.[4]

Pion production measurements are an alternative to a jet measurement in a small acceptance detector. Jet (or pion) production is sensitive to $\Delta g(x)$ through gluon + quark and gluon + gluon reactions and has high statistics. We will be able to begin measurements in RHIC year-2, the first year of the polarized proton collision with 10% luminosity. At PHENIX, π^0 is clearly identified by mass reconstruction with the EMCal. We will obtain very clear statistics to distinguish between three models of GS95 NLO polarized PDF. Because of the different fragmentation functions of π^0, π^+ and π^- from each quark, we will observe different asymmetries for each. Figure 2 shows asymmetries of π^0, π^+ and π^- with the estimated statistical errors of our A_{LL} measurement of π^0 in one year of 10% luminosity, $32\,\mathrm{pb}^{-1}$ at $\sqrt{s} = 200\,\mathrm{GeV}$. This measurement is similar to the DIS semi-inclusive plus-charged and minus-charged hadron measurement performed in the HERMES and SMC experiments,[5,6] where the researchers measured flavor decomposition of the quark polarization. We will provide more information on the flavor decomposition of the quark polarization, in addition to the gluon polarization, in this measurement.

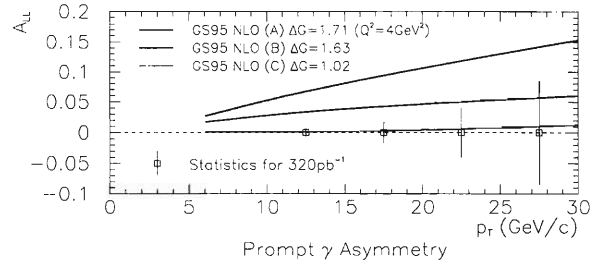

Fig. 1. Statistical errors of our asymmetry measurement of the prompt photon in one year of full luminosity at $\sqrt{s} = 200\,\mathrm{GeV}$. The asymmetry calculations using three models of GS95 NLO polarized PDF are also shown.

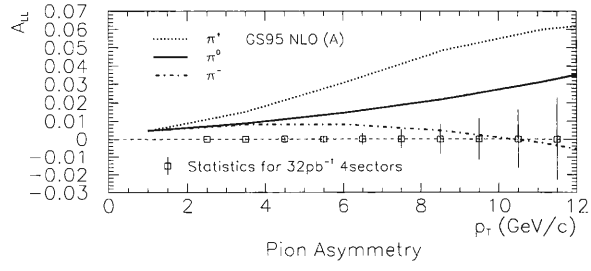

Fig. 2. Asymmetries of π^0, π^+ and π^- with the estimated errors of our A_{LL} measurements of π^0 in one year of 10% luminosity, $32\,\mathrm{pb}^{-1}$ at $\sqrt{s} = 200\,\mathrm{GeV}$.

We will perform the direct measurement of $\Delta g(x)$ at PHENIX using many channels and probes. These channels cover complementary kinematic ranges of the gluon.

References

1) M. Ishihara et al.: RIKEN Accel. Prog. Rep. **34**, 227 (2001).
2) H. D. Sato et al.: RIKEN Accel. Prog. Rep. **34**, 244 (2001).
3) Y. Goto et al.: RIKEN Accel. Prog. Rep. **31**, 54 (1998); A. Bazilevsky et al.: RIKEN Accel. Prog. Rep. **33**, 44 (2000) and references therein.
4) A. Bazilevsky: RIKEN Rev. **28**, 15 (2000).
5) B. Adeva et al.: Phys. Lett. B **420**, 180 (1998).
6) K. Ackerstaff et al.: Phys. Lett. B **464**, 123 (1999).

Prospects for Gluon Polarization Measurement with the PHENIX Muon Arms

H. D. Sato,[*1] M. L. Brooks,[*2] H. En'yo,[*1] N. Hayashi, K. Imai,[*1] K. Kurita, J. M. Moss,[*2] N. Saito, Y. Goto, A. Taketani, and Y. Mao[*3]

One of the major goals of the RHIC spin project is to measure the gluon polarization ($\Delta G(x)/G(x)$; the ratio of the polarized and unpolarized gluon density) in the proton using polarized pp collisions. The experiment will begin in 2001 at $\sqrt{s} = 200\,\mathrm{GeV}$. PHENIX,[1] one of the large experiments at RHIC, is going to measure double-longitudinal spin asymmetries (A_{LL}) for many gluon-induced processes with which the magnitude of $\Delta G(x)$ can be determined.[2] In this paper, we focus on processes which can be studied with the two Muon Arms in PHENIX. Their kinematical acceptance is $1.2 < |\eta| < 2.4$ and $\Delta\phi = 2\pi$.

Since the open heavy-flavor production is dominated by the gluon-gluon fusion process, its asymmetry is sensitive to $\Delta G(x)$.

Production of single muons with a high transverse momentum is known to be dominated by semi-leptonic decays of open heavy-flavors and has a large cross section. 300 k single muons with $p_T > 2\,\mathrm{GeV}/c$ from open charm quarks with a $6pb^{-1}$ luminosity are expected in the first year. This yield corresponds to the statistical error of A_{LL}, $\delta A_{LL}(stat.) = 0.007$, with 50% beam polarization. This accuracy is sufficiently precise to examine the prediction of one of the theoretical models[3] ($A_{LL} \sim 0.02$). It is important to measure A_{LL} for the hadronic decay and punch-through background since (1) A_{LL} for the signal is diluted with it and (2) it will also give us information on $\Delta G(x)$ by itself.

Requiring the coincidence of an electron measured in the two Central Arms, which covers $|\eta| < 0.35$ and $\Delta\phi = \pi$, we can identify open heavy-flavors much more clearly. Figure 1 shows the expected mass spectra for unlike-sign and like-sign $e\mu$ pairs. We used the PYTHIA event generator with the GRV94-LO parton distribution functions. While charm events appear only in the unlike-sign pair, bottom events also contribute to the like-sign pair since some b-quarks decay sequentially ($b \to c \to l$) and the sign of the lepton is flipped. Major sources of the electron background are the Dalitz decay of π^0 and the photon conversion. Most of these can be rejected using the isolation cut with the MVD (multiplicity vertex detector) which covers $|\eta| < 2.5$ around the beam pipe. The reason for this is that within a certain cone angle around a hit by an electron (positron), another hit by the accompanying positron (electron) will be found.[4] Therefore we can obtain A_{LL} for both open charm and open bottom events separately using unlike-sign and like-sign events. Both statistical and systematical errors are estimated to be sufficiently small to distinguish the different models of $\Delta G(x)$ with a $320pb^{-1}$ luminosity.[2]

A_{LL} for the charmonium production will add another constraint to $\Delta G(x)$. The detection of J/ψ is relatively easy and its background is expected to be small for the asymmetry determination. We will obtain roughly 40 k J/ψ's with $6pb^{-1}$, which corresponds to $\delta A_{LL}(stat.) = 0.02$ with 50% beam polarization. We also plan to measure the production cross section and the polarization of J/ψ. Those observables play a

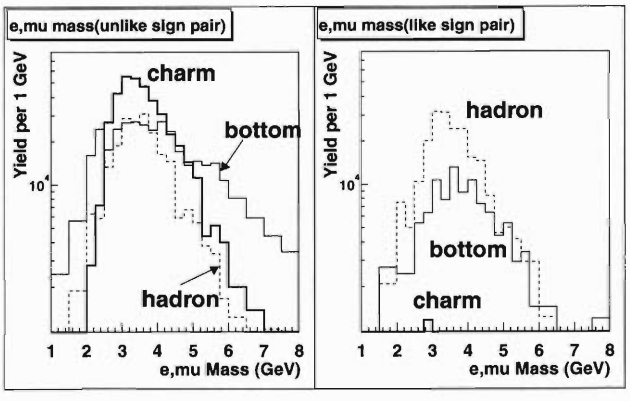

Fig. 1. Expected mass spectra for unlike-sign and like-sign $e\mu$ paris in pp collisions at $\sqrt{s} = 200\,\mathrm{GeV}$ with a $320pb^{-1}$ luminosity.

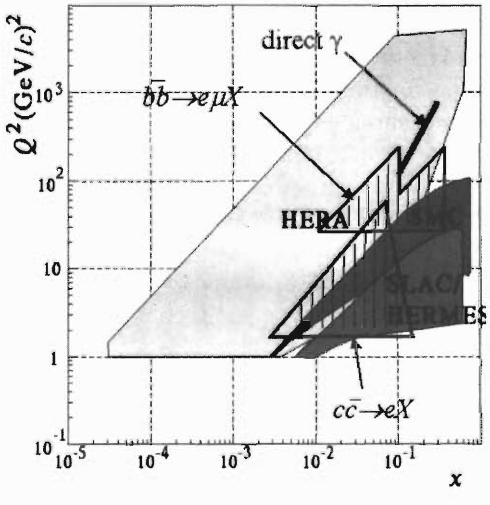

Fig. 2. Sensitive regions of gluon x and Q^2 for the different processes.

*1 Kyoto University
*2 Los Alamos National Laboratory, USA
*3 China Institute of Atomic Energy, China

crucial role in determining the production mechanism of the charmonium.

Figure 2 shows sensitive regions of gluon x and Q^2 for $b\bar{b} \rightarrow e\mu X$, $c\bar{c} \rightarrow eX$ and the direct-photon production process. Since muon channels probe different kinematical regions from those measured in the Central Arms, together they give us a more global picture of $\Delta G(x)$.

References

1) http://www.phenix.bnl.gov/
2) A. Bazilevsky et al.: RIKEN Accel. Prog. Rep. **33**, 44 (2000).
3) T. Gehrmann and W. J. Stirling: Phys. Rev. D **53**, 6100 (1996).
4) W. Xie for the PHENIX Collaboration: American Physical Society Meet., Oct. (2000).

Investigating Contact Interaction by Polarized *pp* Collision

J. Murata

One of the most vital tasks of an experiment using a polarized hadron collider in a new energy region is the study of physics beyond the standard model (SM). In the past few years, several theoretical works have been devoted to the studies of contact interaction (or, compositeness) and new gauge bosons $W'^{\pm}$ and Z'. In these theoretical works,[1] it has been shown that RHIC can reach a similar sensitivity to that of the TEVATRON, due to its polarized beam.

The purpose of the present study is to explore the discovery potential for physics beyond the SM from the experimental perspective. In order to study physics sensitivity and to determine a search window, simulation studies with an event generator are indispensable. Several non-SM scenarios can be examined using PYTHIA. A contact interaction (CI), phenomenologically introduced as a 'residual interaction' which originates from interactions between quark and lepton subconstituents, can be also examined through it. However, as with all other subprocesses, PYTHIA includes only helicity-averaged cross sections for the CI.

The author developed a plug-in program 'POLBEYOND' for PYTHIA by which helicity-dependent matrix elements and spin asymmetries for Drell-Yan and quark-scattering process can be examined. Figure 1 shows the expected single spin asymmetries $A_L = \{\sigma(-) - \sigma(+)\}/\{\sigma(-) + \sigma(+)\}$ at RHIC ($\sqrt{s} = 500\,\mathrm{GeV}$) in $\mu^+\mu^-$ pair production assuming full acceptance and detection efficiency.

The results were obtained for various Λ, which is a model-independent scale parameter of the CI, defined as $F(Q^2) = (1 + Q^2/\Lambda^2)^{-1}$, where $F(Q^2)$ is a 'form factor' of the quark and lepton. Helicity-dependent matrix elements including CI terms were obtained by crossing the electron-quark-scattering formula from the annihilation channel to the exchange channel. Final hadronic spin asymmetries were estimated by accumulating events with the following weight factors: helicity asymmetries of partonic level cross sections, and polarized and unpolarized parton distribution functions. The event generation was controlled by the unpolarized subprocesses, which are already included in PYTHIA for fermion pair creation *via* γ^*/Z production including CI effects. The present result shows that we can expect to observe an anoma-

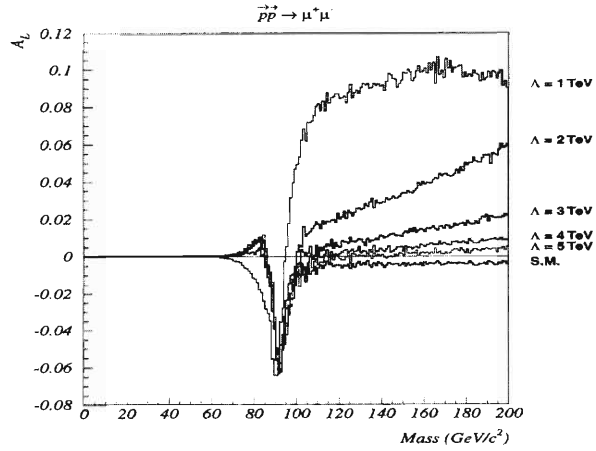

Fig. 1. A_L values are plotted as functions of Drell-Yan mass with selections of Λ and for the case of the SM ($\Lambda \to \infty$). Present results are for the reaction of $pp \to \mu^+\mu^-$ at $\sqrt{s} = 500\,\mathrm{GeV}$, with a constructive interference between the SM and the left-handed CI. GS-A[2] polarized parton distribution function is used.

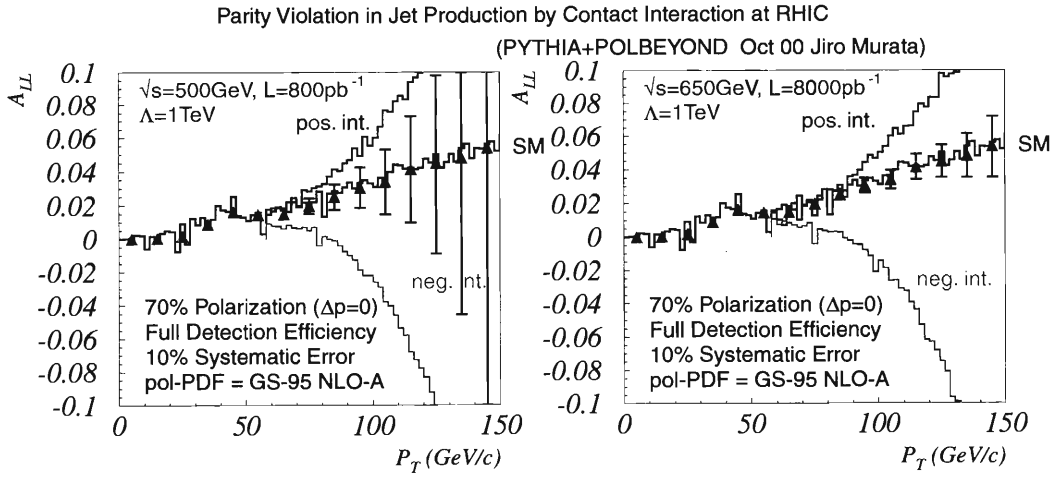

Fig. 2. Parity-violating double-spin asymmetries A_{LL}^{PV} are plotted as functions of jet P_t, for $\sqrt{s} = 500\,\mathrm{GeV}$ with 800 pb^{-1} and $\sqrt{s} = 650\,\mathrm{GeV}$ with 8000 pb^{-1}.

lous parity violation if $\Lambda \sim 1\,\mathrm{TeV}$; however, at least the realistic detector acceptance should be considered in order to predict a more accurate search limit. Furthermore, a full detector simulation is also possible using PYTHIA+POLBEYOND. Although the experimental signature of the Drell-Yan process is clean, its small cross section in pp collisions, which requires sea quarks, limits our sensitivity compared to the already established limits in e^+e^- collisions for the electron-quark CI ($\Lambda > 5.4\,\mathrm{TeV}$) by ALEPH and in $\bar{p}p$ collisions for the muon-quark CI ($\Lambda > 2.9\,\mathrm{TeV}$) by CDF. On the other hand, jet production has a larger cross section and potentially provides better sensitivity. The estimated parity-violating asymmetries in jet production are shown in Fig. 2. It is shown that we can reach more than 3 TeV sensitivity, which is higher than the current limit of 2.7 TeV reported by D0 for the quark-quark CI,[3] with the current RHIC plan. It is also shown that the sensitivity limit can be more than 6 TeV using the RHIC upgrade plan. To summarize, we note that the observation of an anomalous parity violation would directly indicate the presence of new physics.

References

1) P. Taxil: Nuovo Cim. **16** No. 11, 1 (1993); P. Taxil and J.-M. Virey: Phys. Rev. D **55**, 4408 (1997); Phys. Lett. B **404**, 302 (1997); Phys. Lett. B **441**, 376 (1998); J.-M. Virey: Eur. Phys. J. C **8**, 283 (1999).
2) T. Gehrmann and W. J. Stirling: Phys. Rev. D **53**, 6100 (1996).
3) Particle Data Group: Eur. Phys. J. C **15**, 852 (2000).

Polarized Parton Distribution Functions for Future Predictions

Y. Goto, N. Hayashi, M. Hirai,[*1] H. Kobayashi, S. Kumano,[*1] M. Miyama,[*2] T. Morii,[*3] N. Saito, T.-A. Shibata,[*4] and T. Yamanishi[*5]

Based on measurements of polarized deep inelastic scattering (DIS), we determined polarized parton distribution functions (pol-PDFs).[1)] The experimental data of spin asymmetry A_1 at various x and Q^2 are combined in the functional fitting process using a Q^2 evolution for polarized parton distributions.

The functional form of the pol-PDF $\Delta f_i(x, Q^2)$ at $Q^2 = Q_0^2$ $(= 1.0\,\mathrm{GeV}^2)$ is defined using four parameters by taking into account the counting rule,

$$\Delta f_i\,(x, Q_0^2) = A_i\, x^{\alpha_i}\,(1 + \gamma_i\, x^{\lambda_i})\, f_i(x, Q_0^2), \qquad (1)$$

where $f_i(x, Q_0^2)$ is the unpolarized PDF taken from the GRV98 parameterization. The absolute value of pol-PDFs is constrained by the positivity condition,

$$|\Delta f_i(x, Q_0^2)| \leq f_i(x, Q_0^2). \qquad (2)$$

The subscript i denotes the four types of parton distributions: $f_i \in \{u_v, d_v, \bar{q}, g\}$, where u_v and d_v are valence quarks, g is the gluon, and $\bar{q}$ is a sea quark representing all sea quarks:

$$\Delta u_s = \Delta \bar{u} = \Delta d_s = \Delta \bar{d} = \Delta s = \Delta \bar{s} \equiv \Delta \bar{q}. \qquad (3)$$

The SU(3) symmetric sea at $Q^2 = Q_0^2$ is assumed, which is reasonable and within the current experimental accuracy of sea-quark measurement. The first moments of Δu_v and Δd_v are fixed by the β-decays of neutrons and hyperons in accordance with the SU(3) symmetric sea assumption, thus the total number of free parameters is further reduced from 16 to 14.

The χ^2 minimization is performed using the CERN library MINUIT. The parameters are determined by fitting the function to 375 data points of A_1 from DIS experiments that are EMC, SMC, SLAC (E130, E142, E143, E154, E155) and HERMES. We obtained the min. value of $\chi^2 = 322.6$ for the LO and $\chi^2 = 300.4$ for the NLO, suggesting that the NLO is more suitable.

Figure 1 shows the determined polarized parton distribution functions for the NLO. We reported three sets of parameterization, namely, LO, NLO-1 and NLO-2, in our previous publication,[1)] where the NLO-1 function is fitted with 14 free parameters while the NLO-2 function is fitted with 13 free parameters where $\alpha_{\bar{q}}$ is fixed at $\alpha_{\bar{q}} = 1.0$.

A FORTRAN program library used to reproduce the three sets of pol-PDF is available from the AAC home page.[2)] The library uses grid data from pol-PDFs in

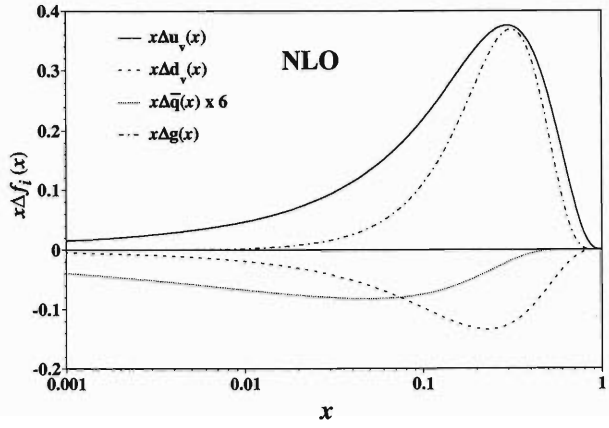

Fig. 1. Polarized parton distribution functions (pol-PDF) in the next-leading-order (NLO-1) at $Q^2 = 1.0\,\mathrm{GeV}^2$.

(x, Q^2) space which covers the kinematical ranges of $10^{-9} \leq x \leq 1.0$ and $1.0 \leq Q^2 \leq 10^5$ GeV^2. The grid data was produced by the same Q^2 evolution program used in the functional fitting. The pol-PDFs and the structure functions g_1 for proton, neutron and deuteron at a specified point of (x, Q^2) are reproduced by interpolating the grid data using the linear (for $\log Q^2$) and cubic spline (for x) interpolation routines. We confirmed that the library reproduces the x and Q^2 dependences of pol-PDFs in our previous publication[1)] as well as the first moments. The library will be useful for future predictions of experimental results.

The study to determine the 1-sigma boundary of uncertainties of pol-PDFs is under way. The 1-sigma boundary can be estimated using the error matrix V_{ij} obtained from the functional fitting. The error of the function F can be calculated using the error propagation formula,

$$(\delta F)^2 = \sum_i \sum_j \frac{\partial F}{\partial a_i} V_{ij} \frac{\partial F}{\partial a_j}, \qquad (4)$$

from the error matrix V_{ij} of parameters a_i and a_j. The level of uncertainty of $\Delta g(x)$ that can be reduced by including results from upcoming measurements at DESY-HERMES, CERN-COMPASS and BNL-RHIC is an interesting subject to which we can apply our pol-PDF analysis.

*1 Saga University
*2 Tokyo Metropolitan University
*3 Kobe University
*4 Tokyo Institute of Technology
*5 Fukui University of Technology

References

1) Y. Goto et al.: Phys. Rev. D **62**, 34017 (2000); hep-ph/0001046.
2) http://spin.riken.bnl.gov/aac/

Future Transversity Measurements at RHIC

D. Boer, M. Grosse Perdekamp, and A. Ogawa*

High-energy, deeply inelastic lepton-nucleon and hadron-hadron scattering cross sections can be described with the help of three independent nucleon helicity amplitudes. Measurements of the nucleon structure functions $F_1(x, Q^2)$, the helicity average, and $g_1(x, Q^2)$, the helicity difference, have explored the helicity conserving part of the cross sections with great experimental accuracy.

In contrast, no information is presently available on the helicity flip amplitude. The absence of experimental measurements is a consequence of the chiral-odd nature of the helicity flip amplitude and the related "transversity quark distributions," $\delta q(x, Q^2)$, which prevents the appearance of helicity flip contributions at leading twist in inclusive deep inelastic scattering experiments.

The current interest in transversity distributions results from recent HERMES[1] and SMC results[2] in semi-inclusive deep inelastic scattering, which suggest that Collins's function $H_1^\perp$ *and* the transversity distribution function δq are different from 0 and measurable. Although precise statements on the shape and magnitude of the functions cannot be made from this data, clearly the prospects of having a tool at hand which, for the first time, provides access to the complete spin structure of nucleons in hard scattering processes are exciting. At DESY a significant fraction (2 years) of the extended HERMES experimental program has been designated for the measurement of the transversity distributions.[3]

In a partonic picture of the nucleon, transversity distributions are interpreted as distributions that describe the probability of probing a quark with spin parallel minus the probability of probing a quark with spin antiparallel in a transversely polarized nucleon target. Some interesting characteristics of transversity distributions are as follows.

- Helicity flip gluon distributions are zero at leading twist and thus there is no mixing between quark and gluon degrees of freedom in the Q^2 evolution.
- The relation between chiral symmetry breaking and transversity in the nucleon.[4]

At RHIC, the proposal of Collins *et al.*[5] and Jaffe *et al.*[6] to utilize two meson interference fragmentation appears to be promising[7] for transversity measurements; studies of the projected asymmetry measurements at RHIC have shown favorable results.[8] The relevant process is pion pair production in pp scattering with one proton transversely polarized. For example,

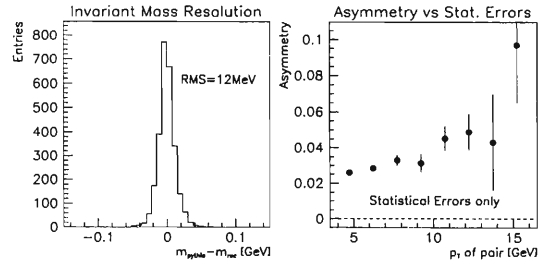

Fig. 1. Simulation studies of two-pion production in the ρ-mass region for the PHENIX detector. Left plot: Invariant mass resolution for pion pairs. Right plot: Projected transverse single-spin asymmetries compared to statistical errors, $\int Ldt = 32\,\mathrm{pb}^{-1}$.

in the ρ/σ invariant mass region, interference occurs between two pions in a superposition of s-wave and p-wave states. The spin-analyzing power of this process is different from 0 in intervals of only a few 100 MeV above and below the ρ-mass and is expected to change sign at the ρ-mass.[6] Therefore, it will be important in RHIC experiments to have sufficient invariant mass resolution to observe the invariant mass dependence of the analyzing power. The invariant mass resolution for pion pairs in the ρ-mass region is shown in Fig. 1 for the example of the PHENIX experiment. The *RMS* of the distribution is 12 MeV which is sufficient for an experimental determination of transversity distributions at RHIC. Projected sensitivities, based on Tang's and Jaffe's model calculations,[6] are shown in the right plot of Fig. 1 assuming the acceptance of the PHENIX detector. The high rates will permit a transversity measurement, and a dedicated run has been added to the future RHIC running schedule.

* Pennsylvania State University, USA

References

1) A. Airapetian et al.: Phys. Rev. Lett. **84**, 4047 (2000).
2) A. Bravar et al.: Nucl. Phys. B **79**, 520 (1999).
3) HERMES Collaboration: The HERMES Physics Program & Plans for 2001–2006, DESY PRC (2000).
4) Talks of R. Jaffe and C. Weiss: Proc. RBRC Workshop on Future Transversity Measurements, BNL, Sept. (2000).
5) J. C. Collins, S. F. Heppelmann, and G. A. Ladinsky: Nucl. Phys. B **420**, 565 (1994); J. C. Collins and G. A. Ladinsky: hep-ph/9411444; J. C. Collins: Proc. RHIC Spin Workshop, Oct. (1999), p.158.
6) R. L. Jaffe et al.: Phys. Rev. Lett. **80**, 1166 (1998); Phys. Rev. D **57**, 5920 (1998); J. Tang: hep-ph/9807560; J. Tang: Thesis, MIT (1999).
7) D. Boer: Proc. RBRC Workshop on Future Transversity Measrements, BNL, Sept. (2000). For a discussion of alternative channels.
8) M. Grosse Perdekamp: 8th Int. Workshop on Deep-

Inelastic Scattering, Liverpool, UK, 2000-8; Talks of A. Ogawa and M. Grosse Perdekamp: Proc. RBRC Workshop on Future Transversity Measurements, BNL, Sept. (2000).

An Electron-Nucleon/Nucleus Collider at BNL

A. Deshpande, G. Garvey,*1 V. W. Hughes,*2 T. Ludlam,*3 L. McLerran,*3 P. Paul,*3 S. Peggs,*3 and R. Venugopalan

In the past one year considerable interest has developed in the experimental and theoretical nuclear physics community to study the scope of a physics program that could be pursued if a high energy electron beam facility is built at BNL and that beam is made to collide with the already existing hadron beams from RHIC. Such a facility is called eRHIC.[1] If the electron beam is polarized then not only could one study unpolarized deep inelastic scattering (DIS) using the unpolarized protons (e-p) or heavy ions (e-A) at RHIC, but also polarized DIS ($\vec{e} \cdot \vec{p}$) using the polarized protons from RHIC.

The nominal electron beam energy under consideration at present is about 10 GeV, but it could be varied between 5 to 12 GeV. The variation of the proton beam energy is already possible in the RHIC accelerators today, although this does affect the luminosity. Using the highest possible value of the proton beam energy possible in the present RHIC of 250 GeV and a 10 GeV electrons from a new facility one could envision DIS with $\sqrt{s} \sim 100$ GeV. For polarized DIS which till now has only been pursued in fixed target mode this would be a factor of ~ 3 to ~ 20 increase in the value of $\sqrt{s}$. The facility would deliver at least $10^{33}\,\mathrm{cm}^{-2}\mathrm{sec}^{-1}$ luminosity. For unpolarized DIS off of heavy ions, it is expected that RHIC would provide beams of 100 GeV/nucleon. This implies that using a 10 GeV electron beam one could attain $\sqrt{s} \sim 60$ GeV for e-A collisions. Using the electron, proton beam energies mentioned above and the the simple relation between the kinematic variables it is obvious that with eRHIC one can reach x as low as few $\times\, 10^{-4}$ and as high as 0.8 for $Q^2 \geq 1\,\mathrm{GeV}^2$. For a nuclear beam one could reach $x \sim 10^{-3}$ values for $Q^2 > 1\,\mathrm{GeV}^2$. Figure 1 shows the $x - Q^2$ kinematic reach of the eRHIC (e-p) compared to the fixed target experiments of the past and present.

In the case of polarized DIS off of proton beams the program for such a collider facility is well defined:[2] eRHIC will enable accucrate measurement of the spin structure function of the proton and of neutron (if $^3He^{+2}$ can be stored in the RHIC ring) in the low-x region which is the source of the largest uncertainty in the first moments $\Gamma_1^{p/n}$ and the Bjorken sum rule. The spin carried by the polarized gluon inside a nucleon is a yet unmeasured quantity. eRHIC would measure that unambiguously and using theoretically and experimentally clean techniques of pQCD analysis at NLO,

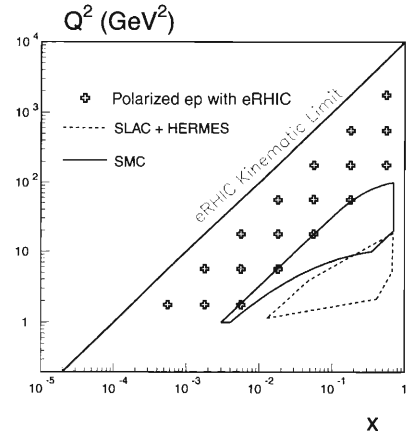

Fig. 1. The $x - Q^2$ kinematic coverage of the eRHIC compared with the present and past fixed target polarized DIS experiments. A future fixed target experiment COMPASS as CERN will cover the same kinematic range as that of SMC.

the photon-gluon-fusion process resulting in di-jet or 2 high p_T oppositely charged tracks, and using photoproduction of di-jets and high p_T tracks. Further eRHIC facility would be unique in its ability to study and resolve the polarized parton distribution inside a polarized photon. Investigations based on charged current e-p scattering would allow a first and unique measurement of the parity violating structure function g_5. There would also be other measurements possible with eRHIC that would be semi-inclusive and exclusive in nature, which will help resolve the spin structure of the nucleon along with the above mentioned measurements with much better accuracy than possible in present day DIS experiments and by those planned to be operational in a few years.

The investigations with e-A scattering would principally be concentrated around finding a novel state of matter of high parton density called in the literature the Colored Glass Condensate (CGC).[2] Indirect evidence for its existance seen from HERA data could be confirmed with direct measurements of e-A at eRHIC. Properties of CGC can be probed by measuring both the inclusive as well as exclusive processes in e-A scattering. Understanding the CGC would be critical in the investigations of QGP underway at RHIC.

*1 Los Alamos National Laboratory, USA
*2 Yale University, USA
*3 Brookhaven National Laboratory, USA

References

1) For full information on the eRHIC project see http://quark.phy.bnl.gov/~raju/eRHIC.html
2) A. Deshpande and V. Hughes: Proc. 2nd Workshop on eRHIC at Yale, BNL Report 52592 (2000).

Computing Center in Japan for RHIC Physics (CC-J)

T. Ichihara, Y. Watanabe, N. Hayashi, S. Yokkaichi, S. Sawada,[*1] Y. Goto, N. Saito, H. En'yo,[*2] H. Hamagaki,[*3] and M. Ishihara

The computing center in Japan (CC-J) for RHIC physics[1] started operation in June 2000 at RIKEN. The CC-J is aimed to be the principle site of computing for PHENIX[2] simulation, a regional PHENIX Asian computing center, and a center for the analysis of RHIC[3] spin physics. Since the PHENIX experiment at RHIC was scheduled to commence in 2000, we started to construct the regional computing center in Japan at the RIKEN Wako campus in April 1999.[4] Prior to the construction, R&D for the CC-J started in 1998 at the RIKEN BNL Research Center (RBRC).

The first PHENIX experiment at RHIC for Au + Au collision was carried out in the summer of 2000. The raw data of approximately 1 TB was transferred from the RHIC Computing Facility (RCF) at the BNL to the CC-J over the Wide Area Network (WAN).[5] The analyses for the first PHENIX experiment have been carried out successfully at the CC-J. The Ring Imaging Cherenkov (RICH) detector demonstrated the good identifications of the electron.[5] The calibration of the Time-of-Flight (TOF) wall was carried out at the CC-J and revealed clear particle identifications for hadrons.[6] A clear π^0 peak was extracted by the calibration of the Electromagnetic Calorimeter (EMCal) and the background was evaluated by mixed event analysis.[7]

The simulation of 100 K events for the PHENIX experiment under several conditions was carried out successfully using the PISA code at the CC-J.[8] A fast Monte Carlo code was developed and simulation using the code was carried out at the CC-J to evaluate the acceptance of the EMCal for π^0.[7]

Table 1 shows the size of the CC-J system. The CC-J is planned to reach its full scale in the three years. At the opening of the CC-J (June 2000), the size of the CC-J was about one-third of the goal, although almost all the planned functions of the CC-J were completed at that time. About 40 user accounts were created.

Figure 1 shows the configuration of the current CC-J system. The main components of the CC-J consist of (1) a High-Performance Storage System (HPSS), (2) Data servers and (3) CPU farms. Since the CC-J handles approximately 200 TB of data for year, the HPSS was installed as a hierarchical storage system.[9]

Three SUN Enterprise 450 (E450) servers have been installed. One E450 server (ccjsun) is used for login, AFS client and general computing. AFS is a worldwide distributed file system. External users are required to log in to the server using Secure Shell (SSH) to access

Table 1. The size of the CC-J system.

	1999	2000	2001
CPU (SPECint95)	2400	5900	13000
Tape Storage (TB)	100	100	100
Disk Storage (TB)	2.0	9	15
Tape I/O (MB/s)	45	45	112

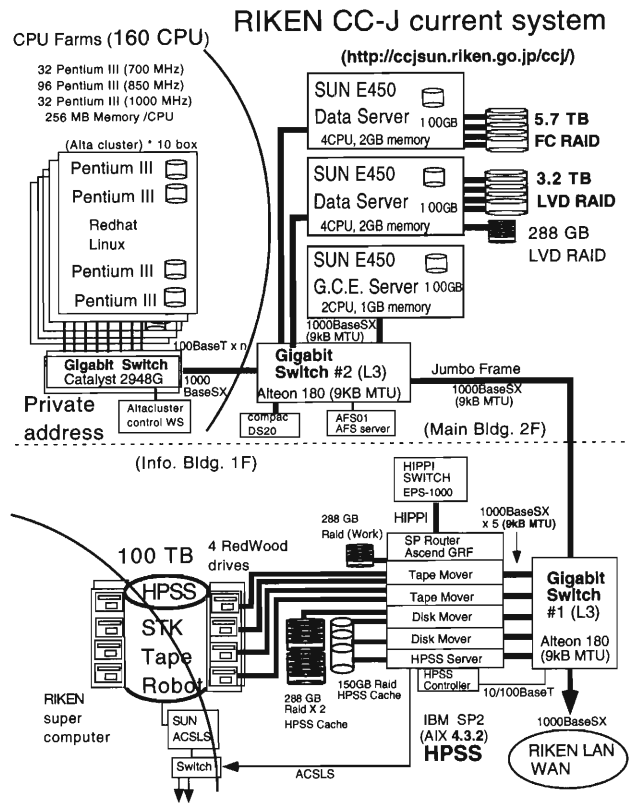

Fig. 1. Configuration of the CC-J system.

the CC-J. Other two E450 servers are used for dedicated data servers. A 3.2 TB SCSI Raid5 disk and a 5.7 TB Fiber Channel (FC) Raid5 disk are connected to the servers. A recent benchmark test for 2 GB file access using Bonnie code revealed that the read access of the FC Raid disk (50 MB/s) is approximately four times faster than that of LVD SCSI Raid disks (12 MB/s). The Veritas File System (VxFS), which is a type of logging file system, were adopted to obtain high performance in file operation and fast file system recovery (fsck) after system failure.

These SUN E450 servers, HPSS servers and switching hubs for the Linux CPU farms are connected by the Gigabit Ethernet to ensure fast file transfer and eleminate network traffic jams.

*1 High Energy Accelerator Research Organization (KEK)
*2 Kyoto University
*3 Center for Nuclear Study, University of Tokyo

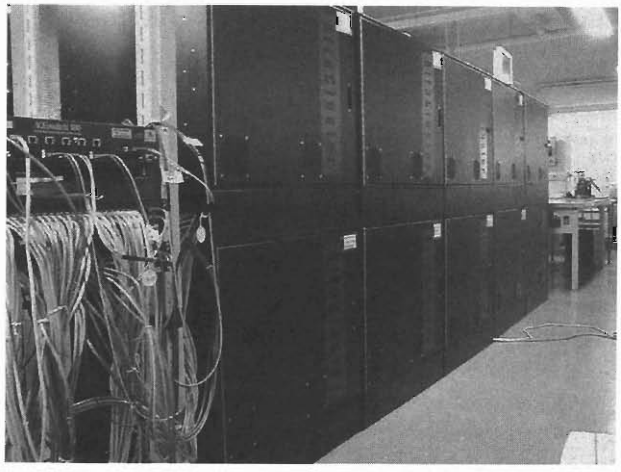

Fig. 2. Linux CPU farms.

The total required CPU performance for CC-J is about 12 k SPECint95 (120 k SPECint2000). The main part of this is for simulation. We adopted the Linux CPU farms to achieve this requirement. The current CPU farms consists of Linux pc's with 160 units of Intel Pentium III processors at 700–1000 MHz. We adopted 10 boxes of Altacluster as a frame. Figure 2 shows a photograph of the current CPU farms. Each node is equipped with a dual CPU, 512 MB of ECC memory, and a 14–18 GB local disk.

We have developed the *kick-start* installation method for Redhat Linux 6.1 to the farms. The installation of Linux for each node can be carried out with a floppy disk and a common NFS server. It takes approximately 10 minutes to install one node and installation can be carried out simultaneously for several nodes. There is no need to use the keyboard or mouse during the installation. The post-installation procedure is carried out automatically following the kick-start installation.

We are currently using Linux kernel 2.2.14 and 2.2.16. The NFSv3 patch for the Linux kernel significantly improved the NFS performance, particularly for the NFS write operation. During job execution, most of the disk IOs are carried out at the local disk equipped for each node. At the beginning and ending of a job, file transfer will be carried out between the Linux local disk and central data server.

To keep the common software environment to be RCF, AFS is used. To access AFS from the Linux farms stably, *mirroring* of the AFS contents to a local data server is carried out daily using the *rsync* utility. AFS contents are accessed from the Linux farms through the NFS; thereby eliminating instabilities from the usage of AFS on the Linux platforms. The mirrored contents of AFS at the CC-J will be mirrored again at the domestic collaborating institutes using the rsync utility for fast update.

Since the PHENIX collaboration uses C++ for its common software, Objectivity/DB was adopted. Therefore, it is necessary to access the PHENIX Objectivity/DB at the RCF from the CC-J and this method has been studied previously.[10)]

The portable batch system (PBS), which is free software, was used for the batch queueing in the early stage of the development. Job scheduler software was developed for the PBS. However, since we encountered freezing problems and instability in PBS, we changed the batch queueing system from PBS to the Load Sharing Facility (LSF) in the summer of 2000. LSF is a commercial product. LSF ensures the stable operation of the batch queueing and offers the convenient features of *fairshare* job scheduling and automatic job recovery after node failure.

RIKEN is currently connected to Inter-Ministry research information network (IMnet) at the speed of 15 Mbps and this bandwidth will be updated to 50 Mbps in early 2001. For the international connection, the CC-J joined the Asia-Pacific Advanced Network (APAN) which has a bandwidth of 70 Mbps over the Pacific Ocean. Thanks to the APAN, stable access to the USA and Europe Energy Science Network (ESnet) sites has been achieved. Since the capability for the huge data transfer (200 TB/year) between the CC-J and the RCF is required, a data duplication facility using SD-3 tape cartridges was constructed at the RCF and started operation in late 2000.[9)]

The CC-J Planning and Coordination Office (PCO) was established. Operation, maintenance and development of the CC-J are carried out under the charge of the PCO. Research plans using the CC-J should be submitted to the CC-J PCO.

The authors are grateful to Professor Bruce Gibbard and the staff of the RCF for their earnest cooperation and discussions. They are also indebted to Professor William A. Zajc, Professor Barbara Jacak and Dr. Dave Morrison for the coordination of the CC-J in the PHENIX collaboration.

References

1) http://ccjsun.riken.go.jp/ccj/
2) http://www.rhic.bnl.gov/phenix/
3) http:/www.rhic.bnl.gov/
4) T. Ichihara et al.: RIKEN Accel. Prog. Rep. **33**, 172 (2000).
5) Y. Akiba et al.: RIKEN Accel. Prog. Rep. **34**, 259 (2001).
6) T. Chujo et al.: RIKEN Accel. Prog. Rep. **34**, 260 (2001).
7) T. Sakaguchi et al.: RIKEN Accel. Prog. Rep. **34**, 261 (2001), and private communications.
8) N. Hayashi et al.: RIKEN Accel. Prog. Rep. **34**, 258 (2001).
9) Y. Watanabe et al.: RIKEN Accel. Prog. Rep. **34**, 254 (2001).
10) S. Yokkaichi et al.: RIKEN Accel. Prog. Rep. **34**, 256 (2001).

Technique for Huge Data (~200 TB/year) Storage and Transfer between US and Japan

Y. Watanabe, H. En'yo,[*1] Y. Goto, H. Hamagaki,[*2] N. Hayashi, T. Ichihara, N. Saito, S. Sawada,[*3] S. Yokkaichi, and M. Ishihara

The data volume of nuclear physics experiments has continuously been increasing. The PHENIX[1] detector at the Brookhaven National Laboratory (BNL),[2] in which the RIKEN Spin Physics project takes part, is producing 20 MB data per second. The 20 MB/s is so large that at such a rate, a CD-ROM is filled in only 30 seconds and the total nominal data volume will reach approximately 300 TB (10^9 Byte) per year. In order to store and manage such a massive amount of data, the primary analysis center for the relativistic heavy-ion collider (RHIC)[3] named the RHIC Computing Facility (RCF)[4] introduced a huge tape library system from StorageTek Inc.[5] as hardware, which includes RedWood tape drives (11 MB/s), SD-3 cartridges (50 GB/cartridge, Fig. 1), and a huge tape robotics library PowderHorn9310 (Fig. 2) which can store up to approximately 6,000 cartridges. This hardware is managed by the high-performance storage system (HPSS),[6] which was developed by several US national laboratories and IBM Inc.

Fig. 1. SD-3 tape cartridge has 50-GB capacity in a small dimension: $100 \times 125 \times 25\,\mathrm{mm}^3$.

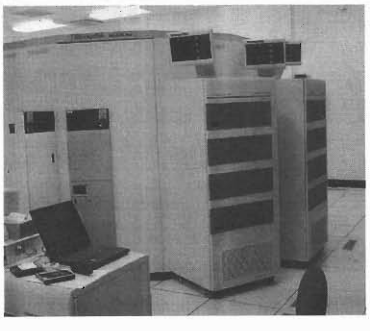

Fig. 2. PowderHorn9310 is one of the largest tape libraries. It can store up to approximately 6,000 cartridges.

In RIKEN, on the other hand, we are constructing the PHENIX Computing Center in Japan (RIKEN CC-J)[7] at Wako campus in order to maximize the physics output of the Spin Physics project by analyzing data produced at the PHENIX detector. It is obviously important to transfer experimental data from BNL to Wako campus. This means that the RIKEN CC-J must also prepare a large storage system as large as that of the RCF. Moreover, it is very important to establish a large data transfer method between the US and Japan. Practically, we do not have a plan to transfer an entire set of raw data but the entire data summary tape (DST) produced after the initial analysis (reconstruction) at the RCF. However, the DST volume is still expected to be as large as 150 TB/year. Table 1 presents the summary of the original estimate for the storage scale.

Figure 3 shows a schematic diagram of the storage system of the CC-J. It is called "*HPSS*" because all the hardware is controlled by HPSS which is the most up-to-date hierarchical storage management (HSM) software. There is a PowderHorn9310 which is the same model as that of the RCF and has 5,000 SD-3 cartridges and 10 RedWood tape drives. It is shared by the Computer and Information Division as a supercomputer's archive, and the CC-J keeps 2,000 cartridges (100 TB) and four drives for its own usage. Five IBM RS/6000SP workstations are working to aid the traffic control of data flow among tapes and cache disks attached on workstations and outside the HPSS (*e.g.*, computers for analysis). They are connected to each other with four types of networks, as shown in Table 2. Each type of network connection has a different function in order to avoid a traffic jam of the data flow. The total volume and number of cache disks are also obviously important for HSM. Our HPSS has a total of 690 GB by five RAID5 disks for cache.

Owing to the HPSS, the storage system is taken for

Table 1. Summary of estimated volume size of data.

	PHENIX	CC-J
Raw Data	290	0
Calibration Data	0.1	0.1
Simulated Data	30	30
Data Summary Tape	150	150
Micro-Data Summary Tape	45	45
Total	~515 TB	~225 TB

*1 Kyoto University
*2 Center for Nuclear Study, University of Tokyo
*3 High Energy Accelerator Research Organization (KEK)

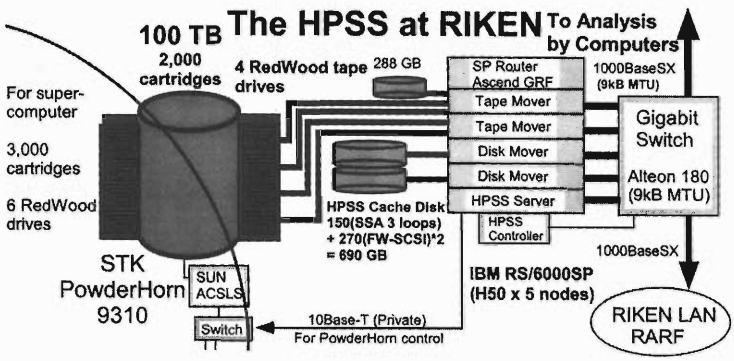

Fig. 3. Schematic diagram of the HPSS at RIKEN.

Table 2. Each RS/6000 is connected to the others with four types of network connections to avoid a traffic jam of the data flow.

	Bandwidth	Purpose
Gigabit Ethernet	1000 Mbps	Data path to outside
SP Switch	1200 Mbps	Data path between RS/6000s
100Base Ethernet	100 Mbps	Control path for HPSS
10Base Ethernet	10 Mbps	Control path for PowderHorn

an extra large (or almost infinite) disk by users which can be accessed with only the ftp interface. As a matter of fact, users must use *pftp* (parallel ftp) which is specially made for the HPSS and has the advantage of higher transfer speed than that of a single cache disk or a single tape drive. Scalability is one of the big advantages of HPSS, which means that the total processing capacity scales almost linearly to the amount of hardware (*e.g.*, workstations, tape drives, cache disks, and tapes). This scalability was not realized until the system built on the distributed computing environment was fabricated. The present HPSS has been measured to have a continual write performance of 50 MB/s (peak), 12 MB/s (sustainable, when employing only two tape drives). Recently, we developed *cftp* (CC-J ftp) by hacking *pftp* for users' convenience and easy management. Users can easily archive/retrieve their own data from HPSS using *cftp*.

The data transfer method between US and Japan is another issue. As mentioned, 150 TB is estimated as a nominal volume of data transferred from US to Japan yearly. It requires 5 MB/s noninterrupted transfer for the entire year over the Pacific Ocean. In fact, 5 MB/s over the Pacific is now achievable. The Asia-Pacific Advanced Network (APAN) which we are using has 70-Mbps (8.8 MB/s) bandwidth between the US and Japan. On the other hand, the measured transfer speed does not exceed 1 MB/s. The 15-Mbps (1.9 MB/s) bandwidth between APAN and RIKEN may be one reason, but 0.2 s of signal delay (round-trip time) between BNL and RIKEN may be more serious. It seems impossible to transfer all the data over the network at present, but it may be possible in the near future. Recently, we were pleased to find out that the bandwidth between APAN and RIKEN will be tripled in the near future. In addition, even 1 MB/s means that approximately 80 GB data can be transferred in one day. A rate of 80 GB/day seems to be an adequate transfer speed except for raw data or DST.

Thus, we decided to transport tapes which contain DST by air. Five MB/s means 3 TB/week which is equal to 60 SD-3 cartridges (Fig. 1) whose dimensions are $100 \times 125 \times 25\,\mathrm{mm}^3$. We can archive 5 MB/s easily by placing these 60 cartridges in a box of $400 \times 125 \times 375\,\mathrm{mm}^3$ and transporting it to the US weekly. We are building up the duplication facility at the RCF to copy data to our cartridges smoothly. It consists of a RedWood tape drive and an RS/6000 workstation with a 200-GB hard disk as a data buffer. The RedWood tape drive and 200 SD-3 cartridges are already installed in the RCF's PowderHorn9310. The procedure is as follows: (1) Each data set for export is stored once in a local buffer disk of the RS/6000. (2) When the total volume of data sets nears 50 GB, the other local disk is set to the next buffer and makes a tape archive of the previous disk by using a standard "tar" utility. (3) Then process (2) is repeated. All hardware is already functioning and the first DST-exporting task is under way.

References

1) http://www.rhic.bnl.gov/phenix/
2) http://www.bnl.gov/
3) http://www.rhic.bnl.gov/
4) http://www.rhic.bnl.gov/RCF/
5) http://www.storagetek.com/
6) http://www.sdsc.edu/hpss/
7) T. Ichihara et al.: RIKEN Accel. Prog. Rep. **34**, 252 (2001); http://ccjsun.riken.go.jp/ccj/

Objectivity/DB System at CCJ for the PHENIX Experiment

S. Yokkaichi, H. En'yo,[*1] Y. Goto, H. Hamagaki,[*2] N. Hayashi,
T. Ichihara, M. Ishihara, S. Sawada,[*3] and Y. Watanabe

Recently, Object-Oriented (OO) techniques for software development have attracted wide interest in the field of experimental particle/nuclear physics. Many experiments in LHC, SLAC, FNAL and RHIC are developing their software using the OO-techniques. The C++ programming language is the most popular OO-programming language and many experiments adopt this language at present.

In C++, it is not very easy to communicate outside of the process in the Object-Oriented manner. Communication between *Objects* on memory is realized using a *pointer* or a *reference*, while it is nonsense to write a *pointer* to a file. A user of C++ has to develop his or her own methods to input/output the *Objects* to/from the files on a disk or to/from inter-process communication methods as a *socket*, because C++ does not support such methods. In other words, C++ supports only the *Objects on memory*, but does not support the *Objects on disk* or *Objects on network*. The Object-Oriented Database (OODB) helps to input/output the *Objects* to/from the disks transparently. The *Objects* persistently exist on the OODB instead of existing transiently on the memory of each process. (For the network case, the Object Request Broker (ORB) helps.)

The Objectivity/DB[1] system is one of the commercial Object-Oriented Database Management Systems. It has been studied through the CERN RD45 project[2] and the ATLAS experiment, and has already been used in the BaBar experiment.

The PHENIX experiment also adopted C++ to develop their online/offline software, and decided to use the Objectivity/DB for their main database. The main DB includes detector calibration data, high voltage values for the detectors, the run information and so on, although there is no plan to include raw data or Data Summary Tapes (DST). The high-voltage data part of this main DB system was already used throughout the last run in 2000. The calibration-data part is partly under development and is used in the reconstruction process, which makes the DST from the raw data. Collaboration-wide license of Objectivity/DB permits the use of the system in any institute in the PHENIX collaboration.

Also in CCJ,[3] we are supporting the access of the PHENIX official database (PHENIX-DB) for regional users who would like to analyze the raw data. Various ways to support the database are discussed. (A) To make a 'snap-shot' of the original PHENIX-DB on BNL using the tool built in the Objectivity/DB system. It supplies a dead copy of the PHENIX-DB on the disk at CCJ and the user can read it and obtain the same data as in BNL. (B) Direct access to the original PHENIX-DB on BNL from CCJ *via* a Wide Area Network (WAN). Objectivity/DB supports two access methods *via* the network. One is *via* the Network File System (NFS), and the other is *via* the Advanced Multi Thread Server (AMS), which is the original technique of Objectivity/DB. In a WAN environment, AMS is a unique solution in fact. We have accessed *via* AMS and measured the overhead time caused by WAN between CCJ and BNL. It is in the order of 20 to 30 minutes for a typical PHENIX official reconstruction routine which requires only 20 to 30 seconds to read a local database. This overhead time is significant. Moreover, possible *locking* of the PHENIX-DB caused by this long-time and unstable access may bother the users in BNL. Users who were accessing the DB were already bothered in the last run by the *locking* of the PHENIX-DB caused by dead processes or living and forgotten processes in BNL.

Now method (A) is adopted in CCJ. Each time a major update is made at BNL, a 'snap-shot' of the PHENIX-DB is created and copied to CCJ by hand using the built-in commands *oobackup*, *oorestore* and *ooinstallfd*. Many users of CCJ have already used the copied DB and analyzed raw data for their own interests as detector calibration.

The current size of the PHENIX-DB is approximately 600 MB, and the copying process takes about 10 minutes. It is not heavy at present, but it is projected that the DB size will reach an order of 10 GB. In such a case, it is difficult to copy the entire DB; thus incremental copying is preferable. There are two methods to realize the incremental copying. One is (C), called *Replication*, supported by the Objectivity/DB system, which makes a copy (or copies) of the DB in real time. Connections between DBs are kept permanently and an update of one DB propagates to other DBs automatically. However, the problem of *locking* in the unstable WAN environment also exists. Another method, (D), uses a special tool developed in the BaBar experiment at SLAC. The people in BaBar use Objectivity/DB for the data storage and copy the data from Objectivity/DB to outside of SLAC incrementally using their special tool.[4] We plan to contact them and study their tool to determine whether it is suitable for our usage or not.

*1 Kyoto University
*2 Center for Nuclear Study, University of Tokyo
*3 High Energy Accelerator Research Organization (KEK)

References

1) http: //www.objectivity.com/
2) http: //wwwinfo.cern.ch/asd/rd45/index.html
3) T. Ichihara et al.: RIKEN Accel. Prog. Rep. **34**, 252 (2001).
4) E. Leonardi and S. J. Patton: Proc. CHEP 2000.

Large-Scale Simulation of Au-Au Collision for PHENIX Year-1

N. Hayashi, T. Ichihara, Y. Watanabe, S. Sawada,[*1] S. Yokkaichi, Y. Goto, H. En'yo,[*2], H. Hamagaki,[*3] M. Ishihara, and C. F. Maguire[*4]

The PHENIX[1] experiment at the Relativistic Heavy Ion Collider (RHIC) successfully started in summer 2000. The first year, PHENIX collected of Au-Au collision data mainly at $\sqrt{s_{NN}} = 130\,\mathrm{GeV}$ (the center of mass energy per nucleon), and its detector configuration evolved during that period. A large number of Monte Carlo simulation (MC) data are necessary to understand the detector characteristics, such as acceptance or efficiency, and to evaluate our reconstruction program. Thus, we started the generation of five different sets of 100 K MC events in various configurations. The five sets are:

- Retracted configuration of the Central Arm with no magnetic field. PHENIX has two Central Arms, East and West. Initially, they were both open against a beam pipe about 40 cm long. In other configurations, the Central Arms are always in a standard position.
- Zero magnetic field strength.
- Full magnetic field strength with 2D (two dimensional) field map.
- Full magnetic field strength with 3D (three dimensional) field map.
- Half magnetic field strength with 3D field map.

RIKEN CC-J (PHENIX Computing Center in Japan)[2] has been established recently and one of its major roles is to produce a large amount of PHENIX simulated data.

The procedure for the project is described as follows.

(1) Minimum bias Au-Au collision event is generated by HIJING event generator[3] and recorded into a file.
(2) It is fed to the GEANT[4]-based PHENIX detector simulator, PISA.[5] This is the most CPU-intensive step.
(3) The output needs to be processed through "response chain" to make a "fake" PHENIX Raw Data File (PRDF) from the GEANT hit file. It is also called a "digitization path" and produces relational data to evaluate reconstruction program at a later time. The relational data describe the relation between the GEANT hit file and PRDF.

Table 1. Typical CPU time and Data size for a job. Presented CPU time is for the Pentium III (850 MHz) processor. Response chain's products are PRDF and relational data for later evaluation.

	CPU (hrs)	Data (MB)
HIJING	0.2	50
PISA	47	850
response	3.5	160 + 270
reconstruction	1.7	40
Total	52.4	1370

(4) The event reconstruction program analyzes this fake PRDF. In principle, it should be exactly the same as one used for real data. Both "response" and "reconstruction" program are coded by C++ language based on the *Root* framework,[6] an Object Oriented data analysis framework.
(5) All generated data are archived into the HPSS[7] (High Performance Storage System) and transferred to BNL to make them available to all PHENIX collaborators.

Typical parameters of one job (1000 events) is shown in Table 1. Each MC data set described above has 100 jobs and in total the factor 5 has to be multiplied to the values listed in this table. This represents 26,000 hours of CPU time and 635 GB of data volume.

In order to archive files into HPSS, *pftp* (parallel ftp) is used. Its speed is about 10 MB/sec.

Because the security at BNL is enhanced using a firewall technique, *ftp* does not work in practical application. We use *scp* (secure copy command) instead of *ftp* to transfer data to BNL. The data transfer speed really depends on the WAN condition, although 100–150 kB/sec for one *scp* session can be achieved. We also use TAPE media to transport some of the data from CC-J to BNL.

*1 High Energy Accelerator Research Organization (KEK)
*2 Kyoto University
*3 Center for Nuclear Study, University of Tokyo
*4 Vanderbilt University, USA

References
1) M. Ishihara and G. Bunce: RIKEN Accel. Prog. Rep. **34**, 227 (2001).
2) T. Ichihara et al.: RIKEN Accel. Prog. Rep. **34**, 252 (2001).
3) http://www-nsdth.lbl.gov/~xnwang/hijing/index.html
4) http://wwwinfo.cern.ch/asd/geant/index.html
5) http://www.phenix.bnl.gov/phenix/WWW/simulation/Simulation.html
6) http://root.cern.ch/
7) Y. Watanabe et al.: RIKEN Accel. Prog. Rep. **34**, 254 (2001).

Analysis of the PHENIX RICH Detector Using CC-J

Y. Akiba,[*1] T. Sakaguchi,[*2] S. Sawada,[*1] K. Shigaki,[*1] and S. Yokkaichi

Among four experiments at the Relativistic Heavy Ion Collider (RHIC), the PHENIX experiment has the best capability for lepton measurements including electrons. The Ring Imaging CHerenkov (RICH) detector is the primary device for electron identification in the PHENIX central arms.[1] It is a threshold-type gas Cherenkov detector with 5120 photomultiplier tubes (PMTs) as photon detectors. Its Cherenkov threshold for pions is 4.9 GeV/c with its CO_2 radiator.

In June 2000, RHIC achieved the first collision, and the first year data were taken during the summer with Au + Au ions at $\sqrt{s_{NN}}$ = 130 GeV. PHENIX has accumulated more than five million events.

In order to establish an effective way of identifying electrons with RICH, fundamental analysis is necessary, including the determination of t_0s (start timing of TACs), TAC conversion coefficients, and gain coefficients for the ADC channels, slewing correction, efficiency correction for each ADC, and geometry correction for the mirrors. Analysis of the RICH performance is also necessary, such as determining the number of fired PMTs for electron candidates, and the number of photo-electrons per Cherenkov ring. Because all of these should be performed with real data and electron production is a relatively rare process, a large amount of PHENIX real data (PRDFs) must be stored and processed. We have copied a large fraction of PRDFs from the RHIC Computing Facility (RCF) to CC-J[2] through WAN, and they have been stored on RAID disks and HPSS. Because of the rich storage area and the number of high performance CPUs at CC-J, the analysis of PRDFs and resulting DSTs has been smoothly iterated. DSTs for about 500 k events were produced, which were used also for the analysis of the PHENIX time-of-flight detector.[3] As an example of the results, Fig. 1 shows the ring-shaped distribution of Cherenkov photons. The radius of the ring is about 6 cm, which is consistent with the design value for the CO_2 radiator. After determining the threshold for the number of photo-electrons per ring, electron candidates can be assigned. Figure 2 shows the E/p ratio for all the tracks and for the electron candidates. Please note that the energy (E) is measured using an electromagnetic calorimeter and the momentum (p) is determined from the track reconstruction. It is evident that our RICH has an excellent capability in distinguishing electrons. We are going to continue to clarify the RICH performance in more detail, and to obtain physics results, such as vector mesons in high temperature, in the near future.

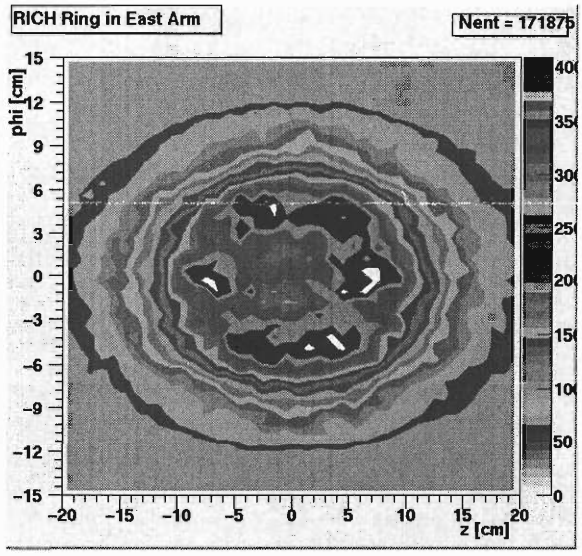

Fig. 1. Accumulated ring image.

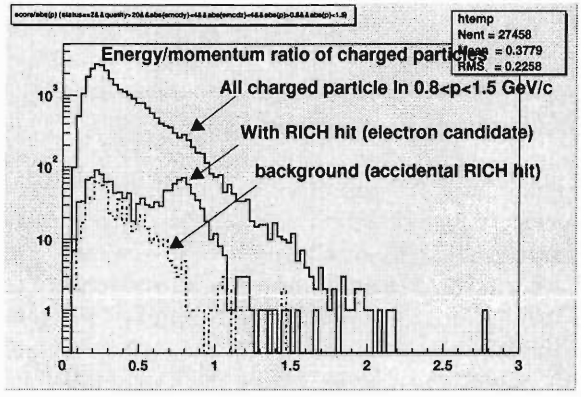

Fig. 2. E/p ratio for all the tracks and the electron candidates determined from RICH.

We would like to thank the members of the Radiation Laboratory for their support of our project, especially Dr. T. Ichihara, Dr. Y. Watanabe, Dr. N. Hayashi, and other CC-J staff. We are indebted to Dr. Y. Goto for the data transfer from RCF to CC-J.

References

1) Y. Akiba et al.: Nucl. Instrum. Methods Phys. Res. A **433**, 143 (1999).
2) T. Ichihara et al.: RIKEN Accel. Prog. Rep. **34**, 252 (2001).
3) T. Chujo et al.: RIKEN Accel. Prog. Rep. **34**, 260 (2001).

*1 High Energy Accelerator Research Organization (KEK)
*2 Center for Nuclear Study, University of Tokyo

Hadron Measurement at RHIC/PHENIX

T. Chujo,[*1] A. Kiyomichi,[*2] H. Ohnishi,[*1] and M. Suzuki[*2]

Heavy ion collisions at ultra-relativistic high energy offer the possibility of producing highly condensed nuclear matter, which may undergo a phase transition from normal nuclear matter to a de-confined state, the Quark Gluon Plasma (QGP). In the summer of year 2000, Relativistic Heavy Ion Collider (RHIC) at Brookhaven National Laboratory (BNL) began its operation as the first Heavy ion collider and energy density producing via heavy ion collisions at RHIC will be able to generate highest energy density ever have, indeed RHIC opens a door to new era to searching and studying for QGP.

The phase transition to QGP should also make a significant difference in the Equation of State (EOF) of nuclear matter and may reveal itself in the dynamical evolution of the interaction region, *i.e.* dynamics of hadrons might change its state before and after the phase transition. Identified hadron measurement arrows not only investigate QGP formation but also to explore dynamical feature of heavy ion interaction. For example, the systematic study of particle yields relates to baryon stopping via proton/anti-proton ratios, to the existence and mechanism of enhanced production of light strange mesons via K/π and K/p ratios, and to comparisons with predictions of chemical and thermal equilibration in these collisions.

The PHENIX experiment collected more than five million of Au+Au collisions at $\sqrt{s} = 130\,\mathrm{GeV}$ per nucleon during year 2000. Generated particle are detected by PHENIX-Central Arm spectrometer. Particle identification is performed by Time-of-Flight (ToF) measurement. The PHENIX Beam/Beam Counter (BBC) provides start timing of ToF measurement. The BBC consists of two arrays on either side of the interaction region; each consisting of 64 photomultiplier tubes equipped with quartz Cherenkov radiators. Timing resolution of BBC achieved 20 ps at central Au+Au collisions. The PHENIX ToF wall provides stop timing of ToF measurement, located about 5.0 m from the vertex. ToF consists of 960 elements of plastic scintillation counters with photomultiplier tube readouts. One million of Au+Au collisions events out of five millions

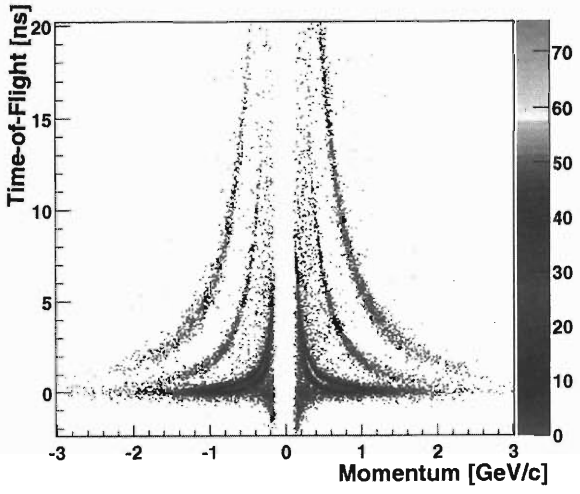

Fig. 1. Identified $\pi^{\pm}$, $K^{\pm}$, proton and anti-proton bands as measured with ToF and tracking detectors.

events are analyzed at CC-J.[1,2] Detector calibration of ToF wall is done at CC-J and finally, ToF resolution is achieved 120 ps for overall ToF measurement. Figure 1 shows the quality of particle identification for hadrons measured with ToF and tracking detectors. Clear separation for particles is seen in this figure.

In summary, PHENIX collected more than five million of Au+Au collisions at $\sqrt{s} = 130\,\mathrm{GeV}$ per nucleon during year 2000. The PHENIX ToF measurements and tracking system are working as we expected and the efforts to withdraw physics from the data are underway.

We would like to thank support from the members of the Radiation Laboratory for our project, especially Dr. T. Ichihara, Dr. Y. Watanabe, Dr. N. Hayashi, and other CC-J staffs.

References

1) T. Ichihara et al.: RIKEN Accel. Prog. Rep. **34**, 252 (2001).
2) Y. Akiba et al.: RIKEN Accel. Prog. Rep. **34**, 259 (2001).

*1 Brookhaven National Laboratory, USA
*2 University of Tsukuba

π^0 Acceptance and Efficiency for PHENIX Electromagnetic Calorimeter

T. Sakaguchi,[*1] S. Botelho,[*2] G. David,[*3] H. Hamagaki,[*1] S. Kametani,[*4] T. Matsumoto,[*1] S. Mioduszewski,[*3] K. Oyama,[*1] T. Thomas,[*3] H. Torii,[*5] and C. Woody[*3] for the PHENIX Collaboration

Directly radiated thermal photons are an interesting probe for investigating the characteristics of the quark gluon plasma (QGP) because they have a long mean free path compared to the size of the nuclear volume involved in relativistic heavy ion collisions. The electromagnetic calorimeter (EMCal) of the PHENIX experiment[1] is a device used for identifying photons, measuring their position and energy, and providing the means to trigger rare events, where photons are produced with a high transverse momentum.[2]

To derive the component of thermal photons from a large background due to γ's from π^0 and η decay, it is necessary to obtain the precise numbers of π^0 and η, the decay photons of which have to be subtracted from the measured inclusive gammas. Also, the π^0 spectra themselves may give information on nuclear effects such as jet quenching. The production cross section of π^0 or η can be derived from the raw counts together with the knowledge of the acceptance and efficiency of the detector.

We have developed a Fast Monte Carlo code which enables faster calculation than by using PISA[3] based on the GEANT simulation code. The software generates π^0's and η's with rapidities and transverse momentums (p_T's) following the given rapidity and p_T distributions, respectively. The particles are generated isotropically in azimuth. The software then generates the secondary γ's decaying from primary particles with a specific branching ratio. The quantities recorded are the four momenta of the primary particles (π^0's and η's) and the secondary γ's. The number of hits in both fiducial areas and veto areas is recorded as well. The software also records the invariant mass spectrum calculated from the decayed gamma of π^0's and η's. The geometry of the calorimeter as instrumented for RHIC Year-1 operation has been implemented using the code with a simple plug-in.

In the simulated and real data analyses, the asymmetry (α) cut and p_T cut are applied to derive a clear π^0 peak in invariant mass spectra. The asymmetry is defined as $\alpha = |E_a - E_b|/(E_a + E_b)$, where E_a and E_b are the energies of γ's. To deduce the production cross section of π^0's from the number of reconstructed π^0's, the acceptance and efficiency should be calculated as a function of α cut and p_T cut.

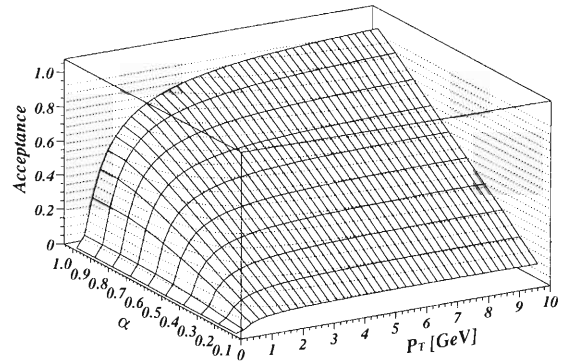

Fig. 1. The acceptance of π^0 as a function of transverse momentum (p_T) and asymmetry (α) cut.

Figure 1 shows the result of the acceptance calculation as a function of p_T and α cut for π^0. The p_T ranges from 0 to 10 GeV with a bin width of 0.25 GeV, which is assumed to be a flat distribution in order to increase statistics at higher p_T, and the α cut ranges from less than 0.1 to 1 with an increase of 0.1. The rapidity distribution is assumed to be flat from -2 to 2, resulting in 1600 particles per event. The smearing effect on energies due to the detector resolution or electric noise is not included. Thus, the calculated value is derived only from the geometric factor of the detector.

We have divided the calculation into 40 energy bins which are mutiplied by 10 asymmetry cuts, resulting in 400 processes. Each calculation takes about 2 hours for 50 K events. Using CC-J, we could run 90 processes simultaneously, and thus obtain the results for a given geometry in about 10 hours.

The software can play a role in efficiency calculations as well. We smear the energy of the photon with a known *in situ* detector resolution, then accept or reject it according to the energy-dependent photon PID efficiency. Finally, we check if the invariant mass of the surviving photon pairs is still within the π^0 mass window used in the data analysis. For this purpose, the software is rewritten in C to enable easy addition or modification. The efficiency calculation will also be performed in the near future.

*1 Center for Nuclear Study, University of Tokyo
*2 University of São Paulo, Brazil
*3 BNL, USA
*4 Advanced Research Institute for Science and Engineering, Waseda University
*5 Department of Physics, Kyoto University

References
1) PHENIX Conceptual Design Report, BNL (1993) (unpublished).
2) G. David et al.: IEEE Trans. Nucl. Sci. **45**, 692 (1998).
3) P. Chand et al.: PHENIX Technical Notes, BNL (1999) (unpublished).

Theoretical Activity in the RIKEN-BNL Collaboration[†]

T. D. Lee and N. P. Samios

This is the first time the theory division of the RIKEN-BNL Research Center (RBRC) is contributing to the RIKEN Accelerator Progress Report. The RIKEN-BNL Research Center was inaugurated on September 22nd, 1997. It is a joint project of the Institute of Physical and Chemical Research (RIKEN) of Japan and the Brookhaven National Laboratory (BNL) of the United States, dedicated to the research of the strong interaction. The Center is located in the same building with the Physics Department of BNL, and maintains close ties with nearby institutions such as Columbia University in the City of New York, the State University of New York at Stony Brook, the Massachusetts Institute of Technology, as well as with RIKEN and BNL.

The Center aims at promoting young physicists: fellow appointments are for up to five years and postdoc appointments are for two to three years. In addition, several tenure-track positions are created jointly with US universities interested in strong-interaction researches. When the Center started, its theory division hired three postdocs (H. Fujii, M. Wingate and Y. Yasui) and two fellows (D. Kharzeev and D. Rischke). Since then seven more postdocs (D. Boer, S. Sasaki, J. Schaffner-Bielich, Y. Nara, Y. Aoki, K. Itakura and K. Orginos) and two more fellows (T. Blum and W. Vogelsang) have been hired. Nine joint-tenure track fellows (S. Bass, D. Kharzeev, A. Kusenko, A. Schäfer, D. Son, M. Stephanov, B. van Kolck, R. Venugopalan, T. Wettig) also have been appointed. Among the four postdocs who have left (Fujii, Yasui, Sasaki, Wingate), two (Fujii and Sasaki) have gone to take permanent positions in University of Tokyo. A fellow (Kharzeev) became a joint-tenure track fellow and then was tenured at BNL. Another fellow (Rischke) is considering an offer of a full-professorship in Europe. In contrast, all the senior scientists (more than a dozen), including the director and deputy director, are volunteers from Japanese and American institutions.

The activities of the Center cover most sub-fields of strong-interaction physics: phenomenological QCD (quantum chromodynamics), perturbative QCD and lattice QCD. Understanding proton spin is one of the biggest challenges in strong-interaction physics today. Another important frontier lies in the understanding of QCD under extreme conditions such as high temperature and density. In both these frontiers the RBRC members have been quite successful, attacking the problems by both perturbative and lattice methods. Our strength in these two rigorous methods has also attracted many creative phenomenologists.

In the fall of 1998 the RBRC completed a 600 Gflops "QCDSP" parallel super computer in collaboration with Columbia University and BNL. It was awarded the Gordon-Bell Prize at the "Super Computing 98" international symposium in the same year. Since then, a new "RIKEN-BNL-Columbia-KEK" lattice QCD collaboration has been very successfully using this computer and its 400 Gflops sister computer at Columbia University. In particular the collaboration pioneered the application of the five-dimensional domain-wall fermion method in lattice QCD. To follow up, RIKEN, Columbia University and IBM Research agreed to start another collaboration to develop a new parallel computer for lattice QCD capable of 10 Tflops called QCDOC (QCD "On a Chip").

The theory division maintains close cooperation with the BNL theory groups as well as the experiment division of the Center, especially in holding seminars and workshops. Four separate series of weekly seminars are held: (1) Spin Physics, Tuesday, organized jointly with experiment division, (2) High-Energy Theory, Wednesday, organized jointly with BNL high-energy theory group, (3) Nuclear Theory, Friday, organized jointly with BNL nuclear theory group, and (4) RBRC Lunch, Thursday, organized by Rischke (97–98) and Blum (98–00). The Spin Physics series gathers both theory and experiment members. Theory seminars are mainly for exchange of ideas with outside theorists. Lunch seminars are mainly for internal exchange. There have been thirty workshops, all published as proceedings. In addition 150 research papers by RBRC staff scientists have been published. In the following are the summary of our research activities for this year.

† We thank RIKEN and the US Department of Energy

Soft-Gluon Effects in Prompt-Photon Production

W. Vogelsang

Prompt-photon production, $pp, p\bar{p}, pN \to \gamma X$, has been a classical tool for constraining the unpolarized gluon density: a photon can be produced in the reaction $qg \to \gamma q$, giving rise also to a distinct clean signal. Using *polarized* proton beams at RHIC is a very promising method for measuring the nucleon's *spin-dependent* gluon density, Δg, which is currently one of the most interesting quantities in nucleon structure. Figure 1 shows theoretical predictions[1] at the 'next-to-leading-order' level of QCD for the spin asymmetry to be expected at RHIC, for various conceivable Δg.

A pattern of disagreement between theoretical predictions and experimental data for unpolarized prompt-photon production has been observed in recent years. The most serious problems are related to the fixed-target region, where NLO theory dramatically underpredicts some data sets. At collider energies, there is less reason for concern, but also here the agreement is not fully satisfactory. In view of this, various improvements of the theoretical framework have been developed.

'Threshold' resummations have been applied[2] to the inclusive prompt-photon cross section. When the initial partons have just enough energy to produce the high-p_T photon and the recoiling jet, the phase space available for gluon bremsstrahlung vanishes, resulting in large logarithmic corrections to the partonic cross section due to imperfect soft cancelations between real-emission and virtual corrections. Threshold resummation organizes this behavior to all orders in α_s. For prompt photons at fixed-target energies, one finds a significant, albeit not sufficient, enhancement of the theoretical prediction.[2]

If the initial partons, *e.g.*, in the Compton process $qg \to \gamma q$ have a nonzero k_T, the γq *pair* in the final state will acquire a net transverse momentum Q_T, which may make the process softer than it would be otherwise and result in an additional enhancement of the photon p_T spectrum. First applications[3] of this idea simply assumed a Gaussian dependence on k_T and had a marked phenomenological success. On the other hand, they were lacking a solid theoretical framework.

This was provided in Ref. 4, where a simultaneous resummation in both threshold and transverse momentum logarithms was achieved. Contributions to the hard scattering function associated with threshold resummation were redistributed over soft gluon transverse momenta, simultaneously conserving energy *and* transverse momentum. Large logarithmic corrections in Q_T arising in the threshold region were resummed *jointly* with threshold logarithms. The possibility of performing this joint resummation is ensured by the factorization properties of the partonic cross section near threshold. The jointly resummed cross section is shown in Fig. 2. A substantial enhancement is found.

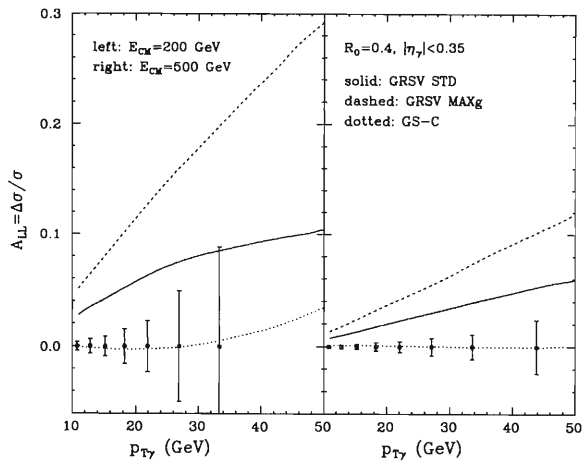

Fig. 1. Double-spin asymmetry for prompt photon production in polarized pp collisions at RHIC.[1]

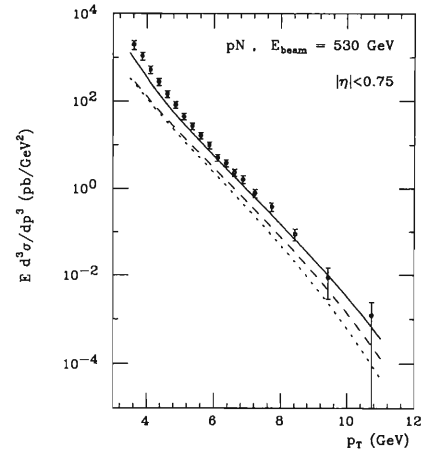

Fig. 2. The prompt-photon cross section at NLO (dotted), with pure threshold resummation (dashed), and with the joint resummation of Ref. 4 (solid). The data are from the E706 experiment.[5]

References

1) S. Frixione and W. Vogelsang: Nucl. Phys. B **568**, 60 (2000); see also, G. Bunce, N. Saito, J. Soffer, and W. Vogelsang: hep-ph/0007218.
2) S. Catani, M. L. Mangano, P. Nason, C. Oleari, and W. Vogelsang: JHEP **9903**, 025 (1999).
3) L. Apanasevich et al.: Phys. Rev. D **59**, 074007 (1999).
4) E. Laenen, G. Sterman, and W. Vogelsang: Phys. Rev. Lett. **84**, 4296 (2000); hep-ph/0010080.
5) E706 Collaboration, L. Apanasevich et al.: Phys. Rev. Lett. **81**, 2642 (1998).

New Understanding of Λ Polarization from Unpolarized Scattering

D. Boer, M. Anselmino*1, U. D'Alesio,*2 and F. Murgia*2

Large asymmetries P_N have been observed in $p+p \to \Lambda^\uparrow + X$ in which the polarization of the Λ is orthogonal to the production plane. Here P_N is defined as

$$P_N = \frac{\sigma(pp \to \Lambda^\uparrow X) - \sigma(pp \to \Lambda^\downarrow X)}{\sigma(pp \to \Lambda^\uparrow X) + \sigma(pp \to \Lambda^\downarrow X)}. \quad (1)$$

The main features of this asymmetry are as follows. The magnitude grows as a function of p_T and $x_F = 2p_L/\sqrt{s}$; above $p_T \approx 1$ GeV it flattens off (for very large p_T it is expected to fall-off completely, but this has not been demonstrated experimentally yet); it is to a large extent $\sqrt{s}$ independent.

Many models exist that try to describe this asymmetry, but none of them allow for a perturbative QCD analysis. However, for large $\sqrt{s}$ and p_T, factorization (see Fig. 1) should hold. The question arises which partonic functions fit into this description, since none of the standard parton distribution and fragmentation functions can generate such asymmetries. Perturbative QCD corrections do not produce large transverse spin effects, since they are proportional to $\alpha_s m_q/\sqrt{\hat{s}}$.

The new proposal[1)] is to use the so-called Polarizing Fragmentation Functions (PFFs).[2)] Such functions describe the fragmentation of an *unpolarized* quark into a transversely polarized hadron (for the case at hand a Λ) plus anything else (Fig. 2). These functions are dependent on the transverse momentum of the Λ compared to the parent quark (orthogonal to the transverse polarization of the Λ); they require final state interactions to be nonzero, but they are allowed by parity and time reversal invariance. It is crucial to note that the polarization only arises in the final state; the initial state only determines the relative amounts of u, d, s quarks, that fragment into the final state. This picture should apply to the current (not to the target) fragmentation region and hence, generates different signatures from for example recombination models.

If fitted in one experiment, the PFFs can be used to predict other observables. Thus the proposed approach is model independent, since it is a factorized description. The polarizing fragmentation effect itself can in principle be modeled, but in any case one does not need to model the process(es) as a whole. This is a huge gain in predictive power.

So far only cross section expressions in terms of the PFFs had been given.[2–4)] Recently the first quantitative study has been performed:[1)] the fit to the P_N data using the PFFs has yielded very good results: reasonable functions were obtained, all qualitative features of the asymmetry were reproduced, including the fact that the asymmetry for $\overline{\Lambda}$ is consistent with zero. These fits will allow to make predictions for near future data and this is in progress.

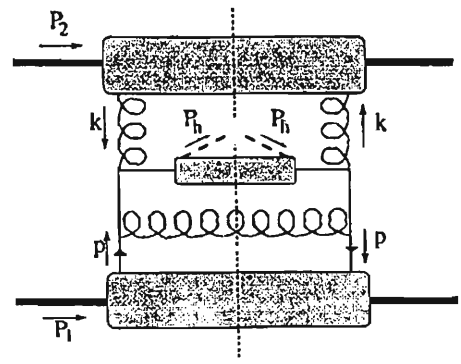

Fig. 1. A factorized diagram contributing to P_N.

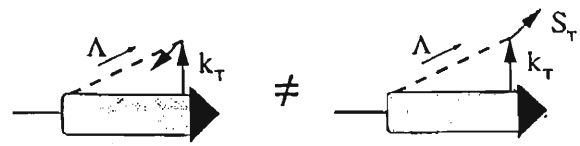

Fig. 2. Nonzero PFF: $(q \to \Lambda^\uparrow(k_T)X) \neq (q \to \Lambda^\downarrow(k_T)X)$.

One near future experimental prospect is that HERMES and COMPASS could measure semi-inclusive DIS[3)] ($\ell p \to \ell' \Lambda^\uparrow X$) in the current fragmentation region. The other important near future option is the BNL-RHIC collider, which can reveal whether $P_N \neq 0$ persists at even larger values of $\sqrt{s}$ and whether it indeed falls off at high p_T. We note that at RHIC energies the scale in the PFFs themselves need not be high (of order p_T), unlike the case of $e^+e^- \to Z \to \Lambda^\uparrow$ jet X, where ALEPH and OPAL have measured transverse polarization to be small (percent level). This could be seen as an indication that the PFFs decrease with energy. Finally, it is worth mentioning that in principle one would also be able to measure P_N in pA or $AA \to \Lambda^\uparrow X$ at RHIC.

*1 Department of Theoretical Physics, University of Torino, Italy
*2 INFN/Department of Physics, University of Cagliari, Italy

References

1) M. Anselmino, D. Boer, U. D'Alesio, and F. Murgia: Phys. Rev. D **63** 054029 (2001); hep-ph/0010291.
2) P. J. Mulders and R. D. Tangerman: Nucl. Phys. B **461**, 197 (1996).
3) D. Boer, R. Jakob, and P. J. Mulders: Nucl. Phys. B **564**, 471 (2000).
4) D. Boer, R. Jakob, and P. J. Mulders: Nucl. Phys. B **504**, 345 (1997); Phys. Lett. B **424**, 143 (1998).

Hard QCD and RHIC Spin Physics

Y. Yasui

The RHIC Spin Physics Project plans to conduct experiments on high-energy polarized pp collision. A 70% polarization of beams and the highest energy of $\sqrt{s} = 500\,\mathrm{GeV}$ at the center of mass system are expected to be realized. The main aim of this Project is to study the origins of the nucleon spin. The Project will provide useful information on the proton spin structure.[1] For example, the gluon component in the polarized proton will be investigated by analyzing the single-photon production process ($pp \to \gamma + X$) and the jets production processes ($pp \to Jets + X$). It is widely believed that the gluon component in the polarized proton plays an essential role in causing the spin crisis problem of the proton spin structure function g_1.

In the parton model, the cross section of the high-energy pp collision is factorized into soft QCD parts (distribution functions and fragmentation functions) and hard QCD parts (cross sections of partonic subprocesses). The nature of the asymptotic freedom makes it possible to analyze the hard parts within the framework of the perturbation theory. As in previous examples, perturbative QCD (pQCD) calculations of the jets production processes are necessary to investigate the spin structure of the proton.

These pQCD calculations have conventionally been carried out using Feynman rules and Feynman diagrams. However calculations for jets production processes often require a large number of Feynman diagrams. To make matter worse, due to the complicated structure of the gauge boson interactions, the calculations are extremely difficult even at lowest order of the perturbation theory (tree level).

Recently, we have seen much progress in the methods of perturbative calculations.[2] Mangano and Parke[3] developed methods for simplifying multijets amplitudes at the tree level. In their methods, they categorized the color structure and the helicity of the initial and final particles. Then, they decomposed the full amplitudes into color-ordered subamplitudes which are described by the spinor helicity basis. They also introduced a new technique using supersymmetry. There were also several breakthroughs on the higher order pQCD calculations. Bern and Kosower[4] introduced a new technique for computing the one-loop-level pQCD amplitude, which is called the string-inspired method and/or the Bern-Kosower rule. The idea is based on the superstring theory. The background field gauge is another powerful method. In this gauge, we can construct the gauge-invariant effective action, which is invariant under the gauge transformation of the classical background field.

In this Project, we are conducting a theoretical study on RHIC Spin Physics. In particular, we are focusing our attention on the hard QCD parts of the jets production processes at the high-energy polarized pp collision. Because of the relatively large value of the QCD coupling constant, higher order corrections are not negligible in the pQCD analysis. However, the non-Abelian structure of the gauge boson coupling and the large number of Feynman diagrams make higher order calculations increasingly difficult. In Ref. 2, we pointed out that the combination of the background field gauge, the color decomposition and the spinor helicity basis is a very powerful method for loop calculations in pQCD. This method simplifies the Feynman rules and reduces the number of intermediate terms and Feynman diagrams required for the calculations. The simplification has been demonstrated in an example of a five-gluon amplitude at the one loop-level ($gg \to ggg$). This is one of the most difficult parts in the calculation of the next to leading order contribution for the three jets production processes.[5] As a simplest example, we show a result of the one-loop-level color-ordered five-gluon amplitude in the maximal-helicity-violating case (the polarizations of all external gluons are $+1$),[2,3]

$$m_{5;1}^{(MHV)} = \frac{i(\sqrt{2})^5 N}{96\pi^2} \frac{1}{\langle 12\rangle\langle 23\rangle\langle 34\rangle\langle 45\rangle\langle 51\rangle} \times [s_{12}s_{23} + s_{23}s_{34} + s_{34}s_{45} + s_{45}s_{51} + \epsilon(1,2,3,4)],$$

where $s_{ij} = 2l_i \cdot l_j$ and $\epsilon(ijkm) = i4\epsilon_{\mu\nu\rho\sigma} l_i^\mu l_j^\nu l_k^\rho l_m^\sigma$. Here, l_i are external gluon momenta. We also use the notation for the spinor helicity basis $\langle ij\rangle = \sqrt{s_{ij}} e^{i\theta_{ij}}$. Here, θ_{ij} is the phase factor[2] and N is the color factor ($N = 3$ for the QCD theory).

In these analyses, we also use computer programs written by analytical manipulation programs, namely, FORM and MAPLE. These programs are widely applicable to pQCD analysis. For example, we can apply these programs immediately to processes which include massless fermions (Ex; $q\bar{q} \to ggg$, $q\bar{q} \to gg\gamma$, etc). The extension of these techniques and methods to theories with a spontaneously broken symmetry such as the electroweak theory is straightforward.

References

1) G. Bunce, N. Saito, J. Soffer, and W. Vogelsang: hep-ph/0007218, ISSN 1344-3879, RIKEN-AF-NP-360, and references therein.
2) Y. Yasui: Phys. Rev. D **61**, 094502 (2000), and references therein.
3) M. Mangano and S. Parke: Phys. Rep. **200**, 301 (1991), and reference therein.
4) Z. Bern and D. A. Kosower: Phys. Rev. Lett. **66** 1669 (1991); Nucl. Phys. B **379**, 451 (1992).
5) Z. Bern, L. Dixon, and D. A. Kosower: Phys. Rev. Lett. **70**, 2677 (1993).

Single Spin Asymmetries in Inclusive Hadronic Reactions

Y. Koike and Y. Kanazawa*

Single transverse-spin asymmetries for large p_T pion production in pp collisions have been receiving considerable attention since the large asymmetry was reported by the FNAL E704 group.[1] An ongoing experiment at RHIC is expected to provide more data on the asymmetry. The process probes particular quark-gluon correlations (higher twist effect) in the nucleon not included in twist-2 parton densities. According to the generalized QCD factorization theorem,[2] the polarized cross section for this process consists of three types of twist-3 cross sections: (A) $G_a(x_1', x_2') \otimes q_b(x) \otimes D_{c\to\pi}(z) \otimes \hat{\sigma}_{ab\to c}$, (B) $\delta q_a(x') \otimes E_b(x_1, x_2) \otimes D_{c\to\pi}(z) \otimes \hat{\sigma}'_{ab\to c}$, and (C) $\delta q_a(x') \otimes q_b(x) \otimes D^{(3)}_{c\to\pi}(z_1, z_2) \otimes \hat{\sigma}''_{ab\to c}$. Here, the functions $G_a(x_1', x_2')$, $E_b(x_1, x_2)$ and $D^{(3)}_{c\to\pi}(z_1, z_2)$ are the twist-3 quantities representing, respectively, the transversely polarized distribution, the unpolarized distribution, and the fragmentation function for the pion, and a, b and c stand for the parton's species. Other functions are twist-2 quantities; $q_b(x)$ the unpolarized distribution (quark or gluon), $\delta q_a(x)$ the transversity distribution, and $D_{c\to\pi}(z)$ the fragmentation function for the pion. The symbol $\otimes$ denotes convolution. $\hat{\sigma}_{ab\to c}$ *etc.* represents the partonic cross section for the process $a + b \to c + anything$ which yields large transverse momentum of parton c. Note that δq_a, E_b and $D^{(3)}_{c\to\pi}$ are chiral-odd.

Qiu and Sterman[3] reported on a systematic QCD analysis of the chiral-even contribution (above (A)). They showed that the (A) term dominates the cross section at large x_F, *i.e.*, pion production in the forward direction with respect to the polarized nucleon beam. Within the valence quark-soft gluon approximation and a model assumption for the valence twist-3 distribution G_a, they reproduced the E704 data reasonably well. In a recent paper,[4] we extended the analysis to one of the chiral-odd contributions ((B) term) and presented a cross-section formula. We also discussed the possibility that this term could be a large source of the asymmetry at large *negative* x_F in parallel with the argument for the chiral-even contribution. It turns out, however, that the (B) term is negligible in *all* kinematic region due to the smallness of the hard cross section, even though the unpolarized twist-3 distribution E_b receives a significant enhancement.[5]

There is another chiral-odd contribution ((C) term) to the asymmetry. In this term, $\delta q_a(x')$ and $D^{(3)}_{c\to\pi}$ can form a closed Fermion loop in the Feynman diagram; therefore, there is no apparent reason for the corresponding hard cross section to be suppressed unlike the case for the (B) term. In addition, the (C) term receives the contribution from the gluon distribution. It is expected to give rise to a large asymmetry at large $x_F \to 1$ as in the case for the (A) term. The analysis of this term is under way.

It is also a well-known experimental fact that hyperons produced in unpolarized nucleon-nucleon collisions are polarized transversely to the production plane.[6] This is also a twist-3 process and its cross section consists of two types of twist-3 cross section: (D) $E_a(x_1, x_2) \otimes q_b(x') \otimes \delta\hat{q}_{c\to Y}(z) \otimes \hat{\sigma}_{ab\to c}$, and (E) $q_a(x) \otimes q_b(x') \otimes \hat{G}^{(3)}_{c\to Y}(z_1, z_2) \otimes \hat{\sigma}'_{ab\to c}$. Here, the new functions $\hat{G}^{(3)}_{c\to Y}(z_1, z_2)$ and $\delta\hat{q}_{c\to Y}(z)$ are the twist-3 fragmentation function and the transversity fragmentation function for the transversely polarized hyperon, respectively.

In our recent analysis,[7] we presented a cross-section formula for the (D) contribution and estimated its magnitude, following the valence quark-soft gluon approximation.[3-5] As expected, it gives rise to a large hyperon polarization at large x_F comparable to the experimental data.[6] Anselmino *et al.* analyzed the same process under the assumption that the spin effect in the fragmentation process (similar to the (E) contribution) is the sole origin of the hyperon polarization.[8] Our analysis shows that (D) should also be considered to fully account for the polarization.

References

1) D. L. Adams et al.: Phys Lett. B **261**, 201 (1991); Phys. Lett. B **264**, 462 (1991); A. Bravar et al.: Phys. Rev. Lett. **77**, 2626 (1996).
2) J. C. Collins, D. E. Soper, and G. Sterman: in *Perturbative Quantum Chromodynamics*, edited by A. H. Mueller, (World Scientific, Singapore, 1989), p.1; J. Qiu and G. Sterman: Nucl. Phys. B **353**, 137 (1991).
3) J. Qiu and G. Sterman: Phys. Rev. D **59**, 014004 (1999).
4) Y. Kanazawa and Y. Koike: Phys. Lett. B **478**, 121 (2000).
5) Y. Kanazawa and Y. Koike: Phys. Lett. B **490**, 99 (2000).
6) G. Bunce et al.: Phys. Rev. Lett. **36**, 1113 (1976); K. Heller et al.: Phys. Rev. Lett. **41**, 607 (1978); E. J. Ramberg et al.: Phys. Lett. B **338**, 403 (1994); P. M. Ho et al.: Phys. Rev. Lett. **65**, 1713 (1990); A. Morelos et al.: Phys. Rev. Lett. **71**, 2172 (1993).
7) Y. Kanazawa and Y. Koike: hep-ph/0012225.
8) M. Anselmino, D. Boer, U. D'Alesio, and F. Murgia: hep-ph/0008186.

* Department of Physics, Niigata University

Gluon Distribution in the Real Photon

M. Imoto*[1] and F. Kawane*[2]

The structure function of a photon has been investigated via deep inelastic electron-photon ($e-\gamma$) scattering. Experimentally, information regarding this function is extracted from the process ($e^+e^- \to e^+e^-$ hadrons). The parton distributions of the photon consist of contributions corresponding to a hadron-part and a point-part of the photon. The hadron-part of the parton distributions for low $Q^2 \leq 1\,\mathrm{GeV}^2$ are represented by the nonperturbative model. The distributions for low Q^2 evolve according to the next-to-leading order Dokshitzer, Gribov, Lipatov, Altarelli and Parisi (NLO-DGLAP) equations. Also, the photon structure function is sensitive to the gluon distribution only at small x, so the shape of the gluon distribution should be determined from data at small x. In Ref. 1, the vector meson dominance model (VMD) is assumed for the photonic input distributions, and the approximate similarity of the vector meson and the pion is utilized. For the photonic input distributions $f^\gamma = q^\gamma (= q^{-\gamma})$, G^γ, we take $f^\gamma(x, q_0^2) = \kappa \frac{4\pi\alpha}{f_\rho^2} f_\pi(x, Q_0^2)$, where the inclusion of the ω and φ mesons in addition to the ρ is indicated by the value of κ. In the valence quark distribution, Regge behavior amplitude is used at small x. However, we express the input distributions of the gluon and the sea quark in the Pomeron exchange cut rather than the Pomeron exchange as follows,

$$xG(x) = b\left(\frac{x^{1-\alpha_C(0)}}{\ln(1/x)}\right)(1-x)^3,$$

$$x\zeta(x) = c\left(\frac{x^{1-\alpha_C(0)}}{\ln(1/x)}\right)(1-x)^5,$$

where $\alpha_C(t) = \{\alpha_P(t) + \alpha_P(t) - 1\}$ gives the position of the branch point trajectory. Taking $\alpha_P(0) \simeq 1.08$, we observe Lipatov behavior[2] $x^{-\lambda}$. The $1/\ln(1/x)$ term arises from the integral over the phase between the two Pomeron-Pomeron poles. Therefore, using Pomeron-cut exchange, we represent the situation where many soft gluon emissions appear at small x and the rise in small x is generated as a result. Also, the $O(Q^2)$ term for the point-like parts of parton distributions is introduced in the framework of NLO-DGLAP equation. Using the above distributions we have shown[1] that predictions for the photon structure function are consistent with experimental data[3] in OPAL at small x. Here, this approach is used in order to investigate the behavior of gluon distribution. In Fig. 1, the x dependence of $xG(x, Q^2)$ is shown at $Q^2 = 100\,\mathrm{GeV}^2$. The solid curve is our result enhanced by a factor $\kappa = 1.0$, and the dashed curve is enhanced by $\kappa = 1.6$ for the photonic input distributions at Q_0^2. Our result with $\kappa = 1.6$ approaches the Glück, Reya and Vogt (GRV) predictions[4] ($\kappa = 1.6$), which are steep in the small x region. Thus we can say that the hadronic component is dominant at very small x. In Fig. 2, we compare the x dependence of our gluon distribution with H1 measurements.[5] Our result is similar to the gluon of SaS 1D[6] and shows the flatter small-x behaviour compared to GRV.[4]

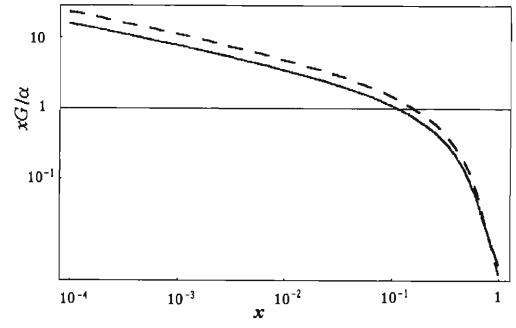

Fig. 1. Small-x behavior for $xG(x)$ at $Q^2 = 100\,\mathrm{GeV}^2$. The solid curve is our result with $\kappa = 1.0$ and the dashed curve is our result with $\kappa = 1.6$.

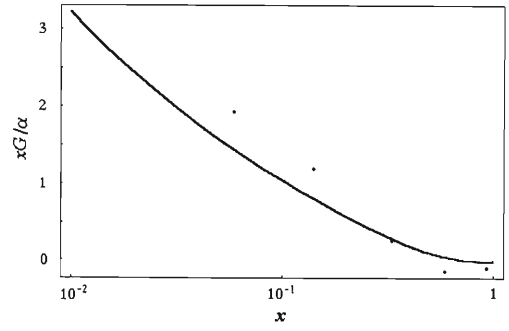

Fig. 2. Prediction for $xG(x)$ at $Q^2 = 75\,\mathrm{GeV}^2$ with HERA (H1) measurements.

*1 College of Science and Technology, Nihon University
*2 Junior College Funabashi Campus, Nihon University

References
1) M. Imoto, H. Kan, and T. Kikuchi: Prog. Theor. Phys. **102**, 819 (1999).
2) L. N. Lipatov: Sov. J. Phys. **23**, 338 (1976); E. A. Kuraev, L. N. Lipatov, and V. S. Fadin: Sov. Phys. JETP **45**, 199 (1977); Y. Balitskii and L. N. Lipatov: Sov. J. Nucl. Phys. **28**, 822 (1978).
3) OPAL Collab., K. Ackerstaff et al.: Phys. Lett. B **412**, 225 (1997).
4) M. Glück and E. Reya: Phys. Rev. D **26**, 2749 (1983); M. Glück, E. Reya, and A. Vogt: Phys. Rev. D **46**, 1973 (1992).
5) H1 Collaboration, T. Ahmed et al.: Nucl. Phys. B **445**, 195 (1995).
6) G. A. Schuler and T. Sjostrand: Z. Phys. C **68**, 607 (1995).

Semi-inclusive Λ_c^+ Production in Polarized *ep* Reaction with Polarized Gluons

S. Oyama,[*1] H.-W. Huang,[*2] and T. Morii

To understand the spin structure of a nucleon in quantum chromodynamics (QCD), it is very important to obtain information on the polarized gluon distribution. Although thus far we have good knowledge of polarized quarks based on the data from numerous polarized experiments and detailed QCD calculations, information on polarized gluons is still lacking. High-energy polarized experiments which are planned, for instance, at eRHIC, are expected to be useful for studying polarized gluons.

To investigate the behavior of polarized gluons, we propose a new semi-inclusive process $e\vec{p} \rightarrow e\vec{\Lambda}_c^+ X$, which can be studied in the forthcoming eRHIC experiment and is very useful for studying polarized gluons. Λ_c^+ consists of u, d and c quarks in a naive quark model, in which the spin wave functions of u and d quarks are antisymmetrically combined and then the spin of Λ_c^+ is the same as that of the c quark. Therefore, we can expect that the spin of Λ_c^+ largely depends on that of the c quark in the hard process. Furthermore, the c quark is produced with a $\bar{c}$ by boson-gluon fusion in the lowest order of QCD. Therefore, one expects that this process can provide rich information on the polarized gluon in the proton. By assuming the helicity of the produced c quark is preserved by hadronizing the c quark to Λ_c^+, we calculated the spin-dependent differential cross section in the lowest order of QCD for $e\vec{p} \rightarrow e\vec{\Lambda}_c^+ X$ and the two-spin correlation asymmetry,

$$A_{LL} = \frac{d\sigma_{++} - d\sigma_{+-} + d\sigma_{--} - d\sigma_{-+}}{d\sigma_{++} + d\sigma_{+-} + d\sigma_{--} + d\sigma_{-+}} = \frac{d\Delta\sigma/dydz}{d\sigma/dydz},$$

where $d\sigma_{+-}$ is the spin-dependent differential cross section for the proton with a positive helicity and the Λ_c^+ with a negative one, and y and z are dimensionless variables used in semi-inclusive deep inelastic scattering. In this calculation, we used the typical parameterization models of the polarized gluon distribution, namely, GS96 set(A)[1] and GRSV96,[2] together with the unpolarized model of GRV95.[3]

The case of the photon-gluon fusion was calculated before at $\sqrt{s} = 50\,\mathrm{GeV}$.[4] Here, we took into account the Z_0 interaction as well as the photon interaction, foreseeing high energy polarized experiments.

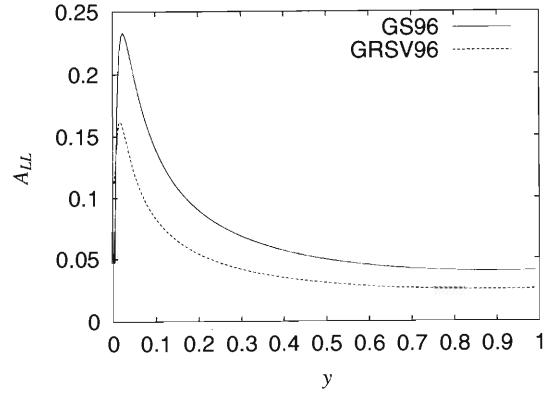

Fig. 1. Two-spin correlation asymmetry, A_{LL}, between the polarized proton and Λ_c^+ at $\sqrt{s} = 100\,\mathrm{GeV}$ and $z = 0.1$. The solid and dashed curves indicate GS96 set(A) and GRSV96, respectively.

Figure 1 shows the calculated result of the two-spin correlation asymmetry, A_{LL}, between the polarized proton and the produced Λ_c^+ at $\sqrt{s} = 100\,\mathrm{GeV}$ and $z = 0.1$, whose energy is planned in the future eRHIC experiment. In Fig. 1, it is evident that the asymmetry largely depends on the models of the polarized gluon distribution in some kinematical region, i.e., the asymmetry is sensitive to the models of the polarized gluon distribution. Therefore, the process we propose here could be useful in testing the models of the polarized gluon distribution, thus providing rich information on the structure of the proton.

References

1) T. Gehrmann and W. J. Stirling: Phys. Rev. D **53**, 6100 (1996).
2) M. Glück, E. Reya, M. Stratmann, and W. Vogelsang: Phys. Rev. D **53**, 4775 (1996).
3) M. Glück, E. Reya, and A. Vogt: Z. Phys. C **67**, 433 (1995).
4) N. I. Kochelev, T. Morii, and S. Oyama: RIKEN Accel. Prog. Rep. **33**, 35 (2000).

*1 Graduate School of Science and Technology, Kobe University
*2 Faculty of Human Development, Kobe University

Single Diffractive Λ_c^+ Productions at Relative Heavy Ion Collider: A Test of Hard Diffractive Factorization and Polarized Gluon Distribution Function

K. Ohkuma*1 and T. Morii*1,*2

Studing the nature of a pomeron which plays a crucial role in diffractive scattering remains a challenging topic. To understand the diffractive process in the framework of Quantum Chromodynamics (QCD), Ingelman and Schlein suggested[1] that by assuming that the pomeron has a partonic structure, the observables of the diffractive process can be calculated by a hard diffractive factorization approach, *i.e.*, the diffractive structure function is given in the factorized form of the pomeron flux and the pomeron structure function. However, the predicted cross sections by the hard diffractive factorization approach for hadron-hadron collisions are several times larger than the experimental data.[2] In order to overcome such inconsistency, Goulianos proposed a phenomenological model.[2] In this model, he introduced a renormalized pomeron flux factor which is generated by renormalizing the standard pomeron flux in a proton to be unity (renormalized pomeron flux model).[2] Further tests using this model for various processes are interesting.

The RHIC experiment will commence soon. One of the important objectives of this experiment is to extract information about the polarized gluon distribution in the proton. The obtained information will be the key to understand the proton spin puzzle. Thus far, there are many models which can excellently reproduce experimental data on the polarized structure function of nucleons. However, the behavior of polarized gluons are quite different among those models. It is interesting to test the models of the polarized gluon distribution in the forthcoming RHIC experiments.

In this work, to test the hard diffractive factorization and polarized gluon distribution model, we propose another diffractive semi-inclusive process: $p+\vec{p} \rightarrow$

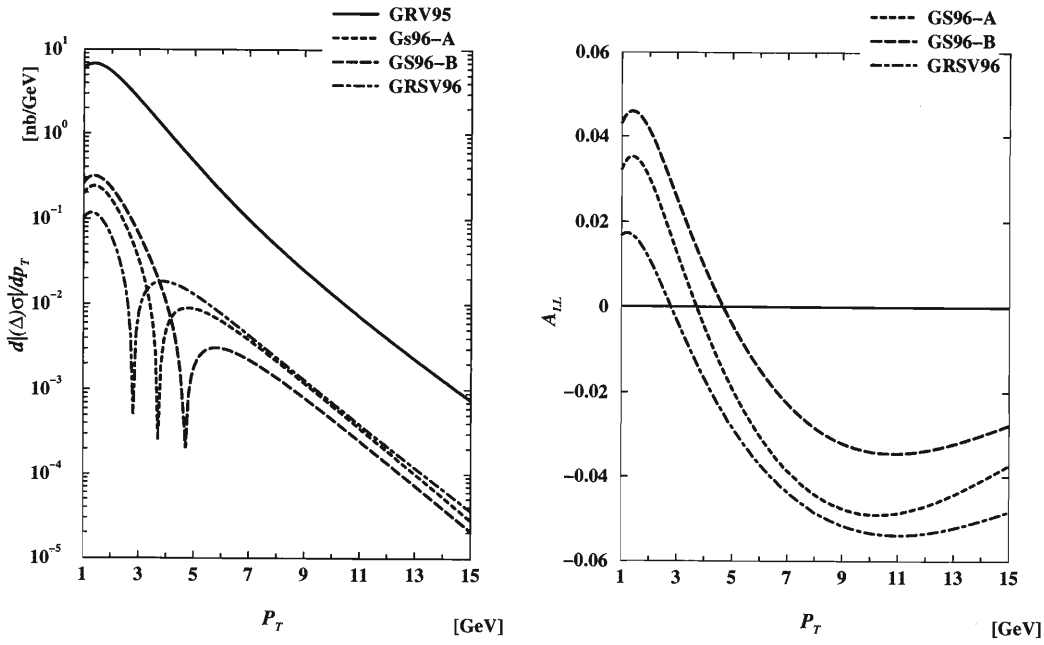

Fig. 1. The unpolarized and polarized differential cross sections (left panel) and the spin-correlation asymmetry (right panel) as a function of p_T at $\sqrt{s} = 500\,\mathrm{GeV}$. The solid line in the left panel represents the unpolarized differential cross section with the GRV95 model for the unpolarized gluon distribution. The dashed, long-dashed and dot-dashed lines indicate the polarized differential cross section calculated using the sets A and B of the GS96 model and the GRSV96 model, respectively, for the polarized gluon distribution. The value of $\frac{d\Delta\sigma}{dp_T}$ is negative for p_T and is larger than the value corresponding to the apparent sharp dip.

*1 Graduate School of Science and Technology, Kobe University
*2 Faculty of Human Development, Kobe University

$p + \vec{\Lambda}_c^+ + X$. We have already analyzed this process in the large p_T region with interesting results.[3)]

In this process, we calculated the spin-correlation differential cross section, $d\Delta\sigma/dp_T$ using the renormalized pomeron flux model and the spin-correlation asymmetry, A_{LL}, defined by

$$\frac{d\Delta\sigma}{dp_T} \equiv \frac{d\sigma_{++} - d\sigma_{+-} + d\sigma_{--} - d\sigma_{-+}}{dp_T},$$

$$A_{LL} \equiv \frac{[d\sigma_{++} - d\sigma_{+-} + d\sigma_{--} - d\sigma_{-+}]/dp_T}{[d\sigma_{++} + d\sigma_{+-} + d\sigma_{--} + d\sigma_{-+}]/dp_T} \equiv \frac{d\Delta\sigma/dp_T}{d\sigma/dp_T},$$

where $d\sigma_{+-}$ denotes the spin-dependent differential cross section with the positive helicity of the target proton and the negative helicity of the produced Λ_c^+. $d(\Delta)\sigma/dp_T$ and A_{LL} will be measured in the forthcoming RHIC experiment. To calculate $d\Delta\sigma/dp_T$ and A_{LL}, we used the GS96[4)] and GRSV96[5)] parameterization models for the polarized gluon distribution function and the GRSV95[6)] model for the unpolarized one.

The p_T distribution of $d(\Delta)\sigma/dp_T$ and A_{LL} for $\sqrt{s} = 500\,\mathrm{GeV}$ are shown in Fig. 1. As shown here, $d\Delta\sigma/dp_T$ and A_{LL} are sensitive to the polarized gluon distribution functions. Note that if the renomalized pomeron flux model is not taken into account in the present process, the polarized diffential and the unpolarized diffential cross sections become several times larger than our calculation. This means that measuring these observables can be a test of the renormalized pomeron flux model. Therefore, the process might be effective for testing not only the hard diffractive factorization but also the polarized gluon distribution function.

References

1) G. Ingelman and P. E. Schlein: Phys. Lett. B **152**, 256 (1985).
2) K. Goulianos: Phys. Lett. B **358**, 379 (1995).
3) K. Ohkuma, K. Sudoh, and T. Morii: hep-ph/0009004.
4) T. Gehrmann et al.: Phys. Rev. D **53**, 6100 (1996).
5) M. Glück et al.: Phys. Rev. D **53**, 4775 (1996).
6) M. Glück et al.: Z. Phys. C **67**, 433 (1995).

Polarized s-Quark Distribution in Semi-Inclusive Λ_c^+ ($\bar{\Lambda}_c^+$) Production

K. Sudoh*

The proton spin puzzle is currently one of the most challenging topics in high-energy spin physics. As is well known, a proton spin is composed of the spins and the orbital angular momenta of quarks and gluons which constitute a proton. The polarized parton distribution function plays an important role in an in-depth description of the spin structure of a proton. However, the polarized sea quark distribution functions remain now poorly clarified.

Recently, the HERMES group has reported that direct measurement of the strange sea is required to explain the violation of the Ellis-Jaffe sum rule.[1] However, we do not have sufficient knowledge to determine the polarized sea quark distribution. Here, I focus on the polarized s or $\bar{s}$ quark distribution.

In this work, to examine the polarized s ($\bar{s}$) quark distribution, I studied semi-inclusive Λ_c^+ and $\bar{\Lambda}_c^+$ leptoproduction, $e^+ + \vec{p} \to \bar{\nu}_e + \vec{\Lambda}_c^+ + X$ and $e^- + \vec{p} \to \nu_e + \vec{\bar{\Lambda}}_c^+ + X$, in unpolarized lepton-polarized proton collisions which might be observed in the forthcoming experiments at e-RHIC or TESLA-$\vec{N}$, where the arrow attached to particles indicates that these particles are polarized. In the naive quark model, since the Λ_c^+ baryon is composed of a heavy c-quark and antisymmetrically combined light u- and d-quarks, we can assume that the polarization of the Λ_c^+ baryon is the polarization of the c-quark. In addition, Λ_c^+ ($\bar{\Lambda}_c^+$) is dominantly produced by the fragmentation of c ($\bar{c}$)-quark which is produced by s ($\bar{s}$)-quark through the t-channel W exchange in the leading order. Hence we can expect that measurement of the produced Λ_c^+ polarization will provide information about the polarized s-quark distribution in a proton.

In these processes, I calculated the double spin asymmetry A_{LL} defined by

$$A_{LL}(p_T) = \frac{d\Delta\sigma/dp_T}{d\sigma/dp_T}, \tag{1}$$

where

$$d\Delta\sigma = \frac{1}{4}\left[d\sigma_{++} - d\sigma_{+-} + d\sigma_{--} - d\sigma_{-+}\right].$$

For instance, in the Λ_c^+ production, the spin-dependent differential cross section generally has a form,

$$d\Delta\sigma(\Lambda_c^+) = \left\{U_{cs}^2 \Delta s(x) + U_{cd}^2 \Delta d(x)\right\} dx \times \left(\frac{d\Delta\hat{\sigma}}{d\hat{t}}\right) d\hat{t} \Delta D_c^{\vec{\Lambda}_c^+}(z) dz, \tag{2}$$

where $\Delta s(x)$ and $\Delta d(x)$ are polarized s-quark and d-quark distribution functions, respectively. Here, I used the GS96[2] (set A) and GRSV96[3] ("standard scenario") parameterizations for the polarized parton distribution. $\Delta D_c^{\vec{\Lambda}_c^+}(z)$ is the polarized fragmentation function and I used the Peterson model,[4] assuming $\Delta D_c^{\vec{\Lambda}_c^+}(z) \simeq D_c^{\vec{\Lambda}_c^+}(z)$.

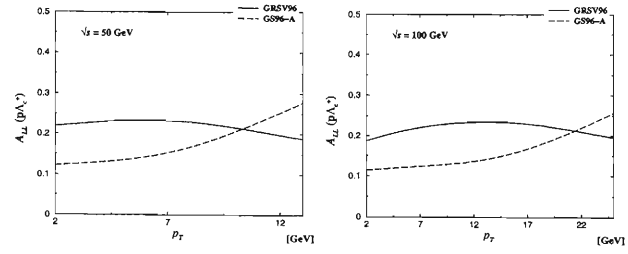

Fig. 1. Double spin asymmetry in $e^+ + \vec{p} \to \bar{\nu}_e + \vec{\Lambda}_c^+ + X$ as a function of p_T at $\sqrt{s} = 50\,\text{GeV}$ (left) and $\sqrt{s} = 100\,\text{GeV}$ (right). Solid and dashed lines represent the "standard scenario" of GRSV96 and set A of GS96, respectively.

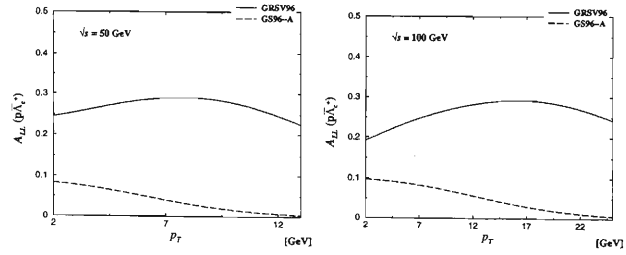

Fig. 2. Double spin asymmetry in $e^- + \vec{p} \to \nu_e + \vec{\bar{\Lambda}}_c^+ + X$ as a function of p_T at $\sqrt{s} = 50\,\text{GeV}$ (left) and $\sqrt{s} = 100\,\text{GeV}$ (right). Lines indicate the same cases as in Fig. 1.

The p_T distribution of A_{LL} in the Λ_c^+ production and the $\bar{\Lambda}_c^+$ production at center-of-mass energy $\sqrt{s} =$ 50–100 GeV are shown in Fig. 1 and Fig. 2, respectively. As shown in the figures, A_{LL} in the $\bar{\Lambda}_c^+$ production largely depends on the models of the polarized parton distribution function, and significant differences can be observed among them. Therefore, I conclude that measuring the double spin asymmetry in this process is very effective not only for testing the model of the parton distribution function but also for extracting the polarized strange sea distribution clearly. On the other hand, for Λ_c^+ production we cannot determine the s-quark distribution clearly, since the contribution from the valence d-quark is large.

* Graduate School of Science and Technology, Kobe University

References

1) HERMES collaboration: Phys. Lett. B **464**, 123 (1999).
2) T. Gehrmann and W. J. Stirling: Phys. Rev. D **53**, 6100 (1996).
3) M. Glück et al.: Phys. Rev. D **53**, 4775 (1996).
4) C. Peterson et al.: Phys. Rev. D **27**, 105 (1983).

Polarized Gluon Distributions from High-p_T Pair Charmed Hadron Leptoproductions

Y.-B. Dong,[*1] T. Morii,[*2] and T. Yamanishi[*3]

Recently, new parametrization sets of the polarized parton distribution functions (pol-PDFs) were obtained from the fitting of polarized deep inelastic scattering (pol-DIS) with high precision for various targets to experimental data.[1] However, knowledge of the behavior of polarized sea quarks and gluons is still limited because it is difficult to directly obtain such information. Thus far, some interesting proposals for studying longitudinally polarized distributions of sea quarks and gluons have been presented.[2,3] For the measurement of the polarized sea quark distribution, several researchers suggest the use of Drell-Yan processes,[2] W-boson productions and the semi-inclusive processes[3] in polarized experiments. For the polarized gluon distribution, some interesting processes are also proposed: direct prompt photon production in polarized proton-polarized proton collisions, open charm and J/ψ-pair production[4] in polarized lepton scattering off-polarized nucleon targets. Recently, the HERMES group at DESY reported the first measurement of the polarized gluon distribution by di-jet analysis of semi-inclusive processes in pol-DIS, although only one data point is given as a function of Bjorken x.[5]

Here, we extend the di-jet analysis of semi-inclusive processes for any hadron pair productions to the charmed hadron pair production in order to obtain accurate information on the polarized gluon distribution in the nucleon. In general, the high-p_T hadron pair production is given by photon-gluon fusion (PGF) and QCD compton at the lowest order of QCD (Fig. 1). The PGF gives us direct information on the polarized gluon distribution in the nucleon, while QCD compton becomes a background to the signal process for extracting the polarized gluon distribution. Here, we consider charmed hadron pair production as the high-p_T hadron pair production since we can safely neglect the contributions of the QCD compton process for heavy-quark pair productions.

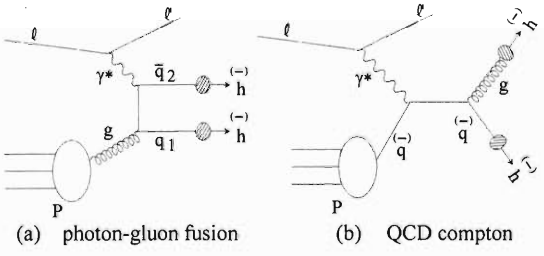

Fig. 1. Lowest-order Feynman diagrams for the high-p_T pair hadron production.

The double-spin asymmetry for a process of $\gamma^* + N \to h_c + \bar{h}_{\bar{c}} + X$ is described as

$$A_{LL} = \frac{d\sigma_{-+} - d\sigma_{++}}{d\sigma_{-+} + d\sigma_{++}} = \frac{d\Delta\sigma}{d\sigma}, \tag{1}$$

where $d\sigma_{-+}$ denotes the cross section for the lepton and nucleon with negative and positive helicities, respectively. The polarized differential cross section can be calculated by

$$\frac{d^3\Delta\sigma}{d\eta dz_1 dz_2} = \Delta g(\eta, Q^2) \int_{z_1}^1 \frac{d\xi_1}{\xi_1} \int_{z_2}^1 \frac{d\xi_2}{\xi_2} \frac{d^3\Delta\hat{\sigma}}{d\eta dz_c dz_{\bar{c}}} \times D_c^{h_c}(\xi_1) D_{\bar{c}}^{\bar{h}_c}(\xi_2), \tag{2}$$

where

$$\eta = \frac{\hat{s}}{s}, \quad z_1 = \frac{P \cdot p_1}{P \cdot q}, \quad z_2 = \frac{P \cdot p_2}{P \cdot q}, \tag{3}$$

and at the partonic level,

$$z_c = \frac{P \cdot p_q}{P \cdot q} = \frac{z_1}{\xi_1}, \quad z_{\bar{c}} = \frac{P \cdot p_{\bar{q}}}{P \cdot q} = \frac{z_2}{\xi_2}. \tag{4}$$

In Eq. (2), Δg and $D_{c(\bar{c})}^{h_c(\bar{h}_c)}$ denote the longitudinally polarized gluon distribution and fragmentation functions from a charmed quark to a charmed hadron, respectively. Here, we take the D^{*+-} meson as the charmed hadron because its fragmentation function has been recently studied extensively.[6]

In the future, we plan to numerically calculate the differential cross section given in Eq. (2) using various parametrization models of the polarized gluon distribution function and to estimate the sensitivity of this process on the polarized gluon.

*1 Institute of High Energy Physics, Academia Sinica, China
*2 Faculty of Human Development, Kobe University
*3 Department of Management Science, Fukui University of Technology

References

1) L. E. Gordon, M. Goshtasbpour, and G. P. Ramsey: Phys. Rev. D **58**, 094017 (1998); G. P. Ramsey: Prog. Part. Nucl. Phys. **39**, 599 (1997); E. Leader, A. V. Sidrov, and D. B. Stamenov: Phys. Rev. D **58**, 114028 (1998); Phys. Lett. B **445**, 232 (1998); Phys. Lett. B **462**, 189 (1999); Y. Goto and Asymmetry Analysis Collaboration: Phys. Rev. D **62**, 034017 (2000).
2) S. Hino and S. Kumano: Phys. Rev. D **59**, 094026 (1999); Phys. Rev. D **60**, 054018 (1999); S. Kumano and M. Miyama: Phys. Lett. B **479**, 149 (2000).
3) T. Morii and T. Yamanishi: Phys. Rev. D **61**, 057501 (2000); Phys. Rev. D **62**, 059901 (2000).
4) A. Bravar, D. von Harrach, and A. Kotzinian: Phys. Lett. B **421**, 349 (1998).
5) A. Airapetian et al.: HERMES Collaboration, Phys. Rev. Lett. **84**, 2584 (2000).
6) J. Binnewies, B. A. Kniehl, and G. Kramer: Phys. Rev. D **58**, 014014 (1998).

Chiral Properties of Domain-Wall Quarks in Quenched QCD

Y. Aoki

Numerical simulation with lattice gauge theory is a powerful nonperturbative tool for analyzing QCD. It respects the gauge symmetry, which is one of the most important aspects of QCD. Another is the chiral symmetry, which has not been satisfactory realized. Against this long-standing problem of lattice gauge theory, the domain-wall fermion[1–3] was proposed with fascinating features. It is a five-dimensional Wilson fermion variant, characterized by the system length in the fifth direction N_s and the domain-wall height M. The four-dimensional physical fermions are defined in terms of those fermions on the five dimensional boundaries.

Analytical studies have shown that this model has the exact chiral symmetry in the limit $N_s \to \infty$ even at finite lattice spacings. Here we test it[4] nonperturbatively for QCD in the quenched approximation, where most of the applications have been done.

We focus on the anomalous quark mass, m_{5q}, which is defined through the symmetry-breaking term of the pseudoscalar channel of the axialvector Ward-Takahashi identity. This quantity can be interpreted as the additive correction of the fermion mass, and is expected to vanish in the limit $N_s \to \infty$ as $m_{5q} \sim e^{-\xi N_s}$.[2]

We investigate two types of gluon action; one is the ordinary Wilson plaquette action and the other is the renormalization group improved action (RG action) of Iwasaki type, which, with the ordinary fermions, leads to much better scaling toward the continuum limit than the plaquette action. We expect that this improved scaling also affects the chiral properties.

Two lattice spacings, $a = 0.1$ and 0.2 fm, were investigated in this study. While a wide range of domain-wall heights, $1.3 \leq M \leq 2.5$, was surveyed for $a = 0.2$ fm, we show the set of results at $M = 1.7$ as a typical example. The domain-wall height at $a = 0.1$ fm was fixed to $M = 1.8$.

In Fig. 1 we show the results of anomalous quark mass. For the same action, one obtains better chiral properties with finer lattices. For the same lattice spacing, the improved action yields better results. One important practical suggestion here is that one should employ improved gauge action such as RG action to reduce the amount of computation.

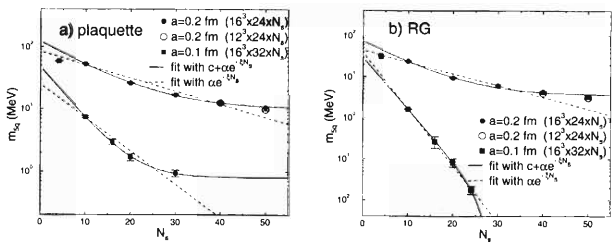

Fig. 1. Anomalous quark mass m_{5q} as a function of the extent of the fifth direction N_s for plaquette action a) and RG action b).

Let us examine the N_s dependence at $a = 0.2$ fm for the plaquette action. The anomalous quark mass decreases as the length of the fifth direction N_s increases. However it does not decrease as fast as $e^{-\xi N_s}$, but rather as $c + \alpha e^{-\xi N_s}$ with $c > 0$. This implies that the chiral symmetry is not realized in the infinite N_s limit. This is also true for all other cases except for $a = 0.1$ fm with RG action, for which the simple exponential fit reproduces the data quite well. These results indicate that the domain-wall fermion fails to realize chiral symmetry in quenched QCD for at least $a \geq 0.1$ fm with the plaquette action and $a \geq 0.2$ fm with the RG action.

There are two other studies available for the anomalous quark mass at $a = 0.1$ for the plaquette action. The authors of Ref. 5 have studied it for $4 \leq N_s \leq 10$. Our results are in very good agreement with theirs. We can find the results for $12 \leq N_s \leq 48$ in a recent paper by the RIKEN-BNL-Columbia collaboration.[6] Their data are consistent with ours, in the region where both of them can be compared, but their point at $N_s = 48$ shows a tendency to decrease still more. Further study is needed to clarify this difference.

We remain interested in the qualitative difference of the anomalous quark mass for two actions and that for different lattice spacings. One way to further investigate this subject is to study the eigenvalues of the four-dimensional Wilson-Dirac operator,[7,8] whose zero mode has one-to-one correspondence to the unit transfer matrix of the domain-wall fermion system in the fifth direction. This might be also a good means for the clarification of the large N_s behavior of m_{5q} at $a = 0.1$ fm for the plaquette action.

This report is a summary of works done in the CP-PACS collaboration.

References

1) D. Kaplan: Phys. Lett. B **288**, 342 (1992); Y. Shamir: Nucl. Phys. B **406**, 90 (1993).
2) V. Furman and Y. Shamir: Nucl. Phys. B **439**, 54 (1995).
3) For a review for the application of the domain-wall fermion to QCD, see, T. Blum: Nucl. Phys. B Proc. Suppl. **73**, 167 (1999).
4) CP-PACS Collaboration, A. Ali Khan et al.: hep-lat/0007014, to appear in Phys. Rev. D.
5) S. Aoki et al.: Phys. Rev. D **62**, 094502 (2000).
6) T. Blum et al.: hep-lat/0007038.
7) R. Edwards et al.: Phys. Rev. D **60**, 034502 (1999).
8) CP-PACS Collaboration, A. Ali Khan et al.: hep-lat/0011032, to appear in Nuc. Phys. Proc. Suppl.

Diquark Correlations and Flavor Dependence of Quark Distributions

H. Mineo,[*1] W. Bentz,[*2] and K. Yazaki[*3]

The valence (v) quark distributions extracted from experimental nucleon structure functions show that $d_v(x)$ is softer than $u_v(x)$. This feature can be explained[1] as an effect of diquark correlations in the scalar ($J = 0$) channel. We investigated[2] the role of the axial vector ($J = 1$) channel as well, using the relativistic Faddeev approach to the Nambu-Jona-Lasinio model and the 'static approximation' of the quark exchange kernel.[3] We consider the three cases shown in Table 1 with different interaction strengths (r_a) in the $J = 1$ channel, fitting the interaction strength in the $J = 0$ channel (r_s) to the experimental nucleon mass in each case. (The constituent quark mass is M = 400 MeV). The resulting values for the scalar diquark mass (M_S) and the contribution of the scalar channel to the baryon number (W_S) show that cases I and III correspond to strong and weak $J = 0$ correlations, respectively. The ratio of the structure functions F_2^n/F_2^p shown in Fig. 1 clearly indicates that the correlations in the J = 1 channel should not be too strong ($W_a < 10\%$). Case II gives a reasonable description of the valence quark distributions. These results, as well as the static properties of the nucleon for the above three cases and the effects of the pion cloud, will be published soon.[2]

Table 1. Parameter sets used in the calculation and resulting values for M_S and W_S.

case	I	II	III
r_a	0	0.25	0.66
r_s	0.73	0.63	0.50
M_S [MeV]	600	684	766
W_S [%]	100	90	60

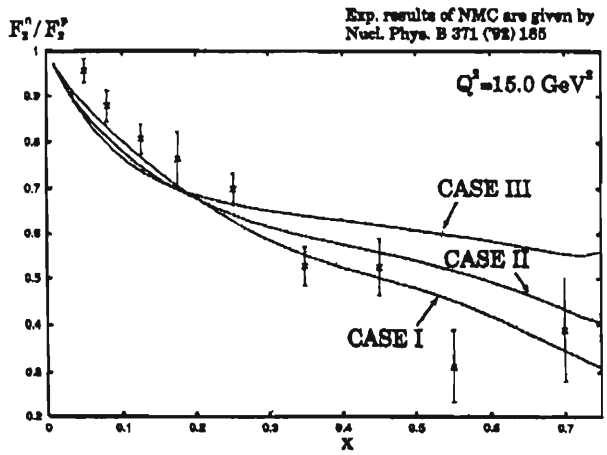

Fig. 1. Ratio of structure functions F_2^n/F_2^p for three cases of Table 1.

References

1) F. E. Close and A. W. Thomas: Phys. Lett. B **312**, 227 (1988).
2) H. Mineo, W. Bentz, and K. Yazaki: to be published.
3) H. Mineo, W. Bentz, and K. Yazaki: Phys. Rev. C **60**, 065201 (1999).

*1 Department of Physics, University of Tokyo
*2 Department of Physics, Tokai University
*3 College of Arts and Sciences, Tokyo Woman's Christian University

Renormalization Group Approach to the $O(N)$ Linear Sigma Model at Finite Temperature

K. Naito, T. Umekawa,* and M. Oka*

The Wilsonian renormalization group (RG) method is applied to finite temperature systems for the study of nonperturbative methods in the field theory.[1] We choose the $O(N)$ linear sigma model as the first step. Under the local potential approximation, we solve the Wilsonian RG equation numerically as a nonlinear partial differential equation. The evolution of the domain is taken into account using the simple cut and extrapolation procedure. The obtained effective potential is shown in Fig. 1. Our procedure is shown to yield the correct solution obtained by the auxiliary field method in the large N limit. To include thermal effects, we employ the imaginary time formalism. In our method, the sum of the Matsubara frequencies is taken before the scale is introduced. Then, the RG equation in this scheme reads

$$\begin{aligned}\frac{dV_t(x)}{dt} = {} & \frac{A_D\Lambda^D}{2}\left\{(N-1)\ln\left(1+\frac{1}{\Lambda^2}\frac{1}{x}\frac{\partial V_t}{\partial x}\right)\right. \\ & \left.+\ln\left(1+\frac{1}{\Lambda^2}\frac{\partial^2 V_t}{\partial x^2}\right)\right\} \\ & +\frac{A_{D-1}\Lambda^{D-1}}{\beta} \\ & \cdot\left\{(N-1)\ln\left(1-\exp\left(-\beta\sqrt{\Lambda^2+\frac{1}{x}\frac{\partial V_t}{\partial x}}\right)\right)\right. \\ & \left.+\ln\left(1-\exp\left(-\beta\sqrt{\Lambda^2+\frac{\partial^2 V_t}{\partial x^2}}\right)\right)\right\}. \quad (1)\end{aligned}$$

The temperature dependence of the condensate ϕ is shown in Fig. 2. We observe a second-order phase transition. The critical exponents are calculated in the Table 1 and are shown to agree with the world best value. However, our apprcach has some numerical unstabilities. Further improvements are necessary.

Table 1. Critical exponents.

	β	δ	γ
Our result	0.38	4.7	1.4
Monte-Carlo[2]	0.384	4.85	1.48

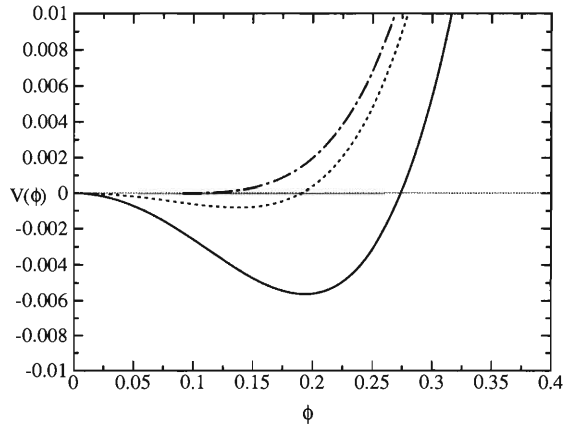

Fig. 1. Effective Potential at the scale $\Lambda = 1.0$ (solid), $\exp(-0.5)$ (dotted), $\exp(-10.0)$ (dash-dotted) respectively.

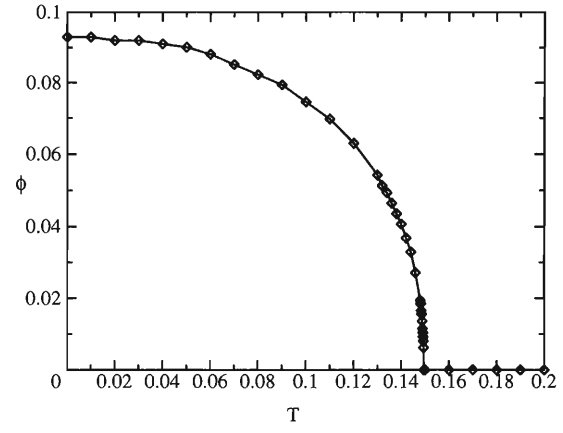

Fig. 2. The temperature dependence of the condensate.

References

1) T. Umekawa, K. Naito, and M. Oka: hep-ph/9905502.
2) K. Kanaya and S. Kaya: Phys. Rev. D **51**, 2404 (1995).

* Tokyo Institute of Technology

Chiral Condensates in a Light-Cone Vacuum

F. Lenz,[*1] M. Thies,[*1] and K. Yazaki[*2]

The standard procedure to characterize the phases of a system by appropriate ground-state expectation values fails in light-cone quantization because of the "triviality" of the vacuum.[1,2] This poses conceptual problems about the light-cone quantization in the nonperturbative regime,[3] though its equivalence to more standard quantizations has been established perturbatively.

We carefully examine the behaviors of the products of field operators when their light-cone time coordinates are close to each other and demonstrate that meaningful quantities serving as order parameters are obtained as expectation values of Heisenberg operators in the equal (light-cone) time limit. These quantities differ from the purely kinematical expectation values of the corresponding Schroedinger operators, for which the light-cone time coordinates of the field operators are chosen to be the same from the beginning.

For the Nambu-Jona-Lasinio (NJL)[4] and the Gross-Neveu (GN)[5] models, we apply the above procedure to define the chiral condensates and describe the spontaneous breakdown of chiral symmetry by deriving the gap equations and the values of the chiral condensates within the framework of light-cone quantization. In these models, dynamical time evolutions of the Heisenberg operators can be approximated by those of free fermions with constituent masses to the leading order of $1/N$ expansion.[6] The results are found to be equivalent to those of more standard approaches.

We thus believe that the light-cone quantization has no conceptual problem even in the nonperturbative regime if the Heisenberg operators are used to define the operators characterizing the nonperturbative features, and can provide us with a practical method of studying hadron structures and hadron spectra.

References

1) M. Burkardt: Adv. Nucl. Phys. **23**, 1 (1996).
2) S. J. Brodsky, H.-C. Pauli, and S. S. Pinsky: Phys. Rep. **301**, 299 (1998).
3) K. Itakura and S. Maedan: Phys. Rev. D **61**, 045009 (2000).
4) Y. Nambu and G. Jona-Lasinio: Phys. Rev. **122**, 345 (1961); Phys. Rev. **124**, 246 (1961).
5) D. J. Gross and A. Neveu: Phys. Rev. D **10**, 3235 (1974).
6) W. Bentz, T. Hama, T. Matsuki, and K. Yazaki: Nucl. Phys. A **651**, 143 (1999).

*1 Institute for Theoretical Physics III, University of Erlangen, Germany
*2 College of Arts and Sciences, Tokyo Woman's Christian University

$K \to \pi\pi$ Decays with Domain Wall Fermions†

T. Blum

Recent measurements of direct CP violation ($\epsilon'/\epsilon \neq 0$) in K meson decays at FNAL and CERN allow an important test of the Standard Model of particle physics, in particular, the Cabibbo-Kobayashi-Maskawa (CKM) mixing paradigm. The effective weak Hamiltonian governing strangeness changing K decays has been computed to next-to-leading order in QCD and QED by the Munich and Rome groups.

$$H^{\Delta S=1} = V_{ud}V_{us}^* \frac{G_F}{\sqrt{2}} \left[\left(1 + \frac{V_{td}V_{ts}^*}{V_{ud}V_{us}^*}\right) \cdot (C_1(\mu)(Q_1(\mu) - Q_{1c}(\mu)) + C_2(\mu)(Q_2(\mu) - Q_{2c}(\mu))) - \frac{V_{td}V_{ts}^*}{V_{ud}V_{us}^*} \vec{C}(\mu) \cdot \vec{Q}(\mu) \right], \quad (1)$$

where V_{ij} are the CKM matrix elements, C_i are Wilson coefficients, and Q_i are effective four quark operators. The CKM matrix elements are fundamental parameters of the Standard Model, and the Wilson coefficients have been computed in weak coupling perturbation theory. The remaining piece of the puzzle is the computation of hadronic matrix elements of the operators of this effective weak Hamiltonian, $\langle\pi\pi|Q_i|K\rangle$. These matrix elements are also needed for a first principles understanding of the empirical $\Delta I = 1/2$ rule of kaon decays. The matrix elements must be computed nonperturbatively. The only viable first principles approach is lattice QCD.

In lattice QCD the recent advance of domain wall (and overlap) fermions which maintain chiral symmetry to a high degree of accuracy allows for a promising new attempt at this long-standing problem. Chiral symmetry of domain wall fermions provides a significant advantage when computing light quark QCD observables since the lattice artifacts that arise when this symmetry is explicitly broken are greatly reduced.

The excellent chiral properties of domain wall fermions allow a further simplification of the lattice calculation. We use lowest order chiral perturbation theory to relate $K \to \pi\pi$ matrix elements to a linear combination of $K \to \pi$ and $K \to |0\rangle$ matrix elements, which are much easier to compute on the lattice. However, this simplification adds a systematic uncertainty since final state interactions of the pions do not appear at lowest order in chiral perturbation theory. In fact, present lattice methods can not treat these interactions.

In the past year we have completed three significant quenched lattice QCD calculations using domain wall fermions. In the first study[1] we precisely determined the residual explicit chiral symmetry breaking effects of domain wall fermions in order that all of our domain wall fermion calculations rest on a sound theoretical foundation. The results were quite satisfactory, and gave us confidence to proceed with the much more complicated matrix element calculations described above.

The second calculation[2] was a first study of operator renormalization using domain wall fermions and the nonperturbative renormalization method of the Rome-Southampton group. The use of this technique with domain wall fermions represents a significant advance over previous studies with conventional lattice fermions. The renormalization of operators is an important aspect of all lattice matrix element calculations.

Finally, in our third study,[3] we have completed the computation of all matrix elements of the effective weak Hamiltonian in Eq. (1) needed to determine ϵ'/ϵ and the $\Delta I = 1/2$ rule, as well as the corresponding operator renormalizations. The final results depend crucially on a complicated combination of all the matrix elements of the operators appearing in Eq. (1) and the precise removal of unphysical divergent terms arising from the lattice regularization. There are many delicate cancelations from both procedures. Thus, great care must be taken in the final analysis to control statistical and systematic uncertainties. We are presently in the final stages of this analysis.

References

1) T. Blum et al.: hep-lat/0007038, to be published in Phys. Rev. D.
2) C. Dawson: hep-lat/0011036; T. Blum et al.: submitted to Phys. Rev. D, hep-lat/0102005.
3) T. Blum: hep-lat/0011042 and R. Mawhinney: hep-lat/0010030 for preliminary results.

† This work was done in collaboration with N. Christ, C. Cristian, C. Dawson, G. Fleming, X. Liao, G. Liu, S. Ohta, A. Soni, P. Vranas, R. Mawhinney, M. Wingate, L. Wu, and Y. Zhestkov. We thank RIKEN, BNL and the U. S. Department of Energy for providing the facilities essential for this work

QCDOC Super Computer for Lattice QCD†

D. Chen,[*1] N. Christ,[*2] Z. Dong,[*2] A. Gara,[*1] K. Garg,[*2] B. Joo,[*3] C. Kim,[*2] L. Levkova,[*2] X. Liao,[*2] R. D. Mawhinney,[*2] S. Ohta,[*4] T. Wettig,[*5] and A. Yamaguchi[*2]

In the fall of 1998 the RIKEN-BNL Research Center (RBRC) completed a 600 Gflops "QCDSP" parallel super computer in collaboration with Columbia University and Brookhaven National Laboratory (BNL). It was awarded the Gordon-Bell Prize at the "Super Computing 98" international symposium in the same year. A new "RIKEN-BNL-Columbia-KEK" lattice quantum chromodynamics (QCD) collaboration has been very successfully using this computer and its 400 Gflops sister computer at Columbia University ever since. In particular the collaboration pioneered the application of the five-dimensional domain-wall fermion method in lattice QCD.[1] To follow up, RIKEN, Columbia University and IBM Research agreed to start another collaboration to develop a new parallel computer for lattice QCD capable of 10 Tflops.[2]

These QCDSP computers are constructed as four-dimensional hypercubic nearest-neighbor networks of twelve thousand (at RBRC) and eight thousand (at Columbia) computing nodes. Each node has a 50 Mflops DSP, 2 Mwords DRAM, and an application specific integrated circuit (ASIC) of 250 K transistors which provides an interface to the memory and eight off-node communication ports.

In the machine now being designed, QCDOC (QCD "On a Chip"), an entire node shrinks to fit in an ASIC of about $(1\,\mathrm{cm})^2$ with 50 M transistors. A PowerPC RISC integer processor and a 1 Gflops 64-bit IEEE floating-point unit replace the DSP. Memory is expanded to 4 MBytes on chip, with possible extension of up to 512 MBytes per node by adding a small, industry-standard, DIMM memory card. Twelve, instead of eight, serial ports are each capable of 1 Gbit/sec off-node communication. They support a six-instead of a four-dimensional network which can be easily partitioned into five- or four-dimensional sublattices (see the example in Fig. 1).

The on-chip memory is joined to the processor with a very high bandwidth bus which provides a maximum data transfer rate between memory and processor of 8 Gbytes per second. This removes a troublesome bottleneck in the QCDSP design and should permit generic 'C' code to run with a reasonable efficiency on the new QCDOC computer. In addition, each QCDOC ASIC is equipped with an Ethernet controller and Ethernet access to JTAG debugging control. The Ethernet controller will provide communications between each node and the host computer as well as access to disk storage. An 8,192-node QCDOC machine will have an equal number of 100 Mbit/sec Ethernet ports, connected to provide a total possible bandwidth to disk as large as 25 Gbytes/sec. The Ethernet-based JTAG connection will permit Ethernet controlled booting as well as a very powerful, multi-node debugging capability. We expect to achieve a cost performance for QCDOC of less than $1 per sustained Mflops in construction and to consume only a couple of Watts per node, making QCDOC about an order of magnitude more cost effective than QCDSP in both its procurement and operation.

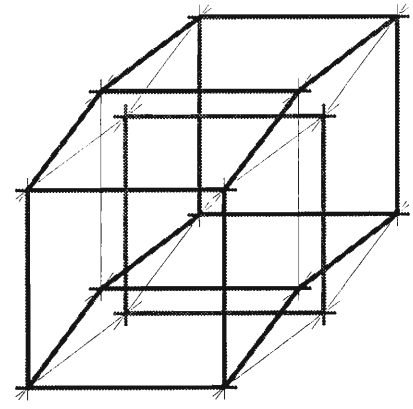

Fig. 1. In this example a 4D hypercubic torus of 2^4 QCDOC nodes is partitioned into 6×2 (red) and 2×2 (blue) 2D tori. Note a factor of 6 allows a flexible choice of lattice sizes. Larger 6D networks will be even more flexible. Periodic boundary conditions are understood.

References

1) T. Blum et al.: hep-lat/0007038, to appear in Phys. Rev. D; see also many contributions from the group in recent "Lattice" series of international symposia, Nucl. Phys. B Proc. Suppl.
2) D. Chen et al.: Proc. on Lattice 2000; hep-lat/0011004.

† We thank RIKEN and the US Department of Energy

*1 IBM T. J. Watson Research Center, Japan
*2 Columbia University, USA
*3 University of Kentucky, USA
*4 Institute for Particle and Nuclear Studies, High-Energy Accelerator Research Organization (KEK)
*5 Yale University, USA

String Tensions and Phase Structure of SU(4) Yang-Mills Theory†

S. Ohta*1 and M. Wingate*2

There are renewed interests in SU(N_c) pure Yang-Mills theory with large (N_c): (1) Finite-temperature phase structure of quantum chromodynamics (QCD) would be easier to understand if the SU(N_c) pure Yang-Mills system has a second order phase transition for $N_c \geq 4$.[1] (2) New developments in M/string theory[2] predict such things as glueball spectrum at large N_c and large g^2 or ratio between different string tensions for $N_c \geq 4$.[3] (3) The dimensionless ratio $T_d/\sqrt{\sigma}$ of the deconfining temperature T_d and string tension σ is expected to be independent of N_c with a value $\sqrt{3/\pi(D-2)}$ with D being the space-time dimensions.[4]

To resolve these issues we numerically investigated the order of deconfining phase transition and the ratio of string tensions for $N_c = 4$.[5] We use single-plaquette action defined in the fundamental **4**-representation of the SU(4) gauge group. Combinations of pseudo-heatbath or Metropolis and over-relaxation algorithms are used in updating 4, 6 and 8×8^3, 12^3, 16^3 or 20^3 lattices. We look at the following observables: plaquette, Polyakov loops, $L(\vec{x}) = (1/N_c)\mathrm{tr}\prod_{t=1}^{L_t} U(\vec{x}, t; \hat{t})$, in **4** (fundamental), **6** (antisymmetric diquark), **10** (symmetric diquark) and **15** (adjoint) representations, deconfinement fraction, and Polyakov loop correlation $\langle L(\vec{0})L(\vec{r})^* \rangle \sim r^{-1}\exp(-F(r)/T) \sim \exp(-L_t\sigma r - \ln r)$ in **4**, **6**, **10** and **15** representations.

On a 6×20^3 lattice we confirmed coexistence of confined and deconfined phases at temperature $\beta = 10.79$: This strongly suggests a first-order deconfining phase transition. We plan further study with finite-size scaling. String tensions in SU(N_c) pure Yang-Mills system is classified by its center Z(N_c) N_c-ality. With $N_c = 4$, the fundamental (**4**) charge has 4-ality $k = 1$, the two diquark (**6** and **10**) charges $k = 2$, and adjoint (**15**) $k = 0$.[3] Note also that $N_c = 4$ is the first example with different string tensions: in SU(3) pure Yang-Mills system the fundamental (**3**) and the symmetric diquark (**6**) tensions are the same.[6] On a 6×16^3 lattice at $\beta = 10.70$ and at a weaker coupling of $\beta = 10.85$ on a smaller lattice of 8×12^3 (see Fig. 1) we find clear difference between **4**- and **6**-string tensions extracted from **4**- and **6**-Polyakov loop correlations. We also find flattening of the adjoint (**15**) correlation in the latter.

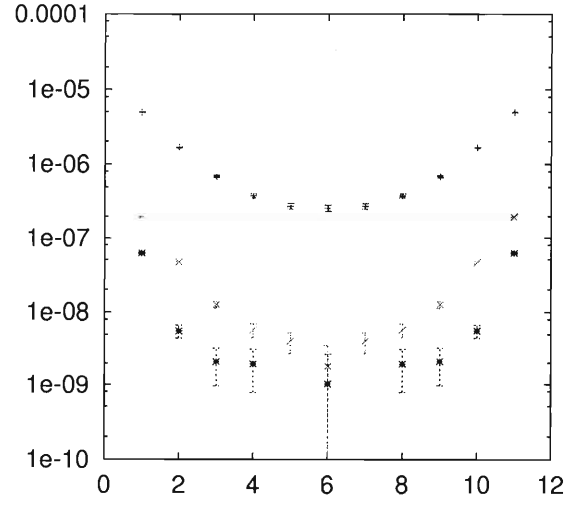

Fig. 1. Polyakov loop correlation function in **4** (top), **6** (middle), and **15** (bottom) representations on a $12^3 \times 8$ lattice at $\beta = 10.85$.

References

1) R. D. Pisarski and M. Tytgat: Proc. 25th Hirschegg Workshop on QCD Phase Transition, Hirschegg, Austria, 1997-1 (1997); hep-ph/9702340.
2) J. Maldacena: Adv. Theor. Math. Phys. **2**, 231 (1998); Int. J. Theor. Phys. **38**, 1113 (1999); hep-th/9711200.
3) M. J. Strassler: Proc. Yukawa Int. Seminar 97, p. 439 (1997); hep-th/9803009.
4) R. D. Pisarski and O. Alvarez: Phys. Rev. D **26**, 3735 (1982).
5) M. Wingate and S. Ohta: to appear Phys. Rev. D, hep-lat/0006016.
6) S. Ohta, M. Fukugita, and A. Ukawa: Phys. Lett. B **173**, 15 (1986).

† We acknowledge helpful conversations with M. Creutz, R. Pisarski, and M. Strassler. We thank RIKEN, BNL and the US Department of Energy.

*1 Institute for Particle and Nuclear Studies, High Energy Accelerator Research Organization (KEK)
*2 Present address: Physics Department, The Ohio State University, USA

Domain-Wall Fermion Lattice QCD Calculation of Nucleons†

T. Blum, S. Ohta,*1 and S. Sasaki*2

The RIKEN-BNL-Columbia-KEK QCD Collaboration have been pursuing the domain-wall fermion (DWF) method in lattice quantum chromodynamics (QCD).[1] In DWF an extra fifth dimension is added to the lattice. By manipulating a "domain-wall" structure in the fermion mass in this fifth dimension, we control the number of light fermion species, chirality and mass in the other four space-time dimensions. In particular: (1) fermion near-zero mode effects are well understood, (2) small chiral symmetry breaking induced by the finite extra dimension is described by a single residual mass parameter in low-energy effective lagrangian, which is very small in the present calculation, and (3) non-perturbative renormalization works well.[2] Here we report our more recent studies about the mass spectrum of the nucleon and its excited state and the nucleon structure.

Our quenched DWF[3] calculation for the first time succeeded in reproducing the large mass splitting between $N(939)$ and $N^*(1535)$ (see Fig. 1). Phenomenological models like the non-relativistic quark model and the MIT bag model have failed here: these models must have only a couple of hundred MeV mass splitting arising from orbital excitation of one valence quark.

We also obtain the isovector vector and axial charges, g_V and g_A, of the nucleon.[4] These quantities are well known from the neutron β decay, $g_V = G_F \cos\theta_c$ and $g_A/g_V = 1.2670(35)$. Here G_F denotes the Fermi constant and θ_c the Cabibbo angle. $g_V = G_F \cos\theta_c$ follows from vector current conservation. In contrast the axial current should receive a strong correction from QCD, resulting in the deviation of the ratio g_A/g_V from unity. In lattice calculations in general the two relevant currents get renormalized by the lattice cutoff. With conventional fermion schemes this renormalization usually makes the calculations rather difficult, if not intractable, even for such simple quantities like g_V and g_A. An important advantage here with DWF is that the lattice renormalizations, Z_V and Z_A, of the currents are identical

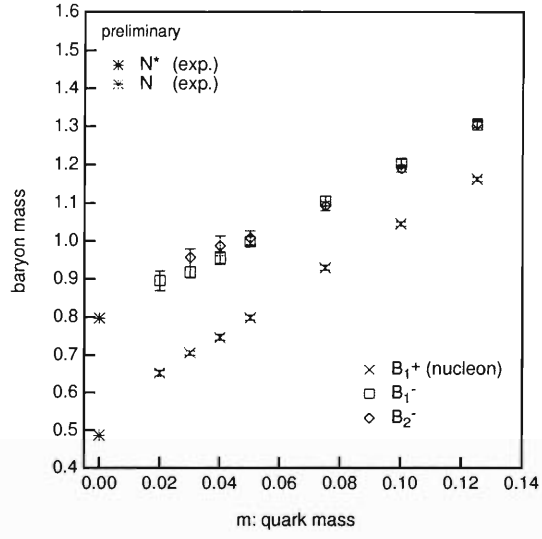

Fig. 1. Dependence of calculated N ($\times$) and N^* ($\square$ and $\diamond$) mass on quark mass. They extrapolate linearly to agree well with experimental values (blasts at zero quark mass). All in lattice units, $a^{-1} \simeq 2\,\mathrm{GeV}$.

so that the lattice ratio $(g_A/g_V)^{\mathrm{lattice}}$ directly yields the continuum value. The longitudinal and transverse quark spin contents, $\Delta q/g_V$ and $\delta q/g_V$, are obtained at the same time. Preliminary values from linear extrapolations in quark mass to zero are: $g_A/g_V = 0.62(13)$, $\Delta q/g_V = 0.36(14)$, and $\delta q/g_V = 0.31(12)$. The quite low value of g_A/g_V is under further investigation.

References

1) T. Blum et al.: hep-lat/0007038, to appear in Phys. Rev. D, and references therein.
2) C. Dawson: hep-lat/0011036; Proc. Lattice 2000, edited by A. Patel et al., Nucl. Phys. B Proc. Suppl. **94**, 295 (2001).
3) S. Sasaki: Proc. NSTAR 2000; hep-ph/0004252, and references therein.
4) T. Blum, S. Ohta, and S. Sasaki: hep-lat/0011011, Proc. on Lattice 2000, edited by A. Patel et al.

† As part of the RIKEN-BNL-Columbia-KEK Collaboration: T. Blum, N. Christ, C. Cristian, C. Dawson, G. Fleming, X. Liao, G. Liu, R. Mawhinney, S. Ohta, A. Soni, P. Vranas, M. Wingate, L. Wu, and Y. Zhestkov. We thank RIKEN, BNL and the US Department of Energy

*1 Institute for Particle and Nuclear Studies, High-Energy Accelerator Research Organization (KEK)
*2 Department of Physics, University of Tokyo

Numerical Lattice Field Theories Using RIKEN VPP Super Computer

S. Kim*1 and S. Ohta*2

Lattice numerical calculation is often the only reliable method to extract quantitative knowledge from non-perturbative quantum field theories such as quantum chromodynamics (QCD), the fundamental theory of the strong interaction. We have been very successful in using RIKEN VPP vector-parallel super computing facility for this purpose. In particular, our calculation of light hadron mass spectrum with quenched approximation of QCD (in which vacuum polarization of quarks are neglected) and staggered fermion quarks is considered the best available.[1] With a very fine lattice spacing of 0.055(1) fm (or the inverse squared coupling of $\beta = 6.5$) and a large volume of $(2.59(5)\ \mathrm{fm})^3$ ($48^3 \times 64$ lattice), a realistic nucleon to ρ-meson mass ratio of 1.23 ± 0.04 (statistical) ± 0.02 (systematic) was obtained without chiral extrapolation, as our lightest quark mass was made so light as about 4.5 MeV. The flavor symmetry breaking which can arise from coarse lattice spacing is no longer visible either.

Another application in lattice QCD where fine spacing and large volume are important is heavy quarkonium spectrum calculation. Again the problem addresses non-perturbative nature of the strong interaction and has many remarkable characters in production or decay of quarkonium.[2] However, it has been difficult to place heavy quarkonium system on a lattice because heavy-quark Compton wavelength (about 1.2 fm for charm and 0.25 fm for bottom) has been too short compared to the available lattice spacing (typically 0.1 fm or larger): such a coarse lattice spacing cannot resolve the structure of heavy quark wave function. On the other hand, sufficiently fine lattice spacing often meant unacceptably small physical lattice volume which cannot accommodate the extent of quarkonium wave function. Thus lattice calculations had to rely on either wild extrapolations from light quark mass region to heavy quark mass region or uncontrolled approximation of expansion in the inverse of heavy quark mass.[3] In order to overcome these problems, we started a quenched QCD calculation of heavy quarkonium mass on a $48^3 \times 64$ lattice at $\beta = 6.8$. With these parameters, lattice spacing is about 0.025 fm and physical volume is about $(1.2\,\mathrm{fm})^3$. These should be sufficient for charmonium and charmed mesons: only interpolation in quark mass is required, and not extrapolation. Thus far, about 400 Monte Carlo samples of gauge configuration have been collected and the analysis is in progress.

A few smaller-scale projects are also in progress:

Phase structure of 3D Thirring model in gauge theory formulation. This needs more accurate determination of the nature of phase transition in view of recent works.[4] Thus, we are studying an application of histogram method to investigate the phase transition of this lattice model.

Phase structure of zero-temperature QCD with staggered-fermion quarks. Here full dynamical treatment of vacuum polarization of quarks is essential, as the phase structure is expected to depend on the number of light quark flavors.[5]

QCD at finite chemical potential. Monte Carlo algorithm for lattice QCD in general relies on the probability distribution interpretation of the Boltzmann kernel of the generating functional path integral,

$$Z = \int [d\psi][d\bar{\psi}][dA_\mu] \exp(-S[\psi, \bar{\psi}, A_\mu]),$$

where ψ denotes quark fields and A_μ gluon fields. If the action functional $S[\psi, \bar{\psi}, A_\mu]$ is real, the Boltzmann factor e^{-S} can be interpreted as a probability distribution over configurations of quarks and gluons and Monte Carlo algorithms are applicable. Unfortunately this does not hold for conventional lattice QCD system at finite quark chemical potential: the Boltzmann factor becomes complex. We are pursuing a different lattice formulation which can circumvent this problem.

References

1) S. Kim and S. Ohta: Phys. Rev. D **61**, 074506 (2000); hep-lat/9912001.
2) G. T. Bodwin, E. Braaten, and G. P. Lepage: Phys. Rev. D **51**, 1125 (1995); Phys. Rev. D **55**, 5853 (1997).
3) C. Bernard: Proc. Lattice 2000, Nucl. Phys. B (Proc. Suppl.), **94**, 159 (2001); hep-lat/0011064, and references therein.
4) S. Hands and B. Lucini: Phys. Lett. B **461**, 263 (1999); hep-lat/9906008.
5) F. R. Brown et al.: Phys. Rev. D **46**, 5655 (1992); hep-lat/9206001, and references therein.

*1 Sejong University, Korea
*2 Institute for Particle and Nuclear Studies, High-Energy Accelerator Research Organization (KEK)

The Spectrum of the QCD Dirac Operator

T. Wettig

The spectrum of the QCD Dirac operator, $D = \gamma_\mu(\partial_\mu + gA_\mu)$, is of great theoretical interest, in particular because of its relation to spontaneous chiral symmetry breaking. The Banks-Casher formula, $\Sigma \equiv |\langle\bar{\psi}\psi\rangle| = \pi\rho(0)/V$, relates the chiral condensate to the spectral density of D defined by $\rho(\lambda) = \langle\sum_n \delta(\lambda-\lambda_n)\rangle$, where the λ_n are the Dirac eigenvalues and the average is over the gauge fields weighted by the QCD action.

In various regions of the parameter space, the Dirac spectrum can be computed analytically.[1] To better understand the results of lattice gauge simulations, we are particularly interested in QCD in a finite volume V. Figure 1 shows the energy scales that are relevant at finite V. For energies below the rho mass, QCD can be described by an effective chiral Lagrangian $\mathcal{L}_{\rm eff}$. However, perturbative calculations break down for small energies of order $1/V\Sigma$, *i.e.* chiral perturbation theory only works above this scale. For energies below the so-called Thouless energy, given by $E_c \sim f_\pi^2/\Sigma\sqrt{V}$, the theory is dominated by the zero-momentum modes in $\mathcal{L}_{\rm eff}$, *i.e.* the kinetic terms can be neglected. In this regime QCD is described by a zero-dimensional effective theory known as chiral random matrix theory (RMT). While it is possible (but very hard) to compute nonperturbative results from $\mathcal{L}_{\rm eff}$, chiral RMT provides a much more convenient mathematical tool (the results agree). There is a finite overlap region, $1/V\Sigma < E < E_c$, in which both chiral RMT and chiral perturbation theory are applicable.

A typical nonperturbative quantity is the microscopic spectral density ρ_s of the Dirac operator,

$$\rho_s(z) = \lim_{V\to\infty} \frac{1}{V\Sigma}\,\rho\left(\frac{z}{V\Sigma}\right) .$$

This quantity describes the distribution of the individual low-lying Dirac eigenvalues. The result of an SU(2) lattice simulation,[2] compared with the analytical RMT result, is shown in Fig. 2.

The disconnected scalar susceptibility is defined on the lattice in terms of the Dirac eigenvalues,

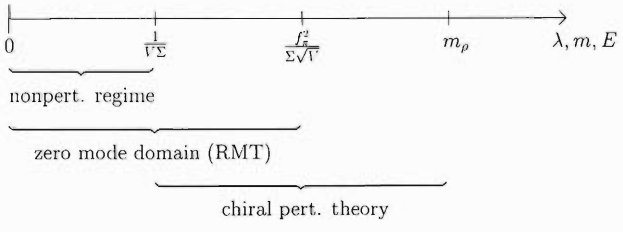

Fig. 1. Applicability of various effective theories for QCD in a finite volume.

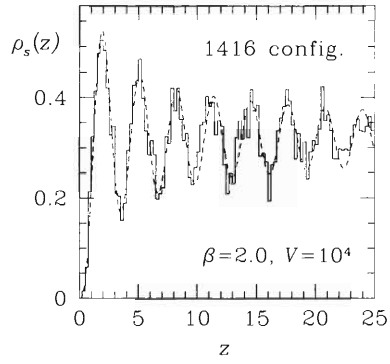

Fig. 2. Microscopic spectral density of D on the lattice (histogram) and in chiral RMT (dashed line).

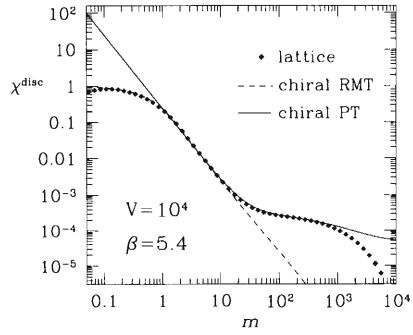

Fig. 3. Disconnected scalar susceptibility on the lattice, in chiral RMT, and in chiral perturbation theory. (The chiral RMT curve is hidden by the data for small m.)

$$\chi^{\rm disc}_{\rm lattice}(m) = \frac{1}{N}\left\langle \sum_{k,l=1}^{N} \frac{1}{(i\lambda_k+m)(i\lambda_l+m)} \right\rangle - \frac{1}{N}\left\langle \sum_{k=1}^{N} \frac{1}{i\lambda_k+m} \right\rangle^2 .$$

This quantity is of interest since it diverges at the chiral phase transition with a universal critical exponent. The result of an SU(3) lattice simulation,[3] compared with the analytical results of chiral RMT and chiral perturbation theory, is shown in Fig. 3. Clearly, there is an overlap regime in which both theories describe the data (m plays the role of an energy).

I would like to thank M. Göckeler, H. Hehl, P. E. L. Rakow, and A. Schäfer for fruitful collaborations.

References

1) J. J. M. Verbaarschot and T. Wettig: Annu. Rev. Nucl. Part. Sci. **50**, 343 (2000).
2) M. E. Berbenni et al.: Phys. Rev. Lett. **80**, 1146 (1998).
3) M. E. Berbenni et al.: Nucl. Phys. B Proc. Suppl. **83**, 974 (2000).

Parity and CP Violation in Hot QCD

D. Kharzeev*

One of the most exciting aspects of relativistic heavy ion physics is the possibility to produce some truly exotic phases of matter. In this report we describe the recent work[1,2] on the topological effects near the deconfinement phase transition, and the related possibility to excite $\mathcal{P}$ and $\mathcal{CP}$ odd metastable vacuum states.

Consider a linear sigma model with a field Φ. Then the effects of the anomaly enter exclusively through a term $\sim \det(\Phi)$. As in the nonlinear sigma model, when the chiral symmetry is spontaneously broken, this term generates a mass for the η'. However, in the nonlinear sigma model, at large N, there is *only* a mass term for the η'; four point interactions between η''s are induced by the anomaly, but are suppressed by higher powers of $1/N^2$.

For U fields which are constant in spacetime, the potential for U is

$$V(U) = \frac{f_\pi^2}{2}\left(\mathrm{tr}\left(M(U+U^\dagger)\right) - a(\mathrm{tr}\,\ln U - \theta)^2\right). \quad (1)$$

The pion decay constant $f_\pi = 93\,\mathrm{MeV}$, while M is the quark mass matrix. When $M = 0$, $m_{\eta'}^2 \sim a$, so $a \sim \lambda_{\eta'}^2/N$.

Taking $M_{ij} = \mu_i^2 \delta^{ij}$, any vacuum expectation value (v.e.v) of U can be assumed to be diagonal, $U_{ij} = e^{i\phi_i}\delta^{ij}$. The potential reduces to

$$V(\phi_i) = f_\pi^2\left(-\sum_i \mu_i^2 \cos(\phi_i) + \frac{a}{2}\left(\sum_i \phi_i - \theta\right)^2\right). \quad (2)$$

This is minimized for

$$\mu_i^2 \sin(\phi_i) + a\left(\sum \phi_i - \theta\right) = 0\,. \quad (3)$$

Note that as $\sum \phi_i$ arises from $\mathrm{tr}\,\ln U$, it is defined modulo 2π.

Now consider the limit of vanishing a: then there automatically other solutions besides $\phi = 0$, $\phi = 2\pi, 4\pi$, *etc.* These solutions are equivalent to the trivial vacuum, and so there is nothing new. But for small values of a, the term linear in a will only move the stationary point a little bit from 2π, 4π, *etc.* Because a is nonzero, they will become metastable, distinct from the usual vacuum. From (3), these states will act like regions of nonzero θ. Parity and CP are both violated spontaneously in such a region.

What are the signatures of such exotic states? Most notably, when the anomaly term a becomes small, there is maximal violation of isospin. At zero temperature, the nonet of pseudo-Goldstone bosons — the π's, K's, η, and η', are, to a good approximation, eigenstates of $SU(3)$ flavor. When the anomaly term becomes small, while the charged pseudo-Goldstone bosons remain approximate eigenstates of flavor, the neutral ones do not. Without the anomaly, the π^0 becomes pure $\bar{u}u$, the η pure $\bar{d}d$, and the η' pure $\bar{s}s$. Consequently, these three mesons become light. This is especially pronounced for the η, as it sheds all of its strangeness, to become purely $\bar{d}d$. Thus the η and η' would be produced copiously, and would manifest itself in at least two ways. First, light η's and η''s decay into two photons, and so produce an excess at low momentum. Secondly, these mesons decay into pions, which would be seen in Bose-Einstein correlations. Further, through Dalitz decays, the enhanced production of η's and η''s will enhance the yield of low mass dileptons.

There is another way to observe parity violation, by measuring the following variable globally, on an event-by-event basis:

$$\mathbf{J} = \sum_{\pi^+\pi^-} \frac{(\vec{p}_{\pi^+} \times \vec{p}_{\pi^-}) \cdot \hat{z}}{|\vec{p}_{\pi^+}||\vec{p}_{\pi^-}|}\,, \quad (4)$$

here $\vec{z}$ is the beam axis, and $\vec{p}$ are the three momenta of the pions. This and similar observables are currently under experimental study by the STAR Collaboration at RHIC.

References

1) D. Kharzeev, R. Pisarski, and M. Tytgat: Phys. Rev. Lett. **81**, 512 (1998).
2) D. Kharzeev and R. Pisarski: Phys. Rev. D **61**, 111901 (2000).

* Physics Department, Brookhaven National Laboratory, USA

Signature Neutrinos from Ultrahigh-Energy Photons

A. Kusenko*

The origin of ultrahigh-energy cosmic rays,[1] with energies beyond the Greisen-Zatsepin-Kuzmin (GZK) cutoff,[2] remains an outstanding puzzle.[3] Many of the proposed explanations invoke new sources, such as superheavy relic particles or topological defects, which can generate photons at both low and high red shifts. To understand the origin of the ultrahigh-energy cosmic rays (UHECR), it is crucial to distinguish such sources from more conventional astrophysical ones. The latter tend to produce more protons than photons. In addition, the "astrophysical" candidate sources such as, *e.g.*, active galactic nuclei, have formed at relatively low red shift. In contrast, topological defects could operate at much higher red shifts.

Sources of ultrahigh-energy photons that were active at red shift $z > 3$ can be identified by observation of neutrinos produced in interactions of energetic photons with the background photons.[4] This may help understand the origin of UHECR.

At red shift z the cosmic microwave background radiation (CMBR) has temperature $T_{CMB}(z) = 2.7(1 + z)\,\mathrm{K}$. Because of this, at high red shift the photon-photon interactions can produce pairs of muons and charged pions, whose decays generate neutrinos. This is in sharp contrast with the $z \lesssim 1$ case, where the photons do not produce neutrinos as they lose energy mainly by scattering off the radio background through electron-positron pair production and subsequent electromagnetic cascade. The ratio of the CMBR density to that of universal radio background (RB) increases at higher z, and the process $\gamma\gamma_{CMB} \to \mu^+\mu^- \to e^+e^-\bar{\nu}_\mu\nu_\mu\bar{\nu}_e\nu_e$ can produce neutrinos. The threshold for this lowest-energy neutrino-generating interaction is $\sqrt{s} > 2m_\mu = 0.21\,\mathrm{GeV}$, or $E_\gamma > E_{\mathrm{th}}(z) = \frac{10^{20}\mathrm{eV}}{1+z}$.

At $z < 1$ the main source of energy loss for photons is electromagnetic cascade that involves e^+e^- pair production (PP) on the radio background photons.[3] The radio background is generated by normal and radio galaxies. Its present density is higher than that of CMB photons in the same energy range. The radio background determines the mean interaction length for the e^+e^- pair production. At red shift z, however, the comoving density of CMB photons is the same, while the comoving density of the radio background is lower. Let z_R be the value of red shift at which the scattering of high-energy photons off CMBR dominates over their scattering off RB. Based on the models of RB, we take $z_R \sim 3$. Another source of energy losses in the electromagnetic cascade is the synchrotron radiation by the electrons in the intergalactic magnetic field (IGMF). This is an important effect for red shift $z < z_M$, where $z_M \sim 5$ corresponds to the time when IGMF is weak, and the synchrotron losses are not significant.

Let us now consider the propagation of photons at $z > z_{\min} = \max(z_R, z_M)$. In particular, we are interested in the neutrino-generating process $\gamma\gamma_{CMB} \to \mu^+\mu^-$. Although the cross section for the electron pair production is higher than that for the muon pair production, neutrinos are nevertheless produced. This is because the high-energy photons are continuously regenerated in the electromagnetic cascade.[3] The energy attenuation length λ_{eff} is much greater than the pair production interaction length $\lambda(\gamma\gamma_{CMB} \to e^+e^-)$.

Since $\lambda_{\mathrm{eff}} \gg \lambda(\gamma\gamma_{CMB} \to \mu^+\mu^-)$, in the absence of dense radio background all photons with $E > E_{\mathrm{th}}$ pair-produce muons and pions before their energy is reduced by the cascade. Due to the kinematics, one of the two muons has a much higher energy than the other, in full analogy with the e^+e^- case. Muons decay before they can interact with the photon background. Each energetic muon produces two neutrinos and an electron. The latter can regenerate a photon via inverse Compton scattering. This process can repeat until the energy of a regenerated photon decreases below the threshold for muon pair production.

The flux of neutrinos from muon decays depends on the cosmological evolution of sources.[4] Signature neutrinos can be observed by such future detectors as HiRes, Pierre Auger, EUSO, OWL, ICE CUBE, and others.

This work was supported in part by the US Department of Energy grant DE-FG03-91ER40662, Task C, as well as by a grant from UCLA Council on Research.

References

1) M. Takeda et al.: Phys. Rev. Lett. **81**, 1163 (1998); M. A. Lawrence, R. J. Reid, and A. A. Watson: J. Phys. G **17**, 733 (1991); D. J. Bird et al.: Phys. Rev. Lett. **71**, 3401 (1993); Astrophys. J. **424**, 491 (1994); N. Hayashida et al.: Astrophys. J. **522**, 225 (1999); astro-ph/0008102.
2) K. Greisen: Phys. Rev. Lett. **16**, 748 (1966); G. T. Zatsepin, and V. A. Kuzmin: Pisma Zh. Eksp. Teor. Fiz. **4**, 114 (1966).
3) For review, see, *e.g.*, P. L. Biermann: J. Phys. G **23**, 1 (1997); P. Bhattacharjee and G. Sigl: Phys. Rep. **327**, 109 (2000).
4) A. Kusenko and M. Postma: hep-ph/0007246.

* Department of Physics and Astronomy, UCLA, USA

Light-Front Realization of Chiral Symmetry Breaking

K. Itakura and S. Maedan*

Finding an appropriate method of describing the chiral symmetry breaking is one of the most important problems in the light-front (LF) formalism. This is because while in the usual quantization scheme the chiral symmetry breaking is attributed to a nontrivial vacuum structure, the vacuum in the LF quantization is kinematically forced to be the Fock vacuum and thus has no structure in it. More strictly speaking, the dispersion relation

$$p^- = \frac{p_\perp^2 + m^2}{2p^+}$$

tells us that the sign of light-front energy p^- and longitudinal momentum p^+ are correlated, and thus imposing the semipositivity of the LF energy $p^- \geq 0$ indicates that p^+ is also positive. If the $p^+ = 0$ state with divergent LF energy is removed, then we have only positive longitudinal momentum, which excludes the mixing of particle states with the vacuum state having zero momentum. On the one hand, this property is considered to be a great merit of the LF formalism. Due to the simplicity of the vacuum, we can describe excited states as valence states, which reminds us of the constituent picture of hadrons. On the other hand, the constituent picture is considered to be realized by the dynamical chiral symmetry breaking. As mentioned above, this phenomenon is, in the usual formulation, described by determining a new vacuum which breaks the chiral symmetry but is energetically favored. Therefore a question comes to mind: How can the chiral symmetry breaking be realized in the LF quantization which has a trivial vacuum?

In recent years, we have been studying this problem using the chiral Yukawa model and the Nambu-Jona-Lasinio model. Details can be found in Ref. 1 and also a review of our approach is given in Ref. 2. Based on careful analyses of the models, we found clear answers to the following three fundamental questions:

(1) *How is the LF chiral transformation different from the ordinary chiral transformation?* This should be asked because the LF chiral transformation is defined only on the "good" spinor component ψ_+ (independent degrees of freedom):

$$\psi_+ \longrightarrow e^{i\gamma_5\theta}\psi_+,$$

where $\psi = \psi_+ + \psi_-$, $\psi_\pm = 2^{-1/2}\gamma^0\gamma^\pm\psi$.

(2) *How does a gap equation for the chiral condensate emerge?* Finding a gap equation, a nonlinear equation for an order parameter, is a standard and important step to reach the symmetry breaking.

(3) *What is the consequence of the coexistence of nonzero chiral condensate $\langle\bar{\psi}\psi\rangle \neq 0$ and the trivial Fock vacuum?*

In the LF formalism, the longitudinal zero mode of a scalar field and half of the spinor component (the "bad" component ψ_-) are not independent degrees of freedom.Therefore, we have constraint equations (the zero-mode and fermionic constraints) which make the analysis extraordinarily difficult.

Answers to Question 1) were achieved after we solved the constraints classically. We have verified that the LF chiral transformation is eventually equivalent to the usual chiral transformation in the massless fermion case.

The answer to Question 2) is based on our recognition that the nonlinear constraints themselves are the keys to the gap equation. Indeed, we found that the constraints become the gap equation if we treat them nonperturbatively in a quantum theory. We also noted that it was very important to carefully treat the infrared divergences in p^+ integrals when we identified the constraints with the gap equations. By solving the gap equation, we obtained a nonzero chiral condensate.

Question 3) is intimately related to another important problem: reconciliation between the invariance of the vacuum under the LF chiral transformation $Q_5^{\rm LF}|0\rangle = 0$ and the nonzero chiral condensate. Both are understood by the modified chiral transformation laws for the dependent variables:

$$[Q_5^{\rm LF}, \bar{\psi}i\gamma_5\psi] \neq -2i\bar{\psi}\psi$$

where both fermion bilinear operators contain the bad component and thus have different forms depending on the solutions of the constraints (gap equations). The unusual transformation law of the bad component also indicates a surprising result

$$[Q_5^{\rm LF}, H] \neq 0.$$

Eventually, the characteristic features of the LF chiral symmetry in the broken phase are found to be that the chiral charge Q_5 is no longer conserved and that the transformation for the scalar and pseudoscalar fields is modified. We have also succeeded in computing the light-cone wave functions of the scalar and pseudoscalar mesons in the Nambu-Jona-Lasinio model.

References

1) K. Itakura and S. Maedan: Phys. Rev. D **61**, 045009 (2000); Phys. Rev. D **62**, 105016 (2000).
2) K. Itakura and S. Maedan: hep-ph/0102330.

* Department of Physics, Tokyo National College of Technology

Transport Model for Relativistic Nuclear Collisions

Y. Nara, S. E. Vance,[*1] and P. Csizmadia[*2]

Data from the first run at the Relativistic Heavy Ion Collider (RHIC) at Brookhaven National Laboratory have shown a large elliptic flow[1] and a moderate number of charge particles.[2] Collisions at RHIC energies are different from those in previous experiments at lower energies since many minijets (semi-hard partons) are produced in the initial condition.

Many microscopic models of heavy-ion interactions such as [3–6] do not include parton degrees of freedom and only include soft hadronic resonance and Regge physics which are crucial in understanding interactions at AGS and SPS energies. On the other hand, the HIJING model[7,8] focuses only on the minijet initial condition and at present does not include either parton or hadron rescattering. Thus, new models that include both partonic and hadronic physics are needed. One attempt at the development of such a model can be found in Ref. 9. In this report, a new transport model is presented through which the importance of the rescattering of the initially produced partons at RHIC energies can be studied.

This model contains the following elements. First, minijets produced in AA collisions are calculated assuming Eikonal approximation for pQCD (HIJING) as an initial condition of parton transport. Using this initial condition, we evolve the initially produced partons using the relativistic Boltzmann equation in which the parton-parton cross sections are calculated from pQCD. The processes $g + g \to g + g$, $g + g \leftrightarrow q + \bar{q}$, $g + q \to g + q$ and $g + \bar{q} \to g + \bar{q}$, along with radiation associated with the outgoing partons (final state radiation) are included. This calculation is a full 3-D simulation where assumptions such as boost invariance are not made. Once the partons finish rescattering, the minijets are fragmented into hadrons. Future additions to this model must be to include the rescattering of the produced hadrons.

The effect of these interactions is to increase u and d quarks jets by 80%, s quark jets by 50%, and c quark jets by 20%. In addition, these newly produced jets are shown to have smaller mean p_T. Figure 1 shows the gluon transverse momentum distributions from our calculations at $\sqrt{s} = 130\,A\,\mathrm{GeV}$ for central Au+Au collisions ($b < 3\,\mathrm{fm}$). The result of the rescattering including the final-state radiation of the gluon jets is a loss of energy of minijets at high p_T and a slight increase in the low $1\,\mathrm{GeV} < p_T < 2\,\mathrm{GeV}$ region. The transverse energy (dE_T/dy) at mid-rapidity decreases due to the parton-parton collisions.[9] The effect of the final state radiation among minijet interactions are small in our model. In comparison, other models of jet energy loss, such as the HIJING jet quenching calculation, increase hadron yields. In this work, soft mode of the plasma is treated by string and we do not include interaction of strings. Instead of strings, soft gluons can be included. Then we can follow the time evolution of the soft mode.

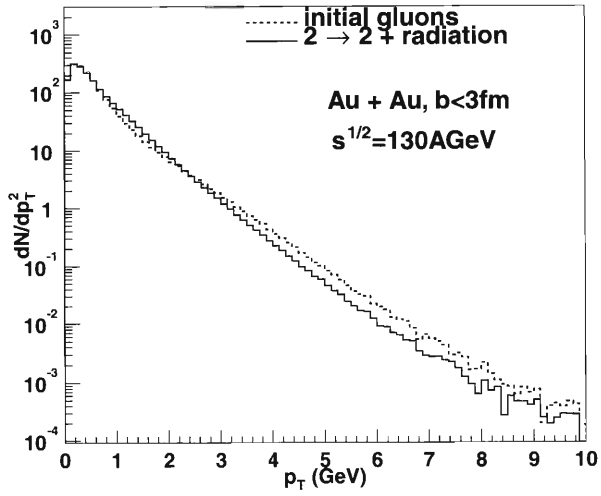

Fig. 1. Minijet gluon transverse momentum distributions for Au+Au collisions ($b < 3\,\mathrm{fm}$) at $\sqrt{s} = 130\,A\,\mathrm{GeV}$. The dotted line denotes the gluon distribution from the initial conditions and the solid line represents gluon distribution after rescattering.

Other possible signatures of this scattering phase are the K^+/π^+ yields as a function of p_T and the acoplanarity of the D and $\bar{D}$ meson pair. Work is in progress to extract those observables.

References
1) STAR Collaboration: Phys. Rev. Lett. **86**, 402 (2000).
2) PHOBOS Collaboration: Phys. Rev. Lett. **85**, 3100 (2000).
3) B. Andersson et al.: Z. Phys. C **57**, 485 (1993).
4) H. Sorge: Phys. Rev. C **52**, 3291 (1995).
5) K. Werner: Phys. Rep. **87**, 232 (1993).
6) S. A. Bass et al.: Prog. Part. Nucl. Phys. **41**, 225 (1998).
7) X. N. Wang and M. Gyulassy: Phys. Rev. D **44**, 3501 (1991).
8) M. Gyulassy and X. N. Wang: Comp. Phys. Comm. **83**, 307 (1994).
9) B. Zhang, C. M. Ko, B. -A. Li, and Z. Lin: Phys. Rev. C **61**, 067901 (2000).

*1 Physics Department, Brookhaven National Laboratory, USA
*2 KFKI Research Institute for Particle and Nuclear Physics (RMKI), Hungary

Properties of Gluons in Color Superconductors

D. H. Rischke

Cold, dense quark matter is a color superconductor.[1] Thanks to asymptotic freedom, one can compute quantities of this phase at large quark chemical potentials, μ, in a controlled way. For instance, the magnitude of the color-superconducting gap parameter, ϕ, can be self-consistently computed from a Dyson–Schwinger equation in one-loop approximation.[2] Commonly, one uses the "hard, dense loop (HDL) approximation"[3] for the gluon propagator in the loop. In cold, dense quark matter, quark particle-hole excitations constitute the dominant contribution to the gluon self-energy. In the HDL approximation, however, the quarks are assumed to be those in a normal conductor, not of a superconductor. This is in principle incorrect, and the correct solution could lead to changes in the magnitude of ϕ.

In order to test this hypothesis, one has to compute the quark loop in the gluon self-energy with quark propagators appropriate for a color-superconducting medium, resum the resulting expression to obtain the gluon propagator, and finally use this modified propagator when solving the gap equation.

This is an ambitious program which has not been completed up to date. I report here on a first step in this direction, namely the computation of the gluon self-energy in the limit of vanishing gluon energy and momentum.[4] In this limit, the self-energy of electric gluons determines the Debye mass, and that of magnetic gluons the Meissner mass. The results for the Debye and Meissner masses in color superconductors with $N_f = 2$ and $N_f = 3$ flavors of massless quarks are summarized in Table 1. Calculations of the gluon self-energy for $N_f = 2$ and $N_f = 3$ at non-vanishing energy and momentum are presently under way.

Table 1. Results for the Debye and Meissner masses in two- and three- flavor color superconductors, $m_g \equiv \sqrt{N_f/6}\, g\, \mu/\pi$.

flavor	gluon color	$-\Pi^{00}_{aa}(0)$	$\Pi^{ii}_{aa}(0)$
2	1 – 3	0	0
2	4 – 7	$\frac{3}{2}\, m_g^2$	$\frac{1}{2}\, m_g^2$
2	8	$3\, m_g^2$	$\frac{1}{3}\, m_g^2$
3	1 – 8	$\frac{21-8\ln 2}{18}\, m_g^2$	$\frac{21-8\ln 2}{54}\, m_g^2$

References

1) D. Bailin and A. Love: Phys. Rep. **107**, 325 (1984).
2) For instance, R. D. Pisarski and D. H. Rischke: Phys. Rev. D **61**, 051501, 074017 (2000).
3) M. Le Bellac: *Thermal Field Theory*, (Cambridge University Press, Cambridge, 1996).
4) D. H. Rischke: Phys. Rev. D **62**, 034007, 054017 (2000).

Phases of QCD at High Baryon Density

T. Schäfer

We have studied the phase structure of QCD at very high baryon density $\rho \gg \Lambda_{QCD}^{-3}$. In this regime the natural degrees of freedom are quasiparticles and holes in the vicinity of the Fermi surface. Since the Fermi momentum is large, asymptotic freedom implies that the interaction between quasiparticles is weak. We know from the theory of superconductivity that the Fermi surface is unstable in the presence of even an arbitrarily weak attractive interaction. At very large density, the attraction is provided by one-gluon exchange between quarks in a color anti-symmetric $\bar{3}$ state. QCD at high density is therefore expected to behave as a color superconductor.[1,2)]

Color superconductivity implies that the local gauge symmetry is broken by a Higgs mechanism. There is a gap in the fermion excitation spectrum and gauge fields are screened by the Meissner effect. In addition to that, color superconductivity can lead to the breakdown of global symmetries. In particular, for $N_f > 2$, chiral symmetry is broken even at asymptotically large baryon density.

If the density is large, the gap can be calculated in weak coupling perturbation theory. The gap equation is dominated by magnetic gluon exchange and we find[3)]

$$\Delta = 512\pi^4 \mu g^{-5} \exp\left(-\frac{3\pi^2}{\sqrt{2}g}\right). \qquad (1)$$

In this regime, we can also study the phase structure.[3)] The superconducting order parameter depends sensitively on the number of flavors and their masses. For two degenerate flavors the superconducting phase breaks color $SU(3) \to SU(2)$ but leaves chiral symmetry unbroken.[2)] In the case of three degenerate flavors the color $SU(3)$ and chiral $SU(3) \times SU(3)$ symmetry are broken, but a diagonal $SU(3)_V$ symmetry survives. If the strange quark mass is included, one finds a first order phase transition between this two phases. For $N_f > 3$ chiral symmetry is broken, but the chiral symmetry breaking pattern is different from the one at zero density. For $N_f = 1$, one finds a spin 1 superconductor where the color and rotational symmetry are broken according to $SU(3) \times SO(3) \to SO(3)$.

References

1) D. Bailin and A. Love: Phys. Rep. **107**, 325 (1984).
2) R. Rapp, T. Schäfer, E. V. Shuryak, and M. Velkovsky: Phys. Rev. Lett. **81**, 53 (1998); M. Alford, K. Rajagopal, and F. Wilczek: Phys. Lett. B **422**, 247 (1998).
3) T. Schäfer: nucl-th/0010049, and references therein.

Signals of Hypermatter at RHIC

J. Schaffner-Bielich, R. Mattiello,[*1] and H. Sorge[*2]

We investigated the production and decay of possible bound states of one hyperon with a nucleon and of two hyperons at the Relativistic Heavy Ion Collider (RHIC) at Brookhaven National Laboratory.[1] Up to 200 hyperons may be produced in a single central collision of two gold nuclei at RHIC. This opens up the possibility of forming and detecting new states of matter with hyperons. The production rates for forming dibaryon states with hyperons has been estimated using the wave function coalescence model. The initial phase space distribution of the single baryons was taken from the event generator RQMDv2.4. The wave function of the dibaryon states was approximated by a Hulthen wave function. We obtained production estimates in the range of 10^{-2} to 10^{-4} per central collision. The rapidity distribution is flat, enabling detection at forward and backward rapidity and at mid-rapidity. The production numbers will be enhanced if a chirally restored phase or a quark-gluon plasma is formed in the collision. In the former case, the baryon masses drop and thus more baryons are produced. In the latter case, the number of strange quarks will increase in the plasma, generating more strange hadrons in the final state.

The strange dibaryons, if formed and bound, can be detected by their weak decay. We calculated the lifetime as well as the branching ratios of various strange dibaryon candidates. We use SU(3) symmetry to describe the weak nonleptonic decay of hyperons. The weak operator is assumed to be proportional to the Gell-Mann matrix λ_6 which ensures hypercharge violation $|\Delta Y| = 1$, the $\Delta I = 1/2$ rule and the Lee-Sugawara relation for the parity-violating amplitudes. The parity-violating as well as the parity-conserving amplitudes can be described effectively by the Lagrangian:

$$\begin{aligned}\mathcal{L} = & D\mathrm{Tr}\bar{B}B\left[P,\lambda_6\right] + F\mathrm{Tr}\bar{B}\left[P,\lambda_6\right]B \\ & + G\mathrm{Tr}\bar{B}P\gamma_5 B\lambda_6 + H\mathrm{Tr}\bar{B}\lambda_6\gamma_5 BP \\ & + J\mathrm{Tr}\bar{B}\{P,\lambda_6\}\gamma_5 B.\end{aligned}$$

Here, B stands for the baryons and P for the pseudoscalar mesons. The five parameters D to J are fitted to the measured 14 amplitudes and the fit results in a reasonable description of all measured amplitudes. We note that the standard model for the weak nonleptonic decay of hyperons, the pole model, fails to explain the parity-conserving amplitudes.[2] The nonmesonic decay modes of the strange dibaryons are modeled by the exchange of pions and kaons using the above interaction for the weak vertex and SU(6) symmetry for the strong vertex. The wave function of the dibaryons is again assumed to be of Hulthen-like shape with varying binding energy.

The calculated lifetimes of the strange dibaryons are somewhat shorter than the ones for hyperons in free space, *i.e.* the decay lengths are about $c\tau = 1$–$5\,\mathrm{cm}$. The lifetime decreases with binding energy as the two baryons are closer together in phase-space. We also find that the branching ratios depend sensitively on the binding energy. The mesonic decay dominates at small binding energies of approximately 1–3 MeV, while the nonmesonic decay is most pronounced for larger binding energies. This is to be expected as this behaviour has been observed experimentally for the weak mesonic and nonmesonic decay of hypernuclei. In particular, the nonmesonic decay is of interest for heavy-ion experiments, as it involves only two hadrons in the final state. For a possible bound dilambda state, we find that the main decay channel is $\Lambda\Lambda \to \Sigma^- + \mathrm{p}$, the same as for the hypothetical H-dibaryon.[3] The $\Xi^0\mathrm{p}$ dibaryon decays mainly to a Λ and a proton, while the $\Lambda\Xi^0$ dibaryon can be seen by its decay to a Ξ^- and a proton. Doubly negatively charged dibaryons, like the $\Sigma^-\Xi^-$, can decay to two Σ^-'s, a unique decay prong.

Strange dibaryons, bound or not, can be detected by the following means:

(1) Experiments with a time-projection chamber can track for unique exotic decays like a charged particle decaying to two charged particles or tracks forming a vertex a few cm outside the target.

(2) Experiments sensitive to hyperons can look for peaks in the invariant mass spectrum of pp, pΛ, $\Lambda\Lambda$, pΞ^-, and $\Lambda\Xi^-$ by background subtraction using event mixing. This method is sensitive to both bound states as well as unbound states close to the threshold with a small decay width.

(3) The strong interaction force of $\Lambda\Lambda$ and $\Lambda\Xi^-$ and possible resonance structures can be probed in correlation functions as they depend sensitively on final-state interactions. Note that the Coulomb potential does not mask the strong interactions so that information about the presently unknown hyperon-hyperon forces can be extracted directly.[4]

*1 Niels Bohr Institute, Denmark
*2 State University of New York, USA

References
1) J. Schaffner-Bielich, R. Mattiello, and H. Sorge: Phys. Rev. Lett. **84**, 4305 (2000).
2) J. F. Donoghue, E. Golowich, and B. R. Holstein: Phys. Rep. **131**, 319 (1986).
3) R. L. Jaffe: Phys. Rev. Lett. **38**, 195 (1977).
4) A. Ohnishi, Y. Hirata, Y. Nara, S. Shinmura, and Y. Akaishi: Nucl. Phys. A **670**, 297 (2000).

Bottom-Up Thermalization in Heavy-Ion Collisions

R. Baier,[*1] A. H. Mueller,[*2] D. Schiff,[*3] and D. T. Son[*2]

It is possible that at RHIC, for the first time, heavy-ion collisions occur at energies high enough to be described by perturbative QCD. At the Large Hadron Collider (LHC), perturbative QCD is expected to work even better. The relevant hard scale is the saturation scale Q_s, estimated to be 1 GeV at RHIC and 2–3 GeV at LHC.[1–5]

The single most important issue in the physics of heavy-ion collisions is thermalization. The conventional argument in favor of thermalization is that at larger collision energies, more gluons are freed in the first moment after the collision, and these gluons collide more frequently with each other. However, the distribution of these gluons is initially very far from thermal equilibrium. In addition, the strong coupling constant decreases at high energies, making thermalization harder to achieve. Whether the system has enough time to equilibrate before falling apart is thus a delicate issue requiring detailed consideration of different physical processes.

In a recent paper,[6] we show that in the limit $Q_s \gg \Lambda_{\rm QCD}$ corresponding to very large nuclei and/or a very high collision energy, thermalization occurs relatively fast while the system is still undergoing one-dimensional expansion. The unexpected feature of our analysis is the manner in which thermalization occurs. During the first period, the most important process is the emission of soft gluons. At first, these soft gluons are too few to have any influence on the evolution of the whole system, but at approximately time $\tau \sim \alpha^{-3/2} Q_s^{-1}$, where α is the strong coupling constant at the scale Q_s, soft gluons begin to dominate the Debye screening even while their density is still much smaller than that of the hard ones. The number of soft gluons becomes comparable to that of the hard ones at time $\tau \sim \alpha^{-5/2} Q_s^{-1}$, after which most gluons are soft. The soft gluons then collide very frequently with each other and achieve thermal equilibration amongst themselves. At first, the temperature of the thermal bath formed by soft gluons is $\alpha^{1/2} Q_s$, and soft gluons carry only a fraction $\alpha^{1/2}$ of the total energy. The system as a whole is still not in thermal equilibrium, since most of the energy is carried by a small number of hard gluons. These few gluons collide with the soft gluons of the thermal bath and constantly lose energy to the latter, heating up the soft thermal bath. During this time, the temperature of the soft thermal bath grows linearly with time, $T \sim \alpha^3 Q_s^2 \tau$. Full thermalization is achieved when the primary hard gluons have lost all their energy. Parametrically, this happens at $\tau \sim \alpha^{-13/5} Q_s^{-1}$, at which time the temperature of the system achieves the maximal value of $\alpha^{2/5} Q_s$.

We have derived the kinetic equations that describe the evolution of the system during the last period $Q_s \tau \gg \alpha^{-5/2}$. At these times, the system is characterized by the temperature of the soft sector T and the energy spectrum of the hard gluons $\epsilon(p)$, which evolve with time according to the following equations

$$\frac{1}{\tau}\frac{\partial}{\partial \tau}(\tau \epsilon(p)) = \frac{\alpha^2 N^{\frac{1}{2}}}{p^{\frac{1}{2}}} \int_0^1 dx\, h(x) \left[x^{\frac{1}{2}} \epsilon\left(\frac{p}{x}\right) - \frac{1}{2}\epsilon(p) \right],$$

$$\frac{1}{\tau^{4/3}}\frac{\partial}{\partial \tau}(\tau^{4/3} g_E T^4) = b h_0 \alpha^2 N^{\frac{1}{2}} \lim_{p \to 0} p^{\frac{1}{2}} \epsilon(p),$$

where $g_E = \pi^2 (N_c^2 - 1)/15$, $N = \frac{1}{3}(N_c^2 - 1) T^3$, $h(x) = h_0 (1 - x + x^2)^{5/2} (x - x^2)^{-3/2}$, $b \approx 4.96$, and

$$h_0 = \frac{2}{\pi^{1/2}} \frac{N_c^2}{(N_c^2 - 1)^{1/2}} \ln^{1/2}[\alpha^5 (Q_s \tau)^2].$$

Surprisingly, the time dependence of the temperature of the soft sector in the (admittedly narrow) region $\alpha^{-5/2} \ll Q_s \tau \ll \alpha^{-13/5}$ can be found almost analytically, and the result depends only on the total number of primary hard gluons (but not on their distribution function).

Although the analysis requires a small coupling, one can hope that many qualitative features of this picture are already present in heavy-ion collisions at LHC or even at RHIC energies. At the very least, the finding gives us confidence that thermalization always occurs in heavy-ion collisions at sufficiently high energies.

References

1) L. V. Gribov, E. M. Levin, and M. G. Ryskin: Phys. Rep. **100**, 1 (1983).
2) J.-P. Blaizot and A. H. Mueller: Nucl. Phys. B **289**, 847 (1987).
3) L. McLerran and R. Venugopalan: Phys. Rev. D **49**, 2233 (1994); Phys. Rev. D **49**, 3352 (1994); Phys. Rev. D **50**, 2225 (1994).
4) J. Jalilian-Marian, A. Kovner, L. McLerran, and H. Weigert: Phys. Rev. D **55**, 5414 (1997).
5) K. J. Eskola, K. Kajantie, P. V. Ruuskanen, and K. Tuominen: Nucl. Phys. B **570**, 379 (2000).
6) R. Baier, A. H. Mueller, D. Schiff, and D. T. Son: Phys. Lett. B, in press; hep-ph/0009237.

*1 Universität Bielefeld, Germany
*2 Columbia University, USA
*3 Université Paris-Sud, France

Isospin Dense Matter and Quark-Hadron Continuity

M. A. Stephanov*1 and D. T. Son*2

Good knowledge of QCD in the regime of finite temperature and baryon density is crucial for understanding a wide range of phenomena, from heavy-ion collisions to neutron stars and cosmology. To understand the regime of finite baryon density, one should be able to follow the transition from hadronic to quark degrees of freedom by increasing the density of a *conserved* charge (such as baryon number), *i.e.*, without invoking the temperature. This is the motivation for us to turn to QCD at finite chemical potential μ_I of *isospin* (more precisely, of the third component, I_3). Nature provides us with nonzero μ_I systems in the form of isospin-asymmetric matter. However, such matter contains both isospin density *and* baryon number density. In contrast, the idealized system considered in this report does not carry baryon number: the chemical potentials of the two light quarks, u and d, are equal in magnitude, $|\mu_I|/2$, and opposite in sign.

Small isospin densities—When μ_I is small compared to the chiral scale (m_ρ), we can use chiral perturbation theory. For zero quark mass and zero μ_I, the pions are massless Goldstone bosons of spontaneously broken $\mathrm{SU}(2)_L \times \mathrm{SU}(2)_R$ chiral symmetry. The Lagrangian describing the pion fields to lowest order in μ_I, m and derivatives has the form:

$$\mathcal{L}_{\text{eff}} = \frac{f_\pi^2}{4}\mathrm{Tr}\nabla_\nu\Sigma\nabla_\nu\Sigma^\dagger - \frac{m_\pi^2 f_\pi^2}{2}\mathrm{ReTr}\Sigma, \tag{1}$$

where the covariant derivative is defined as

$$\nabla_0\Sigma = \partial_0\Sigma - \frac{\mu_I}{2}(\tau_3\Sigma - \Sigma\tau_3). \tag{2}$$

Using Eq. (1) one can straightforwardly determine the vacuum alignment of Σ as a function of μ_I and the spectrum of excitations around the vacuum.

(i) For $|\mu_I| < m_\pi$, the system is in the same ground state as when $\mu_I = 0$: $\overline{\Sigma} = 1$. This is because the lowest-lying pion state costs a positive energy $m_\pi - |\mu_I|$ to excite, which is impossible at zero temperature.

(ii) When $|\mu_I|$ exceeds m_π it is favorable to excite π^- quanta, which form a Bose condensate. In the language of the effective theory, such a pion condensate is described by a tilt of the chiral condensate $\overline{\Sigma}$,

$$\overline{\Sigma} = \cos\alpha + i(\tau_1\cos\phi + \tau_2\sin\phi)\sin\alpha;$$
$$\cos\alpha = m_\pi^2/\mu_I^2. \tag{3}$$

The tilt angle α is determined by minimizing the vacuum energy. The energy is degenerate with respect to the angle ϕ, corresponding to the spontaneous breaking of the $\mathrm{U}(1)_{L+R}$ symmetry generated by I_3 in the Lagrangian (1). The ground state is a pion superfluid, with one massless Goldstone mode. Since we start from a theory with three pions, there are two massive modes which can be identified with π^0 and a linear combination of π^+ and π^-. At the condensation threshold, $m_{\pi^0} = m_\pi$ and the mass of the other mode is $2m_\pi$, while for $|\mu_I| \gg m_\pi$, both masses approach $|\mu_I|$.

The isospin density is determined by differentiating the ground state energy with respect to μ_I and is equal to:

$$n_I = f_\pi^2\mu_I\sin^2\alpha = f_\pi^2\mu_I\left(1 - \frac{m_\pi^4}{\mu_I^4}\right). \tag{4}$$

Asymptotically high isospin densities—In the opposite limit of very large isospin densities, or $|\mu_I| \gg m_\rho$, the description in terms of quark degrees of freedom applies since these degrees of freedom are weakly interacting due to asymptotic freedom. In our case of large negative μ_I, or n_I, the ground state consists of d quarks and $\bar{u}$ antiquarks which, neglecting the interaction, fill two Fermi spheres with equal radii $|\mu_I|/2$. Turning on the interaction between the fermions leads to instability with respect to the formation and condensation of Cooper pairs, similar, to an extent, to the diquark pairing at high baryon density. In our case, $\mu_I < 0$, the Cooper pair consists of a $\bar{u}$ and a d in the color singlet channel. The order parameter has the same quantum numbers as the pion condensate at lower densities,

$$\langle\bar{u}\gamma^5 d\rangle \neq 0. \tag{5}$$

Due to the Cooper pairing, the fermion spectrum acquires a gap Δ at the Fermi surface, where

$$\Delta = b|\mu_I|g^{-5}e^{-c/g}, \qquad c = 3\pi^2/2, \tag{6}$$

and g should be evaluated at the scale $|\mu_I|$.

Quark-hadron continuity—Since the order parameter (5) has the same quantum numbers and breaks the same symmetry as the pion condensate in the low-density regime, it is plausible that there is no phase transition along the μ_I axis. In this case, the Bose condensate of weakly interacting pions smoothly transforms into the superfluid state of $\bar{u}d$ Cooper pairs. The situation is very similar to that of strongly coupled superconductors with a "pseudogap," and possibly of high-temperature superconductors. This also parallels the continuity between nuclear and quark matter in three-flavor QCD as conjectured by Schäfer and Wilczek. We hence conjecture that in two-flavor QCD one can move continuously from the hadron phase to the quark phase without encountering a phase transition. Since a first-order deconfinement phase transition at intermediate isospin chemical potential cannot be rigorously ruled out (though it is unlikely), this conjecture needs to be verified by lattice calculations.

*1 University of Illinois at Chicago, USA
*2 Columbia University, USA

An Effective Theory of Nuclear Matter

U. van Kolck*

The description of relativistic heavy-ion collisions requires an understanding of the hadronic phase of the QCD phase diagram. We have been developing a systematic framework to predict matter at finite baryonic density ρ and temperature T based on QCD, through the use of effective field theory (EFT) methods. The most general Lagrangian involving low-energy degrees of freedom and consistent with the symmetries of QCD is constructed. Interactions are ordered according to an expansion in powers of momenta (related to ρ and T). To any given order, observables are written in terms of a finite number of parameters, which in principle can be calculated from details of the QCD dynamics (for example, through lattice methods). As in the case of a pion gas,[1] the breakdown of the expansion in T at finite ρ should signal the position of the transition.

Two EFTs are being considered. At lowest energies, nucleons have only contact interactions. At higher energies, pions (but not heavier mesons) are accounted for explicitly as well, and chiral symmetry plays an essential role in guaranteeing that the nuclear potential has an expansion in momenta.

The two-nucleon system has been investigated[2] — including some issues of renormalization stemming from the singular nature of the potential[3]—and the three-nucleon system solved[4] in leading order. We are currently working on the four-nucleon system in order to complete the determination of the leading few-nucleon forces. Due to the Pauli principle, interactions with more than four nucleons should involve derivatives and thus be suppressed.

At the same time, the first steps are being taken in developing the tools for calculating nuclear matter properties. Using Monte Carlo methods in a spatial lattice, we have solved[5] exactly the toy problem of nucleons interacting *via* two-body contact forces with free coefficients, at finite T. Generalization to EFT interactions is in progress.

References

1) P. Gerber and H. Leutwyler: Nucl. Phys. B **321**, 387 (1989).
2) U. van Kolck: Prog. Part. Nucl. Phys. **43**, 337 (1999).
3) S. R. Beane, P. F. Bedaque, L. Childress, A. Kryjevski, J. McGuire, and U. van Kolck: quant-ph/0010073.
4) P. F. Bedaque, H. W. Hammer, and U. van Kolck: Nucl. Phys. A **676**, 357 (2000).
5) H. M. Müller, S. E. Koonin, R. Seki, and U. van Kolck: Phys. Rev. C **61**, 044320 (2000).

* University of Arizona, USA

Looking for a Colored Glass Condensate in High Energy Collisions

R. Venugopalan*

We have learnt from HERA that the gluon density in a proton grows very rapidly at small values of x_{Bj}. At sufficiently small values of x_{Bj}, if the density of gluons in a proton is so large that they begin to overlap, the many body repulsive and attractive interactions among the gluons conspire to form a novel state of matter we will call a Colored Glass Condensate[1] (CGC). The reason for this terminology is as follows. The matter is colored since gluons carry color charge; it is a glass because there is a formal analogy between the infrared properties of this theory and that of a spin glass; it is a condensate because most of the gluons are concentrated in a narrow band of momentum states of high occupation number.

The properties of the colored glass condensate are described by a classical effective field theory (EFT) of QCD.[2] The EFT is characterized by a bulk scale Q_s^2—the gluon density per unit area of modes with x's greater than the x value of interest. Since it is the only scale in the EFT, if $Q_s \gg \Lambda_{QCD}$, the physics of the CGC can be studied using weak coupling techniques. It has been shown recently[3] that Wilsonian renormalization group techniques can be applied to the EFT—the scale Q_s grows with decreasing x_{Bj}. In the limit of low parton densities, the standard QCD evolution equations, known by the acronyms DGLAP and BFKL, are recovered.[4] The regime of high parton densities is described by a non-linear renormalization group equation. In the large N_c limit, it agrees with an equation derived by Balitsky and Kovchegov independently using different techniques.[5]

Since the current and future generation of collider experiments will begin probing large parton densities, it will be interesting to look for signatures of the CGC. In the context of heavy ion collisions, A. Krasnitz and I have shown that the initial energy and number distribution of produced gluons is directly and simply related to the scale Q_s of the condensate.[6] Further, J. Bjoraker and I have shown that the equilibration time and the initial temperature of the quark gluon plasma can be related to the scale Q_s.[7] This was also shown independently by Baier, Mueller, Schiff and Son, who also included $2 \to 3$ processes that were not included in our approach.[8] Work is underway to see if RHIC data can be understood in this framework.

Signatures of the CGC can also be observed in pA and eA collisions. We will focus here on eA collisions.[9] In a high energy eA collider (the proposed eRHIC at BNL) the properties of the CGC can be studied through a variety of inclusive and semi-inclusive measurements. For instance, one expects a striking deviation in $dF_2/d\ln(Q^2)$ (F_2 is the electromagnetic form factor of a nucleus) versus Q^2 for a fixed x — from the QCD-DGLAP predictions. A maximum is also predicted in the ratio F_L/F_T. Note that the longitudinal structure function F_L will be measured at eRHIC for the first time. Semi-inclusive measurements will provide striking measures of the CGC. For instance, one expects hard diffractive events — those events with a hard final state ($M_X \gg \Lambda_{QCD}$) and a large rapidity gap — to be about 30% of the cross-section! Also, diffractive versus inclusive vector meson production should be very different depending on whether the size of the meson R_V is larger or smaller than $1/Q_s$. If $R_V > 1/Q_s$, (as for the ρ, the ω, and the ϕ) then one expects $\sigma^V_{\text{diffractive}} = 0.5\sigma^V_{\text{inclusive}}$. For $R_V < 1/Q_s$, $\sigma^V_{\text{diffractive}} \ll \sigma^V_{\text{inclusive}}$ (as is the case for the Υ).

References

1) L. McLerran: BNL-Rep. 52606, 59 (2000), see Ref. 9.
2) L. McLerran and R. Venugopalan: Phys. Rev. D **49**, 2233 (1994); Phys. Rev. D **49**, 3352 (1994); Phys. Rev. D **50**, 2225 (1994).
3) J. Jalilian-Marian, A. Kovner, L. McLerran, and H. Weigert: Phys. Rev. D **55**, 5414 (1997).
4) J. Jalilian-Marian, A. Kovner, A. Leonidov, and H. Weigert: Nucl. Phys. B **504**, 415 (1997); Phys. Rev. D **59**, 014015 (1999).
5) Y. V. Kovchegov: Phys. Rev. D **60**, 034008 (1999); I. Balitsky: Nucl. Phys. B **463**, 99 (1996); E. Iancu, A. Leonidov, and L. McLerran: SACLAY-T00-166; BNL-NT-00-24, Los Alamos e-Print Archive; hep-ph/0011241.
6) A. Krasnitz and R. Venugopalan: Phys. Rev. Lett. **84**, 4309 (2000); hep-ph/0007108.
7) J. Bjoraker and R. Venugopalan: Phys. Rev. C **63**, 024609 (2001).
8) R. Baier, A. H. Mueller, D. Schiff, and D. Son: hep-ph/0009237.
9) Proc. of the eRHIC Summer Meet., BNL Formal Rep. BNL-52606, (2000).

* Brookhaven National Laboratory, USA

Leading Local Operator Analysis of $\Phi' \to \Phi\pi\pi$ Processes

H. Fujii

Quarkonium (Φ) is a QCD bound state of a heavy quark Q and a heavy antiquark $\bar{Q}$, such as J/ψ and Υ. Due to the heavy mass of its constituents, its size is very small as compared with the typical QCD scale $\Lambda_{\rm QCD}^{-1} \sim 1$ fm. Quarkonium is, therefore, thought to be a clean theoretical laboratory to carry out the perturbative treatment (asymptotic freedom). However, the nonperturbative aspects must be taken into account properly[1] when studying the interaction of quarkonium with other light hadrons, which is essential for drawing a conclusion from the anomalous suppression of J/ψ observed in heavy-ion experiments.

Here we calculate the decay rate of $\Phi' \to \Phi\pi\pi$ based on the factorization ansatz at the scale of the quarkonium size. The coupling between $\Phi^{(\prime)}$ and soft gluons is described by the perturbation theory, which leads to the multipole expansion of the color fields. Then the hadronization amplitude of the soft gluons to the light hadrons is estimated using the low-energy theorem.

In the leading order of the multipole expansion, the amplitude for $\Phi' \to \Phi\pi\pi$ is written as

$$\mathcal{M}^{ab} = \frac{g^2}{6}\langle\phi\pi^a\pi^b|r^i E^{iA}\frac{1}{H_8+\epsilon'+iD^0}r^j E^{jA}|\phi'\rangle,$$

where g is the strong coupling constant, E^A the color electric fields and r the relative coordinate between Q and $\bar{Q}$. This expression simply indicates that the initial quarkonium (internal) state changes into the octet state via the color E1 transition, propagates with the Hamiltonian H_8 with energy $-\epsilon' - iD^0$, and returns to the singlet state again via the color E1 transition.

Although crude, we approximate this amplitude by a factorized form:

$$\mathcal{M}^{ab} \sim \frac{g^2}{2}\frac{a_0^2}{\epsilon_0} d\ \langle\pi^a\pi^b|E^{iA}E^{iA}|0\rangle,$$

where $\delta^{ij}(a_0^2/\epsilon_0)d \equiv \frac{1}{3}\int_0^\Delta \frac{dQ}{\Delta}\langle\phi|r^i(H_8+\epsilon'+Q)^{-1}r^j|\phi'\rangle$ is calculable using the quarkonium wave function, and $\Delta = m_{\Phi'} - m_\Phi$.

The remaining part of the pion matrix element contains the physics of the long-distance part. We evaluate this part using the low-energy theorem for the QCD stress tensor:[2]

$$\mathcal{M}^{ab} \sim \left(\frac{a_0^2}{\epsilon_0}d\right)\left(\frac{4\pi^2}{9}\right)sF(s)\delta^{ab},$$

where $s = (p_1+p_2)^2$, and the form factor (Omnès function) $F(s)$ obtained from the $\pi\pi$ phase shift data is included here in order to take the pion final state interactions into account.

In numerical calculation, we take the Coulomb wave function for the quarkonium internal state ϕ, fixing the parameters with the binding energy $\epsilon_0 = 2m_D - 2m_{J/\psi}$ and $m_c = 1.5\,\text{GeV}$ for J/ψ (similarly for Υ). The resulting decay widths listed in Table 1 agree with the experimental values within a factor of 5. In our framework, the shape of the pion invariant mass distribution is determined mainly by the matrix element $\langle\pi\pi|\mathbf{E}\cdot\mathbf{E}|0\rangle$. Based on Fig. 1, we find the need for a form factor which enhances the rate in the 0.5 GeV region, as well as the importance of the chiral symmetry constraint which suppresses the rate in the threshold region. Note that we did not attempt any fitting in this calculation.

Table 1. Decay width for $\psi' \to J/\psi\pi\pi$ and $\Upsilon' \to \Upsilon\pi\pi$ in unit keV.

mode	$F_{\rm omn}$	$F=1$	exp.
$\psi' \to \psi\pi\pi$	260	70	135 ± 20
$\Upsilon' \to \Upsilon\pi\pi$	2.3	0.64	12 ± 4

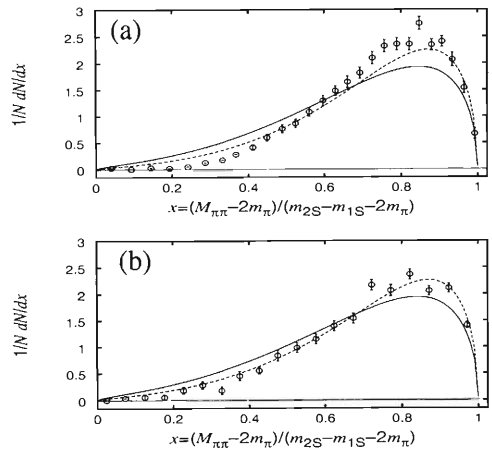

Fig. 1. Distribution of the invariant mass $m_{\pi\pi}$ for (a) $\psi' \to J/\psi\pi\pi$ and (b) $\Upsilon' \to \Upsilon\pi\pi$ decays. Data are taken from Fig. 7 of Ref. 3. The solid (dashed) line indicates the result without (with) the form factor F.

This result suggests that our simple framework correctly describes the process of quarkonium interactions up to a factor of 5. However, it is known that the process $\Upsilon(3S) \to \Upsilon(1S)\pi\pi$ has a different feature compared to that shown in Fig. 1; accordingly, it seems that other elements need to be included.

References
1) H. Fujii and D. Kharzeev: Phys. Rev. D **60**, 114039 (1999), and references therein.
2) M. Voloshin and V. Zakharov: Phys. Rev. Lett. **45**, 688 (1980).
3) H. Albrecht et al. (ARGUS): Z. Phys. C **35**, 283 (1987).

8. Miscellaneous

Topological Modes of Solidification in Liquids with a Confined Geometry

S. Ishimoto,[*1] T. Kobayashi,[*2] K. Morimoto,[*1] I. Nomura,[*3] S. Suzuki,[*1]
Y. Takahashi,[*4] I. Tanihata, and T. Tsuru[*1]

On cooling liquid hydrogen, argon, nitrogen and neon in a small copper cell from the upper side, we found new modes of solidification with topological natures,[1] *i.e.*, an evolution of a "solid string" and a pileup of half-ellipsoidal solid films inside the liquid. The string continued to develop as a three-dimensional knotwork in the liquid surrounded by the solid growing on the cold sidewall until the entire liquid solidified. The string was found to have a structure with a bubble front and a following tubular solid. Therefore, these modes are understood as ways of forming void spaces in a confined liquid required for contraction of the volume during the solid growth. When these liquids were solidified in a closed cell, it was expected that a porous isotropic solid would grow at the center part. However, these topological modes and solid tubes have not been reported to our knowledge.

The main part of our experimental apparatus was a unit of two small cells for solidification and made of pure copper as shown in Fig. 1. The upper cell was a flat cylinder with its axis in the vertical direction. The lower cell was a hole of 25 mm in diameter with its axis in the horizontal direction bored in a rectangular block of copper (72 mm × 72 mm × 10 mm). Both sides of the hole were sealed with 5-mm-thick silica windows. A straight hole of 7 mm in diameter drilled in the copper block connected these cells. The unit was firmly attached to a helium continuous-flow cryostat. Gas was introduced into the upper cell through its top flange. An appropriate amount of gas was first introduced and, then, liquid helium was slowly introduced to the upper part of the heat exchanger.

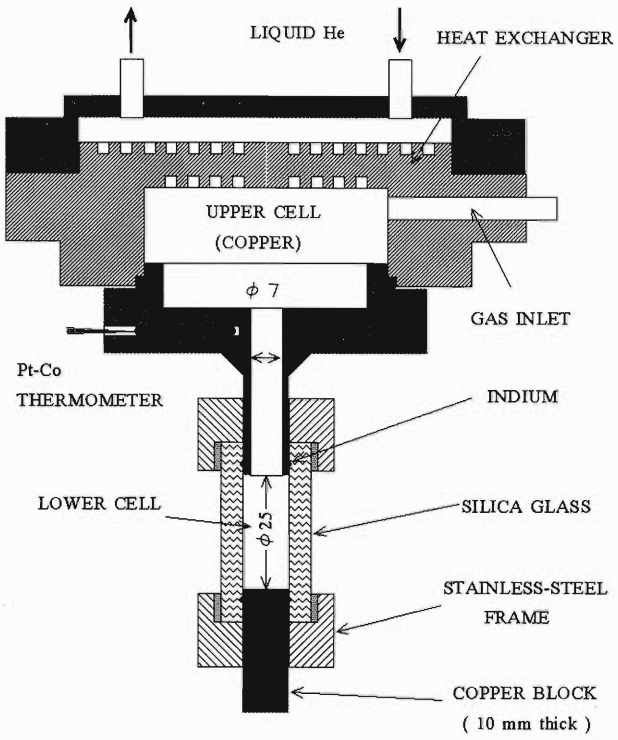

Fig. 1. Experimental apparatus.

The gas liquefied and solidified. Solidification first took place in the upper cell and blocked the holes, confining the liquid in the lower cell. Figure 2 shows a hydrogen string near 13.8 K. The front of the string moved downward, forming a transparent and uniform solid string after it. It reached then reflected off the copper sidewall or the growing solid surface, and moved straight ahead to the opposite side until it was reflected again there.

Figure 3 shows an argon string near 83.8 K. The argon string was thick, uniform and straight. The front part had the brightness of metallic silver, which was clearly the total reflection. Sometimes we observed bubbles moving upward inside the lines. This indicated clearly that the string was a tube made of a thin solid wall and not a solid bar. The moving bubbles inside the argon tubular string, which show the situation most clearly, are shown in Fig. 4. A bubble appeared at the base of the string. In the diffusive transmitted light, the remnant seemed to be a pair of thin parallel lines

Fig. 2. Hydrogen string near $T_t = 13.8$ K.

*1 High Energy Accelerator Research Organization
*2 Faculty of Science, Tohoku University
*3 National Institute for Fusion Science
*4 Research Center for Nuclear Physics, Osaka University

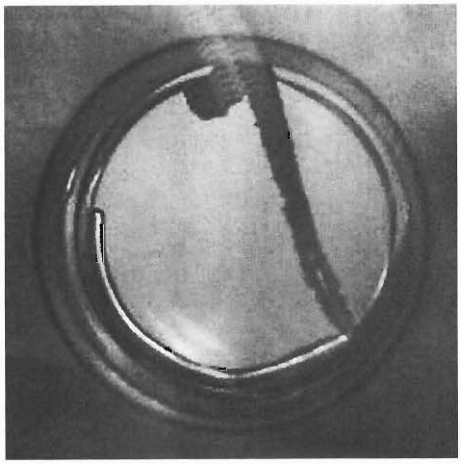

Fig. 3. Argon string near $T_t = 83.8\,\mathrm{K}$.

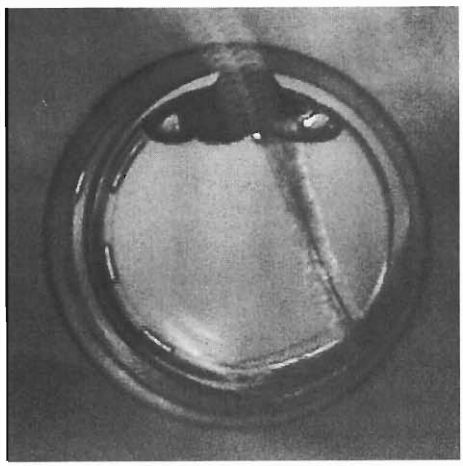

Fig. 4. Bubbles moving inside the solid tube of string in liquid argon.

which appeared similar to a transparent plastic tube. We also observed strings in nitrogen and neon liquid.

In conclusion, we observed that the liquid with a confined geometry generally adopts several topological modes of solidification, when the volume of the system must contract in the solid formation. The most interesting mode is the evolution of the solid string. We found a peculiar structure of the string, in that it consists of a bubble front and a following solid tube.

References

1) S. Ishimoto, T. Kobayashi, K. Morimoto, I. Nomura, S. Suzuki, Y. Takahashi, I. Tanihata, and T. Tsuru: RIKEN-AF-NP-354, KEK Preprint 2000-42 H, to be published.

Possible Mobile TeV Muon Source for Disasters Prevention

K. Nagamine

For the purpose of probing the internal structure of a very large object such as a volcanic mountain, the near-horizontal cosmic-ray muons with energies higher than GeV, produced as secondary cosmic rays by the interaction of the primary cosmic-ray protons in the atmospheric air, are most suitable (range of 1 TeV muon in a rock mountain: 1 km), provided that the size of the detection system is realistically large for a limited muon flux ($10^{-2}/(\mathrm{cm}^2 \cdot \mathrm{s} \cdot \mathrm{str} \cdot \mathrm{TeV})$ at 1 TeV). The basic idea of the method can be summarized as follows: a) The cosmic-ray muon energy spectrum and its dependence on the vertical zenith angle are almost unique. b) The range of cosmic-ray muons through the mountain is uniquely determined by electromagnetic interactions. c) Thus, the intensity of cosmic-ray muons (N_μ) penetrating through rock with thickness X is uniquely determined. d) The cosmic-ray muon path through the mountain can be determined by employing a position-sensitive detection method. Based on test experiments conducted at Mt. Tsukuba[1] and Mt. Asama, a new method for the prediction of volcanic eruptions *via* the detection of near-horizontal muons passing through the active part of the volcano has been proposed.

In order to overcome the intensity-limitation problem, it is indispensable to consider the use of an accelerator. A reasonable way to obtain a mobile TeV source might be to produce muons using the some modest low-energy proton accelerator and accelerate the thus-produced muons up to TeV by employing an acceleration scheme developed in either $\mu^+\mu^-$ colliders or in a neutrino factory.

It is also interesting to point out that many of the active volcanoes are situated near the seaside. Thus, an on-ship mobile 1 TeV accelerator, if it is realized at all, will be the most powerful tool to explore a time-dependent change in the inner structure of a volcano.

A "compact" and mobile TeV muon source can be realized by employing various new acceleration schemes and the ultraslow muon method.[2] Here, we consider the most compact scheme of TeV muon source to be realized by the presently available technologies and consider mounting it onto a "mobile" aircraft carrier ship.

The scheme shown in Fig. 1 is currently proposed. For the muon production, a compact proton accelera-

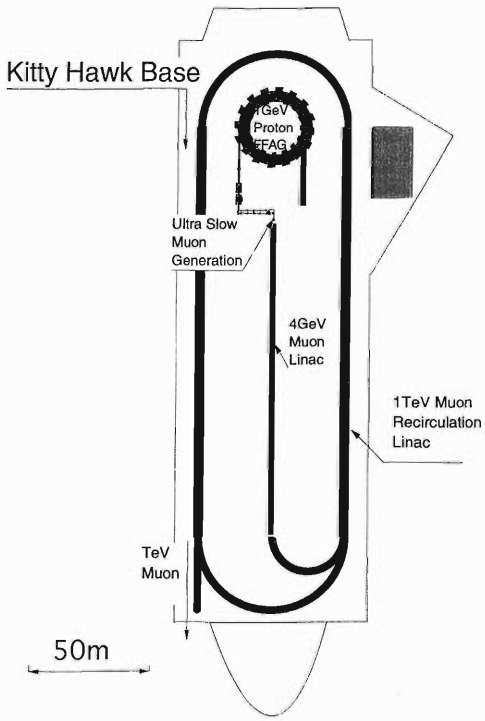

Fig. 1. Schematic view of a mobile 1 TeV muon source.

Table 1. The expected performance of the mobile TeV muon source.

	Expected numbers (s^{-1})	Conditions	Remarks
N_p	1.9×10^{12}	0.8 GeV×3 μA	
$N^{tot}_{\pi^+}$	2.4×10^{11}	4cm Carbon	$\sigma^{tot}_{\pi^+}$: 28 mb
N_{μ^+}	6.0×10^{9}	Pion Capture: 2.9 T, 20 cm bore×1.5 m	Ref. [4]
$N^{\mu\text{-}stop}$	2.9×10^{9}	Muon Decay: 3.0 T, 25 cm bore×10 m 20 ×100 μm W	P_μ: 88(42) MeV
$N_{th.Mu}$	1.2×10^{8}	$\epsilon_{th.Mu}$: 0.04	2000 K hot W
$N_{u.s.\mu^+}$	1.0×10^{8}	ϵ_{ion} : 0.8	Laser Resonant Ionization
$N^{Acc}_{\mu^+}(1\ TeV)$	10^8	$\epsilon_{cap.}$: 1.0 $\epsilon_{acc.}$: 1.0	

$N^{tot}_{\pi^+}$: total π^+ at production target, N_{μ^+}: total μ^+ at the exit of decay solenoid, N^{stop}_{μ} : μ^+ stopping number at thermal Mu producing material, $N_{th.Mu}$: thermal Mu yield, $N_{u.s.\mu^+}$: ultra-slow μ^+ yield after thermal Mu ionization.

tor either a conventional synchrotron or a FFAG (fixed field alternating gradient) synchrotron up to 1 GeV will be used. There, with minimum use of proton linac, a compact synchrotron can be constructed within a circular space of 50 m diameter. Then, following the installation of a super-super muon channel with a large acceptance and superconducting pion collector and a superconducting decay solenoid,[3] the ultra-slow μ^+ generation setup will be installed using hot tungsten for thermal muonium (Mu) production and laser resonant ionization of the Mu.[2] The thus-realized intense and high-quality muon ion source will have various advantages for further acceleration up to TeV energy: (1) an extremely small phase space, and (2) a small energy spread (± 0.2 eV).

A compact linac will be employed to accelerate μ^+ from 0.2 eV to 4 GeV. Then, a recirculating accelerator as realized for the electron accelerator at CEBAF will be used to accelerate μ^+ from 4 GeV to 1 TeV. According to the latest arguments,[4] the entire installation will require the space shown in Fig. 1. A small energy spread is very helpful for a compact design of the "arc" for the recirculation linac. The expected performance of the proposed muon accelarator is summarized in Table 1; easily a 10^{10} increase will be realized from the value for cosmic-ray muons referred at the beginning. The required space should be compared to the space of 80 m $\times$ 350 m available for the existing Kitty Hawk air craft carrier.

The author thanks Dr. G. Reece for helpful discussion and Dr. K. Shimomura for providing the drawing.

References

1) K. Nagamine et al.: Nucl. Instrum. Methods Phys. Res. A **356**, 585 (1995).
2) K. Nagamine et al.: Phys. Rev. Lett. **74**, 4811 (1995).
3) K. Ishida and K. Nagamine: KEK Proc. 98-5 II, (1998), p.12.
4) J. S. Berg: AIP Conf. Proc. **580**, p.13 (2000).

IV. NUCLEAR DATA

Measurement of Neutron Production Cross Sections by High-Energy Heavy Ions

H. Sato,[*1] H. Iwase,[*1] T. Nakamura,[*1] T. Kurosawa,[*2]
N. Nakao,[*3] and Y. Uwamino

We measured the double-differential cross sections (DDX) of neutrons from thin C, Al, Cu, and Pb targets bombarded by 135 MeV/nucleon C, Ne, and He ions, and by 95 MeV/nucleon Ar ion.

The experimental spectra were compared with the calculation using the two heavy-ion Monte Carlo codes of the internuclear-cascade and evaporation model (HIC)[1] and the quantum molecular dynamics model (QMD).[2]

The measurements were carried out in the E4 experimental room in the RIKEN Ring Cyclotron. A schematic view of the experimental setup is shown in Fig. 1. The NE213 liquid scintillator (12.7 cm diameter by 12.7 cm thick), which was designed to expand the dynamic range of output pulses for high-energy neutron measurements, was used as the E counter, and the NE102A plastic scintillator (15 cm by 15 cm square and 0.5 cm thick) used as the ΔE counter was placed in front of the E counter to discriminate charged particles from noncharged particles, neutrons and photons.

The target thicknesses are 1 mm of C, 0.6 mm of Al, 0.3 mm of Cu, and 0.3 mm of Pb. The direction of the incident beam was rotated around the target from 0 to 110 degrees using the beam swinger, in order to measure the energy-angle distribution of neutrons produced from the target by the time-of-flight (TOF) method having the flight path of 847 cm. The measurements were carried out at 0, 15, 30, 50, 80, and 110 degrees.

Figures 2 and 3 show the experimental and calculated neutron energy spectra. The neutron energy spectra measured in the forward direction have a peak near the projectile energy per nucleon. This peak is due to a knock-on process in which a neutron is knocked out by the direct collision between the target nucleon and the projectile nucleon. This peak becomes more prominent in the forward direction and for a lighter target. The high-energy end of neutrons in the forward direction reaches about 300–400 MeV.

Two calculations using HIC and QMD show a tendency to underestimate the high-energy neutron components beyond the peak. At large angles, the calculated spectra are in good agreement with the measured spectra. In general, the QMD gives better agreement with the experimental results, especially for a heavy target, than the HIC.

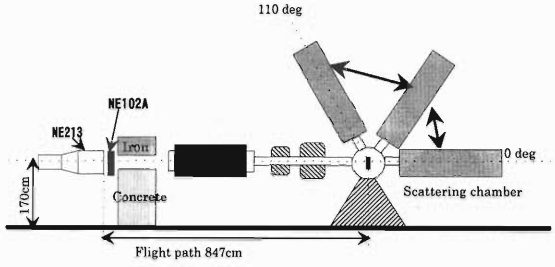

Fig. 1. Schematic view of the experimental setup.

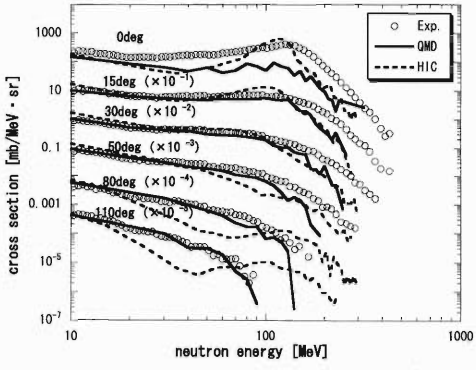

Fig. 2. Double-differential cross sections for 135 MeV/nucleon C ion on Pb target.

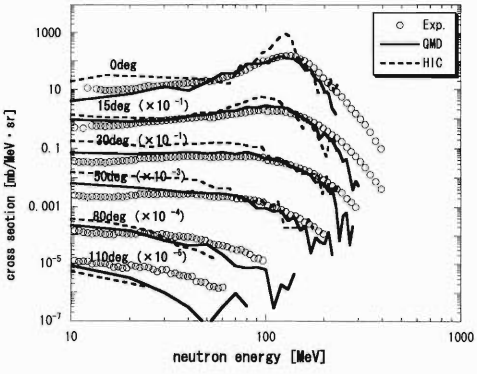

Fig. 3. Double-differential cross sections for 135 MeV/nucleon Ne ion on C target.

References

1) H. W. Bertini, T. A. Gabriel, R. T. Santoro, O. W. Hermann, N. M. Larson, and J. M. Hunt: ORNL-TM-4134 (1974).
2) J. Aichelin: Phys. Rep. **202**, 233 (1991).

*1 Tohoku University
*2 Electrotechnical Laboratory
*3 High Energy Accelerator Research Organization

V. DEVELOPMENT OF ACCELERATOR FACILITIES

RI Beam Factory Project: Progress Report

Y. Yano, T. Katayama, A. Goto, and M. Kase

Figure 1 shows the layout of the Radioisotope Beam Factory (RIBF) which is under construction as an extension of the RIKEN Accelerator Research Facility (RARF). This new facility will add new dimensions to the RARF's existing capabilities. At present, the RARF has a world-class heavy-ion accelerator complex consisting of a K540-MeV ring cyclotron (RRC) and two types of injectors: a variable-frequency Wideröe linac (RILAC) and a K70-MeV AVF cyclotron (AVF). Moreover, its projectile-fragment separator (RIPS) provides the world's most intense light-atomic-mass RI beams. In the factory, a new cyclotron cascade

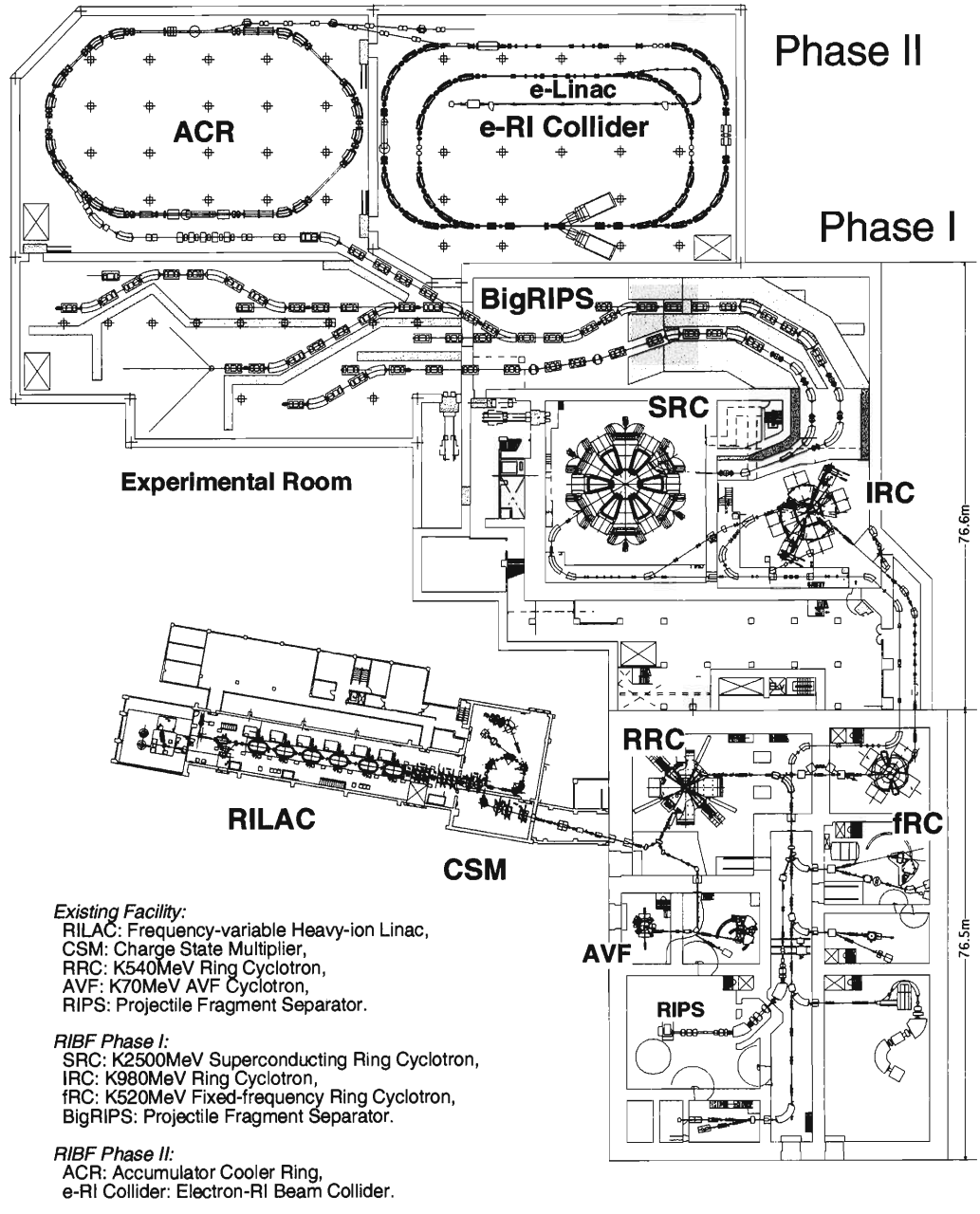

Fig. 1. The layout of the RI Beam Factory (RIBF). The first phase of the RIBF is now under construction and will be completed in 2003. The construction of the second-phase building, the layout of which is preliminarily depicted here, is planned to begin in 2002 and will be completed in 2005.

consisting of a K510-MeV fixed-frequency ring cyclotron (fRC), a K980-MeV intermediate-stage ring cyclotron (IRC) and a K2500-MeV superconducting ring cyclotron (SRC) will be the post-accelerator for the existing RRC. This new cyclotron system will be able to boost the RRC beam's output energy to 400 MeV/nucleon for light ions and 350 MeV/nucleon for very heavy ions. The goal for the beam intensity is higher than 1 pμA.

As in the existing RIPS, RI beams will be generated mostly by projectile fragmentation. In addition, in-flight fission of a uranium beam will be used for the efficient production of very neutron-rich isotopes in the medium mass region. A BigRIPS will be installed to generate such RI beams with much grater magnetic rigidity.

The RIBF includes the multi-use experimental storage rings (MUSES) consisting of an accumulator cooler ring (ACR) and an electron-RI beam collider (e-RI Collider). The MUSES will enable us to conduct various types of advanced experiments: electron scattering on unstable nuclei, precision mass measurements, and atomic physics with cooler electron beams. In the original MUSES project, ion-ion merging or head-on collisions and X-ray spectroscopy of unstable nuclei are planned. We will be requesting the budget to realize these as an RI-beam application program.

The construction of the RIBF is scheduled to be implemented in two phases: in the first phase, the new cyclotrons and the BigRIPS will be built, and the RI-beam experimental installation and the MUSES will be constructed in the second phase.

The construction of the first-phase building, and the fabrication of the IRC, the SRC and the BigRIPS will be completed early in 2003. In 2003, the overall installation and final tuning of these machines will be carried out. We will submit the budget for the fRC in FY2002, and we expect to install this cyclotron during the above-mentioned final tuning work. The first RI-beam production by the BigRIPS is scheduled for the spring of 2004.

The construction of the second-phase building will begin in 2002 and will be completed in 2005. After its completion, major experimental installations, *e.g.*, a large acceptance spectrometer and a gamma-ray detector, will be realized. The ACR will be commissioned in 2006. The first electron scattering experiment on unstable nuclei is scheduled for 2009.

Dependence of Beam Intensity on Plasma Electrode Size and Position for RIKEN 18 GHz Electron Cyclotron Resonance Ion Source

Y. Higurashi,* T. Nakagawa, M. Kidera, Y. Miyazawa, M. Hemmi, T. Chiba, M. Kase, T. Kageyama, A. Goto, and Y. Yano

In the last decade, we have applied many kinds of techniques to increase the beam intensity of highly charged heavy ions produced from the RIKEN 18 GHz electron cyclotron resonance ion source (ECRIS), *e.g.*, by gas mixing, the biased electrode method, the wall coating method and so on, and successfully increased the beam intensity of highly charged heavy ions.[1] This year we focused on the effects of position and size of the plasma electrode on the beam intensity produced from the RIKEN 18 GHz ECRIS, and studied these effects systematically.

Details of the design and performance of the RIKEN 18 GHz ECRIS are described in Ref. 1. Figure 1 shows a cross-sectional view of the RIKEN 18 GHz ECRIS. The axial confinement of plasma is achieved using two solenoid coils which generate a magnetic mirror field. The mirror ratio has the nominal value of 2.8. The maximum magnetic field strength in the axial direction is 1.4 T. To achieve the radial confinement of plasma, we use a hexapole magnet. The field strength at the surface is about 1.4 T, the operational frequency is 18 GHz and the maximum RF power is 1.5 kW.

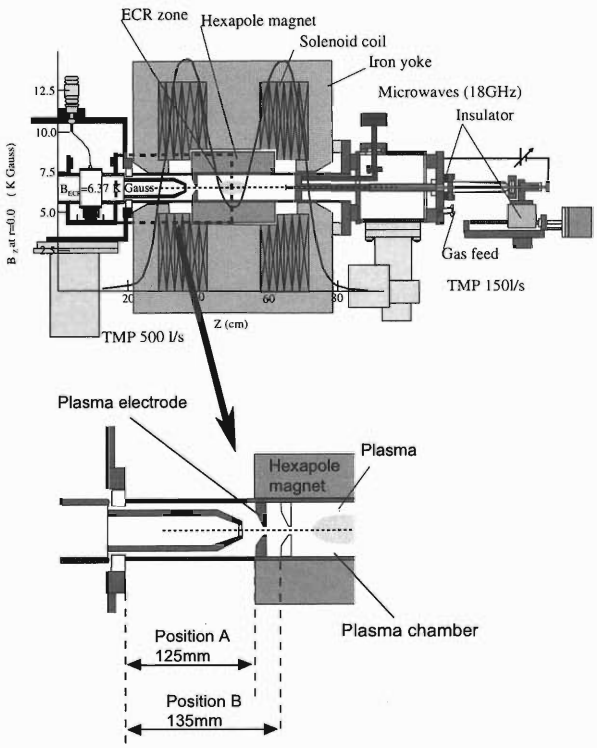

Fig. 1. Cross-sectional view of the RIKEN 18 GHz ECRIS.

* Rikkyo University

In this experiment, to investigate the effect of the electrode position, we measured the beam intensities of Ar ions at two positions, A and B, as shown in Fig. 1. At electrode position A, we measured the beam intensity using plasma electrodes with different hole sizes (8, 10, and 12 mm in diameter) to investigate the effect of hole size.

Figure 2 shows the beam intensities of Ar ions at the two electrode positions. It is clear that the beam intensity of Ar^{8+} increases from 600 to 750 eμA, when changing the electrode from A to B. In this experiment, the extraction voltage was 12 kV, the typical gas pressure was 1.2×10^{-6} Torr, the RF power was 530 W. Incontrast, the number of highly charged Ar ions, such as Ar^{11+} and Ar^{12+}, decreases dramatically. The beam intensity of highly charged heavy ions is strongly dependent on the electrode position. An optimum electrode position to maximize the beam intensity of multi-charged Ar ions may exist.

Figure 3 shows the beam intensities of Ar ions when using electrodes with different hole sizes. Lower charge-state Ar ions (Ar^{8+}) increase with increasing hole size. However, the beam intensity of the higher charge state Ar ions (Ar^{12+} and Ar^{13+}) does not depend on the size of the hole, and is almost constant. From this experimental result, we may conclude that the higher charge-state Ar ions, such as Ar^{12+} and Ar^{13+}, stay in the central part of the ECR plasma, while, the lower charge-state Ar ions, such as Ar^{8+}, exist over a wide area of the ECR plasma.

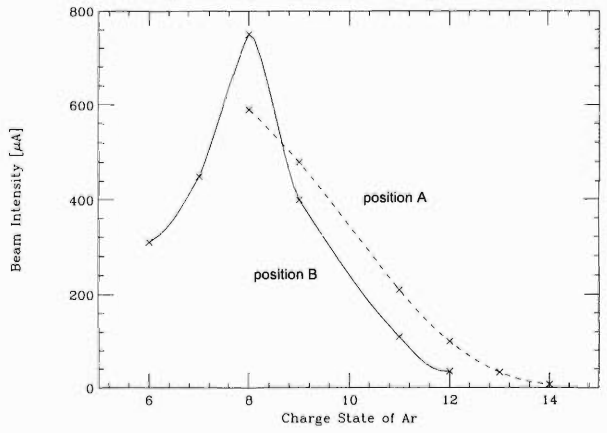

Fig. 2. Beam intensities of Ar ions at two electrode positions (A and B).

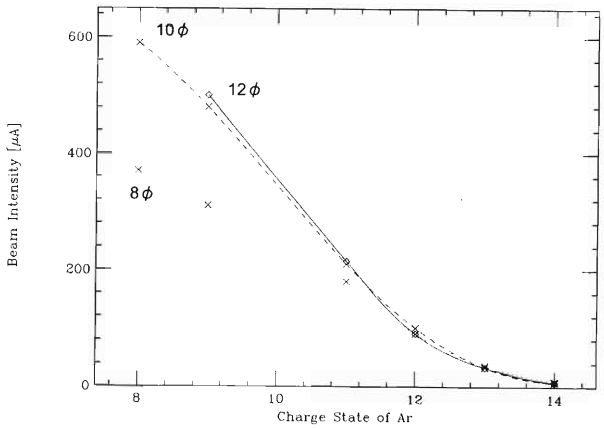

Fig. 3. Beam intensities of Ar ions when using the electrodes of different hole sizes.

References

1) T. Nakagawa, Y. Miyazawa, M. Hemmi, T. Chiba, N. Inabe, M. Kase, T. Kageyama, O. Kamigaito, A. Goto, and Y. Yano: Jpn. J. Appl. Phys. **35**, L1124 (1996) and references therein.

Investigation of Bias Disk Effect in RIKEN 18 GHz ECRIS under the Pulsed Mode Operation of Bias Voltage

Y. Higurashi,* T. Nakagawa, M. Kidera, Y. Miyazawa, M. Hemmi, T. Chiba, M. Kase, T. Kageyama, A. Goto, and Y. Yano

Last decade, many laboratories attemped to increase the beam intensity of highly charged heavy ions produced by Electron Cyclotron Resonance Ion Sources (ECRIS), using many techniques.[1] One of them is the biased electrode method. Although this method is used successfully in many laboratories, the mechanism to increase the beam intensity is still unclear.

In order to investigate the mechanism of enhancement of the beam intensity using an electrode, several experiments have been conducted.[2–4] One of them is the time-resolved measurement.[2] In this experiment, the Frankfurt group found that the ion current reacted promptly against a change of the bias. From this experimental result, they concluded that the bias disk effect is mainly due to the improvements of the extraction conditions at the source. In our experimental results, however, it is clearly seen that the distributions of highly energetic electrons were affected by the biased electrode[3] and that beam intensity is strongly dependent on the position of electrode.[4] In spite of the great success of this method, the mechanism is still unclear. To investigate the mechanism in detail, we conducted a new experiment to learn the time response of the beam intensity. For this test experiment, an electrode (18 mm in diameter) was installed in the plasma chamber of the RIKEN 18 GHz ECRIS, as shown in Fig. 1.

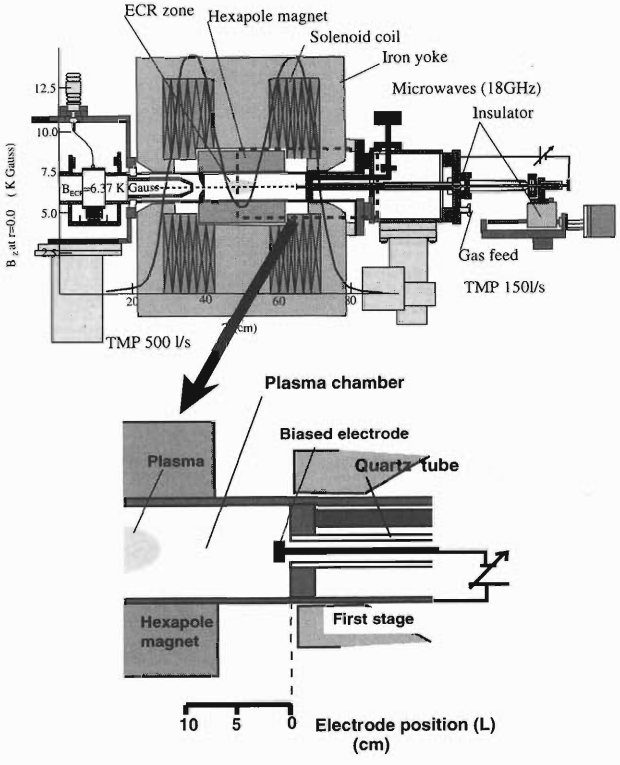

Fig. 1. Cross-sectional view of the RIKEN 18 GHz ECRIS with bias disk.

Initially, to check the dependence of the beam intensity of highly charged heavy ions on the negative bias voltage and the position of the electrode, we have supplied the negative bias voltage in the continuous voltage mode (DC mode). Figure 2 (a) shows the beam intensity of $Ar^{8+,11+}$ ions as a function of electrode position. The gas pressure was 2×10^{-6} Torr. The extraction voltage and RF power were 12 kV and 400 W, respectively. Figure 2 (b) shows the beam intensity of Ar^{8+} as a function of negative bias voltage at the electrode positions of $L = 3.31$ and 6.67 cm. The electrode position of L is defined in Fig. 1. The beam intensity increases with increasing negative bias voltage up to -50 V and then decreases at $L = 3.31$ cm. It corresponds to the position of maximum magnetic field strength (B_{max}) on the axial direction. On the other hand, at $L = 6.67$ cm, the beam intensity gradually increased with increasing bias voltage from 0 to -200 V. Generally speaking, the negative bias voltage which gives the maximum beam intensity gradually increases with increasing L.

To get information on the response time of the ECRIS to the bias voltage, we made time-resolved measurements of the beam intensity when supplying the negative bias voltage the time structure shown in Fig. 3 (a). The maximum and minimum bias voltage were kept at 0 and -50 V, respectively, at the electrode position $L = 3.31$ cm. We changed the Δt from 1 s to 1 ms without changing any other ion source parameters (e.g., magnetic field strength, RF power, gas pressure and extraction voltage). this indicates that the value of $\Delta V/\Delta t$ was changed from 0.05 V/ms to 50 V/ms. If the response time of the beam intensity to the bias voltage is very fast, as described in Ref. 2, the time structure of the beam intensity should not change under the present experimental conditions. However, it is clear that the time structure of the beam intensity of Ar^{8+} was changed at 10 ms, and the saturation time of beam intensity is delayed at less than $\Delta t = 10$ ms, as shown in Fig. 3 (a). From this experimental result, it is concluded that the response time of the extracted beam to bias voltage is slower than 10 ms at the electrode position of $L = 3.31$ cm under this experimen-

* Rikkyo University

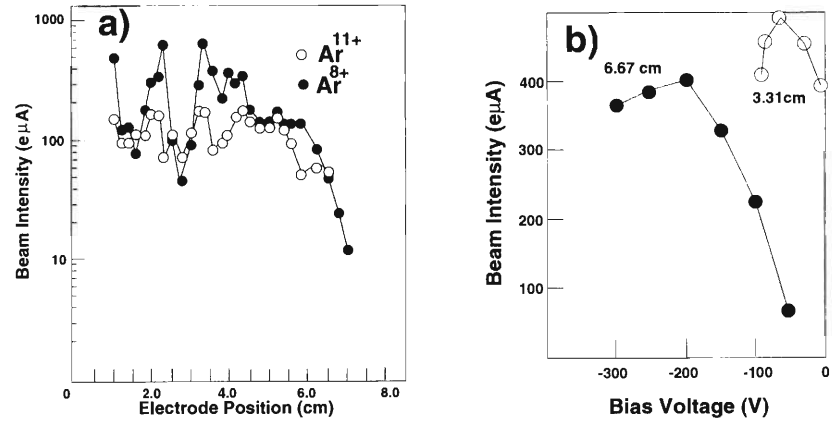

Fig. 2. (a) Beam intensity of $Ar^{8+,11+}$ ions as a function of electrode position. (b) Beam intensity of Ar^{8+} as a function of bias voltage at the electrode position of $L = 3.31$ and 6.67 cm.

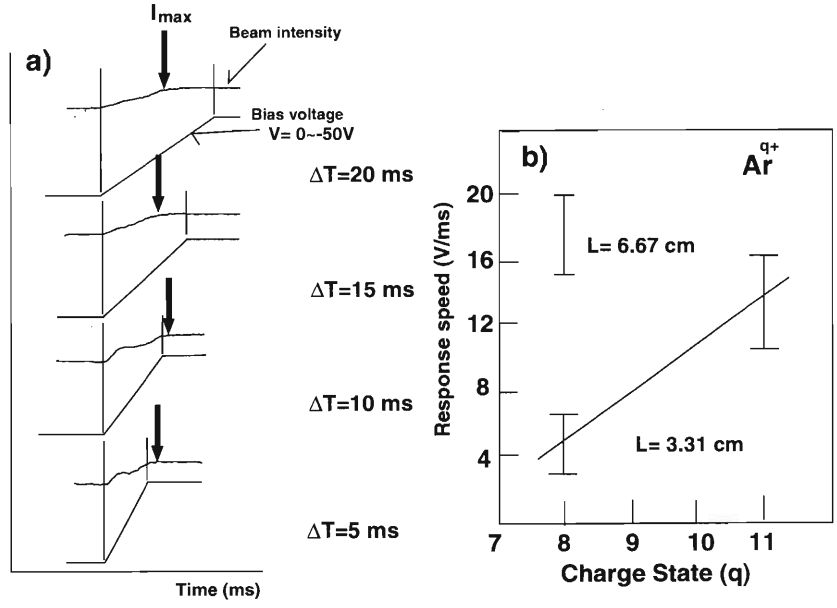

Fig. 3. (a) Time structure of the beam intensity of Ar^{8+}. (b) Fastest response time of the beam intensity of highly charged Ar ions to bias voltage at the electrode position $L = 3.31$ and 6.67 cm.

tal condition, which corresponds to $\Delta V/\Delta t = 5$ V/ms. At $L = 6.67$ cm, we observed that the response time of Ar^{8+} was slower than 5 ms, which corresponds to the 20 V/ms. Figure 3 (b) shows the critical value of $\Delta V/\Delta t$ (it is defined as the value at which the saturation time of the beam intensity starts to be delayed.) for highly charged Ar ions at two positions. The response time of the extracted beam near the ECR zone is much faster the those in the B_{max} region. It is also observed that the response time become faster for higher charge state heavy ions. The electrons from the biased electrode may change the electric field in the plasma. From these experimental results, it may be concluded that the biased electrode does not affect the density of ECR plasma, but simply increases the flow rate of highly charged heavy ions to the extracted region of ion source.

References

1) R. Geller: *Electron Cyclotron Resonance Ion Sources and ECR Plasma* (IOP, Bristol, 1996) and references therein.
2) K. E. Stiebing et al.: Phys. Rev. ST: Accel. Beams. (WEB) **2**, 123501 (1999).
3) M. Kidera, Y. Higurashi, T. Nakagawa, S. Biri, G. Shirkov, M. Hemmi, T. Chiba, M. Kase, T. Kageyama, A. Goto, and Y. Yano: Proc. 14th Int. Workshop on ECR Ion Sources (CEARN, Geneva, 1999), p.86.
4) S. Biri, T. Nakagawa, M. Kidera, Y. Miyazawa, M. Hemmi, T. Chiba, N. Inabe, M. Kase, T. Kageyama, O. Kamigaito, A. Goto, and Y. Yano: Nucl. Instrum. Methods Phys. Res. B **152**, 386 (1999).

Status of Liquid He Free Super Conducting Electron Cyclotron Resonance Ion Source

T. Nakagawa, T. Kurita,* M. Imanaka,* M. Kidera, T. Kawaguchi, and S.-M. Lee*

Recently, for the production of intense beams of highly charged heavy ions, two ECR ion sources have been constructed in RIKEN and Unversity of Tsukuba. At RIKEN, one of the new ion sources will be used to inject an intense beam of highly charged heavy ions, such as Kr and Xe, to the RIKEN AVF cyclotron. In the University of Tsukuba, the ion source will be used to study dynamic behaviors of metal clusters, such as fission and multifragmentation.[1] In this paper, we report the structure and initial results of using the new ECR ion source operated in the Unversity of Tsukuba.

The design of the ion source is described in detail in Ref. 2. Figure 1 shows the cross-sectional view of the liquid-He-free SC-ECRIS. The superconducting solenoid coils are cooled in a small Gifford-McMahon type refrigerator at temperatures below 5 K. The refriderator maintains the superconductivity of solenoid coils without requiring a supply of liquid He. These solenoid coils are used to supply the mirror magnetic field to confine the plasma in the axial direction. The hexapole magnet which consists of 24 segments of permanent magnets is used to confine the plasma in the radial direction. The maximum strengths of the mirror magnetic field are 3 and 2 T at the microwave injection side (B_{inj}) and the beam extraction side (B_{ext}), respectively. The minimum magnetic field strength of the mirror magnetic field (B_{center}) is approximately 0.3 T. The inner and outer diameters of the hexapole magnet are 80 and 174 mm, respectively. The maximum magnetic field strength at the inner surface of the plasma chamber is 1 T. The inner diameter of the plasma chamber is 72 mm. To protect the hexapole magnet from demagnetization due to high temperature, the plasma chamber wall has a double-wall structure to allow the flow of cooling water. The injected microwave frequency is 14.5 GHz. The maximum power is 2 kW. For the production of Xe ions, we used enriched ^{136}Xe gas (enrichment of 85%). As the gas mixing method is very effective for all elements which have heavier masses than that of carbon, in the present case, we used oxygen gas as the mixing gas. Also, a negatively biased electrode placed in the plasma chamber is utilized to increase the beam intensity.[3] The electrode is a circular disc (25 mm in diameter) made of stainless steel.

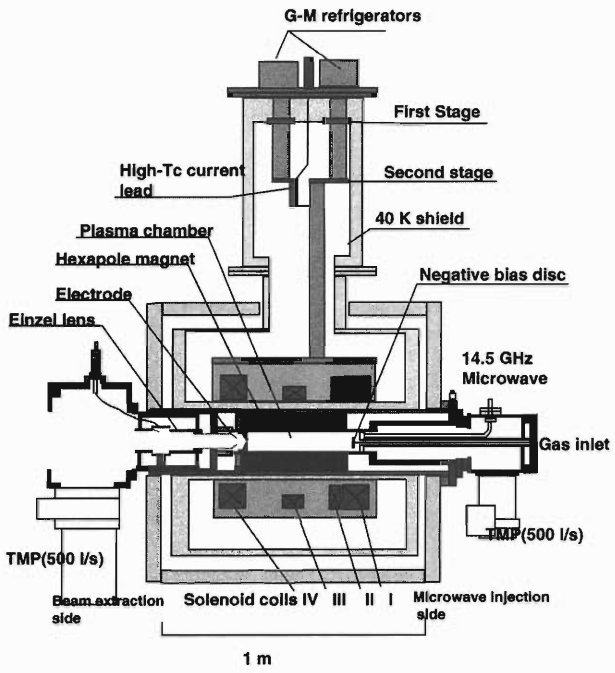

Fig. 1. Cross-sectional view of liquid-He-free SC-ECRIS.

Figure 2 shows the typical charge-state distribution of Xe ions when the ion source was tuned to produce Xe^{30+} ions. The beam intensity of 10 eμA for Xe^{30+} ions was obtained at an injected microwave power of 650 W and an extraction voltage (V_{ext}) of 15 kV. The beam intensity of Xe^{30+} ions produced from liquid-He-free SC-ECRIS is almost the same as those produced from the two ECRISs (upgrade version of the advanced ECRIS in Lawrence Berkeley National Laboratory (AECR-U)[4] and SC-ECRIS in the Laboratorio Nazionale Sud, Catania (SERSE)[5]), which can produce one of the highest beam intensities of highly charged ions in the world. Comparing our results with

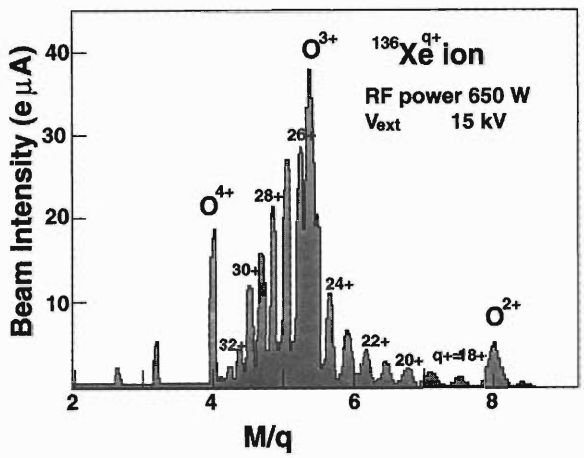

Fig. 2. Charge distribution of Xe ions. The ion source was tuned to produce Xe^{30+} ions.

* University of Tsukuba

those of the two ECRISs, our results are very remarkable, because an injected microwave power higher than 1.2 kW was required to obtain almost the same results in the other two ECRISs.

References

1) F. Chandenzon, C. Guet, B. Huber, D. Jalabert, M. Maurel, E. Monnand, C. Ristori, and J. Rocco: Phys. Rev. Lett. **74**, 3784 (1995).
2) T. Kurita, T. Nakagawa, T. Kawaguchi, and S.-M. Lee: Rev. Sci. Instrum. **71**, 909 (2000).
3) For example, S. Biri et al.: Nucl. Instrum. Methods Phys. Res. B **152**, 386 (1999).
4) Z. Q. Xie: Rev. Sci. Instrum. **69**, 625 (1998).
5) S. Gammino, G. Ciavola, L. Celona, M. Castro, F. Chines, and S. Marletta: Rev. Sci. Instrum. **70**, 3577 (1999).

Plasma Measurements on the Pulsed High-Power Microwave Ion Source at RIKEN

S. Bhattacharjee, T. Nakagawa, M. Kase, A. Goto, and Y. Yano

We have undertaken the development of a novel pulsed high-power microwave ion source at RIKEN[1,2] with a view to obtaining intense, multicharged, pulsed ion beams. This ion source employs short-pulse (0.05–1.0 μs), high-power (~100 kW) microwaves of 9.45 GHz which are launched into a circular conducting tube with a radius smaller than the cutoff value (cutoff frequency ~9.77 GHz), which forms the plasma chamber. The plasma is confined by a minimum-B field generated by permanent magnets surrounding the tube, in the form of a multicusp (10 poles) with a length of 30 cm and inner diameter of 7 cm. The absence of axial magnetic fields generated by electromagnetic coils makes the device compact. A modification of the plasma refractive index at the tube entrance helps the high-power waves to propagate through the peripheral plasma region[3–5] with a reduced wavelength, thereby overcoming the geometrical cutoff limitation. The narrow tube dimension enhances the microwave power density (~100 kW/cm^2), which favors the production of a high-density plasma (> the cutoff density) with a high electron temperature.[4–6]

Our recent measurements[2] using argon as the test gas indicate that the plasma build-up is extended beyond the end of the pulse, with the peak density attained several tens of μs later in the power-off phase, as shown in Fig. 1, where the end of the microwave pulse is also indicated. In general, the plasma build-up time τ_p, defined as the time to obtain the peak density from the end of the pulse, increases with increase in pressure. Depending on the pressure and the microwave power, the ionization frequency in the power-off phase can be sufficiently high so as to balance the plasma losses by recombination and diffusion. This results in a density flat-top that is maintained for several tens of μs, as shown in Fig. 2, and is a unique feature compared to conventional afterglows. These results indicate the generation and maintenance of a high electron temperature in the plasma even in the power-off phase, conforming to our previous time-resolved measurements[4,5] and recent numerical simulations,[6] which indicate that at lower pressures (collision frequencies $\nu_c \cong (0.1 - 1) \times 10^9\,\mathrm{s}^{-1}$), electron temperatures of several keV are obtained and the temperature build-up continues beyond the end of the pulse. Multiply-charged states can be produced by the Auger or electron shake-off processes[7,8] during the transient high-power pulse when the electric field is strong, while stepwise ionization would be predominant in the interpulse regime where the plasma is still active. Both processes are important for the generation of multiply charged states.

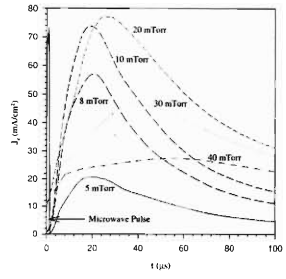

Fig. 1. Temporal variation of the electron current density J_e with pressure p as a parameter.

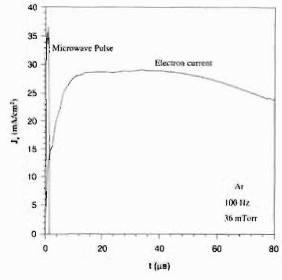

Fig. 2. Temporal variation of the electron current density J_e, showing the development of a density flat-top in the interpulse regime. The discharge pressure p is 36 mTorr and the pulse repetition frequency $f_r = 100$ Hz.

Under pulsed operation, the gaseous breakdown conditions in the narrow tube[9] (plasma chamber) is an important factor which determines the operating pressure of the ion source. The breakdown threshold depends on the ionization energy of the gas, the characteristic diffusion length (which is a function of the tube radius), the pressure and the source frequency. Breakdown occurs initially at the tube entrance by the evanescent electric field. The spatial extent of breakdown was estimated[9] from the microwave discharge theory, and for important waveguide modes, TE_{11}, TM_{01} and TE_{01}, from the requirements of the threshold electric field. It was found that the breakdown extent is the longest (~6 cm) in the case of the TE_{11} mode, followed by that of the TM_{01} (~1 cm) and TE_{01} (~0.5 cm) modes. A numerical calculation[9] of the radial distribution of the electric field indicates that the TE_{11} and TM_{01} modes peak at the tube center while the TE_{01} mode peaks half way to the chamber wall. These results are important for investigating plasma production and density uniformity in the chamber. Figure 3 shows the variation of the peak (electron)

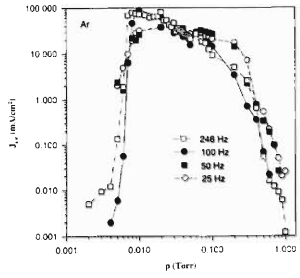

Fig. 3. Variation of the peak electron current density J_{me} with pressure p and pulse repetition frequency f_r as a parameter.

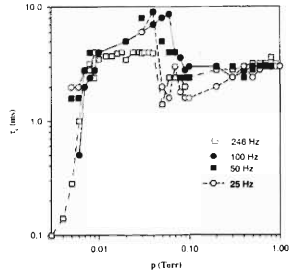

Fig. 4. Variation of the electron confinement time τ_c with pressure p and pulse repetition frequency f_r as a parameter.

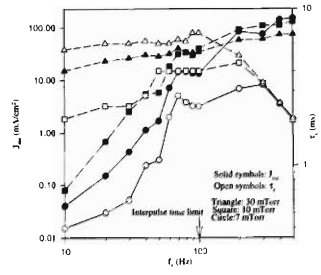

Fig. 5. Variation of the electron confinement time τ_c and the peak electron current density J_{me} with pulse repetition frequency f_r and pressure p as a parameter. Solid symbols: J_{me}, open symbols: τ_c and triangles: 30 mTorr, squares: 10 mTorr and circles: 7 mTorr.

current density J_{me} with pressure p and pulse repetition frequency f_r as a parameter. The plasma can be sustained at a pressure range of 10^{-3} Torr-1 Torr, and for this condition a maximum current density of approximately 100 mA/cm^2 can be obtained. It is noted that for lower values of f_r ($\leq$ 50 Hz), the current is uniform over a wider pressure region.

The particle confinement time was investigated from temporal measurements of the currents in the interpulse (power-off) phase of the high-power microwave pulses. Without external energy to sustain the plasma, particle generation occurs by ionization due to the high electron temperature and losses occur due to volume recombination and diffusion to the walls. Particles are confined by the bottle structure of the minimum-B magnetic field and the plasma space potential which peaks at the tube center. The electron confinement time τ_c may be taken as the sum of the build-up time τ_p and decay time τ_d. τ_d is defined as the time required for the electron current to decay from its peak value to a zero level current when measured with the highest sensitivity ($\sim$0.1 μA). Figure 4 shows the variation of τ_c with pressure p and pulse repetition frequency f_r as a parameter. τ_c was found to increase steadily from $\sim$0.1 ms at 3 mTorr to approximately 10 ms at 40 mTorr, which was the maximum value. Beyond this pressure, τ_c decreased and then tended to be $\sim$3 ms at 1 Torr.

The pulse repetition frequency f_r was found to influence the plasma properties at a lower pressure. Figure 5 shows the variation of J_{me} and τ_c with f_r and pressure p as a parameter. At a lower p (7 mTorr and 10 mTorr) both J_{me} and τ_c are seen to increase rapidly with f_r, however, above 10 mTorr (*e.g.*, 30 mTorr) the dependence on f_r seems to be small. Above 100 Hz, τ_c is seen to decrease, this is because of the limitation in the measurement of τ_c due to a smaller interpulse time. The transition is marked as "Interpulse time limit" in the figure.

High-power pulsed ion sources of the present type have applications to areas where there is a requirement for intense multicharged pulsed ion beams. The achievement of high electron temperature both within the pulse and its maintenance after the end of the pulse will be favorable for the generation of multicharged ions within a short interval of time. The capability to operate at a higher pressure is another advantage, and will be useful in applications where a close coupling of the ion source is required in areas having large pressure gradients, such as where it is required to tolerate vapor loads greater than 10^{-4} Torr. The possibility of obtaining $J_{me} \cong 100\,\mathrm{mA/cm^2}$ at 10 mTorr indicates a high ionization efficiency even at higher pressures. This is due to the realization of a high microwave power density in the narrow tube. The electron confinement time of about 10^4 times greater than the pulse duration will be favorable for the production of higher charged states by having an increased interaction time of energetic electrons with ions.

References

1) S. Bhattacharjee et al.: RIKEN Accel. Prog. Rep. **33**, 200 (2000).
2) S. Bhattacharjee, T. Nakagawa, and Y. Yano: Bull. Am. Phys. Soc. **45**, 230 (2000).
3) S. Bhattacharjee and H. Amemiya: Jpn. J. Appl. Phys. **37**, 5742 (1998).
4) S. Bhattacharjee and H. Amemiya: J. Phys. D: Appl. Phys. **33**, 1104 (2000).
5) S. Bhattacharjee and H. Amemiya: Vacuum **58**, 222 (2000).
6) S. Bhattacharjee, H. Amemiya, and Y. Yano: J. Appl. Phys. (2001), in press.
7) A. Septier: IEEE Trans. Nucl. Sci. **19**, 22 (1972).
8) T. A. Carlson and M. O. Krause: Phys. Rev. A **140**, 1057 (1965).
9) S. Bhattacharjee, H. Amemiya, and Y. Yano: Bull. Am. Phys. Soc. **45**, 369 (2000).

First Beam Measurement of Laser Ion Source at RIKEN

T. Takeuchi,[*1] T. Katayama,[*1] T. Nakagawa, M. Okamura, K. Yano,
B. Sharkov,[*2] and S. Kondrashev[*2]

At RIKEN RI Beam Factory, the maximum intensity of primary beams from the Super-conducting Ring Cyclotron (SRC) is assumed to be 1 pμA. In order to obtain more exultant results in the MUSES project,[1] an upgrade of the beam intensity will be one of the most effective efforts, and thus is the most required. Therefore, we are developing a laser ion source (LIS)[2,3] as a new dedicated pulsed ion source for the MUSES. The average charge state of ions in the expanding laser plasma strongly depends on power density [W/cm^2] deposited by laser beam.[4] To obtain sufficient power density to produce highly-charged-state ions in our LIS system, we optimized the gas mixing ratio, the laser pulse shape and the focal spot size. We then maximized the power density and measured the beam current for the condition of no extraction potential.

A transverse electric atmospheric (TEA) CO_2 laser[5] (wavelength: $\lambda = 10.6\,\mu$m) with the energy of 10 J and the repetition rate of 10 Hz is chosen as a driver for the LIS. Excitation to the laser transition level of 10.6 μm is provided by glow discharge in the gas containing CO_2, N_2, and He. Therefore, the laser output energy and repetition stability depend on the gas mixing ratio of CO_2, N_2, and He. In addition, the optimal condition for gas mixing is different for individual CO_2 laser systems because the discharging characteristic of the preionization and the pumping strongly depends on the shape of the electrodes and the volume in which the gas is contained.[6] For these reasons, we measured the mean energy and the stability of the energy for 20 shots using several gas mixing ratios of CO_2, N_2, and He, as listed in Table 1. We obtained the maximum output energy of 12.1 J for the gas mixing ratio of $CO_2 : N_2 : He = 1 : 2 : 4$, and the best stability for the gas mixing ratio of $CO_2 : N_2 : He = 1 : 1 : 8$.

The pulse shape of the CO_2 laser was measured using a photon drag detector. The typical laser pulse shape obtained is presented in Fig. 1 (a) and (b) for different time scales. A laser pulse usually consists of two components (a short high gain first peak and a low gain long tail).[7] Only the first peak is effective for the generation of laser plasma which produces highly charged heavy ions. Therefore, we maximized the total power of the first peak by varying the gas mixing ratio ($CO_2 : N_2 : He$ = 1 : 1 : 4, 1 : 1 : 8, 1 : 2 : 4, 2 : 1 : 2, 2 : 1 : 4, 2 : 1 : 6, and 3 : 1 : 4). The best result was obtained at the gas mixing ratio of $CO_2 : N_2 : He = 2 : 1 : 4$. The power ratio of the first peak to the total integrated power of the laser pulse was 58 ± 3%. The laser power of the first peak was $P_1 = 110 \pm 30$ MW (the energy: $E_1 = 4.1 \pm 0.6$ J and the pulse duration time is 38 ± 5 ns).

Table 1. Laser mean energy and the stability for 20 shots of TEA CO_2 laser. Total gas pressure is 1.5 kg/cm^2, the conductance is 10 liter/min and the flow is about 1800 Torr liter/sec. Air pressure in the pre-spark gap is 1.3 kg/cm^2.

CO_2:N_2:He	Mean Energy (J)	Standard Deviation (J)	Stability (%)
1:1:4	7.41	0.73	9.90
1:1:8	6.71	0.51	7.56
1:2:4	8.16	0.80	9.80
2:1:4	6.96	0.58	8.43

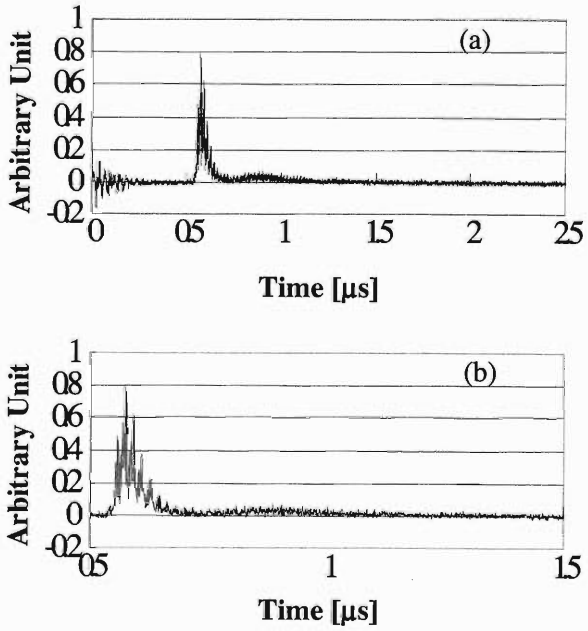

Fig. 1. Typical CO_2 laser pulse shape ((a) rough time scale; (b) zoomed time scale).

A new target chamber (Fig. 2.) designed and manufactured by ITEP was delivered to RIKEN.[8,9] The diameter and height of the chamber are 360 mm and 300 mm, respectively. NaCl is used as the input window material for the infrared laser beam. Two adjustable copper mirrors (plane and focusing mirrors) are installed inside the chamber. The laser beam is reflected by the plane mirror and then focused by a concave mirror with a focal length of 135 mm. The distance between the focusing mirror and the target surface is changeable without breaking the vacuum. A

*1 Center for Nuclear Study, Graduate School of Science, University of Tokyo
*2 Institute of Theoretical and Experimental Physics, Russia

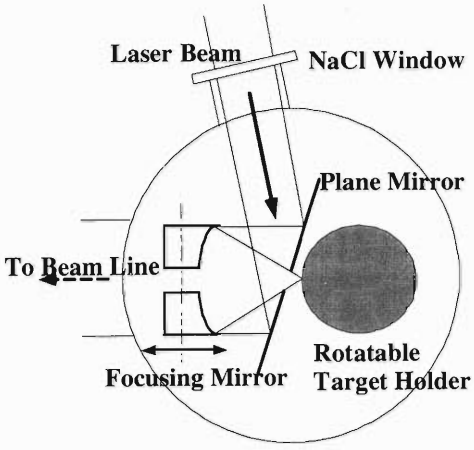

Fig. 2. Schematic view of a new target chamber with a rotatable target and two copper mirrors.

target rotation mechanism enables us to operate sequential laser shots in the order of 10^4 times on a new surface. The focal spot size ($2d_f$) of the CO_2 laser obtained using this target chamber is 44 μm. Our CO_2 laser has an unstable resonator and does not produce a Gaussian-shaped beam. Therefore, we adopted another factor, 50%, for the laser power, as suggested in a Ref. 2. Using this factor, we can estimate the value of the power density on the target surface as

$$I \approx \frac{1}{2}\frac{P_1}{\pi {d_f}^2}.$$

Substituting P_1 and d_f, the power density obtained for our experimental setup is 9×10^{11} W/cm^2.

In the setup mentioned above, we measured the beam current with a Faraday Cup[10] located 3250 mm away from the target. The measured data is shown in Fig. 3. The electrode potential of the Faraday cup was -2 kV. The target material was aluminum. The first peak (consisting mainly of highly-charged-state ions) and a very small hump (consisting mainly of low-charged-state ions) were observed at about 2 μs and

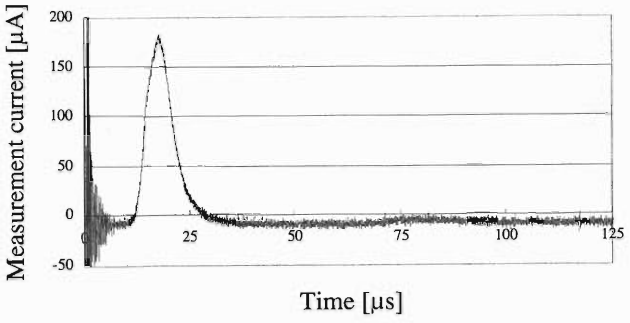

Fig. 3. Faraday Cup signal for the suppressor potential of -2 kV. The target material is aluminum. The Faraday cup is located at a distance of 3250 mm from the target.

about 8 μs, respectively. The measured current for the first peak was 180 μA. The current of the first peak corresponds to the ion current density of 230 μA/cm^2. The energy and pulse duration time of the ions for the first peak were about 551 eV/u and 10 μs (FWHM), respectively. We are planning to increase the beam current using other types of the extraction system for the ion source.[2,11]

References

1) T. Katayama et al.: MUSES Conceptual Design Report 2000, Internal Report.
2) T. Katayama et al.: MUSES Conceptual Design Report 2000, Sect. 2, Internal Report.
3) T. Takeuchi et al.: RIKEN Accel. Prog. Rep. **33**, 202 (2000).
4) B. Sharkov et al.: in *Handbook of Ion Sources*, edited by B. Wolf, (CRC Press, Boca Raton, 1995), p.149.
5) T. Takeuchi et al.: Proc. EPAC2000, (2000), p.1622.
6) V. Yu. Baranov et al.: Preprint of Kurchatov Institute IAE-2398, Moscow, Russian, 1974.
7) R. Scrivens: Doctoral Thesis, May 1999.
8) S. Kondrashev et al.: Rev. Sci. Instrum. **71**, 1409 (2000).
9) S. Kondrashev et al.: Proc. EPAC2000, (2000), p.551.
10) T. Takeuchi et al.: CNS Annu. Rep. **1999**, 36.
11) M. Okamura et al.: Proc. EPAC2000, (2000), p.848.

Development of Long-Lived Carbon Foil for Charge Stripper in RILAC

H. Hasebe,[*1] I. Sugai,[*2] and M. Kase

The production of long-lived C-foils (carbon foils) for the charge stripper of heavy-ion beams has been very important for present heavy-ion accelerators in the RIKEN Accelerator Research Facility (RARF) and it will be more urgently required for the RIKEN RI-Beam Factory (RIBF) project. We have decided to produce C-foils ourselves because the commercially available foils do not satisfy our requirements.

At the end of 1999, a high vacuum evaporation system (EBX-2000C by ULVAC) was purchased and installed in the RILAC building as shown in Fig. 1. The system has a vacuum chamber with a volume of 750 mm × 750 mm × 900 mm and has two oil-sealed pumps and a 5000 l/s cryogenic pump. The ultimate vacuum pressure is 1.0×10^{-5} Pa and it takes less than 15 minutes to evacuate the chamber from atmospheric pressure to 1.3×10^{-4} Pa. In March of 2000, we started to produce C-foils with an ac and a dc arc discharge evaporation source.

After production of the C-foils, their durability under beam irradiation was measured. The beam was $^{136}Xe^{9+}$ with an energy of 32 keV/nucleon and a size of 5 mm × 5 mm. Attention was paid to forming a uniform beam that was as long as possible. C-foils with a thickness of 10 mg/cm^2 were tested. Under these conditions, the lifetime of commercially available C-foils (Arizona Carbon Foil Co.) with the same thickness is limited to within 60 s. The angle between the direction of arc discharge and the foil surface was variable from 0 to 45 degrees. Figure 2 shows the result of the lifetime of a C-foil depending on the angle of arc discharge. The C-foils have long lifetimes in the cases of 0 degrees for the ac discharge and 30 degrees for the dc one. Next, six types of graphite from three companies were tested as a source of the C-foil. The results are shown in Fig. 3. The best results were obtained in the case of OT-5200N(S) for ac discharge and EG-20SH for dc discharge. Figure 4 shows the result depending upon the discharge current. The lifetime becomes longer as the discharge current is increased. The lifetime of C-foils depends upon the parting agent. Three

Fig. 1. High vacuum evaporation system (EBX-2000C by ULVAC).

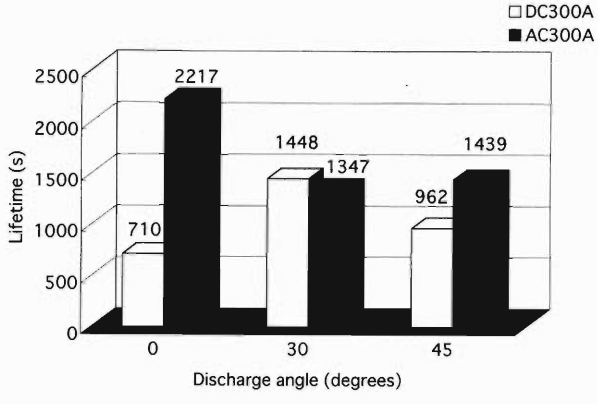

Fig. 2. The result of C-foil lifetime dependence on the direction of arc discharge. Zero degrees corresponds to the discharge direction parallel to the foil surface.

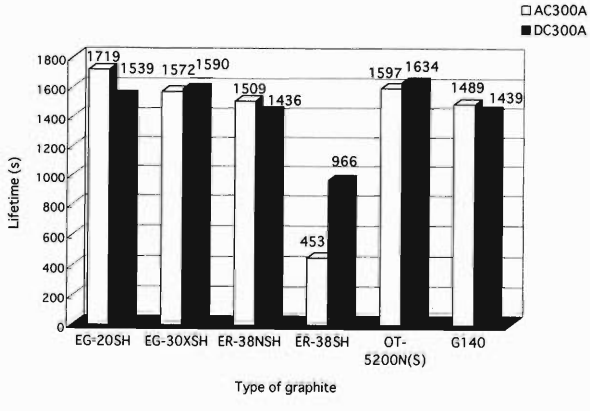

Fig. 3. The dependence of C-foil lifetime on the type of graphite.

*1 SHI Accelerator Service, Ltd.
*2 High Energy Accelerator Research Organization (KEK)

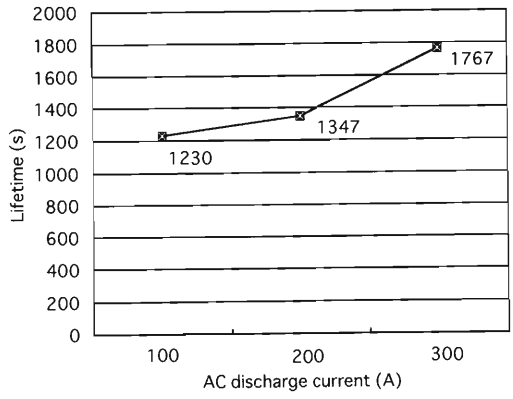

Fig. 4. The dependence of C-foil lifetime on the ac discharge current.

parting agents ($LaCL_3$, NaCl, and $NiCl_2$) were tested and $NiCl_2$ was found to be preferable. The lifetime was improved by 20% when a dc arc discharge was applied with N_2 gas flow.

We have obtained a C-foil with a lifetime 40 times longer than the standard one. We are expecting an increase of durability by an additional twenty percent soon.

Development of Liquid Film Charge Stripper

H. Akiyoshi, T. Chiba, M. Kase, and Y. Yano

Charge strippers are widely used in heavy ion accelerators. Commonly used methods are foil stripping and gas stripping. Gas stripping has the advantages of causing less energy straggling and less multiple scattering, and being able to withstand intense heavy ion beams, but has the disadvantage of producing lower average charge states than foil stripping. Foil stripping has the advantage of producing higher average charge states but has the disadvantage that it breaks down with short lifetimes under bombardment by high-intensity heavy ion beams according to structural changes induced by radiation damage and possibly beam heating.[1] With higher intensity and high-mass beams of RIBF, the foil lifetime is expected to drop markedly to as low as one minute. Substantial progress has been made in developing carbon foil production techniques that result in foil lifetime enhancement factors of up to 2 orders of magnitude as compared to foils fabricated by the conventional method.[2] A different approach to solving the stripper foil lifetime problem was first suggested by Cramer *et al.*,[3] and uses a thin free-standing oil film spun from the edge of a razor-sharp-edged rotating disc touching the surface of an oil reservoir. Leemann *et al.*[4] developed another liquid film stripper based on the same concept. The status of the liquid film charge stripper system in the developing stage for RIBF based on the same concept is described here.

Figure 1 shows a conceptual diagram of the liquid film production apparatus. A disc with diameter 9 cm is rotated by the magnetically suspended motor of a turbomolecular pump. The motor has been modified to be frequency tunable. The lower edge of the disc is immersed in a reservoir of silicone oil. We used SH200 silicone oil with kinematic viscosity of 50 cSt, as suggested in Refs. 3 and 4. The reservoir is suspended by slide rods so that the depth to which the disc is immersed in oil is adjustable over a range from zero to about 3 cm. A 'scraper' is mounted on a separate positioning mechanism so that it can be moved ± 2.5 cm in horizontal direction and ± 4 cm in vertical direction. The disc, the oil reservoir and the 'scraper' are placed in a vacuum chamber.

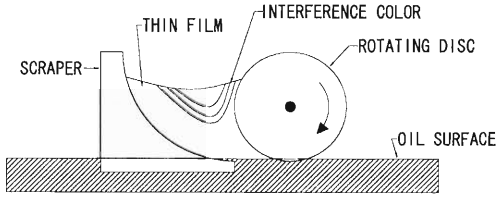

Fig. 1. Conceptual diagram of liquid film charge stripper.

At first, we adopted a disc such as those used in Refs. 3 and 4, and observed the three types of films described in Ref. 3. If the disc is immersed very deeply in the oil, a thick film of large area can be produced when the disc is rotated at a very low frequency. These films exhibited no distinguishable optical interference pattern. The next type of films showed strong interference colors and were of small area. The third type of films was observed to flicker in and out of existence, and showed a large area comparable to the first type of films.

We succeeded in making films with strong interference colors and large area by changing the shapes of the rotating disc and the 'scraper.' Higher rotating frequencies of the disc generally produced larger areas with the thinnest bands, as described in Ref. 4. We observed an area in which no interference color appeared at the upper edge of the film upon increasing the rotating frequency and using oil of lower viscosity. Therefore, the thickness of the thinnest part of the film was assumed to be about 0.3 μm.

The stability of the film became worse when the rotating frequency was increased. One possible source of this instability is disc vibration. We measured the vibration of the disc using an inductive displacement sensor, and found that the displacement in the normal direction against the disc was as large as about 50 μm when the disc was rotated at 30 Hz. It is likely that the vibration is large when the disc is rotated at 30 Hz, because the motor we adopted is normally operated at a much higher frequency when it is used for the rotation of a turbomolecular pump rotor. The present rotation mechanism has another problem as its size is too large to arrange the beam duct. Modification of the rotation mechanism is in progress.

References

1) E. Baron: IEEE Trans. Nucl. Sci. **26**, 2411 (1979).
2) I. Sugai, M. Oyaizu, H. Kawakami, C. Ohmori, T. Hattori, K. Kawasaki, M. J. Borden, and R. J. Macek: Nucl. Instrum. Methods Phys. Res. A **362**, 70 (1995).
3) J. G. Cramer, D. F. Burch, R. Rodenberg, and P. B. Cramer: Nucl. Instrum. Methods **185**, 29 (1981).
4) B. T. Leemann, P. Merrill, H. K. Syversrud, R. Wada, and R. B. Yourd: IEEE Trans. Nucl. Sci. **28**, 2794 (1981).

Construction of a Test Cavity for Sliding Rf Contacts

O. Kamigaito, N. Sakamoto, E. Ikezawa, Y. Miyazawa, T. Chiba, M. Hemmi, S. Kohara, A. Goto, M. Kase, Y. Yano, K. Uno,* and T. Sakata*

Sliding rf contacts or contact fingers, are indispensable for frequency-tuning mechanisms in rf cavities, such as movable shorting-plates and tuners. A typical rf contact is illustrated in Fig. 1. The main body of the contact is a finger-shaped metallic plate, which is usually made of copper-beryllium alloy and plated with silver. On the surface of each finger, one or two pieces of silver tips are welded. The plate is fixed on the boundary of the shorting plate, and the silver tips are pressed onto the cavity wall by the elasticity of the fingers. When the electric current across the silver tips is large, pneumatic cylinders are used from the back of the fingers to press the tips firmly. At present, various types of rf contacts are commercially available in different sizes and materials. The guaranteed limit of such contacts against the current density is around 60 A/cm at maximum for rf frequencies below 100 MHz.

There is a growing demand for the sliding rf contacts which can withstand much higher current density.[1,2] However, it has been very difficult to examine the limitations of the contacts against the rf current density precisely; conventional measurements with dc-currents do not give substantial information. Therefore, a test cavity has been constructed for the development of the rf contacts for the high current density.

Figure 2 shows the schematic drawing of the test cavity. It is based on the folded-coaxial structure, which gives a low resonant frequency with compact dimensions.[3] The design was made using the computer code MAFIA.

Almost all the components of the cavity are made of oxygen-free copper. The sliding rf contacts are set on the shorting plate surrounding the inner conductor. Pneumatic cylinders for the contacts are also prepared on the shorting plate. The water channels are arranged based on the heat calculation. The total water flow is 52 l/min. The cavity is equipped with a turbomolecular pump of 350 l/s.

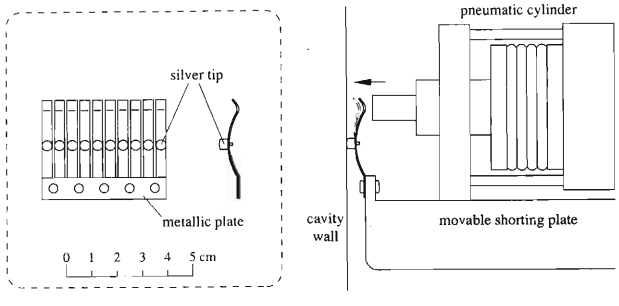

Fig. 1. Conceptual drawing of an rf contact.

According to the MAFIA calculation, the current density reaches 100 A/cm when the gap voltage is 210 kV. The gap voltage is monitored with the calibrated signal from the loop pickup on the base plate. Therefore, the current density is deduced from the pickup signal during the operation. There are five viewing ports for monitoring the contacts. Two of them are located in the ceiling plate and the other three are on the sidewall.

Table 1 shows the rf characteristics of the cavity. The measured resonant frequency is in good agreement with that using the MAFIA calculation. The measured Q-value is about 75% of the calculated ones. From this result, the estimated power loss is 39 kW for the current density of 100 A/cm.

This cavity can be also used for the investigation of the sparking under a high rf voltage. The top piece of the inner conductor can be replaced by an electrode which has the same shape as the drift tube of the CSM cavities.[1,4] When the distance between the electrode and the trimmer is 20 mm, the surface electric field reaches 16 MV/m for a gap voltage of 120 kV. This field strength is the same as that required in the CSM

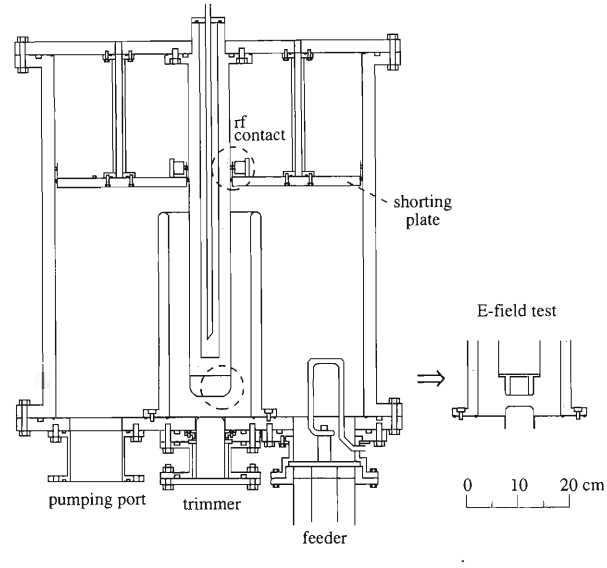

Fig. 2. Schematic drawing of the test cavity.

Table 1. Frequency and Q-value of the test cavity.

f_{calc} (MHz)	Q_{calc}	f_{meas} (MHz)	Q_{meas}	Q_{meas}/Q_{calc} (%)
69.0	13,900	69.8	9,600	69.0

* Sumitomo Heavy Industries, Ltd.

cavities.

The test cavity is already set in the RILAC building. High-power tests have just started using one of the amplifier systems for the CSM.[5)]

References

1) O. Kamigaito et al.: RIKEN Accel. Prog. Rep. **33**, 206 (2000).
2) N. Sakamoto et al.: RIKEN Accel. Prog. Rep. **32**, 208 (1999).
3) O. Kamigaito et al.: Rev. Sci. Instrum. **70**, 4523 (1999).
4) O. Kamigaito et al.: RIKEN Accel. Prog. Rep. **34**, 322 (2001).
5) Y. Murakami et al.: Proc. 12th Symp. on Accelerator Science and Technology, Wako, (1999), p.239.

New Control System for the RIKEN Ring Cyclotron Using EPICS

M. Kobayashi-Komiyama, I. Yokoyama, M. Kaji,[*1] M. Sugimoto,[*2]
M. Nagase, T. Tanabe, and M. Kase

In the last progress report, we reported the necessity of renewing the present control system of the RIKEN Ring Cyclotron (RRC).[1] One reason for this is some current operational problems, mainly occurring around the touch panel, man-machine interface recently, and the other reason is the request to expand the system to achieve compatibility with the RIKEN RI Beam Factory (RIBF) project. To maintain compatibility with the present control system, a partial system replacement plan has been under investigation since last year by using the Experimental Physics and Industrial Control System (EPICS).[2] Considering the fact that the RRC is constantly in operation, the system replacement must be carried out in stages. Under the present condition of RRC operation, we cannot take a sufficiently long period at any one time to replace the large quantity of low level control parts. Therefore, we are attempting to replace only the high level control parts of the system, including the touch panel as the first stage, and the low level control parts are being left as they are. However, by this replacement method, the maximum control ability of the present equipment is expected to be realized. The actual replacement is planned for the end of March 2001.

In Fig. 1, the part surrounded by the dashed line is newly introduced to the system to replace the minicomputer, Mitsubishi M60/AR, which is the host computer in the present system. Our present system is based on a CAMAC serial crate network and is supported by two types of modules, communication interface modules (CIMs) and device interface modules (DIMs). These modules were originally developed by RIKEN in order to assist the main computer in its tasks. Almost all magnet power supplies and beam diagnostic devices such as beam profile monitors, beam baffles, beam slits, main differential probes and Faraday cups are controlled by them. As shown in Fig. 1, only high level control parts are replaced in the first stage of the system replacement. This means that the low level control parts including a CAMAC loop are left as they are and they must be controlled by EPICS. In the EPICS control system, VME single board computers are used as Input/Output Controllers (IOCs), which function as distributed servers of EPICS. EPICS IOC applications consist of the IOC core, record support, device support and driver support. When using hardware not currently supported by EPICS, a hardware driver and/or device support routine needs to be created. Since CIM and DIM are our original modules, the device supports to control them must be developed by us.

On the other hand, we create graphic user interfaces (GUIs) for operation on the EPICS Workstation (EWS) which is used as the Operator Interface (OPI). The EPICS protocol between IOC and OPI is called the Channel Access (CA) protocol. The CA client applications run on OPIs such as Motif-based Editor/Display Manager (MEDM) and Archiver (AR, EPICS logging tool). In our new system, we create GUIs by using MEDM/DM2K if our objective opera-

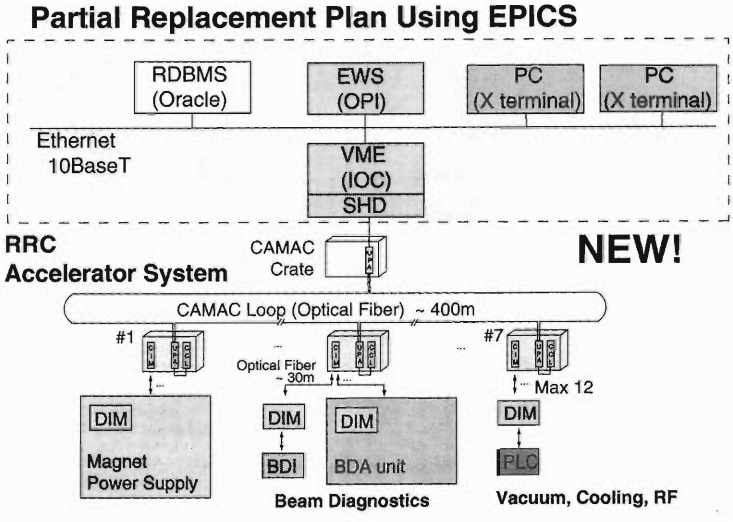

Fig. 1. New control system using the EPICS.

*1 Mitsubishi Electric Corporation
*2 Mitsubishi Electric Control Software Corporation

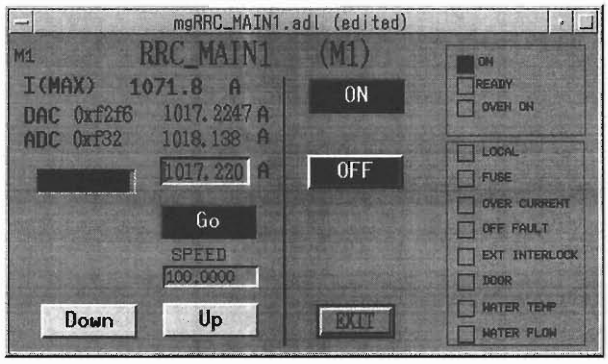

Fig. 2. Sample of GUI created by using MEDM.

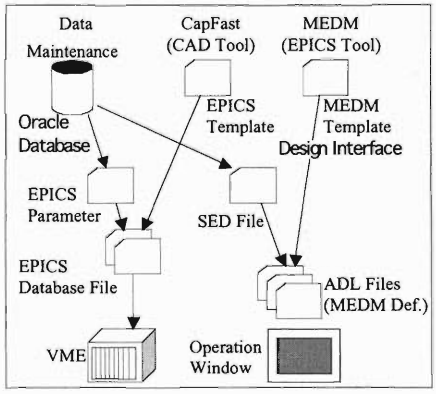

Fig. 3. EPICS configuration generation.

tions are realized using the objects prepared in them (DM2K is the upgraded version of MEDM, which was developed by BESSY[3]). As mentioned later, the configuration files of the operation windows on MEDM are automatically generated using data stored in an Oracle database. When we require more complex functions on GUI, we must create them by writing programs in C. In the new system, we prepared programs to show the graph of data measured by a profile monitor, a Faraday cup and a main differential probe. Though MEDM has a graph object, it has functions which are too simple for our requirements. However, for the present, almost all operation windows were created by MEDM. Figure 2 is a sample GUI created by MEDM for the control of a magnet power supply.

Also as shown in Fig. 1, we newly introduced Oracle to our system. We planned to consolidate all accelerator system data on this relational database management system. It concretely manages the properties of the control devices such as the device name, control address and specifications.

The preliminary system for controlling the magnet power supplies, profile monitors and Faraday cups of the RRC was tested last year, and we obtained results which indicated that the fundamental operations could be performed using EPICS. This year, we are testing the operation of all the accelerator devices which are controlled by the CAMAC-CIM/DIM system. In order to do this, the EPICS database file must be prepared for each operation; the details of this are mentioned in Ref. 4. This is a text-based configuration file of the real-time process database in the IOC core, and is generated from an EPICS template file and an EPICS parameter file. Figure 3 shows the scheme for generating the EPICS database files and the MEDM definition files automatically from the Oracle database. The EPICS template file has the control logic for specific types of equipment such as magnet power supplies and profile monitors. There are two files for control of the magnet power supplies, and eight files for each beam diagnostic device, and some for others in the system now. On the other hand, the EPICS parameter file has a set of parameters for each existing device. They are automatically created by programs written by PL/SQL in Oracle. The parameters in this file are required by its related EPICS template file.

At present, almost all RRC devices connected to the CAMAC-CIM/DIM system can be controlled by EPICS. Now we are examining how to maintain the operational log, and we are attempting to use AR.

Moreover, we have also decided to replace the high level control part of the RILAC control system by using EPICS as well as the RRC. In the present RILAC control system, the same minicomputer is used in the same position as in the RRC system. Therefore, the control of the devices in the RILAC will be made possible only by adding the operational data into the Oracle database. However, it is available only for the devices controlled by the CAMAC-CIM/DIM system. The RILAC has a more complex control system than the RRC because of its longer history. Some devices are controlled by the CAMAC-CIM/DIM system as well as the RRC system, while others are controlled by a GP-IB and a programmable logic controller (PLC), and a network I/O (NIO) system in the future. As the first stage of the investigation of the RILAC system replacement, we are attempting to operate the magnet power supplies controlled by GP-IB by EPICS. There are no significant differences in the construction of the EPICS database between a CAMAC-CIM/DIM system and a GP-IB. The device supports will be developed for each GP-IB device, and their operation will be tested from the same GUI as the CAMAC system. The results of the test have not been obtained yet. We continue the investigation of the RILAC control system as well as the RRC control system.

References

1) M. Kobayashi-Komiyama et al.: RIKEN Accel. Prog. Rep. **33**, 204 (2000).
2) http://www.aps.anlgov/epics/
3) http://www-csr.bessy.de/control/
4) M. Kaji et al.: Proc. 12th Symp. on Accelerator Science and Technology, Wako, (1999), p.441.

CORBA-EPICS Server

T. Tanabe, T. Masuoka, and M. Kase

The common object request broker architecture (CORBA)[1] is the standard distributed object architecture for an open software bus, which allows object components created by different operating systems (OSs) and languages to interoperate. We have investigated the possibility of using CORBA for communication in the new control system for Radio Isotope Beam Factory (RIBF).[2] Riken Accelerator Research Facility (RARF) controls are currently being upgraded with Experimental Physics and Industrial Control System (EPICS)[3] so a mechanism must be developed to allow for the old and the new controls to communicate with each other. CORBA is often used to integrate legacy systems with various kinds of wrapper softwares. However, in our case, it is easier to set up a gateway computer which acts as a translator between the two systems. The CORBA-EPICS (CE) server scheme fulfils this need.

The CORBA server used for the test is the one used for the main-coil power supply of an intermediate-stage ring cyclotron (IRC). The version of EPICS installed in a Sun Workstation (Ultra10 Model 360, Solaris 2.6) is R3.13.2 and a portable channel access (CA) server program runs in it. The ORB is VisiBroker[4] for C++ ver. 3.3. Sun Workshop3 C++ 4.2 was used for the compiler. Since CORBA and EPICS environments are in different network segments, some routing operation is required. Figure 1 shows the system configuration for this server.

The characteristics of the developed software are as follows:

- Fully multithreaded operation is performed to allow simultaneous operation from both directions.
- It is possible to read, write and execute in either direction.
- The CORBA client knows the record name and data so that the CORBA server calls the CA client to access the CA server.

The operation from EPICS to CORBA is initiated by a CA client. It specifies the records to process in the CE server and a modified portable CA server program passes data to the CORBA client program in it. This CORBA client connects CORBA servers in the CORBA domain. A sample program (excas) has been modified to accommodate the following functions in the CA server:

- To make new record-type definitions for CORBA operations.
- To determine the necessary CORBA operation for the corresponding record type.
- To get/put necessary records for a CA client.
- To stop scanning the record when the task is finished.

From CORBA to EPICS, the CORBA client has to know the records to be accessed in the CA server in the EPICS domain. After the CORBA server program receives the call from the CORBA client, it calls a CA client in the CE server to connect to CA servers in the EPICS domain. Schematic diagrams of both operations are given in Fig. 2 (a) and (b).

The interface definition language (IDLs) defined in the CORBA part are in the following.

```
module C_E_SERVER {interface CORBA_to_EPICS
{       any  EpicsGet( in string Str_Epics );
        long EpicsPut( in string Str_Epics ); }; };
module E_C_SERVER {interface EPICS_to_CORBA
{       any  CorbaGet( in string Str_Corba );
        long CorbaPut( in string Str_Corba ); }; };
```

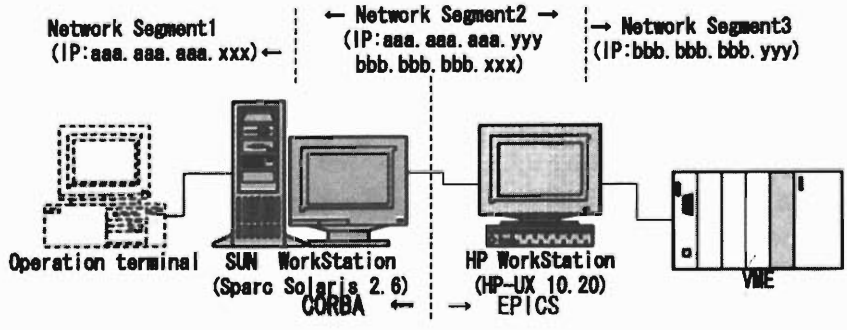

Fig. 1. CORBA-EPICS server system configuration.

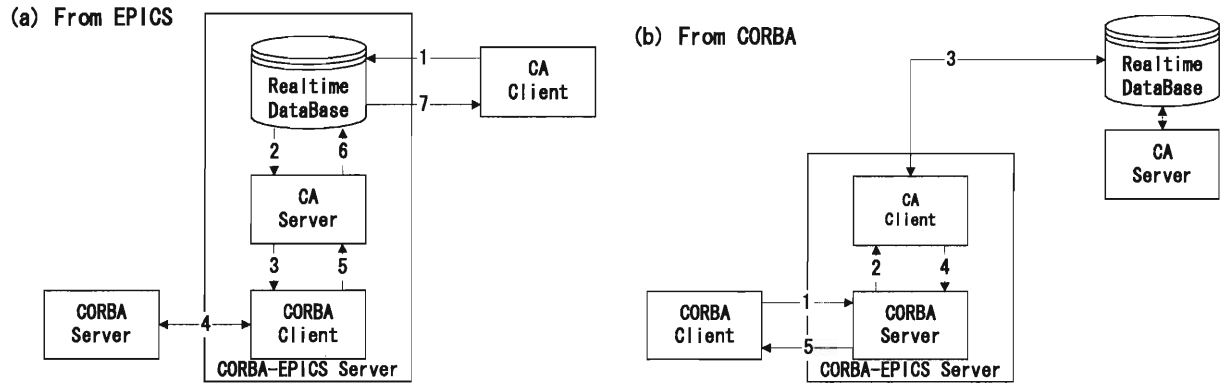

Fig. 2. (a) Schematic diagram of EPICS to CORBA operation. 1. The client accesses a record (put/get). 2. The record accessed is referred to by the CA server program (put/get). 3. The data set in the record are delivered to the CORBA client program (put/get). 4. Received data are delivered to the CORBA server (put/get). The data from the CORBA server returns to the CORBA client (get). 5. & 6. A reply from the CORBA server is reflected in the record (get). 7. The CA client gets a result from the record (get). (b) Schematic diagram of CORBA to EPICS operation. 1. The record to be accessed is specified in the CORBA server (put/get). 2. Received data are delivered to the CA client (put/get). 3. Data are put to or get from the specified record (put/get). 4. Acquired data are delivered to the CORBA server (get). 5. The data are delivered to the CORBA client via CORBA (get).

The "any" data type has been chosen for these operations because there are several different data types allowed in EPICS calls.

There are a few aspects to be modified if the CE server is used in real controls. First, data consistencies have to be monitored and maintained in some ways if "put" operations from both sides are permitted. Second, in this test, it was assumed that one record contained one piece of data. It is necessary to modify the CORBA part of programs if multiple data such as arrays are used for the record.

References

1) http://www.omg.org/
2) http://accelconf.web.cern.ch/accelconf/e00/PAPERS/TUP4B15.pdf
3) http://www.aps.anl.gov/epics/docs/
4) http://www.inprise.com/

Construction of the High-Energy Part of the CSM

O. Kamigaito, N. Sakamoto, M. Kase, E. Ikezawa, S. Kohara, M. Hemmi,
Y. Miyazawa, T. Chiba, Y. Chiba, A. Goto, and Y. Yano

As reported in the last issue,[1] the low-energy part of the charge-state multiplier (CSM) was constructed based on the quarter-wavelength resonator, which has shown good rf characteristics such as a wide variability of the frequency and high Q-values. This year, the high-energy part of the CSM was designed based on the same principle, and the resonant cavities of the accelerator section were constructed.

Figure 1 shows a conceptual drawing of the CSM. The "unit" of the CSM is a combination of two accelerator cavities and one decelerator cavity. The number of units has been reduced to three, while it was four in the original design,[2] because of the lack of space in the RILAC building. Although the maximum energy at the charge stripper decreases by 20% compared to the original value, a uranium beam of one particle microampere will still be available at a final energy of 100 MeV/u.

The acceptable charge-to-mass ratio (A/q) of the high-energy part of the CSM was chosen to be the same as that of the first unit. Using the CSM frequency f, A/q of the accelerator cavities is $32{,}000/f^2$, which gives the same limitation as the RILAC, and that for the decelerator cavities is expressed as $A/q = 16{,}000/f^2$. The input and output energies of each tank

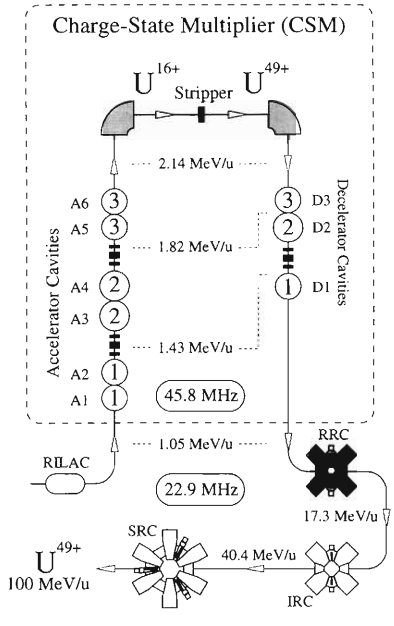

Fig. 1. Conceptual drawing of the CSM. The cavities are represented by open circles. The numbers in the circles indicate the "unit" of the CSM. The energy and frequency are chosen for the uranium acceleration up to 100 MeV/u after the SRC, as an example. The stripping efficiency in the CSM is 12% in this case.

are proportional to the square of the frequency. Table 1 summarizes the coefficients of this relationship.

Each cavity in the same unit has the same shape and dimensions except for the drift tubes. The number of gaps of the third-unit cavities is chosen to be six while the others are eight, so that the cavity length can be made less than 1.3 m. The required gap voltages are approximately 500 kV, as shown in Table 1, which might be a critical condition for the cw-mode operation.

Schematic drawings of the cavities of the high-energy part are shown in Figs. 2 and 3. The dimensions were optimized using the MAFIA code. The stroke of the shorting plate was determined so that the frequency range from 36 to 76.4 MHz could be covered. The estimated current density on the sliding contacts around the shorting plate is 60 A/cm at maximum.

Before making the full structure, the lower parts of the accelerator cavities were constructed, as shown in Figs. 2 and 3. They are operated at a fixed frequency of 75.5 MHz. All the components except for the base plate of the cavity are made of oxygen-free copper. The base plate is made of steel which is plated with copper by 50 μm. An important point in this structure is that the cavity wall is cut from a single piece of copper block in order to avoid possible vacuum leakage and to keep the machining accuracy. The drift tubes have an inner diameter of 35 mm and an outer diameter of 55 mm. They are aligned within an accuracy of $\pm$0.15 mm. The water channels are arranged based on the heat calculation. The total water flow per tank is 600 l/min. Each cavity is equipped with a turbomolecular pump of 520 l/s and a cryogenic pump of 4000 l/s.

Table 2 summarizes the rf characteristics of the cavities. As shown in Table 2, the measured frequencies are in good agreement with those obtained by MAFIA

Table 1. Design parameters of the high-energy part of the CSM.

Tank	C_{in} [a]	C_{out} [b]	V_{gap} (kV)	L_{gap} (mm)
A3	6.78	7.71	470	93
A4	7.71	8.65	470	99
D2	8.65	6.78	470	96
A5	8.65	9.40	500	104
A6	9.40	10.16	500	108
D3	10.16	8.65	500	106

a: The input energy is given by E_{in} (MeV/u) $= C_{in} \times f^2 \times 10^{-4}$, where f is the CSM frequency in MHz.
b: Same as *a* but for the output energy.

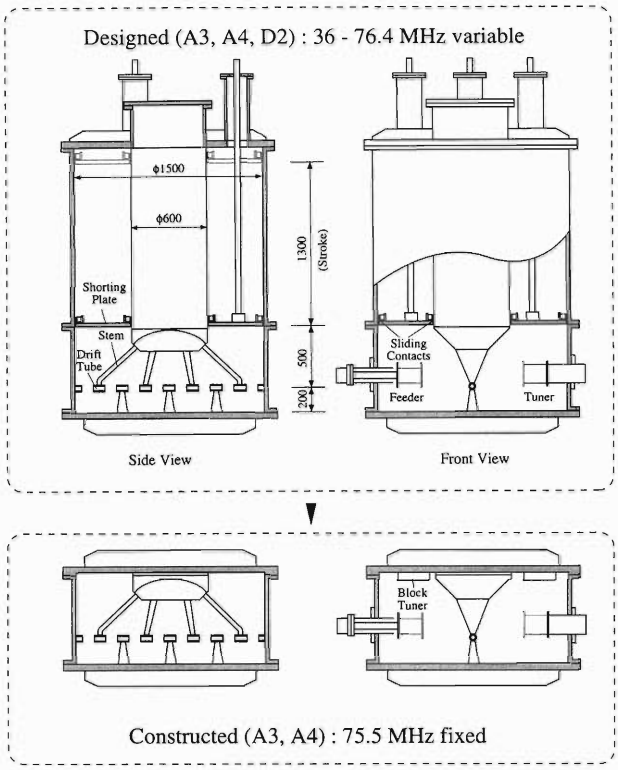

Fig. 2. Schematic drawing of a second-unit cavity.

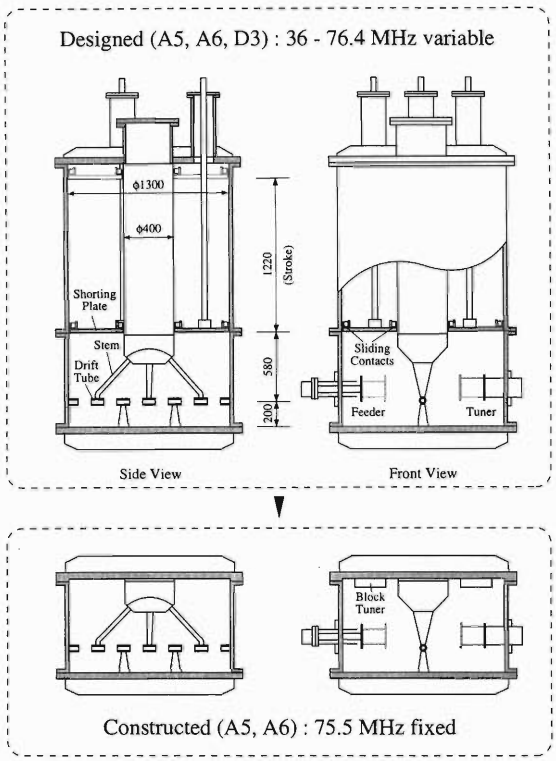

Fig. 3. Schematic drawing of a third-unit cavity.

prediction. The measured Q-values are about 70–80% of the calculated ones. The estimated power losses per cavity are around 70 kW at maximum, which can be supplied by the existing power amplifier.[3)]

Table 2. RF characteristics of the high-energy part of the CSM.

Tank	A3	A4	A5	A6
Height (mm)	747	734	820	812
f_{calc} (MHz)	73.5	73.5	73.5	73.5
Q_{calc}	32,000	31,000	31,000	30,000
f_{meas} (MHz)	75.5	75.5	75.5	75.5
Q_{meas}	25,000	24,200	23,700	23,100
Q_{meas}/Q_{calc}	0.78	0.78	0.76	0.77
P_{loss} (kW)	67	72	63	67

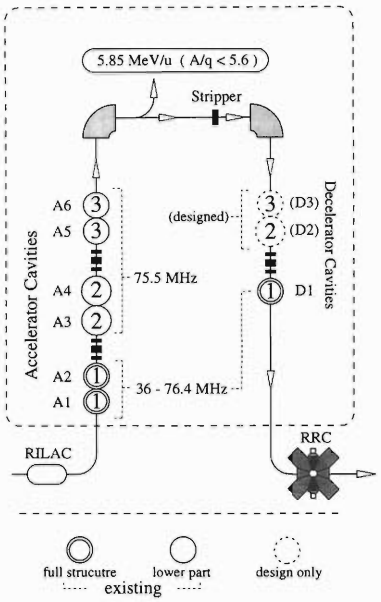

Fig. 4. Present status of the CSM.

The cavities of the high-energy part, as well as those of the first unit, have already been settled in the RILAC building. High-power tests of the cavities have been performed since September 2000. The installation of various utilities[4)] and the beamline[5)] is also in progress. The present status of the CSM is illustrated in Fig. 4. By using the accelerator cavities, ions which have a mass-to-charge ratio of less than 5.6 will be accelerated up to 5.85 MeV/u. The first beam test is expected to be performed in the spring of 2001.

References

1) O. Kamigaito et al.: RIKEN Accel. Prog. Rep. **33**, 206 (2000).
2) O. Kamigaito et al.: RIKEN Accel. Prog. Rep. **32**, 191 (1999).
3) Y. Murakami et al.: Proc. 12th Symp. on Accelerator Science and Technology, Wako, (1999), p.239.
4) E. Ikezawa et al.: RIKEN Accel. Prog. Rep. **34**, 3 (2001).
5) N. Fukunishi et al.: RIKEN Accel. Prog. Rep. **34**, 327 (2001).

Indication System for Charge-State Multiplier Resonator Voltage

S. Kohara, T. Ohki,* T. Aihara,* M. Fujimaki, O. Kamigaito, and M. Kase

An indication system for the resonator voltage of the charge-state multiplier (CSM)[1] has been designed and constructed in order to display the condition of the resonance voltage in the control room at RILAC. The amplitude, the phase and the tuning of the frequency of the resonator voltage are all controlled by control circuit to ensure good operation of the rf system.

The CSM consists of six acceleration resonators, a charge stripper and three deceleration resonators. The resonant frequency is varied from 36.0 to 76.4 MHz. The maximum gap voltage of the resonator is 500 kV. The voltage ratio of the voltage pickup to the resonator voltages is about 3.33×10^{-6}; the maximum pickup voltage is 1.67 V. Each CSM resonator has two voltage pickups; one is used as the control signal for the automatic control system and the other is used as the voltage indication signal. The voltage pickup on the upstream side is connected to a selector switch through a coaxial cable to indicate the resonator voltage.

A block diagram of the indication system for the resonator voltage of the CSM is shown in Fig. 1. The system consists of a remote control unit, selector switch, dividers, oscilloscope, vector voltmeter, and personal computer control system. The remote control unit is installed in the control room. The selector switch is installed in the basement of the RILAC vault. The remote control unit can be operated in two ways; one is manual control with the internal mode and the other is the personal computer control with the external mode. The remote control unit sends an ON/OFF signal to the selector switch in order to choose the resonator voltage of the CSM. Other input channels of the selector switch which do not correspond to the remote control unit are terminated to 50 Ω so that interference among the input channels does not occur due to by rf noise. In the external operation mode, the remote control unit is connected to the WE7000 measuring station through an I/O module and controlled with the personal computer. The ON/OFF status of the input channel of the selector switch is shown on the display of the personal computer. Communication between the personal computer and WE7000 measuring station is carried out through an ethernet module.

The chosen resonator voltage and the reference signal from the synthesizer are sent to the vector voltmeter and the oscilloscope in the control room through a coaxial cable to display the amplitude and the phase. The resonator voltage is compared with the reference signal to measure the phase. The oscilloscope is employed to monitor the condition of the resonance voltage. The operator adjusts the control circuit of the rf system when the resonance voltage is abnormal or unstable. Output terminals for the amplitude and the phase of the vector voltmeter are connected to the WE7000 measuring station through an isolated digitizer module. These data on the resonator voltage are sent to the personal computer through the ethernet module for the monitoring and recording. The recorded data are then used for parameter setting at the start of the rf system and for analysis of the stability of the resonator voltage.

References

1) O. Kamigaito et al.: Proc. 12th Symp. on Accelerator Science and Technology, Wako, (1999), p.233.

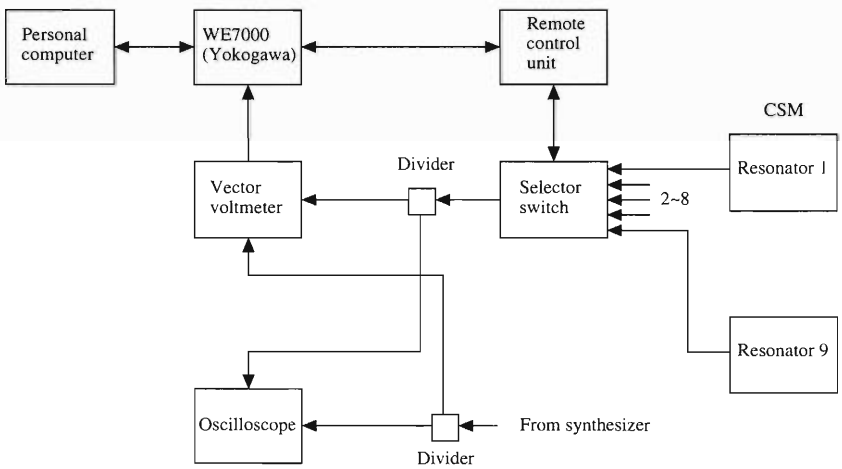

Fig. 1. Block diagram of the indication system for the resonator voltage of the CSM.

* SHI Accelerator Service, Ltd.

Compact Beam Diagnostic System for CSM

M. Fujimaki and M. Kase

A beam diagnosis device for CSM (charge state multiplier) was developed. This beam diagnosis chamber is required to be compact to enable installation in the space between the CSM accelerators which are as small as 130 mm. Three detectors of the phase probe (Fig. 1 ⑤), the profile monitor (Fig. 1 ③) and the Faraday cup (Fig. 1 ④) as well as the gate valve (Fig. 1 ②) are installed in this chamber.

The structure of the gate valve is shown in Fig. 2. The beam entrances to the vacuum chamber are closed with the gate valve by one movement, simultaneously separating the diagnosis chamber from the beam-line vacuum. Therefore, the profile monitor and the Faraday cup can be maintained without breaking the vacuum for the beam line.

Although the profile monitor and the Faraday cup are designed to be smaller than the former design, these two detectors cannot operate simultaneously because they share the same space in the beam center. This is a disadvantage of this diagnosis chamber. We plan to improve this problem beginning immediately.

Because it seldom breaks down, the phase probe is arranged on the outside of the gate valve. The phase probe is installed in the section of the short beam pipe which connects the CSM cavity with the diagnosis chamber. The phase probe has a ring electrode with a diameter of 40 mm and a thickness of 8 mm, and its signal line exits the chamber through the vacuum-sealed SMA connector whose ground side is floated.

The gate valve, the profile monitor and the Faraday cup are actuated by air cylinders. Each air cylinder is equipped with a speed controller so that these devices do not collide mechanically with each other. It must be adjusted so that insertion is slow and withdrawal quick. A control circuit was designed for the solenoid-operated valves. In the case of vacuum trouble or when an electric power down occurs, the gate valve is closed after the profile monitor and the Faraday cup have been withdrawn completely. To guarantee this sequence there is a small buffer tank for air pressure upperside solenoid-operated valves when an electric power down occurs.

The control system for the profile measurements was improved so that the probe head will return to the outside position immediately after the measurement is finished.

Additionally, a limitation circuit is included so that the profile monitor can be removed forcibly when the Faraday cup is inserted. The Faraday cup operation has priority in the control system, because it works as

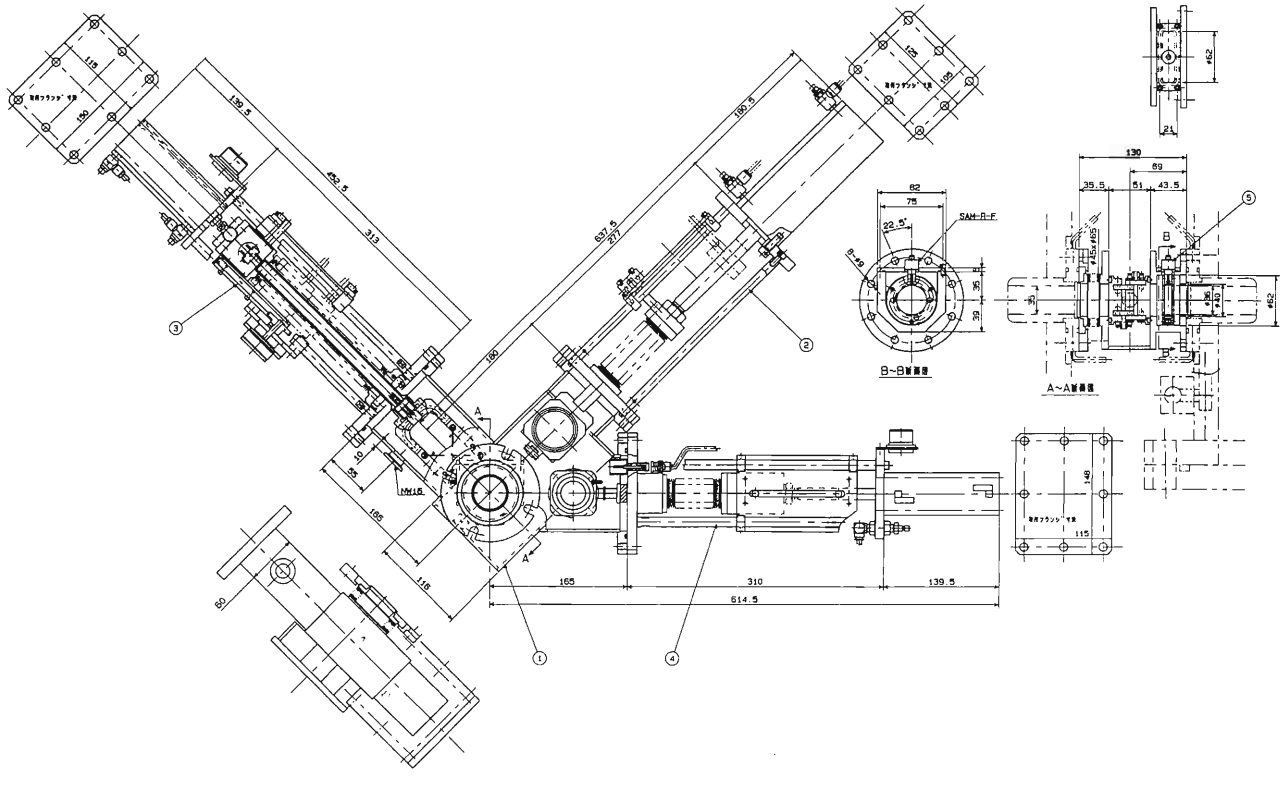

Fig. 1. The cutting view from the diagnosis chamber.

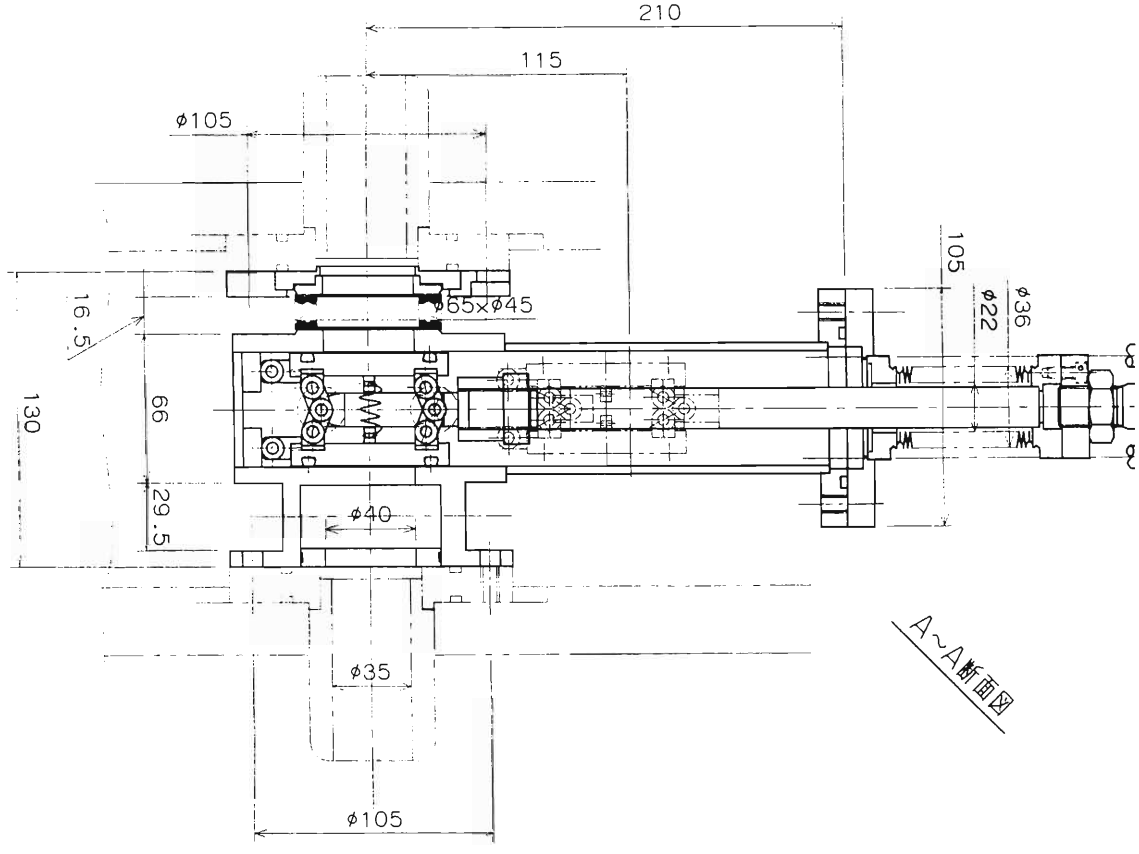

Fig. 2. The side view of the gate valve mechanism.

a beam-stopping device in the beam interlock system. It is designed to work in an emergency although the insertion speed is set to be slow as mentioned above. Scanning of the profile monitor should be programmed as it starts to scan the beam if the Faraday cup in the same space is accurately withdrawn and another Faraday cup downstream is accurately inserted.

New Beam Transport System of RILAC

N. Fukunishi, M. Fujimaki, E. Ikezawa, O. Kamigaito, M. Kase, and Y. Yano

We have started the construction of a new beam transport system for RIKEN heavy-ion linac (RILAC) in order to insert a charge state multiplier (CSM)[1] system between RILAC and RIKEN Ring Cyclotron (RRC). The new beam transport system is illustrated in Fig. 1. It has one main line and six branches. The main line transfers ions from RILAC to RRC *via* CSM. CSM consists of three separate sections: an accelerator, a charge stripper and a decelerator. The accelerator consists of six accelerating cavities (CSM A1–A6 in Fig. 1) and increases the stripping energy to produce highly charged ions required by RI Beam Factory (RIBF) project.[2] The bending magnet BM90 separates the desired charge state from the others by utilizing the difference in magnetic rigidity. Four successive dipole magnets (SW, BA-A, BA-B and BM85) bend the beams further. The total bending angle is 355 degrees. This structure produces a space for the decelerator section of CSM. The decelerator consists of one decelerating cavity (CSM D1), and slows down ions to their initial velocities so that RRC can accept them without changing its injection radius. The decelerated ions are transferred to RRC using the existing beam line. The section from the charge stripper to the decelerator is designed to be achromatic and isochronous like a ring cyclotron. These features are effective to avoid complicated coupling of the longitudinal motion driven by CSM and the horizontal motion caused by the beam line magnets. The results of ion-optical studies are shown in Fig. 2.

The six branches (beam line e1–e6) aim to provide beams accelerated by CSM for use in several experiments. The maximum beam energy is now 6 MeV/nucleon whereas that of RILAC is limited to 4 MeV/nucleon. It enables us to conduct new types of experiments in RILAC facility. The most important example is the search for super-heavy elements *via* a sub-barrier fusion reaction. Experiments for super-heavy elements have been performed in the E1 experimental hall of RRC facility using the lowest energy beams of RRC. Because RILAC facility is more suitable for this experiment after the installation of CSM,

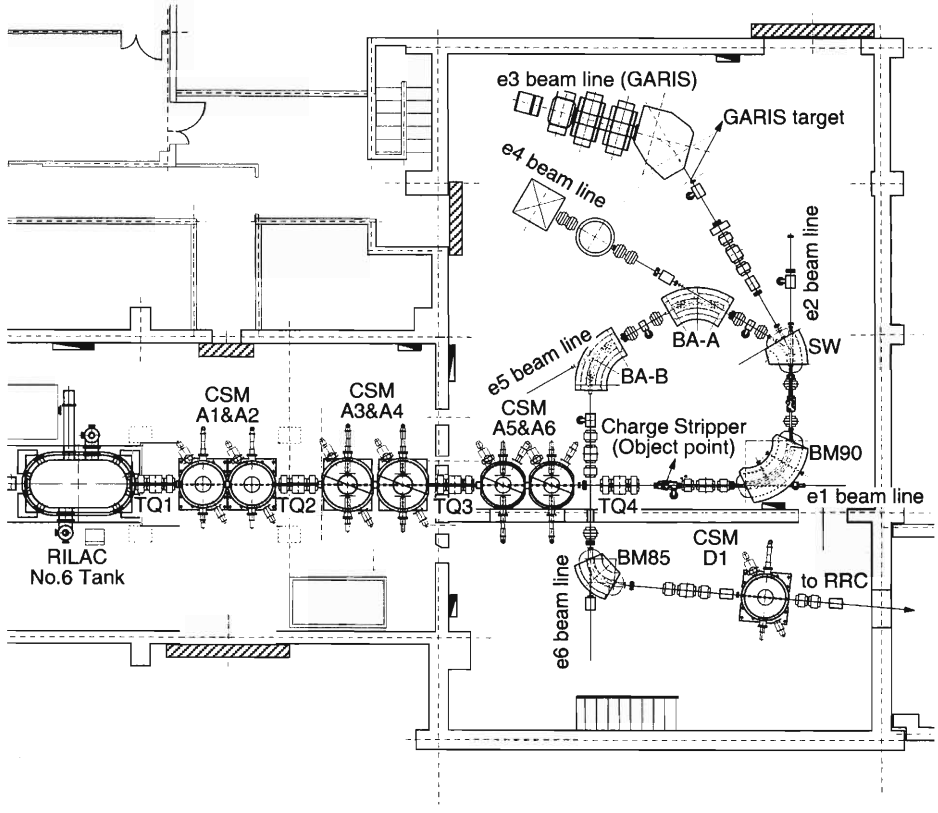

Fig. 1. The new beam transport system in RILAC facility is illustrated. CSM consists of six acceleration cavities (A1–A6), a charge stripper and a decelerator (D1). The beam transport system has one trunk line from RILAC to RRC and six branches for experiments. Four sets of quadrupole magnets (TQ1–TQ4) are newly fabricated.

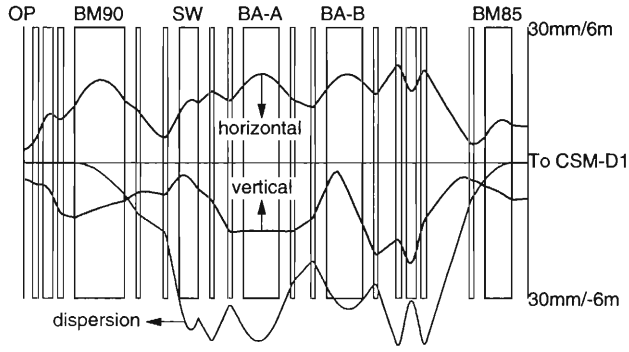

Fig. 2. Beam envelope and dispersion are calculated for the beam transport system from the object point (OP) to the decelerator section of CSM. The emittance assumed here is 22.4π mm · mrad for both horizontal and vertical directions. The momentum spread is assumed to be 0.15%. Rectangular boxes represent dipole and quadrupole magnets.

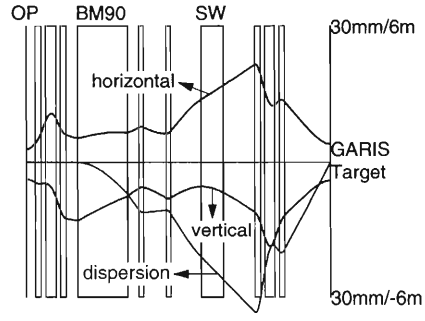

Fig. 3. Beam envelope and dispersion are calculated for the beam transport system from the object point (OP) to the target of GARIS. The emittance assumed here is 22.4π mm · mrad for both horizontal and vertical directions. The momentum spread is assumed to be 0.15%. Rectangular boxes represent dipole and quadrupole magnets.

the experimental setup including the gas-filled recoil isotope separator (GARIS) was moved to RILAC facility.

In the case of GARIS experiments, we first accelerate ions using CSM and produce a waist beam at the charge stripper position. A charge-stripping process is not necessary for GARIS experiments but emittance matching is performed there. Ions are transferred to the target of GARIS through BM90 and SW magnets. We adopted both point-to-point and waist-to-waist imaging for the section from the object point to the target so that the beam tuning can be easily performed. The results of ion-optical studies are shown in Fig. 3.

The maximum magnetic rigidity is limited to 2.1 Tm for the beam lines e2 and e3 and 1.2 Tm for beam lines e4, e5 and e6. In contrast, the maximum magnetic rigidity of the beams accelerated by CSM is 4 Tm. Beam line e1 accepts all the beams because there is no insertion of bending magnets.

Table 1. Specifications of newly constructed dipole magnets.

Type	BM90	SW		BM85
Deflection angle (degree)	90	30	60	24
Curvature radius (m)	1.4	1.6	0.8	0.8
Maximum field (T)	1.50	1.50		1.50
Pole gap (mm)	60	60		60
Pole face rotation (degree)	25/25	0/0	0/30	25/25
Total number of coil windings	432	432		432
Maximum excitation current (A)	200	200		200
Maximum voltage (V)	65	37		42

The new beam transport system is mainly composed of the devices used in the old beam lines. What we have newly constructed are three dipole magnets, four quadrupole triplets, power supplies for the quadrupole magnets and several beam-monitoring devices. For the new dipole magnets, we use existing power supplies. The specifications of the dipole magnets are summarized in Table 1. We should mention that the tape coil technique is used for these magnets. This technique has been widely used for the magnets of RILAC facility to reduce power consumption and space. Because we use the existing power supplies that were originally designed for magnets with tape coils, magnets with tape coils are best fitted to the power supplies. These dipole magnets were fabricated by TOKIN.

The new quadrupole magnets (TQ1–TQ4) have two features. Firstly, the maximum field gradient is 25 T/m, which is much larger than those of magnets used in other beam lines. A strong focusing power is required to focus a divergent beam produced by the RF fields of CSM. Note that CSM does not contain any quadrupole magnets in its accelerating cavities. The second is that these quadrupole magnets function as a steering magnet. It is due to the lack of space for steering magnets. A dipole field is excited by applying different excitation currents to the four poles of a quadrupole magnet. To this end, we also fabricated new power supplies. The new beam-monitoring devices are designed to be very compact and can be inserted between the accelerating cavities of CSM.

We plan to finish the construction of the beam line by the end of this year and start beam services in January 2001.

References

1) O. Kamigaito et al.: Proc. 12th Symp. on Accelerator Science and Technology, Wako, 1999-10 (RIKEN, 1999), p.233.
2) Y. Yano et al.: Proc. 1997 Particle Accelerator Conference, Vancouver, Canada, 1997-5 (IEEE, 1998), p.930.

Dipole and Quadrupole Magnets for Beam Transport System of RIKEN Heavy-Ion Linac and RI Beam Factory

N. Fukunishi, K. Kusaka, T. Nagafuchi, H. Kouzu, T. Kubo, and Y. Yano

Seven dipole magnets and forty-three quadrupole magnets were completed at the end of July 2000. The specifications of these magnets are summarized in Tables 1 and 2. Two types of quadrupole magnets (Q190 and Q380) are used to focus beams accelerated by a charge state multiplier (CSM).[1] Because the electric field of CSM acts as a strong defocusing lens, the field gradient required by these quadrupole magnets is 25 T/m, which are larger than those required by other quadrupole magnets. The remaining magnets will be used in the beam transport system of RIKEN RI beam factory (RIBF). The first three types of dipole magnets (DM90, DM30 and DM24) bend beams accelerated by IRC, the maximum magnetic rigidity of which is 3 Tm. Other dipole magnets are for the beam transport system from IRC to SRC. The maximum magnetic rigidity is 4.6 Tm in this case. Q220 and Q420 magnets are commonly used for these two beamlines. The maximum field gradient is designed to be 15 T/m, which is the same as those of quadrupole magnets used in the existing RARF facility. The dipole magnets are manufactured by Sumitomo Heavy Industries (SHI) and the quadrupole magnets are manufactured by Toshiba.

The specifications listed in the Tables were easily realized by the present technology for conventional normal-conducting magnets. All the products fulfilled the required specifications. The deviation of the magnetic field is less than 1×10^{-3} in the required region for all the dipole magnets. For quadrupole magnets, Toshiba examined the mixing of other multipole components using the harmonic coil method. Values of the multipole components relative to the quadrupole one are typically 1×10^{-3}.

One interesting point here is to confirm the accuracy of recent magnetic-field calculations by comparing calculations with measured data. We determined the cross-sectional shapes of these magnets by two-dimensional magnetic-field calculations in which the computer code OPERA-2D was used. We also estimated the maximum excitation currents using the computer code OPERA-3D that is very useful for three-dimensional magnetic-field calculations. The end profile of magnets is followed by the existing magnets[2,3] and checked by three-dimensional magnetic-field calculations. We adopted the BH curves of pure iron and low-carbon iron for dipole and quadrupole magnets, respectively. These BH curves are based on measurements.

First, we compare the uniformity of the magnetic fields in Fig. 1. Measured data for two dipole magnets that have the same cross-sectional shape are shown in the figure. Magnetic-field measurements were per-

Table 1. Parameters of dipole magnets.

Type	DM90	DM30	DM24	DM28	DM13
Deflection angle (degree)	90	30	24	27.5	12.5
Curvature radius (m)	2.0	2.0	2.0	3.0	3.0
Maximum field (T)	1.50	1.50	1.50	1.53	1.53
Pole gap (mm)	60	60	60	60	60
Pole face rotation (degree)	24/24	15/15	12/12	0/0	0/0
Size of hollow conductor (mm)	□13-ϕ8	□13-ϕ8	□13-ϕ8	□13-ϕ8	□13-ϕ8
Total number of coil windings	280	280	280	280	280
Maximum excitation current (A)	300	300	300	330	330
Maximum voltage (V)	94.2	41.1	35.6	55.2	29.7
Number of magnets	1	2	2	1	1

Table 2. Parameters of quadrupole magnets.

Type	Q220	Q420	Q190	Q380
Aperture (mm)	70	70	60	60
Length (mm)	220	420	190	380
Effective length (mm)	250	450	220	410
Maximum field gradient (T/m)	15	15	25	25
Size of hollow conductor (mm)	□6-ϕ3	□6-ϕ3	□6-ϕ3	□6-ϕ3
Number of coil windings (/pole)	52	52	63	63
Maximum excitation current (A)	158	158	160	160
Maximum voltage (V)	17.7	27.0	23.1	34.8
Number of magnets	23	8	8	4

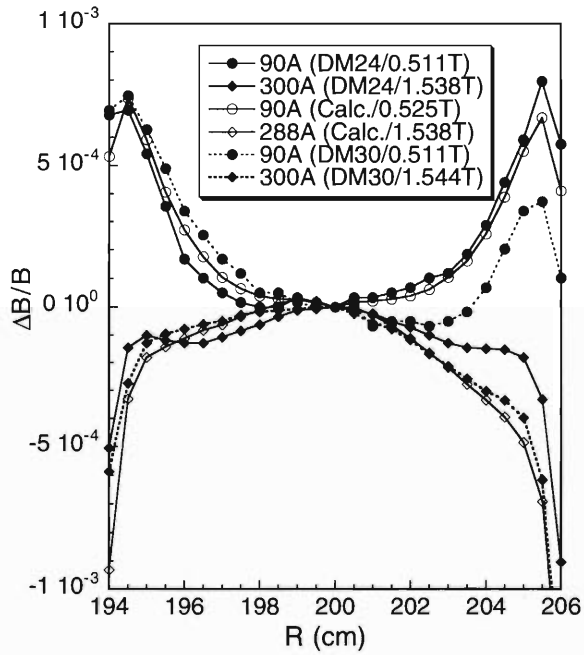

Fig. 1. Deviations of magnetic field ($\Delta B/B$) are illustrated for DM24 and DM30.

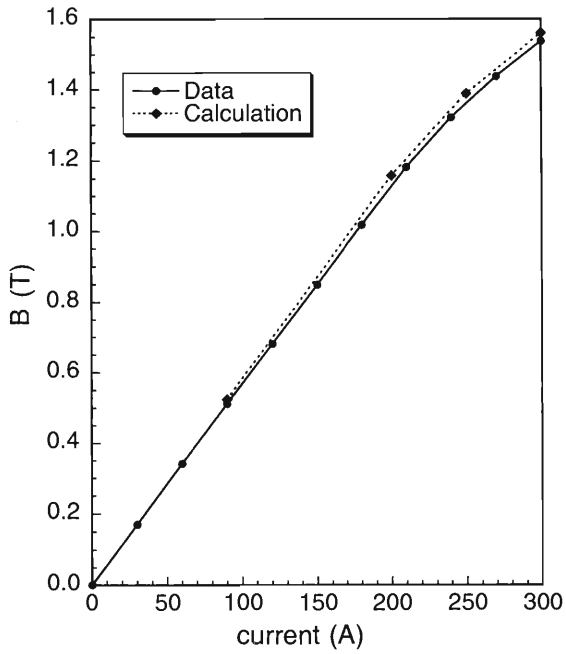

Fig. 2. Magnetic flux density is plotted as a function of excitation current.

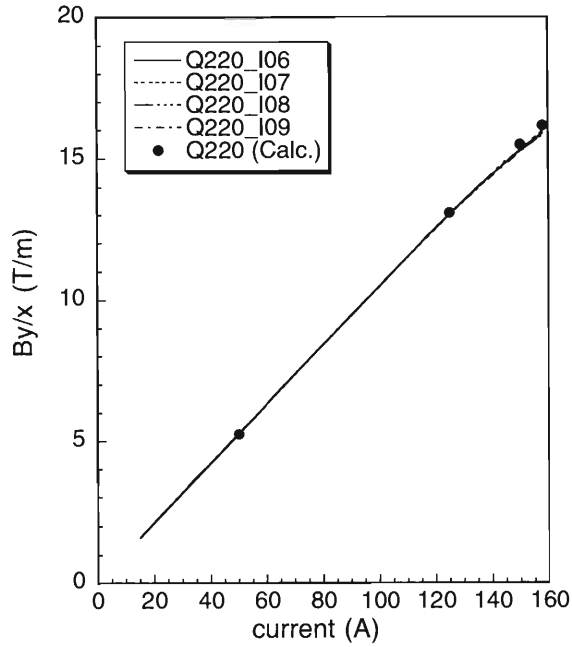

Fig. 3. Field gradient By/x is plotted for Q220 magnets. Measurements were performed for four magnets (I06–I09).

formed by SHI using a Hall probe calibrated by a NMR probe. We find that the maximum difference between the calculation and the measured data is 3×10^{-4} in the region where the radius R is 200 ± 5 cm. The difference is sufficiently small for conventional beamline magnets. We also find that the difference between DM24 and DM30 is 2.5×10^{-4} in the same region. This difference results from errors in processing poles of magnets. This implies that numerical errors in magnetic-field calculation may be smaller than 3×10^{-4}.

Second, we compare the magnetic flux densities at given excitation currents to investigate the effectiveness of three-dimensional magnetic-field calculations. We show magnetic flux density as a function of excitation current in Figs. 2 and 3. Magnetic-field measurements for Q220 magnets are performed by Toshiba using the harmonic coil method. The difference between the calculation and the measured data is 1.5% for DM24 and 2% for Q220, which is sufficiently accurate when we determine maximum excitation currents. However, we should mention that sizable errors exist in three-dimensional magnetic-field calculations. The reason is as follows. A magnetic-field calculation gives the deviation from the ideal magnet made of iron with infinite permeability. For an ideal dipole magnet, the magnetic flux density B is given by the equation $B = I/(\mu_0 \times g)$. Here, I is total ampere turns, μ_0 is the permeability of air and g is the pole gap. In the case of DM24, the present calculation predicts a 11.2% decrease of the magnetic flux density from the ideal magnet. On the contrary, the measured data give a 12.6% decrease. The difference between the calculation and the measured data is more than 10%. The disagreement may be due to the following three reasons. The first is that we neglected relatively less-important structures in our calculations. The second is that the adopted mesh size in the finite-element method is not sufficiently small due to limitations of our computer resource. The last is that the BH curve used in the calculation differs slightly from the actual one. The comparison demonstrated here revealed the limitations of recent three-dimensional magnetic-field calculations.

References

1) O. Kamigaito et al.: Proc. 12th Symp. on Accelerator Science and Technology, Wako, (1999), p.233.
2) K. Hatanaka et al.: Proc. 11th Conf. on Cyclotrons and their Applications, Tokyo, (1987), p.523.
3) M. Kumada et al.: Proc. 2nd Symp. on Accelerator Science and Technology, (1978), p.73.

Construction of the IRC for RIKEN RI Beam Factory

T. Mitsumoto,* A. Goto, M. Kase, J. Ohnishi, O. Kamigaito, N. Sakamoto, K. Ikegami, H. Okuno, Y. Miyazawa, T. Hiasa,* Y. Kumata,* and Y. Yano

The intermediate ring cyclotron (IRC) is a room-temperature ring cyclotron with four sectors that will be utilized in the RIKEN RI-beam factory.[1] It will be installed as the intermediate stage between the existing RIKEN Ring Cyclotron (RRC) and the superconducting ring cyclotron (SRC). The IRC, having a K value of 980 MeV, accelerates the extracted beam from the RRC; the maximum acceleration energy and the maximum magnetic rigidity of the IRC are 126.7 MeV/nucleon and 4.57 Tm, respectively.[2] The main parameters of the IRC are listed in Table 1.

The construction of the IRC started in 1998. The E-sector magnet was completed in April, 2000. All sector magnets were completed in December 2000. Figure 1 (a) shows a photo of the E-sector magnet. Figure 1 (b) shows a photo of the S- and W-sector magnets. Field measurement for the magnetic field of the E-sector magnet was performed. Details of the measurement are described in this report.[3] The field measurement for the other sector magnets will begin in January 2001.

The main coil of the sector magnets consists of 11 pancakes of coils, which are divided into two parts. These parts are excited independently by two power supplies, the M1 power supply for 6 pancakes and the M2 power supply for 5 pancakes. The M1 power supply with the maximum current of 450 Amperes is equipped with a 3-Ampere bypass power supply in order to realize sufficient resolution for the excitation current. The M2 power supply with the maximum current of 450 Amperes is equipped with four 15-Ampere bypass power supplies which realize independent control of the excitation currents of the four sector magnets.

The trim coils of the sector magnet consist of 20 pairs. The first three pairs and the last three pairs of each sector are excited by an independent power supply. The rest of the trim coils are connected in series among sectors. The number of power supplies for trim coils is 38. We adopted a switching type of power supply for trim coils. The volume of the power supply is almost 1/4 that of the dropper type. Table 2 shows the specifications of a 15 kW power supply for

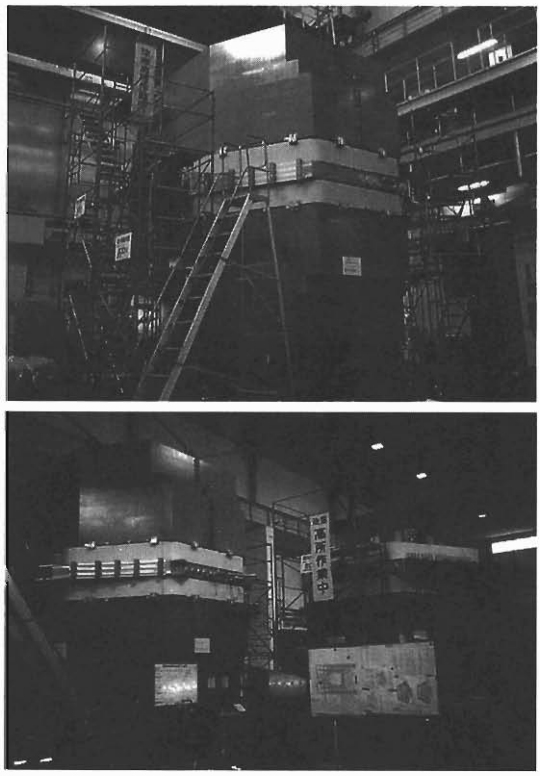

Fig. 1. (a) E-sector magnet was completed at Niihama works, Sumitomo Heavy Industries, Ltd. (b) S- and W-sector magnets. This photo was taken in September 2000.

Table 1. Main parameters of the IRC.

K-value		980 MeV
Number of sectors		4
Harmonics		7
Average radius	Injection	2.77 m
	Extraction	4.15 m
Velocity gain factor		1.5
Number of cavities	Main	2
	Flat-top	1
RF frequency (main resonator)		18.0–38.2 MHz
Cyclotron frequency		2.57–5.45 MHz

Table 2. Specifications of 15 kW switching power supply for trim coil.

Nominal input voltage	400VAC
Maximum output power	15 kW
Nominal output current	500 Amperes
Nominal output voltage	30 V
Efficiency	90% typical
Cooling	Water cooled
Ripple and noise	50 mVp-p
Stability	Maximum output 10 ppm for 8 hours
EMI	Meets CISPR Pub. 22 Class A
Size	486mm(W) 444mm(H) 879mm(D)
Weight	120 kg

* Sumitomo Heavy Industries, Ltd.

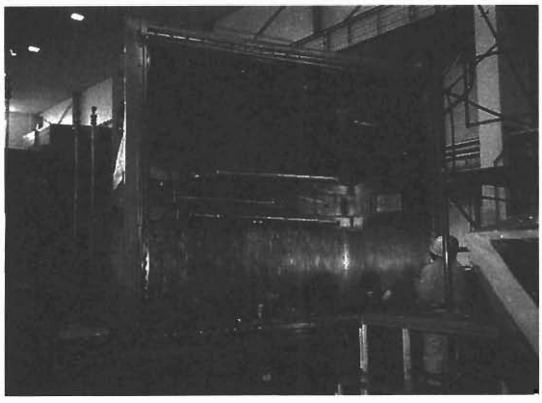

Fig. 2. The first resonator for the IRC. Flapping panels are shown.

the trim coils.

The first main resonator (ES-resonator) was assembled in November, 2000. Figure 2 shows a photo of the resonator. A low-power test was performed. The results of the test are described in this report.[4)]

Manufacturing of all components of the IRC will be completed in March 2001.

References

1) Y. Yano et al.: Proc. 15th Int. Conf. on Cyclotrons and Their Applications, Caen, France, (1998), p.696.
2) T. Mitsumoto et al.: RIKEN Accel. Prog. Rep. **33**, 208 (2000).
3) J. Ohnishi et al.: RIKEN Accel. Prog. Rep. **34**, 333 (2001).
4) N. Sakamoto et al.: RIKEN Accel. Prog. Rep. **34**, 335 (2001).

Magnetic Field Measurement of the IRC Sector Magnets

J. Ohnishi, T. Mitsumoto,* A. Goto, and Y. Yano

The IRC sector magnets are under construction at Sumitomo Heavy Industries, Ltd. and three of four sector magnets have been completed this year. We started the magnetic field measurements of the first completed E-sector magnet in order to verify the magnetic performance and to obtain the magnetic field data necessary for the orbit calculations. This report describes the magnetic field measuring system and preliminary results.

Figure 1 shows a plan view of the field measuring apparatus. Eight Hall probes are placed on the Hall assembly at intervals of 200 mm. The Hall assembly is driven in the radial and the azimuthal directions with pneumatic pistons. This driving system was the same as that developed for the magnetic field measurement of RRC.[1] The parameters of the driving are listed in Table 1. It takes longer than 3 sec for one driving time because the friction of air flow is large in the tube with a length of greater than 30 m. Figure 2 shows a block diagram of the control system. The signals from a DO board on the computer control the electromagnetic valves which supply the driving pistons of the Hall assembly with air. The positional accuracy of the Hall probes was within about 1 mm, which was obtained from alignment error of the rails and the slack of the driving system.

The Hall probes (HHP-MU, AREPOC Ltd.) were calibrated with an NMR gaussmeter in advance. Since the temperature coefficients of the Hall probes were 5–7 $\times 10^{-4}$ per degree, we measured the temperature of the probes and corrected the output voltages by the temperature coefficient of each probe. As a result the measuring accuracy of magnetic fields was within about 5×10^{-4}. The output voltages of the Hall probes and the temperature sensors (Pt resistor) were measured with a data acquisition unit (AT34970A) with a GPIB interface.

Figure 3 shows a time chart of the excitation current pattern. Settlement times when the deviation from the final magnetic field reaches 5×10^{-5} are 2 and 4 hours for the maximum field strength (1.9 T) and low field level (< 1.4 T), respectively, which each include 1.3 hours of the initialisation. Reproducibility of the magnetic field was smaller than 1×10^{-4}. Figure 4 shows the excitation curve of the IRC E-sector magnet. The deviation from the calculation by TOSCA[2] was

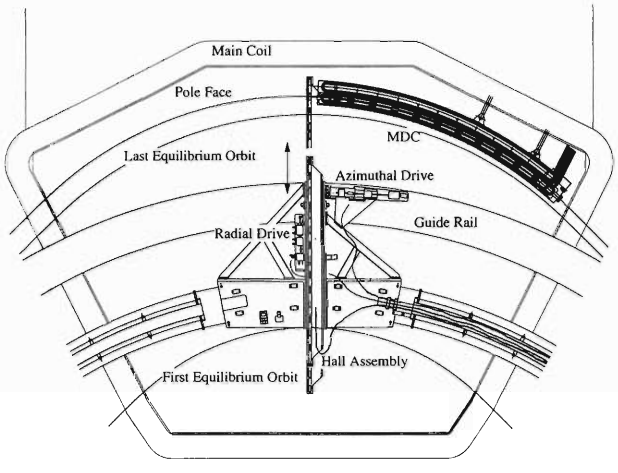

Fig. 1. Plan view of the IRC magnetic field measuring apparatus.

Table 1. Parameters for driving of the Hall assembly.

	Range	Step	Time
R	730mm	10mm, 20mm, 30mm	3.5 sec
Theta	180°	0.25°, 0.50°, 0.75°	3.8 sec

* Sumitomo Heavy Industries, Ltd.

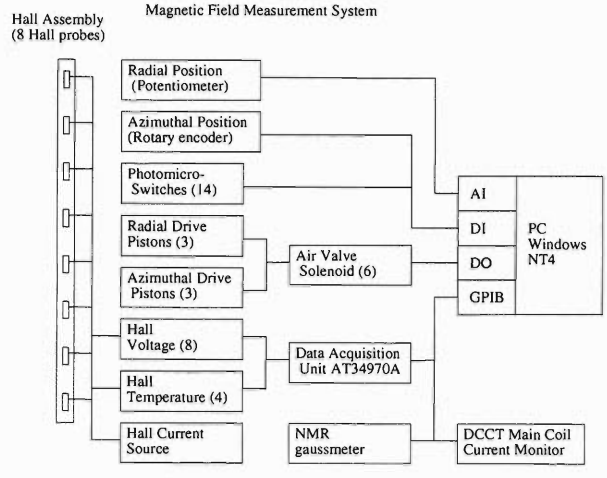

Fig. 2. Block diagram of the control and measurement system.

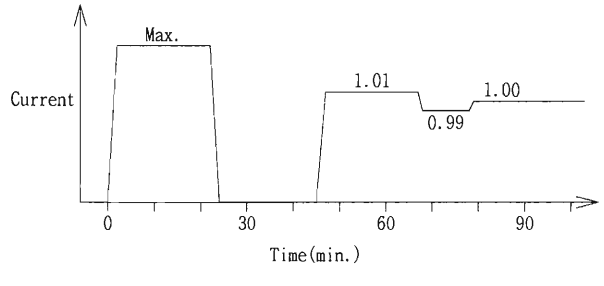

Fig. 3. Time chart of the excitation current pattern.

Table 2. Difference between the measurement and the calculation by TOSCA. Bax indicates magnetic field strength on the centreline of the sector magnet and Bave the average in the region of 90 degrees.

	Bax(R=3500mm) [mT]		Bave(R=3500mm) [mT]		Kb=Bax/Bave	
Current	Measurement	Calculation	Measurement	Calculation	Measurement	Calculation
100A	597	597(−0.04%)	341	343(0.82%)	1.754	1.739(−0.85%)
170A	1006	1009(0.29%)	573	580(1.21%)	1.755	1.739(−0.90%)
240A	1392	1397(0.41%)	792	803(1.27%)	1.756	1.741(−0.85%)
290A	1602	1596(−0.36%)	910	913(0.36%)	1.760	1.748(−0.72%)
380A	1815	1802(−0.76%)	1026	1024(−0.17%)	1.769	1.759(−0.59%)
445A	1918	1904(−0.75%)	1080	1078(−0.22%)	1.776	1.766(−0.53%)

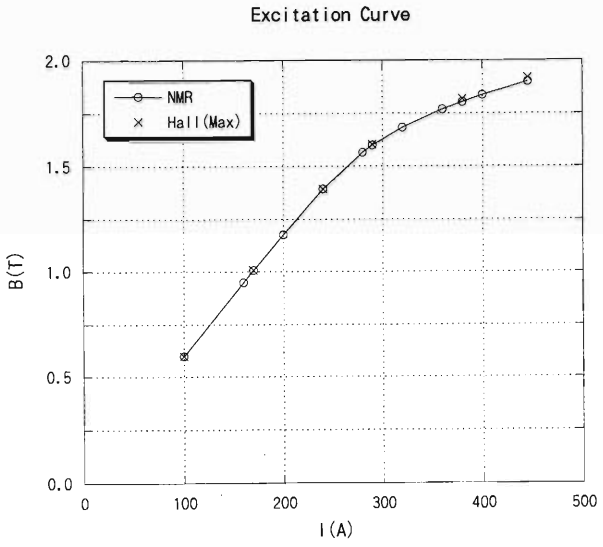

Fig. 4. Excitation curve of the E-sector magnet.

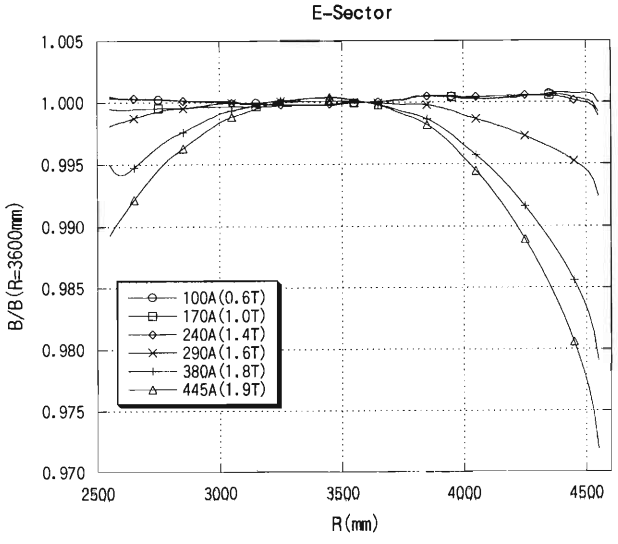

Fig. 5. Magnetic field distributions on the centreline of the E-sector magnet.

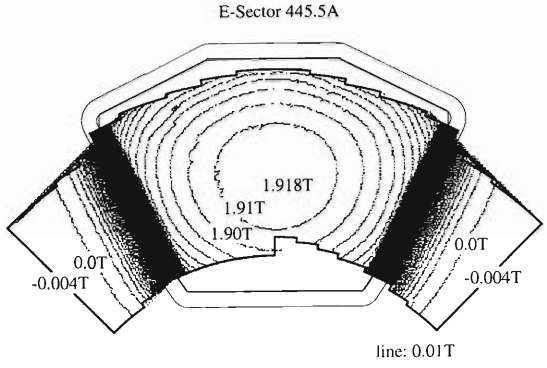

Fig. 6. Contour plot of the magnetic field of the E-sector magnet.

almost within 1%, as evident in Table 2.

Figure 5 shows the magnetic field distributions along the pole centreline of the E-sector magnet. Figure 6 shows an example of a contour plot of the magnetic field obtained from the mapping measurements. The size of the mapping mesh was 10 mm and 0.25° in the radial and the azimuthal directions, respectively, in the pole edge area where the magnetic fields change rapidly. On the other hand, the mesh size was 20 mm and 1.0° in other regions. It took 8.5 hours to measure all of the points of 17196. The measuring time will be improved to about 6 hours by using a digital voltmeter with better performance for the measurement of the Hall voltages.

Next year we will measure the magnetic fields produced by trim coils and the interference with the next sector magnet as well as the other sector magnets, and obtain the magnetic field data necessary for cyclotron operation.

References

1) H. Takebe et al.: RIKEN Accel. Prog. Rep. **16**, 188 (1982).
2) OPERA-3d/TOSCA, Vector Field, Ltd., UK.

Construction of the rf-Resonator for the RIKEN Intermediate-Stage Ring Cyclotron

N. Sakamoto, O. Kamigaito, Y. Miyazawa, T. Mitsumoto, A. Goto, and Y. Yano

The four-sector intermediate-stage ring cyclotron (IRC[1]) in the RIKEN RI-Beam Factory has two single-gap-type accelerating resonators whose operational frequency range is 18.0–40.5 MHz.[2] The resonant frequency is tuned by adjusting two flapping panels which are placed symmetrically to the median plane and finely tuned by block tuners (details are in Ref. 2). The shapes of the resonators are optimized using the computer code MAFIA[3] so that the Q-values are as large as possible. The fabrication of one of the resonators is almost completed and low-power tests have been conducted (Fig. 1).

Fig. 1. The IRC accelerating resonator. The side flange on which the dee electrode is attached is removed.

As shown in Fig. 2, the resonant frequency varies from 17.8 to 41.3 MHz by changing the flapping panel angle from 0° to 90°. The block tuner changes the resonant frequency more than 0.7% over the entire frequency range. The measured results are in good agreement with the MAFIA prediction (Table 1). The unloaded Q-values were obtained from measured loaded Q and SWR. The Q-values were as large as 74–79% of the calculated values.

The higher modes appear at $f > 80$ MHz as shown in Fig. 3. These are well reproduced by a MAFIA calculation; flux patterns of the magnetic field for each mode are schematically illustrated in Fig. 4.

The vertically unbalanced rf field problem is one of the most important issues for this resonator. Misalignment of the flapping panels and dee causes a vertical

Table 1. Measured (Estimated) resonant frequencies and Q-values at the panel angles of 0 deg. and 90 deg.

Flapping panel	0 deg.	90 deg.
Frequency (MHz)	17.83	41.34
	(17.58)	(40.74)
(trimmer) $\Delta f/f$ (%)	0.80	0.80
	(0.80)	(0.80)
$Q_{unloaded}$	21600	29500
	(29300)	(37500)

( ) values estimated using MAFIA code

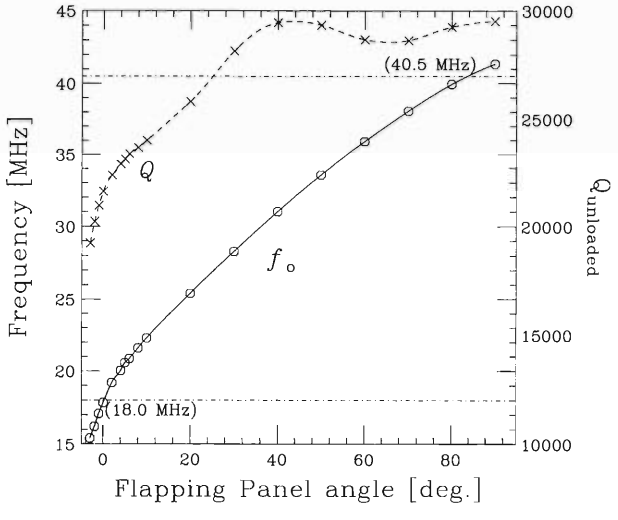

Fig. 2. Measured resonant frequency and unloaded Q-values.

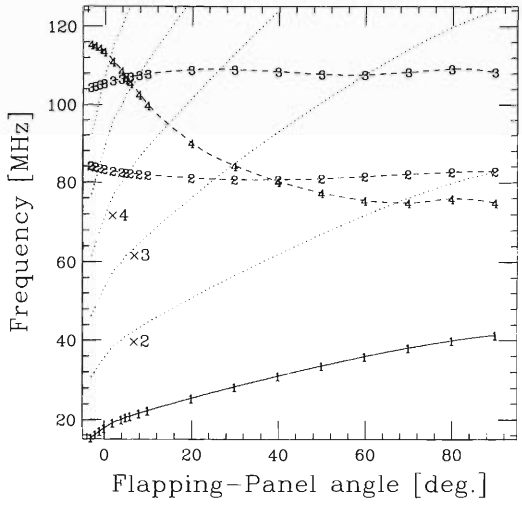

Fig. 3. Frequencies of the higher modes.

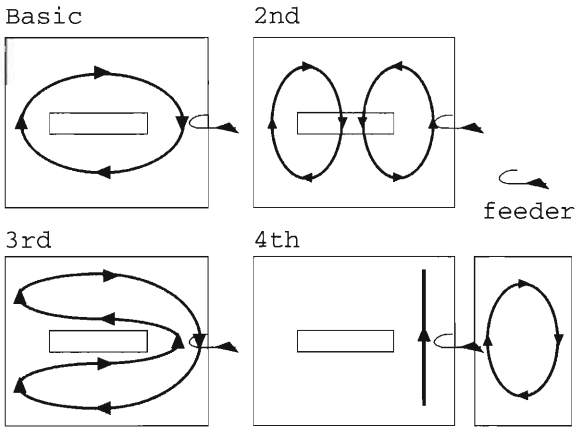

Fig. 4. Schematic views of the magnetic flux pattern of the higher harmonics.

electric field at the median plane and the leakage of the rf field power into the vacuum chamber. In the worst case, elements such as the phase probe are damaged by the leaked rf power. To detect the vertical component of the electric field at the median plane, a balance monitor (capacitive pickup) is installed in the beam chamber outside the resonator. Using this monitor, the leakage can be minimized by offsetting one flapping panel to the other. An example at 18 MHz shown in Fig. 5 indicates that an offset angle of 0.2 degrees is needed to cancel the vertical field due to the misalignment of the dee.

We plan to measure the electric field distribution using a perturbation method. The fabrication of the No. 2 resonator is now in progress.

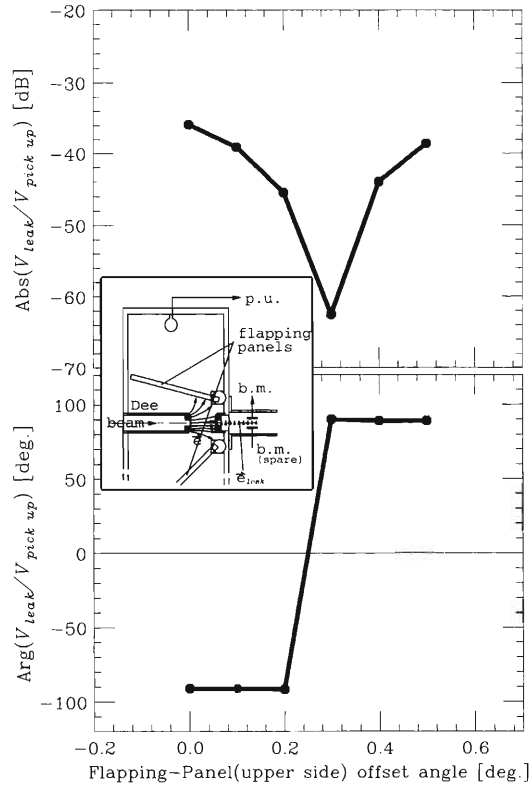

Fig. 5. Leakage field detection. The sign of the phase reflects the direction of the leakage field.

References
1) T. Mitsumoto et al.: Proc. 12th Symp. on Accelerator Science and Technology, Wako, 1999-10, RIKEN (1999), p.183.
2) N. Sakamoto et al.: Proc. 12th Symp. on Accelerator Science and Technology, Wako, 1999-10, RIKEN (1999), p.224.
3) The MAFIA collaboration, User's Guide MAFIA Version 4.0, CST GmbH, Lauteschägerstraße 38, D-64289, Darmstadt, Germany.

Status of the SRC for the RIKEN RI Beam Factory

A. Goto, H. Okuno, J. Ohnishi, T. Mitsumoto, N. Fukunishi, S. Fujishima, T. Tominaka, K. Ikegami, N. Sakamoto, Y. Miyazawa, O. Kamigaito, T. Morikawa, M. Kase, and Y. Yano

We have made significant changes to the design of the sector magnet of the SRC (superconducting ring cyclotron). The changes are as follows:

(1) A pair of large active magnetic-shield coils has been replaced with soft iron slabs that cover the valley regions.

(2) The cold-pole scheme has been replaced with the warm-pole scheme.

In the new design, the cyclotron is almost completely covered with soft-iron slabs about 1 m in thickness, except in the central region. Some of these iron slabs are bridged on the top and bottom of the valley regions between the sector magnets. The others of them are placed vertically between these top and bottom slabs so as to cover the space between the back yokes of the neighboring sector magnets. The total weight of this falling-U-shaped iron-slab structure (referred to as the "iron cover") is about 3,000 tons (the total weight

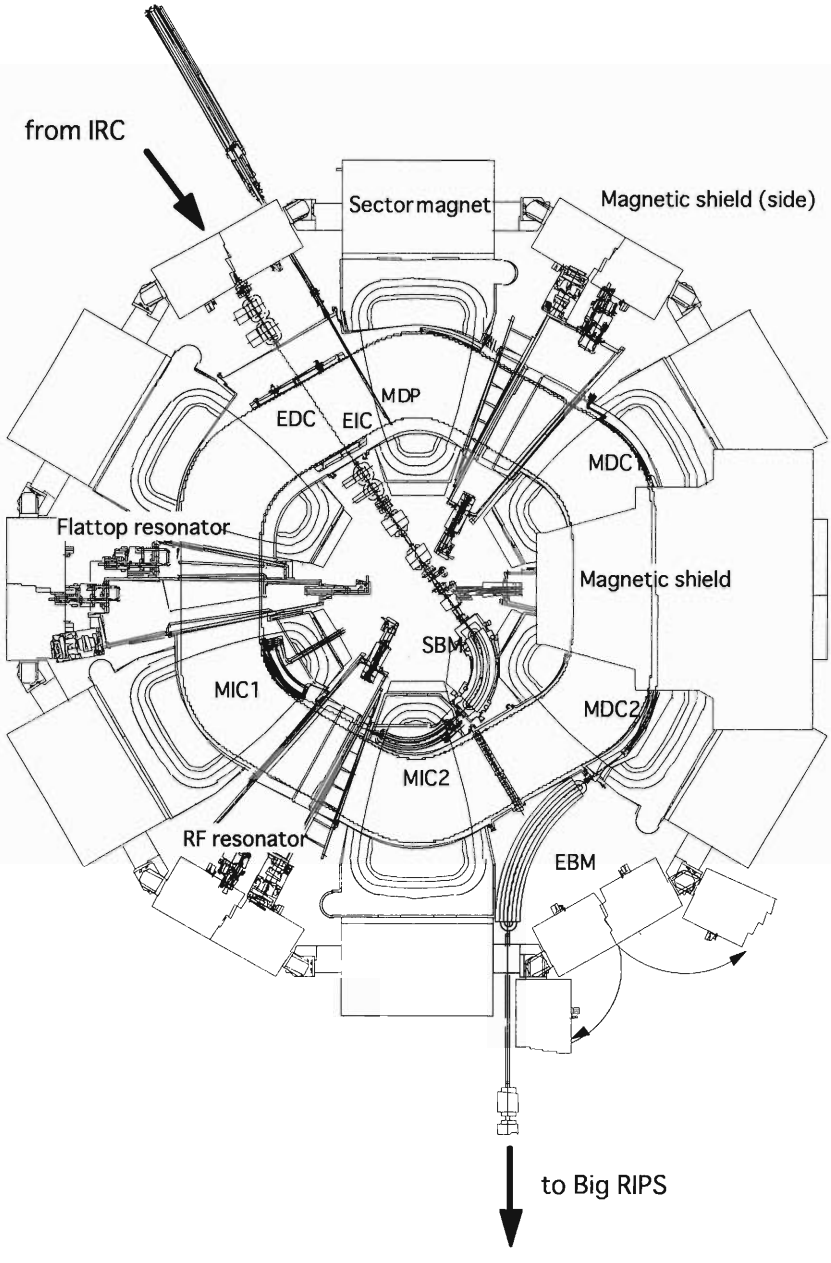

Fig. 1. Plan view of the newly designed SRC.

of the SRC amounts to 7,800 tons). The vertical outside slabs are assembled to form a double-leafed hinged door to be opened when the maintenance is carried out for the rf resonators, vacuum pumps, and so on in the valley region.

The "iron cover" yields the following good results:

(1) The SRC can be self-radiation-shielding.

(2) The stray field in the valley is reduced from 0.5 T to 0.1 T at maximum. The maximum sector field needed to bend, for example, U^{58+} 150 MeV/u is accordingly reduced from 4.3 T to 3.7 T because of this reduction of negative stray field, with the K-value of the SRC being kept at 2,500 MeV. According to this lower flutter, we relocate the operating domain of the vertical betatron frequencies from the values between 1.0–1.5 to those between 0.5–1.0. The decrease of the vertical betatron frequencies causes an increase in the vertical beam size by a factor of about 1.4, but this presents no problem because of sufficient acceptance of the injection and extraction elements. This decrease also makes the tolerances of the main and trim coils and poles tighter, but they are still tolerable. According to the reduction of the maximum sector field, the maximum magnetomotive force required is also reduced from 5.4 MA/sector to about 3.8 MA/sector. Now we adopt the solenoid windings of main coils of 22 layers times 18 turns (30 layers times 20 turns in the old design). The maximum stored energy and the electromagnetic forces exerted on the main coil are greatly reduced from 390 MJ to 235 MJ and from 400 ton/m to 260 ton/m, respectively. This small stray field in the valley allows us to use cryopumps, motors, control devices, and so on in a safe situation.

(3) Superconducting magnetic channels for beam injection and extraction are not necessary. Now all the injection and extraction magnetic channels inside the sector magnets are normal with the moderate power consumption and their structures are very similar to those for the RRC and the IRC.

(4) The shift of the injection and extraction trajectory depending on the negative stray field strength is greatly reduced (almost no shift).

(5) The stray field outside the SRC is reduced: about 200 gauss at the maximum near the yoke and the vertical outside shield-wall. We need neither the active magnetic shielding which is difficult to fabricate nor the thick iron plates enclosing the huge SRC vault. We place the rf oscillators near the SRC like they are for the RRC and the IRC. The SRC vault is now very safe for those working at the site even inside the cyclotron.

For the warm-pole scheme, details are given elsewhere in Ref. 1.

We have decided not to conduct tests of the prototype sector magnet. We learnt many important things from this prototype that has accomplished its mission.

The new design of the sector magnet has almost been finalized. Winding of the main coil is scheduled to start around May 2001. Design of the other components such as the injection and extraction magnetic channels and an rf resonator is currently in progress.

The layout of the newly designed SRC is shown in Fig. 1.

References

1) H. Okuno et al.: RIKEN Accel. Prog. Rep. **34**, 339 (2001).

Design of Sector Magnets for Superconducting Ring Cyclotron

H. Okuno, T. Mitsumoto,[*1] N. Fukunishi, J. Ohnishi, S. Fujishima,[*2] T. Tominaka,[*3]
K. Ikegami, Y. Miyazawa, A. Goto, and Y. Yano

Significant changes have been made to the sector magnets of the superconducting ring cyclotron (SRC), as mentioned in Refs. 1 and 2. Here, the new design will be reported briefly, focusing on the changed parts.

Figure 1 shows a cross-sectional view and a plan view of the sector magnet and its basic parameters are listed in Table 1. The main components of the magnet are its superconducting and normal-conducting coils, a cryostat which consists of 80-K thermal shields and vacuum vessels, poles and a yoke. Two types of superconducting coils are used: a pair of main coils and a group of trim coils. Both coils are located on the upper and lower sides with respect to the midplane. A group of normal-conducting trim coils for fine magnetic-field correction is also arranged on the upper and lower sides of the beam chamber. The cold mass is supported by three types of thermal insulating support (*i.e.*, Fr, Fq, Fz support) from the cryostat wall at room temperature.

In the new design we adopted a warm-pole arrangement, as shown in Fig. 2. The main coil vessel, composed of 50-mm-thick stainless-steel plates, is of a roundish trapezoidal shape. This vessel surrounds the upper iron pole at room temperature. The width of the gap between the 4.5-K vessel and the 300-K iron pole is designed to be more than 110 mm, enough to incorporate an 80-K thermal radiation shield. A pair of approximately 1-m-wide and 20-mm-thick stainless-steel plates link the inner corners of both long-section sides of the coil vessel, as shown in Fig. 1. The plate in the upper corners crosses through the rectangular hole (1.2 m wide and more than 100 mm high) of the warm iron pole. This hole helps to form isochronous fields. Although the mechanical stiffness of this structure decreases compared with that of the cold pole structure, it is still rigid enough to support the electromagnetic forces because the magnetic forces decrease due to the reduction of the total magnetic motive forces, as mentioned in Ref. 2. By adopting the warm pole arrangement we can avoid the problem that soft iron, which has the property of brittleness in the ultralow-temperature region, is used as material for the main support structure against huge magnetic fields as it

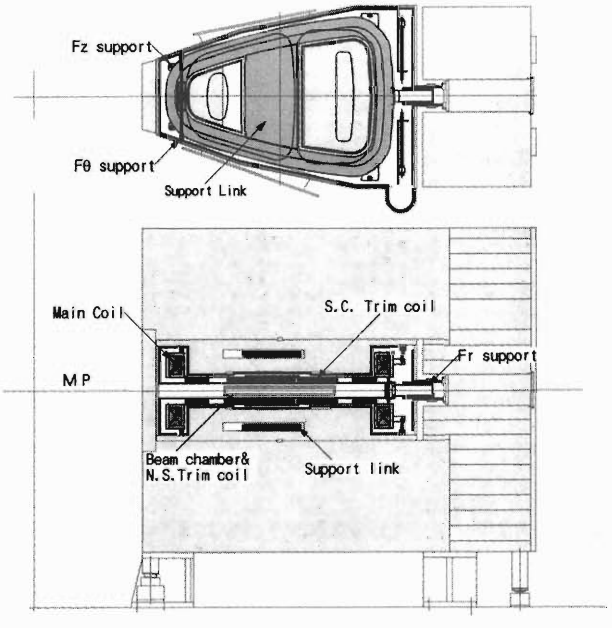

Fig. 1. A cross-sectional view and a plan view of the sector magnet.

Table 1. Main parameters of the sector magnets.

Average radii of beam injection	3.56 m
extraction	5.36 m
Sector angle of main coil	25 degrees
Maximum magnetic field	
in the beam orbital area	3.8 T
in the main coil	4.5 T
in the trim coil	5.1 T
Main-coil's ampere turns per magnets	3.96 MA
Magnetic stored energy for six magnets	240 MJ
Maximum operation currents	
-for main coil	5000 A
-for trim coil	3000 A
Total weight (including the iron cover)	8500 ton

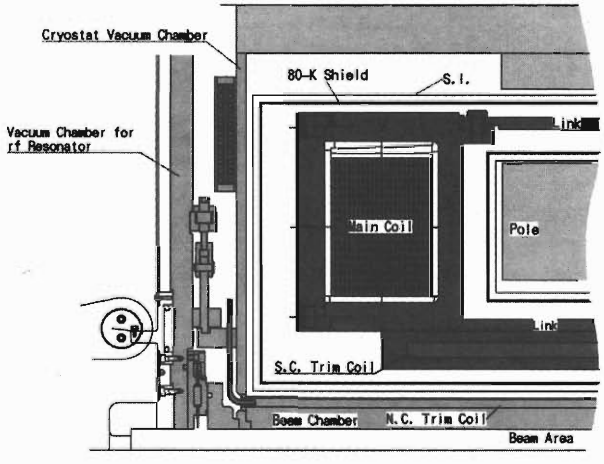

Fig. 2. Warm-pole arrangement.

*1 Sumitomo Heavy Industries, Ltd.
*2 Ishikawajima-Harima Heavy Industries Co., Ltd.
*3 Hitachi, Ltd.

Table 2. Main specifications of the superconducting coils for the sector magnets.

Property	unit	Main Coil	S. C. Trim Coil
Overall size:			
Size	m^2	7.5	7
Number	pairs	6	4 set x 6
Weight	ton	200	9
Coils:			
Winding		Solenoid	Double pancake
Turns/coil		396	16/50/28/32
Nominal current	A	5000	3000
Overall current density	A/mm^2	33.3	25
Stored energy	MJ	235	2
Peak field	T	4.5	5.1
Cooling method		Bath cooling	Two-phase forced flow cooling
Conductor:			
Size	mm^2	8 x 15	8 x 15
Structure		Al stabilized NbTi cable	Al stabilized NbTi cable
Ratio Al:Cu:NbTi		18.5:0.84:1	18.5:0.84:1
Critical current	A	14970@5 T, 4.5 K	14970@5 T, 4.5 K
Stabilized current	A	> 6000 A	-

has been for more than thirty years in the cold pole arrangement.

Table 2 summarizes the specifications of the superconducting coils for the sector magnet. The solenoid winding of 22 layers times 18 turns using superconducting wire of 8 mm × 15 mm (30 layers times 20 turns in the old design) was adopted for the main coil. We apply a cryogenic stabilizing method for the main coil to prevent the coil from quenching. The gaps between turns and between layers of the main coils were designed to be 0.8 mm and 1.5 mm in distance, respectively. These gaps are held with numerous glass-fiber-reinforced plates. Flat plates are adopted for the insulation between turns in order to increase the reliability of electric insulation.

In the old design of the trim coils, solenoid windings using superconducting wire of 2.9 mm × 3.6 mm in size were bath-cooled in He vessels and the cryogenic stabilizing method was applied. However, we have been bothered by the problem that the evacuation of He bubbles, which is important to keep the coils superconducting during bath cooling, is very difficult in the trim coils because they are flat and thin and available spaces in the vertical direction are narrow. In order to solve this problem we decided to adopt the double-pancake windings that are indirectly cooled by forced two-phase helium through a system of tubes attached to the coil casing. The same conductor as that of the main coil will be used for easier winding. The coil is nonstabilized but there are many successful cases using such types of superconducting coils. The design of the details of the superconducting trim coil is currently in progress and is being undertaken carefully to realize the required performances.

References

1) Y. Yano et al.: RIKEN Accel. Prog. Rep. **34**, 301 (2001).
2) A. Goto et al.: RIKEN Accel. Prog. Rep. **34**, 337 (2001).

Design of the Injection and Extraction Systems for the RIKEN Superconducting Ring Cyclotron

S. Fujishima,* H. Okuno, A. Goto, and Y. Yano

Along with the change of the design of the sector magnets of the RIKEN Superconducting Ring Cyclotron (SRC), the design of the injection and extraction systems for the SRC has also been changed significantly compared to the previous design last year.[1] The basic layouts and specifications of the injection and extraction elements were determined by numerical analysis of the injection and extraction trajectories. In the analysis, much care was taken in particular to minimize not only the required fields of the elements but also the differences between various beam trajectories in the elements.

The stray field from the sector magnets depends non-linearly on the magnetic rigidities of the beams, and causes the difference between various beam trajectories in the elements. Larger differences in the trajectories require a wider bore of the element.

In the previous design of the SRC, stray field from the sector magnets had increased to -0.6 T at the maximum and had caused large differences in the trajectories. But, in the present design, stray field from the sector magnets decreased to about -0.06 T because of the iron yoke covering the SRC, so that the differences in the trajectories also decreased.

However, the injection and extraction elements should be installed in a small space limited by the vacuum chamber for the beams or thermal insulating vacuum vessels of the sector magnets, and moreover, should generate sufficiently high fields to bend a beam which has a high magnetic or electric rigidity.

Because of these difficulties, it remains a challenge to design the injection and extraction systems.

Table 1 shows the energies and magnetic rigidities of three typical beams. The beam of $^{238}U^{78+}$ (100 MeV/u) has the lowest magnetic rigidity. The beam of $^{238}U^{88+}$ (350 MeV/u) has the highest magnet rigidity at extraction. The beam of $^{238}U^{49+}$ (100 MeV/u) has the highest magnetic rigidity at injection. The beam of $^{238}U^{88+}$ (350 MeV/u) also has the highest electric rigidity.

Table 1. Energies and magnetic rigidities of typical beams.

	Energy [MeV/u]		B ρ [Tm]	
	Inj.	Ext.	Inj.	Ext.
^{238}U $^{78+}$	40.4	100	2.82	4.51
^{238}U $^{88+}$	115.2	350	4.31	7.94
^{238}U $^{49+}$	40.4	100	4.49	7.18

In the first stage of the analysis, magnetic fields of the sector magnets were calculated with a three-dimensional computer code, "TOSCA." However, the design of the normal-conducting trim coils of the sector magnets has not been optimized perfectly, thus the calculated fields of the sector magnets include about 0.3% error. This causes shifts of the injection and extraction trajectories. To compensate them, the energies of the injection or extraction beams were slightly changed as the length of the first or the last equilibrium orbit become equal to the design value, respectively. And then, to trace the beam trajectories, the equation of motion was solved with using the Runge-Kutta-Gill method. In the calculation, the electric or magnetic field of each element was superimposed on the field of the sector magnets.

Figure 1 shows a schematic layout of the injection and extraction elements, and shows the trajectories of two typical beams of $^{238}U^{78+}$ (100 MeV/u) and $^{238}U^{88+}$ (350 MeV/u). Because of the suppression of the stray field in the valley, the difference between two trajectories is indiscernibly small in the figure. This layout has not been optimized completely, so it may need to be partly modified.

The injection system consists of one superconducting bending magnet (SBM), two normal-conducting magnetic inflection channels (MIC1 and MIC2), and one electrostatic inflection channel (EIC). The extraction system consists of one electrostatic deflection channel (EDC), three normal-conducting magnetic deflection channels (MDC1, MDC2 and MDC3), and one normal-conducting bending magnet (EBM).

In the previous design, the extraction system did not include the MDC1, and the EDC required a considerably high field of -105 kV/cm. To suppress the required field of the EDC, the MDC1 was added to the system and supplemented the bending power of the EDC.

Because the injection beam will be introduced crossing the EIC and EDC, their respective electrodes have holes to pass the beam. To minimize the hole diameter, each trajectory is adjusted with several steering magnets to cross at the same point on the respective electrodes of the EIC and EDC.

All magentic channels are installed in the gap between upper and lower coils of the sector magnets.

Table 2 shows the specifications of the injection and extraction elements.

Each magnetic element consists of main dipole coils and compensation coils to suppress the fringe field on

* Ishikawajima-Harima Heavy Industries Co., Ltd.

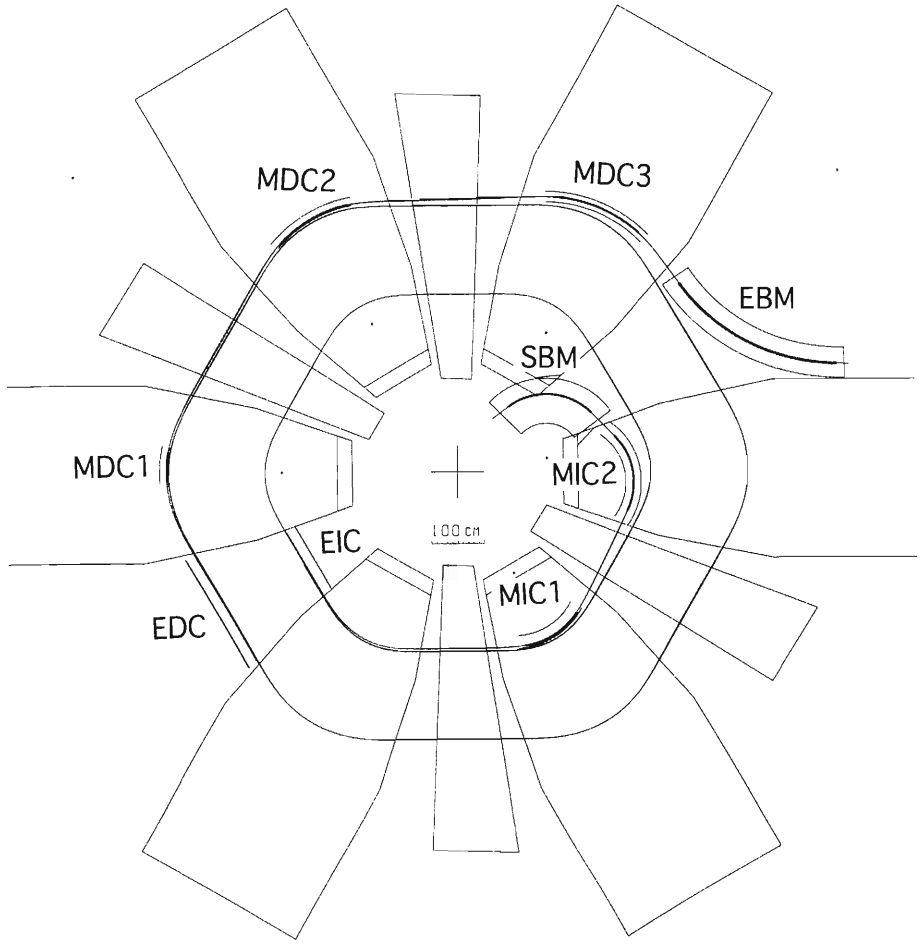

Fig. 1. Schematic layout of the elements and trajectories of typical beams.

Table 2. Specifications of the injection and extraction elements.

	Radius [cm]	Angle [deg.]	Length [cm]	B or E (max.) [T],[kV/cm]
EIC	–	–	130.0	90
MIC1	140.0	49.0	119.7	0.285 (Normal)
MIC2	122.0	72.4	154.2	0.969 (Normal)
SBM	120.6	81.0	170.5	3.794 (Super)
EDC	–	–	228.0	-90
MDC1	220.0	13.0	49.9	- 0.060 (Normal)
MDC2	232.0	37.0	149.8	- 0.200 (Normal)
MDC3	260.0	39.6	179.7	- 0.540 (Normal)
EBM	368.0	54.2	348.1	- 2.102 (Normal)

the first or the last equilibrium orbit.

To reduct fabrication cost, and to improve feasibility, all magnetic channels were specified as normal-conducting magnets.

The length of each element was determined taking into consideration the balance between the difference of the trajectories in the element and the required field of the element.

References

1) S. Fujishima et al.: RIKEN Accel. Prog. Rep. **33**, 218 (2000).

Design of Superconducting Bending Magnet for Superconducting Ring Cyclotron

H. Okuno, S. Fujishima,[*1] T. Tominaka,[*2] K. Ikegami, J. Ohnishi, A. Goto, and Y. Yano

The significant point in the new design of the superconducting ring cyclotron (SRC) is that iron plates of about 1 m thickness cover the valley regions for additional magnetic and radiation shielding. They suppress the leakage field from the sector magnets, decreasing magnetic motive forces for the maximum bending power, which makes the critical parts of the SRC easier to design and produce. A superconducting bending magnet (SBM) for beam injection, which is one of the key elements in the SRC, can also benefit from the additional shield. An iron return yoke can be used for the SBM, while in the previous design, the iron placed in the center region did not work due to saturation without the iron cover. An iron-shielded magnet does not need such a large magnetic motive force and has a simple coil structure compared to an iron-free magnet with an active-shield coil proposed previously.[1] In the following, the design and R&D work of the SBM are described.

The main parameters of the SBM are listed in Table 1. The SBM needs to generate a magnetic field of about 4 T along the beam trajectory with a curvature of about 1.2 m. Figure 1 shows the proposed cross section and a plane view of the SBM. The two coils, the iron poles and the yokes generate the required fields. Flat coils are adopted since they can be wound and supported easily. The iron pole is used for the mandrel in the coil winding. The yoke is divided into two parts: the cold yoke and warm yoke. The cross section of the cold yoke, through which about half of the flux passes, is bilaterally symmetric. This configuration decreases sifting forces and unbalanced forces on the cold mass, while the weight of the cold mass is not as large (about 3 tons). The C-shape of the warm yoke is adopted because the available space for the warm yoke at the side of the sector magnet is very narrow, as shown in Fig. 1 of Ref. 2. A warm duct is installed for the ion beams. Iron shims and water-cooled baffle slits are attached to the duct.

Test coils were fabricated and tested for the design of the real SBM. The main parameters are listed in Table 2. Two types of coil structure were tested: one has vertical channels at every second layer (Coil A) and the other has no vertical channels (Coil B). Their winding method and support structure were designed to be as close as possible to those of the real SBM. The test coil was tested in a field of about 4 T generated with a bias split coil in order to simulate the real operation. Figure 2 shows a photograph of the test coil with the bias coil. Figure 3 shows the results of the excitations of the two coils under real SBM operating conditions. They were tested under the base field of 0 T or 4 T. The results for Coil B are very promising since the quenches occurred at a more severe condition than that of the SBM. Transversal quench propagation velocities were obtained from measurements of voltages between the taps placed at every fifth layer for the two coils. These results show that the normal zones in Coil B propagate in a layer direction more than three times

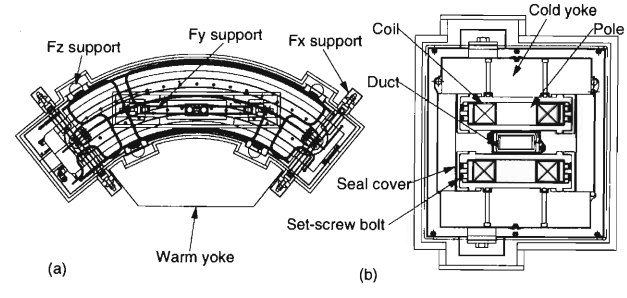

Fig. 1. (a) Plane view of SBM and (b) cross-sectional view of the inside of the cryostat.

Table 1. Main parameters of the SBM.

Item	Value
Type	Flat coil, Iron pole Iron yoke (cold and warm)
Required field	4.0 T
Maximum field in the coil	4.5 T
Stored energy	0.56 MJ
Homogeneity	2-3 x 10^{-3}
Beam bore	40 (H) x 30 (V) mm^2
Radius	1208.4 mm (R. T.)
Angle	75.72 degree
Coil size	55 x 58 mm^2

Table 2. Main parameters of the test coils.

Item	Coil A	Coil B	SBM
Curvature [mm]	960	960	1208
Angle [deg.]	68	68	76
Width of the inner mandrel [mm]	52	52	142
Width and height of the coil [mm^2]	23.3 x 22.5	23.4 x 22.5	58 x 55
Total turn	197	233	1317
He channel (vertical channel)	Each 2 layer	No	Each 20 layer

[*1] Ishikawajima-Harima Heavy Industries Co., Ltd.
[*2] Hitachi, Ltd.

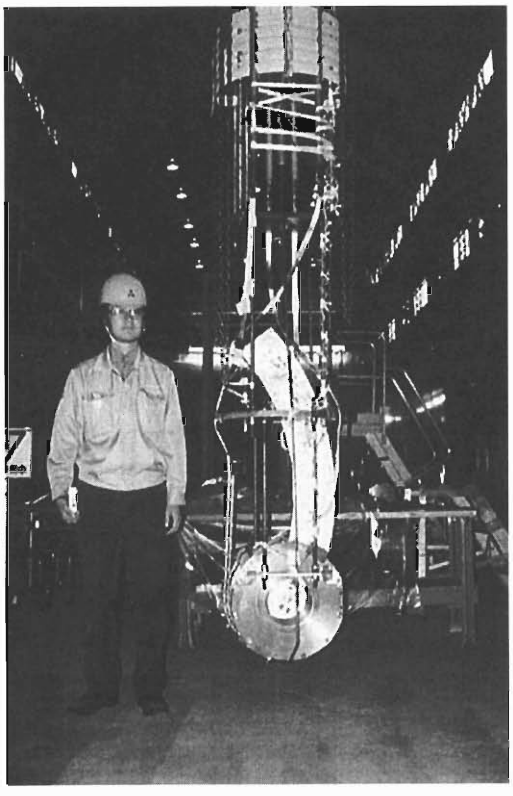

Fig. 2. Assembled test coil.

faster than in Coil A, which means that Coil B is safer than Coil A when quenches occur. From these results, the coil structure of the SBM was designed based on that of Coil B.

The fabrication of the SBM will be completed by

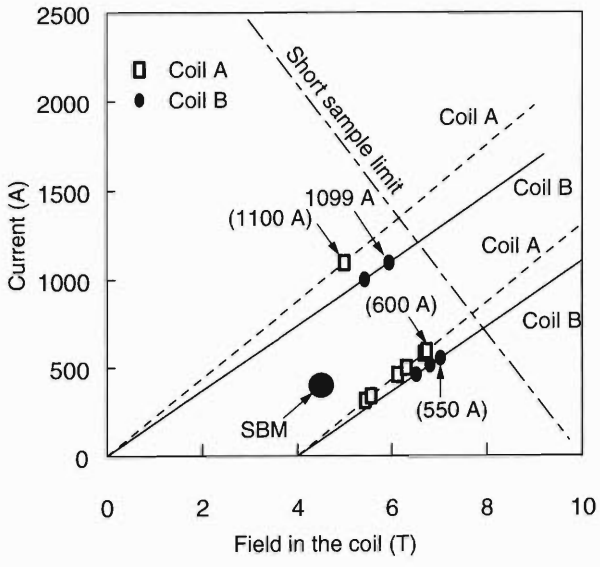

Fig. 3. Quench history. White squares and black circles indicate the points where the quench of Coil A and Coil B occurred, respectively. Lines which start from 0 T (4 T) at zero current indicate excitation curves in the case of the bias-off (bias-on). Currents in parentheses indicate that the excitation terminated for reasons other than quench.

March 2001.

References

1) H. Okuno et al.: RIKEN Accel. Prog. Rep. **33**, 220 (2000).
2) A. Goto et al.: RIKEN Accel. Prog. Rep. **34**, 337 (2001).

Measurement of Outgassing Rates of Materials Used in the Vacuum Chamber for RIKEN Superconducting Ring Cyclotron and Intermediate Ring Cyclotron

K. Sugii, K. Ikegami, A. Goto, and Y. Yano

The vacuum chamber of the RIKEN superconducting ring cyclotron (SRC) and the intermediate ring cyclotron (IRC) which is under construction in the RIKEN RI-Beam Factory Project uses various materials such as stainless steel (SUS), elastomer O-rings and a super insulator. For evaluation of the gas load due to outgassing from these materials and corresponding pumping requirements, measurements of the outgassing rates are indispensable.

A schematic diagram of the experimental setup for the measurement of outgassing rates is shown in Fig. 1. A vacuum chamber is composed of an upper dome and a lower dome. A flat plate having a central circular orifice is mounted between the upper dome and the lower dome. The orifice is 10 mm in diameter, and its conductance is $9.2 \times 10^{-3}\,\mathrm{m^3/s}$ for N^2. The chamber and the flat plate are made of stainless steel (SUS304), and are prepared by electropolishing. A sample for measurement of the outgassing rate is placed into the upper dome. In the case of the measurement of an O-ring sample which is used for sealing, the O-ring was set in a groove (see Fig. 1). Gas flow rate through the orifice (Q) is given by the following equation,

$$Q = C \times (P1 - P2),$$

where $P1$ and $P2$ are the pressures of the upper dome and the lower dome, respectively, and C is the conductance of the orifice. When amounts of outgassing for the upper dome including a sample (Qt) and the upper dome without a sample (Qc) are measured respectively by the above equation, an amount of outgassing for only the sample (Qs) is calculated from

$$Qs = Qt - Qc.$$

In order to reduce the Qc as background and prepare the initial surface state, the chamber was baked at 150°C for about 24 hours, and was then exposed to air. The Qc was measured after these operations. Figure 2 shows amounts of outgassing which were measured for two elastomer O-rings at room temperature. The two types of O-rings are the following: (1) general fluoroelastomer and (2) high-quality fluoroelastomer: FLID ARMOR (NIPPON VALQUA INDUSTRIES, LTD). The size and surface area of each O-ring are ID139.1 × OD153.0 × ϕ 6.98 mm and $1.0 \times 10^{-2}\,\mathrm{m^2}$, respectively. The results are shown as follows: (1) for the general fluoroelastomer when the entire O-ring surface was exposed to ultra-high vacuum (Qga), (2) for the general fluoroelastomer when an O-ring sample was used for vacuum sealing (Qgs), (3) for FLID ARMOR when the whole of O-ring surface was exposed to ultra-high vacuum (Qfa), and (4) for FLID ARMOR when an O-ring sample was used for vacuum sealing

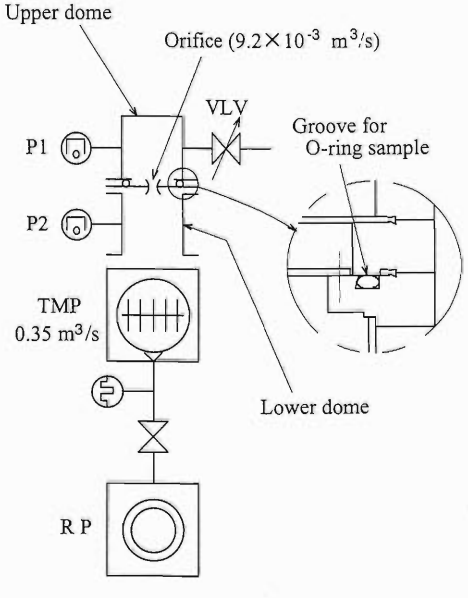

Fig. 1. Experimental setup for measurement of outgassing rate.

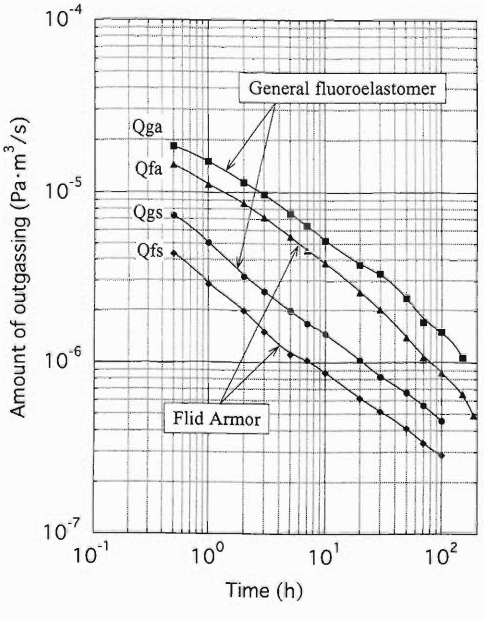

Fig. 2. Measurement results of amounts of outgassing for unbaked fluoroelastomer O-rings.

(Qfs). Outgassing rates of the general fluoroelastomer and FLID ARMOR after pumping for 100 hours were 1.5×10^{-4}Pa m^3/s/m^2 and 8.7×10^{-5}Pa m^3/s/m^2, respectively. From making comparisons at each point between the Qga and the Qfa or the Qgs and the Qfs, we found that the outgassing rate for FLID ARMOR was 56–78% of the value of the general fluoroelastomer. The difference between the O-rings was not significant. The treatment and preservation of O-rings appears to be more important than the choice material for them. Then, from making comparisons at each point, between the Qga and the Qgs, we found that the Qgs was 25–40% of the Qga. (In the case of FLID ARMOR, the Qfs was 20–40% of the Qfa.) Therefore, it is considered that 20–40% of the O-ring surface is exposed to vacuum when the O-ring is set into a groove for vacuum sealing. We consider that these results will be helpful in estimating the amount of outgassing in vacuum systems that use elastomers, such as the SRC or the IRC.

A super insulator which is used as a covering around shields at 80 K for superconducting coils for sector magnets cooled at 4.5 K is used to reduce radiation loss from the wall of the vacuum chamber of the cryostat. Figure 3 shows outgassing rates of the super insulator (SI-1) with time after the start of pumping. The super insulator (SI-1) is multilayerinsulation and i s made of aluminum vaporized polyester sheets. SI-2 values are shown in the graph comparison with the measurement values for SI-1. SI-2 is made of commercially available polyester and its outgassing rate was measured by the National Institute for Fusion Science (NIFS)' group (Akaishi *et al.*).[1] The outgassing rate of SI-1 is 2×10^{-5}Pa m^3/s/m^2 after 10 hours, and of the order of $\sim 10^{-7}$Pa m^3/s/m^2 after 400 hours and is higher than a factor of 3 of that of SI-2.

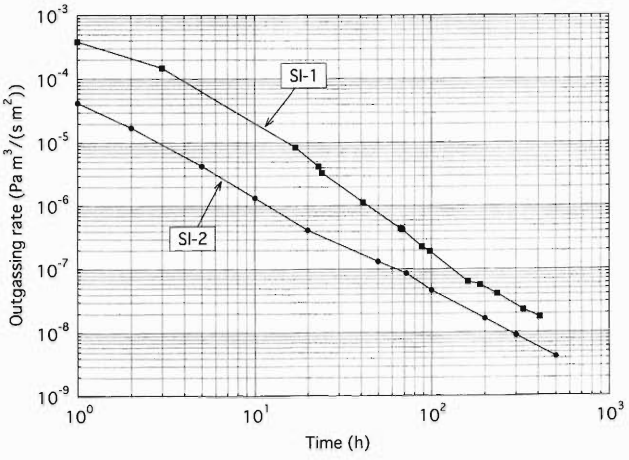

Fig. 3. Measurement result of outgassing rates for super insulators.

These measurement results will be reflected in the design of the pumping system for the vacuum chambers of the SRC and the IRC.

References

1) K. Akaishi et al.: J. Vac. Soc. Japan **37**, 56 (1994).

Helium Cooling System of the RIKEN Superconducting Ring Cyclotron

K. Ikegami, T. Kawaguchi, H. Okuno, M. Ohtake, J. Ohnishi, A. Goto, and Y. Yano

The design of the superconducting ring cyclotron (SRC) having a K-value of 2500 MeV, which is to be built in the RIKEN RI-Beam Factory project, was significantly changed at the beginning of December 1999. Instead of using the superconducting active shield coils of Helmholtz coil type, iron magnetic shields[1] are used for the valley regions of the SRC to reduce the large leakage flux from the six sector magnets. The design of the superconducting main coils and superconducting trim coils of the sector magnet which are set in a single cryostat, was changed as well. The design of the injection system[2] for the SRC was also changed. Only one bending magnet in the injection system will be superconducting.

Figure 1 shows the entire flow of the helium cooling system for the SRC. The cooling system will be a closed-circuit system without liquid nitrogen. It consists of the six cryostats of the sector magnets, the cryostat of the bending magnet in the injection system, a control dewar, a refrigerator, three compressors and five buffer tanks. A control dewar will be located on the top of the six sector magnets. Seven current leads (2 pieces (pcs) of 5 kA and 5 pcs of 100 A) for the twelve main coils are installed in the liquid helium vessel of the control dewar. The total helium mass flow of seven current leads is estimated to be 39 l/h. Fifteen current leads (five pcs of 4 kA and ten pcs of 300 A) of twelve sets of trim coils are also installed in the liquid helium vessel of the control dewar. In this case, the total helium mass flow of fifteen current leads is estimated to be 71 l/h. The superconducting conductors of the coils are electrically connected to the power leads in the liquid helium vessel of the control dewar.

The thermal shields of the cryostats are cooled down to 50 K–60 K by gas helium supplied from the refrigerator. The required capacity of thermal shields is 2900 W at 60 K. Twelve sets of main coils are cooled down to 4.5 K by liquid helium from the refrigerator. Twelve control valves are installed in the control dewar to control the flow of liquid helium. The flow will be adjusted to minimize the temperature difference between each coil. The required capacity of main coils is 353 W at 4.5 K. Twelve sets of trim coils are cooled down to 4.5 K by the two-phase forced cooling method. The helium flow is adjusted similarly using twelve control valves. The required capacity of trim coils is 52 W at

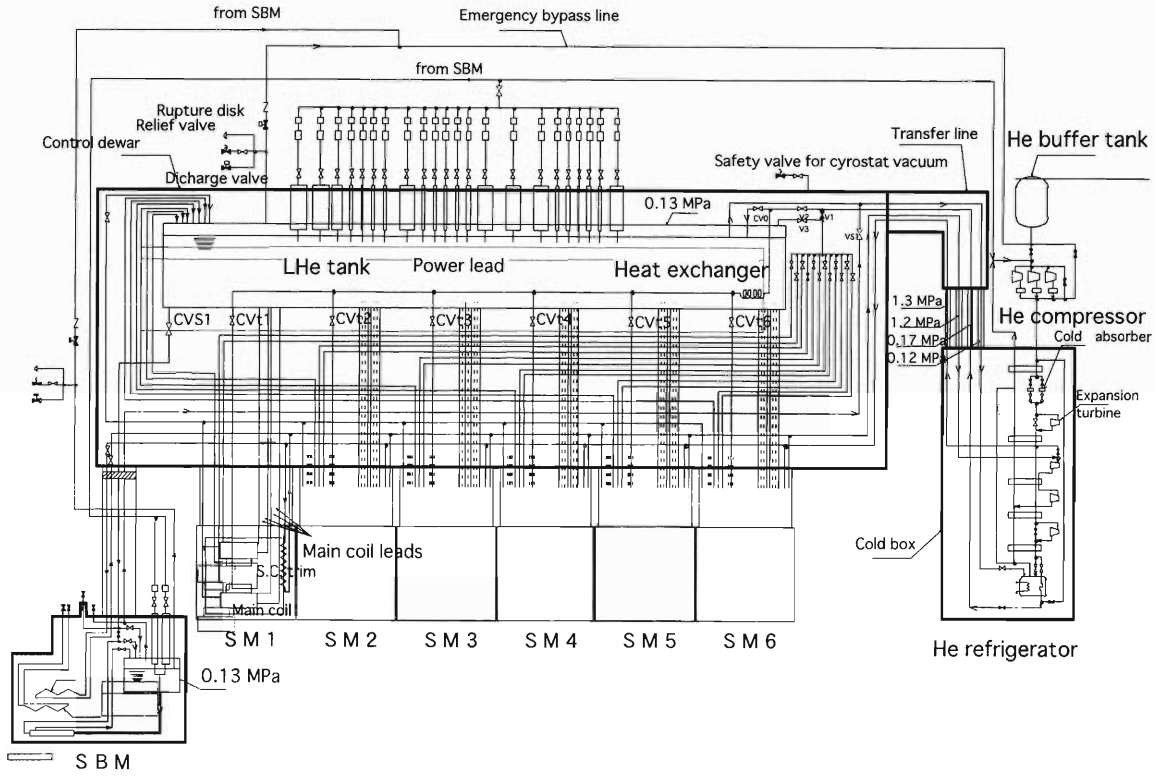

Fig. 1. The helium cooling system for the SRC with a bending magnet.

Table 1. Required capacities of the sector magnets and the bending magnet for the injection system.

Capacity	Sector magnets		Bending magnet
	Main coils	Trim coils	
Coils at 4.5 K	353 W	52 W	40 W
Thermal shield	2900 W		56 W
Current leads	39 ℓ/h	71 ℓ/h	1.7 ℓ/h

4.5 K.

The coil of the superconducting bending magnet is cooled down to 4.5 K through transfer lines connected to the control dewar. A control valve is installed in the control dewar to adjust the helium flow. The total required capacity is 40 W at 4.5 K: 5 W from radiation loss of the wall, 10 W from loss of transfer lines, and 25 W from heat deposit by neutron radiation. The thermal shield loss is 56 W at 60 K. The total helium mass flow for the current leads of the magnet is 1.7 l/h. All required capacities of the SRC are listed in Table 1.

Table 2. Capacities of the refrigerator for the SRC.

Capacity	Refrigerator
Coils at 4.5 K	445 x 1.3 <600 W
Thermal shield	3500 W
Current leads	120 ℓ/h

The refrigerator has a capacity of 600 W (445 W multiplied by a safety factor of 1.3) at 4.5 K for the coils, 3500 W at 60 K for thermal shields, and 120 l/h for current leads, as listed in Table 2. The total refrigeration capacity at 4.5 K is approximately 1.5 kW.

References

1) Y. Yano et al.: RIKEN Accel. Prog. Rep. **34**, 301 (2001).
2) H. Okuno et al.: RIKEN Accel. Prog. Rep. **34**, 339 (2001).

New Liquid Helium Supply and Recovery System

K. Ikegami, M. Ohtake, and Y. Yano

The refrigerator having a maximum capacity of 50 l/h was installed in the RIKEN main building located in the center of RIKEN before ten years ago and is operated to supply liquid helium for the researchers. With year, the refrigerator often was broken down, and had to be repaired it. It's capacity gradually became lower 40 l/h on an average. On the contrary, as researchers using a liquid helium increased with year, it was difficult to supply liquid helium of more than 30000 l per a year by using this old refrigerator to them.

A new liquid helium supply and recover system to supply liquid helium for RIKEN's whole researchers was renovated at the last year. The building for the system is completed at the end of November in this year. The system will be installed in the building after completing at the end of next March. Operation of the system will be started at the beginning of next April.

The system has the maximum capacity of 200 l/h to supply liquid helium consists of pure gas helium cadres, a buffer tank of 15 m^3, a valve stand, a compressor of 355 kW, an oil remover, a liquid nitrogen tank of 11 m^3, an refrigerator of a type of TCF-50 made by LINDE, a liquid helium vessel of 7 m^3, impure gas cadres, a gas dryer and purification device, and a recovery system as shown in Fig. 1. Gas helium from pure gas cadres is introduced to the compressor, compressed, introduced to the refrigerator, and liquefied. Liquid helium made by the refrigerator is saved in the helium vessel and will be supplied to the researchers.

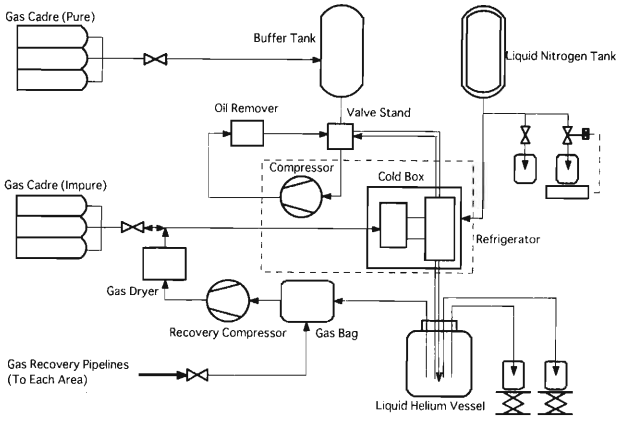

Fig. 1. A block diagram of the liquid helium supply and recovery system.

Table 1. The liquid helium supply and recovery system.

Name	Capacity and size	Type and pressure
Refrigerator	200 ℓ/h at 4.5 K	TCF-50
Circulation compressor	355 KW	1.7 MPa
Gas cadre (pure)	630 m³	14.7 MPa
Gas cadre (impure)	1800 m³	14.7 MPa
Liquid nitrogen tank	11 m³	0.93 MPa
Buffer tank	15 m³	0.93 MPa
Gas dryer	130 Nm³/h	14.7 MPa
Liquid helium vessel	7 m³	0.2013 MPa
Recovery gas bag	120 m³	50 mmAq
Recovery compressor	130 Nm³/h	14.7 MPa
Recovery gas holder	20 m³	50 mmAq
Recovery blower	80 Nm³/h	50 mmAq

The recovery system consists of a recovery compressor of 130 Nm^3/h, a gas bag of 100 m^3, and three recovery stations whose each station has one gas holder of 20 m^3 and one blower. One recovery station is placed near the new building located in south side of RIKEN. The second recovery station connected to the system through a recovery pipe of length of 500 m, is put in RIKEN main building. The third recovery station connected to the second recovery station through a recovery pipe of length of 400 m is put in behind of the east brain building located in east side RIKEN. The RARF (RIKEN accelerator facility) is connected to the third staion through a recovery pipe whose length of 150 m. The recovered gas from each station is saved in the gas bag first. After compressing saved gases to 15 MPa by the recovery compressor, one part of the gas is saved in impure gas cadres through a dryer. Another part of compressed gas after passing dryer, is purified, introduced to the refrigerator and liquefied again. Each capacity of the system is listed in Table 1.

The system and all recovery stations can be operated automatically from the controller using the computer installed the system side.

This system will be used to test as a superconducting bending magnet for the superconducting ring cyclotron (SRC) and the superconducting triplet quadruple magnet for the big projectile fragment separator (BIGRIPS).

Prototype of Superferric Quadrupole Magnets for the BigRIPS Separator (I)

H. Kouzu,[*1] T. Kubo, T. Tominaka,[*2] K. Kusaka, M. Okamura, Y. Yano, O. Ohsaki,[*1] T. Tsuchihashi,[*1] and T. Hirumachi[*1]

In the RIKEN RI-beam factory project, radioactive isotope (RI) beams are to be produced using projectile fragment separators called BigRIPS. Superferric quadrupole magnets (iron-dominated superconducting quadrupole) are to be used for the BigRIPS separators in order to efficiently produce RI beams. A prototype consisting of a superferric quadrupole triplet has been fabricated for R&D studies on the basis of the design reported in Refs. 1 and 2. In this report, we outline the prototype and describe the results of testing.

The prototype quadrupole triplet is installed in a single cryostat. Cross-sectional views are shown in Figs. 1 and 2. The iron yokes and superconducting coils installed in a helium vessel are cooled by the liquid-He bath cooling method. The three quadrupoles are connected rigidly to each other by stainless steel bars. The helium vessel is supported from the vacuum vessel of the cryostat by six axial and eight radial supports that are made of glass-fiber-reinforced plastic (GFRP) or carbon-fiber-reinforced plastic (CFRP). The lengths of the radial supports can be adjusted from the outside of the vacuum vessel in order to align the quadrupoles with respect to the beam axis. An 80 K shield with a cooling pipe surrounds the helium vessel, and is cooled with liquid-N_2. The 80 K shield is supported from the vacuum vessel and the helium vessel.

Three quadrupoles have an identical cross section. Their pole-tip radius and warm bore radius are 170 mm and 140 mm, respectively. The nominal effective lengths of the quadrupoles are 500 (Q500), 800 (Q800), and 500 (Q500) cm, respectively. The maximum pole-tip fields are 2.4 T, corresponding to the field gradient of 14.1 T/m. The main parameters of the quadrupoles

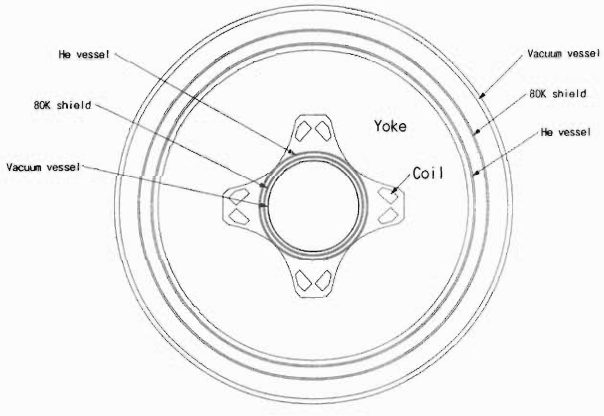

Fig. 2. Cross-sectional view perpendicular to the beam axis.

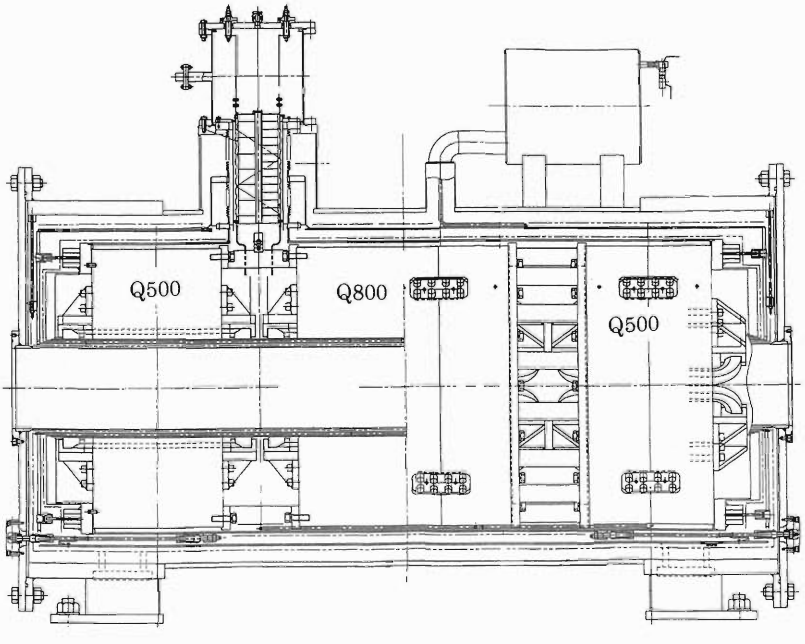

Fig. 1. Cross-sectional view parallel to the beam axis.

*1 Toshiba Corporation
*2 Hitachi Ltd.

Table 1. Main parameters of the quadrupoles.

	Q500(*1)	Q800(*2)
Effective magnetic length (m)	~0.54	~0.84
Pole tip radius (mm)	170	170
Warm clear bore radius (mm)	140	140
Field gradient (T/m)	14.1	14.1
Winding of coil	orderly	orderly
Nominal current per pole (kA)	199	190
Nominal current (A)	142	136
Nominal turn number	1403	1403
Nominal current density (A/mm^2)	115	110
Cross section of coil (mm^2)	1730	1730
Straight length of coil (mm)	440	740
Total length of coil (mm)	640	940
Length of iron (mm)	440	740
Outer radius of yoke (mm)	480	480

(*1) The quadrupole whose design effective length is 500 cm.

(*2) The quadrupole whose design effective length is 800 cm.

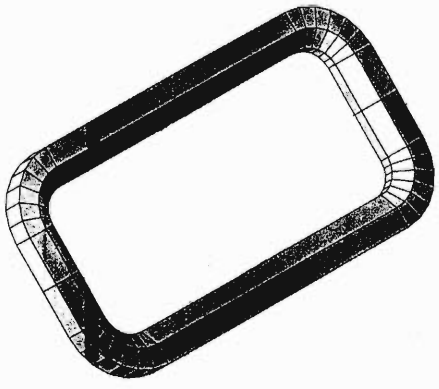

Fig. 3. Schematic view of the superconducting coil.

Table 2. Main parameters of the superconducting wire.

Insulated diameter(mm)	1.15
Bore diameter(mm)	1.10
Cu/super ratio	6.6
RRR of Cu	100-105
Filament diameter(μm)	75

are listed in Table 1.

The superconducting quadrupole coils are of the racetrack type which was described in our previous reports.[1,2] This type allows ordered coil winding. A cross-sectional view and a schematic view of the coil are shown in Figs. 2 and 3, respectively. We used a NbTi superconducting wire whose specifications are summarized in Table 2. The specifications are determined based on the quench protection analysis described in Refs. 1 and 2. Each coil that consists of 53 layers was wound orderly on a mandrel by wet winding method. Epoxy was applied to the coils layer-by-layer during the winding. The epoxy contains fillers so that its thermal contraction rate is similar to that of the superconducting wire. During the winding, the coil was pressurized twice by a plate and the glass tapes that were impregnated with the resin were inserted several times in order to adjust the coil height. The coils were cured at 100°C in an oven after the winding. The design values of the coil height and the coil width are 55.8 mm and 35.8 mm, respectively. Twelve coils in all were wound for the quadrupole triplet (4 coils × 3 quadrupoles). We measured the size of all the coils. The coil height deviation was 0.5 mm except for the first coil, which was 0.9 mm. The width deviation was measured to be within 0.5 mm. Magnetic field calculations reveal that the deviations are within allowable values.

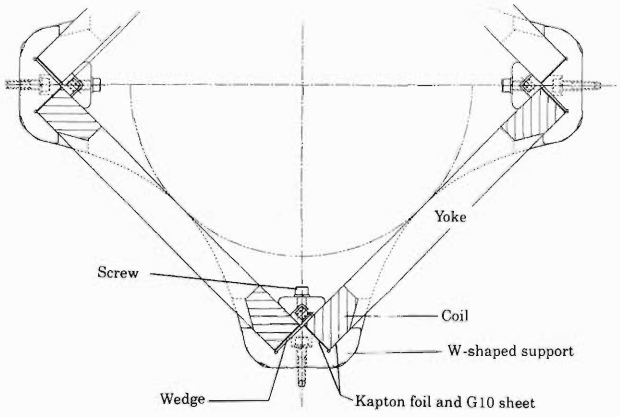

Fig. 4. Coil support.

The coils are supported by the iron yoke, as shown in Fig. 4. A stainless steel bar which we call a 'w-shaped' support is used to support the coils against electromagnetic force. This w-shaped support is placed between the yoke and the coils, being continuous for the length of the yoke. The coils are pushed against the w-shaped support by tightening screws, as shown in Fig. 4. The shimming arrangement is also shown in Fig. 4. The shim between the coil and the w-shaped support is a wedge shaped stainless steel piece, which provides a self-tightening effect when the coils shrink due to cooling. The Kapton foil and the G10 sheet provide electrical insulation. The shim of the copper sheets was also used to adjust the position of the coils.

In order to verify that three quadrupoles were properly fabricated, we tested each quadrupole using a liquid-He open dewar. We measured the field gradients, performed a quench protection test, and observed acoustic emissions. Table 2 summarizes the test results.

The three quadrupoles were successfully excited without quenching up to 163 A, which is about 120% of the maximum operation current. The field gradients were measured by a Hall probe installed in the pole gap. Excitation curves were found to match well with calculations.

Table 3. Dewar test results.

	Q500 A	Q800	Q500 B
Maximum field gradient(T/m)	15.2	15.6	15.3
Maximum current(A)	163	163	163
Maximum excitation rate(A/s)	1	0.75	1
Quench	No	No	No
Detected Voltage in the quench test with heater (at 135A)	166	284	157
Stability judged from acoustic emission	Stable	Stable	Stable

The quench protection test was performed at 136 A, corresponding to the maximum operation current, using heaters attached to the coils. A quench was artificially generated by turning on the heaters at 3 W for a few seconds. We measured the coil voltage generated by quenching and compared it with the prediction by the quench analysis.[2] The coils were designed to be self-protected against quench, so that they can survive without an external resistor. The quench analysis without the external resistor[2] revealed that the generated coil voltage of the Q800 reaches 670 V, which is far below our design criterion, 1 kV.[2] In the case of the Q500, a lower voltage is produced because it has a smaller inductance. However, in the test, an external resistor of 0.48 Ω was used due to the restrictions of the test facility. The measured voltages are listed in Table 3. In the case of the Q800, the coil voltage was measured to be 284 V, while the quench analysis with an external resistor predicts the voltage to be 310 V. This indicates that the quench analysis can well predict the voltage and hence the predicted voltage without the external resistor is reliable. It can be concluded that the coil is self-protected.

Mechanical stability of the coils was tested by observing the acoustic emissions produced by movement of the coil or superconducting wire. An event rate of the acoustic emission increased as the current increased during a virgin excitation. However, the event rate decreased as the current increased after the virgin excitation, which indicates that the coils became stable.

We performed a cooling test and an excitation test after the quadrupoles were assembled and installed in the cryostat. The consumption rate of the liquid-He was measured to be 3.1 l/h when the magnet was not excited, while the consumption rate of the liquid-He was measured to be 4.1 l/h when the magnet was excited at 146 A. These consumption rates are almost the same as those of the design values. Each quadrupole was excited up to 165 A without quenching. Field gradients were measured by a Hall probe installed in the pole gap. Excitation curves were found to match the calculations well, as shown in Fig. 5. Figure 6 shows the inductance derived from the measured current and voltage. The inductance decreases as the current increases due to saturation.

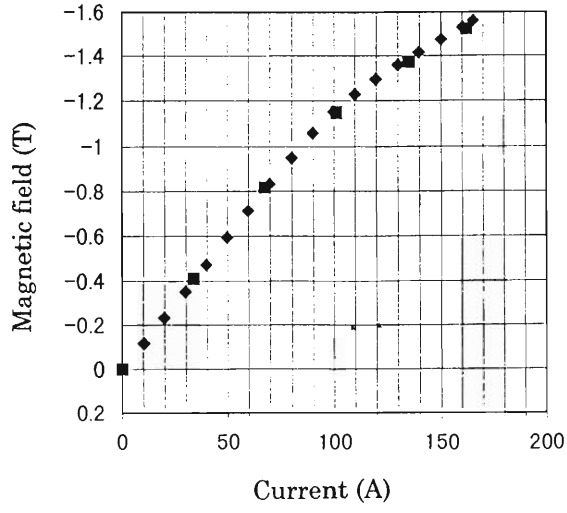

Magnetic field By at $x = 100$ mm, $y = 0$, and $z = 0$.
◆ indicates measured magnetic fields.
■ indicates calculated magnetic fields.

Fig. 5. Excitation curve of the Q800.

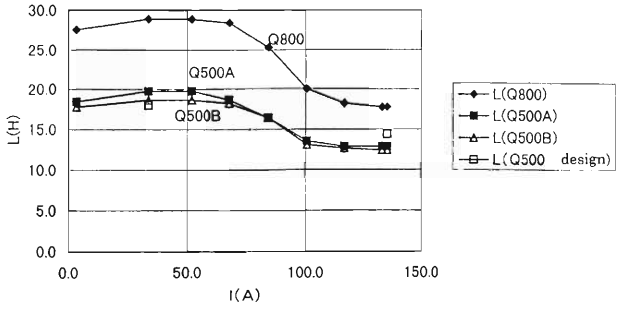

Fig. 6. Inductance vs. excitation current.

The prototype of the superferric quadrupole magnet has been successfully fabricated. As the next step, a precise field-map measurement will be performed in the near future.

References

1) T. Kubo et al.: RIKEN Accel. Prog. Rep. **33**, 238 (2000).
2) T. Hirumachi et al.: IEEE Trans. Appl. Supercond. **10**, 238 (2000).

Prototype of Superferric Quadrupole Magnets for the BigRIPS Separator (II)

T. Tominaka,[*1] T. Kubo, H. Kouzu,[*2] K. Kusaka, M. Okamura, Y. Yano, T. Senba,[*1] and S. Suzuki[*1]

A superferric quadrupole with superconducting sextupole and octupole coils has been constructed as a prototype for the projectile fragment separator named BigRIPS.[1] In our previous report, we designed two types of superferric quadrupole called Type A and Type B.[2,3] The fabrication of the quadrupole in the present report is based on the design of Type B. The fabrication of Type A quadrupoles is described elsewhere.[4] In this report, the design and construction of Type B superferric quadrupole magnet with superconducting sextupole and octupole coils are described, together with the experimental results.

The original design of these quadrupole, sextupole and octupole coils, which have been developed as the superferric quadrupole magnet system at NSCL/MSU[5] was based on results of a two-dimensional magnetic field calculation performed mainly with OPERA-2d, and those of a three-dimensional magnetic field calculation performed with TOSCA/OPERA-3d.[6] The main parameters for one Type B superferric quadrupole magnet system are listed in Table 1. The mechanical parameters are also listed in Table 2. The cross section and schematic view of the prototype quadrupole magnet are shown in Figs. 1 and 2.

In order to reduce the 12-pole component (b6) due to the end effect of the iron pole, a chamfer is adopted. The reduction of the 12-pole component results in a better uniformity of the gradient field. With the chamfer, the uniformity of the field gradient is greatly improved in the low-excitation region, but the uniformity

Table 1. Main parameters of prototype quadrupole (Q), sextupole (S) and octupole (O) coils.

Coil	Q	S	O
Field intensity	14.1 (T/m)	15 (T/m^2)	40 (T/m^3)
Nominal current per pole (kA)	253	28.2	10.1
Nominal current (A)	158	48.6	48.1
Turn number	1600	580	210
Nominal current density (A/mm^2)	115	84	86
Peak field on conductor (T)	3.8	2.9	2.9
Cross section of coil (mm^2)	2209	335	118
Shape of cross section Opening angle (pole angle) & thickness [for shell]	rectangular 47 mm × 47 mm	shell 59(21) deg × 6.5 mm	shell 44(16) deg × 3.0 mm
Inner radius (mm)	-	152.0	159.5
Outer radius (mm)	-	158.5	162.5
Straight length of coil (mm)	450	445	465
Total length of coil (mm)	≈630	≈600	≈600
Nominal effective length (mm)	500	500	500
Inductance (H)	≈ 27	1.3	0.38
Winding of coil	Semi-orderly	random	random

Table 2. Mechanical parameters of prototype quadrupole magnet.

Inner tube for correction coils	SUS316L
Inner diameter (mm)	144
Outer diameter (mm)	151
Outer tube for correction coils	SUS316
Inner diameter (mm)	163
Outer diameter (mm)	166
Pole tip radius (mm)	170
Iron yoke	
Inner diameter (mm)	295
Outer diameter (mm)	480
Length of iron yoke (mm)	450

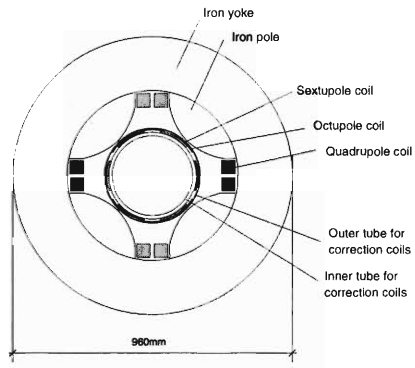

Fig. 1. Cross section of prototype superferric quadrupole magnet (B).

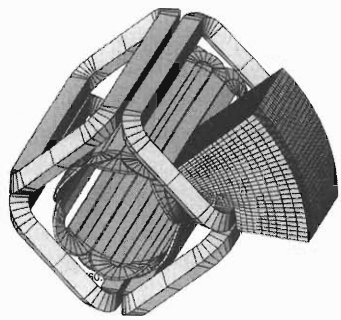

Fig. 2. Schematic view of prototype quadrupole magnet (B), together with sextuple and octupole coils (graphical output of calculational model for TOSCA).

*1 Hitachi, Ltd.
*2 Toshiba Corporation

is a slightly deteriorated in the high-excitation region. We think that the uniformity is improved over the entire excitation region with the chamfer. A comparison between with and without chamfer is also given in Table 3.

All flat quadrupole coils are wet wound with Stycast 2850 FT epoxy and Catalyst 11 in a winding form with a V-shaped groove. As the cross section of the quadrupole coils is diamond-shaped, the latter half of winding is not carried out in a winding form. After the R&D of winding, the coil is cut to observe the cross section. It is observed that the winding of the initial half is a slightly more dense than that of the latter half. After winding, the two outer surface planes are pressed with a jig for the trimming treatment of the cross-sectional shape. The coils are then oven cured. The surfaces of the coils are finally treated with Stycast 2850 FT epoxy and Catalyst 9. A set of four coils is then assembled around the pole tips. The coils are shimmed in place with SUS and GFRP spacers. All sextupole and octupole thin coils are also wet wound in a racetrack shape with Stycast 2850 FT epoxy and Catalyst 11 in a flat winding form. The sextupole and octupole coils are then deformed into a saddle shape and oven cured. Finally, the sextupole and octupole coils are assembled on the tube of SUS316L (designed as the inner tube of a helium vessel), together with the insulating plate of GFRP and then rigidly fixed to the outer SUS tube and the key connecting the inner and outer tubes to sustain a large electromagnetic force. The parameters of the superconducting wires are summarized in Table 4.

In order to verify the magnet performance, the prototype magnet has been tested in an open vertically oriented helium vessel up to 120% of nominal operation current. One quench for the quadrupole coil at 119% of nominal operation current and one quench for the sextupole coil at 120% of nominal operation current on the excitation of the octupole coil were observed. For the rough measurement of the magnetic field produced due to the quadrupole, sextupole and octupole coils, seven Hall probes were installed in the middle plane vertical to the magnet (or beam) axis. As a result, an agreement between the measured and calculated results has been obtained, as shown in Fig. 3. In Fig. 3, the measured results are indicated by stars, and the calculated results by diamonds. In order to measure the strain of the supporting tube sextupole and octupole coils due to the electromagnetic force, four strain gauges were installed on the inner supporting tube. As a result, it was confirmed that the measured azimuthal strain (1.7×10^{-4}) roughly agrees with the calculated value (1.3×10^{-4}).

The superferric quadrupole magnet with correction coils which produces field intensities of 14.1 T/m, 15 T/m^2, and 40 T/m^3, over a 120-mm radius with uniformity of approximately 0.5%, have been constructed and successfully tested with the confirmation of their magnet performance.

Table 3. Comparison between with and without chamfer.

Type	With chamfer	Without chamfer
Chamfer Axial and radial lengths (mm)	19 × 30	-
Field gradient (T/m)	4.0 – 14.1	4.0 – 14.1
Current per pole (kA)	46.1 – 253	46.1 – 253
Effective length (m)	0.544 – 0.513	0.555 – 0.515
b_6 ($\times 10^{-4}$)	-23.5 – 40.8	-43.2 – 35.9
b_{10} ($\times 10^{-4}$)	-2.0 – 2.6	-1.4 – 2.5

Table 4. Main parameters of superconducting wire for prototype quadrupole (Q), sextupole (S) and octupole (O) coils.

Coil	Q	S and O
Insulated diameter (mmϕ)	1.15	0.71
Bare diameter (mmϕ)	1.10	0.648
Cu/super Ratio	6.6	4.0
RRR of Cu	100 – 150	100 – 150
Filament diameter (μmϕ)	75	45
Number of filament	28	42
Insulator	Formvar	Formvar
I_c (A)	415 @4T, 4.2K	250 @3T, 4.2K

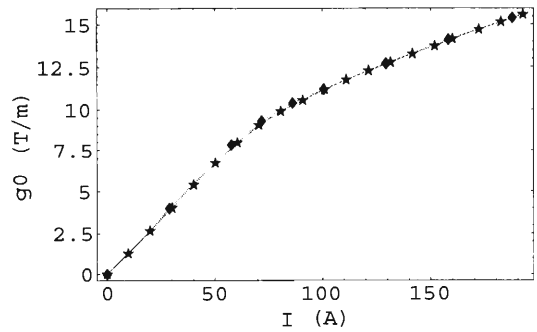

Fig. 3. Comparison between measured and calculated excitation curves of field gradients.

References

1) T. Kubo et al.: RIKEN Accel. Prog. Rep. **33**, 236 (2000).
2) T. Kubo et al.: RIKEN Accel. Prog. Rep. **33**, 238 (2000).
3) T. Hirumachi et al.: IEEE Trans. Appl. Supercond. **10**, 236 (2000).
4) H. Kouzu et al.: RIKEN Accel. Prog. Rep. **34**, 350 (2001).
5) A. F. Zeller et al.: IEEE Trans. Appl. Supercond. **9**, 693 (1999).
6) OPERA-2d and OPERA-3d/TOSCA, Vector Field, Ltd., Oxford, UK.

Pulsing Magnet Power Supply for the RIKEN RI-Beam Factory Project

H. Kouzu,* T. Kubo, K. Kusaka, Y. Yano, Y. Chiba, C. Yamazaki,* and T. Saito*

In the RIKEN RI-beam factory project,[1] radioactive isotope (RI) beams will be produced using projectile fragment separators called BigRIPS. Two BigRIPS separators will be constructed, so that two different RI-beam experiments can be conducted at the same time. These two BigRIPS separators will share primary beams from the SRC cyclotron by means of time sharing. A pulsing dipole magnet will be installed in the beam line from the SRC cyclotron to the BigRIPS production targets. The primary beams will be transported to one line when the pulsing dipole magnet is excited. On the other hand, they will be transported to another line when the pulsing dipole magnet is not excited. A power supply for the pulsing dipole magnet has been designed and fabricated. In this report, we describe the design and the test results of the pulsing dipole magnet power supply.

As regards the type of pulsing dipole magnet, we choose a c-type dipole magnet with a bending radius of 5.5 m and a bending angle of 20 degrees. The field strength is 1.41 T and the pole gap is 60 mm. The main parameters of the pulsing dipole magnet are listed in Table 1. The pulsing magnet is large compared with ordinary pulsing magnets.

The pulsing magnet will be operated in both pulse and DC modes. In the case of the pulse mode, both flat-top period and flat-base period are 450 ms or longer. Its operation pattern is shown in Fig. 1. The output current is 0 A during the flat-base period. Both flat-top and flat-base periods can be changed depending on the requirement of the experiments. Furthermore, the ratio of these two periods can be changed as well.

Table 1. Parameters of the pulsing magnet.

Magnetic rigidity	7.52Tm
Bending radius	5.5m
Bending angle	20degree
Dipole field strength	1.41T
Pole gap	60mm
Turn number per pole	24
Hollow conductor size	13.5mm×13.5mm-ϕ8mm
Nominal current	1445A
Resistance	33.3mΩ
Inductance	25.9mH
Good field region	±50mm
Magnetic field uniformity	Better than 4×10^{-4}
Weight	6.3t

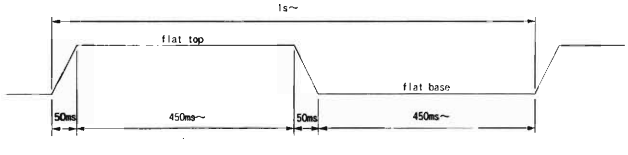

Fig. 1. Operation pattern of the pulsing mode.

The switching time should be as short as possible since primary beams cannot be delivered to the BigRIPS during this period. We aimed at a switching time shorter than 50 ms. Current accuracy, such as ripples, long-time stability, and reproducibility, is required to be better than 1×10^{-4} p-p for both flat-top and flat-base periods. The current accuracy for the flat-base period is defined in terms of the flat-top current. This current accuracy must be achieved within 50 ms.

The pulsing magnet power supply consists of two circuits: one is a forcing circuit and the other is the main circuit. These two circuits are connected in series. A schematic block diagram of the circuit is shown in Fig. 2. The forcing circuit provides the pulsing magnet with a high voltage in order to quickly raise the current from the flat-base to the flat-top. On the other hand, the main circuit controls the current accurately by using a transistor dropper. This current control begins to work when the current almost reaches the flat-top. In the case of the DC mode, only the main circuit is operated. The main parameters of the pulsing magnet power supply are listed in Table 2.

The operating sequence of the pulse mode is as follows:

Sequence 1: Two gate turn off thyristors (G1, G2) in the forcing circuit and a transistor dropper (Tr) in the main circuit are turned on. The current rises quickly due to the high voltage produced by an electric charge stored in a condenser (C1) in the forcing circuit.

Sequence 2: G2 is turned off and Tr in the main circuit starts controlling the current just before the current

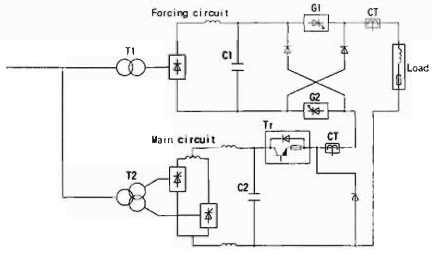

T1, T2: Transformer
C1, C2: Condenser
G1, G2: Gate turn off thyrister
Tr: Transistor dropper
CT: Current transformer

Fig. 2. Schematic block diagram of the pulsing magnet power supply.

* Toshiba Corporation

Table 2. Parameters of the pulsing magnet power supply.

Maximum output current	1600A
Maximum output voltage	2170V
Load resistance	33.3mΩ
Load inductance	25.9mH
Ripple	$\leqq 1\times10^{-4}$p-p(*1)
Reproducibility	$\leqq 1\times10^{-4}$p-p(*1)
Stability	$\leqq 1\times10^{-4}$p-p(*1)
Operation mode	Pulse/DC
Rising switching time	≦50ms
Descending switching time	≦50ms
Flat top time	≧450ms
Repetition period	≧1s

(*1)Ranging from 50% of maximum current to 100%.

reaches the flat-top current.
Sequence 3: The current is accurately controlled by Tr during the flat-top period.
Sequence 4: G1 and Tr are turned off. Energy stored in the pulsing magnet recovers to C1 and the current decreases towards the flat-base. The power supply is switched off and the output current is not controlled during the flat-base period.

The maximum output current and voltage are chosen to be 1600 A and 2170 V, based on the design of the circuit and the pulsing dipole magnet. The maximum current is chosen to be 10% larger than the magnet current listed in Table 1, because the design of the pulsing magnet has not been finalized.

In designing the power supply, we have made circuit simulation by using the code EMTDC,[2] in order to find the conditions that achieve the required current accuracy within 50 ms. It is found that the output current must rise as fast as 20 ms, and current control by the transistor dropper must begin when the output current reaches about 98% of the flat-top current. This is because it takes time to damp current fluctuation. The output voltage is determined based on the simulation results.

We fabricated the power supply, and performed a test operation by using a test load in order to measure switching time and current accuracy. The inductance and the resistance of the test load are 5.6 mH and 10.5 mΩ, respectively. Voltage in the test is lower than that in the case of using the pulsing magnet because the inductance of the test load is lower than that of the pulsing magnet. The output voltage is about 800 V.

The operation test was performed at 1600 A and 800 A, respectively. The test results are summarized in Table 3. In order to optimize the rising switching time, the timing of sequence 2 is adjusted during the measurement. An example of observed output currents is shown in Fig. 3 for the case of rising. The rising switching time at 1600 A and 800 A are measured to be 35 ms and 44 ms, respectively. The rising switching time of 800 A is longer than that of 1600 A, because the turn-off time of G2 is optimized for 1600 A. An example of observed output currents is shown in Fig. 4 for the case of descending. The descending switching time at 1600 A and 800 A is measured to be 17 ms and

Table 3. Test results.

Ripple(@1600A)	2.9×10^{-5}p-p
Ripple(@800A)	5.1×10^{-5}p-p
Stability(@1600A)	1.0×10^{-4}p-p
Stability(@800A)	1.0×10^{-4}p-p
Reproducibility(1600A)	0.45×10^{-4}p-p
Reproducibility(800A)	0.33×10^{-4}p-p
Rising time(@1600A)	35ms
Rising time(@800A)	44ms
Descending time(@1600A)	17ms
Descending time(@800A)	11ms

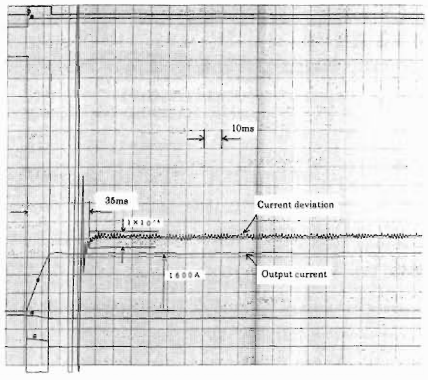

Fig. 3. Example of observed currents for the case of rising.

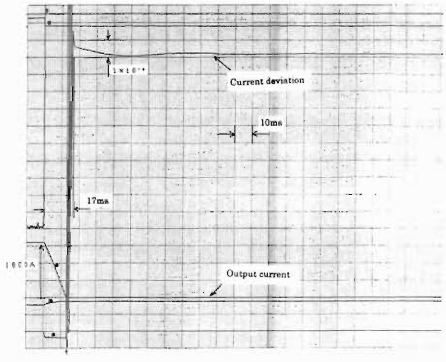

Fig. 4. Example of observed currents for the case of descending.

11 ms, respectively. These values well achieve the requirement. Long-time stability and reproducibility are well achieved.

It is expected that the similar results will be obtained when the actual pulsing magnet is used as the load, although some adjustments are needed.

The specifications required for the pulsing magnet power supply have been achieved. The power supply will be tested again in the combination with the pulsing magnet to be fabricated in a few years.

References

1) Y. Yano et al.: Proc. 15th Int. Conf. on Cyclotrons and Their Applications, Caen, France, (1998) p.696.
2) EMTDC, Manitoba HVDC Research Centre, Canada.

New Lattice Design of ACR for MUSES

K. Ohtomo,* T. Tanabe, N. Inabe, M. Wakasugi, and T. Katayama

The Accumulator Cooler Ring (ACR)[1] is newly designed to study the accumulation and cooling of RI beams for Multi-USe Experimental Storage rings (MUSES). RI beams with large momentum spreads and emittances, after passing through a fragment projectile separator (Muses-RIPS), should be manipulated before injecting them into the ACR. The longitudinal momentum spread of $dp/p = \pm 0.5\%$ is reduced to $\pm 0.15\%$ by debuncher cavities[2] located 80 m downstream from the M-RIPS. The transversely horizontal emittance is expected to become large due to a degrader in the M-RIPS.[3] Solenoids or skew quadrupoles should be installed in the injection beam line to transfer emittance from the horizontal plane to the vertical one. A rapid repetitive cycle of multiturn injection and RF stacking is required to build up a RI beam current. The cooling time required in electron cooling (EC) and stochastic cooling (SC) should be approximately as small as the RF stacking time, which is a 50–100 msec period. The lattice of the ACR should be designed to fulfill the following conditions which are important for rapid cooling and effective accumulation.

(1) A large acceptance in the horizontal plane ($A_x = 125\pi$ mm mrad), in the vertical plane ($A_y = 40\pi$ mm mrad) and a large momentum spread acceptance ($\Delta p/p = \pm 1.0\%$).

(2) A long dispersion-free space (10 m long) with small β_x function (less than 5 m) for the EC.

(3) A pair of dispersion-free spaces (6 m long) for the SC pickup and the SC kicker. The betatron phase advance $\Delta\mu^{pk}$ between them should be $k\pi/2$ (k: odd integer) and the local transition γ_{tr}^{pk} should be nearly the same as relativistic γ for efficient cooling.[4] Here, γ_{tr}^{pk} is defined as

$$\frac{1}{\gamma_{tr}^{pk\,2}} = \alpha^{pk} = \frac{1}{\Delta L}\int_{SCpickup}^{SCkicker} \frac{D_x}{\rho} ds,$$

where α^{pk} is a local momentum compaction factor, ΔL the distance from the SC pickup to the SC kicker, D_x the horizontal dispersion, and ρ the curvature of the orbit.

(4) A space with certain dispersion (3 m long) for multiturn injection. A pair of spaces, where the beta-

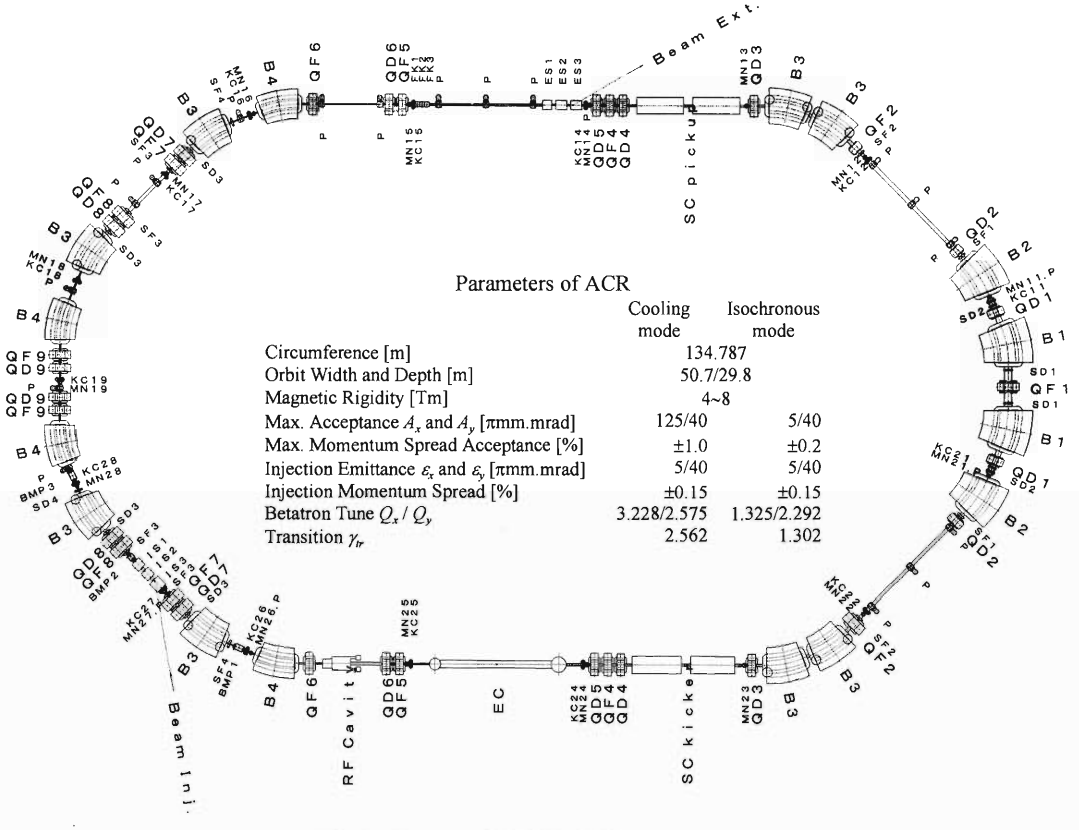

Fig. 1. Layout of ACR with parameters.

* Sumitomo Heavy Industries, Ltd.

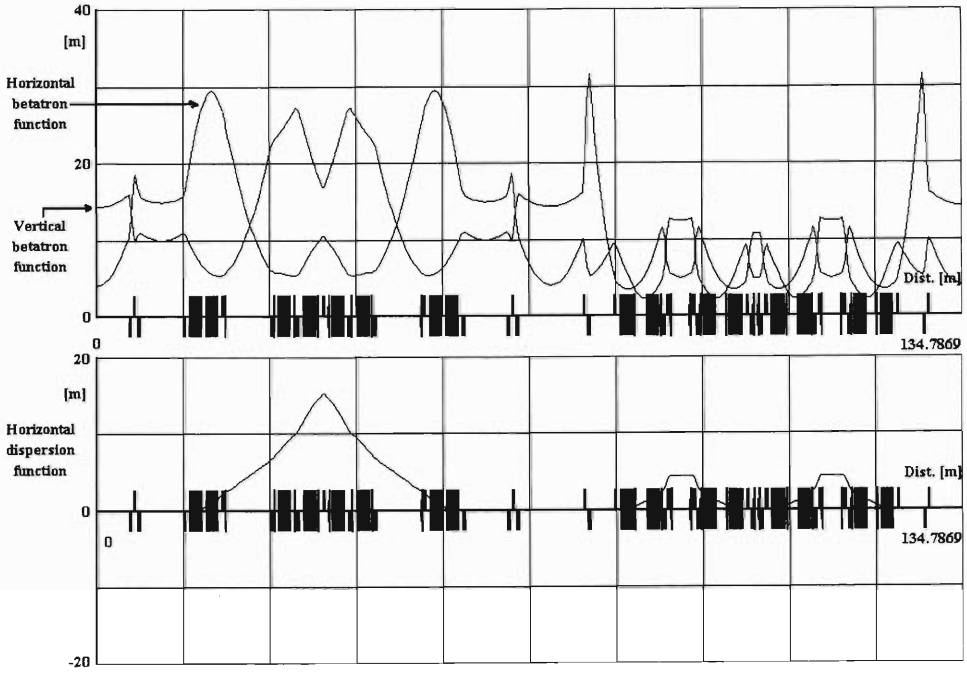

Fig. 2. Twiss functions.

tron phase advance is nearly π between them, is also required for the installation of bump magnets.

(5) A dispersion-free space (3 m long) for a tunable RF stacking cavity.

According to the above requirements, the ACR lattice has been designed using MAD[5] and WinAGILE.[6] The resultant layout with parameters and Twiss functions is shown in Figs. 1 and 2.

The ACR consists of two types of lattice arcs which are connected in long straight sections. One lattice, called A-arc, has large dispersion to satisfy condition (3) mentioned above. Another lattice, B-arc, has relatively small dispersion to satisfy condition (4) and to adjust betatron tunes of the total ACR.

The A-arc is described as follows:

$$\text{A-arc} = \text{SC–QD3–B–B–QF2–QD2–B–QD1–B–QF1–B–QD1–B–QD2–QF2–B–B–QD3–SC},$$

where QF1,2 and QD1,2 are focusing and defocusing quadrupoles, respectively, and B is a bending magnet. The dispersion function increases along the bending arc and reaches the maximum of 15.3 m at QF1. The total arc functions as a dispersion suppressor. From the SC kicker to the SC pickup, $\Delta\mu_x^{pk}$ and $\Delta\mu_y^{pk}$ are $3\pi/2$ and γ_{tr}^{pk} is 1.688.

The B-arc is described as follows:

$$\text{B-arc} = \text{B–B–QD7–QF7–INJ–QF8–QD8–B–B–QF9–QD9–(symm.)–QD9–QF9–B–B–QD8–QF8–QF7–QD7–B–B},$$

where QF7,8,9 and QD7,8,9 are focusing and defocusing quadrupoles, respectively, and INJ the injection point. The B-arc is a two-folded structure and each half-arc is a dispersion suppressor. The injection point is located at the first arc where the dispersion has a maximum of 4.38 m in the B-arc. Also, the tune of the B-arc is adjusted so that the total horizontal betatron tune Q_x becomes 3.228, nearly $k/4$ (k: odd integer), to obtain good efficiency by multiturn injection, and the total vertical betatron tune Q_y becomes 2.575, far from the strong resonance lines.

The connection section is described as follows:

$$\text{STR} = \text{QD4–QF4–QD5–(EC or EXT)–QF5–QD6–RF–QF6},$$

where QF4,5,6 and QD4,5,6 are focusing and defocusing quadrupoles, respectively, RF the RF cavity, and EXT the extraction. The horizontal and vertical betatron functions at the center of EC are 4.03 m and 14.34 m, respectively, enabling the electron flow of the EC to cover RI beams with large emittance.

The total ACR is described as follows:

$$\text{ACR} = \text{A-arc–STR(EC)–B-arc–STR(EXT)}.$$

The large-momentum spread operation requires sextupole magnet correction. However, an excessive sextupole correction results in a reduction of the dynamic aperture. The dynamic aperture with bare lattice and sextupole correction was determined and it was verified to be several times as large as the designed value of acceptance. Also, 20000 turn tracking has been performed with particles having dp/p of $\pm 1\%$ and bound-

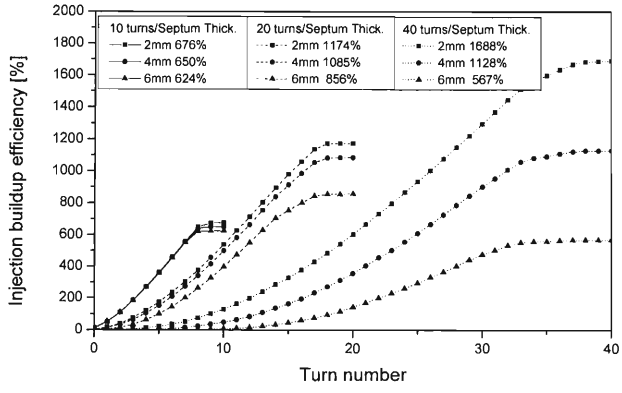

Fig. 3. Multiturn injection efficiency with various parameters. Bump fields decay linearly. Injection beam emittance is 5π mm mrad, ACR acceptance is 125π mm mrad, injection beam momentum displacement is +1%, and injection beam momentum spread is ±0.15%.

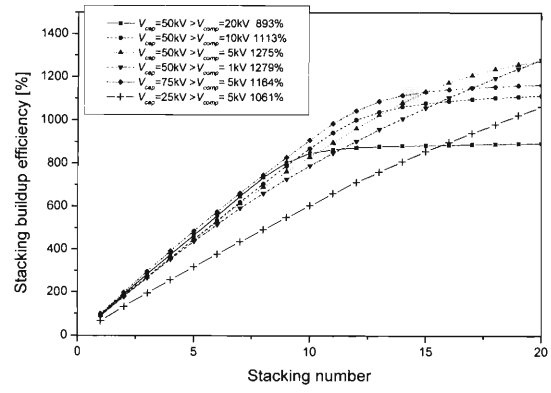

Fig. 4. RF stacking efficiency with various RF voltages. V_{cap} is the initial RF voltage at the capturing process, whereas V_{comp} is the final RF voltage at the compressing process by RF buckets.

ary emittances ϵ_x/ϵ_y of $150/48\pi$ mm mrad; all particles have survived.

Multiturn injection efficiency was determined with fixed parameters, which are the injection beam emittance and acceptance in Fig. 1, and optimized parameters, which are the turn number of multiturn, thickness of injection septum, and betatron function of injection beam line. It was proved that the total buildup efficiency reached about 1000%, as shown in Fig. 3.

The RF stacking process has been simulated in the same manner as the optimized parameters, which are the stack number of RF stacking, and the initial and final RF voltages. It was observed that the total buildup efficiency reached about 1000%, as shown in Fig. 4.

Currently, the cycle of multiturn injection, RF stacking, and cooling is expected to be 5–10 Hz and the total beam current might be built up 600–2000 times the injected beam at the ACR.

The isochronous mode operation in Fig. 1, which means that the ACR will be used as a mass spectrometer of RI beams, should be studied carefully in the future.

References

1) K. Ohtomo et al.: Proc. of European Particle Accelerator Conf. 2000, p.566 (2000).
2) K. Ohtomo and T. Katayama: RIKEN Accel. Prog. Rep. **31**, 225 (1997).
3) C. C. Yung: MUSES Meet. (2000).
4) M. Wakasugi et al.: Proc. of European Particle Accelerator Conf. 2000, p.1274 (2000).
5) H. Grote and F. C. Iselin: CERN/SL/90-13 Rev.5 (1996).
6) P. J. Bryant: Proc. of European Particle Accelerator Conf. 2000, p.1357 (2000).

Space-Charge-Dominated Ion Beams Cooled by Electron Cooling

M. Takanaka

At low energies, a high-current beam is led to betatron-tune shift, resonance trapping, emittance growth, and instability by a self-induced field. Electron cooling is a very effective method for decreasing longitudinal and transverse emittances of low-current beams. When ion beams are stored, electron-cooled, and stable in a ring, how large are the beam currents? In order to answer this question, we studied space-charge-dominated beams using beam-tracking simulation.

In the beam-tracking simulation, we took the following sources of force into account: (1) longitudinal monopole space-charge impedance, (2) transverse space-charge field, (3) transverse dipole broadband impedance based on the broadband impedance model, (4) electron-cooling force, (5) solenoid field of the electron-cooling section, (6) beam twist due to the toroid field at both ends of the electron-cooling section, (7) a constantly focusing section and the drift electron-cooling section of which the ring is assumed to consist, and (8) RF field for beam bunching.

Using 40,000 macroparticles, we simulated U_{238}^{92+} ion beams at 150 MeV/u. Table 1 shows the parameters of the ring and the electron cooling used for the simulation.

We present the simulation results of coasting U_{238}^{92+} ion beams of 33 mA and 330 mA and the results of a bunched beam of 33 mA. The beams initially had a Gaussian momentum distribution with a spread of 10^{-3} at sixfold rms, and transverse rms emittances of 10^{-6} m×rad and 2×10^{-6} m×rad for the beam currents of 33 mA and 330 mA, respectively.

Figure 1 shows the evolution of the coasting beam of 33 mA. The electron cooling is evidently more effective in decreasing the momentum spread than in decreasing the transverse emittances. The momentum spread reached an equilibrium at 13 ms. Figure 2 shows that the beam has a dense core at the center of the cross section. Part of the beam betatron oscillates with a betatron amplitude several times larger than the core. Ions in the core have their incoherent tunes shifted over 2 and are isolated from the rest. This indicates that even if part of the core beam is trapped into a resonance due to imperfection of the ring magnets, it escapes the resonance easily because a very small increase in the betatron amplitude causes a large tune shift, and that the electron cooling confines the beam transversely.

Since the core beam has a very small betatron amplitude, it is difficult to observe the tune of the core beam practically using monitors.

Figure 3 shows the evolution of the coasting beam of 330 mA. The electron cooling was not sufficient for the momentum spread and the transverse emittances to decrease. Figure 4 shows that there is no core structure due to the electron cooling evident from the transverse beam profile or the betatron-tune distribution.

Between 33 mA and 330 mA is a threshold of beam current at which beams are confined by the electron cooling.

Table 1. Parameters of the ring and the electron cooling.

Circumference $2\pi r$	134.8 m
Transition γ	2.562
Betatron tune (ν_x/ν_y)	3.228/2.575
Chromaticity (ξ_x/ξ_y)	0.0151/0.0001
Beta function (β_x/β_y)	$r/\nu_x/r/\nu_y$
Beta function at EC section center (β_x^*/β_y^*)	4.0/14.3 m
Inner radius of the chamber	4.0 cm
RF harmonics	16
Electron current	4. A
Section length	3.6 m
Electron beam radius	28.4 mm
Cathode temperature kT_c	0.1 eV
Solenoid field	2 kG
Expansion factor	20.

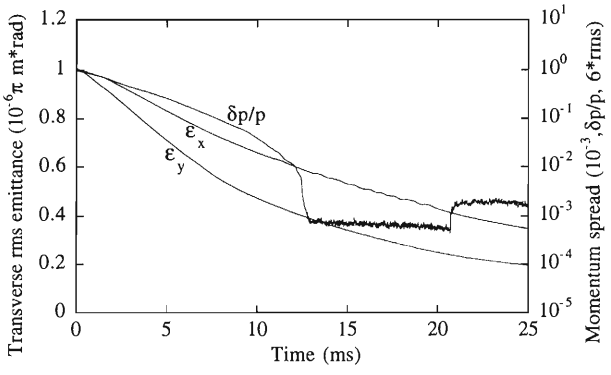

Fig. 1. Evolution of a coasting U_{238}^{92+} ion beam of 33 mA during electron cooling. The bandwidth of the longitudinal space-charge impedance changed from 13 GHz to 16 GHz at 21 ms.

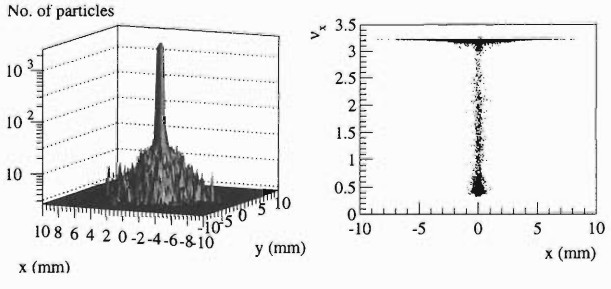

Fig. 2. Transverse beam profile and betatron-tune distribution of the coasting U_{238}^{92+} ion beam of 33 mA at 25 ms.

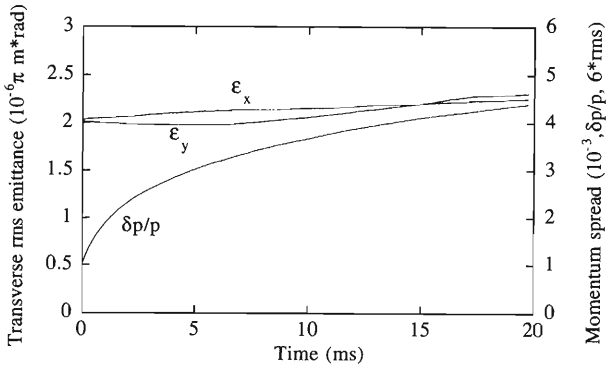

Fig. 3. Evolution of a coasting U_{238}^{92+} ion beam of 330 mA during electron cooling.

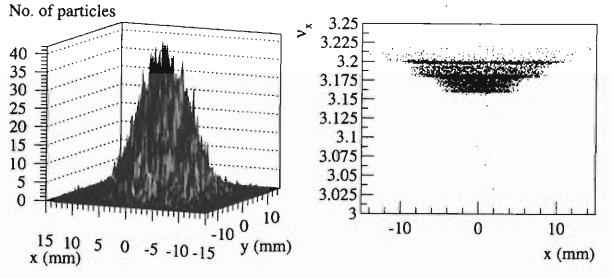

Fig. 4. Transverse beam profile and betatron-tune distribution of the coasting U_{238}^{92+} ion beam of 330 mA at 20 ms.

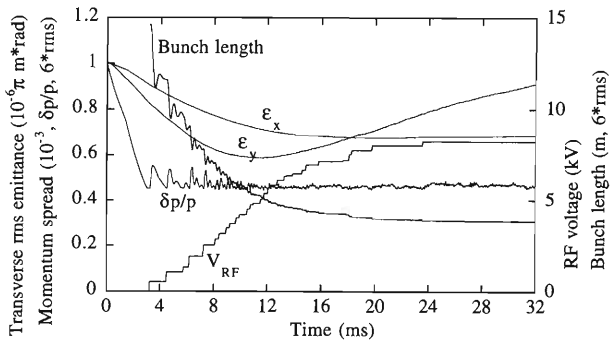

Fig. 5. Evolution of the bunching of a U_{238}^{92+} ion beam of 33 mA during electron cooling.

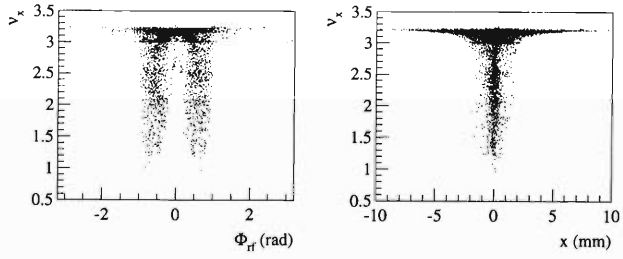

Fig. 6. Incoherent betatron-tune distribution of the bunched U_{238}^{92+} ion beam of 33 mA along the bunch at 20 ms.

After the coasting beam of 33 mA was cooled to a momentum spread of 4.5×10^{-4}, it was bunched using an RF system. During the bunching, the RF voltage increased in such a way that the momentum spread was maintained at 4.5×10^{-4}. Figure 5 shows the evolution of the bunching. After 25 ms, the momentum spread did not decrease, and the RF voltage was constant. In contrast, not only did the vertical emittance increase at 11 ms, but also the horizontal emittance slowly increased at 20 ms. Figure 6 shows that the bunched beam loses a dense core at the bunch center. The electron cooling became insufficient to confine the beam at the bunch center where the instantaneous beam current was 150 mA.

By a beam-tracking simulation of a space-charge dominated beam, we confirmed that the beam confined by the electron cooling contains a small, dense core or cores. The ions in the cores have their incoherent betatron tune shifted largely, for example, over 1 by the space-charge effects. We ensured that U_{238}^{92+} ion beams of 150 MeV/u can be confined to about 150 mA at the instantaneous beam current in the ring with the parameters listed in Table 1.

In analyzing the results of the simulation, checking whether beams contain the cores or not becomes an important factor for determining the beam confinement.

Development of the Kicker Magnet for MUSES

T. Ohkawa,[*1] T. Takeuchi,[*2] M. Wakasugi, and T. Katayama

In the MUSES project, kicker magnets are used for the ion-beam injection and fast extraction. The injection kicker field must fall from approximately 90% to 10% of the full strength and the extraction kicker field must rise from approximately 10% to 90% of the full strength during the time interval between bunches. The high performance of the kicker magnet is important in the efficiency of beam injection and extraction. In this paper, the development of kicker magnets for MUSES are presented.

We have adopted a traveling-wave-type kicker magnet, which is often used to generate a high magnetic field with a rapid rise and fall time.[1)] When the PFN is charged at 100 kV, the kicker magnet is expected to produce a magnetic field of 0.084 T with a flat top of 1 μs and a rise time of 95 ns. The design parameters are listed in Table 1 and a photograph of the kicker magnet is shown in Fig. 1.

Table 1. Parameters of the kicker magnet.

ITEM	DESIGN VALUE
Gap height	30 mm
Gap width	130 mm
Total core length	225 mm
Cell number	9
Inductance of unit cell	0.136 μH
Capacitance of unit cell	108.9 pF
Characteristic impedance	25 Ω
Gap field	0.084 T
Coil current	2000 A
PFN voltage	100 kV
Field rise time	95 ns

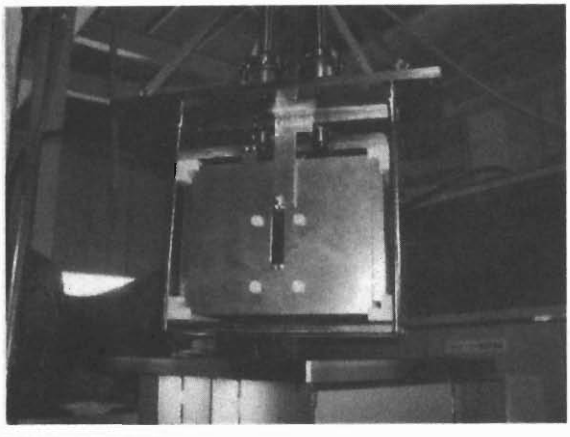

Fig. 1. Photograph of the kicker magnet.

As shown in Fig. 2, the power supply of the kicker magnet consists of a DC high-voltage power supply, a PFN, a thyratron, and a terminator. Table 2 presents the parameters of the power supply. We use the transmission cable with a length of 100 m so that reflected current does not disturb the waveform at the flat top.

To avoid the mismatch of impedance between the kicker magnet and feedthrough, we have developed a feedthrough with a coaxial structure whose characteristic impedance is designed to be 25 Ω. The structure of the feedthrough is shown in Fig. 3.

The impedance of the feedthrough from the connector to the inlet of the kicker magnet measured by the TDR method is shown in Fig. 4. The result of the measurement shows that the impedance of the feedthrough is approximately 27 Ω except at the part of the connector.

A current transformer (PEARSON-110) and a single-turn long search coil are used for the measure-

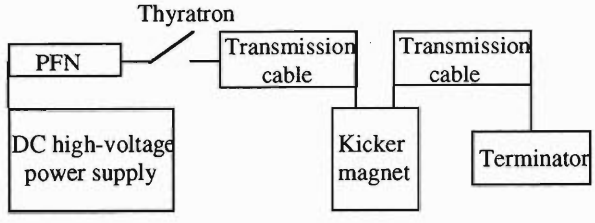

Fig. 2. Schematic of the kicker magnet system.

Table 2. Parameters of the power supply.

ITEM	DESIGN VALUE
Charging voltage	100 kV
Current	2000 A
Pulse width	1125 ns
Pulse interval	more than 0.3 s
Repetition	1 Hz
Jitter	±5 ns
Thyratron	CX1171(EEV)
Termination resistance	24±2 Ω (variable)

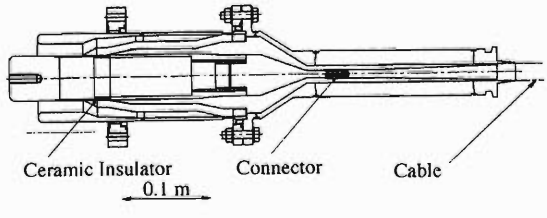

Fig. 3. Structure of the feedthrough.

[*1] Mitsubishi Heavy Industries, Ltd.
[*2] Center for Nuclear Study, Graduate School of Science, University of Tokyo

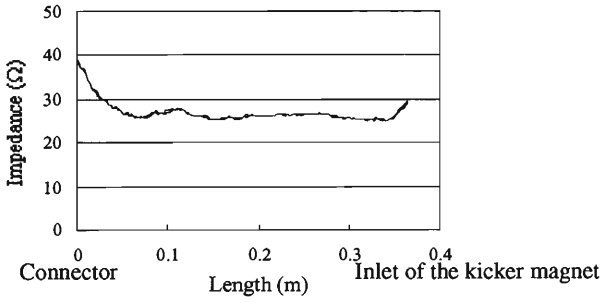

Fig. 4. Impedance of the feedthrough.

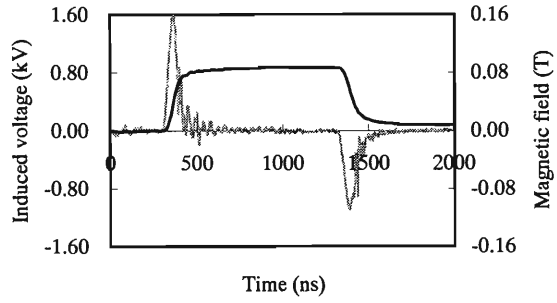

Fig. 6. Magnetic field and induced voltage.

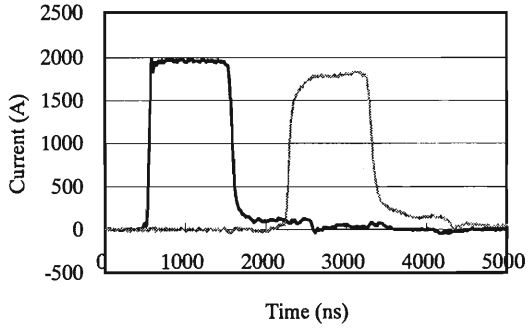

Fig. 5. Current waveforms at the outlet of the thyratron and inlet of the termination resistor.

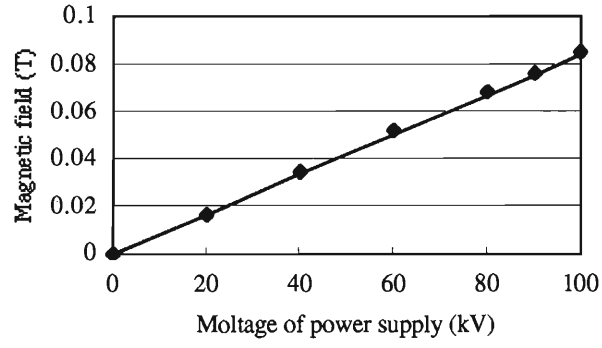

Fig. 7. Dependence of the peak magnetic field on voltage of the power supply.

ment of the current and the magnetic field, respectively. The search coil is a one-turn coil 5 mm wide and 470 mm long. The diameter of the wire is 0.5 mm. Output voltages are measured with a high-voltage probe and digital oscilloscope. The waveform of the magnetic field is obtained by integrating the induced voltage at the end of the search coil.

Figure 5 shows the current waveforms at the outlet of the thyratron and inlet of the termination resistor. Reflection currents are observed immediately after falling due to the mismatch of impedance between the PFN and transmission cable. Figure 6 shows the waveforms of the induced voltage and the magnetic field in the core gap at 100 kV. The rise time of the waveform is approximately 104 ns, flat-top time is 922 ns. The rise time of the magnetic field becomes longer than the expected value (95 ns).

The dependence of the peak magnetic field on voltage of the power supply is shown in Fig. 7. The difference between the measured result and the calculated result is less than ±3%.

We intend to perform further tests and study the ultimate kick strength and amplitude stability.

References

1) T. Ohkawa et al.: Proc. EPAC2000, p.2113 (2000).

Ferrite Evaluation Test for MUSES

Y. Chiba and K. Ohtomo

The ferrite core used for accelerator cavities has unfavorable features in that its loss factor (inverse of magnetic Q-value) rapidly increases with rf power level and a "high loss effect"[1] occurs above the threshold power level. The high loss effect is characterized by a short period, less than a few ms, of normal cavity voltage followed by a voltage decrease at the onset of rf excitation. During the high loss period, the loss factor increases further and also the appearance of noise in the amplitude and phase of the cavity voltage was reported.[1] These features govern the rise in core temperature under high-voltage operation and limit the maximum voltage sustained by a core; they impose serious limitations in the design of a ferrite-loaded cavity. To investigate these problems, a ferrite test cavity[2,3] was constructed as part of the MUSES project at RIKEN.

The accumulation cooler ring (ACR)[4] in MUSES uses a cavity frequency in the vicinity of 33 MHz. Characteristics of a Ni-Zn ferrite sample, type V2F from TDK Co., Ltd., were measured at 33 MHz using the test cavity. The core is a candidate for the ACR cavity and has a size of 127 (inner diameter) × 203 (outer diameter) × 25.4 (thickness) mm.

The measurement was carried out by varying the rf input power at a fixed bias current. A pulse excitation of 20 ms duration with 5% duty was used. The data were obtained at two positions on the time scale. The first was at 0.5 ms after the rise in pulse excitation and the second was at 16 ms after the rise. These corresponded to before and after the onset of the high loss effect, respectively. Tuning and impedance matching were adjusted as accurately as possible for each data point.

The effective value of relative permeability (μ), stored energy density (Em) in the ferrite averaged over the radius, power dissipation (Pt) in the entire volume of the ring core, loss factor of the ferrite, and rf voltage (Vf) across the core thickness at the inner radius were deduced from measured data on the basis of the radial-mode field distribution because the test cavity was a radial-mode resonator with an open aperture at the inner radius. For simplicity of analysis, a radially constant effective μ was assumed, although actual μ increases with the radius due to a $1/r$ decrease in the bias magnetic field. Results for μ of 3.9, 8.2 and 15.4, which correspond to bias fields of 5530, 2270, and 780 AT/m, respectively, are given below. Figure 1 shows loss factor vs Em and Fig. 2, Pt vs Vf.

A decrease in voltage due to the high loss effect was observed on the oscilloscope in the range of rf power level where separation of the two data lines was recognized in both figures. The threshold of the high

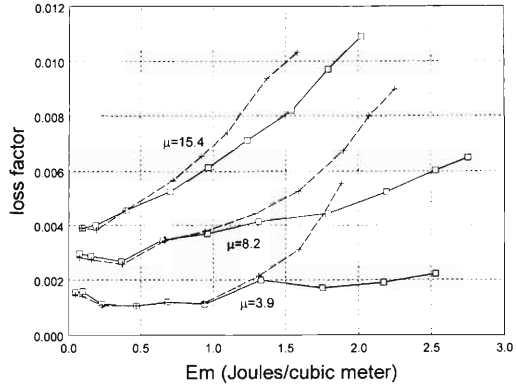

Fig. 1. Loss factor (inverse of magnetic Q-value) of the ferrite at 33 MHz as a function of stored energy density (Em) in the ferrite. Square and plus marks show the data obtained at 0.5 and 16 ms after the rise in rf excitation, respectively.

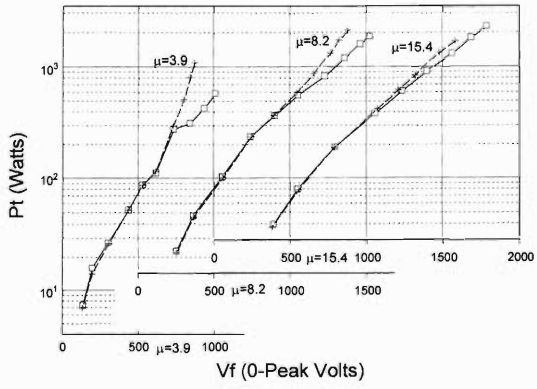

Fig. 2. Total power loss (Pt) in the ferrite core at 33 MHz as a function of the rf peak voltage (Vf) across the core thickness at the inner radius. Square and plus marks indicate the same as in Fig. 1.

loss effect in Em was estimated to be about 0.5 to 1.2 J/m^3 from Fig. 1. These figures are larger than those (0.3 ± 0.1 J/m^3) given in Ref. 1. No appearance of noise in the high loss region was observed in any case. If the self heating of about 300 W in this core can be cooled, the maximum usable voltage of the core would be 700 to 900 volts (peak value), corresponding to the μ range of 4 to 15 as shown in Fig. 2.

References

1) J. E. Griffin and G. Nicholls: IEEE Trans. Nucl. Sci. **26**, 3965 (1979).
2) K. Ohtomo and Y. Chiba: RIKEN Accel. Prog. Rep. **33**, 251 (2000).
3) K. Ohtomo et al.: Proc. EPAC2000, (2000), p.1987.
4) K. Ohtomo et al.: RIKEN Accel. Prog. Rep. **34**, 357 (2001).

Helical Partial Snake Magnet for AGS

M. Okamura, T. Tominaka,[*1] T. Takeuchi,[*2] and T. Katayama

For AGS synchrotron, Brookhaven National Laboratory has introduced a partial snake, which helps to overcome the imperfection resonances that appear during the acceleration of polarized protons. The existing partial snake is a solenoid magnet located at the C10 straight section of the AGS, and its field rises at the same rate as that of the AGS main magnet. The longitudinal (Bz) component of the solenoidal partial snake introduces linear coupling of the transverse coordinates of the beam. This linear coupling appears on the single turn first-order transfer matrix of the AGS, and one of its effects is to realize additional intrinsic resonances which cause depolarization of the beam. To achieve high polarization in RHIC, overcoming intrinsic resonance in the AGS is indispensable. In order to reduce the coupling caused by the solenoidal magnet, an alternative partial snake which is a helical dipole magnet has been proposed. The AGS partial helical snake would be composed of a single normal conducting helix with steering magnets on either side.

The designed 3D view is shown in Fig. 1. The effective magnetic length is 1500 mm and the bore is 150 × 150 mm in a square shape. Required magnetic field strength for 9 degree spin rotation at $G\gamma = 8.68$ beam is 1.61 T. Here, G is called the 'anomalous magnetic moment' and is 1.7928 for protons. γ represents the mass ratio in relativistic motion. Due to the use of a helical structure with a 360-degree rotation of the magnetic field, deflections of beam orbits will be canceled. However, considering the fringing fields in the real magnet, there should be a correct rotation angle which is less than 360 degrees. The optimized rotation angle of the iron pole determined using TOSCA is 334.67 degrees and its length is 1393.2 mm. Considering the 3D-effect, the size, height and width of the return yoke were determined not to exceed 1.5 T of the field strength in the iron, except in the pole face region. The yoke would be laminated in order to form such a complex twisted structure. The assumed current is 198000 A turn for 1.61 T. The design parameters are summarized in Table 1.

Figure 2 shows a comparison of the helical snake with the existing solenoidal snake. In this graph, the integrated longitudinal field along the beam trajectories are plotted for the both snakes. The operating $G\gamma$ of the AGS is from 4.7 to 47. Therefore, within the entire energy range of the AGS, the helical partial snake induces much less longitudinal field and has a great advantage in suppressing the coupling resonance. We believe that the new snake system will be effective in reducing depolarization in the AGS.

Table 1. Design Parameters.

Parameter	Value
Coils	
Current density (A/cm^2)	754
Total current (A turn)	198000
Power dissipation (kW)	19
Conductor size (mm)	11.5 x 11.5
Diameter of hollow (mm)	7.5
Total turns	1728
Inductance (mH)	95
Number of turns	168 (14 x 12)
Yoke	
Height (mm)	560
Width (mm)	870
Rotation angle (degrees)	334.67
Length (mm)	1393
Packing factor (%)	99

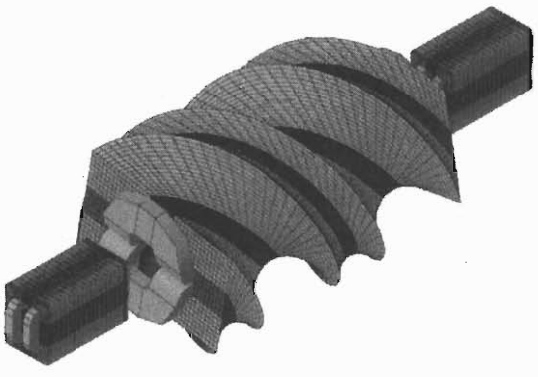

Fig. 1. 3D view of helical partial snake.

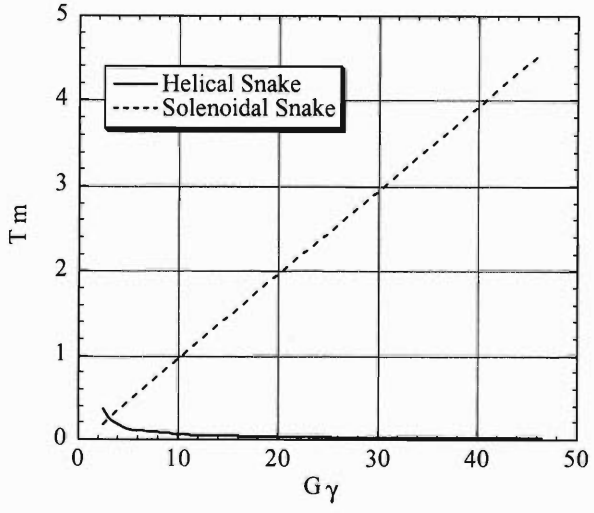

Fig. 2. Comparison of integrated longitudinal field.

*1 Hitachi, Ltd.
*2 Center for Nuclear Study, Graduate School of Science, University of Tokyo

VI. RADIATION MONITORING

Routine Work for Radiation Safety in the Ring Cyclotron Facility

S. Fujita, S. Ito, H. Sakamoto,[*1] A. Uchiyama,[*2] N. Hirao,[*2] M. Kase, and Y. Uwamino

Here we report on the residual radioactivity and leakage radiation level of the Ring Cyclotron Facility.

Residual radioactivities in the Ring Cyclotron Facility were measured at various locations using ionization-chamber survey meters.

The measurements were performed after almost every beam experiment as well as during the routine overhaul period. The routine overhaul started immediately after the experiment which was carried out with a polarized deuteron beam of 270 MeV in the E4 experimental vault from Aug. 1 to 3, 2000. The dose rates at the deflectors of the RIKEN Ring Cyclotron and the AVF Injector Cyclotron were measured from Aug. 22 to 23. These values were measured immediately before the maintenance of deflectors during the routine annual overhaul, and Fig. 1 shows them over the last fifteen years.

In the period from Oct. 1, 1999 to Sep. 30, 2000, dose rates were measured along the beam lines. The spots **a**–**z**, marked by bullets in Fig. 2, are the places where the dose rates exceeded 50 μSv/h. Table 1 summarizes the observed dose rates and gives the dates

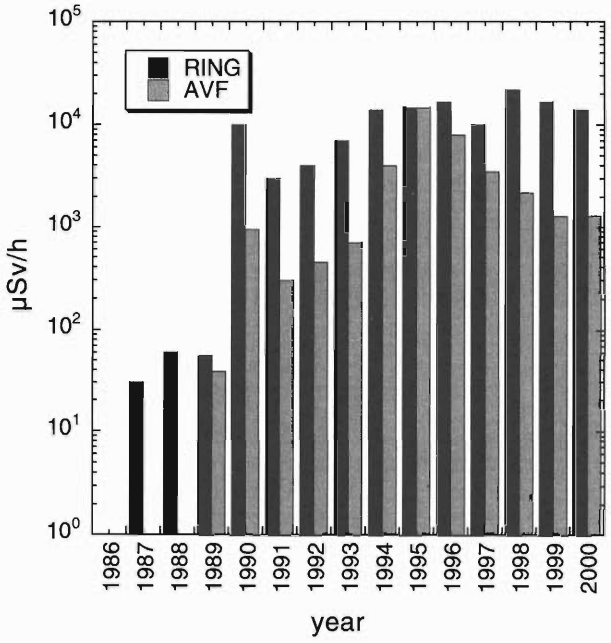

Fig. 1. Variation of the dose rates at the deflectors of the RIKEN Ring Cyclotron and the AVF Injector Cyclotron.

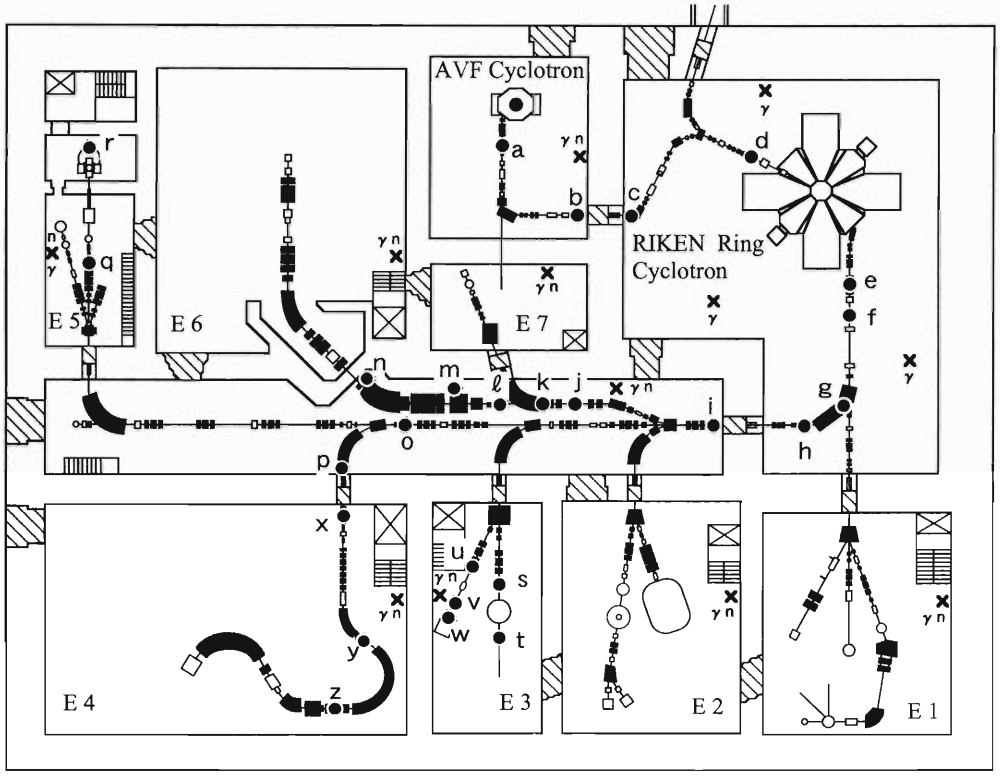

Fig. 2. Layout of the RIKEN Ring Cyclotron facility as of 2000. Measured locations of residual radioactivities along the beam lines are shown by bullets **a**–**z**.

*1 SHI Accelerator Service, Ltd.
*2 Faculty of Science, Science University of Tokyo

Table 1. Summary of the dose rates measured along the beam lines using ionization-chamber survey meters. The detection points **a**–**z** indicate the measured locations shown in Fig. 2.

Detection point	Measured dose rate (μSv/h)	Date	Particle	Energy (MeV/u)	Intensity (enA)	Period (days)
a	100	May 10, '00	Ca-40	100	85	3
b	55	May 10, '00	Ca-40	100	85	3
c	200	Aug 7, '00	d	270	100	2
d	72	Aug 7, '00	d	270	100	2
e	6000	May 2, '00	d	270	110	2
f	2000	May 2, '00	d	270	110	2
g	200	May 2, '00	d	270	110	2
h	150	May 2, '00	d	270	110	2
i	350	Jan 6, '00	d	135	320	6
j	83	Apr 14, '00	O-18	100	4400	10
k	680	May 10, '00	Ca-40	100	85	3
l	150	May 10, '00	Ca-40	100	85	3
m	10000	Apr 18, '00	O-18	100	4400	10
n	350	Apr 14, '00	O-18	100	4400	10
o	300	Jan 6, '00	d	135	320	6
p	450	Jan 6, '00	d	135	320	6
q	50	Jul 25, '00	He-4	135	800	1
r	200	Jul 25, '00	He-4	135	800	1
s	120	Jan 25, '00	N-14	135	5	1
t	120	Jan 25, '00	N-14	135	5	1
u	100	Aug 1, '00	N-14	135	800	2
v	1800	Nov 16,'99	N-14	135	700	2
w	3000	Feb 15, '00	N-14	135	800	1
x	250	Oct 29,'99	p	210	660	2
y	800	May 2, '00	d	270	110	2
z	150	Nov 29,'99	d	70	82	7

when the measurements were performed. The maximum dose rate was 10 mSv/h at the target chamber of the RIKEN projectile-fragment separator, denoted by **m** in Fig. 2. Whenever we observed a high dose rate, we roped off the area and posted a sign warning that it was dangerous to remain in that area for a long period of time.

We also continuously monitor the leakage radiation from the Ring Cyclotron Facility.

Having analyzed the collected data of leakage neutrons, we found that the radiation levels in the controlled area were much lower than the allowable dose limit. The leakage of γ-rays and neutrons was below the detection limit of the environmental monitors. We evaluated the radiation level at the boundary of the accelerator facility using the monitor which was installed in the computer room on the ground floor immediately above a bending magnet which guided the beams from the ring cyclotron vault to the distribution corridor. As a result, we obtained a radiation level of approximately 5 μSv/year which was much lower than the allowable dose limit (1 mSv/year).

Improvement of Drain System in the Ring Cyclotron Facility

S. Fujita, Y. Uwamino, S. Ito, H. Sakamoto,[*1] A. Uchiyama,[*2] N. Hirao,[*2] and M. Kase

The drain system of the Ring Cyclotron Facility has been working steadily since 1986, and we have been monitoring the radioactive wastewater continuously.

The concentration of radionuclides in the wastewater is measured using the method of evaporating a sample of water until it is dry. During the time interval between the sampling and the measurement — that is, about 10 days — the wastewater is kept in a storage tank and the new wastewater is contained in another tank. This time-consuming process has been necessary since very-low-concentration limits were applied to the radioactive wastewater in the Japanese legislation for radiation safety.

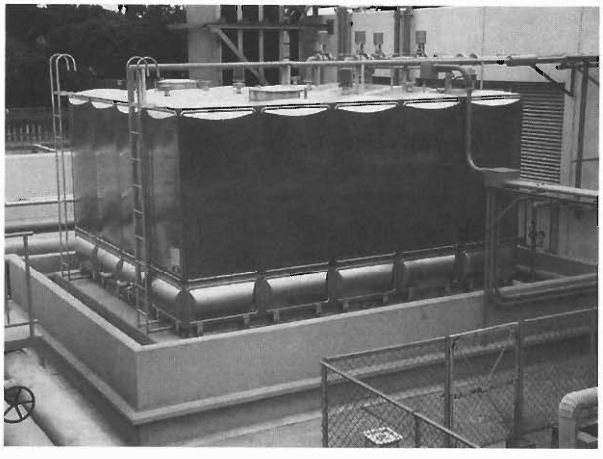

Fig. 1. Storage tank on the rooftop.

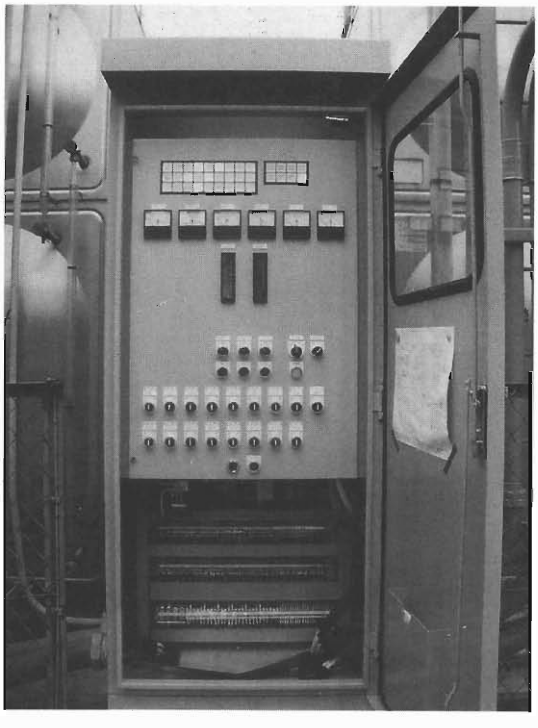

Fig. 2. New control panel board in front of the storage tank.

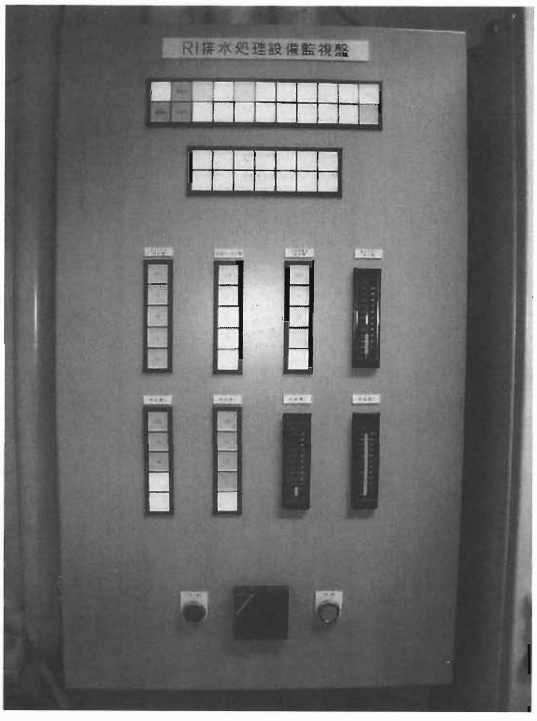

Fig. 3. New monitor panel board in the radiation safety control office.

The former drain system consisted of two 1-m^3 tanks and a 1.5-m^3 tank in the 2nd basement for storage, and two 2.5-m^3 tanks on the roof for dilution and automatic radioactivity measurement.

The volume of the wastewater, however, has augmented due to an increase in the number of users, and we recently needed large storage tanks to meet the current demand. Hence we built two storage tanks with capacities of 20 m^3 on the roof of the Ring Cyclotron Facility this year, as shown in Fig. 1. The control and the monitor panel boards for the entire drain system were replaced, and Figs. 2 and 3 show them, respectively.

*1 SHI Accelerator Service, Ltd.
*2 Faculty of Science, Science University of Tokyo

VII. LIST OF PUBLICATIONS

1. Accelerator development and accelerator physics

H. Okuno, T. Tominaka, S. Fujishima, A. Goto, and Y. Yano: "Design study of the superconducting magnets for the injection system of the superconducting ring cyclotron", Proc. 15th Int. Conf. on Magnet Technology (MT15), Beijing, China, 1997-10, pp. 57–60 (1997).

H. Okuno, T. Tominaka, S. Fujishima, A. Goto, and Y. Yano: "Design study of the injection and extraction systems for the RIKEN superconducting ring cyclotron", Proc. 15th Int. Conf. on Cyclotrons and Their Applications 98, Caen, France, 1998-06, edited by Eric Baron and Marcel Lieuvin, IOP Publishing, London, pp. 37–40 (1998).

J.-W. Kim, A. Goto, T. Mitsumoto, T. Kawaguchi, H. Okuno, T. Kubo, T. Tominaka, S. Fujishima, K. Ikegami, N. Sakamoto, S. Yokouchi, K. Sugii, J. Ohnishi, T. Morikawa, T. Wada, and Y. Yano: "Trim coil design for RIKEN superconducting ring cyclotron", Proc. 15th Int. Conf. on Cyclotrons and Their Applications 98, Caen, France, 1998-06, edited by Eric Baron and Marcel Lieuvin, IOP Publishing, London, pp. 207–210 (1998).

N. Sakamoto: "Design of the rf resonators for the new booster ring cyclotrons in the RIKEN RI Beam Factory", Proc. 15th Int. Conf. on Cyclotrons and Their Applications 98, Caen, France, 1998-06, edited by Eric Baron and Marcel Lieuvin, IOP Publishing, London, pp. 223–226 (1998).

J.-W. Kim, A. Goto, T. Mitsumoto, T. Kawaguchi, H. Okuno, T. Kubo, T. Tominaka, S. Fujishima, K. Ikegami, N. Sakamoto, T. Morikawa, K. Sugii, J. Ohnishi, S. Yokouchi, T. Wada, and Y. Yano: "A single-turn extraction study for the RIKEN superconducting ring cyclotron", Proc. 15th Int. Conf. on Cyclotrons and Their Applications 98, Caen, France, 1998-06, edited by Eric Baron and Marcel Lieuvin, IOP Publishing, London, pp. 503–506 (1998).

Y. Yano, A. Goto, and T. Katayama: "Overview of RIKEN RI Beam Factory Project", Proc. 15th Int. Conf. on Cyclotrons and Their Applications 98, Caen, France, 1998-06, edited by Eric Baron and Marcel Lieuvin, IOP Publishing, London, pp. 696–703 (1998).

Y. Goto: "Sensitivity to gluon polarization at RHIC", Nucl. Phys. B (Proc. Suppl.) **79**, 588–590 (1999).

S. Kohara, T. Nakagawa, O. Kamigaito, M. Fujimaki, M. Kidera, T. Aihara, T. Ohki, H. Hasebe, H. Yamauchi, M. Kase, A. Goto, and Y. Yano: "Status report on RIKEN heavy ion linac", Proc. 12th Symp. on Accelerator Science and Technology, Wako, 1999-10, edited by Y. Yano, RIKEN, pp. 168–170 (1999).

M. Kidera, T. Nakagawa, K. Takahashi, S. Enomoto, T. Minami, M. Fujimaki, E. Ikezawa, O. Kamigaito, M. Kase, A. Goto, and Y. Yano: "New method for trace element analysis using the electron cyclotron resonance ion source and heavy ion linac", Proc. 12th Symp. on Accelerator Science and Technology, Wako, 1999-10, edited by Y. Yano, RIKEN, pp. 188–190 (1999).

K. Sugii, K. Ikegami, S. Yokouchi, A. Goto, and Y. Yano: "Vacuum system for the RIKEN superconducting ring cyclotron", Proc. 12th Symp. on Accelerator Science and Technology, Wako, 1999-10, edited by Y. Yano, RIKEN, pp. 281–283 (1999).

K. Sugii, K. Ikegami, M. Ohtake, S. Yokouchi, A. Goto, and Y. Yano: "Influence of external magnetic field on the performance of cold cathode gauges", Proc. 12th Symp. on Accelerator Science and Technology, Wako, 1999-10, edited by Y. Yano, RIKEN, pp. 284–286 (1999).

T. Kawaguchi, H. Okuno, A. Goto, J. Ohnishi, T. Tominaka, T. Mitsumoto, and Y. Yano: "Superconducting sector magnets for the RIKEN superconducting ring cyclotron", Proc. 12th Symp. on Accelerator Science and Technology, Wako, 1999-10, edited by Y. Yano, RIKEN, pp. 322–324 (1999).

N. Fukunishi, S. Ito, Y. Uwamino, and Y. Yano: "Shielding design of RIKEN RI Beam Factory", Proc. 12th Symp. on Accelerator Science and Technology, Wako, 1999-10, edited by Y. Yano, RIKEN, pp. 349–351 (1999).

N. Fukunishi, K. Kusaka, H. Sakurai, T. Kubo, T. Nagafuchi, H. Okuno, T. Mitsumoto, S. Fujishima, M. Kase, A. Goto, and Y. Yano: "Design studies on beam transport system of RIKEN RI Beam Factory", Proc. 12th Symp. on Accelerator Science and Technology, Wako, 1999-10, edited by Y. Yano, RIKEN, pp. 438–440 (1999).

M. Takanaka and T. Katayama: "Transverse instability due to the space charge during the electron-cooling bunching of ion beams", Proc. 1999 Particle Accelerator Conf., New York, USA, 1999-03, edited by A. Luccio and W. MacKay, Brookhaven National Laboratory, New York, pp. 1719–1721 (1999).

T. Kawaguchi, H. Okuno, A. Goto, T. Mitsumoto, T. Tominaka, J. Ohnishi, and Y. Yano: "Development of sector magnets for the RIKEN superconducting ring cyclotron", Teion Kougaku **34**, 405–413 (1999).

T. Kawaguchi, H. Okuno, A. Goto, T. Mitsumoto, T. Tominaka, J. Ohnishi, and Y. Yano: "Development of sector magnets for the RIKEN superconducting ring cyclotron", Teion Kougaku **34**, 414–423 (1999).

S. Bhattacharjee, T. Nakagawa, and Y. Yano: "Particle confinement time in a plasma produced by short-pulse high-power microwaves", Bull. Am. Phys. Soc. **45**, 230–231 (2000).

S. Bhattacharjee, H. Amemiya, and Y. Yano: "Mi-

crowave breakdown of gas in a circular tube with a radius below the cut-off value", Bull. Am. Phys. Soc., **45**, 369–369 (2000).
S. Bhattacharjee and H. Amemiya: "Production of pulsed microwave plasma in a tube with a radius below the cut-off value", J. Phys. D **33**, 1104–1116 (2000).
Y. Kawamura, D. Li, R. Shlomo, T. Tanabe, and K. Toyoda: "Laser undulator radiation", Nucl. Instrum. Methods Phys. Res. A **445**, 241–246 (2000).
V. Banerjee, A. Chakrabarti, A. Bandyopadhyay, S. Chattopadhyay, A. Polley, T. Nakagawa, O. Kamigaito, A. Goto, and Y. Yano: "Design of a two-ion-source (2-IS) beam transport line for the production of multi charged radioactive ion beams", Nucl. Instrum. Methods Phys. Res. A **447**, 345–349 (2000).
S. Bhattacharjee and H. Amemiya: "General properties of high power short pulse microwave plasmas", Proc. 17th Symp. on Plasma Processing, Nagasaki, 2000-01, edited by H. Sugai, Division of Plasma Electronics, Japan Soceity of Applied Physics, Tokyo, pp. 61–64 (2000).
M. Niimura, M. Lamoureux, A. Goto, and Y. Yano: "Dynamic simulations of the interchange instability, ion production, and electron heating processes in an electron cyclotron resonance ion source plasma", Rev. Sci. Instrum. **71**, 846–849 (2000).
S. Bhattacharjee and H. Amemiya: "Pulsed microwave plasma production in a conducting tube with a radius below cutoff", Vacuum **58**, 222–232 (2000).

2. Nuclear physics and nuclear instrumentation

K. Varga and Y. Suzuki: "Solution of few-body problems with the stochastic variational method I. Central forces with zero orbital momentum", Comput. Phys. Commun. **106**, 157–168 (1997).
F. Soramel, C. Signorini, L. Müller, Z. C. Li, A. Andrighetto, Z. H. Liu, A. Yoshida, Y. Pu, T. Fukuda, K. E. G. Löbner, K. Rudolph, C. Zotti, and J. L. Sida: "Influence of break-up on fusion of ^{9,11}Be+^{209}Bi", Perspectives in Heavy Ion Physics: 3rd Japan-Italy Joint Symposium '97, Padova, Italy, 1997-10, edited by C. Signorini, F. Soramel, and T. Kishida, World Scientific, Singapore, pp. 83–91 (1997).
T. Kikuchi, T. Motobayashi, N. Iwasa, Y. Ando, M. Kurokawa, S. Moriya, H. Murakami, T. Nishio, J.-Z. Ruan, S. Shirato, S. Shimoura, T. Uchibori, Y. Yanagisawa, T. Kubo, H. Sakurai, T. Teranishi, Y. Watanabe, M. Ishihara, M. Hirai, T. Nakamura, S. Kubono, M. Gai, R. H. France III, K. I. Hahn, T. Delbar, P. Lipnik, and C. Michotte: "Experimental determination of the E2 component in the Coulomb dissociation of ^{8}B", Phys. Lett. B **391**, 261–266 (1997).
Y. Suzuki, J. Usukura, and K. Varga: "New description of orbital motion with arbitrary angular momenta", J. Phys. B **31**, 31–48 (1998).
G. Ryzhikh, J. Mitroy, and K. Varga: "The stability of the ground state for positronic sodium", J. Phys. B **31**, L265–L271 (1998).
M. Oi, N. Onishi, N. Tajima, and T. Horibata: "Signature and angular momentum in 3d-cranked HFB states", Phys. Lett. B **418**, 1–6 (1998).
T. Ohnishi, H. Sakai, H. Okamura, S. Ishida, H. Otsu, N. Sakamoto, T. Uesaka, T. Wakasa, Y. Satou, T. Fujita, and E. J. Stephenson: "Measurement of a complete set of analyzing powers for deuteron elastic scattering from ^{40}Ca at 270 MeV and an investigation of tensor potentials", Phys. Lett. B **438**, 27–34 (1998).
M. R. Ahmady, V. Elias, and E. Kou: "Nonperturbative QCD contribution to gluon-gluon-η' vertex", Phys. Rev. D **57**, 7034–7036 (1998).
M. R. Ahmady, E. Kou, and A. Sugimoto: "Nonspectator contribution: A mechanism for inclusive $B \to X_s\eta'$ and exclusive $B \to K^{(*)}\eta'$ decays", Phys. Rev. D **58**, 14015-1–14015-5 (1998).
T. Ariga and K. Suda: "Gas flow simulation of a gas cell of IGISOL", RIKEN Rev., No. 19, p. 13 (1998).
Y. Mochizuki, K. Takahashi, H.-Th. Janka, W. Hillebrandt, and R. Diehl: "^{44}Ti: its effective decay rate in young supernova remnants and its abundance in Cassiopeia A", Astron. Astrophys. **346**, 831–842 (1999).
E. Ideguchi, X. Zhou, Y. Gono, S. Mitarai, T. Morikawa, M. Kidera, H. Tsuchida, M. Shibata, H. Watanabe, M. Miyake, A. Odahara, M. Oshima, Y. Hatsukawa, S. Hamada, H. Iimura, M. Shibata, T. Ishii, T. Kishida, and M. Ishihara: "A new high spin isomer in ^{146}Eu", Eur. Phys. J. A **6**, 387–390 (1999).
S. N. Nakamura, K. Bartlett, G. A. Beer, D. R. Gill, R. Hayano, T. Ito, M. Iwasaki, L. Lee, G. Mason, A. Olin, H. Outa, M. Salomon, R. Seki, T. Taniguchi, T. P. Terada, G. Trayling, Y. Yamashita, and S. Yen: "Observation of kaonic hydrogen atom X-ray", Hyperfine Interact. **118**, 45–51 (1999).
C. Petrascu, S. Bianco, A. M. Bragadireanu, F. L. Fabbri, C. Guaraldo, M. Iliescu, T. M. Ito, V. Lucherini, M. Bregant, E. Milotti, A. Vacchi, E. Zavattini, M. Augsburger, D. Chatellard, P. Knowles, F. Mulhauser, L. A. Schaller, L. Schellenberg, H. Schneuwly, J.-P. Egger, D. Varidel, W. H. Breunlich, M. Cargnelli, B. Gartner, R. King, B. Lauss, J. Marton, J. Zmeskal, T. Ponta, S. N. Nakamura, T. Koike, R. S. Hayano, M. Hori, T. Ishikawa, T. Ishiwatari, M. Iwasaki, Y. Akaishi, G. Beer, A. C. Sanderson, and R. Seki: "Disentangling the K-complex of kaonic hydrogen with DEAR", Hyperfine Interact. **118**, 53–57 (1999).
S. N. Nakamura, K. Nagamine, T. Matsuzaki, K. Ishida, N. Kawamura, S. Sakamoto, M. Iwasaki,

M. Tanase, M. Kato, K. Kurosawa, H. Sugai, I. Watanabe, K. Kudoh, N. Takeda, and G. H. Eaton: "Measurement of the K_β/K_α ratio for muon alpha sticking X-rays in muon catalyzed d-t fusion at the RIKEN-RAL Muon Facility", Hyperfine Interact. **118**, 209–212 (1999).

T. Matsuzaki, K. Nagamine, K. Ishida, S. N. Nakamura, N. Kawamura, M. Tanase, M. Kato, K. Kurosawa, M. Hashimoto, H. Sugai, K. Kudoh, N. Takeda, and G. H. Eaton: "Muon catalyzed fusion and muon to ^{3}He transfer in solid T_2 studied by X-ray and neutron detection", Hyperfine Interact. **118**, 229–234 (1999).

C. Guaraldo, S. Bianco, A. M. Bragadireanu, F. L. Fabbri, M. Iliescu, T. M. Ito, V. Lucherini, C. Petrascu, M. Bregant, E. Milotti, A. Vacchi, E. Zavattini, M. Augsburger, D. Chatellard, P. Knowles, F. Mulhauser, L. A. Schaller, L. Schellenberg, H. Schneuwly, J.-P. Egger, D. Varidel, W. H. Breunlich, M. Cargnelli, B. Gartner, R. King, B. Lauss, J. Marton, J. Zmeskal, T. Ponta, S. N. Nakamura, T. Koike, R. Hayano, M. Hori, T. Ishikawa, T. Ishiwatari, M. Iwasaki, Y. Akaishi, G. A. Beer, A. C. Sanderson, and R. Seki: "The DEAR case", Hyperfine Interact. **119**, 253–261 (1999).

T. Matsuzaki, K. Nagamine, M. Tanase, M. Kato, K. Kurosawa, K. Ishida, S. N. Nakamura, I. Watanabe, and G. H. Eaton: "Tritium gas handling system for muon catalyzed fusion research at RIKEN-RAL Muon Facility", Hyperfine Interact. **119**, 361–363 (1999).

K. Matsuta, T. Onishi, M. Fukuda, T. Minamisono, M. Mihara, M. Sasaki, T. Yamaguchi, T. Miyake, K. Sato, K. Minamisono, F. Ohsumi, Y. Muramoto, S. Oui, C. Ha, K. Tanaka, K. Kidera, A. Morishita, T. Tsubota, T. Sumikawa, A. Kitagawa, M. Torikoshi, M. Kanazawa, T. Nishio, S. Koda, T. Ohtsubo, S. Fukuda, Y. Nojiri, S. Momota, A. Ozawa, K. Yoshida, T. Suzuki, T. Kobayashi, I. Tanihata, S. S Hanna, J. R. Alonso, G. F. Krebs, T. J. M. Symons, and K. Tanaka: "Spin polarization of β-emitting fragments in high energy heavy ions on Be collisions", Hyperfine Interact. **120/121**, 713–717 (1999).

T. Kishida, Y. Gono, M. Shibata, H. Watanabe, T. Tsutsumi, S. Motomura, E. Ideguchi, X. Zhou, T. Morikawa, T. Kubo, and M. Ishihara: "A windowless gas target for secondary beam production", Nucl. Instrum. Methods Phys. Res. A **438**, 70–72 (1999).

T. Horibata, M. Oi, N. Onishi, and A. Ansari: "Erratum to "Band structures of ^{182}Os studied by GCM based on 3D-CHFB"", Nucl. Phys. A **651**, 435–436 (1999).

M. Fukuda, M. Mihara, T. Fukao, S. Fukuda, M. Ishihara, S. Ito, T. Kobayashi, K. Matsuta, T. Minamisono, S. Momota, T. Nakamura, Y. Nojiri, Y. Ogawa, T. Ohtsubo, T. Onishi, A. Ozawa, T. Suzuki, M. Tanigaki, I. Tanihata, and K. Yoshida: "Density distribution of ^{8}B studied via reaction cross sections", Nucl. Phys. A **656**, 209–228 (1999).

T. Suzuki, R. Kanungo, O. Bochkarev, L. Chulkov, D. Cortina-Gil, M. Fukuda, H. Geissel, M. Hellström, M. Ivanov, R. Janik, K. Kimura, T. Kobayashi, A. A. Korsheninnikov, G. Münzenberg, F. Nickel, A. A. Ogloblin, A. Ozawa, M. Pfützner, V. Pribora, H. Simon, B. Sitár, P. Strmeň, K. Sumiyoshi, K. Sümmerer, I. Tanihata, M. Winkler, and K. Yoshida: "Nuclear radii of ^{17,19}B and ^{14}Be", Nucl. Phys. A **658**, 313–326 (1999).

N. Saito: "RHIC spin physics: Status of polarized collider and spin-flavor structure of the nucleon", Nucl. Phys. B (Proc. Suppl.) **79**, 584–587 (1999).

Zs. Fülöp, M. Golovkow, T. Kato, K. Kimura, H. Kudo, Y. Mochizuki, H. Otsu, A. Ozawa, H. Petrascu, H. Sakurai, T. Suzuki, I. Tanihata, Y. Wakasaya, K. Yoshida, R. N. Boyd, and E. Somorjai: "Production of ^{44}Ti at the RIKEN RIPS facility", Nuclei in the Cosmos V, Proc. Int. Conf. on Nuclear Astrophysics, Volos, Greece, 1998-07, edited by N. Prantzos et al., Editions Frontieres, Paris, pp. 281–284 (1999).

Y. Mochizuki: "The long half-life of highly ionized ^{44}Ti", Nuclei in the Cosmos V, Proc. Int. Conf. on Nuclear Astrophysics, Volos, Greece, 1998-07, edited by N. Prantzos et al., Editions Frontieres, Paris, pp. 285–288 (1999).

H. Ogawa, K. Asahi, K. Sakai, A. Yoshimi, M. Tsuda, Y. Uchiyama, T. Suzuki, K. Suzuki, N. Kurokawa, M. Adachi, H. Izumi, H. Ueno, T. Shimoda, S. Tanimoto, N. Takahashi, W. D. Schmidt-Ott, M. Schaefer, S. Fukuda, A. Yoshida, M. Notani, T. Kubo, H. Okuno, H. Sato, N. Aoi, K. Yoneda, H. Iwasaki, N. Fukuda, N. Fukunishi, M. Ishihara, and H. Miyatake: "Magnetic moment and electric quadrupole moment of ^{18}N ground state", Phys. Lett. B **451**, 11–18 (1999).

K. Krueger, C. Allgower, T. Kasprzyk, H. Spinka, D. Underwood, A. Yokosawa, G. Bunce, W. H. Huang, Y. Makdisi, T. Roser, M. Syhers, N. I. Belikov, A. A. Derevshchikov, Y. A. Matulenko, L. V. Nogach, S. B. Nurushev, A. I. Pavlinov, A. N. Vasiliev, M. Bai, S. Y. Lee, Y. Goto, N. Hayashi, T. Ichihara, M. Okamura, N. Saito, H. En'yo, K. Imai, Y. Kondo, Y. Nakada, M. Nakamura, H. D. Sato, H. Okamura, H. Sakai, T. Wakasa, V. Baturine, A. Ogawa, V. Ghazikhanian, G. Igo, S. Trentalange, and C. Whitten: "Large analyzing power in inclusive $\pi^\pm$ production high x_F with a 22-GeV/c polarized proton beam", Phys. Lett. B **459**, 412–416 (1999).

N. Kawamura, K. Nagamine, T. Matsuzaki, K. Ishida, S. N. Nakamura, S. Sakamoto, I. Watanabe, M. Iwasaki, M. Tanase, M. Kato, K. Kurosawa, H. Sugai, K. Kudoh, N. Takeda, and G. H. Eaton:

"Measurements of ^{3}He accumulation effect on muon catalyzed fusion in the solid/liquid DT mixtures", Phys. Lett. B **465**, 74–80 (1999).

Y. Fujita, H. Akimune, I. Daito, H. Fujimura, M. Fujiwara, M. N. Harakeh, T. Inomata, J. Jänecke, K. Katori, A. Tamii, M. Tanaka, H. Ueno, and M. Yosoi: "Mirror-symmetry structure of $A = 27$, $T = 1/2$ nuclei studied through strong, weak, and electromagnetic interactions", Phys. Rev. C **59**, 90–100 (1999).

K. Kusaka, H. Toki, and S. Umisedo: "Nonperturbative renormalization of a fermion mass term in the mass-independent renormalization scheme", Phys. Rev. D **59**, 116010-1–116010-10 (1999).

A. A. Korsheninnikov, M. Golovkov, A. Ozawa, E. Kuzmin, E. Nikolskii, K. Yoshida, B. G. Novatskii, A. Ogloblin, I. Tanihata, Zs. Fülöp, K. Kusaka, K. Morimoto, H. Otsu, H. Petrascu, and F. Tokanai: "Observation of an excited state in ^{7}He with unusual structure", Phys. Rev. Lett. **82**, 3581–3584 (1999).

Y. Mochizuki: "The origin of neutron star glitches", Proc. of Workshop on Birth and Evolution of Neutron Stars, Tokyo, 1998-12, pp. 114–126 (1999).

Y. Mochizuki: "^{44}Ti: its effective decay rate in young supernova remnants and its abundance in Cassiopeia A", Proc. of Workshop on Birth and Evolution of Neutron Stars, Tokyo, 1998-12, pp. 186–193 (1999).

K. Kusaka, T. Sakai, and H. Toki: "Bethe-Salpeter approach for mesons in the pion channel within the dual Ginzburg-Landau theory", Prog. Theor. Phys. **101**, 721–747 (1999).

H. Madokoro and M. Matsuzaki: "Relativistic and non-relativistic mean field investigation of the superdeformed bands in ^{62}Zn", Prog. Theor. Phys. **101**, 1027–1041 (1999).

N. Dinh Dang and U. Garg: "Introduction to the proceedings on selected topics in nuclear collective excitations", RIKEN Rev., No. 23, p. 1 (1999).

Y. Matsui: "Nucleon-trinucleon scattering with Yamaguchi potential", RIKEN Rev., No. 25, pp. 66–67 (1999).

S. Bianco, A. M. Bragadireanu, F. L. Fabbri, C. Guaraldo, M. Iliescu, T. M. Ito, V. Lucherini, C. Petrascu, M. Bregant, E. Milotti, A. Vacchi, E. Zavattini, M. Augsburger, D. Chatellard, P. Knowles, F. Mulhauser, L. A. Schaller, L. Schellenberg, H. Schneuwly, J.-P. Egger, D. Varidel, W. H. Breunlich, M. Cargnelli, B. Gartner, R. King, B. Lauss, J. Marton, J. Zmeskal, T. Ponta, S. N. Nakamura, T. Koike, R. Hayano, M. Hori, T. Ishikawa, T. Ishiwatari, M. Iwasaki, Y. Akaishi, G. A. Beer, A. C. Sanderson, and R. Seki: "The DEAR case", Riv. Nuovo Cimento **22**, 1–45 (1999).

X. Zhou, E. Ideguchi, T. Kishida, M. Ishihara, H. Tsuchida, Y. Gono, T. Morikawa, M. Shibata, H. Watanabe, M. Miyake, T. Tsutsumi, S. Motomura, and S. Mitarai: "Weak coupling in ^{143}Nd", Chin. Phys. Lett. **17**, 264–266 (2000).

J. Y. Huh, C. S. Lee, Y. K. Kwon, J. Y. Kim, Y. Gono, T. Morikawa, H. Watanabe, M. Shibata, S. Motomura, T. Tsutsumi, T. Fukuchi, T. Kishida, E. Ideguchi, X. Zhou, A. Odahara, S. Kubono, J. H. Ha, M. K. Cheoun, C. Lee, J. C. Kim, C. B. Moon, S. J. Chae, Y. K. Kim, and J. S. Chai: "Observation of intermediate bands feeding the positive-parity yrast band in ^{155}Gd", Eur. Phys. J. A **7**, 11–14 (2000).

T. Ohnishi, H. Sakai, H. Okamura, S. Ishida, H. Otsu, N. Sakamoto, T. Uesaka, T. Wakasa, and Y. Satou: "Measurement of deuteron elastic scattering at E_d = 270 MeV and a comparison with sudden approximation", Few Body Systems Suppl. 12: Few Body Problems in Pysics '99, Kashiwa, 1999-08, edited by S. Oryu, M. Kamimuna, and S. Ishikawa, Springer, Wien, pp. 153–156 (2000).

H. Sakai, K. Sekiguchi, H. Kato, A. Tamii, T. Ohnishi, K. Yako, S. Sakoda, Y. Maeda, M. Hatano, N. Sakamoto, T. Uesaka, Y. Satou, H. Okamura, K. Suda, and T. Wakasa: "Precise measurement of dp scattering at 270 MeV", Few Body Systems Suppl. 12: Few Body Problems in Pysics '99, Tokyo, 1999-08, edited by S. Oryu, M. Kamimura, and S. Ishikawa, Springer, Wien, pp. 403–408 (2000).

K. Sekiguchi, H. Sakai, and H. Okamura: "Measurement of cross sections and vector and tensor analyzing powers for d-p elastic scattering at E_d = 270 MeV", Few Body Systems Suppl. 12: Few Body Problems in Pysics '99, Kashiwa, 1999-08, edited by S. Oryu, M. Kamimura, and S. Ishikawa, Springer, Wien, pp. 474–478 (2000).

H. Okamura: "Fast data acquisition system for the spectrometer SMART at RIKEN", Nucl. Instrum. Methods Phys. Res. A **443**, 194–196 (2000).

A. Ozawa, O. V. Bochkarev, L. Chulkov, D. Cortina-Gil, H. Geissel, M. Hellström, M. Ivanov, R. Janik, K. Kimura, T. Kobayashi, A. A. Korsheninnikov, G. Münzenberg, F. Nickel, A. A. Ogloblin, M. Pfutzner, V. Pribora, H. Simon, B. Sitár, P. Strmen, K. Summerer, T. Suzuki, I. Tanihata, M. Winkler, and K. Yoshida: "Production cross-sections of light neutron-rich nuclei from ^{40}Ar fragmentation at about 1 GeV/nucleon", Nucl. Phys. A **673**, 411–422 (2000).

L. Chulkov, O. V. Bochkarev, D. Cortina-Gil, H. Geissel, M. Hellström, M. Ivanov, R. Janik, K. Kimura, T. Kobayashi, A. A. Korsheninnikov, G. Münzenberg, F. Nickel, A. A. Ogloblin, A. Ozawa, M. Pfützner, V. N. Privora, M. V. Rozhkov, H. Simon, B. Sitár, P. Strmen, K. Summerer, T. Suzuki, I. Tanihata, M. Winkler, and K. Yoshida: "Total charge-changing cross sections for neutron-rich light nuclei", Nucl. Phys. A **674**, 330–342 (2000).

N. Dinh Dang, K. Tanabe, and A. Arima: "Damping of multiphonon giant resonances", Nucl. Phys. A **675**, 531–558 (2000).

R. Kanungo, I. Tanihata, Y. Ogawa, and A. Ozawa: "Halo structure in ^{19}C: A Glauber model analysis", Nucl. Phys. A **677**, 171–186 (2000).

K. Asahi: "Nuclear and fundamental physics with spin-polarized nuclei", Nuclear Study **44**, No. 4, pp. 45–63 (2000).

S. N. Nakamura, K. Nagamine, T. Matsuzaki, K. Ishida, N. Kawamura, Y. Matsuda, M. Tanase, M. Kato, K. Kurosawa, H. Sugai, and G. H. Eaton: "The first observation of muon-to-alpha sticking K_β X-rays in muon catalyzed D-T fusion", Phys. Lett. B **473**, 226–232 (2000).

H. Kurasawa and T. Suzuki: "Effects of the Dirac sea on the giant monopole states", Phys. Lett. B **474**, 262–268 (2000).

T. Nakatsukasa, N. R. Walet, and G. D. Dang: "Local harmonic approaches with approximate cranking operators", Phys. Rev. C **61**, 014302-1–014302-15 (2000).

X. Zhou, H. Tsuchida, Y. Gono, A. Odahara, E. Ideguchi, T. Morikawa, M. Shibata, H. Watanabe, M. Miyake, T. Tsutsumi, S. Motomura, T. Kishida, S. Mitarai, and M. Ishihara: "Level structure in ^{143}Nd", Phys. Rev. C **61**, 014303-1–014303-11 (2000).

M. Tanifuji, S. Ishikawa, Y. Iseri, T. Uesaka, N. Sakamoto, Y. Satou, K. Itoh, H. Sakai, A. Tamii, T. Ohnishi, K. Sekiguchi, K. Yako, S. Sakoda, H. Okamura, K. Suda, and T. Wakasa: "Reaction mechanism and characteristics of T_{20} in d+^{3}He backward elastic scattering at intermediate energies", Phys. Rev. C **61**, 024602-1–024602-8 (2000).

N. Dinh Dang, K. Eisenman, J. Seitz, and M. Thoennessen: "Statistical analysis of the hot giant dipole resonance with the phonon damping model", Phys. Rev. C **61**, 27302-1–27302-3 (2000).

V. Y. Denisov and S. Yamaji: "Single- and double-phonon giant monopole resonances in a nonlinear approach", Phys. Rev. C **61**, 044318-1–044318-9 (2000).

N. Dinh Dang, T. Suzuki, and A. Arima: "Giant dipole resonance in neutron-rich nuclei within the phonon damping model", Phys. Rev. C **61**, 64304-1–64304-2 (2000).

A. Ansari, N. Dinh Dang, and A. Arima: "Hot giant dipole resonance with thermal fluctuation corrections in the static path approximation", Phys. Rev. C **62**, 11302-1–11302-4 (2000).

Y. M. Zhao, N. Yoshinaga, S. Yamaji, J. Q. Chen, and A. Arima: "Nucleon-pair approximation of the shell model", Phys. Rev. C **62**, 014304-1–014304-9 (2000).

Y. M. Zhao, S. Yamaji, N. Yoshinaga, and A. Arima: "Nucleon-pair approximation of the nuclear collective motion", Phys. Rev. C **62**, 014315-1–014315-10 (2000).

Y. M. Zhao, N. Yoshinaga, S. Yamaji, and A. Arima: "Validity of SD-pair truncation of the shell model", Phys. Rev. C **62**, 014316-1–014316-9 (2000).

N. Dinh Dang and A. Arima: "Extended renormalized random phase approximation", Phys. Rev. C **62**, 024303-1–024303-7 (2000).

K. Tanabe and N. Dinh Dang: "Exact form of the random phase approximation equation at finite temperature including the entropy effect", Phys. Rev. C **62**, 024310-1–024310-11 (2000).

Y. M. Zhao, N. Yoshinaga, S. Yamaji, and A. Arima: "Relationship between fermion dynamical symmetric model Hamiltonian and nuclear collective motion", Phys. Rev. C **62**, 024322-1–024322-6 (2000).

Y. Fujita, B. A. Brown, H. Ejiri, K. Katori, S. Mizutori, and H. Ueno: "Separation of isoscalar, isovector, orbital, and spin contributions in $M1$ transitions in mirror nuclei", Phys. Rev. C **62**, 44314–44314 (2000).

J. Golak, H. Kamada, H. Witala, W. Glöckle, J. Kuroś-Zolnierczuk, R. Skibiński, V. V. Kotlyar, K. Sagara, and H. Akiyoshi: "Faddeev calculations of proton-deuteron radiative capture with exchange currents", Phys. Rev. C **62**, 054005-1–054005-16 (2000).

H. Kurasawa and T. Suzuki: "Effects of the neutron spin-orbit density on the nuclear charge density in relativistic nuclear models", Phys. Rev. C **62**, 54303-1–54303-4 (2000).

R. Bieber, W. Glöckle, J. Golak, M. N. Narakeh, D. Hüber, H. Huisman, N. Kalantar-Nayestanaki, H. Kamada, J. G. Messchendorp, A. Nogga, H. Sakai, N. Sakamoto, M. Seip, M. Volkerts, S. Y. Van der werf, and H. Witala: "Three-nucleon force and the A_y puzzle in intermediate energy $\vec{p}$ + d and $\vec{d}$ + p elastic scattering", Phys. Rev. Lett. **84**, 606–609 (2000).

A. Ozawa, T. Kobayashi, T. Suzuki, K. Yoshida, and I. Tanihata: "New magic number, $N = 16$, near neutron, drip line", Phys. Rev. Lett. **84**, 5493–5495 (2000).

A. A. Korsheninnikov, M. Golovkov, A. Ozawa, E. Kuzmin, E. Nikolskii, K. Yoshida, B. G. Novatskii, A. Ogloblin, I. Tanihata, Zs. Fülöp, K. Kusaka, K. Morimoto, H. Otsu, H. Petrascu, and F. Tokanai: "Excited state of ^{7}He and its unique structure", Phys. Scr. T **788**, 199–202 (2000).

Y. Mochizuki: "Half-lives of unstable nuclei produced in supernovae", Proc. 2nd Symp. on Science of Hadrons under Extreme Conditions, pp. 139–141 (2000).

T. Ichihara, Y. Watanabe, N. Hayashi, S. Sawada, S. Yokkaichi, A. Taketani, Y. Goto, H. En'yo, and H. Hamagaki: "PHENIX computing center in Japan", Proc. CHEP 2000, pp. 581–584 (2000).

N. Dinh Dang: "Single and multiphonon resonances within the Phonon Damping Model", Proc. Int. Symp. on Quasiparticle and Phonon Excitations in Nuclei (Soloviev 99), RIKEN, 1999-12, edited by N.

Dinh Dang and A. Arima, World Scientific, Singapore, pp. 45–53 (2000).
T. Suzuki: "A few topics on giant resonance states", Proc. Int. Symp. on Quasiparticle and Phonon Excitations in Nuclei (Soloviev 99), Wako, 1999-12, edited by N. Dihn Dang and A. Arima, World Scientific, Singapore, pp. 264–271 (2000).
Y. Mochizuki: "Effective decay rate of ^{44}T and supernova remnants Cassiopeia A, RX J0852.0-4622", Proc. 12th Symp. of Association of Japanese Theoretical Astronomers, pp. 147–147 (2000).
M. Matsuo, T. Nakatsukasa, and K. Matsuyanagi: "Adiabatic selfconsistent collective coordinate method for large amplitude collective motion in nuclei with pairing correlations", Prog. Theor. Phys. **103**, 959–979 (2000).
H. Kamada, T. Uesaka, W. Glöeckle, H. Sakai, S. Gojuki, K. Itoh, T. Ohnishi, H. Okamura, N. Sakamoto, S. Sakoda, Y. Satou, K. Sekiguchi, K. Suda, A. Tamii, T. Wakasa, H. Witala, and K. Yako: "A model for the ^{3}He$(\vec{d},p)^4$He reaction at intermediate energies", Prog. Theor. Phys. **104**, 703–708 (2000).
T. Otsuka, N. Shimizu, S. Haruyama, M. Honma, T. Mizusaki, A. Taketani, Y. Utsuno, and Y. Watanabe: "Monte Carlo Shell Model calculations for atomic nuclei and their parallel computing", Prog. Theor. Phys. Suppl., No. 138, pp. 24–27 (2000).
Y. Watanabe, N. Shimizu, S. Haruyama, M. Honma, T. Mizusaki, A. Taketani, Y. Utsuno, and T. Otsuka: "A workstation farm optimized for Monte Carlo Shell Model calculations: Alphleet", Prog. Theor. Phys. Suppl., No. 138, pp. 43–44 (2000).

3. Atomic and solid-state physics

Y. Kobayashi, Y. Yoshida, K. Hayakawa, K. Yukihira, J. Nakamura, H Haesslein, S. Nasu, N. Inabe, Y. Watanabe, A. Yoshida, M. Kase, A. Goto, Y. Yano, E. Yagi, and F. Ambe: "In-beam Mössbauer spectrometers for materials science at RIKEN Accelerator Research Facility", Hyperfine Interact. C **3**, 273–276 (1998).
V. V. Krishunamurthy, I. Watanabe, K. Nagamine, C. Geibel, G. Sparn, and F. Steglich: "μ^+SR study of heavy-fermion magnetism in $Ce(Cu_{1-x}Ni_x)_2Ge_2$", Hyperfine Interact. **120/121**, 607–610 (1999).
J. Arai, T. Ishiguro, I. Watanabe, and K. Nagamine: "μSR study in $La_{2-x}Sr_xCu_{1-y}Zn_yO_4$ with x $\simeq$ 1/8", J. Low Temp. Phys. **117**, 377–382 (1999).
I. Watanabe, M. Akoshima, Y. Koike, S. Ohira, and K. Nagamine: "μ^+SR study on $Bi_2Sr_2Ca_{1-x}Y_x(Cu_{1-y}Zn_y)_2O_{8+\delta}$ around the hole concentration of $\frac{1}{8}$ per Cu", J. Low Temp. Phys. **117**, 503–507 (1999).
M. Akoshima, H. Noji, Y. Koike, T. Nishizaki, N. Kobayashi, I. Watanabe, and K. Nagamine: "Transport and μSR studies at $p\sim\frac{1}{8}$ in the Bi-2212 and Y-123 phases", J. Low Temp. Phys. **117**, 1163–1167 (1999).
Y. Yamazaki: "Trapping, cooling and extraction of antiprotons, and the ASACUSA project", Non-neutral Plasma Physics III, edited by John J. Bollinger, et al., American Institute of Physics, New York, pp. 48–58 (1999).
T. Ichioka, H. Higaki, M. Hori, N. Oshima, K. Kuroki, A. Mohri, K. Komaki, and Y. Yamazaki: "Multiring trap as a reservoir of cooled antiprotons", Non-neutral Plasma Physics III, edited by John J. Bollinger, et al., American Institute of Physics, New York, pp. 59–64 (1999).
K. Awaga, N. Wada, I. Watanabe, and T. Inabe: "Unusual crystal structures and properties of nitronylnitrooxide radicals. Possible RVB states in molecule-based magnets", Philos. Trans. R. Soc. London. A **357**, 2893–2922 (1999).
I. Watanabe, M. Akoshima, Y. Koike, and K. Nagamine: "Anomalous slowing down of Cu-spin fluctuations observed by muon spin relaxation in the Zn-substituted Bi_2 $Sr_2Ca_{1-x}Y_x(Cu_{1-y}Zn_y)_2O_{8+\delta}$ system around the hole concentration of $\frac{1}{8}$ per Cu", Phys. Rev. B **60**, R9955–R9958 (1999).
Y. Yamamoto, Y. Miyako, S. Kawarazaki, T. Takeuchi, M. Ocio, P. Pari, J. Hammann, I. Watanabe, K. Nishiyama, K. Shimomura, and K. Nagamine: "Low temperature properties of the heavy-fermion $Ce(Ru_{1-x}Rh_x)_2Si_2$ at the magnetic-nonmagnetic boundaries", Physica B **259/261**, 66–67 (1999).
V. V. Krishunamurthy, I. Watanabe, S. Ohira, K. Nishiyama, K. Nagamine, M. Ishikawa, D. H. Eom, and N. Takeda: "μ^+SR observation of magnetic ordering and non-Fermi liquid scaling in $CeCoGe_{1.8}Si_{1.2}$", Physica B **259/261**, 374–375 (1999).
I. Watanabe and K. Nagamine: "μSR study of magnetically ordered state of the Zn-substituted La-Sr system", Physica B **259/261**, 544–545 (1999).
I. Watanabe, M. Akoshima, Y. Koike, and K. Nagamine: "μSR study on the magnetic state of the Zn-substituted Bi-2212 system", Physica B **259/261**, 557–558 (1999).
W. Higemoto, K. Nishiyama, I. Watanabe, K. Nagamine, A. Asamitsu, H. Kuwahara, and Y. Tokura: "μ^+SR study on $(Nd_{1-y}Sm_y)_{0.5}MnO_3$", Physica B **259/261**, 822–823 (1999).
T. Nishimura and I. Shimamura: "Elastic scattering of positrons from Ne, Ar, CH_4, and SiH_4", RIKEN Rev., No. 25, pp. 12–13 (1999).
T. Iitaka and T. Ebisuzaki: "Efficient algorithm for calculating two photon absorption spectra", RIKEN Rev., No. 25, pp. 84–86 (1999).
H. Ikeda, N. Kuroda, Y. Tanaka, T. Kambara, K. Yoshikawa, and R. Yoshizaki: "Magnetic properties

of Bi-2223 tapes irradiated by Xe ion", Advances in Superconductivity XII, Morioka, 1999-10, edited by T. Yamashita and K. Tanabe, Springer, Tokyo, pp. 377–378 (2000).

Y. Kanai, K. Iemura, and X.-M. Tong: "Production of doubly excited He atoms in collisions of He^{2+} ions with alkaline-earth atoms", AIP Conf. Proc., **500**, 606–615 (2000).

M. Hase, K. Ishioka, M. Kitajima, K. Ushida, and S. Hishita: "Dephasing of coherent phonons by lattice defects in bismuth films", Appl. Phys. Lett. **76**, 1258–1260 (2000).

Y. Yamazaki, Y. Morishita, S. Ninomiya, and R. Hutton: "Production of meta-stable multi-Rydberg states: Resonant electron transfer into slow highly charged ions", Butsuri **55**, 430–433 (2000).

E. Yagi: "Ion beam materials analysis-NRD (nuclear reaction detection method)", Ion beam materials analysis and materials modification, edited by Fuminori Fujimoto and Kenichiro Komaki. Uchida Rokakuho Publishing, Tokyo, pp. 37–58 (2000).

N. Ishikawa, A. Iwase, Y. Chimi, O. Michikami, H. Wakana, and T. Kambara: "Defect production induced by primary ionization in ion-irradiated oxide superconductors", J. Phys. Soc. Jpn. **69**, 3563–3575 (2000).

Y. Nagashima, T. Kurihara, F. Saito, Y. Itoh, A. Goto, and T. Hyodo: "Stable, high-efficiency moderator with tungsten mesh", Jpn. J. Appl. Phys. **39**, 5356 5357 (2000).

E. Yagi: "Application of accelerators in various research fields: Solid state physics", Kasokuki Kougaku Handbook, edited by Y. Hirao, M. Odera, H. Kamitsubo, and T. Fuketa, Nihon Genshiryoku Sangyo Kaigi, Tokyo, pp. 235–254 (2000).

A. Igarashi, I. Shimamura, and N. Toshima: "Photodetachment cross sections of the positronium negative ion", New J. Phys. (Web) **2**, 17.1–17.14 (2000).

Y. Chimi, A. Iwase, N. Ishikawa, N. Kuroda, and T. Kambara: "Radiation annealing induced by electronic excitation in iron", Nucl. Instrum. Methods Phys. Res. B **164/165**, 408–414 (2000).

T. Kambara, Y. Kanai, T. M. Kojima, Y. Nakai, A. Yoneda, K. Kageyama, and Y. Yamazaki: "Acoustic emission from fast heavy-ion irradiation on solids", Nucl. Instrum. Methods Phys. Res. B **164/165**, 415–419 (2000).

V. V. Krishunamurthy, I. Watanabe, K. Nagamine, H. Kuwahara, and Y. Tokura: "Critical spin dynamics in $Nd_{1-x}Sr_xMnO_3$ with $x \approx 0.5$", Phys. Rev. B **61**, 4060–4069 (2000).

M. Matsuda, K. Katsumata, R. S. Eccleston, S. Brehmer, and H.-J. Mikeska: "Magnetic excitations and exchange interactions in the spin-1/2 two-leg ladder compound $La_6Ca_8Cu_{24}O_{41}$", Phys. Rev. B **62**, 8903–8908 (2000).

N. Nishida, S. Kaneko, H. Sakata, H. Kajiwara, M. Matsumoto, T. Mochiku, K. Hirata, and T. Kambara: "Studies of boundary effects and symmetry of Cooper pairing in $Bi_2Sr_2CaCu_2O_x$ by LT-STS", Physica B **284/288**, 967–968 (2000).

V. Krishnamurthy, K. Nagamine, I. Watanabe, K. Nishiyama, S. Ohira, M. Ishikawa, D. H. Eom, and T. Ishikawa: "Non-Fermi liquid behavior in $CeCoGe_{3-x}Si_x$ alloys", Physica B **289**, 47–51 (2000).

V. Krishnamurthy, I. Watanabe, K. Nagamine, H. Kuwahara, and Y. Tokura: "Spin dynamics in $Nd_{1-x}Sr_xMnO_3$ with x = 0.5", Physica B **289**, 56–60 (2000).

S. Ohira, T. Ishida, T. Nogami, I. Watanabe, F. L. Pratt, and K. Nagamine: "μSR studies on the organic radical magnet, 4-arylmethyleneamino-TEMPO", Physica B **289**, 123–127 (2000).

T. M. Briere, J. Jeong, T. P. Das, S. Ohira, and K. Nagamine: "Ab initio molecular orbital studies of the positive muon and muonium in 4-arylmethyleneamino-TEMPO derivatives", Physica B **289**, 128–131 (2000).

J. Jeong, T. M. Briere, N. Sahoo, T. P. Das, S. Ohira, K. Nishiyama, and K. Nagamine: "Hartree-Fock investigation of muon trapping in the chemical ferromagnet 4-(*p*-chlorobenzylideneamino)-TEMPO", Physica B **289**, 132–136 (2000).

M. Matsuda, I. Watanabe, and K. Nagamine: "Magnetic ordering in $La_2Cu_2O_5$", Physica B **289**, 161–164 (2000).

M. Mekata, K. M. Kojima, I. Watanabe, K. Nagamine, and H. Ikeda: "Magnetic ordering and fluctuations in Ising spin nets $Rb_2Co_{1-x}Mg_xF_4$", Physica B **289**, 194–197 (2000).

J. Arai, T. Ishiguro, M. Hirai, H. Shinmen, J. Yokoyama, I. Watanabe, and K. Nagamine: "Zn-induced magnetic order detected by μSR around $x = \frac{1}{8}$ in $La_{2-x}Sr_xCu_{1-y}Zn_yO_4$", Physica B **289**, 347–350 (2000).

F. L. Pratt, S. J. Blundell, Th. Jestädt, B. W. Lovett, A. Husmann, I. M. Marshall, W. Hayes, A. Monkman, I. Watanabe, K. Nagamine, R. E. Martin, and A. B. Holmes: "μSR of conducting and non-conducting polymers", Physica B **289**, 625–630 (2000).

Y. Miyake, K. Shimomura, Y. Matsuda, R. J. Scheuermann, P. Bakule, S. Makimura, P. Strasser, S. N. Nakamura, K. Ishida, T. Matsuzaki, I. Watanabe, and K. Nagamine: "Construction of the experimental set-up for ultra slow muon generation by thermal Mu ionization method at RIKEN-RAL", Physica B **289**, 666–669 (2000).

A. Fukaya, I. Watanabe, S. Ohira, and K. Nagamine: "Radio-frequency muon spin resonance of Haldane-gap systems, $Ni(C_2H_8N_2)_2NO_2(ClO_4)$ and NiC_2O_4 2·(2-methylimidazole)", Physica B **289/290**, 185–188 (2000).

J. Kim, F. Saito, Y. Nagashima, T. Kurihara, A. Goto, Y. Itoh, and T. Hyodo: "The design of a spin-polarized slow positron beam", Rad. Phys. Chem. **58**, 759–762 (2000).

N. Suzuki, A. Takamori, J. Baba, J. Matsuda, T. Hyodo, Y. Okamoto, and H. Miyagi: "Positron annihilation study of high impact polystyrene", Radiat. Phys. Chem. **58**, 593–596 (2000).

N. Suzuki, Y. Nagai, and T. Hyodo: "Can a newly developed AMOC technique be applied to determine the *para*-positronium lifetime?", Radiat. Phys. Chem. **58**, 777–780 (2000).

H. Torii, Y. Morishita, Y. Yamazaki, K. Komaki, K. Kuroki, R. Hutton, K. Ishii, K. Ando, H. Masuda, M. Sekiguchi, M. Hori, E. Widmann, and R. S. Hayano: "Spectroscopy of high Rydberg states of highly charged ions and antiprotonic helium atoms", RIKEN Rev., No. 31, pp. 30–33 (2000).

Y. Iwai, S. Thuriez, Y. Kanai, H. Oyama, K. Ando, R. Hutton, H. Masuda, K. Nishio, K. Komaki, and Y. Yamazaki: "High-resolution soft X-ray measurements in slow Ne^{9+} ions transmitted through a microcapillary", RIKEN Rev., No. 31, pp. 34–37 (2000).

Y. Nakai, T. Kambara, K. Ando, H. Oyama, and Y. Yamazaki: "Plan of multiple ionization experiment with ultra fast TW-laser in RIKEN", RIKEN Rev., No. 31, pp. 45–47 (2000).

M. Wada, I. Katayama, S. Okada, Y. Ishida, T. Nakamura, Y. Nakai, T. M. Kojima, Y. Kanai, T. Kambara, Y. Yamazaki, Y. Okada, K. Noda, H. Kawakami, and S. Ohtani: "Slow or trapped RI-beams from projectile fragment separators and their laser spectroscopy", RIKEN Rev., No. 31, pp. 56–58 (2000).

Y. Kanai, D. Dumitriu, Y. Iwai, T. Kambara, M. Kitajima, T. M. Kojima, A. Mohri, Y. Morishita, Y. Nakai, N. Oshima, H. Oyama, M. Wada, and Y. Yamazaki: "Present status of slow highly charged ion facility at RIKEN", RIKEN Rev., No. 31, pp. 62–64 (2000).

N. Oshima, T. M. Kojima, D. Dumitriu, A. Mohri, H. Oyama, T. Kambara, Y. Kanai, Y. Nakai, M. Wada, and Y. Yamazaki: "A new positron accumulator with electron plasma", RIKEN Rev., No. 31, pp. 65–69 (2000).

T. M. Kojima, N. Oshima, D. Dumitriu, H. Oyama, A. Mohri, and Y. Yamazaki: "An ion trap for cooling MCIs with cold positrons", RIKEN Rev., No. 31, pp. 70–73 (2000).

H. M. Shimizu, T. Ikeda, H. Kato, K. Kawai, H. Miyasaka, T. Oku, W. Ootani, C. Otani, H. Sato, Y. Takizawa, and H. Watanabe: "Development of superconductor radiation detectors", RIKEN Rev., No. 31, pp. 74–80 (2000).

E. Yagi: "The study on the state of hydrogen dissolved in metals by means of the channelling method", Zairyo to Kankyo **49**, 282–287 (2000).

4. Radiochemistry, radiation chemistry, and radiation biology

K. Matsumoto: "Foliar uptake and translocation of radionuclides in plants", Data Base for Nuclear Base Technology, Radiation Application Development Association, No. 160006 (1998).

Y. Einaga, O. Sato, T. Iyoda, Y. Kobayashi, F. Ambe, K. Hashimoto, and A. Fujishima: "Characterization of cobalt iron cyanide by ^{57}Fe Mössbauer spectroscopy", Hyperfine Interact. C **3**, 236–239 (1998).

Y. Kobayashi, Y. Yoshida, A. Yoshida, Y. Watanabe, N. Aoi, K. Hayakawa, K. Yukihira, S. Nasu, J. Nakamura, and F. Ambe: "In-beam Mössbauer spectroscopy for materials science at RIKEN accelerator research facility", Proc. Specialist Research Meet. on Solid State Physics with Probes of Radiations and Nuclei, edited by S. Nasu, Y. Kawase, and Y. Maeda, Research Reactor Institute, Kyoto University, pp. 88–90 (1998).

Y. Einaga, O. Sato, T. Iyoda, Y. Kobayashi, F. Ambe, K. Hashimoto, and A. Fujishima: "Characterization of cobalt-iron cyanide by ^{57}Fe Mössbauer spectroscopy", Proc. Specialist Research Meet. on Solid State Physics with Probes of Radiations and Nuclei, edited by S. Nasu, Y. Kawase, and Y. Maeda, Research Reactor Institute, Kyoto University, pp. 114–117 (1998).

S. Enomoto and N. Takematsu: "Theoretical consideration on the distribution of rare earth elements in various organs of rats and mice", Biomed. Res. Trace Elements **10**, 53–56 (1999).

S. Ambe: "Multitracer studies on the absorption of radionuclides via plant roots", Data Base for Nuclear Base Technology, Radiation Application Development Association, No. 160005 (1999).

T. Arie: "Stidies on the foliar uptake of radionuclides in the air and their translocation in soybean plant", Data Base for Nuclear Base Technology, Radiation Application Development Association, No. 160013 (1999).

T. Shinonaga: "Studies on the uptake of radionuclides by various plants from soil and on the subcellular distribution of radionuclides in plants", Data Base for Nuclear Base Technology, Radiation Application Development Association, No. 160014 (1999).

C. H. Bae, T. Abe, H.-Y. Lee, D.-C. Kim, K.-S. Min, K.-S. Choi, T. Matsuyama, T. Nakano, and S. Yoshida: "Characterization of albino tobaccos (*Nicotiana tabacum* L.) derived from leaf blade-segments cultured *in vitro*", J. Plant Biotech. **1**, 101–107 (1999).

T. Funayama, I. Narumi, M. Kikuchi, S. Kitayama, H. Watanabe, and K. Yamamoto: "Identification and disruption analysis of the *recN* gene in the extremely

radioresistant bacterium *Deinococcus radiodurans*", Mutat. Res. **435**, 151–161 (1999).
H. Wang, N. Takematsu, and S. Ambe: "Effects of soil acidity on the uptake of trace elements in soybean and tomato plants", Appl. Radiat. Isot. **52**, 803–811 (2000).
H. Tamano, E. Igasaki, S. Enomoto, N. Oku, N. Itoh, T. Kimura, K. Tanaka, and A. Takeda: "Hepatic zinc response via metallothionein induction after tumor transplantation", Biochem. Biophys. Res. Commun. **270**, 1140–1143 (2000).
K. Ushida, M. Hase, K. Ishioka, and M. Kitajima: "Use of coherent phonon spectroscopy as a probe for distribution of defects in solids", Nonlinear Opt. **26**, 145–152 (2000).
F. Saito, Y. Nagashima, T. Kurihara, I. Fujiwara, R. Iwata, N. Suzuki, Y. Itoh, A. Goto, and T. Hyodo: "Spot ^{18}F positron source electro-deposited on a graphite rod", Nucl. Instrum. Methods Phys. Res. A **450**, 491–494 (2000).
T. Matsuyama, T. Abe, C.-H. Bae, Y. Takahashi, R. Kiuchi, T. Nakano, T. Asami, and S. Yoshida: "Adaptation of Restriction Landmark Genomic Scanning (RLGS) to plant genome analysis", Plant Mol. Biol. Rep. **18**, 331–338 (2000).
C. H. Bae, T. Abe, N. Nagata, N. Fukunishi, T. Matsuyama, T. Nakano, and S. Yoshida: "Characterization of a periclinal chimera variegated tabacco (*Nicotiana tabacum* L.)", Plant Sci. **151**, 93–101 (2000).
F. Saito, N. Suzuki, Y. Itoh, A. Goto, I. Fujiwara, T. Kurihara, R. Iwata, Y. Nagashima, and T. Hyodo: "Automatic ^{18}F positron source supply system for a monoenergetic positron beam", Rad. Phys. Chem. **58**, 755–757 (2000).
K. Ushida, M. Hase, K. Ishioka, and M. Kitajima: "Study on ion-irradiated materials as probed by coherent phonon spectroscopy", Radiat. Chem., No. 70, pp. 26–30 (2000).
H. Suzuki, H. Kumagaya, K. Oohashi, S. Enomoto, and F. Ambe: "Uptake of 15 trace elements in arbuscular mycorrhizal marigold measured by the multitracer technique", Soil Sci. Plant Nutr. **46**, 283–289 (2000).

5. Material analysis

K. Kholmurodov, K. Yasuoka, T. Ebisuzaki, and B. Smith: "Tuning DL_POLY for vector computers", HPC Profile, No. 24, pp. 10–11 (1999).
J. Kawai, K. Hayashi, and K. Maeda: "EXEFS", Adv. X-ray Anal. **42**, 83–90 (2000).
H. Hamanaka, T. Hasegawa, K. Hasegawa, K. Maeda, and S. Yumoto: "PIXE analysis of Al compounds using a wavelength-dispersive spectrometer with PSPC(3)", Report of Research Center of Ion Beam Technology Hosei University, No. Suppl.18, pp. 139–140 (2000).
J. Kawai, Y. Mizutani, T. Sugimura, M. Sai, T. Higuchi, Y. Harada, Y. Ishiwata, A. Fukushima, M. Fujisawa, M. Watanabe, K. Maeda, S. Shin, and Y. Gohshi: "High resolution soft X-ray absorption spectroscopy for the chemical state analysis of Mn", Spectrochim. Acta B **55**, 1385–1395 (2000).

6. RIKEN-BNL Collaboration on Spin Physics Program

K. Itakura and S. Maedan: "Effects of topology on the light front", **Nucl. Phys. A 670,** 76c–79c (2000).
D. Boer, R. Jakob, and P. J. Mulders: "Angular dependences in electroweak semi-inclusive leptoproduction", Nucl. Phys. B **564**, 471–485 (2000).
D. Boer and P. J. Mulders: "Color gauge invariance in the Drell-Yan process", Nucl. Phys. B **569**, 505–526 (2000).
K. Itakura and S. Maedan: "Dynamical chiral symmetry breaking on the light front: DLCQ approach", Phys. Rev. D **61**, 045009-1–045009-18 (2000).
D. T. Son and M. A. Stephanov: "Inverse meson mass ordering in the color-flavor-locking phase of high-density QCD", Phys. Rev. D **61**, 074012-1–074012-8 (2000).
K. Itakura and S. Maedan: "Dynamical chiral symmentry breaking on the light front II: The Nambu-Jona-Lasinio model", Phys. Rev. D **62**, 15016-1–15016-19 (2000).
K. Suzuki, A. Hayashigaki, K. Itakura, J. Alam, and T. Hatsuda: "Validity of the color dopole approximation for diffractive production of heavy quarkonium", Phys. Rev. D **62**, 031501-1–031501-4 (2000).
D. Boer: "Double transverse spin asymmetries in vector boson production", Phys. Rev. D **62**, 094029-1–094029-9 (2000).
D. T. Son: "Hydrodynamics of nuclear matter in the chiral limit", Phys. Rev. Lett. **84**, 3771–3774 (2000).
D. T. Son and M. A. Stephanov: "QCD at finite isospin density", Phys. Rev. Lett. **86**, 592–595 (2000).
D. Boer: "Transverse polarization distribution and fragmentation functions", RIKEN Rev., No. 28, pp. 26–30 (2000).

VIII. LIST OF PREPRINTS

2000

RIKEN-AF-NP

338 T. Suzuki, R. Kanungo, O. Bochkarev, L. Chulkov, D. Cortina, M. Fukuda, H. Geissel, M. Hellstrom, M. Ivanov, R. Janik, K. Kimura, T. Kobayashi, A. A. Korsheninnikov, G. Munzenberg, F. Nickel, A. A. Ogloblin, A. Ozawa, M. Pfützner, V. Pribora, and H. Simon: "Nuclear radii of ^{17,19}B and ^{14}Be"

339 R. Kanungo, I. Tanihata, and C. Samanta: "Soft dipole resonance in ^{11}Li"

340 K. Sugawara-Tanabe, S. Yamaji, and A. Arima: "The pseudospin symmetry in the Dirac equatin with deformed potential"

341 T. Suzuki: "A few topics on giant resonance states"

342 Y. Goto, N. Hayashi, M. Hirai, H. Horikawa, S. Kumano, M. Miyama, T. Morii, N. Saito, T.-A. Shibata, E. Taniguchi, and T. Yamanishi: "Polarized parton distribution functions in the nucleon"

343 Y. M. Zhao, R. F. Casten, and A. Arima: "The NpNn scheme for heavy odd-A and doubly odd nuclei"

344 Y. M. Zhao, R. F. Casten, and A. Arima: "Effective valence proton numbers for nuclei near the Z = 64 subshell"

345 N. Itagaki, S. Okabe, and K. Ikeda: "Important role of the spin-orbit interaction in forming the $1/2^+$ orbital structure in Be isotopes"

346 N. Dinh Dang and A. Arima: "Extended renormalized random phase approximation"

347 H. Iwasaki, T. Motobayashi, H. Akiyoshi, Y. Ando, N. Fukuda, H. Fujiwara, Zs. Fülöp, K. I. Hahn, Y. Higurashi, M. Hirai, I. Hisanaga, N. Iwasa, T. Kijima, T. Minemura, T. Nakamura, M. Notani, S. Ozawa, H. Sakurai, S. Shimoura, S. Takeuchi, T. Teranishi, Y. Yanagisawa, and M. Ishihara: "Quadrupole deformation of ^{12}Be studied by proton inelastic scattering"

348 S. Ishimoto, T. Kobayashi, K. Morimoto, I. Nomura, S. Suzuki, Y. Takahashi, I. Tanihata, and T. Tsuru: "A windowless solid hydrogen target"

349 N. Dinh Dang, V. Kim. Au, and A. Arima: "Electromagnetic cross sections of double giant dipole resonances in ^{136}Xe and ^{208}Pb within the phonon damping model"

350 A. Ozawa, T. Kobayashi, T. Suzuki, K. Yoshida, and I. Tanihata: "A new magic number, N = 16, near to the neutron drip-line"

351 A. Ozawa, O. Bochkarev, L. Chulkov, D. Cotia, H. Geissel, M. Helstrom, M. Ivanov, R. Janik, K. Kimura, T. Kobayashi, A. A. Korsheninnikov, G. Munzenberg, F. Nickel, A. A. Ogloblin, M. Pfützner, V. Pribora, H. Simon, B. Sitar, P. Strmen, K. Sümmerer, T. Suzuki, I. Tanihata, M. Winkler, and K. Yoshida: "Production cross-sections of light neutron-rich nuclei from ^{40}Ar fragmentation at about 1 GeV/nucleon"

352 R. Kanungo, I. Tanihata, Y. Ogawa, H. Toki, and A. Ozawa: "Halo structure in ^{19}C: Aglauber model analysis"

353 H. Kurasawa and T. Suzuki: "Effects of the neutron spin-orbit density on nuclear charge density in relativistic models"

354 S. Ishimoto, T. Kobayashi, K. Morimoto, I. Nomura, S. Suzuki, Y. Takahashi, I. Tanihata, and T. Tsuru: "Topological modes of solidification in liquids with a confined geometry"

355 S.-G. Zhou, J. Meng, and S. Yamaji: "Relativistic mean field description of nitrogen isotopes"

356 N. Dinh Dang: "Description of single- and multiple-phonon giant dipole resonances within the phonon damping model"

357 H. Iwasaki, T. Motobayashi, H. Akiyoshi, Y. Ando, N. Fukuda, H. Fujiwara, Zs. Fülöp, K. I. Hahn, Y. Higurashi, M. Hirai, I. Hisanaga, N. Iwasa, T. Kijima, A. Mengoni, T. Minemura, T. Nakamura, M. Notani, S. Ozawa, H. Sagawa, H. Sakurai, S. Shimoura, S. Takeuchi, T. Teranishi, Y. Yanagisawa, and M. Ishihara: "Low lying intruder 1-state in ^{12}Be and the melting of the N = 8 shell closure"

358 H. Madokoro, J. Meng, M. Matsuzaki, and S. Yamaji: "Relativistic mean field description for the shears band mechanism in ^{84}Rb"

359 N. Saito: "Polarized parton distribution functions in the nucleon"

360 G. Bunce, N. Saito, J. Soffer, and W. Vogelsong: "Prospects for spin physics at RHIC"

361 N. Dinh Dang, A. Ansari, and A. Arima: "Angular-momentum effect on the width of hot giant dipole resonance within the phonon damping model"

362 A. Ansari, N. Dinh Dang, and A. Arima: "Thermal shape and orientation fluctuation corrections for the hot giant dipole resonance within the static path approximation"

363 Y. M. Zhao and A. Arima: "On predominance of 0^+ ground states in even-even many-body system using random two-body interactions: Single-j cases"

364 H. Sagawa, T. Suzuki, H. Iwasaki, and M. Ishihara: "Low energy dipole strength in light drip line nuclei"

365 K. Yoneda, H. Sakurai, T. Gomi, T. Motobayashi, N. Aoi, N. Fukuda, U. Futakami, Z. Gacsi, Y. Higurashi, N. Imai, N. Iwasa, H. Iwasaki, T. Kubo, M. Kunibu, M. Kurokawa, Z. Liu, T. Minemura, A. Saito, M. Serata, S. Shimoura, S. Takeuchi, Y. X. Watanabe, K. Yamada, Y. Yanagisawa, K. Yogo, A. Yoshida, and M. Ishihara: "Large deformation of the neutron-rich isotope ^{34}Mg from in-beam γ-ray spectroscopy using RI beam fragmentation"

366 Y. Goto: "Sensitivities of the gluon polarization measurement at PHENIX"

367 K. Kurita: "Study of the spin structure of the nucleon with RHIC-PHENIX"

368 Y. M. Zhao, R. F. Casten, and A. Arima: "Systematics of nuclear deformation for large regions"

369 H. Kumagai, A. Ozawa, N. Fukuda, K. Sümmerer, and I. Tanihata: "Delay-line PPAC to high-energy light ions"

370 A. Arima, W. Bentz, T. Suzuki, and T. Suzuki: "Delta-hole interaction in nuclei and the Gamow-Teller strength in ^{90}Nb*"

371 K. Asahi, K. Sakai, H. Ogawa, H. Miyoshi, K. Yogo, A. Goto, T. Suga, H. Ueno, Y. Kobayashi, A. Yoshimi, T. Kubo, Y. X. Watanabe, H. Imai, K. Yoneda, N. Fukuda, N. Aoi, M. Ishihara, W.-D. Schmidt-Ott, G. Neyens, and S. Teughels: "Electromagnetic moments of neutron-rich nuclei measured with polarized radioactive ion beams"

372 T. Motobayashi: "Nuclear astrophysics experiments with intermediate-energy radioactive ion beams"

373 I. Tanihata: "Nuclear radii and change in shell structure a halo driven new magic number N = 16"

374 N. Dinh Dang, V. Kim. Au, T. Suzuki, and A. Arima: "Pygmy and giant dipole resonances in neutron-rich nuclei within quasiparticle representation of phonon damping model"

375 M. Ishihara: "In-beam gamma-ray spectroscopy with RIB on very neutron-rich nuclei"

376 A. Ozawa, O. Bochkarev, L. Chulkov, D. Cortina, H. Geissel, M. Hellstrom, M. Ivanov, R. Janik, K. Kimura, T. Kobayashi, A. A. Korsheninnikov, G. Munzenberg, F. Nickel, Y. Ogawa, A. A. Ogloblin, M. Pfützner, V. Pribora, H. Simon, B. Sitar, P. Strmen, K. Sümmerer, T. Suzuki, I. Tanihata, M. Winkler, and K. Yoshida: "Measuremets of interaction cross-sections for light neutron-rich nuclei at relativistic energies and determination of effective matter radii"

377 N. Dinh Dang, T. Suzuki, and A. Arima: "Description of Gamow-Teller resonance within phonon damping model"

378 M. Hirai, H. Kobayashi, and M. Miyama: "Determination of polarized parton distribution functions"

379 M. Petrascu, I. Tanihata, K. Morimoto, T. Kobayashi, K. Katori, I. Cruceru, M. Giurgiu, A. Isbasescu, H. Petrascu, R. Ruscu, M. Chiba, S. Nishimura, A. Ozawa, T. Suda, K. Yoshida, C. Bordeanu, and A. Tudorica: "Neutron pair pre-emission in the fusion of ^{11}Li halo nuclei with Si targets"

380 N. Dinh Dang and A. Arima: "Phonon damping model using random-phase-approximation operators"

RIKEN-AF-NC

17 Y. K. Batygin: "Particle-in-cell code BEAMPATH for beam dynamics simulations with space charge"

18 P. Zenkevich, T. Katayama, and A. Sidorin: "Problems of ion beam stability for MUSES storage rings"

19 A. Sidorin and I. Mesh: "Ion bunch stability in the double storage ring"

20 E. Syresin and T. Tanabe: "A proposal and simulations of a DSR electron cooling system"

21 A. Siminov, A. Sidorin, E. Syresin, I. Meshkov, T. Tanabe, and T. Katayama: "Computer simulation of ECOOL and IBS process in ACR and DSR using BETACOOL program"

22 T. Katayama and D. Koshkarev: "New injection scheme for accumulator cooler ring"

23 D. Koshkarev: "Electron cooling and intrabeam scattering"

24 G. Shirkov, Y. Alexandrov, V. Presendorf, V. Shevtsov, R. Komisarov, M. Koryovkina, E. Shirkova, O. Stekalovsky, N. Tokareva, A. Tuzikov, V. Vatulin, E. Vasina, V. Fomin, A. Anisimov, R. Veselov, A. Golubev, S. Grushin, V. Povyshev, A. Sadovoi, and E. Don: "Physical and numerical basement of ECR plasma simulation with particle-in-cell model"

25 A. Sidorin, P. Zenkevich, A. Bolshakov, and T, Katayama: "Optimization of intense ion beam parameters on ACR by use of the electron cooling system"

IX. PAPERS PRESENTED AT MEETINGS

1. Accelerator development and accelerator physics

T. Uesaka, T. Wakui, T. Ohnishi, H. Okamura, Y. Satou, S. Ishida, N. Sakamoto, H. Otsu, T. Wakasa, T. Nonaka, G. Yokoyama, K. Itoh, K. Sekiguchi, S. Haruyama, T. Ikeda, M. Wakasugi, H. Sakai, and Y. Yano: "Polarized ^{3}He project at RIKEN", 7th RCNP Int. Workshop on Polarized ^{3}He Beams and Gas Targets and Their Application, Kobe, Jan. (1996).

S. Watanabe and T. Katayama: "Power supply system for the RIKEN-MUSES project", 6th European Particle Accelerator Conf. (EPAC '98), (MSL), Stockholm, Sweden, June (1998).

T. Kawaguchi, H. Okuno, A. Goto, T. Mitsumoto, T. Kubo, T. Tominaka, J.-W. Kim, K. Ikegami, and Y. Yano: "Design of the sector magnets for the RIKEN superconducting ring cyclotron", 15th Int. Conf. on Cyclotrons and Their Applications (Cyclotrons '98), (GANIL), Caen, France, June (1998).

T. Kawaguchi, H. Okuno, A. Goto, T. Mitsumoto, T. Tominaka, and Y. Yano: "Design of structure and quench-stability of sector magnets for RIKEN superconducting ring cyclotron", Applied Superconductivity 98, (LBL), Parm Springs, USA, Sept. (1998).

M. Takanaka and T. Katayama: "Transverse instability due to the space charge during the electron-cooling bunching of ion beams", 1999 Particle Accelerator Conf., (Brookhaven National Laboratory), New York, USA, Mar. (1999).

T. Kurita, T. Nakagawa, T. Kawaguchi, and S. M. Lee: "Design of electron cyclotron resonance ion source using liquid-helium-free superconducting solenoid coils", 8th Int. Conf. on Ion Sources (ICIS '99), (Kyoto University), Kyoto, Sept. (1999).

T. Hirumachi, T. Tominaka, T. Kubo, H. Sakurai, T. Nagahuchi, K. Kusaka, M. Okamura, T. Fujioka, T. Tsuchihashi, O. Osaki, T. Senba, and S. Suzuki: "Design of a superferric quadrupole magnet for the RIKEN RI-Beam Factory project", 16th Int. Conf. on Magnet Technology (MT16), (National High Magnetic Field Laboratory), Ponte Vedre Beach, USA, Sept. (1999).

N. Sakamoto: "Model test of the RIKEN-IRC main resonator", 12th Symp. on Accelerator Science and Technology, Wako, Oct. (1999).

N. Sakamoto: "Design of the RIKEN-SRC RF system", 12th Symp. on Accelerator Science and Technology, Wako, Oct. (1999).

S. Kohara, O. Kamigaito, M. Kase, E. Ikezawa, Y. Miyazawa, T. Chiba, and A. Goto: "Model test of a resonator for flat-top acceleration system in the RIKEN AVF cyclotron", 12th Symp. on Accelerator Science and Technology, Wako, Oct. (1999).

T. Tanabe, T. Rizawa, K. Ohtomo, T. Katayama, E. Syresin, A. Sidorin, and I. Meshkov: "Electron coolers for the MUSES project", 12th Symp. on Accelerator Science and Technology, Wako, Oct. (1999).

S. Bhattacharjee and H. Amemiya: "General properties of high power short pulse microwave plasmas", 17th Symp. on Plasma Processing, (The Association of Super-advanced Electronics Technologies (ASET)), Nagasaki, Jan. (2000).

A. Goto and Y. Yano: "Construction of the superconducting ring cyclotron for the RIKEN RI-Beam Factory", 1st Workshop on Future Plan for Ion Beam Application at JEARI-Takasaki, Takasaki, Feb. (2000).

T. Takeuchi, T. Katayama, T. Nakagawa, M. Okamura, K. Yano, B. Sharkov, S. Kondrashev, and A. Shumshurov: "Laser ion source for RIKEN MUSES project", 7th European Particle Accelerator Conf. (EPAC2000), Vienna, Austria, June (2000).

T. Takeuchi, T. Katayama, T. Nakagawa, M. Okamura, K. Yano, B. Sharkov, and S. Kondrashev: "Laser ion source for RIKEN MUSES project", 7th European Particle Accelerator Conf. (EPAC2000), Vienna, Austria, June (2000).

K. Ohtomo, N. Inabe, T. Katayama, T. Tanabe, and M. Wakasugi: "New lattice design of Accumulator Cooler Ring for MUSES", 7th European Particle Accelerator Conf. (EPAC2000), Vienna, Austria, June (2000).

K. Ohtomo, Y. Chiba, T. Rizawa, and M. Wakasugi: "Ferrite evaluation test for MUSES", 7th European Particle Accelerator Conf. (EPAC2000), Vienna, Austria, June (2000).

T. Rizawa, T. Katayama, T. Tanabe, S. Takama, and A. Yamashita: "Design study of the ACR electron-cooler for RIBF", 7th European Particle Accelerator Conf. (EPAC2000), Vienna, Austria, June (2000).

T. Tanabe, T. Masuoka, and M. Kase: "Preliminary design of RIBF control system using CORBA and RTOS", 7th European Particle Accelerator Conf. (EPAC2000), Vienna, Austria, June (2000).

S. Bhattacharjee: "Interpulse plasmas of high power short pulse microwaves", 27th IEEE Int. Conf. on Plasma Science (ICOPS 2000), New Orleans, USA, June (2000).

H. Hasebe, E. Ikezawa, Y. Miyazawa, M. Hemmi, T. Aihara, T. Ohki, and H. Yamauchi: "Development of long-life carbon-foil by flashlight irradiation method", 24th Linear Accelerator Meet. in Japan, (Hokkaido University), Sapporo, July (2000).

A. Goto: "Beam dynamics in cyclotrons", Accelerator School 2000, (BATAN), Yogyakarta, Indonesia, Sept. (2000).

2. Nuclear physics and nuclear instrumentation

Y. Gono: "In-beam gamma-ray spectroscopy", Int. Workshop on JHF Science (JHF98), (KEK), Tsukuba, Mar. (1998).

Y. Gono: "A windowless gas target for secondary beam production", 19th World Conf. of INTDS, Nuclear Targets Preparation, Characterization and Use, (Oak Ridge National Laboratory), Oak Ridge, USA, Oct. (1998).

A. Goto, K. Sakai, T. Suzuki, K. Yogo, K. Asahi, H. Ogawa, A. Yoshimi, M. Nagakura, T. Suga, M. Utsuro, and M. Hino: "Measurement of energy distribution in spallation neutron source for Sisythus UCN production method", 1999 Fall Meet. of Physical Society of Japan, Matsue, Jan. (1999).

K. Morimoto, F. Tokanai, M. Nishimura, and I. Tanihata: "Development of beam monitor using scintillating fiber", 54th Ann. Meet. of Physical Society of Japan, Higashihiroshima, Mar. (1999).

N. Dinh Dang and U. Garg: "Introduction to the proceedings on Selected Topics in Nuclear Collective Excitations", RIKEN Symp. and Workshop on Selected Topics in Nuclear Collective Excitations, Wako, Mar. (1999).

N. Dinh Dang, K. Tanabe, and A. Arima: "Microscopic description of the hot giant dipole resonance", RIKEN Symp. and Workshop on Selected Topics in Nuclear Collective Excitations, Wako, Mar. (1999).

N. Dinh Dang, K. Tanabe, and A. Arima: "Damping of giant dipole resonance as a probe into the order-to-chaos transition in hot nuclei", RIKEN Symp. and Workshop on Selected Topics in Nuclear Collective Excitations, Wako, Mar. (1999).

K. Asahi, H. Ogawa, K. Sakai, A. Yoshimi, M. Tsuda, Y. Uchiyama, T. Suzuki, K. Suzuki, N. Kurokawa, M. Adachi, A. Yoshida, S. Fukuda, M. Notani, T. Kubo, H. Okuno, H. Sato, N. Fukunishi, N. Aoi, K. Yoneda, H. Iwasaki, N. Fukuda, M. Ishihara, H. Izumi, H. Ueno, T. Shimoda, S. Tanimoto, N. Takahashi, H. Miyatake, W. D. Schmidt-Ott, and M. Schoefer: "Nuclear moments measurements with polarized radioactive beams", 4th Int. Workshop on Laser Spectroscopy on Beams of Radioactive Nuclei, (Adam Mickiewicz University), Poznan, Poland, May (1999).

T. Suda: "Photodisintegration of few-nucleon systems", Nuclear Science Seminar, (University of Tokyo), Tokyo, May (1999).

T. Nakatsukasa: "Selfconsistent determination of collective coordinates", Nuclear Theory Seminar at Niigata University, Niigata, May (1999).

T. Nakatsukasa: "Selfconsistent determination of collective coordinates", Seminar at Nuclear Theory Group of University of Tokyo, Tokyo, May (1999).

T. Nakatsukasa: "Selfconsistent determination of collective coordinates", Nuclear Theory Colloquium at Kyoto University, Kyoto, June (1999).

T. Nakatsukasa: "Selfconsistent determination of collective subspace", Nuclear Theory Seminar at Tokyo Metropolitan University, Hachioji, June (1999).

Y. Mochizuki: "Exotic nuclear rod model for the origin of neutron star glitches", Seminar at National Astronomy Observatory, Mitaka, June (1999).

T. Nakatsukasa: "Determination of collective coordinates for low-energy collective motion", Nuclear Theory Seminar at Chiba University, Chiba, July (1999).

H. Sakai, K. Sekiguchi, H. Kato, A. Tamii, T. Ohnishi, K. Yako, S. Sakoda, Y. Maeda, M. Hatano, N. Sakamoto, T. Uesaka, Y. Satou, H. Okamura, K. Suda, and T. Wakasa: "Precise measurement of $d\ p$ elastic scattering at 270 MeV", Asia Pacific Conf. on Few-Body Problems in Physics (APFB 99), (Science University of Tokyo), Kashiwa, Aug. (1999).

T. Ohnishi, H. Sakai, H. Okamura, S. Ishida, H. Otsu, N. Sakamoto, T. Uesaka, T. Wakasa, Y. Satou, and T. Nonaka: "Measurement of deuteron elastic scattering at $E_d = 270$ MeV and a comparison with sudden approximation", Asia Pacific Conf. on Few-Body Problems in Physics (APFB 99), (Science University of Tokyo), Kashiwa, Aug. (1999).

Y. Mochizuki: "^{44}Ti in Cas A as a test of models of core collapse supernovae", Int. Conf. on Astrophysics at High T and Low Tau, (RIKEN & Ohio State University), Sedona, USA, Aug. (1999).

K. Katori: "Roles of nucleon spin in nuclear structure", Polusion99, (RCNP of Osaka University), Osaka, Aug. (1999).

R. Kanungo, I. Tanihata, Y. Ogawa, A. Ozawa, and H. Toki: "Halo structure in ^{19}C", 1999 Fall Meet. of Physical Society of Japan, Matsue, Sept. (1999).

A. Yoshimi, K. Asahi, K. Sakai, H. Ogawa, T. Suzuki, M. Nagakura, T. Suga, A. Goto, and K. Yogo: "The characteristics of ^{129}Xe nuclear spin maser", 1999 Fall Meet. of Physical Society of Japan, Matsue, Sept. (1999).

K. Sakai, Y. Uchiyama, T. Suzuki, M. Nagakura, A. Goto, K. Asahi, H. Ogawa, A. Yoshimi, Y. Mizumura, K. Yogo, T. Suga, M. Utsuro, K. Okumura, and M. Hino: "Spin-flip magnetic deceleration of neutrons for the UCN production (I)", 1999 Fall Meet. of Physical Society of Japan, Matsue, Sept. (1999).

Y. Mochizuki: "Exotic nuclear rod model for the origin of neutron star glitches", 1999 Fall Meet. of Physical Society of Japan, Matsue, Sept. (1999).

A. Ozawa: "Measurements of interaction cross sections for unstable nuclei", Fuantei-kaku, Hyper-Kaku Goudou Benkyoukai, (Ministry of Education, Science, Sports and Culture), Wako, Sept. (1999).

K. Asahi: "Nuclear moments measurements with polarized radioactive nuclear beams at RIKEN", Int. Workshop on Symmetry and Spin, (Faculty of Math-

ematics and Physics, Charles University), Prague, Czech Republic, Sept. (1999).

Y. Mochizuki: "Exotic nuclear rod model for the origin of neutron star glitches", Seminar at Tokyo Institute of Technology, Tokyo, Sept. (1999).

T. Suda: "Photodisintegration reactions of ^{3}He and ^{4}He at TAGX", 2nd KEK-Tanashi Int. Symp. on Hadron and Nuclear Physics with Electromagnetic Probes, Tanashi, Oct. (1999).

Y. Watanabe, N. Shimizu, S. Haruyama, M. Honma, T. Mizusaki, A. Taketani, Y. Utsuno, and T. Otsuka: "A workstation farm optimized for Monte Carlo Shell Model calculations: Alphleet", 5th Int. Conf. on Computational Physics (ICCP5), (Kanazawa University), Kanazawa, Oct. (1999).

T. Otsuka, N. Shimizu, S. Haruyama, M. Honma, T. Mizusaki, A. Taketani, Y. Utsuno, and Y. Watanabe: "Monte Carlo Shell Model calculations for atomic nuclei and their parallel computing", 5th Int. Conf. on Computational Physics (ICCP5), (Kanazawa University), Kanazawa, Oct. (1999).

Y. Mochizuki: "Exotic nuclear rod model for the origin of neutron star glitches", Physical Society Meet. of Korea, Pusan, Korea, Oct. (1999).

R. Kanungo, I. Tanihata, and C. Samanta: "Inverse proton reactions of unstable nuclei with halo", RCNP-TMU Symp. on Spins in Nuclear and Hadronic Reactions, Ibaraki, Oct. (1999).

T. Suda: "eA (RI) collider for charge form factor measurements", Int. Workshop on Physics on eA Collider at MUSES, Wako, Nov. (1999).

S. Takeuchi, S. Shimoura, T. Motobayashi, H. Akiyoshi, Y. Ando, N. Aoi, Zs. Fülöp, T. Gomi, K. Higurashi, M. Hirai, N. Iwasa, H. Iwasaki, Y. Iwata, H. Kobayashi, M. Kurokawa, T. Minemura, S. Ozawa, H. Sakurai, M. Serata, T. Teranishi, K. Yamada, Y. Yanagisawa, Z. Liu, and M. Ishihara: "Charge exchange reaction of ^{14}Be", YITP Workshop on Structure and Reaction of Unstable Nuclei, Kyoto, Nov. (1999).

N. Dinh Dang and A. Arima: "Introduction to the proceedings on quasiparticle and phonon excitations in nuclei", RIKEN Int. Symp. on Quasiparticle and Phonon Excitations in Nuclei, Wako, Dec. (1999).

K. Morimoto: "Application for experiments using heavy ion beam", RIKEN Symp. on Application of Superconductor Radiation Detectors, STJ Workshop, Wako, Dec. (1999).

Y. Mochizuki: "Exotic nuclear rod model for the origin of neutron star glitches", Seminar at Tokyo Metropolitan University, Hachioji, Dec. (1999).

Y. Mochizuki: "^{44}Ti in Cas A, SN 1987A, and in laboratories", Seminar at University of Tokyo, Tokyo, Dec. (1999).

Y. Mochizuki: "Effective halflife of ionized ^{44}Ti and supernova remnants Cas A, RX J0852.0-4622", Symp. of Japanese Theoretical Astronomers, Tokyo, Dec. (1999).

T. Kishida: "The future project at the RIKEN Accelerator Research Facility", Workshop on Frontier of Gamma-ray Spectroscopy and Short-lived Nuclei, (JAERI), Tokaimura, Dec. (1999).

T. Nakatsukasa: "Extention of the RPA with Green's function method to deformed states", Workshop on Frontier of Gamma-ray Spectroscopy and Short-lived Nuclei, (JAERI), Tokaimura, Dec. (1999).

K. Sekiguchi, H. Sakai, and H. Okamura: "Measurement of cross section and analyzing powers for dp scattering at intermediate energies and three-nucleon force effects", 14th Int. Spin Physics Symp. (SPIN 2000), (Research Center for Nuclear Physics, Osaka University), Osaka, Jan. (2000).

Y. Mochizuki: "^{44}Ti in supernova remnants Cas A, RX J0852-4642", Int. Symp. on the Origin of Matter and Evolution of Galaxies 2000 (OMEG2000), (CNS University of Tokyo, RIKEN, NAO, and KEK), Tanashi, Jan. (2000).

K. Ishida: "Muon catalyzed fusion experiment at RIKEN-RAL (II)", Present Status of Nuclear Fusion Research and Muon Catalyzed Fusion, Wako, Jan. (2000).

T. Matsuzaki: "Muon catalyzed fusion research at RIKEN-RAL", Present Status of Nuclear Fusion Research and Muon Catalyzed Fusion, Wako, Jan. (2000).

R. Kanungo, I. Tanihata, Y. Ogawa, A. Ozawa, and H. Toki: "Halo structure in ^{19}C", 10th RIKEN Winter School on Nuclear Physics with Electromagnetic Probes at RIKEN RI-Beam Factory, Akita, Jan. (2000).

T. Nakatsukasa and K. Yabana: "Random-phase approximation with Green's function method in deformed states", 10th RIKEN Winter School on Nuclear Physics with Electromagnetic Probes at RIKEN RI-Beam Factory, Akita, Jan. (2000).

K. Asahi: "Electromagnetic moments of unstable nuclei", 10th RIKEN Winter School on Nuclear Physics with Electromagnetic Probes at RIKEN RI-Beam Factory, Akita, Jan. (2000).

Y. Mochizuki: "Half-lives of unstable nuclei produced in supernovae", Workshop on Hadron Physics at Extreme Conditions, (JAERI), Tokaimura, Jan. (2000).

K. Sakai and K. Asahi: "Experimental test of neutron deceleration for Sisyphus UCN production", Workshop on Nuclear Physics and Fundamental Physics with Neutrons V, (KEK), Tsukuba, Jan. (2000).

T. Ichihara, Y. Watanabe, N. Hayashi, S. Sawada, S. Yokkaichi, A. Taketani, Y. Goto, H. En'yo, and H. Hamagaki: "PHENIX Computing Center in Japan (CC-J)", Int. Conf. on Computing in High Energy and Nucler Physics (CHEP 2000), (INFN), Padova, Italy, Feb. (2000).

Y. Mochizuki: "How nuclear and atomic physics affects

on the maximum luminocity and the decay time of type Ia supernovae", RIKEN Workshop on Structure and Reaction of Nuclei: Assignments and Prospects towards 21th Century, Wako, Feb. (2000).

H. Kato, Y. Satou, and H. Sakai: "Measurement of deuteron polarization transfer coefficients at highly excited continuum of ^{12}C", 2000 Fall Meet. of the Physical Society of Japan, Niigata, Mar. (2000).

Y. Mochizuki: "^{44}Ti in Cas A as a test of models of core collapse supernovae", 2000 Spring Ann. Meet. of Astronomy Society of Japan, Tokyo, Mar. (2000).

K. Sekiguchi, H. Sakai, and H. Okamura: "Measurement of cross section and analyzing powers for dp scattering at intermediate energies", 2000 Spring Meet. of the Physical Society of Japan, Suita, Mar. (2000).

H. Kato, H. Sakai, and A. Tamii: "Measurement of polarization transfer coefficients in $\vec{d}p$ elastic scattering at 270 MeV", 2000 Spring Meet. of the Physical Society of Japan, Suita, Mar. (2000).

M. Hatano, T. Wakui, and H. Sakai: "Development of a polarized proton solid target by means of integrated solid effect at high temperature and low magnetic field", 2000 Spring Meet. of the Physical Society of Japan, Suita, Mar. (2000).

N. Kawamura, K. Nagamine, T. Matsuzaki, K. Ishida, S. N. Nakamura, Y. Matsuda, S. Sakamoto, M. Tanase, M. Kato, K. Kurosawa, H. Sugai, K. Kudoh, N. Takeda, and G. H. Eaton: "Muon catalyzed fusion experiment for D-T mixture at RIKEN-RAL muon facility: μCF in cryo-solid", 2000 Spring Meet. of the Physical Society of Japan, Suita, Mar. (2000).

H. Ogawa, K. Asahi, M. Nagakura, T. Suzuki, A. Goto, T. Suga, K. Yogo, H. Miyoshi, T. Honda, K. Sakai, A. Yoshimi, H. Ueno, Y. Watanabe, N. Imai, K. Yoneda, N. Aoi, N. Fukuda, Y. Kobayashi, A. Yoshida, T. Kubo, H. Sakurai, W.-D. Schmidt-Ott, G. Neyens, and S. Teughels: "The measurement of ^{15}C magnetic moment", 2000 Spring Meet. of the Physical Society of Japan, Suita, Mar. (2000).

T. Suzuki, H. Ogawa, K. Asahi, H. Miyoshi, M. Nagakura, A. Goto, T. Suga, K. Yogo, T. Honda, K. Sakai, A. Yoshimi, H. Ueno, N. Imai, K. Yoneda, N. Fukuda, Y. Watanabe, N. Aoi, Y. Kobayashi, A. Yoshida, T. Kubo, H. Sakurai, W.-D. Schmidt-Ott, G. Neyens, and S. Teughels: "Electric quadrupole moment of neutron halo nucleus ^{17}B", 2000 Spring Meet. of the Physical Society of Japan, Suita, Mar. (2000).

K. Yogo, H. Ogawa, K. Sakai, A. Yoshimi, T. Suzuki, M. Nagakura, A. Goto, T. Suga, and K. Asahi: "Cross polarization effect on LMR of ^{18}N implanted in Mg", 2000 Spring Meet. of the Physical Society of Japan, Suita, Mar. (2000).

Y. Mochizuki: "Nuclear γ-ray astronomy", 2000 Spring Meet. of the Physical Society of Japan, Higashiosaka, Mar. (2000).

K. Asahi: "Electromagnetic moments of light neutron-rich nuclei measured with polarized radioactive ion beams", Int. RIKEN Symp. on Shell Model 2000, Wako, Mar. (2000).

H. Ogawa, K. Sakai, T. Suzuki, M. Nagakura, H. Miyoshi, K. Asahi, K. Yogo, A. Goto, T. Suga, T. Honda, A. Yoshimi, H. Ueno, N. Imai, Y. Watanabe, K. Yoneda, N. Fukuda, N. Aoi, Y. Kobayashi, W.-D. Schmidt-Ott, G. Neyens, S. Teughels, A. Yoshida, T. Kubo, and M. Ishihara: "The measurement of ^{15}C magnetic moment and ^{17}B electric quadrupole moment", Int. RIKEN Symp. on Shell Model 2000, Wako, Mar. (2000).

K. Sekiguchi, H. Sakai, and H. Okamura: "Measurement of cross sections and analyzing powers for the d-p elastic scattering at intermediate energies", 16th IUPAP Int. Conf. on Few-Body Problems in Physics, Taipei, Taiwan, Mar. (2000).

H. Sakai: "Polarization transfer measurements for dp scattering at 270 MeV", 16th IUPAP Int. Conf. on Few-Body Problems in Physics, Taipei, Taiwan, Mar. (2000).

T. Uesaka, H. Sakai, H. Okamura, A. Tamii, Y. Satou, T. Ohnishi, K. Sekiguchi, K. Yako, K. Suda, S. Sakoda, J. Nishikawa, M. Hatano, H. Kato, Y. Maeda, N. Sakamoto, T. Wakasa, and K. Itoh: "^{3}He$(\vec{d},p)^4$He reaction at intermediate energies", 16th IUPAP Int. Conf. on Few-Body Problems in Physics, Taipei, Taiwan, Mar. (2000).

T. Kishida: "Secondary fusion reaction of high spin isomeric beams", Work on Science with Low-energy Radioactive Nuclear Beams 2000, (High Energy Acclerarater Research Organization), Tanashi, Mar. (2000).

T. Kishida: "Gas target system for production of secondary beams and study of nuclear structure", Work on Science with Low-energy Radioactive Nuclear Beams 2000, (High Energy Acclerarater Research Organization), Tanashi, Mar. (2000).

H. Ogawa, K. Asahi, M. Nagakura, T. Suzuki, A. Goto, T. Suga, K. Yogo, H. Miyoshi, T. Honda, K. Sakai, A. Yoshimi, H. Ueno, Y. Watanabe, N. Imai, K. Yoneda, N. Aoi, N. Fukuda, Y. Kobayashi, A. Yoshida, T. Kubo, H. Sakurai, W.-D. Schmidt-Ott, G. Neyens, and S. Teughels: "Electromagnetic moment of ^{17}B and ^{15}C", Work on Science with Low-energy Radioactive Nuclear Beams 2000, (High Energy Acclerarater Research Organization), Tanashi, Mar. (2000).

T. Suda: "e-A collider at RIKEN/MUSES", Workshop on eA Collider, (Gesellschaft Schwerionenforschung), Darmstadt, Germany, Mar. (2000).

K. Ishida: "X-ray studies on muon sticking and regeneration in D-T μCF", Workshop on Muon Catalyzed Fusion Studies: Interaction between Theoretical and *Experimental* Studies, (KEK-MSL and RIKEN-MUON), Tsukuba, Mar. (2000).

T. Matsuzaki: "Recent experimental results on t-t muon catalyzed fusion", Workshop on Muon Catalyzed Fusion Studies: Interaction between Theoretical and *Experimental* Studies, (KEK-MSL and RIKEN-MUON), Tsukuba, Mar. (2000).

K. Yoneda, H. Sakurai, T. Gomi, T. Motobayashi, N. Aoi, N. Fukuda, U. Futakami, Z. Gacsi, K. Higurashi, N. Imai, N. Iwasa, H. Iwasaki, T. Kubo, M. Kunibu, M. Kurokawa, Z. Liu, T. Minemura, A. Saito, M. Serata, S. Shimoura, S. Takeuchi, Y. Watanabe, K. Yamada, Y. Yanagisawa, K. Yogo, A. Yoshida, and M. Ishihara: "Gamma-ray spectroscopy of ^{34}Mg via RI beam fragmentation", 5th Int. Conf. on Radioactive Nuclear Beams (RNB5), (CERN and the ISOLDE collaboration), Divonne, France, Apr. (2000).

M. Matsuo, T. Nakatsukasa, and K. Matsuyanagi: "Adiabatic collective path for large amplitude shape dynamics", YITP Workshop on Dynamical Process in Nuclear Structure and Low-Intermediate Energy Heavy-Ion Nuclear Reactions, (Kyoto University), Kyoto, Apr. (2000).

A. Ozawa: "Nuclear radii and halo", Int. Symp. on Exotic Nuclear Structures, (ATOMKI), Debrecen, Hungary, May (2000).

S. N. Nakamura: "Measurement of the Fermi coupling constant", NuFact '00 Workshop (Muon Storage Ring for a Neutrino Factory), (Lawrence Berkeley National Laboratory), Monterey, USA, May (2000).

T. Matsuzaki: "Tritium gas handling system at RIKEN-RAL muon facility", RIKEN Symp. on Scientific Research Using Tritium and Related Engineering, Wako, May (2000).

N. Dinh Dang: "Single and multiphonon resonances at zero and finite temperatures within the phonon damping model", Structure of Nucleus at the Dawn of the Century (Bologna 2000), (University of Bologna), Bologna, Italy, May (2000).

T. Matsuzaki: "Muon catalyzed fusion research at RIKEN-RAL muon facility", Denki Kagakukai the 4th Seminar, Tokyo, June (2000).

T. Ohnishi, H. Sakai, H. Okamura, T. Niizeki, K. Sekiguchi, N. Sakamoto, T. Uesaka, H. Ohnuma, Y. Satou, and K. Yakou: "Study of spin-isospin excitations in ^{11}Be via the $(d,^2\mathrm{He})$ reaction at 270 MeV", Int. Conf. on Giant Resonances (GR2000), (RCNP of Osaka University), Osaka, June (2000).

K. Katori: "Isospin symmetry-structure study at new high-resolution course of RCNP", Int. Conf. on Giant Resonances (GR2000), (RCNP of Osaka University), Osaka, June (2000).

N. Dinh Dang: "Description of the hot GDR, multiphonon GDR in stable nuclei, and GDR in unstable nuclei within the phonon damping model", Int. Conf. on Giant Resonances (GR2000), (RCNP of Osaka University), Osaka, June (2000).

V. Kim Au, N. Dinh Dang, and A. Arima: "Electromagntic cross sections of double giant dipole resonances in ^{136}Xe and ^{208}Pb within the phonon damping model", Int. Conf. on Giant Resonances (GR2000), (RCNP of Osaka University), Osaka, June (2000).

K. Eisenman, J. Seitz, N. Dinh Dang, and M. Thoennessen: "Evolution of the giant dipole resonance width with nuclear temperature in ^{120}Sn", Int. Conf. on Giant Resonances (GR2000), (RCNP of Osaka University), Osaka, June (2000).

A. A. Korsheninnikov, M. Golovkov, A. Ozawa, K. Yoshida, I. Tanihata, Z. Fulop, K. Kusaka, K. Morimoto, H. Otsu, H. Petrascu, F. Tokanai, D. Bogdanov, M. Chelnokov, A. Fomichev, V. Gorshkov, Y. Oganessian, A. Rodin, S. Sidorchuk, S. Stepantsov, G. Ter-Akopian, R. Wolskii, W. Mittig, P. Roussel-Chomaz, H. Savajols, E. Kuzmin, E. Nikolskii, and A. Ogloblin: "Superheavy hydrogen ^{5}H. Spectroscopy of ^{7}He", Int. Conf. on Nuclear Physics, Clustering Phenomena in Nuclear Physics, St. Petersburg, Russia, June (2000).

Y. Mochizuki: "Ionization effects of ^{44}Ti in Cas A, RX J0852-4622, and SN 1987A", Int. Symp. on Nuclei in the Cosmos 2000, (Univesity of Aarhas), Aarhus, Denmark, June (2000).

N. Nakao, T. Kurosawa, T. Nakamura, and Y. Uwamino: "Development of quasi-monoenergetic neutron field and measurements of response function of organic scintillator for neutron energy range from 66 to 206 MeV", Int. Workshop on Neutron Field Spectrometry in Science, Technology and Radiation Protection, (Physikalisch-Technische Budesanstalt), Pisa, Italy, June (2000).

A. A. Korsheninnikov, M. Golovkov, I. Tanihata, D. Bogdanov, M. Chelnokov, A. Fomichev, V. Gorshkov, Y. Oganessian, A. Rodin, S. Sidorchuk, S. Stepantsov, G. Ter-Akopian, R. Wolskii, W. Mittig, P. Roussel-Chomaz, H. Savajols, E. Kuzmin, E. Nikolskii, and A. Ogloblin: "Superheavy hydrogen ^{5}H", Nucleus-Nucleus Collisions 2000, (GANIL, GSI), Strasbourg, France, July (2000).

N. Nakao, T. Shibata, T. Nunomiya, T. Nakamura, E. Kim, T. Kurosawa, S. Taniguchi, M. Sasaki, H. Iwase, Y. Uwamino, S. Ito, P. Wright, and D. R. Perry: "Deep penetration experiment at ISIS", 5th Specialists' Meet. on Shielding Aspects of Accelerators, Targets and Irradiation Facilities (SATIF-5), (OECD/Nuclear Energy Agency), Paris, France, July (2000).

Y. Mochizuki, I. Tanihata, and Y. Yano: "Video: The quest for the origin of the elements", CNS/RIKEN Symp. on Physics of RI-Beam at Low Energy, Wako, Aug. (2000).

Y. Mochizuki: "Recent topics in neutron star physics and in nuclear gamma ray astronomy", Lecture Series (invited) at 14th Symp. of Hokkaido Theoretical

Nuclear Physics Group, Sapporo, Aug. (2000).

T. Nakatsukasa and K. Yabana: "Linear response theory in the continuum", RIKEN Workshop on Computational Physics Approaches in Nuclear Mean Field Theory, Wako, Aug. (2000).

T. Nakatsukasa and K. Yabana: "The RPA with Green's function method on 3D real space", 55th Ann. Meet. of Physical Society of Japan, Niigata, Sept. (2000).

A. Ozawa: "A new magic number, N = 16, near to the neutron drip-line", 55th Ann. Meet. of Physical Society of Japan, Niigata, Sept. (2000).

Y. Aoki, K. Yoshida, T. Nakagawa, K. Nakagawa, and J. Kasagi: "Hot Giant Dipole Resonace of ^{209}Bi", 55th Annual Meeting of the Physical Society of Japan, Niigata, Sept. (2000).

Y. Mochizuki, I. Tanihata, and A. Ozawa: "On the magic numbers related to r-process nucleosynthesis", 55th Annual Meeting of the Physical Society of Japan, Niigata, Sept. (2000).

H. Sakai: "$\vec{d}p$ and $\vec{n}d$ scatterings at intermediate energy and three-nucleon force effects", 17th European Conf. on Few-Body Problems in Physics, (University of Évora), Évora, Portugal, Sept. (2000).

K. Yoshida: "DGR observed through heavy ion reactions", Symp. on "2 Phonon Giant Resonance" and "Change of Nuclear Lifetime", (Laboratory of Nuclear Science, Tohoku University), Sendai, Sept. (2000).

H. Kato, Y. Satou, and H. Sakai: "Deuteron polarimeter DPOL and calibration of the system", 14th Int. Spin Physics Symp. (SPIN 2000), (RCNP, Osaka University), Osaka, Oct. (2000).

T. Ohnishi, H. Sakai, H. Okamura, T. Niizeki, K. Sekiguchi, N. Sakamoto, T. Uesaka, H. Ohnuma, Y. Satou, and K. Yakou: "Systematic study of spin-isospin excitations in neutron rich light nuclei via the (d,^{2}He) reaction at 270 MeV", 14th Int. Spin Physics Symp. (SPIN2000), (RCNP of Osaka University), Osaka, Oct. (2000).

T. Wakui, M. Hatano, H. Sakai, A. Tamii, and T. Uesaka: "Development of a polarized proton target in a low magnetic field at high temperature", 14th Int. Spin Physics Symp. (SPIN2000), (RCNP of Osaka University), Osaka, Oct. (2000).

T. Uesaka, J. Nishikawa, H. Okamura, H. Sakai, M. Hatano, K. Itoh, H. Kato, Y. Maeda, T. Ohnishi, T. Saito, N. Sakamoto, S. Sakoda, Y. Satou, K. Sekiguchi, K. Suda, A. Tamii, N. Uchigashima, K. Yako, S. Yamamoto, T. Wakasa, and T. Wakui: "Role of deuteron internal variables in the ^{3}He$(d,p)^4$He reaction", 14th Int. Spin Physics Symp. (SPIN2000), (RCNP of Osaka University), Osaka, Oct. (2000).

Y. Mochizuki: "Evolution of the elements in the universe", Lecture Series (invited) at Department of Physics, Shizuoka University, Shizuoka, Oct. (2000).

T. Nakatsukasa and K. Yabana: "Linear response theory in the continuum", Nuclear Physics Seminar at Tohoku University, Sendai, Oct. (2000).

Y. Mochizuki: "Retardation of ^{44}Ti decay in supernova remnants and its importance", Seminar at Department of Physics, Chiba University, Chiba, Oct. (2000).

Y. Mochizuki: "Exotic nuclear rod model for the origin of neutron star glitches", Seminar at Department of Physics, Sophia University, Tokyo, Oct. (2000).

A. Ozawa: "New magic number, N = 16, near the neutron drip line", 2000 Symp. on Nuclear Data, (JAERI), Tokaimura, Nov. (2000).

A. Ozawa: "Measurement of interaction cross-sections and related topics", Int. Symp. on Perspectives in Physics with Radioactive Isotope Beams 2000, Hayama, Nov. (2000).

Y. Mochizuki: "Retardation of ^{44}Ti decay in supernova remnants and its importance", Nuclear Physics Seminar at Hosei University, Tokyo, Nov. (2000).

S. Fujii and S. Fujii: "Shell-model calculations for lambda hypernuclei using microscopic effective interactions", RIKEN-RCNP Workshop on Exotics in Hadron Many Body Systems, Nara, Nov. (2000).

Y. Mochizuki: "Exotic nuclear rod model for the origin of neutron star glitches", Theoretical Nuclear Physics Seminar at the University of Tokyo, Tokyo, Nov. (2000).

A. Ozawa: "Recent RI beam program at RIKEN and related topics", Int. Symp. on Nuclear Physics (ISNP2K), (Bhabha Atomic Research Center), Mumbai, India, Dec. (2000).

Y. Mochizuki: "How can glitches in neutron stars occur?", Lecture at Department of Physics, Ryukyu University, Okinawa, Dec. (2000).

Y. Mochizuki: "Nuclear Astrophysics: Evolution of the elements in the universe", Lecture Series (invited) at Department of Physics, Ryukyu University, Okinawa, Dec. (2000).

Y. Mochizuki: "On the magic numbers related to r-process nucleosynthesis", 13th Symp. of Association of Japanese Theoretical Astronomers, Kyoto, Dec. (2000).

Y. Mochizuki: "Retardation of ^{44}Ti decay in supernova remnants and its importance", Theoretical Nuclear Physics Seminar at the University of Tokyo, Tokyo, Dec. (2000).

3. Atomic and solid-state physics

I. Watanabe, M. Akoshima, Y. Koike, and K. Nagamine: "Possibility of '$\frac{1}{8}$ problem' in Zn-doped Bi-2212 system", Int. Workshop on JHF Science (JHF98), (Meson Science Laboratory, High Energy Accelerator Research Organization and Meson Science Association), Tsukuba, Mar. (1998).

N. Wada, A. Yamaguchi, H. Yano, K. Awaga, I.

Watanabe, S. Ohira, and K. Nagamine: "Two-dimensional $S = 1$ spin-gap antiferromagnet m-MPYNN·BF_4", Int. Workshop on JHF Science (JHF98), (Meson Science Laboratory, High Energy Accelerator Research Organization and Meson Science Association), Tsukuba, Mar. (1998).

S. Ohira, I. Watanabe, R. Imachi, N. Ishida, T. Nogami, and K. Nagamine: "μSR studies on organic radical ferromagnets, 4-anylmethyleneamino-TEMPO", Int. Workshop on JHF Science (JHF98), (Meson Science Laboratory, High Energy Accelerator Research Organization and Meson Science Association), Tsukuba, Mar. (1998).

J. Arai, T. Ishiguro, I. Watanabe, and K. Nagamine: "μSR study in $La_{1-x}Sr_xCu_{0.99}Fe_{0.01}O_4$", Int. Workshop on JHF Science (JHF98), (Meson Science Laboratory, High Energy Accelerator Research Organization and Meson Science Association), Tsukuba, Mar. (1998).

K. Shimomura, I. Watanabe, and K. Nagamine: "Muon dynamics in GaAs under laser irradiation", Int. Workshop on JHF Science (JHF98), (Meson Science Laboratory, High Energy Accelerator Research Organization and Meson Science Association), Tsukuba, Mar. (1998).

V. V. Krishunamurthy, I. Watanabe, H. Kuwahara, Y. Tokura, and K. Nagamine: "Magnetism and non-Fermi liquid scaling in Kondo lattice systems", Int. Workshop on JHF Science (JHF98), (Meson Science Laboratory, High Energy Accelerator Research Organization and Meson Science Association), Tsukuba, Mar. (1998).

T. Takabatake, D. T. Adroja, I. Watanabe, and K. Nagamine: "μSR studies of a Heavy-Fermion compound Ce_7Ni_3 with inequivalent Ce sites", Int. Workshop on JHF Science (JHF98), (Meson Science Laboratory, High Energy Accelerator Research Organization and Meson Science Association), Tsukuba, Mar. (1998).

I. Watanabe, M. Akoshima, Y. Koike, and K. Nagamine: "Magnetic instability observed by μSR in Zn-doped Bi-2212 system at the hole density of $\frac{1}{8}$", NEDO Workshop on Strongly Correlated Electron Systems, Los Angels, USA, Mar. (1998).

I. Watanabe, M. Akoshima, Y. Koike, and K. Nagamine: "μSR on magnetic state of Zn-doped Bi-2212 system", Int. Conf. on Strongly Correlated Electron Systems (SCES98), Paris, France, July (1998).

I. Watanabe and K. Nagamine: "μSR study of magnetically ordered state of Zn-doped La-Sr system at hole density of around $\frac{1}{8}$", Int. Conf. on Strongly Correlated Electron Systems (SCES98), Paris, France, July (1998).

V. V. Krishunamurthy, I. Watanabe, S. Ohira, K. Nishiyama, K. Nagamine, M. Ishikawa, and D. H. Eom: "μ^+SR observation of magnetic ordering and non-Fermi liquid scaling in $CeCo(Ge_{1.8}Si_{1.2})$", Int. Conf. on Strongly Correlated Electron Systems (SCES98), Paris, France, July (1998).

Y. Yamamoto, Y. Miyako, T. Takeuchi, I. Watanabe, K. Nishiyama, K. Shimomura, and K. Nagamine: "Low temperature properties of the Heavy-Fermion $Ce(Ru_{1-x}Rh_x)_2Si_2$ at the magnetic-nonmagnetic boundaries", Int. Conf. on Strongly Correlated Electron Systems (SCES98), Paris, France, July (1998).

V. V. Krishunamurthy, I. Watanabe, K. Nagamine, H. Kuwahara, and Y. Tokura: "μ^+SR observation of critical spin dynamics at the ferromagnetic ordering in $Nd_{0.5}Sr_{0.5}MnO_4$", 11th Int. Conf. on Hyperfine Interactions, Durban, South Africa, Aug. (1998).

V. V. Krishunamurthy, I. Watanabe, K. Nagamine, C. Geibel, G. Sparn, and F. Sterlich: "μ^+SR study on Heavy-Fermion magnetism in $Ce(Cu_{1-x}Ni_x)_2Ge_2$", 11th Int. Conf. on Hyperfine Interactions, Durban, South Africa, Aug. (1998).

I. Watanabe, M. Akoshima, Y. Koike, and K. Nagamine: "Possibility of '$\frac{1}{8}$ problem' in Zn-doped Bi2212 system", 3rd Workshop on Neutron Science Project: Science and Technology in the 21st Century Opened by Intense Spallation Neutron Source, (JAERI), Tokaimura, Mar. (1999).

Y. Koike, M. Akoshima, T. Adachi, N. Kakinuma, H. Noji, T. Nishizaki, N. Kobayashi, I. Watanabe, and K. Nagamine: "$\frac{1}{8}$ problem in the La-, Bi and Y-based cuprates and new anomalies in the overdoped region of the La-based cuprate", 2nd Int. Conf. on New Theories, Discoveries, and Applications of Superconductors and Related Materials, Las Vegas, USA, May (1999).

I. Watanabe, M. Akoshima, Y. Koike, and K. Nagamine: "μ^+SR study on $Bi_2Sr_2Ca_{1-x}Y_x(Cu_{1-y}Zn_y)_2O_{8+\delta}$ around the hole concentration of $\frac{1}{8}$ per Cu", Int. Conf. on Physics and Chemistry of Molecular and Oxide Superconductors (MOS99), Stockholm, Sweden, July (1999).

J. Arai, T. Ishiguro, I. Watanabe, and K. Nagamine: "μ^+SR study in $La_{2-x}Sr_xCu_{1-y}Zn_yO_4$ with $x \sim \frac{1}{8}$", Int. Conf. on Physics and Chemistry of Molecular and Oxide Superconductors (MOS99), Stockholm, Sweden, July (1999).

M. Akoshima, H. Noji, Y. Koike, T. Nishizaki, N. Kobayashi, I. Watanabe, and K. Nagamine: "Transport and μ^+SR at $P \sim \frac{1}{8}$ in the Bi-2212 and Y-123 phases", Int. Conf. on Physics and Chemistry of Molecular and Oxide Superconductors (MOS99), Stockholm, Sweden, July (1999).

I. Watanabe, M. Akoshima, Y. Koike, S. Ohira, W. Higemoto, and K. Nagamine: "μSR studies on the '$\frac{1}{8}$ effect' in Zn-substituted Bi2212 system", 22nd Int. Conf. on Low Temperature Physics (LT22), Helsinki, Finland, Aug. (1999).

I. Watanabe, N. Wada, K. Awaga, S. Ohira, and K.

Nagamine: "μSR study on dynamics of dimer spin in the 2D organic antiferromagnet, m-MPYNN·BF_4", 22nd Int. Conf. on Low Temperature Physics (LT22), Helsinki, Finland, Aug. (1999).

I. Watanabe, M. Akoshima, Y. Koike, S. Ohira, W. Higemoto, and K. Nagamine: "μSR study on the spin/charge ordered state of the hole-doped high T_c oxides around the hole concentration of $\frac{1}{8}$", 8th Int. Conf. on Muon Spin Rotation, Relaxation and Resonance (μSR99), Les Diablerets, Switzerland, Aug. (1999).

I. Watanabe, N. Wada, K. Awaga, S. Ohira, and K. Nagamine: "μSR study on the 2D $S = 1$ *Kagomé* organic antiferromagnet, m-MPYNN·(BF_4,ClO_4)", 8th Int. Conf. on Muon Spin Rotation, Relaxation and Resonance (μSR99), Les Diablerets, Switzerland, Aug. (1999).

W. Higemoto, H. Tanaka, I. Watanabe, S. Ohira, A. Fukaya, and K. Nagamine: "Anomalous magnetic field dependence of the muon spin relaxation in $S = 1$ double chain systems $KCuCl_3$ and $TlCuCl_3$", 8th Int. Conf. on Muon Spin Rotation, Relaxation and Resonance (μSR99), Les Diablerets, Switzerland, Aug. (1999).

T. Ishiguro, M. Hirai, H. Shinmen, J. Arai, I. Watanabe, and K. Nagamine: "Zn-induced magnetic order detected by μSR around $x = \frac{1}{8}$ in $La_{2-x}Sr_xCu_{1-y}Zn_yO_4$", 8th Int. Conf. on Muon Spin Rotation, Relaxation and Resonance (μSR99), Les Diablerets, Switzerland, Aug. (1999).

M. Mekata, K. M. Kojima, I. Watanabe, K. Nagamine, and H. Ikeda: "Magnetic ordering and excitation in Ising spin nets $Rb_2Co_{1-x}Mg_xF_4$", 8th Int. Conf. on Muon Spin Rotation, Relaxation and Resonance (μSR99), (Paul Scherrer Institut, EPS, Universitas Turicensis, and ETH), Les Diablerets, Switzerland, Aug. (1999).

M. Matsuda, I. Watanabe, and K. Nagamine: "Magnetic ordering in $La_2Cu_2O_5$", 8th Int. Conf. on Muon Spin Rotation, Relaxation and Resonance (μSR99), (Paul Scherrer Institut, EPS, Universitas Turicensis, and ETH), Les Diablerets, Switzerland, Aug. (1999).

V. V. Krishunamurthy, I. Watanabe, K. Nagamine, H. Kuwahara, and Y. Tokura: "Spin dynamics in $Nd_{1-x}Sr_xMnO_3$ with $x = 0.5$ and $x = 0.55$", 8th Int. Conf. on Muon Spin Rotation, Relaxation and Resonance (μSR99), (Paul Scherrer Institut, EPS, Universitas Turicensis, and ETH), Les Diablerets, Switzerland, Aug. (1999).

F. L. Pratt, S. J. Blundell, Th. Jestädt, B. W. Lovett, A. Husmann, I. M. Marshall, W. Hayes, A. P. Monkman, I. Watanabe, and K. Nagamine: "μSR on conducting and non-conducting polymers", 8th Int. Conf. on Muon Spin Rotation, Relaxation and Resonance (μSR99), (Paul Scherrer Institut, EPS, Universitas Turicensis, and ETH), Les Diablerets, Switzerland, Aug. (1999).

W. Higemoto, I. Watanabe, K. Nagamine, S. Kuroda, and H. Takita: "Investigation of the dynamics of flux line lattice under an electric current", 8th Int. Conf. on Muon Spin Rotation, Relaxation and Resonance (μSR99), (Paul Scherrer Institut, EPS, Universitas Turicensis, and ETH), Les Diablerets, Switzerland, Aug. (1999).

F. L. Pratt, S. J. Blundell, A. Husmann, I. M. Marshall, B. W. Lovett, W. Hayes, S. L. Lee, C. Ager, T. Sasaki, T. Toyoda, V. N. Laukhin, E. Laukhina, I. Watanabe, and K. Nagamine: "BEDT-TTF superconductors studied by μSR", 8th Int. Conf. on Muon Spin Rotation, Relaxation and Resonance (μSR99), (Paul Scherrer Institut, EPS, Universitas Turicensis, and ETH), Les Diablerets, Switzerland, Aug. (1999).

S. Ohira, I. Watanabe, F. L. Pratt, N. Ishida, T. Nogami, and K. Nagamine: "Muon spin relaxation and resonsnce studies on the organic radical magnet, 4-arylmethykeneamino-TEMPO", 8th Int. Conf. on Muon Spin Rotation, Relaxation and Resonance (μSR99), (Paul Scherrer Institut, EPS, Universitas Turicensis, and ETH), Les Diablerets, Switzerland, Aug. (1999).

Y. Miyake, K. Shimomura, Y. Matsuda, R. J. Sheuermann, P. Bakule, S. Makimura, P. Strasser, S. N. Nakamura, K. Ishida, T. Matsuzaki, I. Watanabe, and K. Nagamine: "Set-up for the ultra slow muon experiment by laser resonant ionization method at RIKEN-RAL", 8th Int. Conf. on Muon Spin Rotation, Relaxation and Resonance (μSR99), (Paul Scherrer Institut, EPS, Universitas Turicensis, and ETH), Les Diablerets, Switzerland, Aug. (1999).

A. Kratzer, G. M. Kalvius, T. Takabatake, K. Umeo, D. T. Adroja, Y. Echizen, I. Watanabe, R. Wäppling, D. R. Noakes, C. U. Jackson, and C. E. Stronach: "μSR studies of Ce_7Ni_3", 8th Int. Conf. on Muon Spin Rotation, Relaxation and Resonance (μSR99), (Paul Scherrer Institut, EPS, Universitas Turicensis, and ETH), Les Diablerets, Switzerland, Aug. (1999).

V. V. Krishunamurthy, I. Watanabe, K. Nagamine, J. Kitagawa, M. Ishikawa, and T. Komatsubara: "μ^+SR study of ordering phenomenon in the Heavy-Fermion state of $Ce_3Pd_{20}Ge_6$ single crystal", 8th Int. Conf. on Muon Spin Rotation, Relaxation and Resonance (μSR99), (Paul Scherrer Institut, EPS, Universitas Turicensis, and ETH), Les Diablerets, Switzerland, Aug. (1999).

V. V. Krishunamurthy, K. Nagamine, I. Watanabe, K. Nishiyama, S. Ohira, M. Ishikawa, and D. H. Eom: "Non-Fermi liquid behavior in $CeCoGe_{3-x}Si_x$ alloys", 8th Int. Conf. on Muon Spin Rotation, Relaxation and Resonance (μSR99), (Paul Scherrer Institut, EPS, Universitas Turicensis, and ETH), Les Diablerets, Switzerland, Aug. (1999).

Y. Kobayashi, Y. Yoshida, A. Yoshida, Y. Watanabe, K. Hayakawa, K. Yukihira, F. Shimura, and F. Ambe: "In-beam Mössbauer study of $^{57}Mn/^{57}Fe$ in Si following projectile fragmentation and implantation", Int. Conf. on the Application of the Mössbauer Effect 1999, Garmish-Partenkirchen, Germany, Aug. (1999).

I. Shimamura: "Dynamics of three-body and four-body exotic-atom systems", ITAMP Workshop on Fragmentation and Recombination in Novel 3- and 4-Body Systems, (Institute for Theoretical Atomic and Molecular Physics), Cambridge, USA, Nov. (1999).

M. Akoshima, Y. Koike, I. Watanabe, and K. Nagamine: "Suppression of the high-T_c superconductivity and the stripe correlations in the Bi-2212 and Y-123 phases around $p{\sim}1/8$", Dai 54-kai Ohyobutsuri Gakkai Tohoku-shibu Gakujutsu Koen-kai, Sendai, Dec. (1999).

Y. Morishita: "Study of initially populated states of slow highly charged ions interacting with Ni micro capillary", RIKEN Symp. on Studies on Condensed Matter Physics, Atomic Physics, Hyperfine Interactions and Biomedical Sciences Using RIKEN Accelerators, Wako, Jan. (2000).

T. Azuma and Y. Yamazaki: "Coherent resonant excitation and high resolution spectroscopy", RIKEN Symp. on Studies on Condensed Matter Physics, Atomic Physics, Hyperfine Interactions and Biomedical Sciences Using RIKEN Accelerators, Wako, Jan. (2000).

Y. Koike, M. Akoshima, I. Watanabe, and K. Nagamine: "Transport and μSR studies on the $\frac{1}{8}$ anomaly in the Bi-2212 and Y-123", US-Japan Neutron Scattering Workshop on Stripe in Transition Metals Oxides, Honolulu, USA, Jan. (2000).

Y. Koike, M. Akoshima, I. Watanabe, and K. Nagamine: "$\frac{1}{8}$ anomaly in the Bi-2212 and Y-123 phases", 6th Int. Conf. on Materials and Magnetism of Superconductivity and High Temperature Superconductors, Houston, USA, Feb. (2000).

I. Shimamura, M. Kimura, and G. Ya. Korenman: "Metastable antiprotonic Lithium", Workshop on the Theory of Antimatter Science Using Antiprotons, Atami, Feb. (2000).

Y. Yamazaki: "Production of ultra slow antiproton beams and elementary collision processes with atoms", Workshop on the Theory of Antimatter Science Using Antiprotons, Atami, Feb. (2000).

T. Ishiguro, T. Oda, H. Shinmen, M. Hirai, J. Yokoyama, J. Arai, I. Watanabe, and K. Nagamine: "Zn-substitution effect in $La_{2-x}Sr_xCu_{1-y}Zn_yO_4$ around the optimul doped region studied by μ^+SR", 2000 Spring Meet. of the Physical Society of Japan, Suita, Mar. (2000).

M. Mekata, K. M. Kojima, S. Ito, I. Watanabe, and K. Nagamine: "Process of the ordering of the diluted ising-spin net", 2000 Spring Meet. of the Physical Society of Japan, Suita, Mar. (2000).

M. Akoshima, I. Watanabe, K. Nishimaki, M. Aoyama, Y. Koike, S. Ohira, W. Higemoto, and K. Nagamine: "$\frac{1}{8}$ anomaly in $YBa_2Cu_{3-2x}Zn_{2y}O_{7-\delta}$ observed by μSR", 2000 Spring Meet. of the Physical Society of Japan, Suita, Mar. (2000).

Y. Yoshida, Y. Kobayashi, F. Ambe, A. Yoshida, Y. Yano, and F. Shimura: "Studies on jump process of Fe atoms located at interstitial and substitutional position in Si", 2000 Spring Meet. of the Physical Society of Japan, Suita, Mar. (2000).

M. Wada, S. Okada, Y. Okada, I. Katayama, H. Kawakami, K. Noda, T. Nakamura, S. Ohtani, Y. Nakai, T. M. Kojima, Y. Kanai, T. Kambara, and Y. Yamazaki: "RF ion guide for collecting ions in energetic radioactive beams", 2000 Spring Meet. of the Physical Society of Japan, Suita, Mar. (2000).

T. Kambara, Y. Kanai, T. M. Kojima, Y. Nakai, Y. Yamazaki, and K. Kageyama: "Acoustic emission from solid irradiated by fast heavy ions", 2000 Spring Meet. of the Physical Society of Japan, Suita, Mar. (2000).

Y. Iwai, S. Thuriez, R. Hutton, Y. Kanai, H. Oyama, K. Ando, H. Masuda, T. Azuma, K. Komaki, and Y. Yamazaki: "High resolution soft X-ray spectroscopy of slow highly charged ions through Ni microcapillary", 2000 Spring Meet. of the Physical Society of Japan, Suita, Mar. (2000).

D. Murakoshi, N. Okabayashi, Y. Iwai, H. Torii, K. Kuroki, H. Masuda, K. Komaki, and Y. Yamazaki: "Measurement of charge state distribution of Xe^{q+} transmitted through Ni micro-capillaries", 2000 Spring Meet. of the Physical Society of Japan, Suita, Mar. (2000).

A. Endo, N. Okabayashi, H. Torii, K. Kuroki, K. Komaki, and Y. Yamazaki: "The design of a mini-EBIS using high-T_c superconductors", 2000 Spring Meet. of the Physical Society of Japan, Suita, Mar. (2000).

M. Hoshino, M. Kitajima, Y. Nakai, Y. Kanai, and Y. Yamazaki: "The collision energy-dependence of double electron capture cross sections in low energy C^{4+}-He collision", 2000 Spring Meet. of the Physical Society of Japan, Suita, Mar. (2000).

Y. Morishita, Y. Yamazaki, K. Kuroki, H. Torii, K. Komaki, H. Masuda, R. Hutton, K. Ando, K. Ishii, and M. Sekiguchi: "Visible light emission from slow highly charged ions transmitted through Ni microcapillary (3)", 2000 Spring Meet. of the Physical Society of Japan, Suita, Mar. (2000).

T. Ichioka, H. Higaki, M. Hori, K. Yoshiki Franzen, N. Kuroda, B. Ujbari, N. Oshima, K. Kuroki, A. Mohri, K. Komaki, and Y. Yamazaki: "Development of a trap for experiments using ultracold antiprotons (II)", 2000 Spring Meet. of the Physical Society of Japan, Suita, Mar. (2000).

Y. Yamazaki: "Research of ion-matter interaction at RIKEN RI-Beam Factory", 2000 Spring Meet. of the Physical Society of Japan, Suita, Mar. (2000).

N. Oshima, T. M. Kojima, D. Dumitriu, A. Mohri, H. Oyama, Y. Kanai, T. Kambara, Y. Nakai, M. Wada, and Y. Yamazaki: "Development of a slow positron beam using a rare gas solid moderator", 2000 Spring Meet. of the Physical Society of Japan, Suita, Mar. (2000).

X. Diao, Y. Yoshida, K. Hayakawa, F. Shimura, T. Kambara, and A. Iwase: "IR study on the V-0 pairs and oxygen-interstitials in CZ-Si irradiated by 3.5 GeV Xe", 2000 Spring Meet. of the Physical Society of Japan, Suita, Mar. (2000).

T. Ishida, T. Ise, T. Nogami, S. Ohira, I. Watanabe, and K. Nagamine: "μSR on Ar-CH=N-TEMPO magnets (Ar=Biph,Ph,4-Py)", 78th National Meet. Chemical Society of Japan, Funabashi, Mar. (2000).

I. Shimamura: "Collision calculations for muonic few-body systems", Workshop on Muon Catalyzed Fusion Studies: Interaction between Theoretical and *Experimental* Studies, (KEK), Tsukuba, Mar. (2000).

I. Watanabe, N. Wada, K. Awaga, S. Ohira, and K. Nagamine: "Dynamical and static internal fields in frustrated materials observed by the muon spin relaxation method", Workshop on Frustration and Kiral Ordering for the Cerebration of the Foundation of The Kyoto Institute of Technology, Kyoto, Apr. (2000).

Y. Koike, M. Akoshima, M. Aoyama, K. Nishimaki, I. Watanabe, S. Ohira, W. Higemoto, and K. Nagamine: "$\frac{1}{8}$ anomaly and stripes in the Bi-2212 and Y-123 phases", Int. Workshop on Superconductivity, Structure and Property Relationship for Applications of High-Temperature, Matsue, June (2000).

Y. Kanai, D. Dumitriu, Y. Iwai, T. Kambara, T. M. Kojima, Y. Morishita, Y. Nakai, H. Oyama, N. Oshima, and Y. Yamazaki: "Present status of slow highly-charged ion facility at RIKEN", 10th Int. Conf. on the Physics of Highly Charged Ions (HCI-2000), (American Vacuum Society, University of California, and United States Department of Energy), Berkeley, USA, July (2000).

A. Itoh, T. Majima, H. Tsuchida, Y. Nakai, and T. Kambara: "Charge-state dependence of C_{60} - multifragmentation in collisions of 30 MeV Ne^{2-9+} ions", 10th Int. Conf. on the Physics of Highly Charged Ions (HCI-2000), (American Vacuum Society, University of California, and United States Department of Energy), Berkeley, USA, July (2000).

M. Huang, R. Hutton, Y. Zou, K. Ando, H. Oyama, and M. Huang: "The continuing saga of the Si-like intercombination lines in highly charged ions, Si-like rhodium", 10th Int. Conf. on the Physics of Highly Charged Ions (HCI-2000), (American Vacuum Society, University of California, and United States Department of Energy), Berkeley, USA, July (2000).

R. Hutton, Y. Zou, K. Ando, and H. Oyama: "Optical transitions between spin-aligned levels of highly charged Mg-like ions", 10th Int. Conf. on the Physics of Highly Charged Ions (HCI-2000), (American Vacuum Society, University of California, and United States Department of Energy), Berkeley, USA, July (2000).

M. Hoshino, M. Kitajima, Y. Kanai, Y. Nakai, H. Tanaka, and Y. Yamazaki: "Angular resolved energy gain spectroscopy to study of double electron capture processes in very slow C^{4+}-He collisions", 10th Int. Conf. on the Physics of Highly Charged Ions (HCI-2000), (American Vacuum Society, University of California, and United States Department of Energy), Berkeley, USA, July (2000).

T. Azuma, T. Ito, Y. Takabayashi, K. Komaki, Y. Yamazaki, E. Takada, and T. Murakami: "Resonant coherent excitation of hydrogen-like Ar ions to the n = 3 states", 10th Int. Conf. on the Physics of Highly Charged Ions (HCI-2000), (American Vacuum Society, University of California, and United States Department of Energy), Berkeley, USA, July (2000).

Y. Zou, R. Hutton, S. Huldt, K. Ando, and H. Oyama: "Effects of foil aging properties on the intensities of atomic transition lines following ion-foil interaction", 10th Int. Conf. on the Physics of Highly Charged Ions (HCI-2000), (American Vacuum Society, University of California, and United States Department of Energy), Berkeley, USA, July (2000).

Y. Koike, M. Akoshima, M. Aoyama, K. Nishimaki, T. Kawamata, T. Adachi, H. Noji, I. Watanabe, S. Ohira, W. Higemoto, K. Nagamine, H. Kimura, K. Hirota, K. Yamada, and Y. Endoh: "Impurity effect on the stripes in the La-124, Bi-2212 and Y-123 phases", Int. Symp. on Physics in Local Lattice Distortions (LLD2K), Tsukuba, July (2000).

K. Nagaya, Y. Teranishi, and H. Nakamura: "New way of controlling molecular photodissociation with use of the complete reflection phenomenon", 25th Ann. Meet. of Society for Atomic Collision Research, Okazaki, Aug. (2000).

N. Oshima, T. M. Kojima, D. Dumitriu, A. Mohri, H. Oyama, Y. Kanai, T. Kambara, Y. Nakai, M. Wada, and Y. Yamazaki: "Research plans using slow positron beam", 25th Ann. Meet. of Society for Atomic Collision Research, Okazaki, Aug. (2000).

M. Hoshino, M. Kitajima, Y. Kanai, Y. Nakai, H. Tanaka, and Y. Yamazaki: "Present status of very low energy highly charged ion: Atom collision experiment", 25th Ann. Meet. of Society for Atomic Collision Research, Okazaki, Aug. (2000).

Y. Morishita, H. Torii, Y. Yamazaki, K. Kuroki, K. Komaki, R. Hutton, K. Ando, K. Ishii, H. Masuda, and M. Sekiguchi: "Visible light spectroscopy of

highly charged ions transmitted through a Ni microcapillary", 25th Ann. Meet. of Society for Atomic Collision Research, Okazaki, Aug. (2000).

T. Azuma, T. Ito, Y. Takabayashi, K. Komaki, Y. Yamazaki, E. Takada, and K. Murakami: "Resonant coherent excitation of relativistic highly charged ions: Excitation from the ground state of hydrogen-like ions to the n=3 states", 25th Ann. Meet. of Society for Atomic Collision Research, Okazaki, Aug. (2000).

T. Ito, Y. Takabayashi, T. Azuma, K. Komaki, Y. Yamazaki, E. Takada, and K. Murakami: "Possible application of resonant coherent excitation to high resolution atomic spectroscopy", 25th Ann. Meet. of Society for Atomic Collision Research, Okazaki, Aug. (2000).

T. Nishimura and I. Shimamura: "Calculation of positronium formation cross section on positron-hydrogen molecule collision", 25th Ann. Meet. of Society for Atomic Collision Research, Okazaki, Aug. (2000).

Y. Iwai, S. Thuriez, R. Hutton, Y. Kanai, H. Oyama, K. Ando, H. Masuda, K. Nishio, T. Azuma, K. Komaki, and Y. Yamazaki: "Soft X-ray spectroscopy of slow highly charged ions through microcapillary", 25th Ann. Meet. of Society for Atomic Collision Research, Okazaki, Aug. (2000).

N. Suzuki, Y. Nagai, and T. Hyodo: "Vacancy formation enregy of metals determined by using positron age-momentum correlation technique", 12th Int. Conf. on Positron Annihilation (ICPA-12), München, Germany, Aug. (2000).

L. Wei, N. Suzuki, J. Kim, F. Saito, Y. Itoh, A. Goto, T. Kurihara, Y. Nagashima, and T. Hyodo: "Slow positron yields from a new type of moderator", 12th Int. Conf. on Positron Annihilation (ICPA-12), München, Germany, Aug. (2000).

T. Nakatsukasa and K. Yabana: "Linear response in the continuum", Physics Division Seminar, (Oak Ridge National Laboratory), Oak Ridge, USA, Aug. (2000).

N. Suzuki, Y. Nagai, Y. Itoh, A. Goto, and T. Hyodo: "Vacancy formation energy of metals determined by using positron age-momentum correlation technique", 55th Ann. Meet. of Physical Society of Japan, Niigata, Sept. (2000).

T. Nakatsukasa and K. Yabana: "Real-space calculation method of continuum spectra", 55th Ann. Meet. of Physical Society of Japan, Niigata, Sept. (2000).

T. Nakamura, M. Wada, Y. Okada, I. Katayama, S. Ohtani, and H. A. Shuessler: "Precision spectroscopy of the hyperfine structure of $^9Be^+$ ion in a strong magnetic field using a combined linear ion trap", 55th Ann. Meet. of Physical Society of Japan, Niigata, Sept. (2000).

Y. Okada, L. Boesten, M. Wada, T. Nakamura, S. Ohtani, and I. Katayama: "Development of a cryogenic linear ion trap for spectroscopic application", 55th Ann. Meet. of Physical Society of Japan, Niigata, Sept. (2000).

M. Hoshino, M. Kitajima, Y. Nakai, Y. Kanai, H. Tanaka, and Y. Yamazaki: "Angular distribution measurements of electron capture processes for X^{4+}(X=C,N,O)-He collision at low energy region", 55th Ann. Meet. of Physical Society of Japan, Niigata, Sept. (2000).

Y. Takabayashi, T. Ito, T. Azuma, K. Komaki, Y. Yamazaki, E. Takada, and T. Murakami: "Convoy electron production with relativistic heavy ions: Projectile charge state dependence", 55th Ann. Meet. of Physical Society of Japan, Niigata, Sept. (2000).

T. Azuma, T. Ito, Y. Takabayashi, K. Komaki, Y. Yamazaki, E. Takada, and T. Murakami: "Resonant coherent excitation of hydrogen-like Ar ions to the n = 3 states", 55th Ann. Meet. of Physical Society of Japan, Niigata, Sept. (2000).

T. Ito, Y. Takabayashi, T. Azuma, K. Komaki, Y. Yamazaki, E. Takada, and T. Murakami: "Resonant coherent excitation of relativistic highly charged ions II: Possibility of high resolution atomic spectroscopy", 55th Ann. Meet. of Physical Society of Japan, Niigata, Sept. (2000).

T. Majima, A. Itoh, H. Tsuchida, Y. Nakai, and T. Kambara: "Multiionization and multifragmentation processes of C_{60} molecules induced by 30 MeV Ne^{2-9+} impacts: Projectile charge dependences", 55th Ann. Meet. of Physical Society of Japan, Niigata, Sept. (2000).

A. Endo, K. Yoshiki Franzen, H. Torii, K. Komaki, and Y. Yamazaki: "The development of a mini-EBIS using high-T_c superconductors (II)", 55th Ann. Meet. of Physical Society of Japan, Niigata, Sept. (2000).

T. Ichioka, H. Higaki, K. Yoshiki Franzen, Z. Wang, N. Kuroda, M. Hori, N. Oshima, B. Újbári, K. Kuroki, A. Mohri, K. Komaki, and Y. Yamazaki: "Negative hydrogen ions and protons in the trap and their manipulation", 55th Ann. Meet. of Physical Society of Japan, Niigata, Sept. (2000).

Y. Iwai, S. Thuriez, R. Hutton, Y. Kanai, H. Oyama, K. Ando, H. Masuda, K. Nishio, T. Azuma, K. Komaki, and Y. Yamazaki: "High resolution soft x-ray spectroscopy of highly charged ions through Ni microcapillary target (II)", 55th Ann. Meet. of Physical Society of Japan, Niigata, Sept. (2000).

T. Kambara, Y. Kanai, T. M. Kojima, Y. Nakai, Y. Yamazaki, A. Yoneda, and K. Kageyama: "Acoustic emission from solids irradiated by fast heavy ions (II)", 55th Ann. Meet. of Physical Society of Japan, Niigata, Sept. (2000).

Y. Nakai, T. Kambara, A. Itoh, H. Tsuchida, and Y. Yamazaki: "Ionization and fragmentation of C_{60} by fast ion impact- Analysis of TOF spectra profile of fullerene-like fragment ions", 55th Ann. Meet. of

Physical Society of Japan, Niigata, Sept. (2000).

T. M. Kojima, N. Oshima, Y. Kanai, A. Mohri, and Y. Yamazaki: "Development of an ion trap for multi-charged ions cooled with cold positron coolant", 55th Ann. Meet. of Physical Society of Japan, Niigata, Sept. (2000).

N. Oshima, T. M. Kojima, D. Dumitriu, A. Mohri, H. Oyama, Y. Kanai, T. Kambara, Y. Nakai, M. Wada, and Y. Yamazaki: "Development of a slow positron beam using a rare gas solid moderator (II)", 55th Ann. Meet. of Physical Society of Japan, Niigata, Sept. (2000).

M. Takekawa and Y. Ichikawa: "Elastic scattering of electron by OCS molecule", 55th Ann. Meet. of Physical Society of Japan, Niigata, Sept. (2000).

S. Morishima, H. J. Bang, Y. Hagio, T. Mochizuki, T. Maruyama, K. Akimoto, M. Nomura, and E. Yagi: "Concentration quenching of Eu related luminescence in Eu-doped GaN studied by EXAFS analysis", 61st Autumn Meet. 2000 of The Japan Society of Applied Physics, Sapporo, Sept. (2000).

H. J. Bang, S. Morishima, T. Maruyama, K. Akimoto, M. Nomura, and E. Yagi: "Growth and characterization of Tb doped GaN", Int. Workshop on Nitride Semiconductors (IWN2000), (The Japan Society of Applied Physics), Nagoya, Sept. (2000).

I. Shimamura: "Resonances in Coulomb few-body systems", Int. Workshop on Resonances in Few-Body Systems, (ATOMKI), Sárospatak, Hungary, Sept. (2000).

N. Suzuki, H. Saito, Y. Nagai, T. Hyodo, H. Murakami, M. Sano, Y. Itoh, S. A. Kuten, and I. V. Vondarev: "Search for positronium quadrupole interaction in crystalline solids", 43rd Symp. on Radiochemistry, Wako, Oct. (2000).

Y. Yamazaki: "An ion beam to probe ions and an ion beam to probe targets", Quantum Science and Engineering Center Symposium, Kyoto University, Kyoto, Oct. (2000).

Y. Yamazaki: "Energy deposition mechanism with heavy particles: From slow highly charged ions to relativistic heavy ions", RIKEN Symp. on Dynamics of High-Energy and High-Density Excited Valence Electrons in Matter, Wako, Oct. (2000).

T. Kambara: "Acoustic emission from solids irradiated by fast heavy ions", RIKEN Symp. on Dynamics of High-Energy and High-Density Excited Valence Electrons in Matter, Wako, Oct. (2000).

E. Yagi: "The study on the state of hydrogen dissolved in metals by means of the channelling method", Dai 11 Kai Suiso to Zairyou Kinou Kyoudou Kenkyuukai, (The Japan Institute of Metals), Tokyo, Nov. (2000).

T. Kambara, Y. Kanai, T. M. Kojima, Y. Nakai, A. Yoneda, Y. Yamazaki, and K. Kageyama: "Ultrasonic pulse from fast heavy-ion irradiation on solids", 16th Int. Conf. on the Application of Accelerators in Research and Industry (CAARI 2000), Denton, USA, Nov. (2000).

N. Suzuki, Y. Nagai, Y. Itoh, A. Goto, and T. Hyodo: "Vacancy formation energy of metals determined by using positron age-momentum correlation technique", Specialist Research Meet. on Positron Beam Techniques for Science and Engineering, (Research Reactor Institute Kyoto University), Kumatori, Nov. (2000).

N. Oshima, T. M. Kojima, D. Dumitriu, A. Mohri, H. Oyama, Y. Kanai, T. Kambara, Y. Nakai, M. Wada, and Y. Yamazaki: "Present status of the positron cooling for highly charged ions", Specialist Research Meet. on Positron Beam Techniques for Science and Engineering, (Research Reactor Institute, Kyoto University), Kumatori, Nov. (2000).

H. Higaki, T. Ichioka, K. Yoshiki Franzen, N. Kuroda, Z. Wang, S. Yoneda, H. Torii, K. Komaki, and Y. Yamazaki: "Non-neutral plasma and production of ultra slow antiproton beam", 2nd Workshop on the Theory of Antimatter Science by Use of Antiprotons and 8th RIKEN Symp. on the Theory of Atomic and Molecular Processes: Antimatter Science by Use of Antiprotons, Fujiyoshida, Dec. (2000).

I. Shimamura: "Influence of a laser field on the formation of antihydrogen", 2nd Workshop on the Theory of Antimatter Science by Use of Antiprotons and 8th RIKEN Symp. on the Theory of Atomic and Molecular Processes: Antimatter Science by Use of Antiprotons, Fujiyoshida, Dec. (2000).

T. Nakatsukasa and K. Yabana: "Calculations of response function in the continuum", Computational Physics in Condensed Matter Research, (Institute for Solid State Physics, University of Tokyo), Kashiwa, Dec. (2000).

T. Ichioka, H. Higaki, K. Yoshiki Franzen, Z. Wang, N. Kuroda, S. Yoneda, H. Torii, K. Komaki, M. Hori, K. Kuroki, A. Mouri, and Y. Yamazaki: "ASACUSA trap system for high intensity ultra slow antiproton beam", Seminar of Atomic and Molecular Processes in Space, (The Institute of Space and Astronautical Science), Sagamihara, Dec. (2000).

4. Radiochemistry, radiation chemistry, and radiation biology

Y. Einaga, O. Sato, T. Iyoda, Y. Kobayashi, F. Ambe, K. Hashimoto, and A. Fujishima: "Characterization of cobalt iron cyanide by ^{57}Fe Mössbauer Spectroscopy", Int. Conf. on the Applications of the Mössbauer Effect 1997, Rio de Janeiro, Brazil, Sept. (1997).

C. H. Bae, T. Abe, T. Matsuyama, T. Nakano, and S. Yoshida: "Effect of heavy-ion beam irradiation on mutation induction in plants at pollination stage (III)", 93rd Congr. of the Breeding Society of Japan, Yokohama, Mar. (1998).

S. Sharma, J. Kaneko, and N. Ito: "Stimulated emission and exciton complex formation in some insulator crystals irradiated by heavy-ions", 7th Workshop on Fast Ion-Atom Collisions, Debrecen, Hungary, Sept. (1998).

K. Ushida, K. Ishioka, S. Hishita, K. G. Nakamura, and M. Kitajima: "Acceleration of dephasing of coherent phonons induced by ion implantation", 1998 Asian-Pacific Forum on Science and Technology: Optical Probing and Creation of Advanced Photoactive Materials, (Japan Advanced Institute of Science and Technology, Hokuriku), Tatsunokuchi, Nov. (1998).

K. Ushida, K. Ishioka, S. Hishita, K. G. Nakamura, and M. Kitajima: "Effect of disorders artificially generated by ion beam irradiation on the dephasing of coherent phonons", 1st Int. Symp. on Atomic Scale Processing and Novel Properties in Nanoscopic Materials, (The Institute of Scientific and Industrial Research COE, Osaka University), Suita, Nov. (1998).

T. Matsuyama, T. Abe, C. H. Bae, T. Nakano, T. Asami, and S. Yoshida: "RLGS analysis in plant genome", Ann. Meet. of Japan Society for Bioscience, Biotechnology, and Agrochemistry, Fukuoka, Mar. (1999).

Y. Nose, S. Enomoto, S. Ambe, F. Ambe, and I. Yamaguchi: "Multitracer study on biosorption of various trace elements in yeast *Saccharomyces cerevisiae*", RIKEN Symp. on Bio-Trace Elements '99, Wako, Mar. (1999).

C. H. Bae, T. Abe, N. Nagata, T. Matsuyama, T. Nakano, H.-Y. Lee, and S. Yoshida: "A chlorophyll deficient mutant that has an altered amount of chloroplast genes", 1999 Korea-Japan Joint Symp.: New Approaches to Understand Gene Function in Plants and Application to Plant Biotechnology, (Seoul National University), Seoul, Korea, July (1999).

S. Sharma and J. Kaneko: "Extremely short-lived track luminescence of ion irradiated insulator crystals", 10th Int. Conf. on Radiation effects in Insulators, Jena, Germany, July (1999).

K. Kimura, S. Sharma, and J. Kaneko: "New 100 ps-lived uv luminescence of ion track in wide band-gap crystals", 21st Int. Conf. on the Physics of Electronic and Atomic Collisions (XXI-ICPEAC), Sendai, July (1999).

S. Sharma and J. Kaneko: "A new 100 ps-lived luminescence of ion tracks in insulator crystals", 18th Int. Conf. on Atomic Collisions in Solids, Odense, Denmark, Aug. (1999).

H. Tamano, S. Enomoto, E. Igasaki, N. Oku, N. Itoh, K. Tanaka, and A. Takeda: "Tumor growth after subcutaneous transplantation is affected by hepatic zinc metallothionein level", Metallothionein 99, (Osaka University), Osaka, Nov. (1999).

Y. Nose, S. Ambe, S. Enomoto, T. Arie, T. Soshi, and I. Yamaguchi: "Uptake and distribution of various radionuclides in soybean", RIKEN Symp. on Bio-Trace Elements '99.12, Wako, Dec. (1999).

H. Tamano, S. Enomoto, and A. Takeda: "Tumor and trace elements", RIKEN Symp. on Bio-Trace Elements '99.12, Wako, Dec. (1999).

F. Yatagai, T. Nomi, and M. Kusakabe: "Mutation induction by heavy-ion irradiation of gptΔ transgenic mouse", (The Institute of Space and Astronautical Science), Sagamihara, Jan. (2000).

Y. Kobayashi: "In-beam Mössbauer studies of ^{57}Fe($\leftarrow^{57}$Mn) atoms via projectile fragmentation and implantation", RIKEN Symp. on Studies on Condensed Matter Physics, Atomic Physics, Hyperfine Interactions and Biomedical Sciences Using RIKEN Accelerators, Wako, Jan. (2000).

F. Yatagai: "Biological effect of p53 after the heavy-ion exposure", Int. Workshop on Dose-Effect Relationship of Particle Radiations, (National Institute of Radiological Sciences), Chiba, Feb. (2000).

M. Hase, K. Ishioka, K. Ushida, and M. Kitajima: "Dephasing of coherent phonons induced by lattice defects in thin film of bismuth", 28th Workshop of the Surface Science Society of Japan, Tsukuba, Feb. (2000).

Y. Yoshida, A. Saeki, T. Kozawa, S. Seki, K. Ushida, Y. Numata, and S. Tagawa: "Geminate ion recombination in liquid alkane studied by subpicosecond and picosecond pulse radiolysis", 78th National Meet. Chemical Society of Japan, Funabashi, Mar. (2000).

Y. Kobayashi, A. Yoshida, K. M. Kubo, Y. Yamada, and F. Ambe: "Characterization of Fe atoms by means of ^{57}Mn beam and the in-beam Mössbauer technique", 78th National Meet. Chemical Society of Japan, Funabashi, Mar. (2000).

Y. Kobayashi, A. Yoshida, K. M. Kubo, and Y. Yamada: "In-beam Mössbauer studies on valence states of ^{57}Fe ions decayed from ^{57}Mn", Work on Science with Low-energy Radioactive Nuclear Beams 2000, (High Energy Acclerarater Research Organization), Tanashi, Mar. (2000).

Y. Konomi, T. Abe, F. Sugawara, and S. Yoshida: "Salt resistant mutation using heavy-ion beams", 2000 Ann. Meet. of Japan Society for Bioscience, Biotechnology, and Agrochemistry, Tokyo, Apr. (2000).

K. Tokuhara, T. Abe, K. Miyoshi, and S. Yoshida: "Effects of heavy-ion beam irradiation on PLB development in several orchids", 97th Congr. of the Breeding Society of Japan, Tsukuba, Apr. (2000).

H. Tsujimoto, T. Yamada, and T. Abe: "Breakage of wheat chromosomes by irradiation of heavy-ion beam", 97th Congr. of the Breeding Society of Japan, Tsukuba, Apr. (2000).

A. Yoshiki, N. Hiraiwa, C. Yoshida-Noro, N. Fukunishi, M. Kase, Y. Yano, and M. Kusakabe:

"A novel method for production of mutant mice by heavy ion beams", 33rd Ann. Meet. of the Japanese Society of Developmental Biologists, Kochi, May (2000).

H. Tamano, S. Enomoto, E. Igasaki, N. Oku, N. Itoh, K. Tanaka, and A. Takeda: "Tumor growth after subcutaneous injection is affected by hepatic zinc-metallothionein level", 6th Int. Symp. on Metal Ions in Biology and Medicine, (Armed Forces Institute of Pathology), Puerto Rico, USA, May (2000).

H. Tamano, S. Enomoto, and A. Takeda: "Zinc-65 imaging of rat brain tumors", 11th Ann. Meet. of the Japan Society for Biomedical Research on Trace Elements, Nagoya, June (2000).

S. Enomoto, R. Hirunuma, H. Tamano, and Y. Kawamura: "Transfer of various elements from the placenta to the fetus", 11th Ann. Meet. of the Japan Society for Biomedical Research on Trace Elements, Nagoya, June (2000).

K. Matsumoto, R. Hirunuma, S. Enomoto, and K. Endo: "Contents and uptakes of various elements in Se-deficient rat liver cell-fractions", 11th Ann. Meet. of the Japan Society for Biomedical Research on Trace Elements, Nagoya, June (2000).

Y. Taroda, R. Amano, and S. Enomoto: "Concentration and behavior of Mn in the brain of young mice", 11th Ann. Meet. of the Japan Society for Biomedical Research on Trace Elements, Nagoya, June (2000).

K. Ushida, M. Hase, K. Ishioka, and M. Kitajima: "The evaluation of defects formed in solids on ion irradiation as probed by coherent phonon spectroscopy", Gordon Research Conf. on Radiation Chemistry, Plymouth, USA, June (2000).

T. Matsuyama, T. Abe, C.-H. Bae, R. Kiuchi, T. Nakano, T. Asami, and S. Yoshida: "Plant genome DNA analysis by two-dimensional gel elecrophoresis", 2000 Japan-Korea Joint Symp. of Plant Science on Plant Responses to Environments: Molecular Mechanisms and Applications to Biotechnology, (The Botanical Society of Japan), Shizuoka, July (2000).

T. Abe, H. Takahashi, C.-H. Bae, N. Nagata, T. Matsuyama, and S. Yoshida: "Physiological responses of normal and albino tobacco to clomazone treatment", 2000 PGRSA/JSCRP Ann. Meet., (Plant Growth Regulation Society of America), Kailua-Kona, USA, July (2000).

T. Abe, T. Matsuyama, N. Fukunishi, S. Sekido, S. Yoshida, and I. Yamaguchi: "An effective mutation method for plants using heavy-ion beams (II)", 18th Ann. Meet. and Symp. of Japanese Society for Plant Cell and Molecular Biology, Shizuoka, July (2000).

F. Saito, L. Wei, N. Suzuki, J. Kim, Y. Itoh, A. Goto, T. Kurihara, Y. Nagashima, and T. Hyodo: "Separation of ^{18}F for the radio-pharmaceuticals of PET from ^{18}O-water by electro-deposition", 37th Ann. Meet. on Radioisotopes in the Physical Science and Industries, (Japan Radioisotope Association), Tokyo, July (2000).

T. Abe: "Salt tolerant mutants obtained by ion beam irradiation", 37th Gamma Field Symp., (MAFF, Institute of Radiation Breeding NIAR), Mito, July (2000).

M. Hase, K. Ishioka, M. Kitajima, and K. Ushida: "Effect of lattice defects on LO phonon-plasmon coupled modes in n-GaAs", 12th Int. Conf. on Ultrafast Phenomena, (Optical Society of America), Charleston, USA, July (2000).

T. Abe: "Effect of heavy-ion beam irradiation on mutation induction in plants.", 6th VIBRC Colloq. for Young Scientist, (Iwate Biotechnology Research Center), Kitakami, July (2000).

F. Saito, N. Suzuki, J. Kim, L. Wei, Y. Itoh, A. Goto, T. Kurihara, Y. Nagashima, and T. Hyodo: "^{18}F source for a slow positron beam", 12th Int. Conf. on Positron Annihilation (ICPA-12), München, Germany, Aug. (2000).

C. Egawa, Y. Takahashi, S. Enomoto, R. Hirunuma, and H. Shimizu: "Multitracer study on the diffusion of various trace elements in a granite", 2000 Ann. Meet. of the Geochemical Society of Japan, Yamagata, Sept. (2000).

F. Saito, I. Fujiwara, N. Suzuki, J. Kim, L. Wei, Y. Nagashima, T. Kurihara, Y. Itoh, A. Goto, and T. Hyodo: "Electro-deposition of ^{18}F for a slow positron beam source and recovery of ^{18}O-water in synthesis of [^{18}F]FDG", 43rd Meet. of Radiation Chemical Society of Japan, Wako, Sept. (2000).

M. Hase, K. Ishioka, K. Ushida, and M. Kitajima: "Annihilation of coherent LO phonon-plasmon coupled modes by lattice defects in n-GaAs", 25th Int. Conf. on the Physics of Semiconductors (ICPS 25), (IUPAP, The Science Council of Japan, The Physical Society of Japan, and The Japan Society of Applied Physics), Osaka, Sept. (2000).

M. Kitajima, M. Hase, K. Ishioka, and K. Ushida: "Dephasing of coherent phonons by lattice defects", Koushi Kekkan Forum, (The Physical Society of Japan), Niigata, Sept. (2000).

Y. Kobayashi, K. M. Kubo, Y. Yamada, A. Yoshida, H. Ogawa, H. Ueno, K. Asahi, and F. Ambe: "In-beam Mössbauer studides on chemical states of ^{57}Fe atoms decaying from ^{57}Mn", 44th Symp. on Radiochemistry, Kobe, Sept. (2000).

C. Egawa, Y. Takahashi, S. Enomoto, R. Hirunuma, and H. Shimizu: "Multitracer study on the diffusion of various elements in a granite", 44th Symp. on Radiochemistry, Kobe, Sept. (2000).

M. Hase, K. Ishioka, K. Ushida, and M. Kitajima: "Electron-phonon dynamics in ion-implanted semiconductors by using coherent phonon spectroscopy", 43rd Meet. of Radiation Chemical Society of Japan, Wako, Oct. (2000).

A. Saeki, T. Kozawa, S. Seki, K. Ushida, Y. Yoshida,

and S. Tagawa: "Study on geminate ion recombination in n-dodecane using subpicosecond pulse radiolysis", 43rd Meet. of Radiation Chemical Society of Japan, Wako, Oct. (2000).

F. Yatagai, T. Kurobe, T. Nomi, M. Kusakabe, K. Masumura, A. Yoshiki, H. Yamaguchi, K. Kuniya, F. Hanaoka, and Y. Yano: "Mutation induction by heavy ion irradiation of gpt Δ transgenic mice", 14th Ann. Meet. of Japanese Society for Biological Sciences in Space, Fukushima, Oct. (2000).

I. Honda, M. Wada, T. Abe, T. Asami, and S. Yoshida: "Application of heavy-ion bombardment to mutate wheat and barley", 2000 Int. Workshop Molecular Plant Breeding and Utilization of Genetic Resources, (STA, JISTEC, and MAFF), Tsukuba, Nov. (2000).

I. Honda, M. Wada, T. Abe, T. Asami, and S. Yoshida: "A novel barley mutant induced by heavy ion bombardment", 35th Ann. Meet. of the Society for the Chemical Regulation of Plants, Wako, Nov. (2000).

H. Nagase, A. Yoshiki, C. Yoshida-Noro, and M. Kusakabe: "Possible use of somatic and germ-line mutation induced by heavy ion beam (HIB) irradiation in mouse carcinogenesis models", 14th Int. Mouse Genome Conf. (IMGC 2000), Narita, Nov. (2000).

A. Yoshiki, C. Yoshida-Noro, H. Nagase, N. Hiraiwa, A. Kogiso, T. Masuda, and M. Kusakabe: "A novel strategy for mutagenesis in the mouse: Heavy ion beams and fetal phenotype screening (II)", 14th Int. Mouse Genome Conf. (IMGC 2000), Narita, Nov. (2000).

M. Kusakabe, A. Yoshiki, N. Hiraiwa, F. Ike, C. Yoshida-Noro, H. Nagase, and Y. Yano: "A novel strategy for mutagenesis in the mouse: Heavy ion beams and fetal phenotype screening (II)", 14th Int. Mouse Genome Conf. (IMGC 2000), Narita, Nov. (2000).

C. Yoshida-Noro, H. Nagase, A. Yoshiki, and M. Kusakabe: "A novel strategy for mutagenesis in the mouse: Heavy ion beams and fetal phenotype screening (III)", 14th Int. Mouse Genome Conf. (IMGC 2000), Narita, Nov. (2000).

F. Saito, L. Wei, N. Suzuki, J. Kim, Y. Itoh, A. Goto, T. Kurihara, Y. Nagashima, and T. Hyodo: "Development and application of spin polarized positron beams", Specialist Res. Meet. on Positron Beam Techniques and Condensed Matter, (Research Reactor Institute, Kyoto University), Osaka, Nov. (2000).

F. Saito, I. Fujiwara, N. Suzuki, J. Kim, L. Wei, Y. Itoh, A. Goto, T. Kurihara, Y. Nagashima, and T. Hyodo: "Electro-deposited ^{18}F source for slow positron beam", 11th Symp. on Beam Engineering of Advanced Material Syntheses, Tokyo, Nov. (2000).

H. Yasui, T. Takino, J. Fugono, R. Matsushita, J. Takada, R. Hirunuma, S. Enomoto, and H. Sakurai: "Metallokinetic analysis of blood disposition and biodistribution of vanadyl complexes in rats", 2000 Int. Chemical Congr. of Pacific Basin Societies (PACIFICHEM 2000), Honolulu, USA, Dec. (2000).

S. Morimoto, T. Kato, M. Izumi, N. Fukunishi, M. Honma, F. Hanaoka, and F. Yatagai: "Cellular responses after low-dose exposure to heavy ions", 23rd Ann. Meet. of Japanese Society of Molecular Biology, Kobe, Dec. (2000).

C. Yoshida-Noro, A. Yoshiki, H. Nagase, N. Hiraiwa, F. Ike, and M. Kusakabe: "A novel approach for mutagenesis in the mouse: Heavy ion beams and fetal phenotype screening", 23rd Ann. Meet. of Japanese Society of Molecular Biology, Kobe, Dec. (2000).

T. Soshi, T. Arie, and I. Yamaguchi: "Influence of Fusarium on the uptake of radionuclides by tomato", RIKEN Symp. on Bio-Trace Elements 2000, Wako, Dec. (2000).

5. Material analysis

T. Sugimura, J. Kawai, K. Maeda, A. Fukushima, and S. Shin: "F K-edge X-ray absorption spectroscopy for chemical state analysis", Eur. Conf. on Energy Dispersive X-Ray Spectrometry 2000, (University of Mining and Metallurgy), Krakow, Poland, June (2000).

N. Handa, O. Nureki, K. Kurimoto, S. Fukai, I. Kim, H. Sakamoto, Y. Shimura, Y. Muto, and S. Yokoyama: "Crystal structure of the Sex-lethal protein in complex with the *transformer* mRNA precursor at 1.7 Å resolution", 2nd Ann. Meet. of the RNA Society of Japan, Yokohama, July (2000).

T. Sugimura, J. Kawai, K. Maeda, A. Fukushima, S. Shin, M. Motoyama, and T. Nakajima: "F K-edge soft X-ray absorption spectroscopy", 36th Meet. for X-ray Chemical Analysis Japan, (Discussion Group of X-Ray Analysis, The Japan Society for Analytical Chemistry), Neyagawa, Nov. (2000).

K. Maeda, K. Ogiwara, H. Hamanaka, K. Hasegawa, and G. Ito: "Mini position-sensitive spectrometer with a limitted diffraction angle range designed for chemical analysis of adjacent elements", 17th PIXE Symp., Hakodate, Nov. (2000).

6. RIKEN-BNL Collaboration on Spin Physics Program

Y. Nara: "Parton cascade description of nuclear collisions at RHIC", Nihon Genshiryoku Kenkyujyo Kenkyukai Dai 2 Kai Kyokugen Jyouken ni okeru Hadron Kagaku, Tokaimura, Jan. (2000).

Y. Nara: "Parton cascade prediction of baryon distribution in ultra-relativistic heavy ion collisions", 3rd Catania Relativisitc Ion Studies (CRIS 2000), (Italian National Institute of Nuclear Physics (INFN) and the University of Catania), Acicastello, Italy, May (2000).

D. Boer: "Transversely polarized Λ production", 7th Conf. on Intersections of Particle and Nuclear

Physics (CIPANP2000), Quebec City, Canada, May (2000).

Y. Nara: "Hadron observables from hadronic transport model with jet production at RHIC", Structure of Nucleus at the Dawn of the Century (Bologna 2000), (Italian National Institute of Nuclear Physics (INFN) and The University of Bologna), Bologna, Italy, May (2000).

Y. Aoki, A. Ali Khan, S. Aoki, R. Burkhalter, S. Ejiri, M. Fukugita, S. Hashimoto, N. Ishizuka, Y. Iwasaki, Taku Izubuchi, K. Kanaya, T. Kaneko, Y. Kuramashi, T. Manke, K. Nagai, J. Noaki, M. Okawa, H. Shanahan, Y. Taniguchi, A. Ukawa, and T. Yoshie: "Chiral properties of domain-wall quarks in quenched QCD", Int. School of Subnuclear Physics: 38th Course, Theory and Experiment Heading for New Physics, (EMFCSC), Erice, Italy, Aug. (2000).

K. Suzuki and K. Itakura: "Constraints on color dipole-nuclear cross section from diffractive heavy quarkonium production", Int. Workshop on Diffraction in High-Energy Physics (Diffraction 2000), (Universitadella Calabria Universitadi Torino), Centraro, Italy, Sept. (2000).

X. LIST OF SYMPOSIA

(Jan.–Dec. 2000)

1) RIKEN Symp. on Present Status of Nuclear Fusion Research and Muon Catalyzed Fusion
6 Jan., Wako, Muon Science Lab., RIKEN

2) 10th RIKEN Winter School on Nuclear Physics with Electromagnetic Probes at RIKEN RI-Beam Factory: Unstable Nuclei and Hadrons
9–14 Jan., Akita, RI Beam Science Lab., RIKEN

3) Workshop on Jet Tagets at RHIC
26–28 Jan., New York, USA, RIKEN BNL Research Center

4) RIKEN Symp. on Studies on Condensed Matter Physics, Atomic Physics, Hyperfine Interactions, and Biomedical Science Using RIKEN Accelerators
31 Jan., Wako, Cellular Physiology Lab., Muon Science Lab., Applied Nuclear Physics Lab., Atomic Physics Lab., Cyclotron Center, RIKEN

5) RIKEN Workshop on Nuclear Structure and Reaction for the 21st Century
4–6 Feb., Wako, Cyclotron Center, RIKEN

6) RIKEN Int. Workshop on Shell Model 2000
5–8 Mar., Wako, Cyclotron Center, RIKEN

7) Event Generator for RHIC Spin Physics III: Towards Precision Spin Physics at RHIC
6–17 Mar., New York, USA, RIKEN BNL Research Center

8) Predictions and Uncertainties for RHIC Spin Physics
6–31 Mar., New York, USA, RIKEN BNL Research Center

9) Workshop on Muon Catalyzed Fusion Studies: Interaction between Theoretical and Experimental Studies
21–23 Mar., Tsukuba, Muon Science Lab., KEK-MSL and RIKEN-MUON

10) RIKEN Symp. on Scientific Research Using Tritium and Related Engineering
15–16 May, Wako, Muon Science Lab., RIKEN

11) RIKEN Symp. on The Development and Application of Neutron Optics
17–18 May, Wako, Image Information Div., RIKEN

12) Workshop on Physics at RI Beam Factory: The First Experiments
21 June, Wako, RI Beam Science Lab., RIKEN

13) eRHIC Summer Meeting at BNL
26 June–14 July, New York, USA, RIKEN BNL Research Center

14) Spin Physics Topics to be Pursued at EPIC and eRHIC
27 June, New York, USA, RIKEN BNL Research Center

15) Equilibrium and Non-Equilibrium Aspects of Hot, Dense QCD
17–30 July, New York, USA, RIKEN BNL Research Center

16) Meeting on Year-2 RHIC Spin Running
3 Aug., New York, USA, RIKEN BNL Research Center

17) RIKEN Workshop on Cluster Structure of Nuclei: Tensor Force and Nuclear Structure
19–22 Aug., Wako, RI Beam Science Lab., RIKEN

18) CNS/RIKEN Workshop on Physics with Low Energy RIB
23–25 Aug., Wako, Applied Nuclear Physics Lab., RI Beam Science Lab., Radiation Lab., CNS/RIKEN

19) Future Transversity Measurements
18–20 Sept., New York, USA, RIKEN BNL Research Center

20) RIKEN Symp. on Dynamics of High-Energy and High-Density Excited Valence Electrons in Matter
6 Oct., Wako, Beam Technology Div., RIKEN

21) RIKEN Symp. on Recent Topics on Magnetic Correlations in High Tc Superconductors
11 Oct., Wako, Muon Science Lab., RIKEN

22) Int. Workshop on Polarized Partons at High Q^2 Region in Kyoto
13–14 Oct., Kyoto, RIKEN BNL Research Center

23) Int. Spin Physics Symp. on SPIN2000 in Osaka
16–21 Oct., Osaka, RIKEN BNL Research Center

24) RIKEN Conf. on RIB00: Int. Symp. on Perspectives in Physics with Radioactive Isotope Beams 2000
13–16 Nov., Hayama, Applied Nuclear Physics Lab., RI Beam Science Lab., Radiation Lab., RIKEN/CNS

25) RIKEN-GSI Workshop on Electron-(Unstable) Nucleus Collider
17–18 Nov., Wako, RI Beam Science Lab., Beam Physics and Engineering Lab., RIKEN

26) RIKEN-RCNP Workshop on Exotics in Hadron Many Body System
22–24 Nov., Nara, RI Beam Science Lab., RIKEN

27) Workshop on Rapid Stochastic Cooling
23–24 Nov., Minakami, Beam Physics and Engineering Lab., RIKEN

28) RIKEN Symp. on Bio-Trace Elements 2000
1 Dec., Wako, Cyclotron Center, RIKEN

29) 8th RIKEN Symp. on The Theory of Atomic and Molecular Processes: Antimatter Science Using Antiprotons
15–17 Dec., Fujiyoshida, Atomic Physics Lab., RIKEN

XI. LIST OF SEMINARS

(Jan.–Dec. 2000)

Radiation Lab., RI Beam Science Lab., Applied Nuclear Physics Lab., and Beam Technology Div.

1) P. Moller, Los Alamos National Laboratory (USA), 11 Jan.
"Barriers for fission and fusion in the heavy-element region"

2) M. Smith, Oak Ridge National Laboratory (USA), 24 Jan.
"New radioactive beam measurements and theoretical calculations relevant for novae and X-ray bursters"

3) J. Wallenius, KTH (Sweden), 26 Jan.
"Accelerator driven systems for transmutation of long lived nuclear waste"

4) M. G. Itkis, Flerov Laboratory of Nuclear Reactions, JINR (Russia), 27 Jan.
"Fission of heavy and superheavy nuclei at low excitation energies"

5) S. Amari, Washington University (USA), 28 Jan.
"Abundance analysis for presolar grains found in meteorites: Nucleosynthesis studied with isotopic anomaly"

6) A. Gorine, Institute of High Energy Physics (IHEP, Protvino) (Russia), 10 Feb.
"Recent development of fiber detectors using position-sensitive pmt"

7) L. Schroeder, LBNL (USA), 16 Feb.
"Nuclear physics at the Berkeley Lab."

8) A. B. Kurepin, Institute for Nuclear Research, Russian Academy of Sciences (Russia), 22 Feb.
"Possible observation of a phase transition to quark-gluon plasma in nuclear matter"

9) U. Garg, University of Notre-Dame (USA), 24 Feb.
"Additivity of incremental alignment in superdeformation bands in the A 150 region"

10) C. Baktash, Oak Ridge National Laboratory (USA), 13 Mar.
"Research opportunities with radioactive ion beams at ORNL"

11) H. Kamada, Institut für Theoretische Physik II Ruhr-Universität Bochum (Germany), 16 Mar.
"A model for the $^{3}\mathrm{He}(\vec{d},\mathrm{p})^{4}\mathrm{He}$ reaction at intermediate energies"

12) N. V. Giai, Institut de Physique Nucleaire (France), 17 Mar.
"Microscopic description of (p,p') reactions on unstable oxygen, sulfur and argon isotopes"

13) F. Iachello, Yale University (USA), 12 Apr.
"The discovery of supersymmetry in nuclei"

14) Y. Akaishi, KEK (Tsukuba), 28 Apr.
"Coherent lambda-sigma coupling in light hypernuclei"

15) S. Kuyucak, Australian National University (Australia), 10 May
"Description of quadrupole-octupole collectivity in boson models"

16) K. Kazunori, YITP, Kyoto University (Kyoto), 11 May
"Standard theory of big-bang nucleosynthesis and present observation of light elements"

17) T. Muto, Chiba Institute of Technology (Narashino), 15 May
"Nuclear experiment on the giant Gamow-Teller state and pion condensation"

18) C. Samanta, Saha Institute of Nuclear Physics (India), 7 June
"Proton elastic scattering from ^{4,6,8}He and ^{6,7,9,11}Li"

19) M. Thoennessen, MSU (USA), 8 June
"Structure of the particle-unbound nuclei ^{7,9}He and ^{10}Li"

20) H. Utsunomiya, Konan University (Kobe), 16 June
"Photodisintegration of ^{9}Be for nuclear astrophysics"

21) T. Aumann, GSI (Germany), 19 June
"Electromagnetic excitation of relativistic secondary beams"

22) P. von Neumann-Cosel, Institut für Kernphysik, TU Darmstadt (Germany), 19 June
"Electron scattering and elementary excitation modes of nuclei"

23) A. Mengoni, ENEA-Bologna and INFN-Bologna (Italy), 20 June

"Nuclear Physics and Astrophysics at CERN-n TOF"

24) N. Kalantar-Nayestanaki, KVI Groningen (The Netherlands), 23 June
"Probing few-body systems with Bremsstrahlung"

25) S. Shlomo, Cyclotron Institute, Texas A&M University (USA), 7 July
"Microscopic calculation of excitation of isoscalar giant resonances by inelastic alpha scattering"

26) G. Colo', Universita' degli Studi (Italy), 12 July
"Giant resonances in stable and unstable nuclei"

27) H. Nakada, Chiba University (Chiba), 13 July
"Microscopic calculation of nuclear level densities applying the shell model Monte Carlo method"

28) Y. Miake, Institute of Physics, University of Tsukuba (Tsukuba), 18 July
"QGP formation and collective flow in high energy heavy ion collisions"

29) K. Chmielewski, Institut für Theoretische Physik, Universität Hannover (Germany), 28 Aug.
"Elastic and inelastic neutron-deuteron scattering with Δ-isobar excitation"

30) E. Ideguchi, Royal Institute of Technology (Sweden), 30 Aug.
"'Enhanced' superdeformation in ^{91}Tc"

31) S. WenQing, Shanghai Institute of Nuclear Research, Chinese Academy of Science (China), 11 Sept.
"Research on isospin effect of projectile fragmentation reaction and BUU calculation of total reaction cross section"

32) P. K. Sahu, Hokkaido University (Sapporo), 2 Oct.
"Nuclear equation of state and its application to heavy-ion collisions and neutron star"

33) S. WenQing, Shanghai Institute of Nuclear Research, Chinese Academy of Science (China), 4 Oct.
"Program for RIB physics and nuclear astrophysics in China and preliminary plan of Shanghai laser electron gamma source"

34) Y. A. Plis, Joint Institute for Nuclear Research (Russia), 11 Oct.
"The new possibilities for polarized ion beam production"

35) J. Tojo, Kyoto University (Kyoto), 25 Oct.
"Measurement of the analyzing power for proton-carbon elastic scattering in the Coulomb-nuclear interference region with a 22 GeV/c polarized proton beam"

36) Ch. Stoyanov, Institute for Nuclear Research and Nuclear Energy (Bulgaria), 6 Nov.
"Microscopic description of newly discovered mixed symmetry states"

37) M. Zhukov, Chalmers University of Technology (Sweden), 9 Nov.
"Can we discuss a proton halo in ^{8}B?"

38) H. Koura, Waseda University (Tokyo), 27 Nov.
"New mass formula and suggested properties of instable nuclei"

39) A. I. Malakhov, JINR (Russia), 11 Dec.
"Some results and research program of Laboratory of High Energies (JINR, Dubna)"

40) A. P. Kobushkin, Bogolyubov Institute for Theoretical Physics (Ukraine), 11 Dec.
"Deuteron spin structure at short distances from experiments with polarized deuteron beams"

41) P. Moller, Los Alamos National Laboratory (USA), 28 Dec.
"New results from calculations of fission and fusion barriers in five-dimensional, multi-million-grid-point deformation spaces"

42) Y. Hasegawa, Atominstitut (Austria), 28 Dec.
"Quantum mechanics from interference experiment"

Atomic Physics Lab.

1) O. Jagutzki, IKF, Universität Frankfurt (Germany), 2 Feb.
"Position and time resolved MCP read-out with delay-line anodes: Novel techniques, applications and future developments"

2) T. Hirota, University of Tokyo (Tokyo), 16 Feb.
"Chemical composition and evolution of matters in the core region of dark nebulas"

3) E. Lindroth, Stockholm University (Sweden), 6 Mar.
"What is known and what is not known on the high resolution spectroscopy of few body high z system"

4) C. C. Havener, Oak Ridge National Laboratory

(USA), 21 Mar.
"Low energy ion-atom collisions using merged beams"

5) M. Inokuti, Argonne National Laboratory (USA), 28 Mar.
"Dielectric-response function: Data analysis with the use of sum rules and dispersion relations"

6) J. Haynes, Institute of Physics (UK), 29 Mar.
"The future of physics communication"

7) T. Matsumoto, ERATO, JST (Tsukuba), 19 Apr.
"Negative muon capture processes in hydrogen-terminated silicon nanocrystal"

8) A. Czasch, IKF, Universität Frankfurt (Germany), 20 Apr.
"Fragmentation of diatomic molecules in slow scattering processes"

9) H. A. Schuessler, Texas A&M University (USA), 21 Apr.
"Ultra-sensitive trace detection by laser spectroscopy"

10) T. Kuwamoto, Kyoto University (Kyoto), 28 Apr.
"Search for permanent electric dipole moment with cooled Yb atoms"

11) Y. Fukuda, University of Tokyo (Tokyo), 1 May
"VUV spectroscopy of rare gas dimers: Ion core transfer in high Rydberg states"

12) L. G. Christophorou, National Institute of Standards and Technology (USA), 25 May
"Electron interactions with excited atoms and molecules"

13) X.-M. Tong, Cold Trapped Ion Project, ICORP, JST (Chofu), 21 July
"Density functional theory with optimized effective potential: An application to energy structure of hollow atoms and ions"

14) S. Hasegawa, Institute of Space and Astronautical Science (Sagamihara), 23 Aug.
"Acceleration of submicron and micron particles by an electrostatic accelerator"

15) J. Eichler, Hahn-Meitner-Institut Berlin (Germany), 10 Nov.
"Ion-atom collisions at relativistic velocities"

16) C. T. Whelan, University of Cambridge (UK), 24 Nov.
"(e, 2e) and related processes"

17) H. A. Schuessler, Texas A&M University (USA), 4 Dec.
"Nonlinear properties of laser-generated giant surface acoustic wave pulses in solid materials"

18) E. D. Donets, JINR (Russia), 18 Dec.
"Nuclear and atomic researches with an ion trap apparatus, using dense electron beams and strings: Results and project proposals"

RIBF Project Office, Beam Physics and Engineering Lab., Beam Dynamics Div., and Beam Technology Div.

1) M. Xiao, University of Tokyo (Tokyo), 10 Feb.
"Spin dynamics of polarized proton beams in relativistic heavy ion collider (RHIC)"

2) R. Jameson, LANL (USA), 7 Mar.
"Some fundamental questions of space-charge physics"

3) S. Adam, Paul Scherrer Institut (Switzerland), 21 Apr.
"Routine operation of the PSI Accelerator Facility at a beam power of 0.9 megawatt"

4) G. Melin, CEA-Grenoble (France), 18 May
"Evolution of electron cyclotron resonance ion source (ECRIS) of highly charged ions from classical to superconducting sources"

5) G. Shirkov, JINR (Russia), 4 Sept.
"Physical and numerical basement of ECR plasma simulation with particle-in cell model"

6) T. Hori, Sumitomo Heavy Industries Ltd. (Tanashi), 28 Sept.
"Present status and design concept of compact SR source AURORA2S"

7) A. Dael, CEA-Saclay (France), 5 Dec.
"B0 construction and Saclay activities"

8) S. M. Lund, LLNL (USA), 11 Dec.
"Axial bunch compression ion rings through fast bunch"

Radioisotope Technology Div.

1) S. Kodama, Nagasaki University (Nagasaki), 11 Oct.
"Mechanisms of radiation-induced genetic instability"

2) K. Ohta, RIKEN (Wako), 11 Oct.
"The role of Mre-11 in DNA recombination and telomere main tenance"

RIKEN BNL Research Center

1) J. Smith, SUNY, Stony Brook (USA), 5 Jan.
"Variable flavor number schemes for heavy quark electroproduction"

2) J. Raufeisen, Institut für Theoretische Physik, University Heidelberg (Germany), 14 Jan.
"Light-cone approach to nuclear shadowing in DIS and to the Drell-Yan process"

3) E. Souza Fraga, BNL (USA), 20 Jan.
"The role of fermions and dynamical viscosity in nucleating bubbles"

4) S. Raha, BNL (USA)/Bose Institute (Calcutta), 21 Jan.
"Some aspects of strangeness in astrophysics and cosmic rays"

5) Y. Kuramashi, Washington University (USA), 26 Jan.
"Nucleon decay matrix elements from lattice QCD"

6) S. White, BNL (USA), 27 Jan.
"A program of measurements with an internal target at RHIC"

7) M. Baker, BNL (USA), 1 Feb.
"Transversity"

8) F. Maltoni, University of Illinois at Urbana-Champaign (USA), 2 Feb.
"Quarkonium phenomenology: Status and directions"

9) F. Gelis, BNL (USA), 3 Feb.
"Photon and dilepton production by a quark-gluon plasma"

10) R. Rapp, SUNY, Stony Brook (USA), 4 Feb.
"Thermal dileptons: Chiral restoration and QGP radiation"

11) M. Alford, MIT (USA), 9 Feb.
"Scalar mesons and pion scattering on the lattice"

12) J. Ollitrault, Saclay (France), 11 Feb.
"Effects of HBT correlations and momentum conservation on flow at SPS"

13) A. Henneman, Vrije University (The Netherlands), 15 Feb.
"Soffer-like bounds on distribution functions with transverse momentum"

14) M. Neubert, Cornell University (USA), 16 Feb.
"Theory of hadronic B decays"

15) J. Schaffner-Bielich, RIKEN BNL Rresearch Center (USA), 17 Feb.
"Weak decay of strange dibaryons"

16) R. Malfliet, ECT* (Italy), 18 Feb.
"Non-classical behaviour in non-equilibrium quantum systems"

17) S. White, BNL (USA), 22 Feb.
"A_N measurement at RHIC"

18) J. Verbaarshot, SUNY, Stony Brook (USA), 23 Feb.
"Exact results for QCD dirac spectra at zero and finite baryon density"

19) A. Peshier, BNL (USA), 24 Feb.
"Thermodynamics of the QGP at finite chemical potential"

20) S. Bass, Michigan State University (USA), 25 Feb.
"Dynamics of hot bulk QCD matter: From QGP to hadronic freeze-out"

21) W. Guryn, BNL (USA), 29 Feb.
"Summary of the Jet target workshop"

22) D. Bodeker, Niels Bohr Institute (Germany), 1 Mar.
"The dynamics of magnetic scale gluons"

23) S. Jeon, Ernest Orlando LBNL (USA), 3 Mar.
"Charged multiplicity ratio fluctuations as a QGP signal"

24) G. Weiglein, Conseil Européen pour la Recherche Nucléaire (Switzerland), 8 Mar.
"Higgs and electroweak precision physics at present and future colliders"

25) A. Hebecker, University of Heidelberg (Germany), 10 Mar.
"Diffractive parton distributions"

26) D. Wackeroth, University of Rochester (USA), 15 Mar.
"Four-fermion production at present and future e^+e^- colliders: Precise predictions from RACOONWW"

27) D. Rischke, BNL (USA)/RIKEN BNL Research Center (USA), 17 Mar.
"Color superconductivity in cold dense quark

matter"

28) T. Csorgo, Columbia University (USA)/KFKI (Hungary), 23 Mar.
"Back-to-back correlations of bosons and fermions at RHIC"

29) G. J. Lolos, University of Regina (Canada), 24 Mar.
"Mass and helicity modifications in low energy ρ photoproduction"

30) F. Meissner, DESY-Zeuthen (Germany), 27 Mar.
"Spin asymmetry in vector meson production in HERMES"

31) X. Wang, Ernest Orlando LBNL (USA), 30 Mar.
"Multiple scattering and parton energy loss in eA collisions"

32) D. Riska, University of Helsinki (Finland), 31 Mar.
"The strange form factors of the proton: SAMPLE, HAPPEX, and the anapole moment"

33) R. Jakob, Wuppertal University (Germany), 4 Apr.
"Interference fragmentation functions"

34) R. Lebed, Jefferson Laboratory (USA), 11 Apr.
"Masses of orbitally excited baryons in large N_c QCD"

35) M. Diehl, Stanford Linear Accelerator Center (USA), 11 Apr.
"Deeply-virtual Compton scattering"

36) T. Schaefer, RIKEN BNL Research Center (USA)/SUNY, Stony Brook (USA), 13 Apr.
"Gluino condensation and instantons"

37) M. Diehl, Stanford Linear Accelerator Center (USA), 14 Apr.
"Learning more about the proton structure: Parton distributions and beyond"

38) D. Son, Columbia University (USA)/RIKEN BNL Research Center (USA), 20 Apr.
"Avoiding the sign problem: QCD at finite isospin density"

39) A. Muronga, University of Minnesota (USA), 21 Apr.
"Dissipative fluid dynamics for relativistic nuclear collisions"

40) J. Garcia-Bellido, Imperial College (UK), 26 Apr.
"Leptogenesis from preheating in hybrid inflation"

41) N. Saito, RIKEN (Wako)/RIKEN BNL Research Center (USA), 2 May
"Report from DIS2000"

42) E. Simmons, Boston University (USA), 3 May
"Exploring new electroweak interactions for the third generation"

43) T. D. Lee, Columbia University (USA)/RIKEN BNL Research Center (USA), 4 May
"A new method to derive n-dimensional quantum wave functions"

44) A. Dumitru, Columbia University (USA), 5 May
"Coupling of soft and hard modes of chiral condensates in real time lattice simulations"

45) M. Perdekamp, RIKEN BNL Research Center (USA), 9 May
"More report from DIS2000"

46) E. Shuryak, SUNY, Stony Brook (USA)/RIKEN BNL Rresearch Center (USA), 18 May
"Instanton-induced effects and high energy processes"

47) M. Bai, BNL (USA), 23 May
"Improving polarization at AGS"

48) L. Everett, University of Michigan (USA), 24 May
"CP violation and flavor in type I superstring models"

49) R. Kaiser, DESY-Zeuthen (Germany), 30 May
"Polarized electron-nucleon scattering at TESLA"

50) R. Kaiser, DESY-Zeuthen (Germany), 30 May
"The HERMES RICH detector"

51) C. Aragao de Carvalho, Universidade Federal do Rio de Janeiro (Brazil), 31 May
"Phase transitions in field theories"

52) G. Carter, SUNY, Stony Brook (USA), 2 June
"Neutrino propagation in color superconducting quark matter and protoneutron stars"

53) A. Belitsky, SUNY, Stony Brook (USA), 6 June
"Extraction of skewed parton distributions"

54) L. Lellouch, CPT, CNRS Luminy (France), 7 June
"Non-leptonic weak decays from euclidean corre-

lation functions"

55) A. Yelkhovsky, Budker Institute (Russia), 14 June
"Ground state of the helium atom"

56) K. Melnikov, Stanford Linear Accelerator Center (USA), 21 June
"Three loop renormalization of QED and QCD"

57) Z. Bern, UCLA (USA), 28 June
"NNLO QCD"

58) Z. Duan, Yale University (USA), 29 June
"Low energy theory for two flavors at high density QCD"

59) F. Sannino, Yale University (USA), 30 June
"Entropy and phases of chiral gauge theories"

60) S. Pate, New Mexico State University (USA), 6 July
"Polarized lambda production"

61) R. Yoshida, Argonne National Laboratory (USA), 11 July
"Proton structure measurements from HERA"

62) A. Arbuzov, INFN (Italy), 12 July
"Radiative corrections to e^+e^- scattering"

63) S. Bueltmann, University of Virginia (USA), 18 July
"Recent results from E155"

64) M. H. G. Tytgat, Conseil Européen pour la Recherche Nucléaire (Switzerland), 26 July
"Surfing on non-commutative waves"

65) L. Ya. Glozman, University of Graz (Austria), 11 Aug.
"Baryon structure in the low-energy regime of QCD"

66) M. Stratmann, Regensburg University (Germany), 12 Sept.
"Current issues in polarized PDF analyses"

67) S. Nussinov, Tel Aviv University (Israel), 13 Sept.
"The rise and fall of the crossection"

68) M. Nowak, Cracow, 14 Sept.
"Disorder in QCD and diffusion of the light quarks in t"

69) Y. Derbenev, DESY (Germany), 21 Sept.
"Stern gerlach polarization of antiprotons in storage rings"

70) M. Nowak, Jagellonian University (Poland), 22 Sept.
"pi0 $\rightarrow \gamma\gamma$ in dense QCD"

71) M. Stratmann, Regensburg University (Germany), 26 Sept.
"Polarized heavy flavor production in NLO QCD"

72) M. Polyakov, St. Petersburg, INP (Russia)/Ruhr University (Germany), 26 Sept.
"Stratmann and ubar–dbaqr asymmetry in the (polarized) nucleon sea"

73) K. Sasaki, Yokohama National University (Yokohama), 27 Sept.
"Parton distributions in the polarized virtual photon target"

74) G. Sterman, SUNY, Stony Brook (USA)/BNL (USA), 11 Oct.
"Combining threshold and transverse momentum resummations"

75) M.-A. Halasz, University of Pennsylvania (USA), 20 Oct.
"Random matrices and the sign problem in QCD at finite mu"

76) I. Zahed, SUNY, Stony Brook (USA), 27 Oct.
"Non-perturbative approach to high energy scattering in QCD"

77) M. Muehlleitner, DESY (Germany), 1 Nov.
"Higgs pair production at high-energy colliders"

78) T. Fugleberg, BNL (USA), 2 Nov.
"A signal for induced theta vacua"

79) E. Gubankova, North Carolina State University (USA), 3 Nov.
"Solving QCD Hamiltonian for bound states"

80) I. Balitsky, Jefferson Laboratory (USA)/Old Dominion University (USA), 8 Nov.
"Renormalons as dilatation modes in the functional space"

81) F. Laue, M. Calderon, A. Poskanzer, 9 Nov.
"STAR data from RHIC: HBT, h-spectra, flow"

82) S. Soff, BNL (USA), 14 Nov.
"Strangeness, collective flow and correlations as probes of excited nuclear matter"

83) D. Zeppenfeld, University of Wisconsin (USA), 15

Nov.
"Prospects for intermediate mass higgs studies at the LHC"

84) A. Basilevsky, S. Mioduszewski, J. Burward-Hoy, RIKEN BNL Research Center (USA), 16 Nov.
"PHENIX: Transverse energy; Neutral pion production; Charged hadron pt"

85) J. Raufeisen, Ernest Orlando LBNL (USA), 17 Nov.
"QCD coherence effects in high energy reactions with nuclei"

86) D. Boer, RIKEN BNL Research Center (USA), 28 Nov.
"Towards a global transversity analysis"

87) Y. Aoki, RIKEN BNL Research Center (USA), 30 Nov.
"Chiral properties of domain-wall quarks in quenched QCD"

88) J. Bowers, MIT (USA), 1 Dec.
"Crystalline color superconductivity"

89) T. Tait, Argonne National Laboratory (USA), 6 Dec.
"Flavor and supersymmetry breaking from a small extra dimension"

90) A. Zhitnitsky, British Columbia University (Canada), 7 Dec.
"QCD domain walls"

91) J. A. Wirstam, BNL (USA), 7 Dec.
"Effective actions and world-line methods at finite temperature"

92) B. Fox, University of Colorado (USA), 12 Dec.
"Deeply virtual Compton scattering"

93) H. Cheng, Academia Sinica (Taiwan)/BNL (USA), 13 Dec.
"Some aspects of hadronic charmless B decays"

94) D. Kharzeev, BNL (USA), 14 Dec.
"What do we learn from the first data on hadron production at RHIC?"

95) M. Okawa, KEK (Tsukuba), 20 Dec.
"Toward the 2 + 1 flavor QCD simulation with exact fermion algorithm"

Image Information Div.

1) Y. Otake, RIKEN (Harima), 7 June
"The possibility of the detection between the coherency and decoherence"

2) J. Kawarabayashi, Nagoya University (Nagoya), 29 June
"Single electron transistor for radiation measurement application"

3) F. Klose, Spallation Neutron Source (USA), 10 Nov.
"Optical components for reflectometer at SNS (Spallation Neutron Source)"

4) D. Fukuda, University of Tokyo (Tokyo), 13 Nov.
"Development of radiation detectors with superconductive materials"

XII. LIST OF PERSONNEL

RIKEN ACCELERATOR RESEARCH FACILITY

TANIHATA Isao 谷畑勇夫 (Facility Director)
YANO Yasushige 矢野安重 (Vice Facility Director)

Linac Division

FUJIMAKI Masaki 藤巻正樹
KASE Masayuki 加瀬昌之 *1
IKEZAWA Eiji 池沢英二
KOHARA Shigeo 小原重夫

Ring Cyclotron Division

FUJITA Jiro 藤田二郎
INABE Naohito 稲辺尚人
KAMIGAITO Osamu 上垣外修一
KOHARA Shigeo 小原重夫
NAGASE Makoto 長瀬 誠
OGIWARA Kiyoshi 荻原 清
IKEGAMI Kumio 池上九三男
KAGEYAMA Tadashi 影山 正
KASE Masayuki 加瀬昌之 *1
KUBO Toshiyuki 久保敏幸
NAKAGAWA Takahide 中川孝秀
OKUNO Hiroki 奥野広樹

Experimental Support Division

ICHIHARA Takashi 市原 卓
KANAI Yasuyuki 金井保之
MORITA Kosuke 森田浩介
YATAGAI Fumio 谷田貝文夫
KAMBARA Tadashi 神原 正 *1
MATSUZAKI Teiichiro 松崎禎市郎
WATANABE Yasushi 渡邊 康

Radioisotope Facilities Division

KOBAYASHI Yoshio 小林義男
YATAGAI Fumio 谷田貝文夫 *1

Radiation Protection Group

FUJITA Shin 藤田 新 *1
OGIWARA Kiyoshi 荻原 清
ITO Sachiko 伊藤祥子

Administration Division

MANABE Tadashi 真鍋 烈 *2
NUMATA Shigeo 沼田茂男
NAKAMURA Toshiko 中村とし子

Steering Committee

ASAHI Koichiro 旭 耕一郎
HANAOKA Fumio 花岡文雄
KAMBARA Tadashi 神原 正
KATAYAMA Takeshi 片山武司
MANABE Tadashi 真鍋 烈
NAGAMINE Kanetada 永嶺謙忠
TANIHATA Isao 谷畑勇夫
YANO Yasushige 矢野安重
YOSHIDA Shigeo 吉田茂男
GOTO Akira 後藤 彰
ICHIHARA Takashi 市原 卓
KASE Masayuki 加瀬昌之
KATSUMATA Koichi 勝又紘一
MATSUZAKI Teiichiro 松崎禎市郎
SAWA Hiroshi 澤 宏
YAMAZAKI Yasunori 山崎泰規 *3
YATAGAI Fumio 谷田貝文夫

*1 Group Leader, *2 Manager, *3 Chairperson

****
Members (included Special Postdoctral Researcher,
RIKEN Fellow, and Contract Researcher)
****

Cosmic Radiation Laboratory

Members

KATO Hiroshi 加藤 博
MIYASAKA Hiromasa 宮坂浩正
YOSHIDA Atsumasa 吉田篤正

Visiting Members

GOKA Tateo 五家建夫 (NASDA)
KOSHIISHI Hideki 越石英樹 (NASDA)
MATSUMOTO Haruhisa 松本晴久 (NASDA)

Radiation Laboratory

Head

TANIHATA Isao 谷畑勇夫

Members

ICHIHARA Takashi 市原 卓
YOSHIDA Atsushi 吉田 敦
SAITO Naohito 齊藤直人
WATANABE Yutaka 渡邊 裕
HAYASHI Naoki 林 直樹
YASUI Yoshiaki 安井良彰
WATANABE Yasushi 渡邉 康
KISHIDA Takashi 岸田 隆
TAKETANI Atsushi 竹谷 篤
MURATA Jiro 村田次郎
NAITO Kenichi 内藤謙一
ISHII Noriyoshi 石井理修

Visiting Members

AKIBA Yasuyuki 秋葉康之 (KEK)
ANDO Yoshiaki 安藤嘉章 (Coll. Sci., Rikkyo Univ.)
AOI Nori 青井 考 (Dept. Phys., Grad. Sch. Sci., Univ. Tokyo)
ASAI Masato 浅井雅人 (JAERI)
ASAMI Hiroyasu 浅海弘保 (KEK)
AWAYA Yoko 粟屋容子 (Musashino Art Univ.)
BAUMANN Thomas (Natl. Superconducting Cycl. Lab., Michigan State Univ., USA)
BECK F. A. (CRN, France)
BENTZ Wolfgang (Dept. Phys., Grad. Sch. Sci., Univ. Tokyo)
BROGLIA R. (Univ. di Milano, Italy)
BROOKS Melynda (LANL, USA)
BURWARD-HOY Muriel Jane (Dept. Phys., SUNY, Stony Brook, USA)
CASTEN Rick (Phys. Dept., BNL, USA)
CHUJO Tatsuya 中條達也 (Phys. Dept., BNL, USA)
COLO Gianluca (Univ. di Milano, Italy)
CRIST Norman (Columbia Univ., USA)
DOOI Makoto 堂井 真 (Inst. Phys., Univ. Tsukuba)
EN'YO Hideto 延与秀人 (Fac. Sci., Kyoto Univ.)
FLOCARD Hubert (Div. Phys. Theor. IPN, Inst. Phys. Nucl., France)
FUCHI Yoshihide 渕 好秀 (KEK)
FUJII Hirotsugu 藤井宏次 (Grad. Sch. Arts Sci., Univ. Tokyo)
FUJIKAWA Kazuo 藤川和男 (Fac. Sci., Univ. Tokyo)
FUKUDA Mitsunori 福田光順 (Grad. Sch. Sci., Osaka Univ.)
FUKUDA Naoki 福田直樹 (Dept. Phys., Grad. Sch. Sci., Univ. Tokyo)
FUKUDA Tomokazu 福田共和 (KEK)
FURUTAKA Kazuyoshi 古高和禎 (JAERI)
GELBERG Adrian (Koln Univ., Germany)
HAMAMOTO Ikuko 浜本育子 (Univ. Lund, Sweden)
HATSUDA Tetsuo 初田哲男 (Fac. Sci., Kyoto Univ.)
HAYASHIGAKI Arata 林垣 新 (Dept. Phys., Grad. Sch. Sci., Univ. Tokyo)

HORIUCHI Hisashi 堀内 昶 (Fac. Integr. Human Studies, Dept. Fundamental Sci., Kyoto Univ.)
HOTTA Tomohiro 堀田智洋 (Grad. Sch. Arts Sci., Univ. Tokyo)
ICHIMURA Munetake 市村宗武 (Grad. Sch. Arts Sci., Univ. Tokyo)
IDEGUCHI Eiji 井手口栄治 (Dept. Chem. Washington Univ., USA)
IEKI Kazuo 家城和夫 (Coll. Sci., Rikkyo Univ.)
IMAI Kenichi 今井憲一 (Fac. Sci., Kyoto Univ.)
IMOTO Michiko 井本道子 (Lab. Phys., Coll. Sci. Technol., Nihon Univ.)
ISHII Tetsuro 石井哲朗 (JAERI)
IWASAKI Hironori 岩崎弘典 (Dept. Phys., Grad. Sch. Sci., Univ. Tokyo)
IZUMI Hideaki 出水秀明 (Grad. Sch. Sci., Osaka Univ.)
JIN Genming 靳 根明 (Inst. Modern Phys., Chinese Acad. Sci., China)
KAKI Kaori 嘉規香織 (Fac. Sci., Shizuoka Univ.)
KAMAE Tsuneyoshi 釜江常好 (Fac. Sci., Univ. Tokyo)
KASAGI Jirota 笠木治郎太 (Lab. Nucl. Sci., Tohoku Univ.)
KATO Seigo 加藤静吾 (Fac. Ed., Yamagata Univ.)
KIM Jong Chan 金 鐘賛 (Dept. Phys., Seoul Natl. Univ., Korea)
KISTENEV Edouard (Phys. Dept., BNL, USA)
KITAO Kensuke 喜多尾憲助 (Data Eng. Inc.)
KODAIRA Jirou 小平治郎 (Fac. Sci., Hiroshima Univ.)
KOHAMA Akihisa 小濱洋央 (Fac. Sci., Univ. Tokyo)
KOIKE Yuji 小池裕司 (Fac. Sci., Niigata Univ.)
KUMANO Shunzo 熊野俊三 (Fac. Sci. Eng., Saga Univ.)
KUNIHIRO Teiji 國弘悌二 (YITP, Kyoto Univ.)
KUSAKARI Hideshige 草刈英榮 (Fac. Ed., Chiba Univ.)
LIU Guanhua 劉 冠華 (Inst. Modern Phys., Chinese Acad. Sci., China)
LIU Zhong (Inst. Modern Phys., Chinese Acad. Sci., China)
LOMON Earle (Massachusetts Inst. Technol., USA)
MAO Yajun (Phys. Dept., BNL, USA)
MATSUDA Satoshi 松田 哲 (Fac. Integr. Human Studies, Dept. Fundamental Sci., Kyoto Univ.)
MATSUI Tetsuo 松井哲男 (YITP, Kyoto Univ.)
MATSUYANAGI Kenichi 松柳研一 (Fac. Sci., Kyoto Univ.)
MENGONI Alberto (Phys. Div., ENEA, Italy)
MIAKE Yasuo 三明康郎 (Inst. Phys., Univ. Tsukuba)
MIN Byung-Joo 閔 丙珠 (Korea Atomic Energy Res. Inst., Korea)
MITARAI Shiro 御手洗志郎 (Fac. Sci., Kyushu Univ.)
MIYAMA Masanori 深山正紀 (Fac. Sci., Tokyo Metrop. Univ.)
MIYATAKE Hiroari 宮武宇也 (KEK)
MOLLER Peter (LANL, USA)
MORII Toshiyuki 森井俊行 (Fac. Human Dev., Kobe Univ.)
MORIKAWA Tsuneyasu 森川恒安 (Fac. Sci., Kyushu Univ.)
MORINOBU Shunpei 森信俊平 (Fac. Sci., Kyushu Univ.)
MOTOBAYASHI Toru 本林 透 (Coll. Sci., Rikkyo Univ.)
MOTTELSON Ben R. (Nordita; Nordisk Inst. Teoretisk Fysik, Denmark)
MUELLER Ludwig (Phys. Dept., Univ. di Padoba, Italy)
MURAKAMI Takeshi 村上 健 (Natl. Inst. Radiol. Sci.)
MURAKAMI Hiroyuki 村上浩之 (Coll. Sci., Rikkyo Univ.)
NAGAI Yasuki 永井泰樹 (RCNP, Osaka Univ.)
NAGAMIYA Shoji 永宮正治 (KEK)
NAKAJIMA Mitsuo 中島充夫 (Grad. Sch. Nagatsuta, Tokyo Inst. Technol.)
NAKAMURA Shogo 中村正吾 (Fac. Ed., Yokohama Natl. Univ.)
NAKAMURA Takashi 中村隆司 (Tokyo Inst. Technol.)
NAKAMURA Masanobu 中村正信 (Fac. Sci., Kyoto Univ.)
NAKAYAMA Shintaro 中山信太郎 (Fuc. Integr. Arts Sci., Univ. Tokushima)
NEMOTO Yukio 根本幸雄 (RCNP, Osaka Univ.)
NIIZEKI Takashi 新関 隆 (Tokyo Kasei Univ.)
NISHIMURA Jun 西村 淳 (Cen. Integrated Res. Sci. Eng., Nagoya Univ.)
NORO Tetsuo 野呂哲夫 (RCNP, Osaka Univ.)

ODAHARA Atsuko 小田原厚子 (Nishinippon Inst. Technol.)
OGAWA Masao 小川雅生 (Tokyo Inst. Technol.)
OHSHIMA Kazuto 大嶋一人 (Gunma Natl. Coll. Technol.)
OKAMURA Hiroyuki 岡村弘之 (Fac. Sci., Saitama Univ.)
OOISHI Ryutaro 大石竜太郎 (Inst. Phys., Univ. Tsukuba)
ORIHARA Hikonojyo 織原彦之丞 (Cycl. Radioisot. Cen., Tohoku Univ.)
OSHIMA Masumi 大島真澄 (JAERI)
OTSUKA Takaharu 大塚孝治 (Fac. Sci., Univ. Tokyo)
PAN Qiangyan 潘 強岩 (Inst. Modern Phys., Chinese Acad. Sci.)
PENIONZHKEVICH Iouri (Flerov Lab. Nucl. React., Joint Inst. Nucl. Res., Russia)
PIERROUTSAKOU Dimitra (Sez. Napoli (INFN), Italy)
REN Zhongzhou 任 中洲 (Nanjing Univ., China)
SAGAWA Hiroyuki 佐川弘幸 (Cen. Math. Sci., Univ. Aizu)
SAKAGUCHI Harutaka 坂口治隆 (Fac. Sci., Kyoto Univ.)
SAKURAGI Hiroyuki 櫻木弘之 (Fac. Sci., Osaka City Univ.)
SAKURAI Hiroyoshi 櫻井博儀 (Dept. Phys. Grad. Sch. Sci., Univ. Tokyo)
SASAKI Shoichi 佐々木勝一 (Dept. Phys. Grad. Sch. Sci., Univ. Tokyo)
SATO Hikaru 佐藤 皓 (KEK)
SATO Hiroki 佐藤博紀 (Fac. Sci., Kyoto Univ.)
SAWADA Shinya 澤田真也 (KEK)
SCHAEFER Markus (Phys. Inst., Univ. Goettingen, Germany)
SCHMIDT-OTT Wolf-Dieter (Phys. Inst., Univ. Goettingen, Germany)
SEDERWALL Bo (Royal Inst. Technol., Sweden)
SHIBATA Toshiaki 柴田利明 (Tokyo Inst. Technol.)
SHIGAKI Kenta 志垣賢太 (KEK)
SHIMIZU Hajime 清水 肇 (Fac. Ed., Yamagata Univ.)
SHIMIZU Yoshifumi 清水良文 (Fac. Sci., Kyushu Univ.)
SHIMODA Tadashi 下田 正 (Grad. Sch. Sci., Osaka Univ.)
SIGNORINI Cosimo (Phys. Dept., Univ. di Padoba, Italy)
STROE Lucian (Phys. Dept., Univ. di Padoba, Italy)
SUGAWARA Masahiko 菅原昌彦 (Chiba Inst. Technol.)
SUGITATE Toru 杉立 徹 (Fac. Sci., Fac. Sci. Hiroshima Univ.)
SUZUKI Yasuyuki 鈴木宜之 (Fac. Sci., Niigata Univ.)
SUZUKI Katsuhiko 鈴木克彦 (Dept. Phys., Grad. Sch. Sci., Univ. Tokyo)
SUZUKI Toshio 鈴木敏男 (Fac. Eng., Fukui Univ.)
TAJIMA Yasuhisa 田島靖久 (Cycl. Radioisot. Cen., Tohoku Univ.)
TAKADA Eiichi 高田栄一 (Natl. Inst. Radiol. Sci.)
TAKAHASHI Tadayuki 高橋忠幸 (Inst. Space Astro. Sci.)
TAKEMOTO Hiroki 竹本宏輝 (JAERI)
TAKIGAWA Noboru 滝川 昇 (Grad. Sch. Sci., Tohoku Univ.)
TAKIZAWA Makoto 瀧澤 誠 (Showa Coll. Pharm. Sci.)
TAMII Atsushi 民井 淳 (Fac. Sci., Univ. Tokyo)
TANAKA Masahiko 田中雅彦 (KEK)
TANOKURA Atsushi 田野倉 敦 (Fac. Sci. Technol., Sophia Univ.)
TENDOW Yoshihiko 天道芳彦
TERAKAWA Atsuki 寺川貴樹 (Cycl. Radioisot. Cen., Tohoku Univ.)
TORII Hisayuki 鳥井久行 (Fac. Sci., Kyoto Univ.)
TOYAMA Takeshi 外山 毅 (KEK)
TOYOKAWA Hidenori 豊川秀訓 (JASRI)
UEMATSU Tsuneo 植松恒夫 (Fac. Integr. Human Studies, Dept. Fundamental Sci., Kyoto Univ.)
UENO Hideki 上野秀樹 (Lab. Nucl. Studies, Fac. Sci., Osaka Univ.)
UNO Masahiro 宇野正宏 (Min. Ed. Sci. Sports Culture)
WAKAMATSU Masashi 若松正志 (Lab. Nucl. Studies, Fac. Sci., Osaka Univ.)
WAKASA Tomotsugu 若狭智嗣 (RCNP, Osaka Univ.)
WHITE Sebastian (Phys. Dept., BNL, USA)
XU Shuwei 徐 樹威 (Inst. Modern Phys., Chinese Acad. Sci., China)
YAMANISHI Teruya 山西輝也 (Fac. Eng., Fukui Univ. Technol.)

YAMASHITA Yoshiki　山下芳樹　(Hirosaki Univ.)
YAZAKI Koichi　矢崎紘一　(Tokyo Women's Chr. Univ.)
YOKKAICHI Satoshi　四日市　悟　(Fac. Sci., Kyoto Univ.)
YOSHIMURA Koji　吉村浩司　(Int. Cen. Element. Part. Phys., Univ. Tokyo)
YOSHINAGA Naotaka　吉永尚孝　(Fac. Sci., Saitama Univ.)
YOSOI Masaru　與曽井　優　(Fac. Sci., Kyoto Univ.)
ZHANG Yu-Hu　張　玉虎　(Inst. Modern Phys., Chinese Acad. Sci., China)
ZHOU Xiaohong　周　小紅　(Inst. Modern Phys., Chinese Acad. Sci., China)
ZHU Lihua　(China Inst. Atom. Energy, China)

Trainees

BABA Hidetada　馬場秀忠　(Coll. Sci., Rikkyo Univ.)
DEMICHI Kimihiko　出道仁彦　(Coll. Sci., Rikkyo Univ.)
FUKUCHI Tomonori　福地知則　(Fac. Sci., Kyushu Univ.)
FUSAWA Hirofumi　古澤博文　(Fac. Sci., Niigata Univ.)
FUTAKAMI Udai　二上宇内　(Coll. Sci., Rikkyo Univ.)
GOMI Tomoko　五味朋子　(Coll. Sci., Rikkyo Univ.)
HASEGAWA Hirokazu　長谷川浩一　(Coll. Sci., Rikkyo Univ.)
HATANO Michio　波多野道夫　(Dept. Phys., Grad. Sch. Sci., Univ. Tokyo)
HIGURASHI Yoshihide　日暮祥英　(Coll. Sci., Rikkyo Univ.)
HIRAI Masanori　平井正紀　(Fac. Sci. Eng., Saga Univ.)
IKEDA Hiroshi　池田　宙　(Tokyo Inst. Technol.)
INOUE Masaki　井上正樹　(Fac. Sci., Kyushu Univ.)
ISHIDA Tomoyuki　石田智之　(Dept. Phys., Grad. Sch. Sci., Univ. Tokyo)
KANEKO Emi　金子恵美　(Coll. Sci., Rikkyo Univ.)
KANNO Syouko　菅野祥子　(Coll. Sci., Rikkyo Univ.)
KASHIYAMA Osamu　樫山　修　(Fac. Sci., Kyushu Univ.)
KATO Hiromitsu　加藤裕充　(Dept. Phys., Grad. Sch. Sci., Univ. Tokyo)
KAWASAKI Hiroaki　河崎洋章　(Coll. Sci., Rikkyo Univ.)
KINUGAWA Hiroto　衣川裕人　(Coll. Sci., Rikkyo Univ.)
KISHI Chieko　岸　千恵子　(Coll. Sci., Rikkyo Univ.)
KIYOMICHI Akio　清道明男　(Inst. Phys., Univ. Tsukuba)
KOBAYAKAWA Akira　小早川　彰　(Dept. Phys., Grad. Sch. Sci., Univ. Tokyo)
KUNIBU Makoto　國分　誠　(Coll. Sci., Rikkyo Univ.)
KUROKAWA Minako　黒川三奈子　(Tokyo Inst. Technol.)
MAEDA Yukie　前田幸重　(Dept. Phys., Grad. Sch. Sci., Univ. Tokyo)
MATSUURA Taeko　松浦妙子　(Dept. Phys., Grad. Sch. Sci., Univ. Tokyo)
MATSUYAMA Yuuichi　松山裕一　(Coll. Sci., Rikkyo Univ.)
MINEMURA Toshiyuki　峯村俊行　(Coll. Sci., Rikkyo Univ.)
MIURA Motooki　三浦元隆　(Tokyo Inst. Technol.)
MIYAKAWA Takahiko　宮川貴彦　(Fac. Sci., Tokyo Metrop. Univ.)
MORINAGA Mitsutoshi　守永光利　(Dept. Phys., Grad. Sch. Sci., Univ. Tokyo)
MOTOMURA Shinji　本村信治　(Fac. Sci., Kyushu Univ.)
MUTO Ryotaro　武藤亮太郎　(Fac. Sci., Kyoto Univ.)
NAKAJIMA Noriaki　中島典昭　(RCNP, Osaka Univ.)
NAKAMURA Hideki　中村秀樹　(Dept. Phys., Grad. Sch. Sci., Univ. Tokyo)
NAKANO Jo　中野　譲　(Dept. Phys., Grad. Sch. Sci., Univ. Tokyo)
NAKANO Eiji　仲野英司　(Fac. Sci., Tokyo Metrop. Univ.)
NARUSHIMA Koichi　成嶋功一　(Coll. Sci., Rikkyo Univ.)
OHKUMA Kazumasa　大熊一正　(Fac. Human Dev., Kobe Univ.)
ONO Masaya　小野雅也　(Inst. Phys., Univ. Tsukuba)
SAHA Pranab　(KEK)
SAITO Koji　斎藤浩司　(Fac. Sci., Kyushu Univ.)
SAITO Takaaki　斎藤孝明　(Dept. Phys., Grad. Sch. Sci., Univ. Tokyo)
SAITOU Akito　斎藤明登　(Coll. Sci., Rikkyo Univ.)
SAKODA Seitaro　迫田誠太郎　(Dept. Phys., Grad. Sch. Sci., Univ. Tokyo)
SATO Kyosuke　佐藤恭祐　(Coll. Sci., Rikkyo Univ.)

SHIMBO Ken 新保 謙 (Dept. Phys., Grad. Sch. Sci., Univ. Tokyo)
SUDOH Kazutaka 須藤和敬 (Fac. Human Dev., Kobe Univ.)
SUETSUGU Kentaro 末次健太郎 (Tokyo Inst. Technol.)
SUGIMOTO Takashi 杉本 崇 (Tokyo Inst. Technol.)
SUZUKI Miwako 鈴木美和子 (Inst. Phys., Univ. Tsukuba)
TAKESHITA Eri 竹下英理 (Coll. Sci., Rikkyo Univ.)
TOJO Junji 東城順治 (Fac. Sci., Kyoto Univ.)
TOZAWA Yuichi 杜澤優一 (Coll. Sci., Rikkyo Univ.)
TSURUOKA Hiroshi 鶴岡裕士 (Inst. Phys., Univ. Tsukuba)
UCHIGASHIMA Nobuyuki 内ヶ島暢之 (Dept. Phys., Grad. Sch. Sci., Univ. Tokyo)
YAMAMOTO Minoru 山本 稔 (Coll. Sci., Rikkyo Univ.)
YANAKA Shuichi 田中周一 (Fac. Sci., Kyushu Univ.)

RI Beam Science Laboratory

Head

TANIHATA Isao 谷畑勇夫

Members

FUKUYAMA Yoshimitsu 福山祥光
ISHIDA Yoshihisa 石田佳久
KORSHENINNIKOV Alexei A.
KUMAGAI Hidekazu 熊谷秀和
KUSAKA Kensuke 日下健祐
MATSUO Yukari 松尾由賀利
MOCHIZUKI Yuko 望月優子
MORIMOTO Koji 森本幸司
NAKATSUKASA Takashi 中務 孝
NISHI Yuji 西 勇二
NISHIMURA Shunji 西村俊二
OZAWA Akira 小沢 顕
ONISHI Takashi 大西 崇
ONHISHI Tetsuya 大西哲也
SUDA Toshimi 須田利美
SUMIYOSHI Kohsuke 住吉光介
WAKUI Takashi 涌井宗志
YAMAGUCHI Takayuki 山口貴之
YAMAZAKI Toshimitsu 山崎敏光
YOSHIDA Koichi 吉田光一

Visiting Members

AOYAMA Shigeyoshi 青山茂義 (Kitami Inst. Technol.)
ADACHI Shizuko 安達静子 (ICFD)
AHMADY Mohammad (Western Ontario Univ., Canada)
ARATANI Michi 荒谷美智 (Inst. Environ. Sci.)
BOLBOT Michael (Notre Dame Univ., USA)
BOYD Richard (Ohio Univ., USA)
BROCKMANN Roff (Inst. Phys., Univ. Mainz, Germany)
CRUCCERU Ilie (Horia Inst. Eng., Romania)
DATAR Vivek (Bhabha Atom. Res. Cen., India)
DAVID Dean J. (CALTEC, USA)
DEMYANOVA Alla S. (Kurchatov Inst. Atom. Energy, Russia)
DOKE Tadayoshi 道家忠義 (Adv. Res. Inst. Sci. Eng., Waseda Univ.)
ENYO Yoshiko 延與佳子 (Cen. Nucl. Study, Univ. Tokyo)
FOMITCHEV Andrei (JNRF, Russia)
FUJIWARA Mamoru 藤原 守 (RCNP, Osaka Univ.)
FÜLÖP Zsolt (ATOMIKI, Hungary)
GACSI Zoltan (ATOMKI, Hungary)
GEISSEL Hans (GSI, Germany)
GIURGIU Mircea (Horia Inst. Nucl. Eng., Romania)
GOLOVKOV Mikhail S. (Kurchatov Inst., Russia)
GONCHAROV Sergei A. (Kurchatov Inst., Russia)
GORINE Alexander (IHEO, Russia)
GOSWAMI Ranjana (Variable Energy Cycl. Cen. Calcutta, India)
GUNJI Shuichi 郡司修一 (Fac. Sci., Yamagata Univ.)
HASEBE Nobuyuki 長谷部伸行 (Fac. Sci. Eng., Waseda Univ.)
NGUYEN THUC Hien (Hanoi Univ., Vietnam)

HIRENZAKI Satoru　比連崎　悟　(Fac. Sci., Nara Women's Univ.)
HORIGUCHI Masakatu　堀口正勝　(Horiguchi Ironworks)
HORIUCHI Hisashi　堀内　昶　(Fac. Sci., Kyoto Univ.)
IKEDA Kiyomi　池田清美
ISHIHARA Masayasu　石原正泰　(RIKEN BNL Res. Cen.)
ISHIMOTO Shigeru　石元　茂　(KEK)
ITAGAKI Naoyuki　板垣直之　(Fac. Sci., Univ. Tokyo)
IWAMOTO Akira　岩本　昭　(JAERI, Tokai Res. Estab.)
IWASA Naohito　岩佐直仁　(Fac. Sci., Niigata Univ.)
IWASAKI Aiichi　岩崎愛一　(Nishogakusya Univ.)
IZUMIKAWA Takuji　泉川卓司　(Fac. Sci., Niigata Univ.)
IZUYAMA Takeo　伊豆山健夫　(Fac. Sci., Toho Univ.)
KANEKO Kazuya　金子和也　(Kyushu Sangyo Univ.)
KANUNGO Rituparna　(Saha Inst. Nucl. Phys., Calcutta, India)
KATORI Kenji　鹿取謙二
KIKUCHI Jun　菊池　順　(Sci. Eng. Res. Lab., Waseda Univ.)
KIMURA Kikuo　木村喜久雄　(Fac. Eng., Nagasaki Inst. Appl. Sci.)
KOBAYASHI Toshio　小林俊雄　(Fac. Sci., Tohoku Univ.)
KOLATA James　(Notre Dame Univ., USA)
KOUZMINE Evgueni　(Kurchatov Inst, Russia)
KRASZNAHORKAY Attila　(ATOMKI, Hungary)
KUMARU Suresh　(Bhabha Atom. Res. Cen., India)
LE HONG Khiem　(Inst. Phys., Natl. Cen. Sci. Technol., Vietnam)
LIU Xin　(Inst. Nucl. Study, Univ. Tokyo)
MARUYAMA Koichi　丸山浩一　(Inst. Nucl. Study, Univ. Tokyo)
MARUYAMA Tomoyuki　丸山智幸　(Nihon Univ.)
MATSUOKA Nobuyuki　松岡伸行　(RCNP, Osaka Univ.)
MATSUTA Kensaku　松多健策　(Fac. Sci., Osaka Univ.)
MATSUYAMA Yoshitaka　松山芳孝　(Inst. Nucl. Study, Univ. Tokyo)
MINAMISONO Kei　南園　啓　(Fac. Sci., Osaka Univ.)
MINAMISONO Tadanori　南園忠則　(Fac. Sci., Osaka Univ.)
MITTING M.　(GANIL, France)
MIHARA Mototugu　三原基嗣　(Fac. Sci., Osaka Univ.)
MIRGULE Ekanath Tanu　(Bhabha Atom. Res. Cen., India)
MIYAKE Yasuo　三明康朗　(Fac. Sci., Univ. Tsukuba)
MIYAMURA Osamu　宮村　修　(Fac. Sci., Hiroshima Univ.)
MOMOTA Sadao　百田佐多生　(Kochi Univ. Technol.)
MORITA Hiroaki　森田弘明　(Horiguchi Ironworks)
MURAOKA Mitsuo　村岡光男　(Fac. Eng., Aomori Univ.)
NOJIRI Yoichi　野尻洋一　(Kochi Univ. Technol.)
NOMURA Izumi　野村和泉　(NIFS)
OGAWA Kengo　小川健吾　(Coll. Arts. Sci., Chiba Univ.)
OGAWA Yoko　小川洋子　(Fac. Sci., Osaka Univ.)
OGLOBLIN Alexei A.　(Kurchatov. Inst., Russia)
OHTSUBO Takashi　大坪　隆　(Fac. Sci., Niigata Univ.)
OMATA Kazuo　小俣和夫　(Inst. Nucl. Study, Univ. Tokyo)
ORYU Shinsho　尾立晋祥　(Fac. Sci. Technol., Sci. Univ. Tokyo)
OTSU Hideaki　大津秀暁　(Fac. Sci., Tohoku Univ.)
OTSUKA Takaharu　大塚孝治　(Fac. Sci., Univ. Tokyo.)
OYAMATSU Kazuhiro　親松和浩　(Aichi Shukutoku Univ.)
PETRASCU Horia　(Horia Inst. Phys. Nucl. Eng., Romania)
PETRASCU Marius　(Horia Inst. Phys. Nucl. Eng., Romania)
POLLACCO Emmanuel　(EAC, France)
ROUSSEL-CHAMAZ P.　(GANIL, France)
SAGAWA Hiroyuki　佐川弘幸　(Cen. Math. Sci., Univ. Aizu)
SAKAGUCHI Harutaka　坂口治隆　(Grad. Sch., Kyoto Univ.)
SAKAI Hideyuki　酒井英行　(Fac. Sci., Univ. Tokyo)

SAKURAI Hirohisa　櫻井敬久　(Fac. Sci., Yamagata Univ.)
SASA Hiromasa　佐々博政　(Horiguchi Ironworks)
SATO Hiroshi　佐藤　紘　(Seikei Univ.)
SATO Kazuhiro　佐藤和洋　(Tokyo Fire Dept.)
SAVAJOLS H.　(GANIL, France)
SCHROEDER Lee S.　(Laurence Berkeley Lab., USA)
SEKI Ryoichi　関　亮一　(California Univ., USA)
SHERRIL B.　(Michigan State Univ., USA)
SHIBATA Mitihiro　柴田理尋　(Dept. Energy Eng. Sci., Nagoya Univ.)
SHIBATA Toru　柴田　徹　(Sci. Eng., Aoyama Gakuin Univ.)
SUGANUMA Hideo　菅沼秀夫　(RCNP, Osaka Univ.)
SUGAWARA Masahiko　菅原昌彦　(Fundam. Sci., Chiba Inst. Technol.)
SÜMMERER Klaus　(GSI, Germany)
SUZUKI Hideyuki　鈴木英之　(KEK)
SUZUKI Takeshi　鈴木　健　(Fac. Sci., Niigata Univ.)
SUZUKI Tsuneo　鈴木恒雄　(Fac. Sci., Kanazawa Univ.)
SUZUKI Toshio　鈴木敏男　(Sci. Eng., Fukui Univ.)
SUZUKI Yasuyuki　鈴木宣之　(Fac. Sci., Niigata Univ.)
TACHIBANA Takahiro　橘　高博　(Sen. High Sch., Waseda Univ.)
TAKAHASHI Yoshiyuki　高橋義幸　(Alabama Univ., USA)
TAKAHASHI Yutaka　高橋　豊　(Fac. Sci., Osaka Univ.)
TAKANO Masatoshi　鷹野正利　(Fac. Sci. Eng., Waseda Univ.)
TER-AKOPIAN G.　(Dubna, Russia)
THIROLF P.　(Univ. Munchen, Germany)
TOKANAI Fuyuki　門叶冬樹　(JST)
TOKI Hiroshi　土岐　博　(RCNP, Osaka Univ.)
TORBJOEN Baeck　(Stockholm Univ., Sweden)
TOSTEVIN Jeffrey A.　(Univ. Surry, India)
UCHIHORI Yukio　内掘幸夫　(Inst. Rad. Sci.)
UTSUNO Yutaka　宇津野　穣　(Tokai Research Establishment)
UTSUNOMIYA Hiroaki　宇都宮弘章　(Fac. Sci., Konan Univ.)
VARGA Kalman　(Inst. Nucl., Hungarian Acad. Sci., Hungary)
WADA Takahiro　和田隆宏　(Fac. Sci., Konan Univ.)
WINKLER Martin　(GSI, Germany)
YAGI Hirosuke　八木浩輔　(Fac. Sci., Univ. Tsukuba)
YAMADA Shoichi　山田章一　(Fac. Sci., Univ. Tokyo)
YAMAGUCHI Yoshio　山口嘉夫　(Inst. Nucl. Study, Univ. Tokyo)
YORANN Alhassid　(Yale Univ., USA)
YUZUKI Akira　柚木　彰　(Toshiba Corp.)
ZAHAR Mohamed　(Dept. Phys., Notre Dam Univ., USA)
ZHENG Tao　(Fac. Sci. Technol., Sci. Univ. Tokyo)

Trainees

AOKI Yuka　青木由香　(Fac. Sci., Tohoku Univ.)
CHIBA Masami　千葉将充　(Fac. Sci., Tohoku Univ.)
FUZIMURA Takeshi　藤村　岳　(Sci. Eng., Aoyama Gakuin Univ.)
HARA Kenichiro　原　健一朗　(Fac. Sci. Eng., Waseda Univ.)
HARUKI Masamichi　春木正道　(Fac. Sci. Eng., Waseda Univ.)
HIBINO Masaru　日比野　優　(Fac. Sci. Eng., Waseda Univ.)
IHARA Akifumi　井原亜紀史　(Fac. Sci. Eng., Waseda Univ.)
HASHIMOTO Izumi　橋本和泉　(Fac. Sci., Osaka Univ.)
ITO Hiroshi　伊藤浩巳　(Fac. Sci. Eng., Waseda Univ.)
KATO Tomomi　加藤智美　(Fac. Sci., Niigata Univ.)
KATO Toshiyuki　加藤俊幸　(Fac. Sci. Eng., Waseda Univ.)
KAWA Tadahisa　河　忠久　(Fac. Sci., Osaka Univ.)
KAWAMURA Yoshie　川村淑恵　(Fac. Sci. Niigata Univ.)
KIHIRA Eiichi　吉平栄一　(Fac. Sci. Eng., Waseda Univ.)

KITANI Takao 木谷貴雄 (Fac. Sci. Eng., Waseda Univ.)
KIYAMU Atushi 喜谷武篤史 (Fac. Sci. Eng., Ibaraki Univ.)
KOBAYASHI Shingo 小林進吾 (Fac. Sci. Eng., Waseda Univ.)
KOIKE Takayuki 小池貴之 (Fac. Sci. Eng., Waseda Univ.)
KUDO Syuichi 工藤修一 (Fac. Sci., Osaka Univ.)
KURIYAMA Koji 栗山幸治 (Sci. Eng., Aoyama Gakuin Univ.)
MASUMURA Takahiro 増村考洋 (Fac. Sci. Eng., Waseda Univ.)
MIYAKE Toru 三宅 徹 (Fac. Sci., Osaka Univ.)
MUTO Nobuo 武藤信雄 (Fac. Eng., Aoyama Gakuin Univ.)
NAGATOMO Kiyoshi 長友 傑 (Fac. Sci., Osaka Univ.)
NISHIKIDO Humihiko 錦戸文彦 (Fac. Sci. Eng., Waseda Univ.)
OGURA Masako 小倉昌子 (Fac. Sci., Osaka Univ.)
OHZEKI Kazuki 大関和貴 (Fac. Sci., Tohoku Univ.)
OKA Aihiro 岡 晃弘 (Fac. Sci. Eng., Waseda Univ.)
OKUDA Takashi 奥田貴志 (Fac. Sci., Tohoku Univ.)
OKUDAIRA Osamu 奥平 修 (Fac. Sci. Eng., Waseda Univ.)
OZAKI Kiminori 尾崎公教 (Fac. Sci. Eng., Waseda Univ.)
SAKAGUCHI Takao 坂口貴男 (Fac. Sci. Eng., Waseda Univ.)
SASAKI Makoto 佐々木 誠 (Fac. Sci., Osaka Univ.)
SATO Kazunori 佐藤和則 (Fac. Sci., Osaka Univ.)
SEKIGUCHI Masatugu 関口昌嗣 (Fac. Sci., Tohoku Univ.)
SHIMIZU Noritaka 清水則孝 (Fac. Sci., Univ. Tokyo)
SOURI Hirofumi 惣宇利啓史 (Fac. Sci. Eng., Waseda Univ.)
SUGIMOTO Satoshi 杉本 聡 (RCNP, Osaka Univ.)
TAKEMURA Atsushi 竹村 淳 (Fac. Sci., Osaka Univ.)
TAKEMURA Haruyuki 竹村春礼 (Fac. Sci. Eng., Waseda Univ.)
TAKENAKA Sunao 竹中 直 (Fac. Sci. Eng., Waseda Univ.)
TAKENOUCHI Masatoshi 竹之内正俊 (Fac. Sci. Eng., Waseda Univ.)
TAKEUCHI Satoshi 武内 聡 (Fac. Sci., Rikkyo Univ.)
TANAKA Motoyuki 田中基之 (Fac. Sci., Waseda Univ.)
TAZAWA Shinya 田沢伸也 (Fac. Sci., Tohoku Univ.)
TERASAWA Kazuhiro 寺沢和洋 (Fac. Sci. Eng., Waseda Univ.)
TERASAWA Mariko **寺澤真理子** (Fac. Sci., Univ. Tokyo)
TERUHI Shigeru 照日 **繁** (Fac. Sci. Eng., Waseda Univ.)
UMEMURA Tomohiro 梅村朋弘 (Fac. Sci. Eng., Waseda Univ.)
UZIIE Toru 氏家 徹 (Fac. Sci., Tohoku Univ.)
WAKASAYA Yoshiaki 若狭谷義朗 (Fac. Sci. Technol., Sci. Univ. Tokyo)
WANG Haiming 王 海鳴 (Fac. Sci., Univ. Tokyo.)
WATANAE Shigeo 渡邊茂夫 (Fac. Sci., Niigata Univ.)
YAMADA Kazunari 山田一成 (Fac. Sci., Rikkyo Univ.)
YAMAGUCHI Yoshitaka 山口由高 (Fac. Sci., Niigata Univ.)
YAMASHITA Masaki 山下雅樹 (Adv. Res. Inst. Sci. Eng., Waseda Univ.)
YAMASHITA Naoyuki 山下直之 (Fac. Sci. Eng., Waseda Univ.)
YASHIRO Junichi 矢代淳一 (Fac. Sci. Eng., Waseda Univ.)
YOSHIOKA Hideki 吉岡秀樹 (Fac. Sci. Eng., Waseda Univ.)

Applied Nuclear Physics Laboratory

Head

ASAHI Koichiro 旭 耕一郎

Members

KOBAYASHI Yoshio 小林義男
SATO Wataru 佐藤 渉
YOSHIMI Akihiro 吉見彰洋
UENO Hideki 上野秀樹
YONEDA Kenichiro 米田健一郎
WATANABE Hiroshi 渡邊 寛

Visiting Members

EINAGA Yasuaki 栄長泰明 (Fac. Sci., Univ. Tokyo)
IMAI Nobuaki 今井伸明 (Fac. Sci., Univ. Tokyo)
KUBO M. Kenya 久保謙哉 (Fac. Sci., Univ. Tokyo)
OGAWA Hiroshi 小川博嗣 (Fac. Sci., Tokyo Inst. Technol.)
SAKAI Kenji 酒井健二 (Fac. Sci., Tokyo Inst. Technol.)
YAMADA Yasuhiro 山田康洋 (Fac. Sci., Sci. Univ. Tokyo)
NAKAHARA Hiromichi 中原弘道 (Fac. Sci., Tokyo Metrop. Univ.)
SHIMIZU Suguru 清水 俊 (Fac. Sci., Osaka Univ.)
ADACHI Minoru 足立 実
OKADA Takuya 岡田卓也

Trainees

SUZUKI Takayuki 鈴木孝幸 (Fac. Sci., Tokyo Inst. Technol.)
SUGA Toshitaka 須賀敏孝 (Fac. Sci., Tokyo Inst. Technol.)
YOGO Katsunori 余語克紀 (Fac. Sci., Tokyo Inst. Technol.)
GOTO Atsushi 五島 敦 (Fac. Sci., Tokyo Inst. Technol.)
HONDA Toshiki 本多俊樹 (Fac. Sci., Tokyo Inst. Technol.)
HORI Kentaro 堀 健太郎 (Fac. Sci., Sci. Univ. Tokyo)
KATSUMATA Keiichi 勝又啓一 (Fac. Sci., Sci. Univ. Tokyo)
MIYAZAKI Junn 宮崎 淳 (Fac. Sci., Sci. Univ. Tokyo)
MIYOSHI Hisanori 三好永哲 (Fac. Sci., Tokyo Inst. Technol.)
KAMEDA Daisuke 亀田大輔 (Fac. Sci., Tokyo Inst. Technol.)
NAGAKURA Masaki 長倉正樹 (Fac. Sci., Tokyo Inst. Technol.)
SATO Keisuke 佐藤慶介 (Fac. Sci., Tokyo Inst. Technol.)
OONO Kenichi 大野賢一 (Fac. Sci., Tokyo Inst. Technol.)
KAIHARA Jou 貝原星宇 (Fac. Sci., Tokyo Inst. Technol.)
OGAWA Shigeru 小川 茂 (Fac. Sci., Shizuoka Inst. Sci. Tech.)
ONO Yuki 小野祐樹 (Fac. Sci., Sci. Univ. Tokyo)
SAITO Takashi 齋藤 崇 (Fac. Sci., Sci. Univ. Tokyo)
SHIMAZAKI Hideo 島崎秀生 (Fac. Sci., Sci. Univ. Tokyo)
ISHIKAWA Yumiko 石川由美子 (Fac. Sci., Sci. Univ. Tokyo)
SHIMIZU Yasunori 清水康功 (Fac. Sci., Shizuoka Inst. Sci. Tech.)

Atomic Physics Laboratory

Head

YAMAZAKI Yasunori 山崎泰規

Members

IKEDA Tokihiro 池田時浩
KANAI Yasuyuki 金井保之
MORISHITA Yuichiro 森下雄一郎
NAKAMURA Takashi 中村貴志
NISHIMURA Tamio 西村民男
OURA Masaki 大浦正樹
SHIMAMURA Isao 島村 勲
TERANISHI Yoshiaki 寺西慶哲
KAMBARA Tadashi 神原 正
KOJIMA Takao M. 小島隆夫
NAKAI Yoichi 中井陽一
NISHIDA Masami 西田雅美
OSHIMA Nagayasu 大島永康
OYAMA Hitoshi 大山 等
TAKEKAWA Michiya 竹川道也
WADA Michiharu 和田道治

Visiting Members

ANDO Kozo 安藤剛三
AZUMA Toshiyuki 東 俊行 (Dept. Phys., Tokyo Metrop. Univ.)
BRAGE Tomas (Dept. Phys., Univ. Lund, Sweden)
CHIMI Yasuhiro 知見康弘 (JAERI, Tokai Res. Estab.)
DIAO Xungang 刁 訓剛 (Shizuoka Inst. Sci. Tech.)
DUMITRIU Dana (Natl. Inst. Phys. Nucl. Eng., Romania)
EICHLER Jörg (Hahn-Meitner Inst. Berlin, Germany)

FAIFMAN Mark (Russian Res. Cent., Kurchatov Inst., Russia)
FUJIMA Kazumi 藤間一美 (Fac. Eng., Yamanashi Univ.)
HARA Shunsuke 原 俊介 (Dept. Gen. Ed., Tsukuba Coll. Technol.)
HATTORI Toshiyuki 服部俊幸 (Res. Lab. Nucl. React., Tokyo Inst. Technol.)
HINO Ken-ichi 日野健一 (Inst. Appl. Phys., Univ. Tsukuba)
HITACHI Akira 月出 章 (Kochi Med. Sch.)
HUTTON Roger (Dept. Phys., Lund Univ., Sweden)
ICHIMURA Atsushi 市村 淳 (Inst. Space Astr. Sci.)
ICHIOKA Toshiyasu 市岡利康 (Grad. Sch. Arts Sci., Univ. Tokyo)
IGARASHI Akinori 五十嵐明則 (Fac. Eng., Miyazaki Univ.)
IKEDA Hiroshi 池田 博 (Univ. Tsukuba)
INOKUTI Mitio 井口道生 (Argonne Natl. Lab., USA)
ISHII Keishi 石井慶之 (Fac. Sci. Eng., Ritsumeikan Univ.)
ISHIKAWA Norito 石川法人 (JAERI, Tokai Res. Estab.)
ITO Takaomi 伊藤高臣 (Grad. Sch. Arts Sci., Univ. Tokyo)
ITOH Akio 伊藤秋男 (Fac. Eng., Kyoto Univ.)
ITOH Yoh 伊藤 陽 (Fac. Sci., Josai Univ.)
IWAI Yoshio 岩井良夫 (Dept. Phys., Grad. Sch. Sci., Univ. Tokyo)
IWASE Akihiro 岩瀬彰宏 (JAERI, Tokai Res. Estab.)
KAGEYAMA Kensuke 蔭山健介 (Fac. Eng., Saitama Univ.)
KAWATSURA Kiyoshi 川面 澄 (Fac. Eng. Design, Kyoto Inst. Technol.)
KIMURA Kenji 木村健二 (Fac. Eng., Kyoto Univ.)
KIMURA Mineo 季村峯生 (Fac. Eng., Yamaguchi Univ.)
KITAJIMA Masashi 北島昌史 (Fac. Sci. Technol., Sophia Univ.)
KOBAYASHI Nobuo 小林信夫 (Dept. Phys., Tokyo Metrop. Univ.)
KOIKE Fumihiro 小池文博 (Sch. Med., Kitasato Univ.)
KOIZUMI Tetsuo 小泉哲夫 (Dept. Phys., Rikkyo Univ.)
KOMAKI Ken-ichiro 小牧研一郎 (Grad. Sch. Arts Sci., Univ. Tokyo)
KOWARI Kenichi 小割健一 (Dept. Appl. Phys. Chem., Univ. Electro-Commun.)
KURODA Naoshi 黒田直志 (JAERI, Tokai Res. Estab.)
KUROKI Kenro 黒木健郎 (Natl. Res. Inst. Police Sci.)
LINDROTH Eva (Dept. Atom. Phys., Stockholm Univ., Sweden)
MATSUNAMI Noriaki 松波紀明 (Sch. Eng., Nagoya Univ.)
MATSUO Takashi 松尾 崇 (Dept. Pathol., Tokyo Med. Dent. Univ.)
MATSUZAWA Michio 松澤通生 (Dept. Appl. Phys. Chem., Univ. Electro-Commun.)
MITSUKE Koichiro 見附孝一郎 (Inst. Mol. Sci.)
MIZOGAWA Tatsumi 溝川辰巳 (Nagaoka Coll. Technol.)
MOHRI Akihiro 毛利明博
MUKOYAMA Takeshi 向山 毅 (Inst. Chem. Res., Kyoto Univ.)
OHTANI Shunsuke 大谷俊介 (Inst. Laser Sci., Univ. Electro-Commun.)
OKABAYASHI Norio 岡林則夫 (Grad. Sch. Arts Sci., Univ. Tokyo)
OKADA Kunihiro 岡田邦宏 (Fac. Sci. Tech., Sophia Univ.)
OKAYASU Satoru 岡安 悟 (JAERI, Tokai Res. Estab.)
OKUNO Kazuhiko 奥野和彦 (Dept. Phys., Tokyo Metrop. Univ.)
ONO Fumihisa 小野文久 (Dept. Phys., Okayama Univ.)
ROSMEJ Frank B. (GSI, Germany)
SAKAI Akio 坂井昭夫 (Vacuum Products Co.)
SATO Hiroshi 佐藤浩史 (Fac. Sci., Ochanomizu Univ.)
SHIMA Kunihiro 島 邦博 (Tandem Accel. Cen., Univ. Tsukuba)
SHIMAKURA Noriyuki 島倉紀之 (Fac. Sci., Niigata Univ.)
TONUMA Tadao 戸沼正雄 (Adv. Res. Inst. Sci. Eng., Waseda Univ.)
TORII Hiroyuki 鳥居寛之 (Grad. Sch. Arts Sci., Univ. Tokyo)
TOSHIMA Nobuyuki 戸嶋信幸 (Inst. Appl. Phys., Univ. Tsukuba)
TSUCHIDA Hidetsugu 土田秀次 (Fac. Sci., Nara Women's Univ.)
UEDA Kiyoshi 上田 潔 (Res. Inst. Sci. Meas., Tohoku Univ.)
WATANABE Shinichi 渡辺信一 (Dept. Appl. Phys. Chem., Univ. Electro-Commun.)
YAGISHITA Akira 柳下 明 (KEK)

YOSHIDA Yutaka 吉田 豊 (Shizuoka Inst. Sci. Tech.)
ZOU Yaming (Shanghai Jiao Tong Univ., China)

Trainees

EBIHARA Takashi 海老原貴司 (Fac. Sci. Technol., Sophia Univ.)
ENDO Atsumi 遠藤厚身 (Dept. Phys., Grad. Sch. Sci., Univ. Tokyo)
HASEGAWA Tadayuki 長谷川忠之 (Grad. Sch. Eng., Tokai Univ.)
HORI Masaki 堀 正樹 (Dept. Phys., Grad. Sch. Sci., Univ. Tokyo)
HOSHINO Masamitsu 星野正光 (Grad. Sch. Sci. Eng., Sophia Univ.)
KURODA Naofumi 黒田直史 (Dept. Phys., Grad. Sch. Sci., Univ. Tokyo)
MAJIMA Takuya 間嶋拓也 (Grad. Sch. Eng., Kyoto Univ.)
MURAKOSHI Dai 村越 大 (Grad. Sch. Arts Sci., Univ. Tokyo)
NIIGAKI Megumi 新垣 恵 (Coll. Arts Sci., Univ. Tokyo)
OSHIMA Tatsuaki 大島龍明 (Grad. Sch. Sci., Tohoku Univ.)
SAKAGUTI Syuiti 坂口修一 (Grad. Sch. Sci. Tech., Saitama Univ.)
SHIMADA Hiroyuki 島田紘行 (Coll. Arts Sci., Univ. Tokyo)
SONODA Tetsu 園田 哲 (Grad. Sch. Sci., Tohoku Univ.)
TAKABAYASHI Yuichi 高林雄一 (Dept. Phys., Grad. Sch. Sci., Univ. Tokyo)
TAKAHASHI Takehisa 高橋武寿 (Dept. Phys., Grad. Sch. Sci., Rikkyo Univ.)

Muon Science Laboratory

Head

NAGAMINE Kanetada 永嶺謙忠

Members

BAKULE Pavel
HASHI Kenjiro 端 健二郎
KAWAMURA Naritoshi 河村成肇
MATSUDA Yasuyuki 松田恭幸
MATSUZAKI Teiichiro 松崎禎市郎
OHIRA Seiko 大平聖子
STRASSER Patrick
YAGI Eiichi 八木栄一
FUKAYA Atsuko 深谷敦子
ISHIDA Katsuhiko 石田勝彦
KOYAMA Akio 小山昭雄
MATSUSHITA Akira 松下 明
NAKAMURA Satoshi N. 中村 哲
PRATT Francis L.
WATANABE Isao 渡邊功雄

Visiting Members

ADROJA Devashibhai (Fac. Sci., Hiroshima Univ.)
AJIRO Yoshitami 網代芳民 (Fac. Sci., Kyushu Univ.)
AKIMITSU Jun 秋光 純 (Coll. Sci. Eng., Aoyama Gakuin Univ.)
AKIMOTO Katsuhiro 秋本克洋 (Inst. Mater., Univ. Tsukuba)
AKOSHIMA Megumi 阿子島めぐみ (Fac. Eng., Tohoku Univ.)
ARAI Juichiro 新井重一郎 (Sci. Univ. Tokyo)
ASAI Kichizo 浅井吉蔵 (Univ. Electro-Commun.)
AWAGA Kunio 阿波賀邦夫 (Grad. Sch. Arts Sci., Univ. Tokyo)
BOGDANOVA N. Ludmila (Inst. Theor. Exp. Phys., Russia)
BRIERRE Tina M. (KEK)
BROWN Douglas H. (KEK)
DAS Prasad Tara (Dept. Phys., State Univ. New York, Albany, USA)
FUJIOKA Manabu 藤岡 学 (Cycl. Radioisot. Cen., Tohoku UIniv.)
FUKUSHIMA Kenji 福島謙二
HIGEMOTO Wataru 髭本 亘 (KEK)
HONDA Morihiro 本田守広 (Inst. Cosmic Ray Res., Univ. Tokyo)
HIYAMA Emiko 肥山詠美子 (KEK)
IKEDA Susumu 池田 進 (KEK)
ITO Atsuko 伊藤厚子
IWASAKI Masahiko 岩崎雅彦 (Dept. Phys., Tokyo Inst. Technol.)
KADONO Ryosuke 門野良典 (KEK)

KAMIMURA Masayasu 上村正康 (Fac. Sci., Kyushu Univ.)
KATO Mineo 加藤岑生 (JAERI, Tokai Res. Estab.)
KINO Yasushi 木野康志 (Fac. Sci., Tohoku Univ.)
KOIKE Youji 小池洋二 (Fac. Eng., Tohoku Univ.)
KUNO Yoshitaka 久野良孝 (KEK)
KUROSAWA Kiyoyuki 黒沢清行 (JAERI, Tokai Res. Estab.)
MACRAE Roderick M. (Notre Dame Radiation Lab., USA)
MAKIMURA Syunsuke 牧村俊助 (KEK)
MARUTA Goro 丸田悟朗 (KEK)
MEKATA Mamoru 目方 守 (Fac. Eng., Fukui Univ.)
MINAMISONO Tadanori 南園忠則 (Fac. Sci., Osaka Univ.)
MIYAKE Yasuhiro 三宅康博 (KEK)
MIYAKO Yoshihito 都 福仁 (Fac. Sci., Osaka Univ.)
MOCHIKU Takashi 茂筑高士 (Natl. Res. Inst. Metals)
MORITA Masato 森田正人 (Fac. Sci., Josai Univ.)
MORITA Reiko 森田玲子 (Josai Jr. Coll. Women)
NISHIDA Nobuhiko 西田信彦 (Fac. Sci., Tokyo Inst. Technol.)
NISHIYAMA Kusuo 西山樟生 (KEK)
PONOMAREV Leonid I. (Kurchatov Inst., Russia)
SAKAMOTO Shinichi 坂元眞一 (KEK)
SATO Kazuhiko 佐藤一彦 (Fac. Sci., Saitama Univ.)
SHIMOMURA Koichiro 下村浩一郎 (KEK)
STORCHAK Vyacheslav G. (Kurchatov Inst., Russia)
SUGAI Hiroyuki 須貝宏行 (JAERI, Tokai Res. Estab.)
TAKABATAKE Toshiro 高畠敏郎 (Grad. Sch. Adv. Sci. Matter, Hiroshima Univ.)
TAKEDA Keiji 武田啓司 (Hokkaido Univ.)
TAKIGAWA Masashi 瀧川 仁 (Inst. Solid State Phys.)
TANASE Masakazu 棚瀬正和 (JAERI, Takasaki)
TORIKAI Eiko 鳥養映子 (Fac. Eng., Yamanashi Univ.)
UEDA Kazuo 上田和夫 (Inst. Solid State Phys.)
UMEO Kazunori 梅尾和則 (Fac. Sci., Hiroshima Univ.)
WADA Nobuo 和田信雄 (Grad. Sch. Arts Sci., Univ. Tokyo)
WATANABE Tsutomu 渡部 力 (Int. Chr. Univ.)
YAMADA Kazuyoshi 山田和芳 (Inst. Chem. Res., Kyoto Univ.)

Trainees
MIYADERA Haruo 宮寺晴夫 (Grad. Sch., Univ. Tokyo)
TANAKA Hiroyuki 田中宏幸 (Grad. Sch., Nagoya Univ.)
TOYODA Akihisa 豊田晃久 (Grad. Sch., Univ. Tokyo)

Magnetic Materials Laboratory

Head
KATSUMATA Koichi 勝又紘一

Members
HAGIWARA Masayuki 萩原政幸
MATSUDA Masaaki 松田雅昌

Beam Physics and Engineering Laboratory

Head
KATAYAMA Takeshi 片山武司

Members
CHOUFFANI Khalid
NAKAMURA Masato 中村仁音
OKAZAKI Kiyohiko 岡崎清比古
HAMAGAKI Manabu 浜垣 学
OKAMURA Masahiro 岡村昌宏
SAKUMI Akira 作美 明

TAKANAKA Masao 高仲政雄
WATANABE Tamaki 渡邉 環
YANAGISAWA Yoshiyuki 柳澤善行
YUN Chong-Cheoul 尹 鍾哲
TAMBA Moritake 丹波護武
XIAO Meiqin 肖 美琴
YOKKAICHI Satoshi 四日市 悟

Visiting Members

BOLSHAKOV Alexander (ITEP, Russia)
CHAI Jong-Seo (CALK, Korea)
DIKANSKI Nikolai (Budka Inst. Nucl. Phys., Russia)
HARA Tamio 原 民夫 (Toyota Technol. Inst.)
HASHIMOTO Yuichi 橋本雄一 (Canon Inc.)
HATTORI Toshiyuki 服部俊幸 (Res. Lab. Nucl. React., Tokyo Inst. Technol.)
JAMESON Robert (Los Alamos Natl. Lab., USA)
KATO Shigeki 加藤茂樹 (KEK)
KOCHKAREV Dmitry (ITEP, Russia)
KONDRASHEV Sergei (ITEP, Russia)
KOROTAEV Iouri (JINR, Russia)
MATSUMOTO Takashi 松元貴志 (CNS, Univ. Tokyo)
MESHKOV Igor (JINR, Russia)
MOON Sang-ik (CALK, Korea)
OGAWA Masao 小川雅生 (Tokyo Inst. Technol.)
OGURI Yoshiyuki 小栗慶之 (Res. Lab. Nucl. React., Tokyo Inst. Technol.)
SAKAKIBARA Takeshi 榊原 剛 (Chuo Univ.)
SAKAMOTO Yuichi 坂本雄一 (Nichimen Co.)
SERATA Masaki 世良田真来 (Coll Sci., Rikkyo Univ.)
SHARKOV Boris (ITEP, Russia)
SIDORIN Anatoly (JINR, Russia)
SKRINSKY Alexander (ITEP, Russia)
SYRESIN Evgeny (JINR, Russia)
TAKEUCHI Takeshi 竹内 猛 (CNS, Univ. Tokyo)
YUKITAKE Mitsuteru 雪竹光輝 (Hitachi Ltd.)
ZENKEVITCH Pavel (ITEP, Russia)
GALSTER Wilfried (CNS, Univ. Tokyo)
HAMAGAKI Hideki 浜垣秀樹 (CNS, Univ. Tokyo)
HIRANO Midori 平野みどり (CNS, Univ. Tokyo)
KOHNO Kiyoji 河野清次 (CNS, Univ. Tokyo)
KUBONO Shigeru 久保野 茂 (CNS, Univ. Tokyo)
KUBOTA Shogo 久保田昌吾 (CNS, Univ. Tokyo)
MIYACHI Takashi 宮地 孝 (CNS, Univ. Tokyo)
NISHIMURA Shunji 西村俊二 (CNS, Univ. Tokyo)
NOTANI Masahiro 野谷将広 (CNS, Univ. Tokyo)
OHSHIRO Yukimitsu 大城幸光 (CNS, Univ. Tokyo)
OZAWA Kyoichiro 小沢恭一郎 (CNS, Univ. Tokyo)
SAKAGUCHI Takao 坂口貴男 (CNS, Univ. Tokyo)
SHIMOKOSHI Fumio 霜越文夫 (CNS, Univ. Tokyo)
SHIMOURA Susumu 下浦 享 (CNS, Univ. Tokyo)
TAKAKU Seisaku 高久清作 (CNS, Univ. Tokyo)
TANAKA Yoshito 田中義人 (CNS, Univ. Tokyo)
TERANISHI Takashi 寺西 高 (CNS, Univ. Tokyo)
UESAKA Meiko 上坂明子 (CNS, Univ. Tokyo)
WATANABE Shin-ichi 渡辺伸一 (CNS, Univ. Tokyo)
YAMAMOTO Yasushi 山本 泰 (CNS, Univ. Tokyo)
YAMAZAKI Norio 山崎則夫 (CNS, Univ. Tokyo)

Cellular and Molecular Biology Laboratory

Head

SHIBATA Takehiko　柴田武彦

Members

LING Feng　凌　　楓

Cellular Physiology Laboratory

Head

HANAOKA Fumio　花岡文雄

Members

YATAGAI Fumio　谷田貝文夫

Visiting Members

ANDO Koichi　安藤興一　(Natl. Inst. Radiol. Sci.)
FURUSAWA Yoshiya　古澤佳也　(Natl. Inst. Radiol. Sci.)
HAMA Yoshimasa　浜　義昌　(Sci. Eng. Res. Lab., Waseda Univ.)
HASE Yoshihiro　長谷純宏　(JAERI, Takasaki Rad. Chem. Res. Estab.)
HOSHINO Kazuo　星野一雄　(Natl. Inst. Radiol. Sci.)
ITO Hisao　伊東久夫　(Sch. Med., Chiba Univ.)
ITSUKAICHI Hiromi　五日市ひろみ　(Natl. Inst. Radiol. Sci.)
KANAI Tatsuaki　金井達明　(Natl. Inst. Radiol. Sci.)
KASAI Kiyomi　笠井清美　(Natl. Inst. Radiol. Sci.)
KAWACHI Kiyomitsu　河内清光　(Natl. Inst. Radiol. Sci.)
KOBAYASHI Yasuhiko　小林泰彦　(JAERI, Takasaki Rad. Chem. Res. Estab.)
MATSUFUJI Naruhiro　松藤成弘　(Natl. Inst. Radiol. Sci.)
MINOHARA Shinichi　簑原伸一　(Natl. Inst. Radiol. Sci.)
MURAKAMI Masahiro　村上正弘　(Natl. Inst. Radiol. Sci.)
SAITO Mizuho　斉藤瑞穂　(Natl. Inst. Radiol. Sci.)
SASAKI Hiroshi　佐々木　弘　(Fac. Med., Kyushu Univ.)
SHIKAZONO Naoya　鹿園直哉　(JAERI, Takasaki Rad. Chem. Res. Estab.)
SOGA Fuminori　曽我文宣　(Inst. Nucl. Study, Univ. Tokyo)
TANAKA Atsushi　田中　淳　(JAERI, Takasaki Rad. Chem. Res. Estab.)
TOMURA Hiromi　外村浩美　(Natl. Inst. Radiol. Sci.)
WATANABE Masami　渡辺正己　(Fac. Pharm., Nagasaki Univ.)
YAMASHITA Shoji　山下昌次　(Natl. Saitama Hospital)

Trainees

LI Ryonpha　李　玲華　(Natl. Inst. Radiol. Sci.)

Plant Functions Laboratory

Head

YOSHIDA Shigeo　吉田茂男

Members

ABE Tomoko　阿部知子
MATSUYAMA Tomoki　松山知樹
SAKAMOTO Koichi　阪本浩一

Visiting Members

FURUKAWA Koji　古川浩二　(Mukoyama Orchids Ltd.)
HAMATANI Misako　浜谷美佐子　(Hiroshima City Agric. Forest. Promot. Cen.)
HARA Yasuhide　原　靖英　(Kanagawa Inst. Agric. Sci.)
HASHIMOTO Takashi　橋本　隆　(Dept. Biosci., NAIST)
HONDA Ichiro　本多一郎　(Natl. Agric. Res. Cent., MAFF)

KITAURA Takeo　北浦健生　(Kanagawa Inst. Agric. Sci.)
MIYOSHI Kazumitsu　三吉一光　(Fac. Bioresource Sci., Akita Pref. Univ.)
SATO Fumihiko　佐藤文彦　(Dept. Agric. Chem., Kyoto Univ.)
SATO Shinobu　佐藤　忍　(Inst. Biol. Sci., Tsukuba Univ.)
SUZUKI Kenichi　鈴木賢一　(Suntory Ltd.)
TSUJIMOTO Hisashi　辻本　壽　(Kihara Biol. Res. Inst., Yokohama City Univ.)

Trainees
KOMOMI Yuki　許斐佑紀　(Fac. Sci. Tech., Sci. Univ. Tokyo)

Microbial Toxicology Laboratory
Head
YAMAGUCHI Isamu　山口　勇

Members
ARIE Tsutomu　有江　力
NOSE Yasuhiro　能勢泰寛
SOSHI Takayuki　曽雌隆行

CYCLOTRON CENTER
Chief Scientist
YANO Yasushige　矢野安重

RIBF Project Office
Head
YANO Yasushige　矢野安重

Members
DINH DANG Nguyen
INABE Naohito　稲辺尚人
KIM Ka-hae　金　佳恵
KOHAMA Akihisa　小濱洋央
KUBO Toshiyuki　久保敏幸
MADOKORO Hideki　間所秀樹
MIYASAKA Hiromasa　宮坂浩正
WAKASUGI Masanori　若杉昌徳
YAMAJI Shuhei　山路修平

Visiting Members
ANSARI Ahmad　(Inst. Phys., India)
ARAKAWA Kazuo　荒川和夫　(JAERI, Takasaki Rad. Chem. Res. Estab.)
ARIMA Akito　有馬朗人　(Former President, RIKEN)
BANDYOPADHYAY Arup　(Variable Energy Cycl. Cen., India)
BAO Jing-Dong　(Peking Normal Univ., China)
CHAKRABORTY Tapan　(Variable Energy Cycl. Cen., India)
CHATTOPADHYAY Subrata　(Variable Energy Cycl. Cen., India)
COLO Gianluca　(Univ. Milano, Italy)
EISENMAN Kaury　(Michigan State Univ., USA)
FUJINAWA Tadashi　藤縄　雅　(Mitsubishi Electric Co., Ltd.)
FUJISHIMA Shiro　藤島史郎　(I.H.I.)
FUKUDA Mitsuhiro　福田光宏　(JAERI, Takasaki Rad. Chem. Res. Estab.)
HIASA Toshikazu　日朝俊一　(Sumitomo Heavy Ind., Ltd.)
HIRUMACHI Tamiko　蛭町多美子　(Toshiba Corp.)
HONMA Toshihiro　本間寿広　(N.I.R.S.)
KAWAGUCHI Takeo　川口武男　(Mitsubishi Electric Co., Ltd.)
KIDO Syuuichi　木戸修一　(Hitachi Ltd.)
KOSSENKO Grigori　(Omsk State Univ., Russia)
KOZU Hideo　神津秀雄　(Toshiba Corp.)
KUNO Kazuo　久野和雄　(Mitsubishi Electric Co., Ltd.)
MASUNO Shin-ichi　益野真一　(Mitsubishi Electric Co., Ltd.)

MASUOKA Toshikatu 益岡俊勝 (Hitachi Zosen Corp.)
MATSUI Ju-Mei 松井重明 (Mitsubishi Electric Co., Ltd.)
MENG Jie (Peking Univ., China)
MIDORIKAWA Shouichi 緑川章一 (Fac. Eng., Aomori Univ.)
MIRONOV Vladmir (J.I.N.R., Dubna, Russia)
MITSUMOTO Toshinori 密本俊典 (Sumitomo Heavy Ind., Ltd.)
MORIKAWA Tetsuya 森川鐵也
MOTONAGA Shoushichi 元永昭七
NAKAZAWA Taro 中沢太郎
OHKAWA Tomohiro 大川智宏 (Mitsubishi Res. Inst. Inc.)
OHTOMO Kiyotaka 大友清隆 (Sumitomo Heavy Ind., Ltd.)
POLLEY Asis (Variable Energy Cycl. Cen., India)
SAKURAGI Hiroyuki 櫻木弘之 (Fac. Sci., Osaka City Univ.)
SEITZ Jeremy (Michigan State Univ., USA)
SEKINE Hirotaka 関根弘隆
SHEN Caiwan (Inst. Theor. Phys., China)
SIDORIN Anatoly (J.I.N.R., Dubna, Russia)
STOYANOV Chavdar (Sch. Bulg. Acad. Sci. Nucl. Phys., Bulgaria)
TANAKA Yasushi 田中保志 (Kyokuto Boeki Kaisha, Ltd.)
TEZUKA Hirokazu 手塚洋一 (Dept. Liberal Arts, Fac. Literature, Toyo Univ.)
THOENNESSEN Michael (Michigan State Univ., USA)
TOMINAKA Toshiharu 冨中利治 (Hitachi Ltd.)
UESAKA Tomohiro 上坂友洋 (Fac. Sci., Saitama Univ.)
VO Van Thuan (Inst. Nucl. Sci. Tech., Vietnam Atom. Ener., Vietnam)
ZHOU Shan-Gui (Peking Univ., China)

Trainees
ASANO Tomomasa 浅野大雅 (Fac. Sci., Konan Univ.)
ICHIKAWA Takatoshi 市川隆敏 (Fac. Sci., Konan Univ.)
OZAWA Shuichi 小澤修一 (Coll. Sci., Rikkyo Univ.)

Beam Dynamics Division

Head
GOTO Akira 後藤 彰

Members
FUKUNISHI Nobuhisa 福西暢尚
KAMIGAITO Osamu 上垣外修一
OHNISHI Jun-ichi 大西純一
OKUNO Hiroki 奥野広樹
SAKAMOTO Naruhiko 坂本成彦
SATOU Yoshiteru 佐藤義輝
SUZUKI Naoki 鈴木直毅

Visiting Members
CHAKRABARTI Alok (Variable Energy Cycl. Cen., India)
FUJISAWA Takashi 藤沢高志 (N.I.R.S.)
ITOH Yoshiko 伊東芳子 (Adv. Res. Inst. Sci. Eng., Waseda Univ.)
KIM Jaehong
OKAMURA Hiroyuki 岡村弘之 (Fac. Sci., Saitama Univ.)
SAITO Fuminori 斉藤文修
VOROJTSOV Serguei (J.I.N.R., Dubna, Russia)
WEI Long (I.H.E.P, China)

Trainees
KUMASAKA Hirokazu 熊坂弘一 (Fac. Sci., Saitama Univ.)
MORI Masahiro 森 雅広 (Fac. Sci., Saitama Univ.)
SAKODA Seitaro 迫田誠太郎 (Fac. Sci., Univ. Tokyo)
SATOMI Takehisa 里見竹永 (Fac. Sci., Saitama Univ.)

SEKIGUCHI Kimiko 関口仁子 (Dept. Phys., Sch. Sci., Univ. Tokyo)
SUZUKI Ryoko 鈴木涼子 (Fac. Sci., Saitama Univ.)
TAKI Reiko 瀧 玲子 (Fac. Sci., Saitama Univ.)

Liquid Helium Service Division

Head

YANO Yasushige 矢野安重

Members

IKEGAMI Kumio 池上九三男
OTAKE Masao 大竹政雄

Beam Technology Division

Head

KASE Masayuki 加瀬昌之

Members

AKIYOSHI Hiromichi 秋吉啓充
BHATTACHARJEE Sudeep
FUJIMAKI Masaki 藤巻正樹
FUJITA Jiro 藤田二郎
FUJITA Shin 藤田 新
IKEZAWA Eiji 池沢英二
ITO Sachiko 伊藤祥子
KAGEYAMA Tadashi 影山 正
KIDERA Masanori 木寺正憲
KIMURA Kazuie 木村一宇
KOHARA Shigeo 小原重夫
MASUDA Akiko 益田晶子
MORITA Kosuke 森田浩介
NAGASE Makoto 長瀬 誠
NAKAGAWA Takahide 中川孝秀
OGIWARA Kiyoshi 荻原 清
TANABE Toshiya 田辺敏也
USHIDA Kiminori 丑田公規
YONEDA Akira 米田 晃

Visiting Members

ABE Yasuhisa 阿部恭久 (Yukawa Inst. Theor. Phys., Kyoto Univ.)
ABURAYA Takashi 油谷崇志 (NASDA)
ALEXANDROV Vladmir (J.I.N.R., Dubna, Russia)
ANZAWA Osamu 安沢 修 (NASDA)
AOKI Jiro 青木司郎 (NASDA)
AOYAMA Kazuhiro 青山和広 (NASDA)
ARAI Nobuaki 荒井修亮 (Grad. Sch. Inf., Kyoto Univ.)
ARITOMO Yoshihiro 有友嘉浩 (J.I.N.R., Dubna, Russia)
BABA Shinji 馬場信次 (NASDA)
BANERJEE Vaishali (Variable Energy Cycl. Cen., India)
BHATTACHARYA Sudeb (Saha Inst. Nucl. Phys., India)
BHATTACHARYA Sankar (Variable Energy Cycl. Cen., India)
CHEVTSOV Vladmir (J.I.N.R., Dubna, Russia)
CHIBA Toshiya 千葉利哉
FUJIOKA Manabu 藤岡 学 (Cycl. Radioisot. Cen., Tohoku Univ.)
FUJIWARA Ichiro 藤原一郎 (Dept. Economy, Otemon Gakuin Univ.)
FURUSE Kaoru 古瀬 馨 (NASDA)
FUTAMI Yasuyuki 二見康之 (N.I.R.S.)
GOKA Tateo 五家建夫 (NASDA)
HARADA Toru 原田 融 (Fac. Soc. Inf., Sapporo Gakuin Univ.)
HASHIMOTO Osamu 橋本 治 (Fac. Sci., Tohoku Univ.)
HATANAKA Kichiji 畑中吉治 (RCNP, Osaka Univ.)
HATSUKAWA Yuichi 初川雄一 (JAERI, Tokai Res. Estab.)
HATTORI Toshiyuki 服部俊幸 (Res. Lab. Nucl. React., T.I.T.)
HAYANO Ryugo, S. 早野龍五 (Fac. Sci., Univ. Tokyo)
HEMMI Masatake 逸見政武
HIEDA Kohtaro 檜枝光太郎 (Coll. Sci., Rikkyo Univ.)

HIROSE Takayuki 広瀬孝幸 (NASDA)
HIROTA Teruo 廣田輝夫 (Yanagawa Engineering Co., Ltd.)
HONMA Michio 本間道雄 (Cen. Mathe. Sci., Univ. Aizu)
HORIBATA Takatoshi 堀端孝俊 (Fac. Eng., Aomori Univ.)
HORIUCHI Hisashi 堀内 昶 (Grad. Sch. Sci., Kyoto Univ.)
HYODO Toshio 兵頭俊夫 (Grad. Sch. Arts Sci., Univ. Tokyo)
ICHIMURA Munetake 市村宗武 (Fac. Comput. & Inf., Hosei Univ.)
IDESAWA Masanori 出澤正徳 (Univ. Electro-Commun.)
IIO Seiji 飯尾晴二 (Sumitomo Heavy Ind., Ltd.)
IKEDA Akitsu 池田秋津 (Shizuoka Inst. Sci. & Tech.)
IKEZOE Hiroshi 池添 博 (JAERI, Tokai Res. Estab.)
ISHIZUKA Takeo 石塚武男 (Fac. Sci., Saitama Univ.)
ITO Yasuo 伊藤泰男 (Atomic Energy Res. Cen., Univ. Tokyo)
ITOH Kazuya 伊藤和也 (Tandem Accel. Cen., Univ. Tsukuba)
IWAI Satoshi 岩井 敏 (Nuclear Development Co., Ltd.)
IWAMOTO Akira 岩本 昭 (JAERI, Tokai Res. Estab.)
IWATA Ren 岩田 錬 (Cycl. Radioisot. Cen., Tohoku Univ.)
JEONG S. C. (High Energy Accel. Res. Organization)
KAMIMURA Masayasu 上村正康 (Fac. Sci., Kyushu Univ.)
KANAMORI Takashi 金森 崇 (NASDA)
KATAYAMA Ichiro 片山一郎 (High Energy Accel. Res. Organization)
KATO Kiyoshi 加藤幾芳 (Fac. Sci., Hokkaido Univ.)
KATSURAGAWA Hidetsugu 桂川秀嗣 (Fac. Sci., Toho Univ.)
KAWAI Jyun 河合 潤 (Grad. Sch. Eng., Kyoto Univ.)
KAWAZU Akira 河津 璋 (Techno Riken Co., Ltd.)
KOBAYASHI Takao 小林高夫 (Sansho Setsubi Corp.)
KOMIYAMA Misaki 込山美咲
KUBOYAMA Satoshi 久保山智司 (NASDA)
KUDO Hisaaki 工藤久昭 (Fac. Sci., Niigata Univ.)
KUMADA Masayuki 熊田雅之 (N.I.R.S.)
KURIHARA Toshikazu 栗原俊一 (High Energy Accel. Res. Organization)
LEE San-mu 李 相茂 (Inst. Phys., Univ. Tsukuba)
LU Hongfeng (Peking Univ., China)
MAKIHARA Akiko 槙原亜紀子 (NASDA)
MATSUDA Sumio 松田純夫 (NASDA)
MATSUNAMI Noriaki 松波紀明 (Sch. Eng. Nagoya Univ.)
MATSUO Junko 松尾純子 (Yuuai Corp.)
MATSUSE Takehiro 松瀬丈浩 (Fac. Textile Sci. Tech., Shinshu Univ.)
MATSUYANAGI Kenichi 松柳研一 (Grad. Sch. Sci., Kyoto Univ.)
MATSUZAKI Masayuki 松崎昌之 (Fac. Ed., Fukuoka Univ. Ed.)
MECHTCHERIAKOV Nikolai (Inst. Theor. Eng. Phys., Russia)
MELIN Gerard (Service Ions, Atoms Agregate, CEA, France)
MINAMISONO Tadanori 南園忠則 (Grad. Sch. Sci., Osaka Univ.)
MIYATAKE Hiroari 宮武宇也 (High Energy Accel. Res. Organization)
MIYAZAWA Yoshitoshi 宮沢佳敏
MIZUSAKI Takahiro 水崎高浩 (Fac. Sci., Univ. Tokyo)
MURAKAMI Tetsuya 村上哲也 (Grad. Sch. Sci., Kyoto Univ.)
MUTA Atsushi 牟田 淳 (Inst. Phys., Univ. Tsukuba)
MUTO Kazuo 武藤一雄 (Fac. Sci., T.I.T.)
NAGAI Yuki 永井由紀 (NASDA)
NAGASHIMA Yasuyuki 長嶋泰之 (Grad. Sch. Arts Sci., Univ. Tokyo)
NAKADA Hitoshi 中田 仁 (Fac. Sci, Chiba Univ.)
NAKAMURA Takashi 中村尚司 (Cycl. Radioisot. Cen., Tohoku Univ.)
NAKAO Noriaki 中尾徳晶 (High Energy Accel. Res. Organization)
NEMOTO Norio 根本規生 (NASDA)
NOMURA Toru 野村 亨 (High Energy Accel. Res. Organization)
NOZAKI Tadashi 野崎 正 (Purex Co.)

OGANESSIAN Yuri (J.I.N.R., Dubna, Russia)
OGAWA Kengo 小川建吾 (Fac. Sci., Chiba Univ.)
OHIRA Hideharu 大平秀春 (NASDA)
OHTA Kiyoshi 太田 清 (Fac. Sci., Saitama Univ.)
OHTSUKI Tsutomu 大槻 勤 (Lab. Nucl. Sci., Tohoku Univ.)
OHYA Jiro 大矢次郎 (NASDA)
OHZONO Hironobu 大園浩之 (NASDA)
ONISHI Naoki 大西直毅 (Fac. Eng., Yamanashi Univ.)
OOI Makito 大井万紀人 (Dept. Phys., Sch. Sci., Univ. Tokyo)
OOTOMO Hiromitsu 大友洋光 (NASDA)
POPOV Anatoli (Univ. Latvia, Latvia)
SAGARA Kenshi 相良建至 (Fac. Sci., Kyushu Univ.)
SAKAI Hideyuki 酒井英行 (Dept. Phys., Sch. Sci., Univ. Tokyo)
SATO Ken-ichi 佐藤憲一 (Dept. Phys., Tohoku Coll. Pharm.)
SATO Osamu 佐藤 理 (Mitsubishi Res. Inst. Inc.)
SEKINE Toshiaki 関根俊明 (JAERI, Takasaki Rad. Chem. Res. Estab.)
SHIMADA Osamu 島田 修 (NASDA)
SHINDO Hiroyuki 新藤浩之 (NASDA)
SHINOZUKA Tsutomu 篠塚 勉 (Cycl. Radioisot. Cen., Tohoku Univ.)
SHIRKOV Grigori (J.I.N.R., Dubna, Russia)
SOMEKAWA Shuji 染河秀治 (NASDA)
SUEKI Keisuke 末木啓介 (Fac. Sci., Tokyo Metrop. Univ.)
SUGAI Isao 菅井 勲 (KEK)
SUGAWARA-TANABE Kazuko 田辺和子 (Otsuma Women's Coll.)
SUGIYAMA Hiroki 杉山大樹 (NASDA)
SUZUKI Masami 鈴木正美 (Irie Koken Co., Ltd.)
SUZUKI Toshio 鈴木俊夫 (Coll. Hum. Sci., Nihon Univ.)
TAGISHI Yoshihiro 田岸義宏 (Inst. Phys., Univ. Tsukuba)
TAJIMA Naoki 田嶋直樹 (Fac. Eng., Fukui Univ.)
TAKADA Norio 高田憲生 (NASDA)
TAKAGI Syunji 高木俊治 (Mitsubishi Res. Inst. Inc.)
TAKEMASA Tadashi 武政尹士 (Kyoto Univ. Edu.)
TAKIGAWA Noboru 滝川 昇 (Fac. Sci., Tohoku Univ.)
TANABE Kosai 田辺孝哉 (Fac. Sci., Saitama Univ.)
TANAKA Kazuhiro 田中和広 (Medical Dept., Juntendo Univ.)
TOHYAMA Mitsuru 遠山 満 (Kyorin Univ.)
TOMODA Toshiaki 友田敏章 (Fac. Eng., Aomori Univ.)
TOYOKAWA Hiroyuki 豊川弘之 (Electrotechnical Lab., Agency Ind. Sci. Tech.)
TSUBAKI Noriyuki 椿 則幸 (NASDA)
UEHARA Takashi 上原 丘 (Nuclear Development Co., Ltd.)
URITANI Akira 瓜谷 章 (Dept. Phys., Grad. Sch. Sci., Nagoya Univ.)
UTSUNOMIYA Hiroaki 宇都宮弘章 (Fac. Sci., Konan Univ.)
VUONG Kim-Au (Inst. Physics-Hanoi-Vietnam, Vietnam)
WADA Ryoichi 和田良一 (Texas A&M Univ., USA)
WADA Takahiro 和田隆宏 (Fac. Sci., Konan Univ.)
WAKAI Masamiti 若井正道 (Grad. Sch. Sci., Osaka Univ.)
YABANA Kazuhiro 矢花一浩 (Fac. Sci., Niigata Univ.)
YAMAKI Tsutomu 八巻 務
YAMAZAKI Hirohito 山崎寛仁 (Lab. Nucl. Sci., Tohoku Univ.)
YOKOYAMA Ichiro 横山一郎
YOSHIDA Nobuaki 吉田宣章 (Fac. Inf., Kansai Univ.)
YOSHINAGA Naotaka 吉永尚孝 (Fac. Sci., Saitama Univ.)
YOSHIOKA Yasuhiro 吉岡康弘 (NASDA)
ZHAO Yuliang (Fac. Sci., Tokyo Metrop. Univ.)
ZHAO Yu Min (South East Univ., China)

Trainees

FUJIMOTO Rintaro　藤本林太郎　(Dept. Phys., Sch. Sci., Univ. Tokyo)
HARUYAMA Seigo　春山征吾　(Dept. Phys., Sch. Sci., Univ. Tokyo)
HIGURASHI Yoshihide　日暮祥英　(Coll. Sci., Rikkyo Univ.)
IWASE Hiroshi　岩瀬　広　(Fac. Sci., Tohoku Univ.)
KOSHIMIZU Masanori　越水正典　(Dept. Eng., Grad. Sch. Eng., Univ. Tokyo)
KURITA Tetsuro　栗田哲郎　(Inst. Phys., Univ. Tsukuba)
MAKIHARA Yasuhiro　牧原康裕　(Dept. Phys., Grad. Sch. Sci., Nagoya Univ.)
NISHIKAWA Jun　西川　純　(Fac. Sci., Saitama Univ.)
NUNOMIYA Tomoya　布宮智也　(Fac. Sci., Tohoku Univ.)
SASAKI Michiya　佐々木道也　(Grad. Sch. Sci., Tohoku Univ.)
SATO Hisaki　佐藤寿樹　(Fac. Eng., Tohoku Univ.)
SHIOMI Tomoyuki　潮見大志　(Fac. Eng., Tohoku Univ.)
SUDA Kenji　須田健嗣　(Fac. Sci., Saitama Univ.)
TSURUTA Kaoru　鶴田　薫　(Interdisciplinary Grad. Sch. Eng. Sci., Kyushu Univ.)
UMEBAYASHI Tsutomu　梅林　励　(Dept. Eng., Grad. Sch. Eng., Univ. Tokyo)
YAGITA Takanori　八木田貴典　(Interdisciplinary Grad. Sch. Eng. Sci., Kyushu Univ.)
YAMAMOTO Sumiko　山本純子　(Fac. Sci., Toho Univ.)
YASHIMA Hiroshi　八島　浩　(Fac. Eng., Tohoku Univ.)

Radioisotope Technology Division

Head

YATAGAI Fumio　谷田貝文夫

Members

ENOMOTO Shuichi　榎本秀一
YANAGIYA Takahiro　柳谷隆宏
HIRUNUMA Rieko　蛭沼利江子
OZAKI Takuo　尾崎卓郎
TAMANO Haruna　玉野春南

Visiting Members

GORDON Alasdair
KAGAWA Yasuhiro　香川康浩　(Toray Res. Cen. Inc.)
KATO Takesi　加藤武司
KAWAMURA Yoshihiro　川村昌寛
MAEZAWA Hiroshi　前澤　博　(Fac. Med. Technol., Univ. Tokushima)
MORIMOTO Shigeko　森本茂子
OGURA Koichi　小倉紘一　(Coll. Ind. Technol., Nihon Univ.)
YANG Yongfeng　楊　永峰
AMANO Ryohei　天野良平　(Fac. Med., Kanazawa Univ.)
HIMENO Seiichiro　姫野誠一郎　(Sch. Pharm. Sci., Kitasato Univ.)
INAGE Hiroko　稲毛寛子　(Showa Women's Univ.)
MATSUMOTO Ken-ichiro　松本謙一郎　(Showa Pharmaceutical Univ.)
MINAI Yoshitaka　薬袋佳孝　(Cen. Art. Sci., Musashi Univ.)
MINAMI Takeshi　南　武志　(Dept. Living Sci., Kinki Univ., Toyooka Jr. Coll.)
NABEKURA Tomohiro　鍋倉智弘　(Fac. Pharm. Sci., Kinki Univ.)
NAKANISI Tomoko　中西友子　(Univ. Tokyo)
NAKANISHI Yukiko　中西由季子　(Showa Women's Univ.)
OGURA Yasunitsu　小椋康光　(Fac. Pharm. Sci., Chiba Univ.)
SAKURAI Hiromu　桜井　弘　(Kyoto Pharmaceutical Univ.)
SHIBATA Sadao　柴田貞夫　(Natl. Inst. Radiol. Sci.)
SHINOHARA Atsushi　篠原　厚　(Osaka Univ.)
SUZUKI Hiroyuki　鈴木弘行　(RI Res. Cen., Chiba Univ.)
SUZUKI Kazuo　鈴木和夫　(Fac. Pharm. Sci., Chiba Univ.)
TAGAMI Keiko　田上恵子　(Natl. Inst. Radiol. Sci.)
TAKAHASHI Masaaki　高橋正昭　(Coll. Agric., Osaka Pref. Univ.)
TAKAHASHI Yoshio　高橋嘉夫　(Fac. Sci., Hiroshima Univ.)

TAKEDA Atsushi 武田厚司 (Sch. Pharm. Sci., Shizuoka Univ.)
UCHIDA Shigeo 内田滋夫 (Natl. Inst. Radiol. Sci.)
YAMASAKI Mineo 山崎峰夫 (Nara Med. Univ.)
YANAGA Makoto 矢永誠人 (Fac. Sci., Shizuoka Univ.)
YASUI Hiroyuki 安井裕之 (Kyoto Pharmaceutical Univ.)

Trainees
INOUE Kensuke 井上憲介 (Fac. Sci. Eng., Waseda Univ.)
KITO Masatoshi 鬼頭昌利 (Fac. Sci. Eng., Waseda Univ.)
KUROBE Toshihiro 黒部利博 (Fac. Sci. Eng., Waseda Univ.)
OKA Toshitaka 岡 壽崇 (Fac. Sci. Eng., Waseda Univ.)
GOTO Sachiko 後藤佐智子 (Fac. Pharm. Sci., Nagasaki Univ.)
FUGONO Jun 畚野 純 (Kyoto Pharmaceutical Univ.)
FURUKAWA Jun 古川 純 (Univ. Tokyo)
IGARASHI Kaori 五十嵐香織 (Showa Women's Univ.)
KANAYAMA Yousuke 金山洋介 (Fac. Med., Kanazawa Univ.)
MAETSU Hitomi 前津仁美 (Fac. Sci., Shizuoka Univ.)
NAKAYAMA Akihiro 中山明弘 (Kyoto Pharmaceutical Univ.)
OHYAMA Takuya 大山拓也 (Fac. Sci., Shizuoka Univ.)
OIDA Takashi 笈田多加史 (Fac. Sci., Shizuoka Univ.)
SHIOBARA Yamato 塩原大和 (Fac. Pharm. Sci., Chiba Univ.)
TSUJI Takae 辻 孝枝 (Fac. Med., Kanazawa Univ.)
YOSHIDA Shozo 吉田昭三 (Nara Med. Univ.)
YOSHIDA Tsutomu 吉田 努 (Fac. Sci., Shizuoka Univ.)

ADVANCED ENGINEERING CENTER

Research Instruments Development Division

Head
SENOO Katsumi 妹尾克己

Members
IKEGAMI Yuji 池上祐司
NOMIYA Yoshio 野宮芳雄
SHIMODA Susumu 霜田 進
SUGAHARA Seigo 菅原正吾
URAI Teruo 浦井輝夫
YAMADA Shogo 山田正吾
KITSUNAI Tokuji 橘内徳司
SHIGA Tsunenobu 志賀常信
SHIRAISHI Akira 白石 明
TAJIMA Norio 田島典夫
WATANABE Tokuji 渡辺徳治
YAMADA Yutaka 山田 豊

Contracting Members
KANEKO Naoe 金子直恵
KUBO Ushizo 久保丑蔵
MATSUMOTO Akira 松本 昭
NIIOKA Yuzo 新岡勇三
SASAMOTO Tetsuji 笹本哲司
TAKAHASHI Kiyoji 高橋清二
TOKIWA Saburo 常盤三郎
YAMAMOTO Sumio 山本澄雄

Surface Characterization Division

Head
IWAKI Masaya 岩木正哉

Members
NAKAO Aiko 中尾愛子
WATANABE Kowashi 渡辺 剛

KOBAYASHI Tomohiro 小林知洋

ADVANCED COMPUTING CENTER

Computational Science Division

Head

EBISUZAKI Toshikazu 戎崎俊一

Members

IITAKA Toshiaki 飯高敏晃

Image Information Division

Head

SHIMIZU Hirohiko 清水裕彦

Members

OTANI Chiko 大谷知行
OKU Takayuki 奥 隆之
WATANABE Hiroshi 渡辺 博
KAWASAKI Yoshiya 川崎賀也
SATO Hiromi 佐藤広海
TAKIZAWA Yoshiyuki 滝澤慶之
MIYASAKA Hiromasa 宮坂浩正
ADACHI Tomohiro 安達智宏

Visiting Members

KURAKADO Masahiko 倉門雅彦
SAKAI Kenji 酒井健二

BIOGENIC RESOURCES CENTER

Experimental Animal Research Division

Head

KUSAKABE Moriaki 日下部守昭

Members

HIRAIWA Noriko 平岩典子
IKE Fumio 池 郁生
KOJIMA Masayo 小島雅代
YOSHIDA-NORO Chikako 野呂知加子
TSUKADA Teruyo 塚田晃代
YAMANOUCHI Jyun 山之内 淳
HUJIWARA Kyoko 藤原恭子
KOGISO Aya 小木曽 彩
KUBOTA Yukihiko 久保田幸彦
POIRIER Christophe
YAMAGUCHI Hirotake 山口弘毅
YOSHIKI Atsushi 吉木 淳

Visiting Members

YODA Yoshika 依田賀香 (Japan Sci. Technol. Corp.)

RIKEN BNL Research Center

Head

LEE Tsung-Dao*1
SAMIOS Nicholas P.*2

*1 Director, *2 Deputy Director

Experimental

Group Leader

ISHIHARA Masayasu 石原正泰

Deputy Group Leader
BUNCE Gerry M.

Members
BAZILEVSKY Alexander
ICHIHARA Takashi 市原 卓
SAITO Naohito 齊藤直人
KURITA Kazuyoshi 栗田和好
DESHPANDE Abhay
WATANABE Yasushi 渡邊 康
GOTO Yuji 後藤雄二
GROSS PERDEKAMP Matthias

Visiting Members
JACAK Barbara V.
KOBAYASHI Hideyuki 小林秀幸

Theory

Group Leader
LEE Tsung-Dao

Deputy Group Leader
BALTZ Anthony J.

Members
AOKI Yasumichi 青木保道
BOER Daniel
NARA Yasushi 奈良 寧
RISCHKE Dirk-Hermann
VOGELSANG Werner
BLUM Thomas C.
ITAKURA Kazunori 板倉数記
ORIGINOS Konstantinos N.
SCHAFFNER-BIELICH Jurgen

Visiting Members
BASS Steffen A. (Duke Univ., USA)
BODEKER Dietrich (Niels Bohr Inst., Denmark)
GYULASSY Miklos (Columbia Univ., USA)
JAFFE Robert L. (Massachusetts Inst. Technol., USA)
KUSENKO Alexander (Univ. California, Los Angels, USA)
MAWHINNEY Robert (Columbia Univ., USA)
OHTA Shigemi 太田滋生 (KEK)
SCHAEFER Thomas (State Univ. New York, Stony Brook, USA)
SHURYAK Edward V. (State Univ. New York, Stony Brook, USA)
SON Dam Thanh (Columbia Univ., USA)
STEPHANOV Mikhail A. (Univ. Illinois, Chicago, USA)
VENUGOPALAN Rajagopal
WETTIG Tilo (Yale Univ., USA)
van KOLCK Ubirajara (Arizona Univ., USA)

Administration
ESPOSITO Pamela
GREENBERG Rae
HEINZ Tammy Anne
ITO Taeko 伊藤妙子

Administrative Manager
NODA Toshihito 野田淑人

Deputy Administrative Manager
HORIE Hironori 堀江博憲

International Frontier Research Group on Earthquakes

Members

WATANABE Hiroshi　渡辺　博

Safety Center

Members

FUKAZAWA Kunio　深沢国雄
KAGAYA Satoru　加賀屋　悟
MIYAGAWA Makoto　宮川真言
SHINOHARA Shigemi　篠原茂己
YOSHIKI Hajime　吉識　肇
HARASAWA Kaoru　原沢　薫
KOBAYASHI Hiroshi　小林　博
SHIMAGAKI Masayuki　嶋垣正之
UWAMINO Yoshitomo　上蓑義朋

AUTHOR INDEX

RIKEN Accelerator Progress Report Vol. 34

理化学研究所加速器年次報告　第34巻（2001）

印　刷　平成13年（2001）3月21日
発　行　平成13年（2001）3月30日

発行者　理化学研究所
代表者　小林俊一
〒351-0198　埼玉県和光市広沢2番1号
電話（048）462－1111

編集者　理化学研究所加速器研究施設
運営委員会

印刷所　三美印刷株式会社
〒116-0013　東京都荒川区西日暮里5-9-8

定価5,000円
（消費税別）

理化学研究所

埼玉県　和光市　広沢